AD-A237 569

DTIC
ELECTE
JUN 28 1991

WRDC-TR-90-2065

HYDROGEN-FUELED SCRAMJET INVESTIGATION

W. T. Pescnke
T. J. Barber, L. Chiappetta
T. J. Anderson, W. J. Eckerle

United Technologies Research Center
Silver Lane
East Hartford, CT 06108

February 1991

Final Report for Period February 1987 – April 1990

APPROVED FOR PUBLIC RELEASE;
DISTRIBUTION IS UNLIMITED

Accession For
NTIS GRA&I ☑
DTIC TAB ☐
Unannounced ☐
Justification
By
Distribution/
Availability Codes
Dist | Avail and/or Special
A-1

91-03678

91 6 27 098

Aeropropulsion and Power Laboratory
Wright Research and Development Center
Air Force Systems Command
Wright-Patterson Air Force Base, Ohio 45433-6563

NOTICE

When Government drawings, specifications, or other data are used for any purpose other than in connection with a definitely Government-related procurement, the United States Government incurs no responsibility or any obligation whatsoever. The fact that the government may have formulated or in any way supplied the said drawings, specifications, or other data, is not to be regarded by implication, or otherwise in any manner construed, as licensing the holder, or any other person or corporation; or as conveying any rights or permission to manufacture, use, or sell any patented invention that may in any way be related thereto.

This report is releasable to the National Technical Information Service (NTIS). At NTIS, it will be available to the general public, including foreign nations.

This technical report has been reviewed and is approved for publication.

John R. Smith

JOHN R. SMITH
Program Manager
Propulsion Development Branch

William C. Burson Jr.

WILLIAM C. BURSON JR, Chief
Propulsion Development Branch
Advanced Propulsion Division

FOR THE COMMANDER

Paul D. Copp

PAUL D. COPP, LtCol, USAF
Deputy Director
Advanced Propulsion Division
Aero Propulsion & Power Directorate

If your address has changed, if you wish to be removed from our mailing list, or if the addressee is no longer employed by your organization please notify WRDC/POPR, WPAFB, OH 45433-6563 to help us maintain a current mailing list.

Copies of this report should not be returned unless return is required by security considerations, contractual obligations, or notice on a specific document.

UNCLASSIFIED

SECURITY CLASSIFICATION OF THIS PAGE

REPORT DOCUMENTATION PAGE

Form Approved OMB No. 0704-0188

1a. REPORT SECURITY CLASSIFICATION UNCLASSIFIED	1b. RESTRICTIVE MARKINGS
2a. SECURITY CLASSIFICATION AUTHORITY	3. DISTRIBUTION/AVAILABILITY OF REPORT Approved for public release; distribution is unlimited
2b. DECLASSIFICATION/DOWNGRADING SCHEDULE	
4. PERFORMING ORGANIZATION REPORT NUMBER(S) R90-957663-1	5. MONITORING ORGANIZATION REPORT NUMBER(S) WRDC-TR-90-2065
6a. NAME OF PERFORMING ORGANIZATION United Technologies Research Center 6b. OFFICE SYMBOL (If applicable)	7a. NAME OF MONITORING ORGANIZATION Wright Research and Development Center Aero Propulsion and Power Laboratory (WRDC/POPR)
6c. ADDRESS (City, State, and ZIP Code) Silver Lane East Hartford, CT 06108	7b. ADDRESS (City, State, and ZIP Code) Wright-Patterson Air Force Base, OH 45433-6563
8a. NAME OF FUNDING/SPONSORING ORGANIZATION 8b. OFFICE SYMBOL (If applicable)	9. PROCUREMENT INSTRUMENT IDENTIFICATION NUMBER F33615-86-C-2695
8c. ADDRESS (City, State, and ZIP Code)	10. SOURCE OF FUNDING NUMBERS PROGRAM ELEMENT NO. 62203F; PROJECT NO. 3012; TASK NO. 13; WORK UNIT ACCESSION NO 75

11. TITLE (include Security Classification)
Hydrogen-Fueled Scramjet Investigation

12. PERSONAL AUTHOR(S) W. T. Peschke, T.J. Barber, L. Chiappetta, T. J. Anderson, W.J. Eckerle

13a. TYPE OF REPORT	13b. TIME COVERED	14. DATE OF REPORT (Year, Month, Day)	15. PAGE COUNT
Final	FROM Feb 87 TO April 90	1991 February	558

16. SUPPLEMENTARY NOTATION

17. COSATI CODES			18. SUBJECT TERMS (Continue on reverse if necessary and identify by block number)
FIELD	GROUP	SUB-GROUP	Supersonic Mixing and Combustion, Hydrogen Computational Fluid Dynamics, Optical Diagnostics.

19. ABSTRACT (Continue on reverse if necessary and identify by block number)

This report documents an experimental and analytical study of the supersonic mixing and combustion processes associated with a free-shear layer. A specific objective of the program comprised quantifying the effects on the mixing and combustion processes of pressure gradients associated with the production of shock waves in the flowfield. An experiment was conducted in a generic supersonic combustion configuration that incorporated the essential characteristics of scramjet combustors currently being considered for flight application. The objective of the analytical effort was to evaluate mixing and combustion models in current state-of-the-art Computational Fluid Dynamics (CFD) codes.

The experiments provided accurate data used to formulate code input conditions and to evaluate codes that were formulated for application in current high-speed propulsion design activities. Species concentration, total and static temperature, and pitot pressure profiles were measured in a shearlayer experiment in which gaseous hydrogen was injected tangentially into a Mach 3 (nominal) vitiated airstream. In this experiment, hydrogen was

20. DISTRIBUTION/AVAILABILITY OF ABSTRACT ☒ UNCLASSIFIED/UNLIMITED ☐ SAME AS RPT. ☐ DTIC USERS	21. ABSTRACT SECURITY CLASSIFICATION UNCLASSIFIED
22a. NAME OF RESPONSIBLE INDIVIDUAL John R. Smith	22b. TELEPHONE (Include Area Code) 22c. OFFICE SYMBOL 513-255-52175 WRDC/POPR

DD Form 1473, JUN 86 Previous editions are obsolete. SECURITY CLASSIFICATION OF THIS PAGE

UNCLASSIFIED

19. ABSTRACT (Continued)

injected adjacent to the upperwall of the test section. A nonintrusive optical diagnostic technique was used in conjunction with intrusive probing to define the flowfield initial conditions and to characterize the detailed features of the flowfield subsequent to hydrogen injection and combustion. In addition to those conducted at the entrance of the test section, i.e., upstream of the hydrogen injection location, these surveys were performed at two axial stations corresponding to 50 and 100 boundary-layer momentum thicknesses (based on the test section entrance flow profiles) from the point of hydrogen injection.

Convective Mach numbers, calculated on the basis of the undisturbed test section entrance flow conditions, ranged from approximately 0.03 for low equivalence ratio injection into a low total temperature (1820 R) airstream to approximately 0.38 during high equivalence ratio tests in which the airstream total temperature was approximately 3720 R. The corresponding relative Mach numbers were 0.06 and 0.65. At a distance, x from the injection slot of 100 momentum thicknesses, Θ, the shear layer appeared to have assumed its characteristic asymptotic behavior. Under reacting conditions at the elevated temperature, the shear-layer growth rate, db/dx, at $x/\Theta = 100$ corresponded closely to the calculated rate for the experimental test condition employed. Similar measurements made during non-reacting mixing experiments did not compare as favorably with the results of the analysis. This is attributed, at least in part, to the fact that the hydrogen jet was generally underexpanded relative to the local static pressure of the airflow measured immediately upstream from the injection location.

As an adjunct to the study of non-reacting and reacting shear-layer mixing in a slowly varying static pressure field, the effect of inducing a more severe adverse pressure gradient in the flowfield was assessed. In making this assessment, both the shear-layer and mixing-layer growth rates were examined. (The mixing layer is defined herein as the distance between the test section upper wall and the shear-layer outer edge.) A shock wave was caused to intersect the shear-layer mixing region by strategically locating a 6-degree compression ramp in the supersonic flow. The effect of this shock interaction with the mixing layer on the mixing and combustion processes was measured using the aforementioned probing techniques.

At $x/\Theta = 100$, during combustion tests, the consequences of the shock wave-mixing layer interaction included an increase in the mixing layer growth rate of 35 percent based on pitot thickness and a displacement of the low-speed edge of the shear layer toward the airflow, although the shear-layer growth rate was unchanged with respect to the free shear-layer growth rate. Based on the limited quantity of data acquired, for essentially matched (when properly expanded) hydrogen and air velocities, occurring during the low-temperature non-reacting mixing tests, the shear-layer growth rates measured at $x/\Theta = 100$ and 50 both decreased relative to the free shear-layer rates as a consequence of the shock interaction.

Recommendations are made to further examine the separate effects of injection Mach number and injection pressure mismatch on the shear- and mixing-layer growth rates, since both supersonic combustor performance and film-cooling efficacy rely heavily on the understanding of mixing-layer behavior.

Comparisons are made between the data acquired at the two measuring stations and between the measured data and the computational results. The data that characterize the growth of the mixing region are compared with available semiempirical models as well as the CFD results. Combustion data are compared with the results of a cycle analysis and the CFD computations.

It was found that the level of agreement between the predicted and measured stagnation temperature and pitot pressure profiles at two axial locations in the flowfield was only fair. It was concluded that the computed results were sensitive to the distribution of grid nodes in the vertical (cross-stream) direction. It was also noted that large errors in the length scale determination (used in an algebraic model for the turbulent viscosity) could be produced by a poor or inadequate grid node distribution, but the use of a K-epsilon model is not faced with such limitations.

Computed axial wall static pressure distributions were not in good agreement with the measured data. It was noted that, for supersonic, internal flows in which two parallel streams of dissimilar gases mix, slight variations in flow properties and/or in initial conditions can significantly alter the wave pattern induced by the two-stream interaction. It is recommended that, owing to its greater flexibility when used in complex flow situations, the k-epsilon turbulence model be used in future efforts of this type.

SUMMARY

This report documents a research program that was conducted to acquire experimental data characterizing supersonic shear-layer mixing and combustion in a representative supersonic combustor configuration, and to use these data in comparisons with the results of computations employing selected Computational Fluid Dynamics (CFD) codes. A two-dimensional test apparatus measuring 3-in. high x 6-in. wide was employed that incorporated tangential slot injection of gaseous hydrogen into a supersonic vitiated airstream. The test apparatus used incorporated the following characteristics:

- Water-cooled side-, upper-, and lower-wall surfaces in which the coolant flowrates and bulk coolant inlet and outlet temperatures were each recorded. The lower duct wall comprised several separate cooled blocks, including mounting blocks for installation of intrusive instrumentation which could be installed at any axial location in the surface. Each sidewall incorporated three windows for optical access.

- An adjustable slot in a rearward-facing step in the upper wall through which gaseous hydrogen fuel or a gaseous nitrogen purge flow could be admitted. Although the current effort employed sonic injection, the upper wall included removable blocks that can be modified to permit supersonic injection of fuel.

- A constant flow cross-sectional area between the supersonic nozzle exit and the axial location at which the hydrogen was injected. The hydrogen injection slot height was 0.292 in. and the thickness of the water-cooled splitter plate was 0.08 in. Downstream from the injection location, the upper wall was angled at two degrees to compensate for boundary-layer growth. The test-section exit-to-entrance area ratio was thus approximately 1.32.

- Provision for installing a compression ramp on the lower surface so as to induce the occurrence of a shock that could interact with the free-shear layer mixing region.

Measurements of static temperatures and hydrogen and water vapor concentrations were made using Coherent Anti-Stokes Raman Spectroscopy (CARS). Total temperatures and pitot pressures were measured simultaneously using a Dual Sonic Orifice (DSO) probe. The data, comprising traverses of the CARS beams and the probe across the free shear-layer from the vitiated-airstream into the hydrogen layer, were acquired during non-reacting and combustion tests in which the gaseous hydrogen was introduced at flowrates corresponding to nominal equivalence ratios of 0.5 or 1.0. Wall static pressure distributions were recorded for the various steady-state conditions examined. Similar data were acquired for both the "constant-pressure " free shear-layer flowfield and for the case in which a shock wave was induced to interact with the mixing region by inserting a six-degree ramp in

the flowfield. Schlieren and shadowgraph flow visualization data and direct visualization of the mixing and combustion events were recorded on video tape.

Noteworthy results and conclusions from this investigation include the following:

The shear-layer growth rate determined through measurements of the pitot thickness during free shearlayer combustion experiments was approximately 0.05 at both low- and high-equivalence ratio hydrogen injection, as predicted by semiempirical analysis.

No significant change in that growth rate was detected to occur during further combustion experiments in which a shock wave was induced to interact with the shear-layer mixing region. The extent of the mixing region, defined as the region between the upper wall of the test section and the outer edge of the shear layer, did however increase significantly under the influence of the shock wave interaction.

Four computational fluid dynamics (CFD) codes were considered in the course of the study, comprising two NavierStokes (NS) and two Parabolized Navier-Stokes (PNS) treatments. Preliminary examination showed that both NS codes produced comparable results and that the PNS codes required further development before they could be used routinely to simulate flows of interest to the current study. Only one of the Navier-Stokes codes was available through U.S. Government sources. Thus, the computational effort was directed toward the use of this code, i.e., the SPARK code. Based on the results of this study involving these codes, the following observations were made:

In general, the level of agreement between the predicted and measured stagnation temperature and pitot pressure profiles at two axial locations was only fair. It was concluded that the computed results were sensitive to the distribution of grid nodes in the cross-stream direction.

Computed axial wall static pressure distributions were in poor agreement with the measured data. It was noted that, for supersonic internal flows in which two parallel streams of dissimilar gases are mixed, small variations in the flow properties and initial conditions can alter significantly the resulting wave pattern.

It is recommended that the data developed during this effort be used to examine whether suitable grids can be developed to improve the level of agreement between computed and experimental results. Owing to its greater flexibility in applications involving complex flows, the k-epsilon turbulence model should be used in future efforts of this type. Corrections for compressibility should be incorporated into this model.

PREFACE

This work reported herein was done for the United States Air Force Aero Propulsion and Power Laboratory under Contract F33615-86-C-2695. The Air Force Program Monitor was Mr. John Smith and the UTRC Program Manager and Principal Investigator was Mr. W. T. Peschke. Dr. T. J. Barber served as a co-principal investigator and managed the activities in CFD code evaluation. T. J. Anderson conducted the effort involving the acquisition of temperature and species data using Coherent Anti-Stokes Raman Spectroscopy (CARS). Mr. L. Chiappetta performed the CFD code evaluations and contributed heavily as well to the data reduction and presentation. Mr. R Elmquist developed the initial conditions for the CFD code evaluations. Dr. W. J. Eckerle, formerly of Clarkson University, formulated the Thermal Compression analysis. Dr. R. N. Guile served as a technical advisor, assisted in the preparation of reports, and initiated a number of useful discussions regarding the technical effort. Mr. I. W. Kay aided in the reduction of data acquired using the dualsonic orifice probe. Mr. R.P.C. Lehrach performed the cycle analyses for the combustion experiment. The successful design of the experimental apparatus was accomplished under a United Technologies capital improvement program by Mssrs. J. Flori and D. Bombara of the UTRC Design Group and the apparatus was fabricated in the UTRC Model Shop as part of the Corporate investment. Mr. J. McNamara conducted the operation of the facility during tests and Mr. P. Hamel assembled and restructured the experimental apparatus as required by the conditions established in the test matrix. Mr. Scott Boucher aided in the operation of the CARS apparatus. Mrs. J. S. Fournier coordinated and performed the computerized data reduction.

The authors appreciate the support of the United Technologies Research Center in providing the supersonic combustion test apparatus and in providing for the enhancement of the capability of the CARS optical diagnostic apparatus to enable the simultaneous acquisition of multiple-species data and the quantification of those data.

TABLE OF CONTENTS

	Page
SUMMARY	iii
PREFACE	v
INTRODUCTION	1
TASK 1: SUPERSONIC COMBUSTION EXPERIMENT	3
Experimental Apparatus	3
Instrumentation	4
Test Section and Facility	4
Traversing Probe	4
Traversing CARS	5
Experimental Procedures	5
Definition of Initial Conditions	5
Mixing and Combustion Experiments	7
Data Reduction Procedures	8
Experimental Results	11
Free Shear-Layer Tests	11
Pressure Gradient Tests	15
DISCUSSION OF EXPERIMENTAL RESULTS	18
Flowfield Structure	18
Shear- and Mixing-Layer Growth	18
Shear-Layer Growth Rate	18
Mixing Layer Growth Rates	20
Mixing Efficiency	22
Cycle Analysis	23

TABLE OF CONTENTS (concluded)

	Page
Task 2: EVALUATION OF CFD METHODS	**24**
Computer Codes	24
Selection of Cases	27
Data Available for Comparison to CFD Results	27
Model Assumptions	29
Boundary Conditions	29
Turbulence Models	30
Chemical Kinetics Models	31
Comparisons of Computed Results and Data	32
Reacting Flow Cases (AFS3A and AFS4A)	32
Mixing Cases (AFS5 and AFS6)	35
Shock Generator Cases (AFS7 and AFS8)	36
TASK 3: THERMAL COMPRESSION ANALYSIS	**38**
Wave Analysis	38
Example Problem	40
CONCLUDING REMARKS	**41**
RECOMMENDATIONS	**44**
LIST OF SYMBOLS	**45**
REFERENCES	**47**
TABLES	**51**
FIGURES	**64**
APPENDIX A - EXPERIMENTAL CONSIDERATIONS	A-1
APPENDIX B - CARS DATA ACQUISITION AND ANALYSIS	B-1
APPENDIX C - CALCULATION OF STAGNATION TEMPERATURES USING THE DSO PROBE TECHNIQUE	C-1
APPENDIX D - PLOTS OF EXPERIMENTAL DATA	D-1
APPENDIX E - THERMAL COMPRESSION ANALYSIS	E-1

TABLES

Table		Page
1.	Summary of Mixing and Combustion Tests	51
2	Nominal Flow Conditions for Mixing and Combustion Tests	54
3	Mixing Conditions	55
4	Shear-Layer Growth Rates	56
5	Summary of Mixing-Layer Growth Rates	57
6.	Summary Of Flow Simulations	58
7.	Flow Conditions For Reacting Flow Cases	59
8.	Flow Conditions For Mixing Cases	60
9.	Flow Conditions Shock Generator Cases	61
10.	Calculated Wave Structure For Free Shear-layer Combustion - using Thermal Compression Analysis	62
11.	Calculated Wave Structure For Shear-layer Combustion With Pressure Gradient - using Thermal Compression Analysis	63

FIGURES

Figure		Page
1	Test section geometric features and measuring station (axial) locations. Test section width = 6 in. window width W = 2 in., slot height HS = 0.292 in.	64
2	View through Station 1 window showing fuel injection slot. Flow from left to right.	65
3	Supersonic mixing and combustion experiment.	66
4	Hydrogen-fueled scramjet combustor instrumentation.	67
5	Double sonic orifice probe.	68
6	DSO probe installation.	69
7	Mobile CARS apparatus installed around test section.	70
8	Initial conditions for high temperature case: total temperature.	71
9	Initial conditions for high temperature case: pitot pressure.	72
10	Initial conditions for high temperature case: static pressure.	73
11	Initial conditions for high temperature case: Mach number.	74
12	Initial conditions for high temperature case: total pressure.	75
13	Initial conditions for high temperature case: static temperature.	76
14	Initial conditions for high temperature case: mass flux.	77
15	Shadowgraph Image of Hydrogen Injection at Equivalence Ratio of 1. Air Total Temperature = 1800 R.	78
16	Shadowgraph Image of Hydrogen Injection of Equivalence Ratio of 0.5 Air Total Temperature = 1800 R.	78
17	Pitot pressure profiles from probe measurements at Stations 2 and 3 during combustion tests at an equivalence ratio of 1. Free shear-layer.	79
18	Pitot pressure profiles from probe measurements at Stations 2 and 3 during combustion tests at an equivalence ratio of 0.5. Free shear-layer.	80

FIGURES (continued)

Figure		Page
19	Pitot pressure profiles from probe measurements at Stations 2 and 3 during non-reacting tests at an equivalence ratio of 1. Free shear-layer.	81
20	Pitot pressure profiles from probe measurements at Stations 2 and 3 during non-reacting tests at an equivalence ratio of 0.5. Free shear-layer.	82
21	Total temperature profiles from probe measurements at Stations 2 and 3 during combustion tests at an equivalence ratio of 1. Free shear-layer.	83
22	Total temperature profiles from probe measurements at Stations 2 and 3 during combustion tests at an equivalence ratio of 0.5. Free shear-layer.	84
23	Total temperature profiles from probe measurements at Stations 2 and 3 during non-reacting tests at an equivalence ratio of 1. Freeshear-layer.	85
24	Total temperature profiles from probe measurements at Stations 2 and 3 during non-reacting tests at an equivalence ratio of 0.5. Free shear-layer.	86
25	Nitrogen mole fraction profiles from CARS measurements at Stations 2 and 3 during combustion tests at an equivalence ratio of 1.0. Free shear-layer.	87
26	Static temperature profiles from CARS measurements at Stations 2 and 3 during combustion tests at an equivalence ratio of 1.0. Free shear-layer.	88
27	Static temperature profiles from CARS measurements at Station 3 during non-reacting tests at nominal equivalence ratios of 0.5 and 1. Free shear-layer.	89
28	Hydrogen profiles from CARS measurements at Stations 2 and 3 during combustion tests at an equivalence ratio of 1.0. Free shear-layer.	90
29	Hydrogen profiles from CARS measurements at Station 2 during non-reacting tests at nominal equivalence ratios of 0.5 and 1. Free shear-layer.	91

FIGURES (continued)

Figure		Page
30	Water vapor profiles from CARS measurements at Station 2 during combustion tests at nominal equivalence ratios of 0.5 and 1. Free shear-layer.	92
31	Water vapor profiles from CARS measurements at Stations 2 and 3 during combustion tests at an equivalence ratio of 1. Free shear-layer.	93
32	Pitot pressure profiles from probe measurements at Stations 2 and 3 during non-reacting tests at an equivalence ratio of 1.0. Shock interaction.	94
33	Pitot pressure profiles from probe measurements at Stations 2 and 3 during combustion tests at an equivalence ratio of 1.0. Shock interaction.	95
34	Total temperature profiles from probe measurements at Stations 2 and 3 during non-reacting tests at an equivalence ratio of 1.0. Shock interaction.	96
35	Total temperature profiles from probe measurements at Stations 2 and 3 during combustion tests at an equivalence ratio of 1.0. Shock interaction.	97
36	Static temperature profiles from CARS measurements at Stations 2 and 3 during combustion tests at an equivalence ratio of 1. Shock interaction.	98
37	Static temperature profiles from CARS measurements at Stations 2 and 3 during combustion tests at an equivalence ratio of 0.5. Shock interaction.	99
38	Hydrogen concentration profiles from CARS measurements at Stations 2 and 3 during non-reacting tests at an equivalence ratio of 1.0. Shock interaction.	100
39	Water vapor concentration profiles from CARS measurements at Stations 2 and 3 during combustion tests at an equivalence ratio of 0.5. Shock interaction.	101
40	Estimated test section flow field characteristics, free shear layer tests; $\bar{P} = P/P_{2j}$ (distance measured from nozzle exit).	102

FIGURES (continued)

Figure		Page
41	Estimated test section flowfield characteristics, pressure gradient tests; $\bar{P} = P/P_2$ (distance measured from nozzle exit).	103
42	Estimated flowfield characteristics near injection region; $\bar{P} = P/P_2$	104
43	Enlargement of a shadowgraph image depicting features of the fuel injector flow field for an equivalence ratio of 1. Low temperature flow condition.	105
44	Mixing layer nomenclature: F = Fuel, A = Air, ℓ = mixing-layer height, b = shear-layer thickness.	106
45	Shear-layer growth rate as a function of equivalence ratio for current test conditions.	107
46	Shear-layer growth rate variation relative to air stagnation temperature. Equivalence ratio = 1.	107
47	Definition of pitot thickness (a) ref. 32, (b) present investigation.	108
48	Example of pitot thickness measurement.	109
49	Relationships between shear-layer growth rates and jet Mach number for equivalence ratio of 1. Fuel jet stagnation temperature = 520 R.	110
50	Definition of mixing layer thickness based on total temperature (a) with combustion and (b) non-reacting.	111
51	Definition of mixing layer thickness based on hydrogen concentration.	112
52	Definition of mixing layer thickness based on static temperature.	112
53	Definition of mixing layer thickness based on water vapor mole fraction.	113
54	Estimated mixing efficiency for current experiment.	114
55	Duct geometry used for cycle calculations.	115
56	Results of cycle analyses of test configuration (a) Injected $\phi = 1$; (b) Injected $\phi = 0.5$. See Fig. 55 for subscript notation.	116
57	Calculated nozzle static pressure distribution.	117

FIGURES (continued)

Figure		Page
58	Comparison between computed and measured total temperature profiles.	117
59	Comparison between computed and measured pitot pressure profiles.	117
60	Comparison between computed and measured stagnation temperature profiles for $\phi = 1$ (case AFS3A).	118
61	Comparison between computed and measured pitot pressure profiles for $\phi = 1$ (case AFS3A).	119
62	Comparison between computed and measured wall static pressure distributions for $\phi = 1$ (case AFS3A).	120
63	Comparison between computed and measured stagnation temperature profiles for $\phi = 0.5$ (case AFS4A).	121
64	Comparison between computed and measured pitot pressure profiles for $\phi = 0.5$ (case AFS4A).	122
65	Comparison between computed and measured wall static pressure distributions for $\phi = 0.5$ (case AFS4A).	123
66	Comparison between computed and measured stagnation temperature profiles for $\phi = 1$ (case AFS3AR2).	124
67	Comparison between computed and measured stagnation temperature profiles for $\phi = 1$ (case AFS3AR5).	125
68	Comparison between computed static temperature and CARS measurement at Stations 2 and 3 during combustion test at an equivalence ratio of 1. Free shear-layer.	126
69	Comparison between computed hydrogen mass fraction and CARS measurement at Stations 2 and 3 during combustion test at an equivalence ratio of 1. Free shear-layer.	127
70	Comparison between computed water vapor mass fraction and CARS measurement at Stations 2 and 3 during combustion test at an equivalence ratio of 1. Free shear-layer.	128
71	Comparison between computed and measured stagnation temperature profiles for $\phi = 0.5$ (case AFS5).	129

FIGURES (continued)

Figure		Page
72	Comparison between computed and measured pitot pressure profiles for ϕ = 0.5 (case AFS5).	130
73	Comparison between computed and measured wall static pressure distributions for ϕ = 0.5 (case AFS5).	131
74	Comparison between computed and measured stagnation temperature profiles for ϕ = 1 (case AFS6).	132
75	Comparison between computed and measured pitot pressure profiles for ϕ = 1 (case AFS6).	133
76	Comparison between computed and measured wall static pressure distributions for ϕ = 1 (case AFS6).	134
77	Comparison between computed and measured stagnation temperature profiles for ϕ = 1 (case AFS6R2).	135
78	Comparison between computed and measured stagnation temperature profiles for ϕ = 1 (case AFS6R3).	136
79	Comparison between computed and measured static temperature at Station 3 during non-reacting test at an equivalence ratio of 0.5. Free shear-layer.	136
80	Comparison between computed and measured hydrogen mass fractions at Station 3 during non-reacting test at an equivalence ratio of 0.5. Free shear-layer.	138
81	Comparison between computed and measured water-vapor mass fractions at Station 3 during non-reacting test at an equivalence ratio of 0.5. Free shear-layer.	139
82	Comparison between computed and measured stagnation temperature profiles for ϕ = 1 (case AFS7).	140
83	Comparison between computed and measured pitot pressure profiles for ϕ = 1 (case AFS7).	141
84	Comparison between computed and measured stagnation temperature profiles for ϕ = 1 (case AFS8).	142
85	Comparison between computed and measured stagnation temperature profiles for ϕ = 1 (case AFS8R1).	143

FIGURES (concluded)

Figure		Page
86	Flowfield for example calculation.	144
87	Flow deflection due to combustion (Ref. 51).	145
88	Geometry for calculation in Ref. 51.	145
89	Calculated wave structure for free shear-layer combustion, thermal compression analysis, E.R. = 1, λ = 0.349.	146
90	Calculated wave structure for combustion with pressure gradient, thermal compression analysis, E.R. = 1, λ = 0.349, ramp angle = 4.8 deg.	147
B-1	Multiple species CARS spectrometer.	B-10
B-2	Stategy For H_2-air Supersonic Combustion.	B-11
B-3	H_2 Q-branch v = 0 population. Normalized to the population at 300 K.	B-12
B-4	Sample N_2 and H_2O spectra.	B-13
B-5	CARS measurement profiles of temperature and N_2, H_2, and H_2O mole fractions.	B-14
B-6	CFD comparisons (lines) with CARS data for sample runs. Triangles, circles from two similar tests.	B-15
C-1	Comparison between type 'K' thermocouple temperature and calculated test section entrance total temperature	C-10
C-2	DSO probe calibration.	C-11
D-1.	Test section wall static pressure taps (o) and thermocouples (•). W is the window location.	D-2

INTRODUCTION

Supersonic combustion engines received a great deal of attention 10–20 years ago through a number of Air Force sponsored programs which led to testing of hydrogen-fueled engines. Hydrogen-fueled supersonic combustion ramjets (scramjets) hold great promise for producing high propulsive efficiency for flight at hypersonic speeds. Applications of interest include interceptor missiles, advanced high-speed aircraft and an advanced aerospace vehicle which would provide ready access to space and/or rapid point-to-point global transportation.

During the period between circa 1960 and 1970, the United Aircraft Research Laboratories (now United Technologies Research Center) demonstrated a variable geometry scramjet (Refs. 1,2), the Marquardt Corporation tested a dual-mode scramjet (Refs. 3–5), the General Electric Co. worked on a variable-geometry component integration model (Ref.6),and General Applied Science Laboratories developed both research and flight-test module scramjet engines (Refs. 7–10). The Applied Physics Laboratory of the Johns Hopkins University also contributed heavily to the research activities in supersonic combustion and scramjet engines (Refs. 11–15) during this time, under support provided by the United States Navy. Also, during the period 1966 through 1975, the NASA Langley Research Center sponsored the development by the Garrett Air Research Corp. of a Hypersonic Research Engine (Refs. 16–19). More recently, NASA has been developing the technology for an airframe-integrated scramjet engine and has addressed a wide range of key areas including combustors, inlets, structures, advanced diagnostics and computational fluid dynamics (Refs. 20–26). Collectively, their activities have confirmed the feasibility of scramjet operation, helped identify the needs for further research and made significant advances towards developing the critical technologies associated with this engine cycle.

Considerable progress has been made towards the development of the hydrogen scramjet propulsion system and the outlook is promising for major strides to be made owing to advances in critical enabling technologies such as computational fluid dynamics, nonintrusive diagnostics and high-temperature materials. Nevertheless, the technical challenges to the development of scramjet engines are significant in core areas such as inlets, combustors, nozzles, structures, computational fluid dynamics, test facilities and in areas related to the propulsion system such as controls, engine/airframe integration, etc. Studies now underway will serve to quantify these challenges and establish prioritized plans for resolution of the issues involved. While significant effort will be required in all of the critical areas, the issues confronting development of efficient supersonic combustion are readily apparent. Moreover, the supersonic combustor impacts each of the other critical areas, to wit: inlet/combustor interactions have caused severe difficulties for scramjet engine developers, the combustor establishes the flow properties at the nozzle entrance and impacts the nozzle configuration, the combustor environment helps establish many of the more taxing requirements for materials and cooled structures, and the combustor is perhaps the most difficult component to model using

computational fluid dynamics. In view of this , UTRC structured this program to concentrate on the technology of the supersonic combustor.

While development activities are structured to mature those technologies critical to producing an effective propulsion system, research activities are more likely to effect an understanding of the fundamental nature of the supersonic combustion process and include the control of inlet-combustor interactions, the enhancement of combustion resulting from compression and oblique-shock wave interactions with supersonic diffusion flames, and the interrelationships between combustor geometry and spatial fuel-injection staging.

The objective of the experimental and analytical program was to help develop a rational approach to the analysis and design of hydrogen-fueled supersonic combustors. A specific objective of the program was to quantify the influence on the diffusive supersonic combustion process of compression/expansion waves present in supersonic combustor flows. These wave phenomena are indigenous to supersonic combustors due to 1) the nature of the flowfield delivered by the inlet, 2) fluid dynamic interaction between the combustor mainstream and the geometric features of the combustor, and 3) thermally-induced compression resulting from the volumetric expansion of hot gases produced by combustion.

The approach chosen to meet the stated objectives was to conduct a supersonic combustion experiment which was sufficiently generic so that the results would have broad application to this critical technology while retaining the features essential to representing the combustion process in realistic scramjet engines. The experiment was performed in the UTRC Supersonic Combustion Test Facility using a water-cooled research combustion tunnel. This tunnel embodies the essential features of a scramjet combustor and provides access for detailed measurement of the combustion process. Advanced laser diagnostics were employed to obtain combustor temperature and species distributions throughout this combustor. The combustion experiment was modeled using state-of-the-art Computational Fluid Dynamics (CFD) procedures.

The program reported herein was conducted in three tasks, Task 1, a Supersonic Combustion Experiment, Task 2, an Evaluation of CFD Methods, and Task 3, a Thermal Compression Analysis. All three tasks were performed simultaneously during the course of the program but will be discussed serially in this report. The Task 1 discussion comprises descriptions of (1) the apparatus used for the experiments, (2) the instrumentation, (3) experimental procedures, (4) data reduction procedures, and (5) the experimental results. Task 2 discusses (1) the selection of computer codes, (2) the selection of experimental cases for analysis, (3) the data available for CFD code comparisons, (4) model assumptions, and (5) comparisons between the computed results and the experimental data. Under Task 3, a brief discussion of the formulation of a simplified supersonic combustor analysis is presented. Following these reviews of the work performed within each task, a discussion of the program results and concluding remarks are provided.

TASK 1: SUPERSONIC COMBUSTION EXPERIMENT

EXPERIMENTAL APPARATUS

The experimental configuration consists of a two-dimensional, 6-inch wide x 3-inch high test section to which vitiated air was delivered at a nominal Mach number of 3 from a hydrogen-fueled air heater. The oxygen content of the vitiated air delivered to the test section was maintained at near-atmospheric concentration by burning the hydrogen in the heater with the oxygen required to do so. Nominal total temperatures of 2000 R or 4000 R were developed to provide a test section environment in which non-reacting mixing tests or combustion tests were performed. The test section entrance static pressure was typically approximately 6 psia. Mixing and combustion tests were conducted by injecting gaseous, room temperature hydrogen at sonic velocity through a slot in the base of a rearward-facing step spanning the 6-inch width of the test section. A schematic diagram showing pertinent geometric features of the test section is presented in Fig 1*. In the figure, the test section begins at the exit of the supersonic nozzle, designated as x = 0 in the figure. The fuel injection slot is situated at a distance of 13.56 inches from the nozzle exit. The first pair of windows, centered at a distance, x = 14.13 inches, provides for CARS data acquisition at a location immediately upstream from the injection slot. A photograph of the fuel injection slot seen through the first test section window is shown in Fig. 2. The second and third pairs of windows are centered at x = 19.25 and 24.33 inches, respectively. The overall test section length is 30 inches and the length available for mixing is 16.44 inches. For the tests reported herein, the height of the sonic hydrogen injection slot was 0.292 in. The water-cooled splitter separating the slot from the primary airstream was 0.08-in. thick and had a blunt trailing edge. Downstream from the injection slot, the upper wall was angled upward two degrees to compensate for boundary-layer growth. The test section exit-to-entrance geometric area ratio was 1.32.

The test section exit was connected via a circular exhaust duct to an air-driven ejector which served to maintain a sufficiently low backpressure to avoid separated flow in the test section. The ejector motive flow also served to reduce the concentration of unburned hydrogen passing from the test section to the exhaust system. To reduce the likelihood of the occurrence of a detonation of unburned hydrogen in the exhaust, six hydrogen-air torches, whose design is based on the details provided in Ref. 27, were situated at strategic locations in the duct and were ignited to burn continuously during the duration of a mixing or combustion test. Unburned hydrogen entering the duct thus was ignited and burned in a controlled manner. In addition to the above precautions, water was sprayed into the exhaust duct to cool the test gas at the test section exit.

A photograph of the water-cooled copper test section is provided in Fig. 3. The three window locations visible in the photograph correspond to the three measuring stations, at which static

* Figures are listed at the end of this report.

temperature and species data, using Coherent Anti-Stokes Raman Spectroscopy (CARS), and total temperature and pitot pressure data, using a water-cooled Dual Sonic Orifice probe were acquired. The 2-inch x 4-inch windows were film-cooled with nitrogen. Vertical surveys in the lateral plane of symmetry were conducted during both mixing and combustion tests, over a period of approximately 1.5 minutes. The total test duration was 2.5 minutes.

INSTRUMENTATION

Test Section and Facility—Test section wall static pressures were measured during the tests using high-speed digital pressure scanners. The pressure connections to the test section were routinely purged prior to each test to remove condensed water vapor. (A brief discussion describing this procedure and a number of other experimental challenges and procedures is provided in Appendix A.) The test section coolant flowrates and coolant temperature rise were also measured and recorded for each test. The hydrogen delivered to the slot fuel injector was metered using critical flow venturies. The hydrogen injection manifold pressure was also monitored and recorded to establish injection condition data.

A schematic diagram showing the overall facility and test apparatus instrumentation is provided in Figure 4. The flowrates of air, oxygen, and hydrogen to the vitiated air heater were also measured with critical-flow venturies. In addition to total pressure, the reactant total temperatures were measured using thermocouples installed near the venturi total pressure tap. Critical flow through the hydrogen and oxygen venturies was achieved by properly sizing these venturies to operate at the high pressures available, i.e., the gases were provided from trailers in which the gases were stored at approximately 140 atm. Thus, throat static pressures were not recorded for the oxygen or hydrogen venturies. A throat static pressure measurement was however, recorded for the flow through the air venturi. Redundant measurements of the air venturi total and throat pressures and the vitiated-air heater total pressure were made to avoid the loss of data in the event of a partial instrumentation failure. Heater, nozzle transition, and supersonic-nozzle water coolant flowrates and bulk coolant inlet and outlet temperatures were all recorded during each test.

Traversing Probe—Instream total temperatures and pitot pressures were measured using a traversing Dual Sonic Orifice (DSO) probe. A schematic diagram of the probe is provided in Fig. 5. The probe was water-cooled and capable of operating in gas streams with stagnation temperatures as high as 5500 R. To ensure that the water vapor in the gas being passed through the probe remains gaseous, a steam jacket encircles the gas path through the probe. In using the probe, the local stagnation temperature at the probe tip was calculated using the continuity equation for critical flow. The measured quantities are the pressure upstream of the choked tip-orifice, and the temperature and pressure upstream of a second critical-flow orifice located at some distance downstream of the tip-orifice. A vacuum pump provided a sufficiently low backpressure for the probe to ensure that critical flow was maintained through both orifices during use of the probe. A derivation of the

equations used to calculate a stream total temperature from the measured quantities is presented below in the section entitled "Data Reduction Procedures". The probe was traversed vertically in the lateral plane of symmetry of the test section at selected axial distances downstream from the fuel injection slot. The probe motion was governed by a stepping motor that received commands from a programmed controller. The positioning accuracy of the probe drive was better than 0.010 in. The probe tip-orifice diameter was 0.04 inch. On the basis of experimental results, a probe dwell time of 3 seconds per point was sufficient to yield satisfactory pressure and temperature data. A schematic diagram of the probe installation in the test section at a typical axial location is provided in Fig. 6. Generally, the probe could be traversed so as to provide data within 0.03 inch from the lower wall and 0.16 inch from the upper wall. A complete vertical traverse thus was approximately 3 inches in extent.

Traversing CARS—Instream static temperature and hydrogen and water vapor concentration data were obtained using a mobile CARS apparatus. The CARS system used, depicted in Fig. 7, was specifically designed and constructed to operate in typical large-scale experimental facilities. The transmitter and receiver were situated on either side of the test section and were mechanically linked by a bridge structure that straddled the test section. This bridge also supports the optics that transmit the laser beams into the test section through the windows and the CARS and laser beams out of the test section to the receiver. Finally, the lenses used to focus the laser beams to a measurement volume approximately 0.15 mm in diameter and 4 mm in length are mounted on the bridge. Thus, the CARS measurement point could be traversed vertically in the lateral plane of symmetry without moving the transmitter or receiver. This vertical translation was also driven by a stepper-motor and was controlled from a remote location.

In the experiments reported, three gaseous species were monitored to characterize the mixing and combustion processes occurring in the flowfield. Since nitrogen is a primary constituent in air-breathing combustion reactions and its CARS spectrum is well understood, it was selected as the constituent from which to acquire temperature data. Hydrogen and water vapor were also selected since they can provide indications of the levels of mixing and combustion achieved in the flow. Additional details regarding the CARS data acquisition and reduction strategy may be found in Appendix B.

EXPERIMENTAL PROCEDURES

Definition of Initial Conditions—Test section entrance flow surveys were conducted by traversing the DSO probe and the CARS beams vertically in the test section plane of symmetry. These data were acquired at the first measuring station, immediately upstream of the fuel injector splitter trailing edge (see Fig. 1). Pitot pressure and total and static temperature profiles were measured at this location for a range of vitiated-air heater total temperatures from 1800 R to 3900 R. The data provided a record of the variations in initial conditions corresponding to changes in the heater total temperature for an essentially constant heater total pressure. Total temperature and pitot pressure profiles

measured at the entrance of the test section during the development of vitiated-airflow at a heater total temperature of 3140 R are presented in Figs. 8 and 9, respectively. In all of the figures depicting data, Y is the vertical distance measured upward from the lower surface of the test section. The profiles indicate that the total temperature and pitot pressure are uniform to within approximately 3 and 6 percent, respectively for the central portion of the test section entrance flow. It was observed that the upper and lower wall test section entrance static pressure levels were nearly equal for these experiments. Furthermore, the pitot pressure profile data acquired at the test section entrance did not exhibit features that would suggest the presence of strong shock waves in the entrance flow. Thus, a linear static pressure distribution, as depicted in Figure 10, was assumed to exist at the test section entrance. Mach number, total pressure, static temperature, and mass flux profiles were computed using the static pressure data and are presented as Figs. 11 through 14, respectively. The computational procedure yields average Mach numbers of 2.85 and 2.75 for the low- and high-temperature cases, respectively. Calculated mass balances are typically within approximately 2 percent of the measured data. Similar test section entrance data were generated for each mixing or combustion test being evaluated using the CFD analyses. Test-to-test variations in heater conditions resulted in test section entrance conditions for mixing and combustion tests that varied somewhat from those for which detailed profiles were measured. To compensate for these variations, the detailed test section entrance profile levels were scaled according to the total temperature and pressure of the test under analysis. It was observed that the acquired test section entrance pitot pressure and total temperature profiles, irrespective of the heater exit total temperature level used, were similarly shaped. Test section entrance total temperatures varied essentially directly with changes in heater exit total temperature. Thus, to provide test section entrance profile data for experiments, i in which the heater exit conditions differed from those used in the baseline, bl tests, pitot pressure and total temperature profiles for CFD code application were derived through the use of the following ratios:

$$P_p(i) = P_p(bl) \times \frac{P_{htr}(i)}{P_{htr}(bl)} \tag{1}$$

and

$$T_t(i) = T_t(bl) \times \frac{T_{htr}(i)}{T_{htr}(bl)} \tag{2}$$

where P_p and T_t are the test section entrance pitot pressure and total temperature, respectively and P_{htr} and T_{htr} are the htr heater total pressure and total temperature, also respectively. Comparisons were made of the acquired pitot pressure and total temperature profiles for the baseline tests. These comparisons showed that differences between normalized levels of these parameters were not more than 5 percent of the normalizing value, i.e., heater total pressure or total temperature.

Mixing and Combustion Experiments—Hydrogen–air mixing and combustion experiments were performed by delivering vitiated air at nominal (ideal) total temperatures of 2000 and 4100 R, respectively to the test apparatus from the hydrogen fueled heater. A summary of the mixing and combustion experiments conducted is provided in Table 1* according to the experimental run number listed in the first column of the table. The next five columns refer to the heater operation, i.e. the heater total pressure, air, oxygen, and hydrogen weight flowrates, and the heater exit total temperature, respectively. The next four columns list levels of test section entrance total temperature, upper and lower wall static pressures, fuel (hydrogen) flow rate, and fuel–air equivalence ratio, based on a stoichiometric fuel–air ratio of 0.0295. The final column denotes the station at which DSO probe and CARS data were acquired during that test. The set of tests listed under "Initial Conditions", i.e., Runs 9 through 43, provided data that characterized the test section entrance conditions, i.e., flow profiles and wall static pressures, for several heater total pressure and total temperature levels. Initial tests in the experimental effort established that autoignition of the hydrogen would occur only at or above an ideal heater total temperature of 4100 R and that the use of a supplementary hydrogen/oxygen torch did not alter the combustion process. The nominal test section entrance flow conditions established for this elevated temperature level and the low temperature of approximately 2000 R, to be used during non–reacting mixing tests, are listed in Table 2. The vitiated–air heater exit total temperature was calculated from the measured heater pressure and the measured air, oxygen, and hydrogen flowrates delivered to the heater, according to the procedure outlined in the "Data Reduction Procedures". The test section entrance bulk gas total temperature was deduced by reducing the total temperature calculated at the heater exit to reflect the measured heat flux to the water coolant of the heater–to–nozzle transition, supersonic nozzle, and test section entrance duct, also in accordance with the procedure discussed in the "Data Reduction Procedures".

The tests in Table 1 under the heading "Free Shear–Layer Tests" i.e., Runs 44 through 101, comprised the bulk of the experimental effort. These mixing and combustion tests were performed by injecting gaseous, room temperature hydrogen tangentially through the injection slot at flowrates corresponding to nominal fuel–air equivalence ratios of 0.5 or 1.0. The objective of these experiments was to characterize the mixing process occurring in an essentially constant pressure flowfield by probing the flowfield at sites downstream from the injection station and in particular, in the vicinity of the shear layer. Optical (CARS) and probe (DSO) traverses were performed at each of the two axial locations of the windows, i.e., at Measuring Stations 2 and 3 in Fig. 1. The probe and CARS beams were traversed vertically, i.e., in the vertical plane of symmetry, normal to the test section airflow, from the lower surface to the upper surface, crossing the shear layer, at each of the measuring stations. These stations are located at distances of approximately 6 and 11 inches downstream of the fuel injection slot, respectively.

* Tables are listed at the end of this report.

The "Pressure Gradient Tests", Runs 102 through 128 in Table 1, consisted of mixing and combustion experiments in which a six-degree compression ramp was installed on the lower surface of the test section. The ramp served to induce the occurrence of a shock wave which was permitted to intersect the shear-layer mixing region in the vicinity of the second measuring station. Optical and probe traverses were performed at each of the two downstream measuring stations. Room temperature hydrogen was again injected at flowrates corresponding to equivalence ratios of approximately 0.5 and 1.0. The vitiated-air heater total temperature and pressure conditions used for the previous free shear-layer tests were again imposed to enable the acquisition of combustion and non-reacting mixing data.

DATA REDUCTION PROCEDURES

The general data reduction program utilizes input conversion factors to reduce the test data to engineering units. Conversion factors for strain-gauge-type instruments are determined through direct calibration, whereas standard tables of conversion factors for copper/constantan, chromel/alumel or any appropriate thermocouple combination are incorporated into the program. The program also includes several general equations which permit calculation of certain quantities. For example, the rates of flow of air, hydrogen, and replenishment oxygen delivered to the vitiated-air heater are metered using venturis. The program computes the flow rates of these fluids throughout a test with either of the following equations.

$$W = C_D A_{TH} P_T \Gamma \sqrt{\frac{g}{RT_T}} \qquad \text{(choked flow)} \qquad (3)$$

or

$$W = C_D A_{TH} P_{S_{TH}} \Gamma \sqrt{\frac{g}{RT_T}} \sqrt{\frac{2\gamma}{\gamma - 1}\left(\frac{P_T}{P_{S_{TH}}}\right)^{\frac{\gamma-1}{\gamma}} \left[\left(\frac{P_T}{P_{S_{TH}}}\right)^{\frac{\gamma-1}{\gamma}} - 1\right]}$$

$$\text{(unchoked flow)} \qquad (4)$$

The vitiated-air heater combustion efficiency was calculated as a temperature-rise combustion efficiency based on a measured air heater total pressure. That is, the heater combustion efficiency is

$$\eta_T = \frac{(T_{T_{act}})_c - T_{T_{ref}}}{T_{T_{id}} - T_{T_{ref}}} \qquad (5)$$

where $T_{T_{id}}$ is the ideal total temperature calculated using the UTRC thermochemcial equilibrium program for the measured air, hydrogen, and oxygen flowrates delivered to the heater and $T_{T_{ref}}$ is a reference temperature reflecting the initial enthalpy levels of the reactants. $(T_{T_{act}})_c$ is the experimentally determined heater exit total temperature corrected for heat transfer through the heater walls. The uncorrected value of this temperature is $T_{T_{act}}$, deduced from the measured total pressure, using the critical flow relationship expressed by Eq. (1). In Eq. (1), A_{TH} is the supersonic nozzle throat area, P_T is the measured heater total pressure, and $\dot{W}$ is the total flow rate through the heater, deduced from direct measurement of the heater reactant flow rates, i.e., air, hydrogen fuel, and replenishment oxygen.

Since the air heater was water-cooled, the measured temperature rise of the coolant was used to adjust the calculated heater exit total temperature, $T_{T_{act}}$. The corrected average heater exit temperature, $(T_{T_{act}})_c$, is thus defined as

$$(T_{T_{act}})_c = T_{T_{act}} + \frac{Q_p}{\bar{c}_p \dot{W}} \tag{6}$$

where Q_p is the rate of transfer of heat from the product gas to the heater-duct walls, $\bar{c}_p$ is the average specific heat of the heater exhaust products at temperature, $T_{T_{act}}$, and $\dot{W}$ is the heater gas flow rate. The measured bulk heater-coolant temperature rise, ΔT_c was used to calculate the heat transfer rate to the coolant,

$$Q_c = c_{pc} \dot{W}_c \Delta T_c \tag{7}$$

where c_{pc} is the water-coolant specific heat and $\dot{W}_c$ is the coolant flow rate. Under the assumption that $Q_c = Q_p$, the corrected heater exit temperature and thus, the heater combustion efficiency were calculated.

The measured coolant temperatures for the heater-to-nozzle transition, the supersonic nozzle, and the test section entrance duct were recorded for each test. These data, in conjunction with the coolant flowrates measured for these components, were used to calculate the heat transfer rates to the coolant. Again, assuming that the heat transferred to the coolant was solely from the vitiated air, the test section entrance total temperature was calculated using an equation of the form of Eq. (5).

The test section fuel/air ratio (f/a,) is defined as

$$f/a = \frac{W_F}{W_a + W_{O_2} + W_{HF}} \tag{8}$$

Similarly, the fuel-air equivalence ratio, act, is defined as

$$\phi_{act} = \frac{(f/a)_{act}}{(f/a)_{stoich}} \tag{9}$$

where $(f/a)_{act}$ is determined from Eq. (5) and $(f/a)_{stoich}$ is the stoichiometric fuel/air ratio for the given fuel, including the contribution of air heater fuel and make-up oxygen.

The Dual-Sonic Orifice (DSO) probe enables the calculation of stagnation temperatures at the probe tip which are above the range of available thermocouples. The probe contains two orifices, one of which is located at the probe tip, (see Fig. 5). By aspirating flow through the probe and choking the two orifices, an expression may be derived from the continuity equation which relates the stagnation temperature at the probe tip to the measured stagnation temperature and pressure at the downstream orifice and the measured pressure at the tip orifice. This expression, derived in Appendix C and shown below, uses the nomenclature presented in Fig. 5. Note that the subscripts refer to the upstream and downstream orifices within the probe and should not be misinterpreted as relating to the different probe stations in the test section.

The form of the equation used for total temperature determination is

$$T_{T_1} = K\left(\frac{P_{T_1}}{P_{T_2}}\right)^2 T_{T_2} \tag{10}$$

Calibration of the probe was accomplished by recording data with the probe in a stream of known stagnation temperature (T_{T_1}) and using a rearranged form of Eq. (8) to define a value of the probe coefficient,

$$K = \left(\frac{T_{T_1}}{T_{T_2}}\right)_{CAL} \left(\frac{P_{T_2}}{P_{T_1}}\right)^2_{CAL} \tag{11}$$

As stated above, a complete derivation of equations used when reducing the DSO probe data is presented in Appendix C, extracted from Ref. 28. The design of the particular DSO probes used during the current program (as shown in Fig. 5) provided for minimizing the effects of thermal expansion of the probe tip orifice by locating the tip cooling water passages within approximately 0.020 in. of the throat and also included an internal steam jacket around the main probe gas passage to ensure that gaseous flow conditions prevailed between the two orifices.

A dual Stokes approach was used to acquire CARS data for both the mixing and combustion experiments. Gas static temperature and gaseous species concentration data were extracted from the spectral shapes of the nitrogen and water vapor signatures captured on an optical multichannel detector. Hydrogen concentration was obtained from the spectrally integrated signal acquired on a photomultiplier tube appropriately normalized by a reference-cell hydrogen signal generated in the receiver. Details of the CARS apparatus, data acquisition strategy, and data analysis are included in Appendix B.

EXPERIMENTAL RESULTS

All of the measured profiles of total temperature and pitot pressure, and profiles of static temperature and nitrogen, hydrogen, and water vapor concentrations from the tests indicated in Table 1 are presented in Appendix D. These plotted data are provided in Sections 1 through 6, respectively of that appendix. The measured axial, centerline wall static pressure data acquired from the tests are contained in Section 7 of Appendix D.

In the present section, results from some of the experiments will be discussed.

Free Shear-Layer Tests—Videotape records of features of the test section flowfield were made through one of the accessible windows for several of the mixing and combustion experiments performed. Direct exposures provided observations of the combustion processes. Schlieren and shadowgraph techniques were also employed in attempts to acquire information regarding the flow structure developed during the injection of hydrogen into the airstream. Owing to the high temperatures imposed on the windows by the airflow, severe distortion of the glass was often encountered, particularly at the higher temperatures used to induce combustion. It was determined that the optical sensitivity associated with the use of a knife edge to yield schlieren images was too great and that the thermally induced distortion of the window resulted in useless exposures. Withdrawal of the knife edge, thereby reducing the sensitivity of the optical system to distortion, made the acquisition of acceptable images possible during tests in which the total temperature was on the order of 2000 R. Snadowgraph images reproduced from the videotape recording of the injection region, obtained during reacting hydrogen injection tests, are shown in Figs. 15 and 16. During these two exposures, the fuel-air equivalence ratios were 1.00 and 0.52, respectively. The total temperature of the vitiated air during both of these tests was approximately 1800 R. The flow was from left to right and the (thermal) boundary layer thickness on the wall approaching the 0.08-inch thick water-cooled splitter plate was

approximately 0.5 inch. (The thickness of the splitter plate was dictated by the need to water-cool this component.) The injectant Mach number during these tests was one. At an equivalence ratio of 0.5, the injectant exit static pressure is approximately 6.2 psia while the local wall static pressure is approximately 5 psia. Inasmuch as the equivalence ratios exceeded 0.5 in both of these low-temperature experiments, the flow was slightly underexpanded in each case. Note that the shear layer deflected slightly more toward the upper wall in the lower equivalence ratio case, Fig. 16. A shock wave and its reflection can be seen in the hydrogen injectant flowfield in both cases. It is postulated that an expansion fan, not seen in the photographs, propagates into the hydrogen flow from the splitter trailing edge. The shock wave seen in the figures propagating into the hydrogen is generated as a consequence of the recompression occurring at the downstream end of the recirculation zone formed in the wake of the splitter plate. In both exposures the splitter lip shock can be observed propagating into the freestream airflow. The angular streaks seen in both photographs are deposits of foreign material on the interior surface of the windows, remaining subsequent to the evaporation of condensate produced following a previous test. Attempts to acquire similar shadowgraph information during combustion tests conducted at the higher vitiated-air total temperature were less successful. Owing to the higher air static temperature, window heating was more severe, resulting in substantial distortion of the windows with consequent image degradation, a circumstance that does not impact CARS data characteristics.

Pitot Pressure Profiles—Pitot pressure profiles measured at the two stations during hydrogen combustion at an equivalence ratio of 1 are presented in Fig. 17. Similar data, acquired at an equivalence ratio of 0.5, are displayed in Fig. 18. Equivalent results for non-reacting mixing tests are presented in Figs. 19 and 20. The normalizing parameter, P_{t0} is the measured heater exit total pressure, PT0 in Table 1. The use of this parameter tends to reduce the variations in the data induced by run-to-run variations in heater conditions. The calculated value of the pitot pressure ratio for the supersonic nozzle exit conditions corresponding to these tests is approximately 0.33, in good agreement with the data acquired at a distance, Y of 1.5 inches from the lower surface of the test section in Figs. 17 and 18. The calculated pitot pressure ratios for the sonic hydrogen flow in these tests are approximately 0.12 and 0.06 for equivalence ratios of 1 and 0.5, respectively. The pressure ratios measured with the probe near the upper wall, i.e. within the hydrogen layer appear to correspond to these calculated values. Based on the vertical distance above the lower wall at Station 3 at which a sudden pitot pressure decrease is noted, the edge of the hydrogen mixing region is approximately 2.7 inches above the lower wall or approximately 1 inch below the upper wall for the combustion tests, according to the results shown in Figs. 17 and 18. The corresponding distances for the non-reacting tests, for which the data are shown in Figs. 19 and 20, are 2.4 and 1.3 inches.

Total Temperature Profiles—Representative total temperature profiles measured during the tests described above are presented in Figures 21 and 22 for the combustion tests and in Figs. 23 and 24 for the non-reacting tests. As the DSO probe was traversed from the lower wall (Y = 0) upward through

the mainstream airflow, the total temperature distribution was similar to the distribution measured at the test section entrance shown in Fig. 8. On entering the region of influence of the shear layer, as the probe approached a height, Y of approximately 3 inches above the test section floor, the total temperature continued to decrease and then rapidly rose and fell as the probe traversed the burning region and continued into the cooler, fuel-rich non-burning zone. Based on the height above the test section lower wall at which the total temperature begins to rise above the vitiated-airflow level, the burning edge of the mixing region at Station 3 is approximately 2.8 inches above the lower surface or approximately 0.94 inch below the upper wall, for both equivalence ratios.

Total temperature profiles measured at Stations 2 and 3 during non-reacting tests are exhibited in Figures 23 and 24 for equivalence ratios of 1 and 0.5, respectively. The calculated test section entrance total temperatures were approximately 1800 R for these experiments, yielding a test section entrance air static temperature less than 800 R, well below the accepted autoignition temperature of approximately 1800 R (at a pressure of one atmosphere). Thus, since no reaction appears to occur, the total temperature profiles do not show the temperature rise evident in the higher-temperature experiments. The gradient across the shear layer is essentially uniform, since the temperature variation is produced primarily by the mixing of the hot (vitiated air) and cold (hydrogen) streams.

Nitrogen Concentration Profiles—Static temperatures discussed in the next section were derived from measured nitrogen spectra in accordance with the procedure discussed in Appendix B. The number of data points comprising the profiles exhibited was related primarily to the test duration. At least six data points were generally acquired although during later tests, up to twelve points were obtained. The nitrogen mole fractions were obtained from a spectral fitting process that provided the most accurate concentration measurements at low concentration levels, e.g., less than ten percent. Thus, the data acquired within the non-reacting hydrogen layer exhibit the greatest accuracy. The nitrogen concentration measured nearest the upper test section wall, i.e., where the hydrogen concentration is a relative maximum, is therefore reported without adjustment as derived from the spectral fitting process. The nitrogen concentrations measured in the vitiated airflow were equated to the values calculated using the UTRC Thermochemical Equilibrium program, For each test, a linearized calibration factor was applied to each measured value acquired between the extremes of the vertical traverse.

Representative profiles of nitrogen mole fractions are presented in Figure 25 for tests in which the test section entrance total temperature was approximately 3700 R. Hydrogen was injected into the test section at flow rate corresponding to an equivalence ratio of approximately unity. The data acquired at Measuring Stations 2 and 3 are compared in this figure.

Static Temperature Profiles—Static temperature data consist of averaged temperatures based on approximately 120 laser shots per measurement location. The points in the flowfield that yield the least accurate results occur where the nitrogen concentration is a relative minimum, i.e., embedded in the

hydrogen mixing layer. Fluctuations in the static temperature data are attributable to the occurrence of two phenomena. The weak nitrogen nitrogen signals encountered at points within the hydrogen mixing layer lead to the development of low signal-to-noise ratios. In addition, actual temperature fluctuations that mark the turbulent character of the mixing process between the elevated-temperature vitiated air and the room-temperature hydrogen increase the standard deviation.

Static temperature profiles derived from CARS measurements are displayed in Figs. 26 and 27. In Fig. 26, a comparison is made between profiles acquired at Measuring Stations 2 and 3. Using the Thermochemical Equilibrium program, the calculated nozzle exit vitiatedair static temperature is approximately 1820 R. The test section entrance total temperature, calculated according to the method discussed in the "Data Reduction Procedures", and Mach number calculated using a cycle analysis were used to yield a static temperature of 1847 R. The static temperature of the vitiated-airstream according to the CARS measurements shown in Fig. 26 is on the order of 1600 R. Since the data in Fig. 26 were acquired downstream from the test section entrance and do not account for heat transferred beyond that location, the measured values do not appear to be inconsistent with the calculated vitiated-air temperatures. The high temperatures (greater than 900 R) in the hydrogen mixing layer can be attributed to the poor accuracy that characterizes this measurement technique in regions of low nitrogen concentration.

The static temperatures near the upper wall indicated by the data in Fig. 27 are nearer the levels one might anticipate to occur within the hydrogen layer. Since the room-temperature hydrogen is introduced at sonic velocity, the theoretical static temperature is 433 R which compares favorably with the lowest temperatures indicated in Fig. 27. Furthermore, the static temperatures indicated to occur at a distance of approximately 2.5 inches from the lower wall in Fig. 27 closely approximate a static temperature of 700 R that was estimated for this airflow, corresponding to the total temperature of approximately 1900 R calculated for these tests.

Hydrogen Concentration Profiles—Hydrogen concentrations were derived from the spectrally integrated intensity of the hydrogen CARS signal. Accuracy using this approach is independent of concentration. The mole fractions however, were determined using the calculated static temperature at each point. Calibration was accomplished by adopting a functional relationship between signal intensity and hydrogen density (see Appendix B). The slope of the relationship was anchored by the concentrations in (1) the vitiated-airstream, assuming that no hydrogen existed there, and (2) the point nearest the upper test section wall, within the region of maximum hydrogen concentration.

Profiles of hydrogen mole fractions are presented in Figs. 28 and 29. In Fig. 28, the measured hydrogen concentrations at Measuring Stations 2 and 3 are compared for an equivalence ratio of one. The test section entrance total temperature was approximately 3700 R. As one might anticipate, owing to combustion, the hydrogen mole fraction measured at the downstream location (Run 55) is somewhat less than that measured at the upstream site (Run 64). The difference may have been greater

if the injected hydrogen flowrates were identical, i.e., the hydrogen flowrates for Runs 55 and 64 were 0.17 and 0.15 lb./sec., respectively, corresponding to a 16 percent difference in equivalence ratio. A comparison is made in Fig. 29 of the hydrogen concentrations measured at Station 2 as a function of equivalence ratio variation. The test section entrance total temperature for these tests was approximately 1750 R. The data imply that the greater equivalence ratio (E.R. = 0.98) resulted in greater penetration of the hydrogen than that developed by the lower equivalence ratio, e.g. 2.4 inches from the lower wall for E.R. = 0.98 versus 2.6 inches for an equivalence ratio of 0.53.

Water Vapor Concentration Profiles—Water vapor mole fractions were determined using a method similar to that used for nitrogen determination. Owing to the relatively less-developed state of this capability, concentration values of water vapor are somewhat less accurate than those of the other two species. As is the case with nitrogen concentration, values of water vapor concentration are most accurate at low levels. This determination is also highly dependent on the accuracy of the static temperature measurement.

Representative profiles of water vapor mole fractions are presented in Figs. 30 and 31 for combustion tests in which the test section entrance total temperature was approximately 3750 R. The data displayed in Fig. 30 were acquired at Measuring Station 2 for equivalence rartios of 0.54 (Run 81) and 1.13 (Run 84). The data suggest that the maximum levels of water vapor produced in the tests are equal but the higher equivalence ratio results in the maximum level occurring at a greater distance from the upper test section wall. The data presented in Fig. 31, acquired for an equivalence ratio of 1.13, compare water vapor mole fractions measured at Stations 2 (Run 84) and 3 (Run 92). Owing to the greater distance from the injection site of Station 3, a greater quantity of water vapor is present at that location. Using the UTRC Thermochemical Equilibrium program, the vitiated-air water vapor mole fraction for the test condition used in these tests is approximately 0.27, corresponding to the levels detected at a distance of approximately 2.3 inches from the lower surface of the test section in both figures.

Pressure Gradient Tests—The experimental results to be discussed in this section were acquired during mixing and combustion tests performed with a six-degree compression ramp installed on the lower wall of the test section. The ramp was situated so as to generate a shock wave that would intersect the shear-layer mixing region in the vicinity of the second window (Measuring Station 2) during supersonic flow through the test section. The shock wave thus altered the vitiated-air flowfield and, it was believed, would measurably alter the mixing and combustion processes.

Pitot Pressure Profiles—Representative pitot pressure profiles measured during nonreacting and combustion tests are displayed in Figs. 32 and 33, respectively for hydrogen injection at an equivalence ratio of approximately 1. In these tests, the probe data traverse was initiated from a height of approximately 1.5 inches above the lower test section surface so as to increase the number of data points acquired during the traverse through the mixing layer. As noted in the free shear-layer test

description, the pitot pressure ratio near the upper wall, i.e. within the hydrogen fuel layer is approximately 0.1 for an equivalence ratio of one during combustion tests. Owing to the slightly greater airflow associated with the conduct of the non-reacting mixing tests, the higher hydrogen flowrate results in a fuel pitot pressure ratio of 0.15, comparable to the values measured in Fig. 32. The high pitot pressure ratios measured at Station 2 correspond to the region downstream from the intersection of the two shock waves induced by the interactions of the test section entrance airflow with the fuel layer along the upper wall and the six-degree ramp on the lower wall. The difference between the levels measured at Station 2 in Figs. 32 and 33, representing the influence on the pitot pressure of the combustion process, corresponds to a reduction of approximately 12 percent in the peak level. This compares with a similar reduction experienced without the compression ramp of approximately 11 percent, as indicated by the data in Figs. 17 and 19. The general increase in pitot pressure level appears to correspond to the changes in the upper surface static pressures. As a consequence of the induced compression, the upper wall static pressure in the vicinity of the DSO probe is increased approximately 60 percent during non-reacting tests and approximately 70 percent during combustion at an equivalence ratio of one. In both Figs. 32 and 33, the height above the lower test section wall at which the pitot pressure undergoes a rapid decrease at Station 2 is approximately 2.5 inches, roughly indicating the location of the outer boundary of the hydrogen layer. The abrupt decrease in pitot pressure at Station 2, approximately 1.8 inches from the lower duct surface, appears to correspond to the location of the expansion wave that propagates from the base of the compression ramp. This characteristic appears in all of the pitot pressure profiles recorded at Measuring Station 2 during the shock-interaction experiments.

Total Temperature Profiles—Total temperature profiles measured during the tests described above are presented in Figs. 34 and 35 for the non-reacting and combustion tests, respectively at a nominal equivalence ratio of 1. Close to the upper wall, the measured total temperature of the gas approaches the room temperature level at which the hydrogen was introduced (520 R). In the non-reacting results shown in Fig. 34, the measured total temperature begins to decrease markedly during the probe traverse at a distance of approximately 2.5 inches from the lower wall. At a distance of 3 inches from the lower wall, the total temperature measured at the downstream location is slightly greater than that at the upstream location, Station 2, indicating that more of the vitiated air has mixed with the hydrogen at this location. Figure 35 comprises similar data acquired in the presence of combustion. In the total temperature profile presented in Fig.35, a local temperature rise occurs at a distance of approximately 2.75 inches above the lower test section wall, or 0.81 inch below the upper wall. The measured temperature rise is not substantial although vigorous combustion was visually observed to occur during the performance of the experiment. A total temperature depression occurs at a distance of approximately 2 inches from the lower test section wall in each of the profiles acquired at Measuring Station 2.

During the performance of these tests, a small quantity of water was seen to accumulate on the lower test section wall immediately down-stream from the base of the six-degree ramp. The accumulation comprised condensation of the water in the vitiated-air. Direct observation through the window at Measuring Station 2 during airflow through the test section revealed that some quantity of the condensate was being entrained in the recirculation zone formed by the flow over the ramp base. It is likely that some of this water contributed to the cooling of the air flowing along the lower duct wall and may be responsible for the sudden decrease in air total temperature indicated in the profiles measured at Station 3. Abrupt decreases of this type were not evident in the total temperature profiles recorded during the free shear layer tests.

Static Temperature Profiles—The static temperature profiles in Fig. 36 correspond to the pitot pressure and total temperature profiles presented in Figs. 33 and 35. The CARS data were acquired simultaneously with the probe data at Measuring Station 2. Good agreement exists between the static temperature and total temperature profiles for Runs 121 and 126. The static temperature discrepancy between the two sets of data at the points measured in the vitiated airstream is unexplained at this time. The calculated vitiated-air static temperature for this experiment is between 1850 and 1930 R. This range reflects the differences between the measured upper and lower test section entrance wall static pressures, which yield a Mach number difference between the upper and lower surfaces. Similar profiles for an equivalence ratio of 0.5, measured at Stations 2 and 3 are displayed in Fig. 37. In the profile measured at Station 3 (Run 127), the static temperature rise occurring as a consequence of combustion is approximately 300 R.

Hydrogen Profiles—The hydrogen profile data presented in Fig. 38 correspond to the pitot pressure and total temperature data presented in Figs. 32 and 34 for an equivalence ratio of 1. In these non-reacting tests, the data acquired at Station 2 (Run 112) show the boundary of the hydrogen layer occurring at a distance of approximately 2.7 inches from the lower surface of the test section. This corresponds closely to the hydrogen layer boundary defined by the pitot pressure and total temperature profiles in the previous figures. As explained earlier, the hydrogen mole fraction calculation relies on the use of the measured static temperature. Since the static temperatures deduced to occur at Station 3 were significantly lower, than those measured at Station 2, the calculated hydrogen mole fractions are also lower.

Water Vapor Profiles—Representative water vapor profiles are shown in Fig. 39 for combustion tests in which the equivalence ratio was 0.5. The data were obtained at Measuring Stations 2 (Run 122) and 3 (Run 127). The vitiated-air water vapor mole fraction calculated for this test condition is 0.27. The level indicated by the profile data at Station 2 and approximately 2.7 inches from the lower wall corresponds to the increase due to hydrogen combustion.

DISCUSSION OF EXPERIMENTAL RESULTS

FLOWFIELD STRUCTURE

Numerical estimates of the test section flowfield characteristics were made for comparison with the measured data. These estimates were made using a simple one-dimensional wave analysis. The essential features of the flowfield associated with the free shear-layer experiments are shown in Fig. 40. The wave intersections and the static pressure ratios correspond closely with the results measured during the non-reacting tests. A similar estimate of the flowfield features characterizing the pressure-gradient experiments is depicted schematically in Fig. 41, which also yields pressure levels that correspond approximately with the wall static and pitot pressure levels measured during the non-reacting experiments. To develop this configuration, since the data show that the injected hydrogen is underexpanded, a three-degree compression of the vitiated-air flowfield was assumed to occur. An alternative flowfield configuration for the region in the vicinity of the fuel injection site is shown in Fig. 42. The underexpanded injectant flow leads to an injection pressure ratio with respect to the test section entrance wall static pressure of approximately 2.5 during non-reacting tests and approximately 1.5 during combustion tests. These ratios are halved during injection at an equivalence ratio of 0.5. In Fig. 42, the hydrogen is permitted to expand about the trailing edge of the 0.08-inch thick splitter. If the length of the recirculation region formed behind the splitter is assumed to be three times the splitter thickness, then the hydrogen flow may expand to an area ratio of approximately 1.14, leading to a flow Mach number of 1.44. The impact of these assumed flow characteristics on the mixing process will be discussed in the next section. Once this expansion has occurred, a compression of the hydrogen flow takes place in the manner observed in the shadowgraph photograph displayed as Fig. 43. Simultaneously, a compression of the expanded vitiated-air flow occurs as depicted in Fig. 42.

SHEAR- AND MIXING-LAYER GROWTH

Characteristics of the shear layer were estimated using the semi-empirical analyses based on the investigations by Papamoschou, Roshko, Dimotakis, et al (Refs. 29-32). Basic features of the mixing layer are depicted in Fig. 44 in which ℓ corresponds to the height of the hydrogen-air interface from the duct wall and b represents the width of the shear layer. The growth of the shear layer is defined as db/dx and, as described in the above references, is related to a convective Mach number that is defined in terms of the velocities and densities of the two fluids undergoing mixing. In each case, the stream with the greater velocity is defined as the primary stream (subscript 1) while the lower-velocity stream is the secondary stream (subscript 2). A summary of the calculated mixing parameters is presented in Table 3 for the non-reacting and combustion test conditions. Note that the convective Mach numbers, M_{c1} = 0.027 to 0.38, are low enough that compressibility effects are not dominant.

Shear-Layer Growth Rate—The shear-layer growth rate, db/dx was estimated for each of the test conditions as functions of the equivalence ratio, shown in Fig. 45. Note that since the vitiated-air

velocity (3705 ft/sec.) at the low temperature is not substantially different from the hydrogen injection velocity (3867 ft/sec.), the shear-layer growth is not great, i.e., db/dx = 0.005. In marked contrast, the calculated shear-layer growth for the high-temperature vitiated-air flow is approximately 10 times as great. Note that the growth rate may be expected to vary little as the equivalence ratio is varied.

The effect on the shear-layer growth of varying the test section entrance total temperature was assessed and the results of these calculations are shown in Fig. 46. Over a modest range of temperatures, e.g., 100 degR, the variation in growth rate is not more than approximately 10 percent. Thus, test-to-test variations in total temperature are not expected to play a significant role in varying measured growth rates.

The experimental determination of shear-layer growth rate was made using the measured pitot-pressure data. The method described by Papamoschou (Ref. 32) to define the pitot thickness is depicted schematically in Fig. 47 (a). Owing to the inability to acquire pitot pressure data extremely close to the test section upper surface, it was necessary to extrapolate the acquired data to apply the above criterion. The extrapolation led to the calculation of growth rates that were significantly greater than those estimated for the high total temperature and that varied widely from test-to-test for virtually identical test conditions, a circumstance likely induced by the extrapolation procedure. A modified definition was used in which the lower end of the pitot pressure, corresponding to the inner edge of the pitot thickness, was defined by the set-point value of the injection pitot pressure, as depicted schematically in Fig. 47(b). An example of an actual pitot thickness measurement for a current test is shown in Fig. 48.

The experimental shear-layer growth rates determined using these procedures from the pitot-pressure profiles are presented in Table 4. Data at each measuring station and for each test section entrance total temperature are provided. Note that, in general, the growth rate is essentially invariant with equivalence ratio changes, as predicted. The high-temperature levels measured at Station 3 exceed the low temperature growth rates, although clearly not to the extent predicted by the calculated results presented in Fig. 45. In fact, the growth rates deduced using the pitot thickness measurements, for the nonreacting tests, are not markedly different from the growth rates deduced from the combustion test data, at either Measuring Station.

Shear-layer growth rate was calculated as a function of (injection) jet Mach number for the two test conditions. The results are presented in Fig. 49. Owing to the "primary stream" definition discussed previously, one may expect to see an inverse relationship between jet Mach number and growth rate for the elevated-temperature test condition and a direct relationship for the non-reacting situation. In the light of the previous discussion regarding the jet-to-airstream pressure ratios for the two test conditions, it seems likely that the high growth rates for the low-temperature cases are a consequence of the jet underexpansion associated with these tests. If the jet is permitted to expand, while bounded by the duct wall and the splitter trailing edge recirculation zone, to an area ratio that is

approximately 14 percent greater than the exit of the fuel injection slot, the jet flow will accelerate to a Mach number of approximately 1.4, as depicted in Fig. 42, discussed earlier. Based on this Mach number, a shear layer growth rate $db/dx = 0.053$ corresponding approximately to the level measured at Station 3 during the non-reacting free-shear layer tests would be anticipated. Indeed, examination of the wall static pressure data for these tests suggests that expansion to a Mach number approaching 2 occurs during the non-reacting tests at an equivalence ratio of 1. During tests in which combustion occurred, the injection Mach number attained is approximately 1.2 on the basis of wall static pressure data.

The shear-layer growth rates determined to exist at Measuring Station 2 are 20 to 50 percent greater than those measured at Station 3. In a recent publication (Ref. 34), Dimotakis cites suggestions by P. Bradshaw that several hundred momentum thicknesses are required for the shear layer to assume its observed asymptotic behavior. The CFD calculations performed during the current effort provided an estimate of the momentum thickness of 0.12 in. for the test section entrance airflow. Thus, according to this reasoning, Station 2, situated at approximately 50 momentum thicknesses is not far enough downstream from the splitter plate to attain the predicted linear growth rate. Station 3, on the other hand, situated at approximate 100 momentum thicknesses appears to be sufficiently distant from the injection site to attain asymptotic behavior.

The effect of the single-shock interaction with the mixing layer, produced in the pressure-gradient tests, appears to reduce the growth rates approximately 12 percent at Measuring Station 2, as evidenced by the data in Table 4. The shear-layer growth rates measured during the high-temperature mixing tests at Station 3 appear to remain unchanged under the influence of the shock interaction. During the nonreacting experiments, however, the growth rates decrease by approximately one-third at Station 3 as a consequence of the shock interaction with the mixing layer.

Mixing Layer Growth Rates—The depth of the mixing layer was defined as the region between the upper wall of the test section and the lower edge of the shear layer in the current experiment. The depth, ℓ was determined by measuring the vertical distance between the wall and the outer edge of the shear layer. The mixing region outer edge was, in turn, defined in each of several ways, depending on which of the measured parameters was used for the determination. For the pitot pressure, the lower edge of the pitot thickness, defined previously in Fig. 47 as the point in the profile equal to 95 percent of the local freestream pitot pressure, was used. To use the total temperature profile, the point in the total temperature profile where the temperature began to rise as a consequence of combustion, e.g. as in Fig. 50(a), or the "95- percent point" relative to the local maximum value as in Fig. 50(b) were selected. To base the mixing layer thickness on the hydrogen measurement, the point at which hydrogen was first detected by the CARS measurement, as in Fig.51, was used. The relative-maximum static temperature as shown in Fig. 52 and the location at which a water vapor level exceeding the freestream level was detected by the CARS apparatus, during combustion tests, as depicted in Fig. 53 were also used to

define the mixing layer thickness. The mixing-layer growth rate, $d\ell/dx$ was defined as the quotient of the mixing layer thickness, ℓ and the distance, x from the fuel injection location.

A summary of the data derived, using these definitions for the mixing-layer growth rate, is provided in Table 5. It is interesting to note that the mixing-layer growth rate measured at Station 2, based on pitot pressure measurements is essentially constant for all of the test conditions examined.

The following observations regarding the behavior of the shearand mixing-layers during non-reacting mixing experiments are made on the basis of the pitot pressure data presented in Tables 4 and 5:

- For the limited data acquired, when the hydrogen and vitiated-air velocities were nearly equal (the low-temperature case), the shear-layer thickness at both x/Θ = 50 and 100 diminished subsequent to the shock wave interaction with the mixing layer. The decrease in the shear-layer growth rate was approximately 35 percent at the downstream location and approximately 20 percent at x/Θ = 50, relative to the rates measured without the shock interaction.

- The mixing layer growth rate decreased approximately half the above amount, viz., 18 percent at x/Θ = 100 but did not vary measurably at the closer distance from the injection location.

- The distance between the upper surface of the test section and the inner edge of the shear layer, i.e., that edge nearest the upper surface, did not change at x/Θ = 100 as the shock wave intersected the mixing layer. At x/Θ = 50, however, the inner edge of the shear layer was displaced away from the upper surface 1.2 times its "no-shock" distance.

Observations regarding the behavior of the shear- and mixing-layers based on the results in Tables 4 and 5, made during the performance of the elevated-temperature combustion experiments comprise the following:

- At the axial location, x/Θ = 100, the shear-layer growth rate measured during the interaction of the shock wave with the mixing layer was equal to the "no-shock" growth rate. At the lesser distance, x/Θ = 50, the shock interaction caused a shear-layer growth rate decrease of approximately 15 percent relative to the free shear-layer growth.

- The depth of the mixing layer increased at both axial locations, exhibiting an increase of 35 percent at x/Θ = 100, but only approximately 6 percent at x/Θ = 50 as a consequence of the shock interaction.

- The distance between the upper surface and the inner (low-speed) shear-layer edge increased due to the shock interaction. At x/Θ = 100, the increase was substantial, viz., 80 percent, while at x/Θ = 50, the increase was approximately 35 percent.

The apparent reversal in the shear-layer and mixing-layer growth rates relative to the "no-shock" condition occurring as a consequence of the shock interaction with the mixing layer may be attributed to the reversal in roles of the vitiated-air and hydrogen flows as primary and secondary flows. During the non-reacting tests, the hydrogen flow had the higher velocity. On the other hand, the vitiated air flow velocity was greater than the hydrogen flow velocity during the combustion tests.

Thus, the shear-layer growth rates measured during the high-temperature experiments agree closely with the calculations performed assuming sonic injection. On the other hand, an injection Mach number approaching approximately 1.5 must be assumed to correlate the non-reacting shear-layer growth rates with the predicted rates for the free-shear layer experiments.

The total temperature, hydrogen and water vapor concentration, and static temperature profiles were all examined as described above to yield mixing-layer growth estimates. Compared with the mixing-layer growth rate deduced from pitot pressure measurements, the growth rate derived from total temperature profiles was roughly equivalent only for the non-reacting experiments.

MIXING EFFICIENCY

An estimate was made of the degree of mixing that could be anticipated to occur between the hydrogen and the air in the current experiment. The estimate was based on a modification of an equation developed by Anderson and Rogers(Ref. 33), for multiple-orifice injection. The expression, modified to include the effect on mixing of injection of hydrogen at various angles with respect to the airflow, is

$$\eta_m = (\sin\alpha)\left[1.01 + 0.176\ln\left(\frac{xe^{(1.72(1-\phi))}}{40h}\right)\right] + (1-\sin\alpha)\left(\frac{xe^{(1.72(1-\phi))}}{40h}\right) \tag{12}$$

where h is one-half the height of the combustion test apparatus, α is the injection angle, and complete mixing is assumed to occur in a combustor length that is 40 times the height of the combustor. The estimated mixing efficiency for the current test apparatus as a function of equivalence ratio, ϕ is shown in Fig. 49. Since the length-to-height ratio of the current combustion test apparatus is only 5.48, limited levels of mixing and combustion were expected to occur during the current experiments. Indeed, on the basis of the experimental data acquired, this appeared to be the case.

CYCLE ANALYSIS

Cycle analyses of the current test apparatus were performed using the UTRC RASCAL cycle analysis code written by R. P. C. Lehrach of UTRC. The analyses comprised determinations of the pressure and temperature increases and Mach number decreases that would accompany combustion of the hydrogen in the test section. The duct geometry used for the calculations is depicted in the schematic diagram in Fig. 55. The analysis results, presented in Fig. 56, represent two cases of interest to the experimental effort. In Fig. 56(a), the results of burning of various fractions of the quantity of room-temperature hydrogen introduced at an equivalence ratio of one are presented. In Fig. 56(b), similar results are presented for injection at an equivalence ratio of 0.5.

The experimental pressure rises measured during the elevated-temperature free shear-layer tests when hydrogen was introduced at an equivalence ratio of one were approximately 1.5 to 1.8 times the test section entrance wall static pressure. According to Fig. 56(a), combustion of no more than 30 percent of the injected hydrogen could have occurred under these circumstances. These low levels of combustion are consistent with the predictions of mixing efficiency presented earlier. This level of combustion would induce an average total temperature rise of approximately 6 percent to occur relative to the test section total temperature. Locally one could expect to measure greater temperature rises. Examination of the DSO probe temperature profiles indicates that local total temperature increases of from 250 to 500 degrees were measured, equivalent to 6 to 12 percent of the test section entrance total temperature. It is possible that the probe provided some catalysis of the combustion. Alternatively, the difference observed between the measured and predicted levels falls within the limits of accuracy of the DSO probe measurement.

The points above the lower wall of the test section at which the measured total temperature began to rise during combustion tests coincided with the points at which the measured water vapor concentration began to exceed the freestream level. At this location also, in several of the experiments, the static temperature detected by the CARS technique showed an increase relative to the freestream and mixing-layer levels.

TASK 2: EVALUATION OF CFD METHODS

The data acquired during the experimental program in this investigation were used to evaluate existing computational fluid dynamics (CFD) analyses for supersonic combustor flowfields. The results of this evaluation are described in the present section. The discussion begins with a brief review of the computer codes available. A description then follows of the experimental conditions used to construct evaluation cases, the types of data available from the experiments, and the assumptions used in the analyses of the data. Subsequently, comparisons are presented between computed and measured flow results.

COMPUTER CODES

The approach to conducting this research was to utilize supersonic combustor flowfield analyses already being developed and considered for application in other programs. The present effort did not include a code development task; rather, the emphasis was on selecting and evaluating existing codes for the analysis of mixing-dominated flows with and without combustion.

The experimental test section to be modelled with the codes was designed to provide essentially two-dimensional flow except, of course, in the vicinity of the sidewalls. Fuel was injected through a slot and parallel to the principal flow direction; flow recirculation was expected to be confined to the region immediately downstream of the splitter plate separating the fuel and air streams. The available static pressure data and schlieren photographs indicate that both conditions were satisfied.

The design of this research combustor had two important consequences with respect to the selection of CFD codes for evaluation. First, it was possible to use two-dimensional (2D) flow analyses, which at the time of this study were developed to a greater extent than three-dimensional (3D) flow codes; also, 2D codes are considerably more economical to operate than 3D codes. Second, except as noted above, the flow is essentially axial so that "parabolized" Navier-Stokes (PNS) methods can be used. Two Navier-Stokes and two PNS codes were considered for use in this program. However, it was found that neither of the PNS codes was capable of analyzing the present flow field, as noted in the following discussion.

In the PNS approximation, diffusion in the axial flow direction is assumed to be negligible when compared to diffusion in the other two directions; also, diffusion in the axial direction is assumed to be negligible relative to convection in that direction. As a result of the PNS approximation, terms in the governing equations involving second derivatives in the axial direction are omitted. In addition, the flow is assumed to be steady. Consequently, PNS codes are potentially more economical to use than are Navier-Stokes codes since the solution obtained with a PNS code can be marched in the axial direction.

A suitable computer code for the flow fields of interest in the present program must solve the governing equations for compressible, reacting, turbulent flow in at least two space dimensions.

Several codes were identified as potentially suitable in the evaluation. The codes differ in the method of solution of the governing equations, hydrogen-air chemical reaction rate models, and turbulence models. The codes considered in various phases of this study were SPARK, NASTAR, SCORCH and ESCAPE. Various workers have applied these codes to a variety of flows and compared predicted results to the available data. A brief description of these codes follows.

The majority of calculations for this program were made using the UT-SPARK code, the UTRC version of the two-dimensional SPARK code developed by J. P. Drummond and co-workers at NASA-Langley Research Center (Refs. 35 and 36). Solutions of the time-dependent form of the Navier-Stokes equations are obtained using the explicit, time-marching, finite-difference method due to MacCormack (Ref. 37). The original code used the algebraic turbulence model of Baldwin and Lomax (Ref. 38). At UTRC, the k-epsilon, two-equation turbulence model (Ref. 39) has been added to the code. Hydrogen-air chemical reaction rates are modeled using either a 1-step global or an 18-step reaction mechanism. As noted in the discussion of results, additional chemical kinetics models have been added at UTRC (as part of the NASP effort).

A second Navier-Stokes code was also available for this study. Using its own funding, Pratt and Whitney has developed the NASTAR code (Refs. 40 and 41) which solves the time-independent form of the Navier-Stokes equations using a control volume, implicit method for flows with arbitrary Mach number in general curvilinear geometries. Both the Baldwin-Lomax and k-epsilon turbulence models are available in the code. Kinetics models include the one-step model used in SPARK, a two-step model (Ref. 42) and an eight-step model used in the SCORCH code (see below).

Since initial calculations obtained for the same case using both SPARK and NASTAR showed that the results obtained were similar and since SPARK is available to Government contractors from NASA-Langley (whereas NASTAR is a proprietary code), it was decided to use only the SPARK code as the Navier-Stokes solver for the present program.

Two parabolized Navier-Stokes codes were also considered for use during the program. Under a series of Government-sponsored efforts to develop computer codes for analyzing the flow within various scramjet engine components, Science Applications International Corporation (SAIC) developed the SCORCH code (Ref. 43) for two-dimensional and axisymmetric, chemically reacting, turbulent flows in combustors. The parabolized form of the Navier-Stokes equations were solved using an implicit, space marching finite-difference method. However, the static pressure field is determined using an explicit procedure that essentially determines flow properties along characteristics; the method has been termed a viscous characteristics approach. The k-epsilon model is used to determine the turbulent viscosity and an eight-step, seven-species reaction rate mechanism is used to compute the burning rate of hydrogen.

Initial application of the SCORCH code during other programs showed that it can be used provided that the Mach number away from solid surfaces remains high enough (greater than

approximately two) and that flow conditions vary smoothly in the lateral direction. The latter restriction is probably relevant for any PNS method. The former restriction is inherent in the viscous characteristic method. Thus, the technique can be applied to, say, reacting flows in nozzles and two-dimensional flows in combustors at higher simulated flight Mach numbers than that corresponding to the present experiments. Since the hydrogen fuel is injected at sonic conditions and since heat release in the shear-layer mixing region between the hydrogen and air streams tends to reduce the local Mach number toward unity, it was found that the SCORCH code could not be applied in the present program. In a private communication, SAIC did show how the code can be applied to compute the flow in a combustor with flow conditions somewhat similar to the present conditions (Ref. 44); however, numerous restrictions and approximations were used. Due to its lack of robustness, SCORCH was not used further in the present study.

The second PNS code considered is ESCAPE, a code developed recently at NASA-Langley Research Center from the three-dimensional version of SPARK (Ref. 45). The code solves the parabolized, Navier-Stokes equations in three dimensions using the explicit method of MacCormack (Ref. 37). In this application of MacCormack's method, differencing in the axial direction is approximated in a manner analogous to temporal differencing when the technique is used for approximating the time-dependent form of the Navier-Stokes equations. The pressure distribution in the local crossplane is determined directly from the governing equations. In subsonic regions, the standard procedure (Ref. 46) of neglecting a portion of the static pressure gradient in the axial direction is used to eliminate numerical instabilities caused by upstream propagation of disturbances in subsonic regions. The Baldwin-Lomax turbulence model is used in the original version of the code, but the k-epsilon model was added at UTRC under the NASP program. Both a one-step and a multiple step chemical kinetics mechanism for hydrogen-air combustion are available.

The ESCAPE code was not available until relatively late in the present study. When the code was applied to analyze the experiment of Burrows and Kurkov (Ref. 44), reasonable agreement was found between calculated and measured profiles at the combustor exit (Ref. 45). However, computer run times are considerably longer than anticipated for a PNS code and robustness is lacking for flows of interest in the present effort. The developers have noted that several errors are present in early releases of the code. Since additional time is evidently required before the ESCAPE code can be applied routinely, it was not used in this study.

As a consequence of the above cited considerations, two Navier-Stokes and two parabolized Navier-Stokes codes were identified as applicable to the present problem. The PNS codes were evaluated as part of other programs and were found to require additional development before they can be used routinely to analyze scramjet combustor flow fields. Results obtained using the two Navier-Stokes codes were similar to each other when applied to the same preliminary set of flow conditions obtained early in the experimental program. Since one of these codes (SPARK) is also available to Government contractors, it was selected for use in this program.

The SPARK code has been previously assessed primarily for turbulent, mixing dominated problems. In all such cases, the Baldwin–Lomax algebraic turbulence model was used. Recently however, UTRC assessed the Baldwin–Lomax model and the newly implemented (k–epsilon) model by calculating the inlet pitot pressure and total temperature profiles presented to the test section and comparing these profiles to measured data. The calculations, which were started in the subsonic plenum downstream of the facility heater, were performed using two over lapping grid sections. The grid densities were 100 by 50 in each segment. A constant temperature (cold) wall boundary condition was specified for each calculation section. The calculated static pressure distribution for the entire nozzle calculation is shown in Fig. 57. The calculated–profiles comparison to measured total temperature and pitot pressure data are shown in Figs. 58 and 59, respectively. The Baldwin–Lomax model produced results that show substantially thicker wall boundary–layer development owing to the inability of the model to provide proper comparison of the mixing effects across regions with large density variation. The (k–epsilon) model results, however do show reasonable agreement with the observed flow profiles. These results should be kept in mind in assessing and interpreting the results of the next section.

SELECTION OF CASES

Flow conditions from several experimental tests were used to define six cases to be simulated with the selected computer program. Each case used data from several tests since more than one test was required to obtain a complete set of data using both intrusive and nonintrusive methods. Flow conditions in the airflow just upstream of the fuel injection station (Station 1 in Fig. 1) were obtained in a separate series of tests and scaled to the flow conditions for the simulation of interest as described in the section, "Experimental Procedures".

The six cases are listed in Table 6. Flow conditions specific to each case are presented in the discussion of results (below). For flows in which the shock generator is not present, two mixing cases and two reacting flow cases were run; the equivalence ratio differed in each pair of cases. One mixing and one reacting flow case were run with the shock generator in place. For the two mixing cases, the static pressure of the hydrogen at the exit of the fuel injector increased with increasing equivalence ratio (ϕ). In all cases, the fuel stream was underexpanded relative to the main flow at the injector exit so that for the present case the equivalence ratio is essentially a measure of the extent of underexpansion of the fuel jet. Note that a total of 23 variations of these cases were run in an attempt to improve the level of agreement between measured and computed results and to assess the sensitivity of the computed results to various modeling assumptions. Selected representative results from some of these variations are presented in conjunction with the discussion of results.

DATA AVAILABLE FOR COMPARISON TO CFD RESULTS

The objective of the computations was to provide simulated flow results that could be compared to the available data and thereby provide a means of evaluating existing CFD analyses. During the

experimental program, wall static pressure, pitot pressure, stagnation temperature, static temperature, and concentration data were acquired.

The wall static pressure data were acquired using static pressure taps mounted flush to the walls of the test section. These data can be regarded as the most reliable of the data acquired since such measurements are made using well-established techniques. For external, supersonic flows and for both internal and external subsonic flows, it is relatively easy to predict wall static pressure distributions with reasonable accuracy. For supersonic internal flows in which a second gas of different density is injected parallel to the main flow direction, it is much more difficult to predict accurately the wall static pressure distribution. The reason for this difficulty is that waves incident on the mixing layer between the two streams are both reflected from, and transmitted through, the layer. Small changes in both the angle of incidence and properties within the layer can alter significantly the resulting wave pattern in the test section. It is interesting to note the lack of comparison with the wall static pressure data in published reports of CFD comparisons for the data of Burrows and Kurkov (Ref. 44). For example, results using the ESCAPE code were presented in Ref. 45 only for flow profiles at the exit of the combustor. These results were reproduced at UTRC with the ESCAPE code; however, agreement between predicted and measured wall static pressures for this case were in poor-to-fair agreement. As will be shown subsequently, the wall static pressure variations were not predicted accurately for the present effort either.

Pitot pressure data were acquired using the same probe that provided total temperature data (Figs. 5 and 6). Of the data obtained within the flow field, these are probably the most reliable data as far as the CFD evaluation is concerned. The measurements are easy to make and they are not affected by small variations in flow properties. In principal, CFD results should differ at most from the measured pitot pressures by a vertical displacement of the pitot pressure profile due to errors in computing the vertical location at which an oblique shock wave passes through the flow at the axial station of interest.

Stagnation temperature data were also acquired using the dual-sonic orifice probe. As noted earlier in this report, determination of stagnation temperature using this method is quite difficult; however, it is the only practical method available for use in flows of the type studied here where stagnation temperatures within the flame prohibit the use of thermocouple probes.

Static temperature data were acquired using the CARS technique. As is also evident from the earlier discussion, these data are difficult to obtain with an accuracy suitable for evaluating CFD codes in an unambiguous fashion. On the other hand, the accuracy of CFD results for static temperature can be affected significantly by (a) errors in the determination of the wave pattern in the combustor, and (b) errors in mixing and reaction rate models for the case of reacting flows.

Relatively few species concentration data were acquired during the experimental program. Since extensive processing of the CARS results were required to obtain these data so that concentration

measurements were not available until almost all of the analytical effort was completed. The accuracy of CFD results for species concentrations can be affected by errors in static temperature determination and the accuracy of mixing and reaction rate models. To assess the current state of development of CFD codes, a larger amount of concentration data are required. In spite of these stipulations, some comparisons are presented for tests during which both static temperature and species concentration data were acquired.

MODEL ASSUMPTIONS

In using the CFD codes to simulate the flow in the scramjet combustor, several assumptions were made. In all cases, some of the details of the flow conditions had to be assumed since it was not practical to measure all of the flow boundary conditions. Additional assumptions were made regarding the choice of turbulence model, chemical kinetics scheme, and grid density and distribution.

Boundary Conditions— In the first category of assumptions, it was necessary to estimate flow boundary conditions in the absence of detailed measurements. As noted earlier, the total temperature, static pressure and Mach number profiles at Station 1, Figs. 8, 10, and 11, respectively, were estimated by scaling the available nozzle exit data to the specific experimental condition. It was also assumed that the hydrogen, oxygen and air in the vitiated-air heater reacted completely so that the mass fractions of nitrogen, oxygen and water vapor at Station 1 were computed from the metered flow rates into the heater. Experimentally, it was determined that the heater was operated at high efficiency so that the effect of this assumption was to neglect the concentration of certain radicals generally found in only small amounts in fuel-lean systems; it should be noted that some of these radicals may be important in the ignition process of fuel with air (see below).

It was also necessary to estimate flow conditions at the exit of the hydrogen slot injector from the measured stagnation temperature and pressure and the assumption that the hydrogen flow was sonic at the exit. Since the injector exit is located relatively close to the fuel plenum, the flow at the exit is not fully developed; therefore, a flat (slug) profile was used to represent each of the flow conditions at the exit. Note that boundary layer estimates made for a similar fuel injector used during other experiments at UTRC show that the boundary layers are small relative to the slot height at the exit of the fuel injector.

For the cases computed without the shock generator, the computational domain extended from just upstream of the fuel injector exit to just downstream of the Station 3 measuring station. Usually, 75 grid nodes were used in each coordinate direction. Two different grid node distributions were used in the vertical direction depending on the extent to which the boundary layer along the lower wall of the combustor was resolved. To avoid an excessive number of grid nodes in the axial direction, the region directly downstream of the splitter plate was resolved with a relatively coarse mesh; typically, the flow along the face of the splitter was not required to satisfy the no-slip velocity or inviscid lip boundary condition.

Perhaps as a consequence of assuming the existence of certain flow conditions at the exit of the injector and making some compromises in grid density or distribution for the sake of computational efficiency, wave patterns in the vicinity of the fuel injector were in poor agreement with those obtained from the schlieren system.

In all cases, viscous, no-slip boundary conditions were used along the upper surface of the combustor. The lower boundary was treated as either viscous or inviscid as noted in the discussion of results. All flow conditions at the combustor inlet (Station 1) or injector exit were specified. Flow conditions at the exit of the computational domain were determined by extrapolation from the interior. Inlet and exit flow conditions are thus seen to be specified in a manner consistent with the fact that the flow is supersonic.

For cases in which the effects of the shock generator (6-degree ramp) were simulated, the computational domain was extended to a point approximately one inch upstream of the start of the shock generator. Approximately 100 nodes were used to define the grid in the axial direction and 75 were used in the vertical direction. Viscous, no-slip velocity boundary conditions were used on the upper and lower surfaces. Inlet and exit boundary conditions were specified as in the cases in which the shock generator was not present.

Typically, more than one computation was made for each case. In some cases, the grid node distribution was varied or the lower wall boundary condition was changed from (say) an inviscid to a viscous flow condition.

Turbulence Models— The effects of different turbulence models on the calculated results were also evaluated. For example, the original version of the SPARK code used the Baldwin-Lomax algebraic turbulence model (Ref. 38) to determine the local turbulent viscosity. In this model, the turbulent length scale is determined from the location of the maximum vorticity relative to the nearest solid surface. For unconfined flows about airfoils, this model provides a rapid and accurate means of determining the turbulent viscosity. For confined flows, experience shows that the location of maximum vorticity can vary rapidly, especially if locally separated regions exist in the flow; such regions may exist in the vicinity of incident shock wave-boundary layer interactions. Similar problems in length scale determination occur in the presence of shear layer/mixing regions such as that between the hydrogen fuel and vitiated air streams. As a result, it may be difficult to achieve convergence of the calculation. In other cases, the predicted turbulent length scale may be large enough to produce unrealistically large values of turbulent viscosity.

To provide an alternative turbulence model, the two equation, k-epsilon model was added to the SPARK code (Ref. 39). The characteristic turbulent velocity is obtained from the solution of the partial differential equation for turbulent kinetic energy (k); the turbulent length scale is computed from the

solution of the partial differential equation for turbulent energy dissipation rate (epsilon). The turbulent viscosity is related to k and epsilon algebraically (see Ref. 39).

$$\mu_t = C_\mu \frac{k^2}{\epsilon} \tag{13}$$

It should be noted that the k–epsilon model was developed and calibrated for low–speed flows and that special treatment is required in the immediate vicinity of solid surfaces. Nevertheless, the model is in widespread use and generally avoids some of the problems in length scale determination when algebraic models are used to analyze complex flows. No attempt was made at this time to include corrections for compressibility effects.

Chemical Kinetics Models— When simulating the reacting flow cases, it was also necessary to consider alternative chemical kinetics models. The static temperature of the vitiated–air delivered to the test section was generally less than 1000 K (1800 R). This temperature is often cited as the autoignition temperature for stoichiometric hydrogen–air mixtures at a pressure of one atmosphere. When single– and multiple–step global chemistry models (such as those incorporated in SPARK, ESCAPE, SCORCH and NASTAR) are used, little or no chemical reaction is predicted to occur. Experimentally, substantial chemical reaction occurs, perhaps due to initiation by radical species produced either during vitiation or in small regions of flow recirculation in the corner flow regions of the combustor.

To force chemical reactions to occur to the CFD calculations, the one–step model of Varma, et al. (Ref. 47) was used for most of the calculations presented later in this report. In this model, hydrogen and air are allowed to react at a finite rate; there is no reverse chemical reaction. In a few cases, an ignition delay model was used to define the region in the flow field in which chemical reaction can occur. In this model, ignition is assumed to occur once the level of concentration of a species, crucial to the ignition process, is large enough. A transport equation for the crucial species is solved with a source term directly related to available ignition delay time data (e.g., Ref. 49). Except for a few cases noted later, the crucial species model was not used for most of the simulations run.

The typical chemical kinetics mechanism consists of one or more chemical reactions whose forward and reverse rates are expressed in the form of an Arrhenius rate expression with specific rate

constant, K given by:

$$K = AT^n e^{E/RT} \tag{14}$$

This form is justified on the basis that it can be derived from molecular collision theory and that all chemical reactions occur at the molecular level.

For turbulent flows in which the reactants are contained in small eddies, it is necessary for the reactants to mix thoroughly before chemical reaction can occur. If the temperature is high enough, it is possible for chemical reactions to occur much more rapidly than reactants can mix. That is, the rate at which the combustion process proceeds is limited by the rate of mixing of the reactants contained in individual eddies. The rate of mixing is related to the turbulent time scale which in turn can be determined from the turbulent velocity and length scales. Magnussen and Hjertager proposed a one-step reaction rate model for turbulent flows in which the time scale can be computed directly from k and epsilon (Ref. 48). One case was run using this model. However, whereas the effect of ignition delay was approximated in Ref. 48 from the local concentration of product (water, in the present case), it was simulated in the present calculations using the crucial species model.

COMPARISONS OF COMPUTED RESULTS AND DATA

In this section, the calculated flow results are compared to experimental data for the six flow simulations presented in Table 6. First, results are presented for two reacting flow cases at two different equivalence ratios. Second, results are shown for two nonreacting flow (mixing) cases for two different equivalence ratios: i.e., for two injector to main stream pressure ratios. Finally, results are given for both reacting and mixing cases in which the effects of the shock generator are present.

Reacting Flow Cases (AFS3A and AFS4A)— Calculations were performed for two reacting flow cases using the SPARK code. The flow conditions simulated are listed in Table 7. These cases have been designated AFS3A and AFS4A. Note that several test runs were used to provide a complete set of flow conditions and measured data for each case. Note also that the equivalence ratio presented in Table 7 is based on the metered flow rates of reactants.

The calculations were made initially using the Baldwin-Lomax algebraic turbulence model (Ref. 38) to compute the turbulent viscosity.

Ignition delay time estimates indicated that, for the assumed flow conditions, autoignition of the hydrogen-air mixture was unlikely to occur. The ignition delay time estimates were based upon a correlation of the data of Slack and Grillo (Ref. 49) as supplemented with additional information to include the effects of variations in equivalence ratio on ignition delay time. Contrary to these

estimates, the experimental results indicated that autoignition did occur and that it was not necessary to employ the torch igniter in the conduct of the tests. The experimentally observed autoignition may be attributable to higher temperatures and lower ignition delay times in the wake of the splitter, catalyzing effects of the hydrogen–air reactions due to trace species produced during vitiation, or possibly three–dimensional effects in the vicinity of the side walls.

To provide an unambiguous result for the simulations, a simple chemical reaction rate expression was used in which the effect of ignition delay was ignored (Ref. 47). Since the extent of flame propagation in the present case was mixing controlled, it is believed that the reaction rate model used was adequate.

The calculations were run using a grid with 75 nodes in each direction. No–slip, temperature specified boundary conditions were used along the top wall. The flow along the bottom wall was assumed to be adiabatic and the flow velocity was allowed to slip; mathematically, the lower wall boundary condition is identical to that for a plane of symmetry. By neglecting viscous effects along the lower wall, grid nodes could be concentrated in the shear layer region and near the upper surface Implicit in the method for modeling the lower wall of the combustor was the assumption that the shocks generated by the growth of the boundary layer along this wall are weak and have negligible effect on the results (see below). The calculations were initiated at the downstream end of the splitter plate. Based on previous results, the boundary condition along the vertical face, or lip, of the splitter plate was replaced by a plane of symmetry condition. The effect of the lower wall and splitter plate boundary conditions on the computed results was also investigated.

A comparison between computed and measured stagnation temperature for the higher equivalence ratio case (AFS3A) is shown in Fig. 60 for the two measuring stations (Stations 2 and 3 in Fig. 1). The computed and measured results are generally in reasonable agreement. However, the computed profiles appears to be shifted downward relative to the measured profiles. Note that the computed results also show the peak temperature associated with chemical reaction in the mixing layer. A similar, but more extreme, result is evident for pitot pressure as shown in Fig. 61. Reasons for this shift in position are offered below.

A comparison of measured and computed wall static pressures for both the upper and lower walls of the combustor is presented for case AFS3A in Fig. 62. Here, while the general level is in agreement a detailed comparison is only fair. Evidently, the predicted and observed wave patterns in the combustor differ greatly.

Results for the lower equivalence ratio case (AFS4A) are presented in Figs. 63 through 65 and show similar levels of agreement.

The computed results indicate that only 2 percent of the hydrogen is consumed for Case AFS3A and only 5 percent is consumed for Case AFS4A. These levels are somewhat lower than those estimated on the basis of the total temperature and static pressure measurements.

Attempts were made (1) to explain more fully the discrepancies between the experimental data and the present results, and (2) to improve the level of agreement between the computed and measured results by examining the sensitivity of results to variations in some of the assumptions made when performing these calculations. For example, it was assumed that the turbulent Schmidt number was unity for the results shown above. Based on discussions with P. Drummond of the NASA-Langley Research Center, there is some evidence that the turbulent Schmidt number is closer to 0.5 for hydrogen-air mixing situations. A case was run (AFS3AR1) in which the turbulent Schmidt number was 0.5, but the computed profiles at Stations 2 and 3 differed only slightly from those shown in Figs. 60 through 62.

Recall that the flow along the lower wall was assumed to be inviscid so that effects of both boundary layer displacement and compression waves due to boundary layer growth along the lower wall were neglected. A case (AFS3AR2) was run using the same computational grid but with no-slip conditions along the lower wall. Agreement between the computed and measured results deteriorated as shown in Fig. 66. It is also possible that some of this deterioration can be attributed to higher than expected heat transfer to the cooled lower wall when the no-slip boundary condition was used.

Other cases were run in which the no-slip condition was applied to the face of the splitter plate (AFS3AR3) or the injection Mach number was increased to 1.2 (AFS3AR4); the results obtained were essentially unchanged from those shown in Figs. 60 through 62.

All of the cases described so far were run with the Baldwin-Lomax algebraic turbulence model (Ref. 38) to calculate the turbulent viscosity. Examination of the computed results for both the reacting (and nonreacting) cases indicates that the turbulent viscosity in the shear layer decreases rapidly in the axial direction. In this model, the turbulent length scale is determined from the location of peak vorticity relative to a solid surface. Experience with the Baldwin-Lomax model, obtained with several computer programs applied to problems of confined flows, shows that the method of length scale determination is not always reliable. Cases were also run using the k-epsilon turbulence model. To satisfy the requirements of the turbulence model for the near-wall region and to keep computational times reasonable, the grid nodes in the vertical direction were redistributed, but the number of grid nodes in the vertical direction was kept constant at 75. The no-slip boundary condition was applied at the lower wall. For the higher-equivalence ratio case (AFS3AR5), comparisons between measured and computed stagnation temperature profiles are shown in Fig. 67. Note that this calculation was never converged satisfactorily. After examining the results for several cases run with the k-epsilon model, it was concluded that the grid distribution in the vertical direction should be modified; the number of grid nodes may be adequate, however.

Calculations for the lower equivalence ratio condition were also made using the k-epsilon model (with the same grid as that used for case AFS3AR5) and the level of agreement between computed and measured results was also poor (case AFS4AR2). In addition, a case was run in which the extent of

chemical reaction was limited by using the ignition delay model to limit the extent of the region of the flow in which chemical reaction was possible (case AFS4AR3); the level of agreement was poor in this case, also.

Other than the use of the ignition delay model, no attempt was made to examine the effect of the chemistry model on the computed results. Results obtained for the Burrows and Kurkov experiment (Ref. 44) show that the computed locations of peak values in the stagnation temperature and species concentration profiles are somewhat sensitive to the choice of chemical kinetics mode; models involving a greater number of chemical reactions tend to give somewhat better agreement (see Refs. 41 and 50). In the present study, the level of agreement for both reacting flow and mixing cases was comparable; therefore, it was concluded that the choice of chemical kinetics model was relatively unimportant.

In accordance with an earlier statement, comparisons between computed results for the high equivalence ratio reacting flow case (AFS3A) and CARS data are presented. Comparisons are made in Figs. 68 through 70 of static temperature and hydrogen and water vapor mass fractions, respectively.

Mixing Cases (AFS5 and AFS6)— The flow conditions simulated are given in Table 8. The cases have been designated AFS4 and AFS5. Note that several test runs were used to provide a complete set of flow conditions and measured data for each case. Note also that the equivalence ratio present in Table 8 is based on the metered flow rates of reactants.

Since the flow is nonreacting, the only effect due to different equivalence ratio is that the fuel jet is more underexpanded for case AFS6. The calculations were made initially using the Baldwin–Lomax algebraic turbulence model. The calculations were run using a grid with 75 nodes in each direction. No–slip, temperature specified boundary conditions were used along the top wall. The flow along the bottom wall was assumed to be adiabatic and the flow velocity was allowed to slip.

A comparison between computed and measured stagnation temperature profiles for the lower equivalence ratio case (AFS5) is shown in Fig. 71 for measuring Stations 2 and 3. The computed and measured results are generally in reasonable agreement. However, the computed profiles appear to be shifted downward relative to the measured profile. A similar result is evident for pitot pressure as shown in Fig. 72. Note that the measured stagnation temperatures show some shift between measuring stations. Since the flow is nonreacting, and since the core total temperature should persist, the differences are unexpected. Note however that on the expanded temperature scale used in Fig. 71, the difference is approximately 200 degrees, comparable to the deviations measured between stations at the high–temperature condition.

A comparison of measured and computed wall static pressures for both the upper and lower walls of the combustor is presented for case AFS5 in Fig. 73. Here, the level of agreement is only fair. Evidently, the predicted and observed wave patterns in the combustor differ greatly as noted previously in the discussion of the reacting flow cases.

Results for case AFS6 are presented in Figs. 74 through 76 and show similar levels of agreement.

Results obtained using the k–epsilon were essentially unchanged when this model was used to simulate Case AFS5 and the velocity along the lower surface was allowed to slip (Case AFS5R1). When the k–epsilon model and a no–slip velocity condition on the lower wall were used, the level of agreement between calculated and measured results deteriorated for both flow rates of fuel (Cases AFS5R2 and AFS6R2).

For Case AFS6, it is instructive to examine the effect of grid node distribution when the lower wall boundary condition is the same (i.e., no–slip) and the turbulence model differs (Cases AFS6R2 and AFS6R3). Computed and measured stagnation temperature profiles are compared in Figs. 77 and 78. These results show that the choice of turbulence model has only a small effect on the results. A direct comparison of the computed results in Figs. 74 and 78 (both obtained using the Baldwin–Lomax model) suggest that grid node distribution and/or lower wall boundary condition has a greater effect on the results. Since the lower wall boundary condition can influence the local mixing rate, the effects of grid node distribution and boundary condition cannot be readily determined from the results presented here. Based on a detailed examination of other calculated results using both grids, it is concluded tentatively that the grid node distribution used for the results shown in Figs. 66, 67, 77 and 78 is the principal cause of deterioration of level of agreement. However, taken together, all of the results indicate that the level of agreement is only fair.

Comparisons for the low equivalence ratio, non–reacting flow case (AFS5) between computed and measured static temperature, and hydrogen and water vapor mass fraction are presented in Figs. 70 through 81, respectively.

Shock Generator Cases (AFS7 and AFS8)— Calculations were also performed for two cases in which the shock generator was used. The shock generator consisted of a 6–deg ramp attached to the lower wall beginning at a point upstream of the trailing edge of the splitter plate and terminated by a blunt trailing edge. The flow conditions are presented in Table 9. These cases have been designated AFS7 and AFS8 for the nonreacting and reacting flow conditions, respectively. The calculations were initiated approximately one inch upstream of the start of the shock generator (2.5 inches upstream of the fuel injector).

All of the calculations were made using the k–epsilon turbulence model and no–slip boundary conditions on the lower wall and ramp (shock generator) surfaces.

It was found that steady flow solutions could not be obtained, i.e., the computation did not converge, for any of the cases run with these flow conditions. Of course, it is possible that the flow immediately downstream of the blunt trailing edge of the compression ramp was unsteady. No attempt was made to determine the characteristic frequencies of the computed flow unsteadiness. Video images of the experimental flow field show that the flow is steady in the vicinity of the fuel injector.

Lack of convergence and unsteadiness can be produced in numerical results if the level of heat release is large enough to unstart the supersonic flow. Since in all of the calculations presented in this report, flow conditions are specified completely at the inflow (upstream) boundaries, there is no mechanism to unstart the flow. Consequently, for unstarted flow the boundary conditions become inconsistent and the calculation does not converge; for a code like SPARK which is based on the solution of the time-dependent form of the governing equations, lack of convergence can also be exhibited as unsteadiness that persists. While thermally-induced unstart is one explanation for lack of convergence or unsteadiness, it should be noted that in the present cases the *experimental* flows were always started.

Comparisons between computed and measured profiles of stagnation temperature and pitot pressure are shown for the nonreacting flow case (AFS7) in Figs. 82 and 83, respectively. The level of agreement is poor. However, the measured results show a rapid decrease in what is effectively the freestream region of the main flow. While the shock structure may account for the shape of the measured pitot pressure profile, the abrupt decrease in the total temperature may be related to the cooling effect of the condensate being transported from the ramp-base recirculation region, discussed earlier.

Three cases were run for the reacting flow case (AFS8). In the first case, the chemical kinetics model described in Ref. 47 was used. Computed and measured stagnation temperature profiles are shown in Fig. 84. However, the computed results are unreliable since the predicted level of heat release is high enough to cause thermal choking; in fact, other numerical results for this case show that the supersonic flow was attempting to unstart—the probable cause of lack of convergence.

When the ignition delay model was used (Case AFS8R1) the flow remained supersonic throughout; however, a large amount of heat was released. The results for stagnation temperature are shown in Fig.85.

Finally, the Magnussen-Hjertager chemistry model was used in conjunction with the ignition delay model; however, the heat release rate was still sufficient to unstart the flow.

It should be noted that the measured stagnation temperature in the reacting flow case also shows the rapid decrease in the main flow noted earlier in the nonreacting flow case (see Figs. 84 and 85). Note also that these data show little evidence that chemical reaction in fact occurred in this test. That is, the total temperature rise denoting the occurrence of combustion at Station 2, in Fig. 84 is less than 200 R. Other data as well as the video tape record do indicate that chemical reaction occurred. Consequently, although questions regarding the shape of the measured stagnation temperature profile near the lower wall of the test section remain, the computed results indicate that considerable work remains to be done on improving the physical models used in these simulations.

TASK 3: THERMAL COMPRESSION ANALYSIS

The objective of this task was to formulate a first-order analysis of the supersonic combustor flowfield as part of an effort to develop a combustor preliminary design process. Although ultimately the detailed analysis and design of the supersonic combustor will rely heavily on accurate CFD code computations, a simplified analytical approach yielding first-order designs would be useful and cost-effective. Furthermore, during experimental development efforts, in which the effects on the flow structure and pressure distribution of fuel injector site or flowrate changes are being evaluated, the application of a CFD analysis in parametric studies may be time-consuming and not cost-effective.

A relationship between the supersonic-flow deflection induced by the burning planar hydrogen jet was developed by Edelman (Ref. 51). State-of-the-art CFD codes may also be appropriate to define this thermal compression effect. For the present, the purpose of this task was served by using the former analysis results as a starting point for the first-order analysis.

WAVE ANALYSIS

Computational procedures were developed that can be be used to calculate the pressure wave distribution induced as a consequence of combustion in a hydrogen-fueled supersonic combustor of two-dimensional cross-section as represented by the geometry shown in Fig. 86. The fuel injection site is at the top of the test section. The upper wall divergence angle (FWA) and the fuel injection slot height (FSH) are inputs. The approaching supersonic flow field (assumed as uniform) is prescribed by its Mach number (M(1)), ratio of specific heats (GAM), and duct height (H). The lower wall is flat. Calculations can be performed with and without the compression ramp. The ramp geometry is prescribed by inputting the streamwise location of the ramp leading edge (XRS) measured from the injection station, the forward and rearward ramp angles (Theta(3) and Delta (6)), and the streamwise location of the ramp peak (XRAMBR).

The effect of heat release during combustion on pressure rise is simulated by establishing a shock wave at the interface between the fuel and the air at the injection location. This shock is termed the thermal compression wave. The strength of the shock enters into the calculation by inputting the flow turning angle due to the shock (THETA (2)). The turning angle can be estimated from Edelman's correlation of deflection angle with the ratio of freestream of fuel mass flux shown in Fig. 87. This correlation is based on calculations for the geometry shown in Fig. 88. Assumptions for Edelman's calculation include combustion starting as the two streams mix and equal exit pressures for the two streams. The thermally induced deflection angle is the turning angle of the external streamline, adjacent to the burning fuel layer.

The coordinate system used in the codes is shown in Fig. 86. The origin is on the lower wall at the streamwise location corresponding to the fuel injection slot exit plane. The calculation tracks the interaction of the thermal compression wave with the ramp-generated waves (if present) and the duct

walls. Figure 85 is an example of the flow field breakup with a compression ramp on the lower wall. Key parameters in the calculation are:

M	local Mach number
BETA	shock wave angle relative to incoming flow
ANGLE	wave angle relative to duct lower surface
DELTA	local flow angle relative to duct lower wall
PP1TR	local to incoming total pressure ratio
PP1SR	local to incoming static pressure ratio
THETA	turning angle induced by a wave
NU	Prandtl-Meyer function
XINT	axial position of wave intersection
YINT	vertical position of wave intersection

These are subscripted variables defined by the region number. A separate numbering system is used to identify the intersection points. The sign convention for flow angle is positive for upward flow and negative for downward flow.

Several approximations are used in the formulations. The discontinuity caused by the thermal compression wave at its initiation point is ignored. The flow angle downstream of the thermal compression wave is assumed to be the value that dictates the thermal compression wave strength. Expansion fans are simulated by a wave at the center of a fan bounded by Mach lines corresponding to conditions upstream and downstream of the fan. Sliplines are tracked to their intersection with the next wave. At this point secondary waves are not generated since the downstream regions on each side of the slipline intersection are similar. The flow conditions feeding into the next wave are assumed, then, to be the average of the two conditions on the downstream side of the slipline intersection. Another approximation is that the flow conditions downstream of coalescing waves are determined by forcing the flow angle downstream of the coalescing waves to be the same as the downstream value before the waves coalesced. Secondary waves are not generated at these intersection points.

The codes are written to track the waves through the combustor. Separate subroutines are called to calculate conditions downstream of each type of intersection. This approach provides for a versatile code since the main code can be written to handle all possible orders of the wave intersections. When a compression ramp is included in the calculations, the number of possibilities is quite large.

The output of each code provides Mach number, local-to-entering total pressure ratio, and local to entering static pressure ratio for each region identified in Fig. 86. Listings of both of the codes are provided in Appendix E. The first of the two programs, written in FORTRAN, is identified as S.FOR and provides for investigation of the flowfield involving free shear-layer combustion. The second program, also written in FORTRAN, is designated as S4.FOR and permits calculation of the flowfield

structure with a compression ramp incorporated in the flowfield in the manner examined experimentally during Task 1 of the current program.

EXAMPLE PROBLEM

Results derived from test cases are presented in Figs. 89 and 90 and are used to describe the calculation procedure. The geometry for this example comprises a test section entrance duct that, as in the current experiment, is 3 inches in height. The duct incorporates a fuel injection slot 0.292 inch high and a 0.08-inch thick splitter plate. The upper wall of the test section is angled upward in the downstream direction, starting at the sonic fuel injection slot.

In both of the cases discussed, the test section entrance Mach number was 2.75 and the test section entrance static pressure was 5.4 psia. The fuel-air equivalence ratio was 1 and the resulting mass flux ratio was 0.349. For this mass flux ratio, according to the curves in Fig. 87, at a distance from the injection site, x /D – oo, the induced flow deflection is approximately 4.8 degrees.

Results of the first case, involving free shear-layer combustion, are shown in Fig. 89, and the calculated flowfield conditions are presented in Table 10. The test section entrance flow is deflected 2.8 degrees since the test section divergence is 2 degrees.

The results of the second calculation, performed to include a 4.8 degree compression ramp placed on the lower wall of the test section, are shown in Fig. 90. The calculated flowfield conditions are presented in Table 11. Attempts to perform a similar calculation involving a 6-degree ramp have not been successful.

CONCLUDING REMARKS

Detailed optical and probe measurements have been made in a supersonic shear-layer mixing experiment. Two classes of experiment were conducted. The first was a free shear-layer experiment while the second involved a shock-wave generator that caused an oblique shock wave to interact with the shear layer. Hydrogen and water vapor concentrations and static temperatures were measured using CARS while pitot pressures and total temperatures were measured using a DSO probe. Data were acquired primarily at two vitiated-air total temperatures, i.e., nominally 1800 and 3700 R, yielding non-reacting and reacting hydrogen-air mixing conditions. Convective Mach numbers, calculated on the basis of the undisturbed test section entrance conditions, ranged from approximately 0.03 for the low equivalence ratio, low total temperature condition to approximately 0.38 corresponding to the high equivalence ratio, high total temperature flow condition. DSO probe and CARS surveys were conducted at two axial locations downstream from the tangential slot fuel injector. Based on test section entrance surveys, which yielded initial conditions for the CFD code analyses, the initial boundary layer momentum thickness, Θ was 0.12 inch. The two survey stations at which the probe and CARS data were acquired thus lay at approximately 50 and 100 momentum thicknesses (x/Θ = 50, 100) downstream from the slot injection location.

At the distance, x/Θ = 100, the shear layer appears to have assumed its asymptotic behavior. The shear-layer characteristics measured at the closer distance from the injection site, i.e. at a distance, x/Θ = 50, appear to retain geometric features for which the injection-pressure mismatch with the local airstream pressure is responsible.

Based on measurements of the pitot thickness, performed during elevated-temperature combustion tests, the shear-layer growth rate measured at x/Θ = 100 corresponds closely to the calculated rate. The calculations were made using the semiempirical analyses due to Papamoschou and Dimotakis (Refs. 29-32). Similar measurements made during non-reacting mixing experiments do not compare as favorably with the results of analysis. This was due at least in part to the fact that the hydrogen injection pressure generally exceeded the local airstream static pressure measured immediately upstream of the injection location.

Significant consequences of the shock wave-mixing layer interaction, reflecting measurements made at a distance, x/Θ = 100 from the injection slot, during combustion, are as follows:

- The shear-layer growth rate did not change with respect to the rate measured during the free shear-layer (no-shock) experiments.
- The mixing-layer growth rate increased 35 percent and the distance between the inner (low-speed) shear-layer edge and the adjacent duct surface increased by approximately 80 percent.

Corresponding results, derived from measurements made during non-reacting experiments, comprise the following:

- The shear-layer growth rate decreased approximately 35 percent from the growth rate deduced during the free shear-layer (no-shock) experiments.

- The mixing layer growth rate decreased approximately 19 percent during the same comparison while the distance between the shear-layer inner edge and the adjacent duct surface remained unchanged.

The apparent reversals in the shear- and mixing-layer growth rates may be related to the reversals in the roles of the vitiated-air and fuel streams as primary and secondary flows in terms of their relative velocities. During the high-temperature experiments, the airstream was the primary stream, exhibiting the higher velocity. When the airstream temperature was reduced for the non-reacting experiments, the injected hydrogen velocity exceeded the airstream velocity, thereby becoming the primary flow.

The mixing-layer growth rates derived from optically acquired CARS data exhibited trends that are similar to the trends displayed by the pitot pressure data but only the hydrogen mole fractions, measured at $x/\Theta = 50$, yielded mixing-layer growth rates that were in reasonably good agreement with the pitot pressure results.

In the near field, i.e., at $x/\Theta = 50$, measured growth rates were strongly related to the degree of the underexpansion of the fuel jet. From the standpoint of attaining improved fuel-air mixing, the results measured at Station 2 suggest the benefits that may accrue from under-expanded injection. Measured growth rates at this location during the high-temperature experiment were 60 percent greater than predicted values, based on "ideal" conditions for the injection process. Bearing in mind that the mixing rates of all fuel injection processes in supersonic flows ultimately degenerate to their asymptotic levels in the farfield, it seems clear that mixing enhancement accomplishments must rely on developing rapid mixing behavior close to the point of fuel introduction into the airstream. Since the results of the current effort include information suggesting that enhancement of growth rates may be induced by high pressure and/or high Mach number injection, these processes should be examined further.

Four computational fluid dynamics codes were considered in this study. Two Navier-Stokes and two parabolized Navier-Stokes methods were examined. Both of the PNS codes were determined to require further development before they can be used routinely to simulate the flows of interest in the present study. Since only one of the Navier-Stokes codes (SPARK) is available through Government sources and since preliminary results showed that both codes produced comparable results, the computational effort was directed toward the use of the SPARK code.

For the cases in which the shock generator was not present, computed results were compared with data acquired during the test program. In general, it was found that the level of agreement between predicted and measured stagnation temperature and pitot pressure profiles at two axial locations was fair. Reasons for the discrepancies were examined and it was concluded that the

computed results were sensitive to the distribution of grid nodes in the vertical direction; it is also possible that large errors in the length scale determination (used in an algebraic turbulence model for the turbulent viscosity) were produced by poor or inadequate grid node distribution.

Computed axial static pressure variations were not in good agreement with the measured data. It was noted that, for supersonic internal flows in which two parallel streams of dissimilar gases mix, small variations in flow properties and initial conditions can alter significantly the resulting wave pattern.

The level of agreement was only fair between the predicted and measured profiles for the wedge (shock generator) cases. For the nonreacting flow case (AFS7), questions remain concerning the stagnation temperature data in the region affected by the flow expansion behind the 6-degree ramp. For the reacting flow case (AFS8), it was found that thermally induced unstart was predicted to occur depending on the choice of chemical reaction model.

In all cases, the predicted profiles were displaced vertically relative to the measured profiles. The effects of several of the assumptions used in the analysis were examined, but no improvement in the computed results was obtained.

It is recommended that the data be used to examine whether suitable grids can be developed to improve the level of agreement. Due to its greater flexibility when used in complex flow simulations, the k-epsilon model should be used in future efforts; commonly used corrections for compressibility should be incorporated into this model. It is also evident from the shock generator cases that a more suitable chemical kinetics model should be examined.

RECOMMENDATIONS

On the basis of the current investigation's results, enhancement of the mixing-layer growth rate appeared to occur due to the shock wave interaction with the mixing region. This phenomenon may have significant consequences in improving levels of combustion performance attainable with fuel injection concepts that provide high desirable levels of axial momentum. Obviously, the effect of this interaction also impacts the effectiveness of film-cooling approaches to supersonic combustor thermal management. Although some of the fundamental issues concerning this supersonic combustor fuel delivery concept have been addressed in the current effort, many questions remain. Thus, the following future activities relating to these questions are recommended:

1) Acceleration of the injected hydrogen as a consequence of the injectant pressure mismatch was suggested by the results as being responsible for the greater-than-predicted levels of shear-layer growth. The separate effects of injection Mach number and the degree of pressure mismatch should be isolated and the consequential enhancement of the mixing layer should be quantified.

2) An effort should be made to provide a more detailed description of the initial conditions presented to the mixing process. In particular, the turbulent characteristics of the flowfield immediately preceding the injection site as well as better definition of the velocity field would be of significant value in developing a greater level of agreement between the analytical and experimental results.

3) In parallel with the above work, a more precise definition of the flow phenomena occurring in the regions immediately adjacent to the blunt-based splitter plate should be sought. Since practical supersonic combustors will not be provided with thin-lipped sections owing to the severe thermal environment and the likely need for cooling, a better understanding of these regions of the flowfield is highly desireable.

4) Owing to its greater flexibility in applications involving complex flow situations, additional work should be performed, using the available experimental data to determine whether suitable grids can be developed to improve the level of agreement between the computed and measured results.

5) Additional investigations using a limited set of test conditions should be performed to refine the multi-species CARS diagnostic approach and identify relationships between the flowfield characteristics and the measurement technique.

LIST OF SYMBOLS

a	Speed of sound
A	Cross-sectional area
α	Injection angle
b	Shear-layer thickness
β	Shear-layer spreading angle
C_D	Discharge coefficient
C_P	Specific heat at constant pressure
ϵ	Turbulent energy dissipation rate
f/a	Fuel-air ratio
g	Gravitational constant
γ	Ratio of specific heats
Γ	$\sqrt{\gamma}\left(\frac{2}{\gamma+1}\right)^{\frac{\gamma+1}{2(\gamma-1)}}$
h	Combustor height (or gap)
K	DSO probe calibration constant
k	Turbulent kinetic energy
ℓ	Mixing-layer thickness
μ	Viscosity
M	Mach number
M_r	Relative Mach number
$\mathcal{M}$	Molecular weight
P	Pressure
P_r	Prandtl number
Q	Heat transfer rate
R	Gas constant
Re	Reynolds number
R_T	Recovery factor

ρ	Density
T	Temperature
Θ	Boundary-layer momentum thickness
ϕ	Equivalence ratio (also E.R.)
u	Velocity
$\dot{W}$	Weight flow rate
x	Axial distance

SUBSCRIPTS

a	Air
as	Adiabatic surface
c	Coolant
F	Test section fuel
HF	Heater fuel
htr, o	Heater conditions
j	Jet (injection)
O_2	Oxygen
p	Pitot, product gas
s	Static conditions
T,t	Stagnation conditions
TH	Throat station
2	Test section entrance conditions

REFERENCES

1. Kepler, C.E. and A.J. Karanian: Hydrogen-Fueled Variable Geometry Scramjet (U), Technical Report AFAPL-TR-67-150, January 1968.

2. McFarlin, D.J. and C.E. Kepler: Mach 5 Test Results of Hydrogen-Fueled Variable-Geometry Scramjet (U), Technical Report AFAPL-TR-68-116, October 1968.

3. Dunsworth, L.C. and K.E. Woodgrift: Dual Mode Scramjet, Part I. Inlet Design and Performance Characteristics, AFAPL-TR-67-132, Part I, (Contract AF33(615)-2834), TMC Report S-837, December 1967.

4. Burnette, T.D., A.E. Heins, and G.J. Reed: Dual Mode Scramjet, Part II. Combustor Design and Performance Characteristics, AFAPL-TR-67-132, Part II, (Contract AF 33(615)-2834), TMC Report S-837, December 1967.

5. Burnette, T.D.: Dual Mode Scramjet, Part III. Engine Design and Performance Characteristics, AFAPL-TR-67-132, Part III, (Contract AF33(615)-2834), June 1968.

6. Bahr, D.W.,M.J. Kenworthy, etal: Scramjet Exploratory Development Program, NASA CR-1502, (Contract NAS1-8544), February 1970.

7. Chinitz, W., T. Baurer, H. Hopf, etal: Analytical and Experimental Investigation of the Low Speed Fixed Geometry Supersonic Combustion Ramjet, AFAPL -TR-66-102, Volume I, GASL TR 621, (Contract AF33(615)-2436), January 1967.

8. Investigations of the Low Speed Fixed Geometry Supersonic Combustion Ramjet, AFAPL TR-66-139, GASL TR 633, (Contract AF33(615)-5051), March 1967.

9. Analytical and Experimental Investigation of the Low Speed Fixed Geometry Supersonic Combustion Ramjet, Volume II, Final Contract Work, AFAPL TR-66-102, Vol. II, (Contract AF33(615)-2436), January 1967.

10. Brown.M.L. and R.L.Maxwell: Scramjet Incremental Flight Test Program, Volume 1, Summary, AFAPL TR-67-112, Vol.1, The Marquardt Corp. Report 6131, (Contract AF33(615)-2815), February 1968.

11. Avery, W.H.: Status and Future Trends in High Speed Chemical Propulsion, Symposium on High Speed Propulsion, Northeastern States Navy Research and Development Clinic, CPIA Publication 77, July 1965.

12. Billig, F.S.: Design of Supersonic Combustors Based on Pressure-Area Fields, Eleventh Symposium (Int'l.) on Combustion, Berkeley, CA., pp.755-769, 1967.

13. Billig, F.S. and G.L. Dugger: The Interaction of Shock Waves and Heat Addition in the Design of Supersonic Combustors, Twelfth Symposium (Int'l.) on Combustion, 1969.

14. Dugger, G.L. and F.S. Billig: Ramjet Technology, Chapter 11, Hypersonic Ramjets, JHU TG 610-11, March 1970.

15. Billig, F.S., R.C. Orth, and J.A. Funk: Direct-Connect Tests of a Hydrogen-Fueled Supersonic Combustor, NASA CR-1904, (Contract NOw-62-0604-c), August 1971.

16. Hypersonic Ramjet Experiment Project, Phase I, Conceptual Design Study Report, Volume I, NASA CR 66221, AiResearch Report AP-66-0167-1 (Contract NAS1-5116), February 1966.

17. Same, Preliminary Design Report, Volumes I through IV

18. Andersen, W.L., etal: Hypersonic Research Engine Project, Phase II, Aerothermodynamic Integration Model (AIM) Test Report, NASA CR-132655, AiResearch Report AP-74-10784 (Contract NAS1-6666), May 1975.

19. Engineering Staff: Hypersonic Research Engine Project, Phase II, Aerothermodynamic Integration Model Development, Final Technical Data Report, 10Mar.1968 through 22Apr. 1974, NASA CR-132654, AiResearch Report AP-75-11133, (Contract NAS1-6666), May 1975.

20. Henry, J.R.: Recent Research on Fuel Injection and Mixing and Piloted-Ignition for Scramjet Combustors, Twelfth Symposium (Int'l.) on Combustion, pp.1175-1182, The Combustion Institute, 1969.

21. Anderson, G.Y. and R.C. Rogers: A Comparison of Experimental Supersonic Combustion performance with an Empircal Correlation of Nonreactive Mixing Results, NASA TM- X-2429, October 1971.

22. Henry, J.R. and G.Y. Anderson, Design Considerations for the Airframe-Integrated Scramjet, NASA TM-X-2895, 1973, also presented at the 1st International Symposium on AirBreathing Engines, Marseille, France, June 1972.

23. Pinckney, S.Z.: Subscale, Hydrogen-Burning, AirframeIntegrated Scramjet; Experimental and Theoretical Evaluation of a Water-Cooled Strut, NASA TM-X-72682 May 1975.

24. Guy, R.W., etal: Thermal Design and Analysis of a Hydrogen-Burning Wind Tunnel Model of an AirframeIntegrated Scramjet, NASA TM-X-73931, January 1977.

25. Northam,G.B., C.A.Trexler, and C.R.McClinton: Flameholding Characteristics of a Swept-Strut H2 FuelInjector for Scramjet Applications, 17th JANNAF Combustion Meeting, Hampton,VA, pp.489-507, September 1980.

26. Northam, G.B. and G.Y. Anderson: Supersonic Combustion Ramjet Research at Langley, AIAA Paper 86-0159, AIAA 24th Aerospace Sciences Meeting, Reno, NV, January 6-9, 1986.

27. Repas, G. A.: Hydrogen-Air Ignition Torch, NASA Technical Memorandum 8882, November 1986.

28. Kay, I. W., J. B. McVey, C. E. Kepler, and L. M. Chiappetta: Hydrocarbon-Fueled Scramjet. Technical Report AFAPL-TR-68-146, Vol. VIII - Piloting and Flame Propagation, May 1971.

29. Papamoschou, D. and A. Roshko: Observations of Supersonic Free Shear Layers. AIAA Paper 86-0162, 1986.

30. Papamoschou, D. and A. Roshko: The Compressible Turbulent Shear Layer: An Experimental Study. Journal of Fluid Mechanics, Vol. 19, 1988, pp. 453-477.

31. Dimotakis, P. E.: Turbulent Free Shear Layer Mixing. AIAA Paper 89-0262, 27th Aerospace Sciences Meeting, January 9-12, 1989, Reno, NV.

32. Papamoschou, Dimitri: Experimental Investigation of Heterogeneous Compressible Shear Layers. Ph. D. Thesis, California Institute of Technology, 1986.

33. Anderson, G. Y. and R. C. Rogers: A Comparison of Experimental Supersonic Combustor Performance with an Empirical Correlation of Nonreactive Results, NADA TM X-2429, October 1971.

34. Dimotakis, P. E.: Turbulent Free Shear Layer Mixing and Combustion, 9th International Symposium on Air-Breathing Engines, Athens, Greece, 3-9 September 1989.

35. Drummond, J. P.: Numerical Study of a Ramjet Dump Combustor Flowfield, AIAA Journal, Vol. 23, No. 4, April 1985, pp. 604-611.

36. Drummond, J. P., R. C. Rogers, and M. Y. Hussainni: A Detailed Numerical Model of a Supersonic Reacting Mixing Layer, AIAA/ASME/SAE/ASEE 22nd Joint Propulsion Conference, Huntsville, AL, June 16-18, 1986

37. MacCormack, R. W.: The Effect of Viscosity in Hypervelocity Impact Cratering, AIAA Hypervelocity Impact Conference, Paper 69-354, Cincinnati, OH, April 30 - May 2, 1969.

38. Baldwin, B. S. and H. Lomax: Thin Layer Approximation and Algebraic Model for Separated Turbulent Flows, AIAA Sixteenth Aerospace Sciences Meeting, Paper 78-257, Huntsville, AL, January 16-18, 1978.

39. Launder, B. E. and D. B. Spalding: Lectures in Mathematical Models of Turbulence, London, Academic Press, 1972.

40. Rhie, C. M. and W. L. Chow: Numerical Study of the Turbulent Flow Past and Airfoil with Trailing Edge Separation, AIAA J., Vol. 21, No. 11, November 1983, pp. 1525-1532.

41. Rhie, C. M., S. T. Stowers, and H. B. Ebrahimi: Numerical Analysis of Reacting Flows Using Finite Rate Chemistry Models, AIAA 27th Aerospace Sciences Meeting, Paper No. 89-0459, Reno, NV, January 9-12, 1989.

42. Rogers, R. C. and W. Chinitz: On the Use of a Global Hydrogen-Air Combustion Model in the Calculation of Turbulent Reacting Flows, AIAA 20th Aerospace Sciences Meeting, Paper 82-0112, Orlando, Florida, January 11-14, 1982.

43. Dash, S. M., N. Sinha, D. E. Wolf and B. J. York: Computational Models for the Analysis/Design of Hypersonic Scramjet Components - Part 1: Combustor and Nozzle Models, AIAA/ASME/SAE/ASEE 22th Joint Propulsion Conference, Paper No. 86-1595, Huntsville, AL, June 16-18, 1986.

44. Burrows, M. C. and A. P. Kurkov: Analytical and Experimental Study of Supersonic Combustion of Hydrogen in a Vitiated Airstream, NASA Report TM-X-2828, 1973.

45. Kamath: Parabolized Navier-Stokes Algorithm for Chemically Reacting Flows, AIAA Paper 89-0386, 27th Aerospace Sciences Meeting, Reno, NV, January 9-12, 1989.

46. Vigneron, Y. C., J. V. Rakich, and J. C. Tannehill: Calculations of Supersonic Viscous Flows over Delta Wings, AIAA Paper No. 78-1137. Seattle, WA, July 1978.

47. Varma, A. K., A. U. Chatwani, and F. V. Bracco: Studies of Premixed Laminar Hydrogen-Air Flames Using Elementary and Global Kinetics Models, Combustion and Flame, Vol. 64, 1986, pp. 233-236.

48. Magnussen, B. F. and B. W. Hjertager: On the Mathematical Modeling of Turbulent Combustion With Special Emphasis on Soot Formation and Combustion, Sixteenth Symposium (International) on Combustion, The Combustion Institute, 1976, pp. 719-729.

49. Slack M. and A. Grillo: Investigation of Hydrogen-Air Ignition Sensitized by Nitric Oxide and by Nitrogen Dioxide, NASA CR-2896, October 1977.

50. Evans, J. S., C. J. Schexnayder and H. L. Beach, Jr.: Application of a Two-Dimensional Parabolic Computer Program to Prediction of Turbulent Reacting Flows, NASA Technical Paper 1169, March 1978.

51. Edelman, R.: Diffusion Controlled Combustion for Scramjet Application, Part I, Analysis and Results of Calculations, GASL TR 569, December 1965.

TABLE 1
SUMMARY OF MIXING AND COMBUSTION TESTS

RUN NO.	PTO (psia)	WA (lb/sec)	WO2 (lb/sec)	WH2 (lb/sec)	TTO (R)	TT2 (R)	P2u (psia)	P2L (psia)	WINJ (lb/sec)	ER	MEASURINGSTATION DSO	CARS
INITIAL CONDITIONS												
9	176.64	7.482	0.846	0.070	1977	1915	5.81	5.10	0	0	1	ND
11	175.66	5.417	1.244	0.105	2955	2833	6.38	5.27	0	0	1	ND
12	174.67	5.417	1.244	0.105	2921	2801	6.45	5.39	0	0	1	ND
14	188.03	5.160	1.538	0.126	3310	3174	7.32	5.84	0	0	1	ND
23	179.99	4.129	1.738	0.149	3865	3679	6.44	5.02	0	0	1	ND
36	151.98	4.247	1.318	0.107	3128	2966	4.44	5.13	0	0	1	1
37	151.98	4.254	1.302	0.106	3140	2964	5.18	5.63	0	0	1	1
38	151.15	4.274	1.340	0.104	3048	2882	5.02	5.50	0	0	1	1
39	152.23	4.300	1.318	0.106	3083	2903	5.26	5.66	0.0827	0.49	1	1
40	150.68	4.307	1.330	0.104	2992	2814	5.00	5.62	0	0	1	1
42	174.20	4.165	1.730	0.147	3566	3360	6.19	6.37	0	0	1	1
43	174.68	4.146	1.767	0.148	3584	3368	6.21	6.44	0.884	0.49	1	1
FREE SHEAR-LAYER TESTS												
44	152.07	6.571	0.736	0.059	1869	1789	4.86	4.83	.1091	.5021	3	3
45	150.98	6.624	0.753	0.058	1822	1742	4.61	4.81	.1186	.5446	3	3
46	148.49	6.643	0.760	0.059	1770	1698	4.84	4.85	.2201	1.0024	3	3
47	149.83	6.523	0.738	0.059	1776	1696	4.66	4.78	.1029	.4688	3	3
48	148.63	6.669	0.744	0.057	1728	1654	4.66	4.7[illegible]	.1915	.8863	3	3
49	149.41	4.254	1.313	0.104	3027	2847	4.48	4.84	.0739	.4417	3	3
50	149.92	4.225	1.299	0.104	3094	2914	5.10	5.38	.1575	.9486	3	3
52	152.05	3.640	1.483	0.132	3743	3497	5.30	5.77	.0671	.4329	3	3
53	149.59	3.577	1.487	0.129	3717	3479	5.25	5.74	.1298	.8473	3	3
54	159.20	3.656	1.538	0.130	3849	3601	5.52	6.12	.0671	.4272	3	3
55	157.63	3.552	1.525	0.131	3934	3718	5.49	6.10	.1698	1.1052	3	3
57	150.44	6.622	0.747	0.058	1838	1760	4.58	5.13	.1161	.5299	2	2
58	149.66	6.580	0.749	0.058	1844	1760	4.86	5.09	.1139	.5227	2	2
59	149.69	6.582	0.747	0.058	1828	1750	4.88	5.11	.2131	.9779	2	2
61	156.14	4.365	1.373	0.106	3113	2949	5.20	5.78	.0860	.4988	2	2

TABLE 1 (CONTINUED)

RUN NO.	PTO (psia)	WA (lb/sec)	WC2 (lb/sec)	WH2 (lb/sec)	TTO (R)	TT2 (R)	P2u (psia)	P2L (psia)	WINJ (lb/sec)	ER	MEASURINGSTATION DSO	
CARS												
FREE SHEAR-LAYER TESTS												
62	156.73	4.355	1.349	0.107	3173	3045	6.84	5.84	.1742	1.0162	2	2
63	158.96	3.632	1.530	0.130	3900	3712	5.26	6.09	.0802	.5137	2	2
64	158.83	3.570	1.539	0.130	3932	3754	5.47	6.08	.1463	.9466	2	2
65	154.05	4.230	1.321	0.105	3234	3074	6.23	5.76	.0829	.4968	2	2
66	158.40	3.677	1.514	0.128	3834	3654	5.15	5.66	.0822	.4926	2	2
69	154.09	3.549	1.459	0.125	3935	3707	5.43	5.76	.1528	1.0091	2	2
70	157.02	3.620	1.460	0.128	3951	3727	5.52	5.71	NITR		2	2
71	155.57	3.581	1.466	0.128	3941	3751	5.47	5.51	.1626	1.0651	2	2
72	155.93	3.602	1.482	0.126	3923	3707	5.49	5.49	.1598	1.0397	2	2
74	156.48	3.609	1.536	0.126	3890	3708	5.45	5.53	.1623	1.0667	2	2
77	157.48	3.114	1.692	0.145	4169	3957	5.55	5.72	.1116	.7641	2	2
78	155.46	3.584	1.471	0 130	3930	3740	ATM	5.62	.1565	1.0362	2	2
81	154.75	3.547	1.474	0.128	3940	3750	5.43	5.62	.0814	.5359	2	2
82	152.37	3.512	1.461	0.124	3918	3734	5.47	5.54	.0804	.5347	2	2
84	152.98	3.537	1.465	0.125	3911	3731	5.48	5.57	.1704	1.1266	2	2
88	154.22	3.591	1.438	0.1275	3919	3739	5.54	5.92	.1670	1.0978	3	3
89	153.91	3.559	1.434	0.1262	3914	3761	5.54	5.92	.1474	.9760	3	3
90	153.50	3.552	1.420	0.1260	3947	3767	5.53	5.90	.1561	1.0080	3	3
92	153.59	3.532	1.502	0.1266	3901	3717	5.56	5.89	.1722	1.1311	3	3
93	154.25	3.549	1.481	0.1269	3921	3714	5.57	5.92	.0785	.5160	3	3
94	154.17	3.534	1.487	0.1260	3925	3745	5.57	5.92	.1638	1.0786	3	3
95	148.03	6.374	0.698	0.0578	1927	1855	5.00	5.07	.2250	1.0697	3	3
96	149.05	6.315	0.708	0.0588	1979	1903	5.02	5.08	.1063	.5088	3	3
97	150.54	6.477	0.730	0.0592	1919	1851	5.07	5.12	.2225	1.0465	3	
ND												
99	147.85	6.430	0.705	0.0583	1889	1821	5.01	5.06	.0986	.4646	3	
ND												
100	146.00	6.361	0.702	0.0570	1881	1811	4.93	4.98	.2275	1.0831	3	
ND												
101	146.79	6.375	0.717	0.0574	1885	1817	4.96	5.00	.2252	1.0678	3	
ND												

TABLE 1 (CONCLUDED)

RUN NO.	PTO (psia)	WA (lb/sec)	WO2 (lb/sec)	WH2 (lb/sec)	TTO (R)	TT2 (R)	P2u (psia)	P2L (psia)	WINJ (lb/sec)	ER	MEASURINGSTATION DSO	
CARS												
PRESSURE-GRADIENT TESTS												
102	146.63	6.395	0.717	0.0574	1871	1799	4.36	4.72	.1840	.8699	2	
ND												
103	144.07	6.355	0.722	0.0549	1828	1756	4.67	4.61	.1058	.4989	2	
ND												
104	154.44	3.558	1.451	0.1275	3941	3731	5.59	6.26	.1691	1.1159	2	
ND												
105	153.63	3.537	1.467	0.1260	3925	3727	5.99	6.19	.0398	.2629	2	
ND												
108	153.41	3.523	1.467	0.1260	3931	3751	5.53	6.23	.1539	1.0197	2	
ND												
109	154.44	3.560	1.446	0.1258	3945	3771	5.49	6.46	.1645	1.0840	2	2
110	155.20	3.560	1.479	0.1268	3939	3767	5.53	6.42	.0832	.5456	2	2
111a	154.17	3.513	1.477	0.1264	3949	3777	5.51	6.45	.1644	1.0885	2	2
111b	155.17	3.555	1.488	0.1266	3934	3758	5.96	6.48	.0750	.4918	2	2
112	148.19	6.421	0.711	0.0569	1901	1827	4.79	5.93	.2129	1.0039	2	2
113	147.89	6.385	0.717	0.0574	1909	1835	4.89	5.91	.1098	.5199	2	2
114	147.65	6.339	0.720	0.0578	1924	1848	4.65	5.93	NITR		2	2
121	153.13	3.553	1.482	0.1244	3890	3718	5.11	6.15	.1624	1.0670	2	2
122	152.82	3.534	1.452	0.1245	3920	3748	5.62	6.16	.0843	.5591	2	2
124	146.71	6.510	0.709	0.0560	1822	1754	5.00	5.18	.2114	.9850	3	3
125	144.45	6.449	0.705	0.0542	1800	1728	4.26	5.11	.1114	.5239	3	3
126	154.26	3.554	1.507	0.1254	3899	3713	5.37	6.32	.1646	1.0758	3	3
127	153.67	3.530	1.485	0.1255	3918	3748	5.78	6.42	.0842	.5552	3	3
128	154.57	3.559	1.474	0.1264	3927	3759	5.54	6.37	.2299	1.4196	3	3

TABLE 2
NOMINAL FLOW CONDITIONS FOR MIXING AND COMBUSTION TESTS

A. Low Temperature Case – Mixing Tests
Vitiated Air Heater

Air flowrate, lbm/sec.	6.372
Oxygen flowrate, lbm/sec.	0.670
Hydrogen flowrate, lbm/sec	0.056

Test Section Entrance

Total Temperature, R	1820
Static pressure, psia (avg.)	5.06

B. High Temperature Case – Combustion Tests
Vitiated Air Heater

Air flowrate, lbm/sec	3.560
Oxygen flowrate, lbm/sec.	1.446
Hydrogen flowrate, lbm/sec	0.126

Test Section Entrance

Total Temperature	3720
Static Pressure, psia (avg.)	5.80

TABLE 3
MIXING CONDITIONS

Quantity	$\phi = 1$	$\phi = 0.5$	$\phi = 1$	$\phi = 0.5$
T_{T_2}, R	3720	3720	1820	1820
u_1, ft/sec	5798	5798	3867	3867
u_2, ft/sec	3867	3867	3705	3705
$r = u_2/u_1$	0.667	0.667	0.958	0.958
$s = \rho_2/\rho_1$	0.52	0.26	2.99	5.98
λ_r	0.20	0.20	0.02	0.02
λ_s	0.19	0.19	0.02	0.02
Mc_1	0.380	0.310	0.027	0.030
M_r	0.65	0.65	0.06	0.06
Re/ft, x 10^6	1.45	1.45	3.62	3.62
η_m	0.14	0.32	0.14	0.32
λ	0.349	0.175	0.349	0.175
P_j, psia	8.72	4.36	12.4	6.2
$\bar{P}_{P_j}/\bar{P}_{t_\infty}$	0.120	0.060	0.150	0.075

λ_r = velocity parameter = $(1-r)/(1+r)$

λ_s = velocity-density parameter = $(1-r)(1+s^{1/2})/2(1 + rs^{1/2})$

Mc_1 = Primary convective Mach number = $(u_1-u_2)/a_1$

M_r = Relative Mach number = $(u_1-u_2)/\bar{a}$

Re = Reynolds number of vitiated airstream

η_m = Mixing efficiency (see text)

λ = jet-to-airstream mass flux ratio

TABLE 4
SHEAR-LAYER GROWTH RATES

Test Condition	Total Temp., R.	Equiv. Ratio	Growth Rate, db/dx		Spreading Angle, β	
			Station 2	Station 3	Station 2	Station 3
Free Shear Layer	3720	0.5	0.086	0.050	4.9	2.9
	3720	1.0	0.085	0.051	4.9	2.9
	1820	0.5	0.074	0.063	4.2	3.6
	1820	1.0	(0.107)*	0.058	(6.1)*	3.3
Pressure Gradient	3720	0.5	0.073	0.053	4.2	3.0
	3720	1.0	0.071	0.056	4.1	3.2
	1820	0.5	0.059	0.039	3.4	2.2
	1820	1.0	0.063	0.038	3.6	2.2

* Based on single data point, questionable.

TABLE 5
SUMMARY OF MIXING–LAYER GROWTH RATES

Measuring Station 2 Growth Rate, $d\ell/dx$ Based on:							
Test Condition	Total Temp., R.	Equiv. Ratio	P_p	T_T	XH_2	T	XH_2O
Free Shear Layer	3720	0.5	0.144	0.116	0.137	0.165	0.127
	3720	1.0	0.137	0.100	0.130	0.143	0.127
	1820	0.5	0.140	0.133	0.150	–	–
	1820	1.0	0.176	0.144	0.180	–	–
Pressure Gradient	3720	0.5	0.142	0.113	0.143	0.141	0.190
	3720	1.0	0.156	0.114	0.143	0.173	0.157
	1820	0.5	0.145	0.140	0.127	–	–
	1820	1.0	0.144	0.132	0.127	–	–

Measuring Station 3 Growth Rate, $d\ell/dx$ Based on:							
Test Condition	Total Temp., R.	Equiv. Ratio	P_p	T_T	XH_2	T	XH_2O
Free Shear Layer	3720	0.5	0.082	0.073	0.069	0.100	0.091
	3720	1.0	0.089	0.079	0.074	0.104	0.091
	1820	0.5	0.105	0.093	0.073	–	–
	1820	1.0	0.106	0.091	0.078	–	–
Pressure Gradient	3720	0.5	0.113	0.072	0.087	0.086	0.100
	3720	1.0	0.121	0.070	0.069	0.078	0.091
	1820	0.5	0.084	0.095	0.082	–	–
	1820	1.0	0.088	0.095	0.082	–	–

TABLE 6. SUMMARY OF FLOW SIMULATIONS

Case	Type	Geometry	Eq. Ratio
AFS3A	R	P	0.7
AFS4A	R	P	1.0
AFS5	M	P	0.5
AFS6	M	P	1.0
AFS7	M	W	1.0
AFS8	R	W	1.0

Key: M = mixing case
R = reacting flow case
P = planar
W = shock generator (wedge)

TABLE 7. FLOW CONDITIONS FOR REACTING FLOW CASES

Vitiated Heater	**AFS3A**	**AFS4A**
Air flow rate	3.563	3.618 lbm/sec
Oxygen flow rate	1.525	1.537 lbm/sec
Hydrogen flow rate	0.131	0.130 lbm/sec
Test Section Conditions		
Total temperature	3718	3601 R
Static press. (ave)	5.79	5.82 psia
Fuel Flow Data		
Total temperature	512	516 R
Total pressure	18.09	8.59 psia
Hydrogen flow rate	0.170	0.080 lbm/sec
Equivalence ratio	1.04	0.48
Slot height	0.292	0.292 in.

TABLE 8. FLOW CONDITIONS FOR MIXING CASES

Vitiated Heater	**AFS5**	**AFS6**
Air flow rate	6.632	6.644 lbm/sec
Oxygen flow rate	0.742	0.767 lbm/sec
Hydrogen flow rate	0.062	0.058 lbm/sec
Test Section Conditions		
Total temperature	1789	1698 R
Static press. (ave)	5.00	4.85 psia
Fuel Flow Data		
Total temperature	510	517 R
Total pressure	11.74	23.61 psia
Hydrogen flow rate	0.110	0.220 lbm/sec
Equivalence ratio	0.49	0.95
Slot height	0.292	0.292 in.

TABLE 9. FLOW CONDITIONS SHOCK GENERATOR CASES

Vitiated Heater	**AFS7**	**AFS8**
Air flow rate	6.421	3.553 lbm/sec
Oxygen flow rate	0.711	1.482 lbm/sec
Hydrogen flow rate	0.0569	0.1244 lbm/sec
Test Section Conditions		
Total temperature	1827	3718 R
Static press. (ave)	6.26	5.84 psia
Fuel Flow Data		
Total temperature	543	532 R
Total pressure	23.28	17.70 psia
Hydrogen flow rate	0.212	0.163 lbm/sec
Equivalence ratio	0.97	.099
Slot height	0.292	0.292 in.

TABLE 10. CALCULATED WAVE STRUCTURE FOR FREE SHEAR-LAYER COMBUSTION

using Thermal Compression Analysis

Equivalence Ratio = 1; Mass Flux Ratio = 0.349

REGION	X	Y	MACH NO.	P/P_2	P_t/P_{t2}
1	13.5600	3.0000	2.7500	1.00000	1.00000
2	20.5385	0.0000	2.6384	1.20301	0.99763
3	30.6533	3.9689	2.5330	1.43679	0.99842
4	40.5272	0.0000	2.6083	1.26615	0.99842

TABLE 11. CALCULATED WAVE STRUCTURE FOR SHEAR-LAYER COMBUSTION WITH PRESSURE GRADIENT using Thermal Compression Analysis

Equivalence Ratio = 1; Mass Flux Ratio = 0.349

INTERSECTION POINTS

Intersection	X	Y
1	16.12151	1.89884
2	20.15102	3.60216
3	18.91621	0.87277
4	19.95282	0.36728
5	20.35826	1.45614
6	14.56000	1.00000
7	21.57067	1.29003
8	162.05680	81.41759

FLOW FIELD DATA

Region	Mach No.	P/P_2	P_t/P_{t2}
1	2.75000	1.00000	1.00000
2	2.63835	1.20301	0.99763
3	2.56141	1.36642	0.99589
4	2.45820	1.62518	0.99617
5	2.45676	1.62645	0.99454
6	2.91167	0.76013	0.99589
7	2.79660	0.92142	0.99617
8	2.79509	0.92223	0.99454
9	2.79605	0.92274	0.99670
10	1.18152	1.11234	0.09489
11	2.68422	1.11301	0.99683
12	1.35558	1.35977	0.28624
13	2.45818	1.62522	0.99617

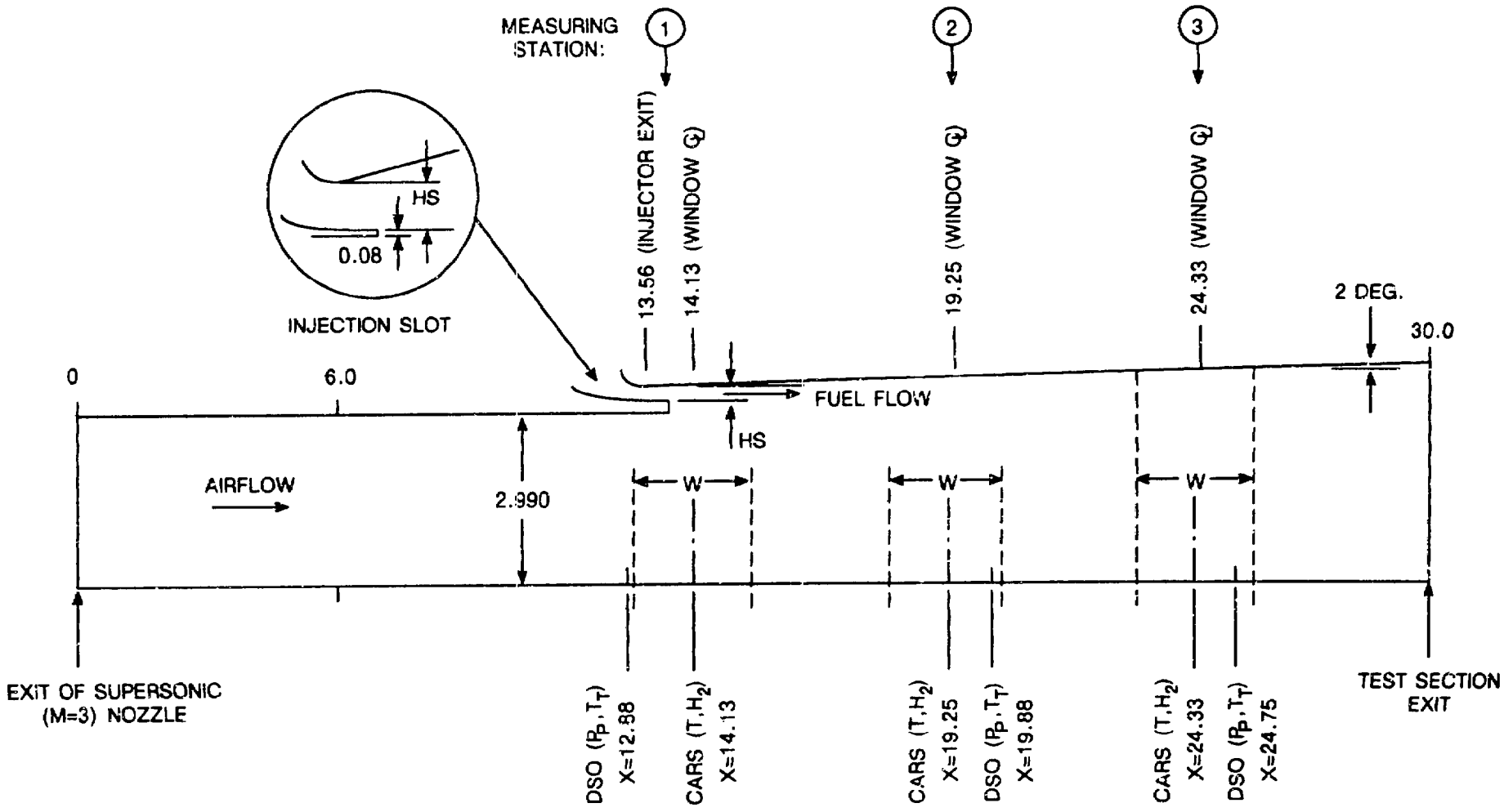

NOTE: ALL DIMENSIONS IN INCHES. X IS DISTANCE FROM EXIT OF SUPERSONIC NOZZLE.

Fig. 1 ***Test section geometric features and measuring station (axial) locations. Test section width = 6 in. window width W = 2 in., slot height HS = 0.292 in.***

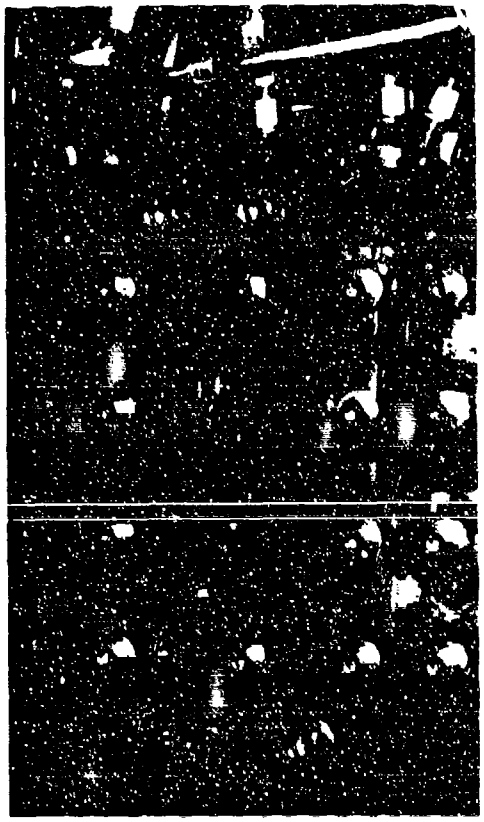

Fig. 2 View through Station 1 window showing fuel injection slot. Flow from left to right.

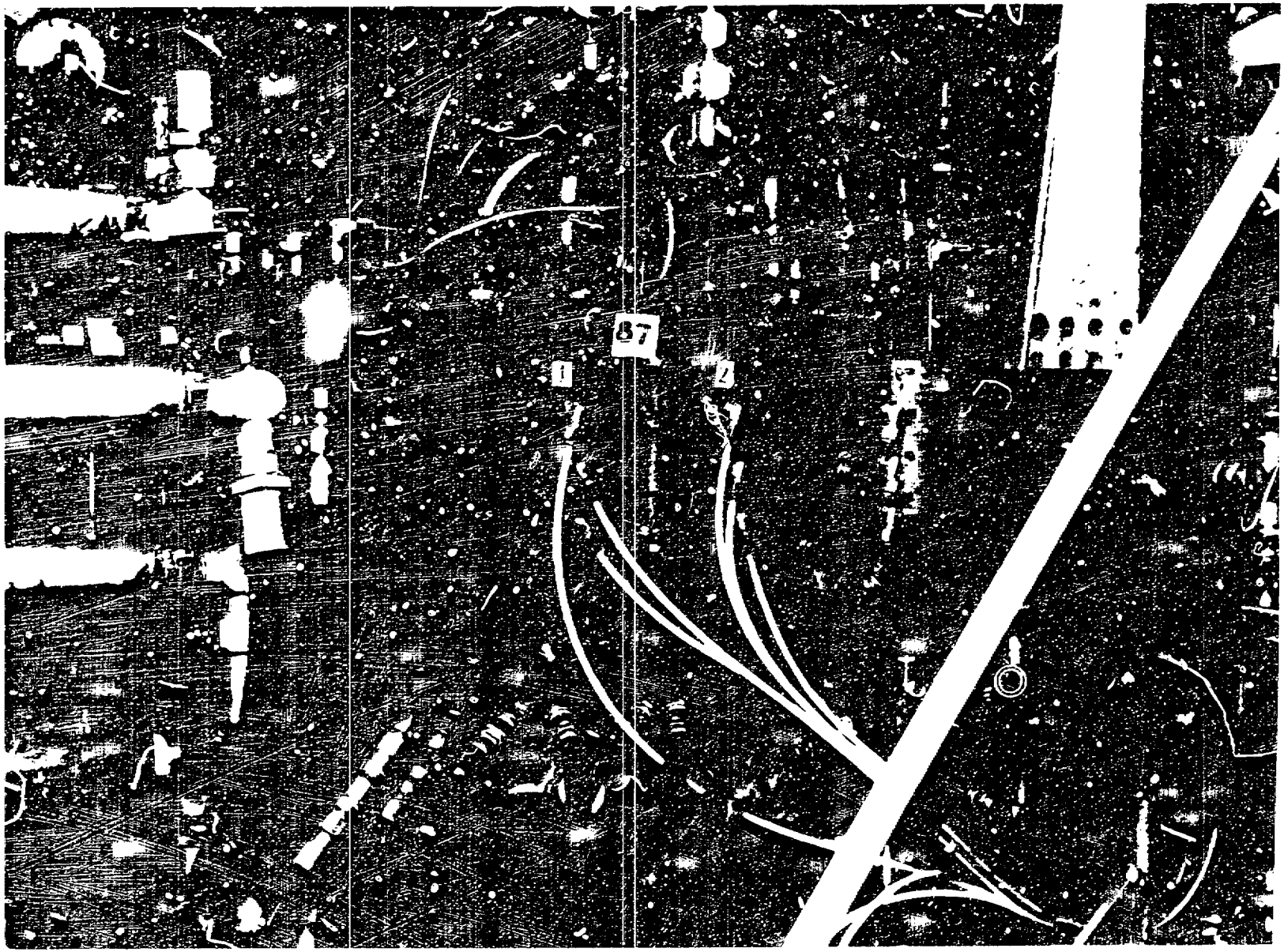

Fig. 3 Supersonic mixing and combustion experiment.

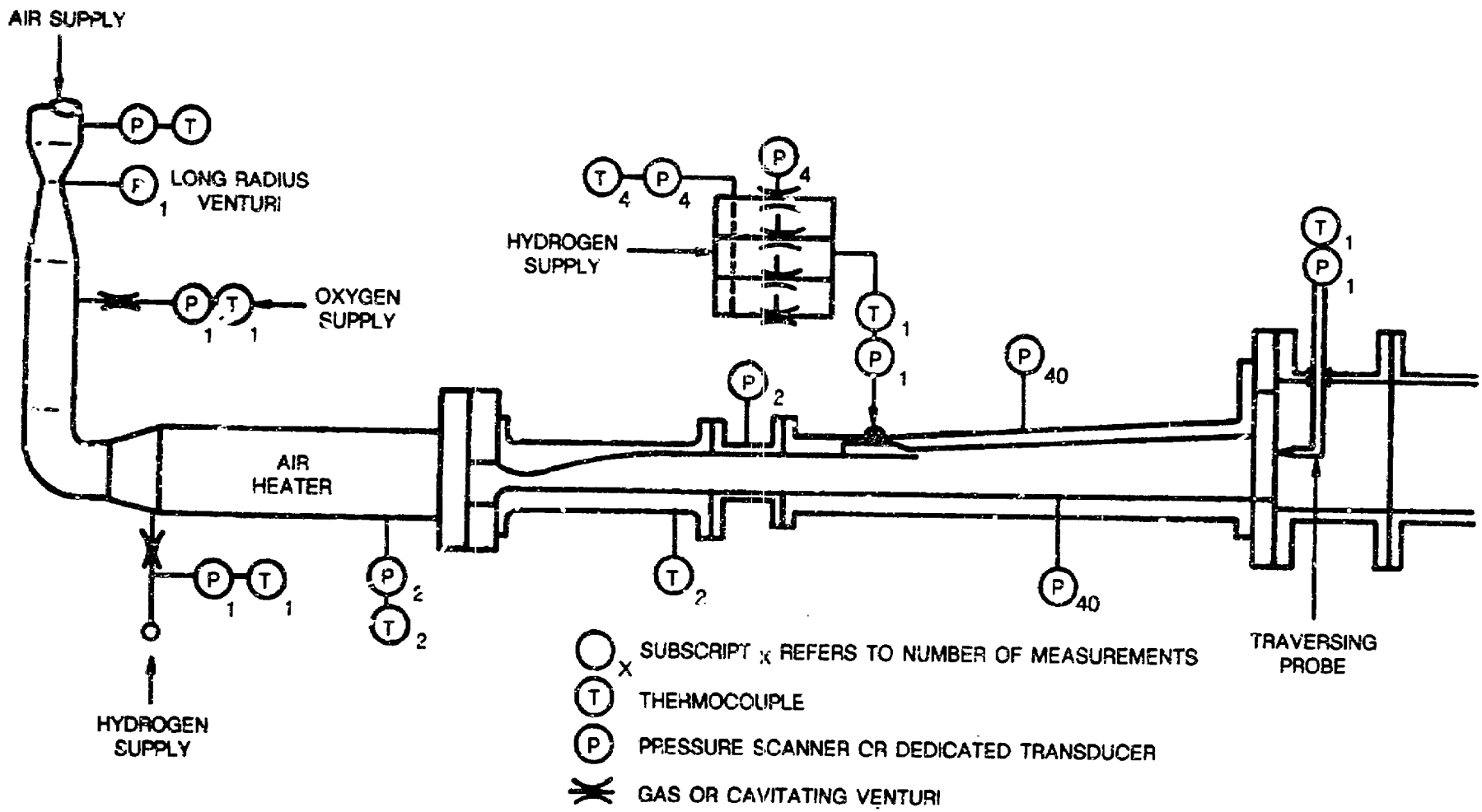

Fig. 4 Hydrogen-fueled scramjet combustor instrumentation.

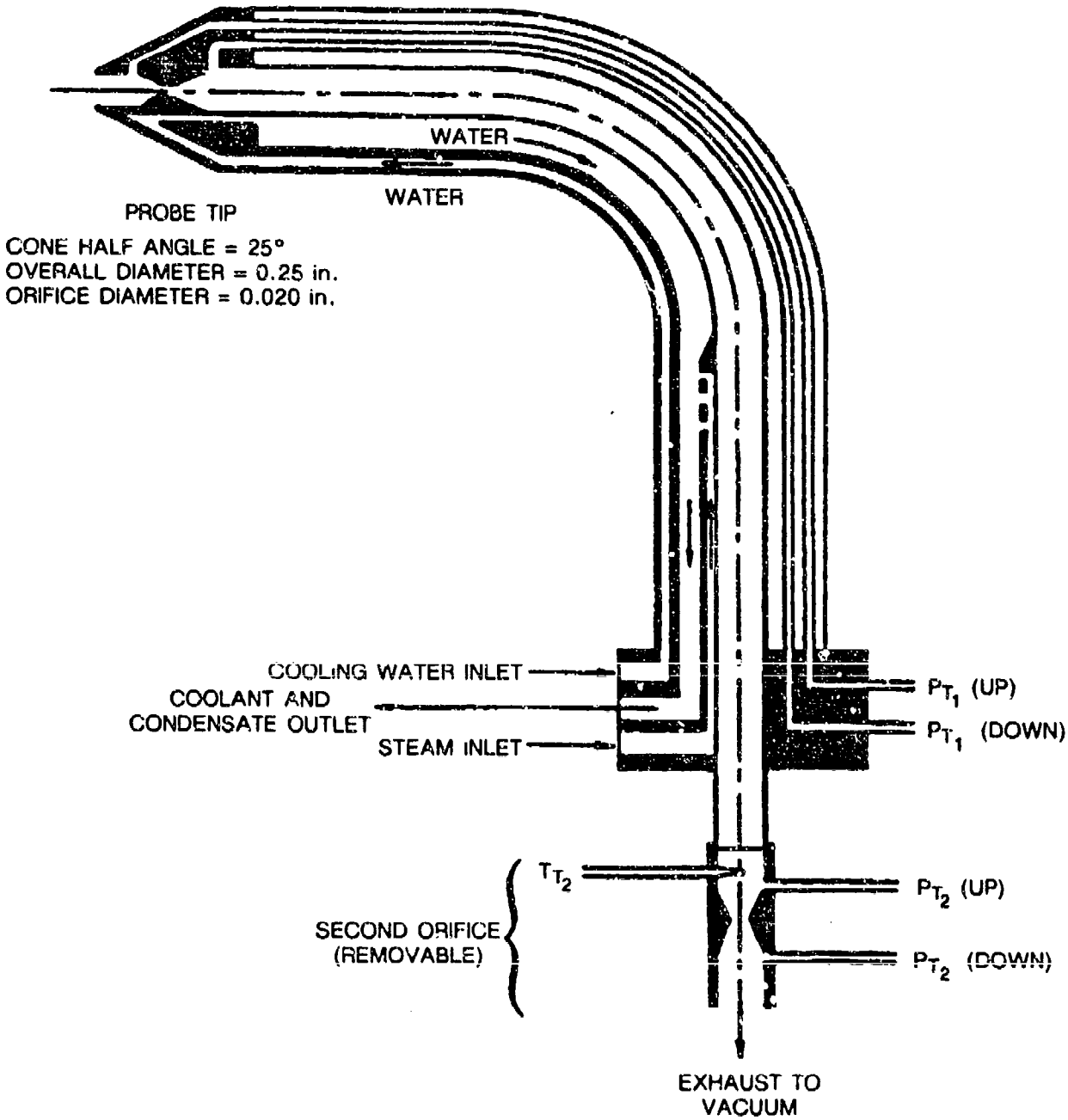

NOTE SUBSCRIPTS SHOWN ON THIS FIGURE REFER TO 1st AND 2nd ORIFICES

Fig. 5 Double sonic orifice probe.

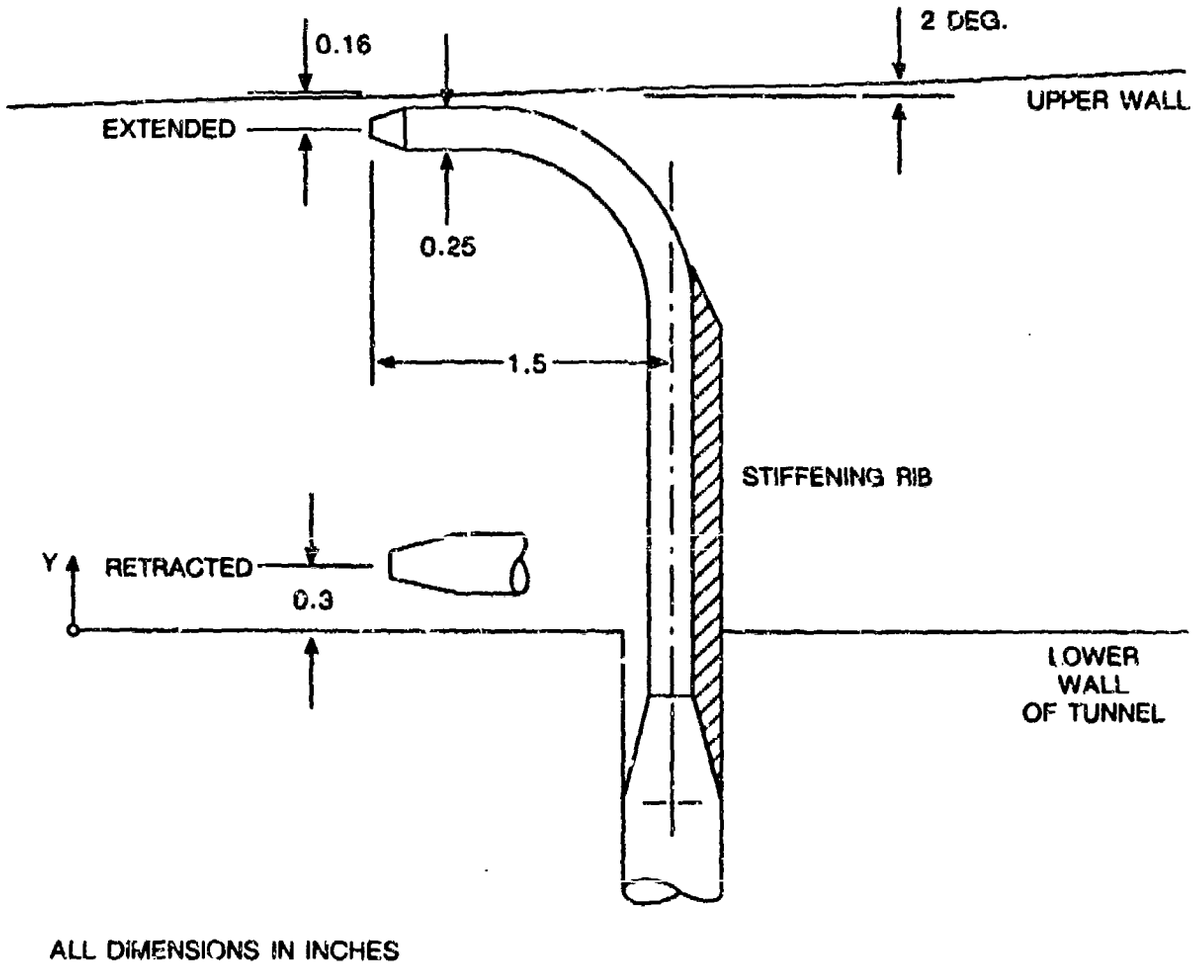

Fig. 6 DSO probe installation.

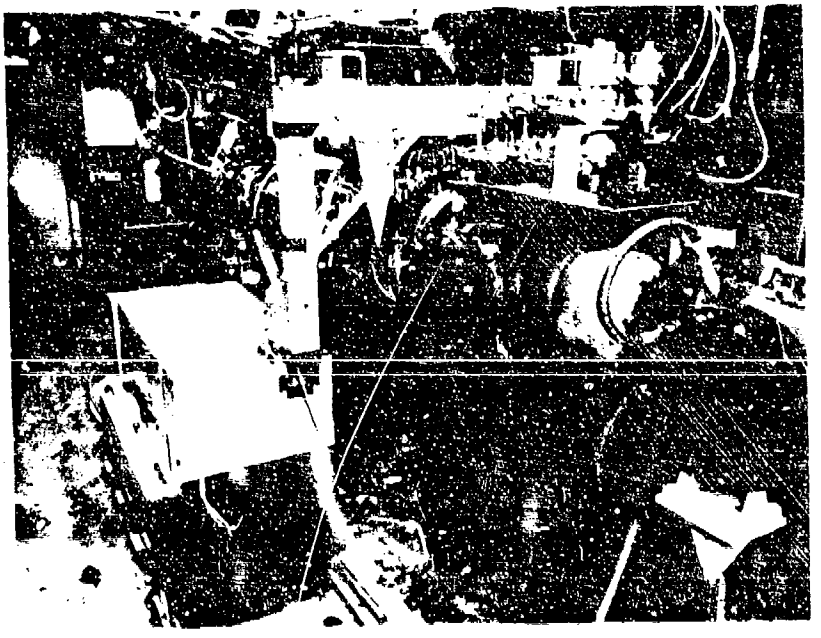

Fig. 7 Mobile CARS apparatus installed around test section.

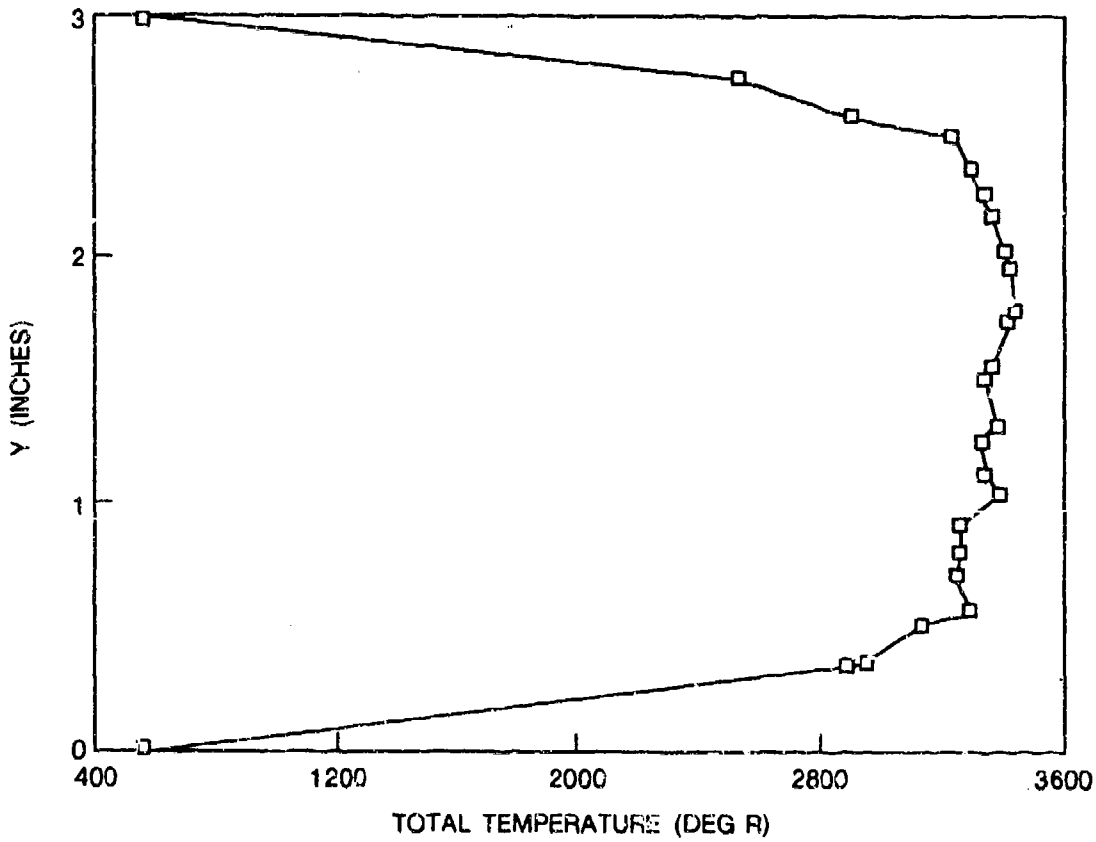

Fig. 8 Initial conditions for high temperature case: total temperature.

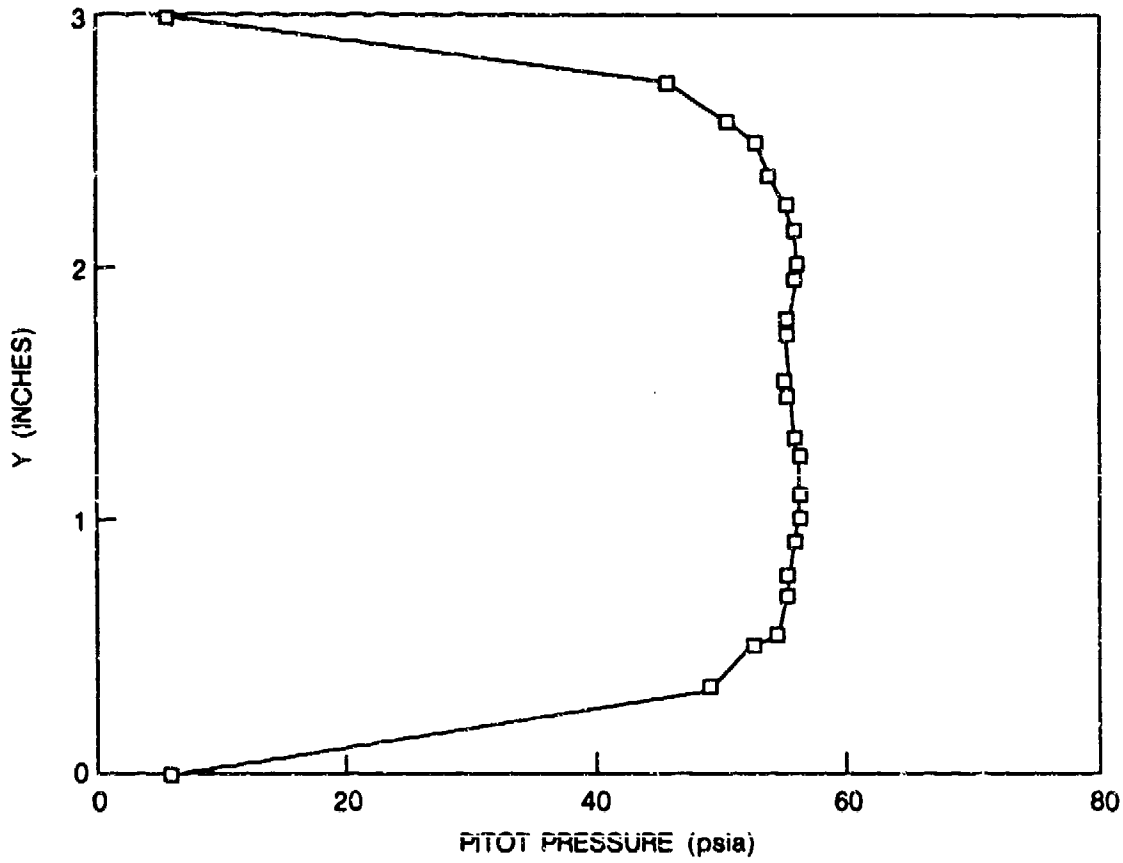

Fig. 9 Initial conditions for high temperature case: pitot pressure.

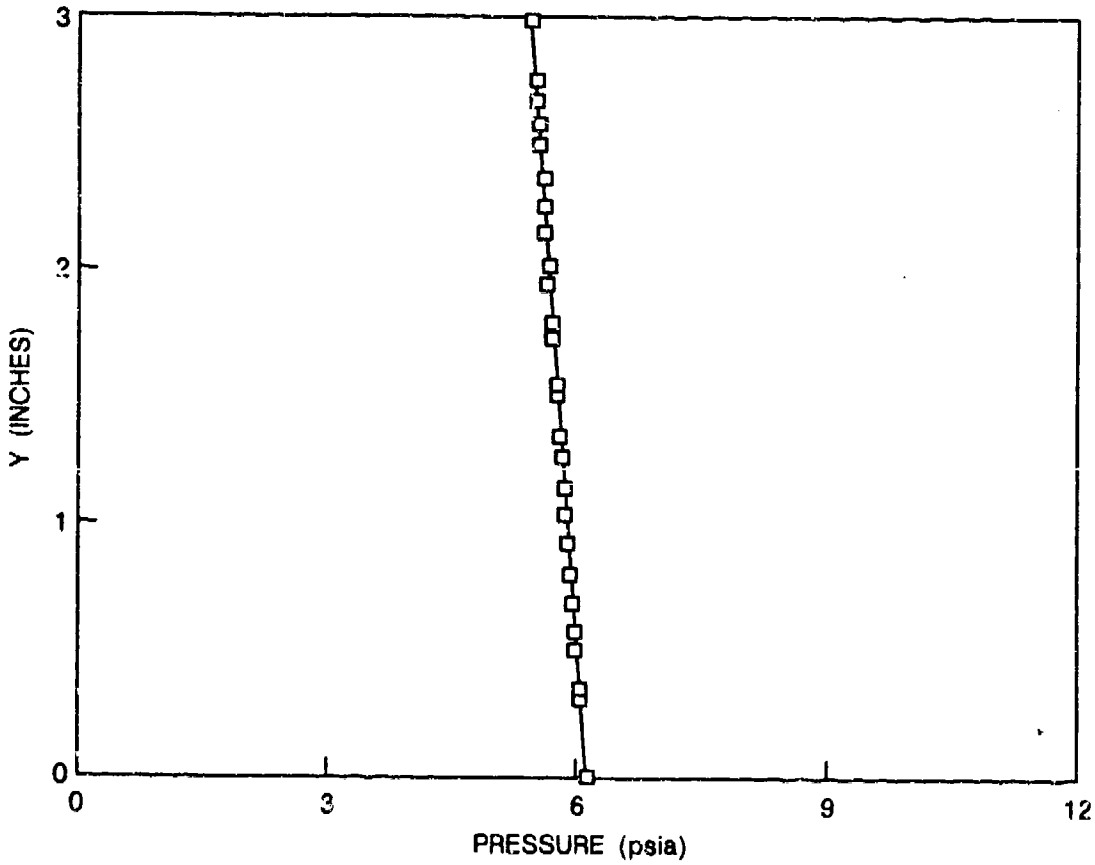

Fig. 10 Initial conditions for high temperature case: static pressure.

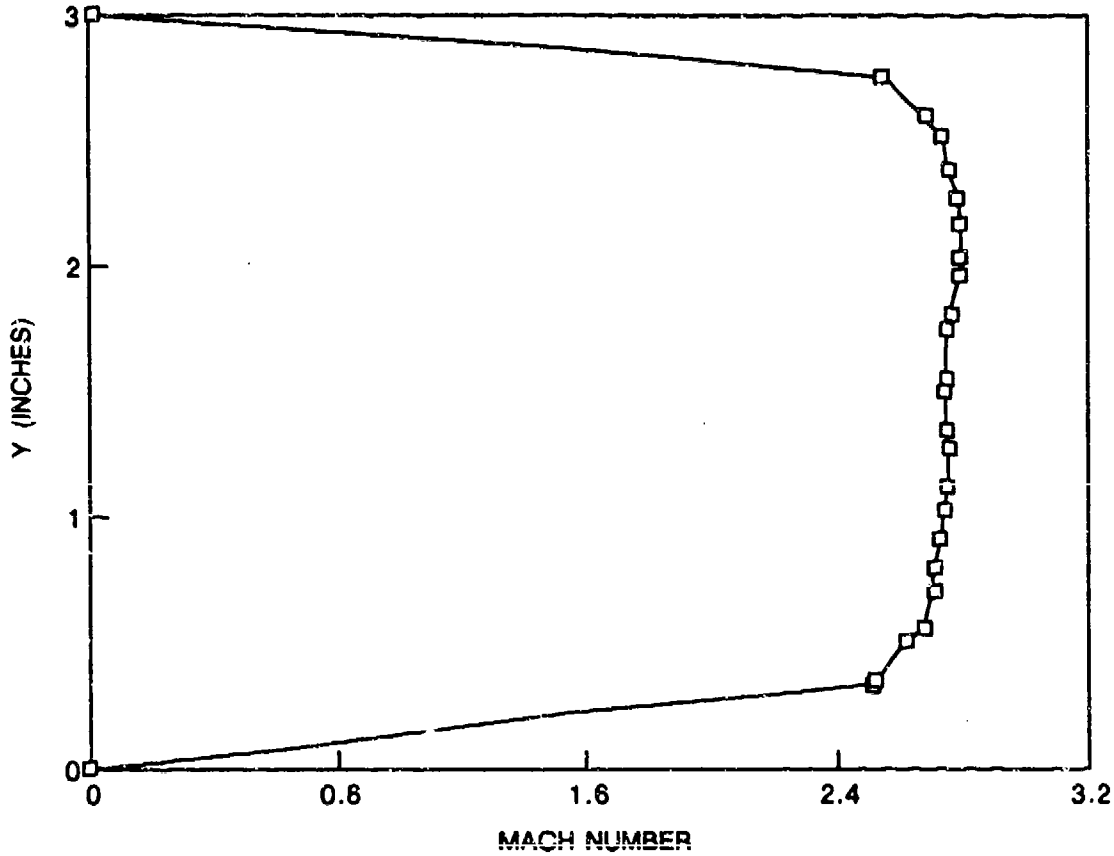

Fig. 11 Initial conditions for high temperature case: Mach number.

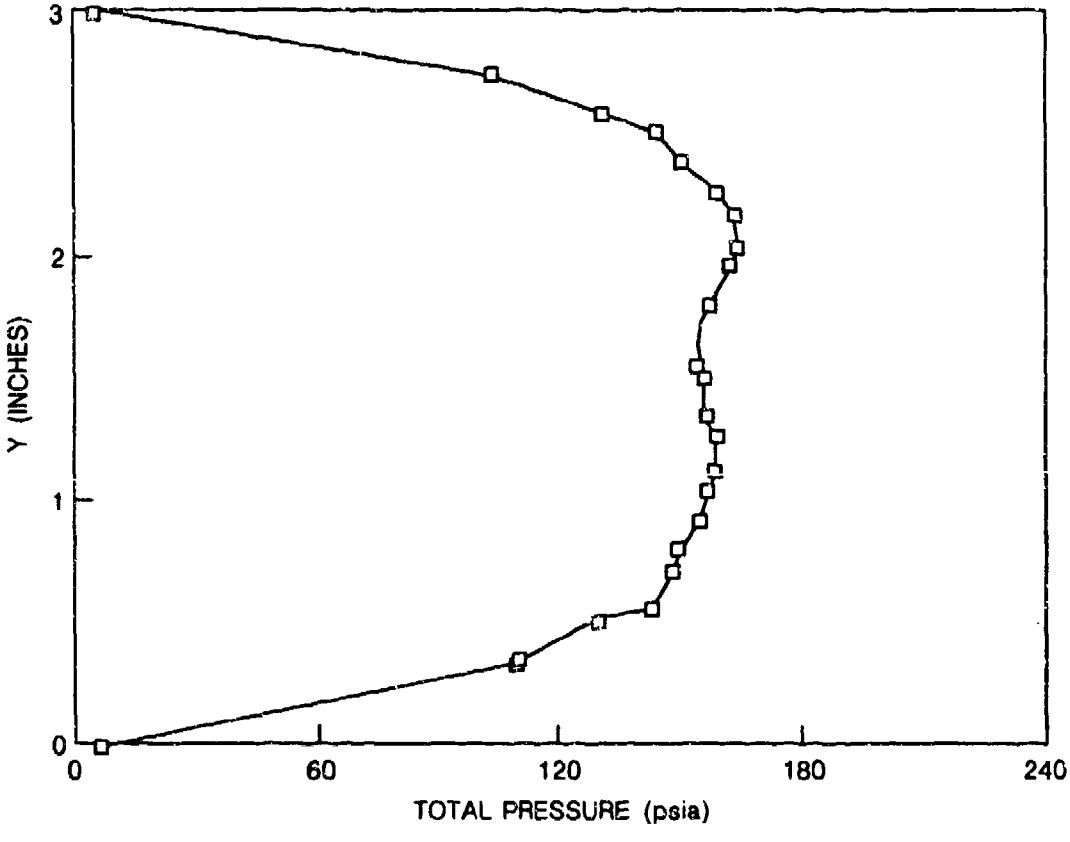

Fig. 12 Initial conditions for high temperature case: total pressure.

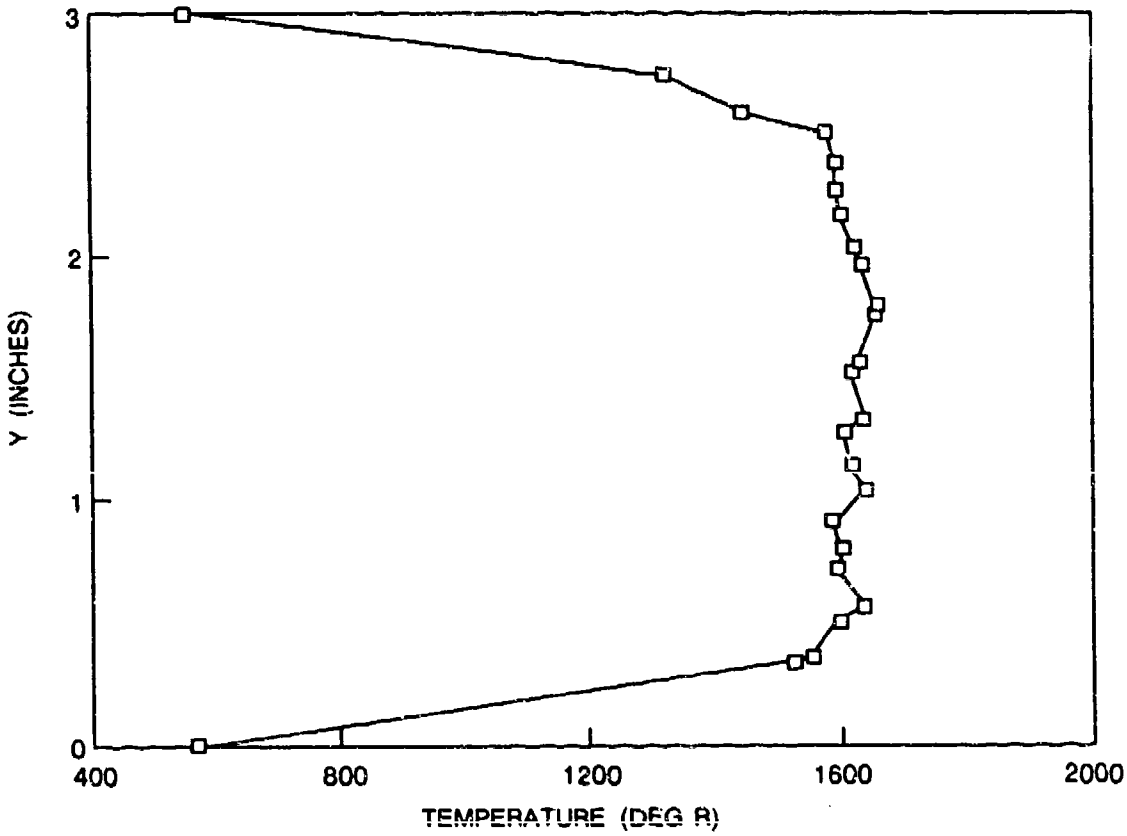

Fig. 13 Initial conditions for high temperature case: static temperature.

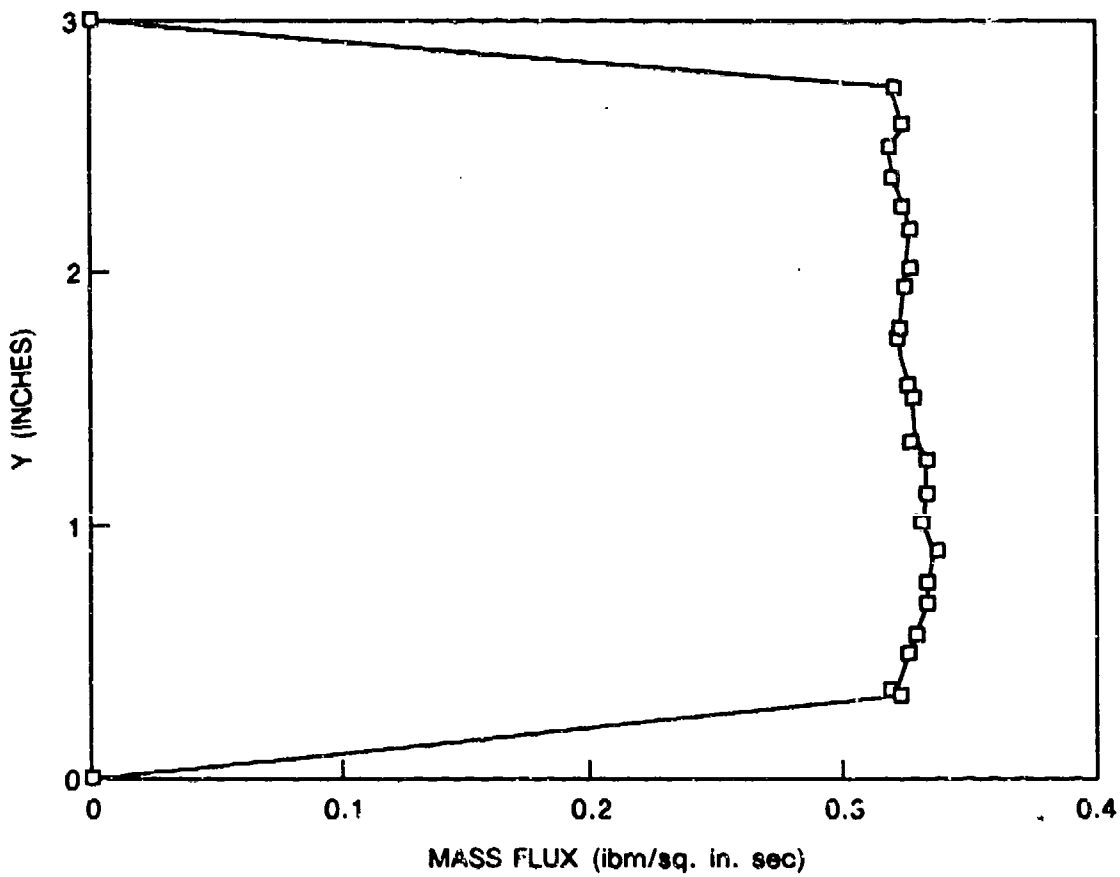

Fig. 14 Initial conditions for high temperature case: mass flux.

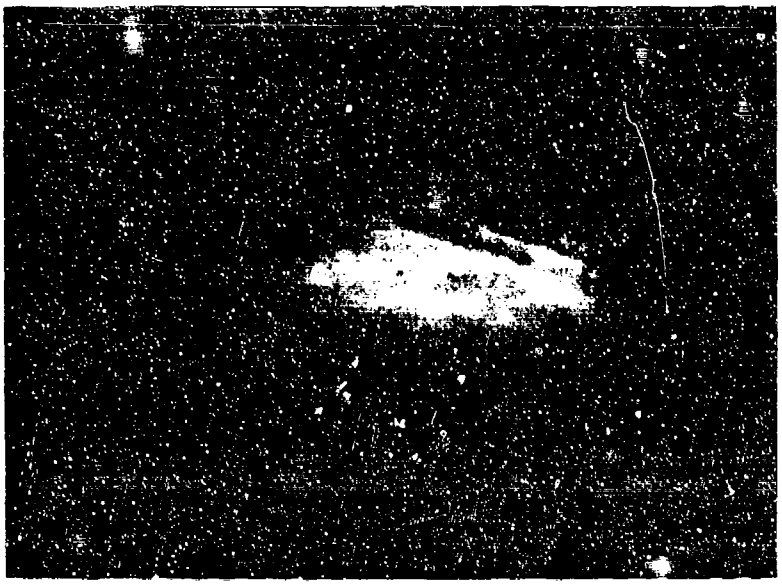

Fig. 15 Shadowgraph Image of Hydrogen Injection at Equivalence Ratio of 1. Air Total Temperature=1800 R.

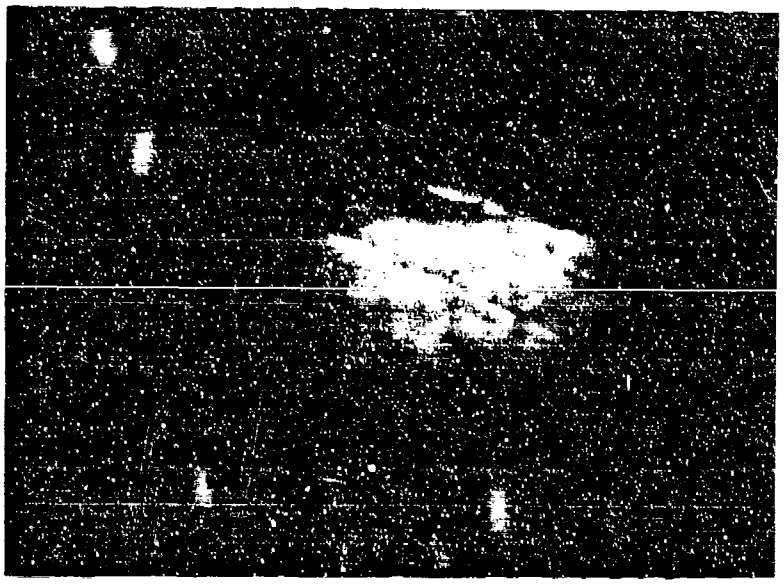

Fig. 16 Shadowgraph Image of Hydrogen Injection at Equivalence Ratio of 0.5. Air Total Temperature=1800 R.

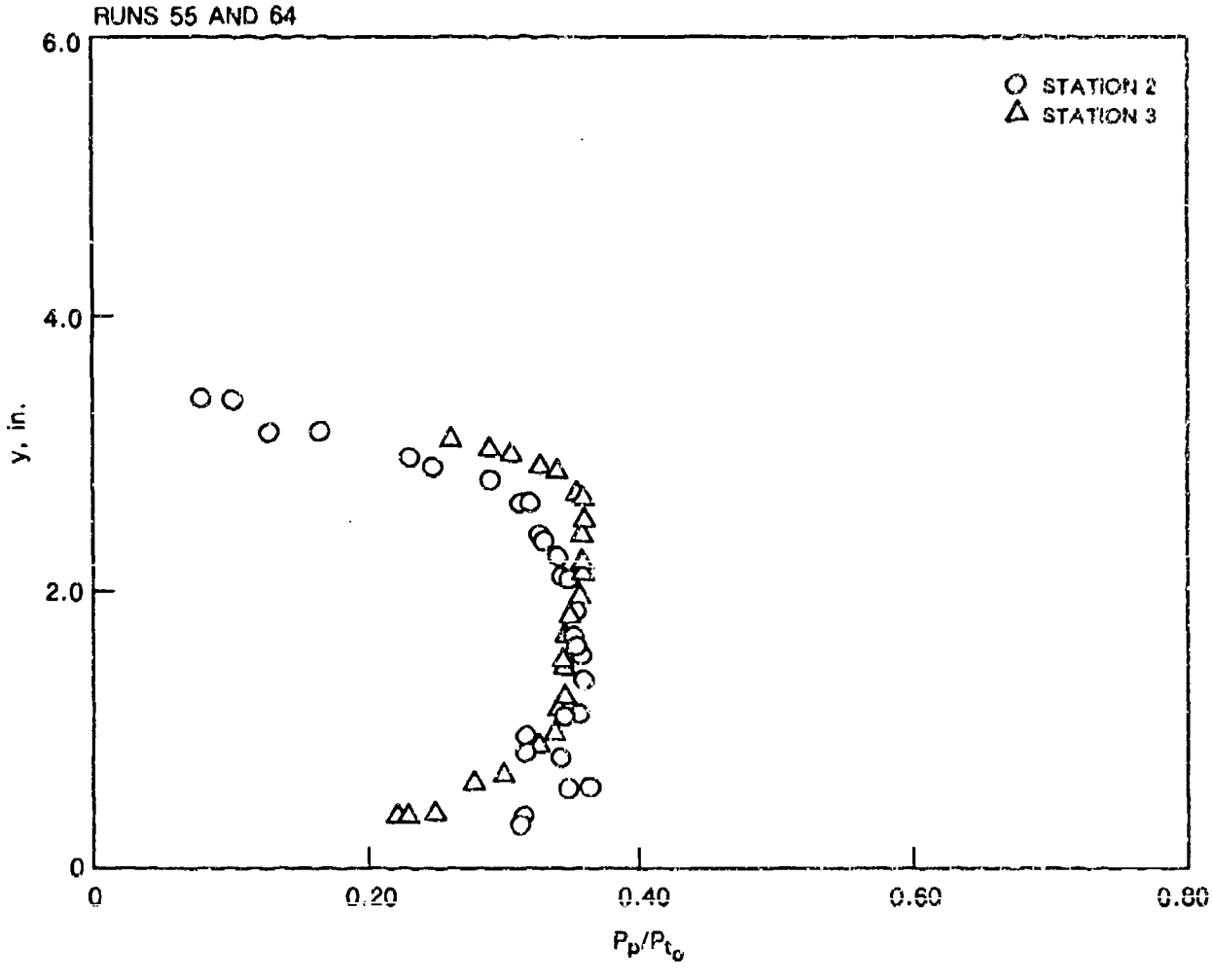

Fig. 17 Pitot pressure profiles from probe measurements at Stations 2 and 3 during combustion tests at an equivalence ratio of 1. Free shear-layer.

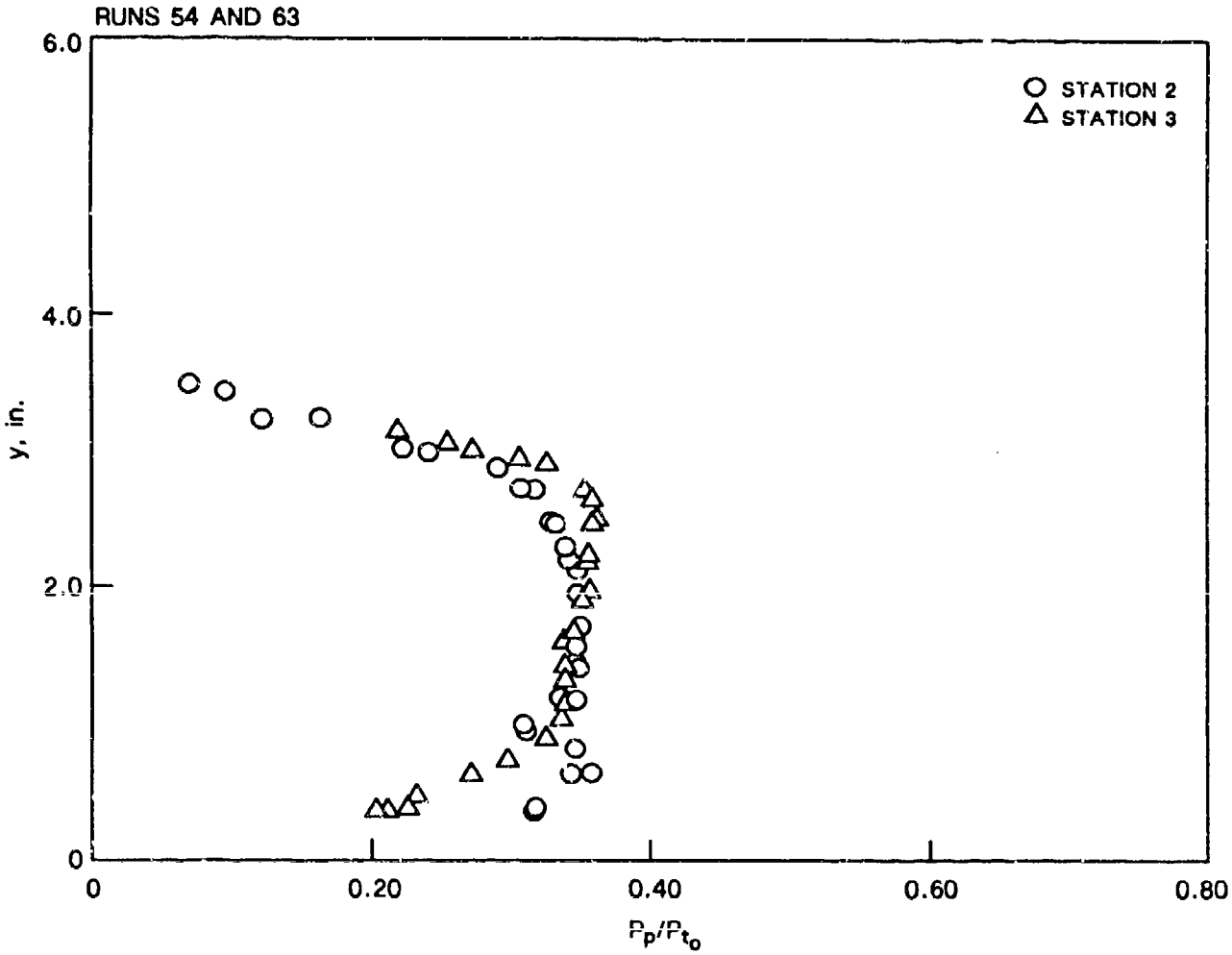

Fig. 18 Pitot pressure profiles from probe measurements at Stations 2 and 3 during combustion tests at an equivalence ratio of 0.5. Free shear-layer.

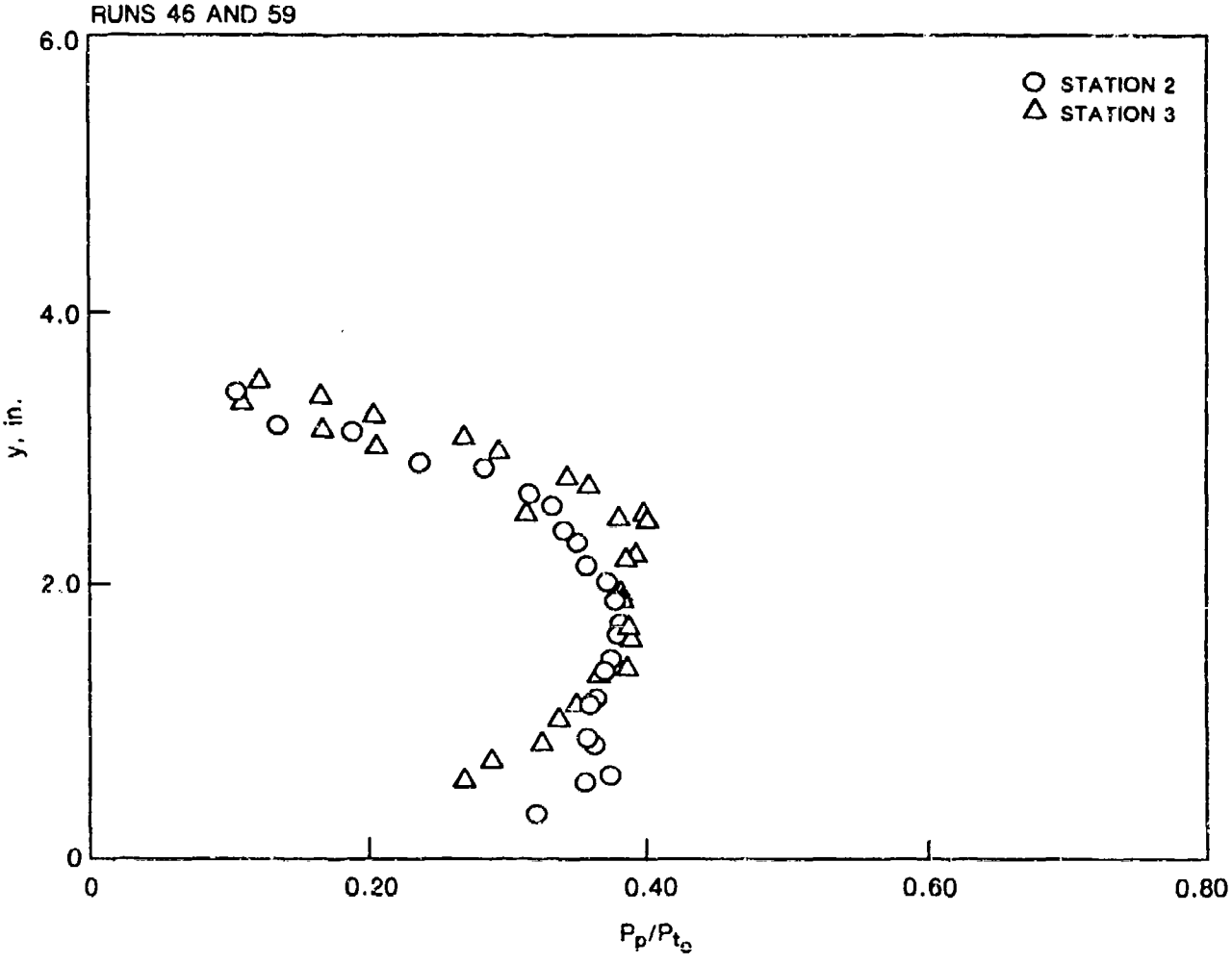

Fig. 19 Pitot pressure profiles from probe measurements at Stations 2 and 3 during non-reacting tests at an equivalence ratio of 1. Free shear-layer.

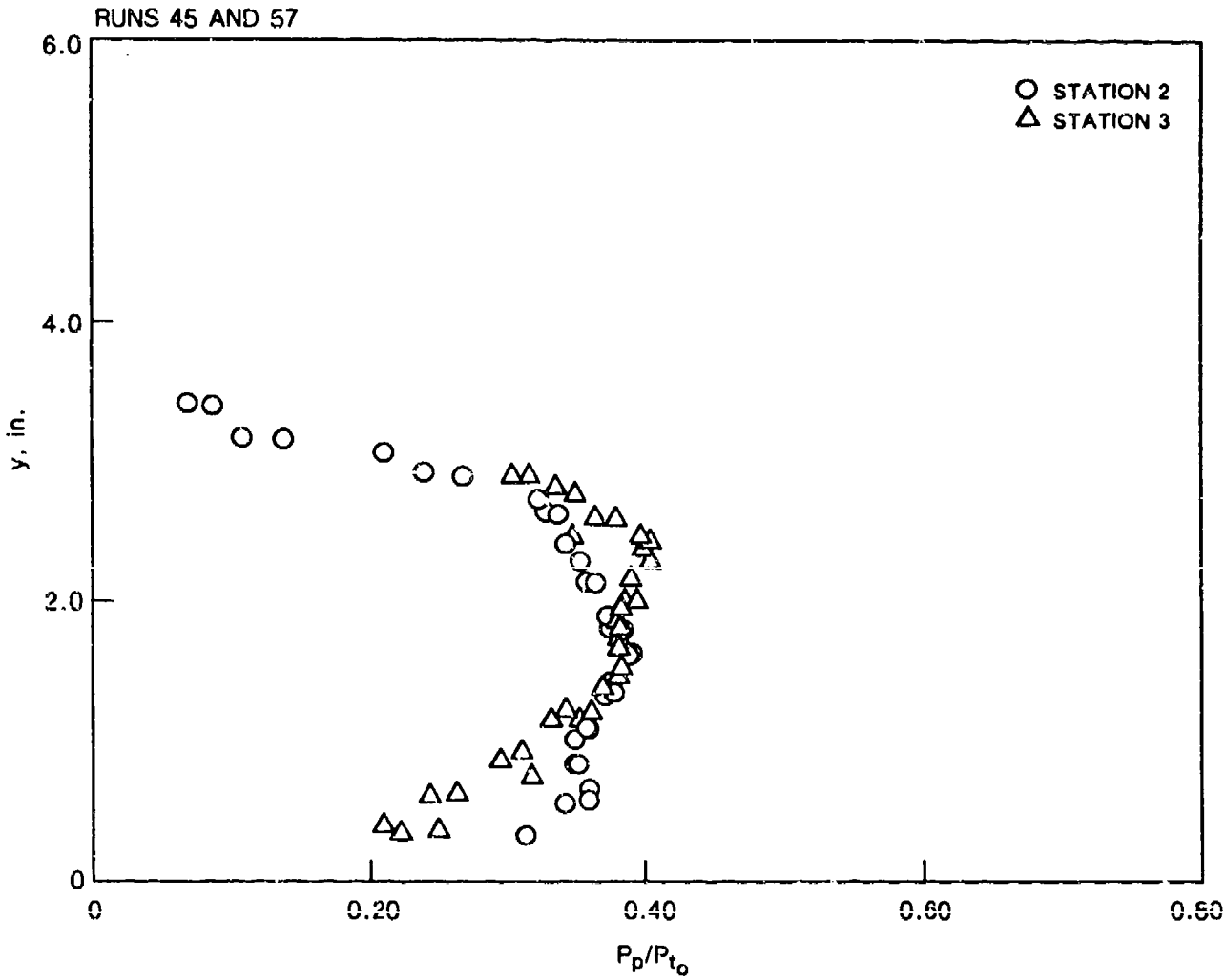

Fig. 20 Pitot pressure profiles from probe measurements at Stations 2 and 3 during non-reacting tests at an equivalence ratio of 0.5. Free shear-layer.

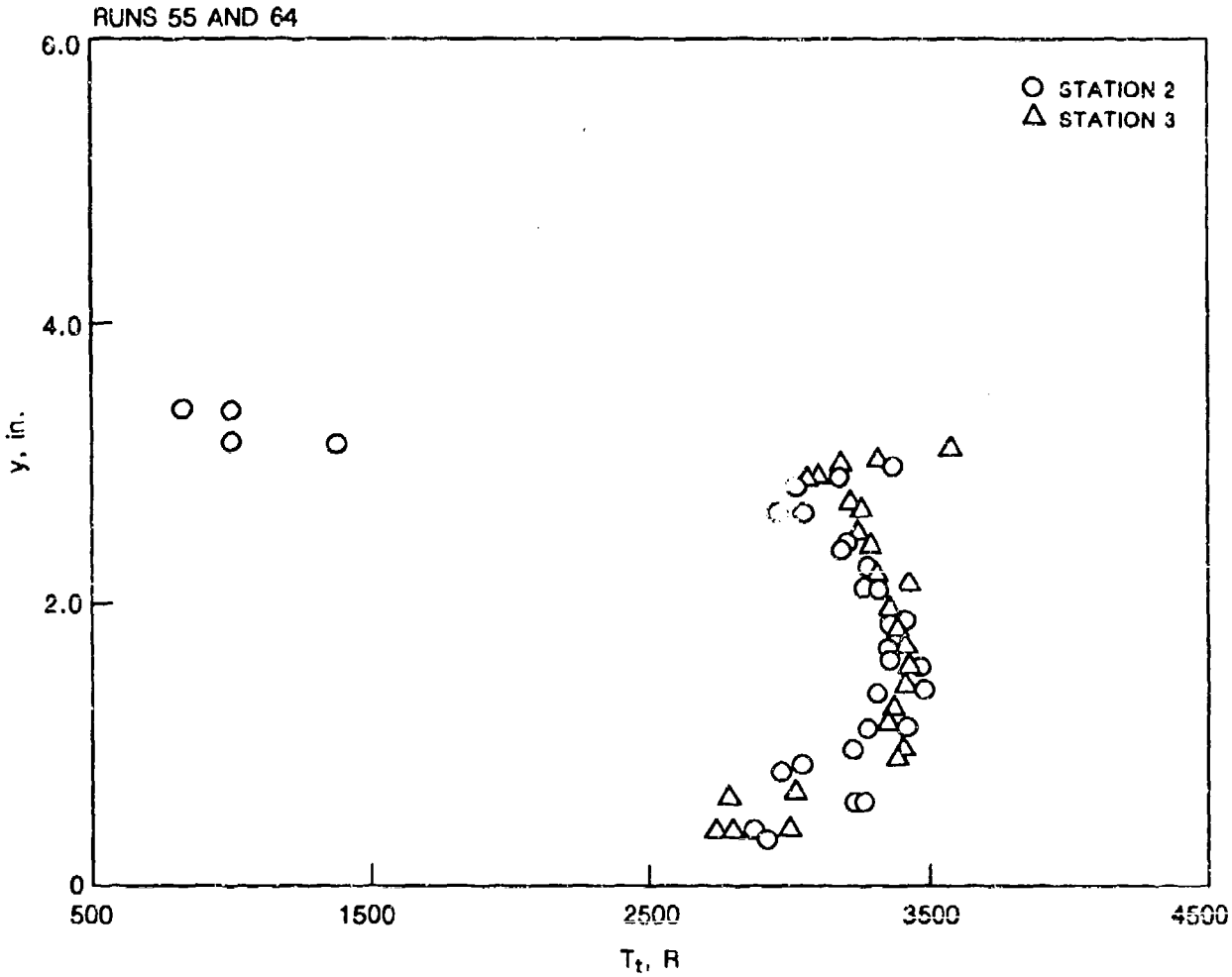

Fig. 21 Total temperature profiles from probe measurements at Stations 2 and 3 during combustion tests at an equivalence ratio of 1. Free shear-layer.

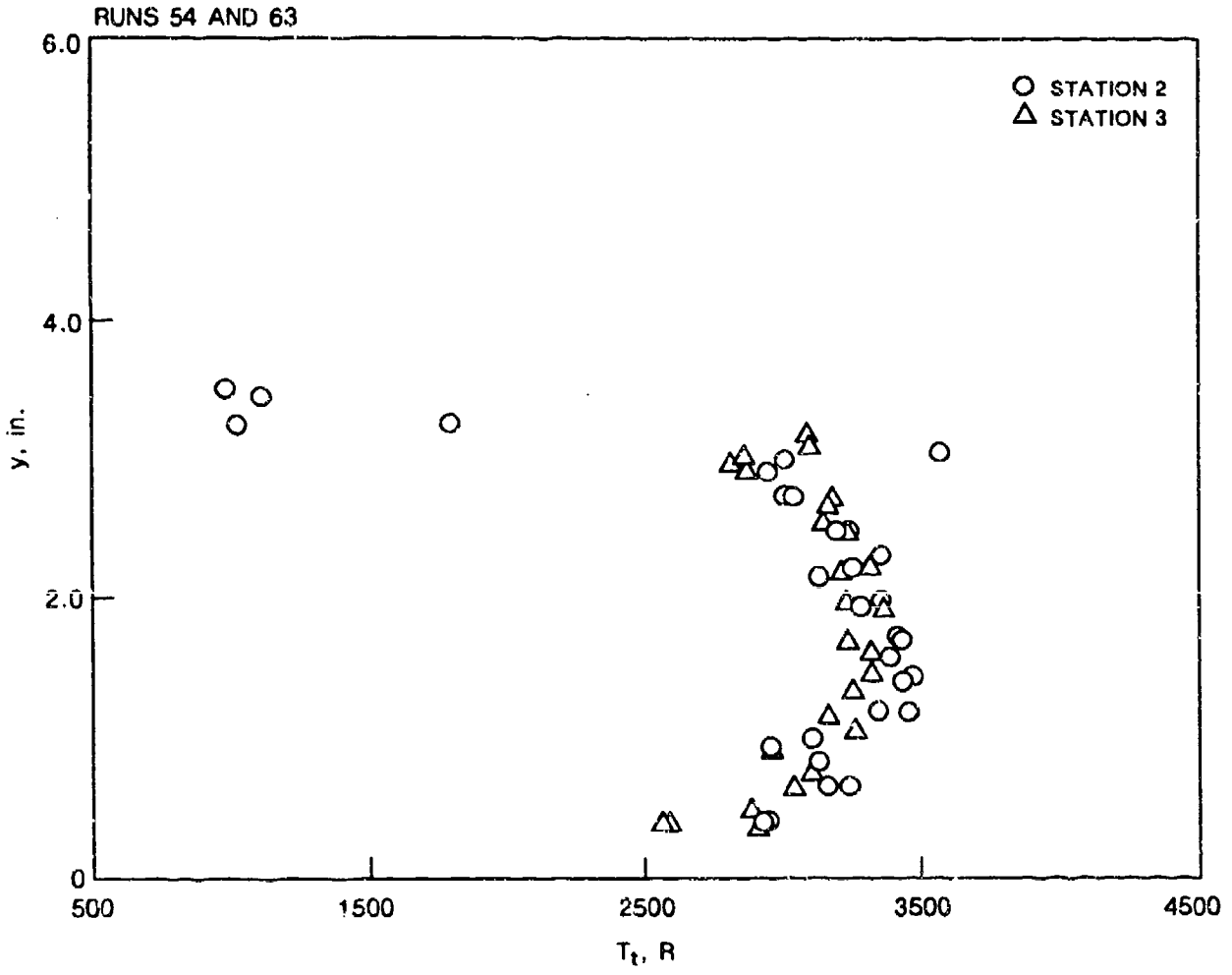

Fig. 22 Total temperature profiles from probe measurements at Stations 2 and 3 during combustion tests at an equivalence ratio of 0.5. Free shear-layer.

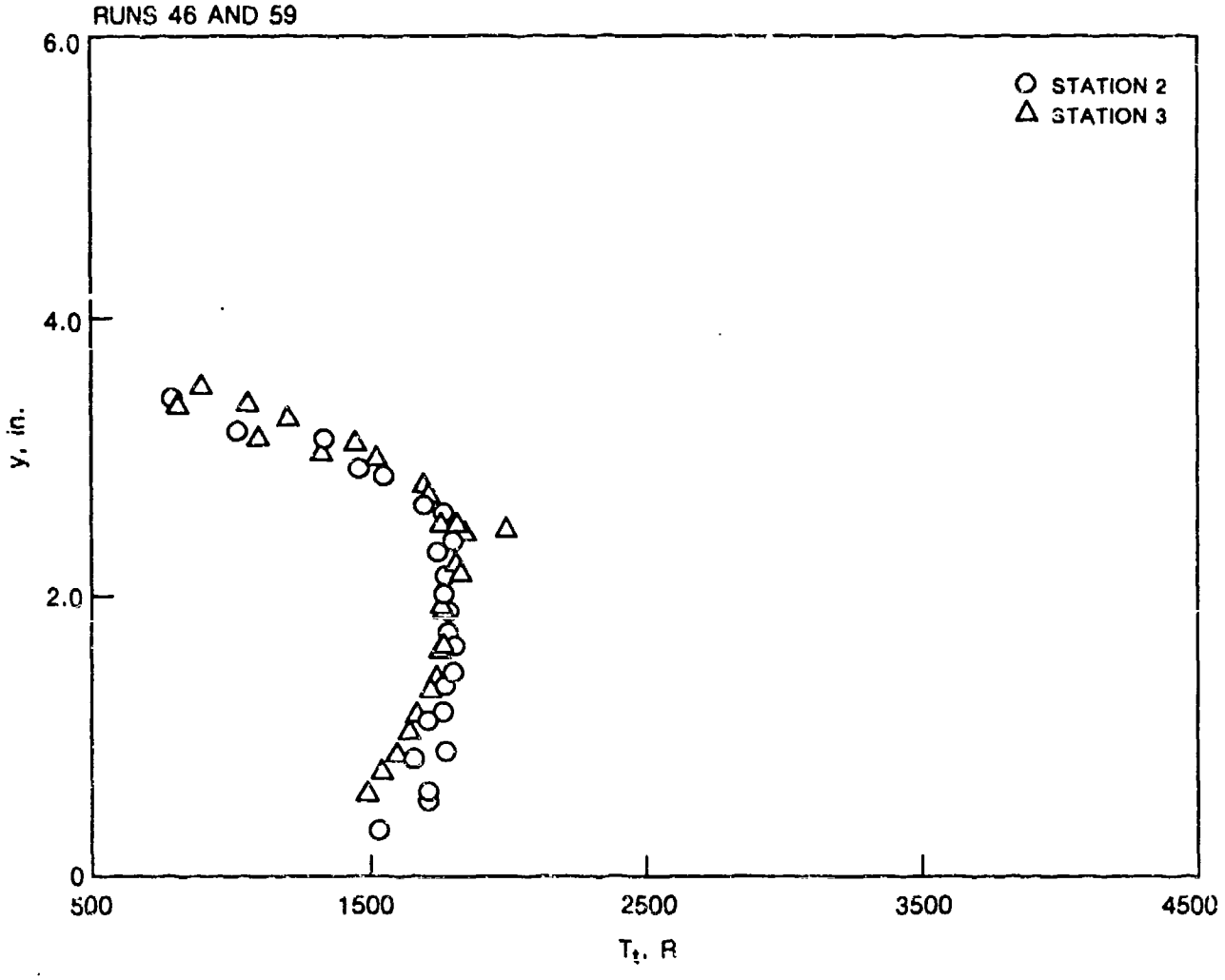

Fig. 23 Total temperature profiles from probe measurements at Stations 2 and 3 during non-reacting tests at an equivalence ratio of 1. Freeshear-layer.

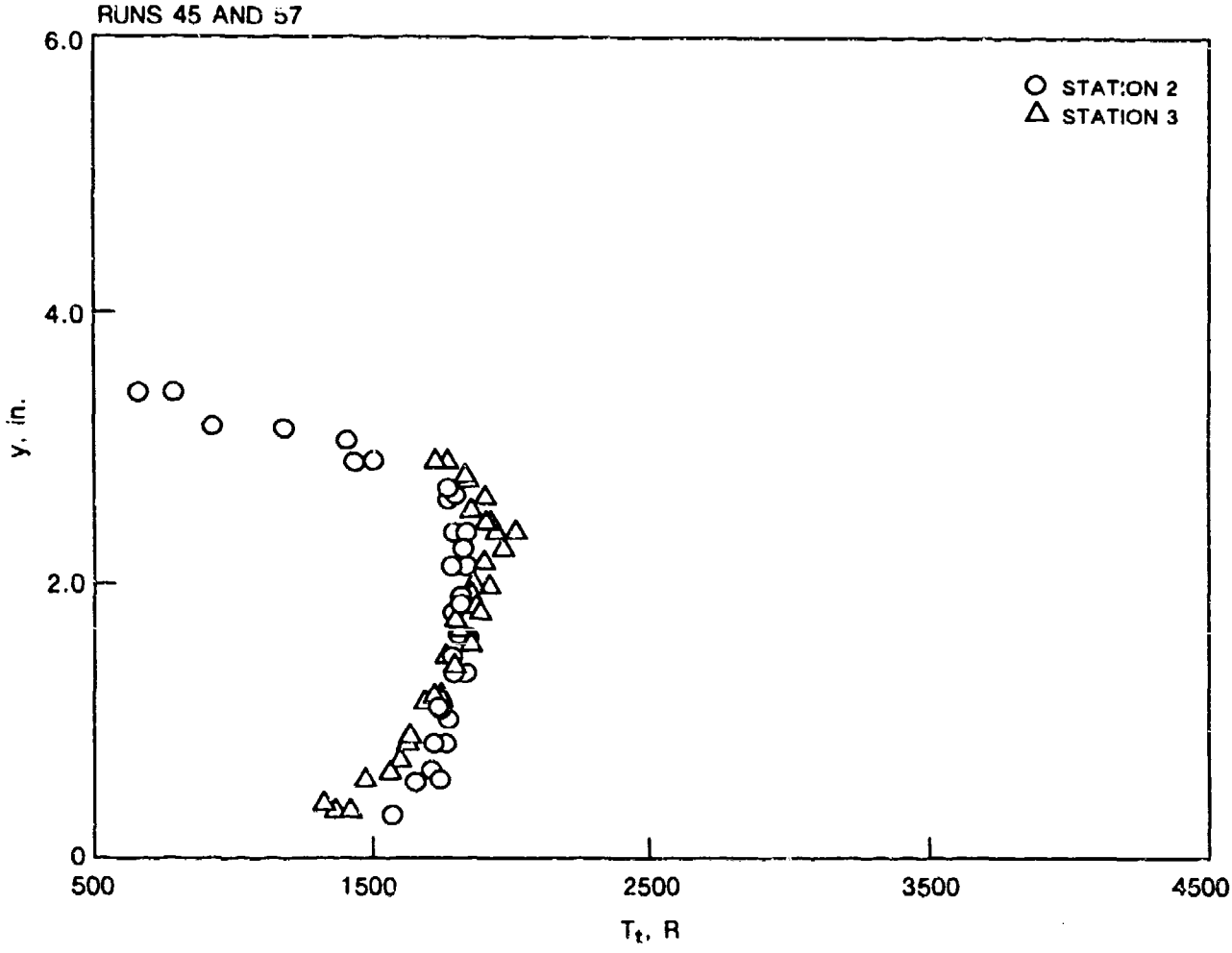

Fig. 24 Total temperature profiles from probe measurements at Stations 2 and 3 during non-reacting tests at an equivalence ratio of 0.5. Free shear-layer.

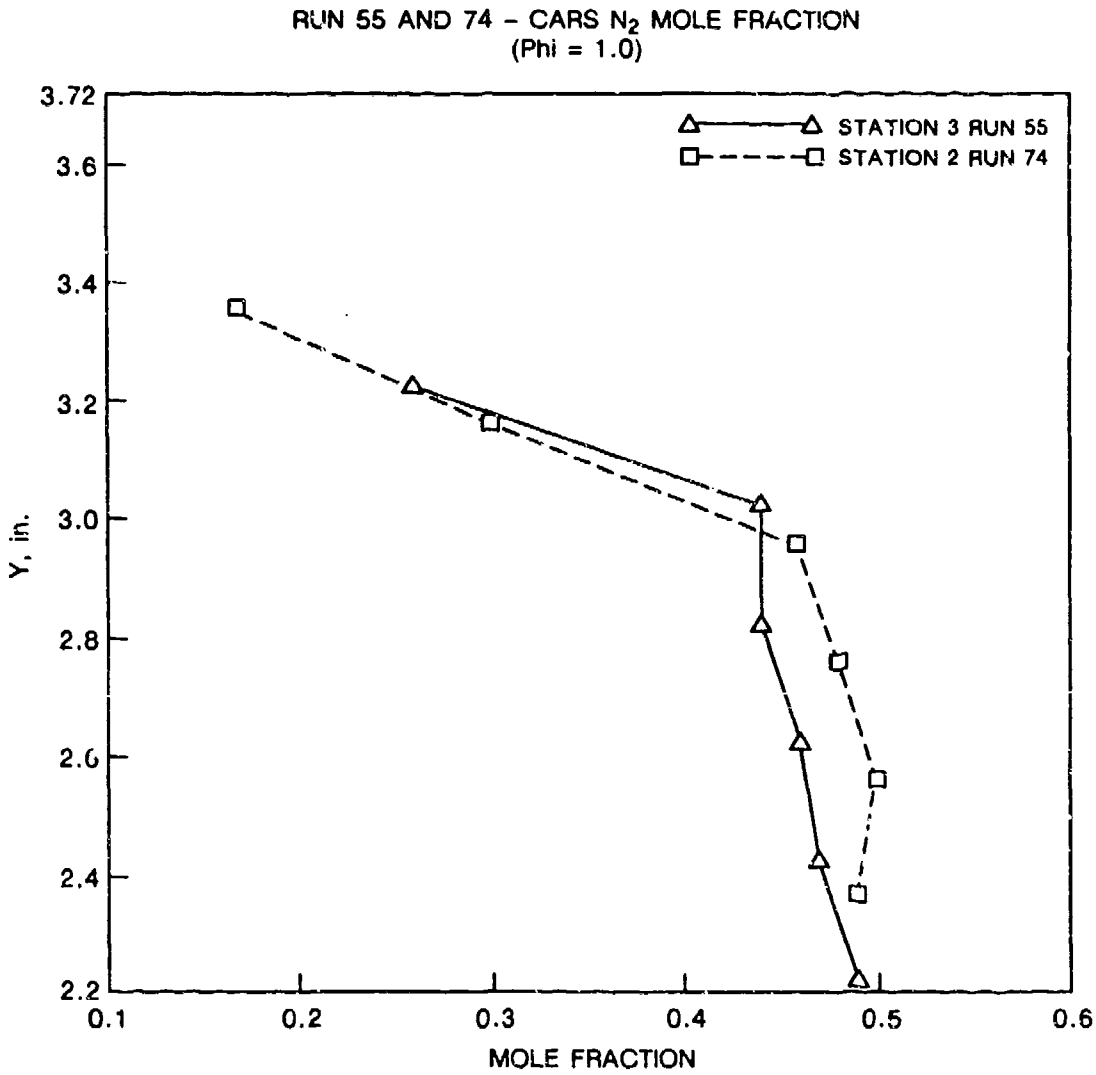

Fig. 25 Nitrogen mole fraction profiles from CARS measurements at Stations 2 and 3 during combustion tests at an equivalence ratio of 1.0. Free shear-layer.

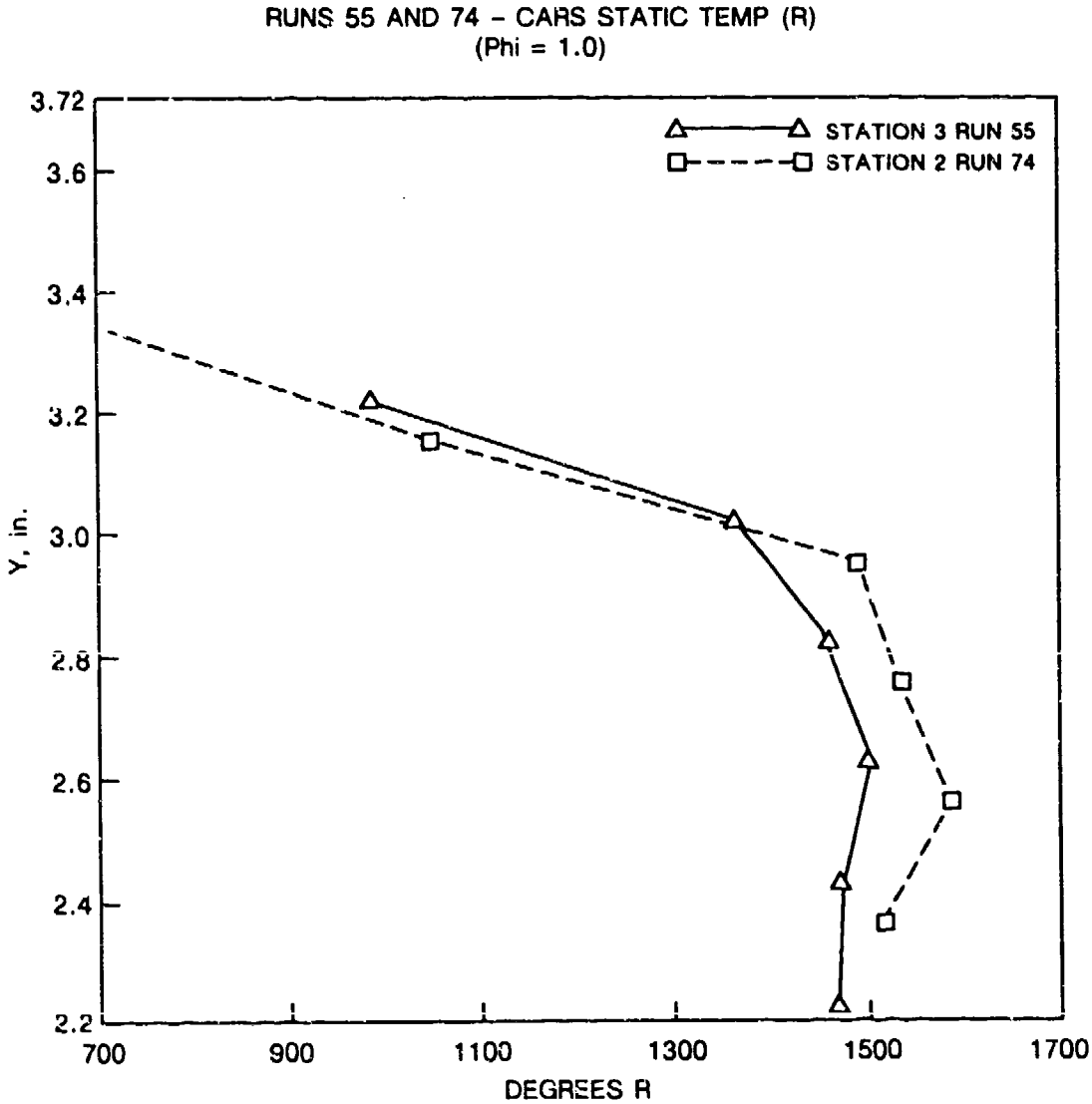

Fig. 26 Static temperature profiles from CARS measurements at Stations 2 and 3 during combustion tests at an equivalence ratio of 1.0. Free shear-layer.

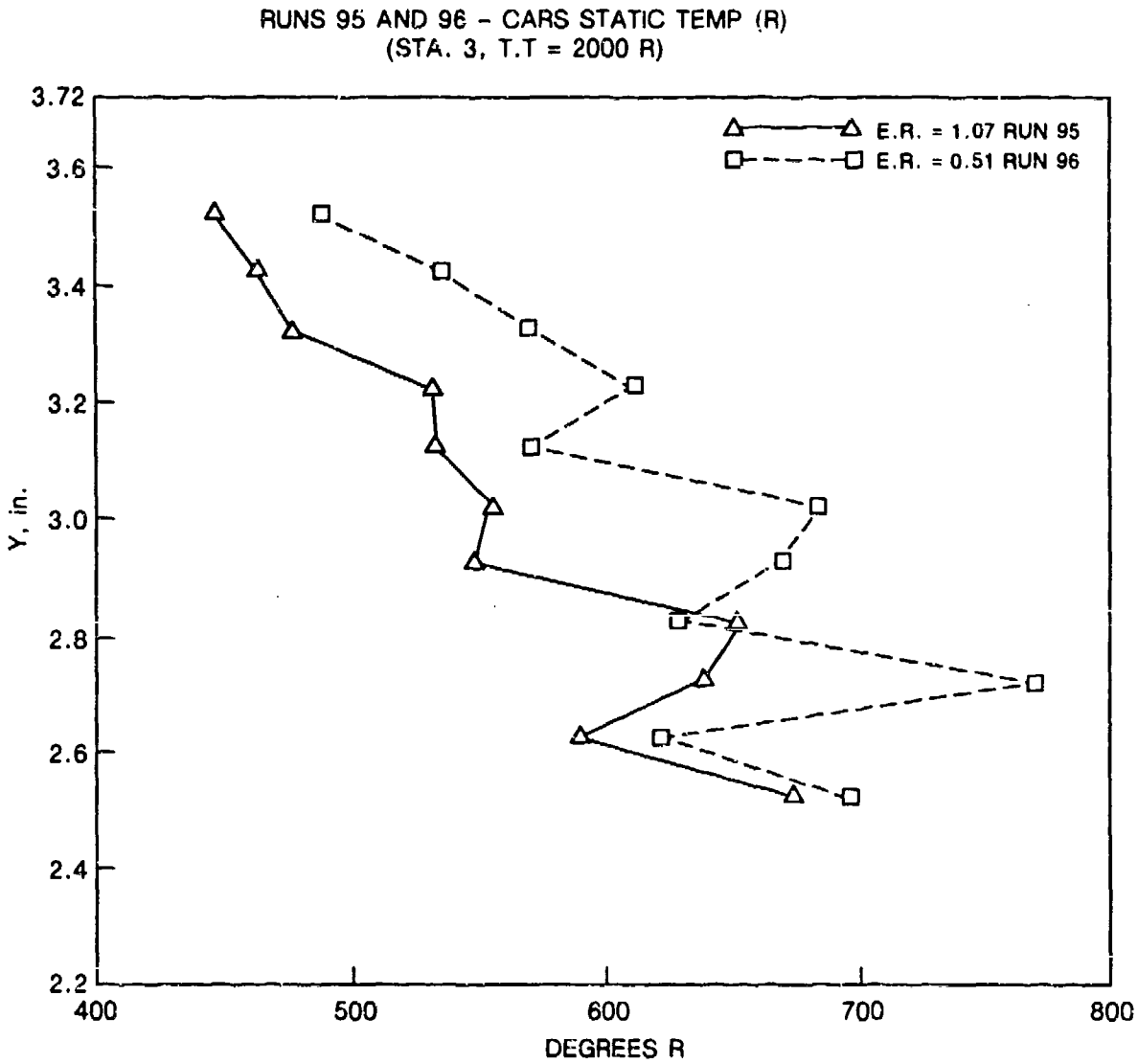

Fig. 27 Static temperature profiles from CARS measurements at Station 3 during non-reacting tests at nominal equivalence ratios of 0.5 and 1. Free shear-layer.

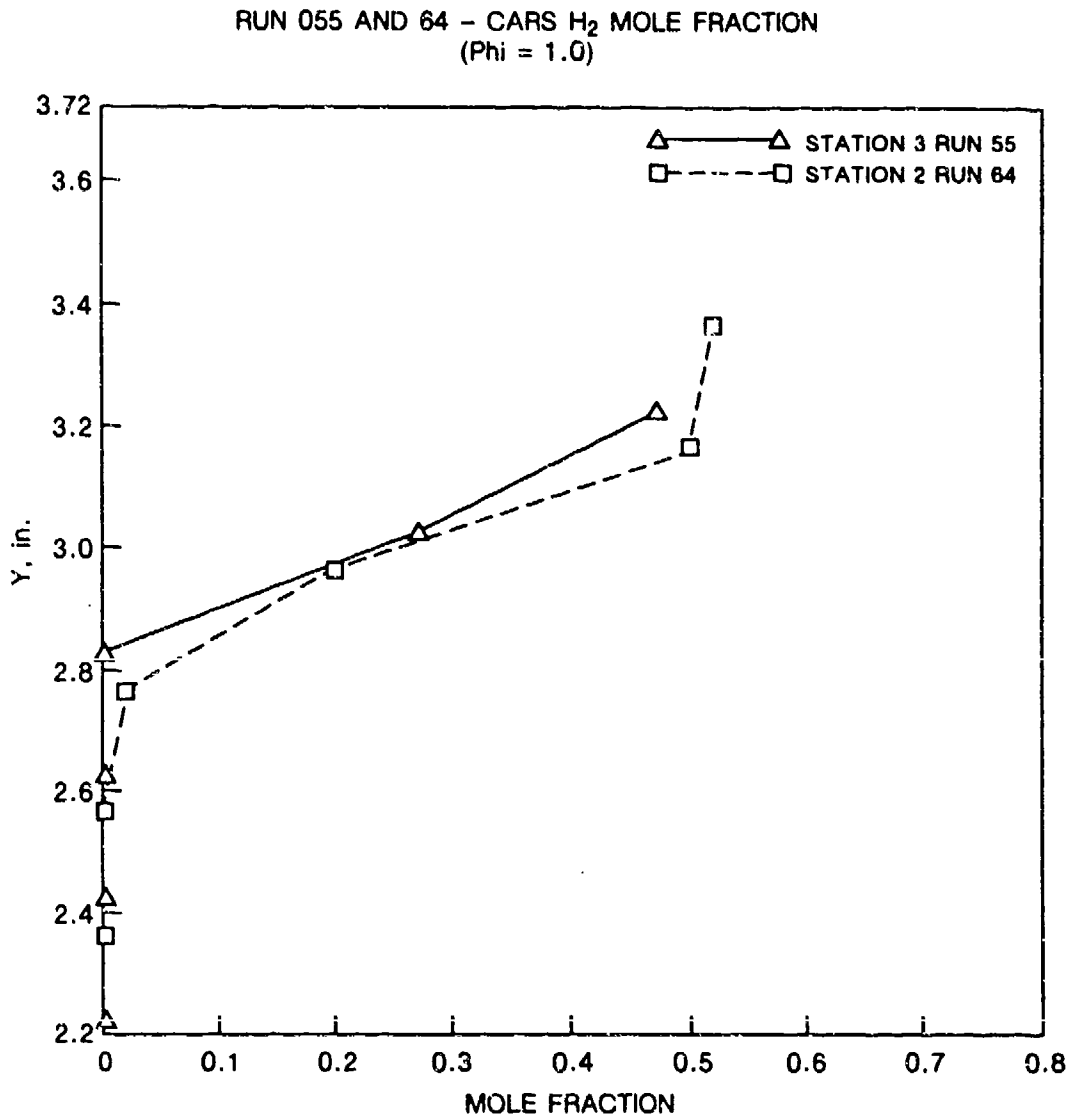

Fig. 28 Hydrogen profiles from CARS measurements at Stations 2 and 3 during combustion tests at an equivalence ratio of 1.0. Free shear-layer.

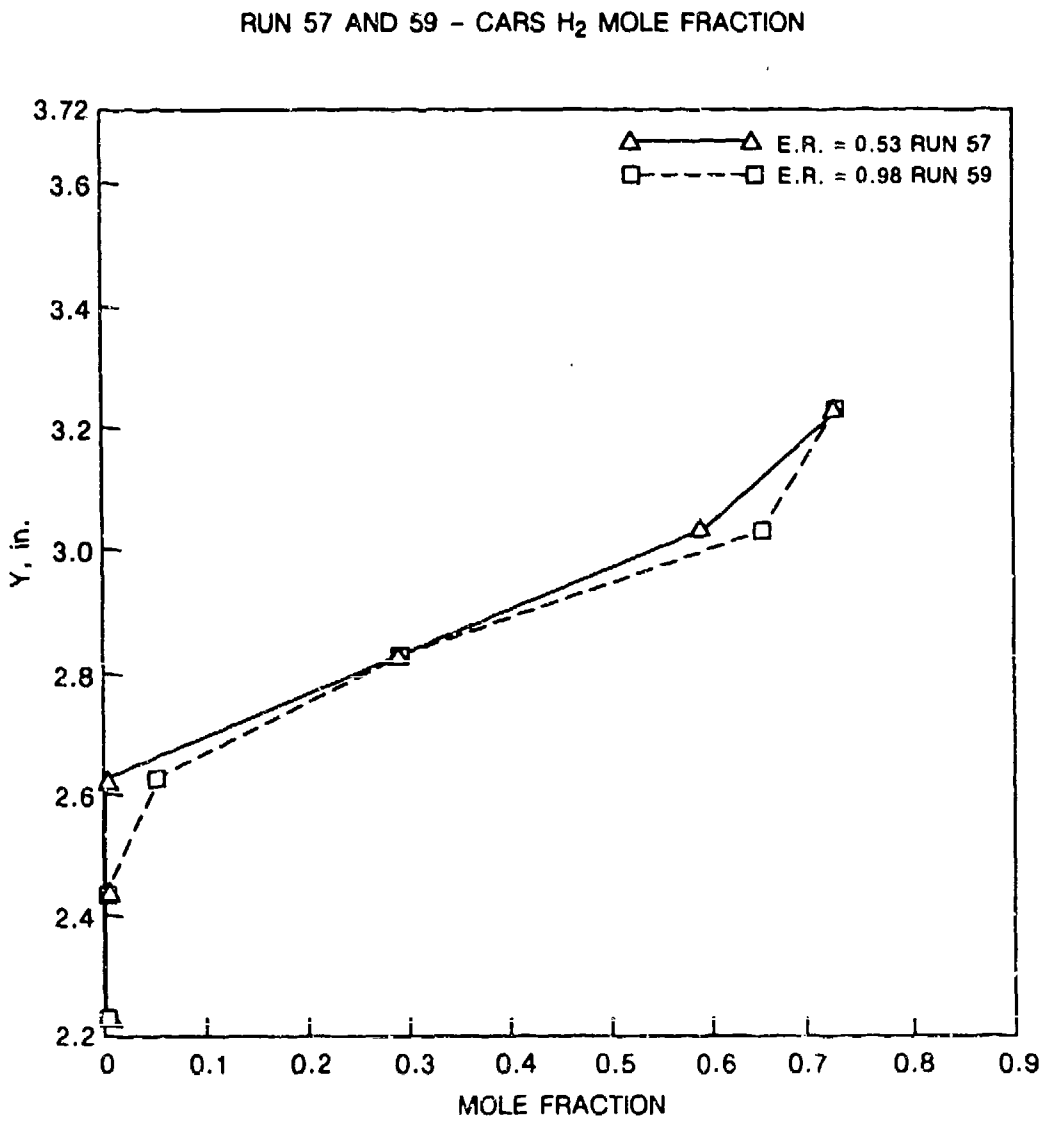

Fig. 29 Hydrogen profiles from CARS measurements at Station 2 during non-reacting tests at nominal equivalence ratios of 0.5 and 1. Free shear-layer.

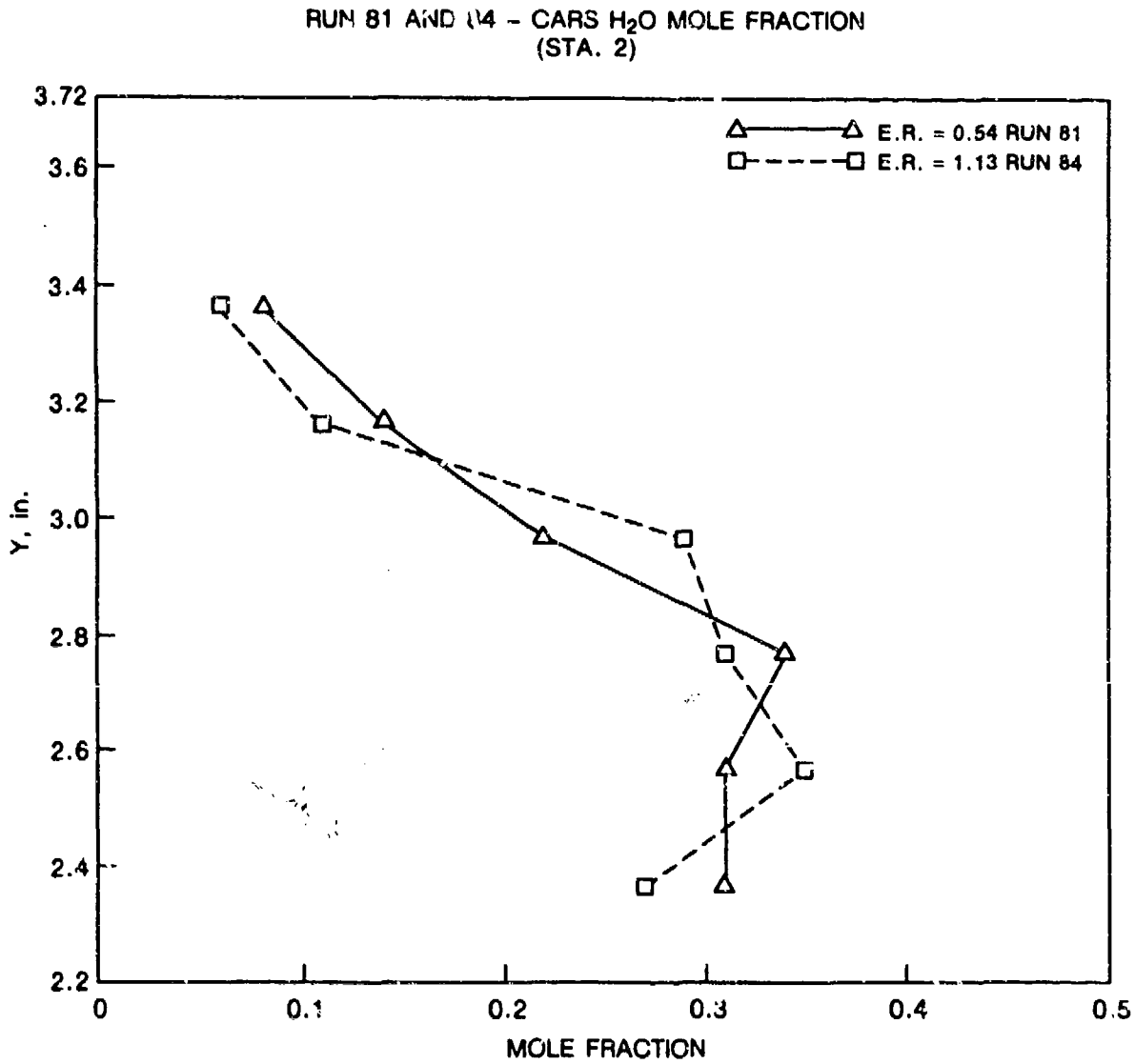

Fig. 30 Water vapor profiles from CARS measurements at Station 2 during combustion tests at nominal equivalence ratios of 0.5 and 1. Free shear-layer.

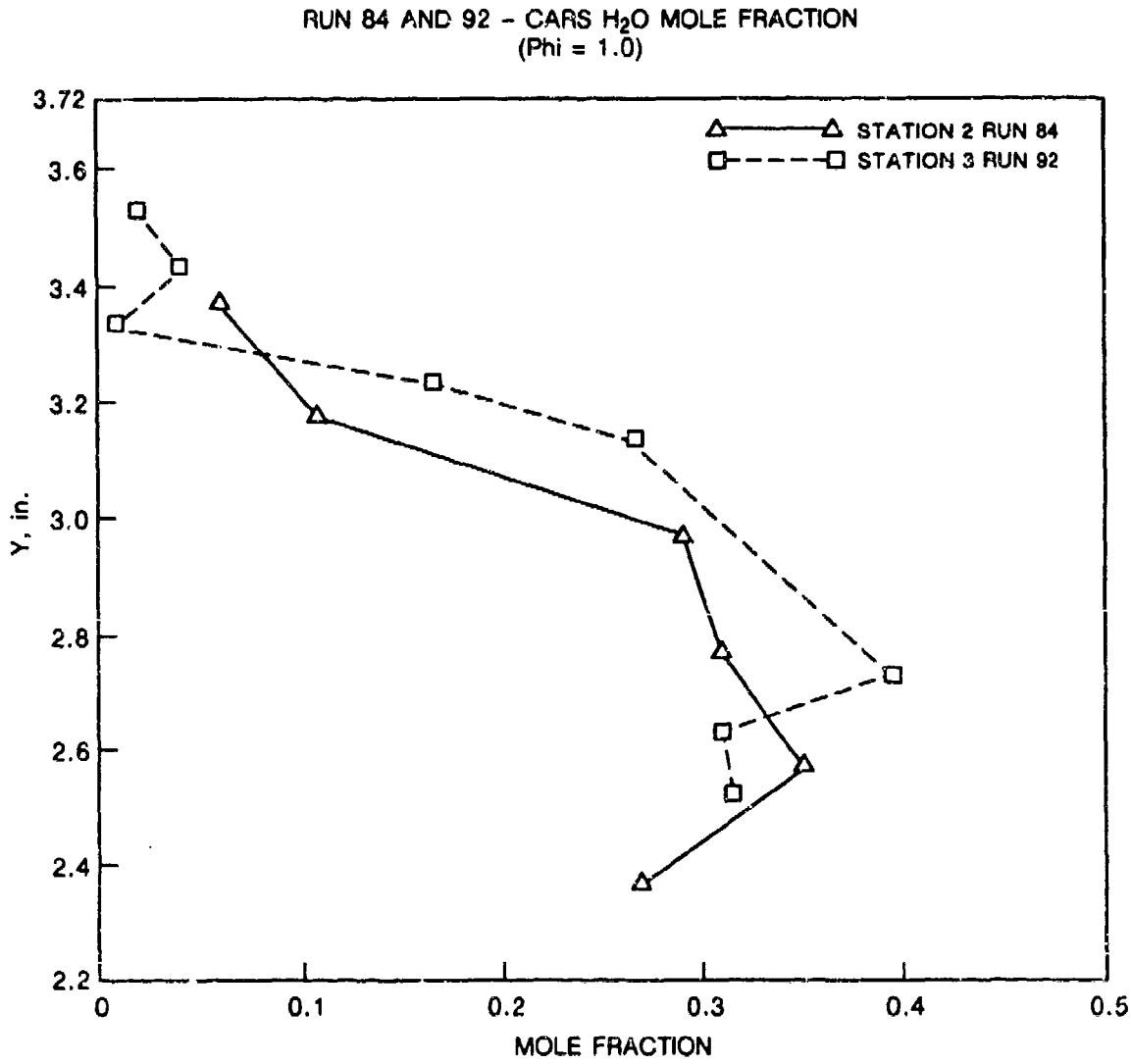

Fig. 31 Water vapor profiles from CARS measurements at Stations 2 and 3 during combustion tests at an equivalence ratio of 1. Free shear-layer.

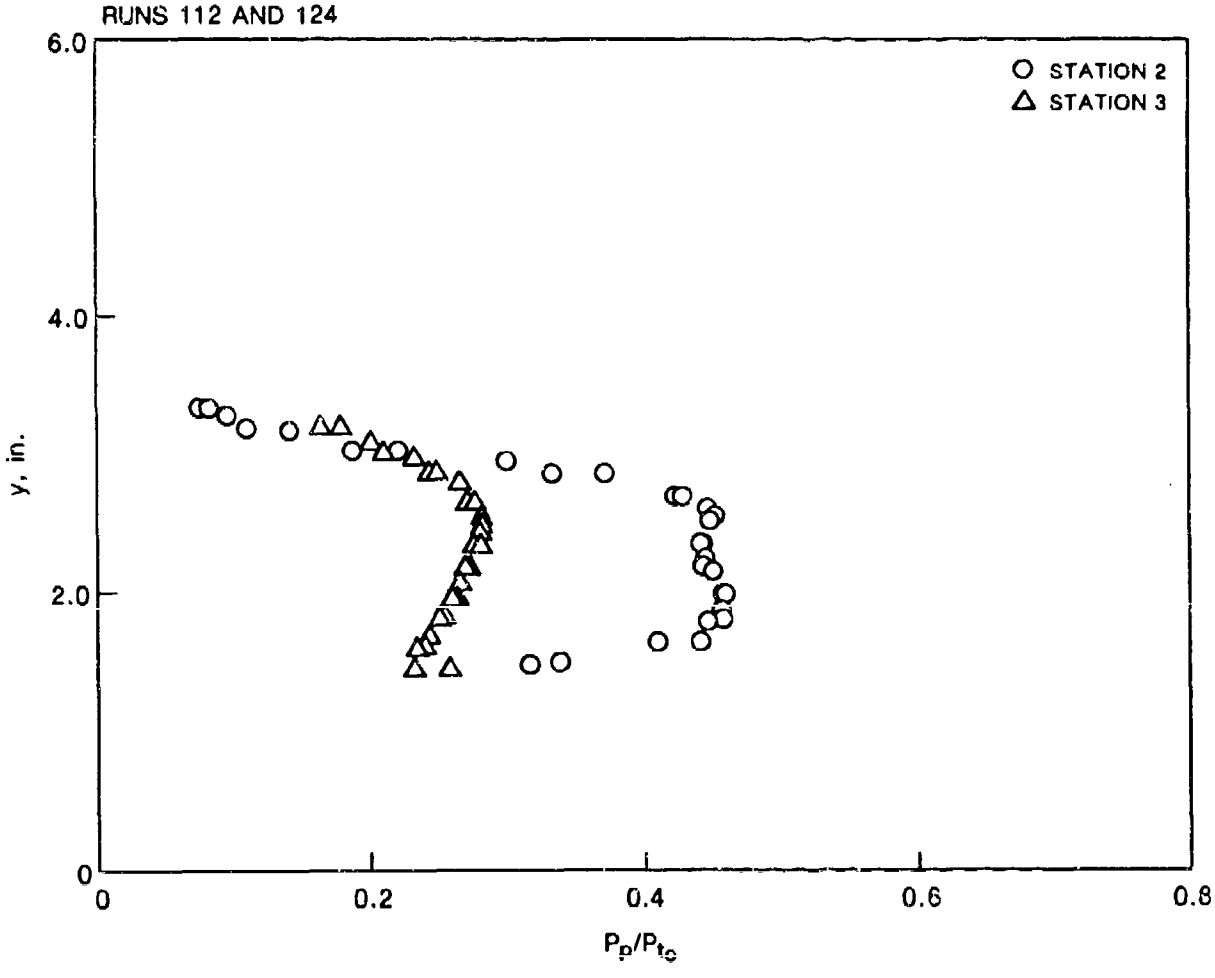

Fig. 32 Pitot pressure profiles from probe measurements at Stations 2 and 3 during non-reacting tests at an equivalence ratio of 1.0. Shock interaction.

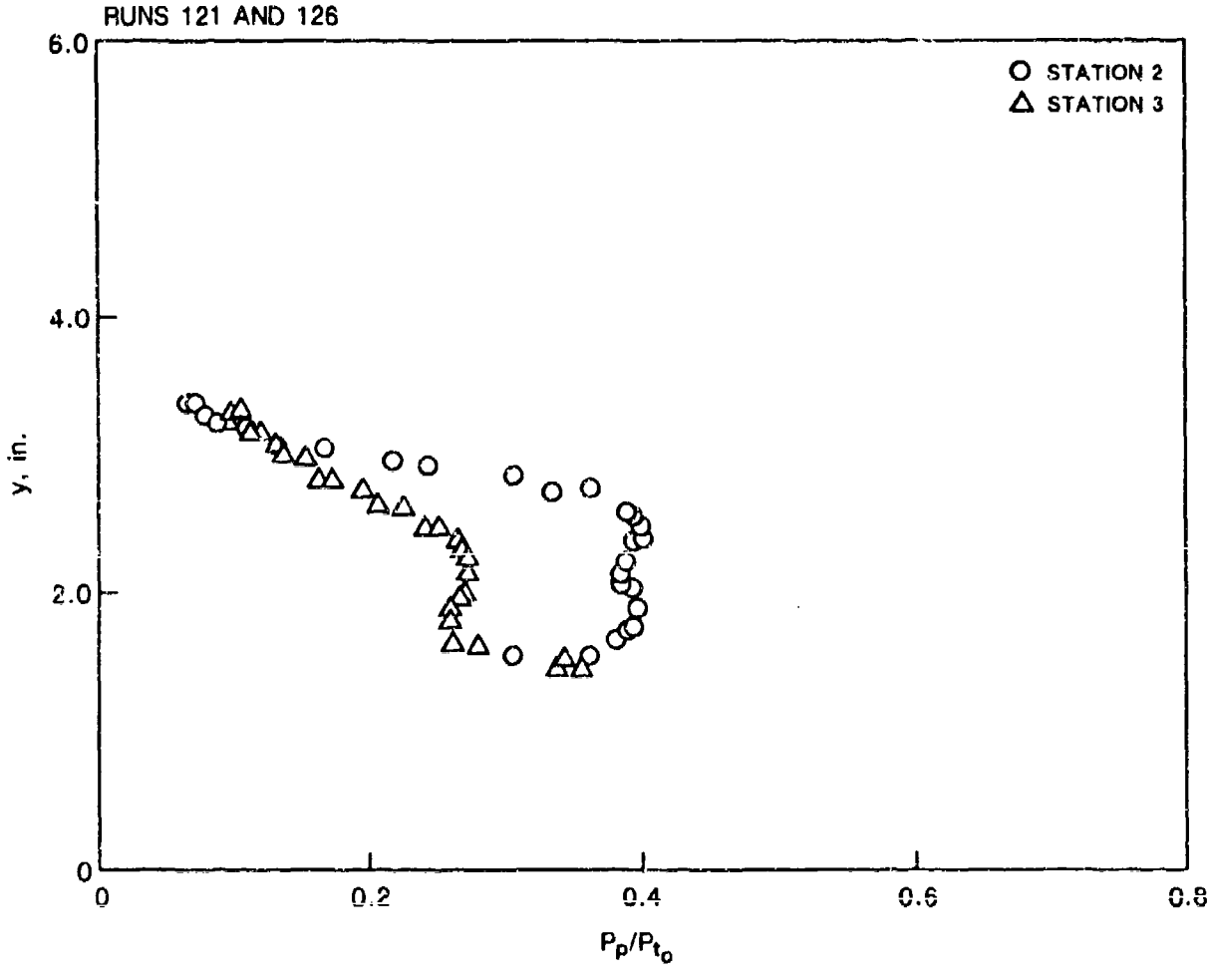

Fig. 33 Pitot pressure profiles from probe measurements at Stations 2 and 3 during combustion tests at an equivalence ratio of 1.0. Shock interaction.

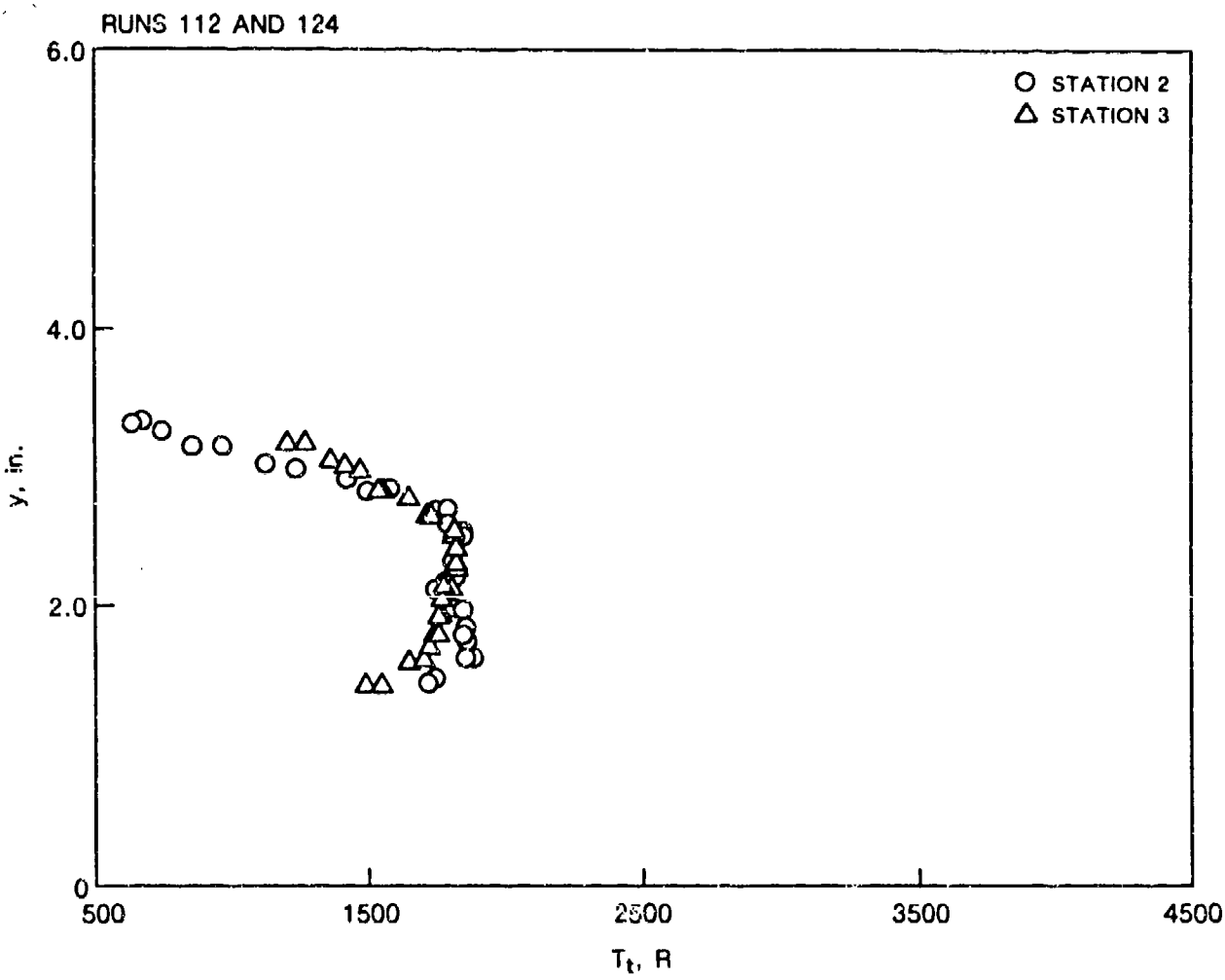

Fig. 34 Total temperature profiles from probe measurements at Stations 2 and 3 during non-reacting tests at an equivalence ratio of 1.0. Shock interaction.

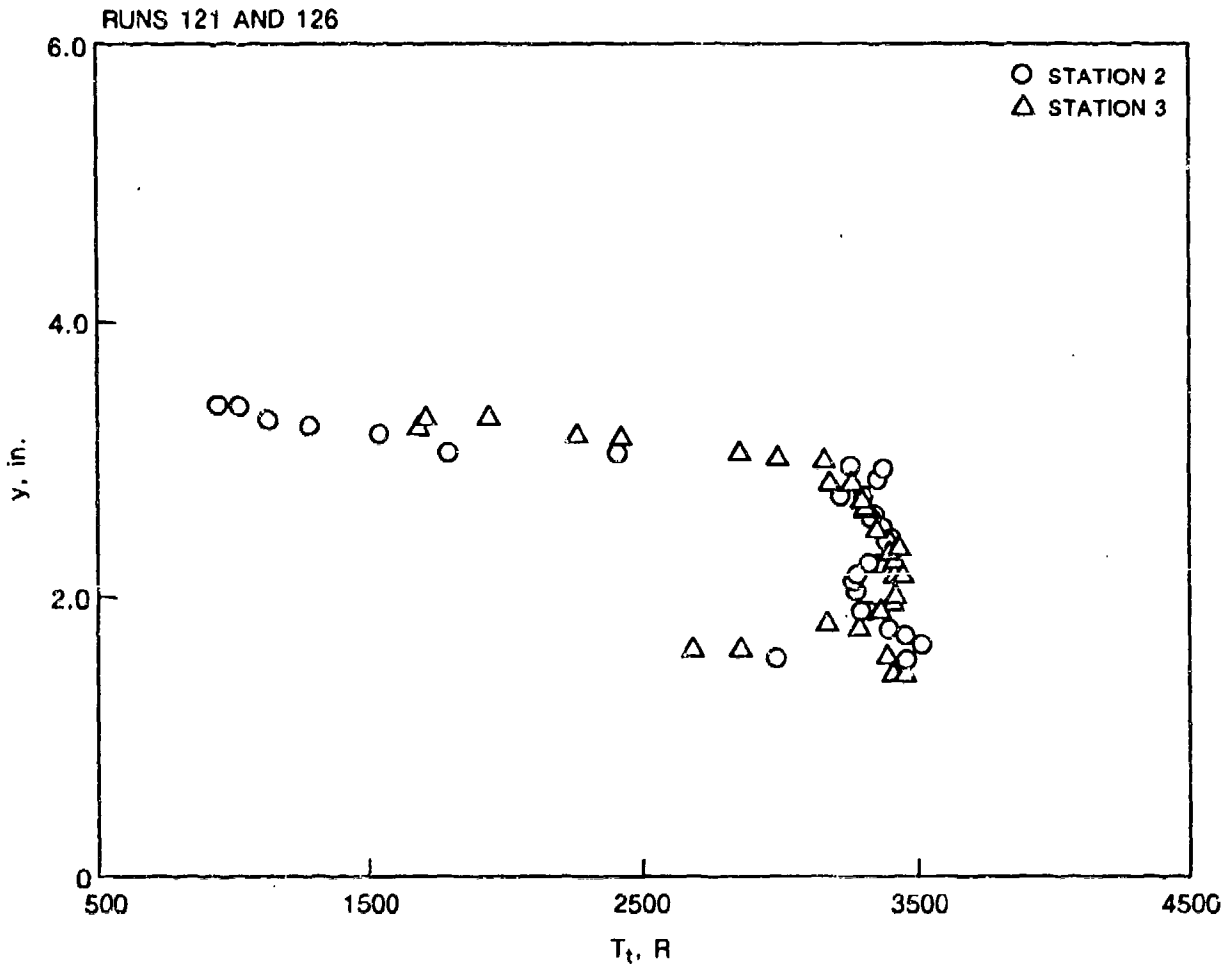

Fig. 35 Total temperature profiles from probe measurements at Stations 2 and 3 during combustion tests at an equivalence ratio of 1.0. Shock interaction.

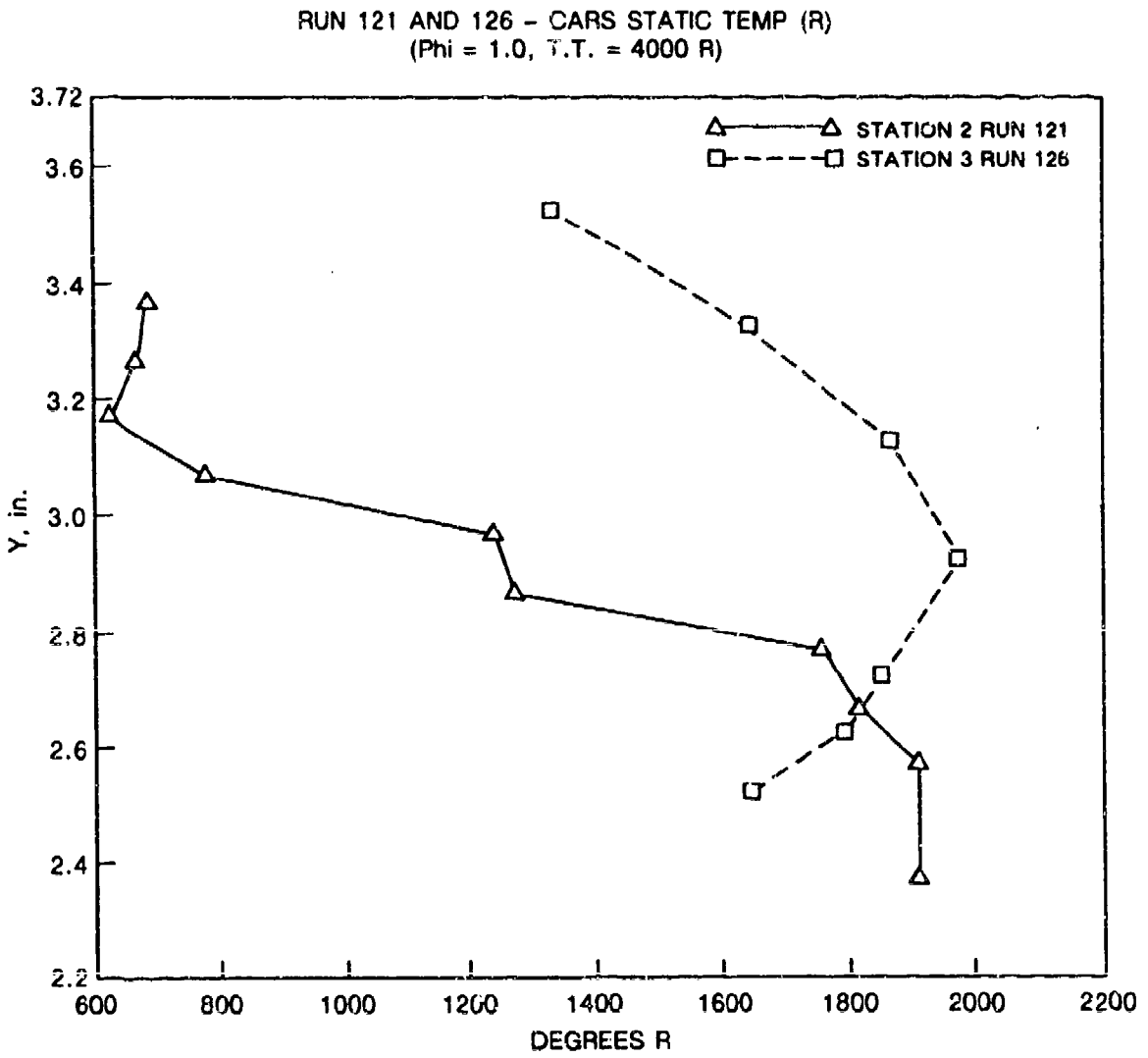

Fig. 36 Static temperature profiles from CARS measurements at Stations 2 and 3 during combustion tests at an equivalence ratio of 1. Shock interaction.

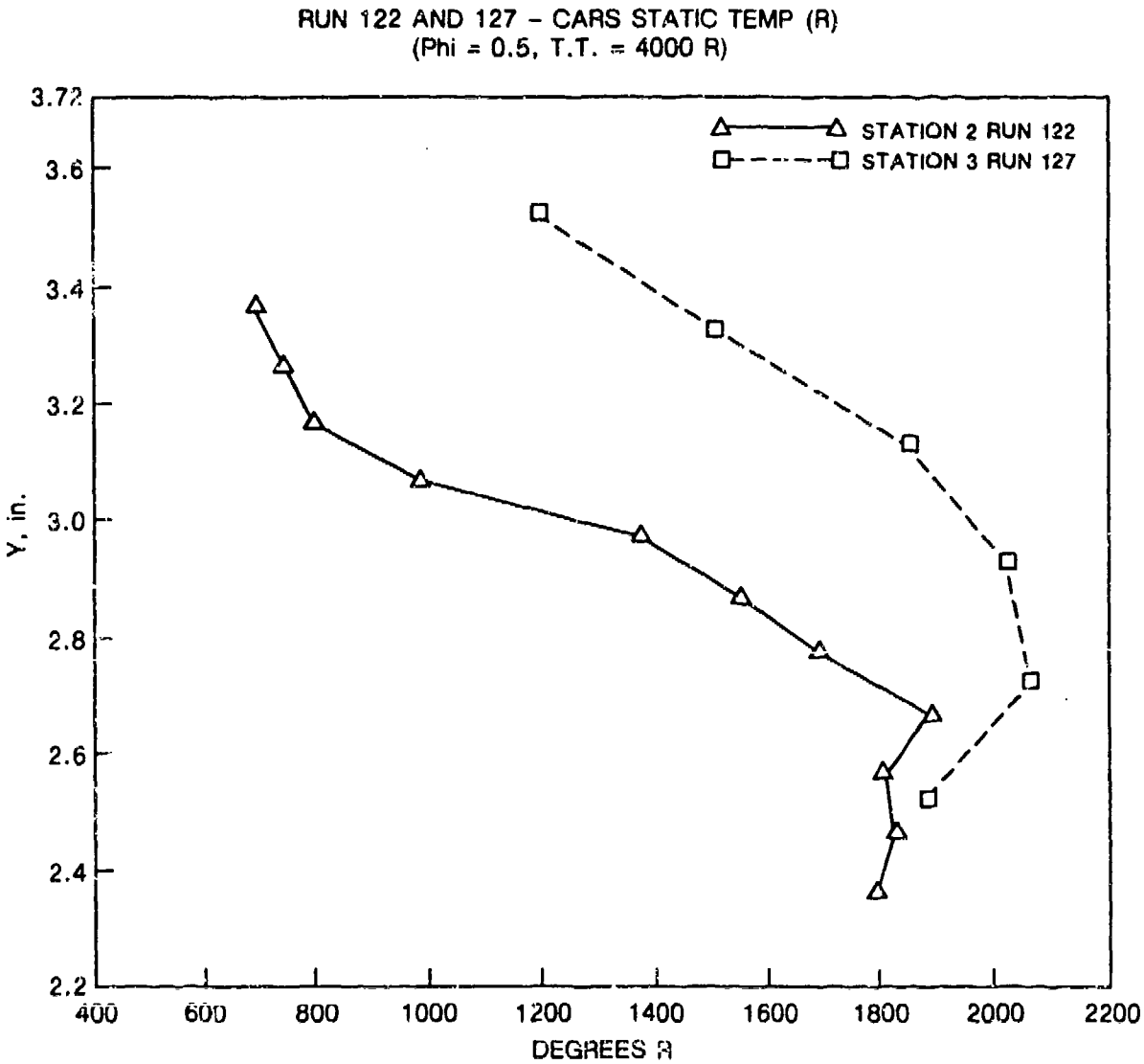

Fig. 37 Static temperature profiles from CARS measurements at Stations 2 and 3 during combustion tests at an equivalence ratio of 0.5. Shock interaction.

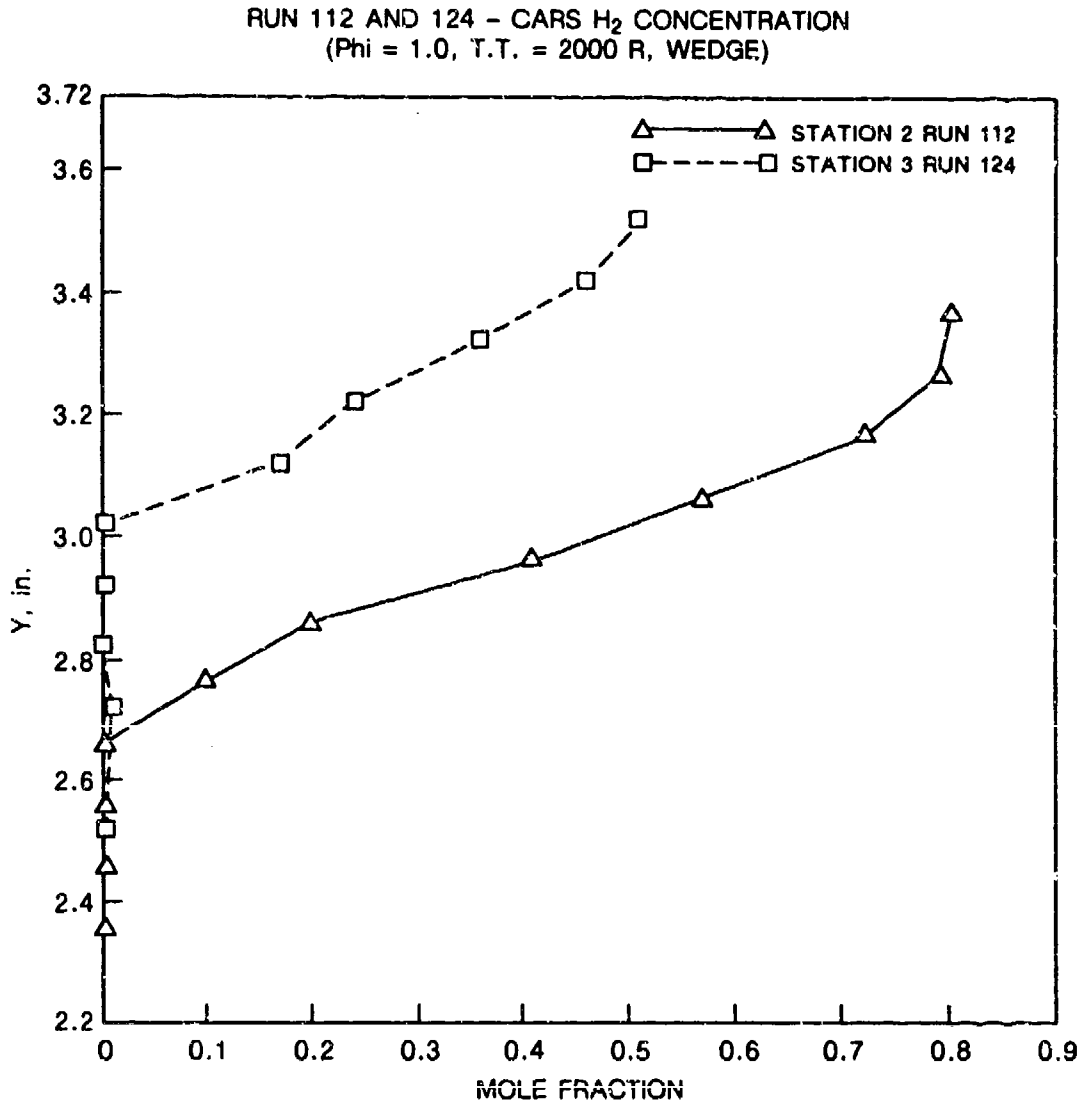

Fig. 38 Hydrogen concentration profiles from CARS measurements at Stations 2 and 3 during non-reacting tests at an equivalence ratio of 1.0. Shock interaction.

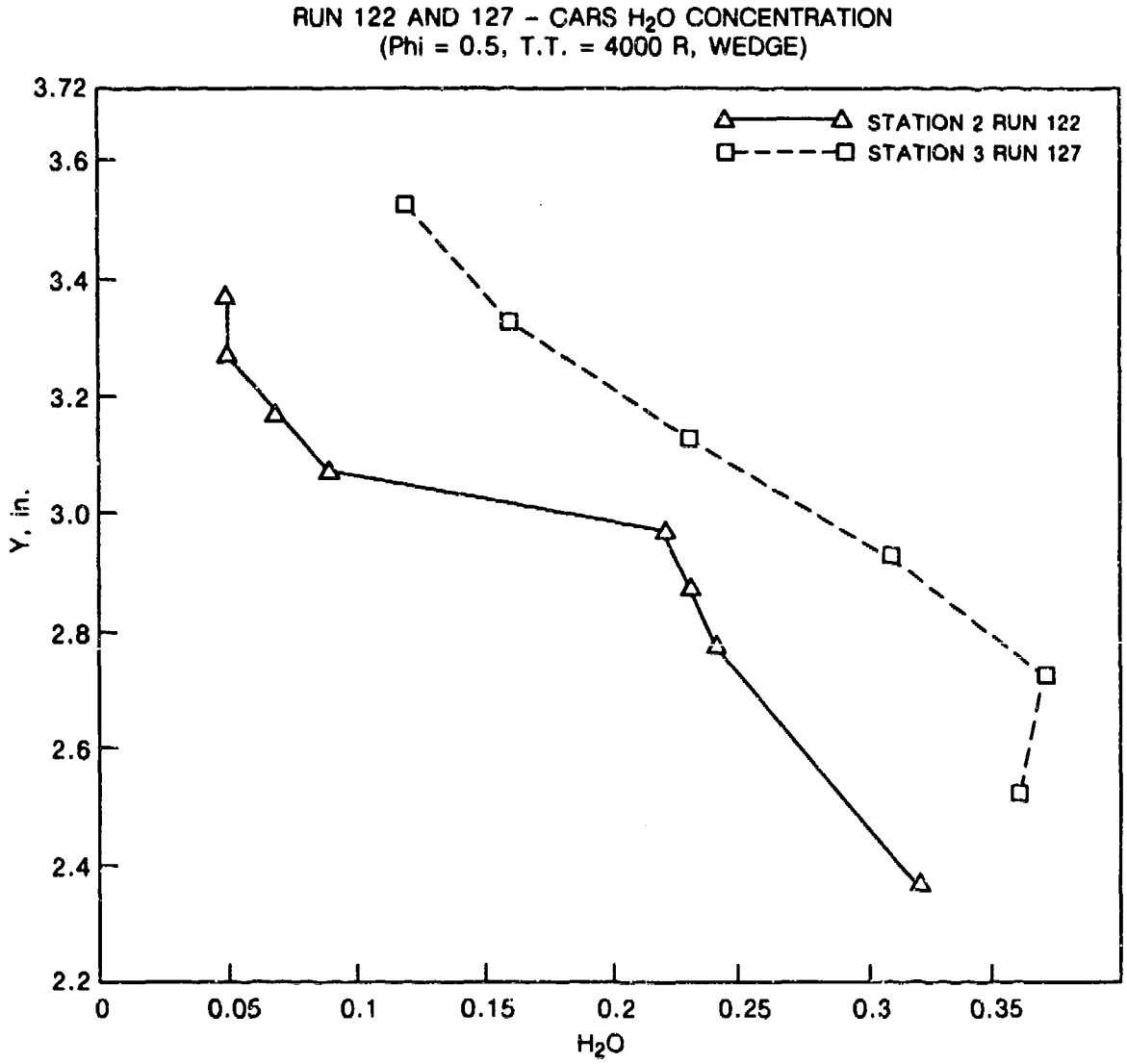

Fig. 39 Water vapor concentration profiles from CARS measurements at Stations 2 and 3 during combustion tests at an equivalence ratio of 0.5. Shock interaction.

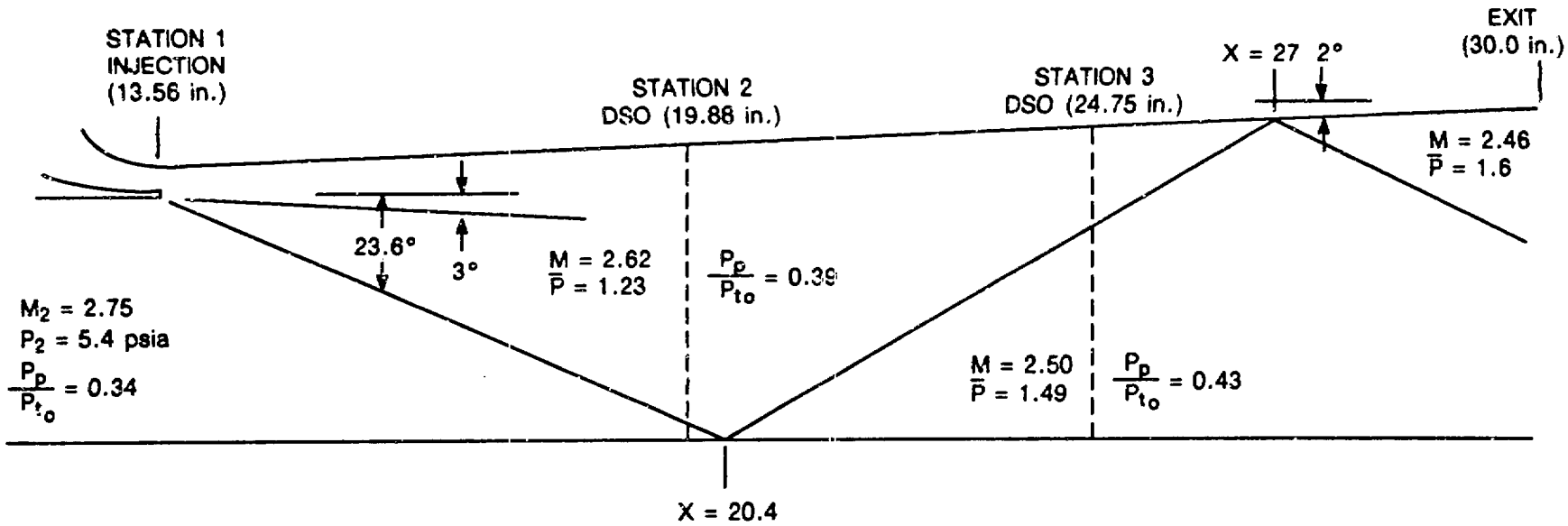

Fig. 40 Estimated test section flow field characteristics, free shear layer tests; $\bar{P} = P/P_{2j}$ (distance measured from nozzle exit).

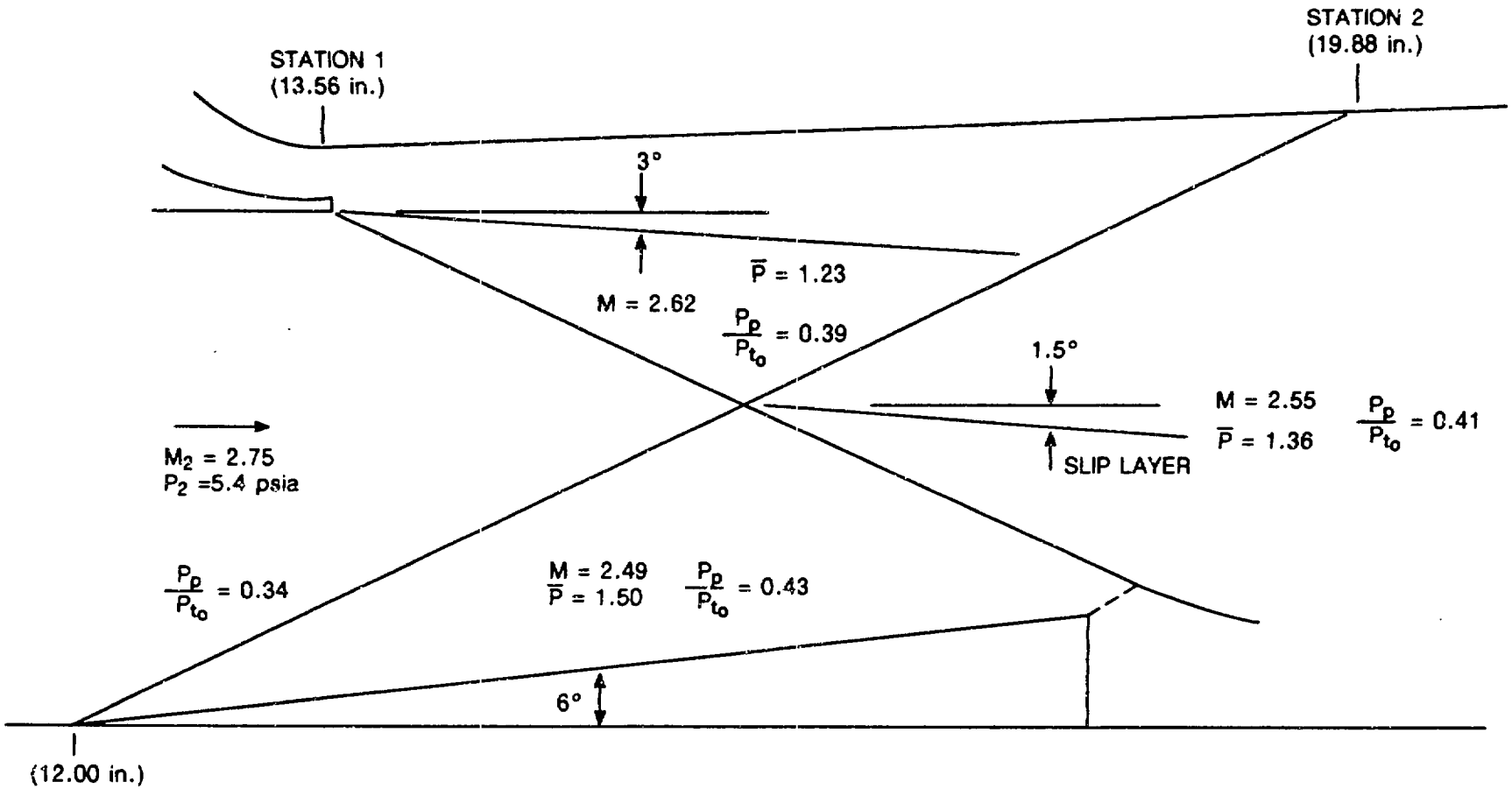

Fig. 41 Estimated test section flowfield characteristics, pressure gradient tests; $\bar{P} = P/P_2$ (distance measured from nozzle exit).

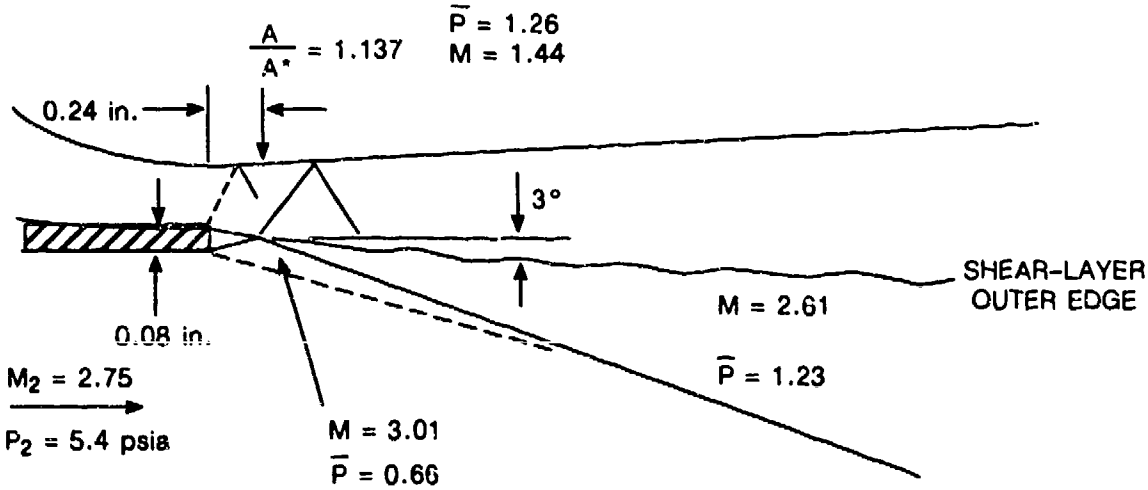

Fig. 42 Estimated flowfield characteristics near injection region; $\bar{P} = P/P_2$

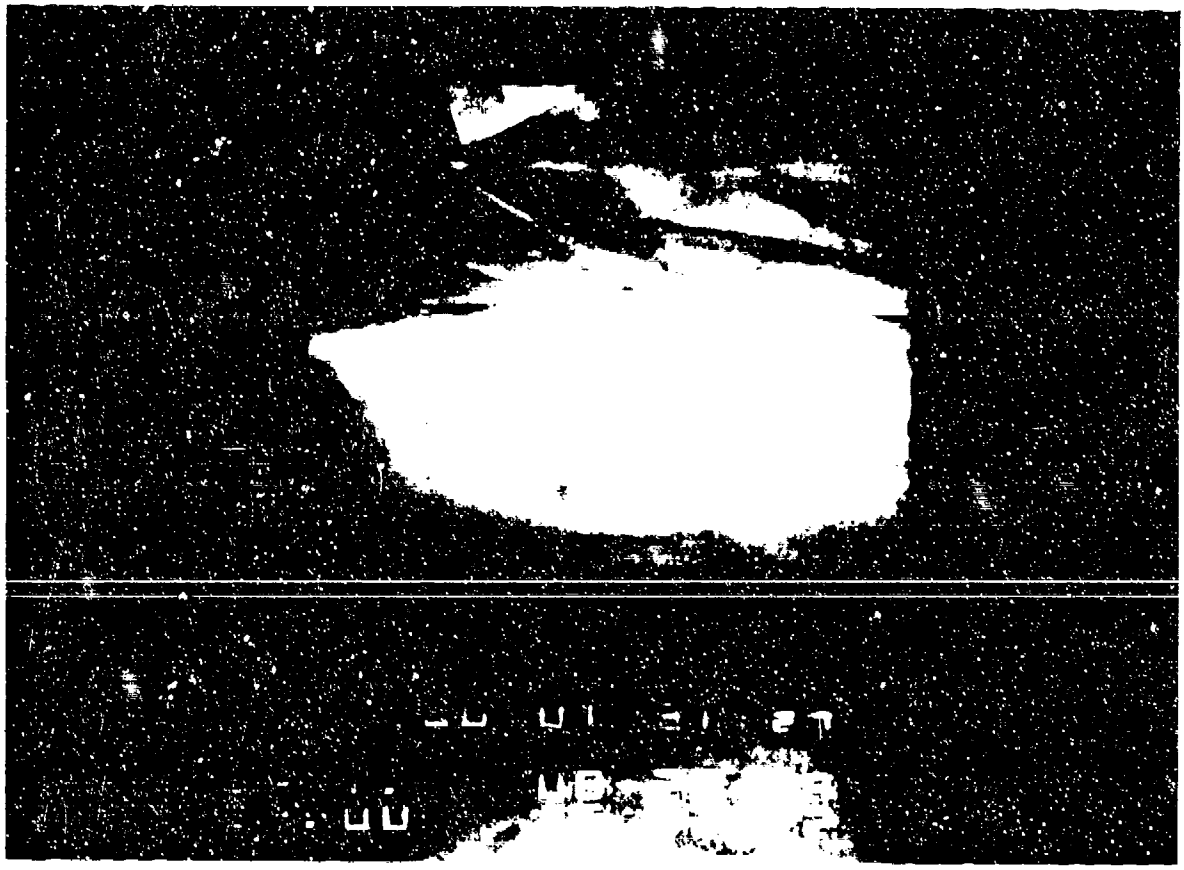

Fig. 43 Enlargement of a shadowgraph image depicting features of the fuel injector flow field for an equivalence ratio of 1. Low temperature flow condition.

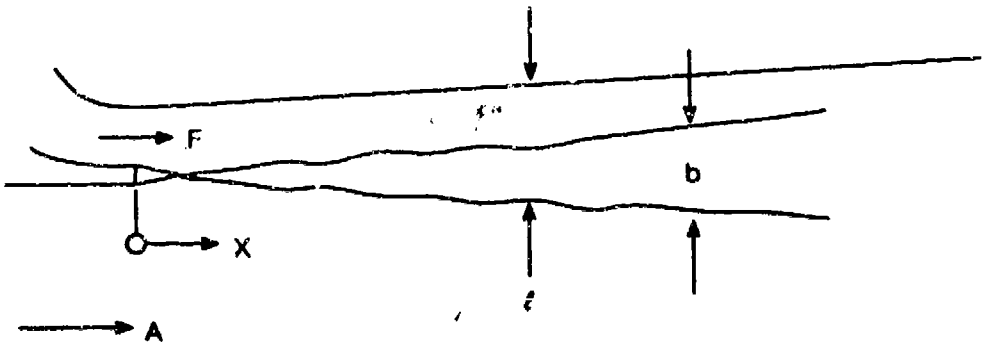

Fig. 44 Mixing layer nomenclature: F = Fuel, A = Air, ℓ = mixing-layer height, b = shear-layer thickness.

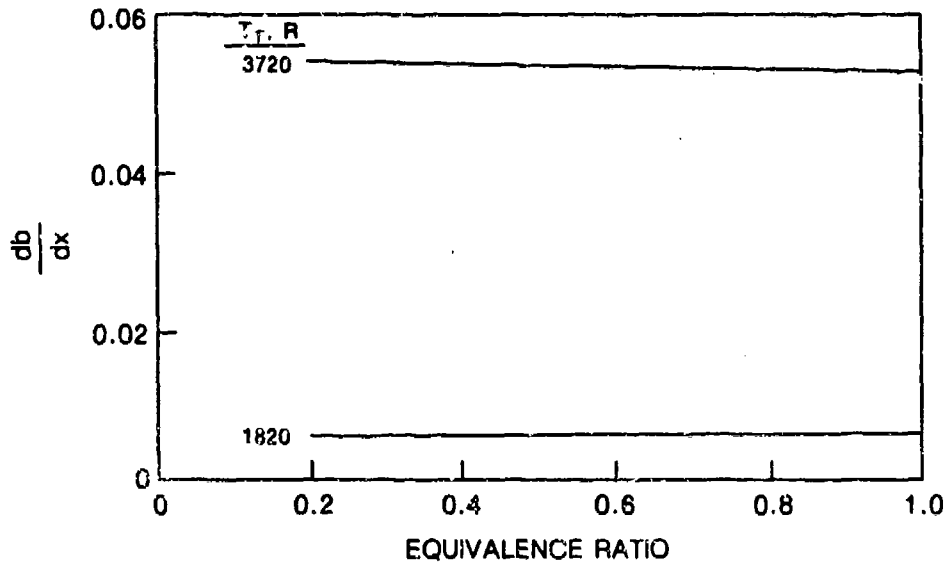

Fig. 45 Shear-layer growth rate as a function of equivalence ratio for current test conditions.

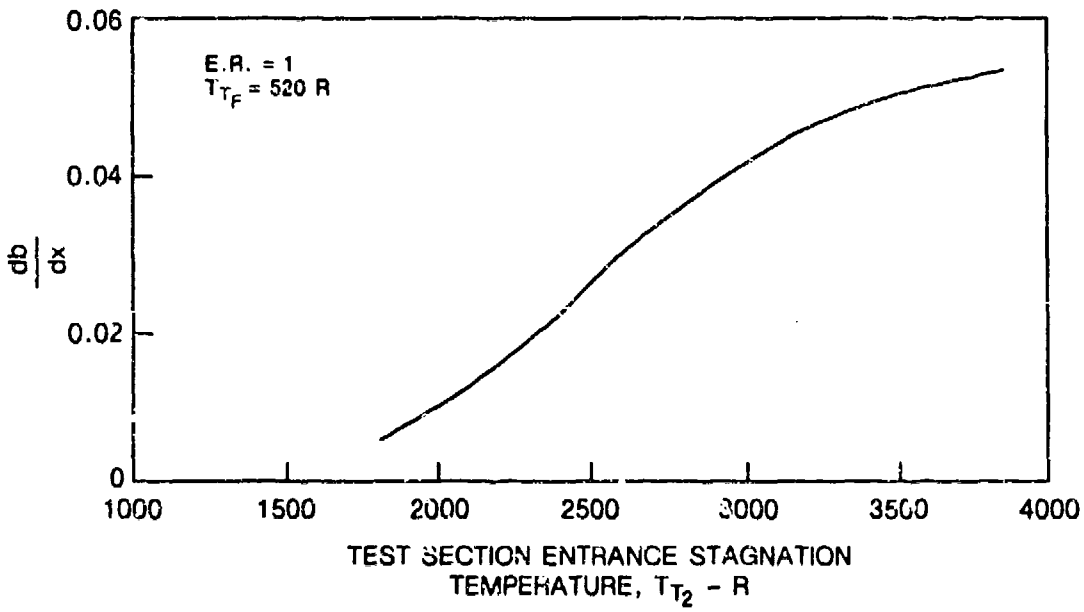

Fig. 46 Shear-layer growth rate variation relative to air stagnation temperature. Equivalence ratio = 1.

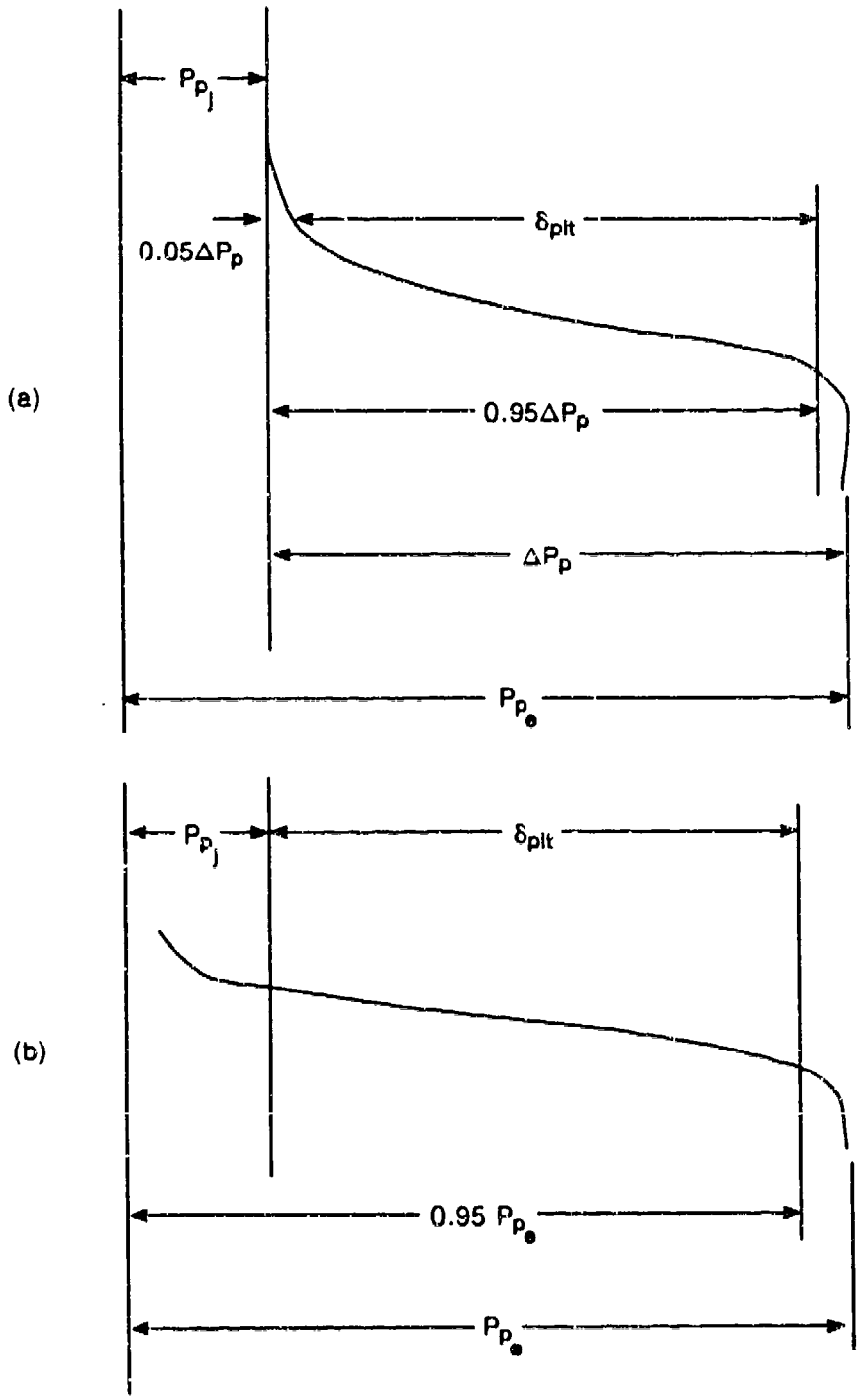

Fig. 47 Definition of pitot thickness (a) ref. 32, (b) present investigation.

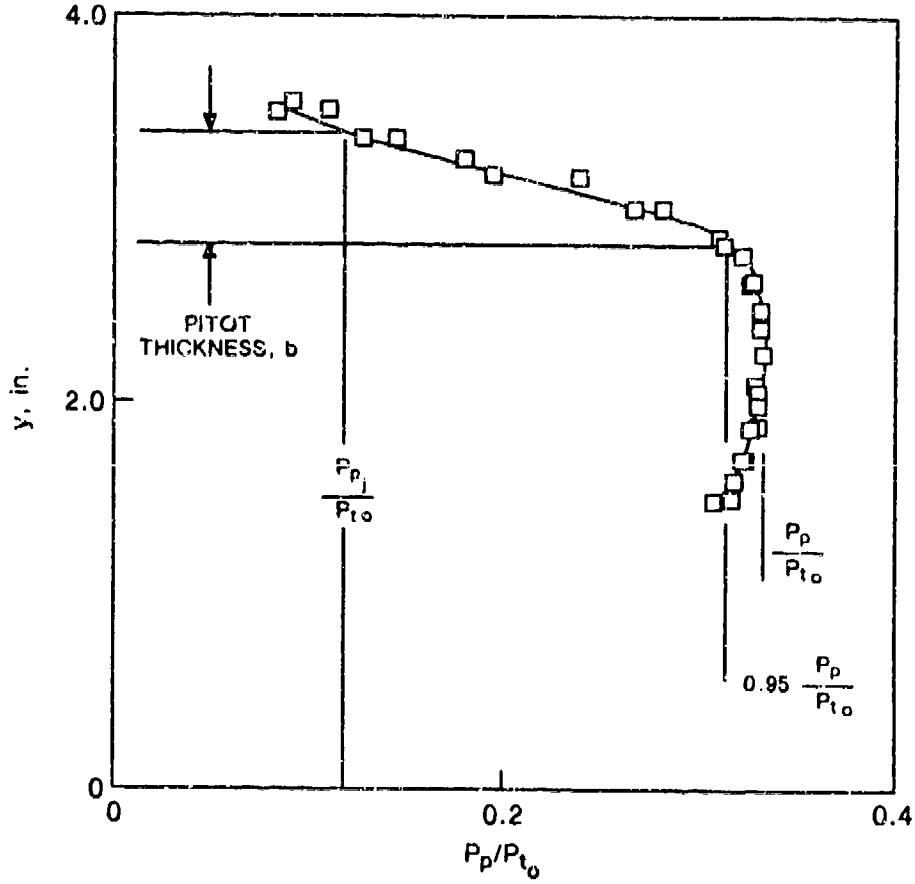

Fig. 48 Example of pitot thickness measurement.

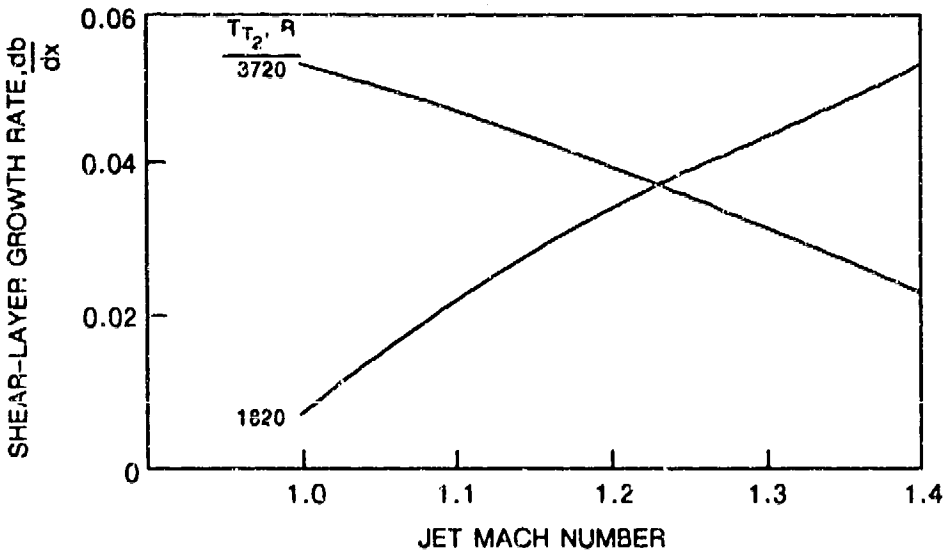

Fig. 49 Relationships between shear-layer growth rates and jet Mach number for equivalence ratio of 1. Fuel jet stagnation temperature = 520 R.

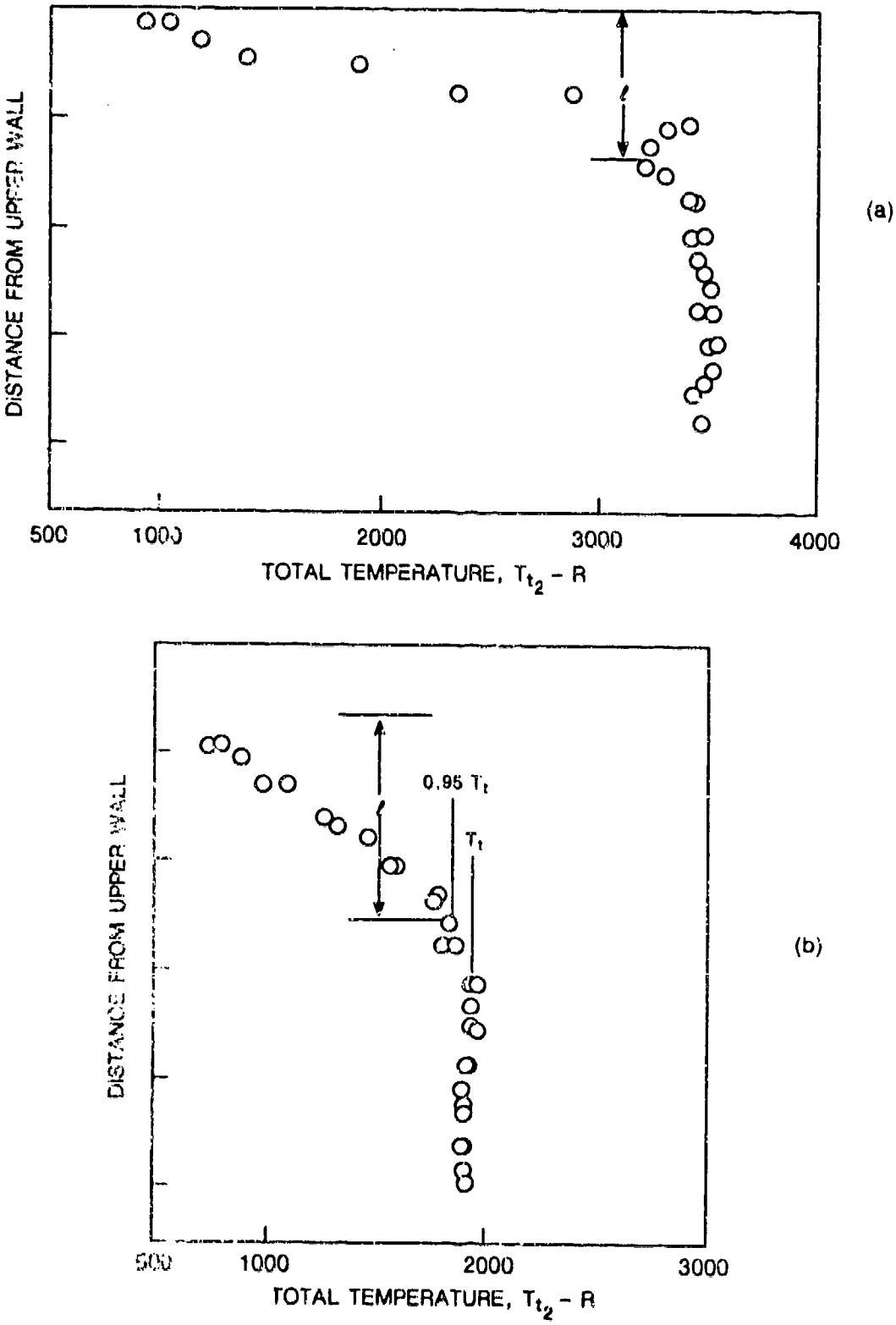

Fig. 50 Definition of mixing layer thickness based on total temperature (a) with combustion and (b) non-reacting.

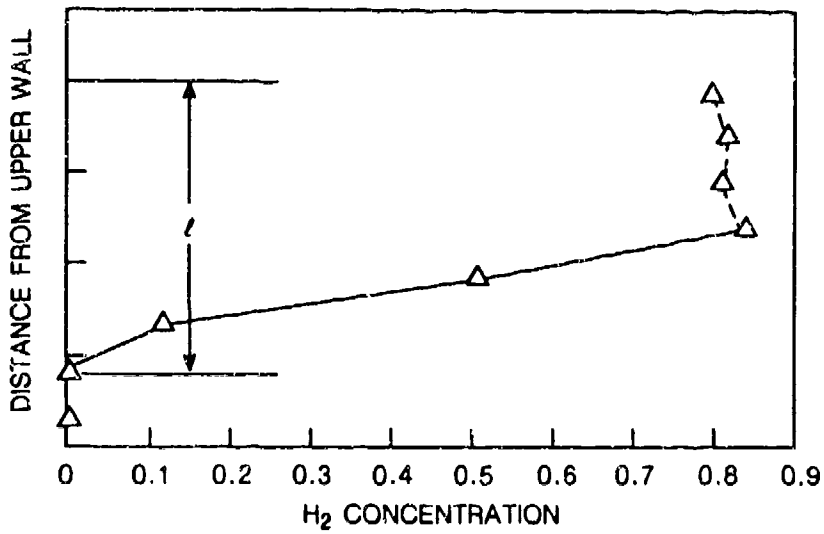

Fig. 51 Definition of mixing layer thickness based on hydrogen concentration.

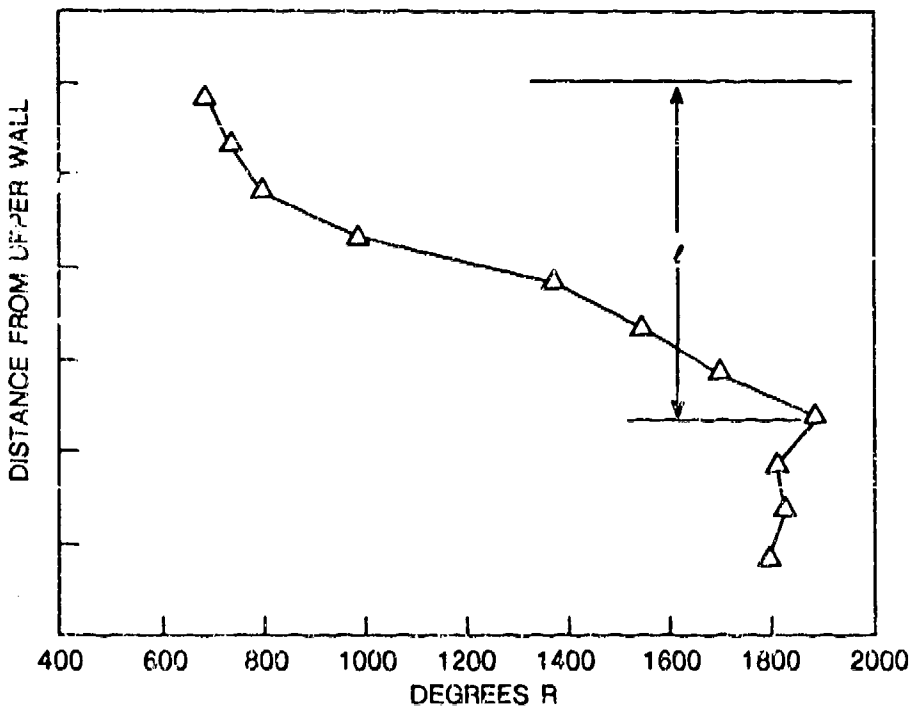

Fig. 52 Definition of mixing layer thickness based on static temperature.

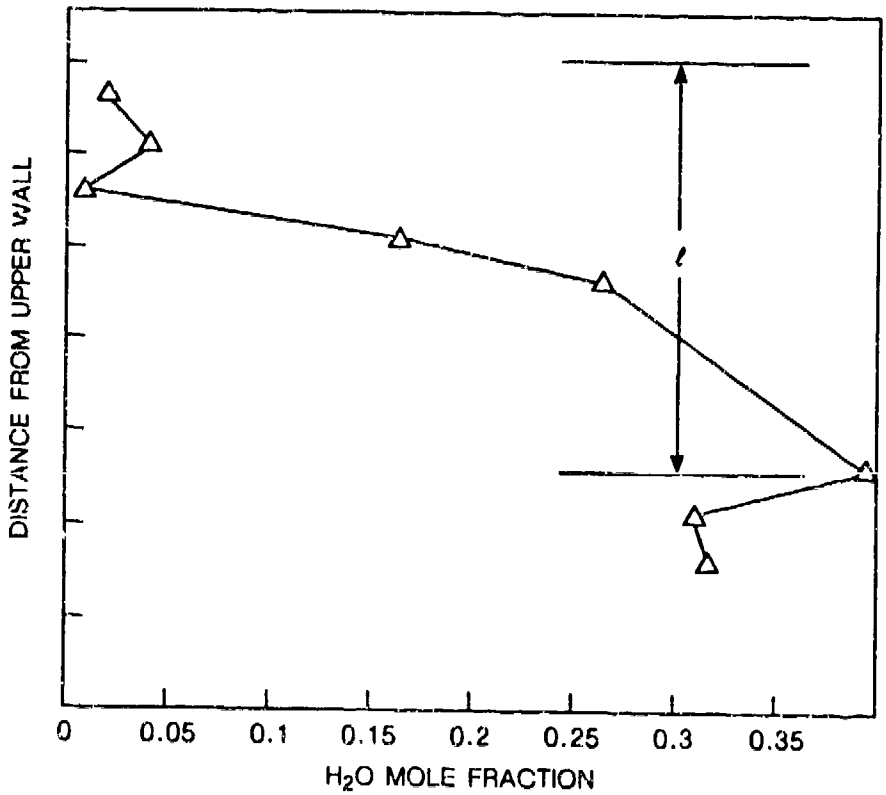

Fig. 53 Definition of mixing layer thickness based on water vapor mole fraction.

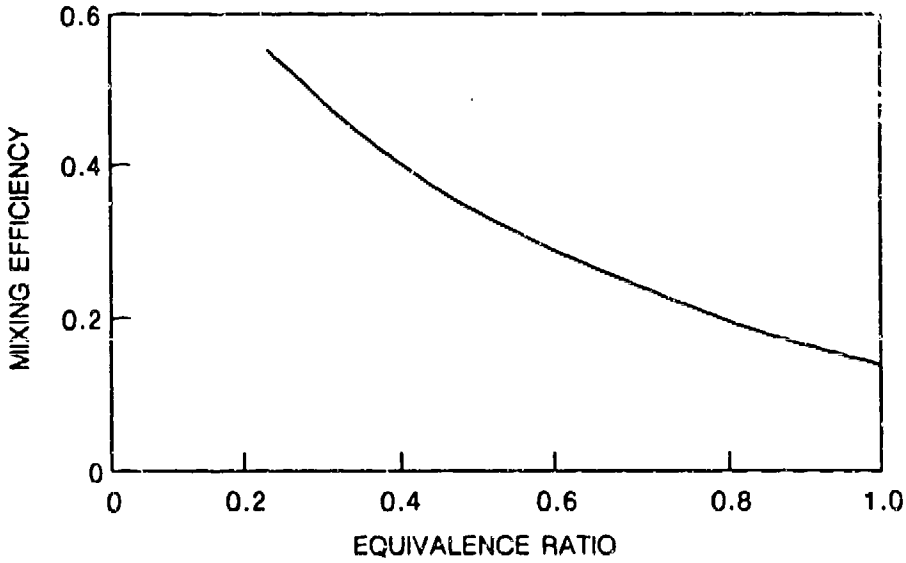

Fig. 54 Estimated mixing efficiency for current experiment.

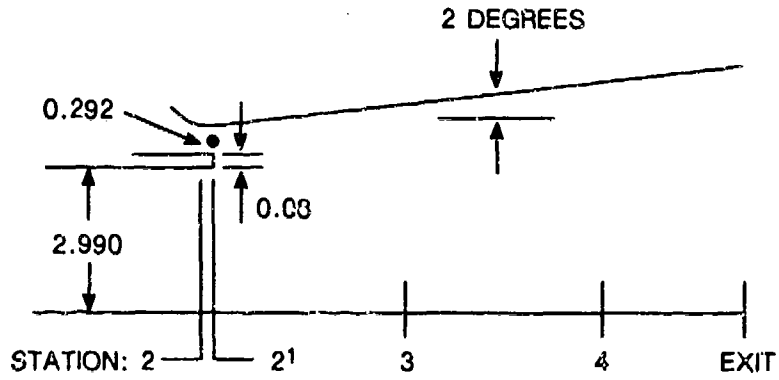

ALL DIMENSIONS IN INCHES

AXIAL STATION	GEO. AREA, FT^2	AREA RATIO, A/A_2
2	0.125	1.000
2^1	0.140	1.124
3	0.148	1.186
4	0.156	1.250
EXIT	0.164	1.315

Fig. 55 Duct geometry used for cycle calculations.

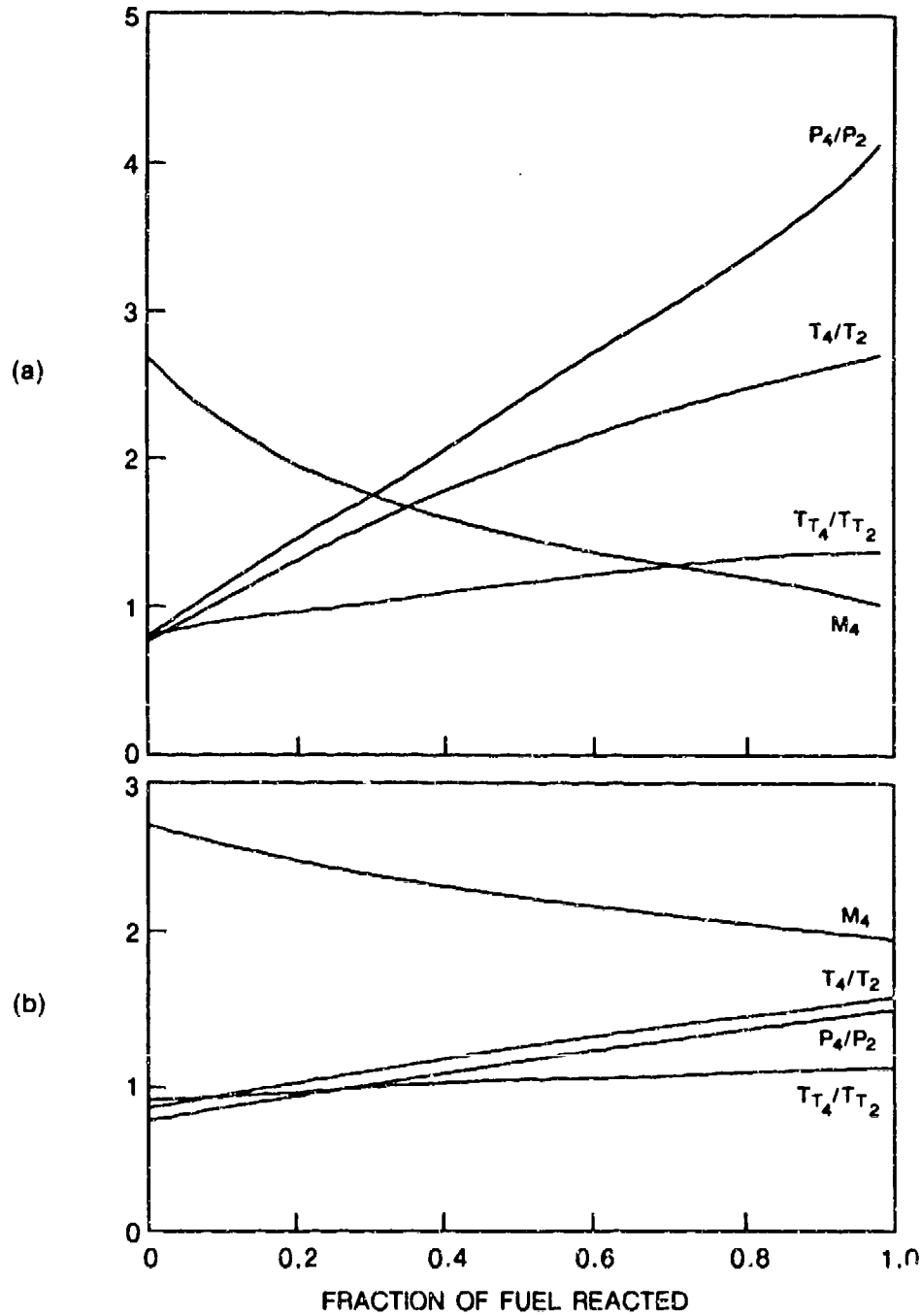

Fig. 56 Results of cycle analyses of test configuration (a) Injected ϕ = 1; (b) Injected ϕ = 0.5. See Fig. 55 for subscript notation.

Fig. 57 Calculated nozzle static pressure distribution.

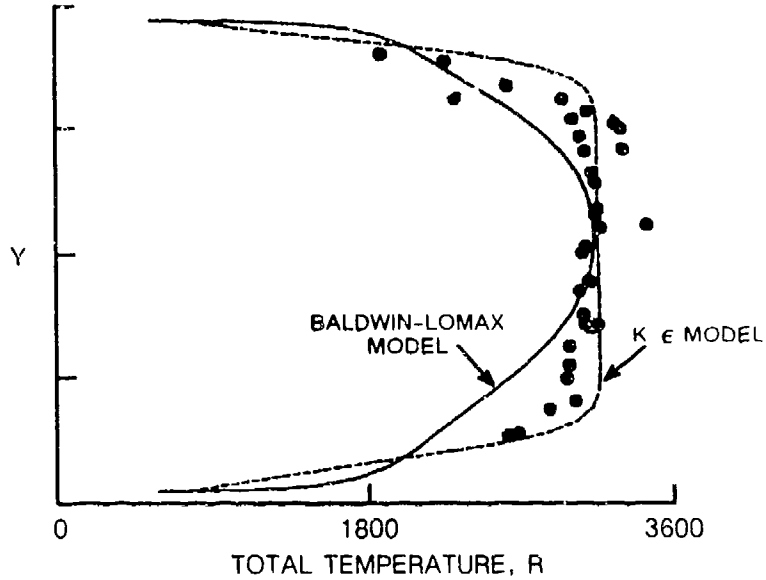

Fig. 58 Comparison between computed and measured total temperature profiles.

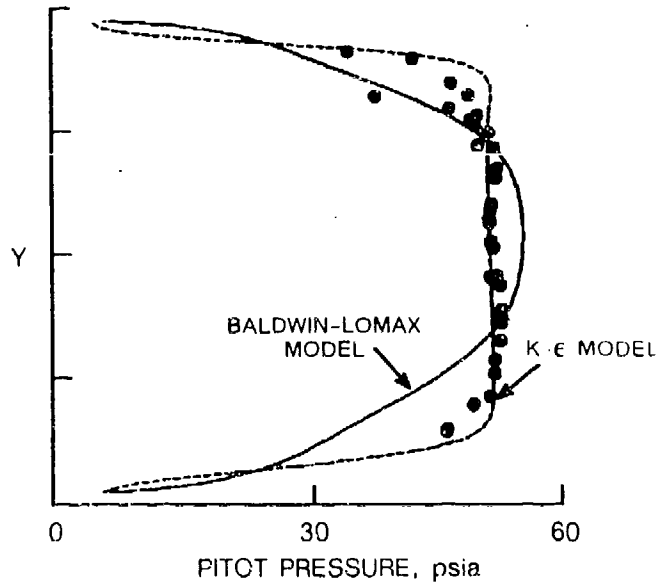

Fig. 59 Comparison between computed and measured pitot pressure profiles.

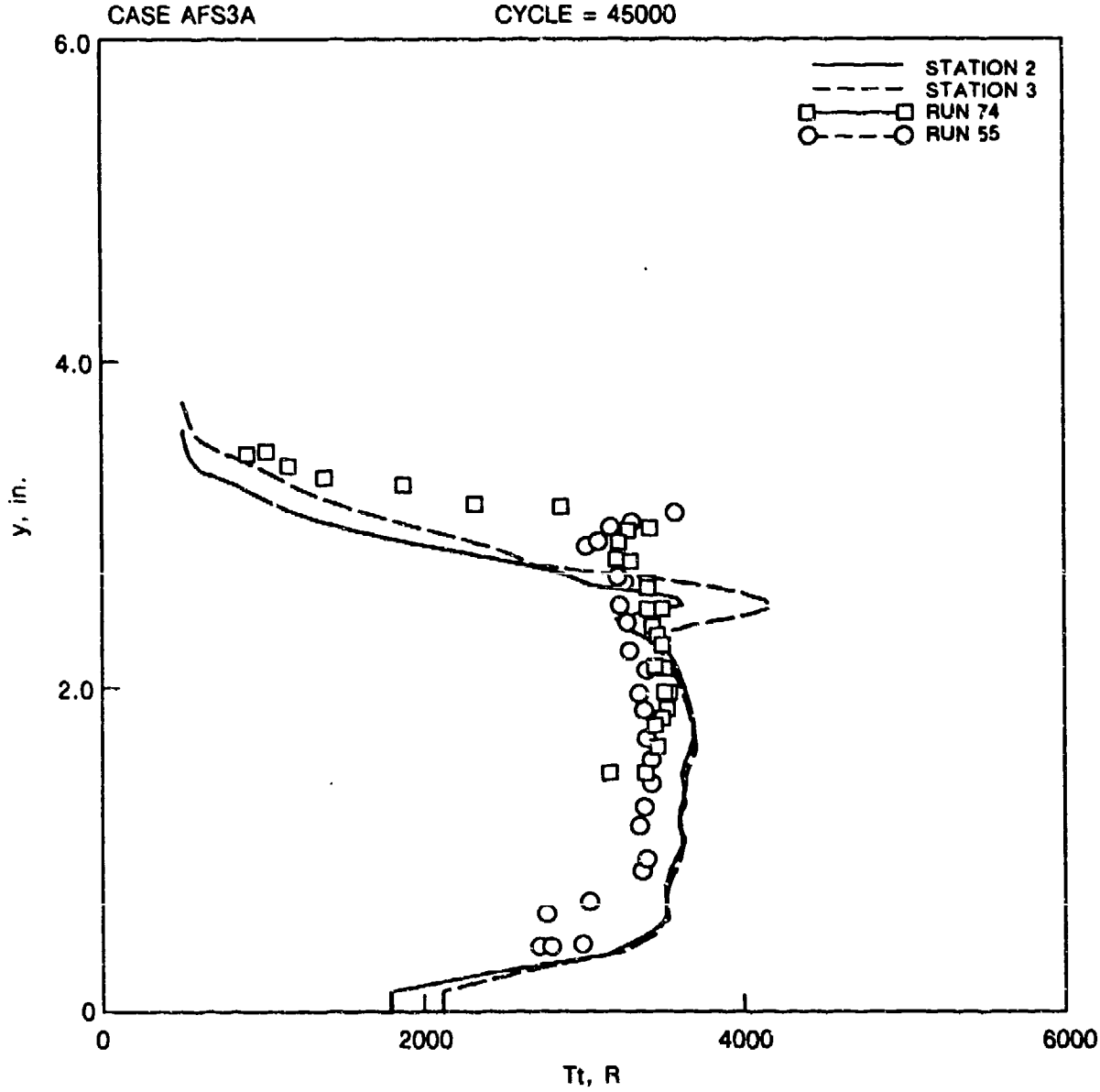

Fig. 60 Comparison between computed and measured stagnation temperature profiles for $\sigma = 1$ (case AFS3A).

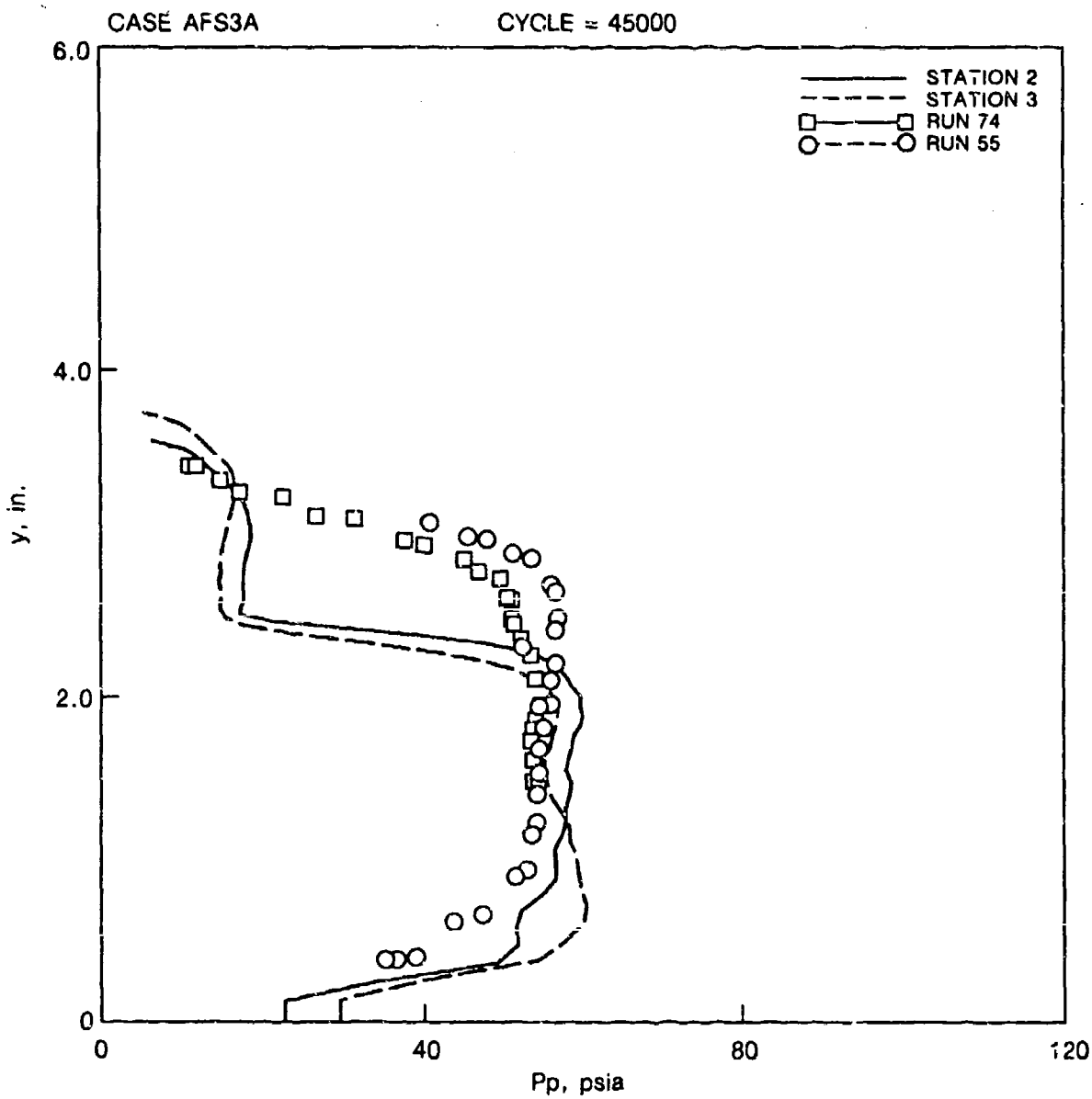

Fig. 61 Comparison between computed and measured pitot pressure profiles for $\theta' = 1$ (case AFS3A).

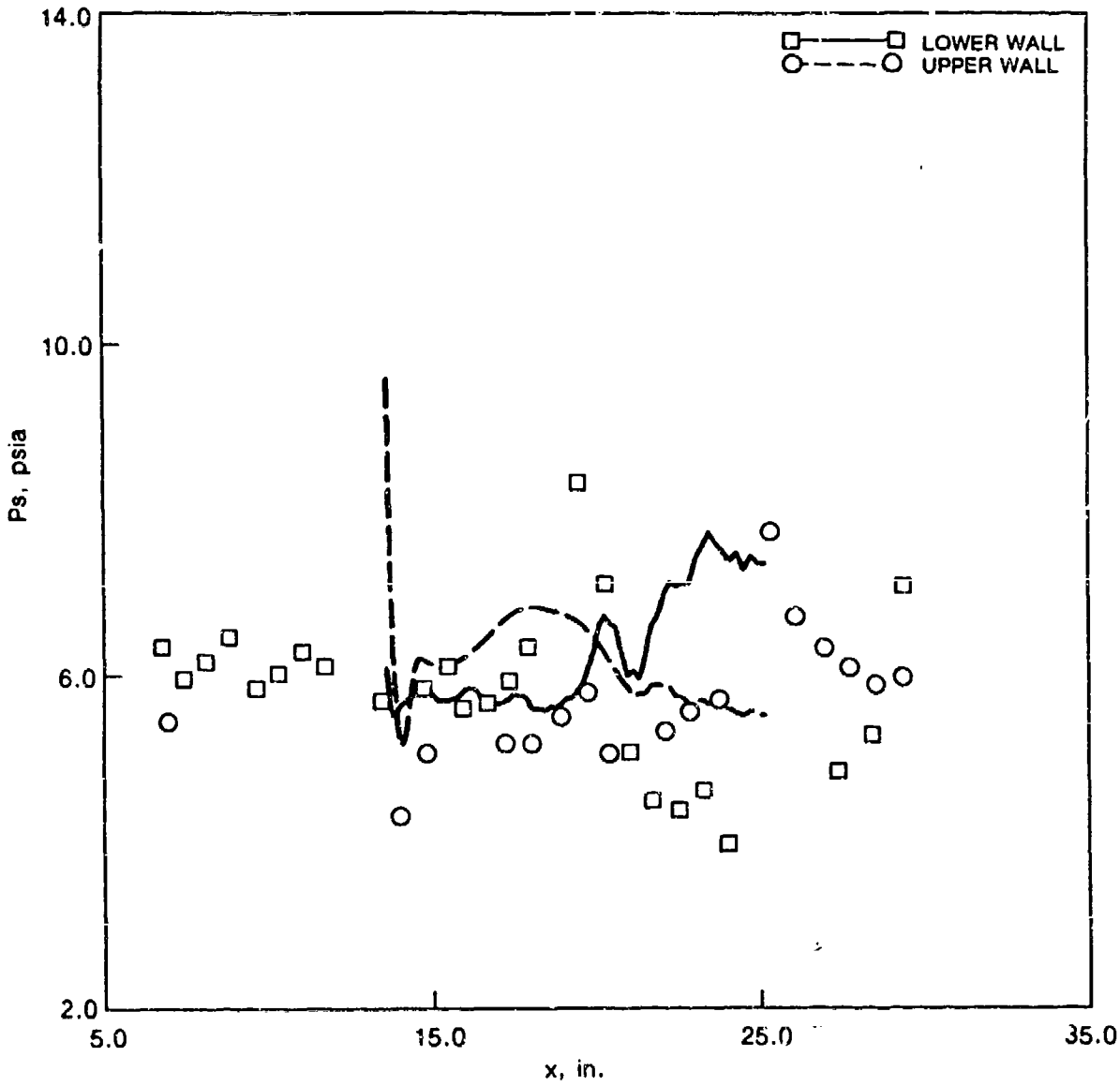

Fig. 62 Comparison between computed and measured wall static pressure distributions for σ = 1 (case AFS3A).

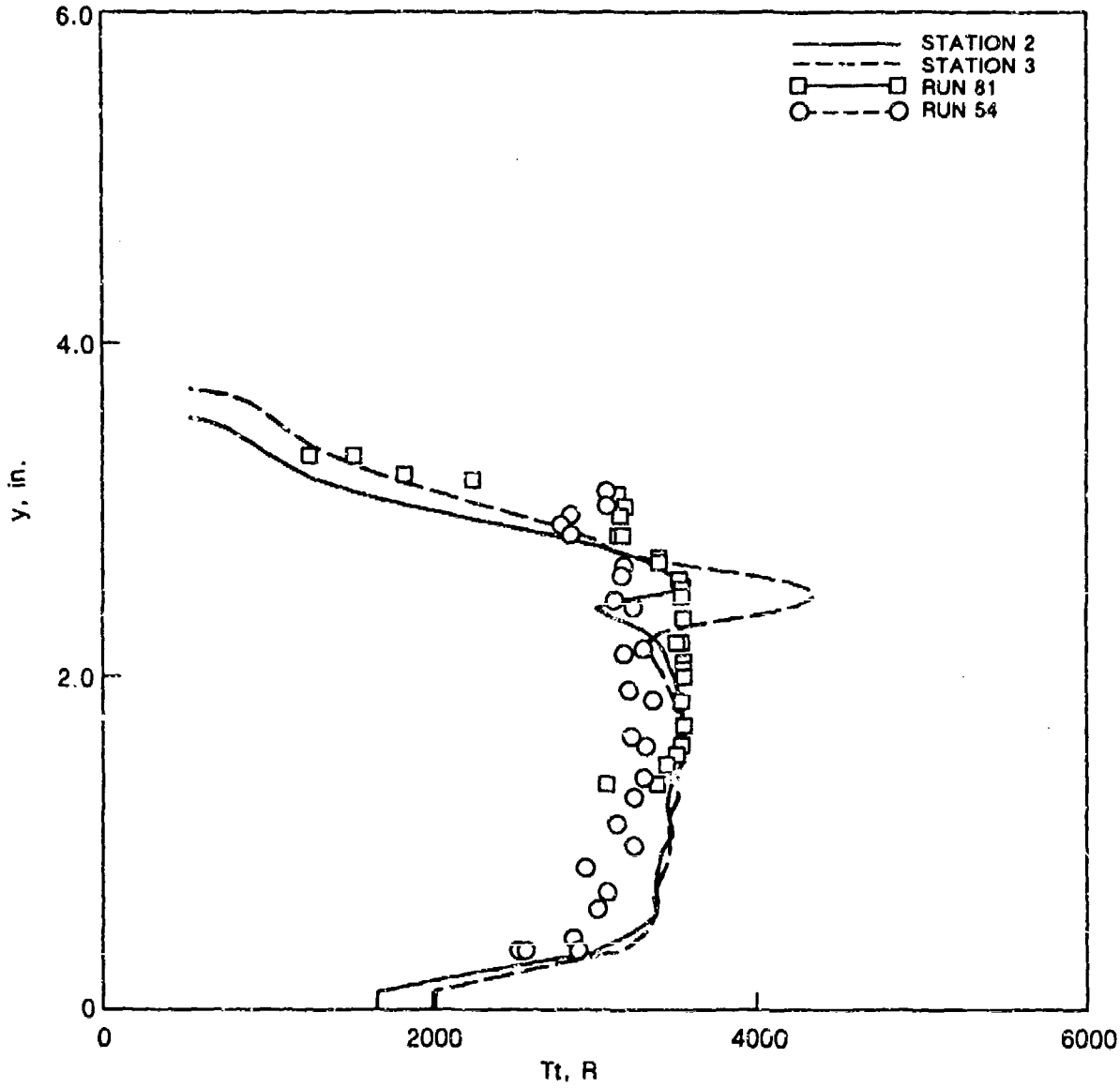

Fig. 63 Comparison between computed and measured stagnation temperature profiles for ϕ = 0.5 (case AFS4A).

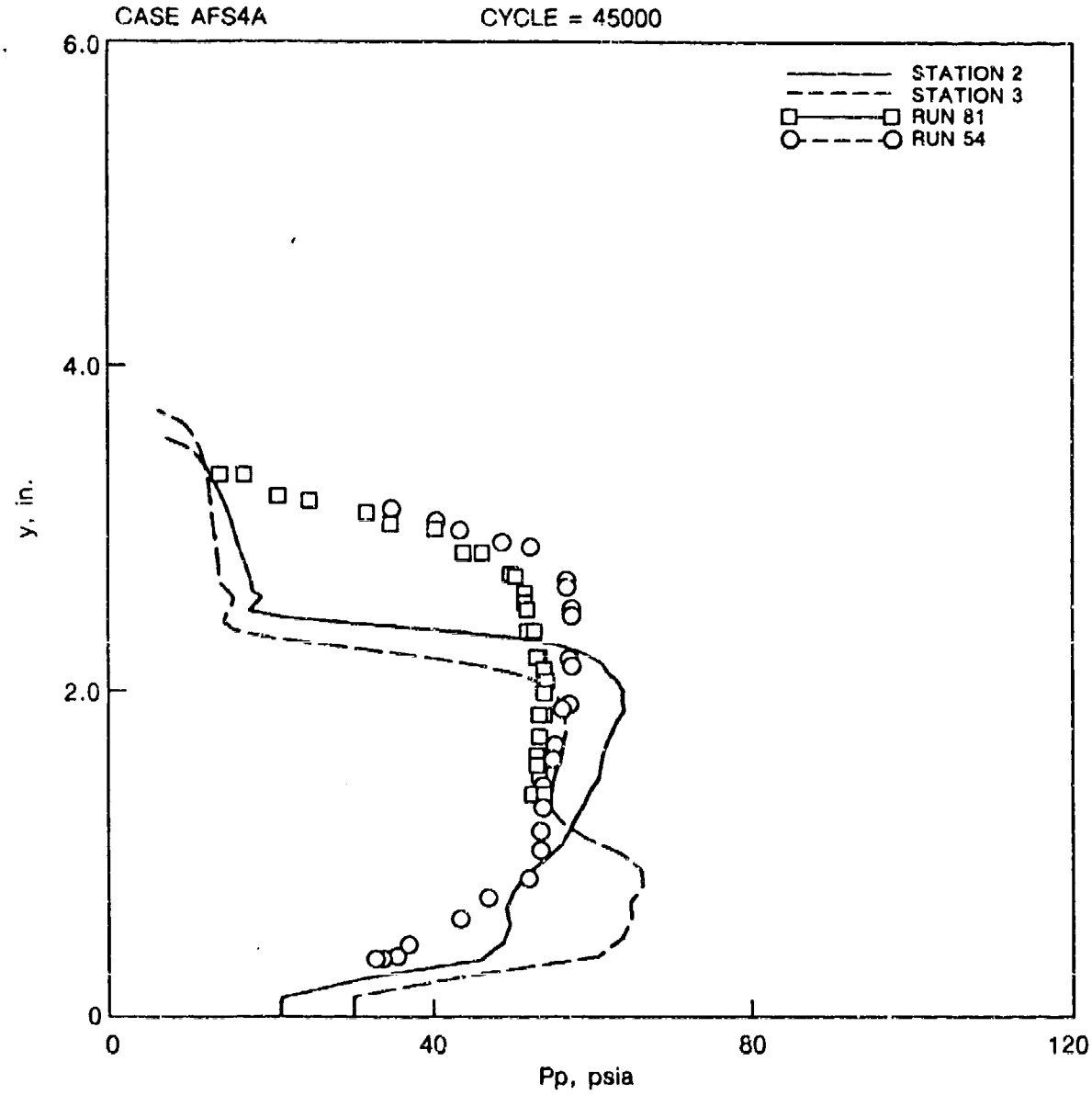

Fig. 64 Comparison between computed and measured pitot pressure profiles for $\delta' = 0.5$ (case AFS4A).

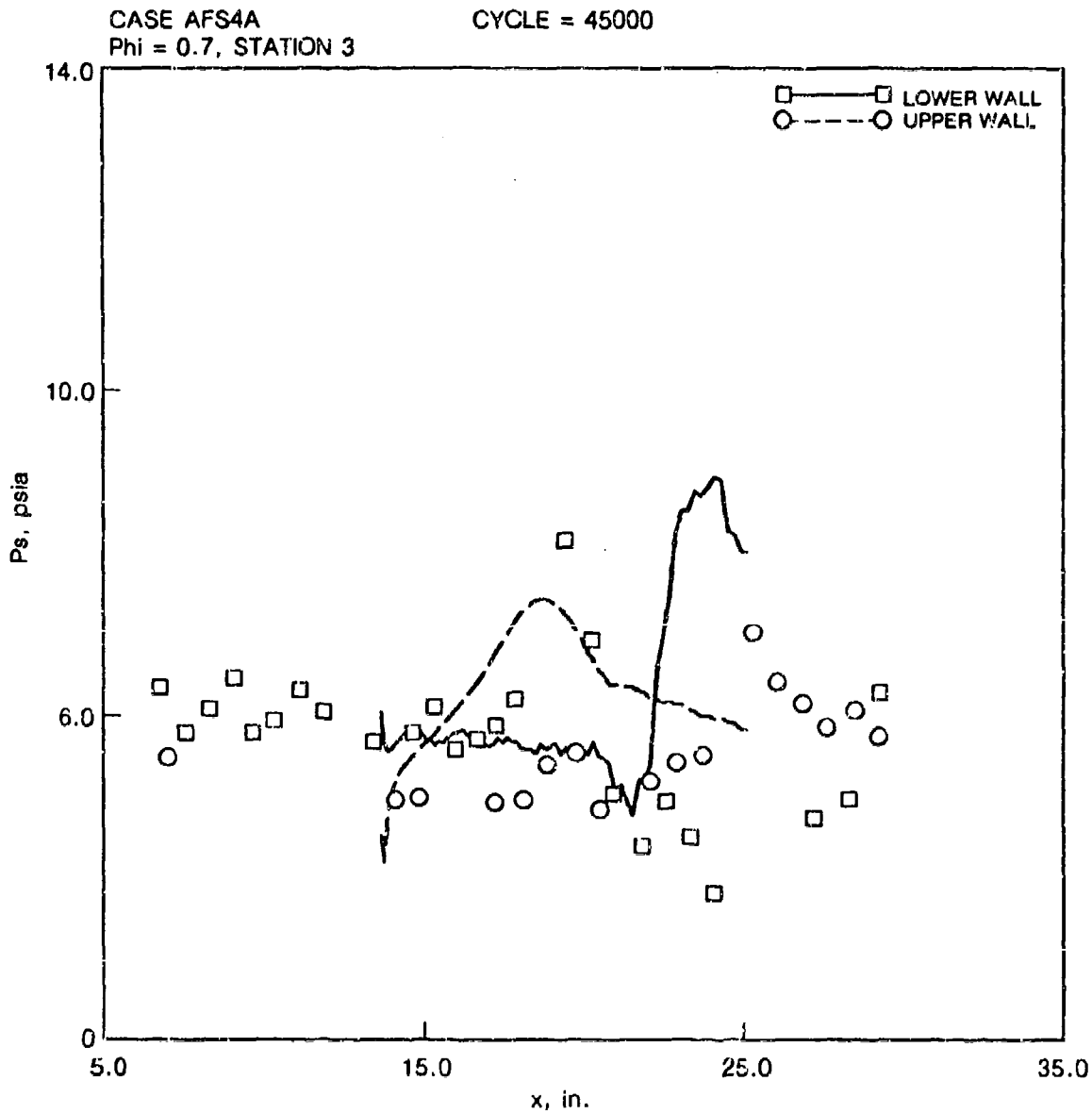

Fig. 65 Comparison between computed and measured wall static pressure distributions for ϕ = 0.5 (case AFS4A).

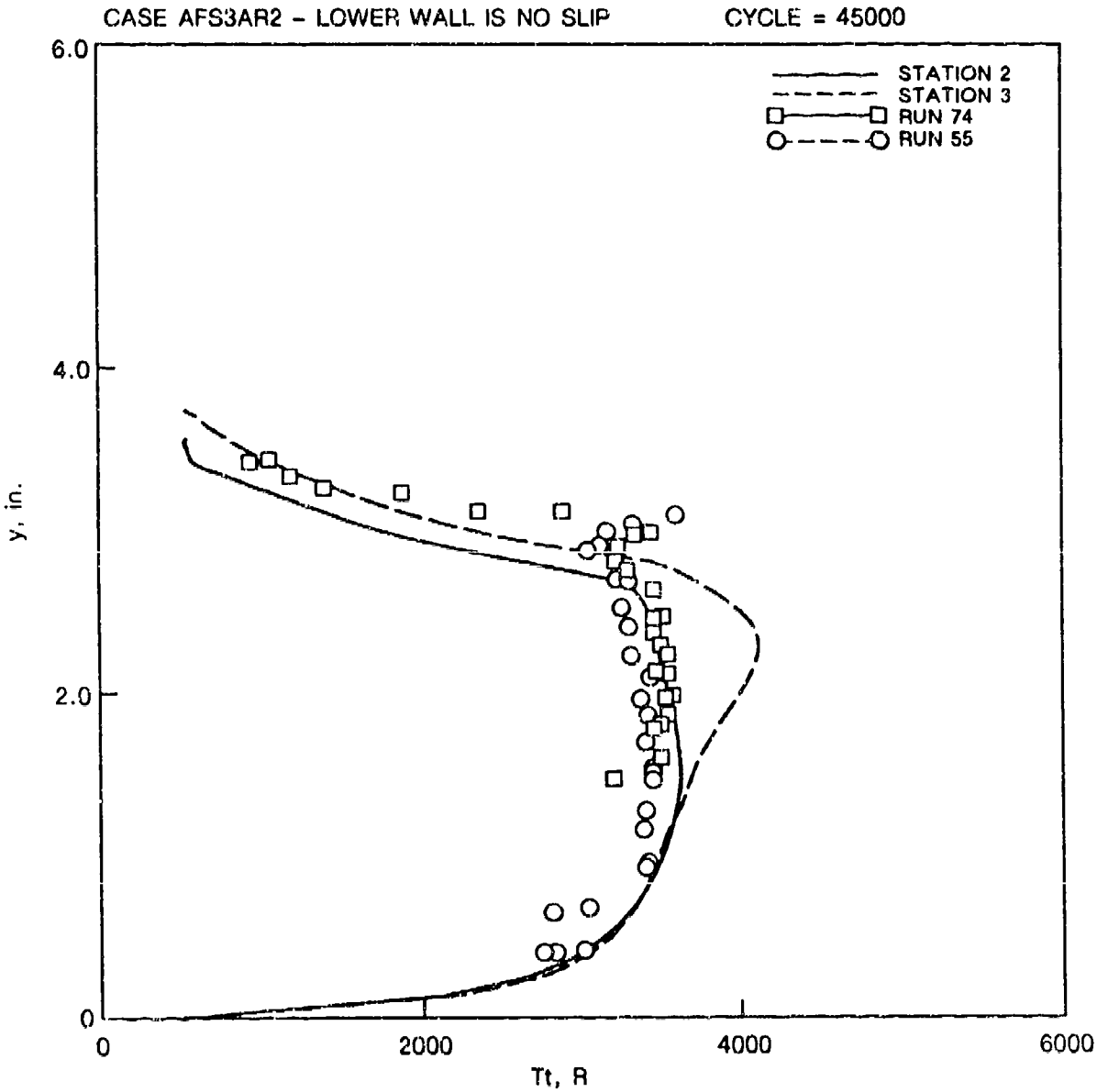

Fig. 66 Comparison between computed and measured stagnation temperature profiles for $\gamma = 1$ (case AFS3AR2).

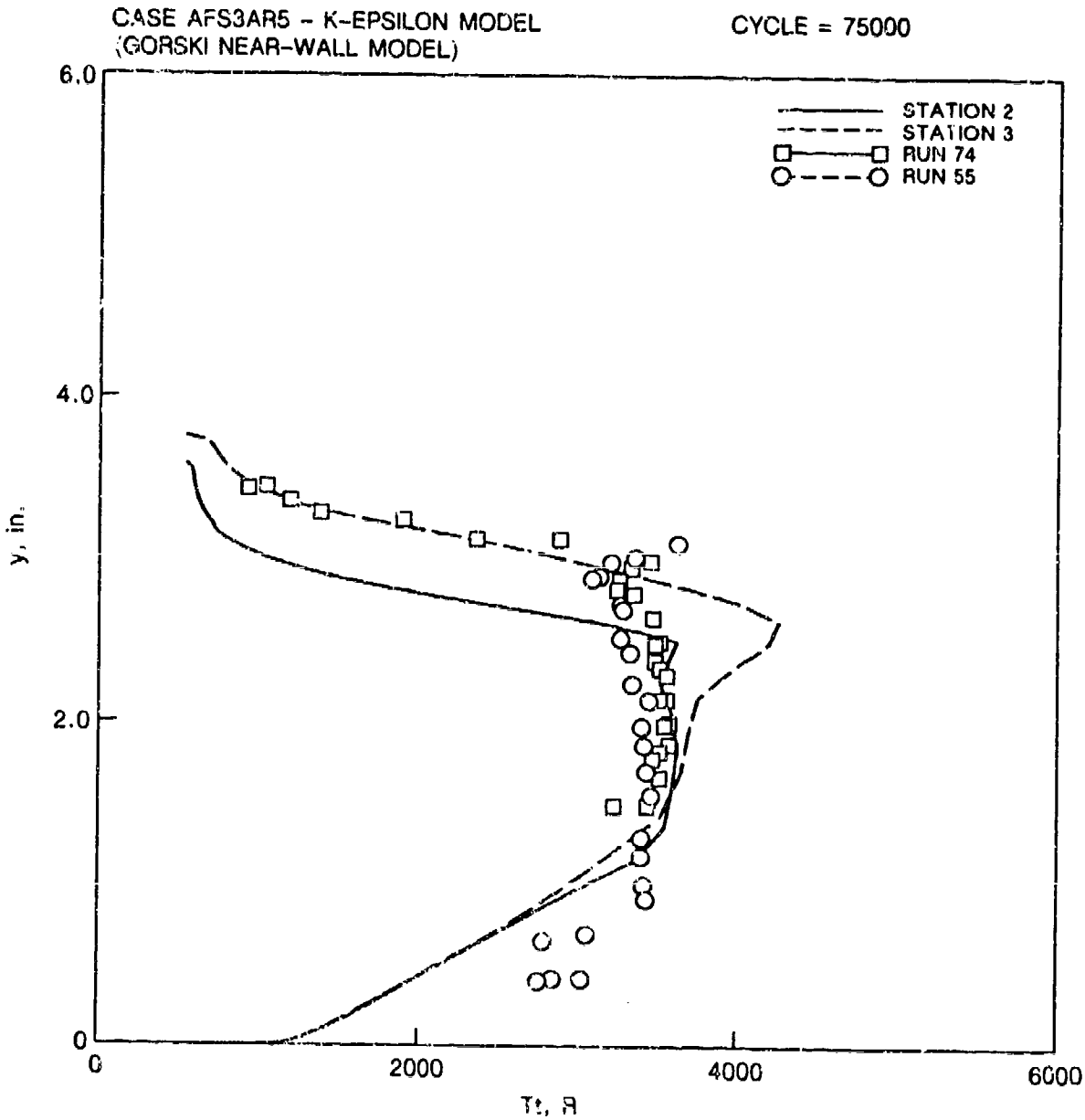

Fig. 67 Comparison between computed and measured stagnation temperature profiles for $\gamma = 1$ (case AFS3AR5).

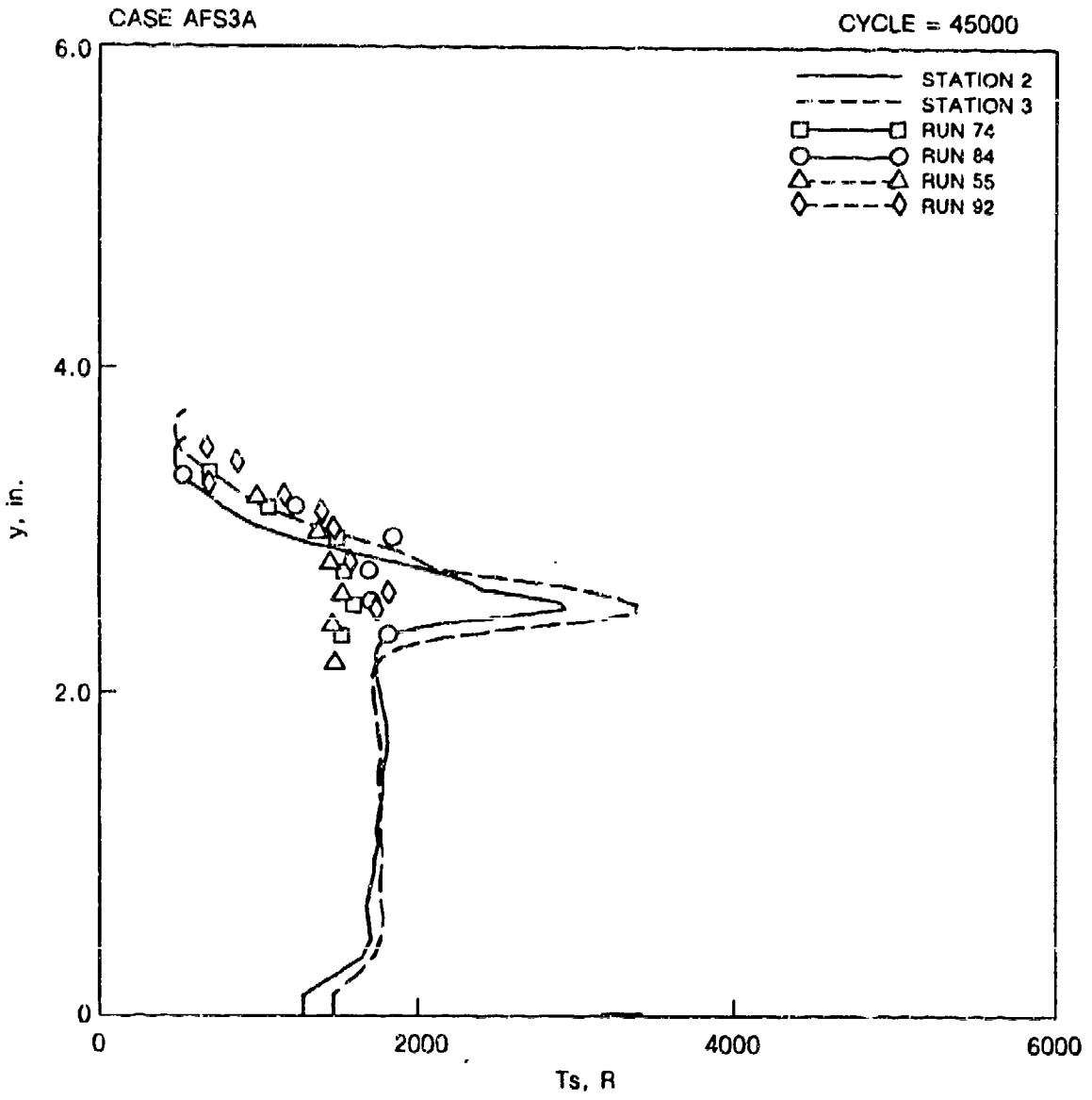

Fig. 68 Comparison between computed static temperature and CARS measurement at Stations 2 and 3 during combustion test at an equivalence ratio of 1. Free shear-layer.

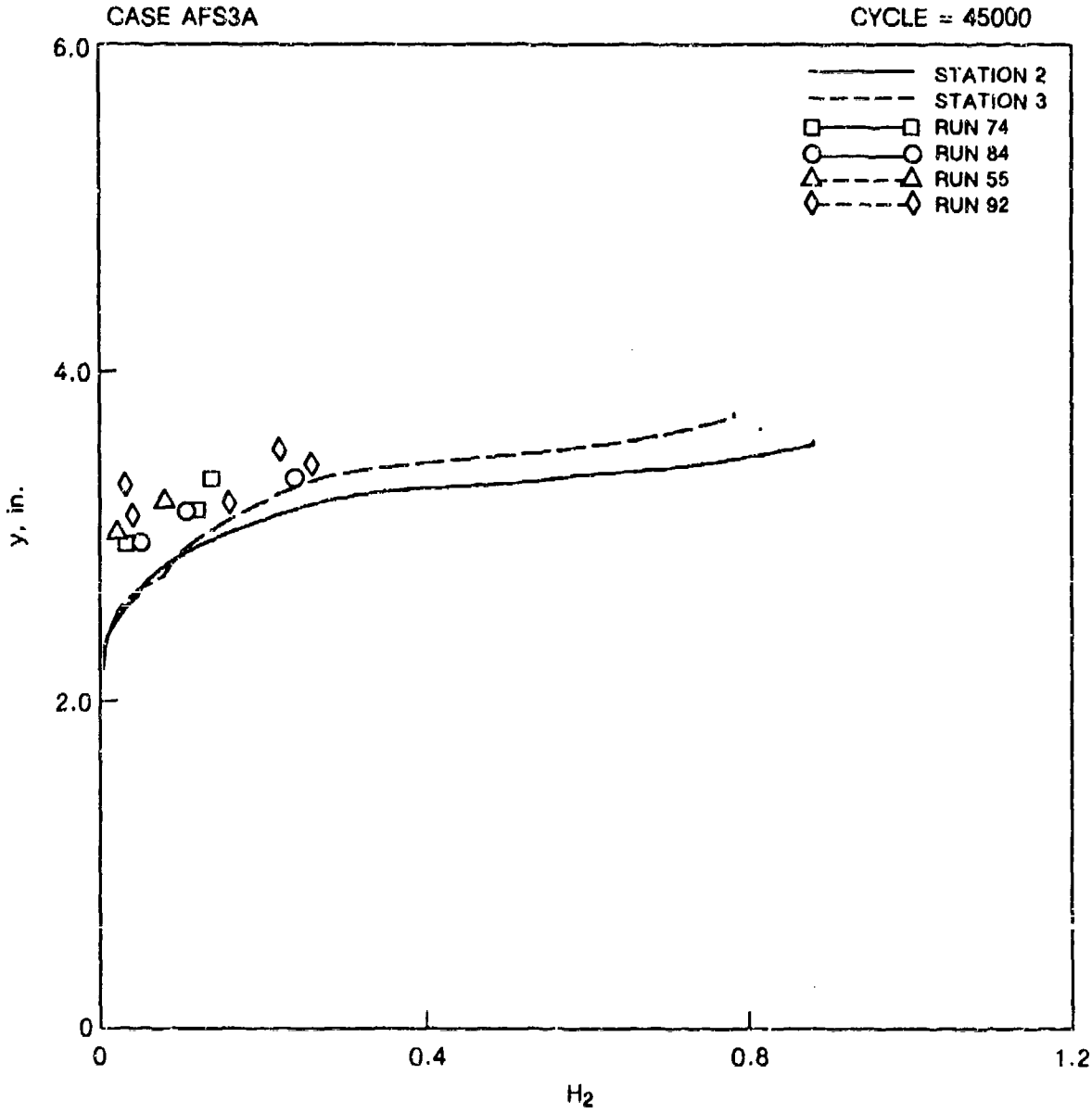

Fig. 69 Comparison between computed hydrogen mass fraction and CARS measurement at Stations 2 and 3 during combustion test at an equivalence ratio of 1. Free shear-layer.

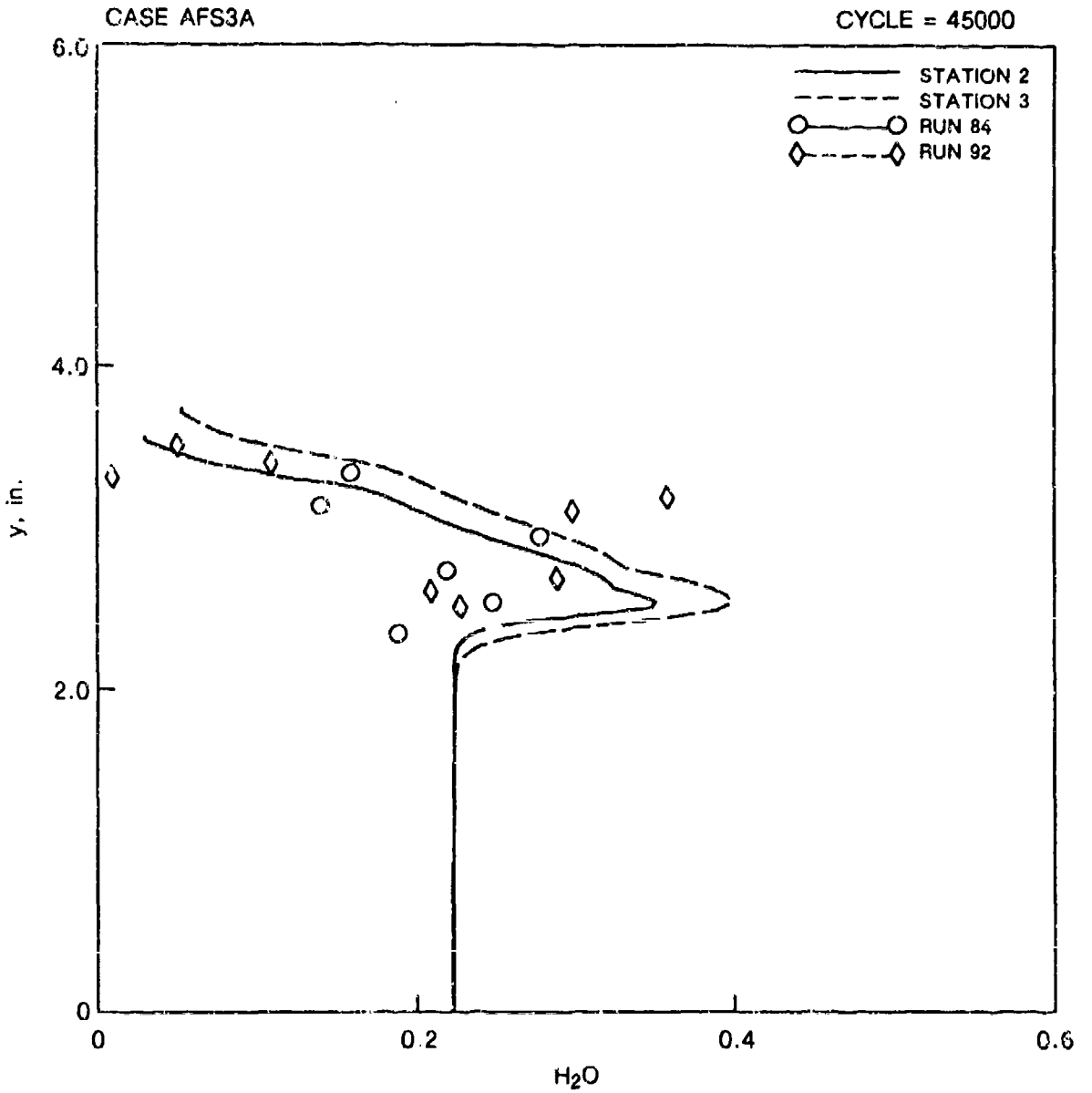

Fig. 70 Comparison between computed water vapor mass fraction and CARS measurement at Stations 2 and 3 during combustion test at an equivalence ratio of 1. Free shear-layer.

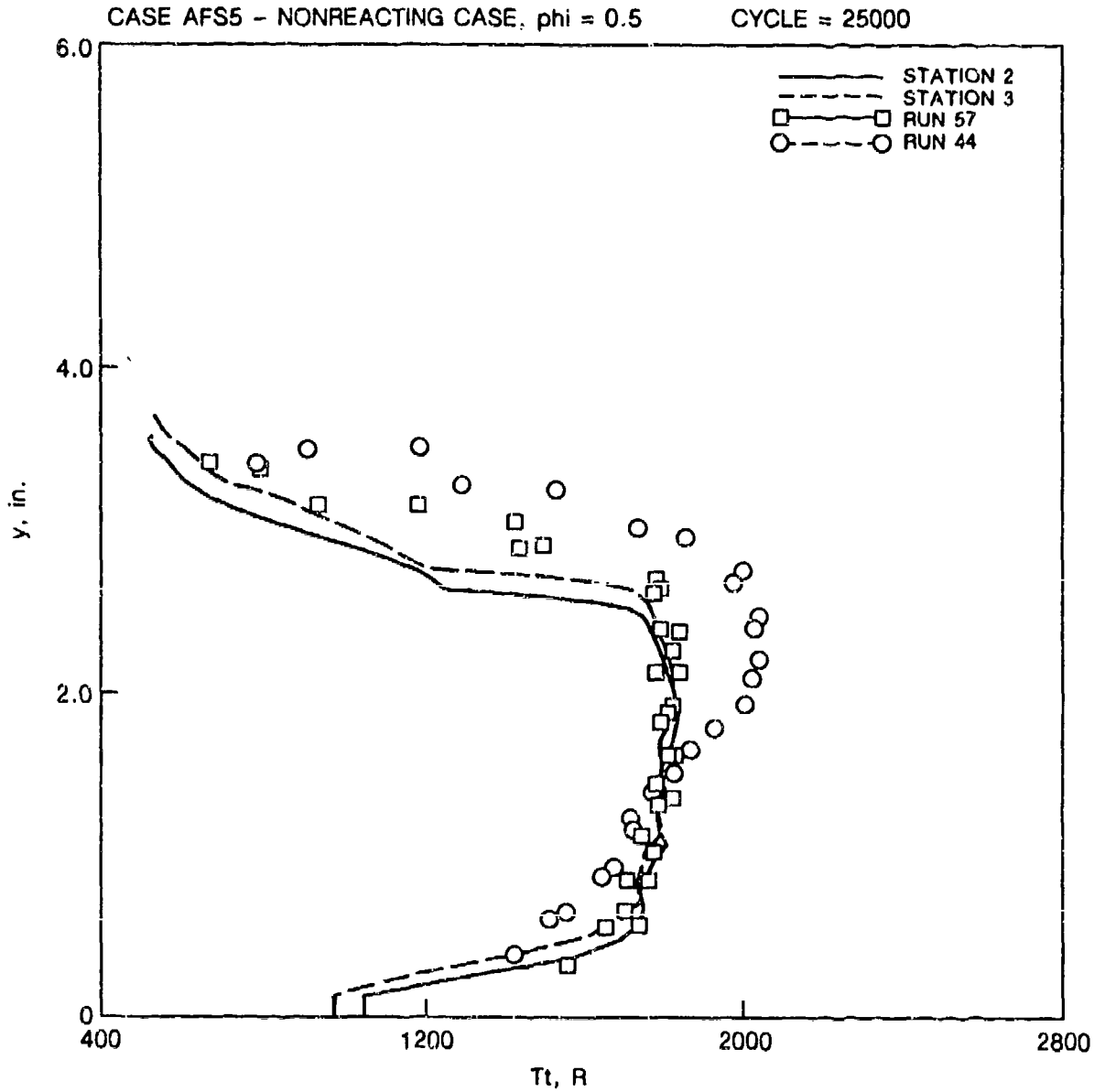

Fig. 71 Comparison between computed and measured stagnation temperature profiles for ϕ = 0.5 (case AFS5).

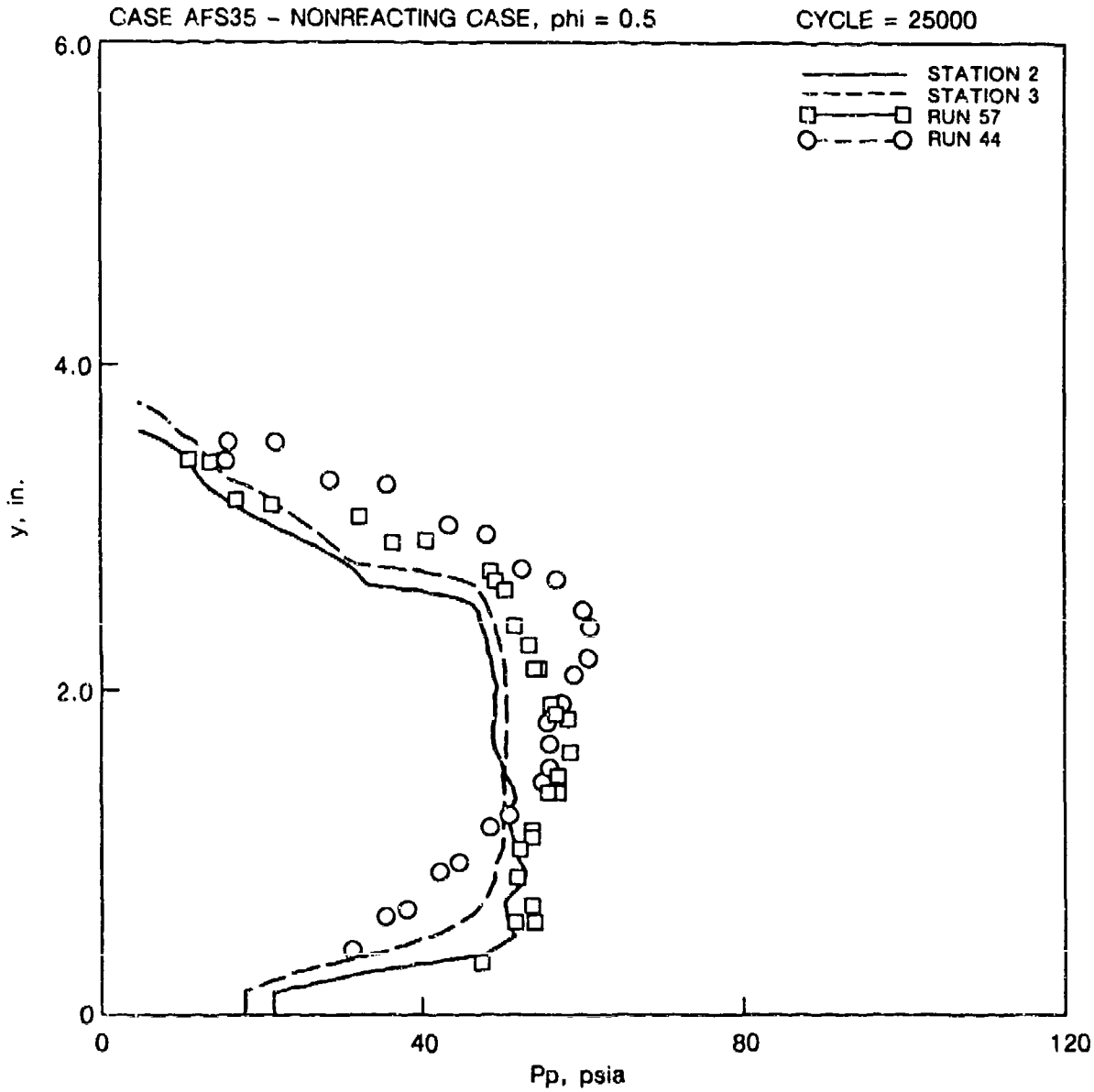

Fig. 72 Comparison between computed and measured pitot pressure profiles for Ø = 0.5 (case AFS5).

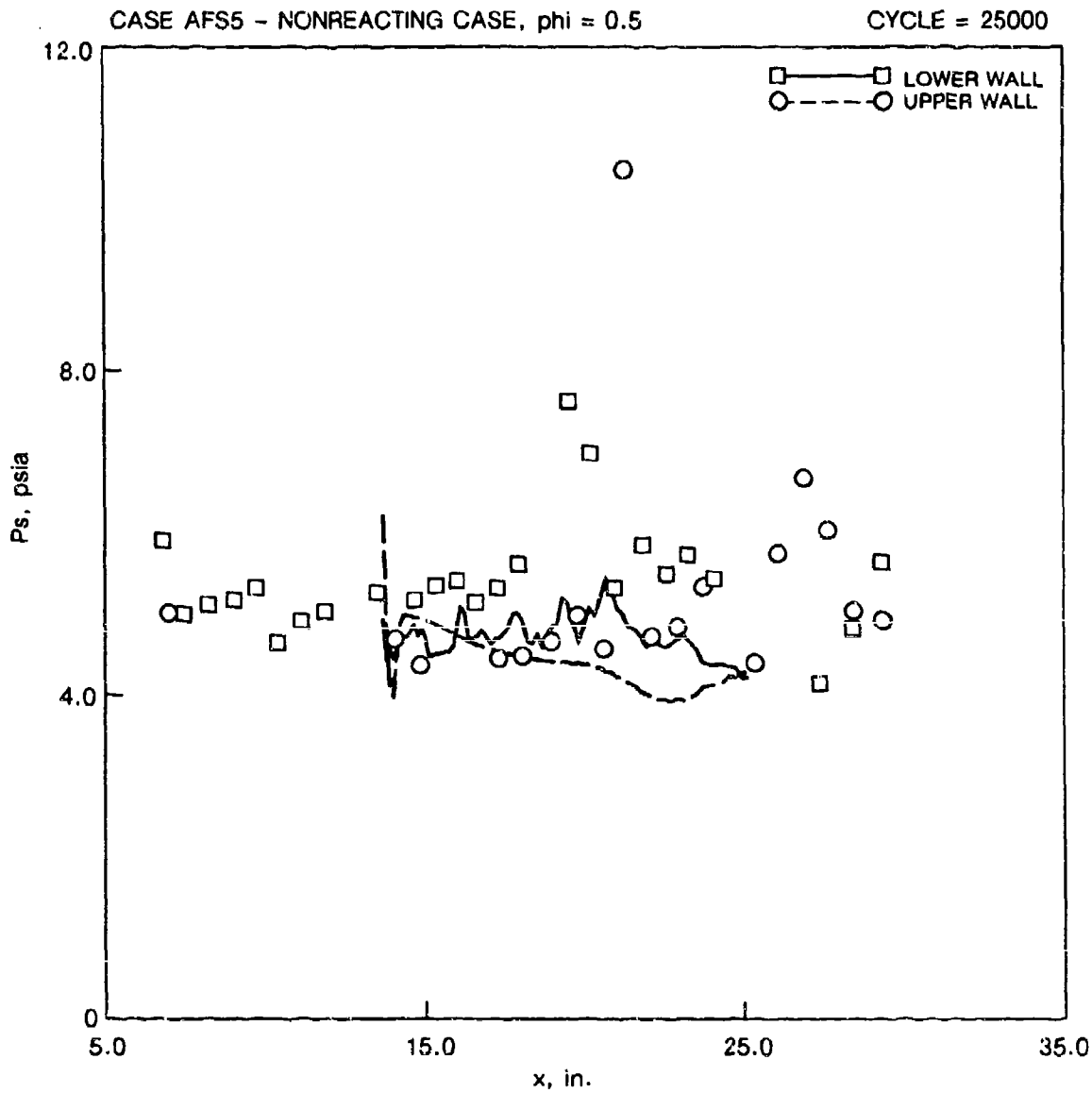

Fig. 73 Comparison between computed and measured wall static pressure distributions for ϕ = 0.5 (case AFS5).

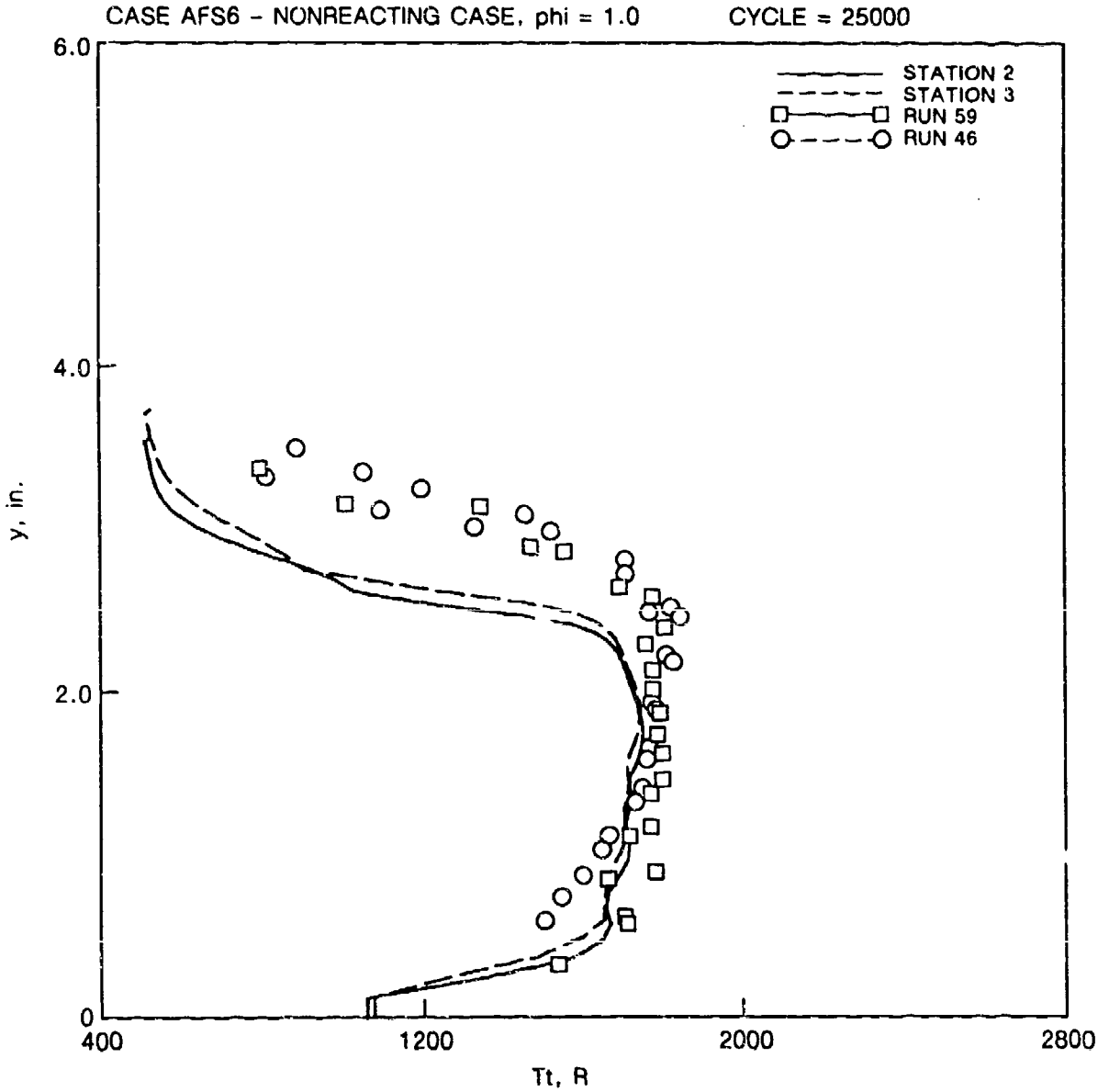

Fig. 74 Comparison between computed and measured stagnation temperature profiles for ϕ = 1 (case AFS6).

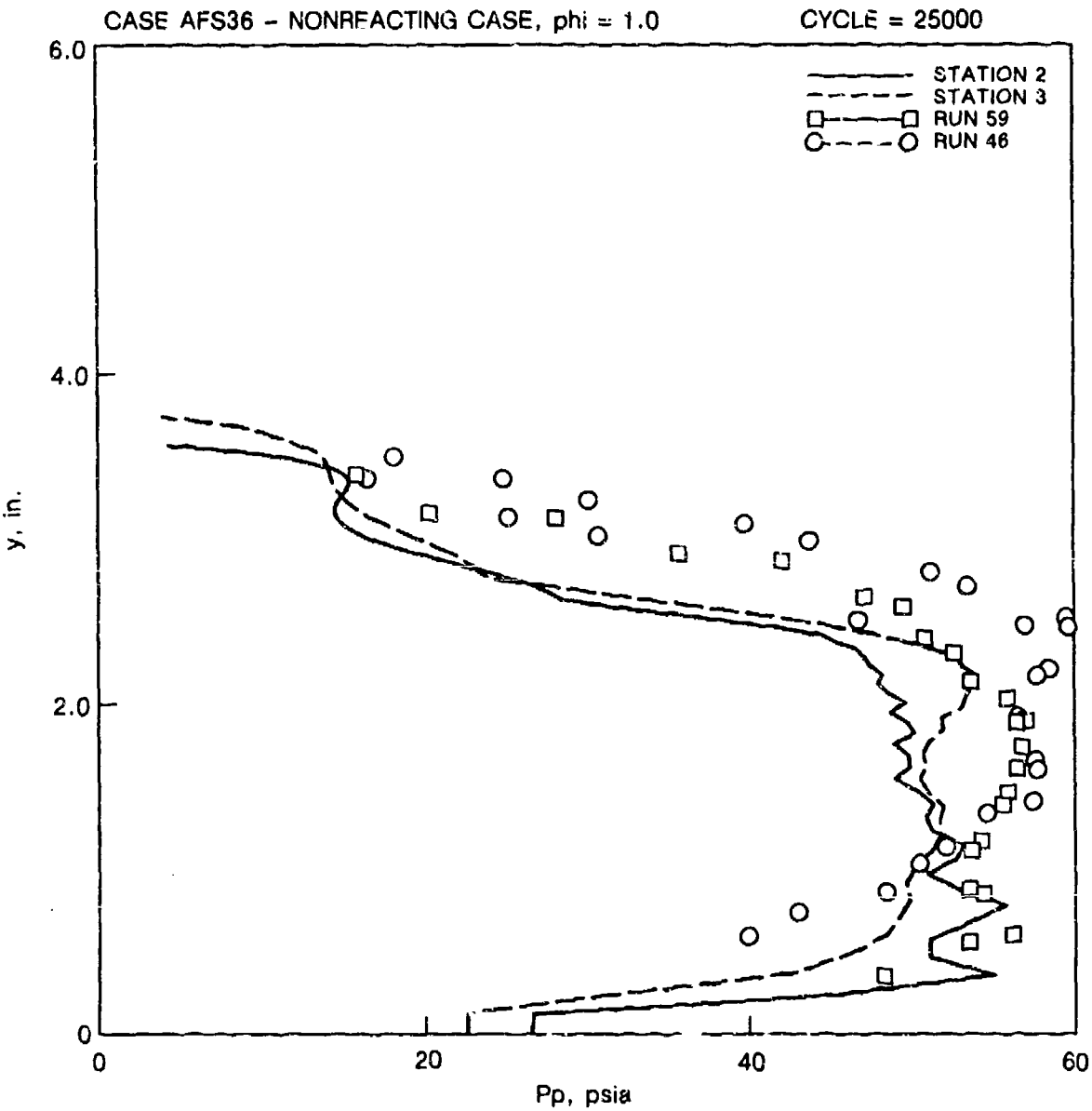

Fig. 75 Comparison between computed and measured pitot pressure profiles for ϕ = 1 (case AFS6).

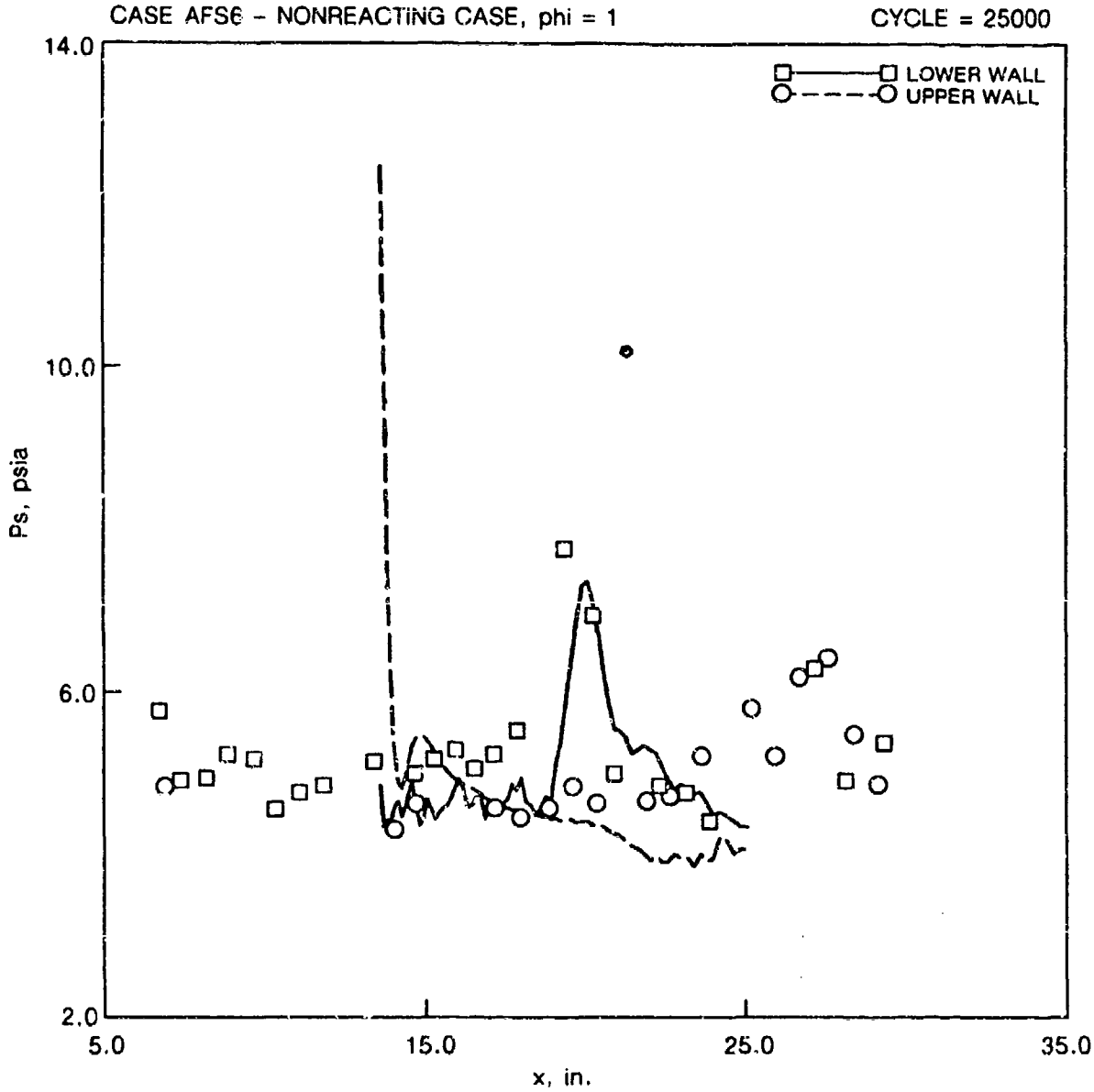

Fig. 76 Comparison between computed and measured wall static pressure distributions for ϕ = 1 (case AFS6).

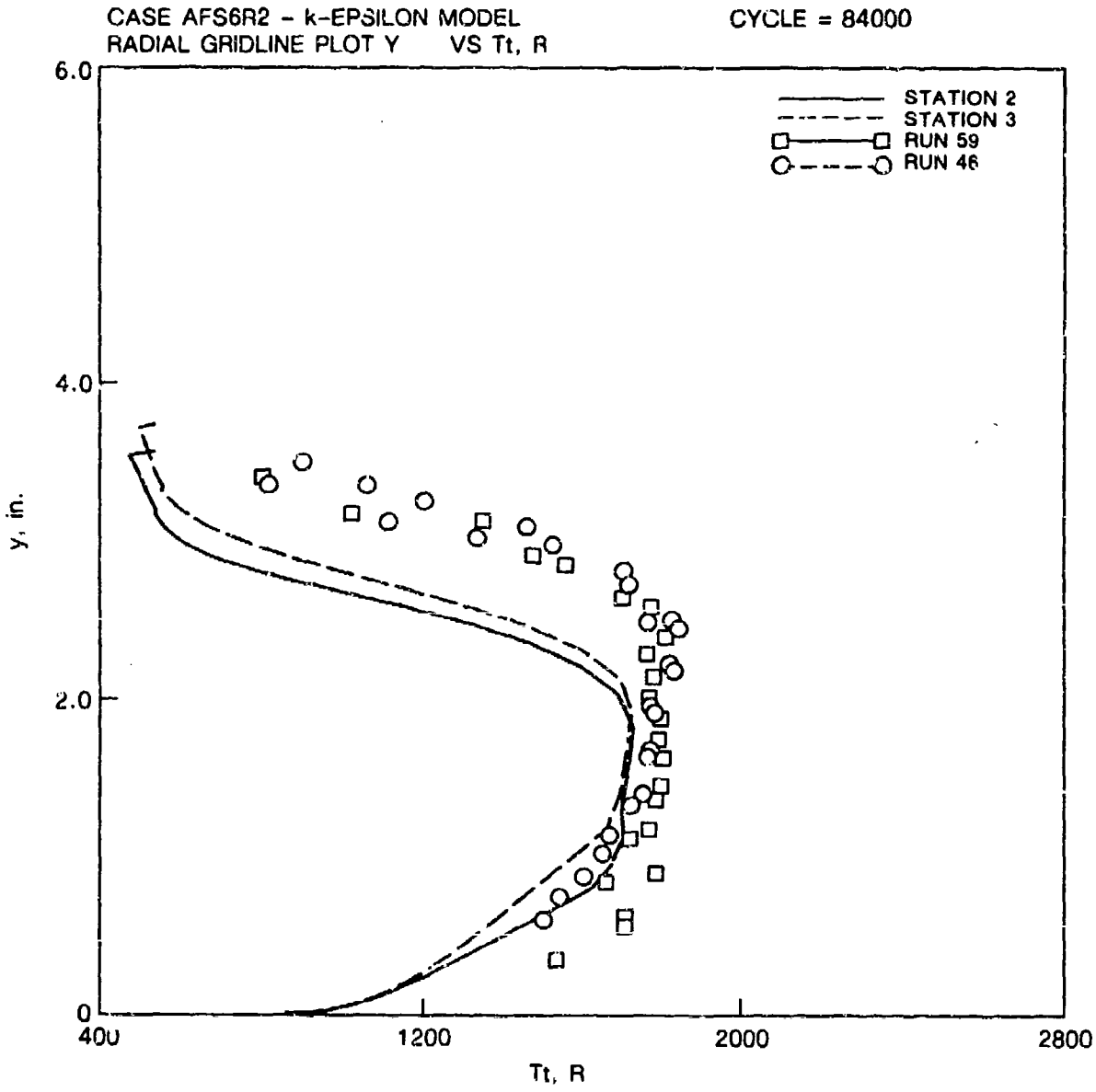

Fig. 77 Comparison between computed and measured stagnation temperature profiles for $\mathscr{X}$ = 1 (case AFS6R2).

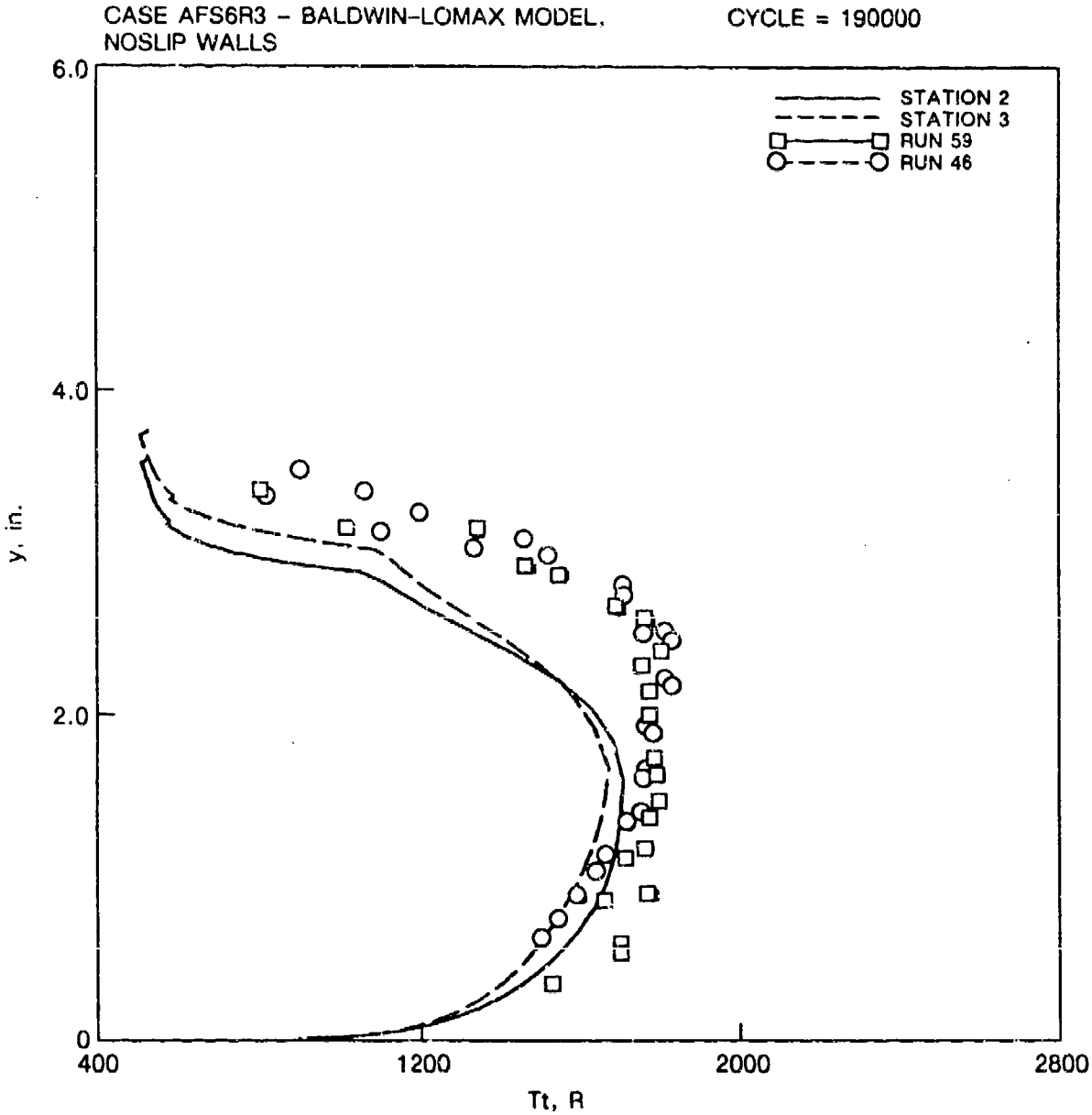

Fig. 78 Comparison between computed and measured stagnation temperature profiles for $\phi = 1$ (case AFS6R3).

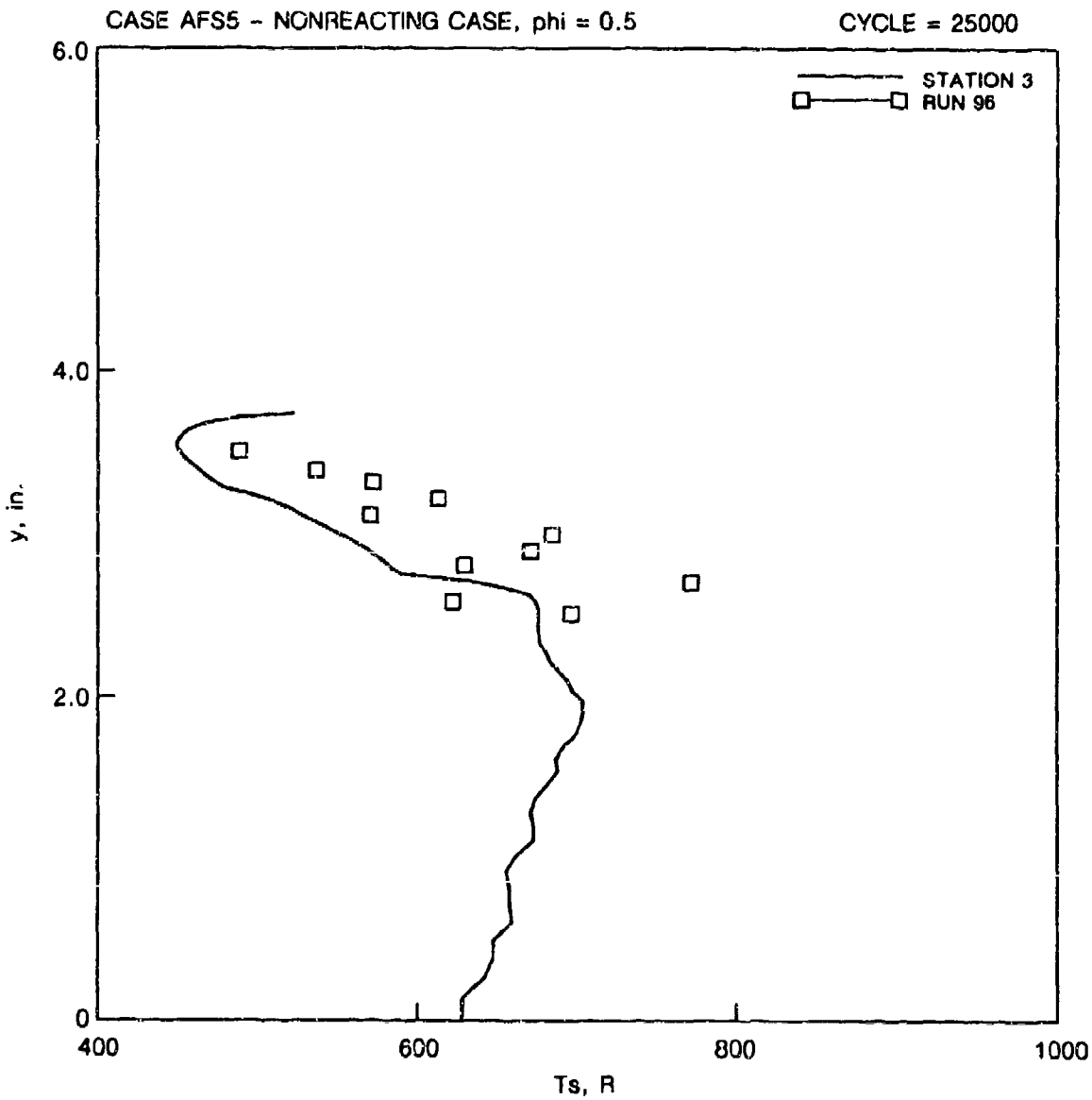

Fig. 79 Comparison between computed and CARS measured static temperature at Station 3 during non-reacting test at an equivalence ratio of 0.5. Free shear-layer.

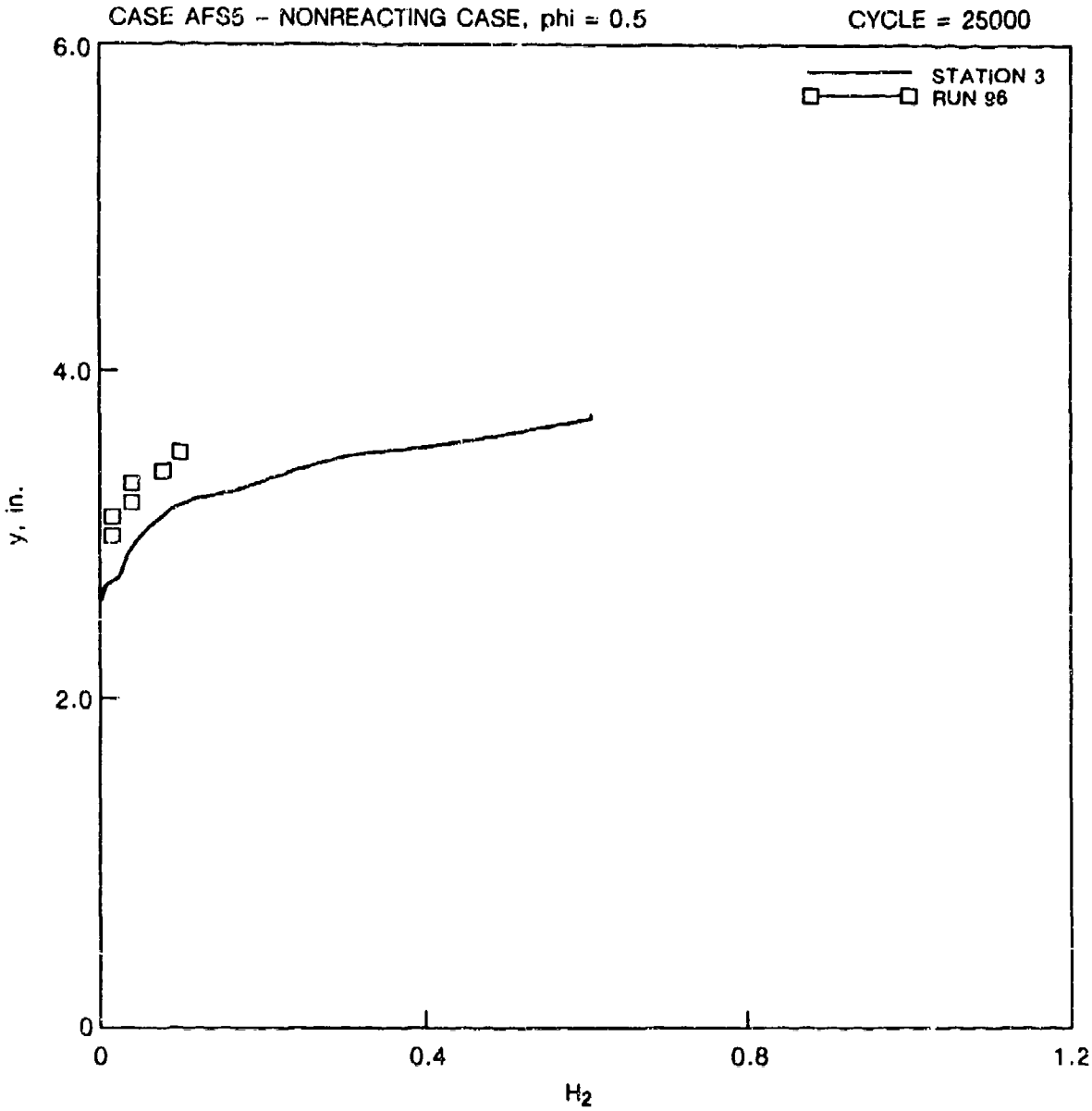

Fig. 80 Comparison between computed and measured hydrogen mass fractions at Station 3 during non-reacting test at an equivalence ratio of 0.5. Free shear-layer.

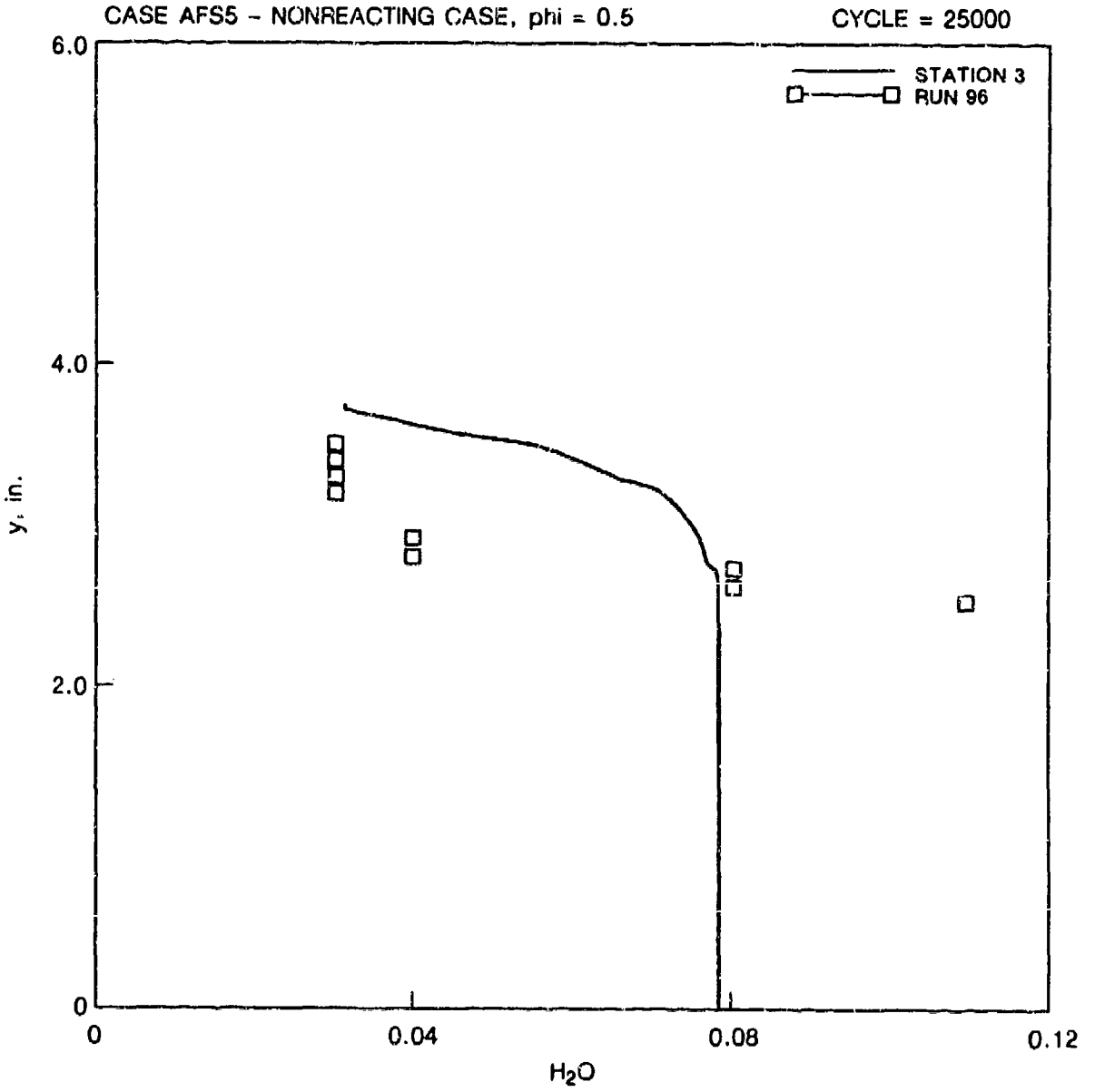

Fig. 81 Comparison between computed and measured water-vapor mass fractions at Station 3 during non-reacting test at an equivalence ratio of 0.5. Free shear-layer.

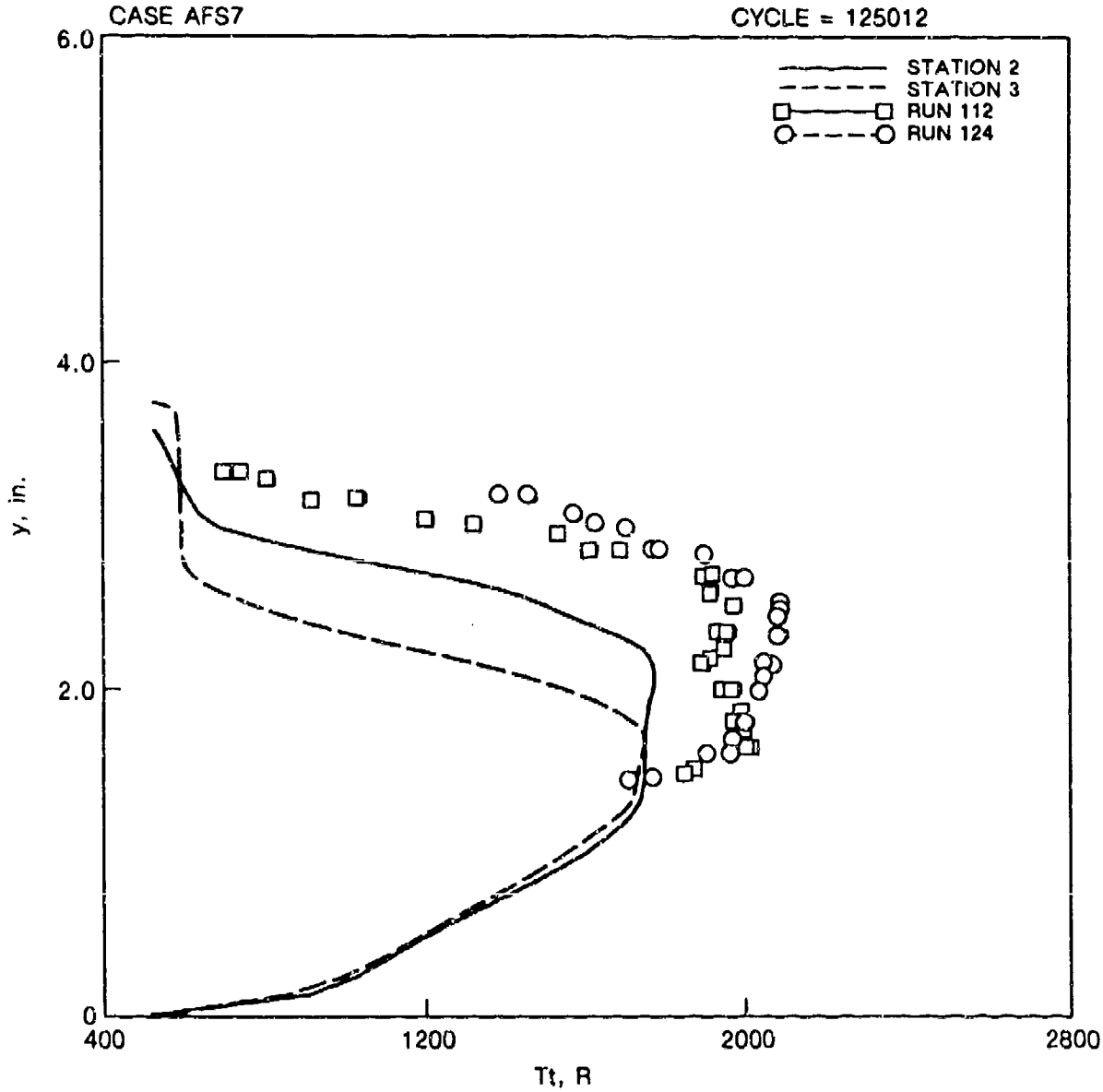

Fig. 82 Comparison between computed and measured stagnation temperature profiles for ϕ = 1 (case AFS7).

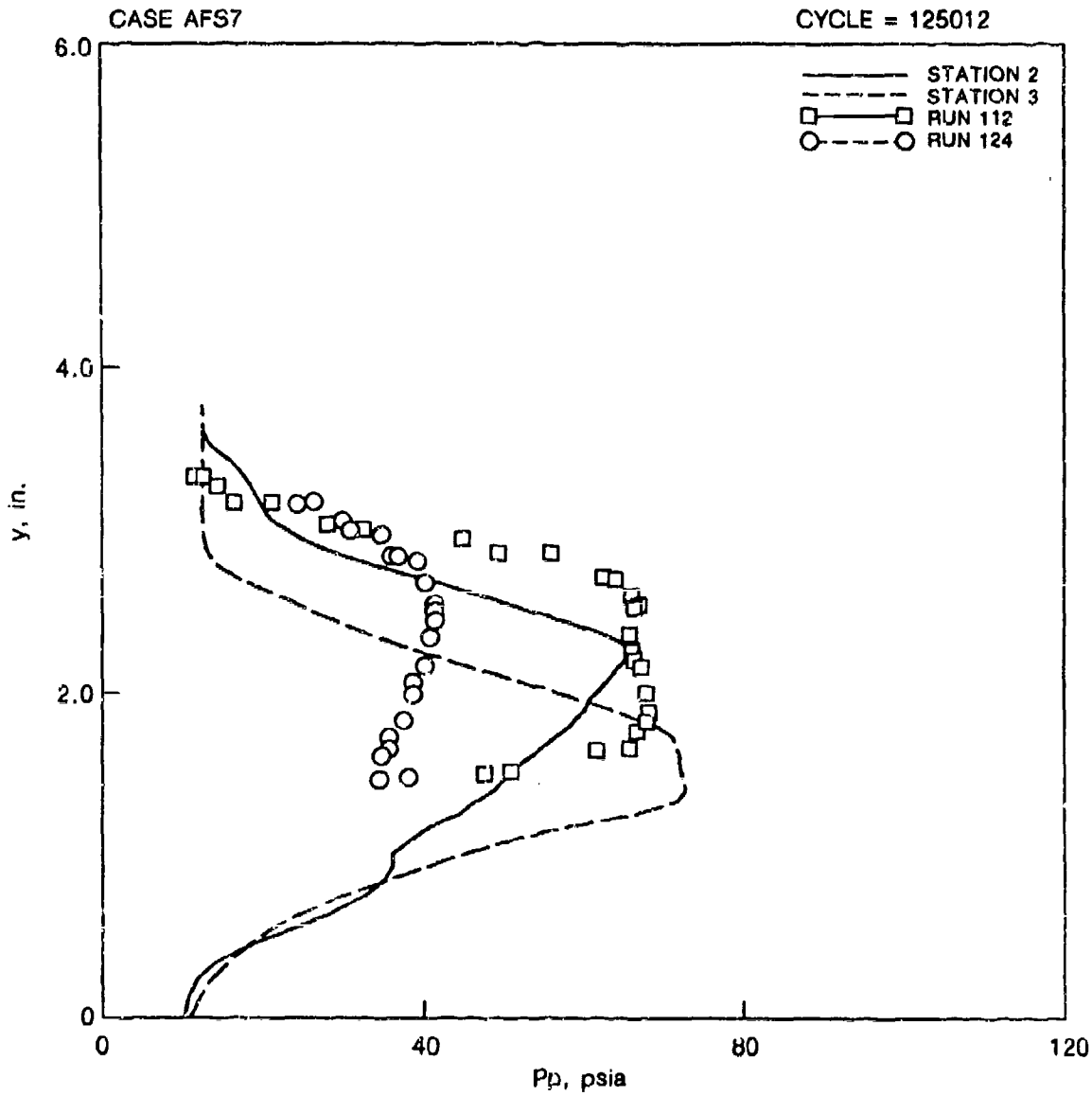

Fig. 83 Comparison between computed and measured pitot pressure profiles for $\phi = 1$ (case AFS7).

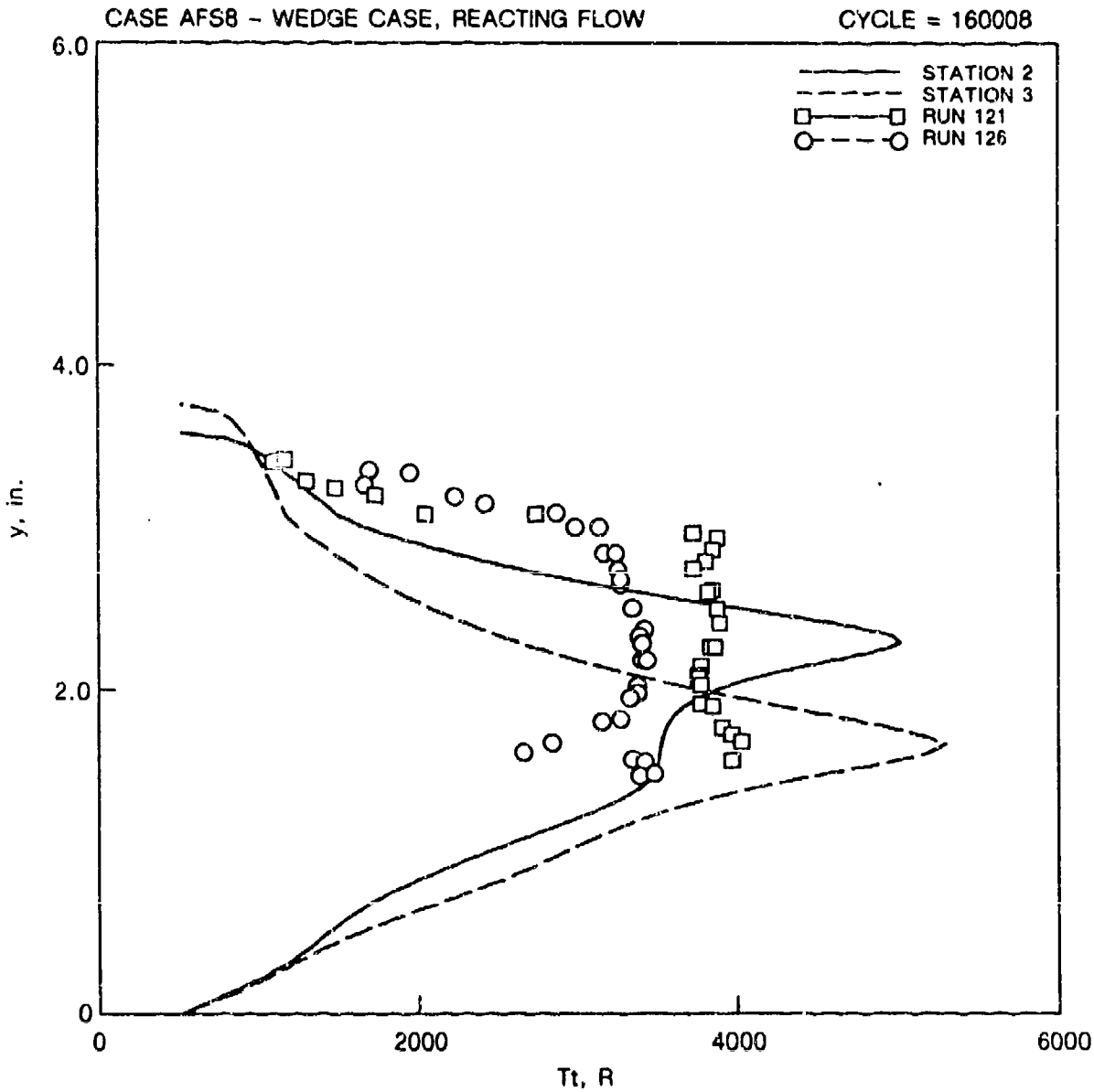

Fig. 84 Comparison between computed and measured stagnation temperature profiles for ϕ = 1 (case AFS8).

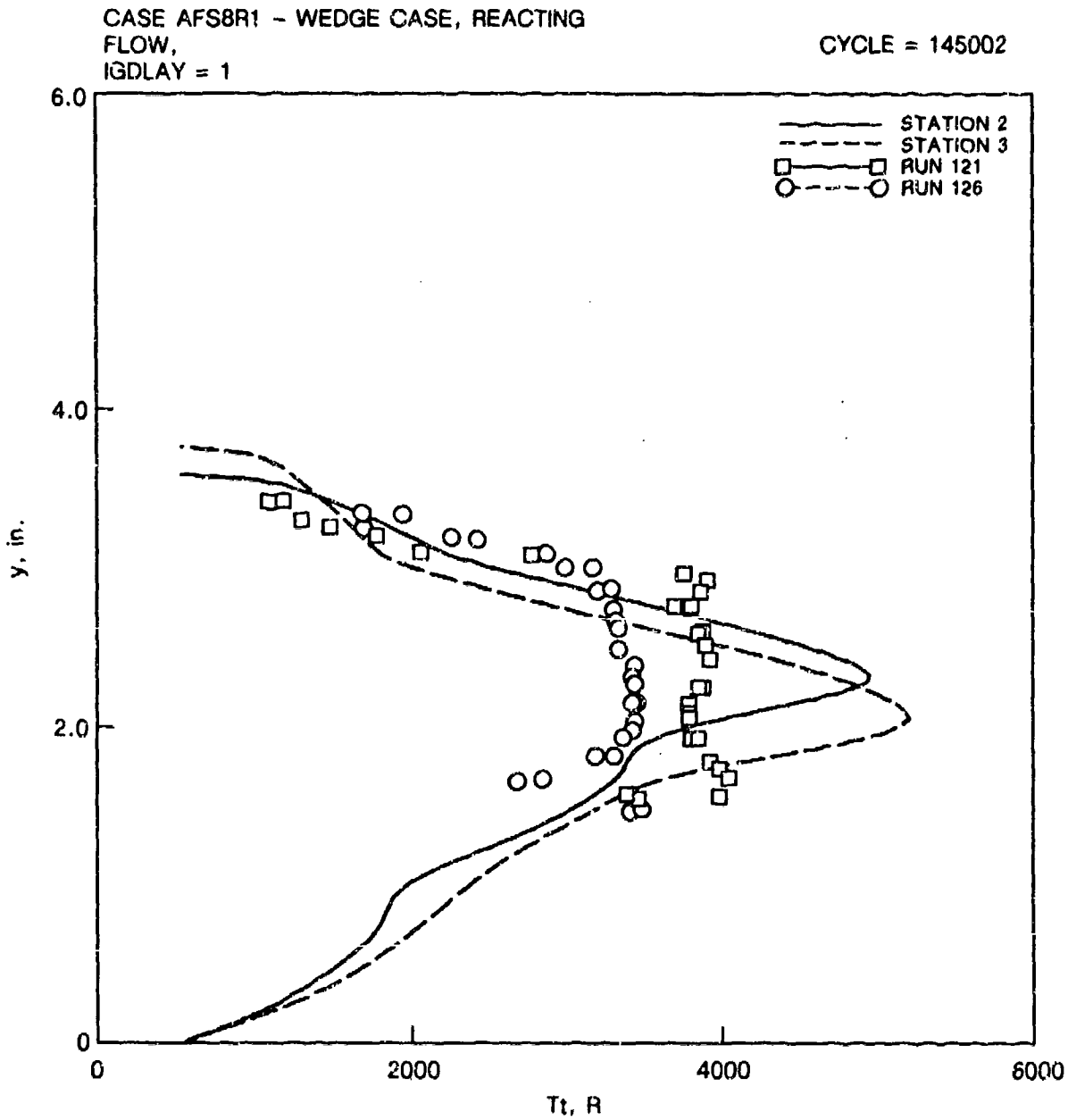

Fig. 85 Comparison between computed and measured stagnation temperature profiles for β = 1 (case AFS8R1).

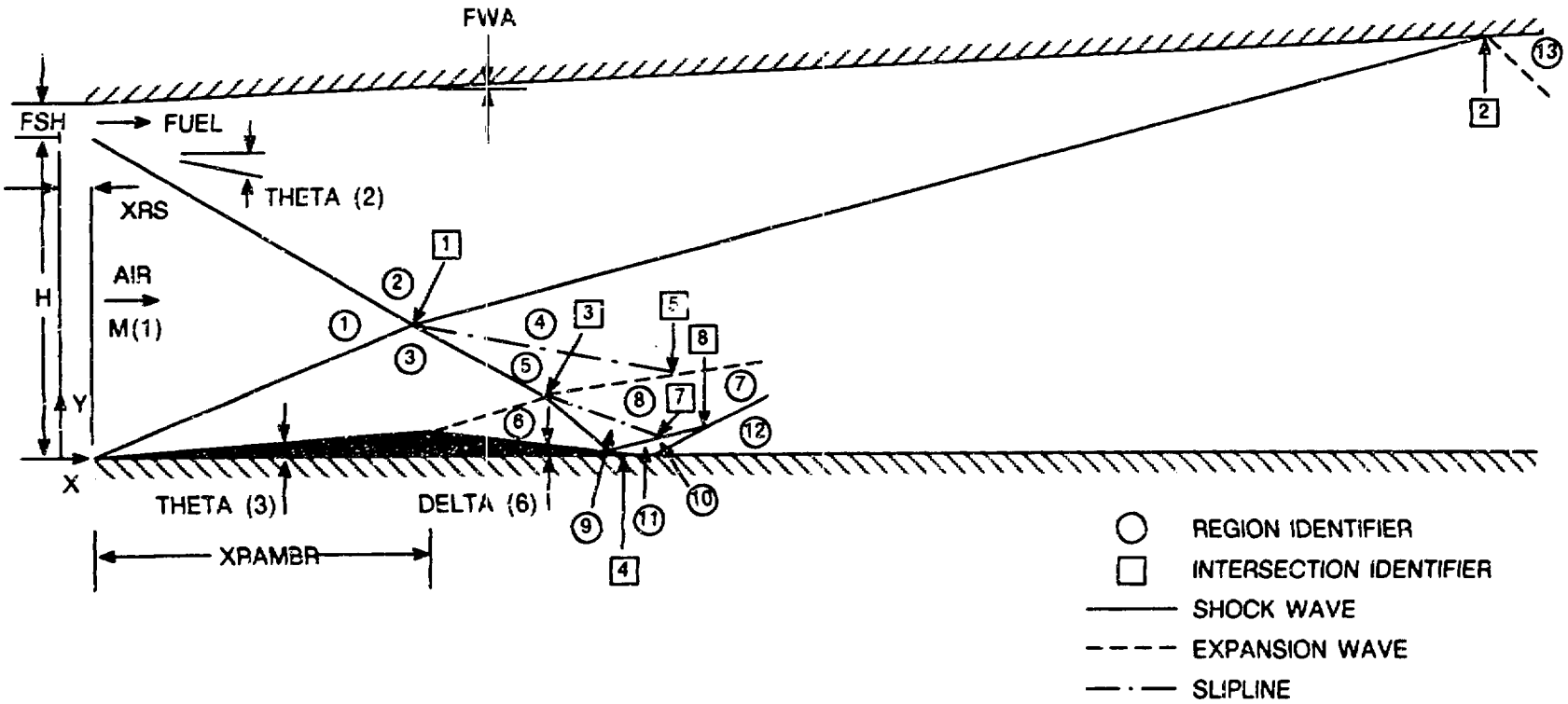

Fig. 86 Flowfield for example calculation.

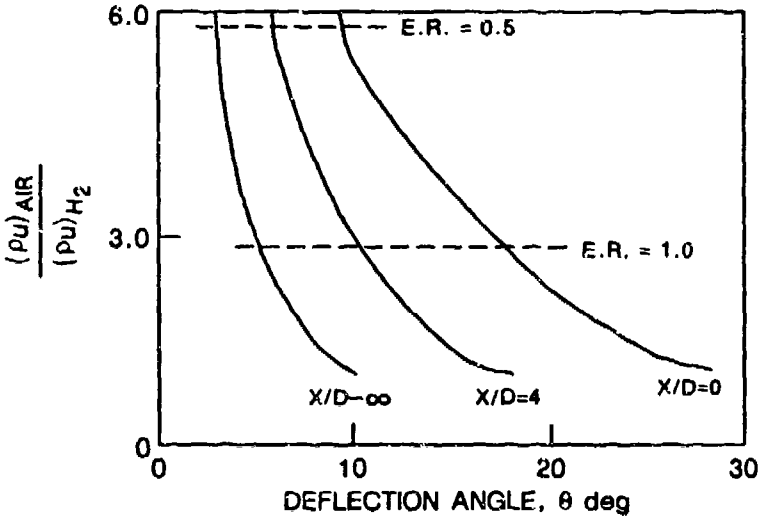

Fig 87 Flow deflection due to combustion (Ref. 51).

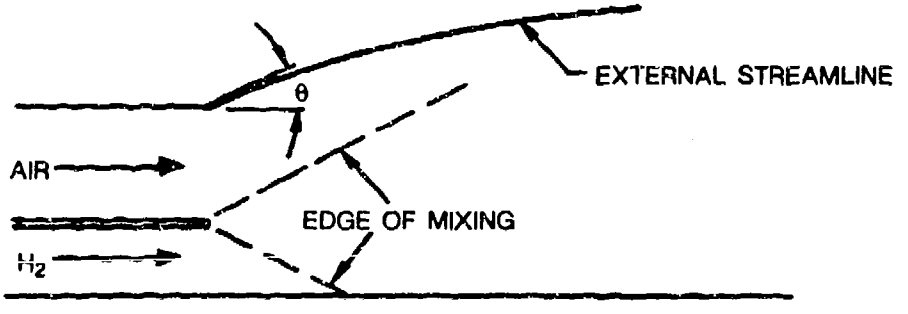

Fig. 88 Geometry for calculation in Ref. 51.

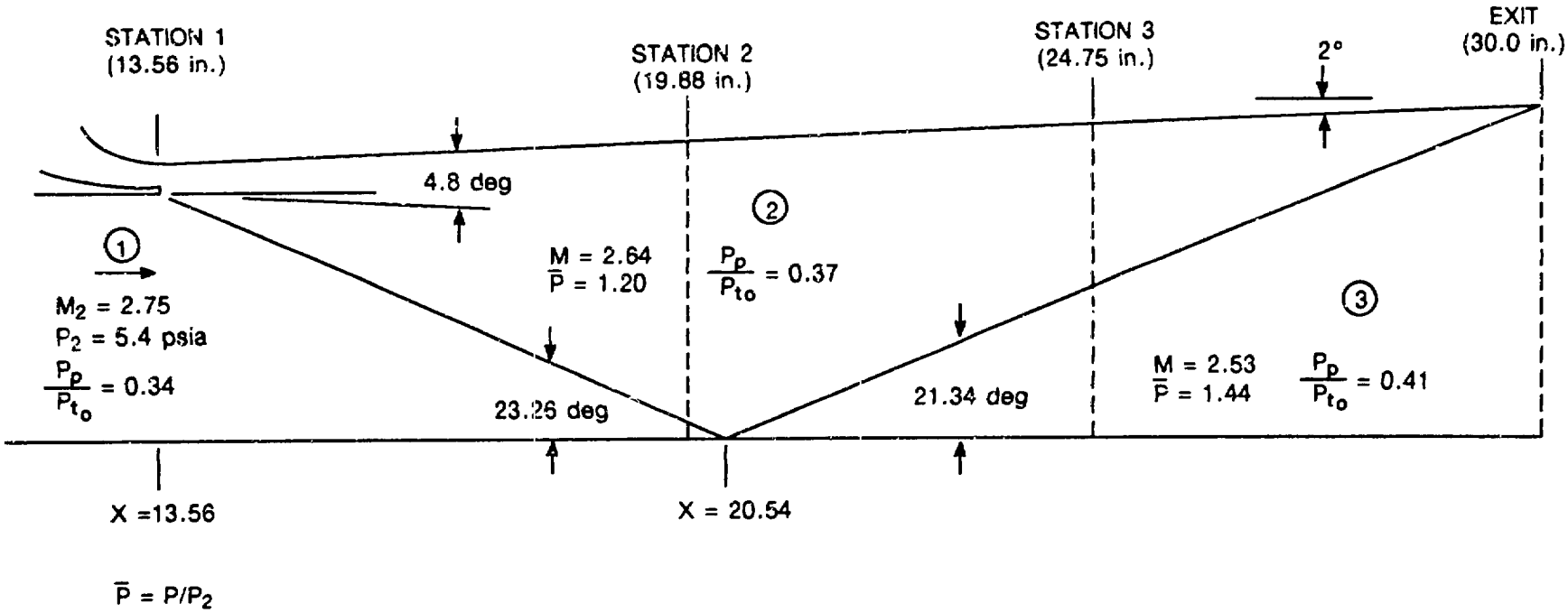

Fig. 89 Calculated wave structure for free shear-layer combustion, thermal compression analysis, E.R. = 1, λ = 0.349.

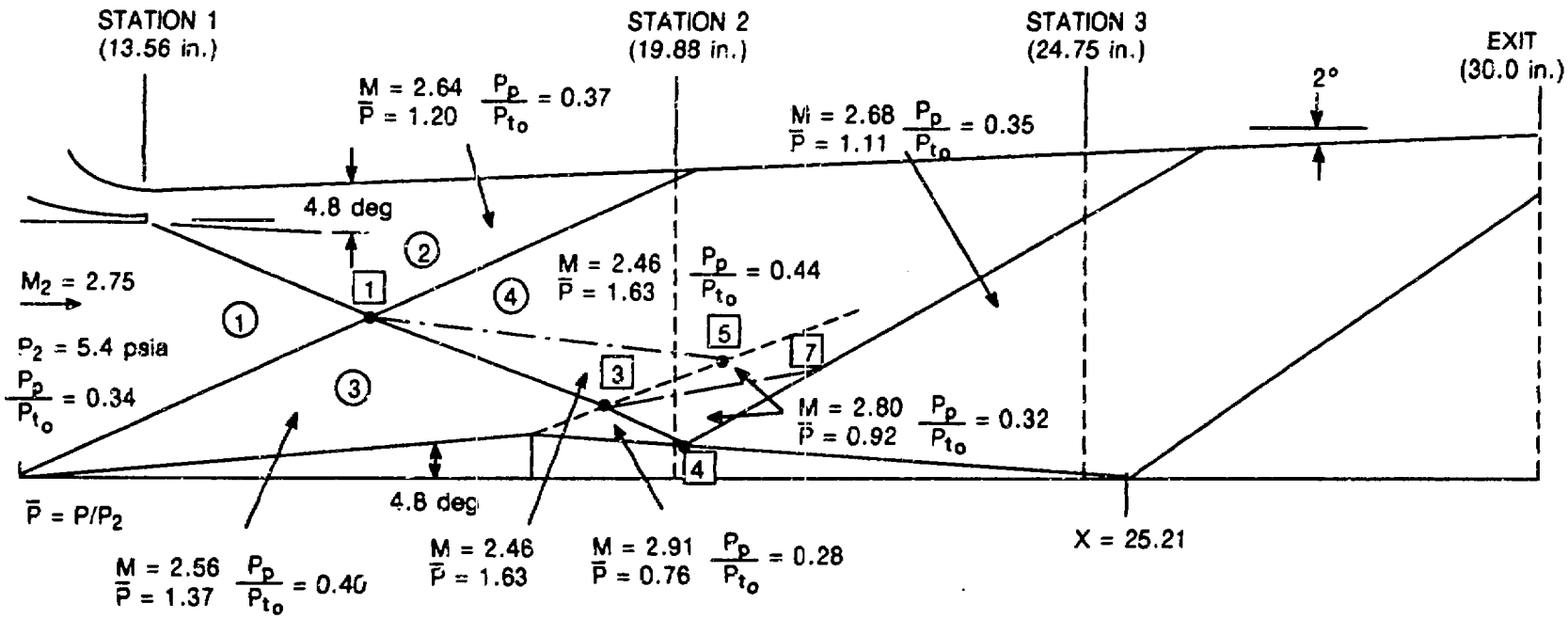

Fig. 90 Calculated wave structure for combustion with pressure gradient, thermal compression analysis, E.R. = 1, λ = 0.349, ramp angle = 4.8 deg.

APPENDIX A
EXPERIMENTAL CONSIDERATIONS

During the course of an experimental investigation, unforeseen difficulties and challenges generally become apparent and require additional effort to enable the program objectives to be met. Most often, these problems, which may require no more than a change in procedure to yield a solution, are not discussed and subsequent investigators must confront the same difficulties. The following problems were faced during the current investigation:

- The need to purge the lines connecting the high-speed digital pressure scanners to the test section pressure taps became apparent early in the experimental effort. Condensed water vapor accumulated in these taps subsequent to the completion of each test. Similar accumulations had been observed to occur during subsonic combustion testing conducted at the UTRC using uncooled test apparatus. This phenomenon is believed to occur commonly, and may be exacerbated through the use of water-cooled hardware. Without removal of this condensate, the wall static pressures would not have been accurately measured. A regulated nitrogen purge system thus was installed to enable purging of these lines between the 16-port scanners and the test section prior to each test.

- During initial hydrogen mixing tests, performed without ejector operation, a detonation occurred in the exhaust duct. To avoid a recurrence of this event, a series of six hydrogen-air torches was installed at points in the exhaust duct where it was believed unburned hydrogen would accumulate. The torches were patterned after those designed by Repas (Ref. A-1). Torch operation is initiated prior to the start of either a mixing or combustion test and is ceased immediately after the test has been completed. Subsequent to their installation, no further detonations were encountered during either mixing or combustion tests.

- As a consequence of the extensive use of copper in the water-cooled heater-to-nozzle transition and supersonic nozzle of the test apparatus, under extreme heater exit temperature conditions substantial deposition of foreign material on the CARS windows occurred. Analysis of the deposited material revealed that the major constituents were copper and nickel oxides traceable to the copper and stainless steel components. The deposits, which accumulated rapidly early in the experimental effort, obscured the optical access and diminished the laser beam intensity and signal strength. A new window mount, employing a nitrogen-purged cavity separating the window from the airflow was designed and fabricated under a Corporate program. This window was used successfully for most of the mixing and combustion tests.

- The redesigned CARS windows provided sufficient access for traversal of the CARS beams and provided for the axial growth of the test section without interference by the window mount. The limited access did not however, permit a sufficiently wide field for schlieren or shadowgraph observation of the flowfield. Under a separate Corporate program, the copper components in the flowfield were redesigned and were fabricated from stainless steel. Subsequent to the installation of these components, the rate at which metallic oxides were deposited on the original windows decreased significantly, making possible the acquisition of photographic records of flowfield features.

- Although schlieren and shadowgraph records of features of the flowfield were acquired during tests at total temperatures of approximately 2000 R, greater total temperatures resulted in more rapid heating of the windows with commensurate distortion of the glass. This distortion, with the resultant image degradation, occurred after protracted exposure at the lower temperatures also, but sufficient time was available to acquire images under this less severe condition. To eliminate the distortion at the higher temperatures, more effective purging of the windows may be attempted although this approach may induce unacceptable perturbations of the flowfield. An alternative approach may be to use a window "sandwich" in which a thin window adjacent to the flow is actively cooled by a gas flowing between it and a more robust outer window.

- Although the DSO probe was designed to survive the test conditions imposed during this experimental effort, some deflection of the probe shaft in response to the aerodynamic loading imposed was observed. To enhance the structural integrity of the probe, a trailing-edge rib was added during the test effort, which reduced the observed deflections.

- Accurate multi-species measurements were difficult to make using an experimental CARS technique applied to a complex and challenging combustion experiment. The CARS diagnostic method is appropriate in this application but refinement to further isolate separate effects of combustion and diagnostic difficulties is needed.

APPENDIX B
CARS DATA ACQUISITION AND ANALYSIS

This text was excerpted from the following reference: Anderson, T. J., and A. C. Eckbreth: Simultaneous Measurement of Temperature and H_2, H_2O Concentrations in Hydrogen-Fueled Supersonic Combustion, AIAA Paper 90-0158, 28th Aerospace Sciences Meeting, January 8–11, 1990, Reno, NV.

Description of the CARS Apparatus—For the measurements described here, a mobile CARS system was employed which was designed for CARS measurements in the harsh environments typical of large-scale combustor test facilities. The system consists of three major subsystems; a transmitter, a receiver and an instrument and control subsystem and is fully described in Ref. B-1.

The transmitter and receiver were located in the test cell and surrounded the combustor as shown in Fig. 7. The transmitter contains a frequency-doubled Nd:YAG laser, dye lasers and the optics necessary to generate the properly phase-matched beams and direct them toward the combustor. The laser pulses at a 20 Hz rate, generating a set of CARS spectra with each laser shot. The pulse length is approximately 10 ns, effectively freezing the flow during a measurement.

Low N_2 concentrations in the supersonic combustor necessitated a modification to the transmitter to improve the CARS signal strength. Because of the low combustor pressure and vitiated air supply, the maximum partial pressure of N_2 in the mainstream flow does not exceed 28 kPa (compared to 80 kPa in a standard atmosphere). At the higher mainstream total temperature conditions, the N_2 pressure may be as low as 20 kPa. To improve signal strength under these conditions, a Nd:YAG amplifier system was installed to approximately double the laser energy available, providing two synchronized 532 nm beams each with pulse energies of approximately 230 mJ.

The receiver, located on the opposite side of the combustor from the transmitter, accepts the laser beams along with the copropagating CARS signals generated in the combustor. The CARS signals are separated from the laser beams and are directed onto a 50 micron diameter optical fiber for transmission to the control room. Both the transmitter and receiver are mounted on rails so that they can be manually moved between runs to any of the combustor window locations.

A bridge structure connects the transmitter and receiver and contains the optics to transmit and focus the laser beams into the combustor, recollimate the CARS and laser beams as they exit the combustor and direct them into the receiver. 300 mm focal length field lenses were used which produced a roughly cylindrical measurement volume approximately 0.15 mm in diameter and 3–4 mm long along the beam axis. Thus, the well-resolved dimension of the measurement volume is aligned transverse to the vertical direction in which large temperature and concentration gradients can occur. The optics in the bridge structure are mounted on a translator system allowing the CARS measurement point to be moved vertically within the combustor without moving the transmitter or

receiver. Driven by a stepper motor system, this operation is accomplished remotely and automatically, providing precise adjustments to pre-chosen measurement points during a run.

The fiber optic carries the CARS signals to the instrument and control subsystem which may be located up to 100 m away from the transmitter. The signals are dispersed in a unique homebuilt spectrometer capable of imaging three disparate spectral regions with good spectral resolution (approximately 2 cm-1) onto adjacent sections of an OMD as shown in Fig.B-1. This device can greatly simplify the acquisition process by requiring only one detector to obtain all of the dispersed spectra. It has been specifically designed for use with dual broadband CARS to image three spectral regions of CARS signals, generated from several species involved in hydrocarbon/air combustion.

CARS Data Acquisition--CARS measurements of three species provide considerable information about H_2-air combustion. Because N_2 is abundant in air-fed combustion and its CARS spectrum is well understood, it is a good source from which to obtain temperature. H_2 and H_2O are also important since they provide indications of mixing and combustion effectiveness in the H_2-air combustion system. The extent of mixing can be determined by monitoring the H_2 concentration in the mainstream air flow and measuring the resulting change in temperature. Combustion will be apparent from a temperature rise and an increase in the H_2O mole fraction.

The dual pump-Stokes technique previously proposed for H_2-air combustion processes (Ref. B-2) makes use of a spectrally narrowed dye beam positioned at a Stokes shift of 1246 cm-1 to monitor the H_2-S(4) rotational transition. A relatively weak transition, its population increases as temperature rises above ambient conditions reducing the signal loss resulting from the decreased concentration within the measurement volume. A broadband dye laser, generating CARS from H_2O at 3657 cm-1, would wave mix to produce a three-color process in the region of N_2 (2331 cm-1) and would reproduce the H_2O spectrum at an adjacent location (2411 cm-1). With this technique, temperature can be monitored from the N_2 spectral shape and the concentrations of the fuel and major combustion product can be determined.

While the dual pump-Stokes CARS technique initially seemed appropriate for these measurements, certain limitations that are critical to supersonic combustion prevented its application. In an open H_2-air diffusion flame, the H_2-S(4) signal is easily detectable at temperatures above 300 K at 101 kPa. In the combustor described, the static temperature of the fuel is reduced to 250 K by the sonic injection and the pressure is only about 40 kPa. These conditions combined to make the H_2 signal very difficult to detect. The low pressure also prevented single shot N_2 spectra from being acquired.

An alternative approach, good for H_2 even at low temperatures, was developed based on some experience with DCM dye in dimethyl sulfoxide (DMSO). This dye mixture,used to generate a Stokes beam for H_2O CARS, is centered at approximately 3600 cm-1, 53 cm-1 from the H_2O bandhead, with an unusually broad spectral width of about 350 cm-1 FWHH. In attempting to shift this mixture to

observe the H_2 Q-branch at 4161 cm-1, it was discovered that, as positioned, the wing of the dye laser spectrum was powerful enough to generate a sufficient CARS signal from the H_2 Q-branch so that it could be observed at all anticipated conditions within the combustor. Signal levels for the H_2 Q-branch were approximately an order of magnitude greater than those acquired from the H_2-S(4) transition using the dual pump-Stokes technique in a 1 atm H_2 diffusion flame. In addition N_2 CARS could be generated directly from a two-color process, increasing the signal level so that single shot spectra could be acquired. Laser pulse energies which provided these capabilities were 200 mJ, 45 mJ and 55 mJ in the pump, H_2/H_2O and N_2 Stokes beams, respectively.

With this information, the CARS strategy in Fig.B-2 was developed. It utilized the dual Stokes approach with one broadband Stokes laser to generate N2 CARS and one to produce CARS from both H_2O and the H_2 Q-branch. Specific characteristics of the approach for each species are described below.

N_2 CARS Data Analysis—For the N_2 Q-branch CARS signal, a broadband Stokes beam, centered at approximately 607 nm, was generated from a frequency doubled Nd:YAG-pumped dye laser using Rhodamine 640 dye in methanol. The spectrum of the N_2 CARS signal was dispersed in the spectrometer and temperature was determined by regression-fitting each spectrum to a library of calculated spectra generated for a range of temperatures(Refs. B-3 through B-5). As a result, a temperature histogram was assembled for CARS signals acquired from a series of laser shots at a given measurement location. Under isothermal conditions at 300 K, the histogram forms a normal distribution and has a demonstrated standard deviation of about 50 K due to shot-to-shot fluctuations in the Stokes beam spectrum. In tube furnace calibrations up to 1800 K, the histogram width remains nearly constant. It can be expected to remain constant or even decrease at higher temperatures since, as the spectrum broadens, its overall shape and, thus the regression fit, depend less on Stokes fluctuations in small regions of the spectrum. In a turbulent combustor, however, real temperature fluctuations contribute significantly to the width of the distribution. In these measurements, an average measured temperature was determined along with a standard deviation. This can be used in direct comparison with CFD results which use a Navier-Stokes analysis with turbulent modeling to determine mean temperatures.

N_2 mole fraction was also derived during the regression fit. It has a large effect on the N_2 CARS spectral shape and, therefore, must be left as a variable in the analysis. The fitting procedure effectively compares the N_2 resonant CARS signal with the nonresonant contributions of all of the gases in the measurement volume. Since the intensity of the resonant signal is much stronger than that of the nonresonant signal at N_2 mole fractions of approximately 20% or greater, the concentration measurement accuracy suffers at these higher concentrations. None the less, concentration measurements can be made at the points of most interest, i.e., in the shear layer region where the N_2 mole fraction is reduced by H_2 mixing and the resonant and nonresonant signals are comparable.

The uncertainty in the non-N_2 make-up of the mixture is an additional source of error in determining the N_2 mole fraction. Because the H_2O nonresonant susceptibility is approximately twice that of the other major constituents, the H_2O relative concentration must be known in order to accurately determine the N_2 mole fraction. For the purposes of the N_2 CARS analysis, a H_2O mole fraction was assumed for the main flow based on heater stoichiometry. As H_2 mixed with the mainstream flow, it was assumed that the N_2, O_2 and H_2O mole fractions were reduced uniformly. Of course, this procedure ignores effects such as combustion and condensation on the relative H_2O concentration. Test analyses were run, however, in which the mixture of nonresonant gases was varied over the anticipated range in the combustor in a regression analysis applied to a N_2 data spectrum. Virtually no variation in temperature was observed for spectra in which N_2 was highly concentrated (greater than approximately 20% mole fraction). For lower concentration levels, the temperature varied by no more than 2% so mixture errors were ignored for the purposes of temperature measurements. Pressure also affects the spectral shape and, therefore, must be accounted for. In this case it was measured from the wall pressure taps and remained relatively constant under all conditions. This along with our experience with the acquisition and analysis of N_2 CARS spectra led to the conclusion that N_2 temperature was the most accurate CARS measurement made with this strategy.

H_2O CARS Data Analysis—H_2O spectra were dispersed in the spectrometer and relative concentration measurements were made using a simplified fitting technique. A calculated library of H2O spectra was developed for a range of temperatures and relative concentrations. An area ratio of a portion of the nonresonant spectrum to the H_2O bandhead was made for each spectrum in the library and a three dimensional array of this ratio verses temperature and mole fraction was produced. During the analysis, the array was entered with the measured temperature and the ratio calculated from the sample spectrum to obtain the H_2O mole fraction.

The synthesis and analysis of H_2O CARS spectra are much more complex than for the diatoms we are studying. The model used to generate the library spectra for these experiments assumed a constant Raman linewidth which may introduce some error, but produces spectra which generally agree with observations, especially near the bandhead region(Ref. B-6). As a result, in generating the ratio of resonant to nonresonant signal intensity, we confined ourselves to regions within 20 cm-1 of the bandhead. The make-up of the nonresonant gases was not a factor in the analysis since all of the other major species (N_2, O_2 and H_2) have nonresonant susceptibilities which are equal to within a few percent (10.2x10-18 for N_2 and 9.82x10-18 for O_2 and H_2 at 298 K).

H_2 CARS Data Analysis—The three-color spectrometer of the mobile CARS system, designed with dual broadband CARS in mind, could not be quickly reconfigured to simultaneously disperse the H_2 Q-branch spectrum with H_2O and N_2. As a result, the integrated spectral intensity of this signal was acquired on a photomultiplier tube. It would be preferable to record the dispersed spectrum,

however, both to simplify the acquisition system and to provide an alternative temperature measurement source using a regression analysis for spectral fit. This will be done in future studies.

Concentration can be determined from the integrated signal intensity but the exact form of the relationship depends on the gas and it environment. As shown in Ref.B-7, the intensity of a CARS signal, I_3, generated by a single isolated Raman transition is

$$I_3 = K_1 I_1^2 I_2 N^2 \varrho^2 (v.J) |h|^2 \tag{B-1}$$

where K_1 is a constant of proportionality, I_1 and I_2 are the pump and Stokes intensities, respectively, ϱ is the population probability density for the given transition, N is the constituent number density and h is the line shape function. The latter complicates matters because it may vary with the transition being monitored and can be a function of pressure, mixture composition and temperature. The effect of pressure on the line shape function is dependent on the pressure regime in which the measurement is made. For these experiments, with pressures at or below 41 kPa, we are operating in the Doppler-broadened regime(Ref.B-8) where the linewidth remains nearly constant with respect to pressure. For H_2, the Doppler linewidth is the same for all transitions to within about 5% (Ref.B9). An analysis by Muller-Dethlefs, et al.(Ref.B-7) indicates that the temperature dependence of the linewidth function integral is T-1/2 and, with our previous assumptions, the spectrally-integrated power for a single transition is

$$P_a = K_2 I_1^2 I_2 N^2 \varrho^2 (v.J) T^{-1/2} \tag{B-2}$$

for H_2 at conditions in the supersonic combustor. (K_2 is another proportionality constant).

Summing over all of the v = 0 Q-branch transitions gives a total signal intensity of

$$S_a = \sum_J P_a = K_2 I_1^2 I_2 N^2 f(T) \tag{B-3}$$

where $f(T) - T^{-1/2} \sum_J \varrho^2(v.J)$ is temperature dependent and its value can be calculated from Boltzmann statistics.

Shot-to-shot fluctuations in the Stokes beam spectrum were significant enough to be considered and a single shot referencing technique was incorporated to eliminate their effect on the single shot

CARS signal intensity. This was accomplished with the installation of a reference cell filled with H_2 in the receiver subsystem. Once the CARS signals from the sample volume were separated from the laser beams, the residual pump and Stokes beams were focused into this cell to generate the reference CARS signal in H_2 at constant conditions. Fluctuations in this signal reflected fluctuations in the H_2 sample signal due to noise in the Stokes spectrum. The spectrally integrated reference intensity measured with a second PMT was recorded with each laser shot and used to eliminate errors in the sample signal intensity due to Stokes noise. The reference signal intensity is of the same form as the sample measurement

$$S_r = K_2' \, I_{1r}^2 \, I_{2r} \, N_r^2 \tag{B-4}$$

except that the laser beam intensities, I_{1r} and I_{2r}, are some fraction of the intensities in the combustor due to window transmittance and filter losses in the receiver. Note that f(T) has been included in the constant, . However, assuming the losses are constant, we eliminate the influence of the Stokes beam intensity by ratioing the two signal intensities

$$S_a' = \frac{S_a}{S_r} = c_r \, N^2 \, f(T) \tag{B-5}$$

where c_r is a lumped constant.

Since the reference cell was maintained at room temperature, the CARS signal generated therein primarily reflected fluctuations in the portion of the Stokes spectrum producing the Q-branch $v = 0$, $J = 1$ CARS signal. This introduced some error when H2 in the measurement volume was at a higher temperature and transitions, $J > 1$, contributed significantly to the CARS signal. An exact correction could be applied only by adjusting the reference temperature to match that of the measurement volume or by recording the single shot dispersed nonresonant spectrum. Since it would be difficult to implement either option from a practical standpoint, a heated reference cell would offer a reasonable compromise by accounting for Stokes fluctuations affecting CARS signals from the higher rotational states, though not necessarily with the proper weighting. Such a technique deserves further consideration for future measurement programs.

Signal intensity will be affected by the Q-branch $v = 0$ population, as well, and, since this varies with temperature, it must be considered. However, as can be seen from Fig. B-3, for temperatures below about 1000 K, the $v = 0$ population varies by no more than 4%. As a result, this factor was ignored at the lower temperatures studied here.

Since the other species concentrations are measured in mole fractions, H_2 concentrations must be converted to a similar form. A calibration was established on each run by using the measurements acquired at the point deepest in the H_2 flow. At that point the N2 mole fraction was small and, therefore, assumed to be the most accurate. Using that value and assuming that the non-H_2 constituents remain in an approximately constant ratio (based on the heater stoichiometry), a method for calculating mole fraction was determined. Signal intensity is related to the concentration by

$$S_a' = c_r \, N_H^2 \, f(T) \tag{B-6}$$

where c is a constant and NH represents H_2 density. Assuming an ideal gas, r this becomes

$$S_a' = c_r \left(\frac{P_H}{kT}\right)^2 f(T) \tag{B-7}$$

where PH is the partial pressure of H_2, k is Boltzmann's constant and T is the local static temperature. H_2 mole fraction in terms of local static pressure, P_s, can be expressed as

$$X_H = \frac{P_H}{P_s} = \frac{kT}{\sqrt{C_r}\,P_s}\sqrt{\frac{S_a'}{f(T)}} \tag{B-8}$$

and ratioing to conditions at the calibration point, designated by [ ]H, results in

$$X_H = \left[\frac{X_H}{T}\sqrt{\frac{f(T)}{S_a'}}\right]_H \cdot T\sqrt{\frac{S_a'}{f(T)}} \tag{B-9}$$

Sample Results—In order to produce spatial profiles with sufficient resolution, an upper limit was required on the separation of the measurement points and a minimum number of points was required to define the curves. However, a minimum number of laser shots at each point was needed in order to overcome the errors introduced by shot-to-shot noise in the Stokes spectral profile and to account for turbulent fluctuations in the sample volume. Because of the limited run time, a compromise was reached in which approximately 120 shots were acquired at each of six to twelve measurement locations. These were concentrated around the mainstream-H2 shear layer since it was the area of most interest. Spacing was 2.5 to 5.0 mm between adjacent points.

Figure B–4 is a sample of the averaged N_2 and H_2O spectra acquired for one run at two of the measurement locations in the translation across the combustor. One can clearly note the decreased temperature at the upper locations (deeper in the H_2 flow) as represented by narrowing of both the N_2 and H_2O spectral peaks. Also, the decreasing mole fraction of each of these species is indicated by the increased level of the nonresonant signal surrounding the resonant peaks. Finally, the presence of large amounts of H_2 is indicated by the H_2–O(5) transition in the tail of the H_2O spectrum.

Sample profiles for one run are shown in Fig. B–5. We can observe the decrease in temperature and mainstream constituent concentration as the measurement point moves upward into the H_2. Fluctuations in the N_2 and H_2O concentrations at the low heights are due to the measurement accuracy at the high concentration levels on the mainstream side of the shear layer. A small amount of combustion appears to have occurred resulting in a slight temperature rise in the H_2–air shear region. The measured decrease in H_2 mole fraction at the upper point (deepest in the H_2) is the result of an error in the temperature measurement introduced by the extremely low N_2 concentration at this point. A shot by shot study indicates that temperature becomes conditionally sampled at this location because it is accurately measured only when sufficient N_2 is available. This occurs only in laser shots in which the measurement point coincides with a location in the turbulent flow where significant amounts of the hot mainstream flow have mixed with the H_2. Below this point in the flow, sufficient N_2 is available on all shots to make accurate temperature measurements.

Data such as that described above have been acquired and are being used in the refinement of two-dimensional computational fluid dynamics (CFD) codes. A sample CFD result is compared to the CARS data in Fig. B–6. While the CARS data are concentrated around the shear and combustion layer regions, the CFD analysis is completed for the entire flow system. It is clear that, while the general trend of the data agrees, the CFD code predicts combustion while very little appears to have actually occurred. Note that mole fractions have been converted to mass fraction for the purpose of this analysis.

REFERENCES

B-1. Anderson, T. J., G. M. Dobbs, and A. C. Eckbreth, "Mobile CARS Instrument for Combustion and Plasma Diagnostics," Appl. Opt., Vol. 25, pp. 4076–4085, November 1986.

B-2. Eckbreth, A. C., T. J. Anderson and G. M. Dobbs, "Multi-Color CARS for Hydrogen-Fueled Scramjet Applications," Appl. Phys. B, Vol. 45, pp. 215-223, 1988.

B-3. Marko, K.A. and Rimai, L., "Space- and Time-Resolved Coherent AntiStokes Raman Spectroscopy for Combustion Diagnostics," Optics Letters, Vol. 4, July 1979, pp. 211-213.

B-4. Eckbreth, A. C., G. M. Dobbs and J. H. Stufflebeam and P. A. Tellex, "CARS Temperature and Species Measurements in Augmented Jet Engine Exhausts," Appl. Opt., Vol. 23, pp. 1328-1339, September 1984.

B-5. Hall, R. J., "Coherent Anti-Stokes Raman Spectroscopy Modeling for Combustion Diagnostics," Opt. Eng., Vol. 22, pp. 322-329, 1983.

B-6. Hall, R. J. and J. A. Shirley, "Coherent Anti-Stokes Raman Spectroscopy of Water Vapor for Combustion Diagnostics," Appl. Spectr., Vol. 37, pp. 196-202, 1983.

B-7. Muller-Dethlefs, K., M. Pealat and J.-P. E. Taran, "Temperature and Hydrogen Concentration Measurements by CARS in an Ethylene-Air Bunsen Flame," Ber. Bunsenges. Phys. Chem., Vol. 85, pp. 803-807, 1981.

B-8. Henesian, M. A., L. Kulevskii, R. L. Byer and R. L. Herbst, "C. W. High Resolution CARS Spectroscopy of H2, D2 and CH4," Opt. Comm., Vol. 18, pp. 125-128, 1976.

B-9. Debarre, D., M. Lefebvre, M. Pealat et al, "Photofragmentation Dynamics of Formaldehyde: H2(v,J) Distributions," J. Chem. Phys., Vol. 83, pp. 4476–4487, 1981.

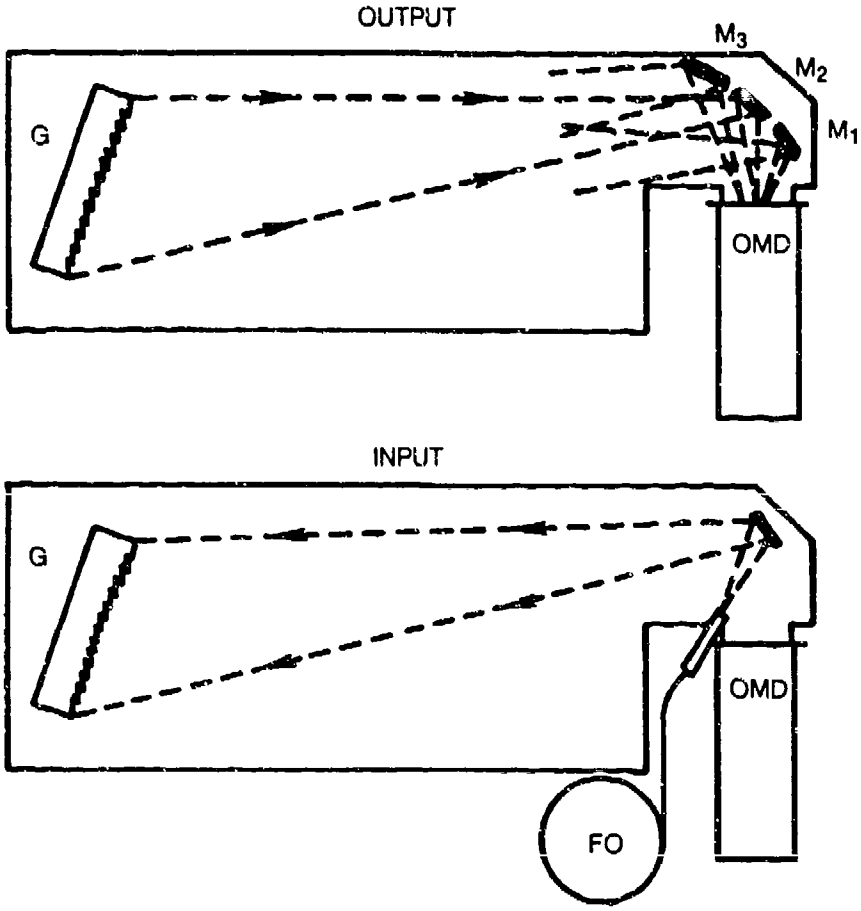

Fig. B-1 Multiple species CARS spectrometer.

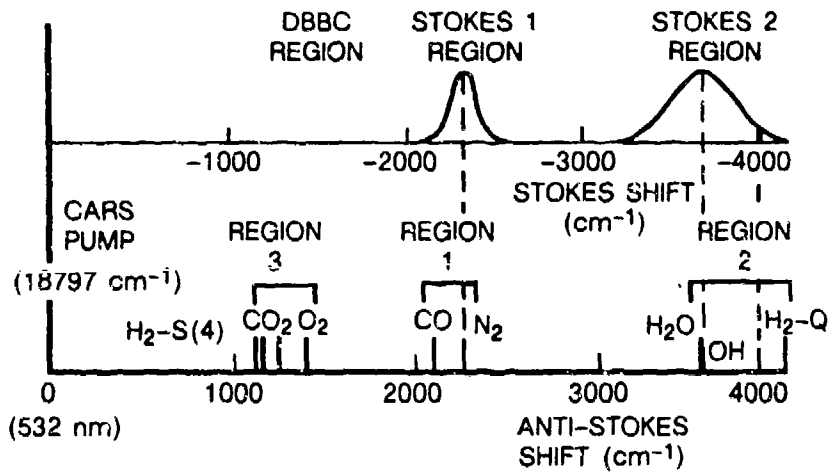

Fig. B-2 Stategy For H_2-air Supersonic Combustion.

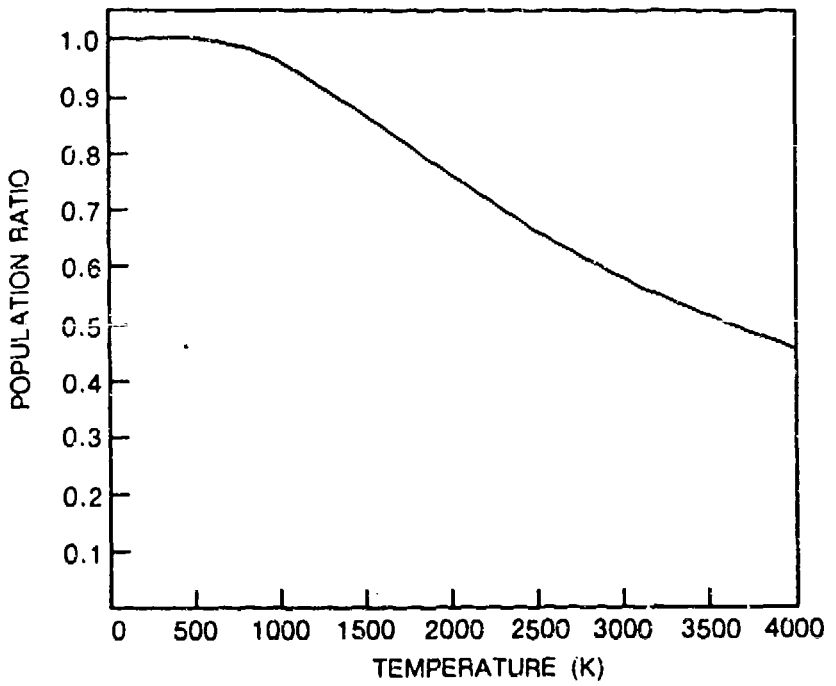

Fig. B-3 H_2 Q-branch v=0 population. Normalized to the population at 300 K.

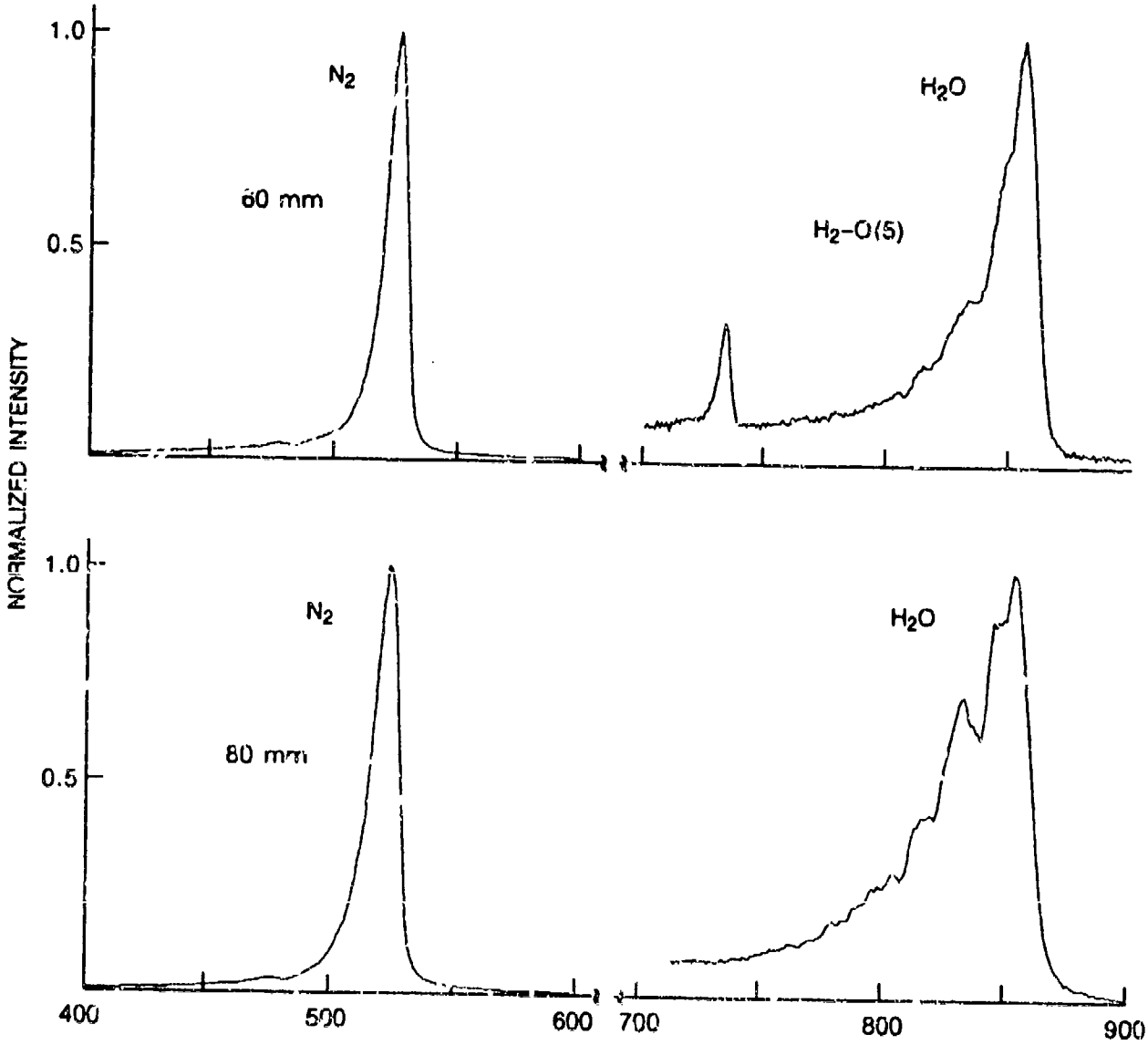

Fig. B-4 Sample N_2 and H_2O spectra.

90-4-21-19

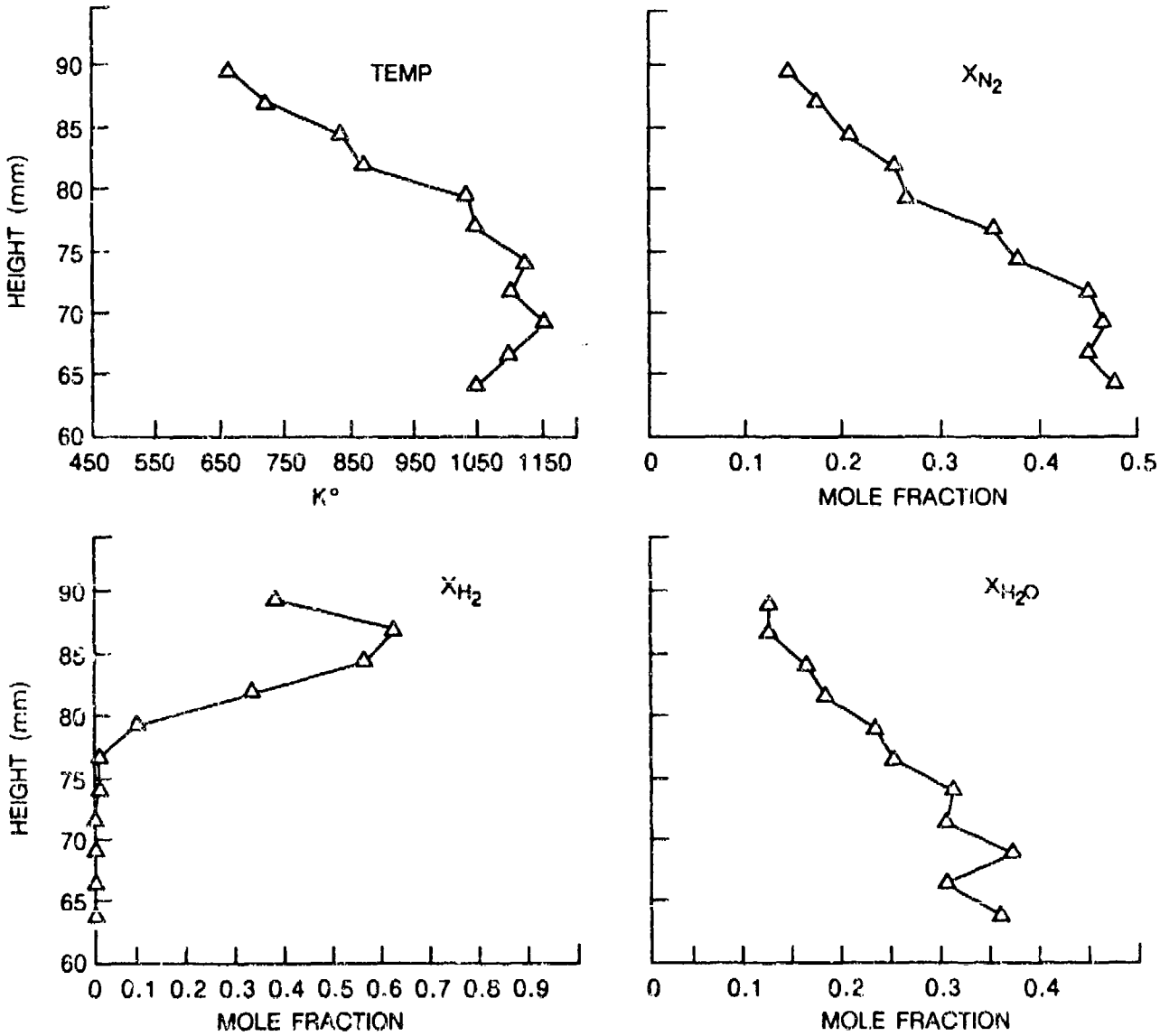

Fig. B-5 CARS measurement profiles of temperature and N_2, H_2, and H_2O mole fractions.

90-4-21-20

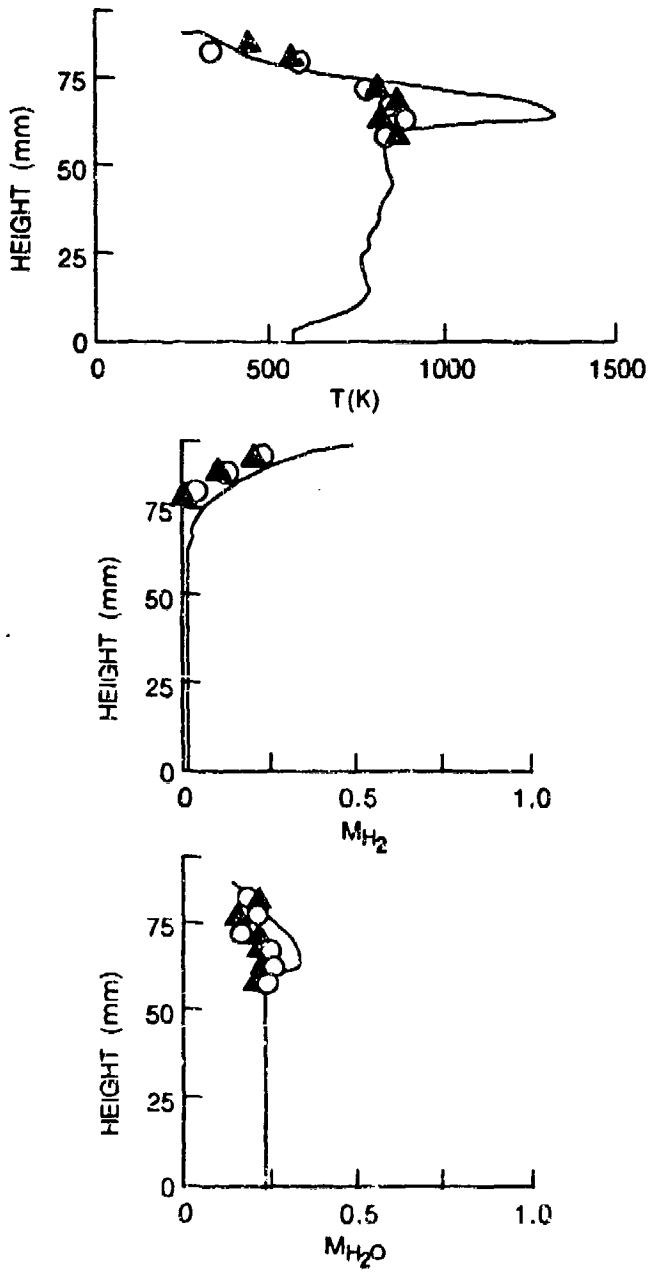

Fig. B-6 CFD comparisons (lines) with CARS data for sample runs. Triangles, circles from two similar tests.

90-4-21-21

APPENDIX C

CALCULATION OF STAGNATION TEMPERATURES USING THE DSO PROBE TECHNIQUE

The Dual Sonic Orifice (DSO) probe enables the calculation of stagnation temperatures at the probe tip which are above the range of available thermocouples. The probe contains two orifices, one of which is located at the probe tip, (see Fig. 5). By aspirating flow through the probe and choking the two orifices, an expression may be derived from the continuity equation which relates the stagnation temperature at the probe tip to the measured stagnation temperature and pressure at the downstream orifice and the measured pressure at the tip orifice. This derivation shown below uses the nomenclature presented in Fig. 5. Note that the subscripts refer to the upstream and downstream orifices within the probe and should not be misinterpreted as relating to the different measuring stations in the test section. For choked-flow conditions, the weight flow through an orifice may be written,

$$W = C_D \sqrt{\frac{\gamma_g \mathcal{M}_0}{R}\left(\frac{2}{\gamma + 1}\right)^{\frac{\gamma+1}{\gamma-1}}} \; \frac{P_T A}{\sqrt{T_T}} \tag{C-1}$$

Equation 1 can be simplified by use of a mass flow function, $\overline{m}^*$, as defined below

$$\overline{m}^* = \sqrt{\frac{\gamma_g \mathcal{M}_0}{R}\left(\frac{2}{\gamma + 1}\right)^{\frac{\gamma+1}{\gamma-1}}} \tag{C-2}$$

and may be written in simplified form as

$$W = C_D \overline{m}^* \frac{P_T A}{\sqrt{T_T}} \tag{C-3}$$

Then, since W_1 must equal W_2,

$$C_{D_1} \overline{m}_1^* \frac{P_{T_1} A_1}{\sqrt{T_{T_1}}} = C_{D_2} \overline{m}_2^* \frac{P_{T_2} A_2}{\sqrt{T_{T_2}}} \tag{C-4}$$

Rearrangement of Eq. (4) yields a convenient expression for the evaluation of T_{T_1} from measurable quantities

$$T_{T_1} = \left(\frac{C_{D_1}}{C_{D_2}}\right)^2 \left(\frac{\overline{m}_1{}^*}{\overline{m}_2{}^*}\right)^2 \left(\frac{A_1}{A_2}\right)^2 \left(\frac{P_{T_1}}{P_{T_2}}\right)^2 T_{T_2} \qquad \text{(C-5)}$$

Since those terms in Eq. (5) containing the discharge coefficient (C_D), the mass flow function ($\overline{m}^*$) and the throat area (A) are usually not known very accurately, the DSO data can be reduced by grouping those terms into a probe coefficient as follows:

$$K = \left(\frac{C_{D_1}}{C_{D_2}}\right)^2 \left(\frac{\overline{m}_1{}^*}{\overline{m}_2{}^*}\right)^2 \left(\frac{A_1}{A_2}\right)^2 \qquad \text{(C-6)}$$

and a simplified form of Eq. (5) can therefore be written, as show below,

$$T_{T_1} = K\left(\frac{P_{T_1}}{P_{T_2}}\right)^2 T_{T_2} \qquad \text{(C-7)}$$

Calibration of the probe can then be achieved by recording data with the probe in a stream of known stagnation temperature (T_{T_1}) and using a rearranged form of Eq. (7) to define a value of the probe coefficient,

$$K_{CAL} = \left(\frac{T_{T_1}}{T_{T_2}}\right)_{CAL} \left(\frac{P_{T_2}}{P_{T_1}}\right)^2_{CAL} \qquad \text{(C-8)}$$

Note that such a calibration yields an accurate evaluation of the combination of terms in Eq. (6), but the value of K so obtained is only valid at the calibration test conditions, since the terms (C_{D_1}/C_{D_2}), $(\overline{m}_1{}^*/\overline{m}_2{}^*)$ and (A_2/A_1) are somewhat dependent upon T_{T_1} and P_{T_1}. These dependencies can, however, be described analytically and can be incorporated into the treatment of the DSO data by suitable adjustment of the probe coefficient, K_{CAL}. This is done by representing the generalized probe coefficient, K, as the product of the experimental value obtained during the probe calibration, K_{CAL}, and a series of terms. K_{C_D}, $K_{\overline{m}^*}$, and K_A, that represent the analytical dependencies

of the respective terms, (C_{D_1}/C_{D_2}) , $(\overline{m}_1{}^*/\overline{m}_2{}^*)$, and (A_2/A_1) on the conditions in the mainstream flow, as shown below:

$$K = (K_{CAL})\,(K_{C_D})\,(K_{\overline{m}^*})\,(K_A) \tag{C-9}$$

where

$$K_{C_D} = \frac{(C_{D_1}/C_{D_2})^2}{(C_{D_1}/C_{D_2})^2_{CAL}} \tag{C-10}$$

$$K_{\overline{m}}{}^* = \frac{(\overline{m}_1{}^*/\overline{m}_2{}^*)^2}{(\overline{m}_1{}^*/\overline{m}_2{}^*)^2_{CAL}} \tag{C-11}$$

and

$$K_A = \frac{(A_1/A_2)^2}{(A_1/A_2)^2_{CAL}} \tag{C-12}$$

In Eq. (12), the "CAL" subscripts are used to denote those values of the various parameters that exist under the conditions of the calibration test. Since, the correction factors shown in Eqs. (10),(11), and (12) are each presented as ratios, it is not as important for the analysis to predict an accurate absolute value of each term (for example, C_{D_1}) as it is to predict the correct functional relationship of that term with the parameters that are different during calibration and testing. Descriptions of the analyses employed for the evaluation of the terms, K_{C_D}, $K_{\overline{m}^*}$, and K_A are presented below.

The discharge coefficient correction term, K_{C_D}, listed as Eq. (10) must be included in the treatment of the DSO probe data because of the dependence of the discharge coefficient for

compressible flow through an orifice on the Reynolds number at the throat, which can be expressed in empirical form (see Ref. C-1) as

$$C_D = 1 - \frac{6.5}{\sqrt{Re^*}} \tag{C-13}$$

Evaluation of the term K_{C_D} for the DSO data therefore only requires that the Reynolds number be evaluated at each DSO orifice for both the test data and the calibration data. By assuming ideal gas conditions and an isentropic expansion from the stagnation conditions, the magnitude of the Reynolds number can be approximated solely in terms of the total pressure and the total temperature at a given orifice as shown below:

$$Re^* = \sqrt{\left(\frac{2}{(\gamma + 1)}\right)^{\frac{\gamma+1}{\gamma-1}}} \sqrt{\frac{g\gamma \mathcal{M}_0}{R}} \frac{P_T D^*}{\sqrt{T_T}} \frac{1}{\mu} \tag{C-14}$$

Note that in calculating values of the Reynolds number using Eq. (14), it must be observed that the properties γ, $\mathcal{M}_0$, and μ are somewhat dependent upon the composition of the sampled gases, and γ and μ are also dependent upon the total temperature. However, except for the temperature dependency of viscosity, these property variations have only a small effect on the Reynolds number, and they may, therefore, be considered as second-order corrections and may safely be neglected in the calculation. Since the viscosity term is a rather strong function of temperature, it must be included as a variable in the calculation procedure. However, by neglecting the influence of changes in species on μ (which are second order effects), the viscosity may be represented by the function shown below which is valid for air up to temperatures of approximately 3500 R (Ref. C-2).

$$\mu = 2.27 \frac{T^{3/2}}{T + 198.6} \times 10^{-8} \frac{lb_f\,sec}{ft^2} \tag{C-15}$$

The mass flow function correction term, $K_{\dot{m}}$, is required to account for different values of γ that exist during a given test in relation to the values that existed during the probe calibration. By combining Eqs. (11) and (12) term $K_{\dot{m}}$ may be written as,

$$K_{\dot{m}} = \frac{\left[\dfrac{\gamma_1 \mathcal{M}_1 \left(\dfrac{2}{\gamma_1+1}\right)^{\frac{\gamma_1+1}{\gamma_1-1}}}{\gamma_2 \mathcal{M}_2 \left(\dfrac{2}{\gamma_2+1}\right)^{\frac{\gamma_2+1}{\gamma_2-1}}}\right]}{\left[\dfrac{\gamma_1 \mathcal{M}_1 \left(\dfrac{2}{\gamma_1+1}\right)^{\frac{\gamma_1+1}{\gamma_1-1}}}{\gamma_2 \mathcal{M}_2 \left(\dfrac{2}{\gamma_2+1}\right)^{\frac{\gamma_2+1}{\gamma_2+1}}}\right]_{CAL}} \qquad \text{(C-16)}$$

Since no reactions occur within the DSO probe (the expansion after the upstream orifice quenches the flow), $\mathcal{M}_1$ must be equal to $\mathcal{M}_2$ at all times for a given test, and the molecular weight terms may be eliminated from Eq. (16). However, in order to evaluate $K_{\dot{m}}$, the composition of the sampled gases must be known since the specific heat ratio is a function of both composition and temperature. Thus, even though the downstream DSO probe orifice is always maintained at the same temperature (approximately 660 R), γ_2 is not generally equal to $\gamma_{2_{CAL}}$ because the sampled species in a given test can be quite different from those of the calibration tests. A theoretical variation of γ with temperature and composition was determined by compiling the results of thermochemical calculations which assumed 100 percent combustion efficiency of various vitiated air-propane mixtures. The resulting functional relationship between γ, T_T and T_{T_0} (the temperature of the vitiated air) was then employed to evaluate $K_{\dot{m}}$ for a given set of test and calibration conditions.

The throat area correction term, K_A, is required to account for the thermal expansion of the DSO probe tip orifice that occurs when the probe is exposed to a high temperature environment. Since the downstream orifice of the DSO probe is always maintained at the same temperature during both testing and calibration, the expression of K_A given in Eq. (12) may be simplified to,

$$K_A = \left(\frac{A_1}{A_{1_{CAL}}}\right)^2 \qquad \text{(C-17)}$$

An expression for A_1 in terms of the temperature of the metal at the probe tip, T_m, assuming a constant value of the linear coefficient of thermal expansion, α, may be written as shown below:

$$A_1 = A_{REF}[1 + \alpha\,(T_m - T_{REF})]^2 \qquad \text{(C-18)}$$

In order to utilize Eq. (18), the metal temperature, T_m, must be known as a function of T_{T_1}; for data reduction purposes the functional relationship of T_m and T_T may be determined by fundamental heat transfer analysis using estimated heat transfer coefficients. However, for the probe configuration shown in Fig. 5, the throat region was cooled to a sufficient degree such that the correction constant, K_A, was assumed to be 1.0 for all conditions.

It should be noted here that since the calculations of K_{C_D}, $K_{\overline{m}^*}$ and K_A all require the knowledge of T_{T_1}, those terms were evaluated by an iterative technique which involved the initial use of values of T_{T_1} based on an uncorrected probe coefficient, K. It should also be emphasized that the maximum correction to the value of the DSO probe coefficient measured during calibration tests was approximately six percent. Therefore, the use of the approximations discussed above in the calculations of K_{C_D}, $K_{\overline{m}^*}$ and K_A could be justified and the use of such corrections would not be expected to detract seriously from the accuracy of the DSO technique for temperature measurements.

CALIBRATION OF THE DSO PROBE

The water-cooled DSO probe used for the data acquisition was calibrated in situ on the geometric centerline of the supersonic combustion test section. An uncooled Type K (chromel-alumel) sheathed thermocouple was used as a reference thermocouple for these tests. The reference thermocouple was fixed immediately adjacent to, i.e., approximately 1/8- inch laterally from, the sensing tip of the DSO probe. The tests were conducted in essentially the same manner as the mixing and combustion tests were conducted. That is, the test gas was delivered to the test section through the supersonic Mach 3 nozzle. Since the reference thermocouple was mounted directly on the DSO probe, the vitiated-air heater total pressure was limited to approximately 100 psia during the calibration to avoid dislodging of the reference thermocouple. The vitiated-air heater total temperature was varied during these tests from approximately 1500 R to approximately 2600 R. The upper limit was set by the capability of the Type K reference thermocouple. The test data were compared and correlated with the calculated heater exit and test section entrance total temperatures, accounting for the heat transfer to the supersonic nozzle, the nozzle entrance transition, and the test section entrance duct upstream of the thermocouple and probe location at Measuring Station 1 in Fig.1.

The results of these calibration tests showed that the total temperature recorded using the sheathed thermocouple situated at the geometric center of the test section entrance corresponded closely to the calculated test section entrance bulk gas temperature. The temperatures measured using the thermocouple were corrected for radiation according to the procedure set forth in Reference C-3. The temperature recovery factor, R_T was estimated as a function of Prandtl number, Pr for turbulent boundary layers according to the following relationship (Ref. C-4):

$$R_T = (Pr)^{1/3} \tag{C-19}$$

The adiabatic surface temperature of the thermocouple, T_{as} is related to the recovery factor, the test section entrance Mach number, M_2, and static temperature, T_2, in the following manner (Ref. C-4):

$$R_T = \frac{2}{(\gamma - 1)M_2^2}\left[\frac{T_{as}}{T_2} - 1\right] \tag{C-20}$$

The recovery correction factor was calculated according to Ref. C-3 using the relationship,

$$\Delta = (T_{T2} - T_{as})/T_{T2} \tag{C-21}$$

The corrected gas temperature was then determined using the following expression, also from Ref. C-3:

$$T_{TTC} = T_{Ti} + \left\{ \frac{K^* rad}{\sqrt{M_2 P_2}} \left(\frac{T_{Ti}}{1000}\right)^{-.18} \left[\left(\frac{T_{Ti}}{1000}\right) - \left(\frac{T_D}{1000}\right) \right] \right\} + T_{Ti}\Delta \tag{C-22}$$

In this relationship, T_{Ti} is the indicated junction temperature, K*rad is a radiation correction, and T_D is the duct wall temperature. The value of K*rad used in this procedure was 3.6, the suggested value from Ref. C-3 for a bare junction in crossflow.

The calibration data relating the calculated test section entrance temperature, T_{T2calc} with the corrected test section entrance temperature, T_{TTC} measured with the Type K (chromel-alumel) thermocouple are shown in Fig. C-1. The relationship between these two parameters appears to be linear over the temperature range investigated and the measured centerline temperatures are nearly equal to the calculated values.

The data relating the DSO probe temperatures, TDSO and the thermocouple temperatures, T_{TTC} are shown in Fig. C-2. Over the range examined, these parameters also appear to be linearly related. A regression analysis of the data yielded the following relationship between these parameters:

$$T_{TTC} = 1.7991\ T_DSO - 400.4136 \tag{C-23}$$

These data thus provided a reliable calibration of the DSO probe under flow conditions similar to those used for the mixing and combustion experiment. Based on these results, a probe constant, K = 0.0281 was derived and used in reducing all of the total temperature data.

REFERENCES

C-1. McLafferty, G. H.: Criteria for Laminar Flow in the Throats of Rocket Exhaust Nozzles, UARL Report No. A-110088-1, February 1962.

C-2. National Advisory Committee for Aeronautics: Equations, Tables and Charts for Compressible Flow. Report 1135, Ames Research Staff, Moffett Field, California, 1953.

C-3. Glawe, G.E., F.S. Simmons, and T. M. Stickney:Radiation and Recovery Corrections and Time Constants of Several Chromel-Alumel Thermocouple Probes in High-Temperature, High Velocity Gas Streams, NACA Technical Note 3766, October 1956.

C-4. Kreith, F.: Principles of Heat Transfer, International Textbook Company, Scranton, PA, 1958.

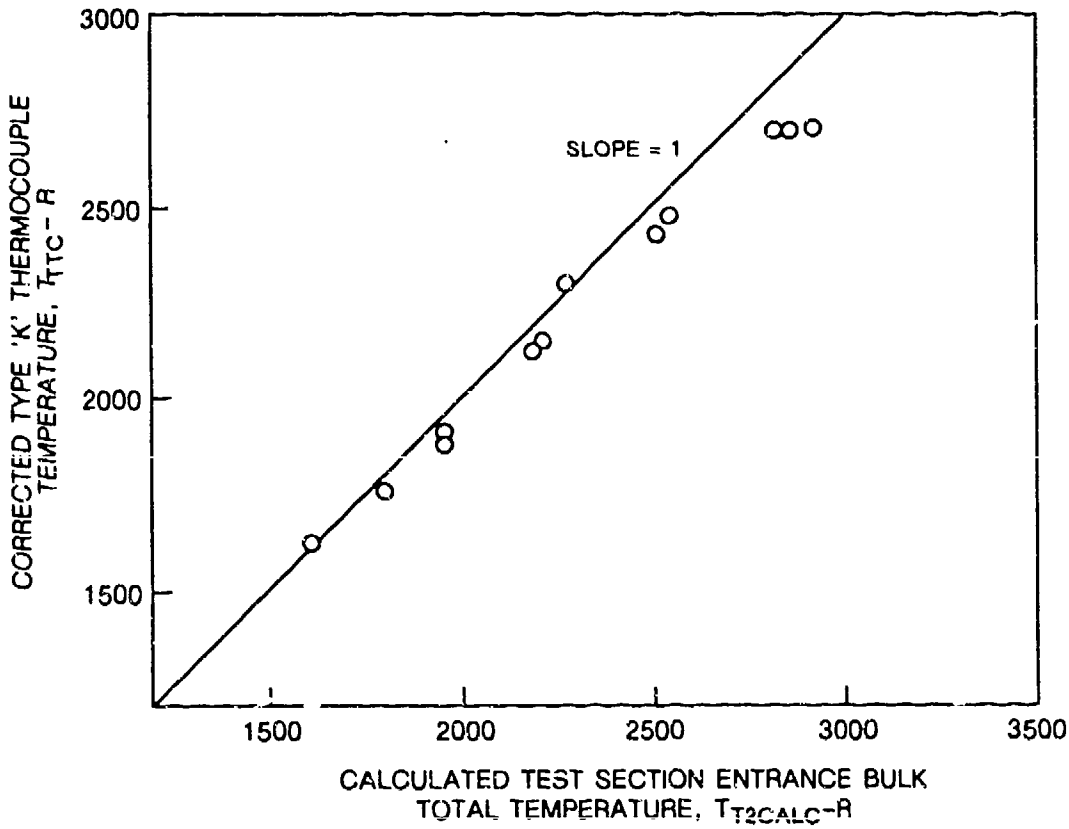

Fig. C-1 Comparison between type 'K' thermocouple temperature and calculated test section entrance total temperature.

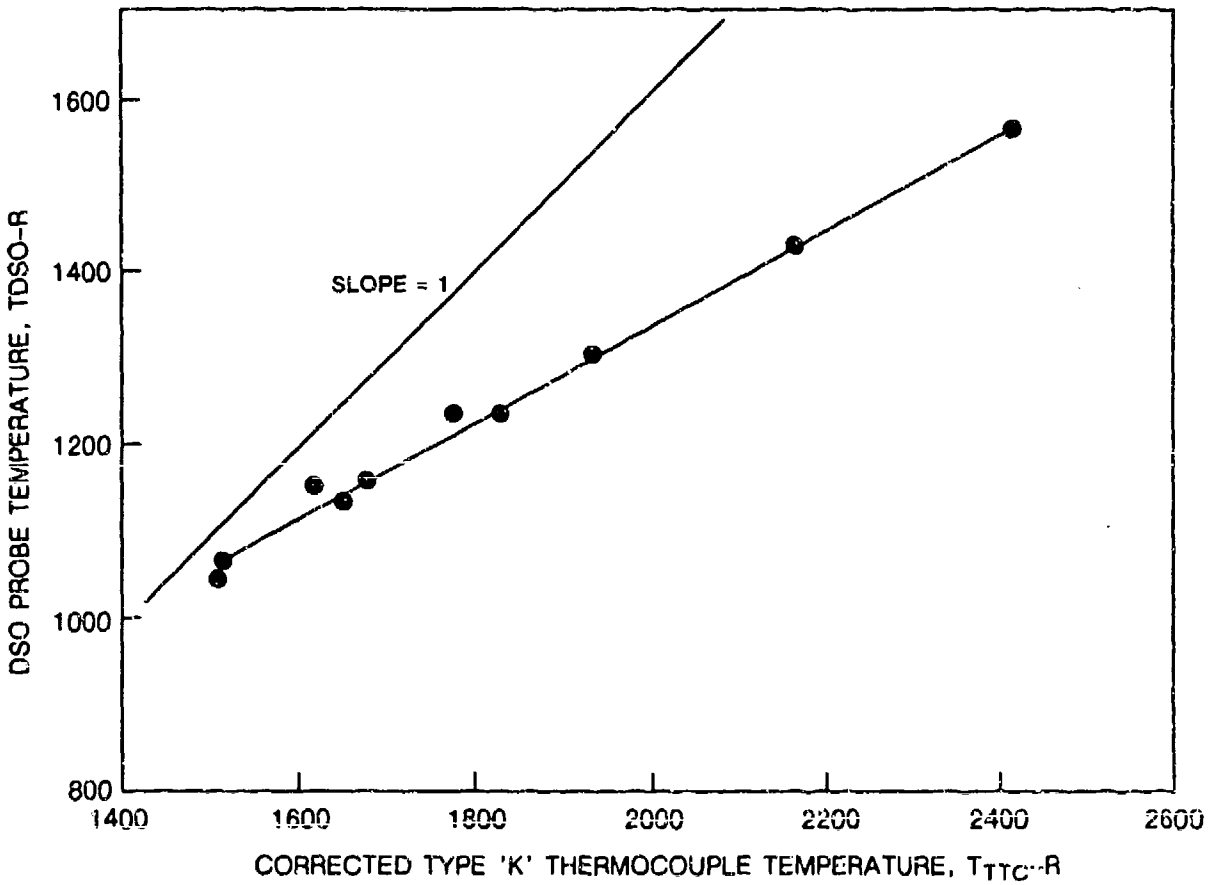

Fig. C-2 DSO probe calibration.

APPENDIX D
PLOTS OF EXPERIMENTAL DATA

The experimentally obtained test-section data, in the form of plots of profiles of the measured parameters, are included in this appendix. Sections D-1 through D-6 contain plots of the profiles of total temperature, pitot pressure, static temperature, and nitrogen, hydrogen, and water vapor mole fractions, respectively, relative to the distance of either the DSO probe tip or the CARS measuring volume from the lower wall of the test section. Section D-7 contains plots of the test section upper and lower wall static pressures measured in the vertical plane of symmetry of the test section. The locations of pressure taps in the test section walls are shown in the drawing displayed as Fig. D-1.

Preceding Sections D-1 through D-6 is a Table D-1 which is a tabulation of the data acquired using the CARS apparatus. Provided in this table is a listing as a function of distance above the lower test section surface of the static temperatures and species molar and mass fractions. The entry headings contain the run number, R(__), the Measuring Station at which the data were acquired, and the nominal equivalence ratio and total temperature.

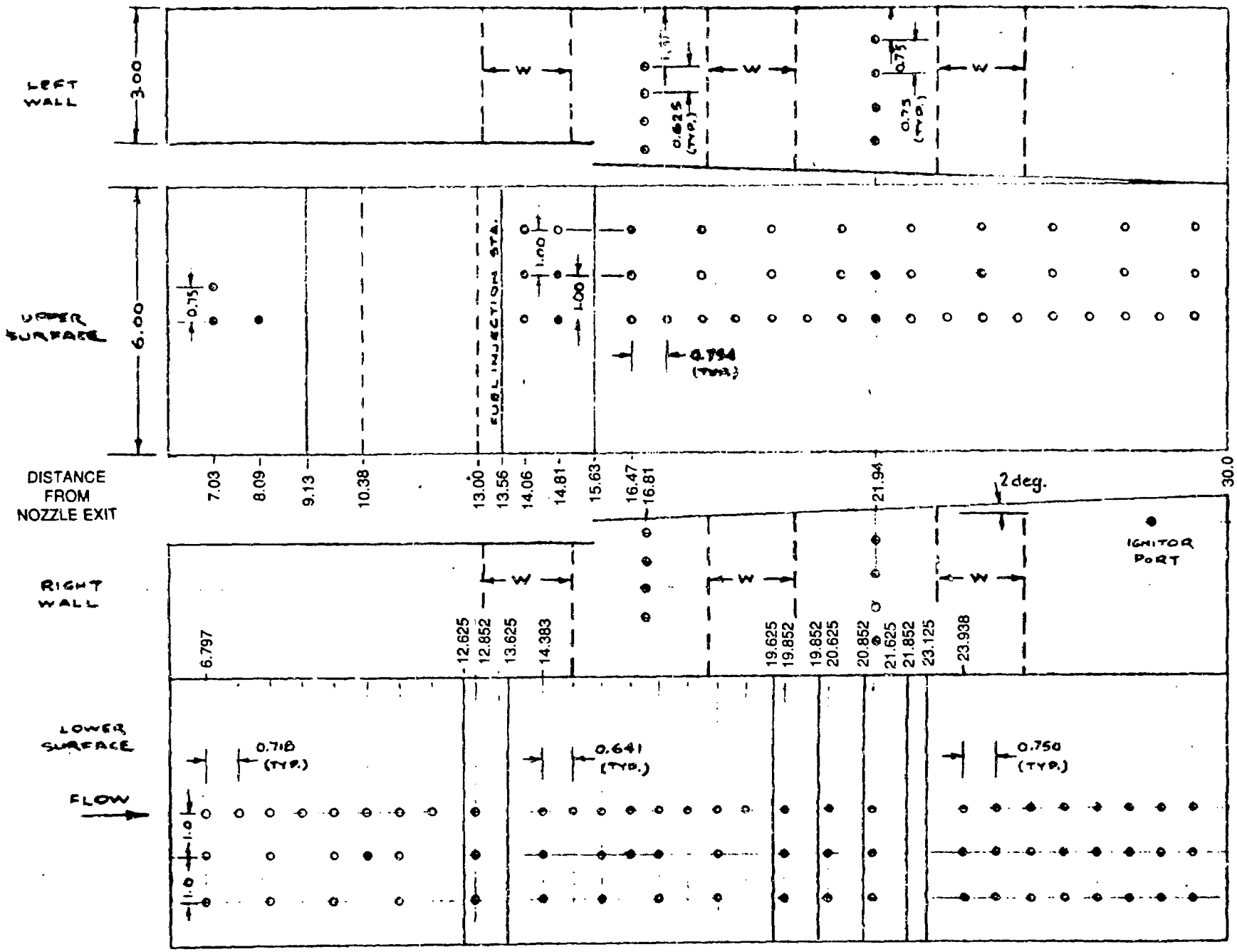

Fig. D-1 Test section wall static pressure taps (o) and thermocouples (•). W is the window location.

TABLE D–1
CARS DATA TABULATION

R046 (STA. 1, PHI = 0, TT = 3000 R)

HEIGHT (IN. FM LWR WALL)	TEMP (R) (S.D.)	MOL. FRAC. N2	MOL. FRAC. H2	MOL. FRAC. H2O	CALC. MASS FRAC. N2	CALC. MASS FRAC. H2	CALC. MASS FRAC. H2O
0.40	1322(213)	–	0	–	–	–	–
0.74	1285(198)	–	0	–	–	–	–
1.08	1236(223)	–	0	–	–	–	–
1.42	1245(265)	–	0	–	–	–	–
1.76	1262(239)	–	0	–	–	–	–
2.10	1254(253)	–	0	–	–	–	–
2.44	1336(234)	–	0	–	–	–	–
2.78	1252(190)	–	0	–	–	–	–
3.12	487(72)	–	0	–	–	–	–

R042 (STA. 1, PHI = 0, TT = 3000R)

HEIGHT (IN. FM LWR WALL)	TEMP (R) (S.D.)	MOL. FRAC. N2	MOL. FRAC. H2	MOL. FRAC. H2O	CALC. MASS FRAC. N2	CALC. MASS FRAC. H2	CALC. MASS FRAC. H2O
0.06	–	–	0	–	–	–	–
0.67	1491(244)	–	0	–	–	–	–
1.29	1679(218)	–	0	–	–	–	–
1.90	1597(252)	–	0	–	–	–	–
2.51	1606(252)	–	0	–	–	–	–
3.13	450(181)	–	0	–	–	–	–

R054 (STA. 3, PHI = 0.5, TT = 3900 R)

HEIGHT (IN. FM LWR WALL)	TEMP (R) (S.D.)	MOL. FRAC. N2	MOL. FRAC. H2	MOL. FRAC. H2O	CALC. MASS FRAC. N2	CALC. MASS FRAC. H2	CALC. MASS FRAC. H2O
2.22	1398(219)	.47	.00	–	.51	.00	–
2.42	1423(286)	.47	.00	–	.51	.00	–
2.62	1433(284)	.53	.00	–	.59	.00	–
2.82	1402(301)	.41	.00	–	.43	.00	–
3.02	1284(332)	.46	.14	–	.50	.01	–
3.22	1041(283)	.27	.44	–	.49	.06	–

(STOICH. H2O ASSUMED)

R055 (STA. 3, PHI = 1.0, TT = 3900 R)

HEIGHT (IN. FM LWR WALL)	TEMP (R) (S.D.)	MOL. FRAC. N2	MOL. FRAC. H2	MOL. FRAC. H2O	CALC. MASS FRAC. N2	CALC. MASS FRAC. H2	CALC. MASS FRAC. H2O
2.22	1469(282)	.49	.00	–	.53	.00	–
2.42	1473(357)	.47	.00	–	.51	.00	–
2.62	1505(176)	.46	.00	–	.50	.00	–
2.82	1460(336)	.44	.00	–	.47	.00	–
3.02	1366(319)	.44	.27	–	.56	.02	–
3.22	985(360)	.26	.47	–	.50	.08	–

(STOIC. H2O ASSUMED)

R057 (STA. 3, PHI = 0.5, TT = 1800 R)

HEIGHT (IN. FM LWR WALL)	TEMP (R) (S.D.)	MOL. FRAC. N2	MOL. FRAC. H2	MOL. FRAC. H2O	CALC. MASS FRAC. N2	CALC. MASS FRAC. H2	CALC. MASS FRAC. H2O
2.22	426(84)	.63	.00	–	–	–	–
2.42	458(83)	.61	.00	–	–	–	–
2.62	455(99)	.63	.00	–	–	–	–
2.82	438(94)	.48	.29	–	–	–	–
3.02	401(79)	.28	.59	–	–	–	–
3.22	400(129)	.18	.73	–	–	–	–

TABLE D–1
CARS DATA TABULATION (continued)

R058 (STA. 3, PHI = 0.5, TT = 1800 R)

HEIGHT (IN. FM LWR WALL)	TEMP (R) (S.D.)	MOL. FRAC. N2	H2	H2O	CALC. MASS FRAC. N2	H2	H2O
2.22	421(67)	.67	.00	–	–	–	–
2.42	466(75)	.67	.00	–	–	–	–
2.62	477(95)	.59	.02	–	–	–	–
2.82	471(79)	.56	.34	–	–	–	–
3.02	468(296)	.28	.59	–	–	–	–
3.22	400(–)	.17	.74	–	–	–	–

R059 (STA. 3, PHI = 1.0, TT = 1800 R)

HEIGHT (IN. FM LWR WALL)	TEMP (R) (S.D.)	MOL. FRAC. N2	H2	H2O	CALC. MASS FRAC. N2	H2	H2O
2.22	376(42)	.71	.00	–	–	–	–
2.42	388(63)	.68	.00	–	–	–	–
2.62	382(44)	.58	.05	–	–	–	–
2.82	411(116)	.37	.29	–	–	–	–
3.02	460(207)	.24	.65	–	–	–	–
3.22	400(295)	.17	.73	–	–	–	–

R062 (STA. 2, PHI = 1.0, TT = 3000 R)

HEIGHT (IN. FM LWR WALL)	TEMP (R) (S.D.)	MOL. FRAC. N2	H2	H2O	CALC. MASS FRAC. N2	H2	H2O
2.36	1354(310)	.68	.00	–	–	–	–
2.56	1346(273)	.67	.00	–	–	–	–
2.76	1320(276)	.60	.00	–	–	–	–
2.96	1192(282)	.60	.31	–	–	–	–
3.16	929(590)	.23	.58	–	–	–	–
3.36	848(–)	.21	.61	–	–	–	–

R064 (STA. 2, PHI = 1.0, TT = 3900 R)

HEIGHT (IN. FM LWR WALL)	TEMP (R) (S.D.)	MOL. FRAC. N2	H2	H2O	CALC. MASS FRAC. N2	H2	H2O
2.36	1566(494)	.51	.00	–	–	–	–
2.56	1527(360)	.55	.00	–	–	–	–
2.76	1618(418)	.60	.02	–	–	–	–
2.96	1407(435)	.49	.20	–	–	–	–
3.16	1348(987)	.25	.50	–	–	–	–
3.36	1000(–)	.24	.52	–	–	–	–

R065 (STA. 2, PHI = 0.5, 3000 R)

HEIGHT (IN. FM LWR WALL)	TEMP (R) (S.D.)	MOL. FRAC. N2	H2	H2O	CALC. MASS FRAC. N2	H2	H2O
2.36	1540(362)	.51	.00	–	–	–	–
2.56	1483(285)	.60	.00	–	–	–	–
2.76	1395(332)	.75	.00	–	–	–	–
2.96	1381(329)	.61	.06	–	–	–	–
3.16	1180(624)	.29	.47	–	–	–	–
3.36	1624(–)	.23	.58	–	–	–	–

TABLE D-1
CARS DATA TABULATION (continued)

R066 (STA. 2, PHI = 0.5, TT = 3900 R)

HEIGHT (IN. FM LWR WALL)	TEMP (R) (S.D.)	MOL. FRAC. N2	MOL. FRAC. H2	MOL. FRAC. H2O	CALC. MASS FRAC. N2	CALC. MASS FRAC. H2	CALC. MASS FRAC. H2O
2.36	1424(448)	.46	.00	-	-	-	-
2.56	1426(401)	.55	.00	-	-	-	-
2.76	1319(432)	.54	.15	-	-	-	-
2.96	1327(590)	.40	.41	-	-	-	-
3.16	1234(1157)	.23	.52	-	-	-	-
3.36	865(-)	.21	.56	-	-	-	-

R070 (STA. 2, PHI = 0, TT = 3900 R)

HEIGHT (IN. FM LWR WALL)	TEMP (R) (S.D.)	MOL. FRAC. N2	MOL. FRAC. H2	MOL. FRAC. H2O	CALC. MASS FRAC. N2	CALC. MASS FRAC. H2	CALC. MASS FRAC. H2O
2.36	1596(286)	.37	0	-	-	-	-
2.56	1592(237)	.36	0	-	-	-	-
2.66	1542(375)	.35	0	-	-	-	-
2.76	1562(308)	.35	0	-	-	-	-
2.86	1555(435)	.36	0	-	-	-	-
2.96	1543(271)	.39	0	-	-	-	-
3.06	1648(398)	.36	0	-	-	-	-
3.16	1579(302)	.38	0	-	-	-	-
3.26	1565(346)	.34	0	-	-	-	-
3.36	1310(239)	.49	0	-	-	-	-

(Pts. at 3.26, 3.06, 2.86, 2.56 in. taken on reverse transit at end of run)

R074 (STA. 2, PHI = 1.0 TT = 3900 R)

HEIGHT (IN. FM LWR WALL)	TEMP (R) (S.D.)	MOL. FRAC. N2	MOL. FRAC. H2	MOL. FRAC. H2O	CALC. MASS FRAC. N2	CALC. MASS FRAC. H2	CALC. MASS FRAC. H2O
2.36	1515(224)	.49	.00	-	.60	.00	-
2.56	1588(267)	.50	.00	-	.61	.00	-
2.76	1535(216)	.48	.00	-	.59	.00	-
2.96	1491(239)	.46	.28	-	.70	.03	-
3.16	1049(292)	.30	.65	-	.79	.12	-
3.36	695(458)	.17	.65	-	.51	.14	-
		(H2 FM RUN 72)			(STOIC. H2O ASSUMED)		

R081 (STA. 2, PHI = 0.5, TT = 3900 R)

HEIGHT (IN. FM LWR WALL)	TEMP (R) (S.D.)	MOL. FRAC. N2	MOL. FRAC. H2	MOL. FRAC. H2O	CALC. MASS FRAC. N2	CALC. MASS FRAC. H2	CALC. MASS FRAC. H2O
2.36	1728(212)	.48	.00	.31	.52	.00	.22
2.56	1772(232)	.52	.00	.31	.57	.00	.22
2.76	1735(202)	.48	.00	.34	.53	.00	.24
2.96	1590(321)	.40	.32	.22	.63	.04	.22
3.16	1149(262)	.25	.78	.14	.63	.14	.23
3.36	875(521)	.12	.75	.08	.43	.19	.18

R082 (STA. 2, PHI = 0.5, TT = 3900 R)

HEIGHT (IN. FM LWR WALL)	TEMP (R) (S.D.)	MOL. FRAC. N2	MOL. FRAC. H2	MOL. FRAC. H2O	CALC. MASS FRAC. N2	CALC. MASS FRAC. H2	CALC. MASS FRAC. H2O
2.36	1740(224)	.50	.00	.36	.54	.00	.21
2.56	1647(199)	.47	.00	.32	.51	.00	.22
2.76	1729(209)	.50	.00	.31	.55	.00	.22
2.96	1660(243)	.45	.25	.27	.67	.03	.26
3.16	1121(253)	.27	.68	.12	.68	.12	.19
3.36	882(431)	.13	.73	.09	.44	.18	.19

TABLE D-1
CARS DATA TABULATION (continued)

R084 (STA. 2, PHI = 1.0, TT = 3900 R)

HEIGHT (IN. FM LWR WALL)	TEMP (R) (S.D.)	MOL. FRAC. N2	MOL. FRAC. H2	MOL. FRAC. H2O	CALC. MASS FRAC. N2	CALC. MASS FRAC. H2	CALC. MASS FRAC. H2O
2.36	1789(183)	.55	.00	.27	.59	.00	.19
2.56	1705(216)	.47	.00	.35	.52	.00	.25
2.76	1685(192)	.45	.00	.31	.49	.00	.22
2.96	1633(197)	.44	.48	.29	.67	.05	.28
3.16	1217(240)	.26	.83	.11	.50	.11	.14
3.36	513(448)	.09	.80	.06	.37	.24	.16

Rev. 1/16/90

R092 (STA. 3, PHI = 1.0)

HEIGHT (IN. FM LWR WALL)	TEMP (R) (S.D.)	MOL. FRAC. N2	MOL. FRAC. H2	MOL. FRAC. H2O	CALC. MASS FRAC. N2	CALC. MASS FRAC. H2	CALC. MASS FRAC. H2O
2.52	1747(261)	.50	.00	.32	.55	.00	.23
2.62	1810(224)	.37	.00	.31	.40	.00	.21
2.72	1685(238)	.50	.00	.39	.57	.00	.29
2.82	1593(265)	.—	.00	.—	–	–	–
2.92	——	.—	.00	.—	–	–	–
3.02	1473(301)	.—	.27	.—	–	–	–
3.12	1393(333)	.36	.35	.27	.62	.04	.30
3.22	1160(333)	.18	.68	.17	.59	.16	.36
3.32	686(389)	.09	.30	.01	.11	.03	.01
3.42	860(417)	.13	.82	.04	.58	.26	.11
3.52	682(297)	.10	.80	.02	.38	.22	.05

R093 (STA. 3, PHI = 0.5)

HEIGHT (IN. FM LWR WALL)	TEMP (R) (S.D.)	MOL. FRAC. N2	MOL. FRAC. H2	MOL. FRAC. H2O	CALC. MASS FRAC. N2	CALC. MASS FRAC. H2	CALC. MASS FRAC. H2O
2.52	1739(236)	.50	.00	.32	.55	.00	.23
2.62	1783(250)	.48	.00	.31	.52	.00	.22
2.72	1670(246)	.50	.00	.33	.59	.00	.25
2.82	1635(231)	.47	.00	.32	.51	.00	.22
2.92	1609(242)	.51	.00	.24	.54	.00	.16
3.02	1544(256)	.46	.00	.22	.48	.00	.15
3.12	1499(250)	.44	.00	.21	.45	.00	.14
3.22	1374(255)	.38	.33	.20	.60	.04	.20
3.32	1129(308)	.31	.48	.20	.64	.07	.27
3.42	857(276)	.23	.55	.13	.50	.09	.18
3.52	788(291)	.18	.64	.11	.48	.12	.19

R094 (STA. 3, PHI = 1.0)

HEIGHT (IN. FM LWR WALL)	TEMP (R) (S.D.)	MOL. FRAC. N2	MOL. FRAC. H2	MOL. FRAC. H2O	CALC. MASS FRAC. N2	CALC. MASS FRAC. H2	CALC. MASS FRAC. H2O
2.52	1768(246)	.50	.00	.32	.55	.00	.23
2.62	1756(226)	.53	.00	.27	.57	.00	.19
2.72	1697(224)	.51	.00	.24	.55	.00	.17
2.82	1697(292)	.51	.00	.—	.48	.00	–
2.92	——	.—	.—	.—	–	–	–
3.02	1457(301)	.45	.00	.13	.44	.00	.08
3.12	1353(366)	.37	.11	.11	.40	.01	.08
3.22	1155(403)	.28	.18	.06	.32	.01	.04
3.32	1006(370)	.21	.26	.04	.26	.02	.03
3.42	849(305)	.20	.86	.04	.69	.21	.10
3.52	790(328)	.15	.75	.03	.50	.18	.06

TABLE D-1
CARS DATA TABULATION (continued)

R095 (STA. 3, PHI = 1.0)

HEIGHT (IN. FM LWR WALL)	TEMP (R) (S.D.)	MOL. FRAC. N2	MOL. FRAC. H2	MOL. FRAC. H2O	CALC. MASS FRAC. N2	CALC. MASS FRAC. H2	CALC. MASS FRAC. H2O
2.52	674(160)	.68	.00	–	.69	.00	–
2.62	590(115)	.65	.00	–	.65	.00	–
2.72	640(121)	.63	.00	–	.63	.00	–
2.82	652(153)	.68	.00	–	.69	.00	–
2.92	548(92)	.52	.09	–	.67	.01	–
3.02	555(150)	.50	.24	–	.73	.03	–
3.12	533(88)	.47	.30	–	.74	.03	–
3.22	532(107)	.51	.42	–	.87	.05	–
3.32	478(142)	.27	.—	–	–	–	–
3.42	465(104)	.23	.48	–	.51	.08	–
3.52	447(244)	.21	.70	–	.60	.14	–

R096 (STA. 3, PHI = 0.5)

HEIGHT (IN. FM LWR WALL)	TEMP (R) (S.D.)	MOL. FRAC. N2	MOL. FRAC. H2	MOL. FRAC. H2O	CALC. MASS FRAC. N2	CALC. MASS FRAC. H2	CALC. MASS FRAC. H2O
2.52	696(167)	.64	.00	.16	.66	.00	.11
2.62	622(131)	.66	.00	.12	.67	.00	.08
2.72	770(173)	.78	.00	.12	.80	.00	.08
2.82	629(115)	.65	.00	.06	.64	.00	.04
2.92	670(149)	.64	.00	.00	.63	.00	.04
3.02	684(163)	.62	.19	.00	.73	.02	.00
3.12	570(123)	.54	.20	.00	.63	.02	.00
3.22	613(141)	.57	.35	.03	.85	.04	.03
3.32	571(117)	.45	.39	.03	.70	.04	.03
3.42	536(206)	.28	.55	.02	.57	.08	.03
3.52	488(137)	.27	.61	.02	.61	.10	.03

R112 (STA. 2, PHI = 1.0, WEDGE)

HEIGHT (IN. FM LWR WALL)	TEMP (R) (S.D.)	MOL. FRAC. N2	MOL. FRAC. H2	MOL. FRAC. H2O	CALC. MASS FRAC. N2	CALC. MASS FRAC. H2	CALC. MASS FRAC. H2O
2.36	1029(148)	.70	.00	.11	.71	.00	.07
2.46	996(144)	.65	.00	.11	.65	.00	.07
2.56	991(150)	.69	.00	.12	.70	.00	.08
2.66	961(147)	.59	.00	.11	.70	.00	.08
2.76	986(140)	.66	.10	.10	.74	.01	.07
2.86	903(135)	.54	.20	.09	.67	.02	.07
2.96	861(154)	.48	.41	.04	.78	.05	.04
3.06	728(115)	.35	.57	.02	.74	.09	.03
3.16	677(190)	.27	.72	.02	.84	.16	.04
3.26	642(215)	.16	.79	.02	.61	.21	.05
3.36	–	.10	.88	.02	.38	.22	.05

TABLE D-1
CARS DATA TABULATION (continued)

R113 (STA. 2, PHI = 0.5, WEDGE)

HEIGHT (IN. FM LWR WALL)	TEMP (R) (S.D.)	MOL. FRAC. N2	MOL. FRAC. H2	MOL. FRAC. H2O	CALC. MASS FRAC. N2	CALC. MASS FRAC. H2	CALC. MASS FRAC. H2O
2.36	999(183)	.49	.00	.10	.48	.00	.06
2.46	982(150)	.58	.00	.13	.58	.00	.08
2.56	1002(180)	.59	.00	.10	.58	.00	.06
2.66	974(163)	.64	.00	.12	.65	.00	.09
2.76	956(173)	.58	.10	.10	.64	.01	.07
2.86	1080(146)	.36	.26	.10	.47	.02	.08
2.96	818(164)	.41	.43	.04	.68	.05	.04
3.06	985(193)	.24	.88	.02	.76	.20	.04
3.16	765(245)	.24	.80	.02	.77	.18	.04
3.26	746(319)	.15	.87	.02	.84	.35	.07
3.36	692(377)	.11	.83	.02	.48	.26	.06

R114 (STA. 2, N2 ONLY, WEDGE)

HEIGHT (IN. FM LWR WALL)	TEMP (R) (S.D.)	MOL. FRAC. N2	MOL. FRAC. H2O	CALC. MASS FRAC. N2	CALC. MASS FRAC. H2O
2.36	965(146)	.50	.10	.49	.06
2.46	964(151)	.56	.12	.56	.08
2.56	944(162)	.56	.10	.55	.06
2.66	941(163)	.54	.12	.54	.08
2.76	981(152)	.56	.10	.55	.06
2.86	962(158)	.56	.10	.57	.06
2.96	983(164)	.65	.09	.65	.06
3.06	944(163)	.66	.07	.65	.04
3.16	925(153)	.73	.06	.72	.04
3.26	834(121)	.69	.03	.67	.02
3.36	785(132)	.72	.03	.70	.02

R121 (STA. 2, PHI = 1.0, WEDGE)

HEIGHT (IN. FM LWR WALL)	TEMP (R) (S.D.)	MOL. FRAC. N2	MOL. FRAC. H2	MOL. FRAC. H2O	CALC. MASS FRAC. N2	CALC. MASS FRAC. H2	CALC. MASS FRAC. H2O
2.36	1912(224)	.44	.00	.37	.49	.00	.27
2.56	1916(248)	.50	.00	.27	.53	.00	.19
2.66	1818(322)	.40	.00	.21	.41	.00	.14
2.76	1764(315)	.42	.00	.28	.44	.00	.17
2.86	1282(370)	.23	.33	.15	.34	.03	.14
2.96	1239(341)	.24	.44	.13	.42	.05	.15
3.06	780(323)	.12	.57	.07	.25	.06	.09
3.16	630(315)	.19	.59	.06	.21	.09	.08
3.26	670(701)	.09	.72	.07	.28	.16	.14
3.36	686(981)	.07	.85	.05	.36	.31	.16

TABLE D-1
CARS DATA TABULATION (continued)

R122 (STA. 2, PHI = 0.5, WEDGE)

HEIGHT (IN. FM LWR WALL)	TEMP (R) (S.D.)	MOL. FRAC. N2	MOL. FRAC. H2	MOL. FRAC. H2O	CALC. MASS FRAC. N2	CALC. MASS FRAC. H2	CALC. MASS FRAC. H2O
2.36	1795(267)	.44	.00	.32	.48	.00	.22
2.46	1828(314)	.46	.00	-	.50	.00	-
2.56	1807(259)	.48	.00	-	.53	.00	-
2.66	1891(296)	.45	.00	-	.53	.00	-
2.76	1694(253)	.43	.00	.24	.45	.00	.16
2.86	1553(323)	.36	.12	.23	.42	.01	.17
2.96	1376(354)	.30	.51	.22	.63	.08	.30
3.06	987(336)	.15	.84	.09	.56	.22	.22
3.16	798(344)	.13	.81	.07	.56	.25	.19
3.26	741(511)	.08	(.82)	.05	.35	.28	.14
3.36	692(510)	.08	(.82)	.05	.32	.23	.13

R123 (STA. 3, PHI = 1.0, WEDGE)

HEIGHT (IN. FM LWR WALL)	TEMP (R) (S.D.)	MOL. FRAC. N2	MOL. FRAC. H2	MOL. FRAC. H2O	CALC. MASS FRAC. N2	CALC. MASS FRAC. H2	CALC. MASS FRAC. H2O
2.52	718(121)	.68	.00	.11	.69	.00	.07
2.72	735(131)	.65	.00	.11	.67	.00	.07
2.92	754(140)	.60	.00	.10	.60	.00	.06
3.12	723(134)	.56	.00	.09	.55	.00	.06
3.22	683(112)	.56	.23	.07	.72	.02	.06
3.32	630(133)	.44	.35	.07	.66	.04	.07
3.42	604(114)	.38	.46	.06	.67	.06	.07
3.52	582(123)	.33	.52	.05	.64	.07	.06

R124 (STA. 3, PHI = 1.0, WEDGE)

HEIGHT (IN. FM LWR WALL)	TEMP (R) (S.D.)	MOL. FRAC. N2	MOL. FRAC. H2	MOL. FRAC. H2O	CALC. MASS FRAC. N2	CALC. MASS FRAC. H2	CALC. MASS FRAC. H2O
2.52	712(122)	.68	.00	.11	.69	.00	.07
2.72	762(118)	.67	.01	.09	.68	.00	.06
2.82	707(115)	.74	.00	.09	.75	.00	.06
2.92	716(128)	.67	.00	.09	.69	.00	.06
3.02	711(122)	.66	.00	.05	.65	.00	.05
3.12	697(135)	.61	.17	.08	.73	.01	.06
3.22	662(125)	.63	.24	.07	.83	.02	.06
3.32	670(125)	.49	.36	.06	.75	.04	.06
3.42	582(102)	.45	.46	.06	.81	.06	.07
3.52	579(132)	.36	.51	.06	.70	.07	.07

TABLE D-1
CARS DATA TABULATION (concluded)

R125 (STA. 3, PHI = 0.5, WEDGE)

HEIGHT (IN. FM LWR WALL)	TEMP (R) (S.D.)	MOL. FRAC. N2	MOL. FRAC. H2	MOL. FRAC. H2O	CALC. MASS FRAC. N2	CALC. MASS FRAC. H2	CALC. MASS FRAC. H2O
2.52	616(116)	.68	.00	.11	.69	.00	.07
2.62	681(140)	.69	.00	.13	.70	.00	.09
2.72	672(126)	.68	.00	.12	.69	.00	.08
2.82	687(117)	.72	.00	.14	.76	.00	.09
2.92	698(138)	.68	.07	.10	.71	.01	.07
3.02	708(120)	.71	.10	.12	.81	.01	.09
3.12	656(142)	.66	.10	.08	.73	.01	.06
3.22	632(167)	.65	.16	.07	.77	.01	.05
3.32	593(102)	.57	.25	.07	.75	.02	.06
3.42	530(103)	.56	.35	.08	.86	.04	.08
3.52	547(110)	.40	.41	.06	.65	.05	.06

R126 (STA. 3, PHI = 1.0, WEDGE)

HEIGHT (IN. FM LWR WALL)	TEMP (R) (S.D.)	MOL. FRAC. N2	MOL. FRAC. H2	MOL. FRAC. H2O	CALC. MASS FRAC. N2	CALC. MASS FRAC. H2	CALC. MASS FRAC. H2O
2.52	1847(278)	.47	.00	.32	.51	.00	.22
2.62	1795(528)	.33	.00	.33	.35	.00	.23
2.72	1855(448)	.38	.00	.36	.42	.00	.26
2.82	2106(878)	.10	.00	.20	.10	.00	.10
2.92	1978(841)	.21	.10	.30	.25	.01	.23
3.02	2084(841)	.06	.14	.29	.07	.01	.22
3.12	1872(745)	.16	.29	.21	.23	.03	.19
3.22	2081(802)	.07	.47	.15	.13	.06	.17
3.32	1646(796)	.11	.56	.10	.23	.08	.13
3.42	1773(726)	.05	.86	.08	.29	.35	.30
3.52	1336(596)	.10	.72	.06	.31	.16	.12

R127 (STA. 3, PHI = 0.5, WEDGE)

HEIGHT (IN. FM LWR WALL)	TEMP (R) (S.D.)	MOL. FRAC. N2	MOL. FRAC. H2	MOL. FRAC. H2O	CALC. MASS FRAC. N2	CALC. MASS FRAC. H2	CALC. MASS FRAC. H2O
2.52	1882(276)	.47	.00	.36	.52	.00	.26
2.62	1975(291)	.45	.00	.30	.48	.00	.21
2.72	2070(333)	.46	.00	.37	.52	.00	.27
2.82	1982(346)	.45	.00	.30	.48	.00	.21
2.92	2023(446)	.38	.10	.31	.46	.01	.24
3.02	1886(416)	.35	.10	.25	.41	.01	.19
3.12	1856(460)	.26	.29	.23	.38	.03	.22
3.22	1570(516)	.25	.50	.18	.52	.07	.24
3.32	1506(513)	.20	.64	.16	.57	.13	.30
3.42	1296(468)	.17	.63	.12	.44	.12	.20
3.52	1195(388)	.14	.47	.12	.25	.05	.14

TOTAL TEMPERATURE

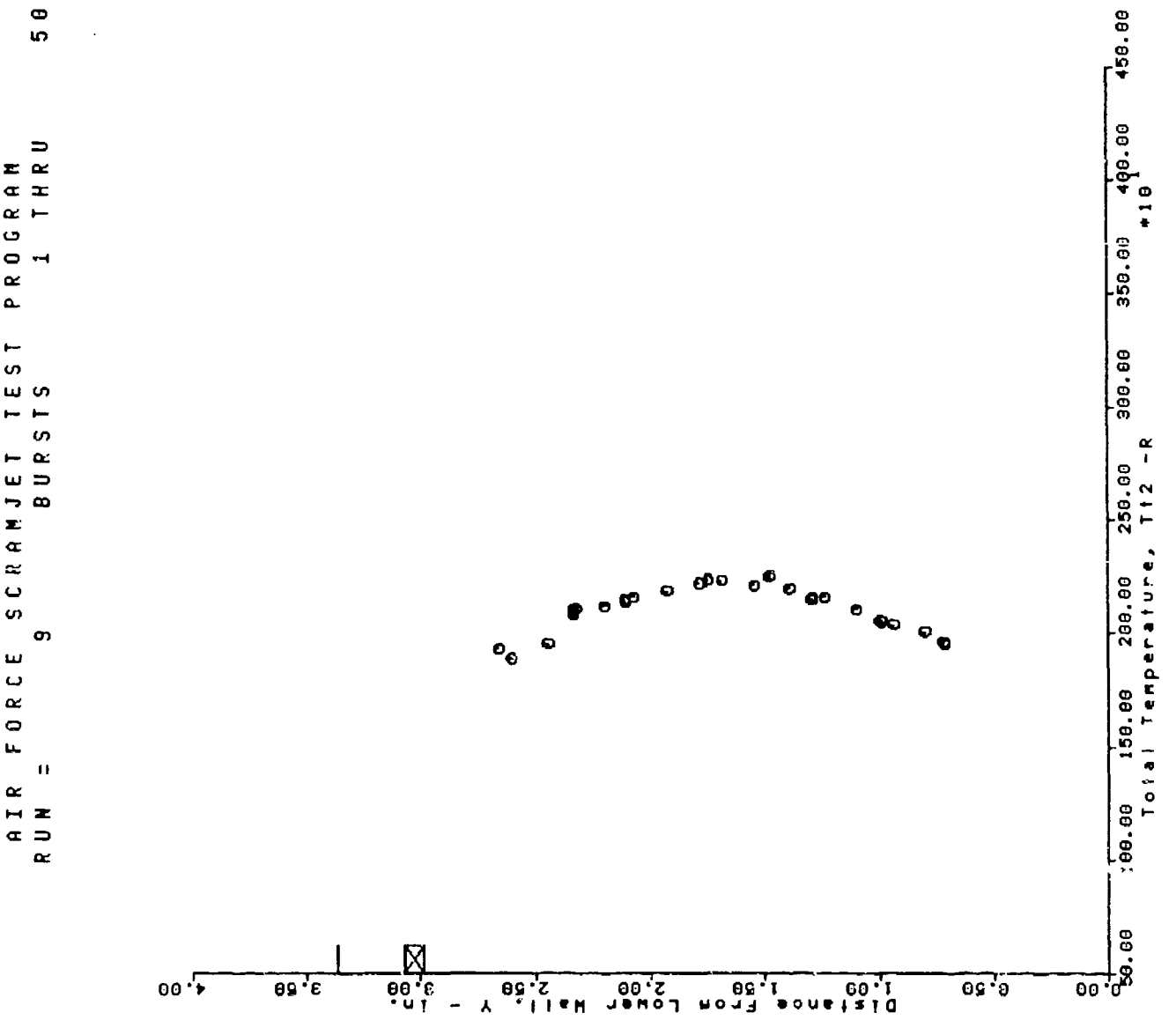

AIR FORCE SCRAMJET TEST PROGRAM
RUN = 11 BURSTS 12 THRU 46

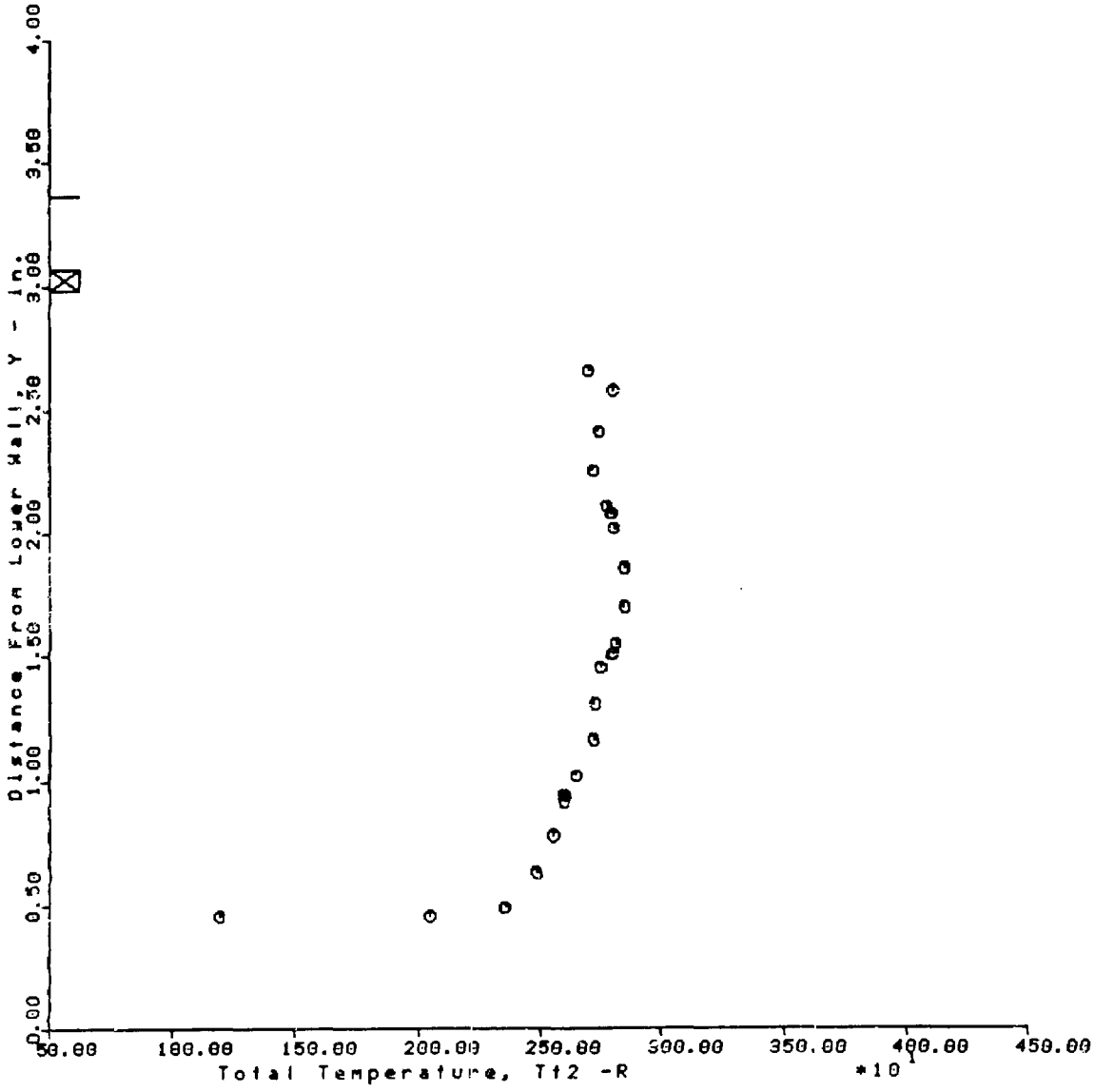

AIR FORCE SCRAMJET TEST PROGRAM
RUN = 14 BURSTS 9 THRU 75

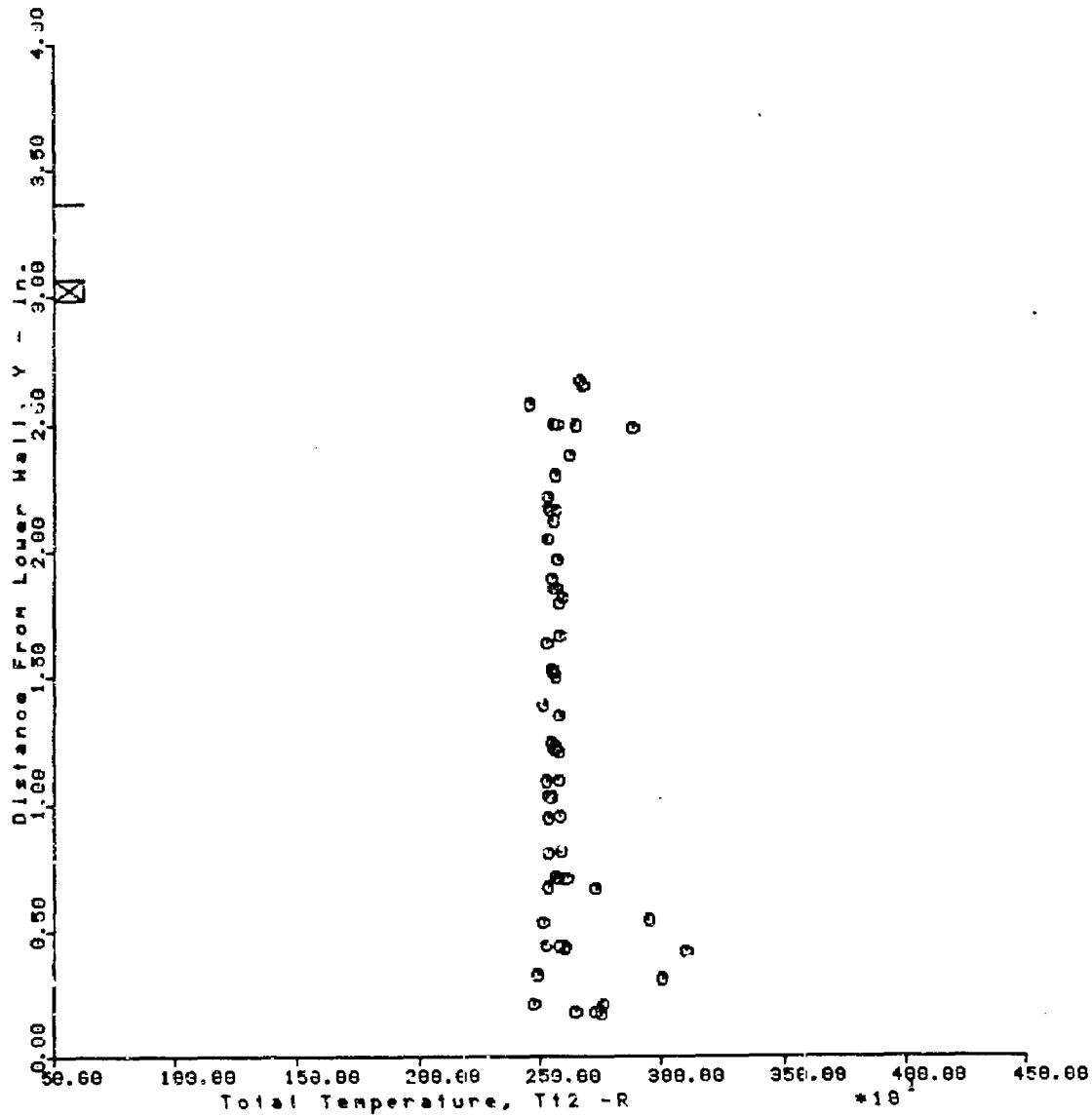

AIR FORCE SCRAMJET TEST PROGRAM
RUN = 23 BURSTS 10 THRU 44

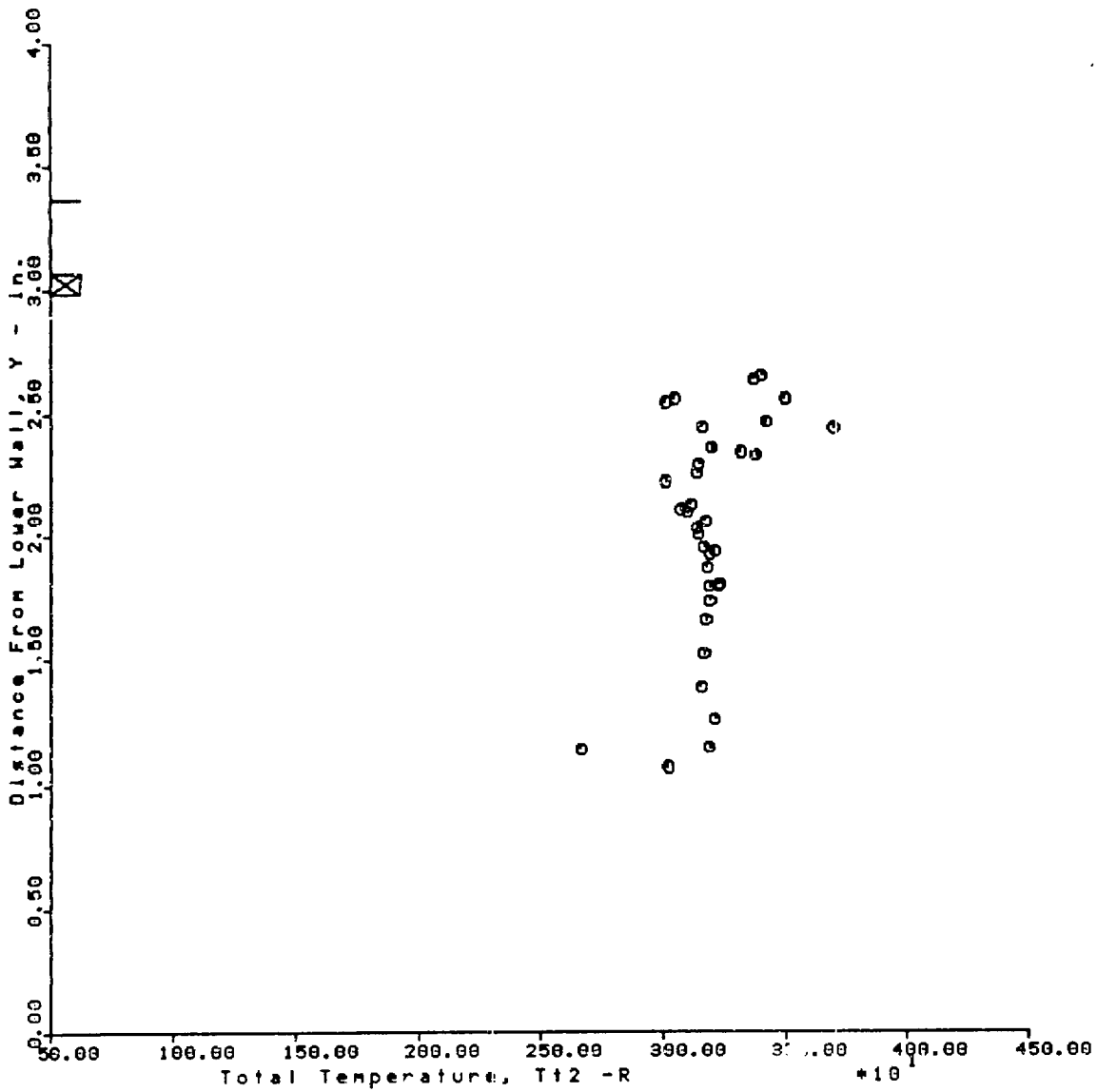

AFS TEST PROGRAM
RUN = 36 BURSTS 38 THRU 74

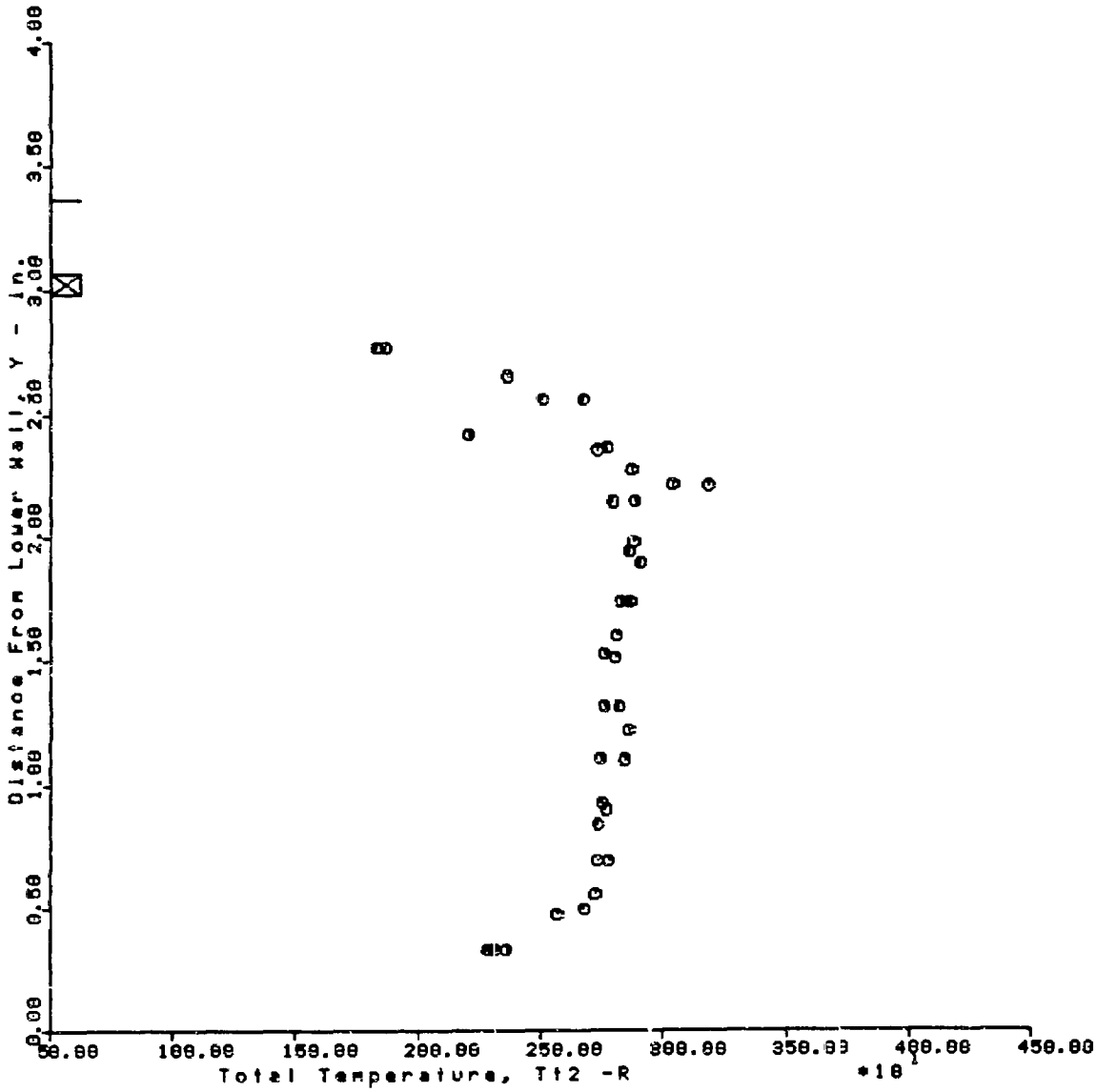

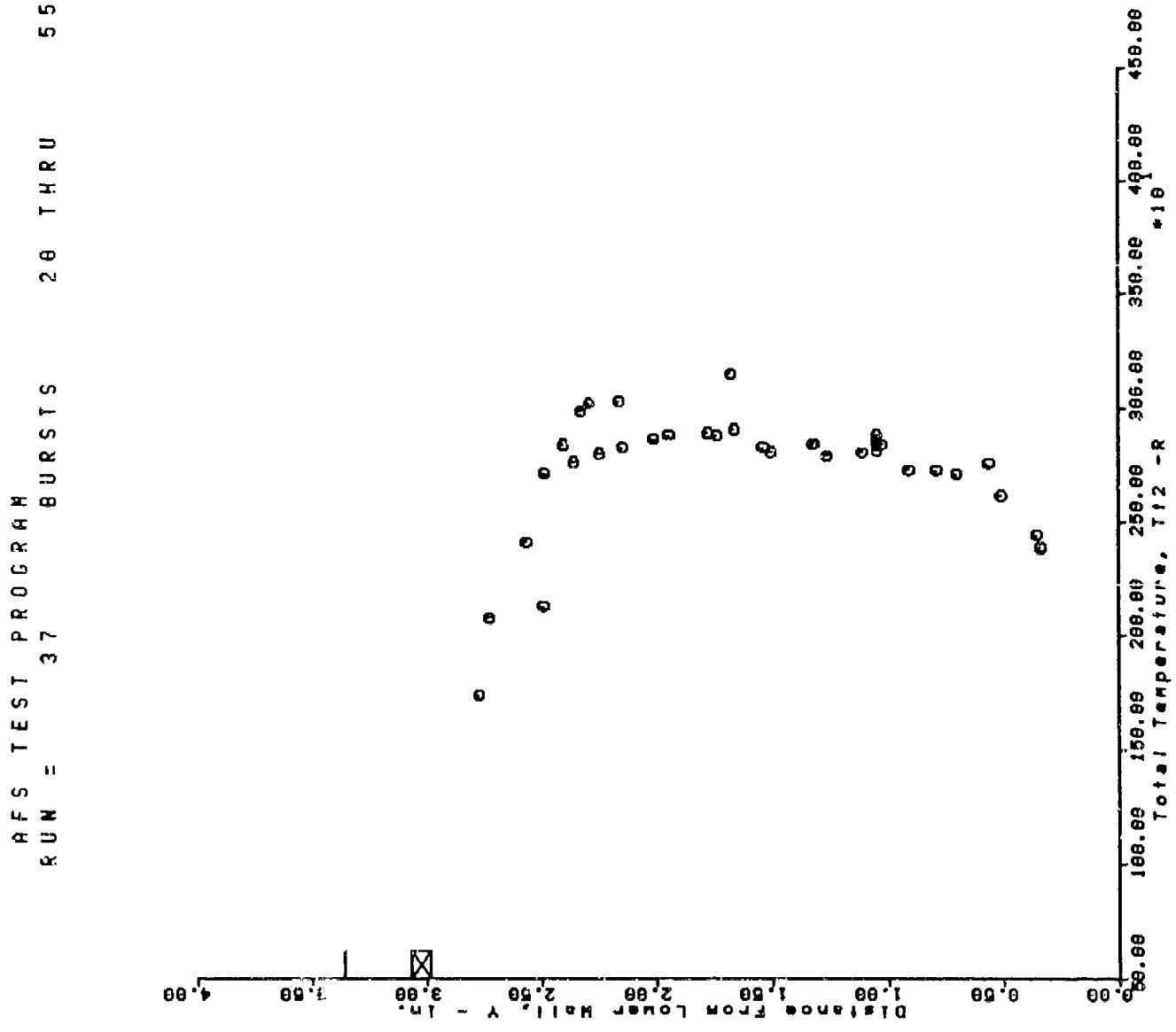
AFS TEST PROGRAM
RUN = 37 BURSTS 20 THRU 55
Distance From Lower Wall, Y - In.
0.00
0.50
1.00
1.50
2.00
2.50
3.00
3.50
4.00
Total Temperature, T12 -R
*10
50.00
100.00
150.00
200.00
250.00
300.00
350.00
400.00
450.00

AFS TEST PROGRAM
RUN = 38 BURSTS 22 THRU 64

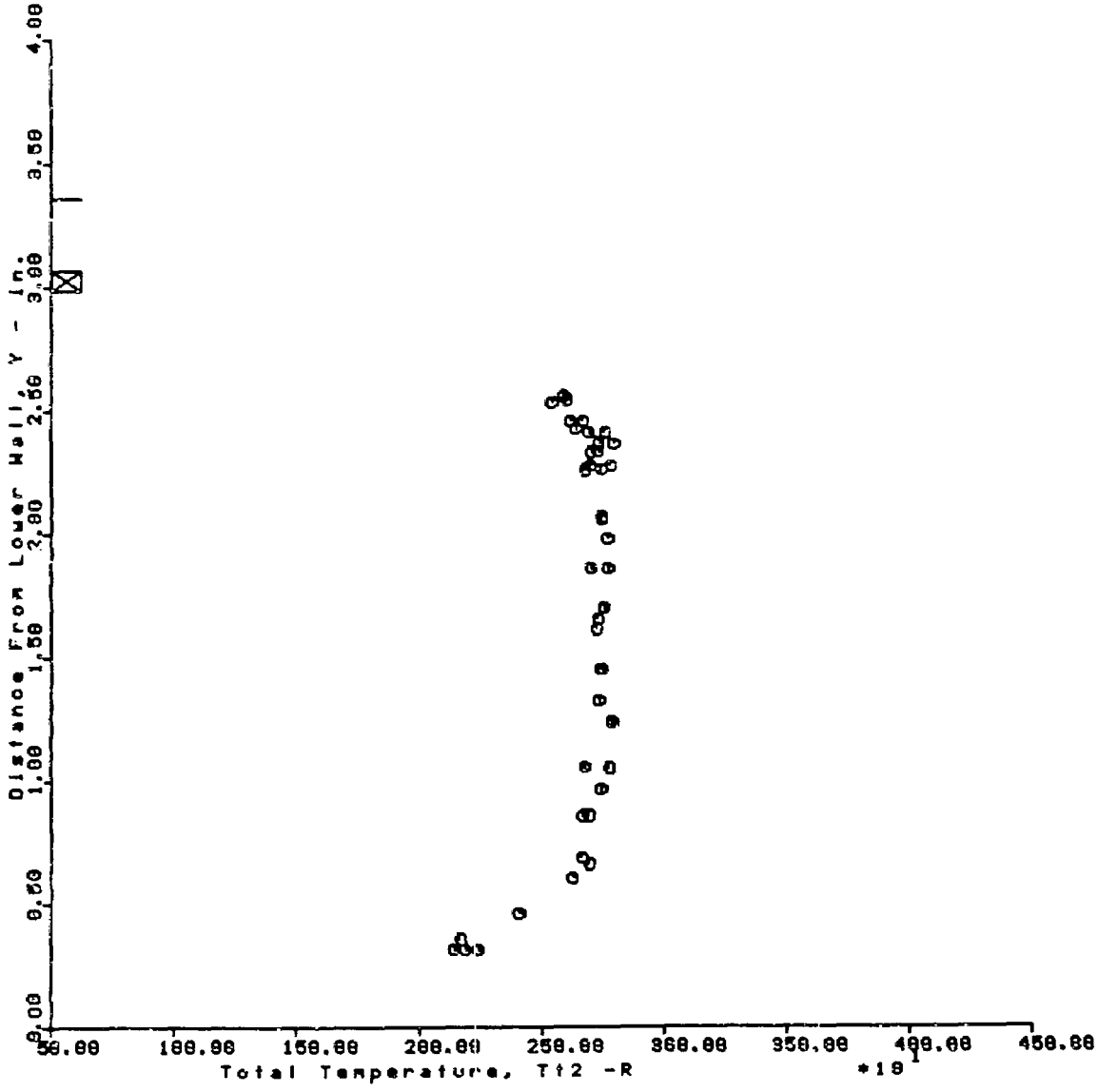

AFS TEST PROGRAM
RUN = 44 BURSTS 26 THRU 50

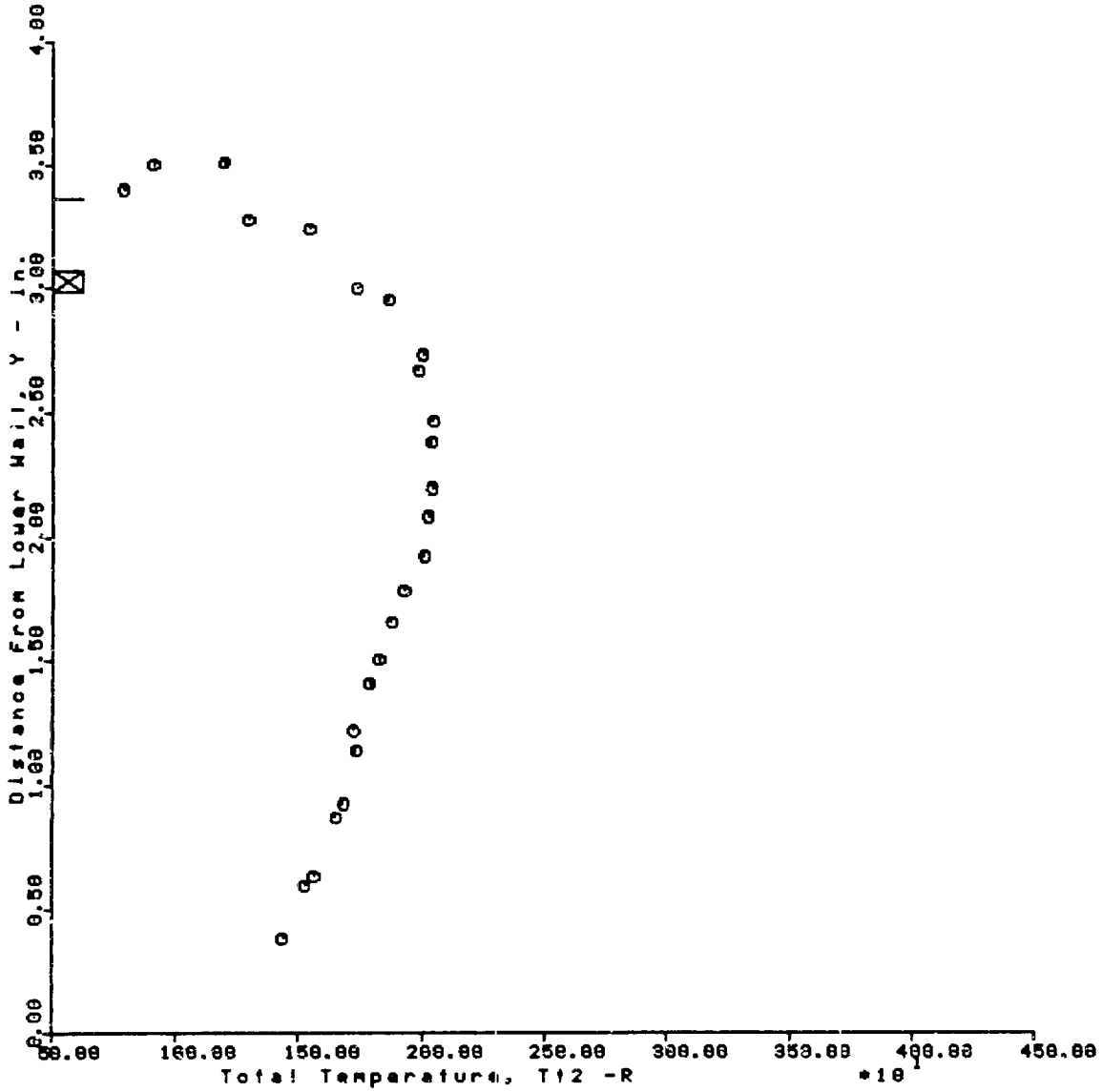

AFS TEST PROGRAM
RUN = 45 BURSTS 25 THRU 50

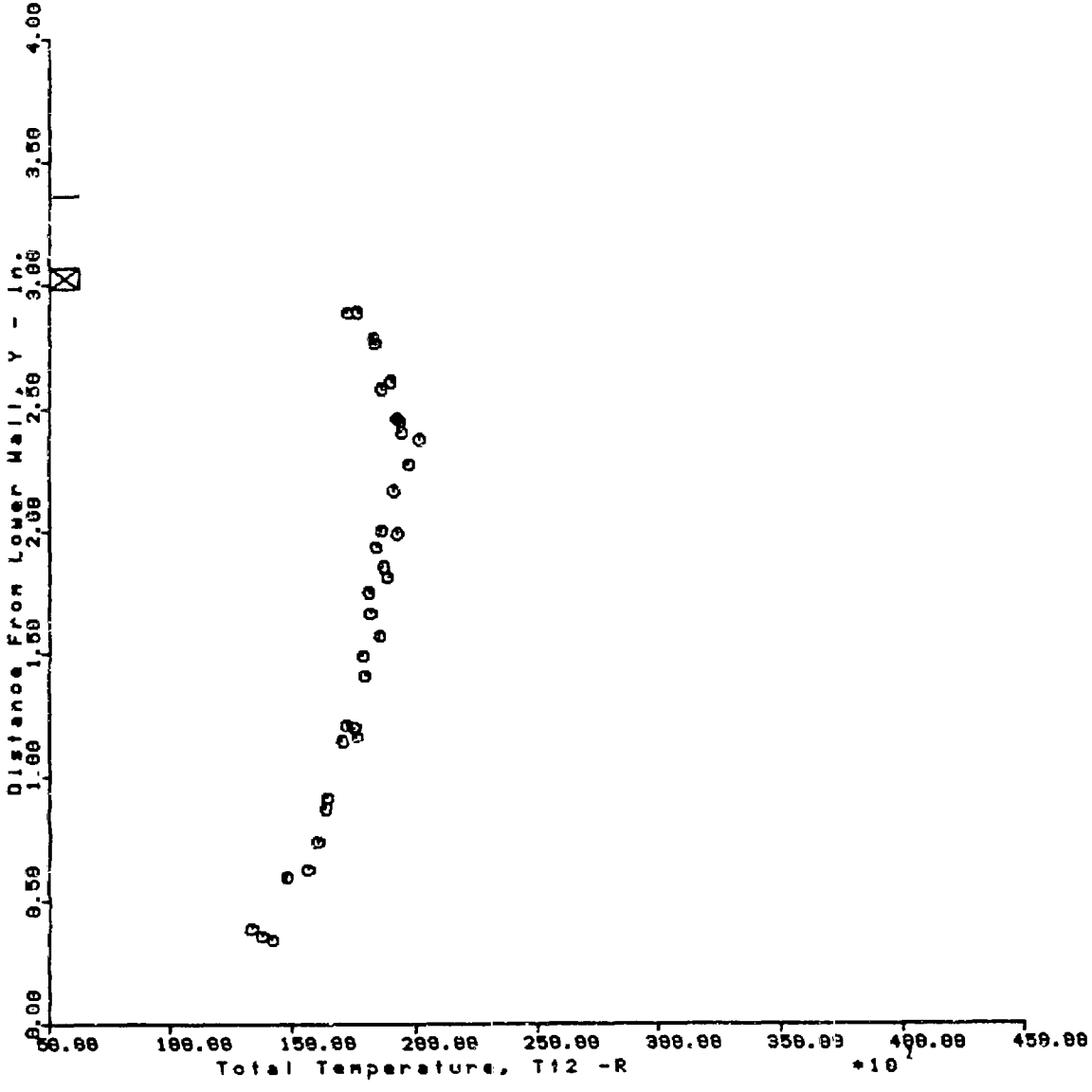

AFS TEST PROGRAM
RUN = 46 BURSTS 27 THRU 53

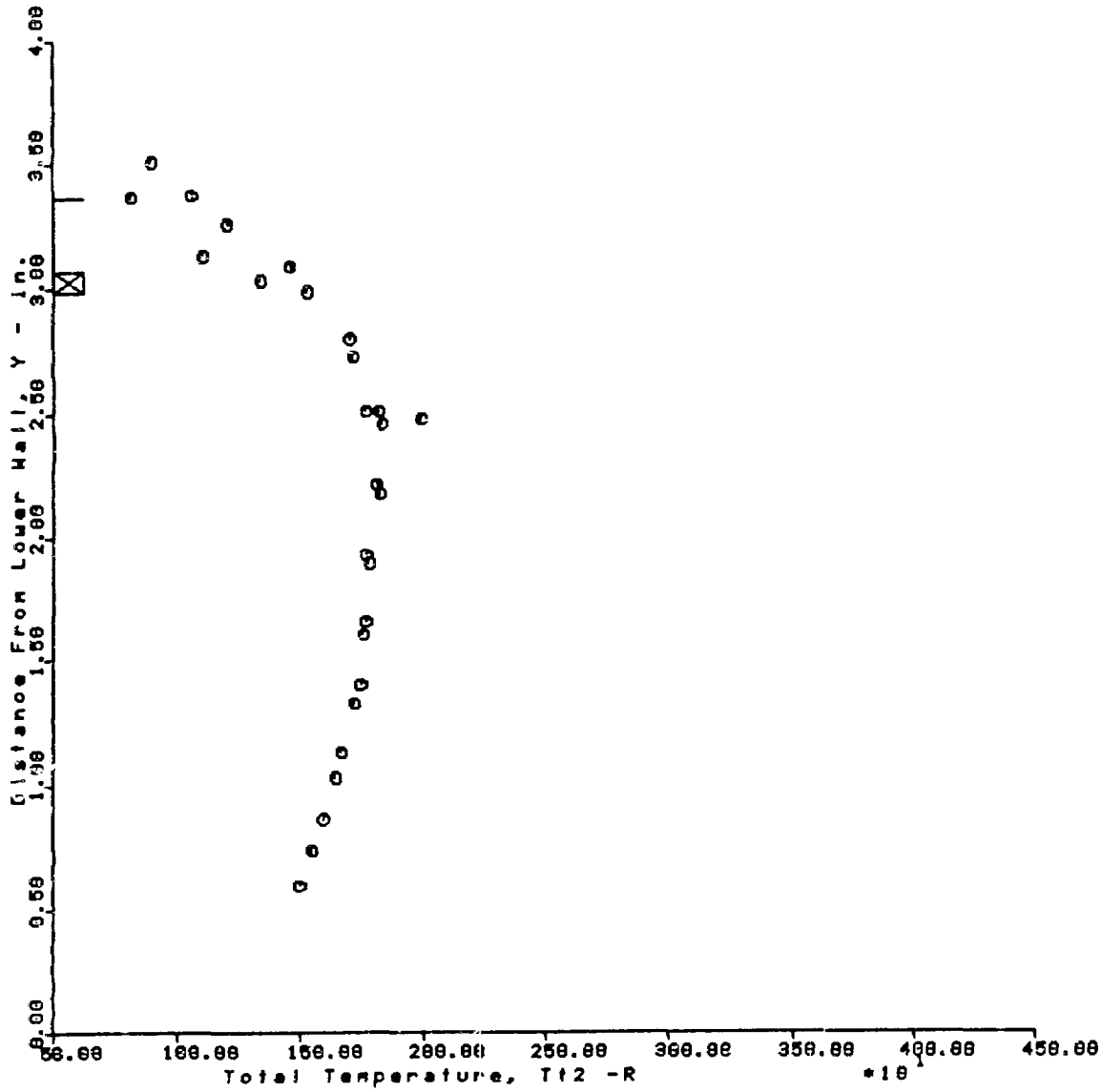

AFS TEST PROGRAM
RUN = 49 BURSTS 43 THRU 64

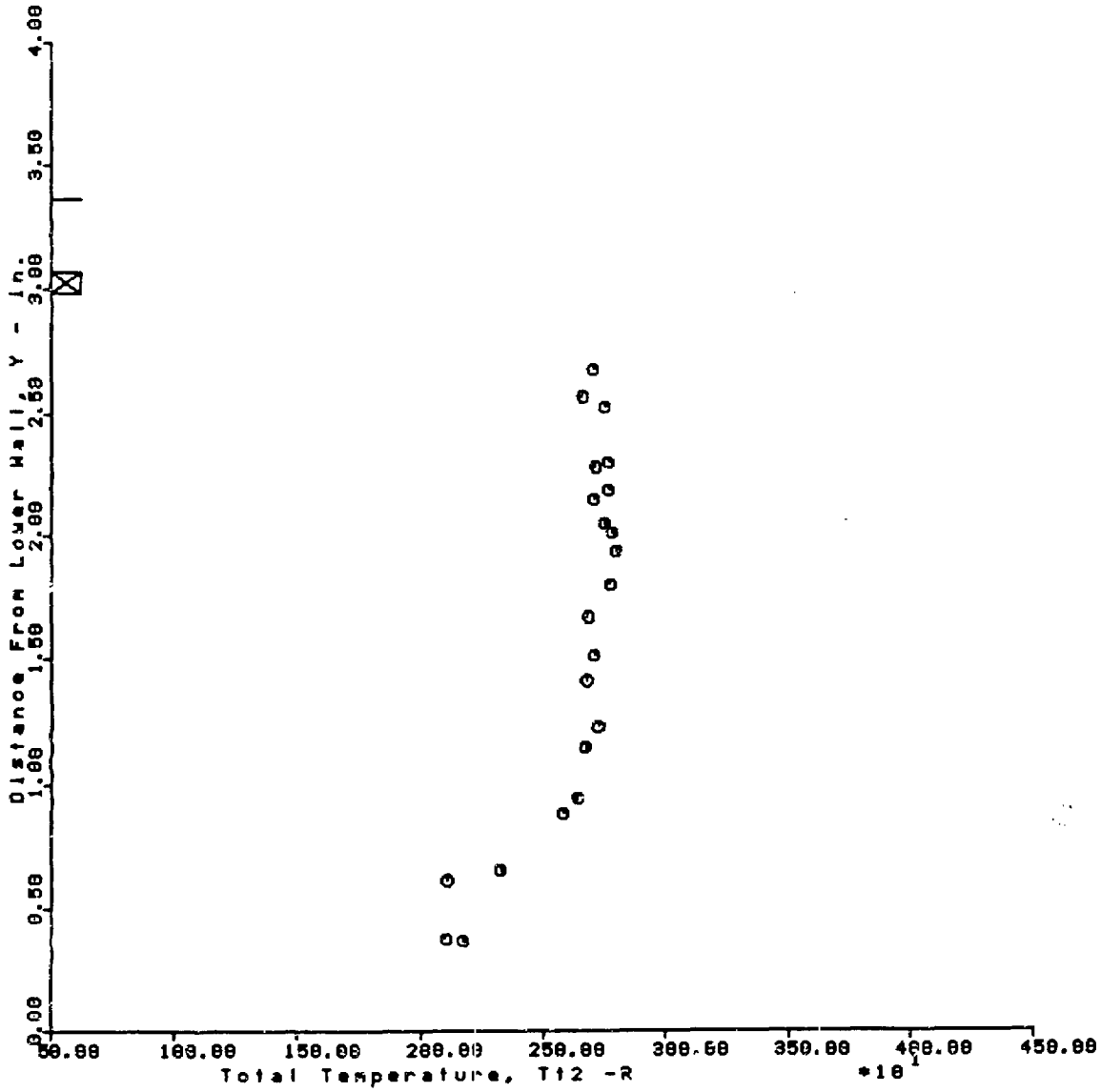

AFS TEST PROGRAM
RUN = 52 BURSTS 25 THRU 60

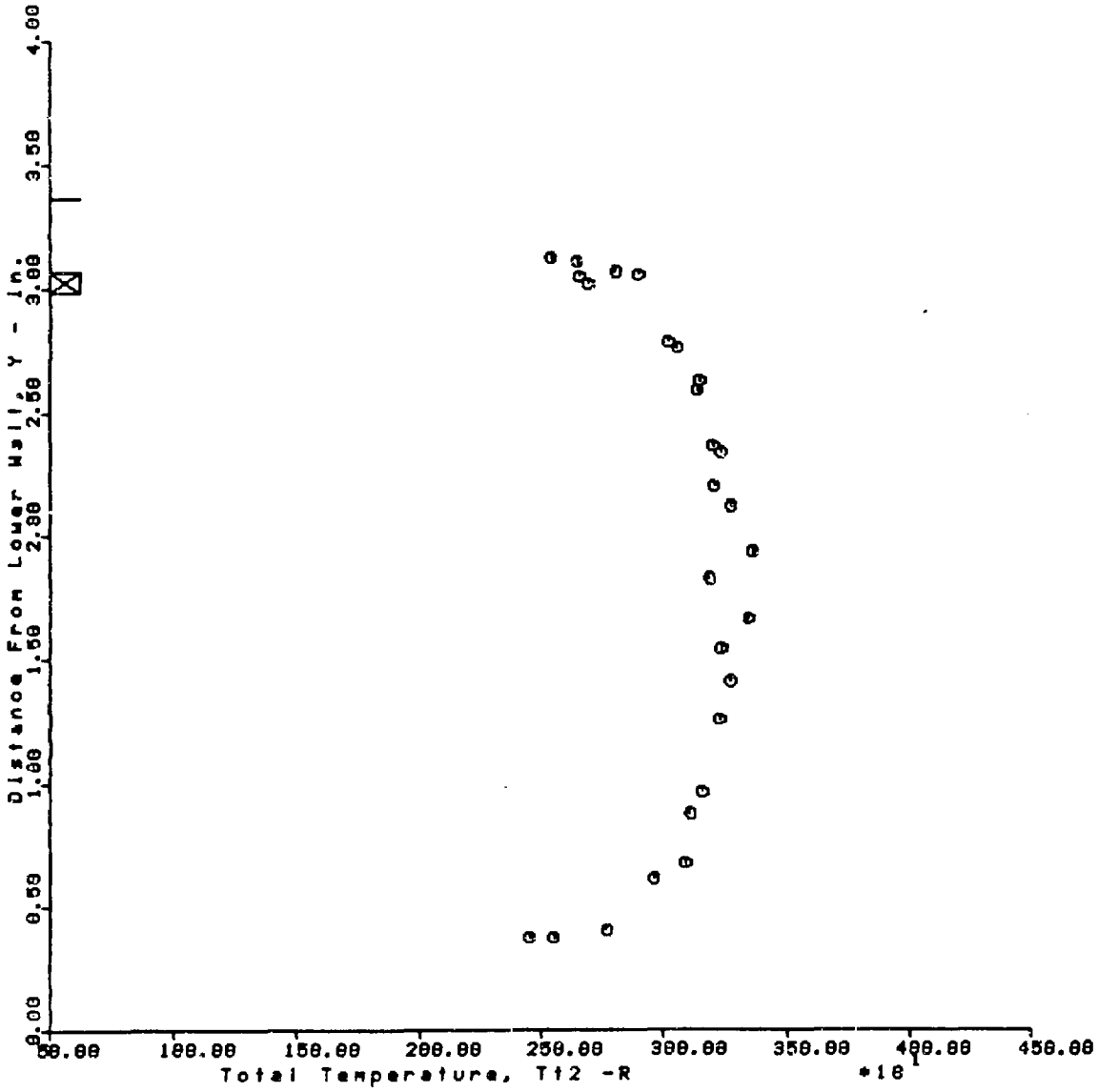

AFS TEST PROGRAM
RUN = 53 BURSTS 26 THRU 59

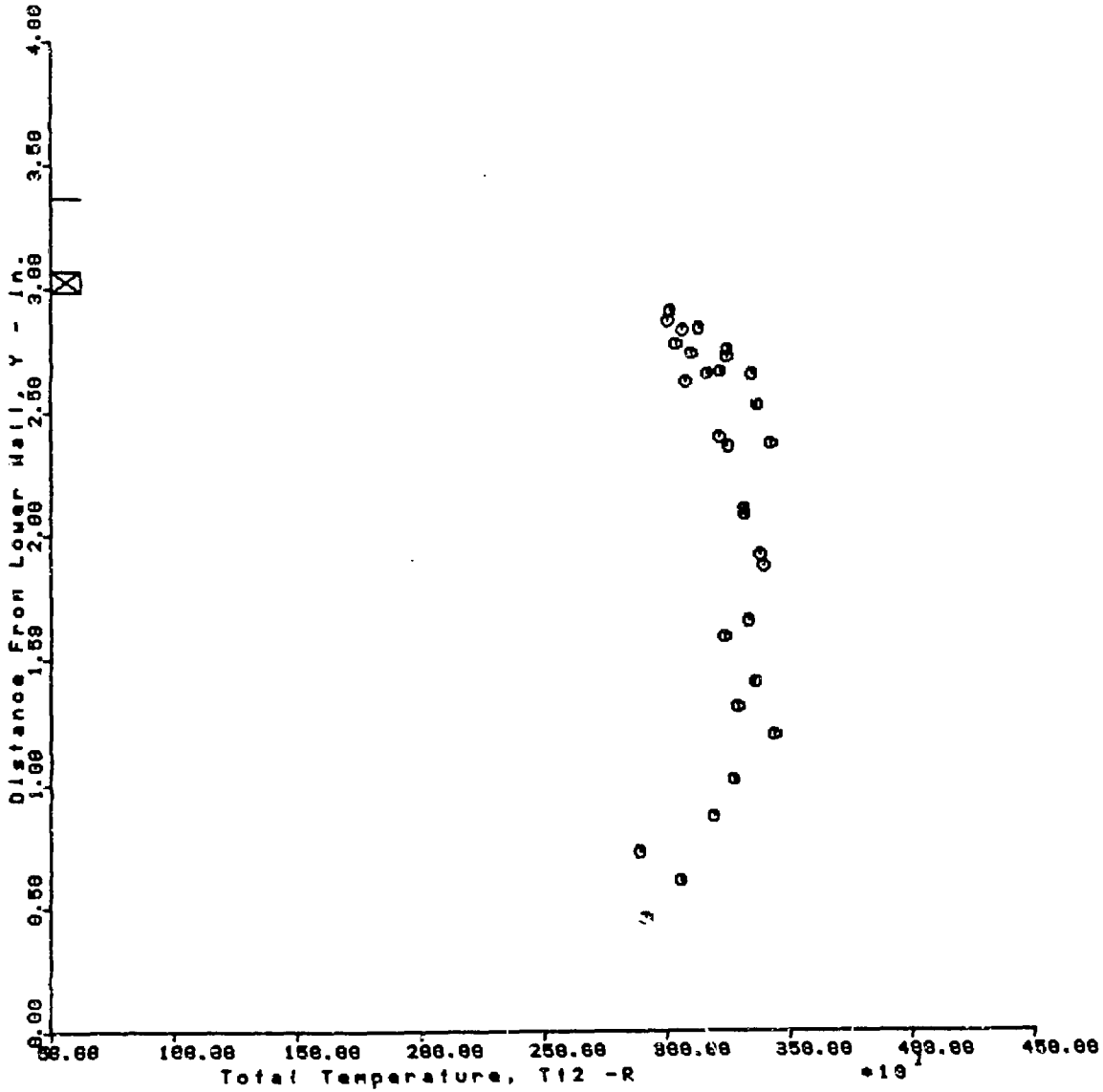

AFS TEST PROGRAM
RUN = 54 BURSTS 27 THRU 52

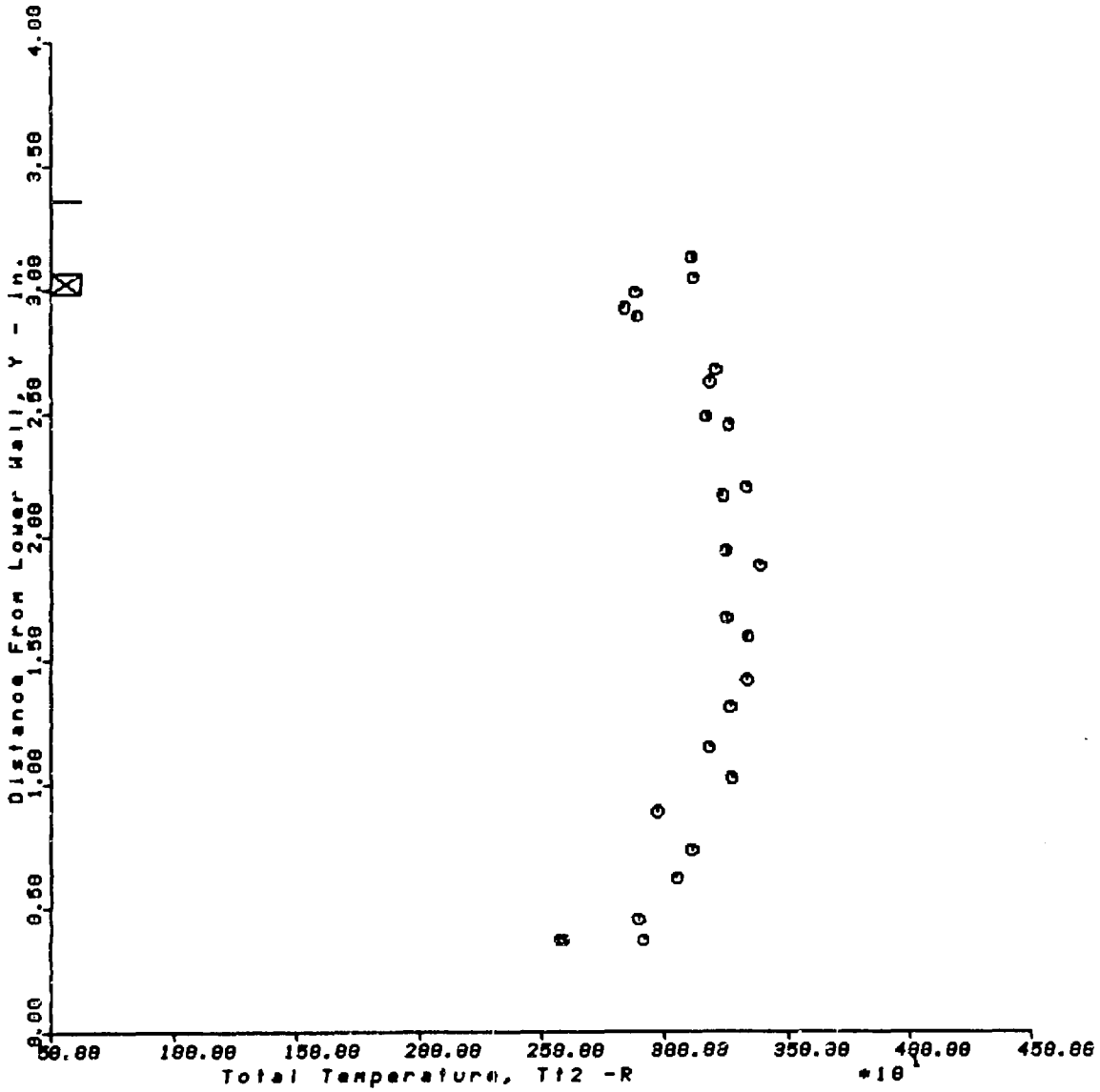

AFS TEST PROGRAM
RUN = 55 BURSTS 26 THRU 50

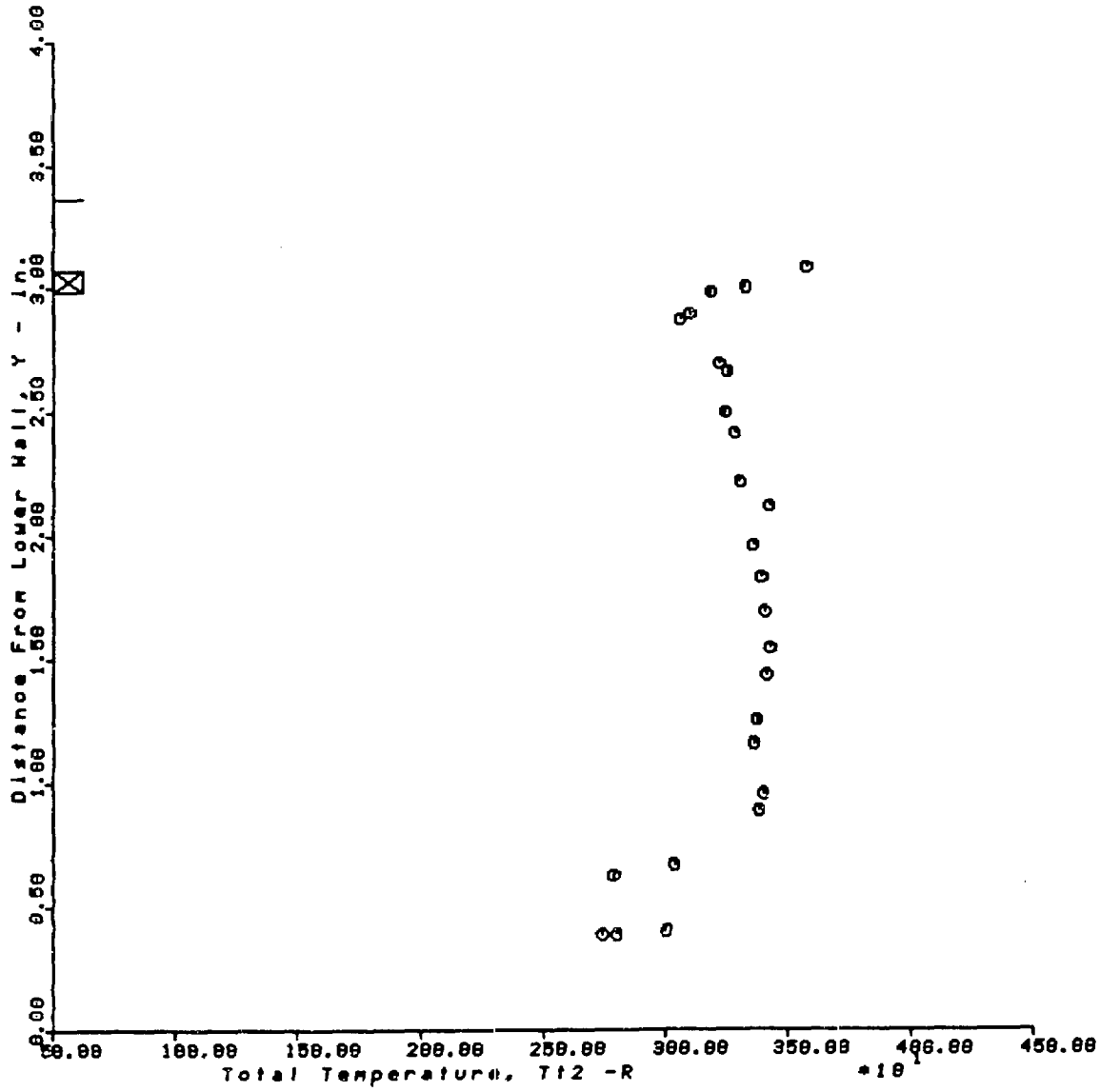

AFS TEST PROGRAM
RUN = 57 BURSTS 27 THRU 58

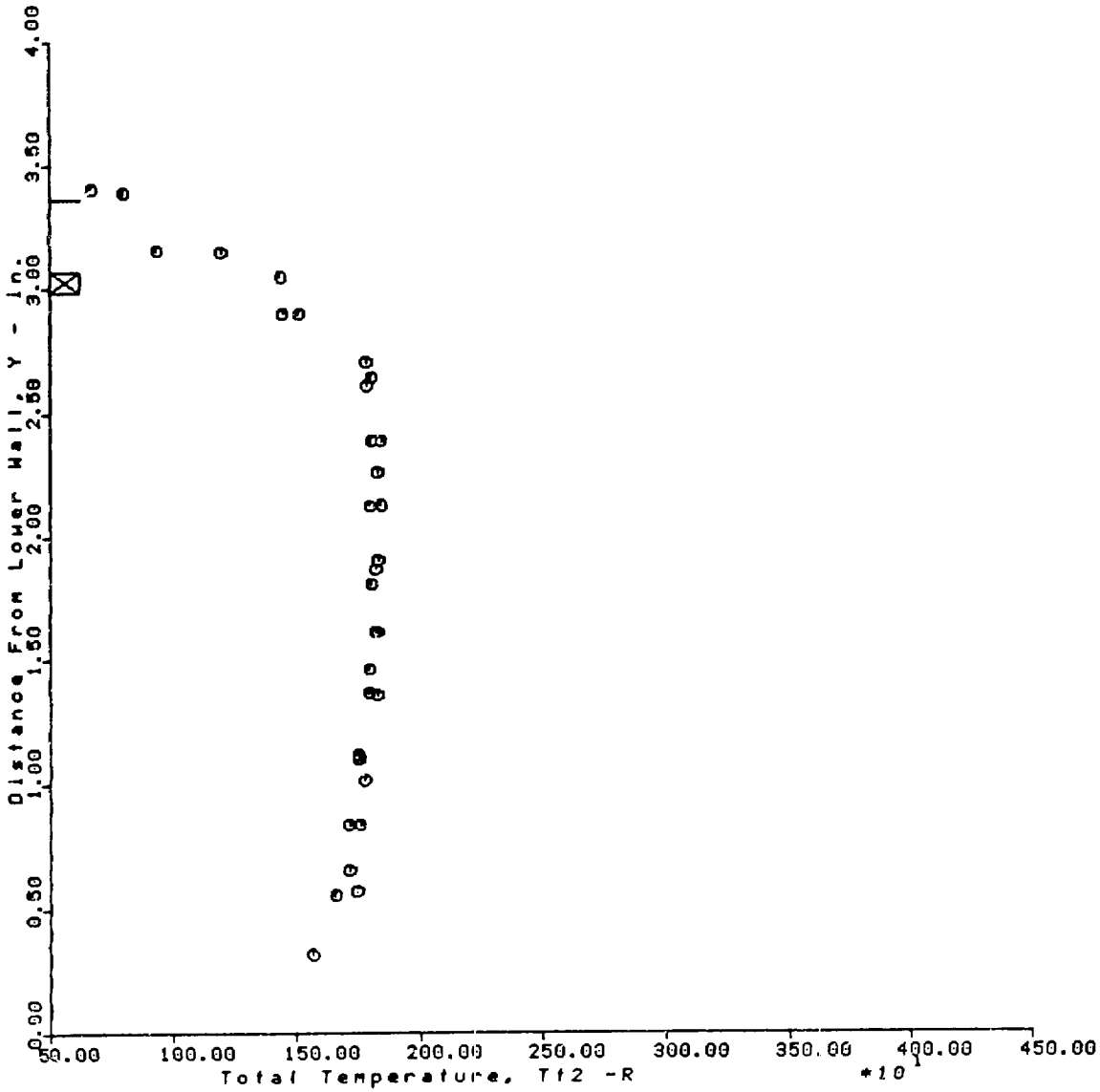

AFS TEST PROGRAM
RUN = 58 BURSTS 26 THRU 48

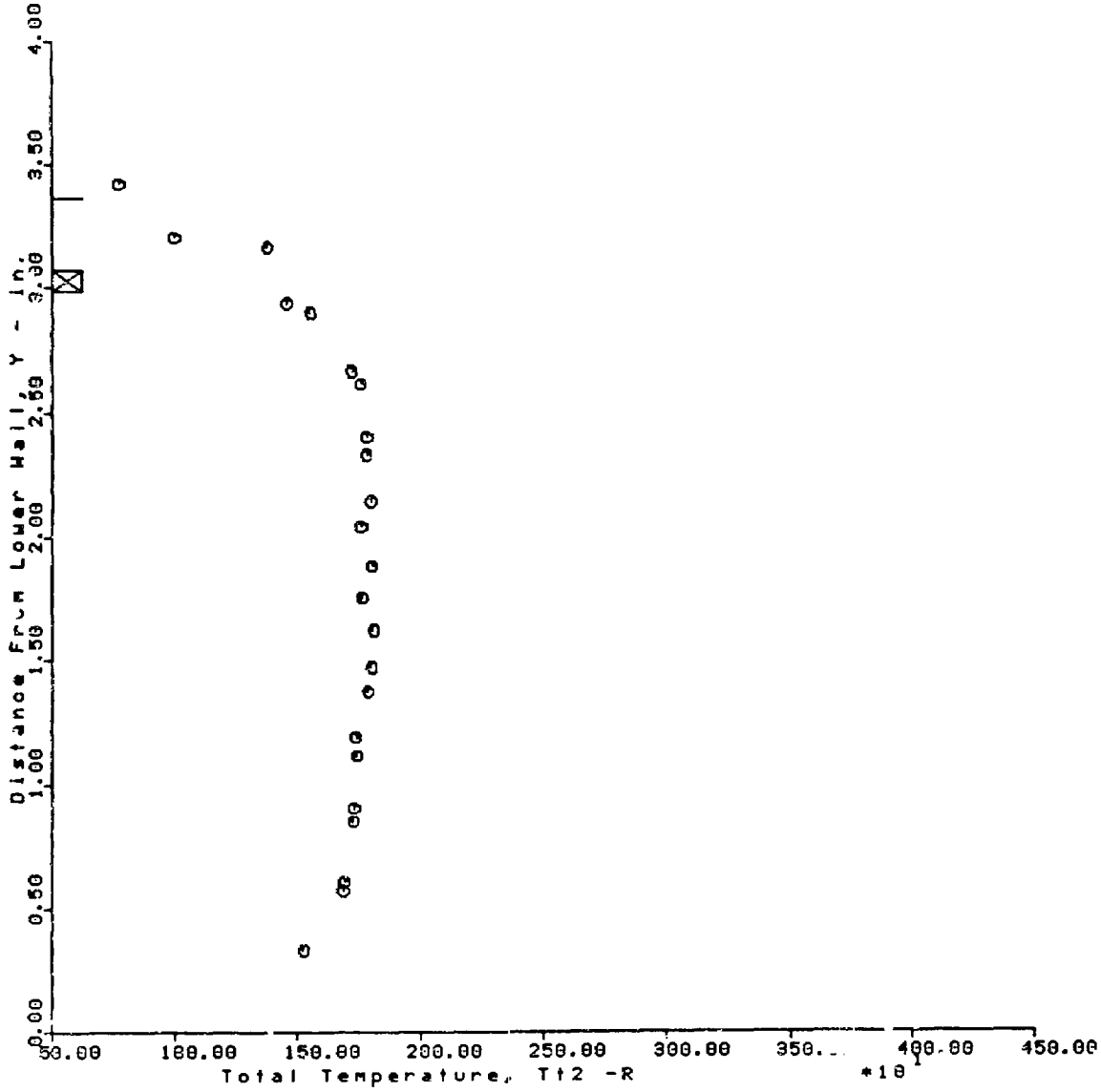

AFS TEST PROGRAM
RUN = 59 BURSTS 25 THRU 47

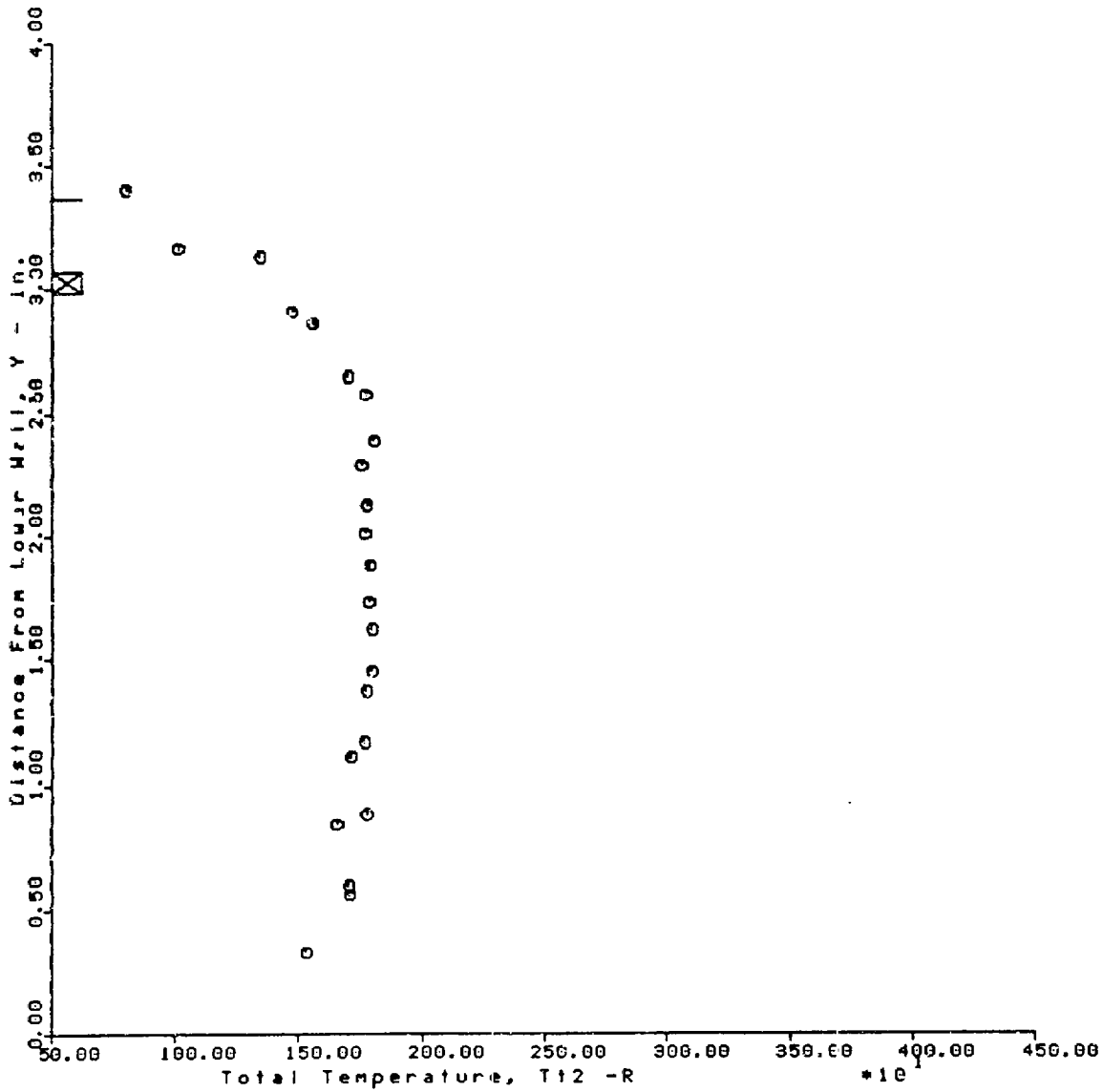

AFS TEST PROGRAM
RUN = 61 BURSTS 26 THRU 46

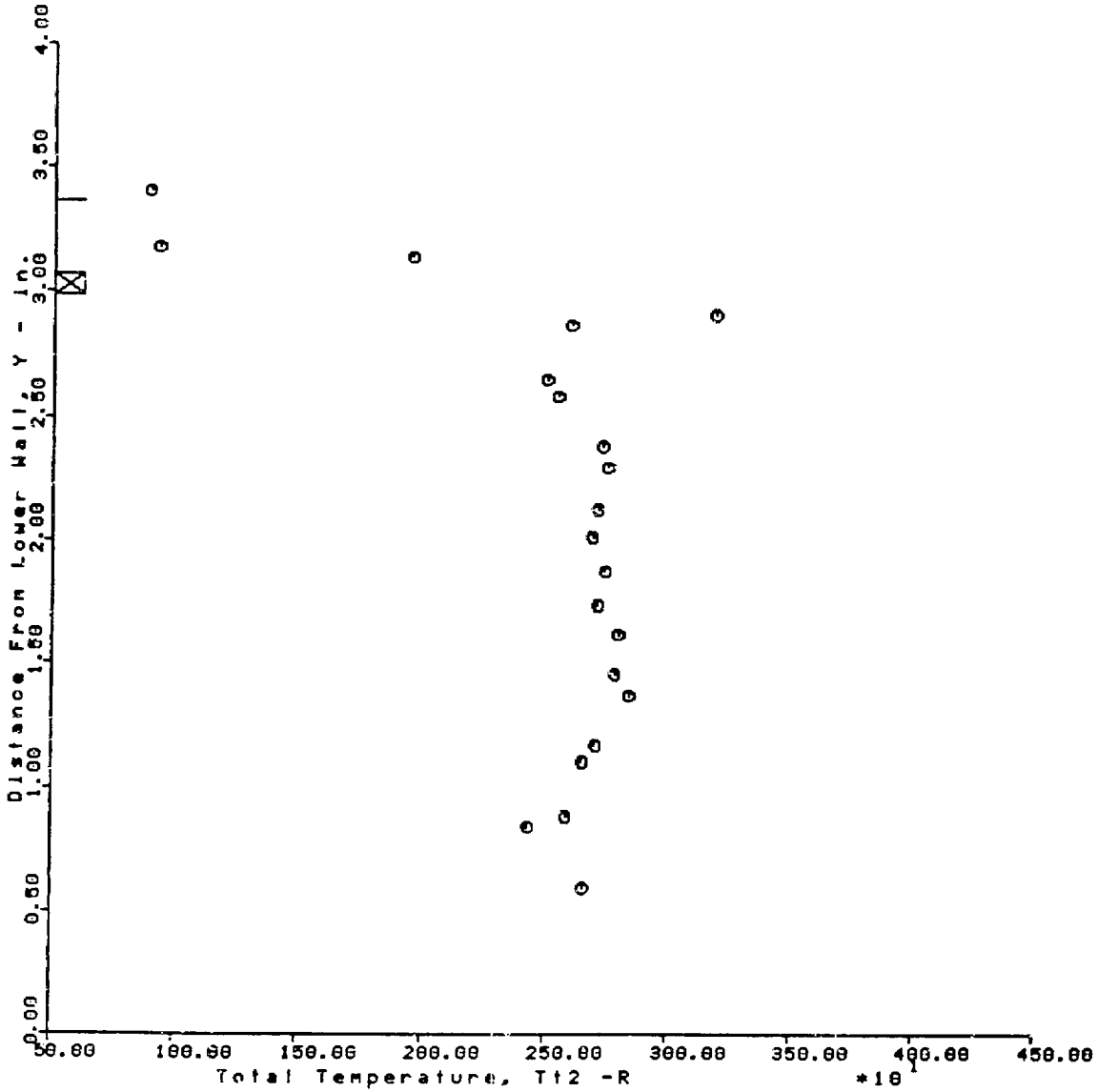

AFS TEST PROGRAM
RUN = 62 BURSTS 29 THRU 58

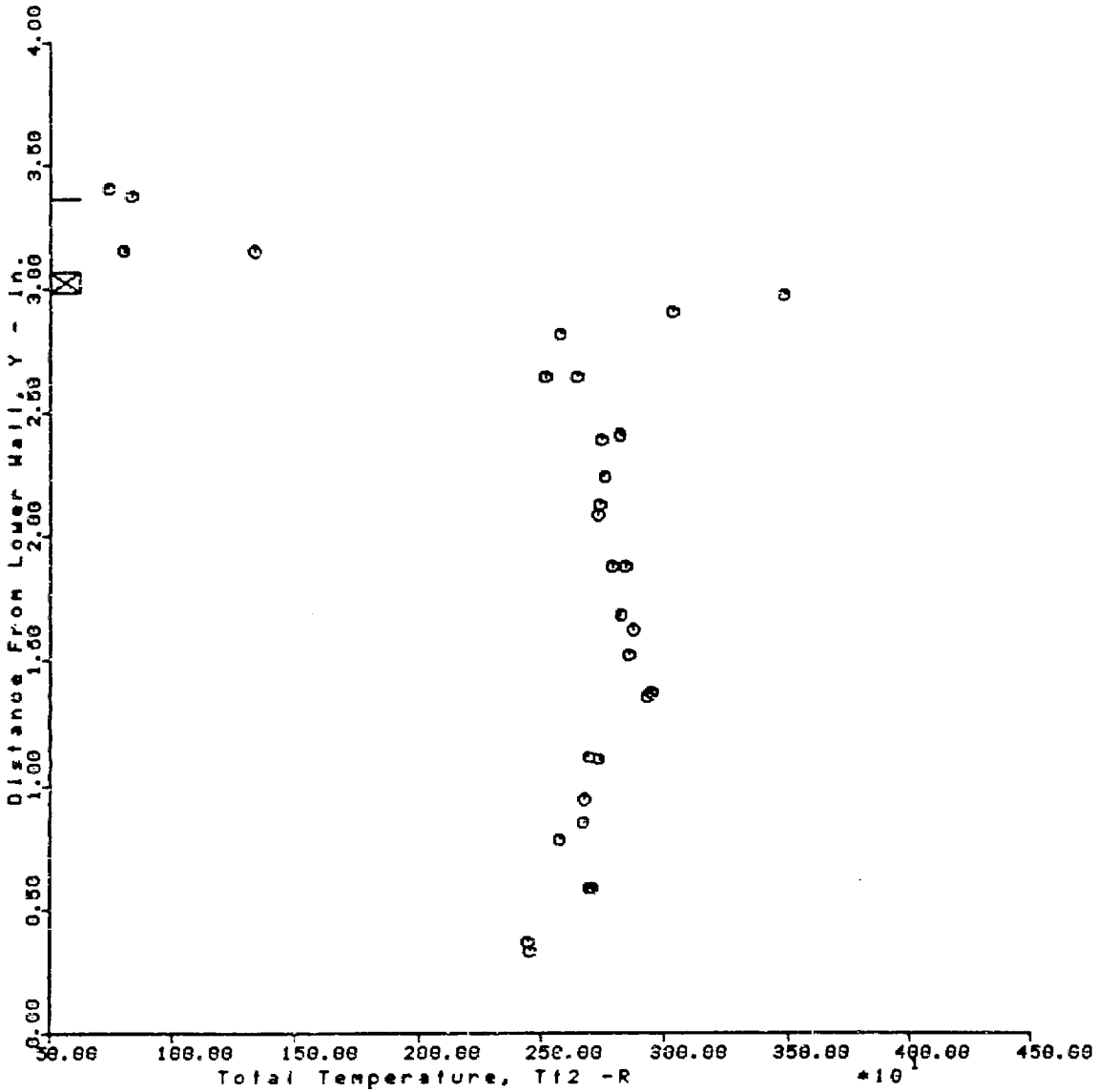

AFS TEST PROGRAM
RUN = 63 BURSTS 33 THRU 62

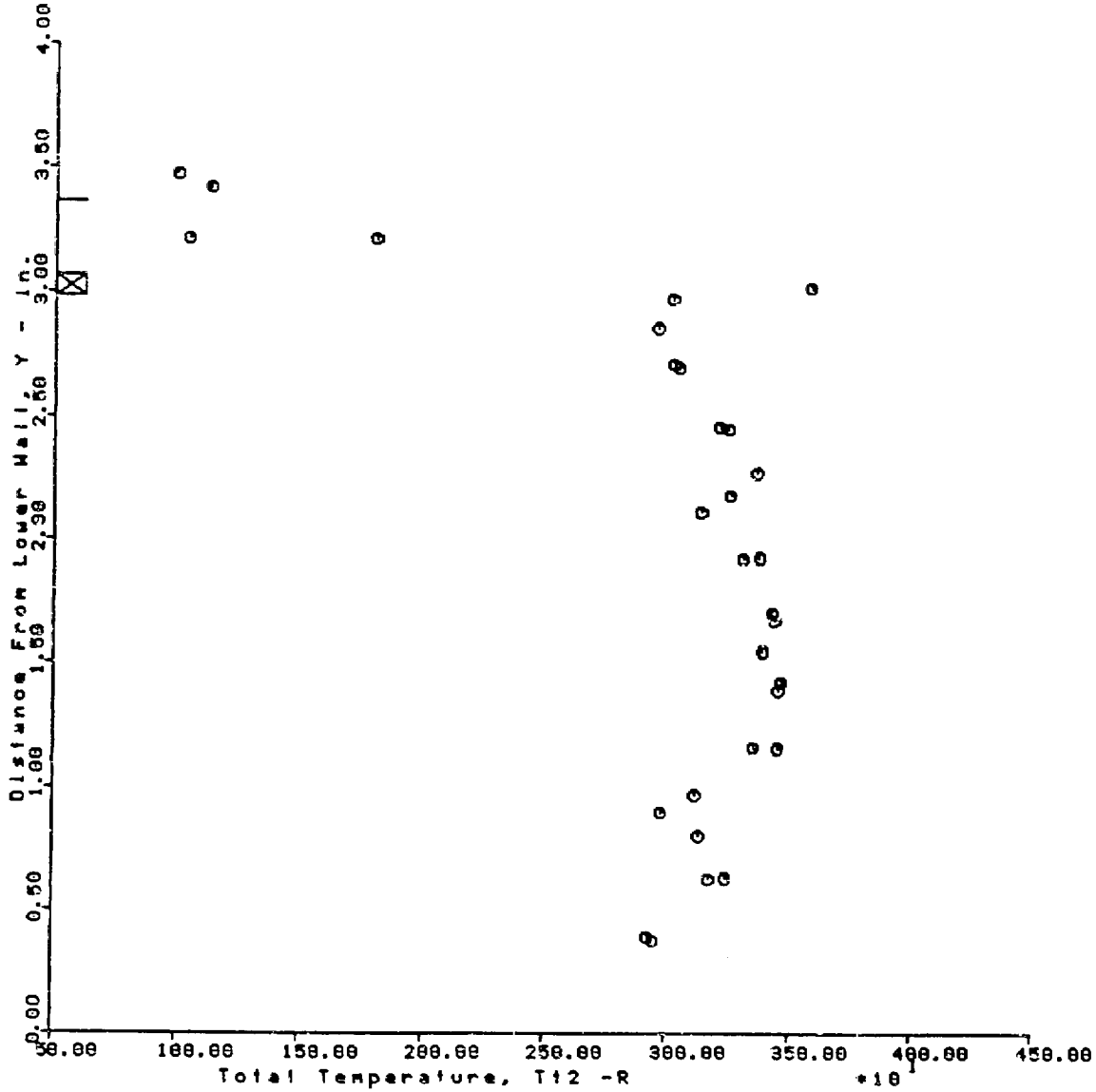

AFS TEST PROGRAM
RUN = 64 BURSTS 27 THRU 56

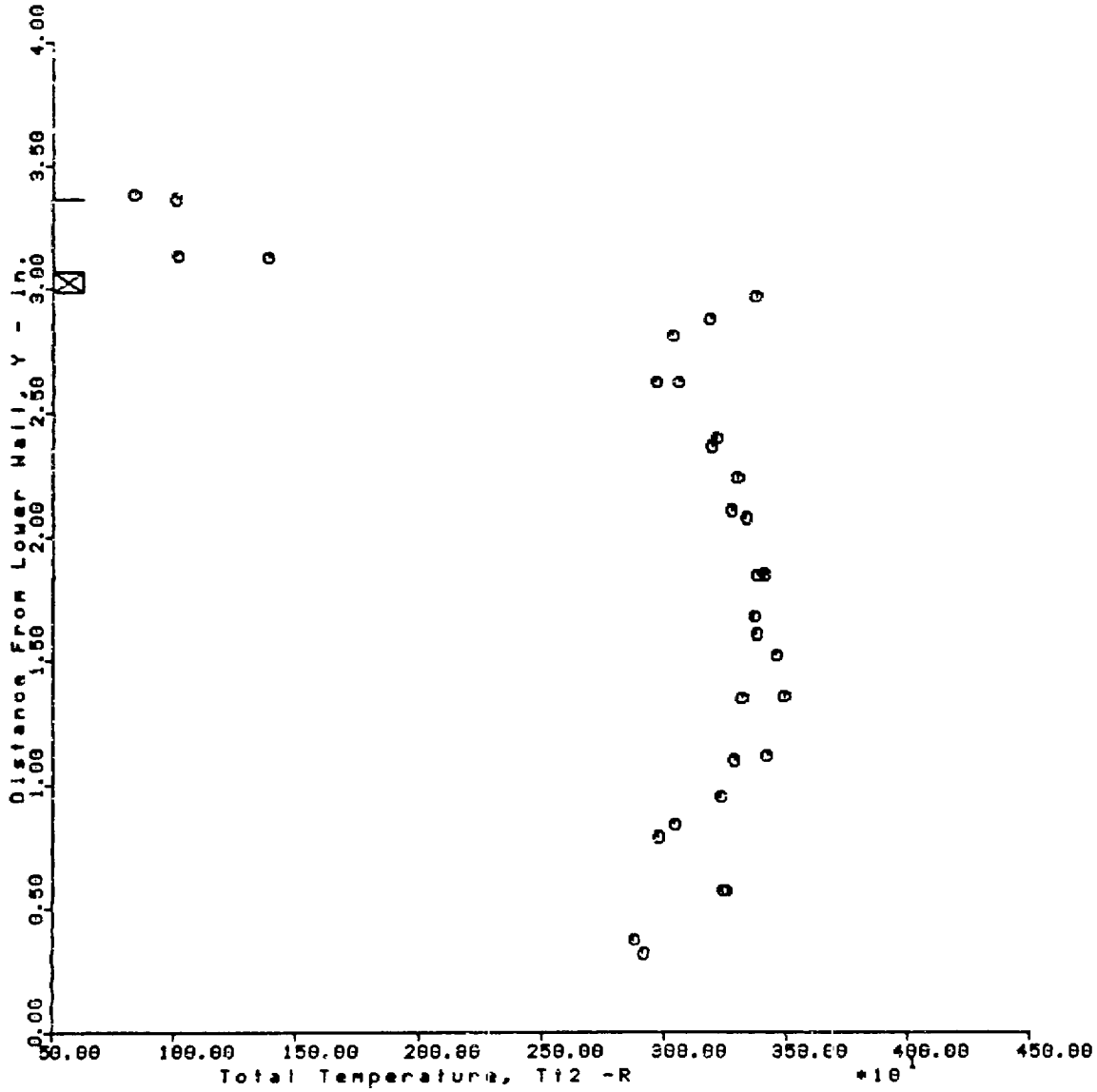

AFS TEST PROGRAM
RUN = 65 BURSTS 38 THRU 59

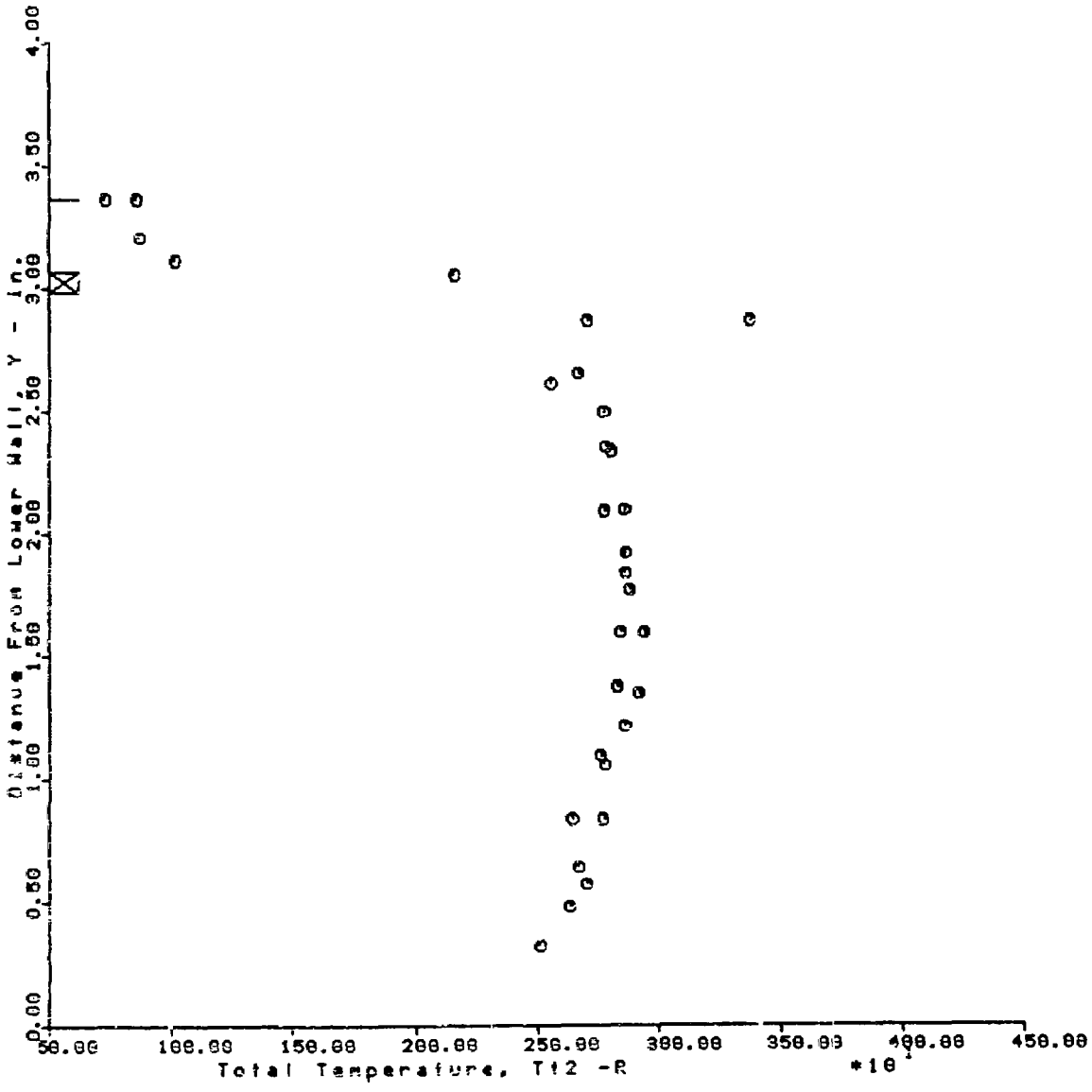

AFS TEST PROGRAM
RUN = 66 BURSTS 38 THRU 59

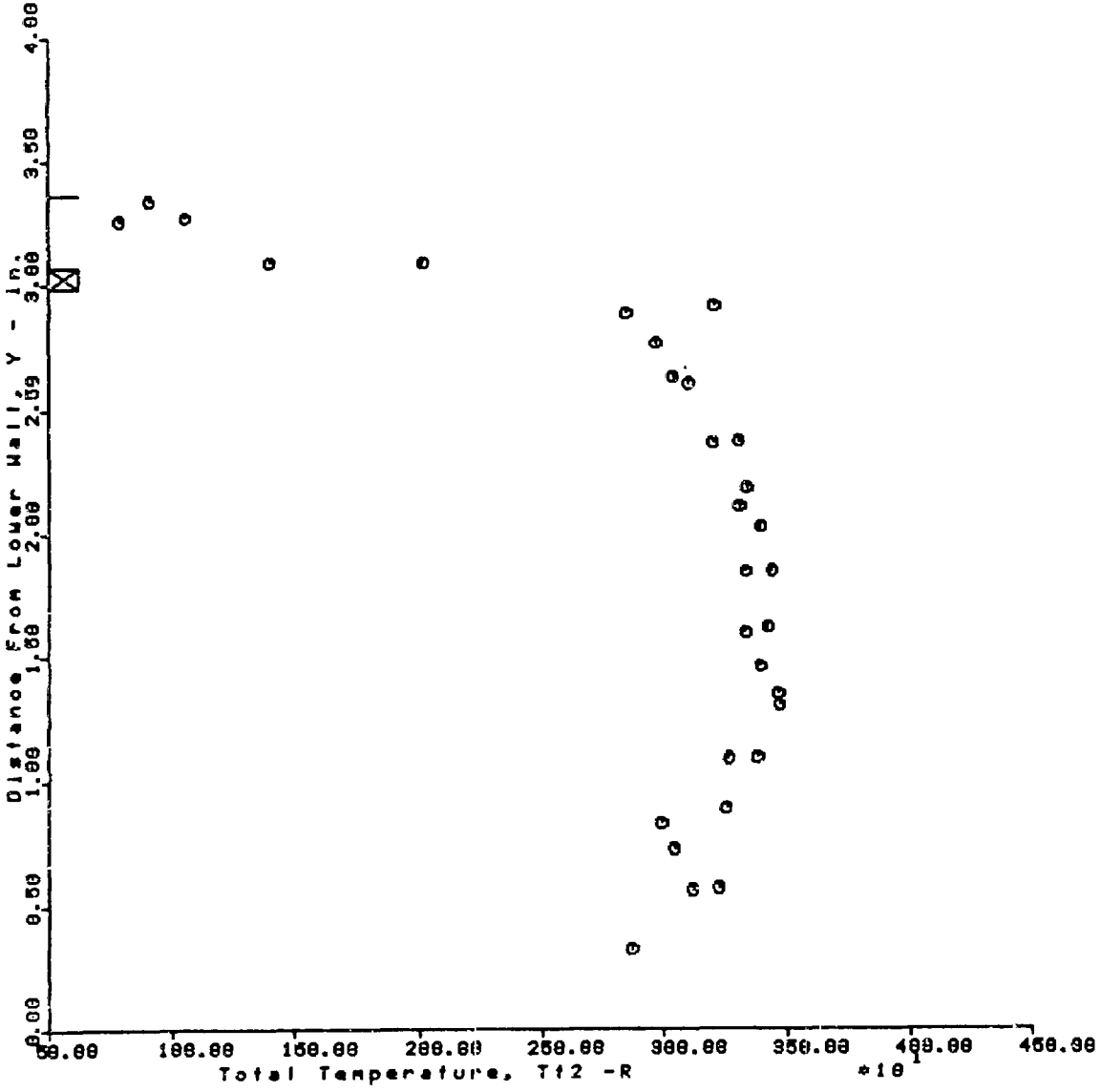

AFS TEST PROGRAM
RUN = 69 BURSTS 34 THRU 63

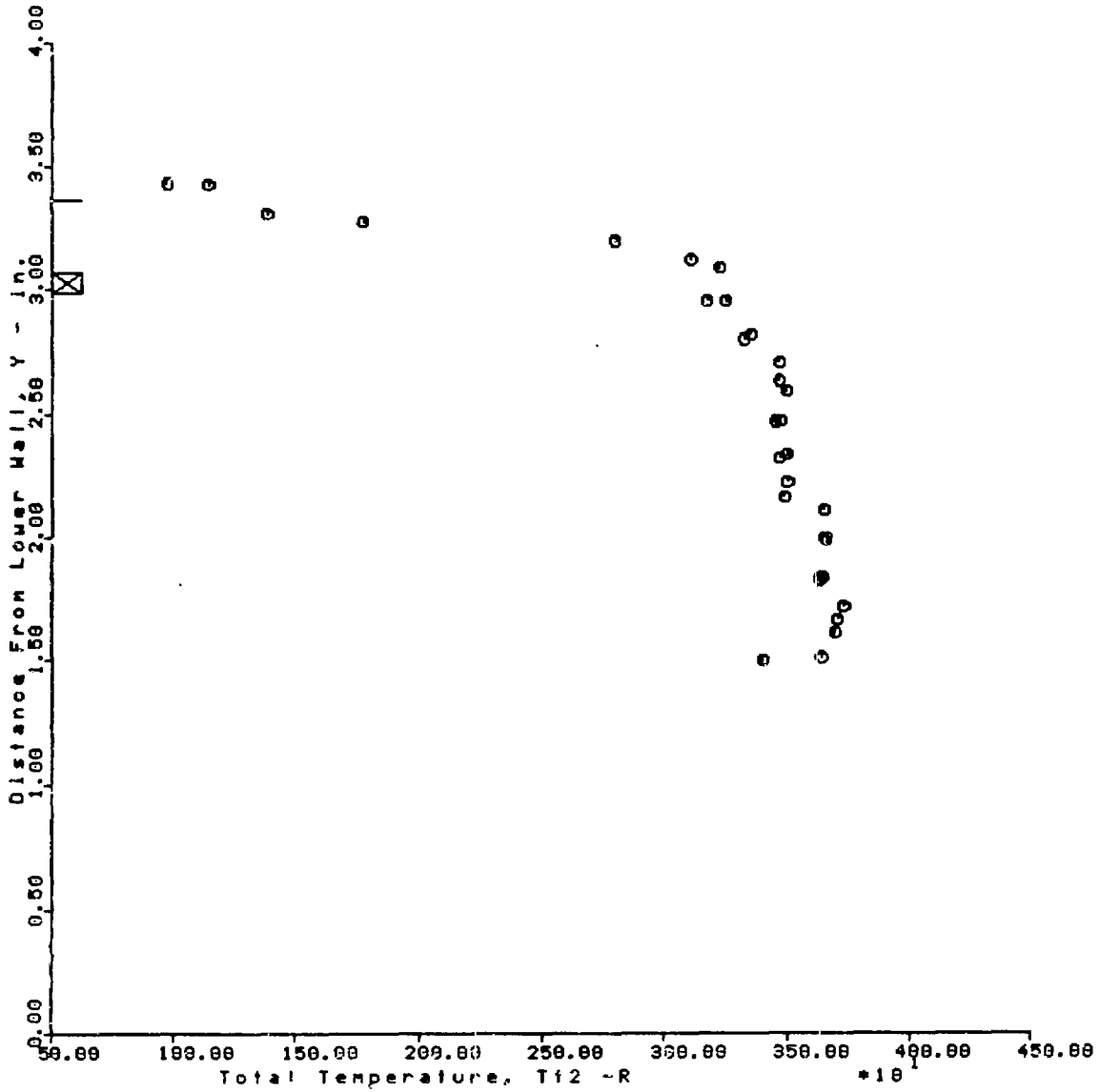

AFS TEST PROGRAM
RUN = 70 BURSTS 22 THRU 51

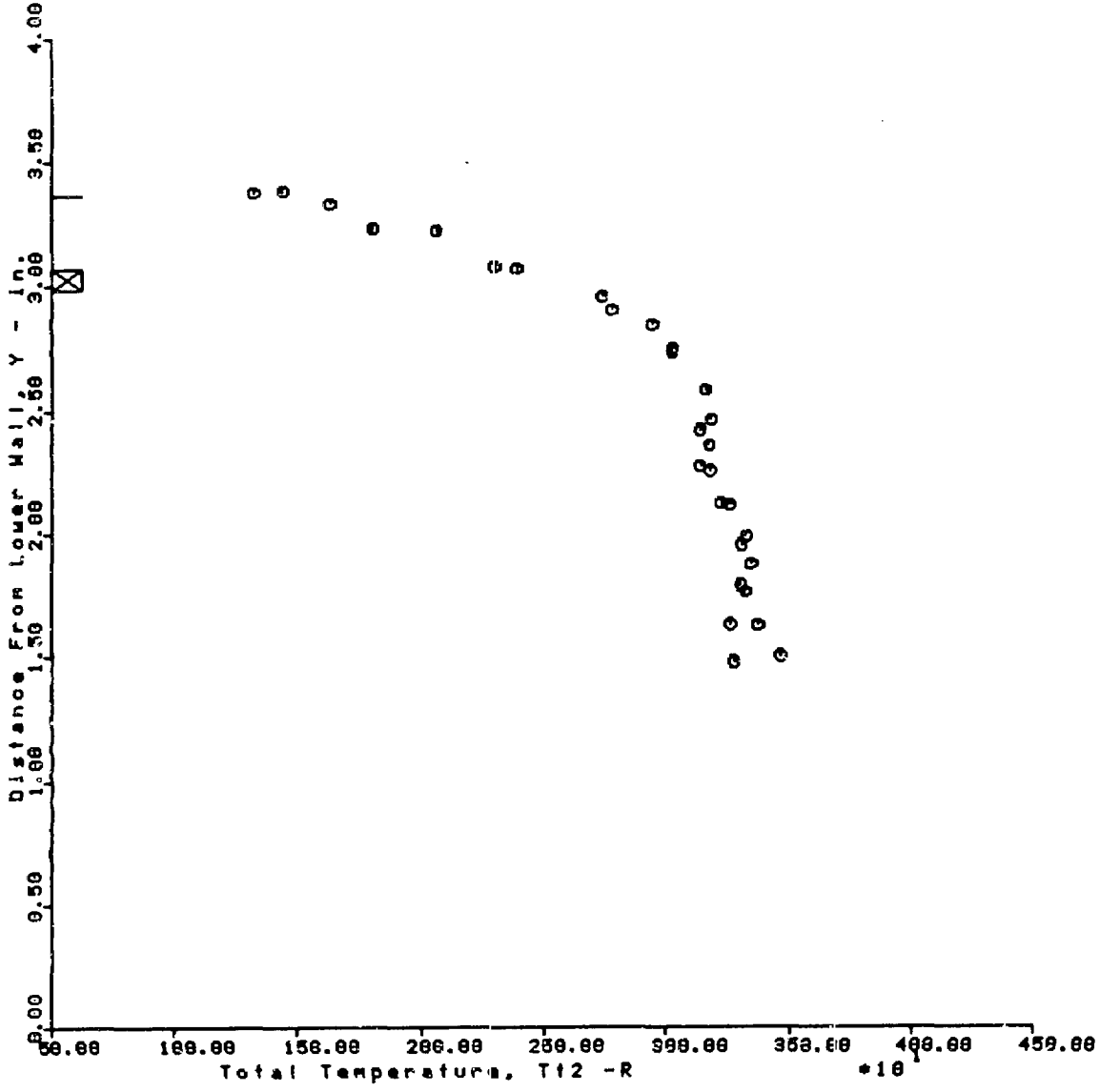

AFS TEST PROGRAM
RUN = 71 BURSTS 34 THRU 63

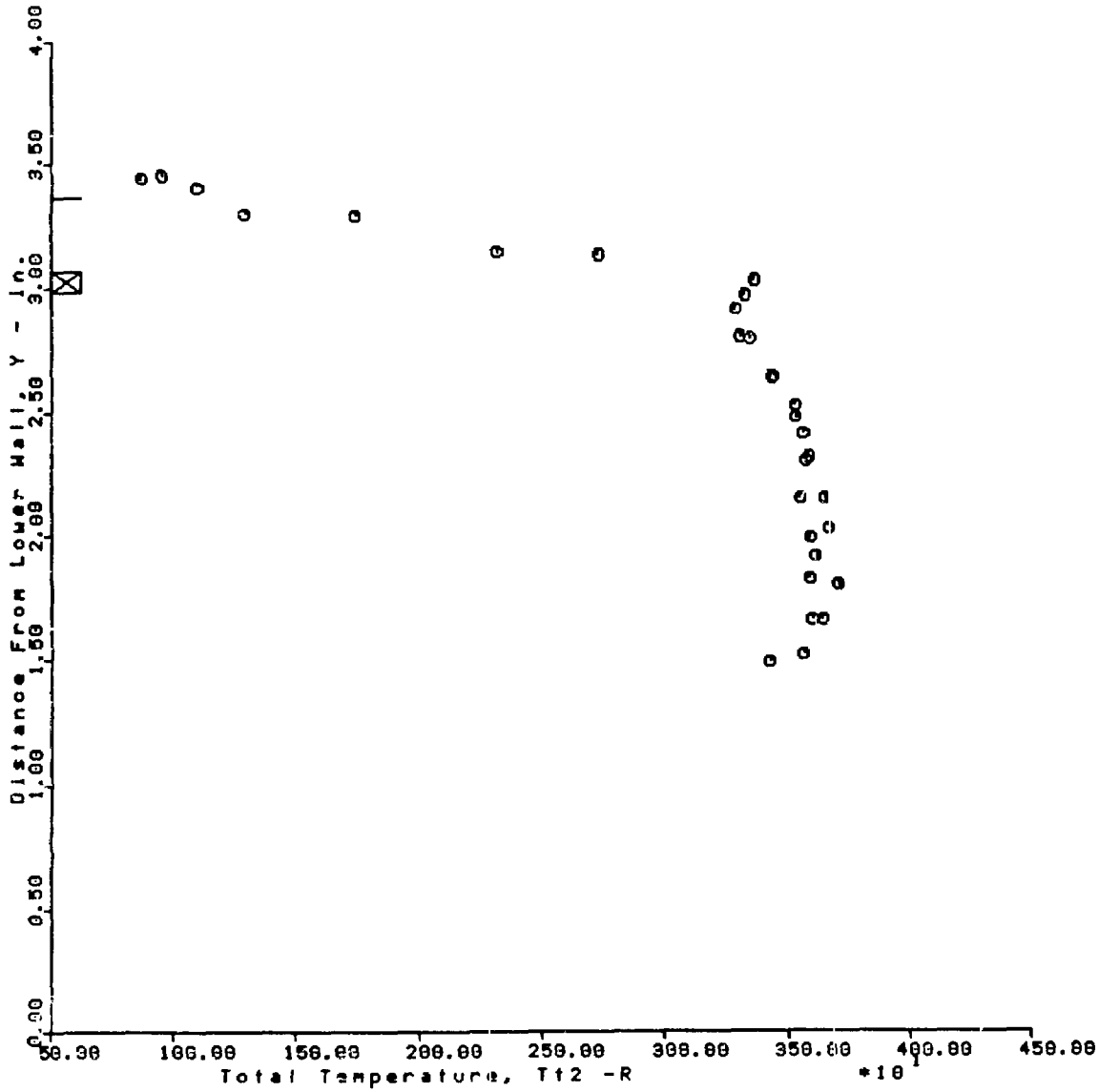

AFS TEST PROGRAM
RUN = 72 BURSTS 33 THRU 62

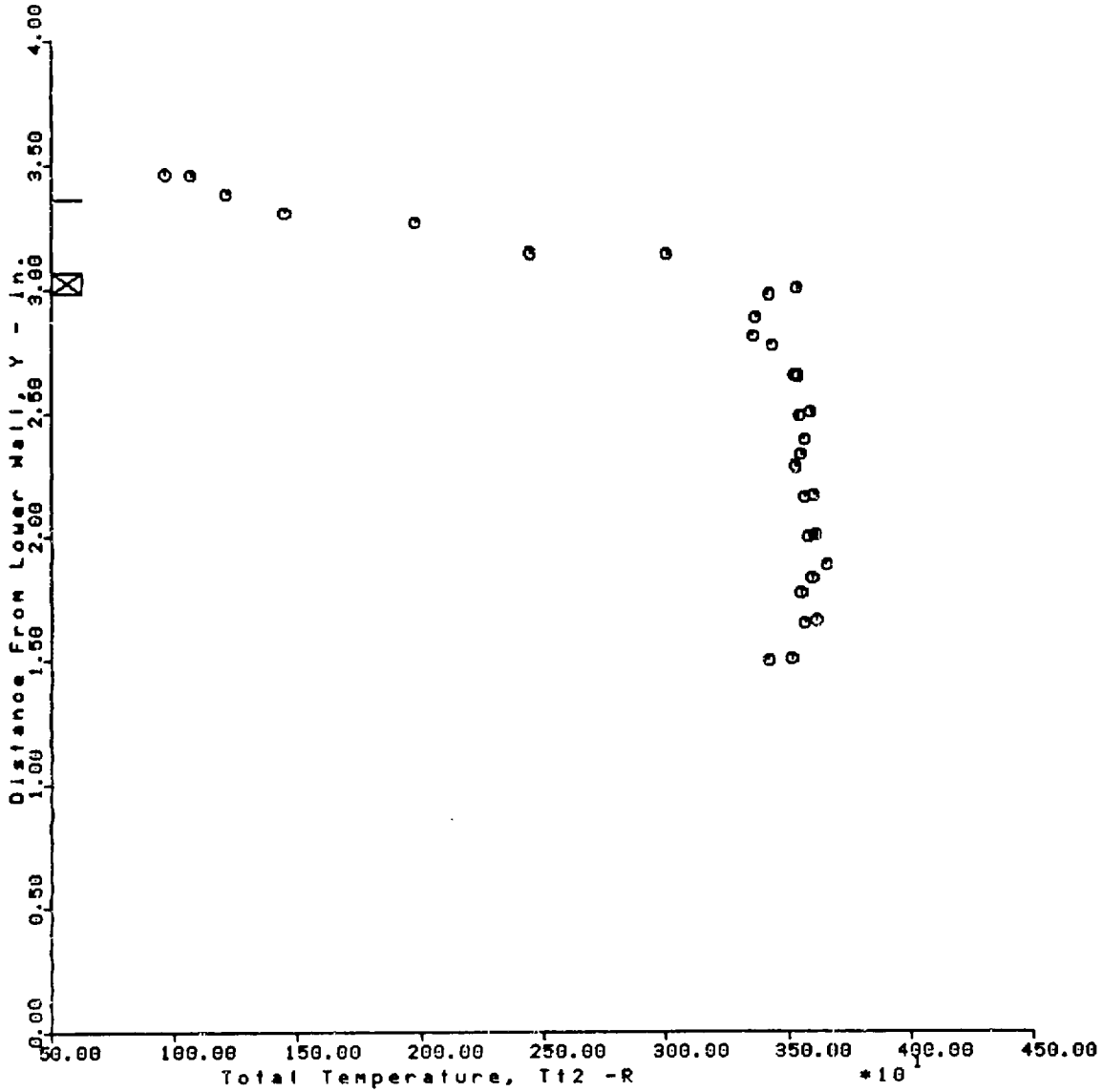

AFS TEST PROGRAM
RUN = 74 BURSTS 34 THRU 63

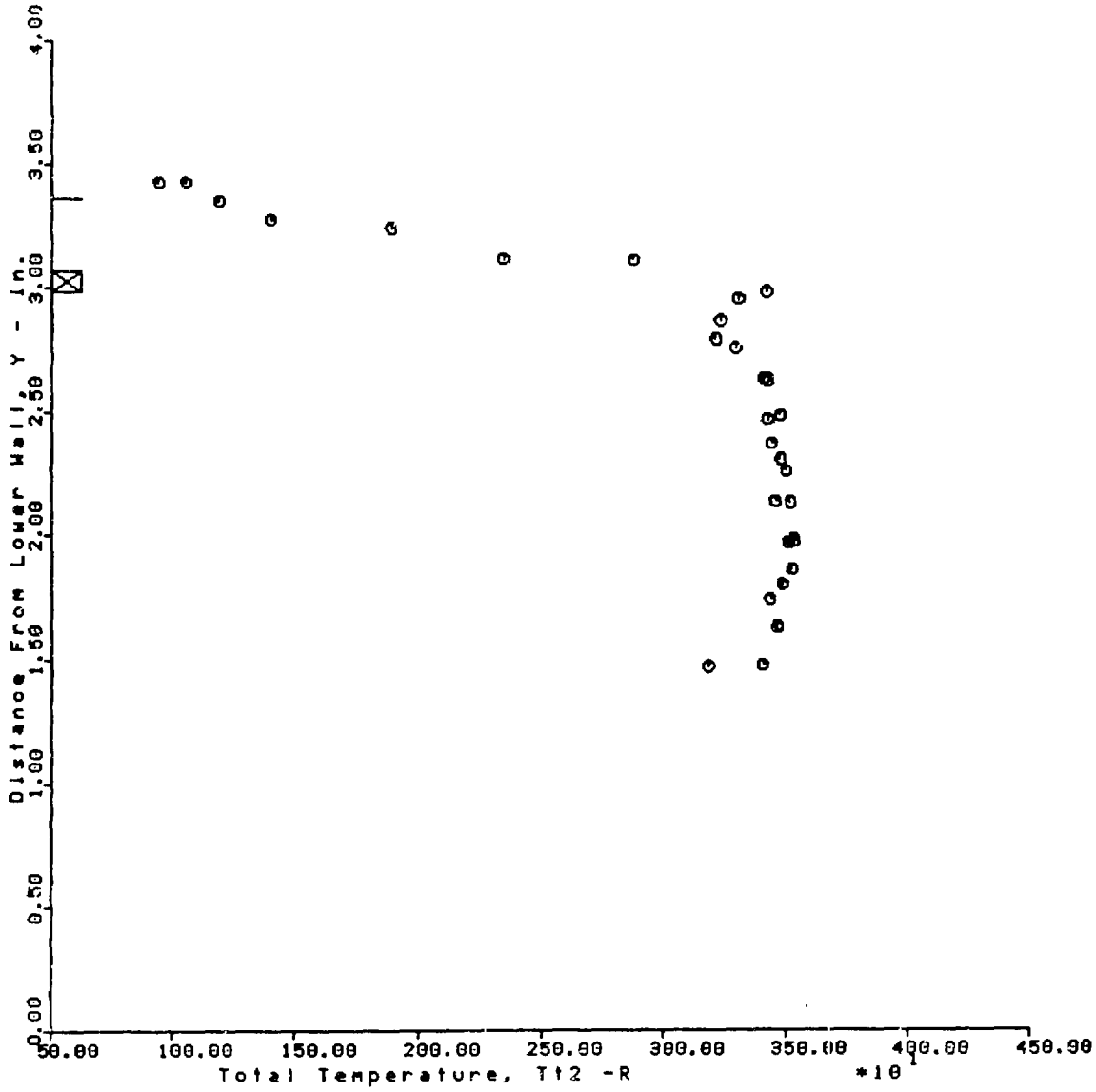

AFS TEST PROGRAM
RUN = 77 BURSTS 28 THRU 60

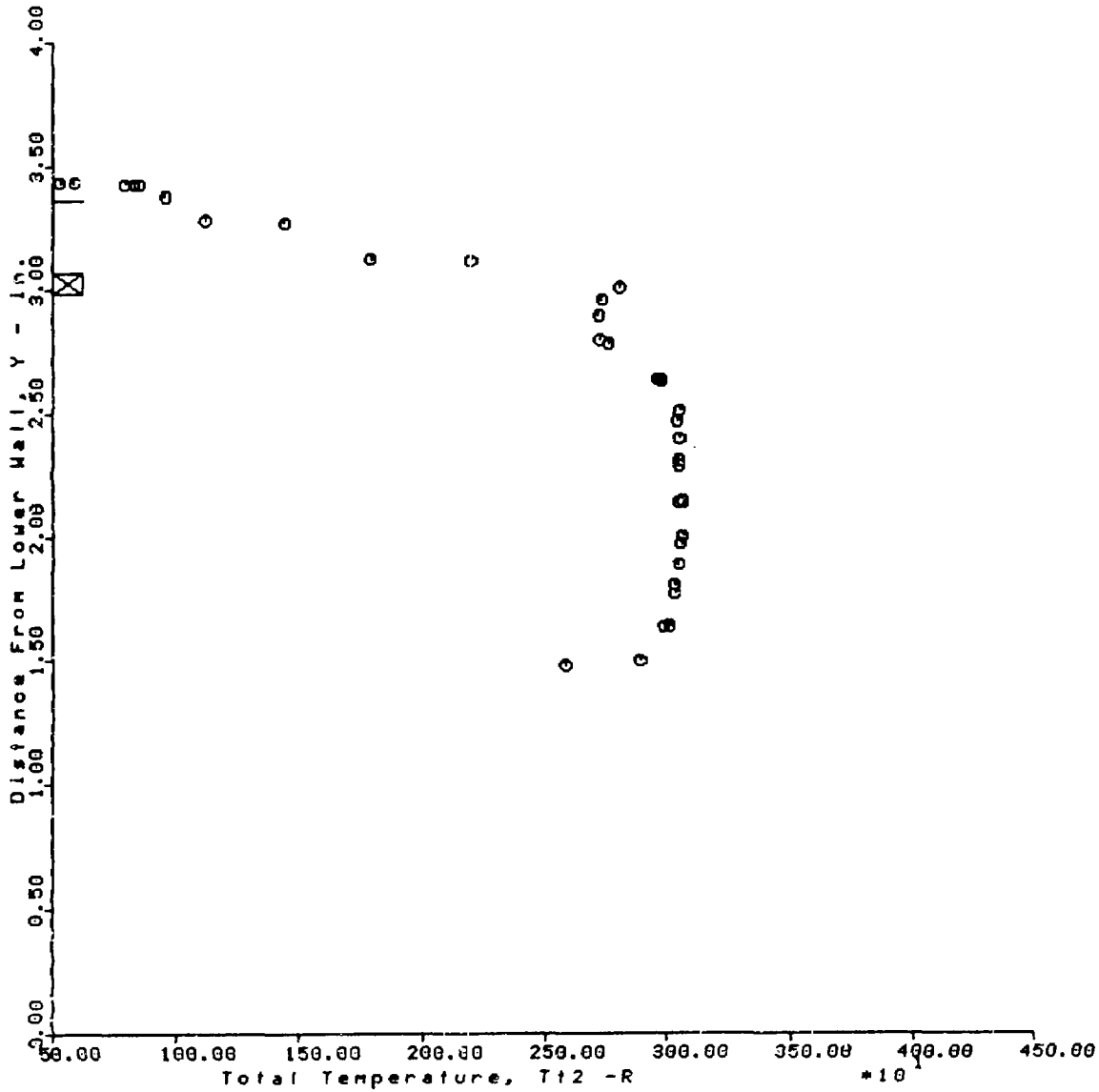

AFS TEST PROGRAM
RUN = 78 BURSTS 31 THRU 45

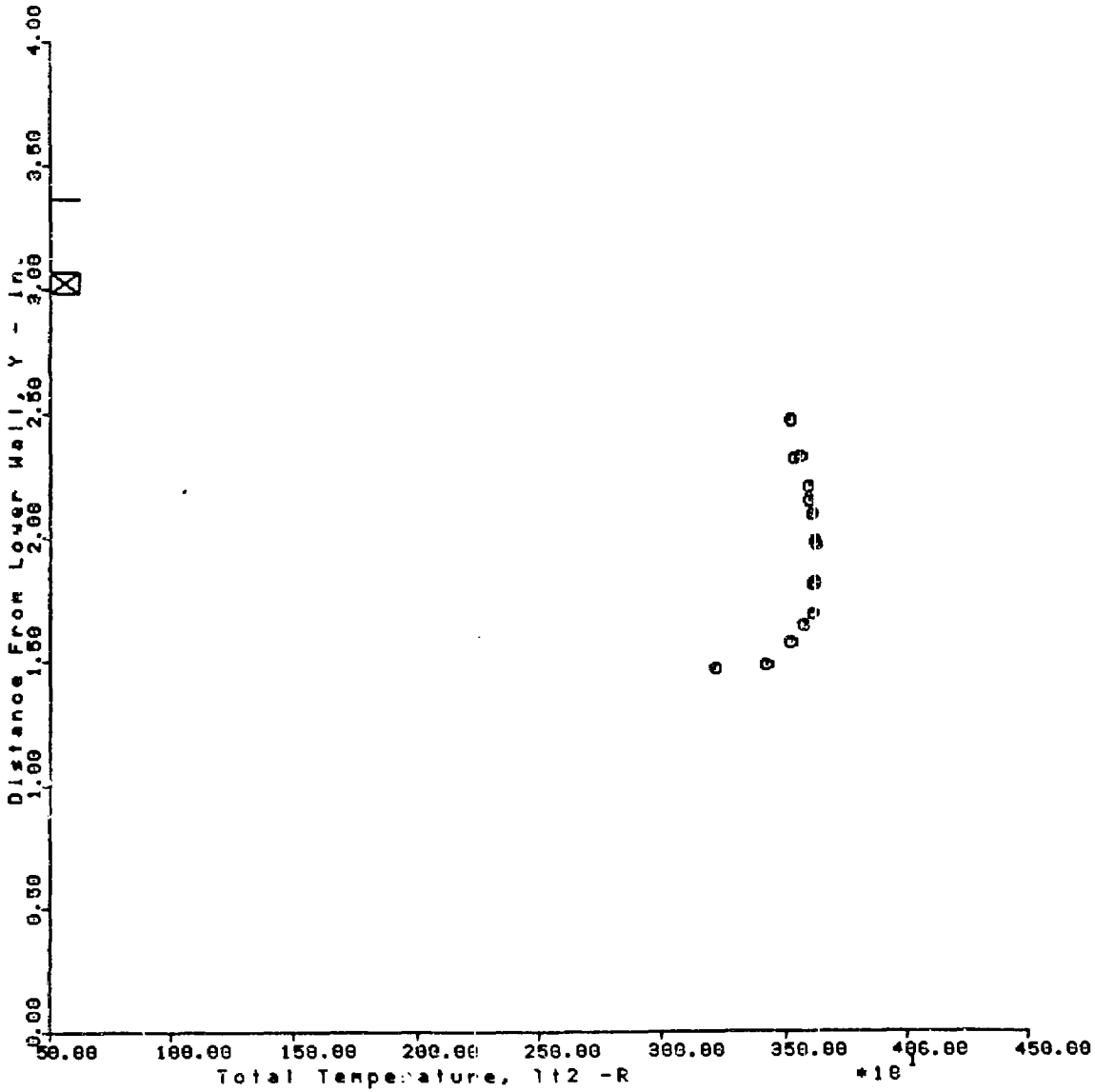

AFS TEST PROGRAM
RUN = 81 BURSTS 38 THRU 59

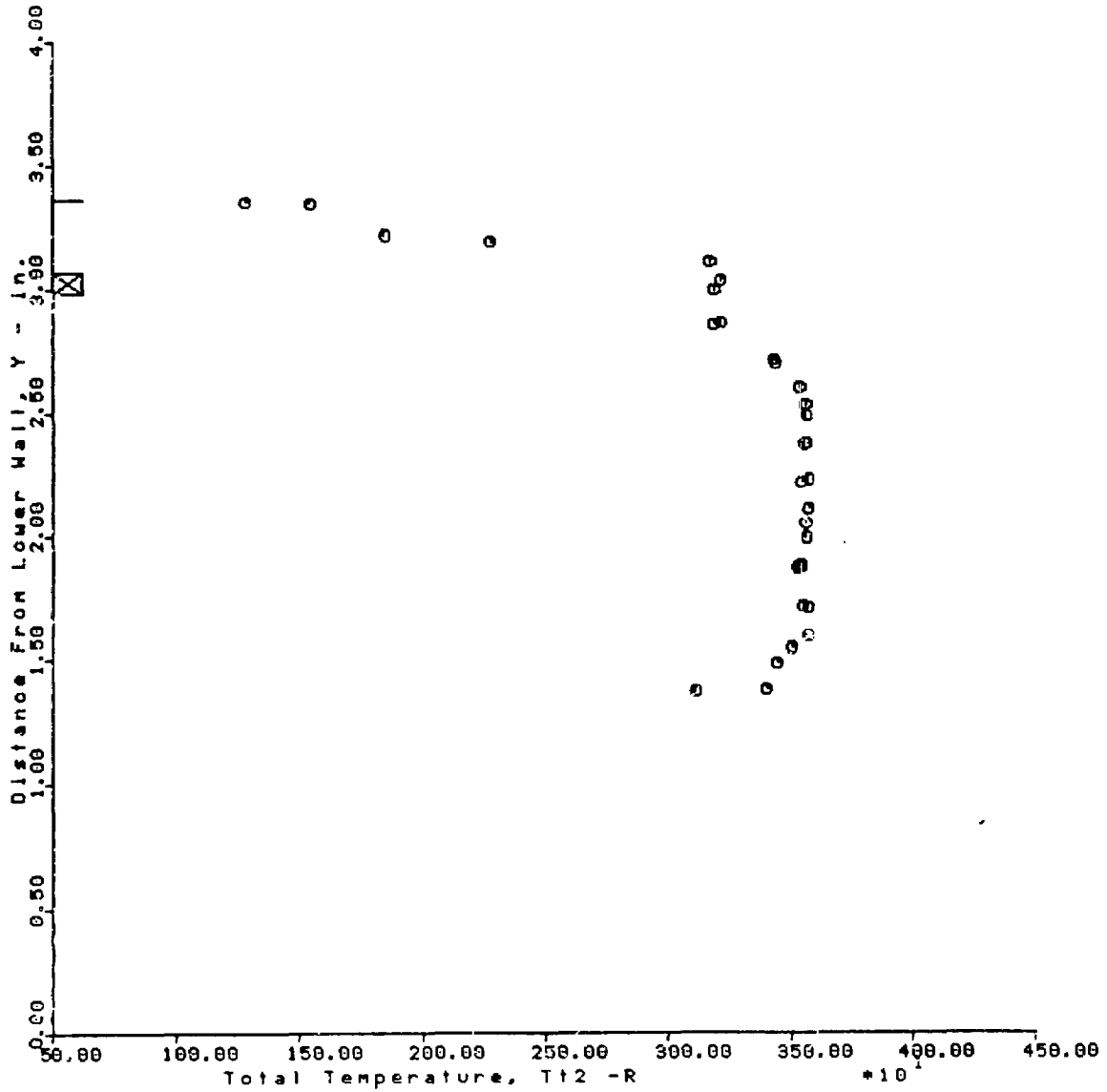

AFS TEST PROGRAM
RUN = 82 BURSTS 38 THRU 58

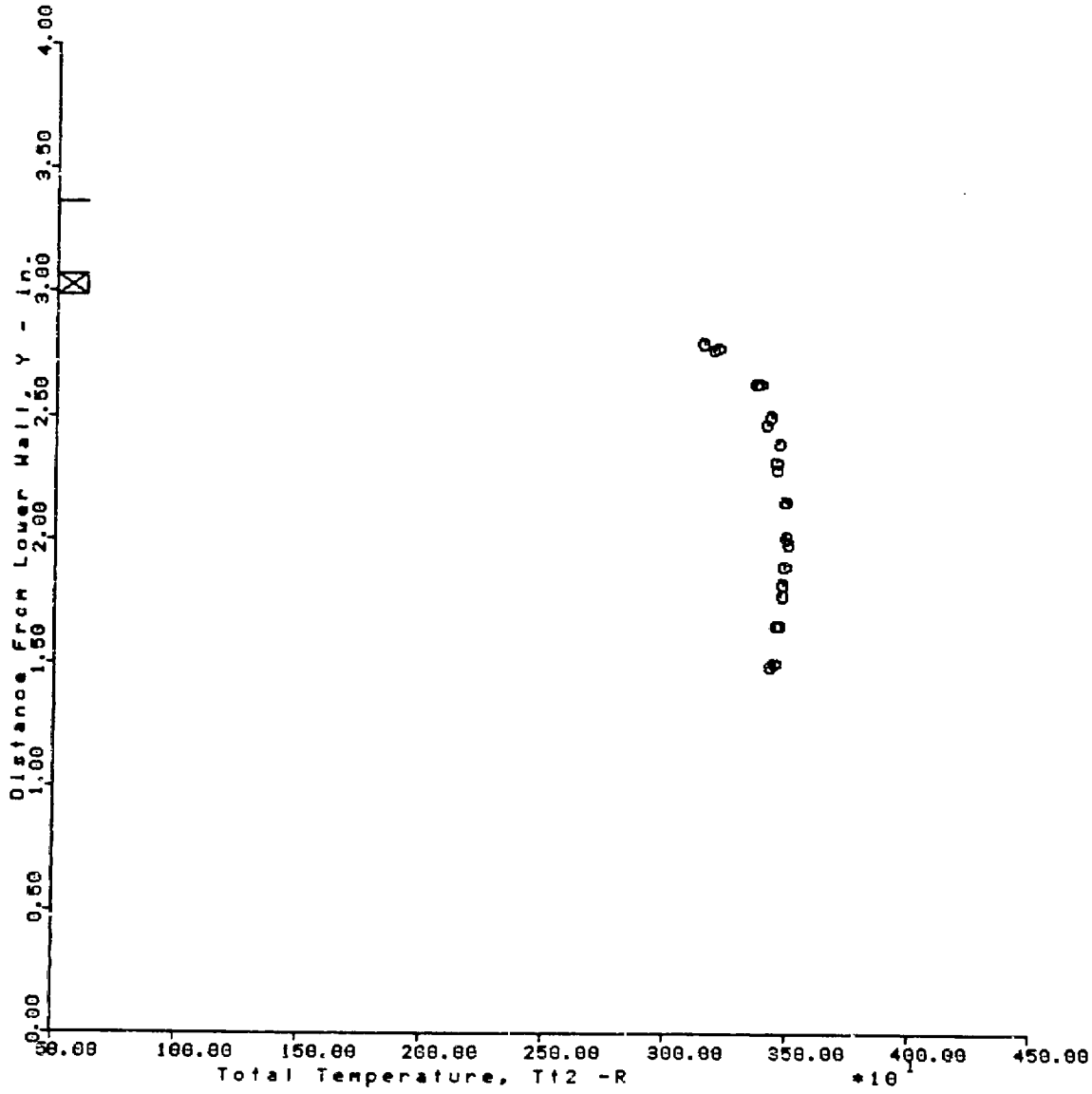

AFS TEST PROGRAM
RUN = 64 BURSTS 30 THRU 59

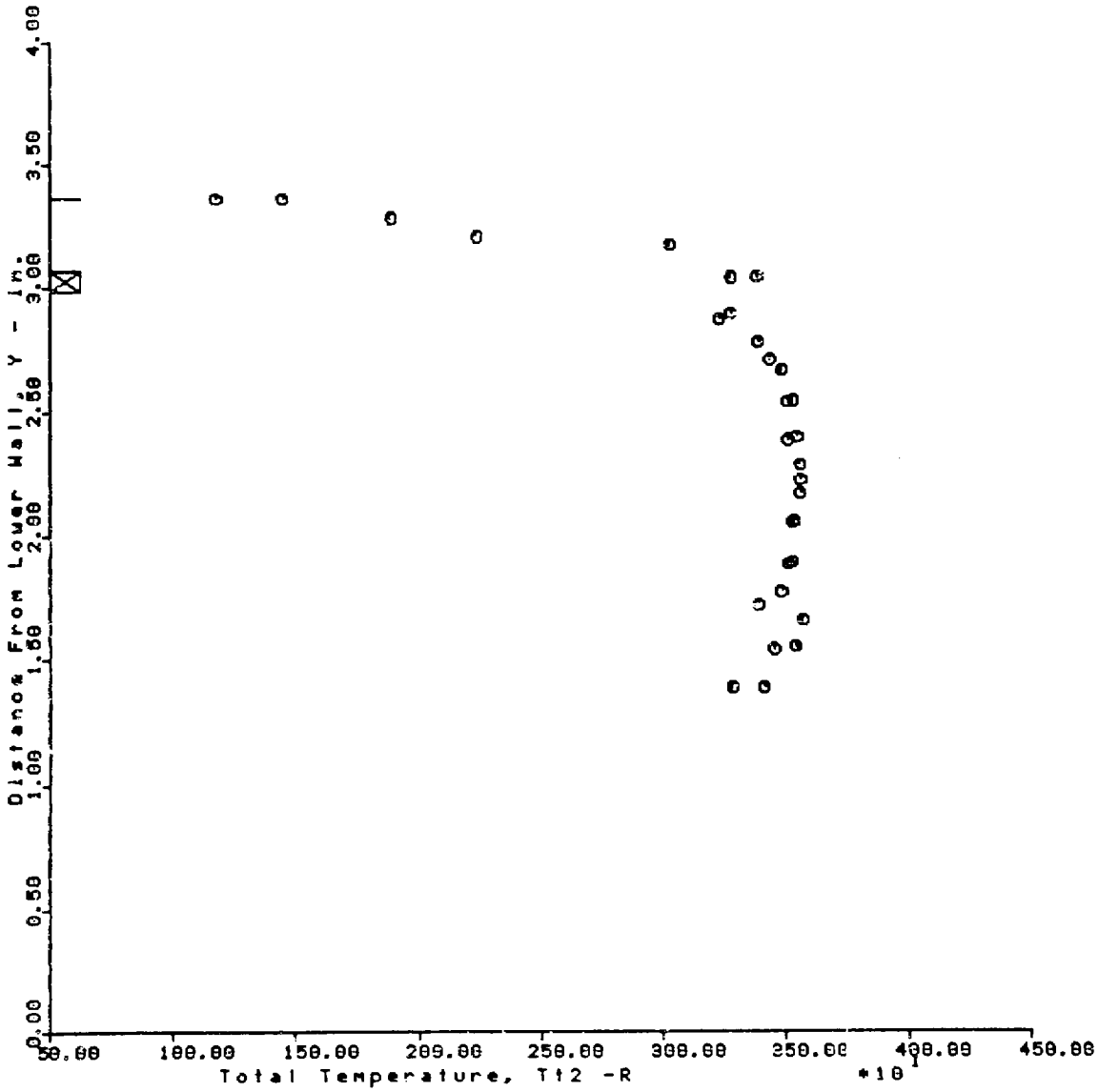

AFS TEST PROGRAM
RUN = 88 BURSTS 47 THRU 64

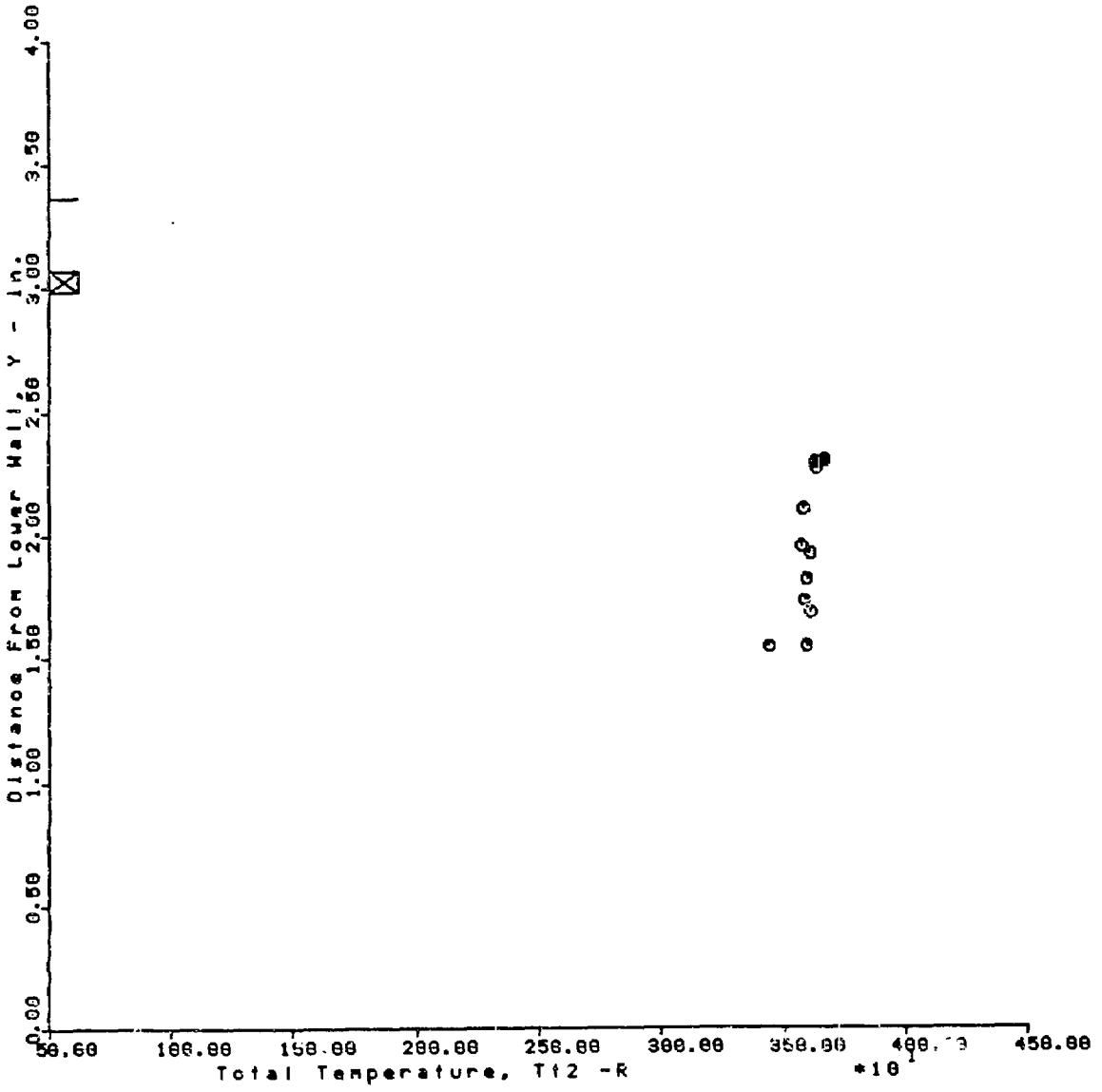

AFS TEST PROGRAM
RUN = 89 BURSTS 54 THRU 64

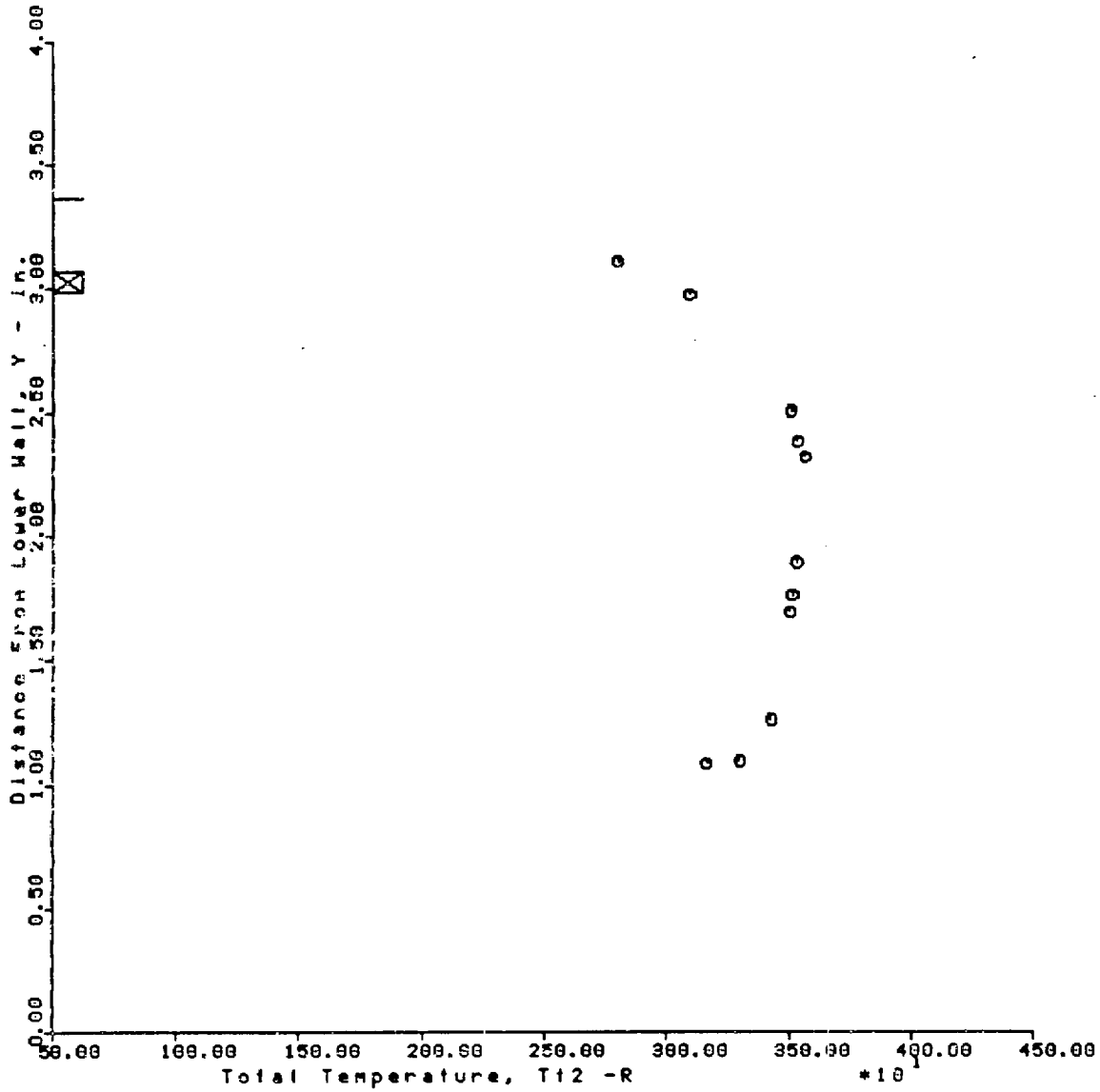

AFS TEST PROGRAM
RUN = 90 BURSTS 29 THRU 45

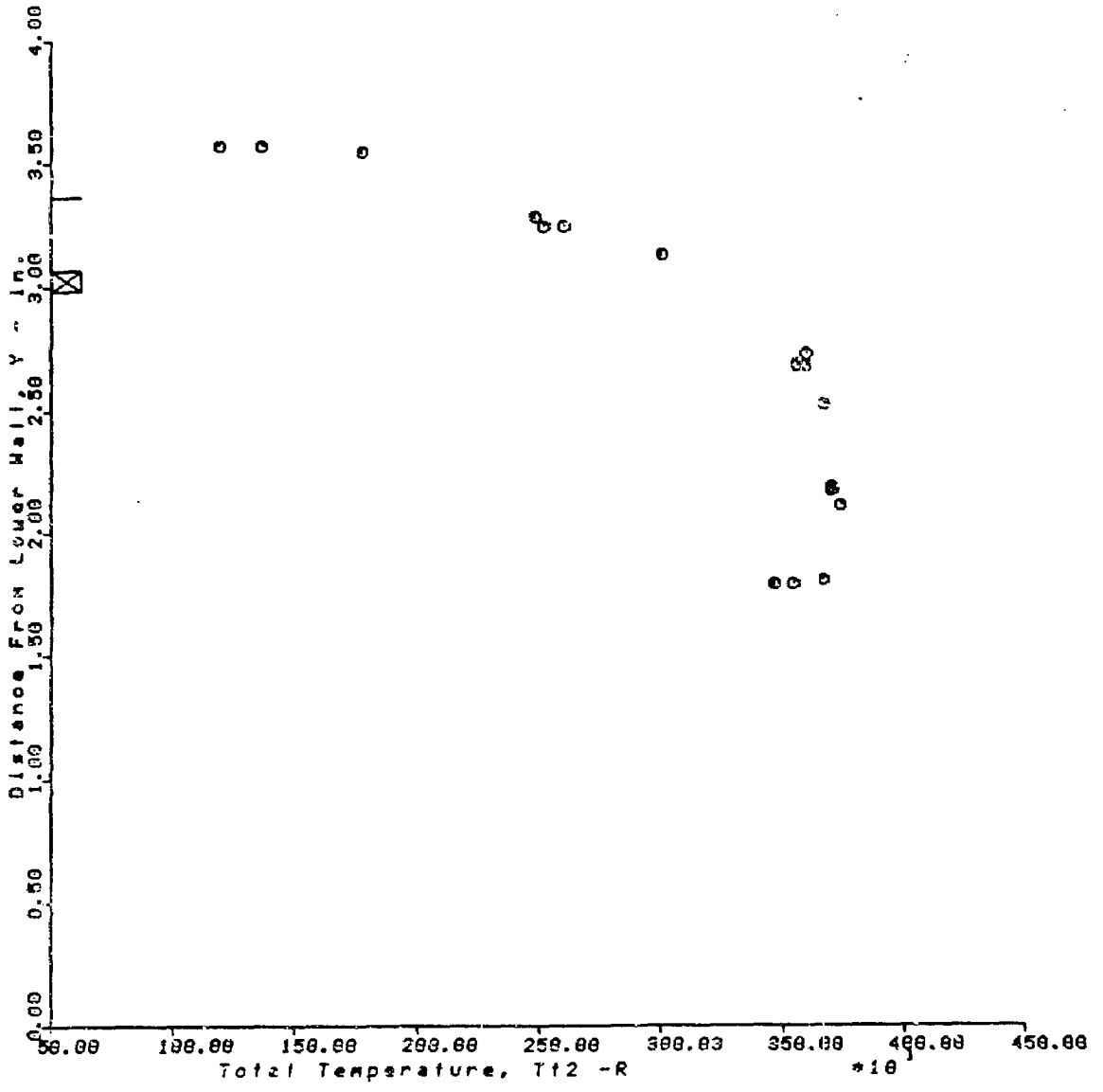

AFS TEST PROGRAM
RUN = 92 BURSTS 38 THRU 58

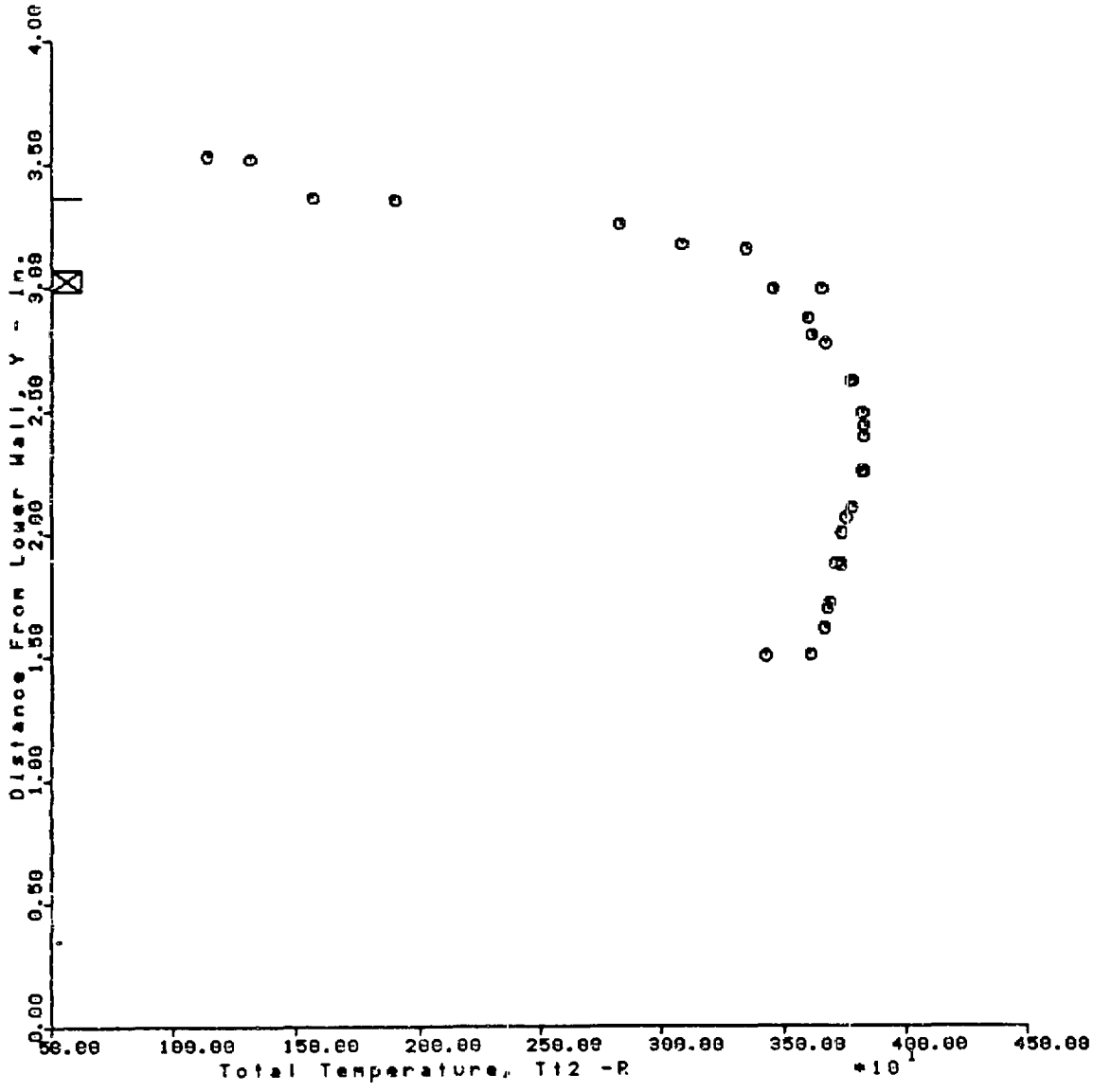

AFS TEST PROGRAM
RUN = 93 BURSTS 25 THRU 54

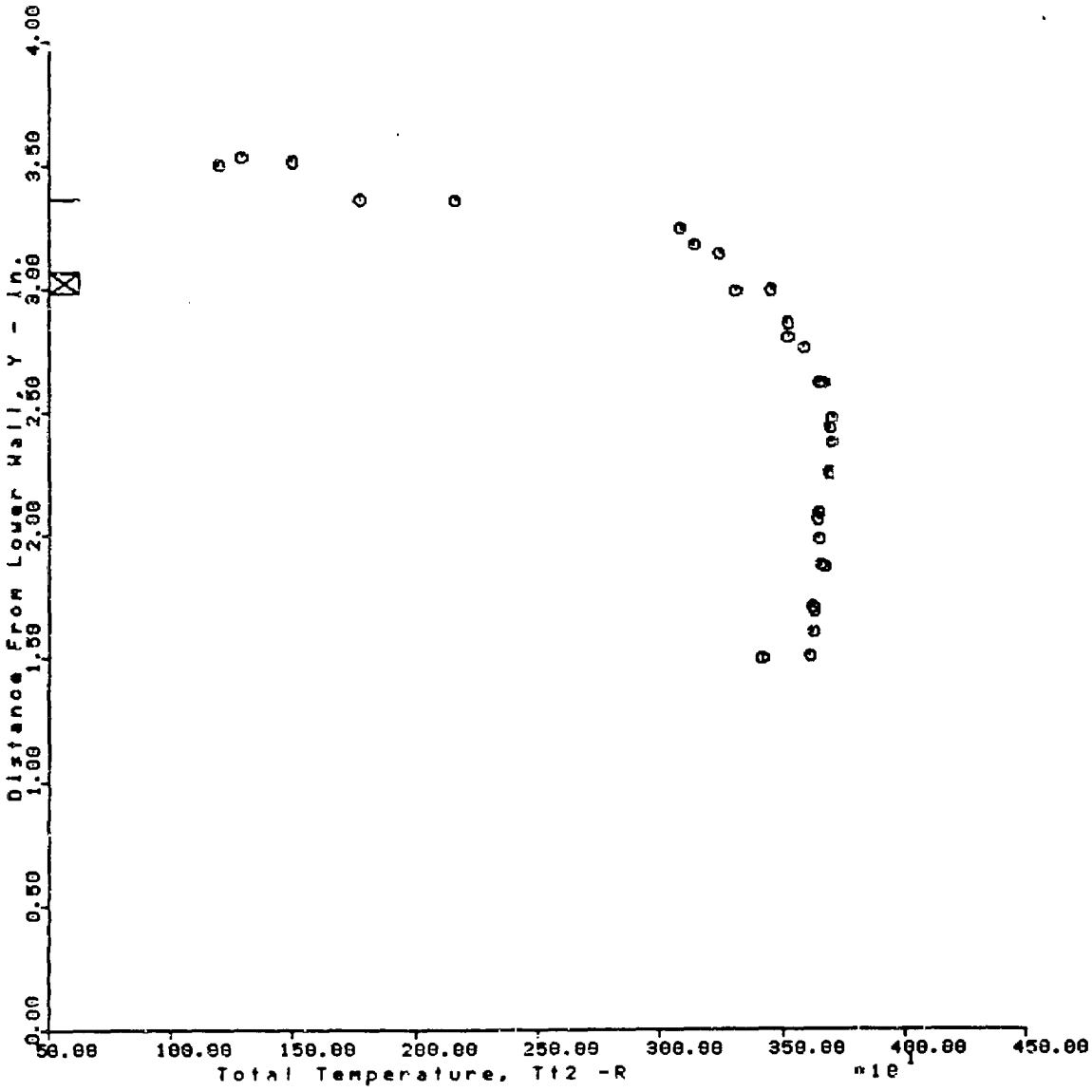

AFS TEST PROGRAM
RUN = 94 BURSTS 28 THRU 57

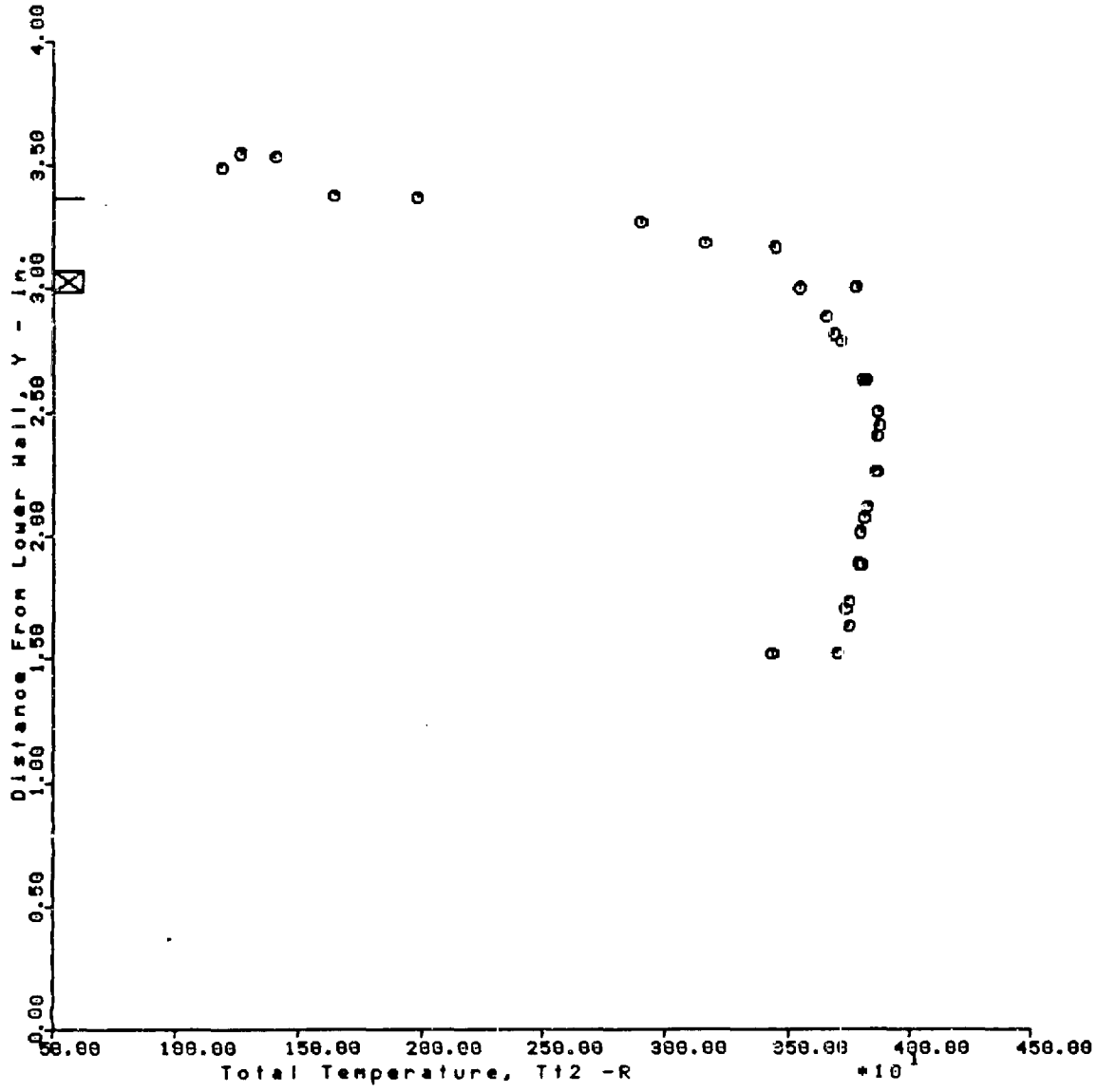

AFS TEST PROGRAM
RUN = 95 BURSTS 29 THRU 57

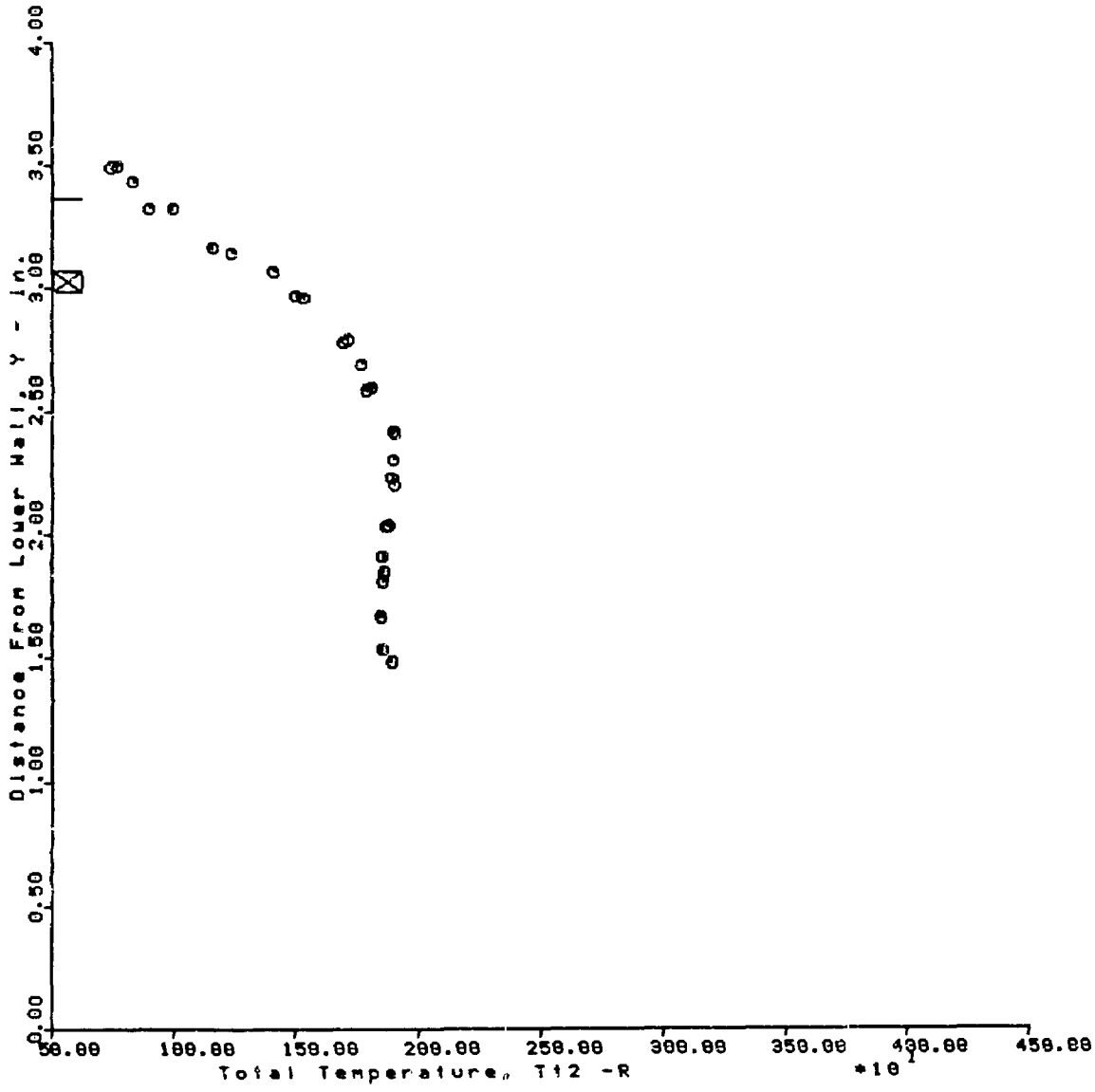

AFS TEST PROGRAM
RUN = 96 BURSTS 28 THRU 56

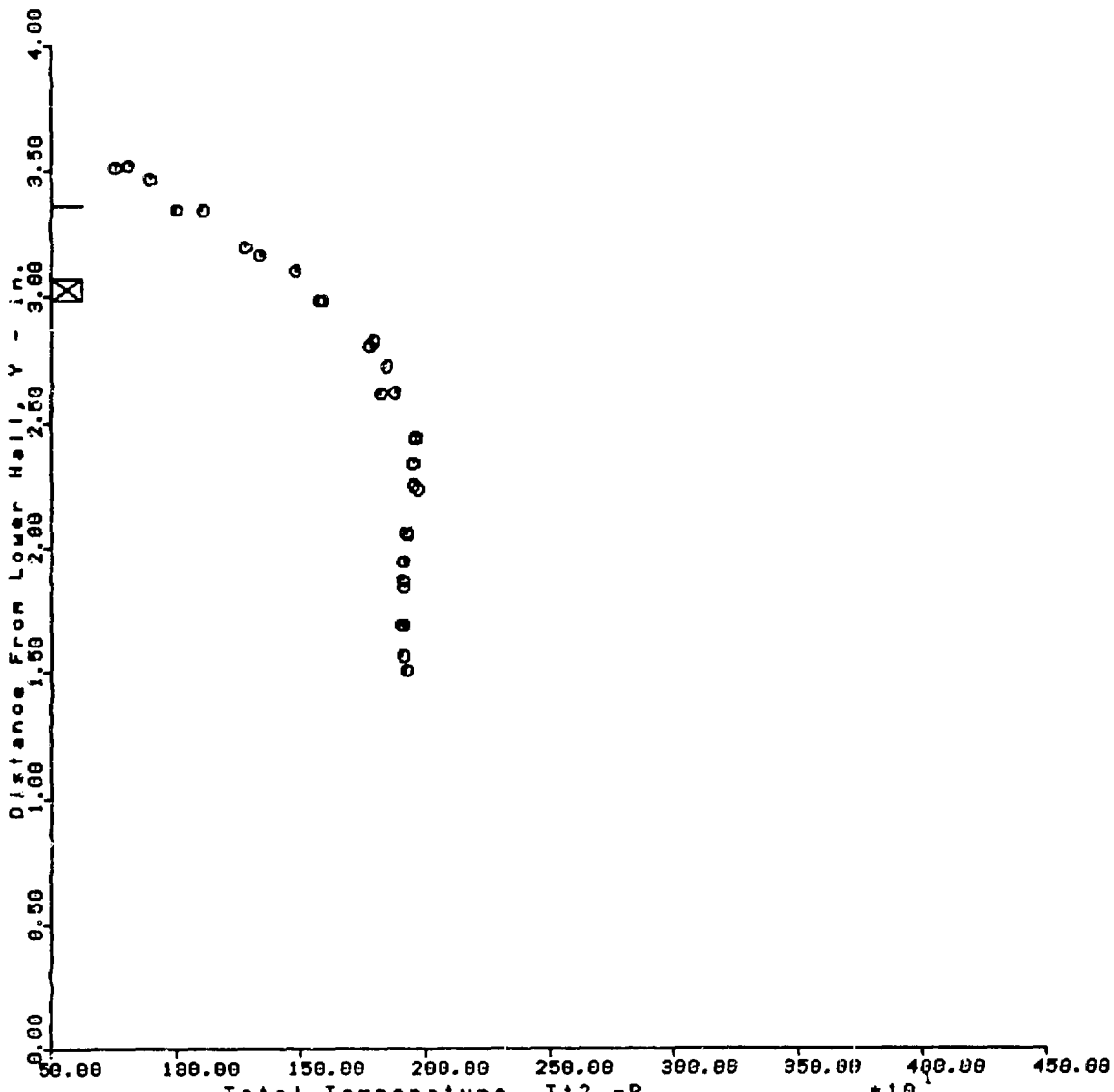

AFS TEST PROGRAM
RUN = 97 BURSTS 40 THRU 52

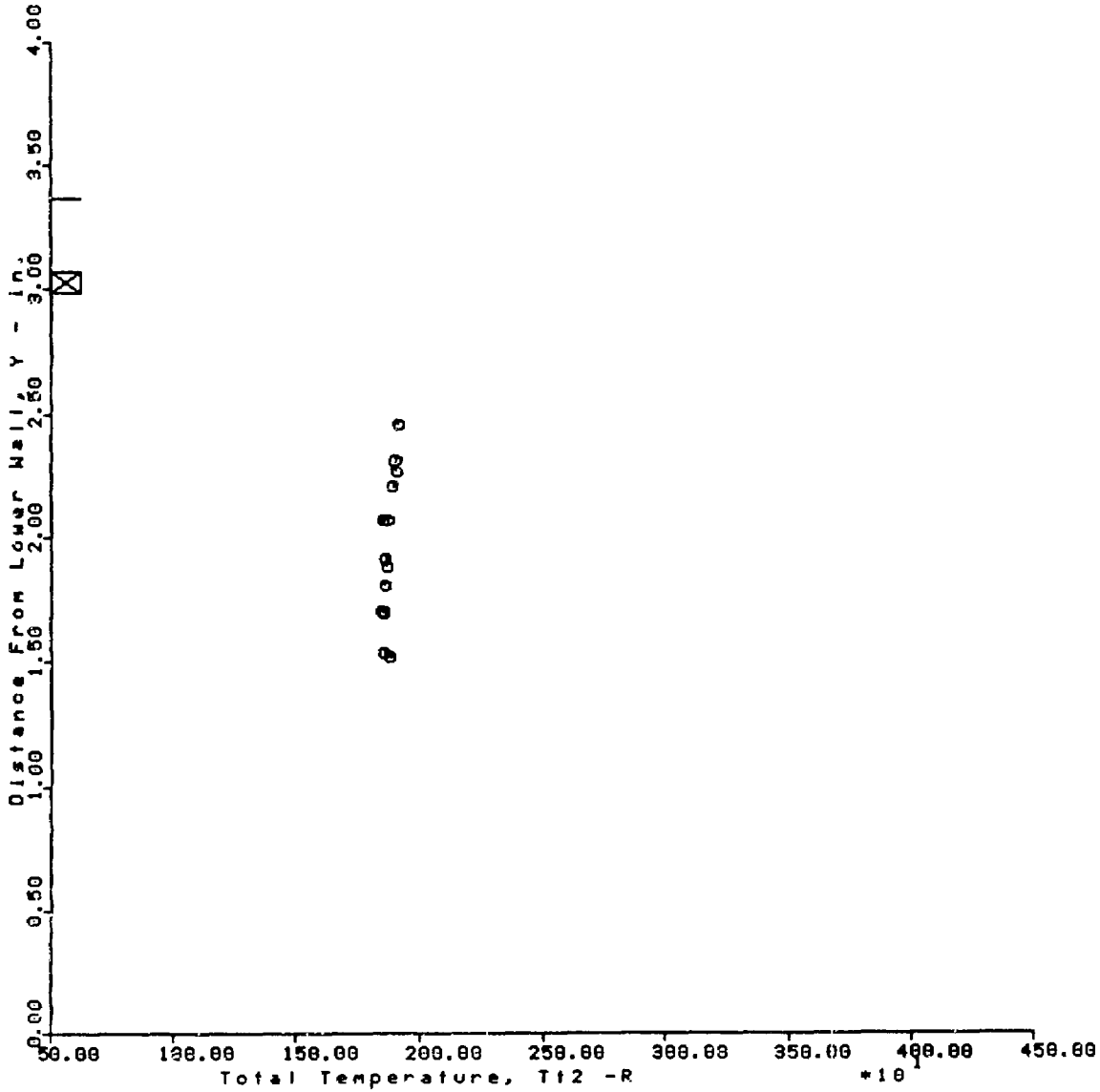

AFS TEST PROGRAM
RUN = 99 BURSTS 42 THRU 71

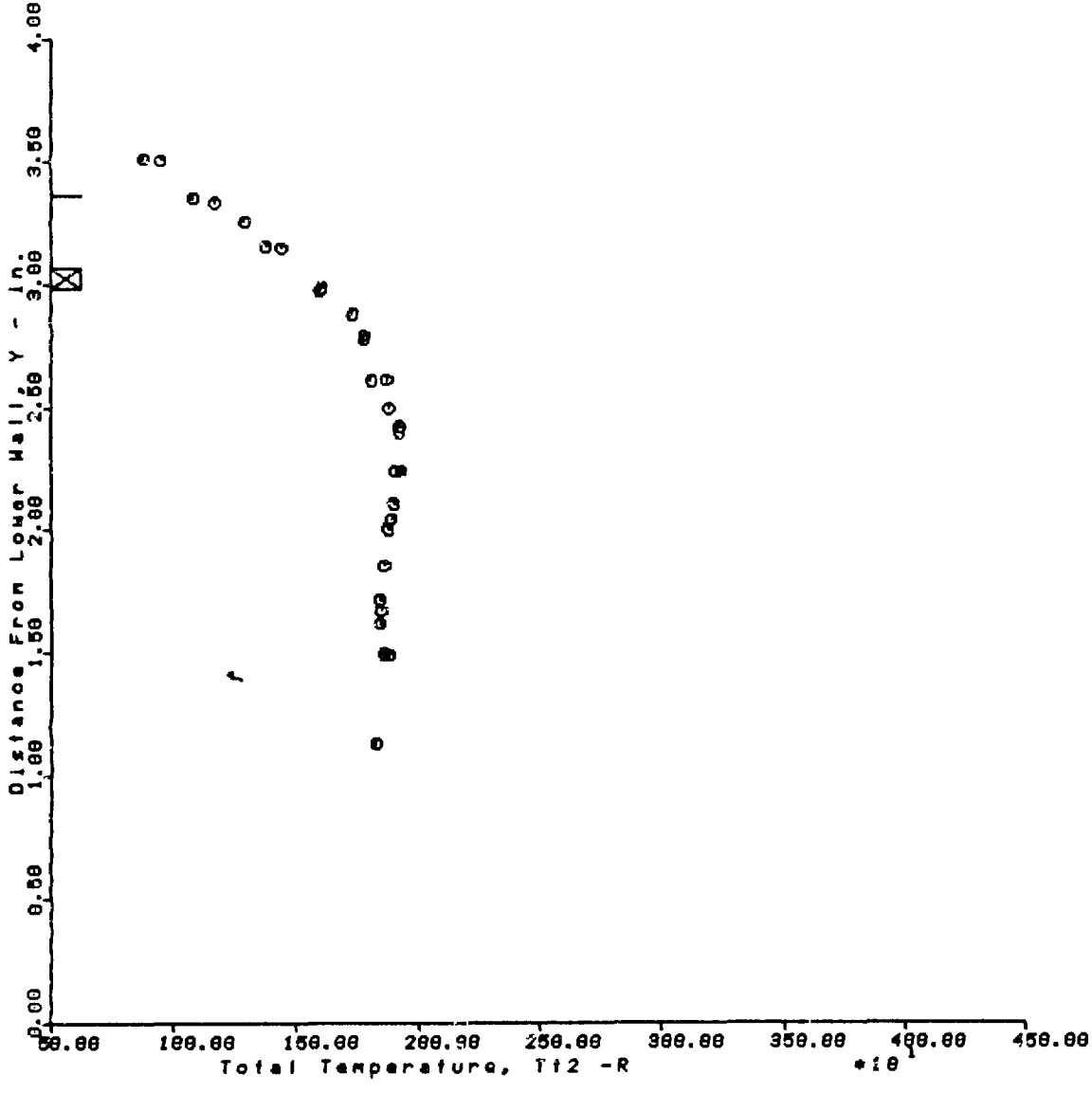

AFS TEST PROGRAM
RUN = 100 BURSTS 38 THRU 66

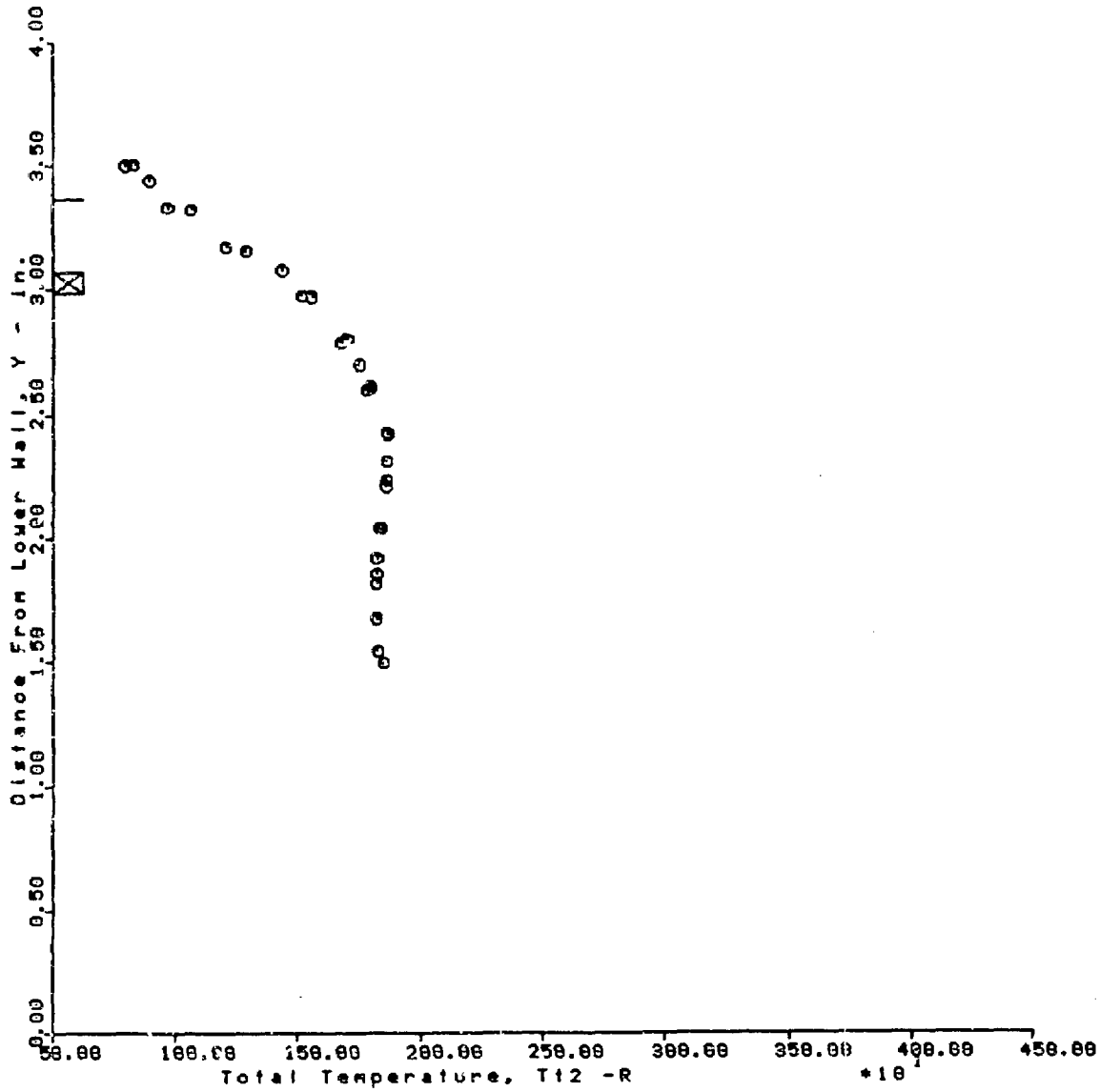

AFS TEST PROGRAM
RUN = 181 BURSTS 35 THRU 63

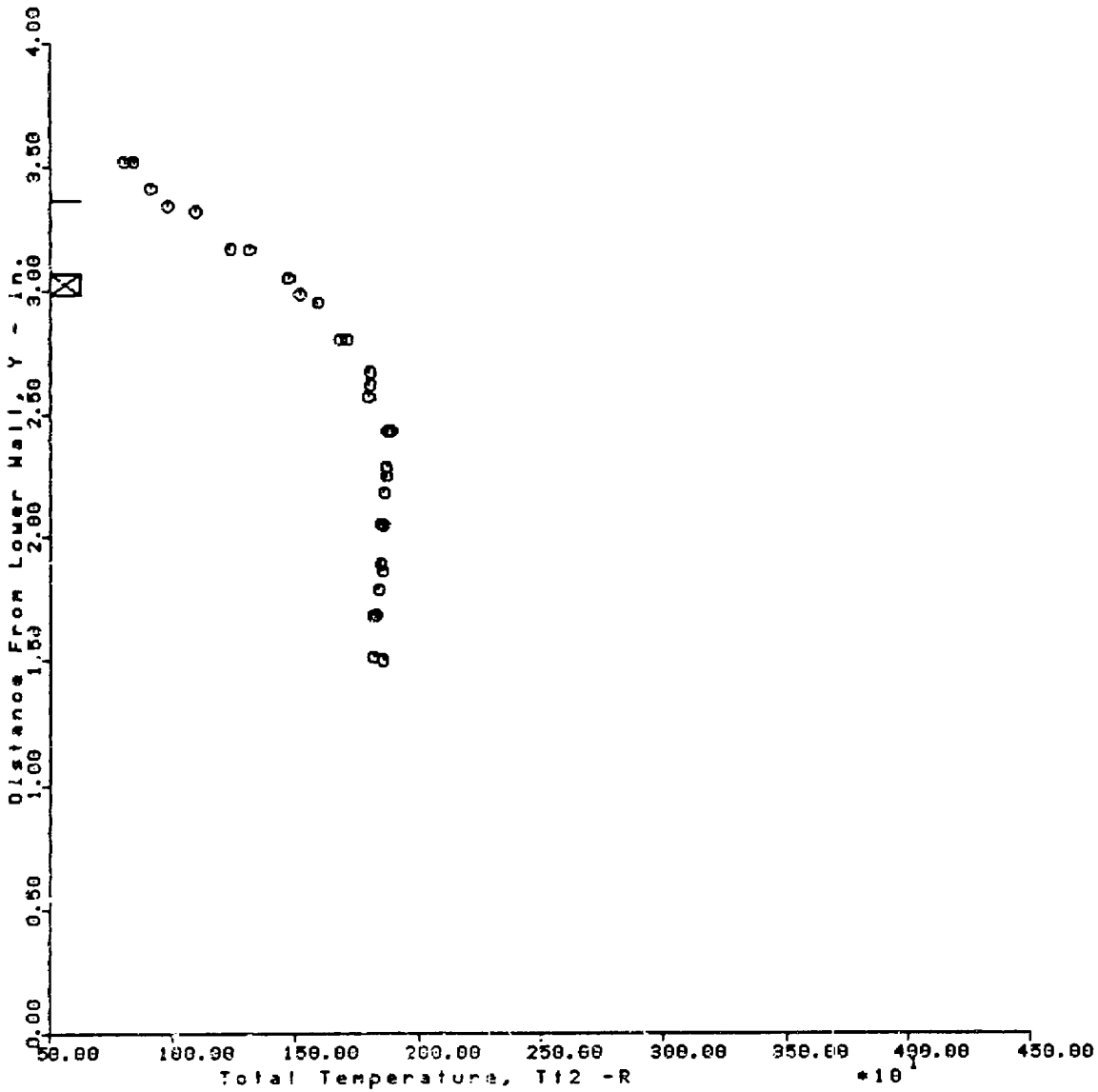

AFS TEST PROGRAM
RUN = 182 BURSTS 38 THRU 66

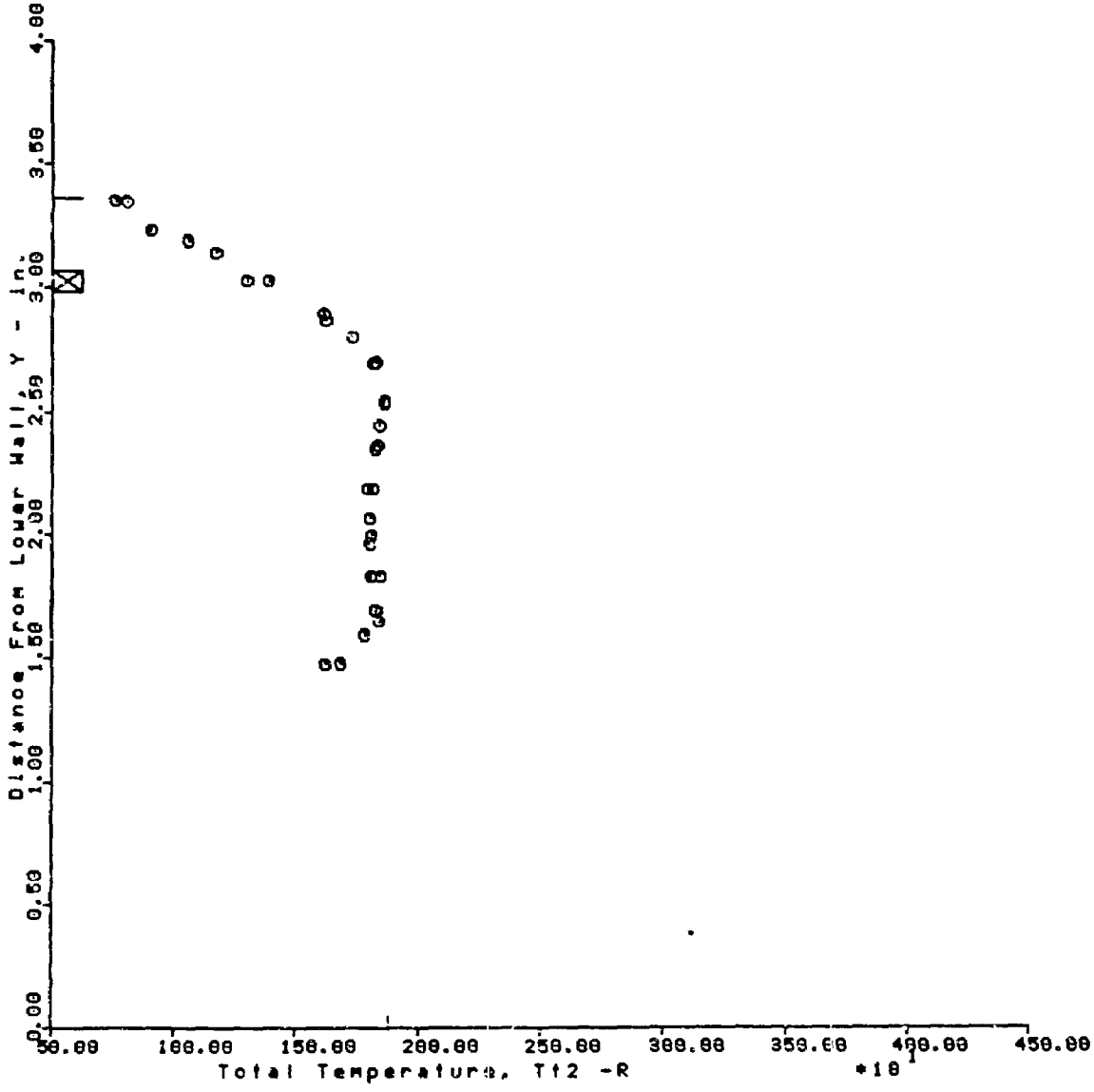

AFS TEST PROGRAM
RUN = 193 BURSTS 29 THRU 57

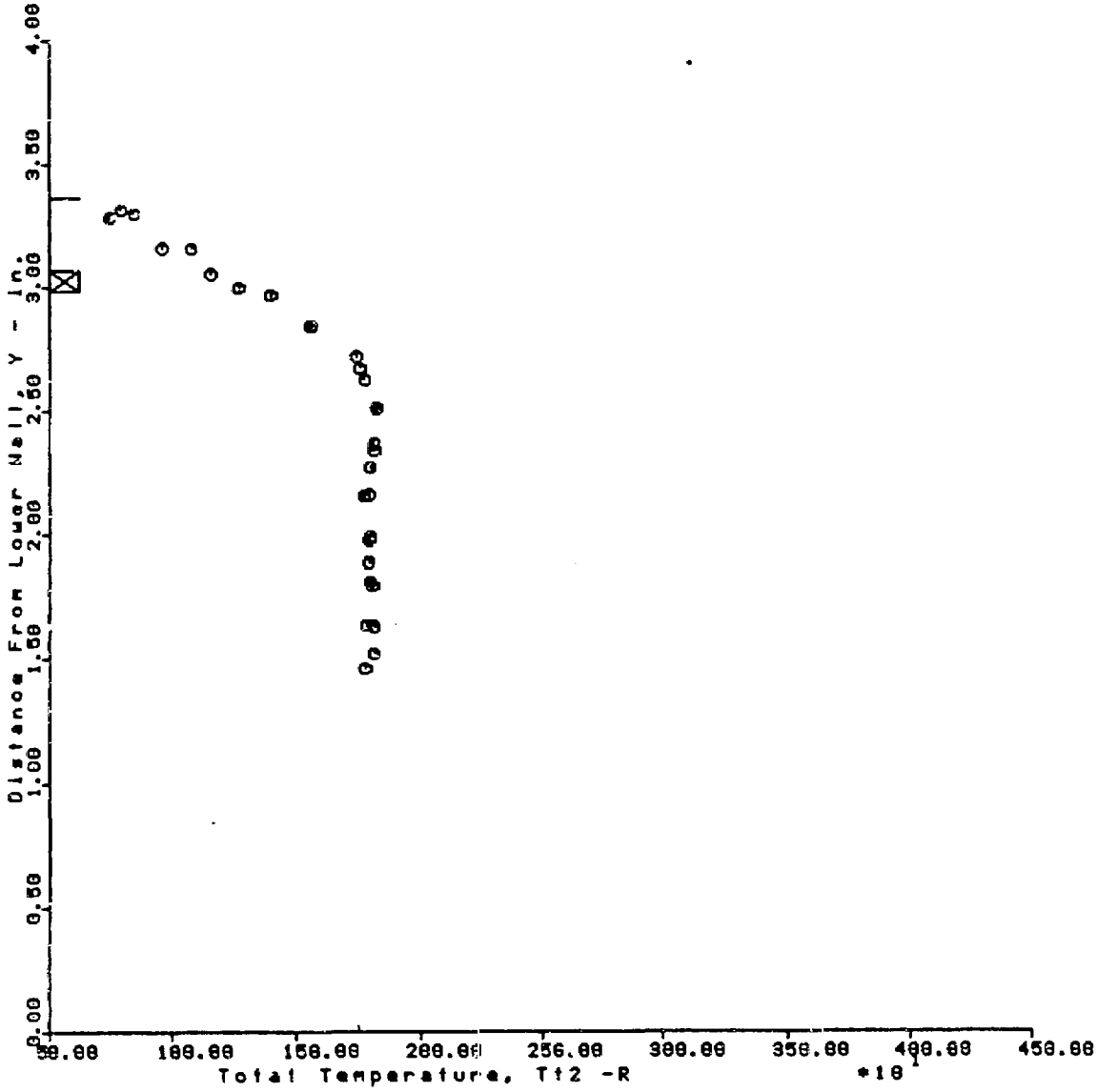

AFS TEST PROGRAM
RUN = 164 BURSTS 46 THRU 74

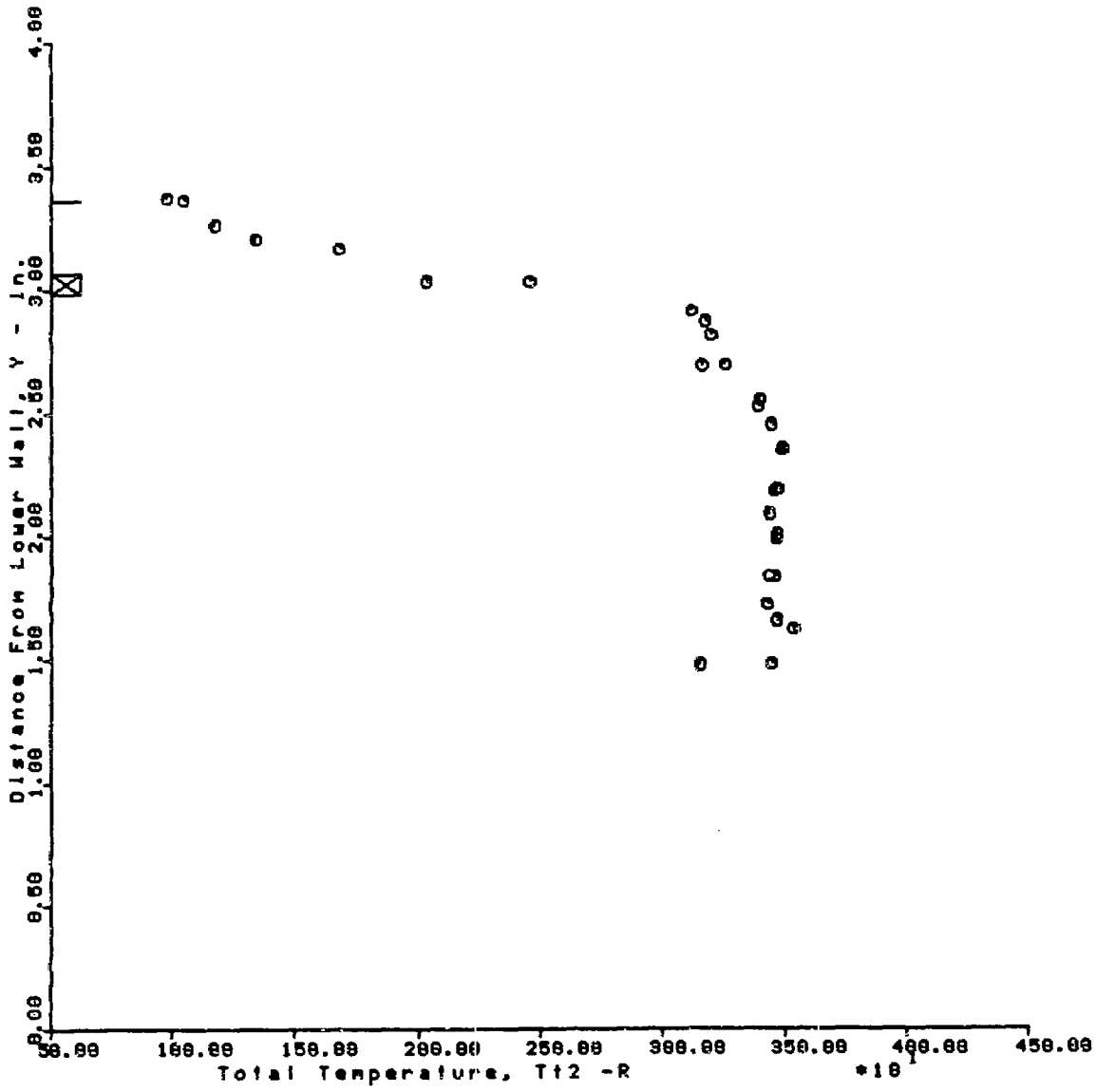

AFS TEST PROGRAM
RUN = 105 BURSTS 30 THRU 50

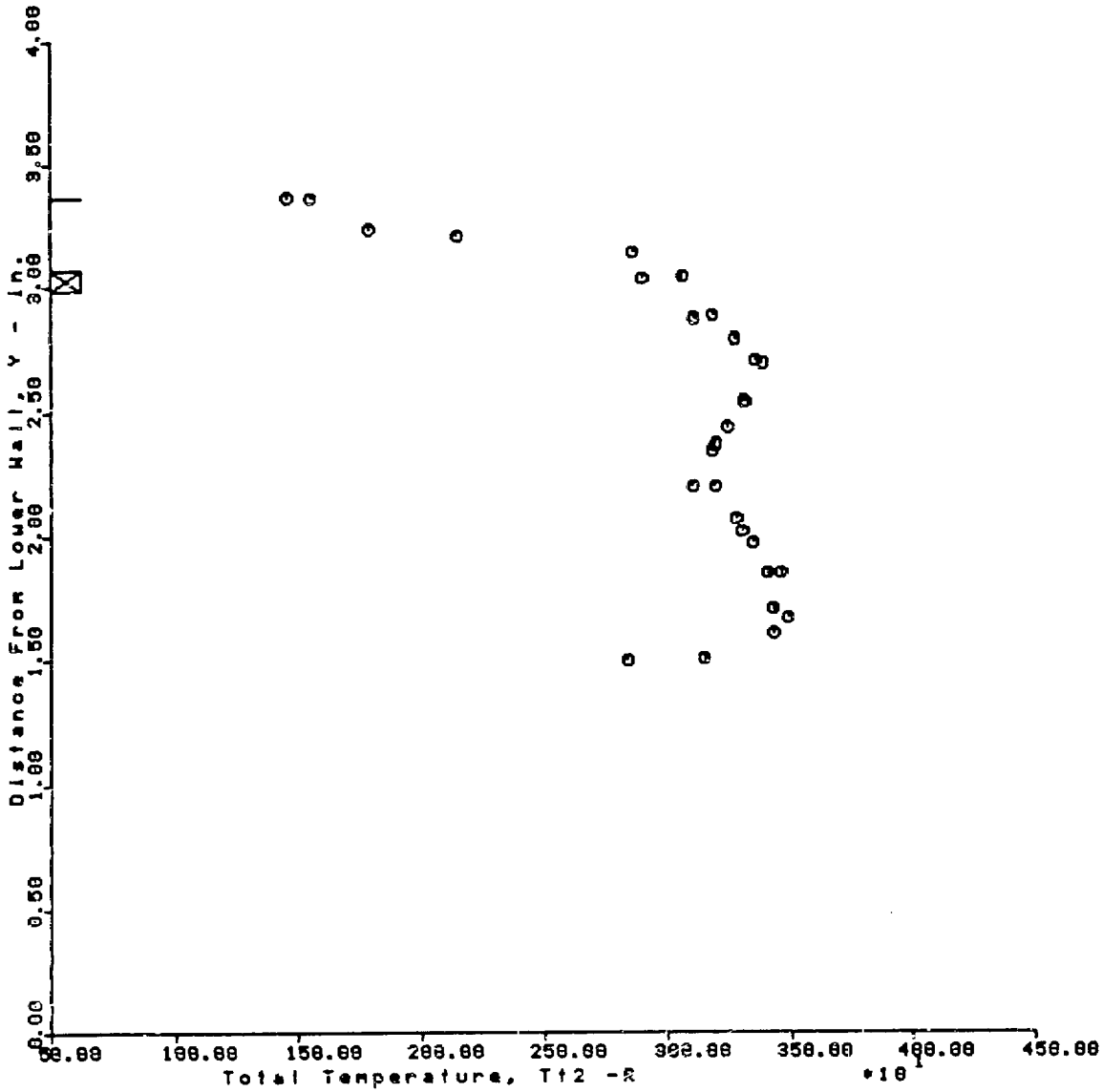

AFS TEST PROGRAM
RUN = 188 BURSTS 28 THRU 56

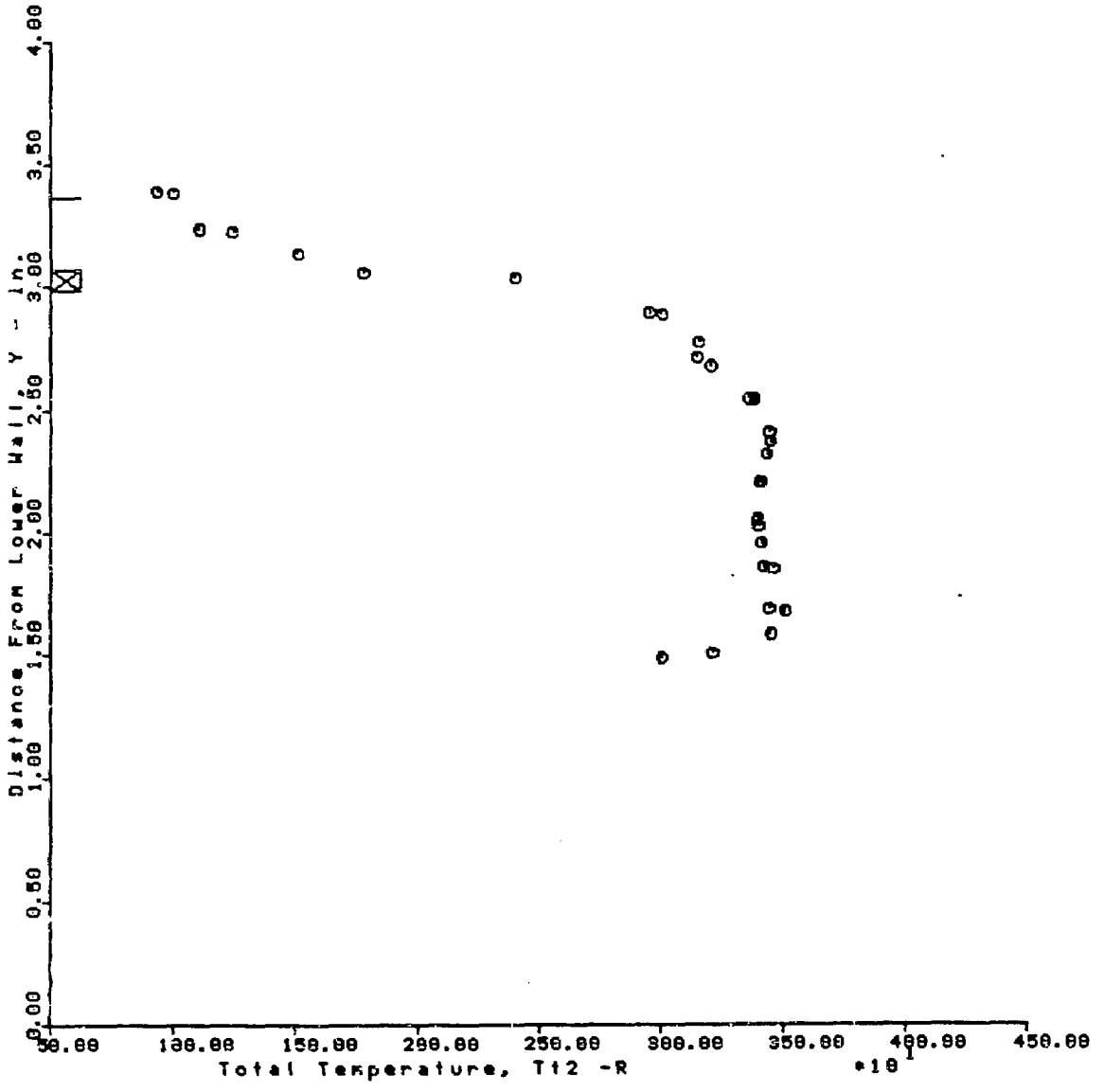

AFS TEST PROGRAM
RUN = 199 BURSTS 32 THRU 60

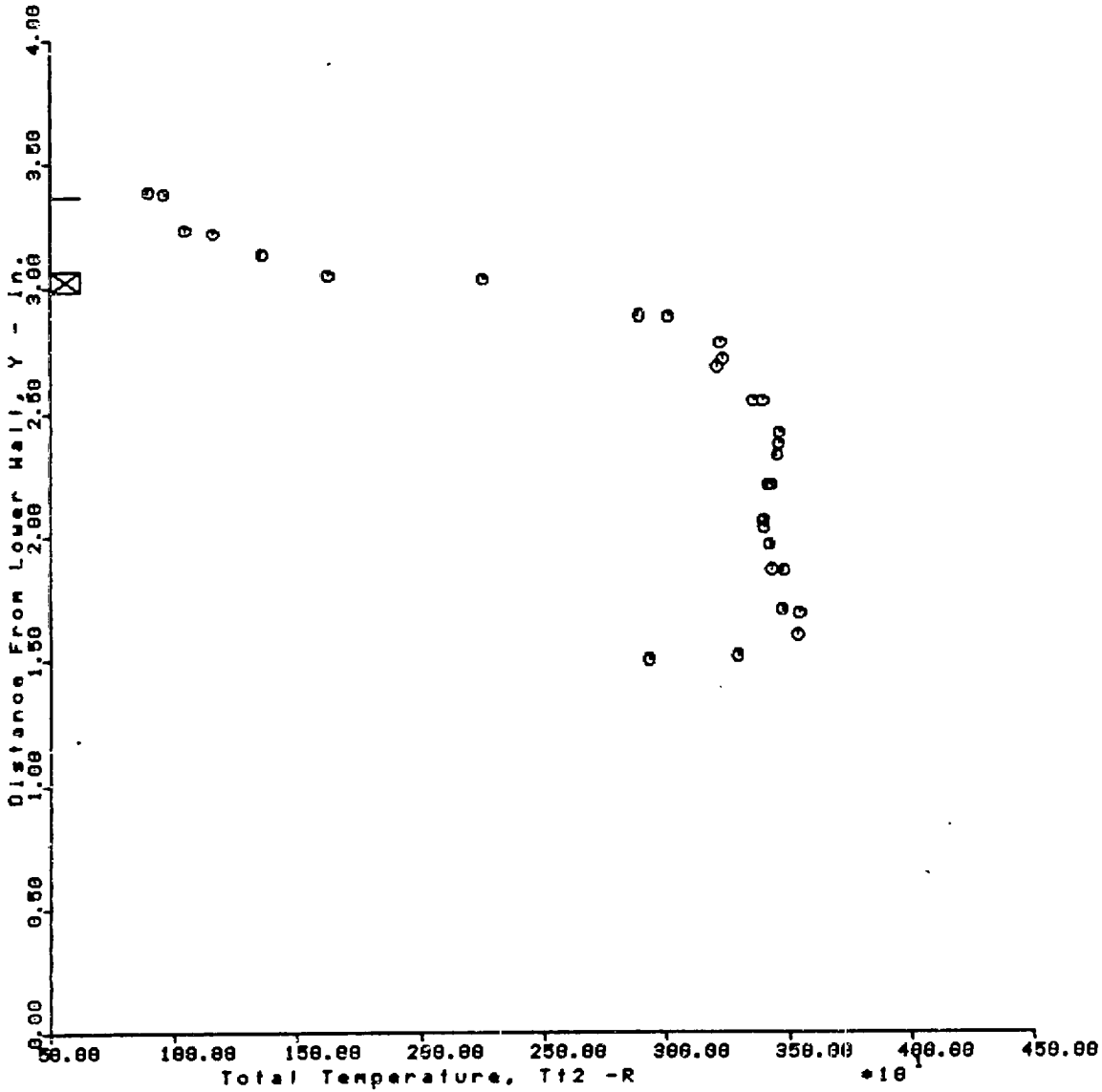

AFS TEST PROGRAM
RUN = 118 BURSTS 36 THRU 58

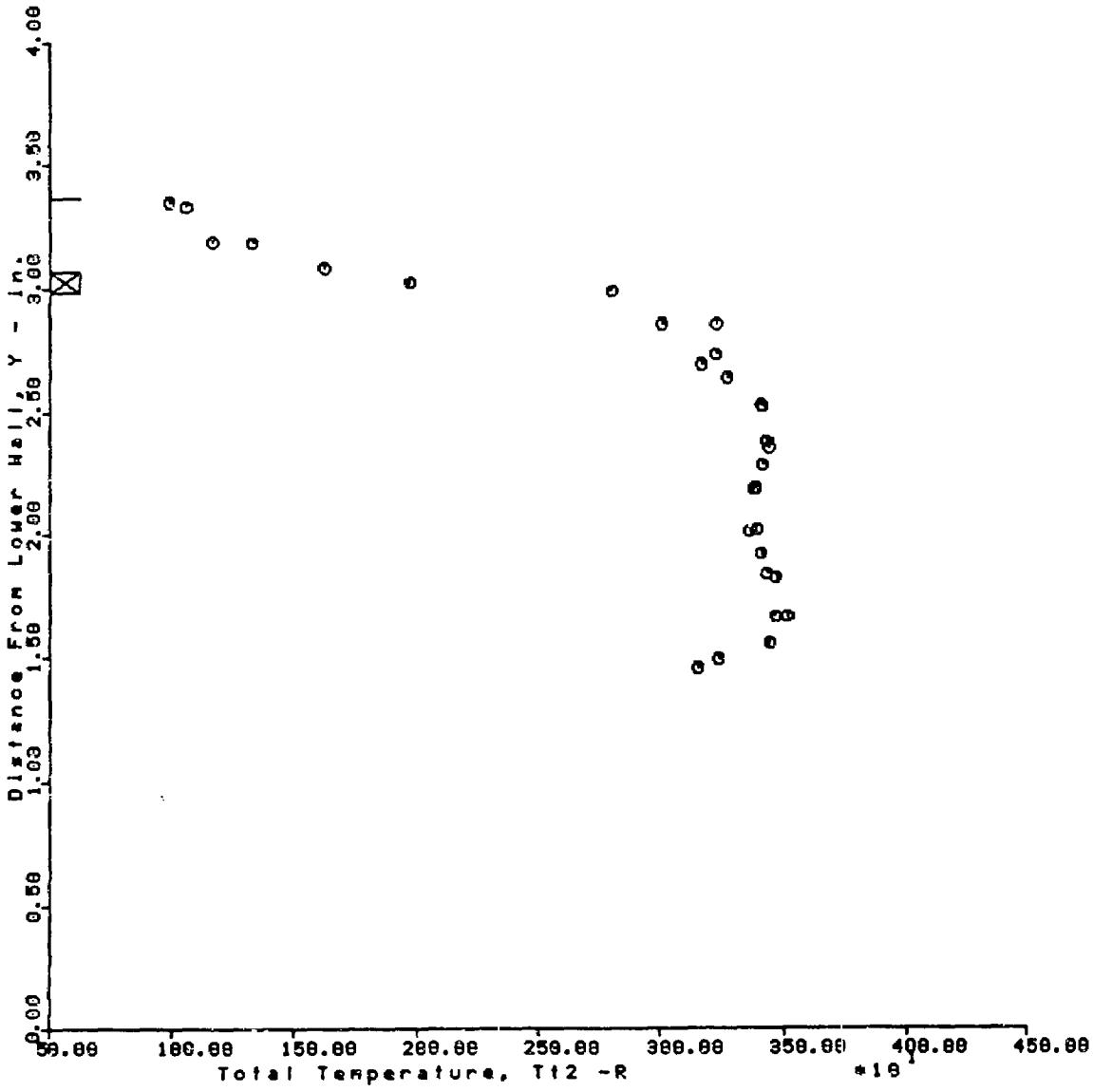

AFS TEST PROGRAM
RUN = 111 BURSTS 25 THRU 53

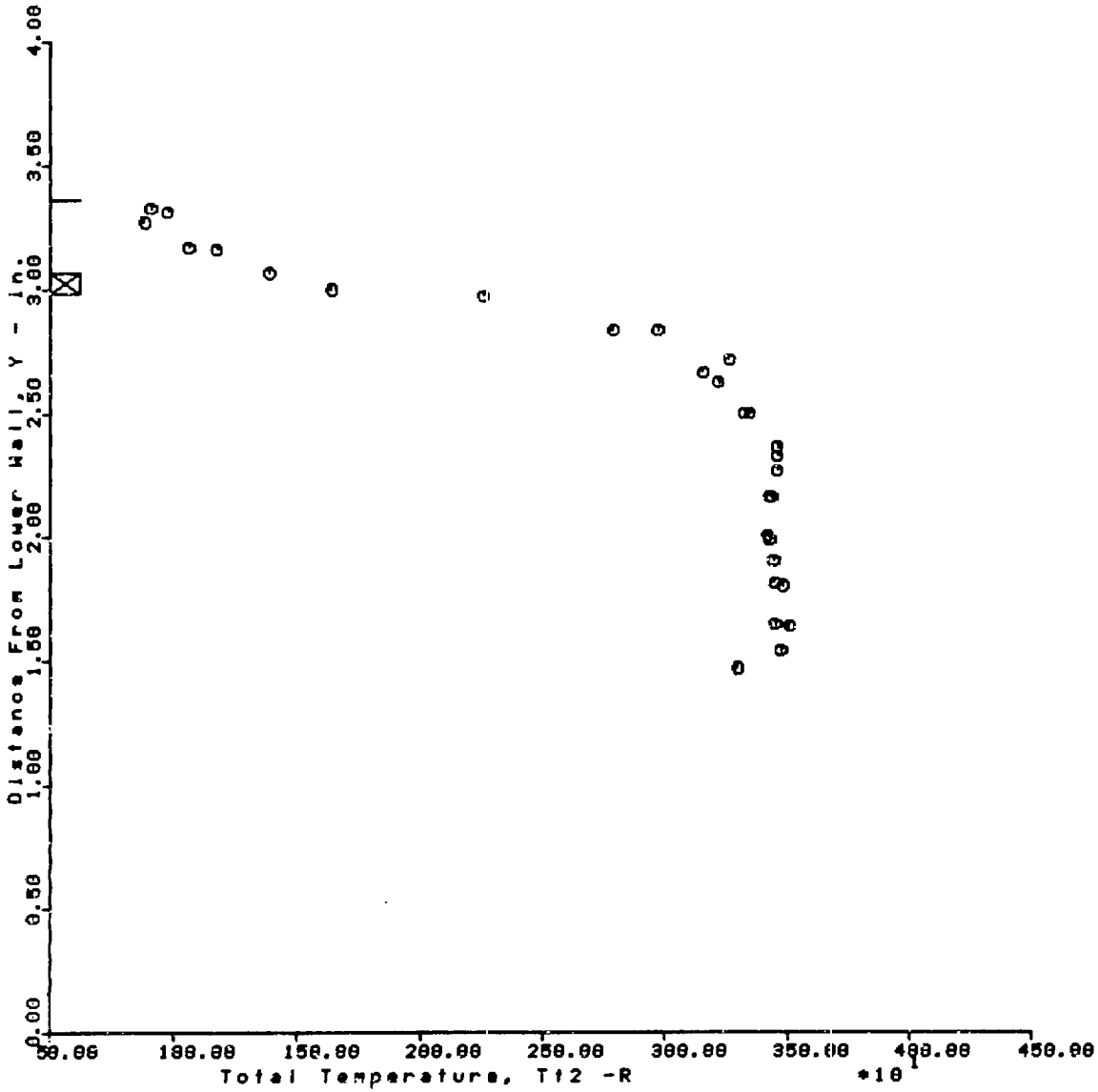

AFS TEST PROGRAM
RUN = 112 BURSTS 31 THRU 59

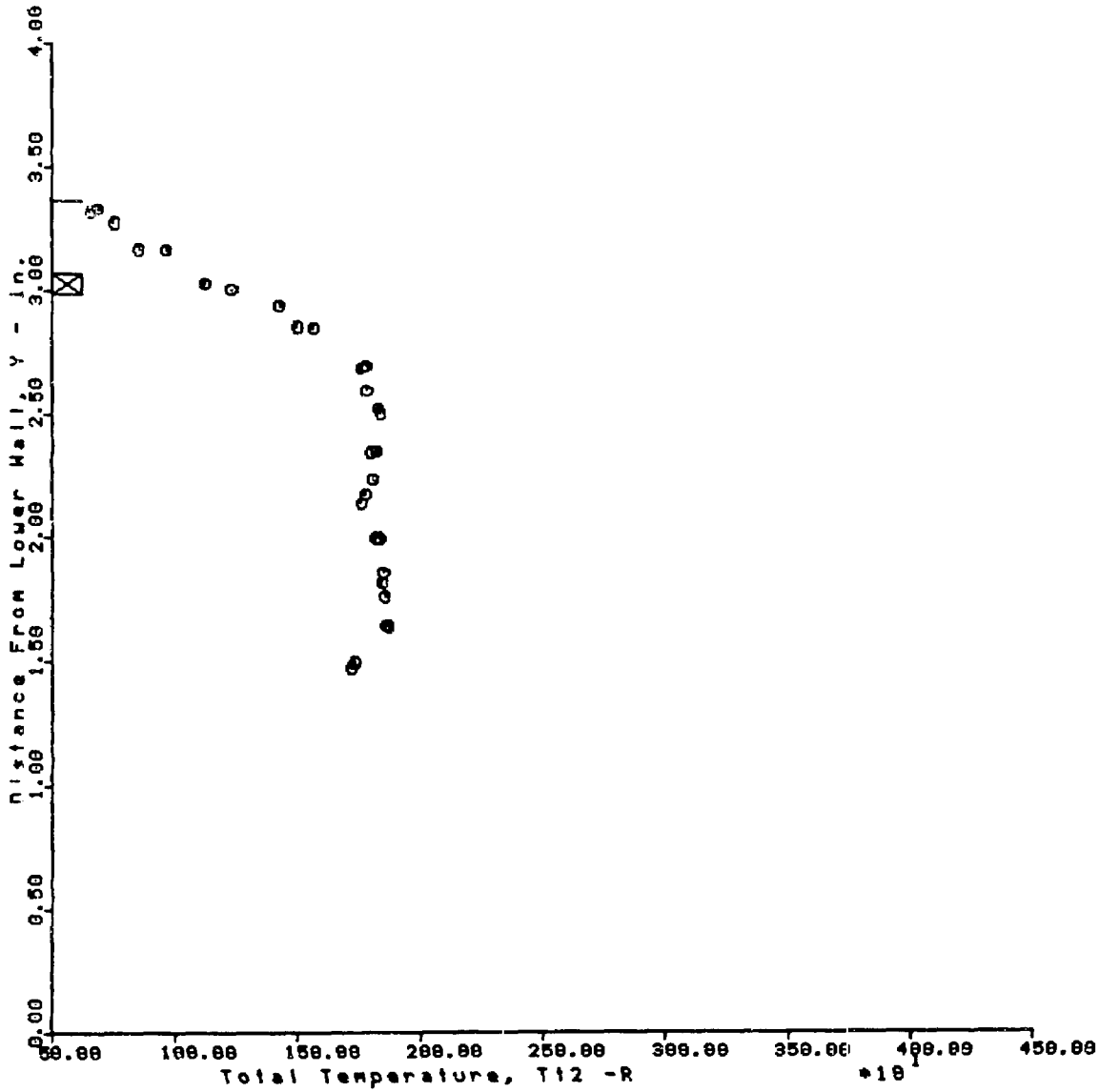

AFS TEST PROGRAM
RUN = 113 BURSTS 29 THRU 57

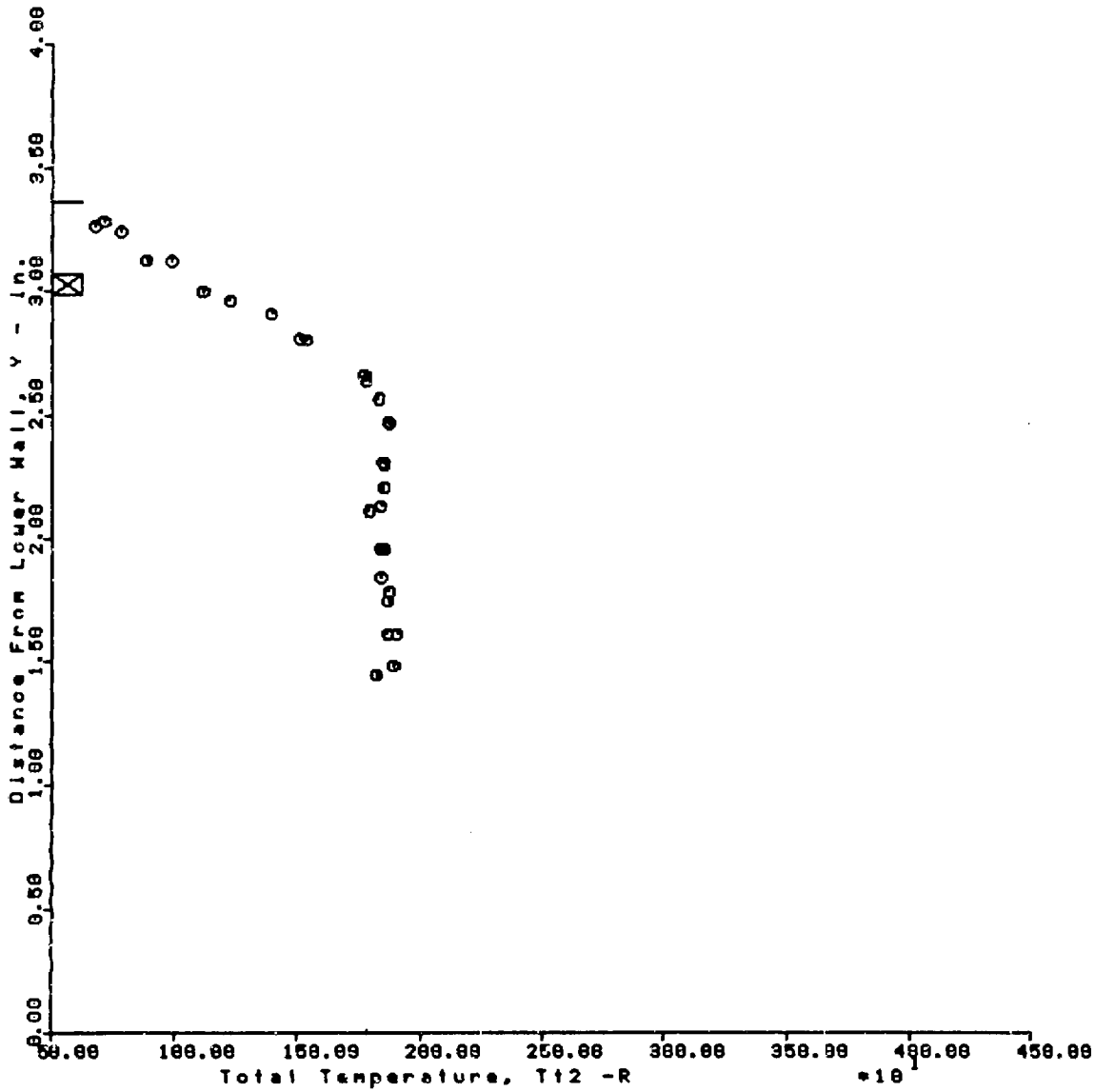

AFS TEST PROGRAM
RUN = 114 BURSTS 25 THRU 53

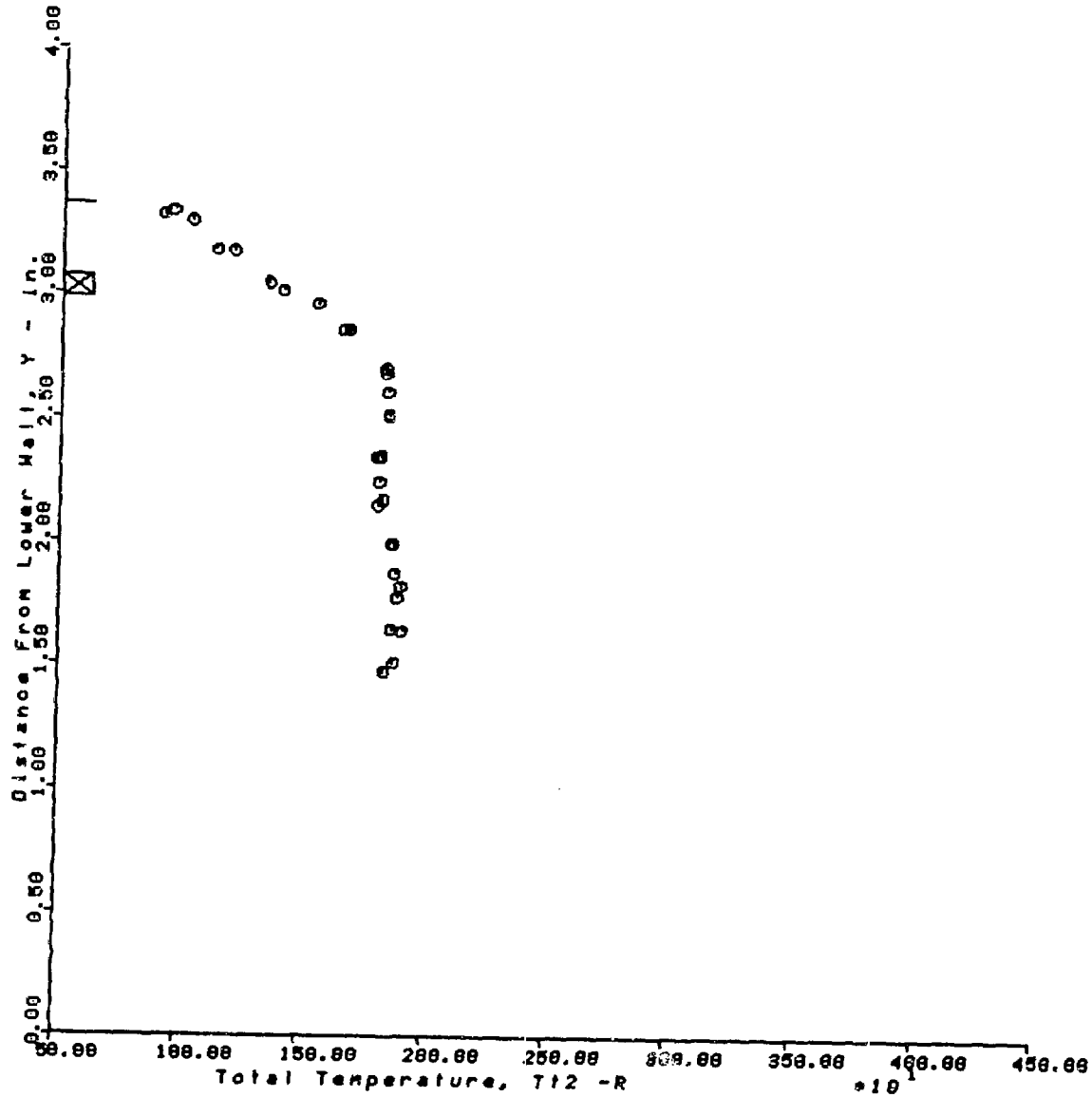

AFS TEST PROGRAM
RUN = 121 BURSTS 33 THRU 61

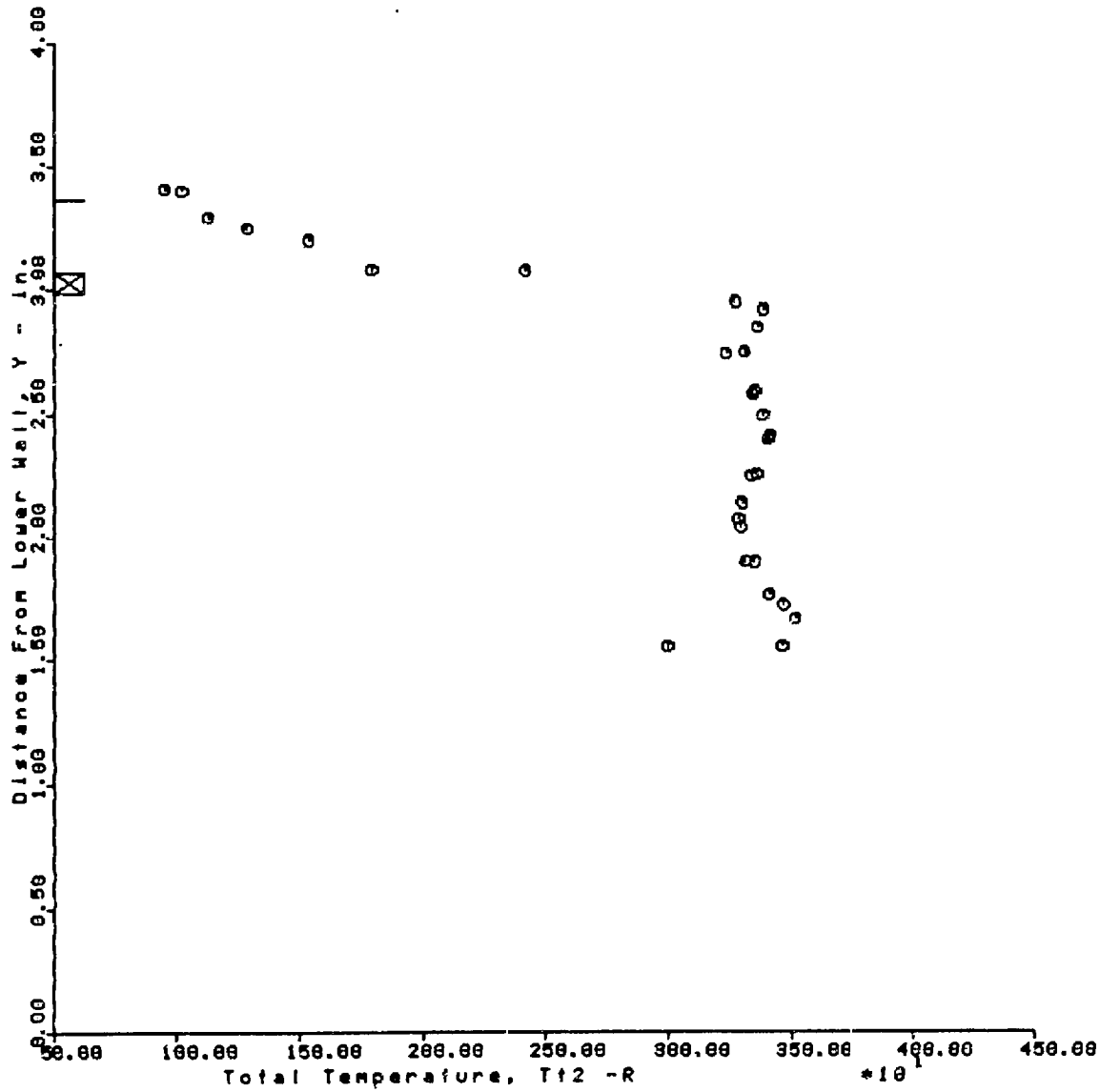

AFS TEST PROGRAM
RUN = 122 BURSTS 31 THRU 59

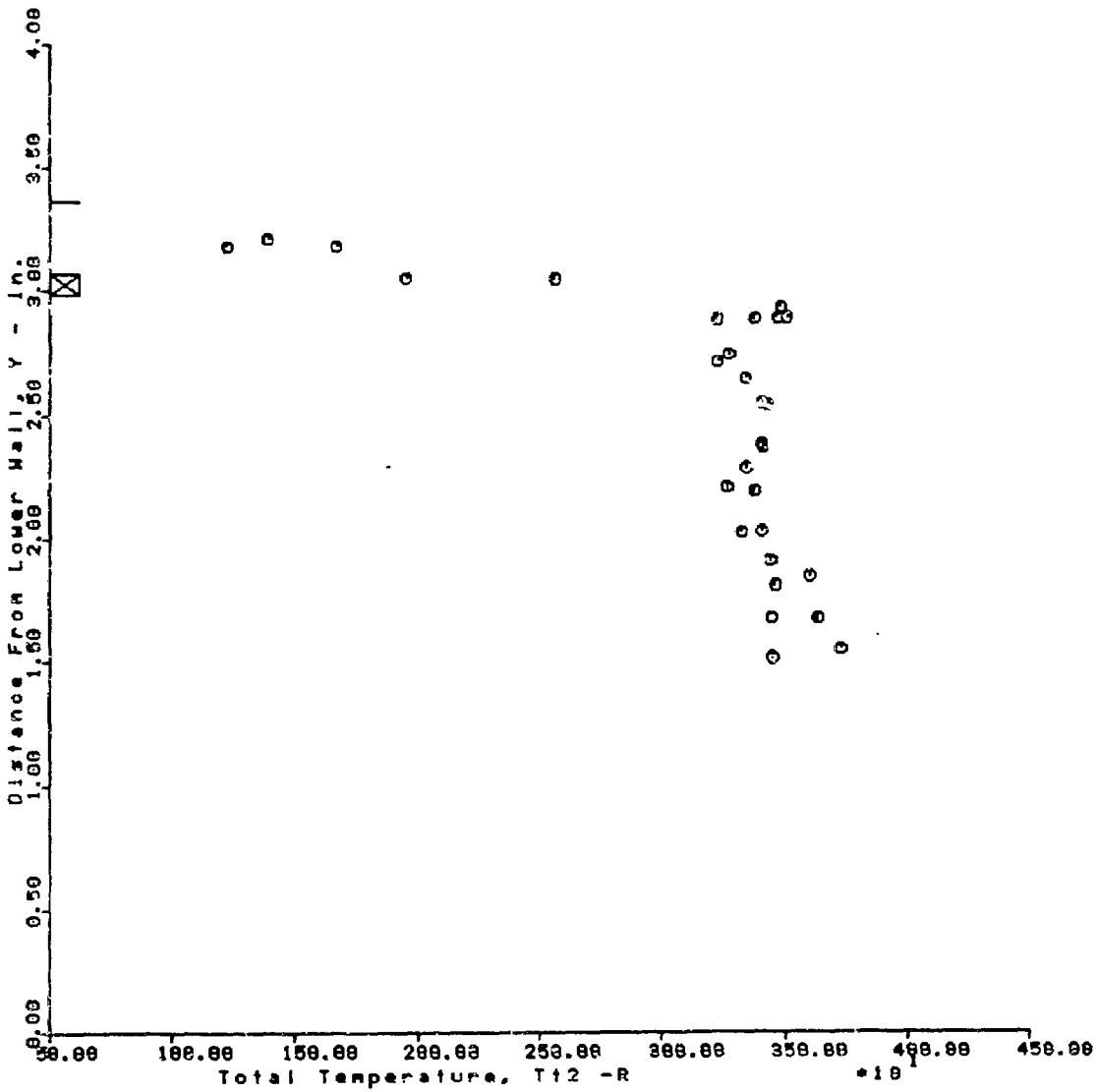

AFS TEST PROGRAM
RUN = 124 BURSTS 25 THRU 53

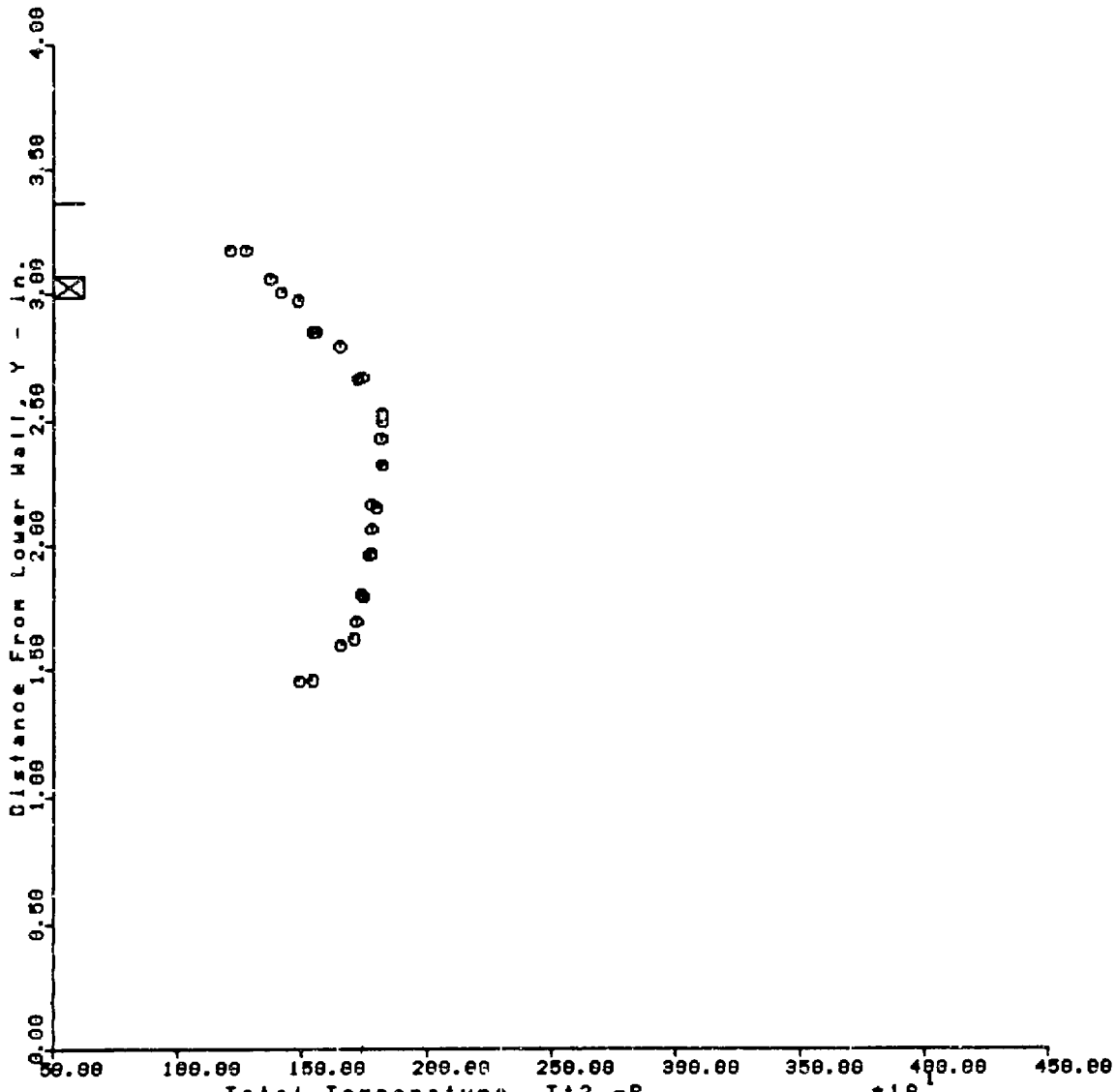

AFS TEST PROGRAM
RUN = 125 BURSTS 25 THRU 54

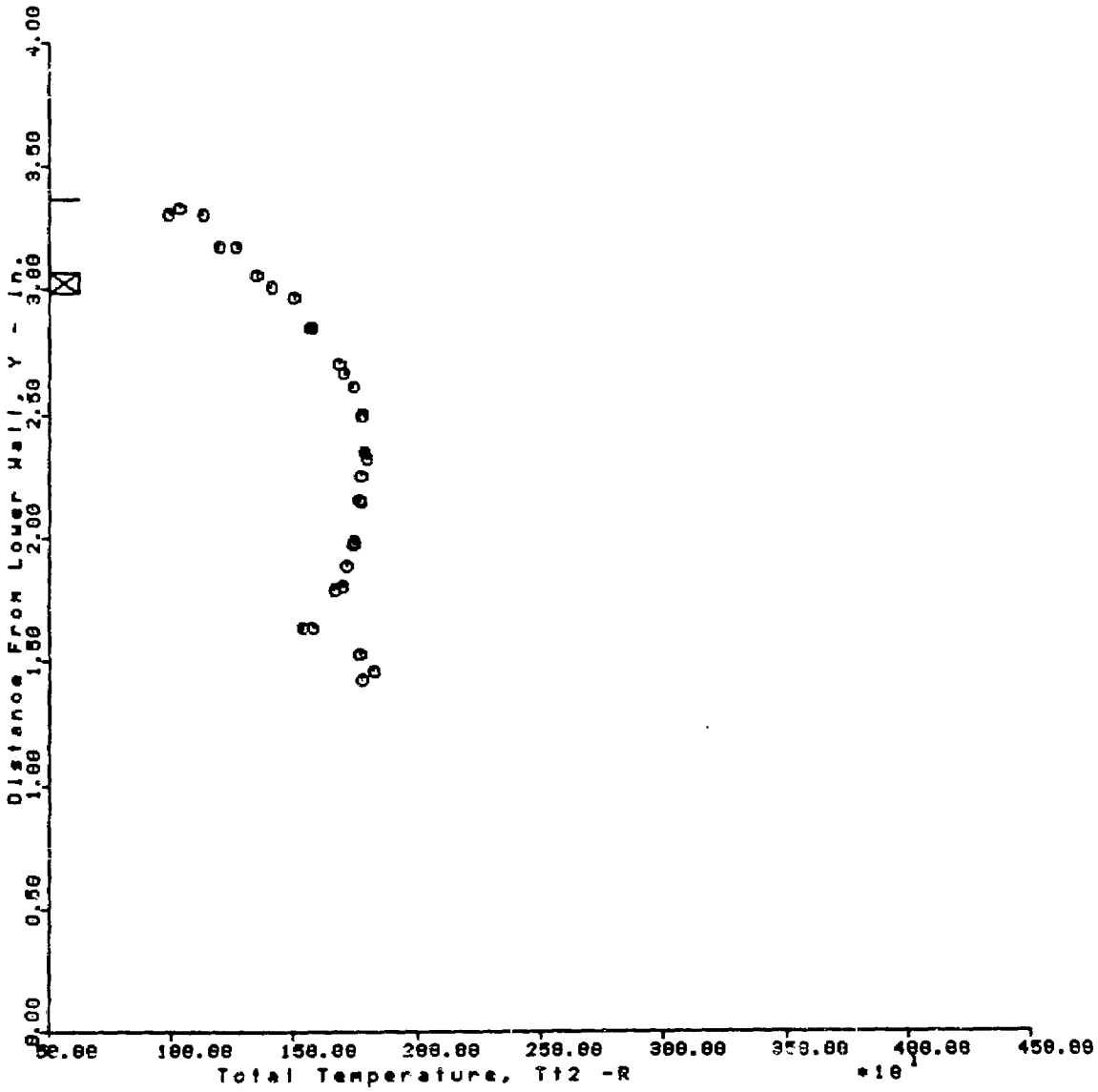

AFS TEST PROGRAM
RUN = 126 BURSTS 27 THRU 56

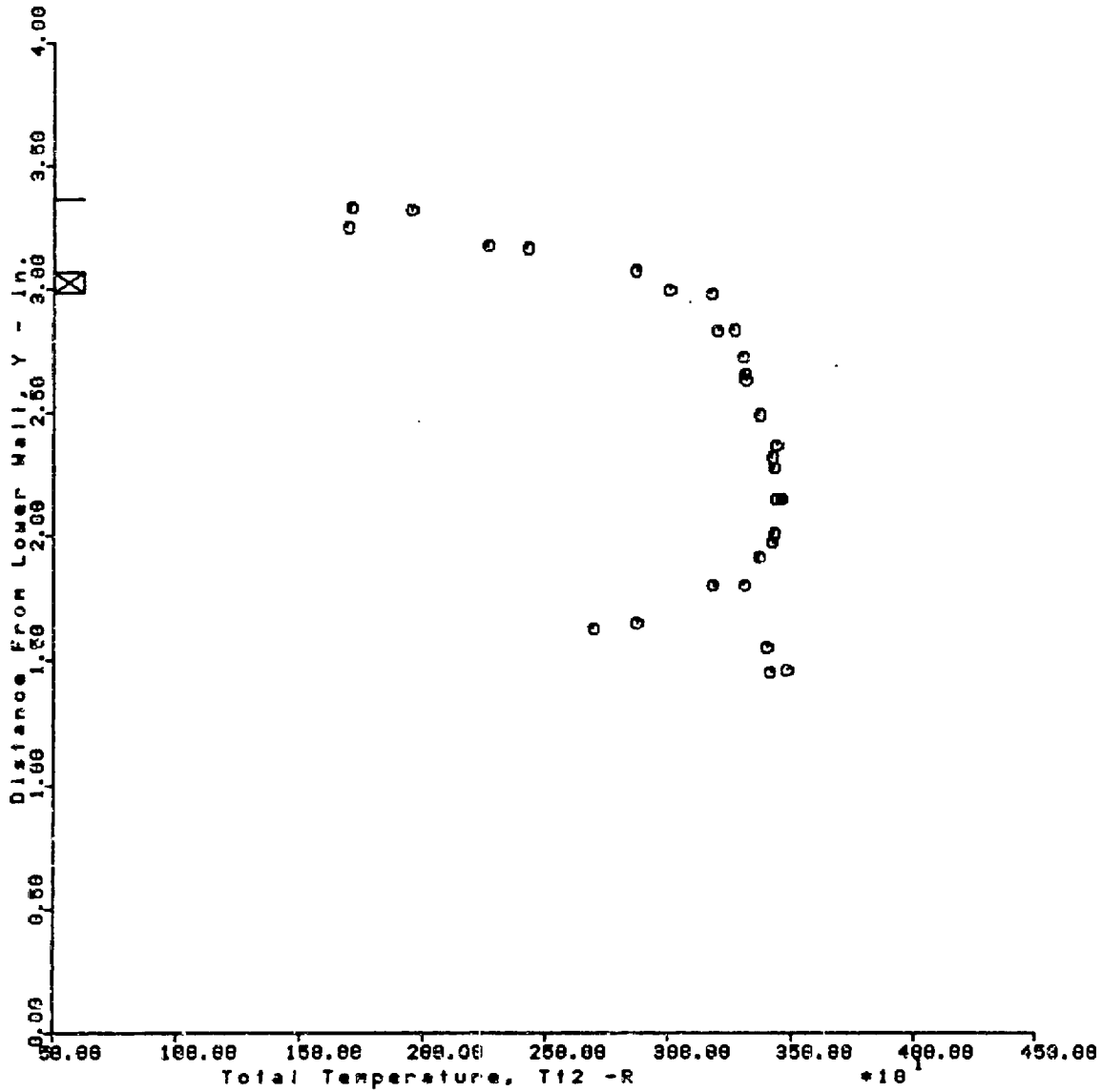

AFS TEST PROGRAM
RUN = 127 BURSTS 27 THRU 55

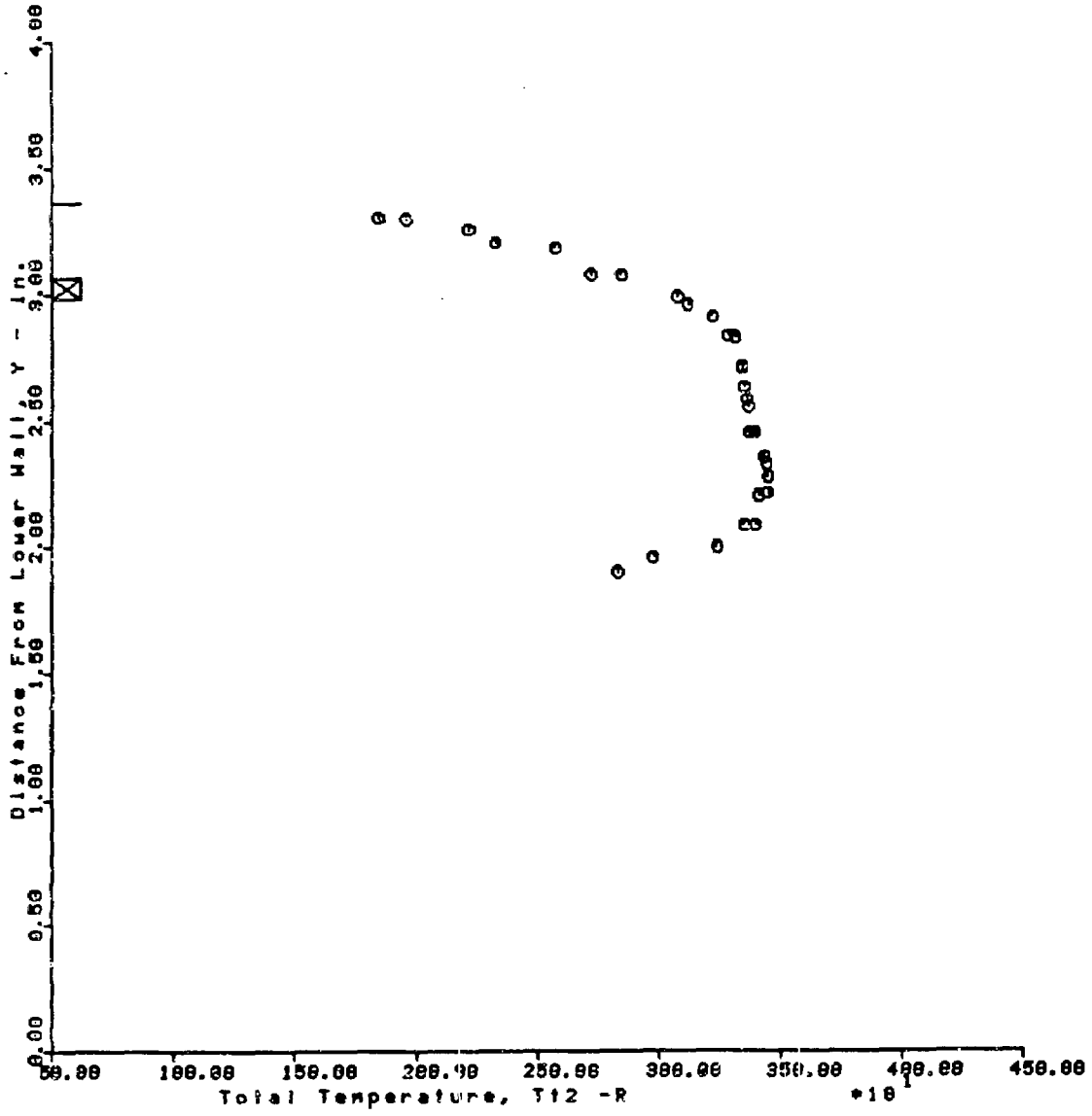

AFS TEST PROGRAM
RUN = 128 BURSTS 25 THRU 53

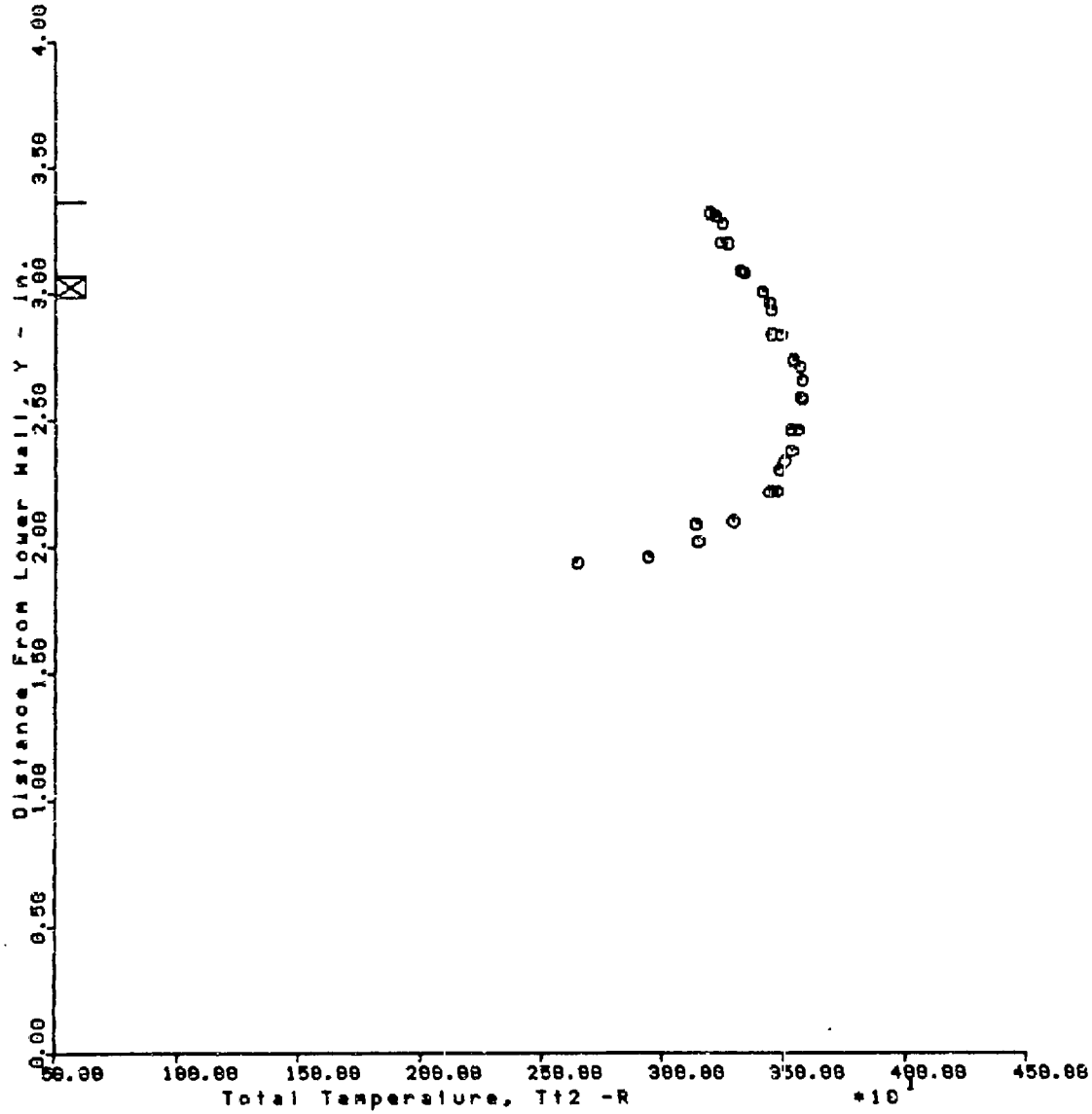

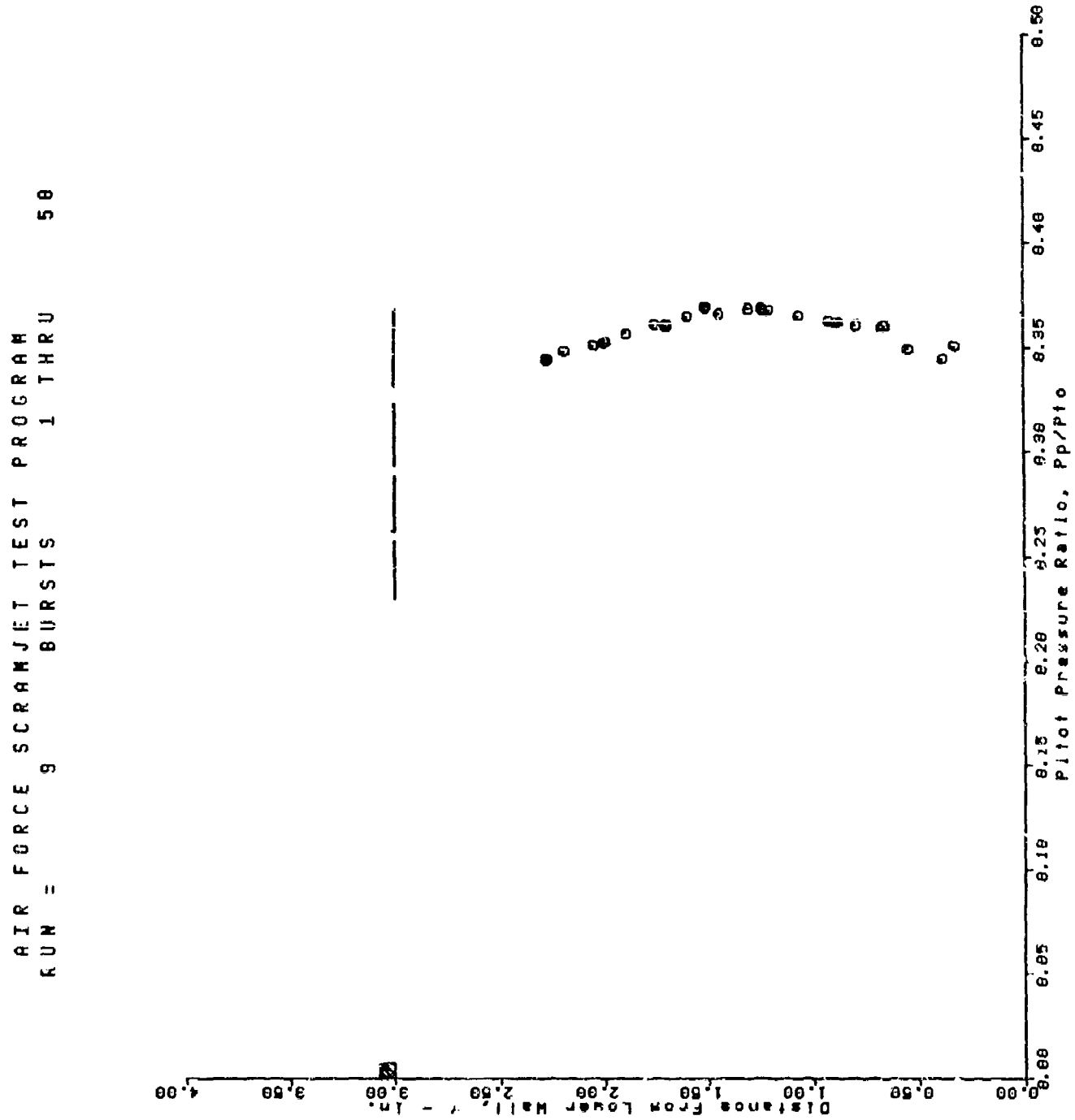
AIR FORCE SCRAMJET TEST PROGRAM
RUN = 9 BURSTS 1 THRU 50
Pitot Pressure Ratio, Pp/Pto
Distance From Lower Wall, y - in.
0.00
0.05
0.10
0.15
0.20
0.25
0.30
0.35
0.40
0.45
0.50
0.00
0.50
1.00
1.50
2.00
2.50
3.00
3.50
4.00

AIR FORCE SCRAMJET TEST PROGRAM
RUN = 11 BURSTS 12 THRU 46

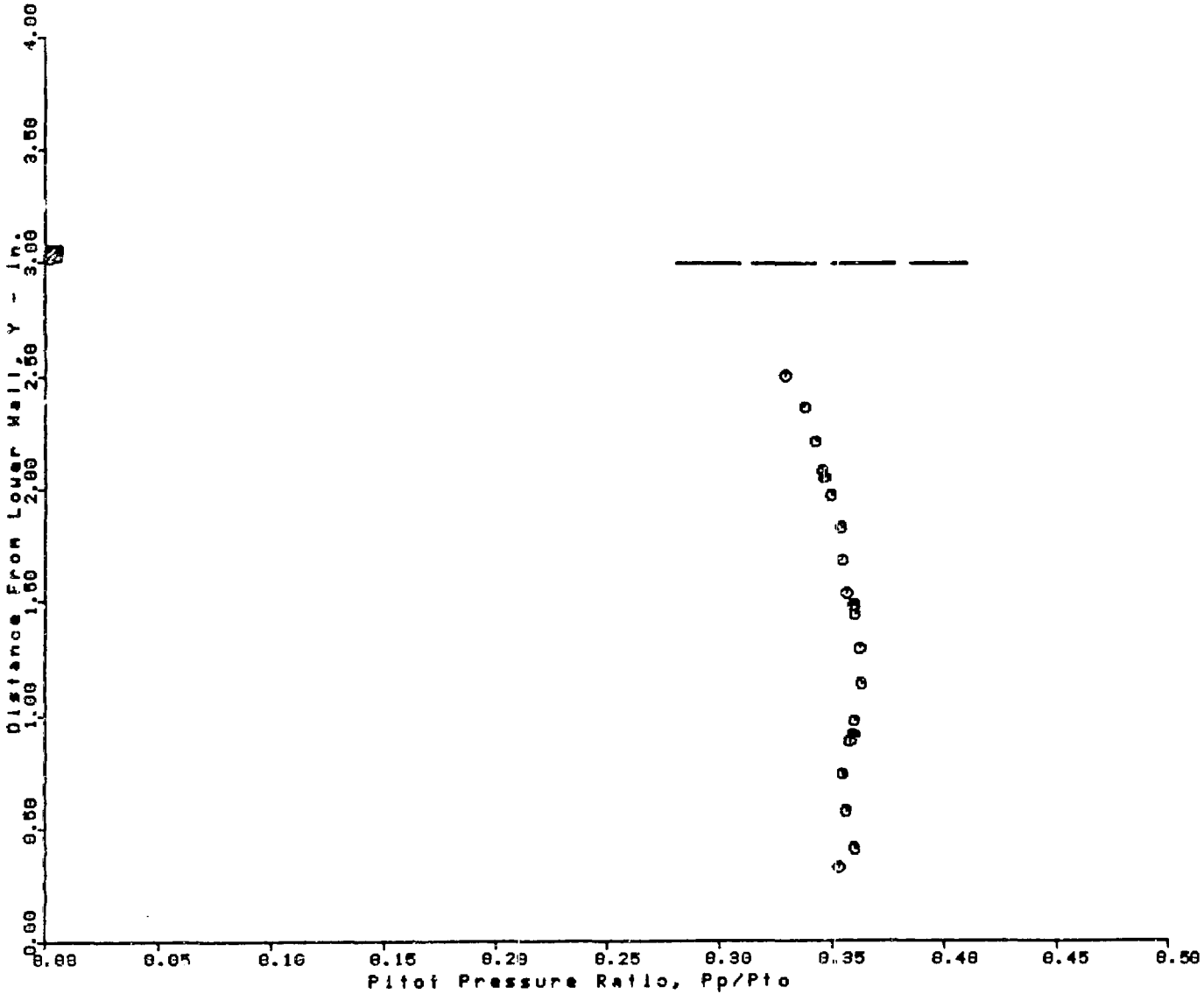

AIR FORCE SCRAMJET TEST PROGRAM
RUN = 12 BURSTS 9 THRU 62

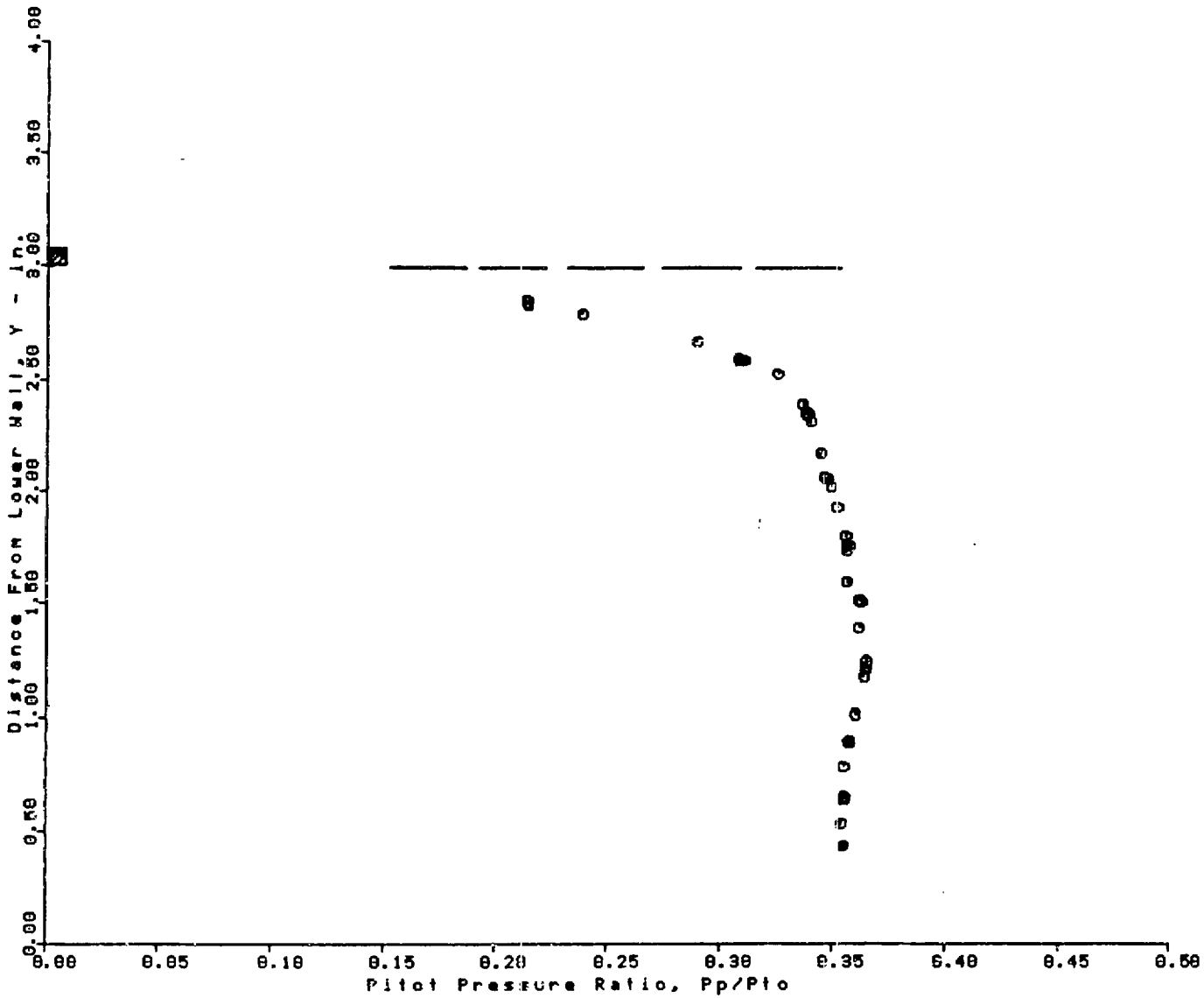

AIR FORCE SCRAMJET TEST PROGRAM
RUN = 14 BURSTS 9 THRU 75

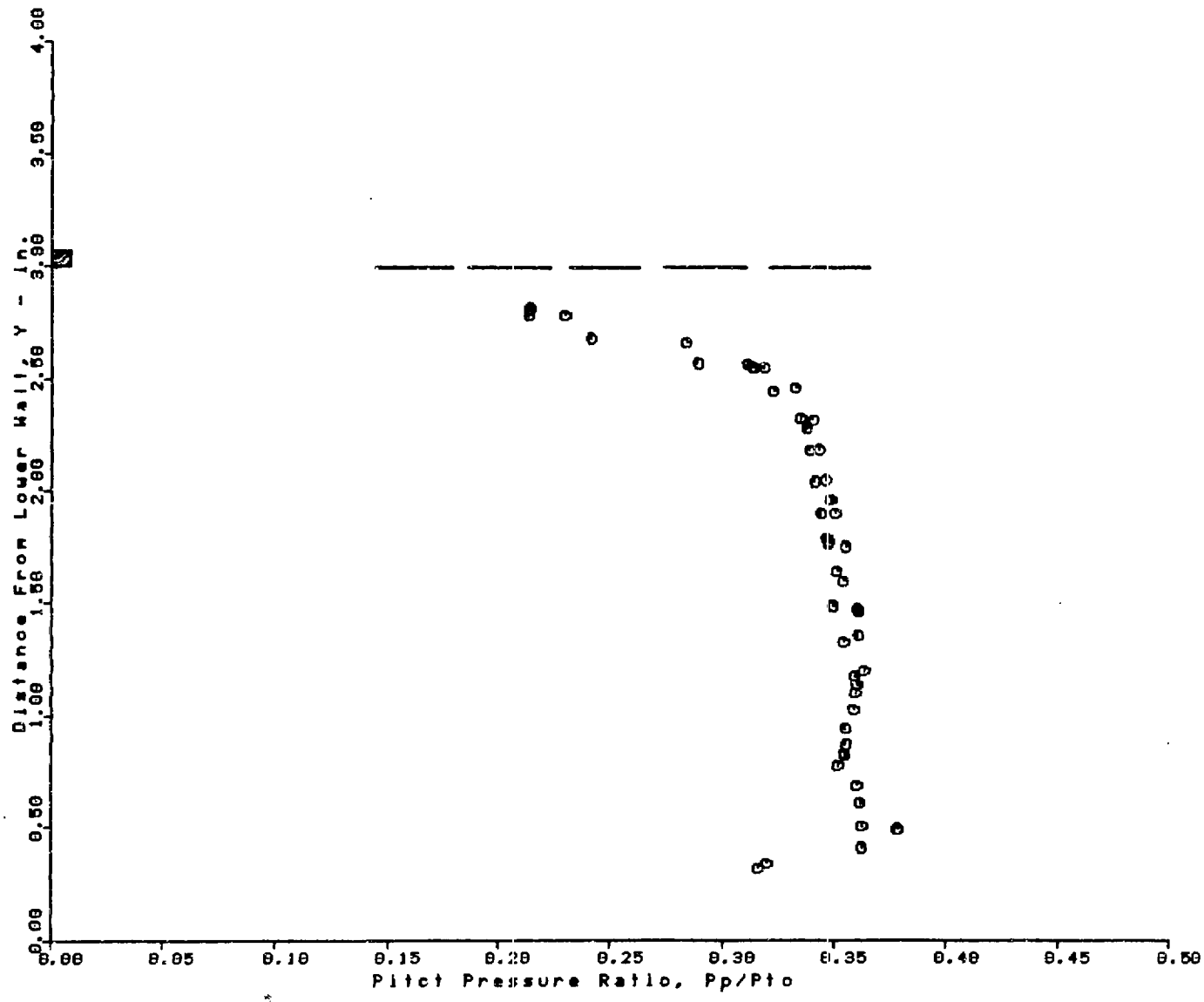

AIR FORCE SCRAMJET TEST PROGRAM
RUN = 23 BURSTS 18 THRU 44

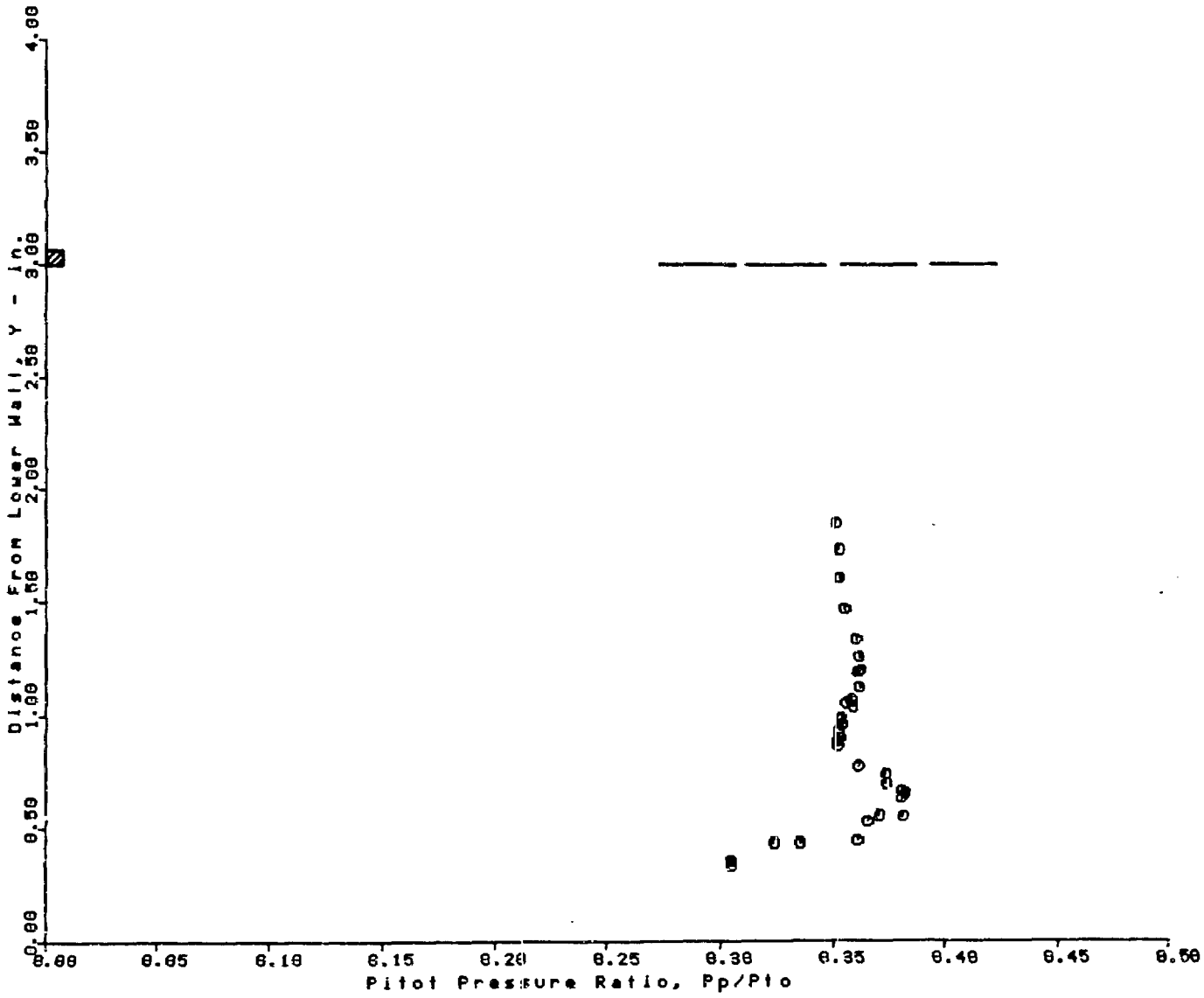

AFS TEST PROGRAM
RUN = 36 BURSTS 38 THRU 74

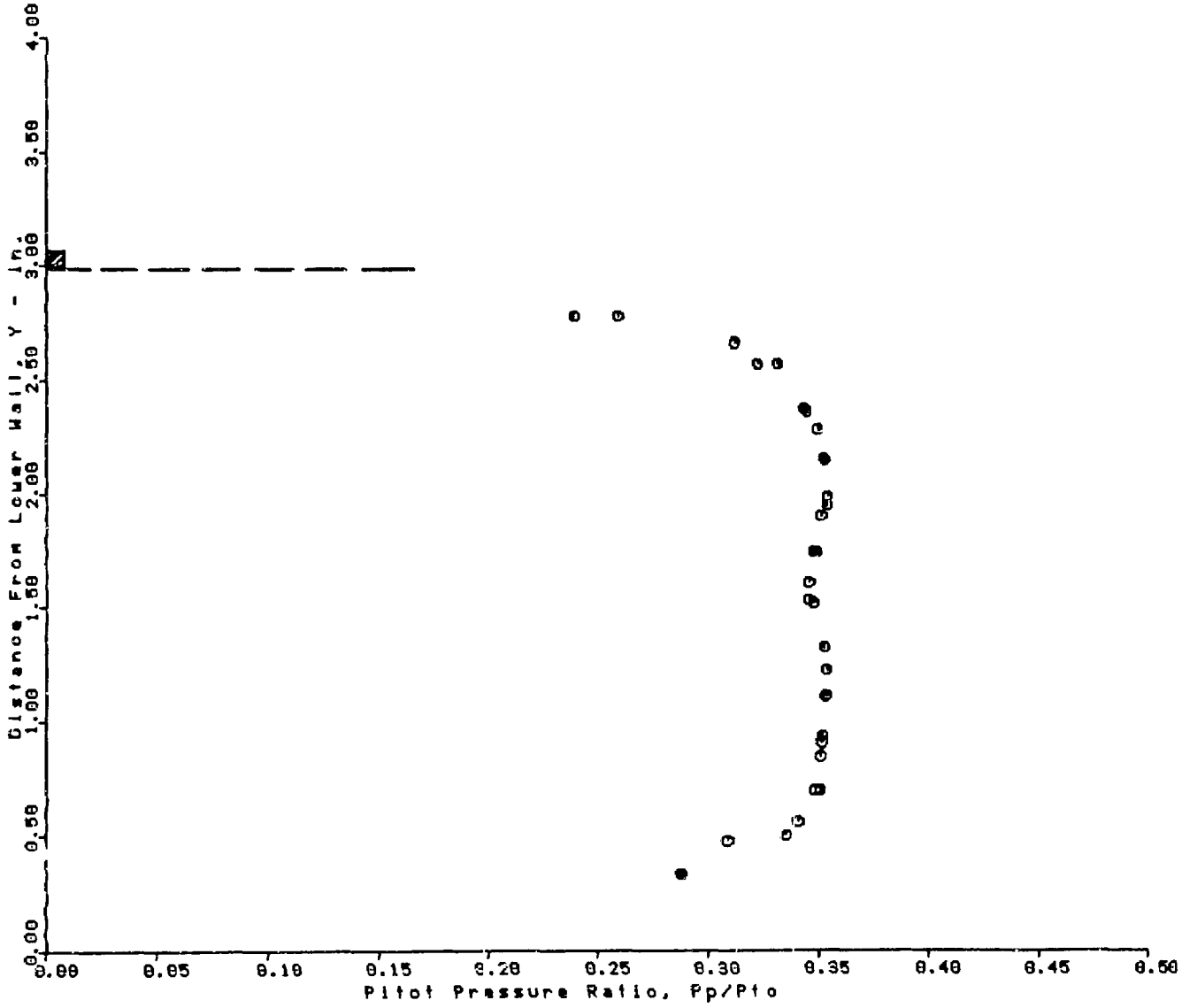

AFS TEST PROGRAM
RUN = 37 BURSTS 20 THRU 55

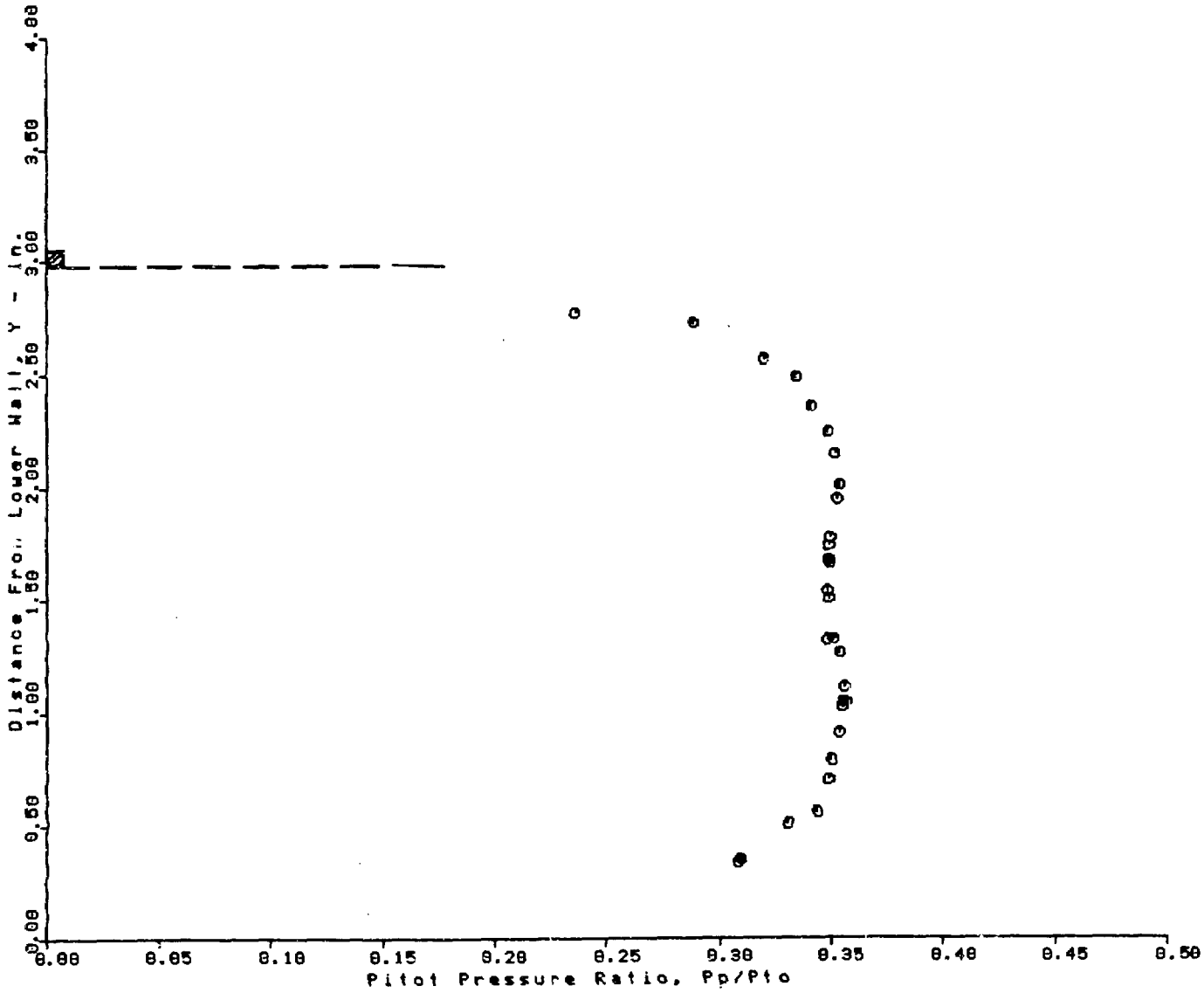

AFS TEST PROGRAM
RUN = 38 BURSTS 22 THRU 64

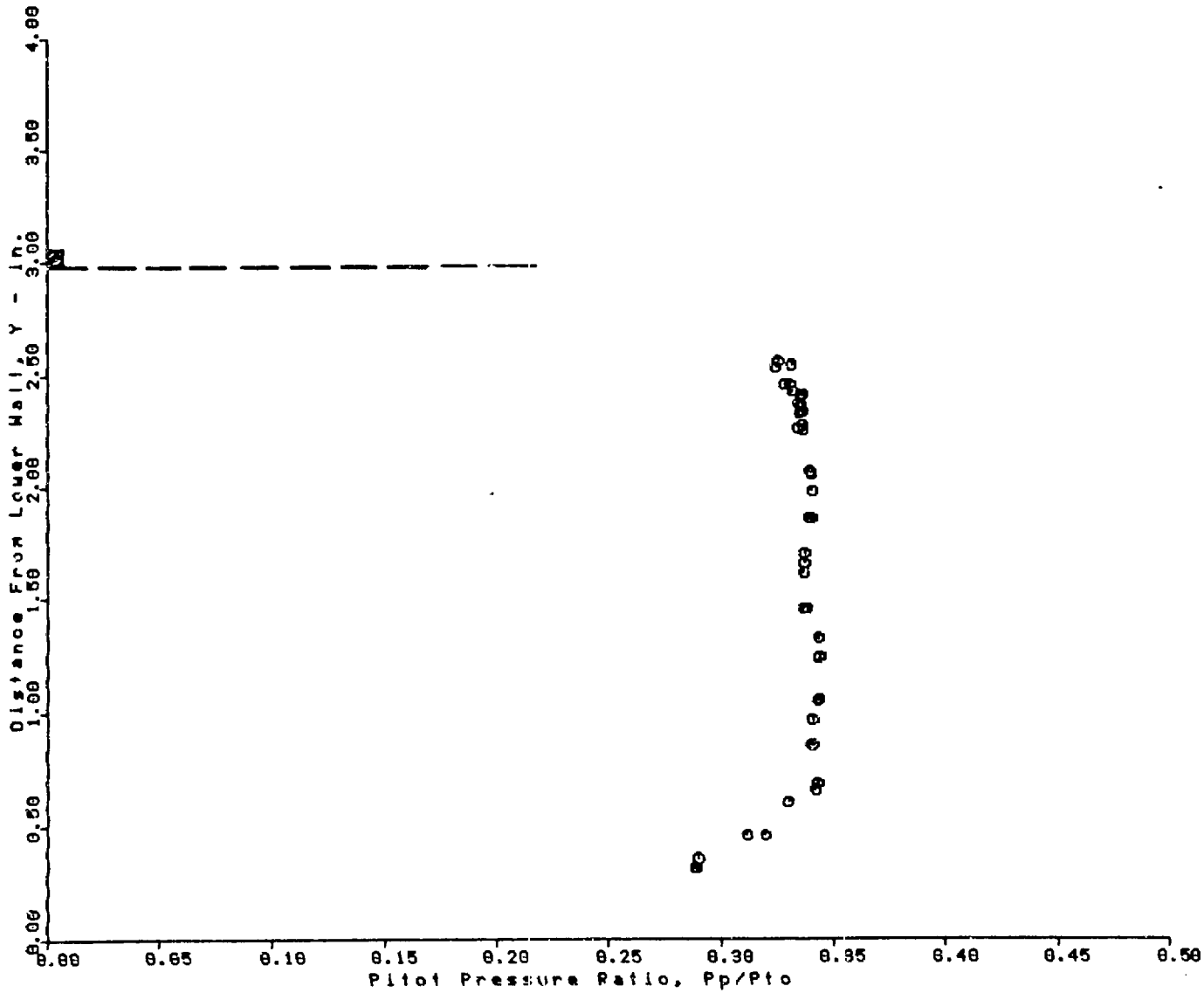

AFS TEST PROGRAM
RUN = 44 BURSTS 26 THRU 58

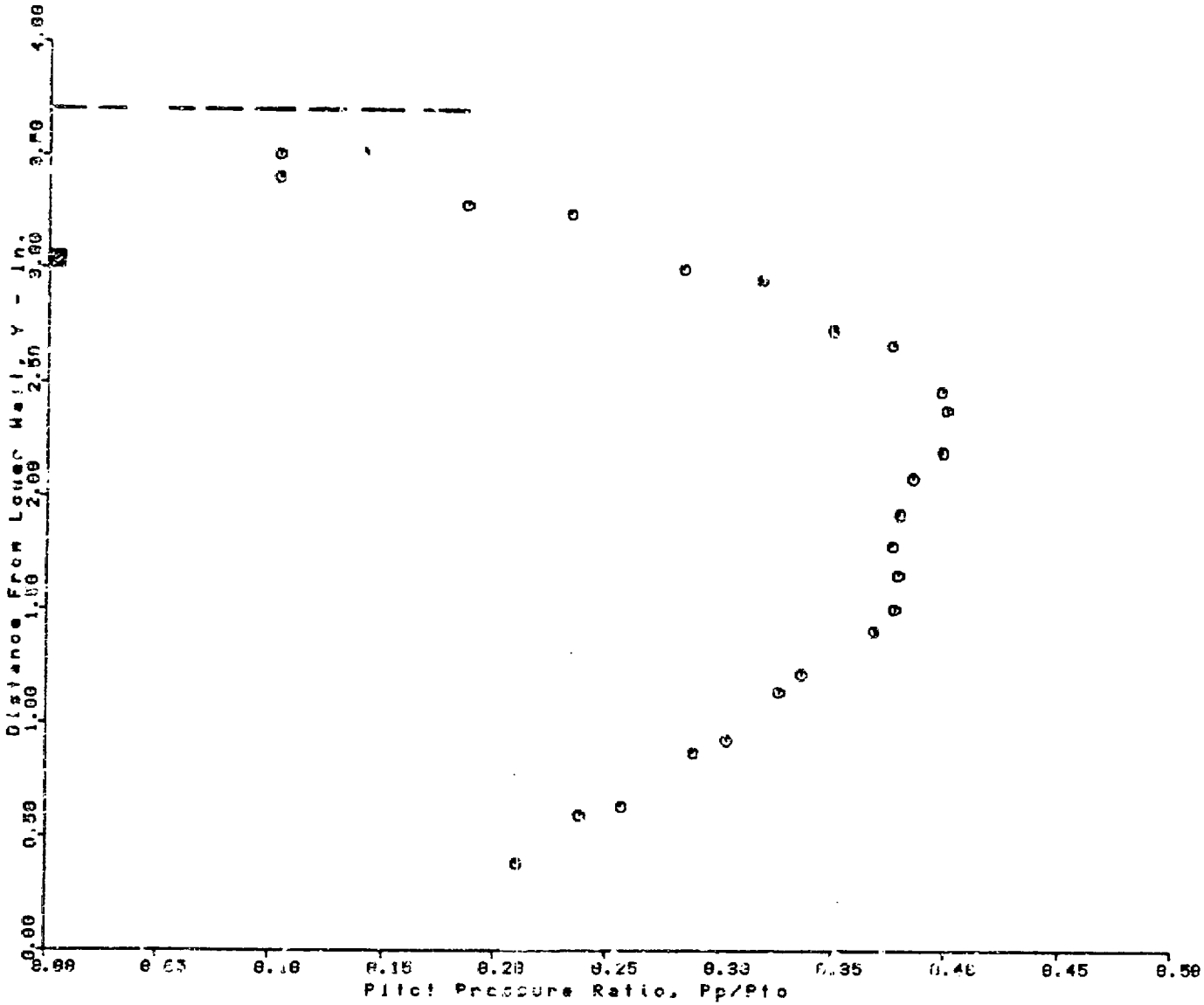

AFS TEST PROGRAM
RUN = 45 BURSTS 25 THRU 58

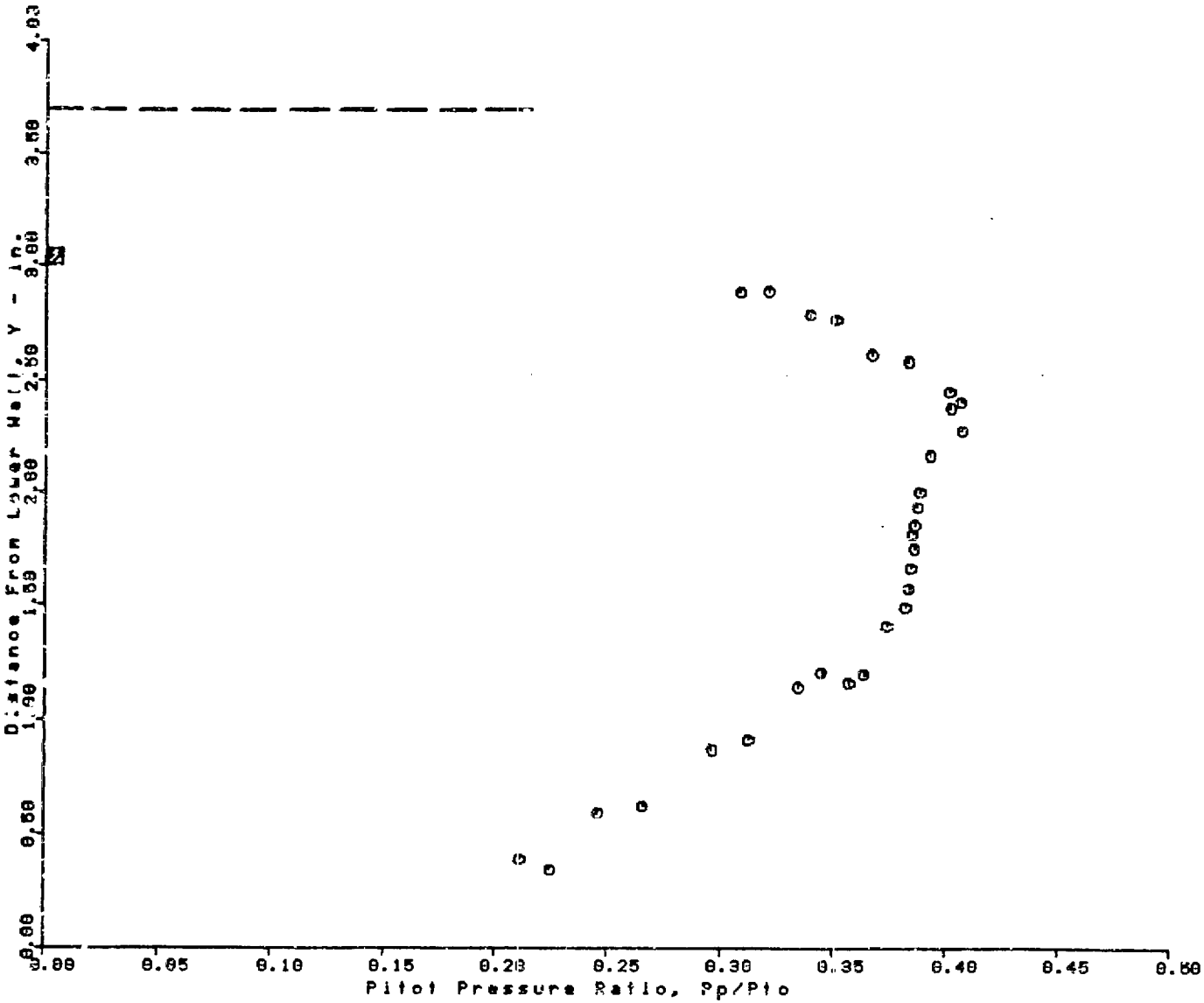

AFS TEST PROGRAM
RUN = 46 BURSTS 27 THRU 53

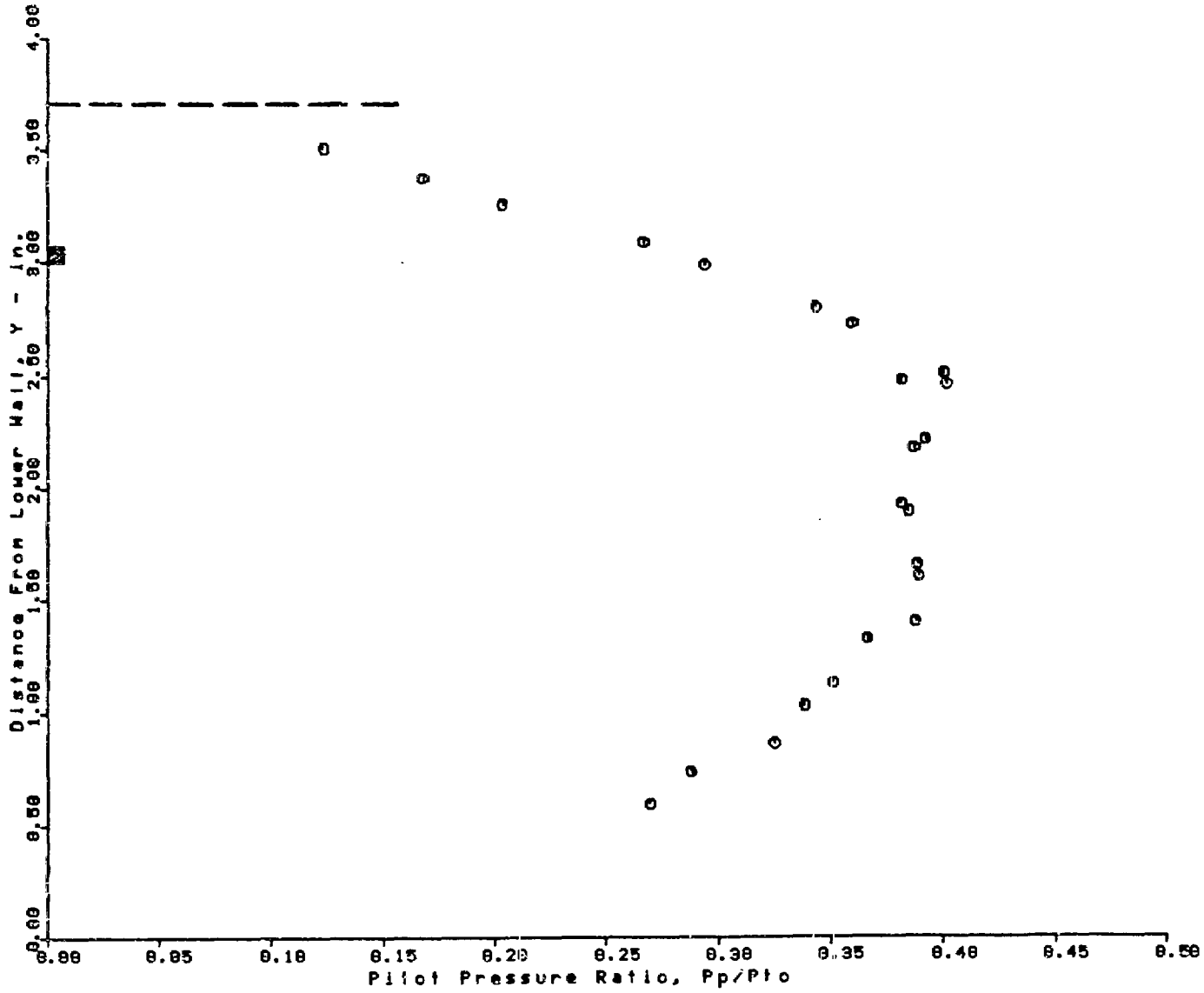

AFS TEST PROGRAM
RUN = 49 BURSTS 43 THRU 64

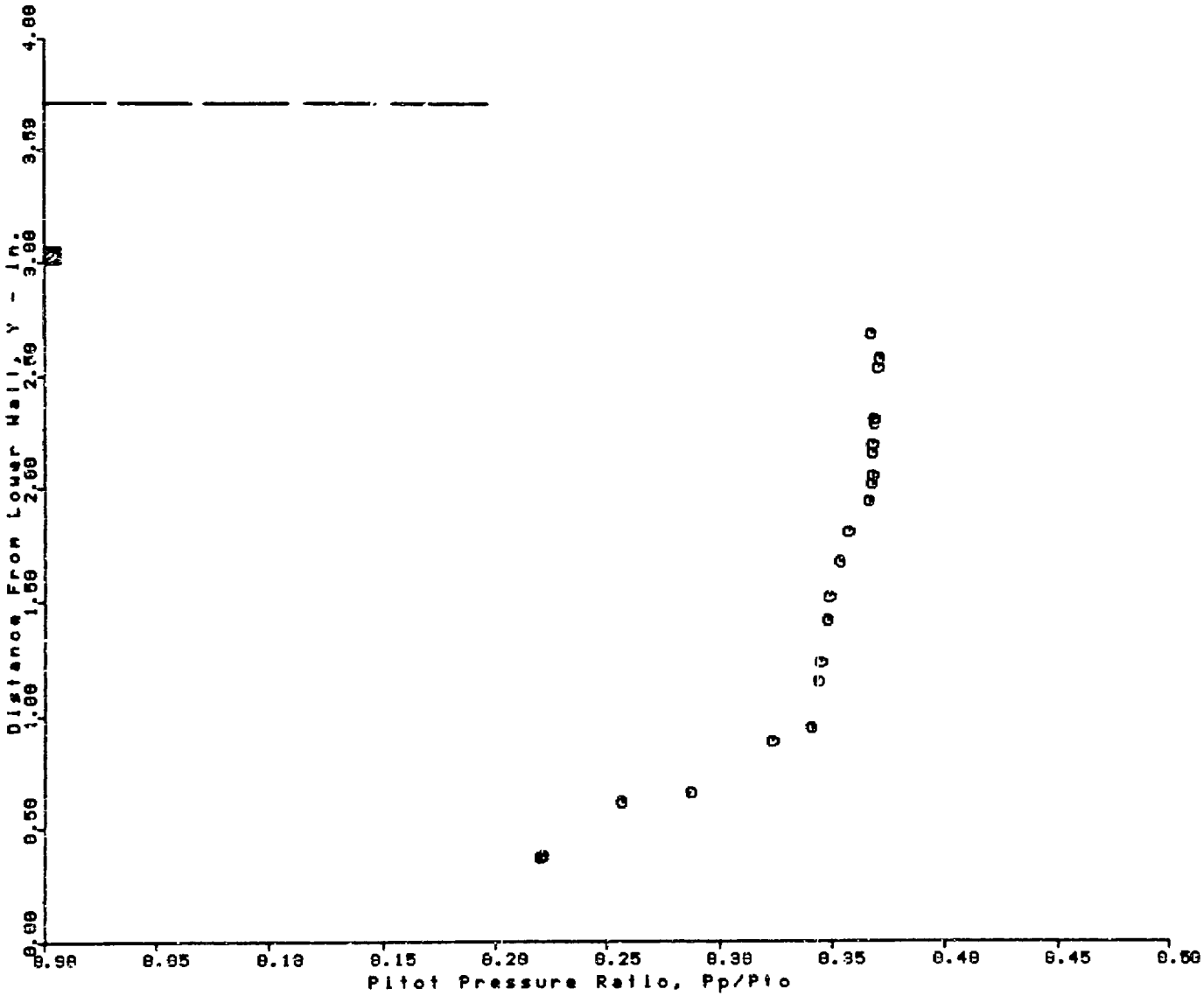

AFS TEST PROGRAM
RUN = 50 BURSTS 30 THRU 66

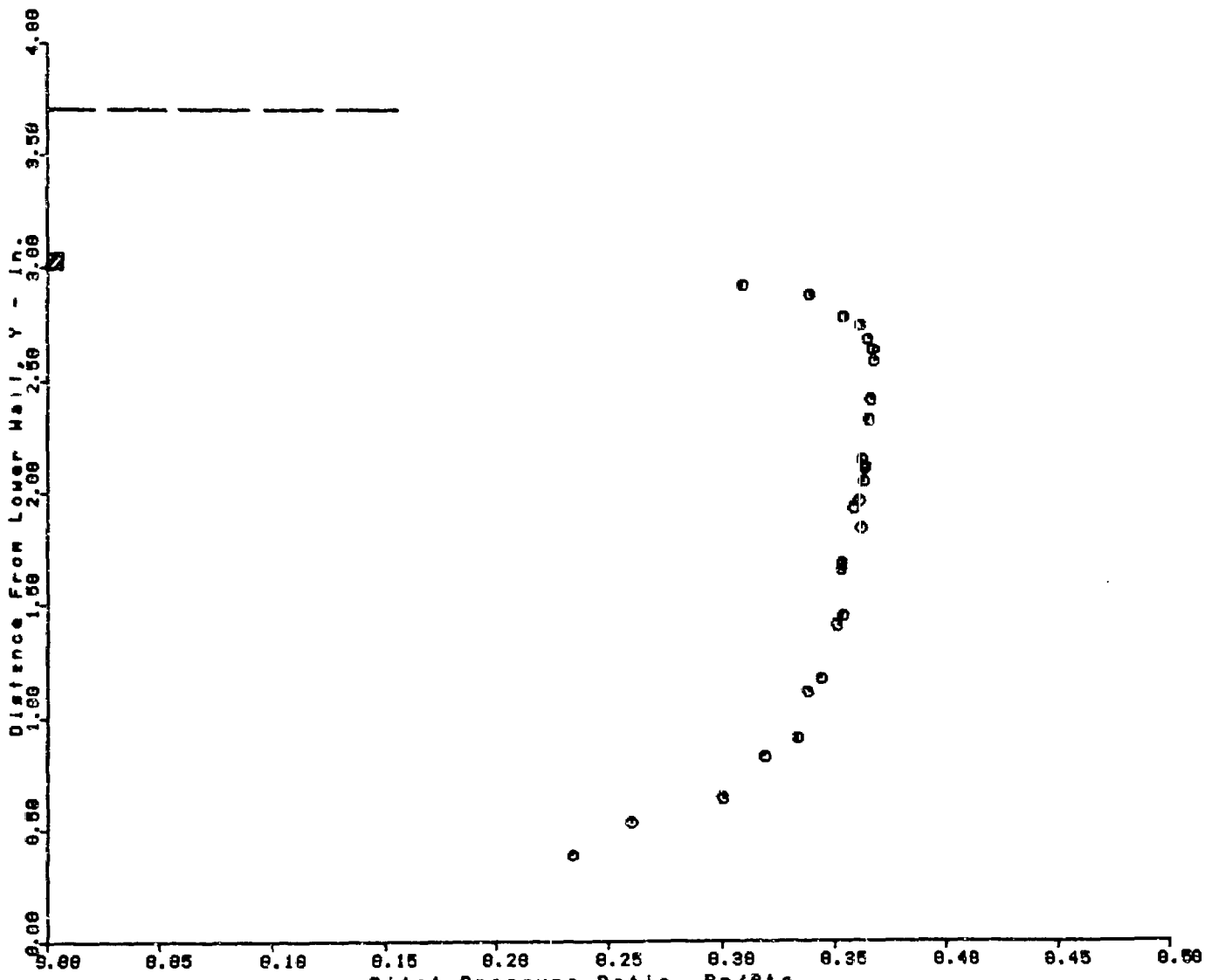

AFS TEST PROGRAM
RUN = 52 BURSTS 25 THRU 60

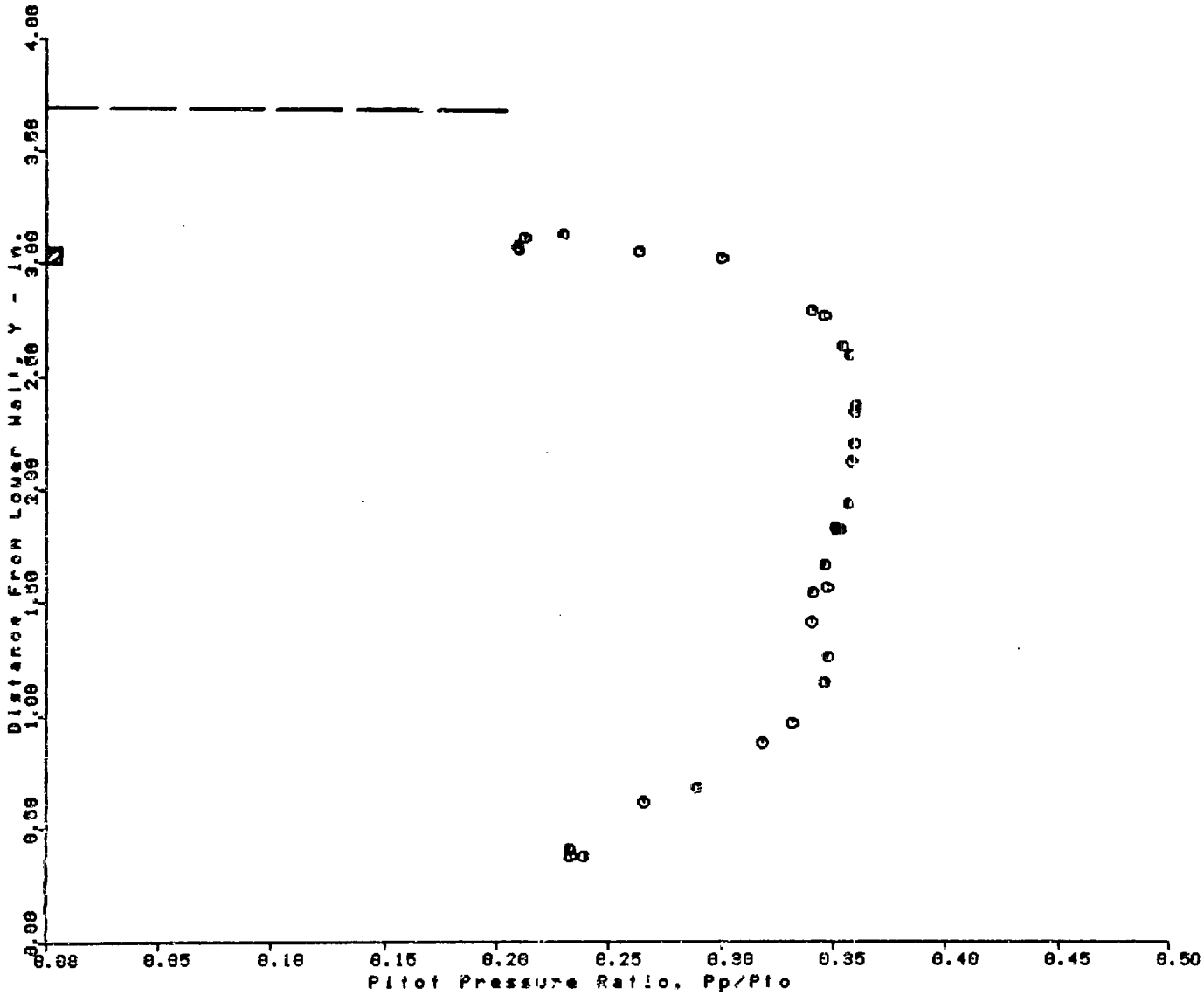

AFS TEST PROGRAM
RUN = 53 BURSTS 26 THRU 59

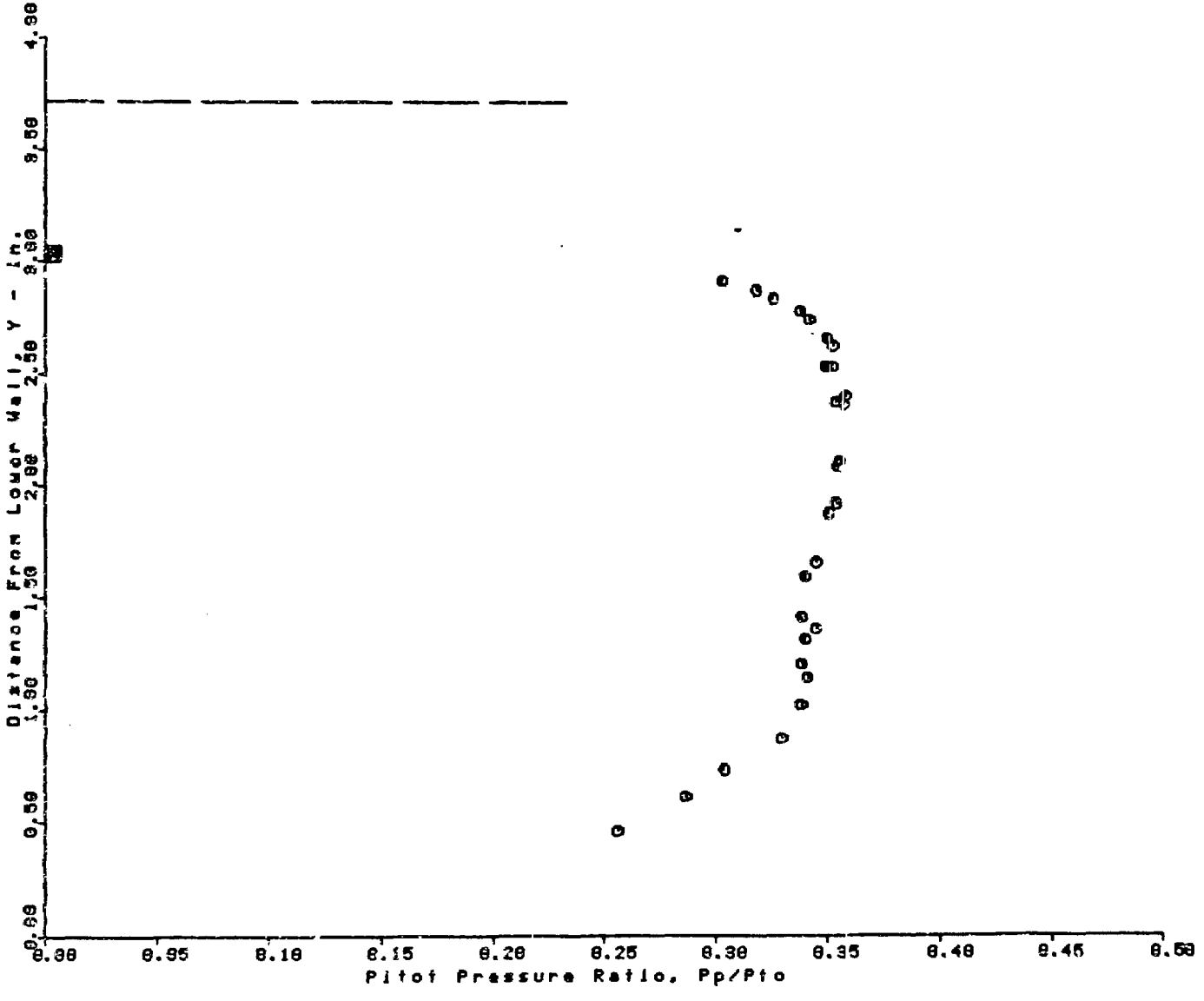

AFS TEST PROGRAM
RUN = 54 BURSTS 27 THRU 52

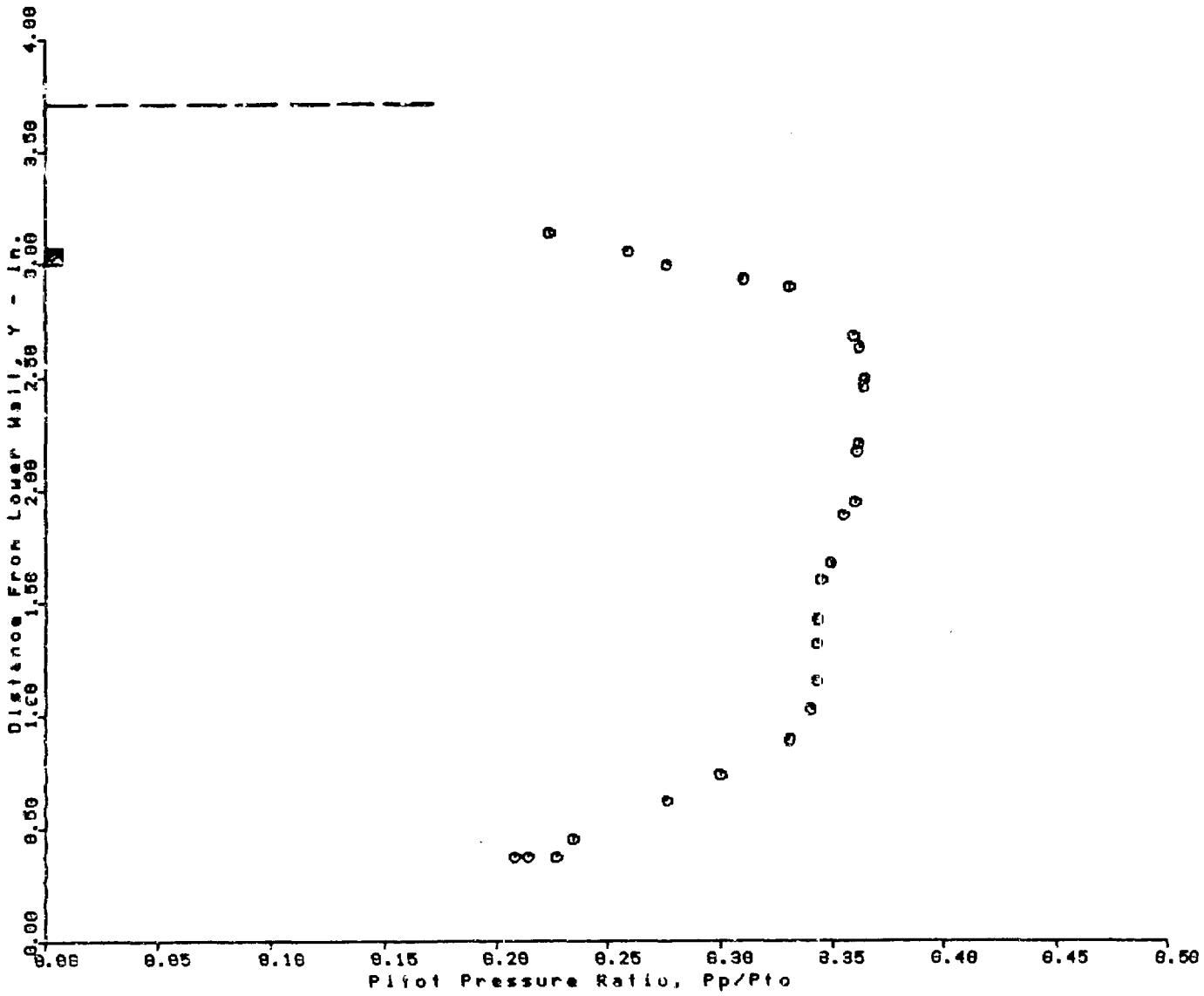

AFS TEST PROGRAM
RUN = 55 BURSTS 26 THRU 50

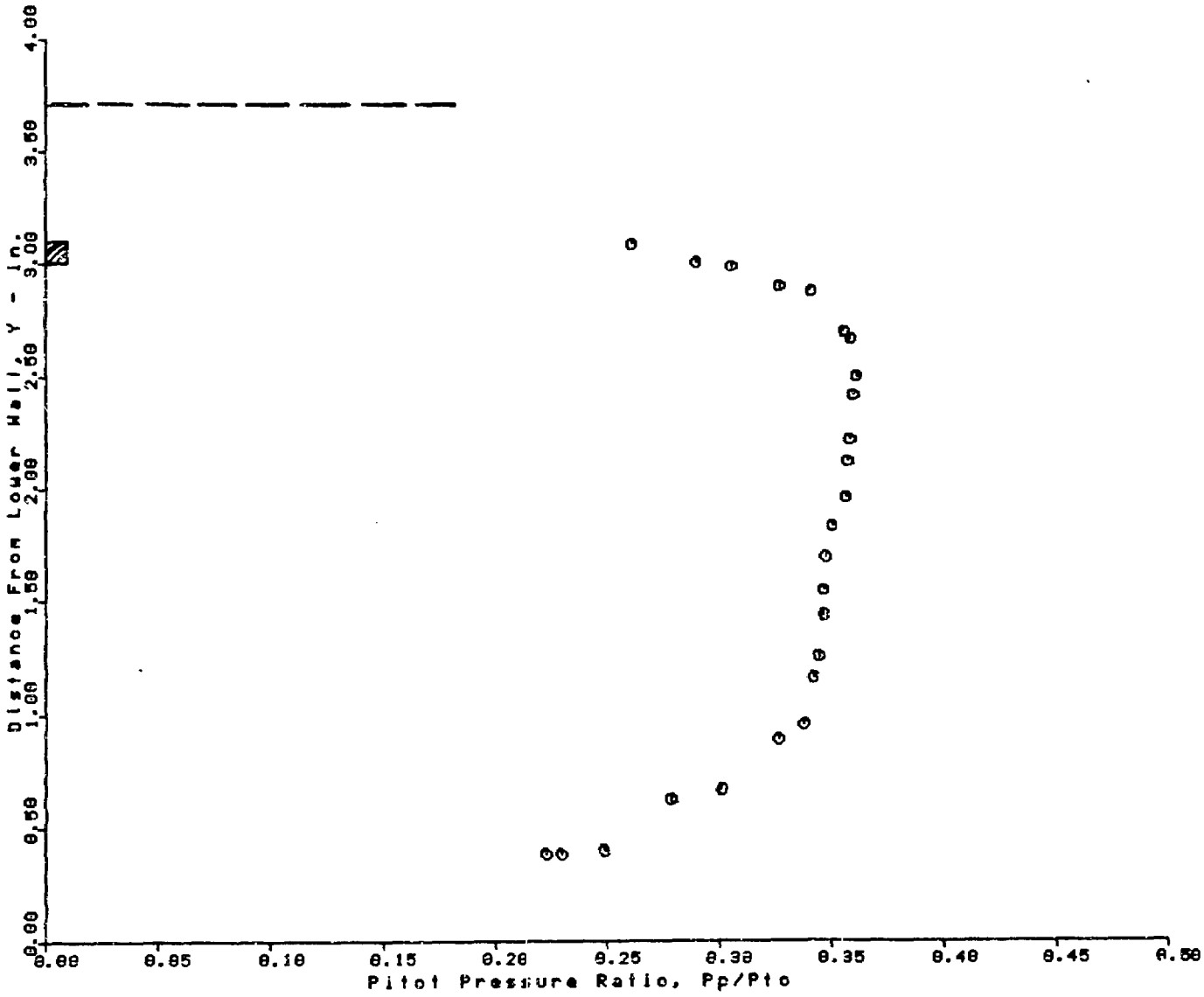

AFS TEST PROGRAM
RUN = 57 BURSTS 27 THRU 58

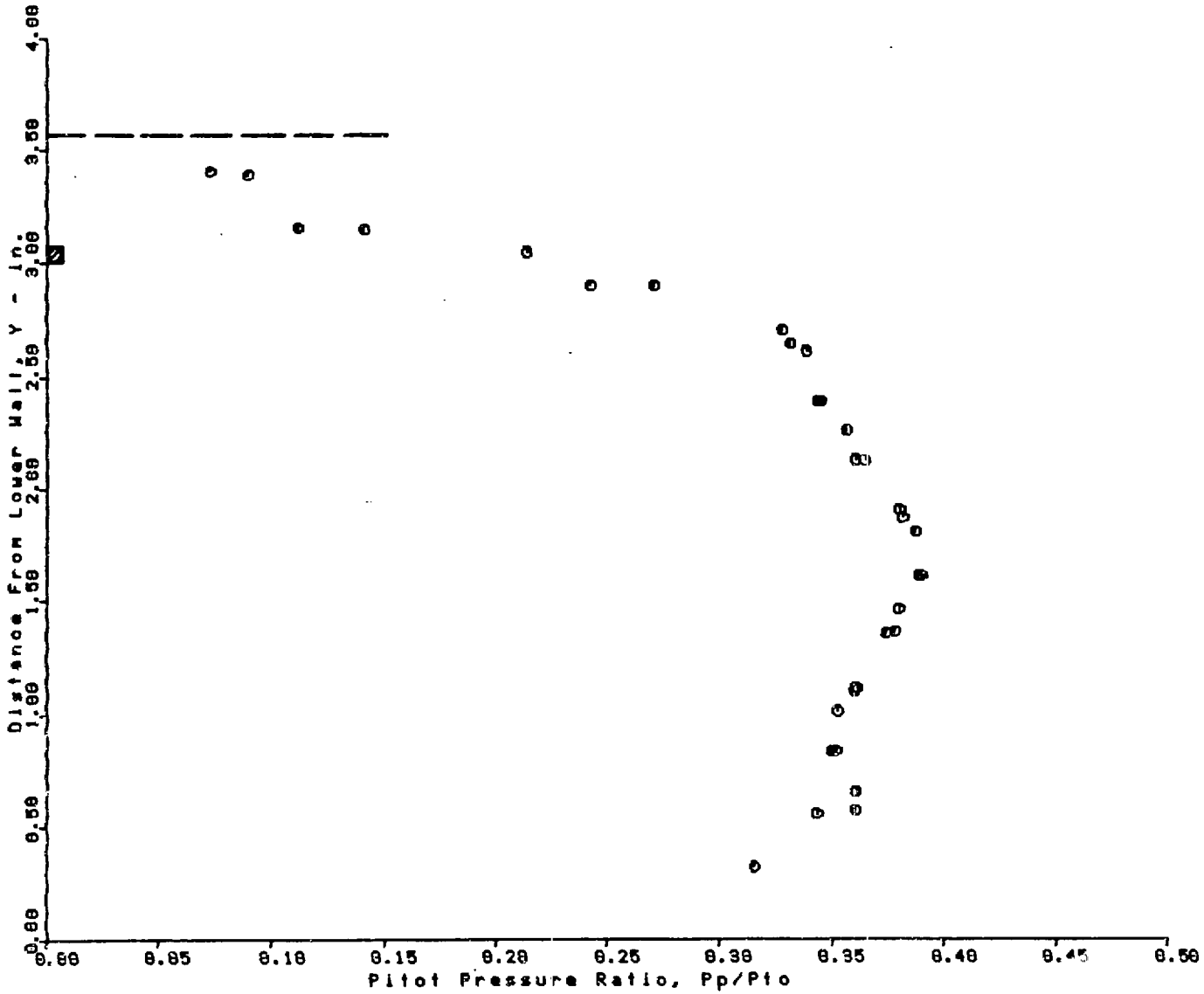

AFS TEST PROGRAM
RUN = 58 BURSTS 26 THRU 48

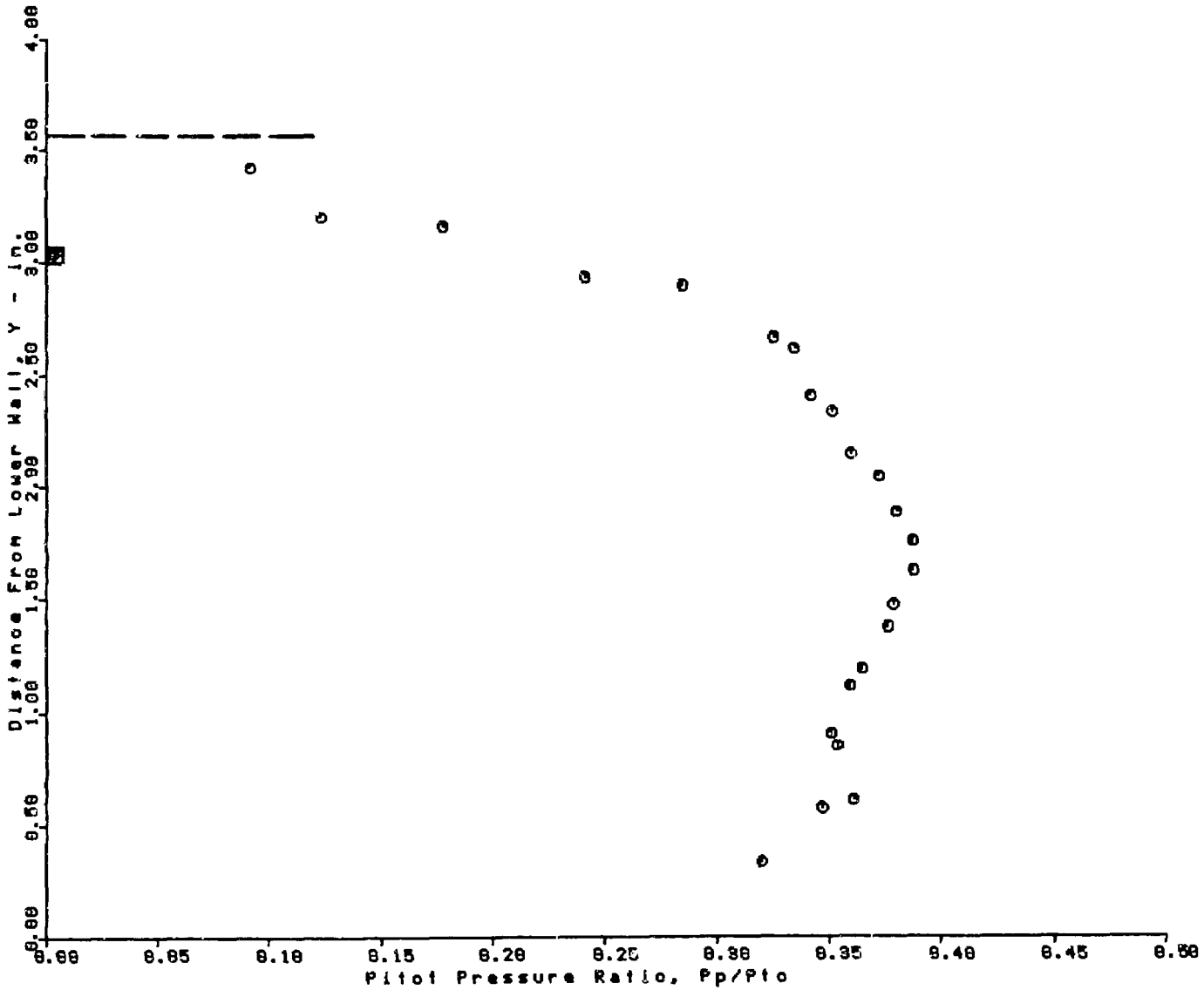

AFS TEST PROGRAM
RUN = 59 BURSTS 25 THRU 47

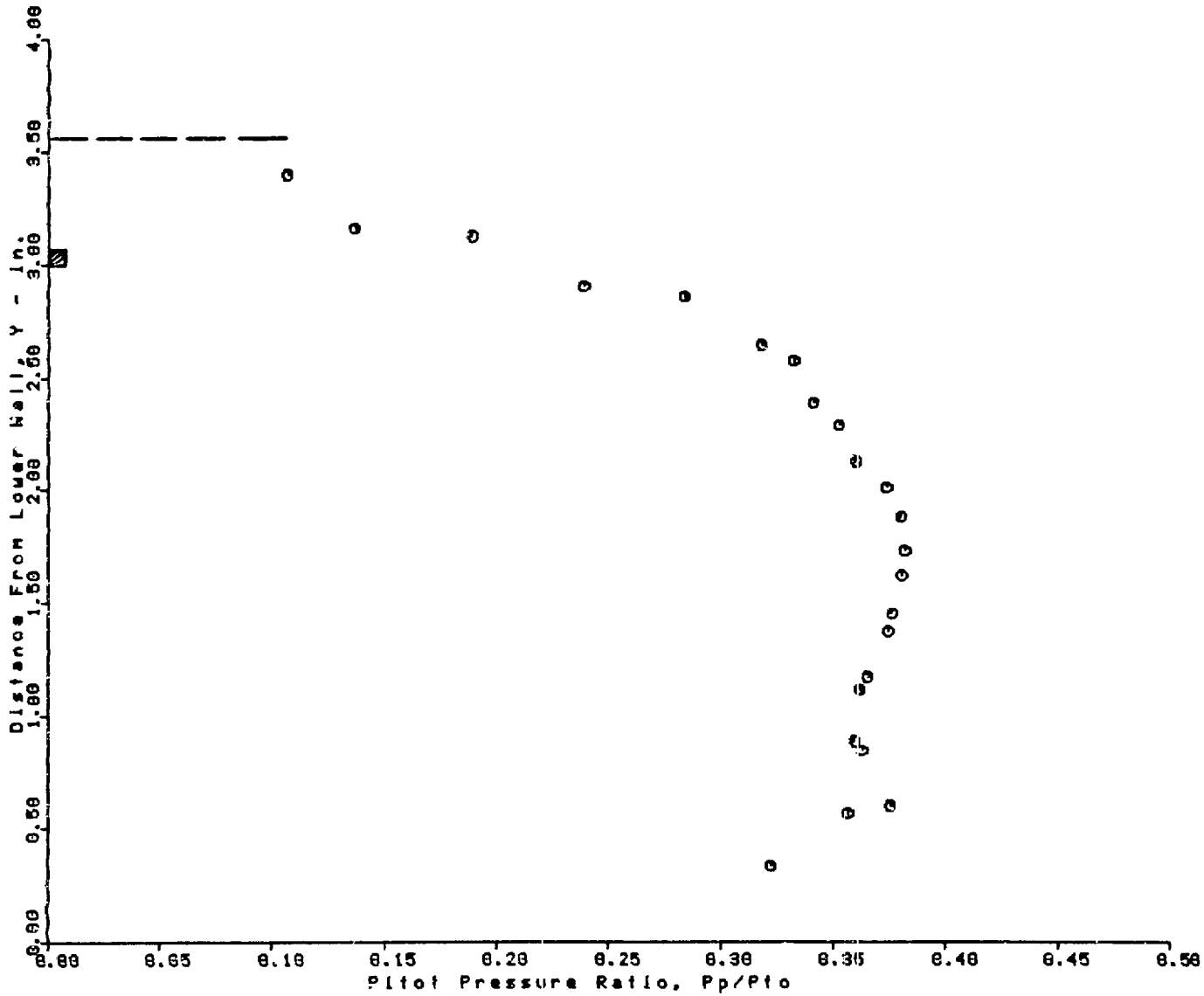

AFS TEST PROGRAM
RUN = 61 BURSTS 26 THRU 46

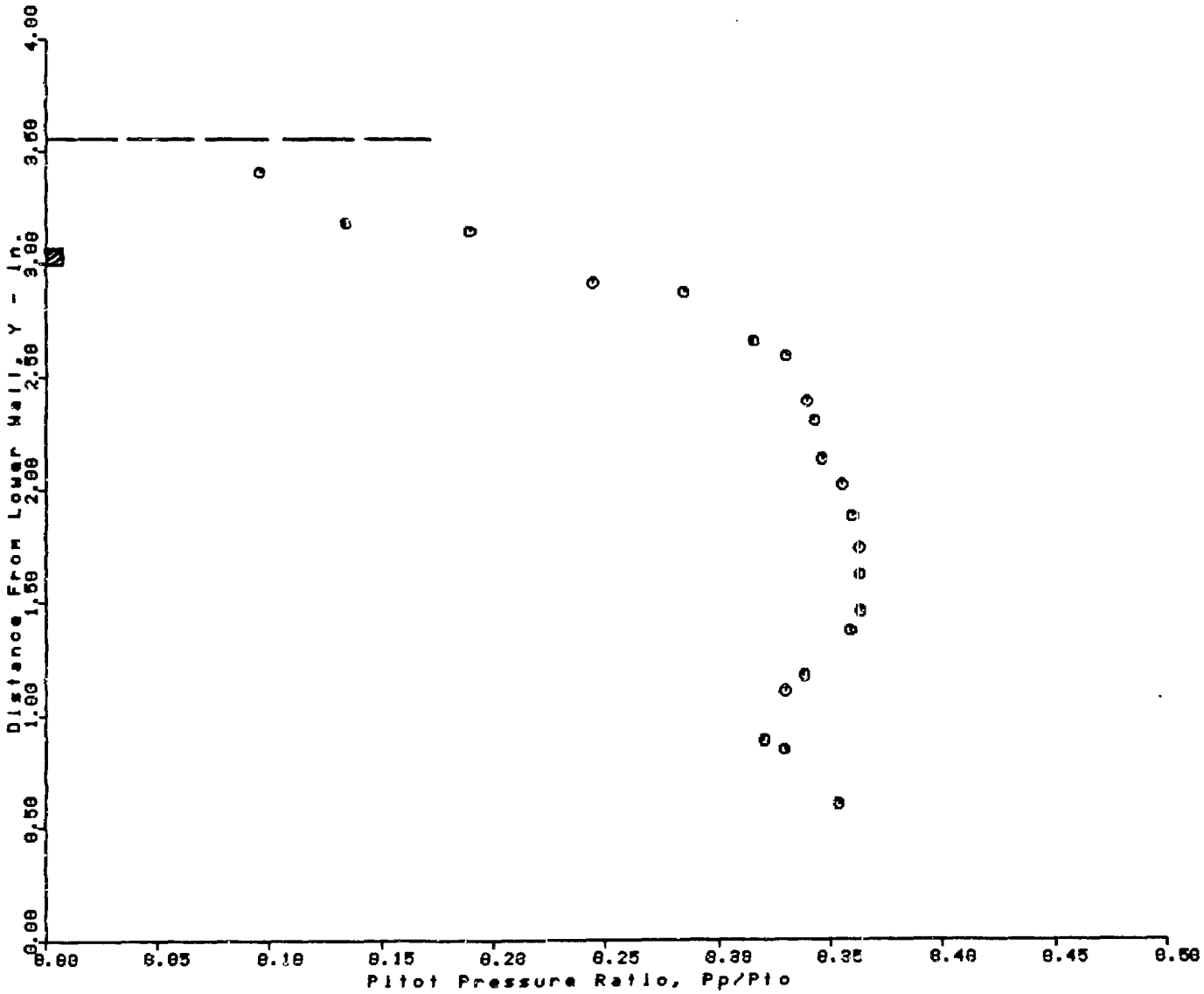

AFS TEST PROGRAM
RUN = 62 BURSTS 29 THRU 58

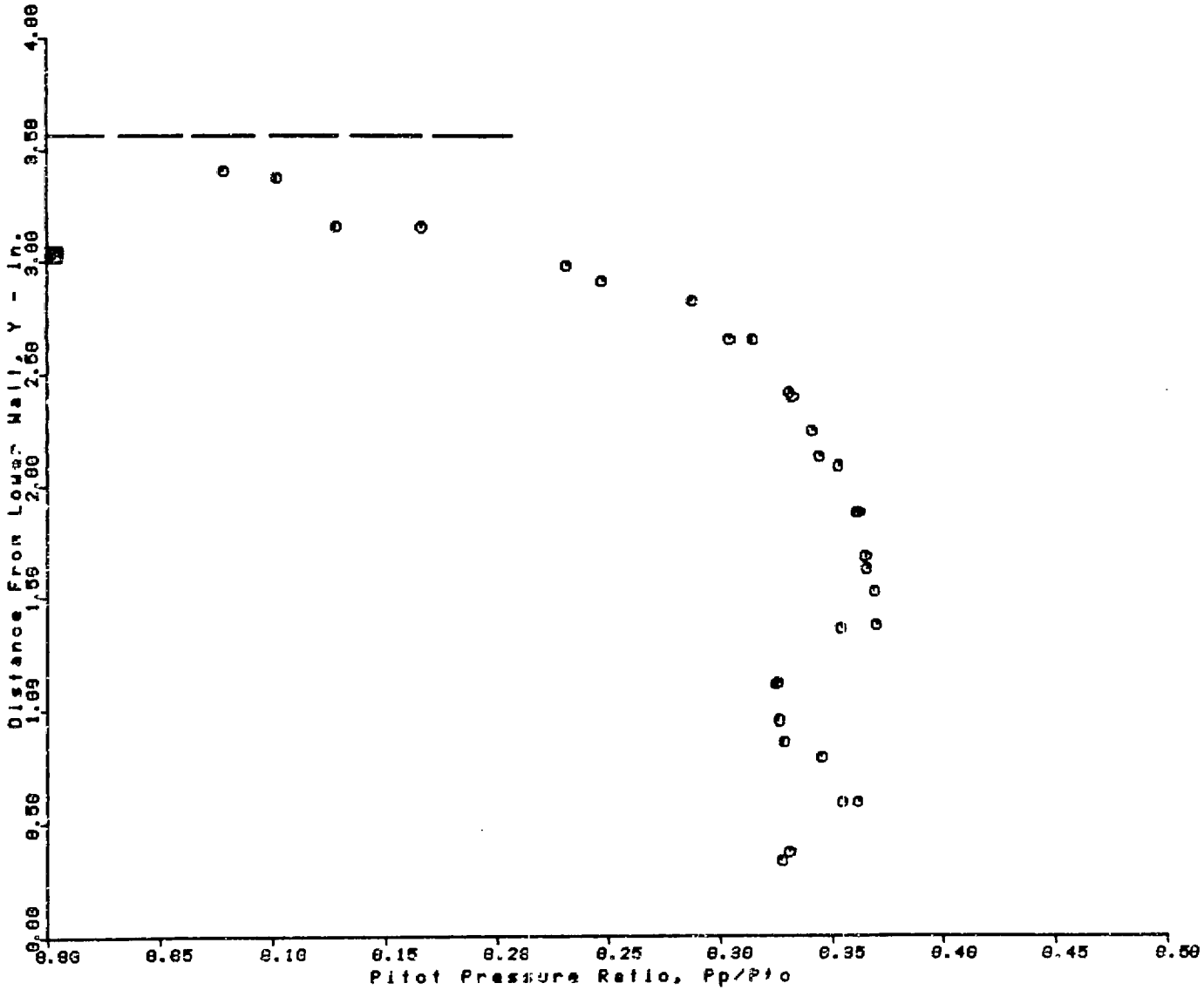

AFS TEST PROGRAM
RUN = 63 BURSTS 33 THRU 62

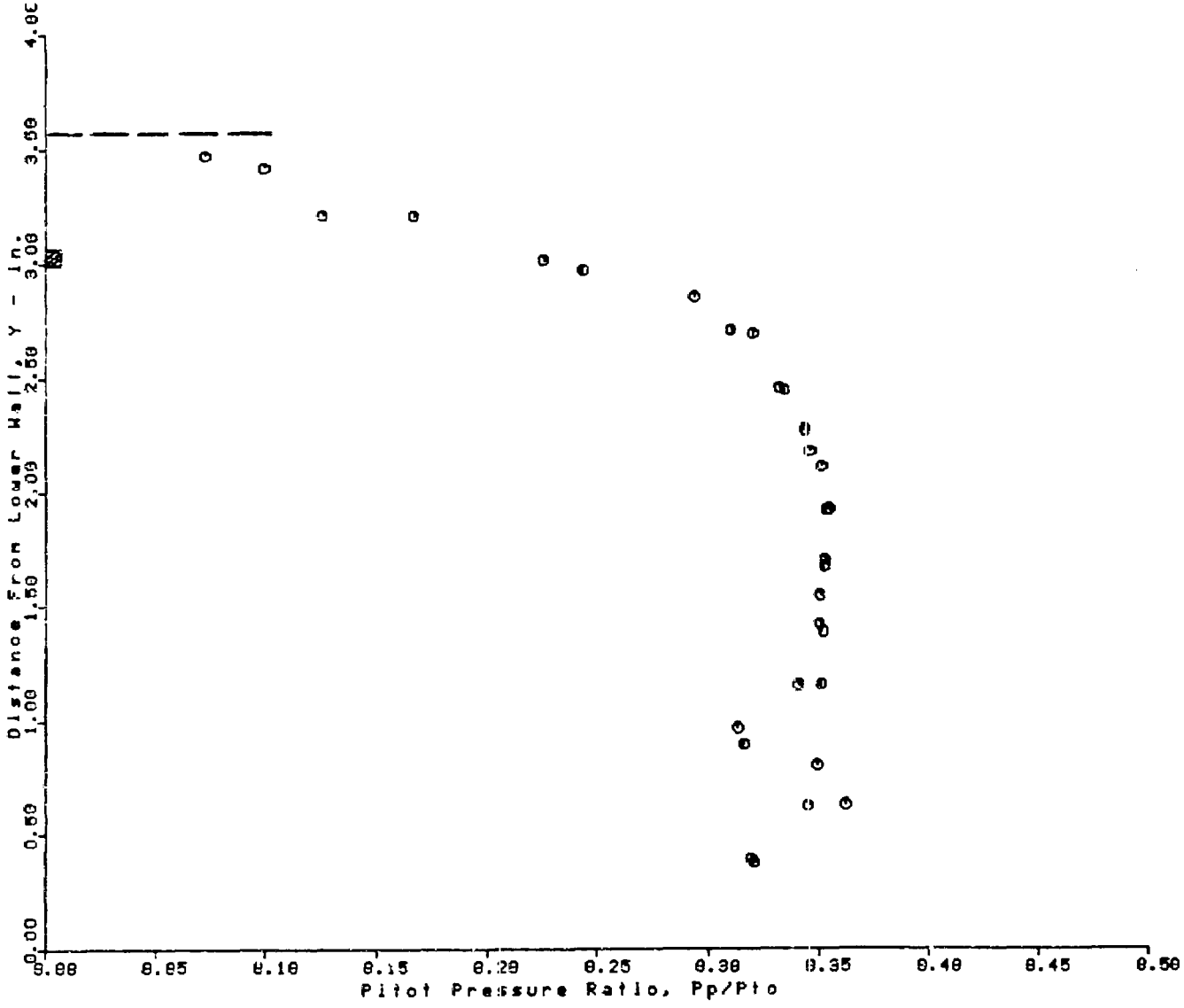

AFS TEST PROGRAM
RUN = 64 BURSTS 27 THRU 56

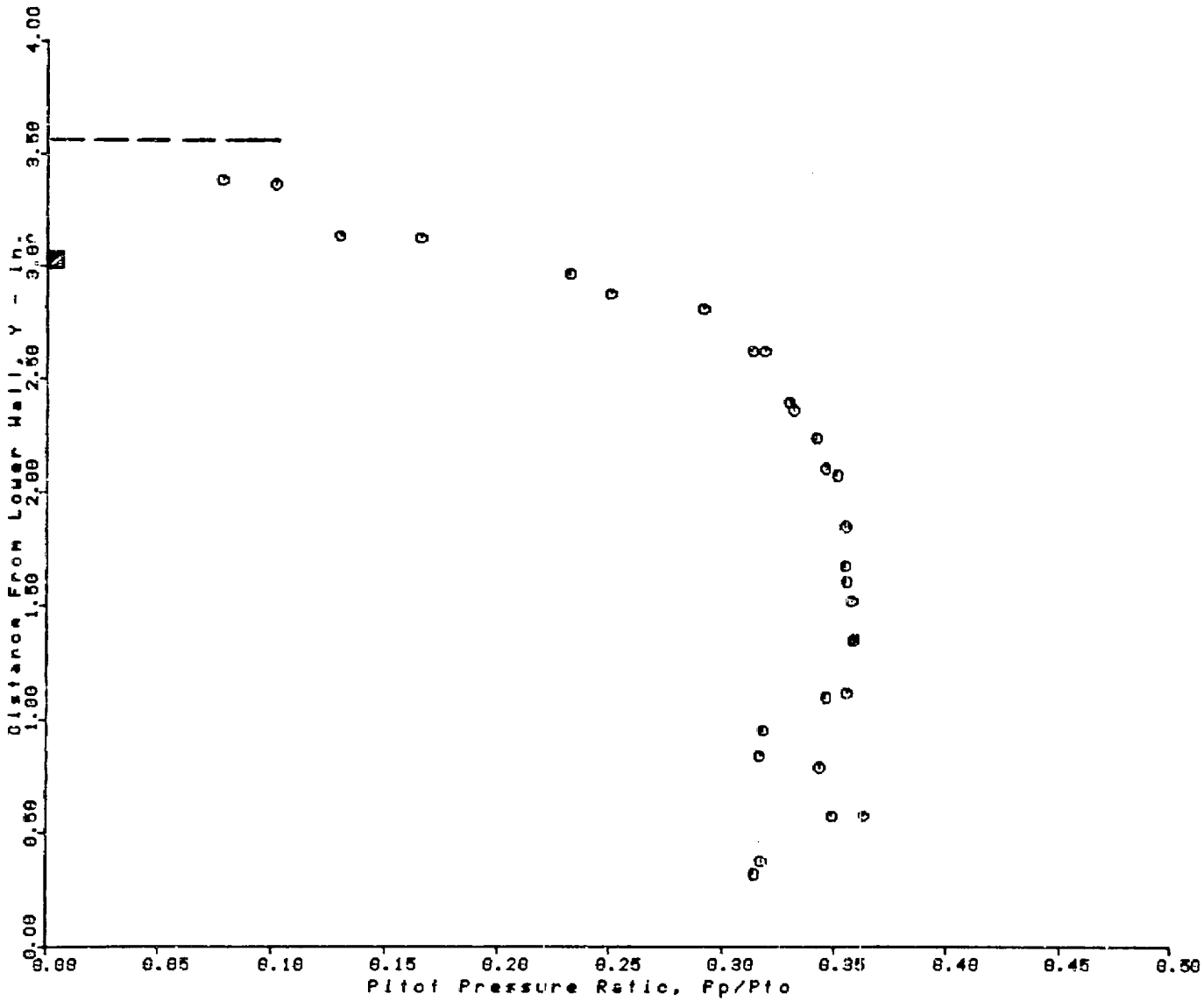

AFS TEST PROGRAM
RUN = 65 BURSTS 38 THRU 59

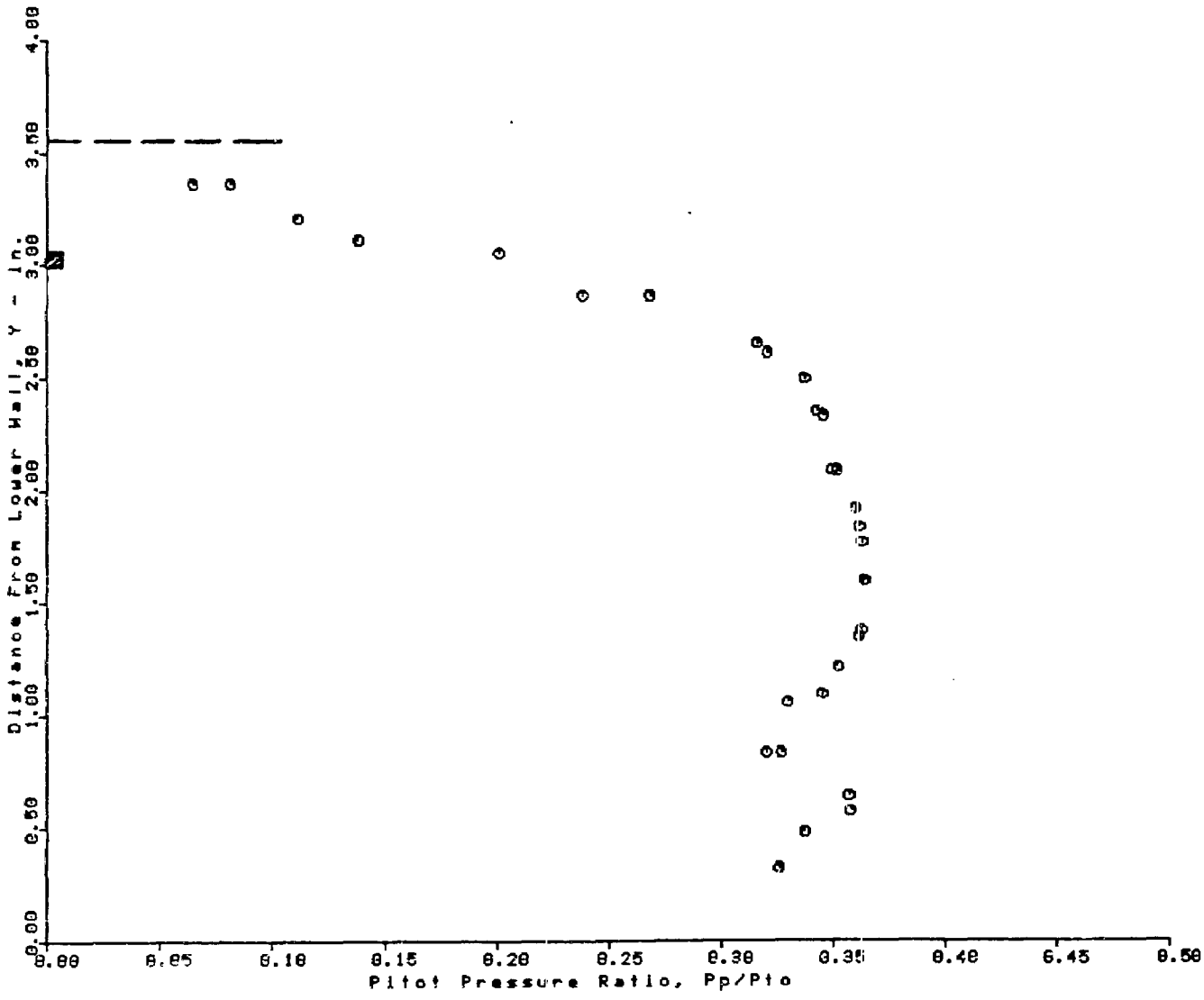

AFS TEST PROGRAM
RUN = 66 BURSTS 30 THRU 59

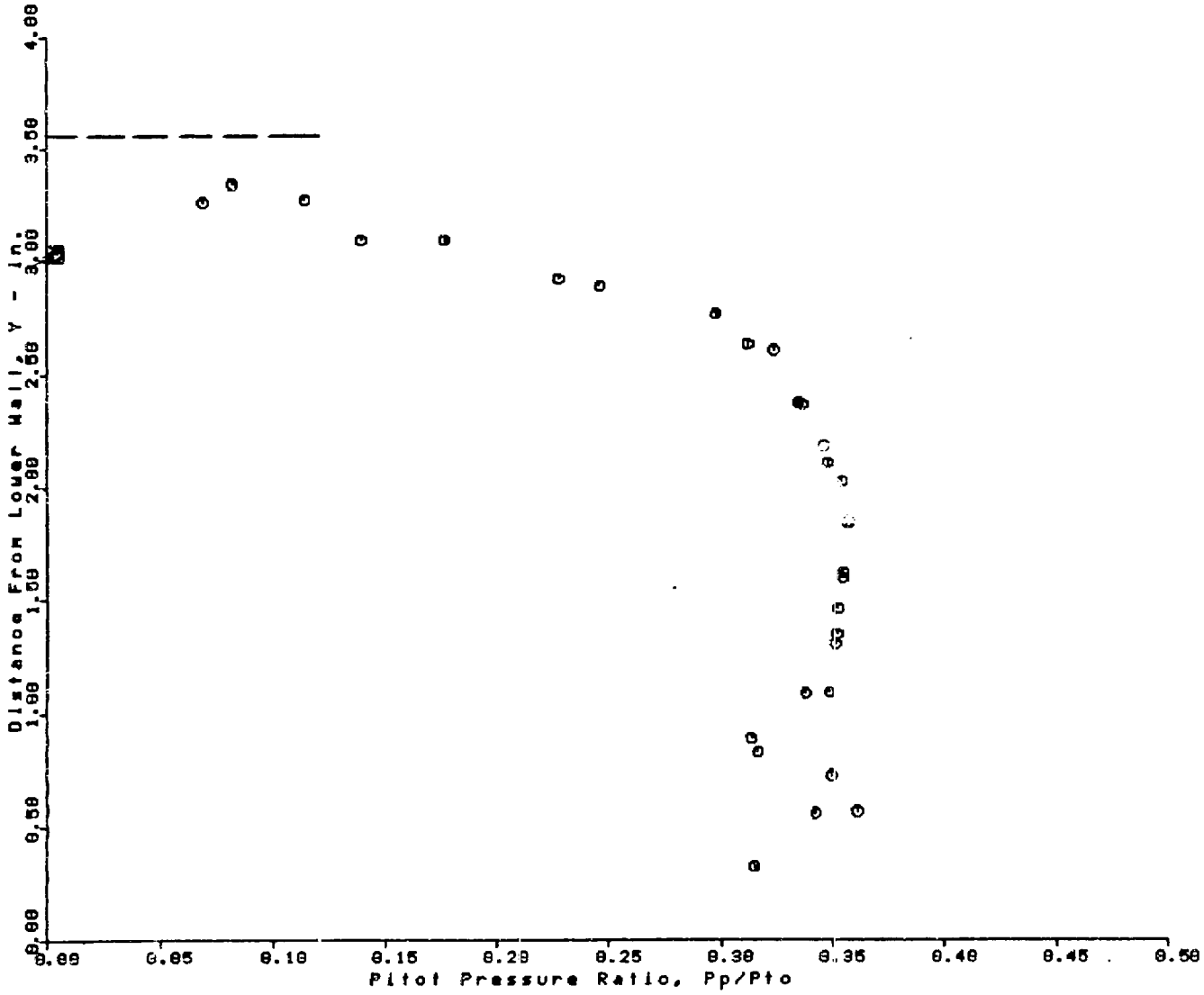

AFS TEST PROGRAM
RUN = 69 BURSTS 34 THRU 63

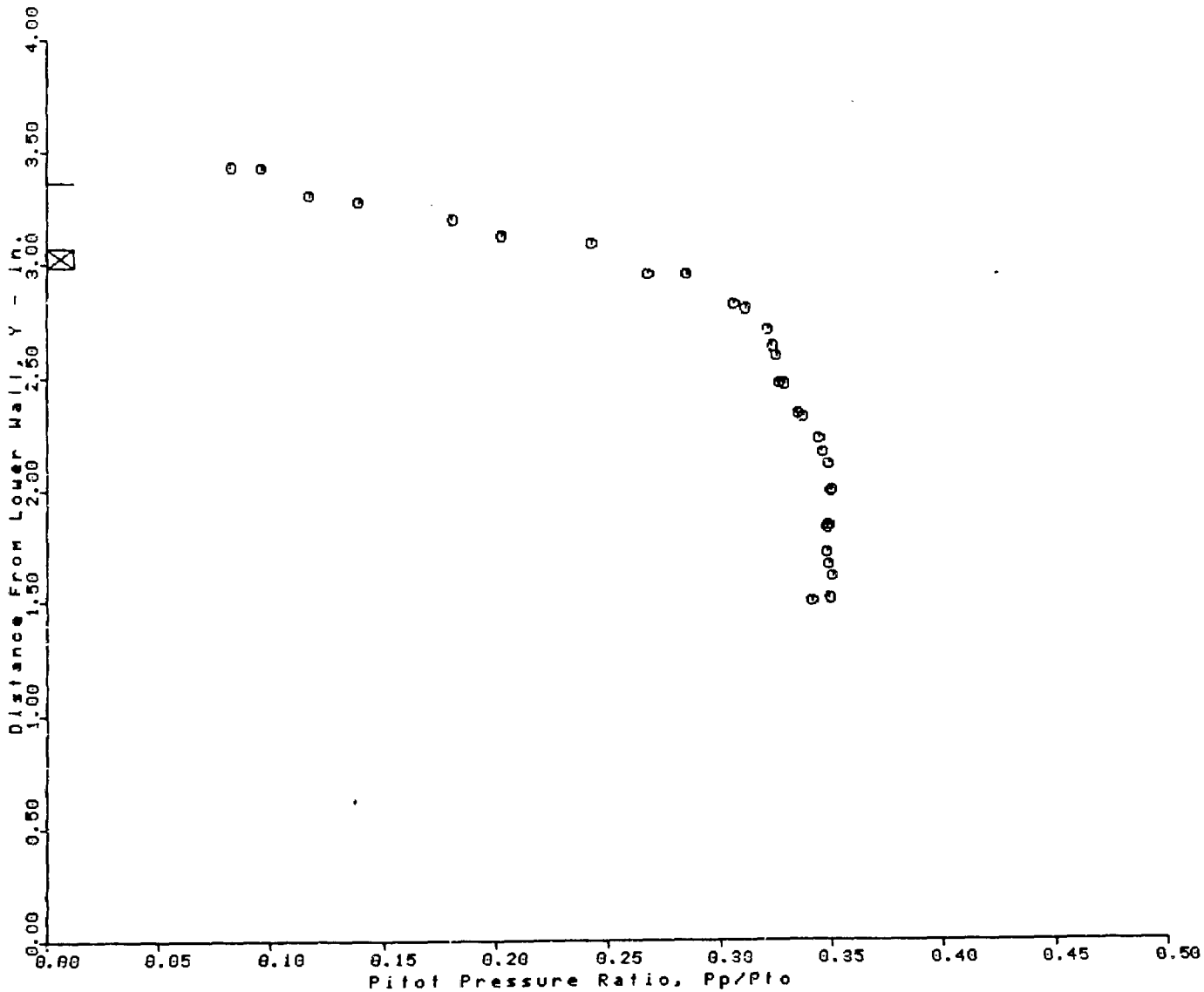

AFS TEST PROGRAM
RUN = 70 BURSTS 22 THRU 51

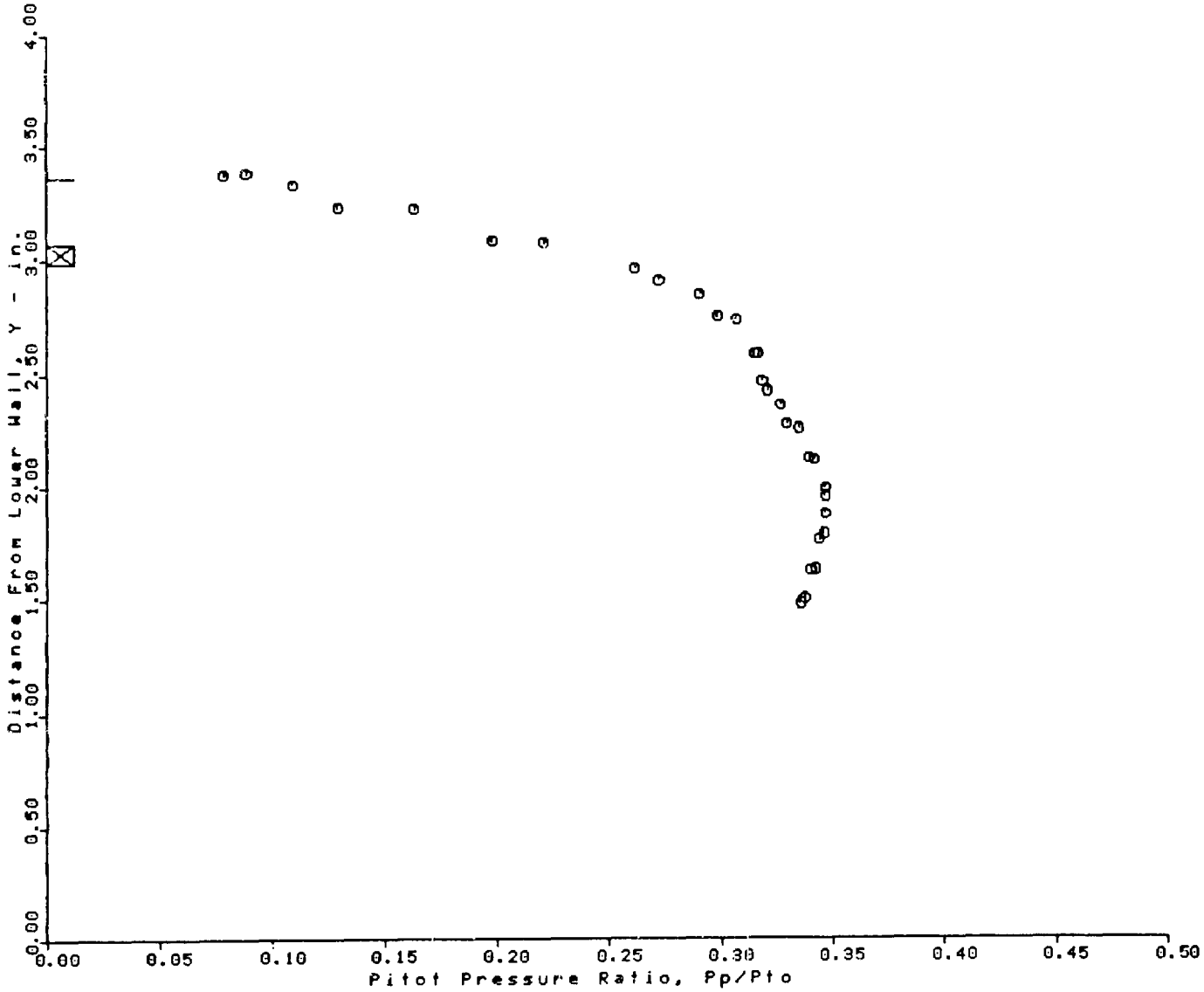

AFS TEST PROGRAM
RUN = 71 BURSTS 34 THRU 63

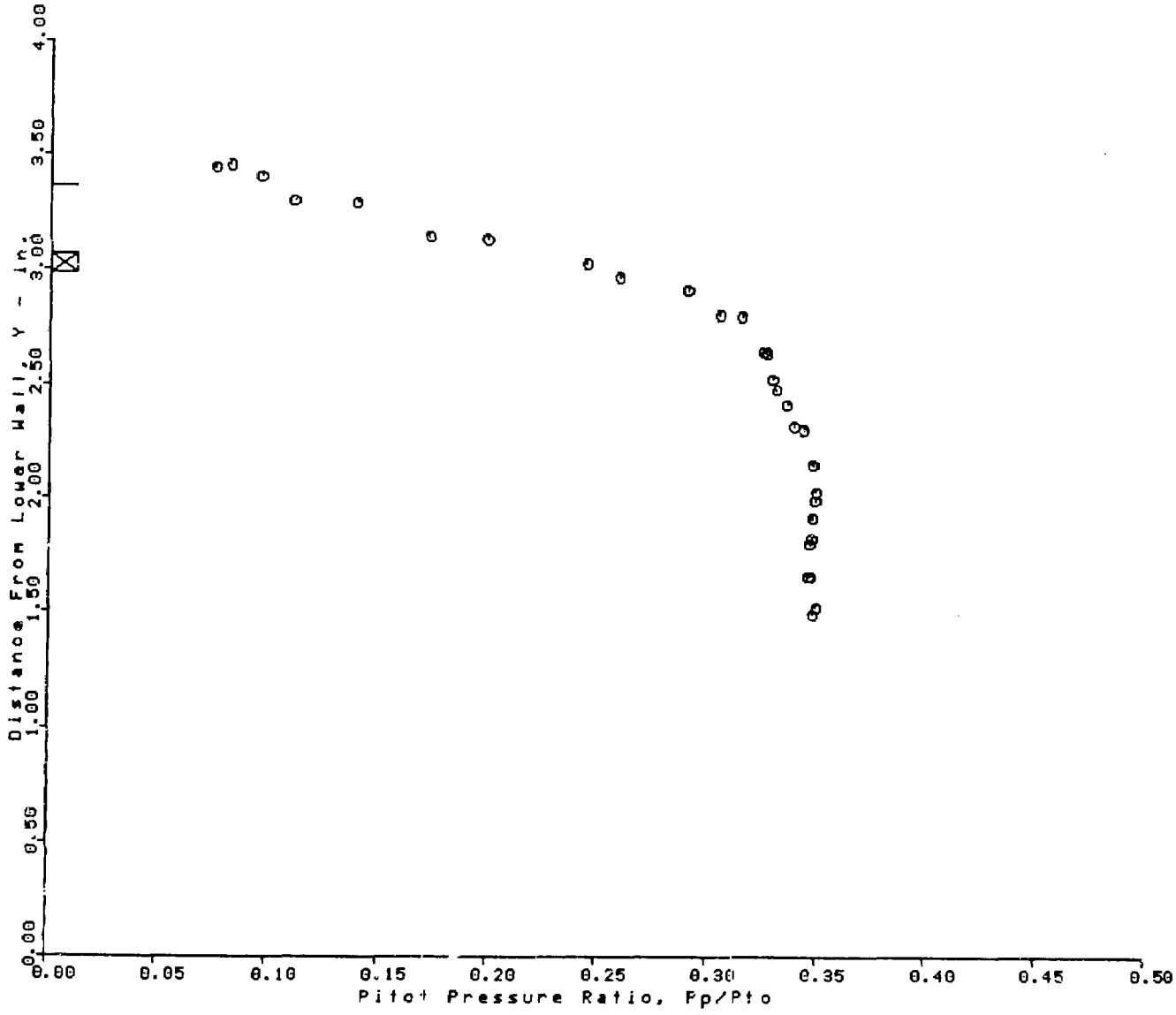

AFS TEST PROGRAM
RUN = 72 BURSTS 33 THRU 62

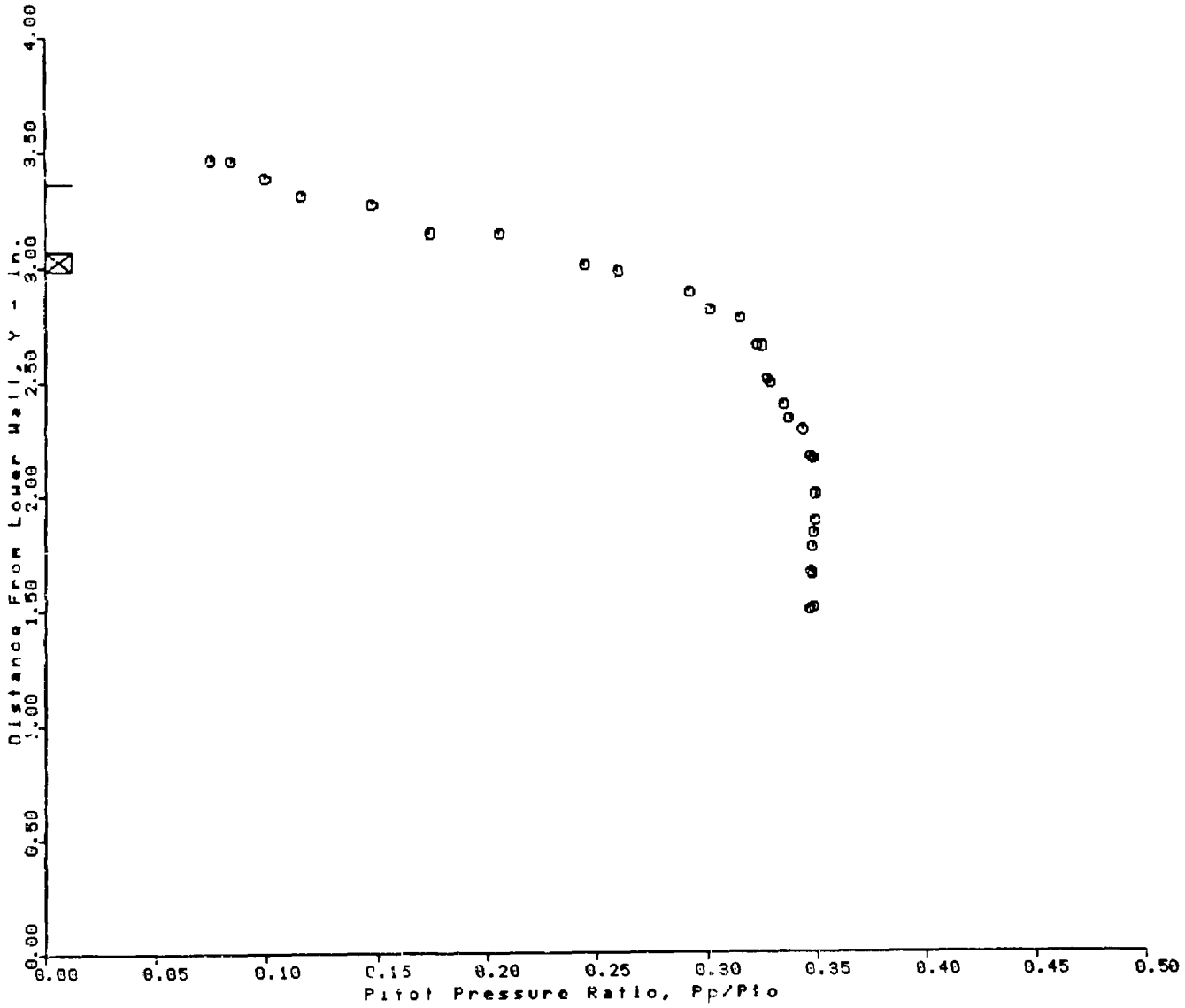

AFS TEST PROGRAM
RUN = 74 BURSTS 34 THRU 63

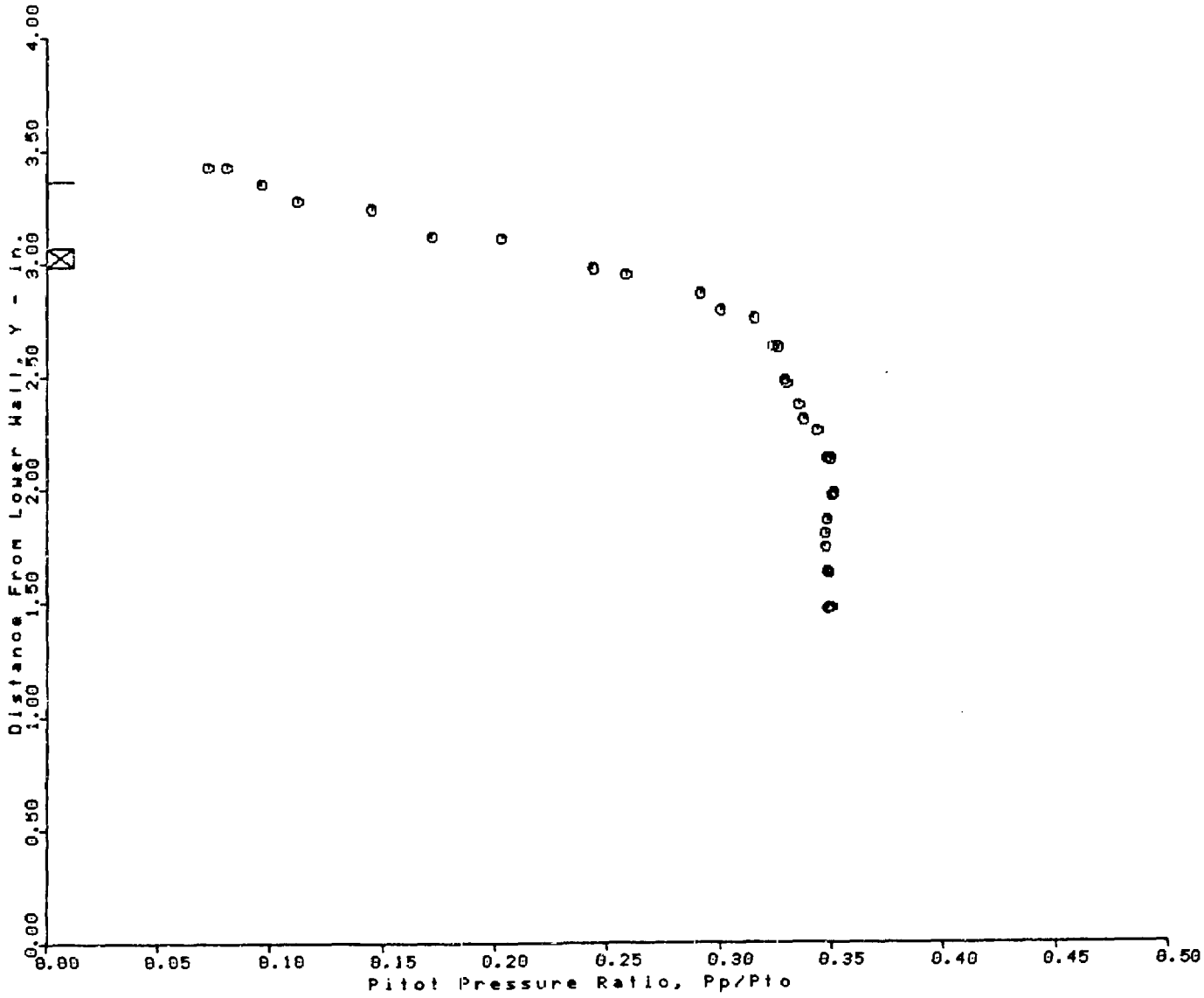

AFS TEST PROGRAM
RUN = 77 BURSTS 28 THRU 68

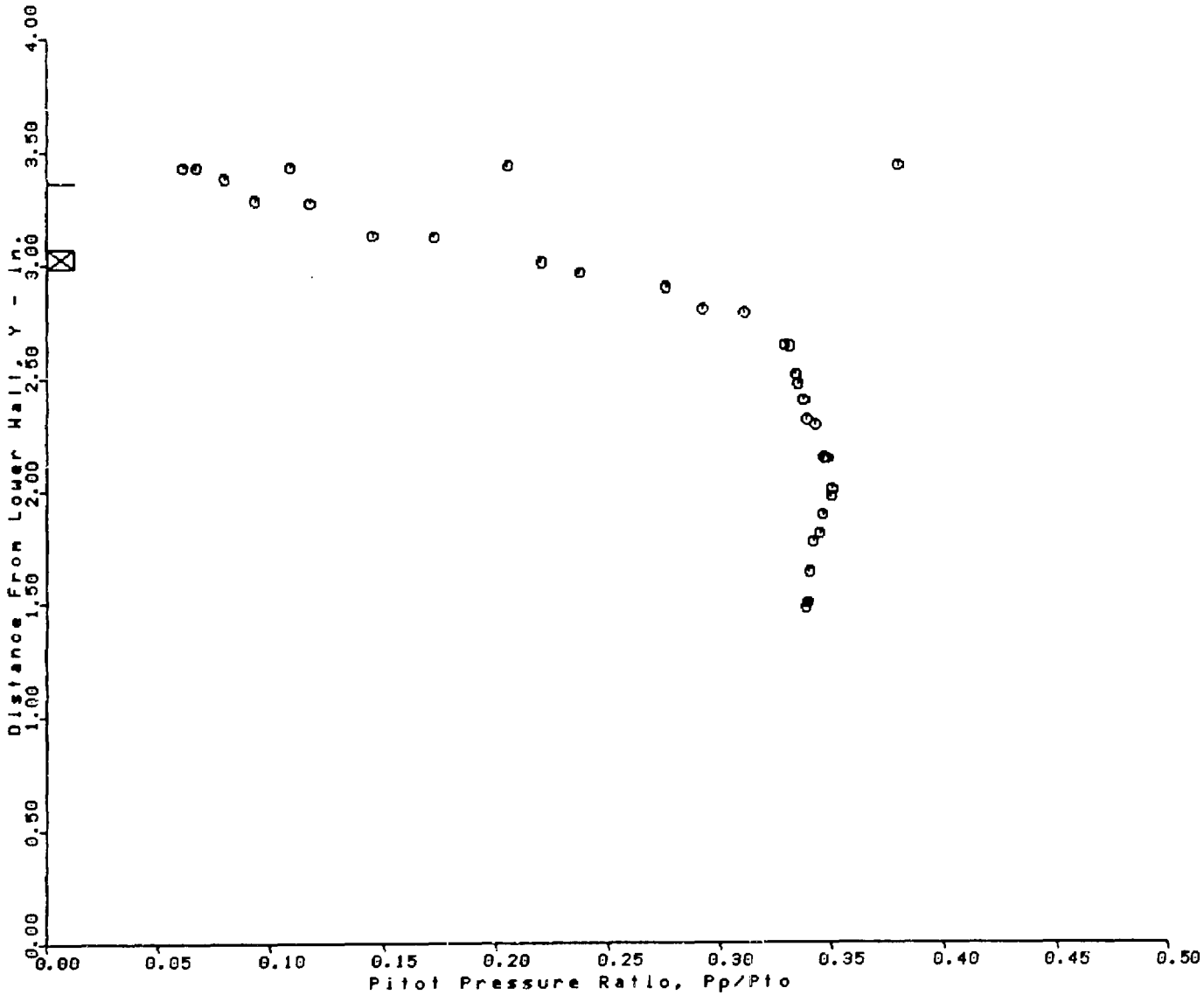

AFS TEST PROGRAM
RUN = 78 BURSTS 31 THRU 45

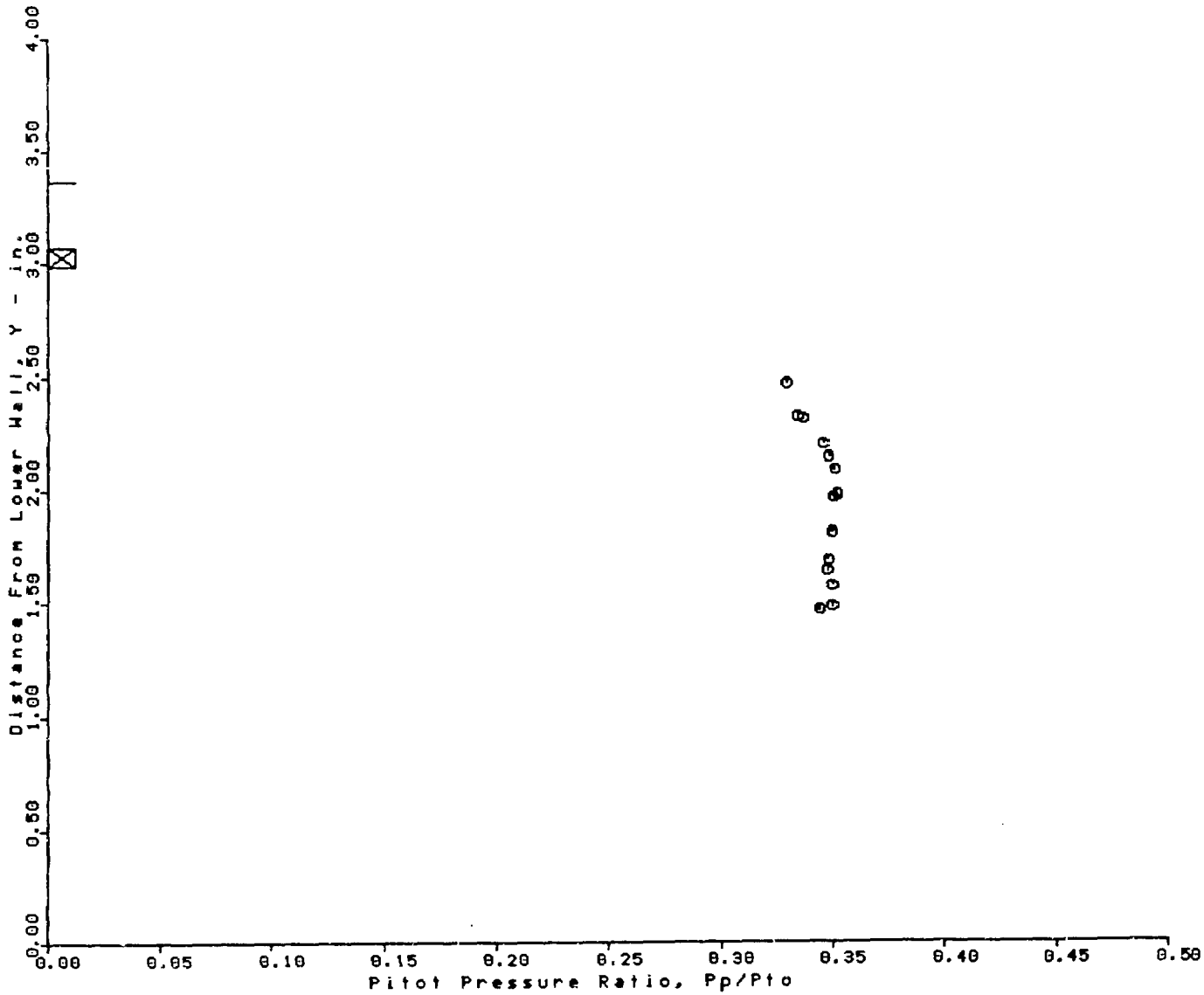

AFS TEST PROGRAM
RUN = 81 BURSTS 30 THRU 59

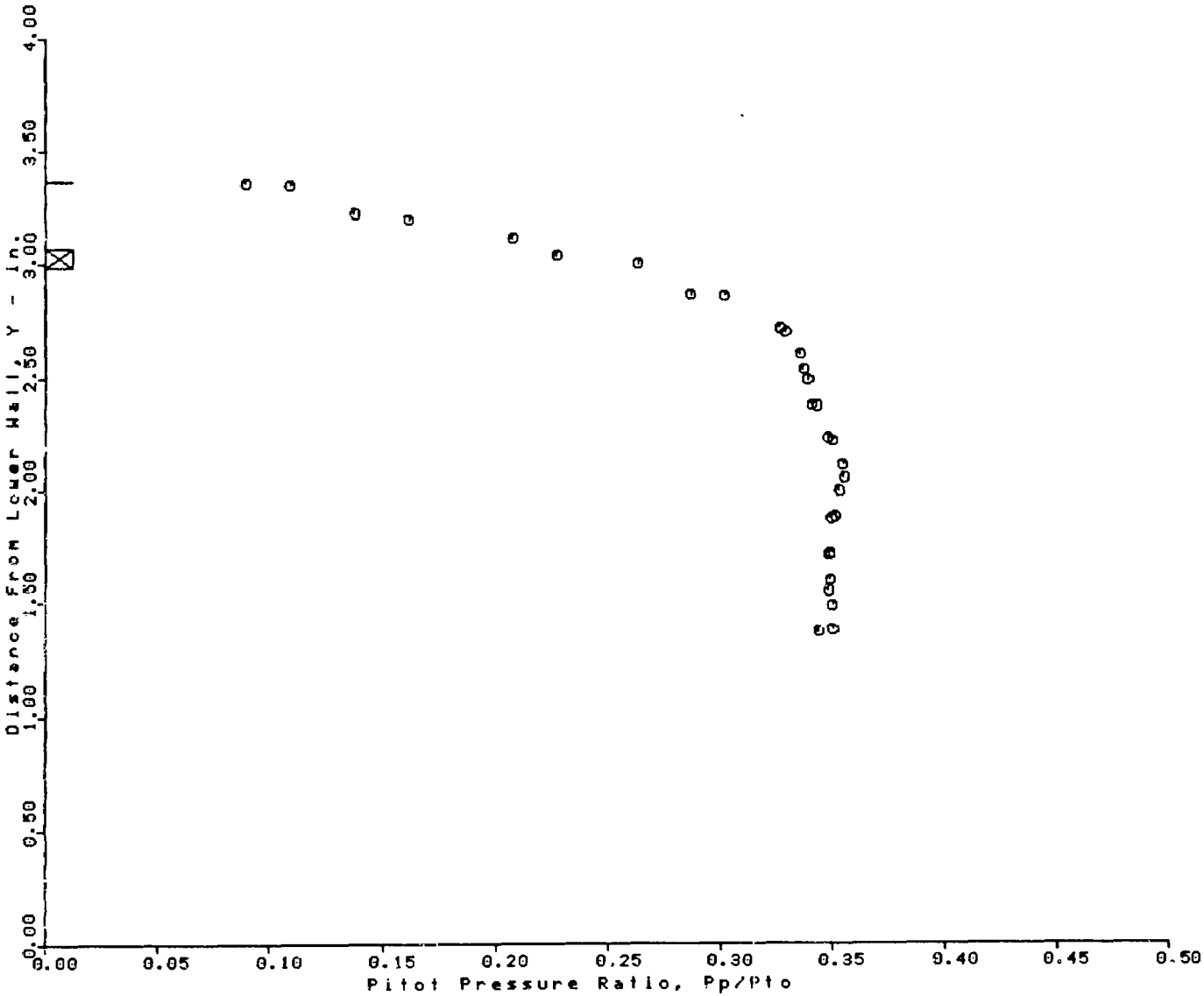

AFS TEST PROGRAM
RUN = 82 BURSTS 38 THRU 58

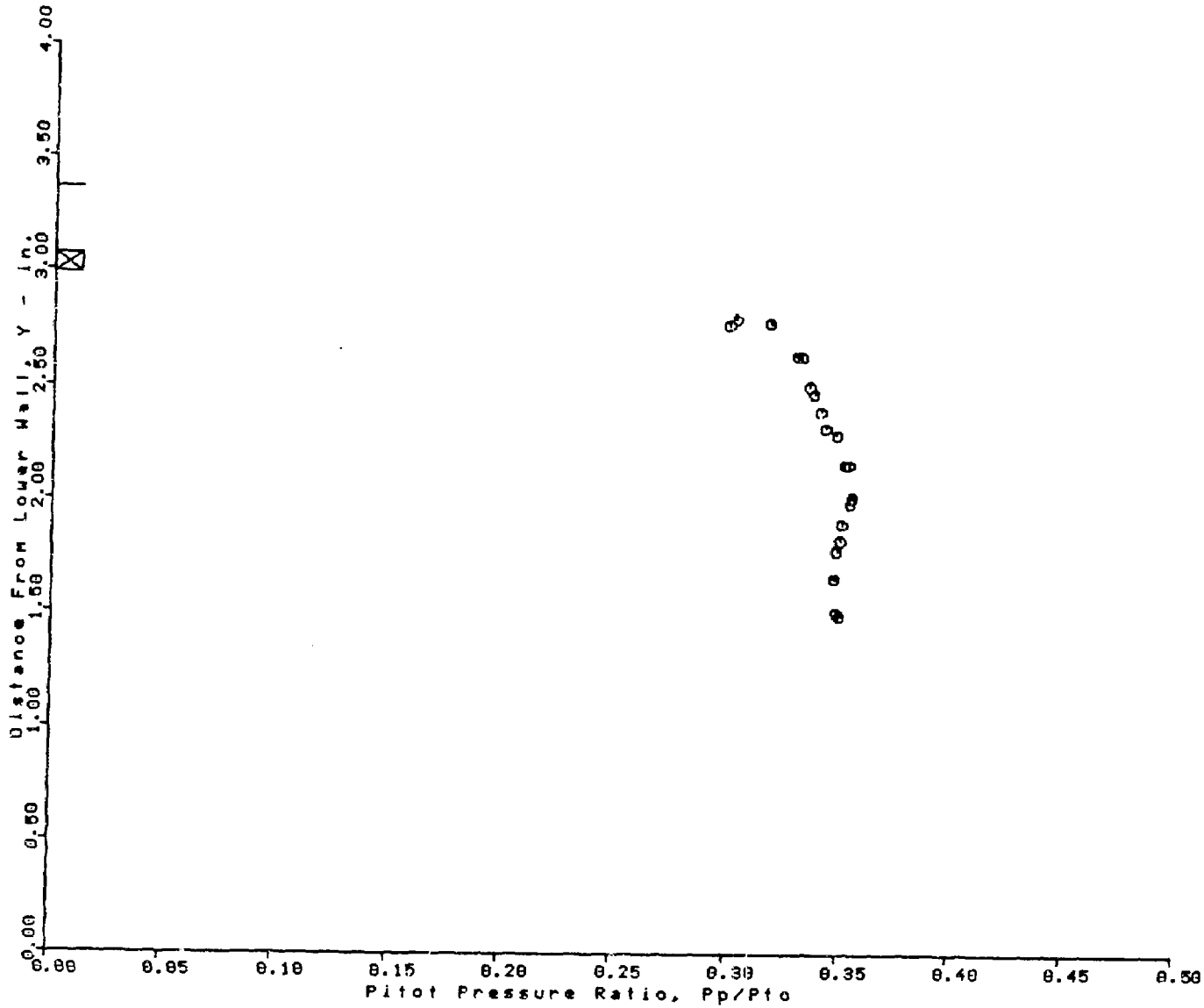

AFS TEST PROGRAM
RUN = 84 BURSTS 30 THRU 59

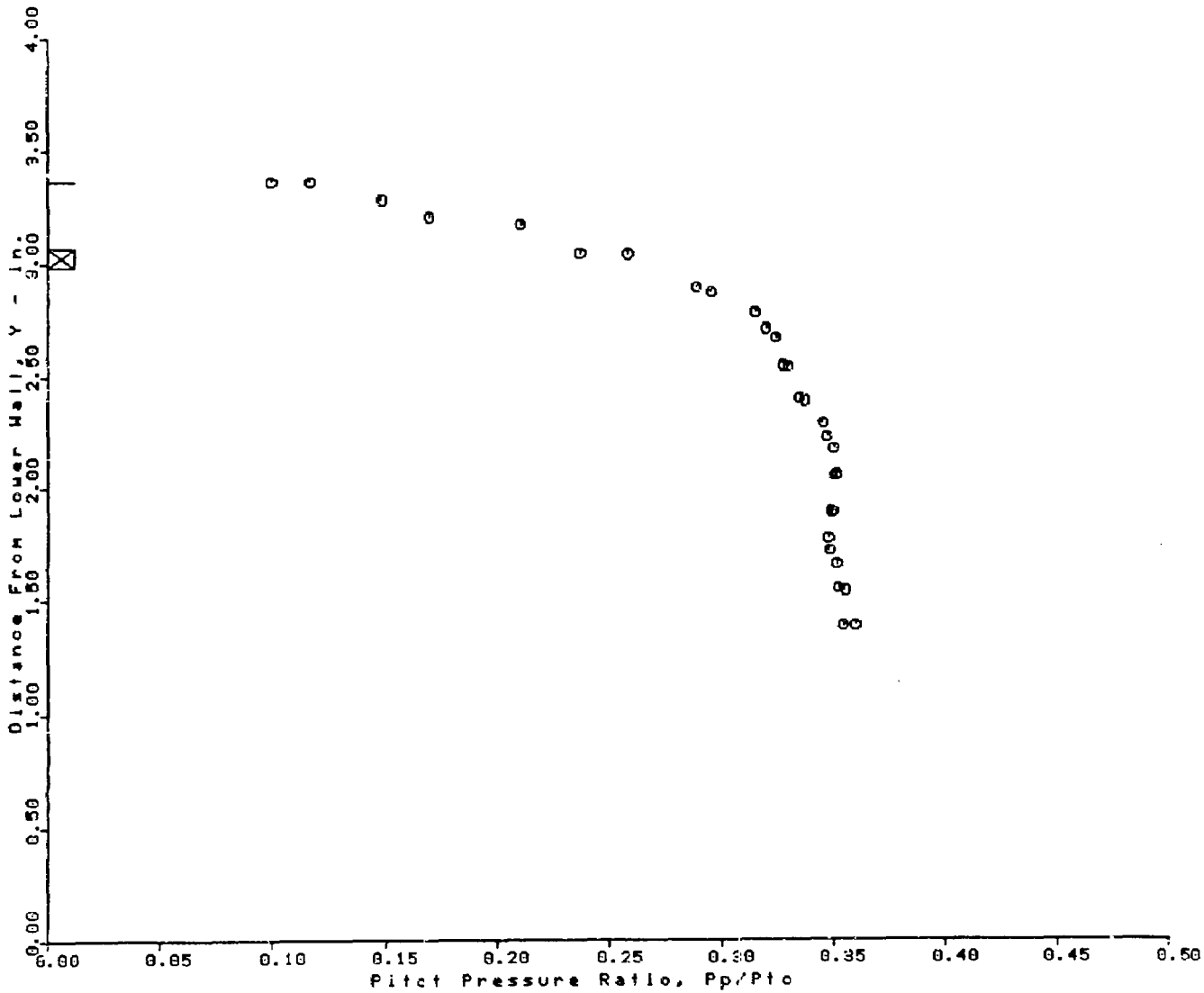

AFS TEST PROGRAM
RUN = 88 BURSTS 47 THRU 64

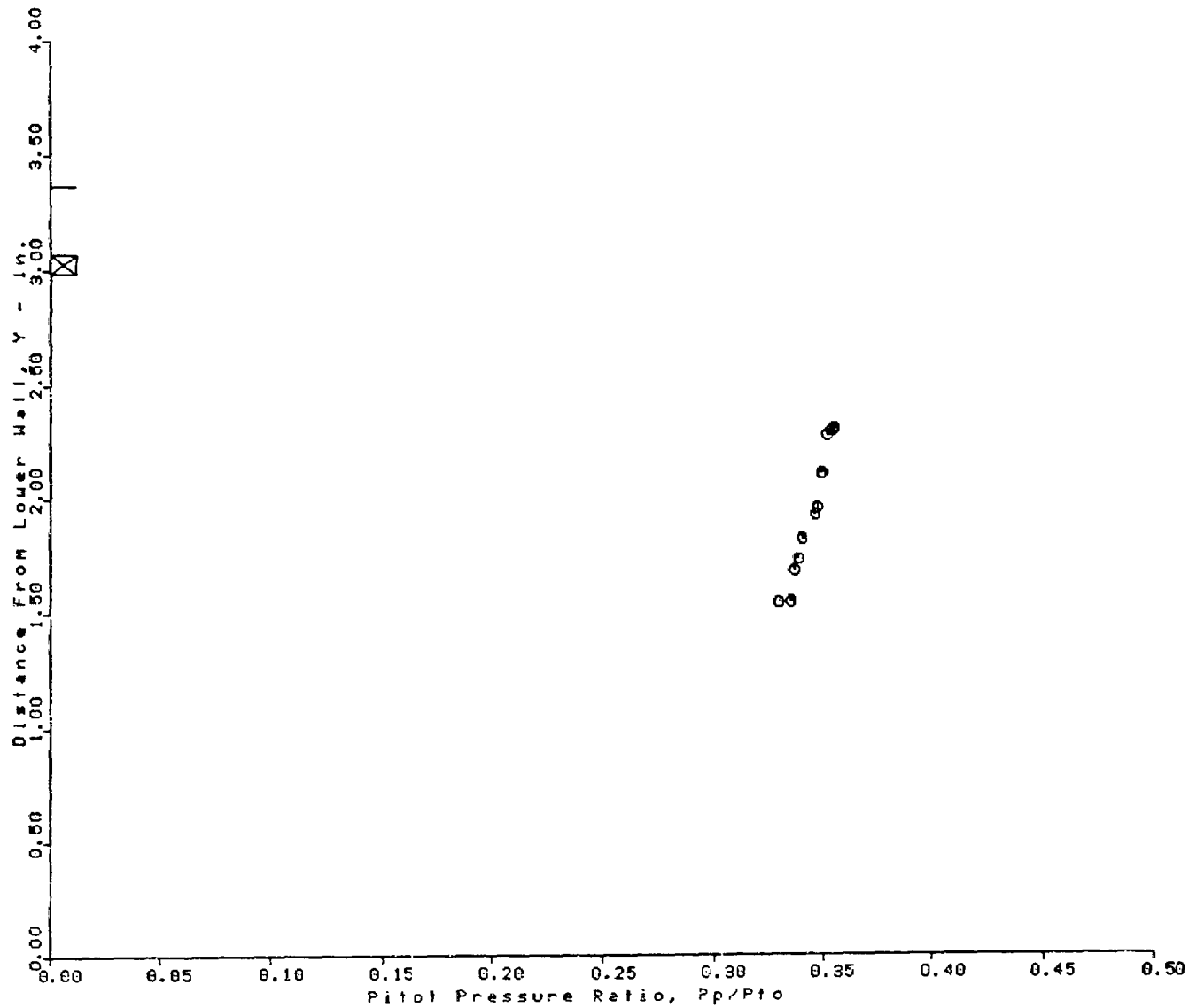

AFS TEST PROGRAM
RUN = 89 BURSTS 54 THRU 64

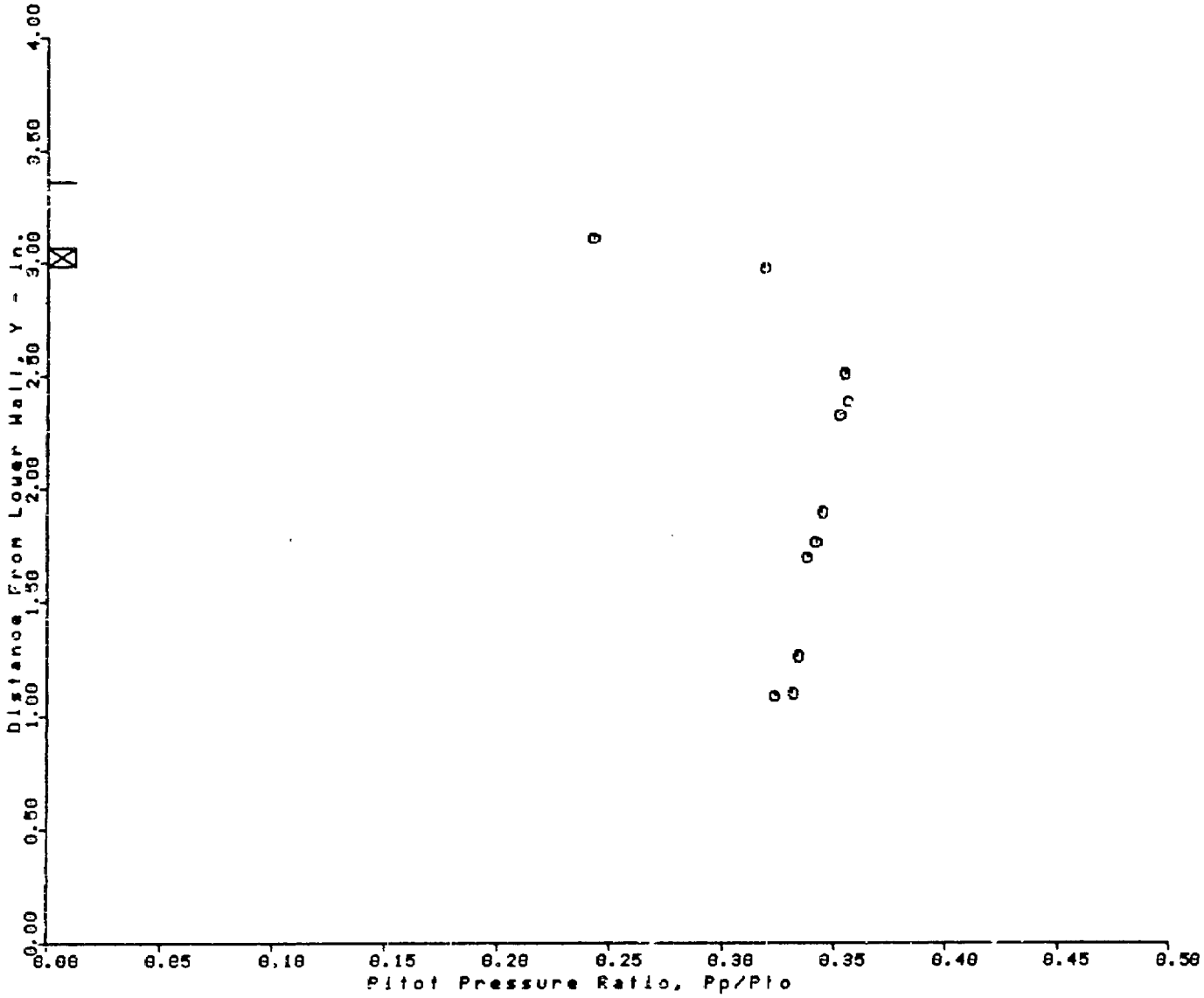

AFS TEST PROGRAM
RUN = 90 BURSTS 28 THRU 45

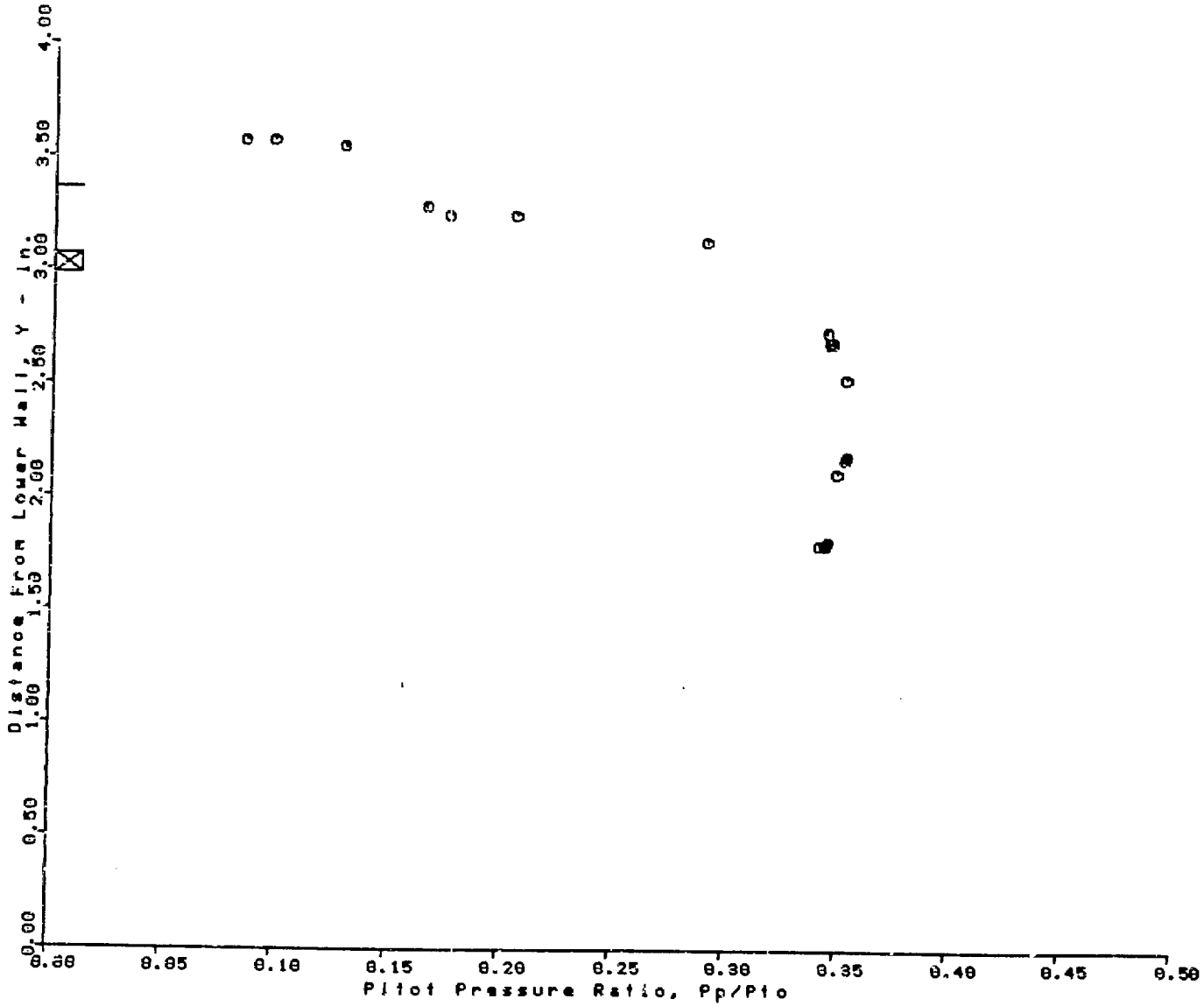

AFS TEST PROGRAM
RUN = 92 BURSTS 30 THRU 56

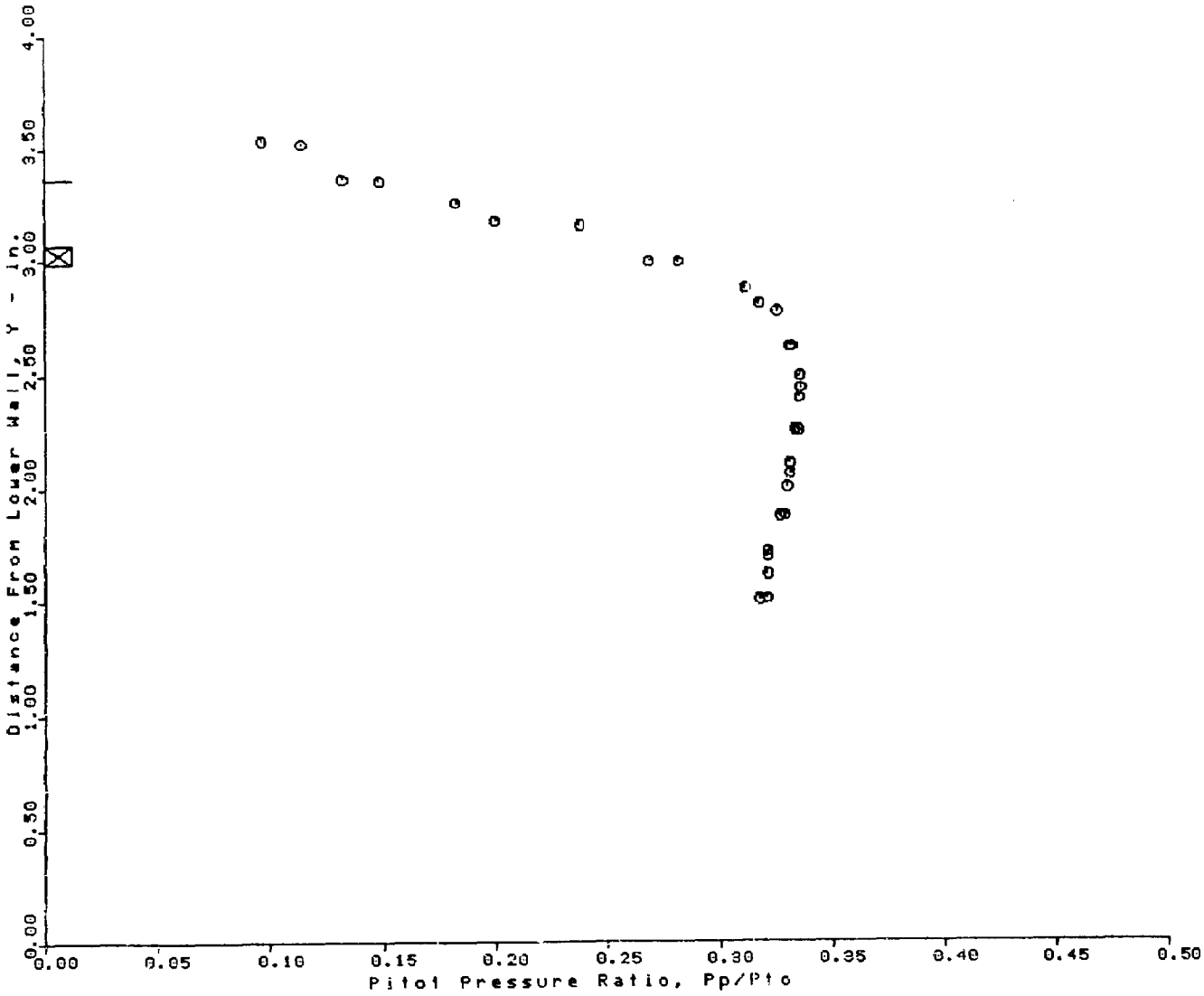

AFS TEST PROGRAM
RUN = 93 BURSTS 25 THRU 54

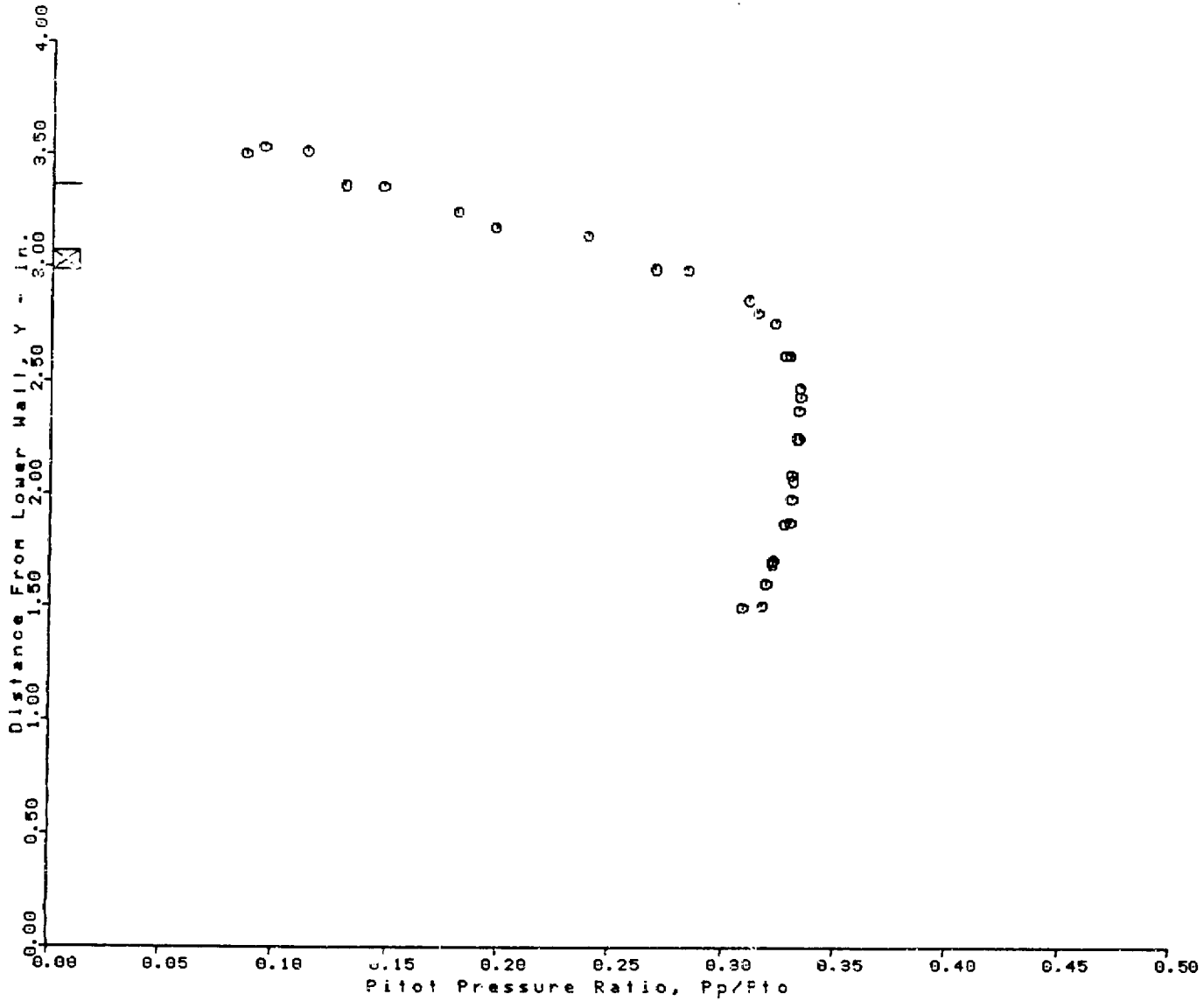

AFS TEST PROGRAM
RUN = 94 BURSTS 28 THRU 57

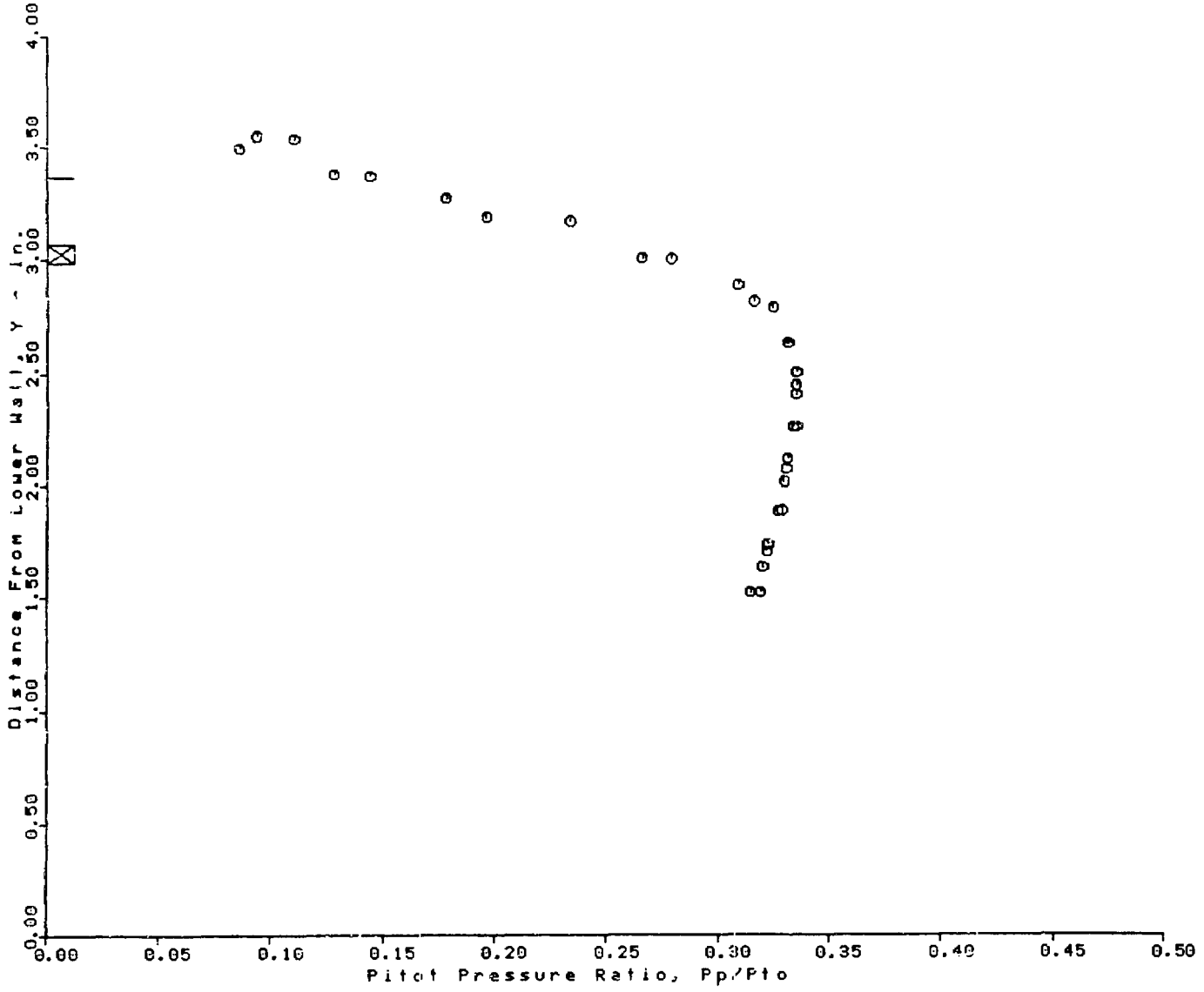

AFS TEST PROGRAM
RUN = 95 BURSTS 29 THRU 57

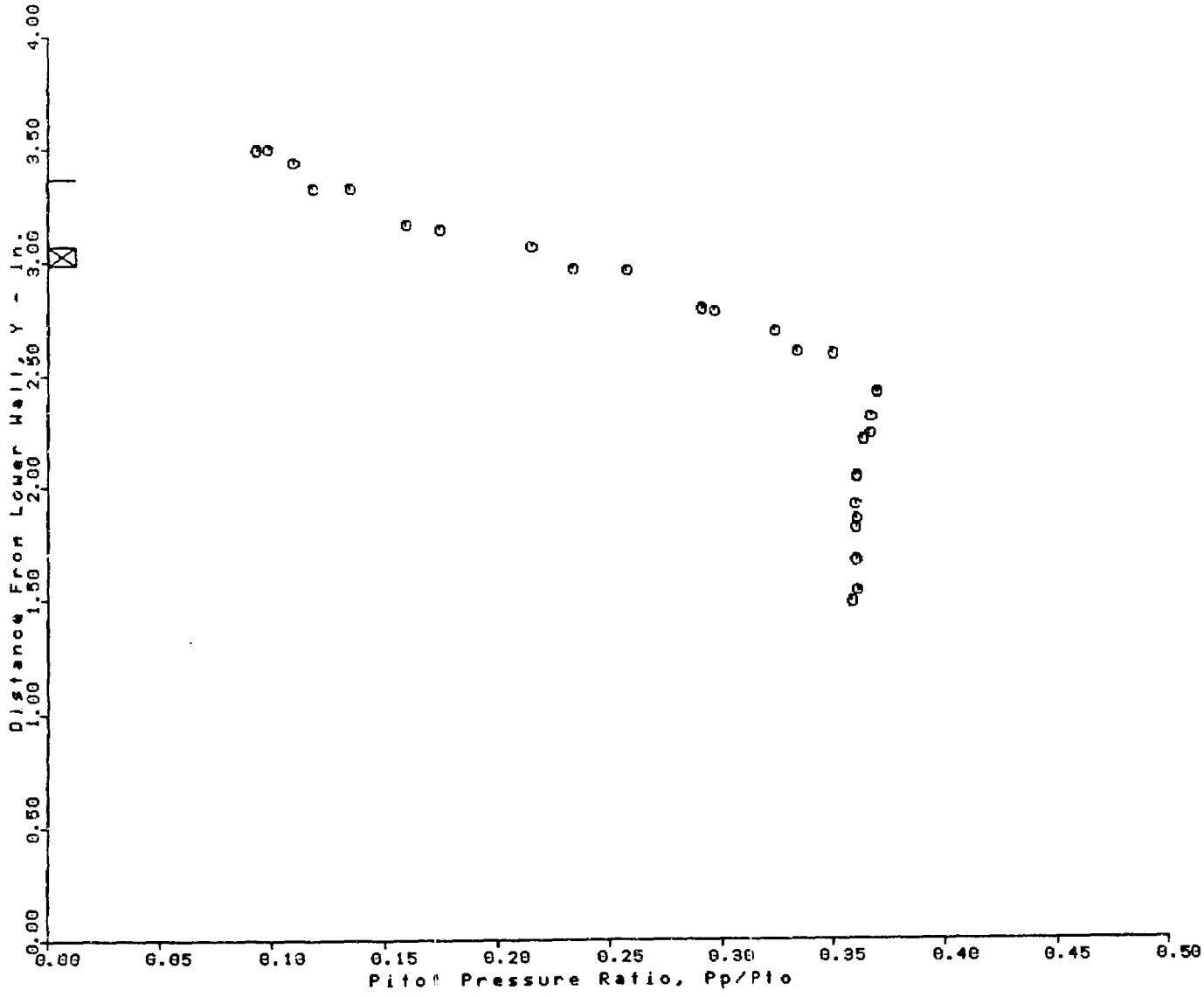

AFS TEST PROGRAM
RUN = 96 BURSTS 28 THRU 56

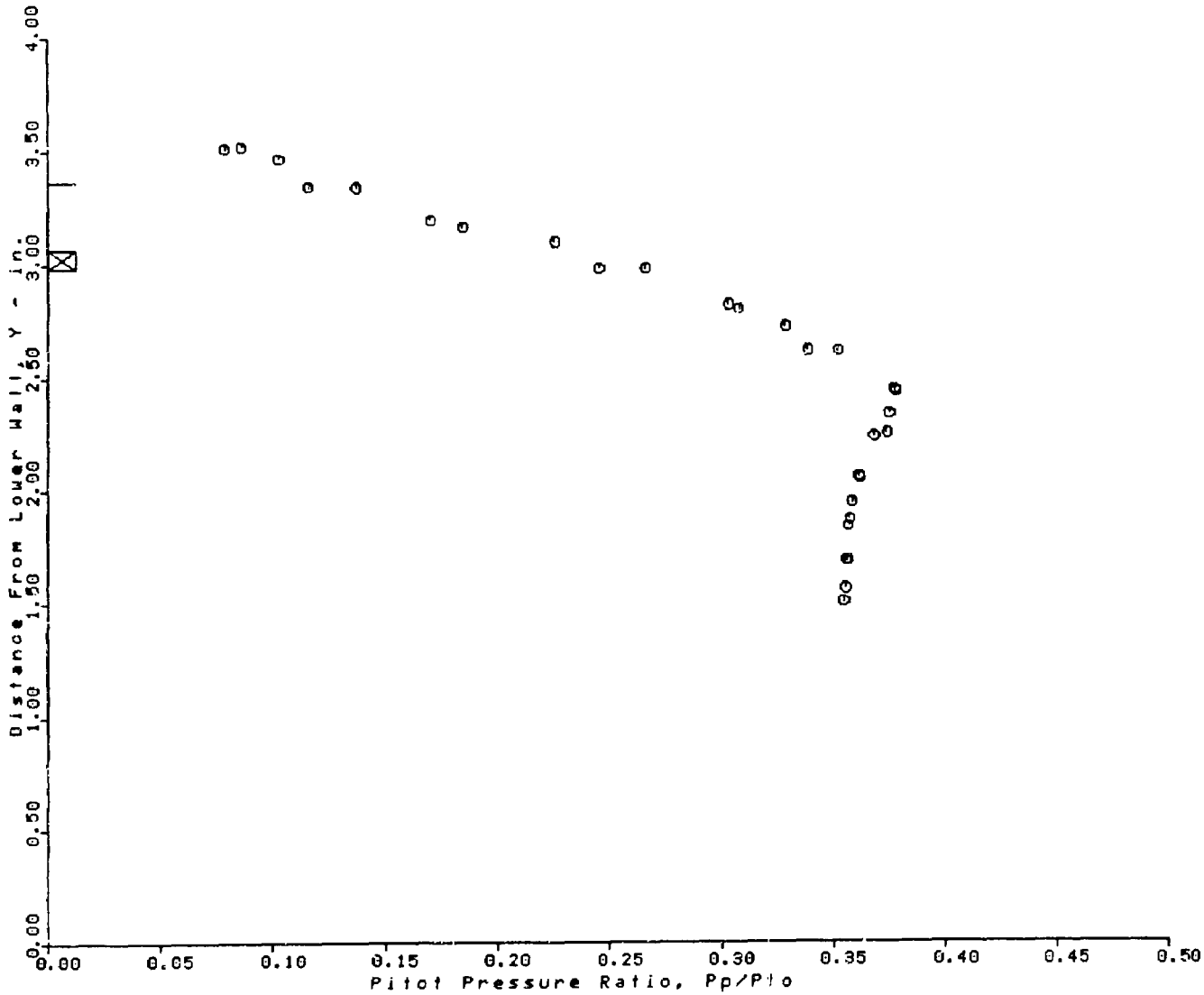

AFS TEST PROGRAM
RUN = 97 BURSTS 40 THRU 52

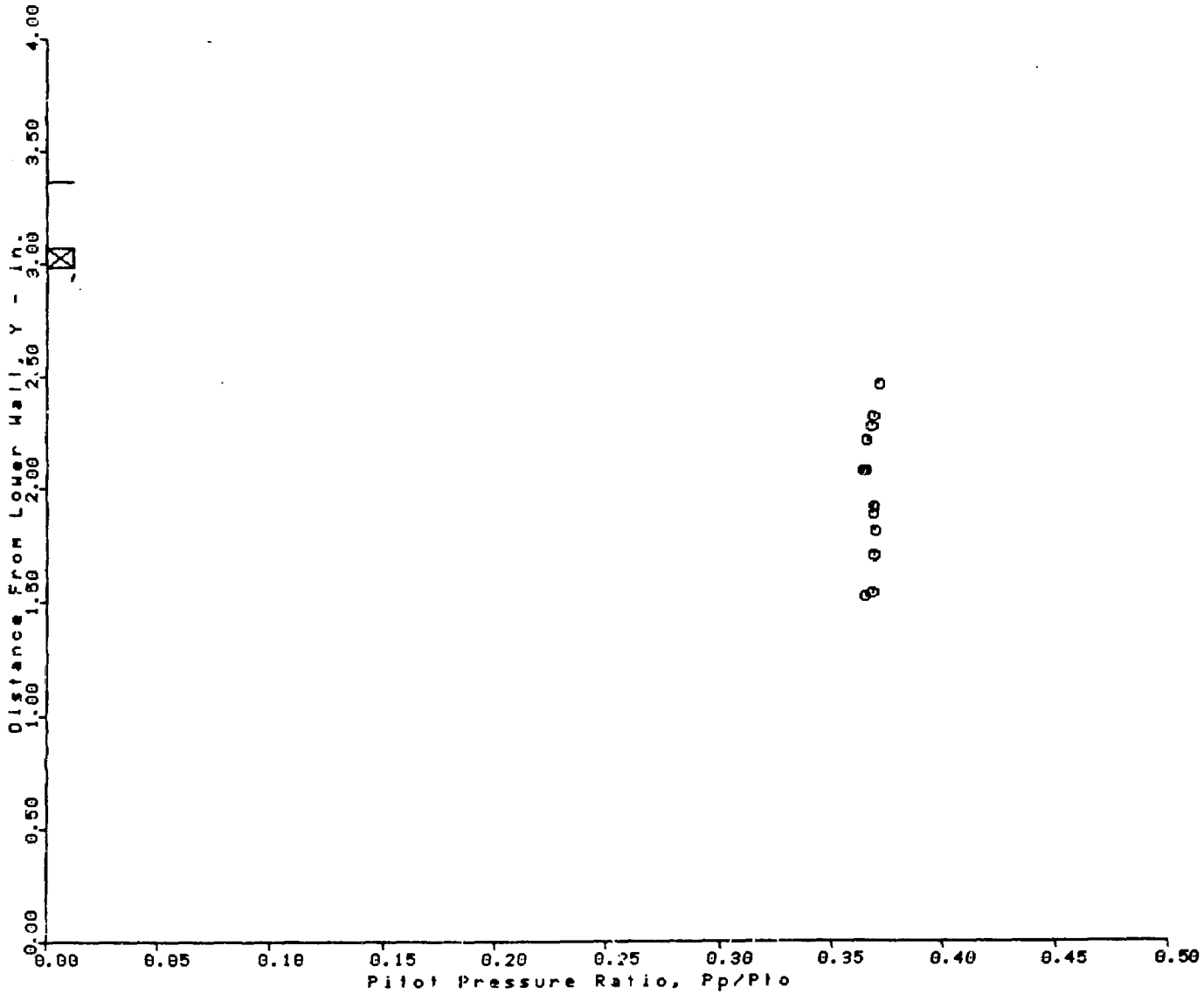

AFS TEST PROGRAM
RUN = 99 BURSTS 42 THRU 71

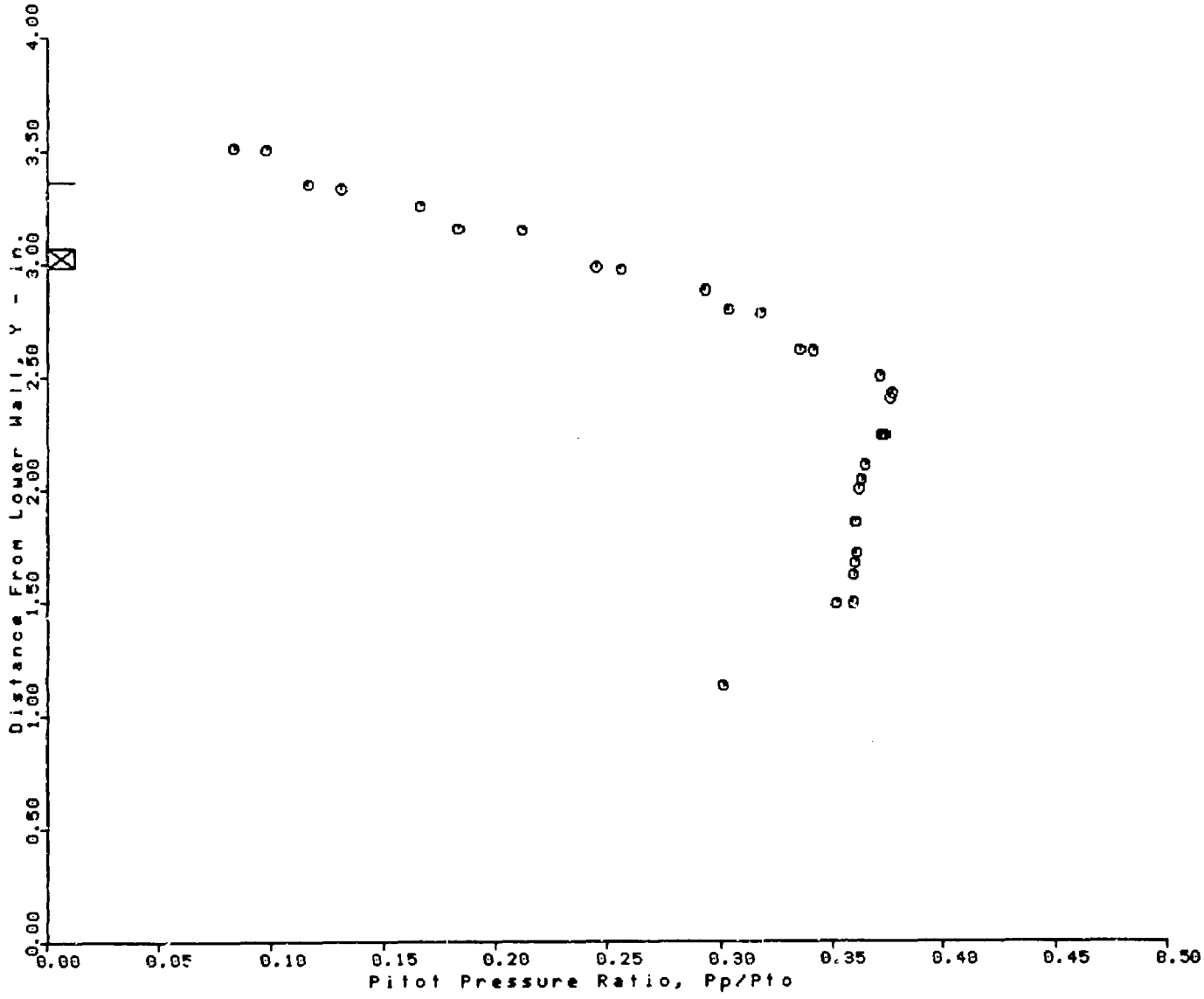

AFS TEST PROGRAM
RUN = 100 BURSTS 38 THRU 66

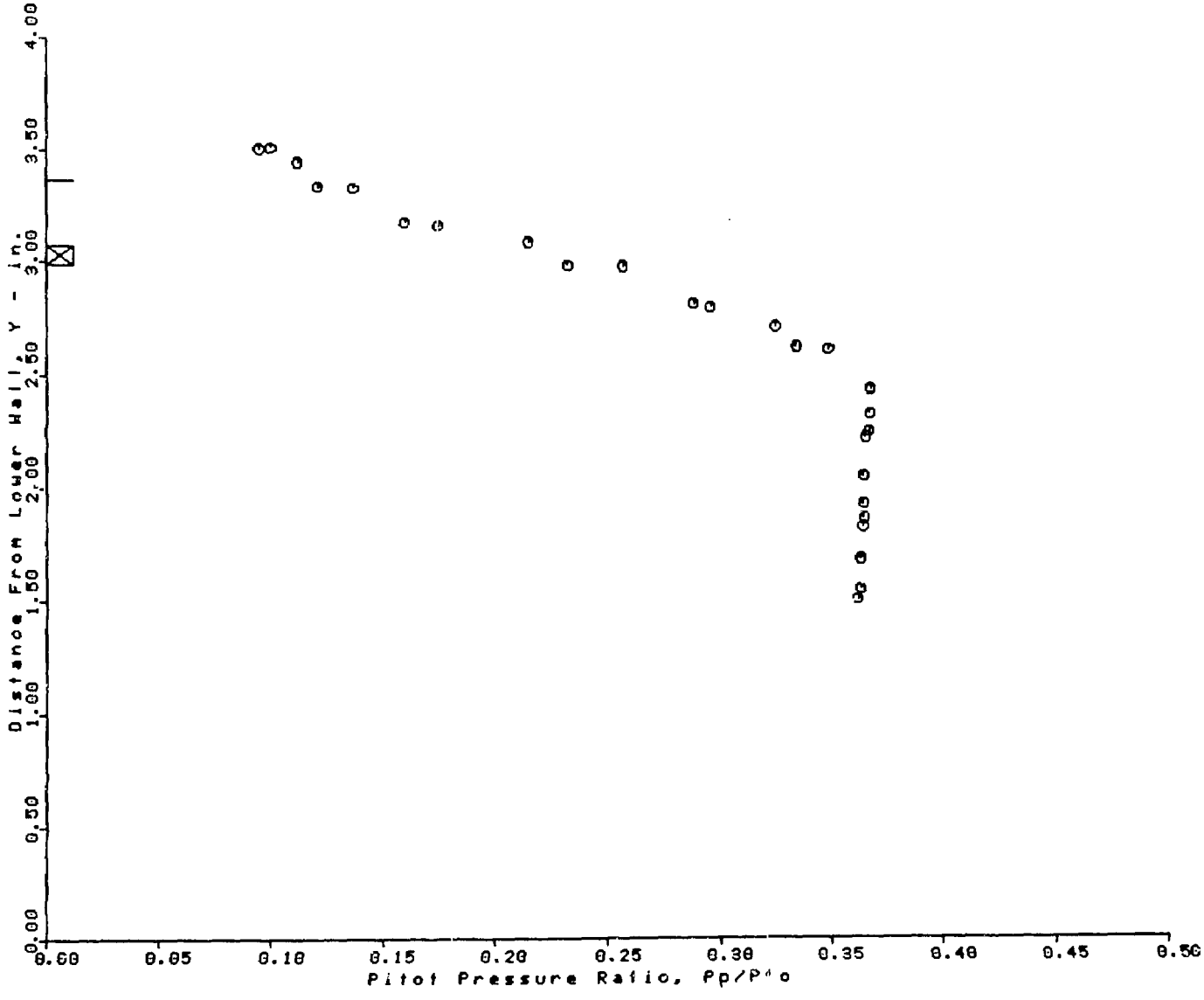

AFS TEST PROGRAM
RUN = 101 BURSTS 35 THRU 63

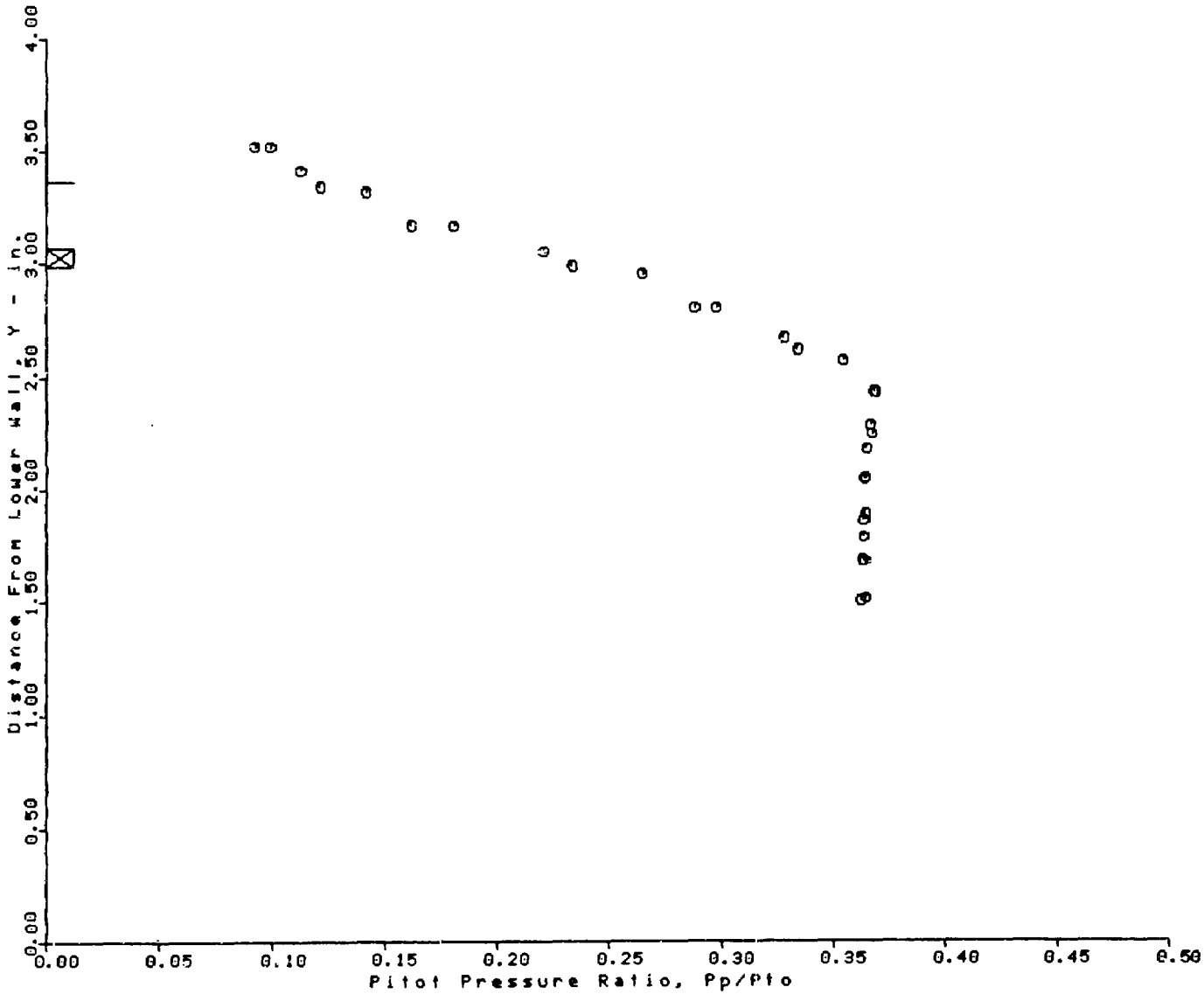

AFS TEST PROGRAM
RUN = 102 BURSTS 38 THRU 66

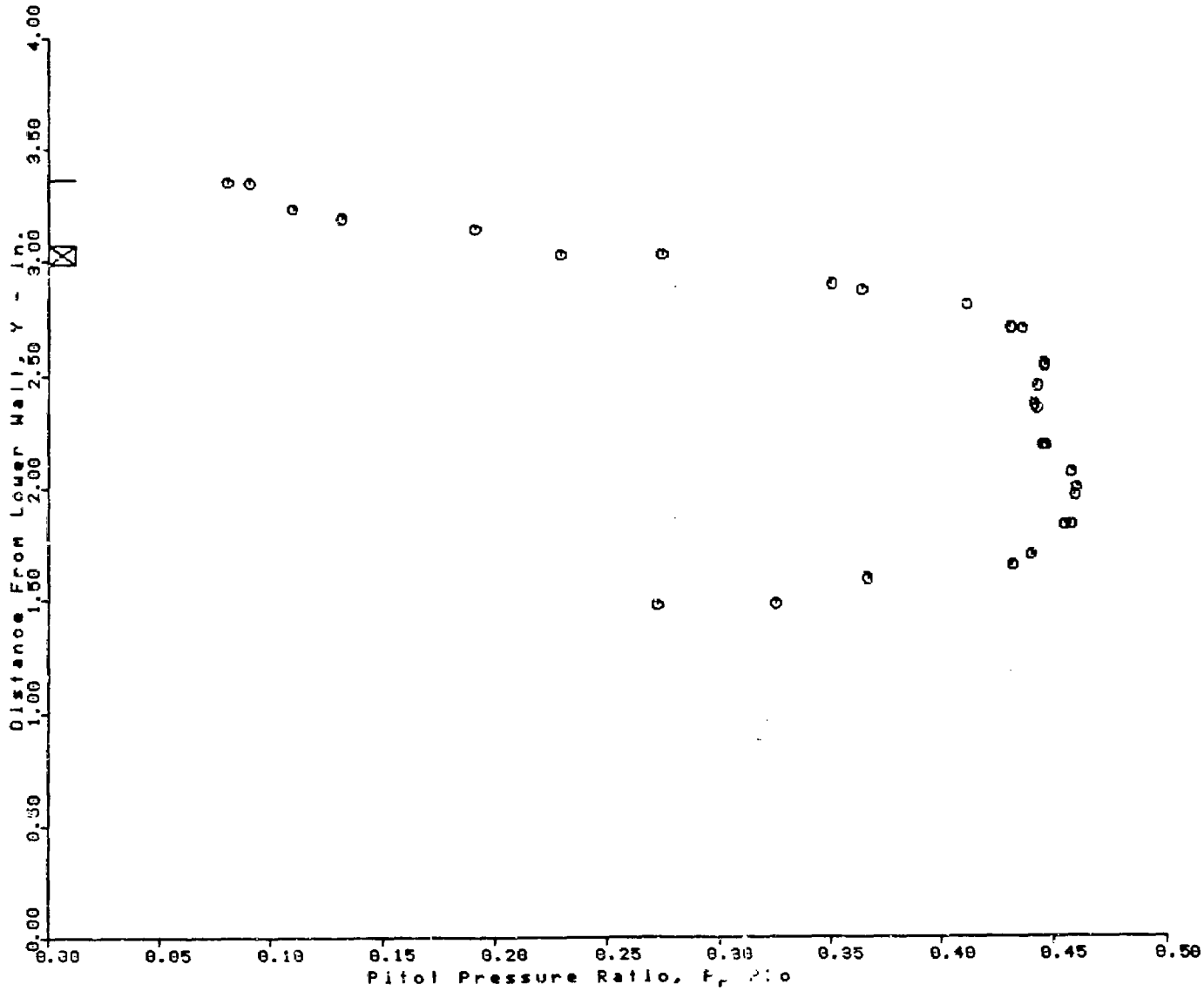

AFS TEST PROGRAM
RUN = 103 BURSTS 29 THRU 57

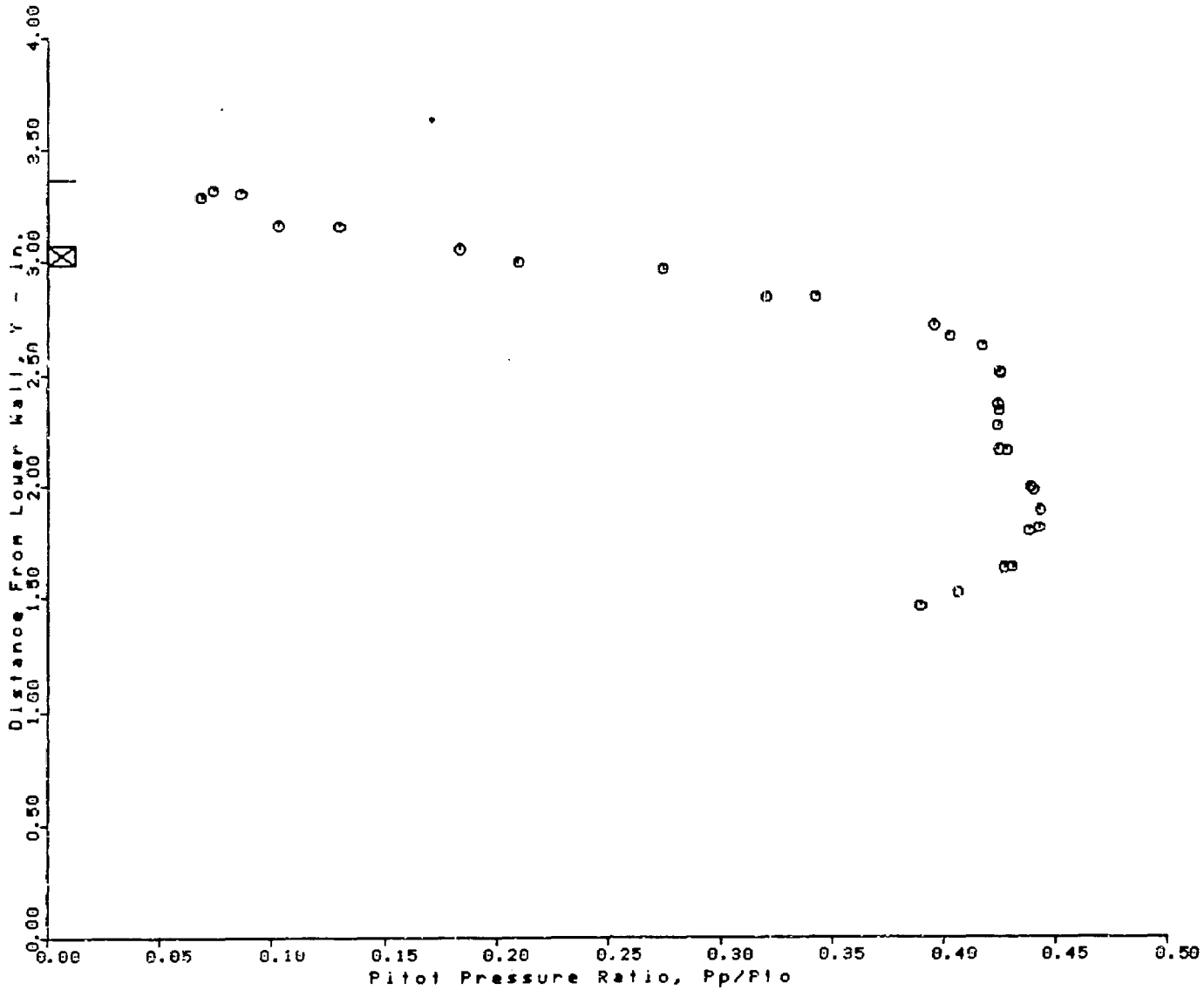

AFS TEST PROGRAM
RUN = 104 BURSTS 46 THRU 74

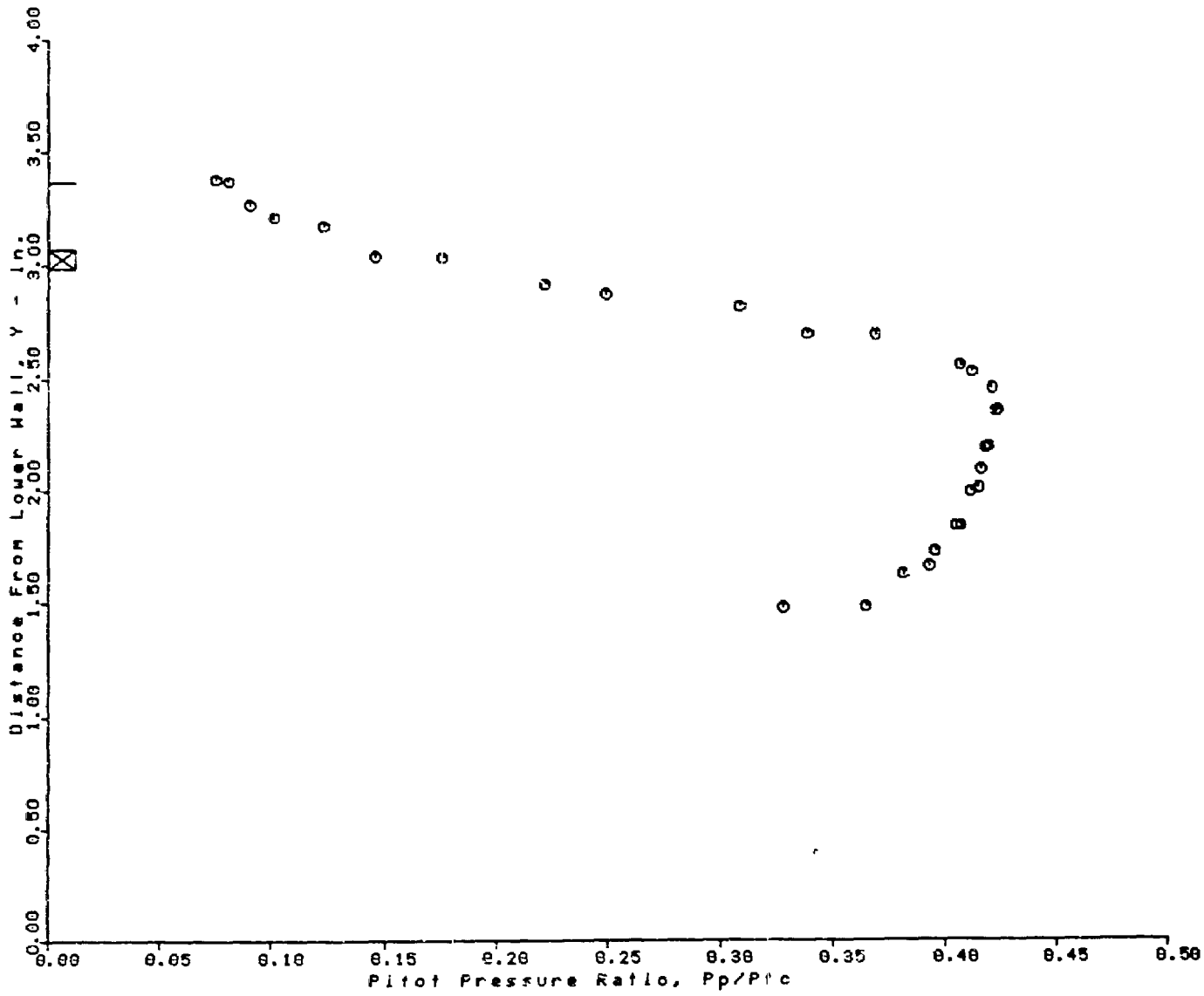

AFS TEST PROGRAM
RUN = 105 BURSTS 30 THRU 58

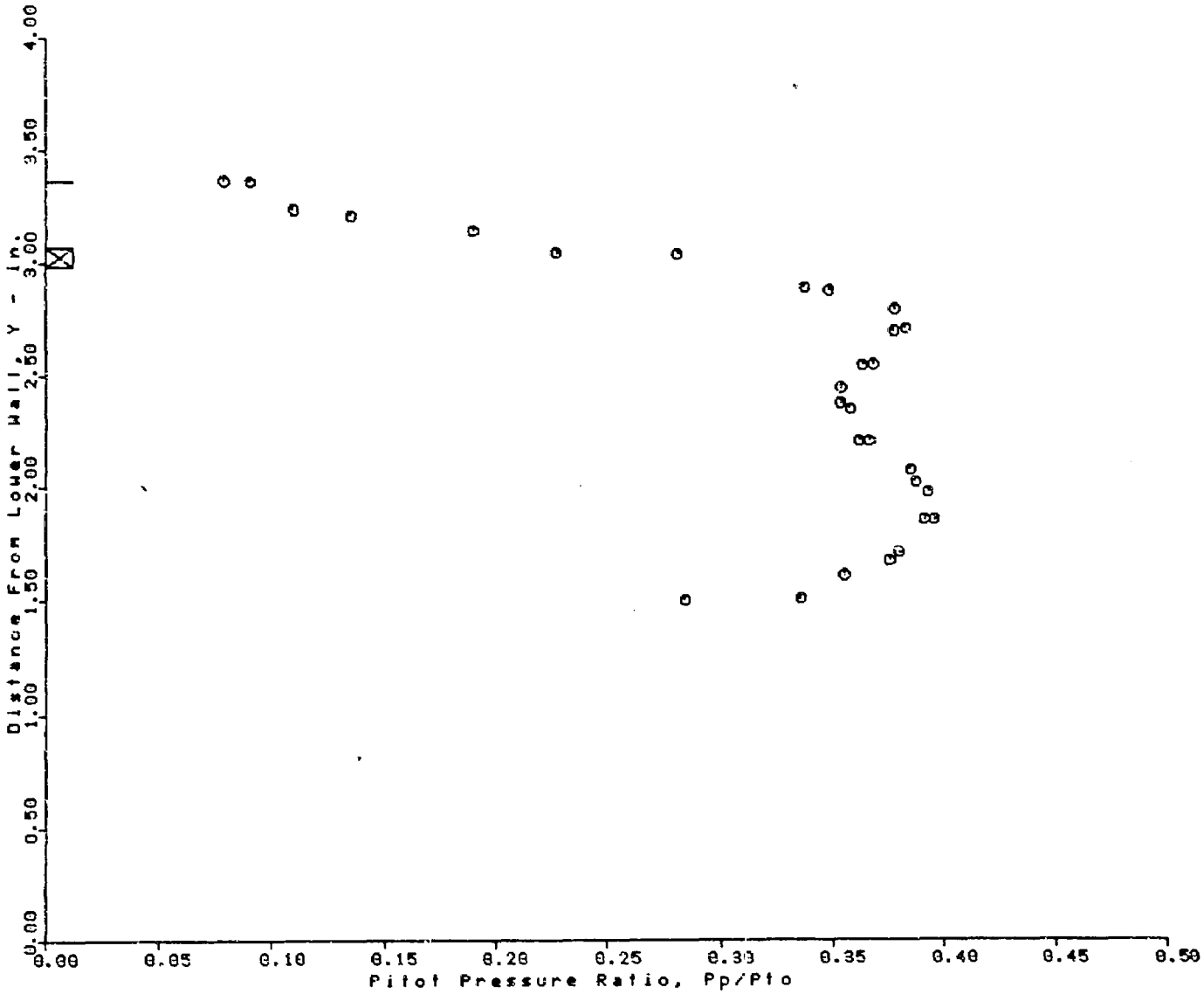

AFS TEST PROGRAM
RUN = 108 BURSTS 28 THRU 56

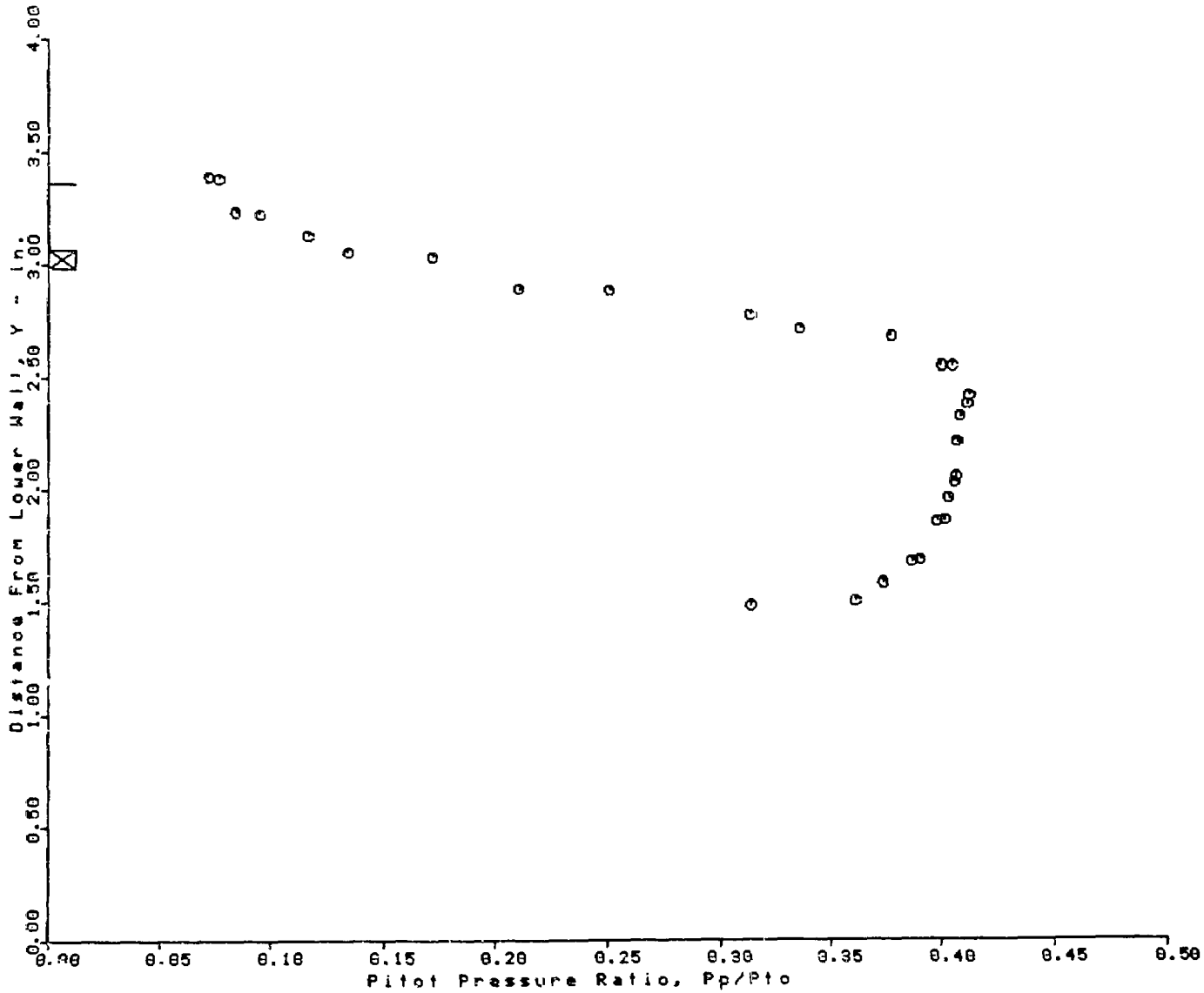

AFS TEST PROGRAM
RUN = 109 BURSTS 32 THRU 60

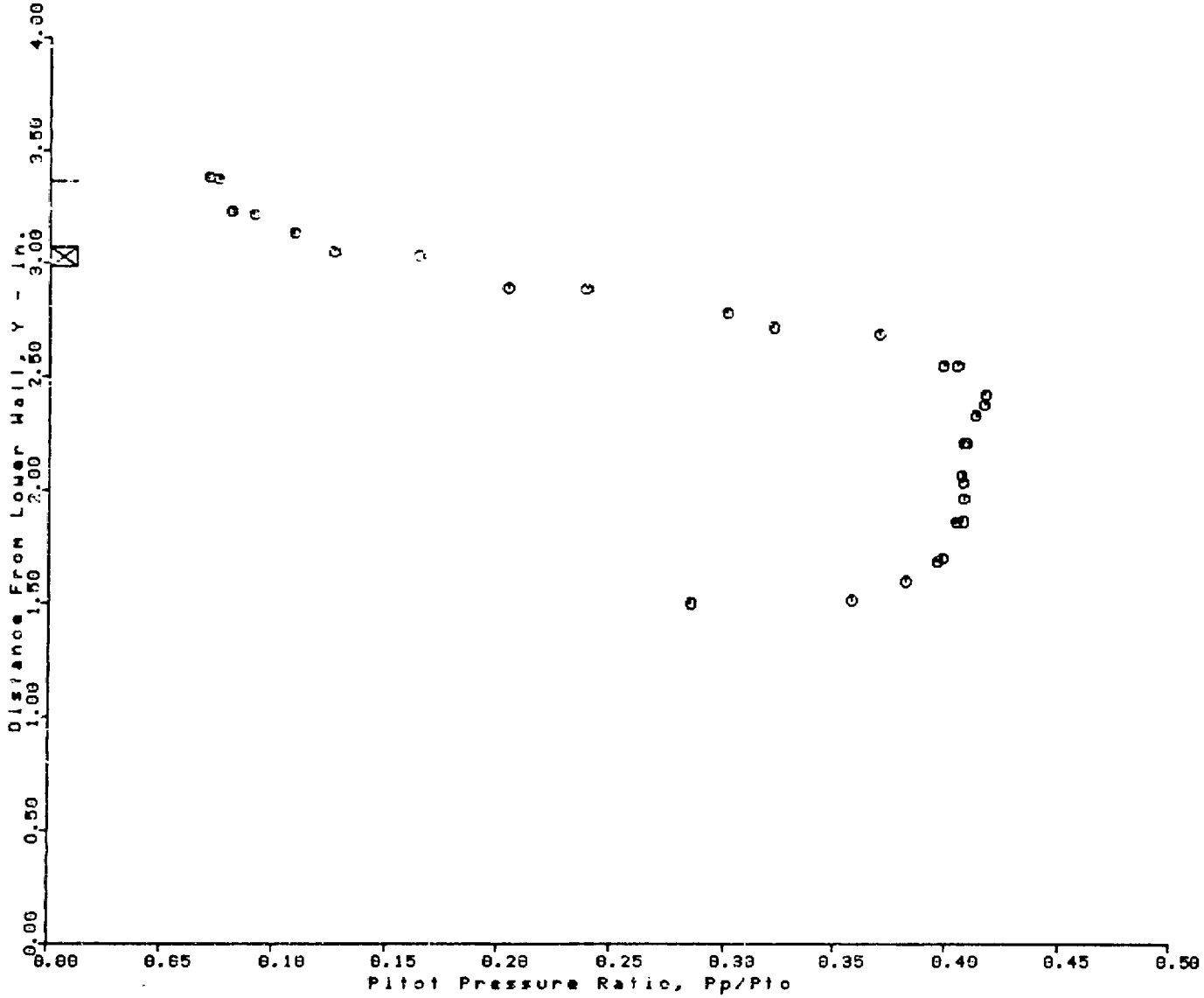

AFS TEST PROGRAM
RUN = 118 BURSTS 30 THRU 50

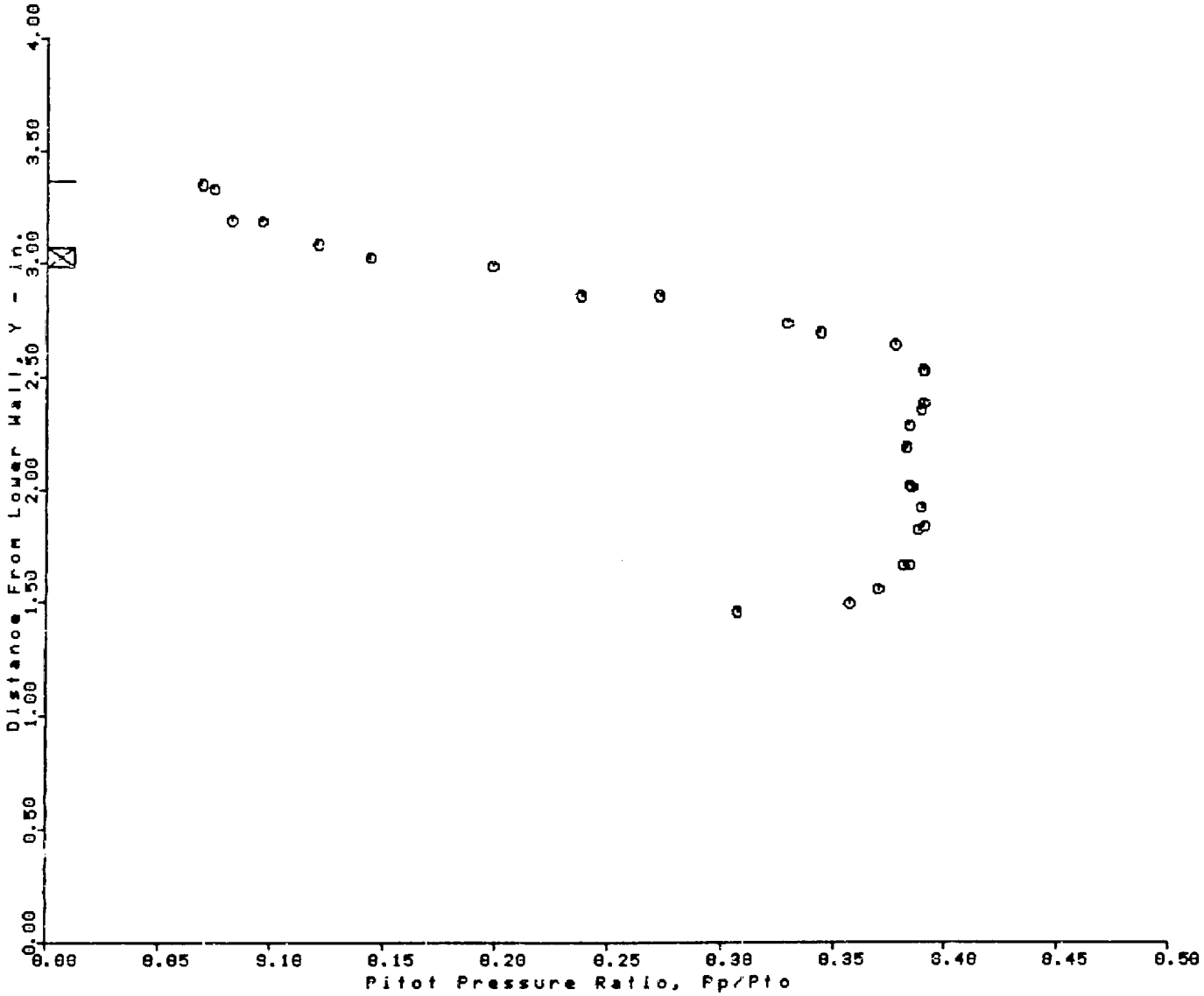

AFS TEST PROGRAM
RUN = 111 BURSTS 25 THRU 53

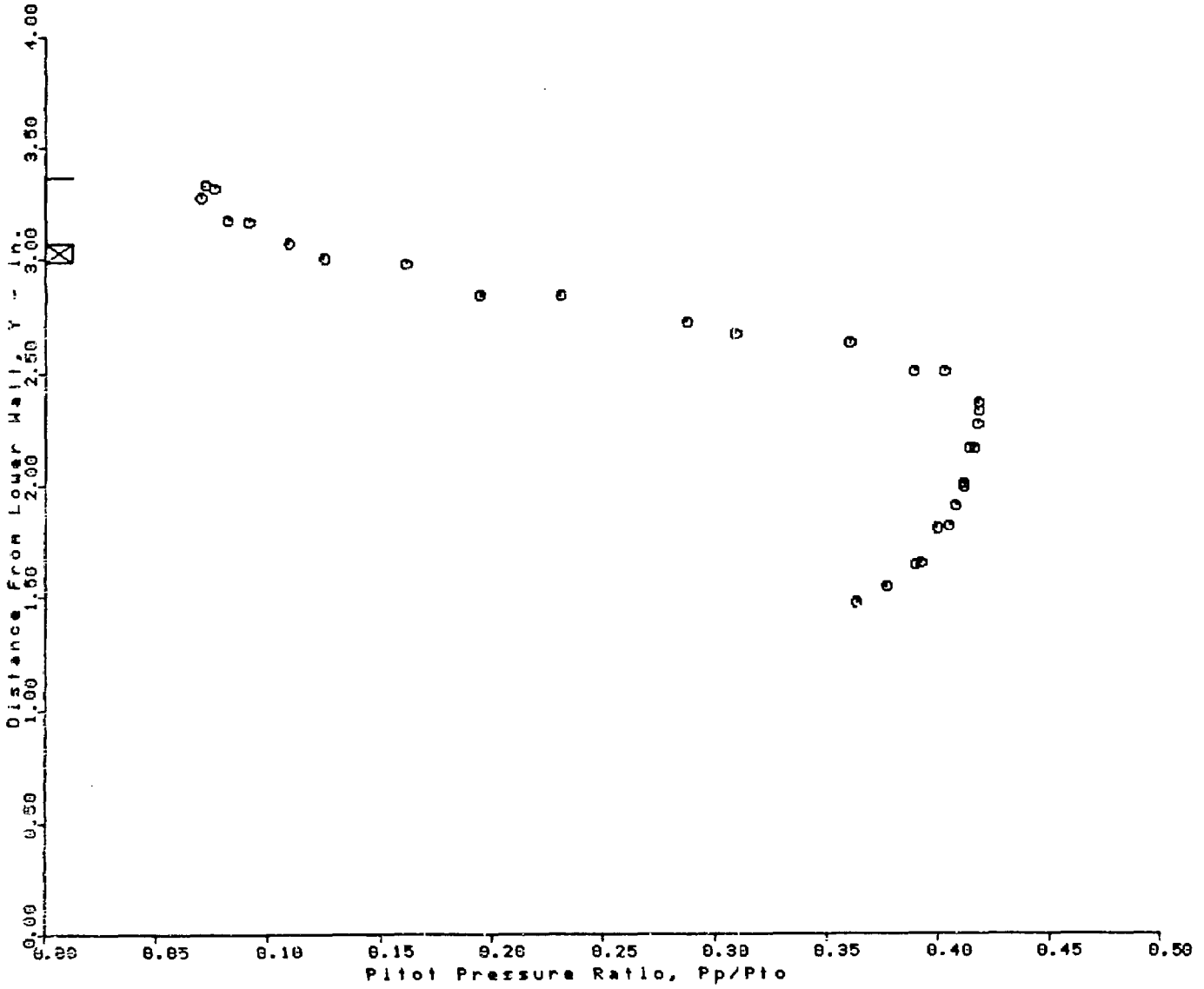

AFS TEST PROGRAM
RUN = 112 BURSTS 31 THRU 59

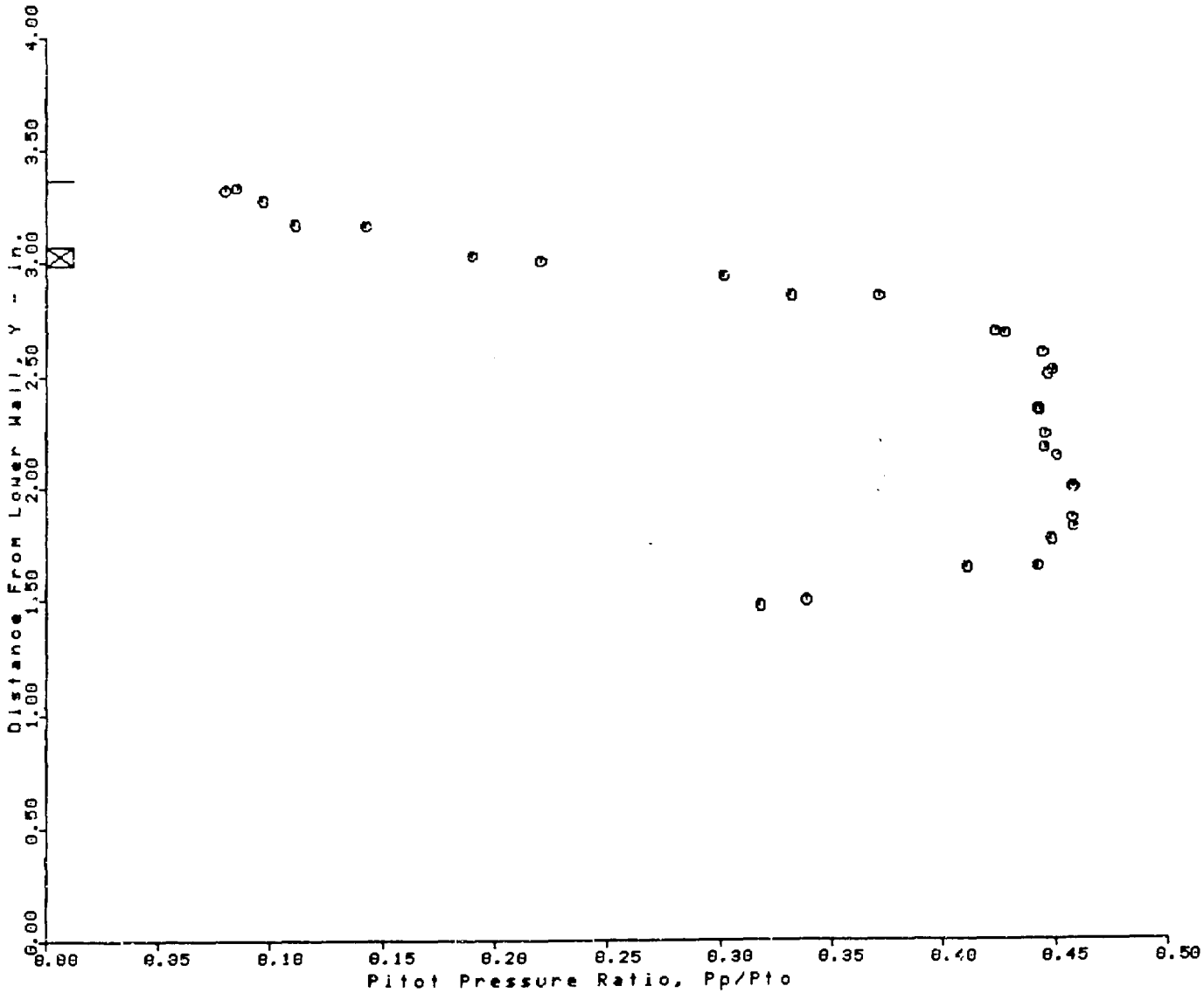

AFS TEST PROGRAM
RUN = 113 BURSTS 29 THRU 57

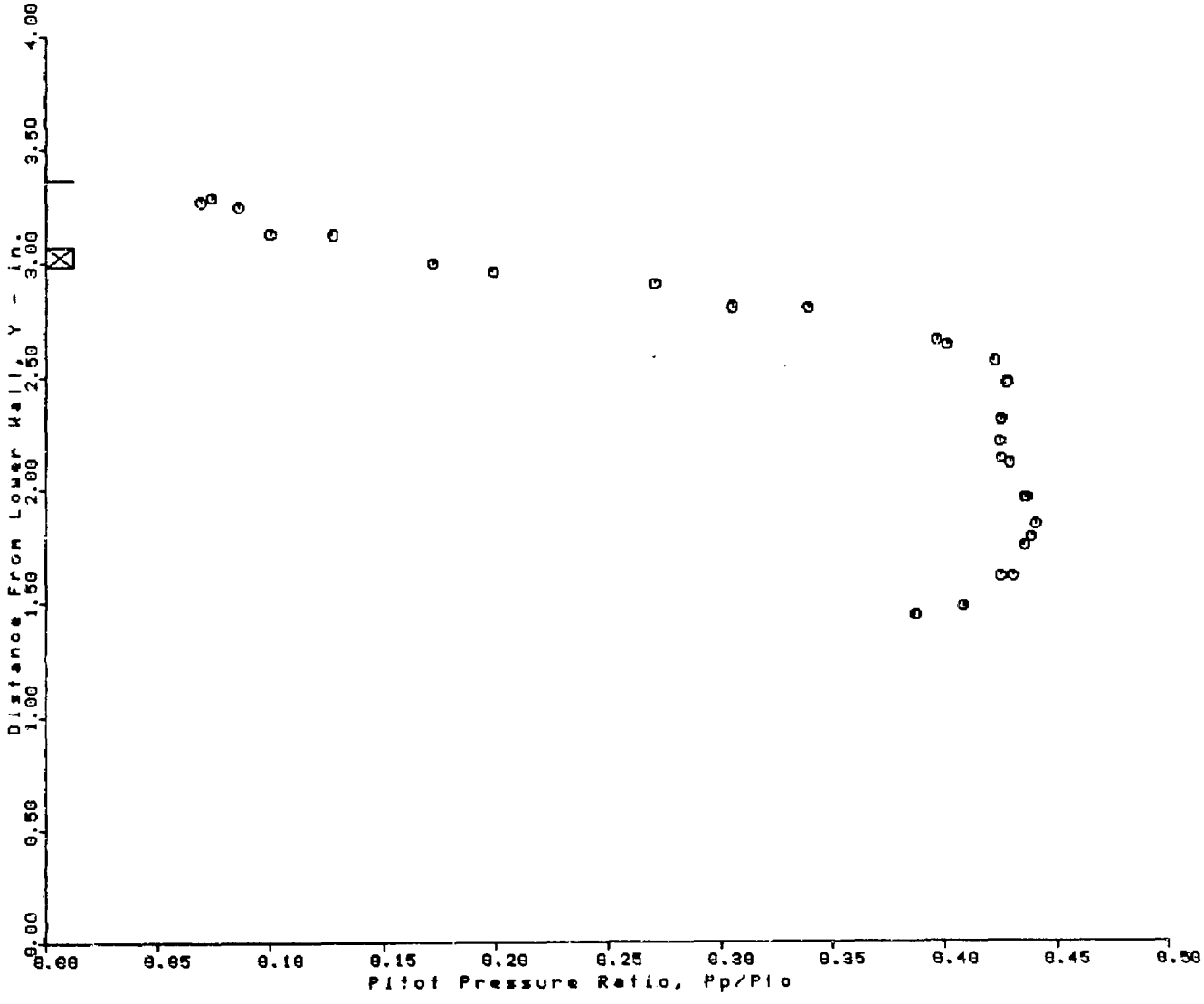

AFS TEST PROGRAM
RUN = 114 BURSTS 25 THRU 53

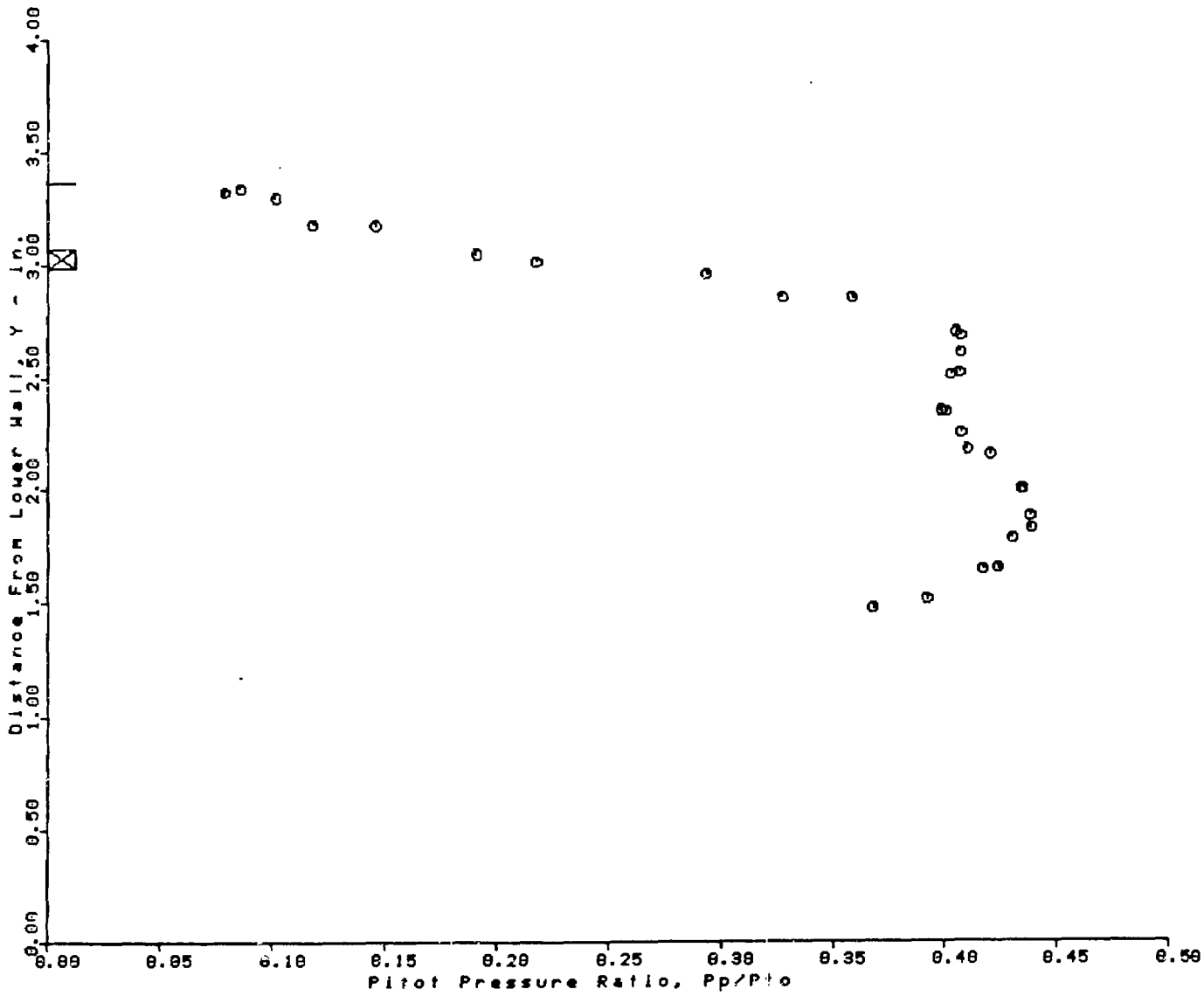

AFS TEST PROGRAM
RUN = 121 BURSTS 33 THRU 61

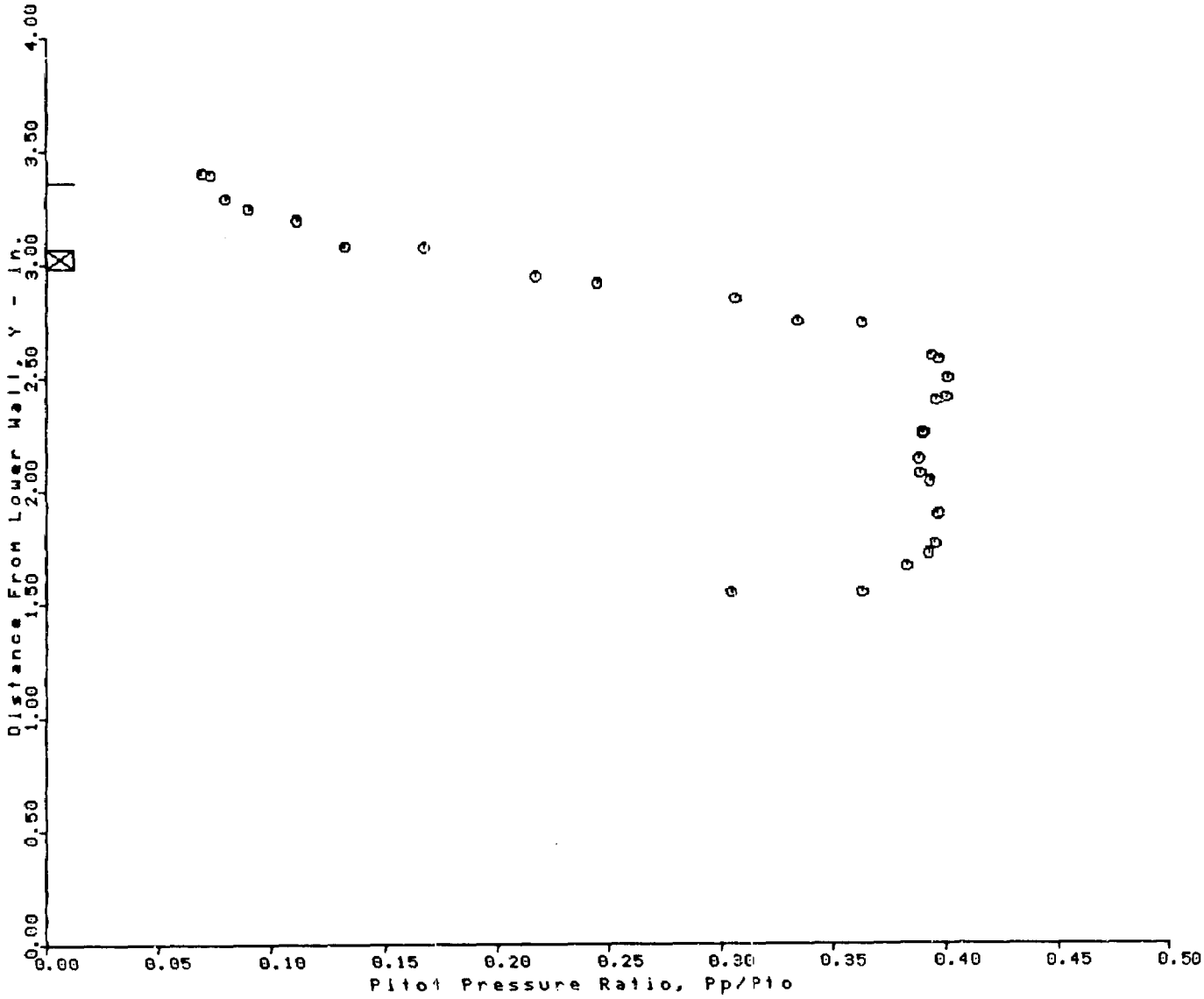

AFS TEST PROGRAM
RUN = 122 BURSTS 31 THRU 59

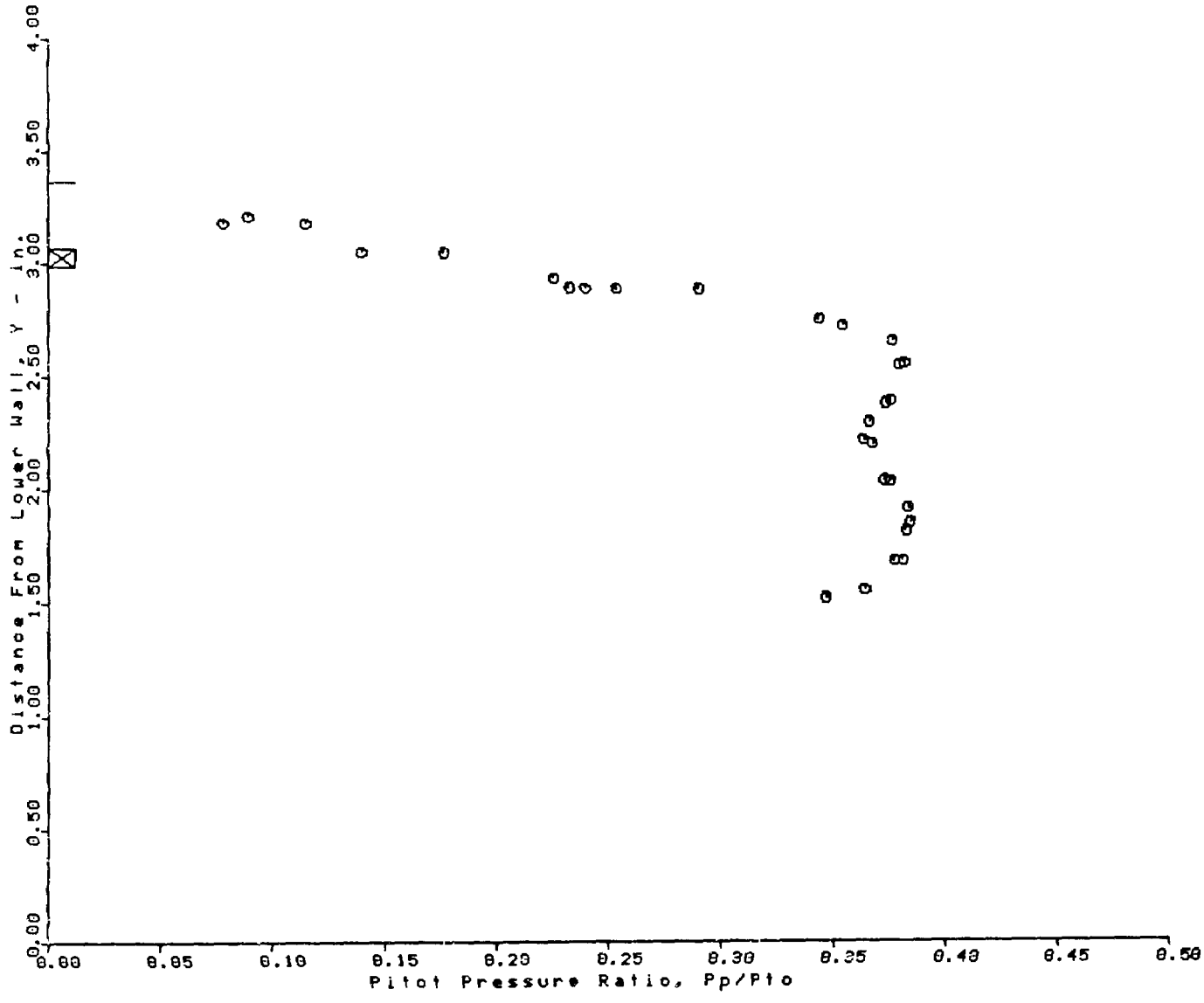

AFS TEST PROGRAM
RUN = 124 BURSTS 25 THRU 53

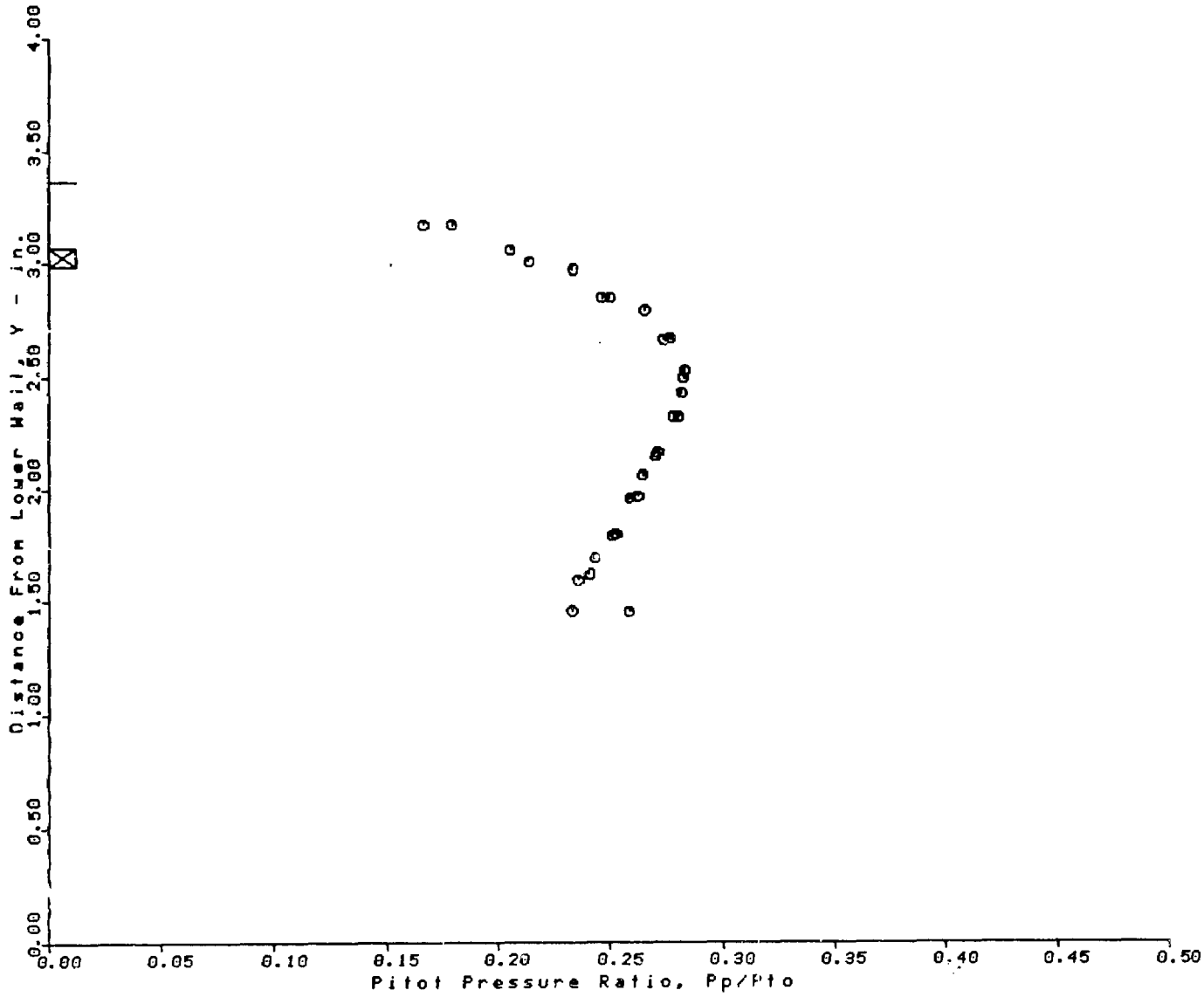

AFS TEST PROGRAM
RUN = 125 BURSTS 25 THRU 54

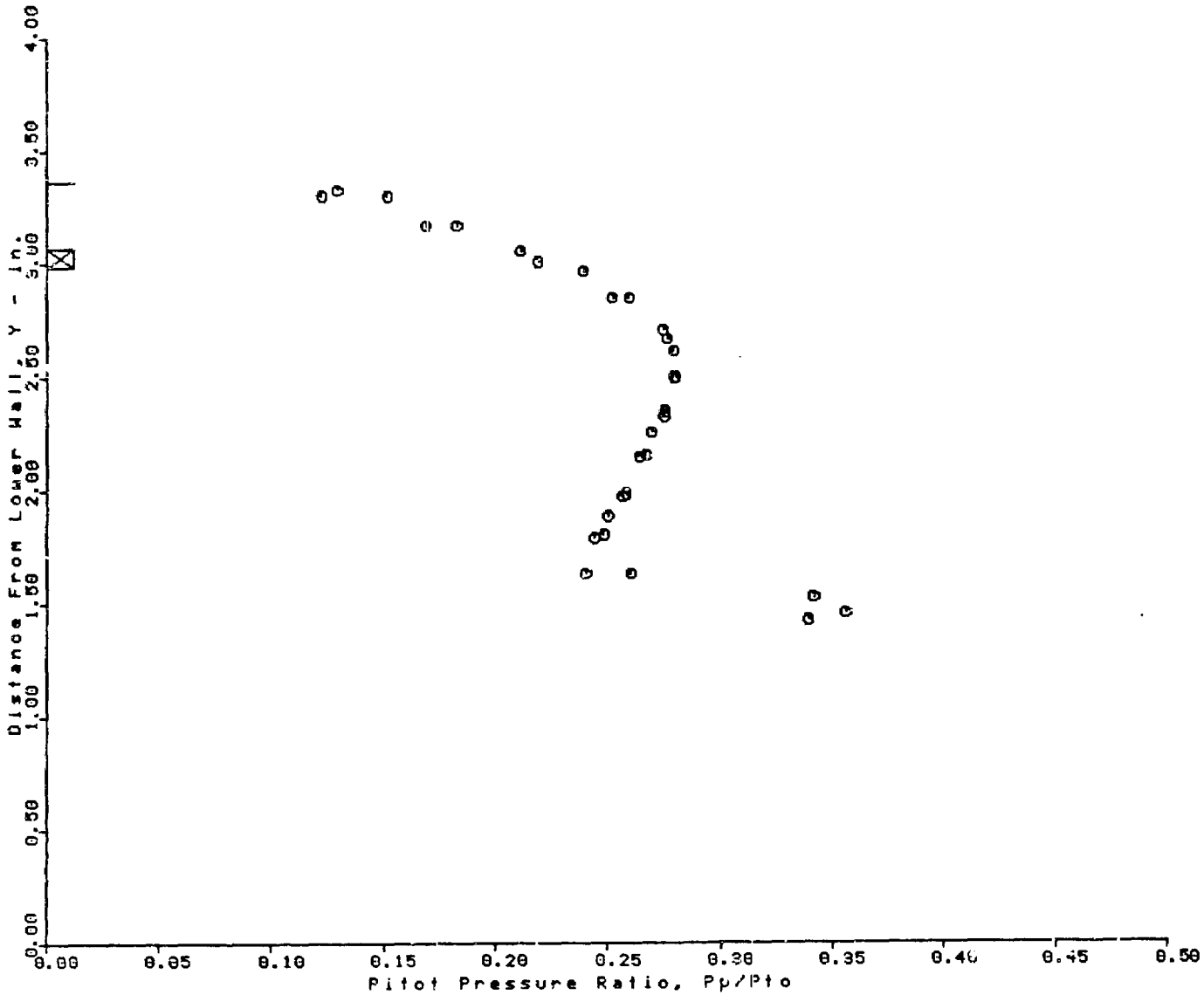

AFS TEST PROGRAM
RUN = 126 BURSTS 27 THRU 55

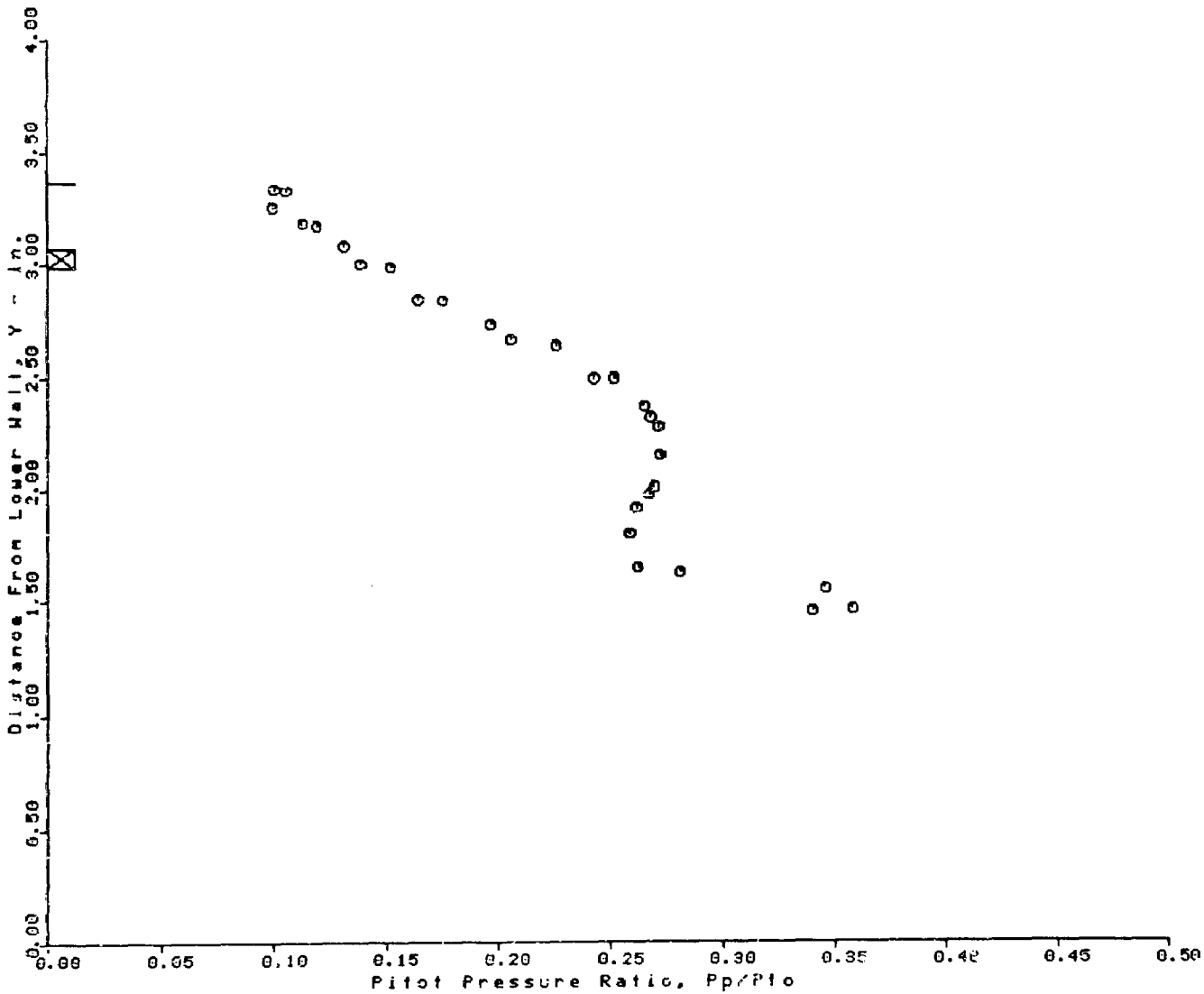

AFS TEST PROGRAM
RUN = 127 BURSTS 27 THRU 55

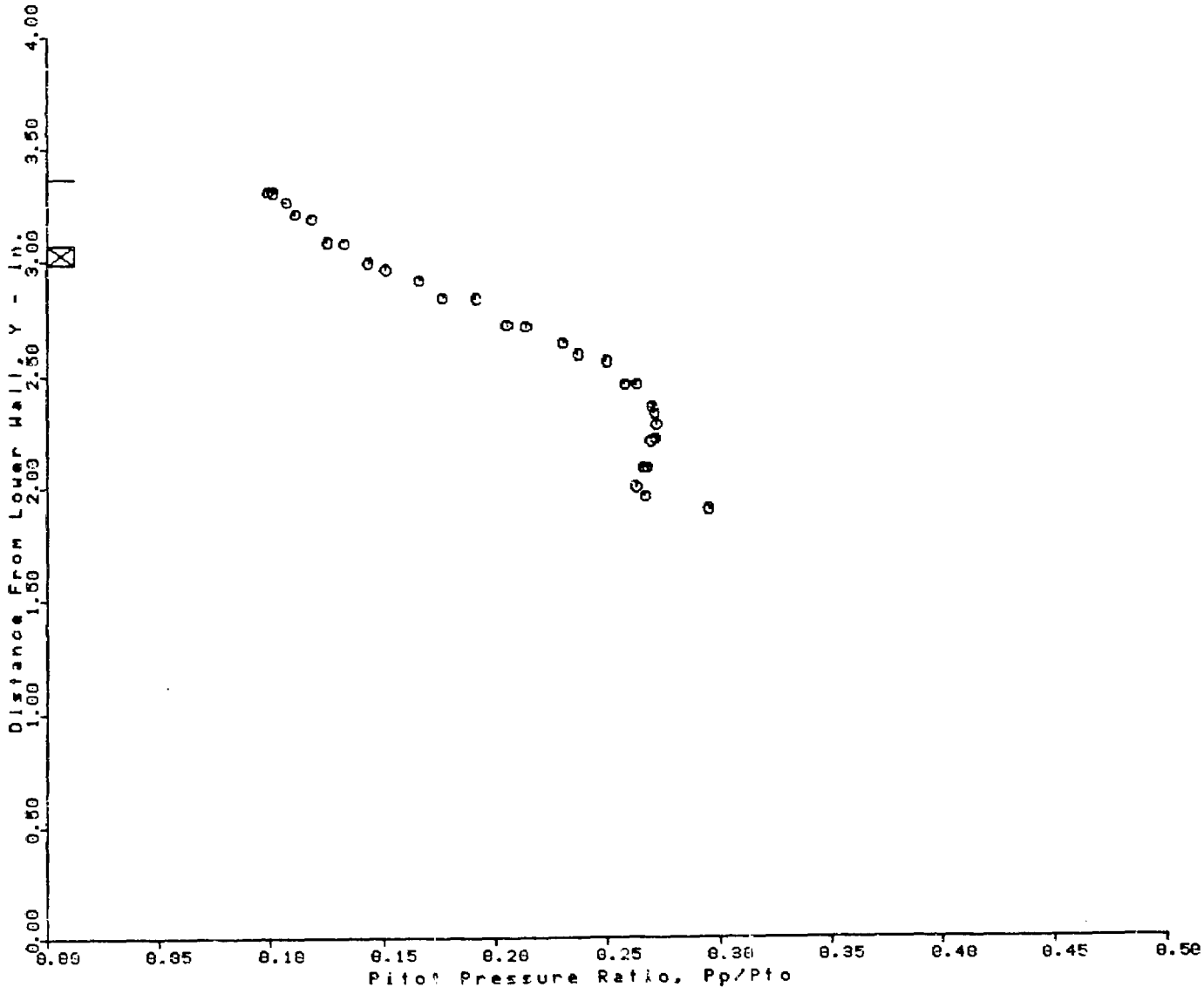

AFS TEST PROGRAM
RUN = 128 BURSTS 25 THRU 53

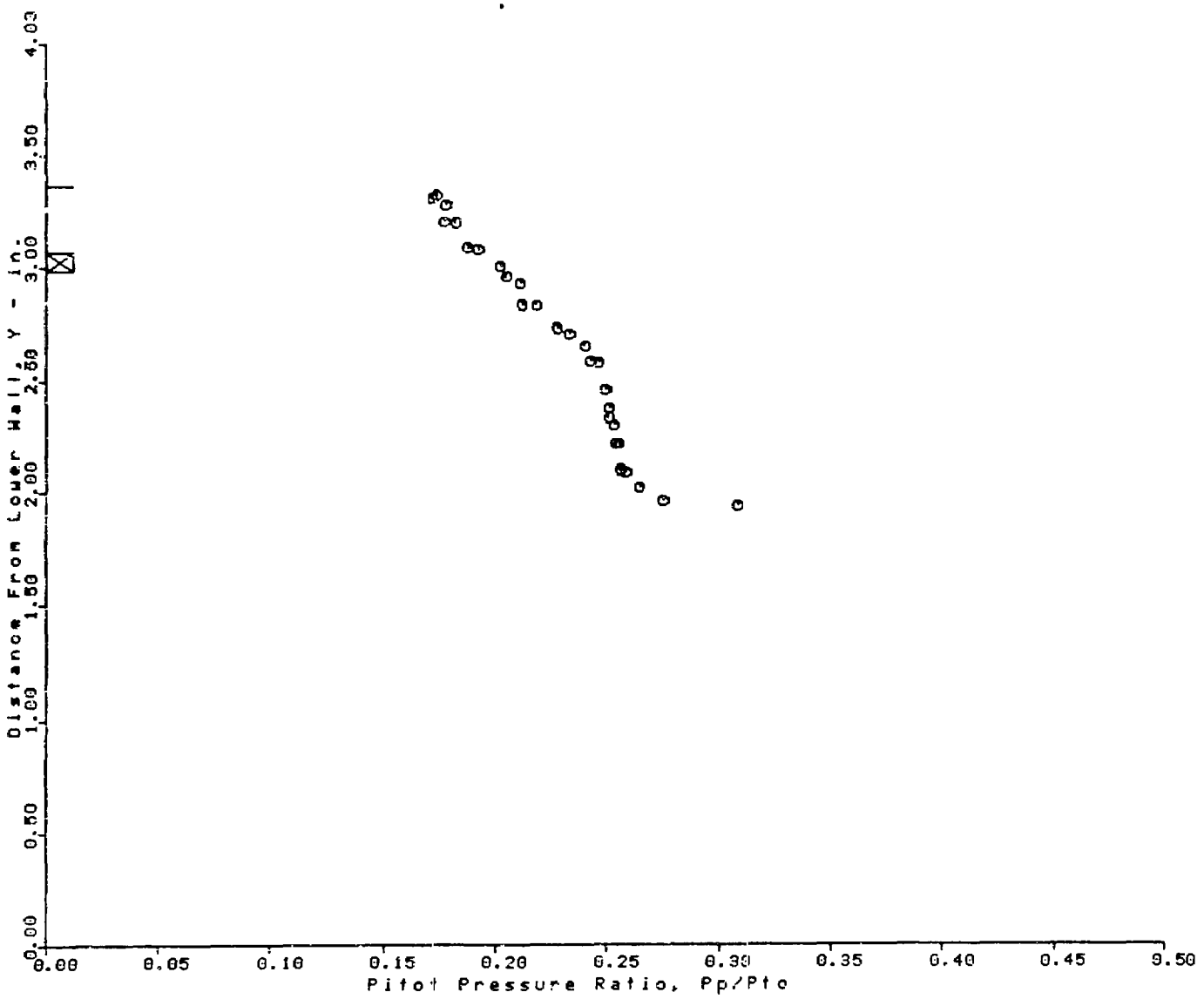

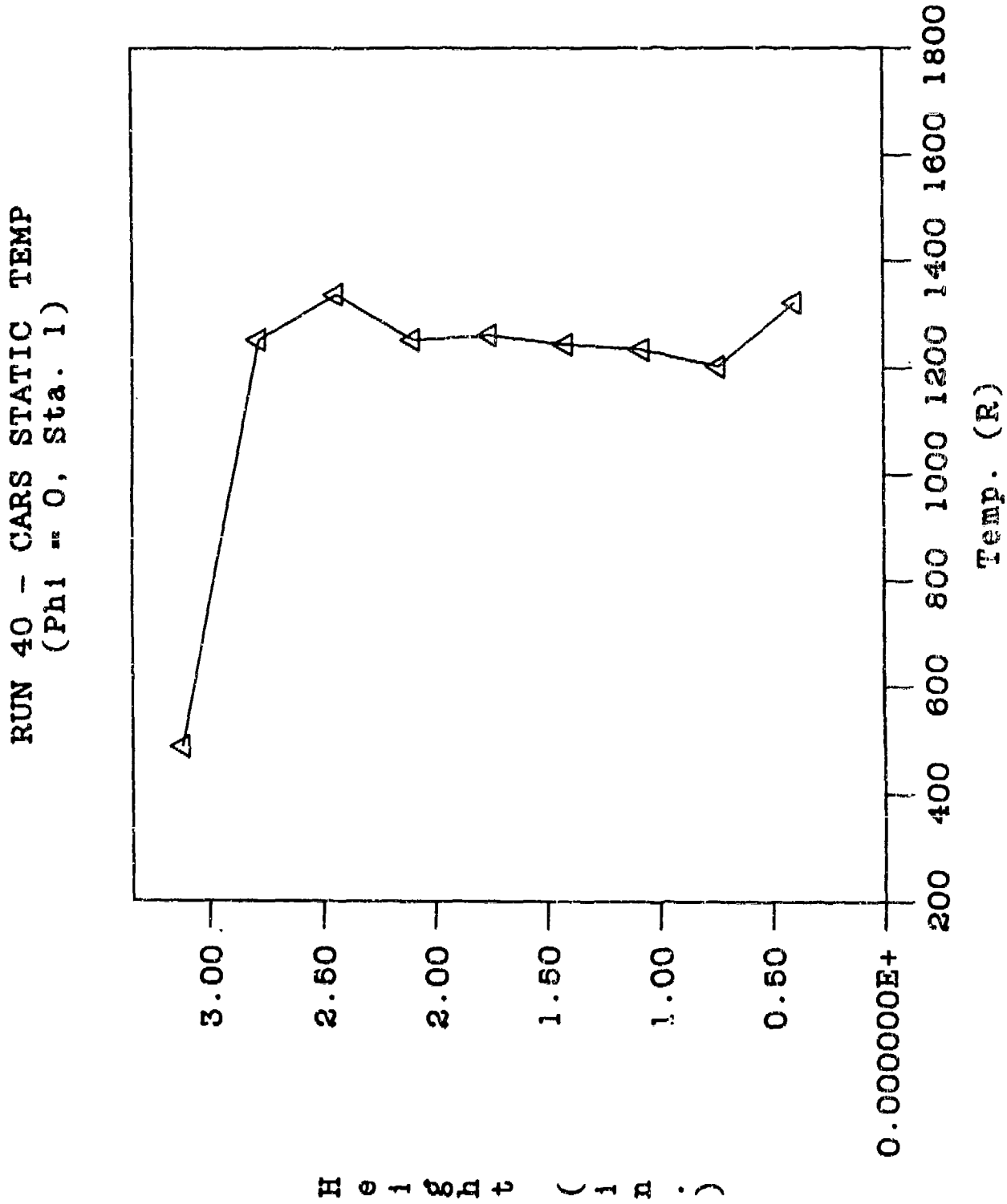
RUN 40 - CARS STATIC TEMP
(Phi = 0, Sta. 1)
Height (in.)
3.00
2.50
2.00
1.50
1.00
0.50
0.0000000E+
200
400
600
800
1000
1200
1400
1600
1800
Temp. (R)

RUN 42 - CARS STATIC TEMP
(Phi = 0, Sta. 1)

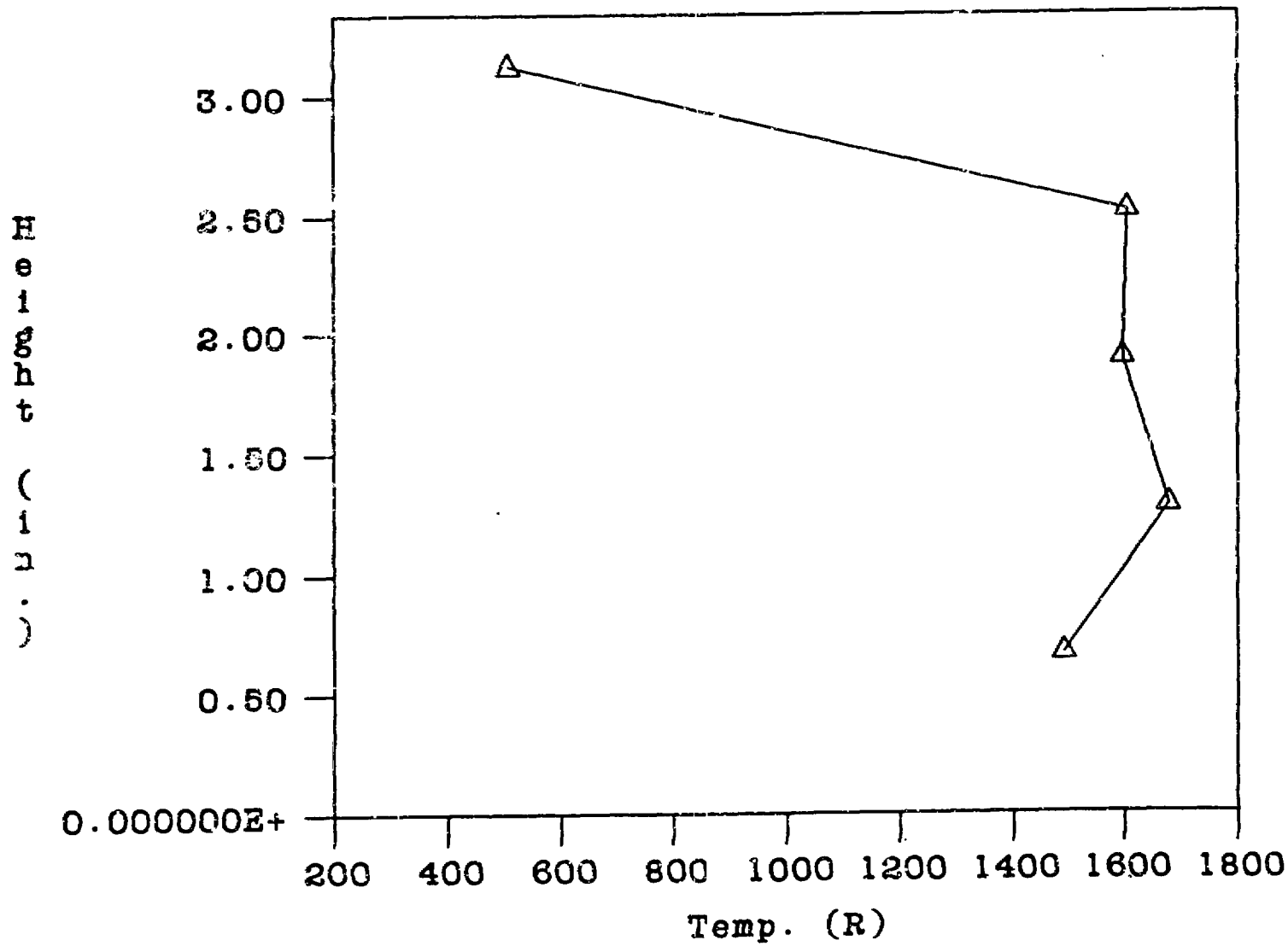

Run 054 - CARS Static Temp (R)
(Phi = 0.5, Sta. 3)

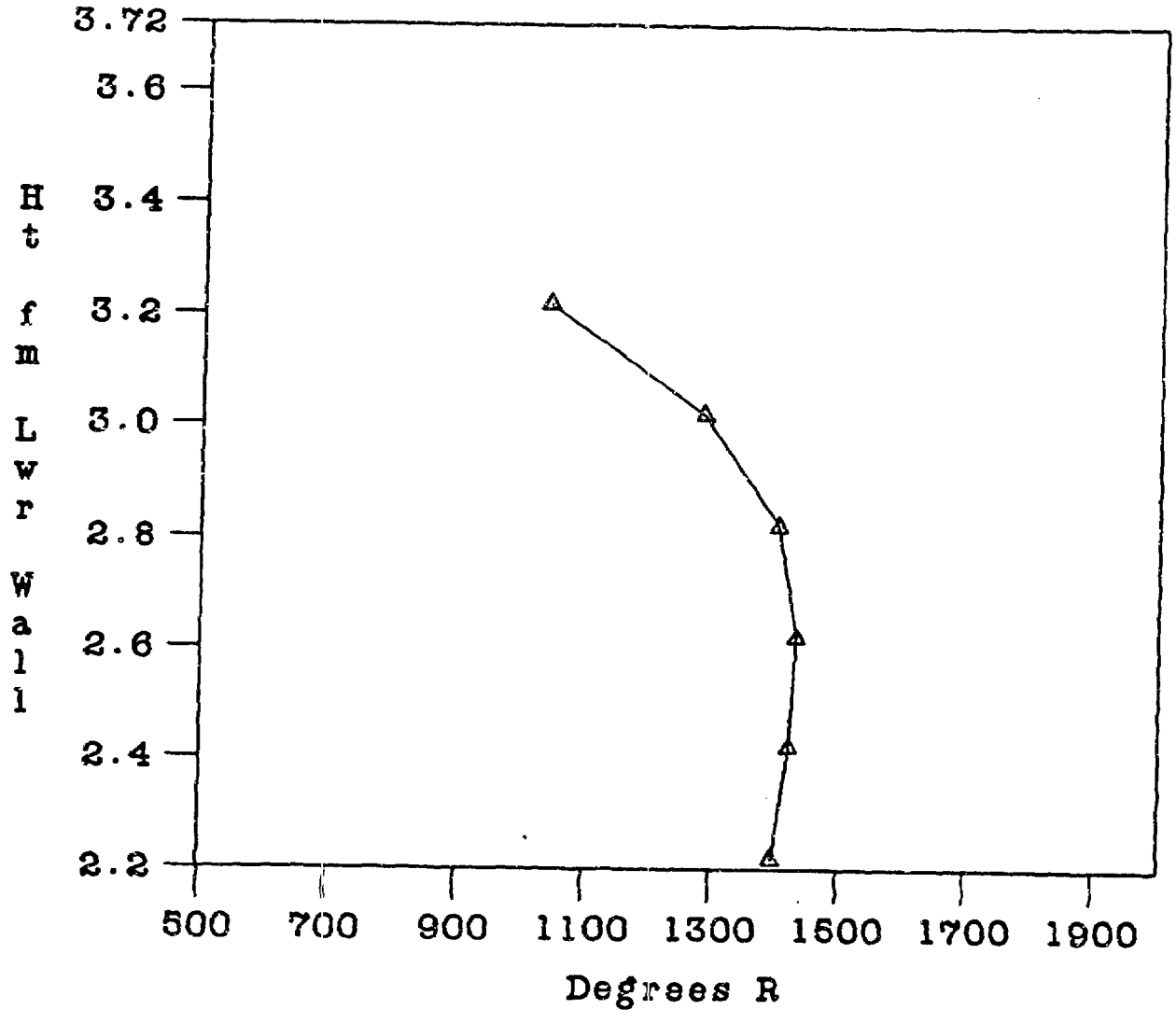

Run 055 - CARS Static Temp (R)
(Phi = 1.0, Sta. 3)

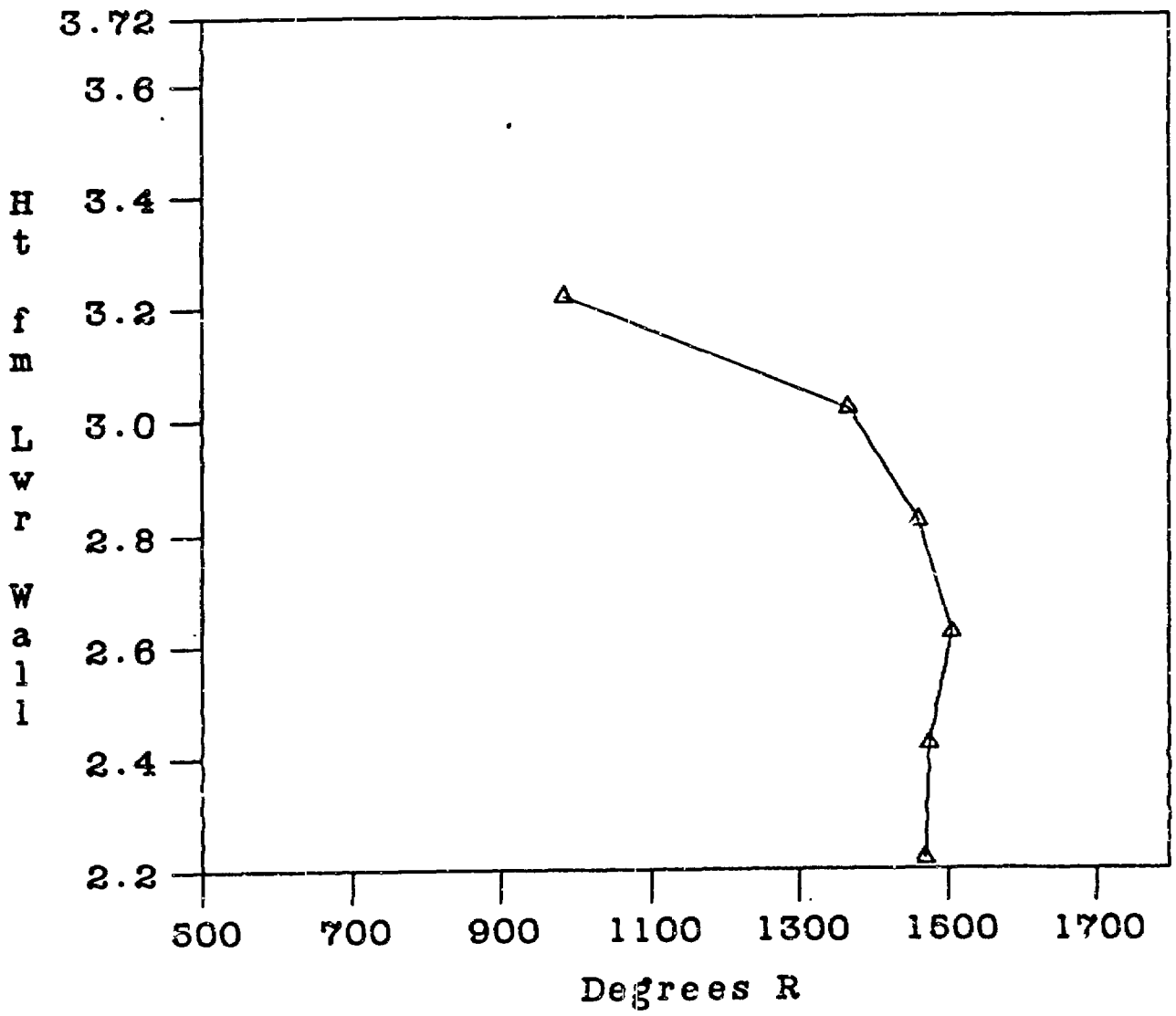

RUN 57 - CARS STATIC TEMP
(Sta. 3)

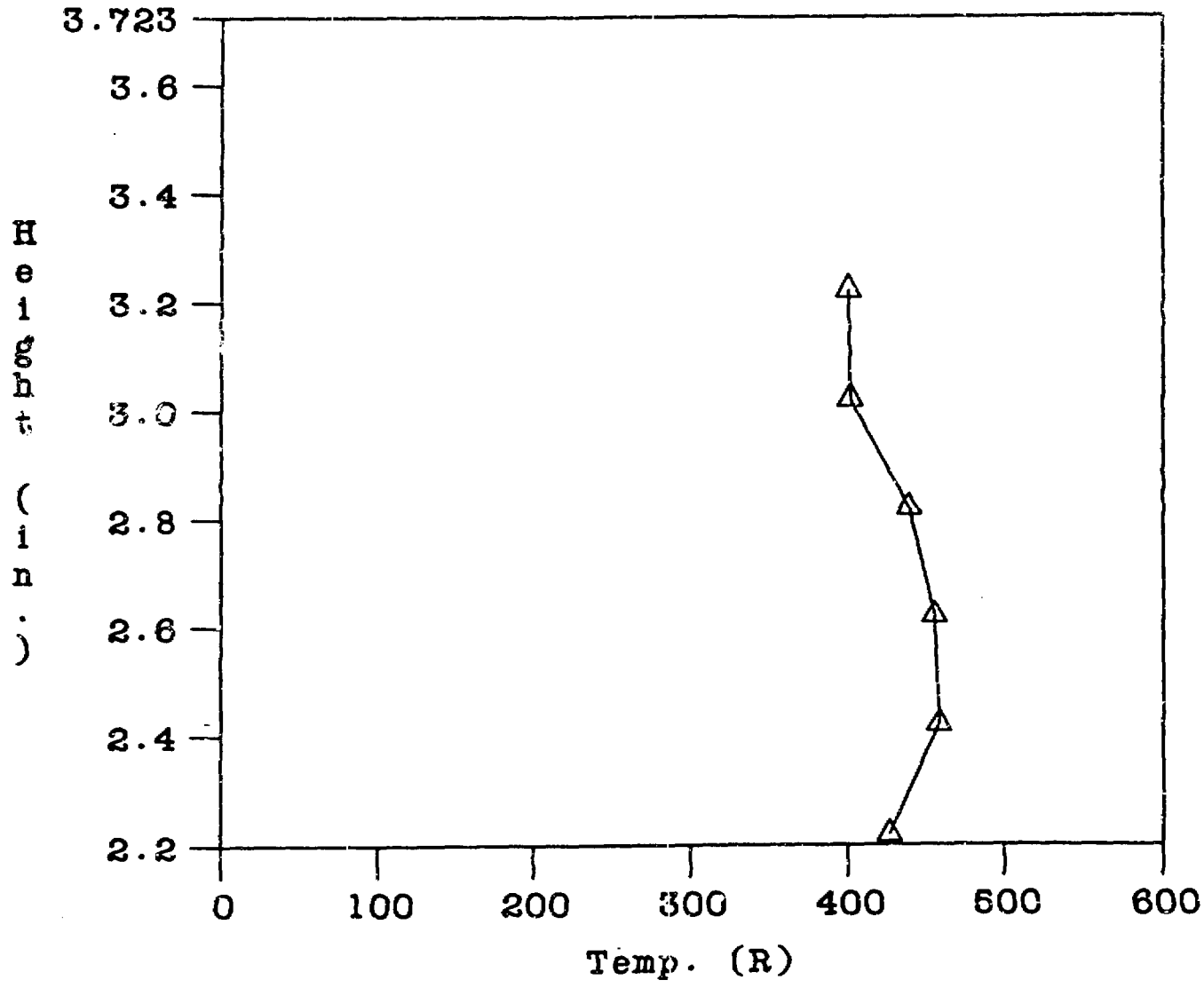

RUN 68 - CARS STATIC TEMP
(Sta. 3)

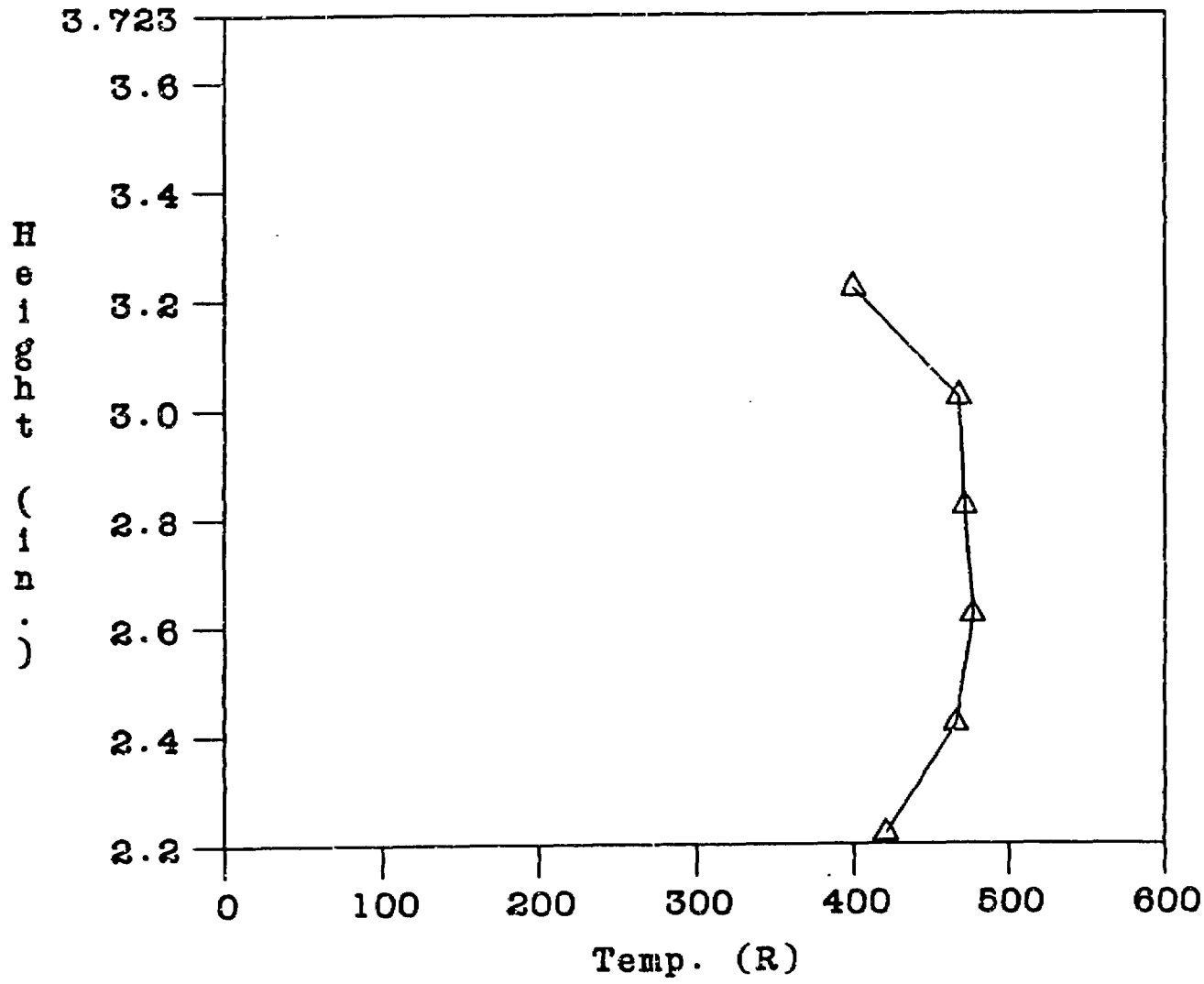

RUN 59 - CARS STATIC TEMP
(Sta. 3)

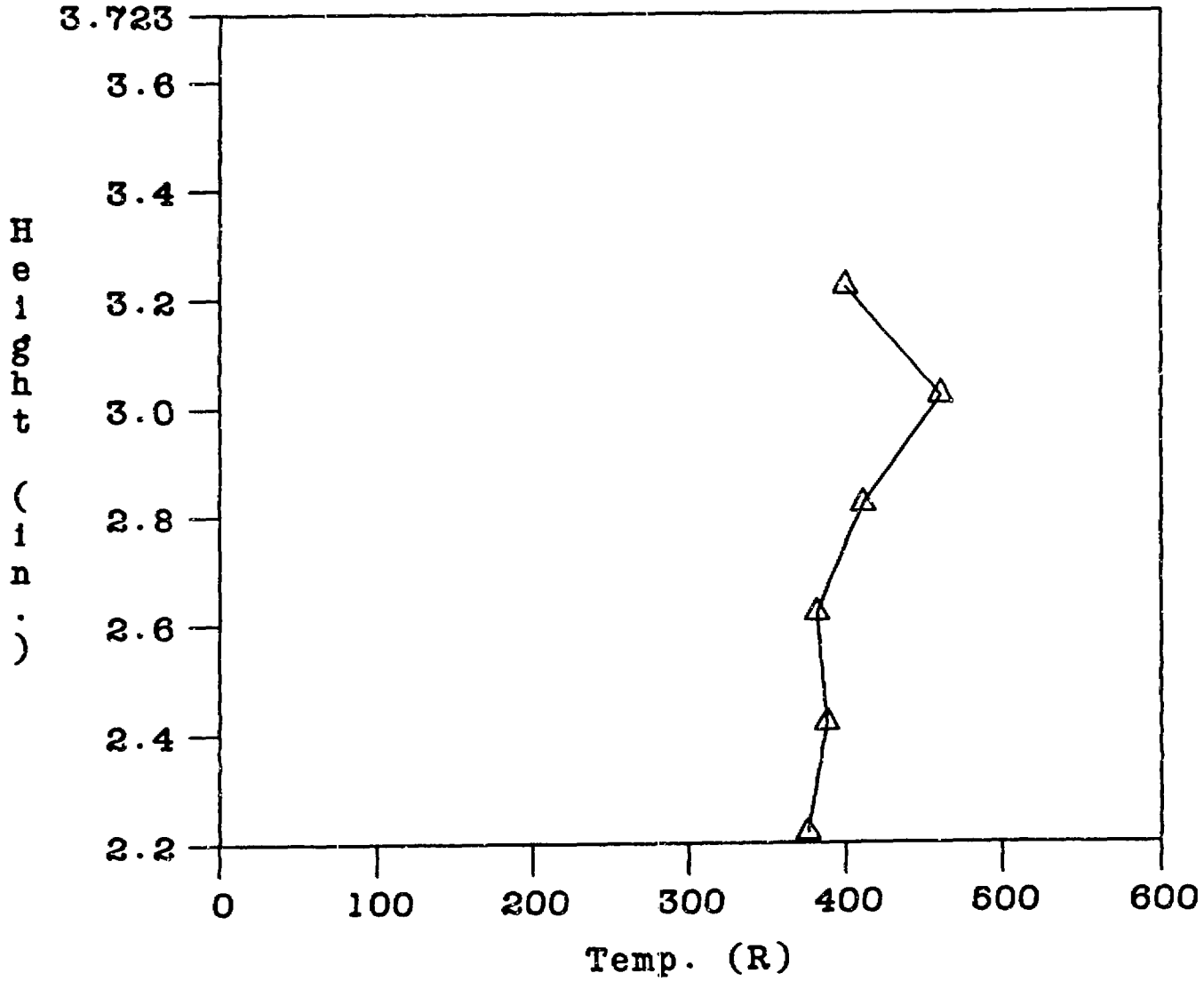

RUN 62 - CARS STATIC TEMP
(Sta. 2)

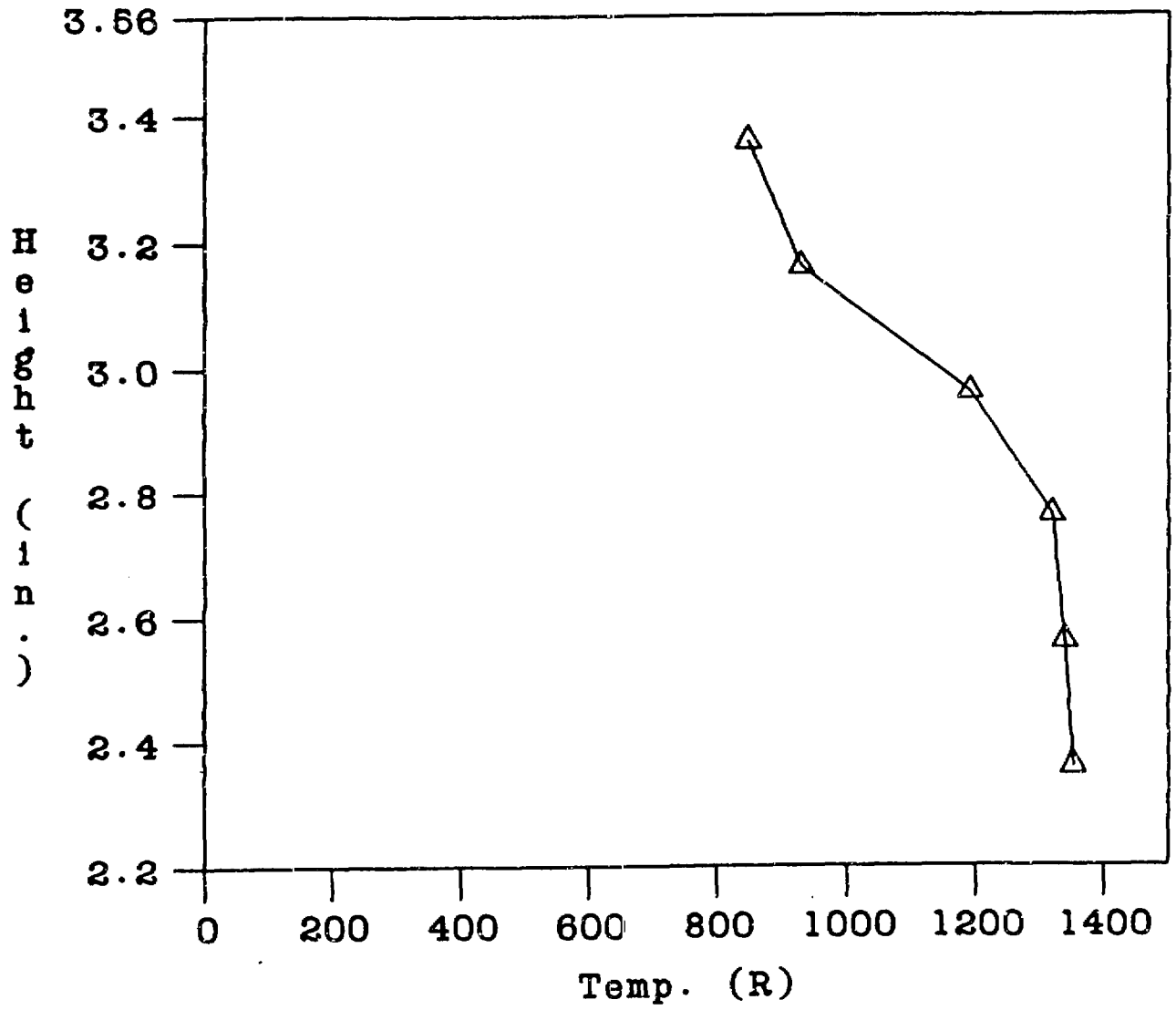

RUN 64 - CARS STATIC TEMP
(Sta. 2)

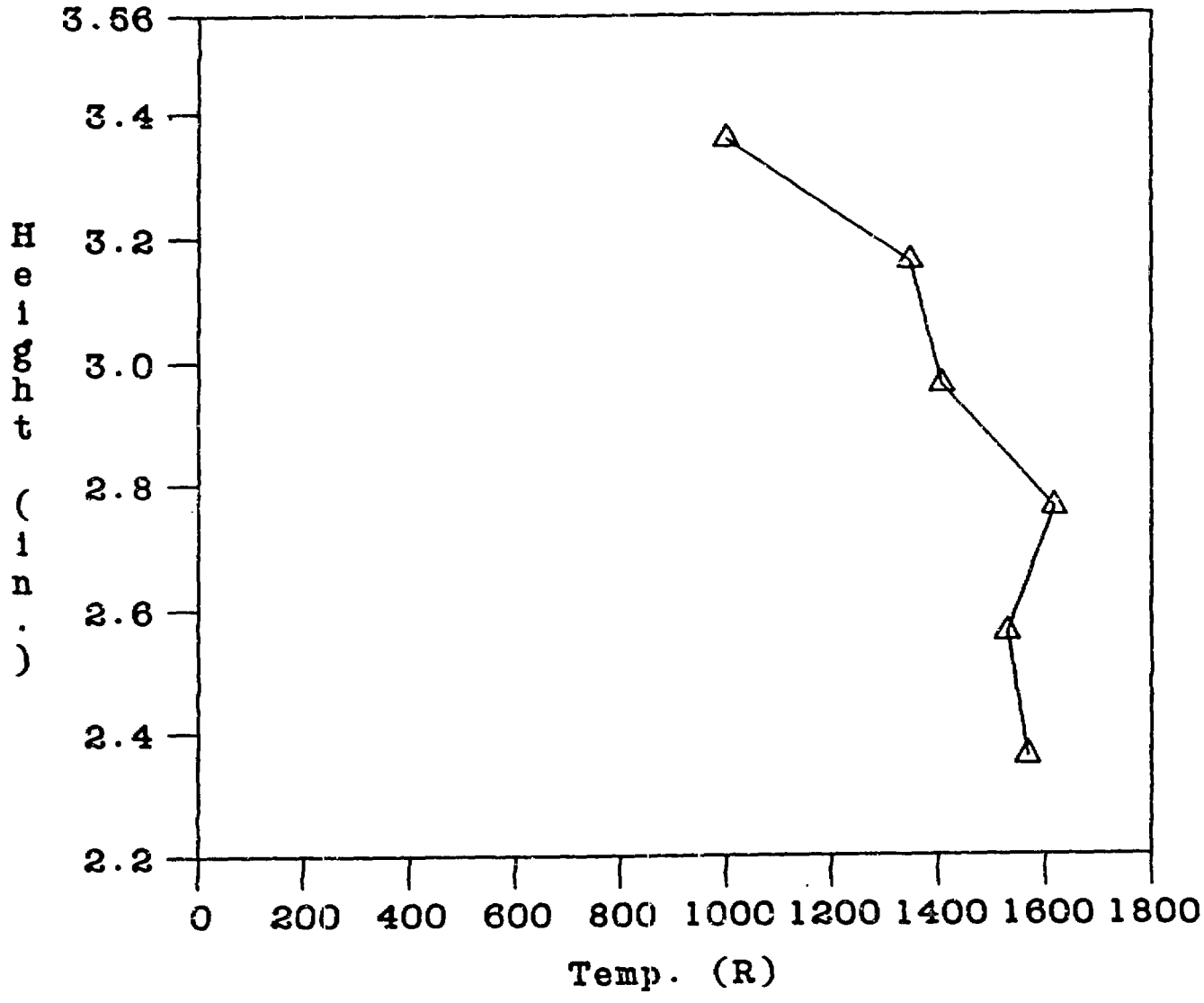

RUN 65 - CARS STATIC TEMP
(Sta. 2)

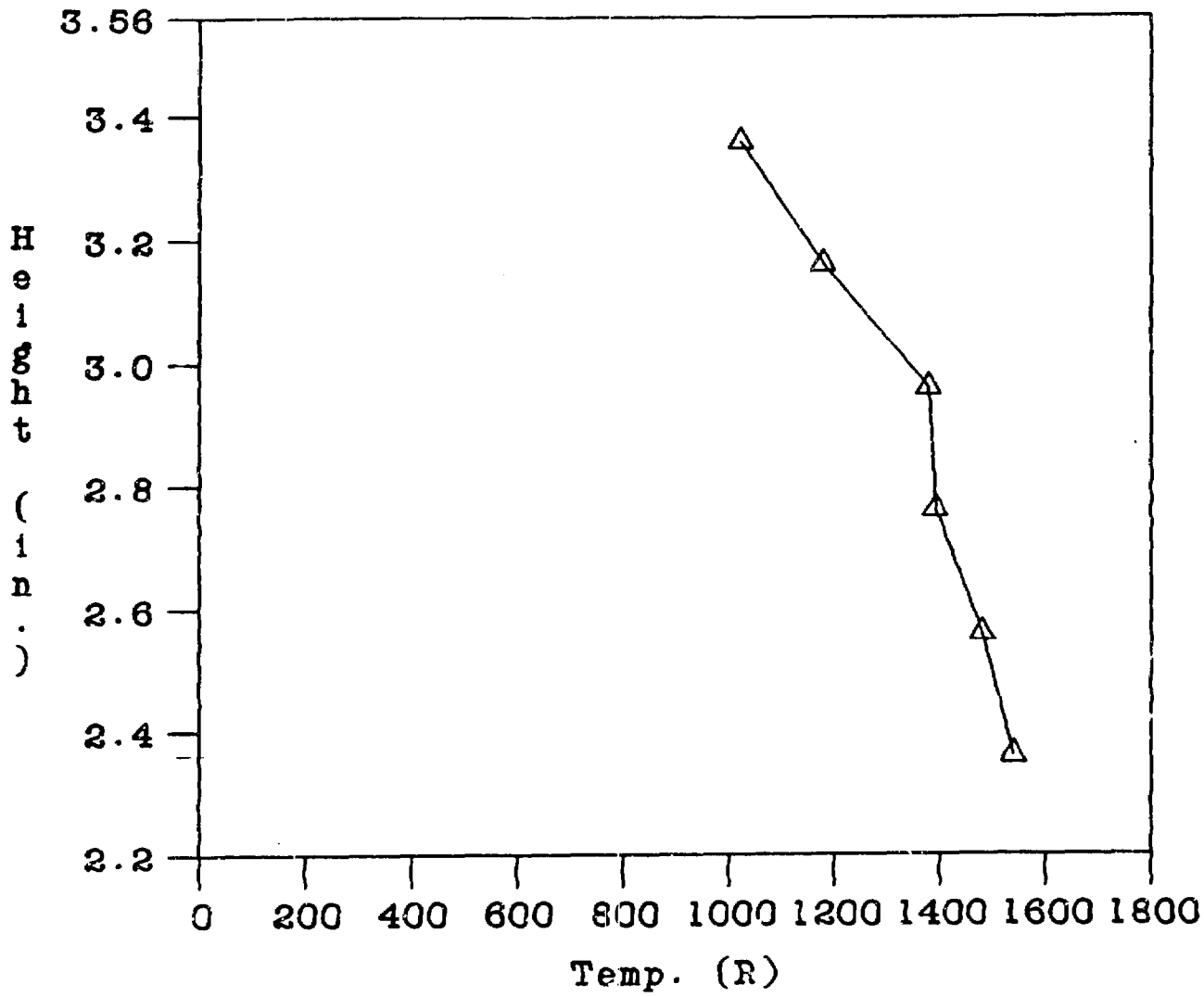

RUN 66 - CARS STATIC TEMP
(Sta. 2)

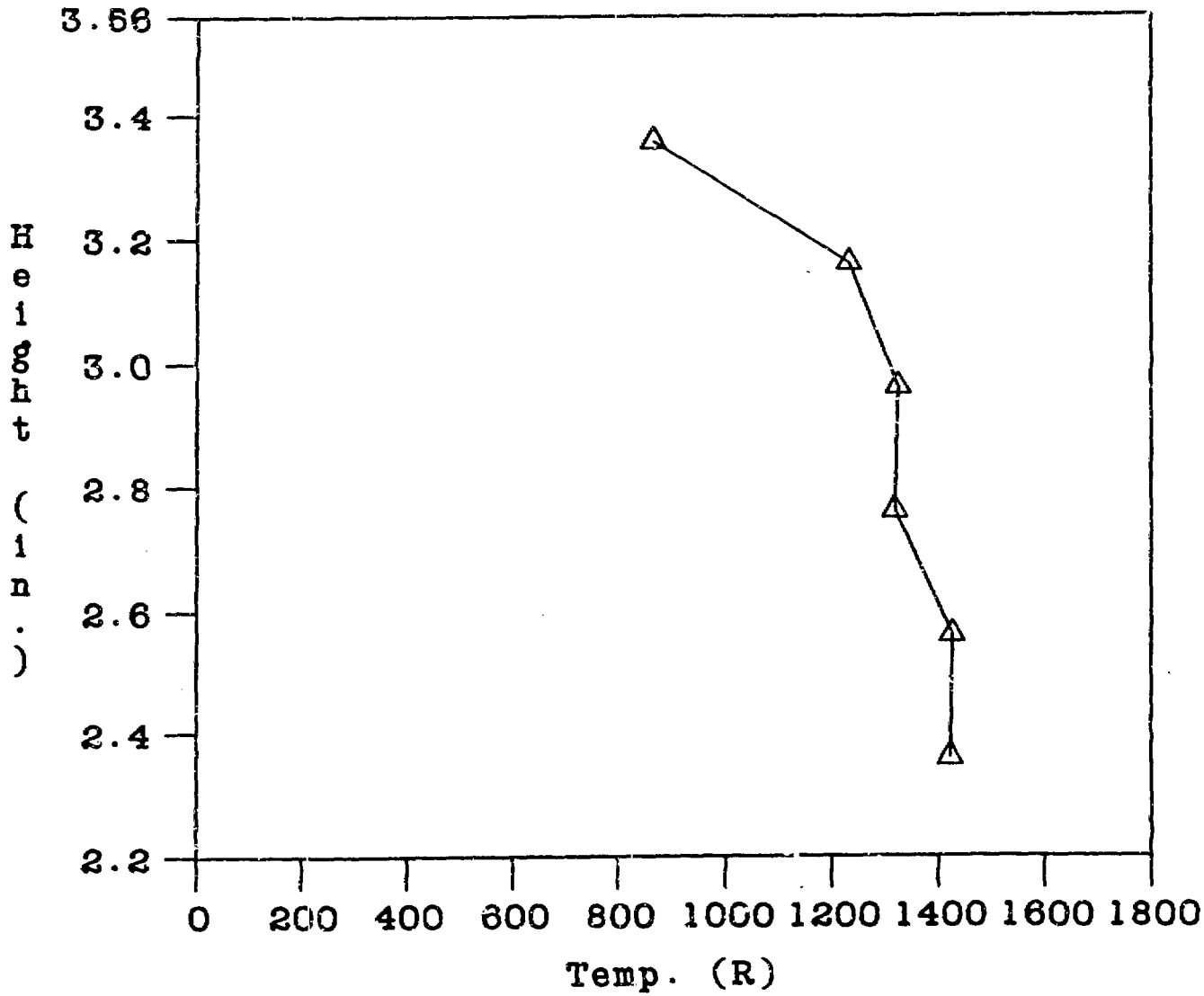

RUN 70 - CARS STATIC TEMP
(Sta. 2)

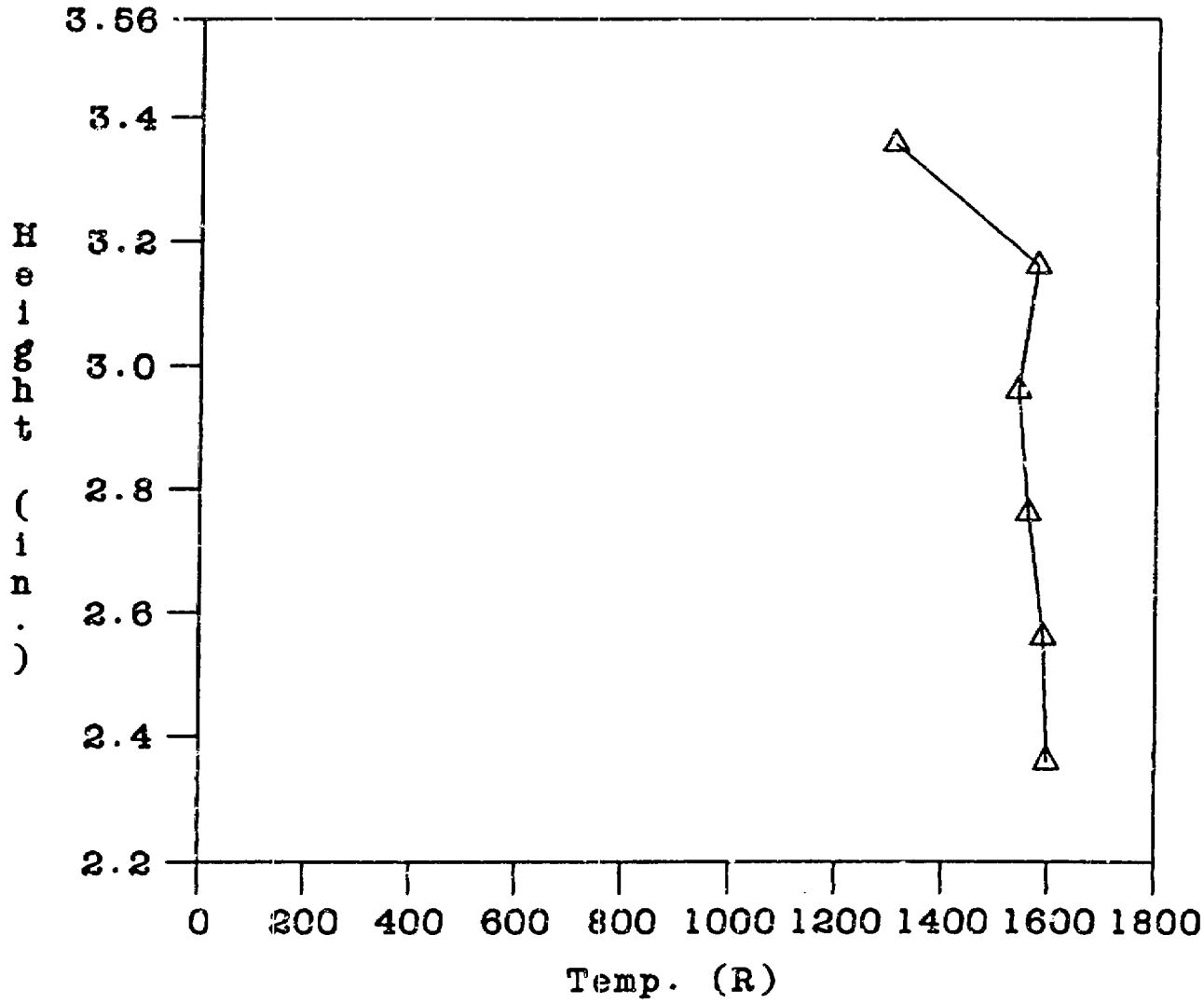

Run 074 - CARS Static Temp (R)
(Phi = 0.5, Sta. 2)

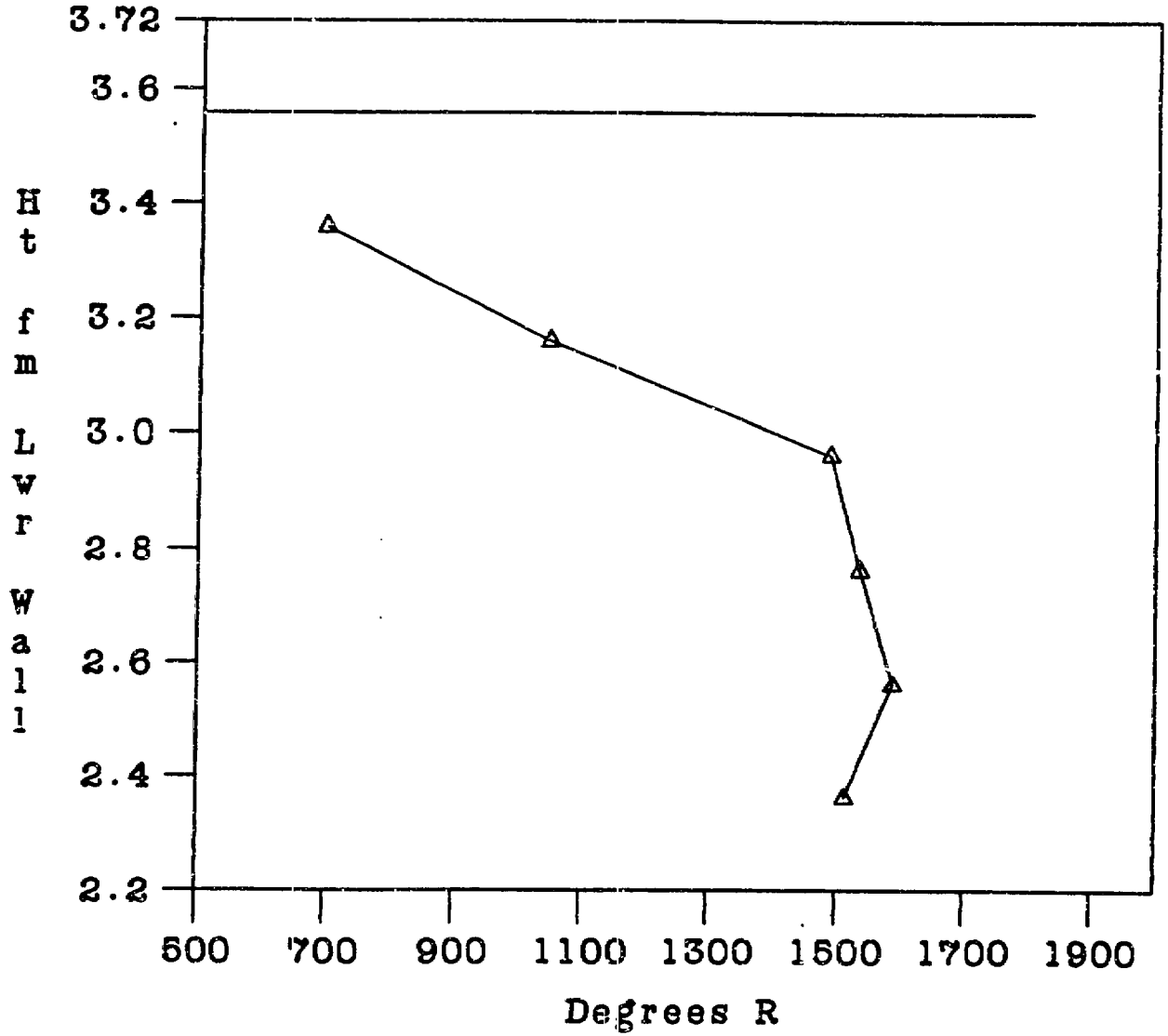

Run 081 - CARS Static Temp (R)
(Phi = 0.5, Sta. 2)

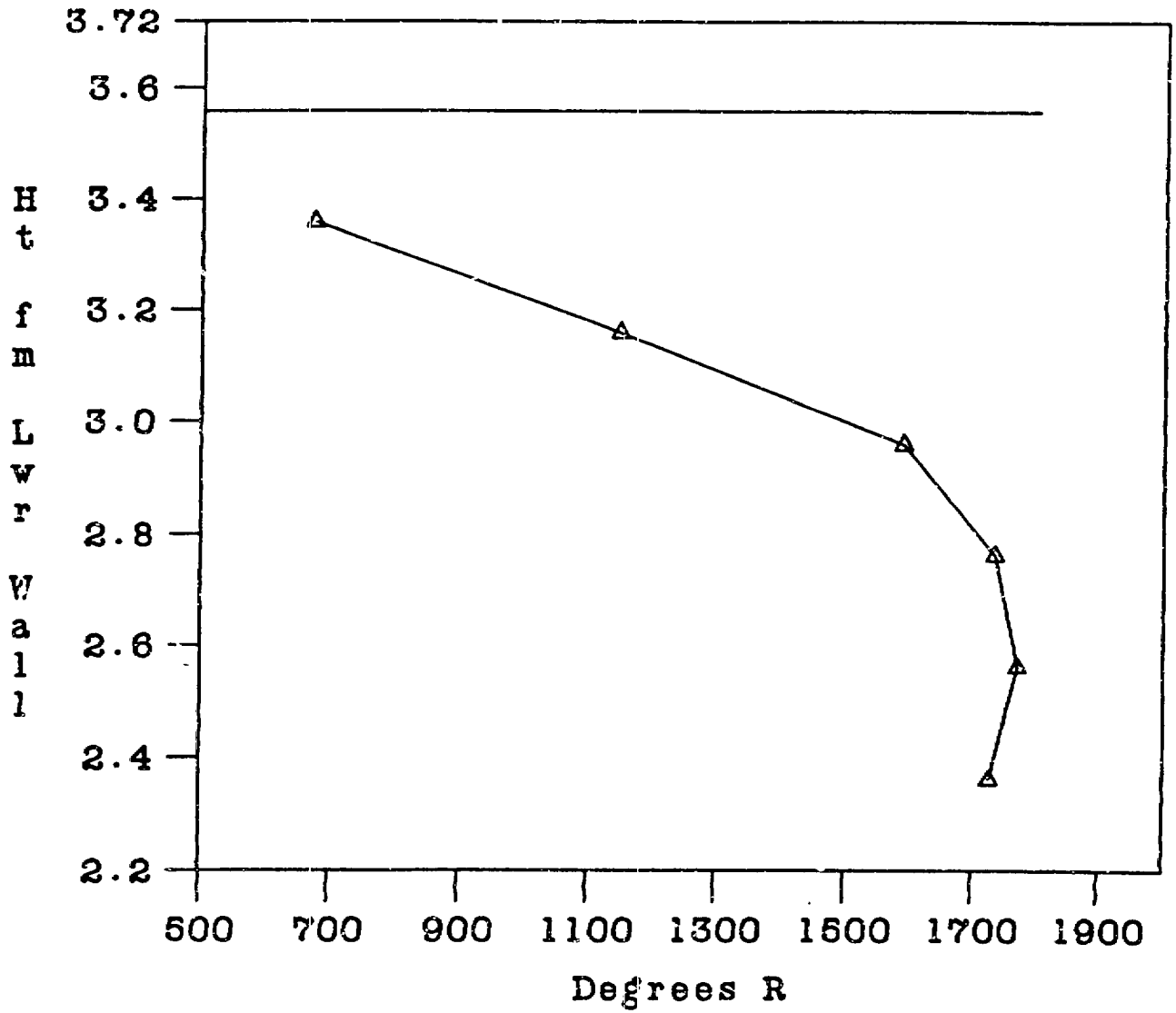

Run 084 - CARS Static Temp (R)
(Phi = 1.0, Sta. 2)

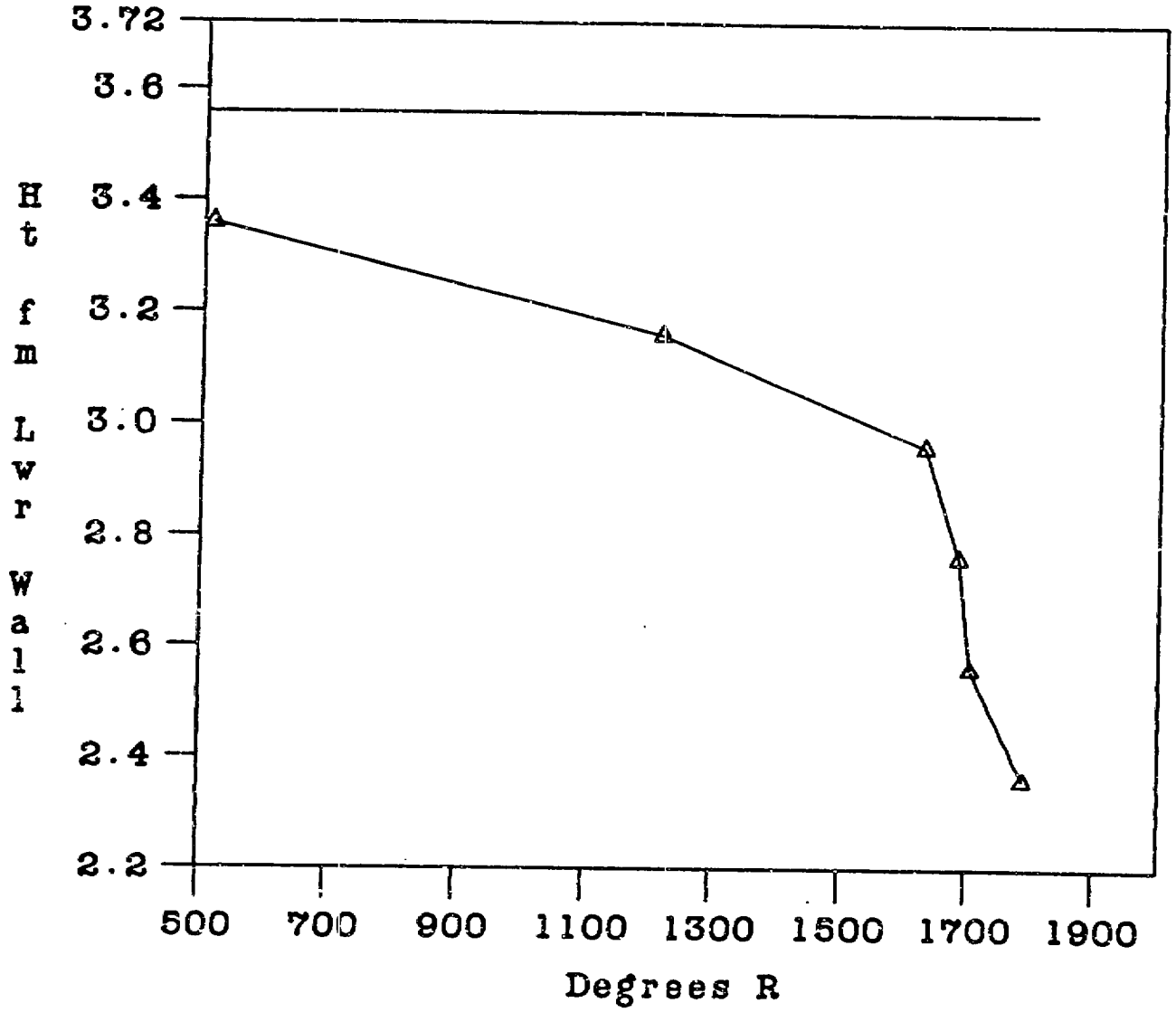

Run 092 - CARS Static Temp (R)
(Phi = 1.0, Sta. 3)

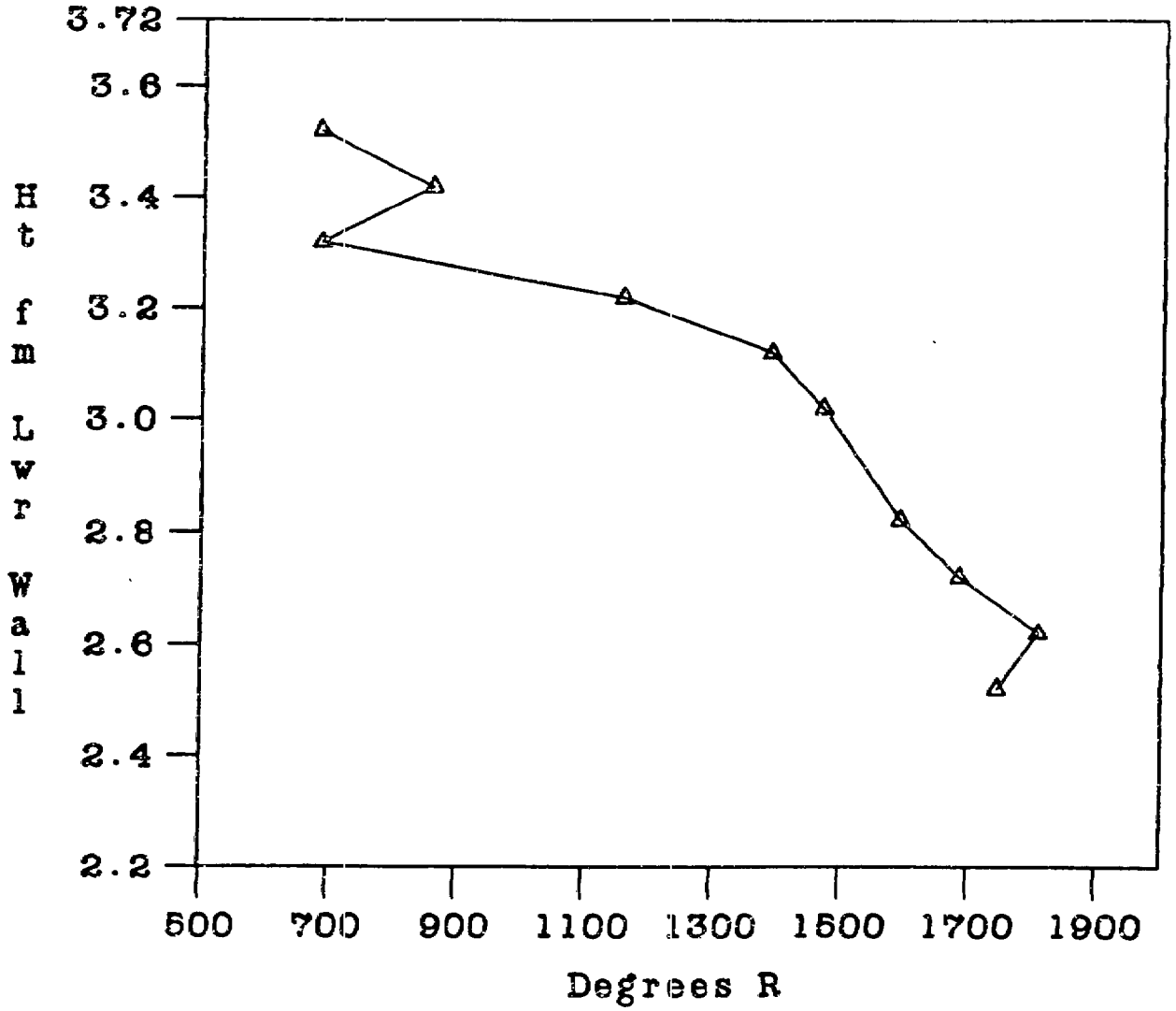

Run 093 - CARS Static Temp (R)
(Phi = 0.5, Sta. 3)

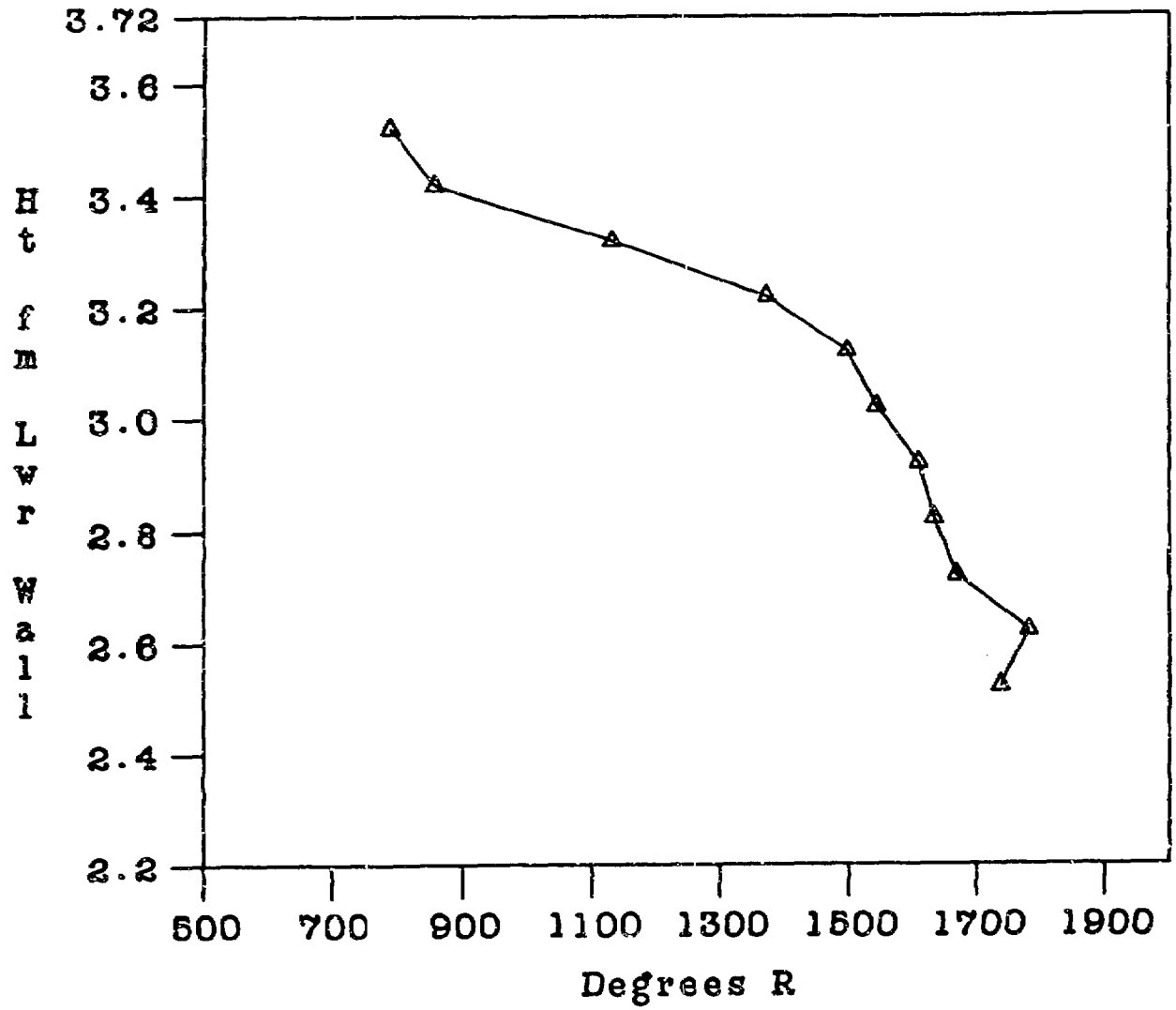

Run 094 - CARS Static Temp (R)
(Phi = 1.0, Sta. 3)

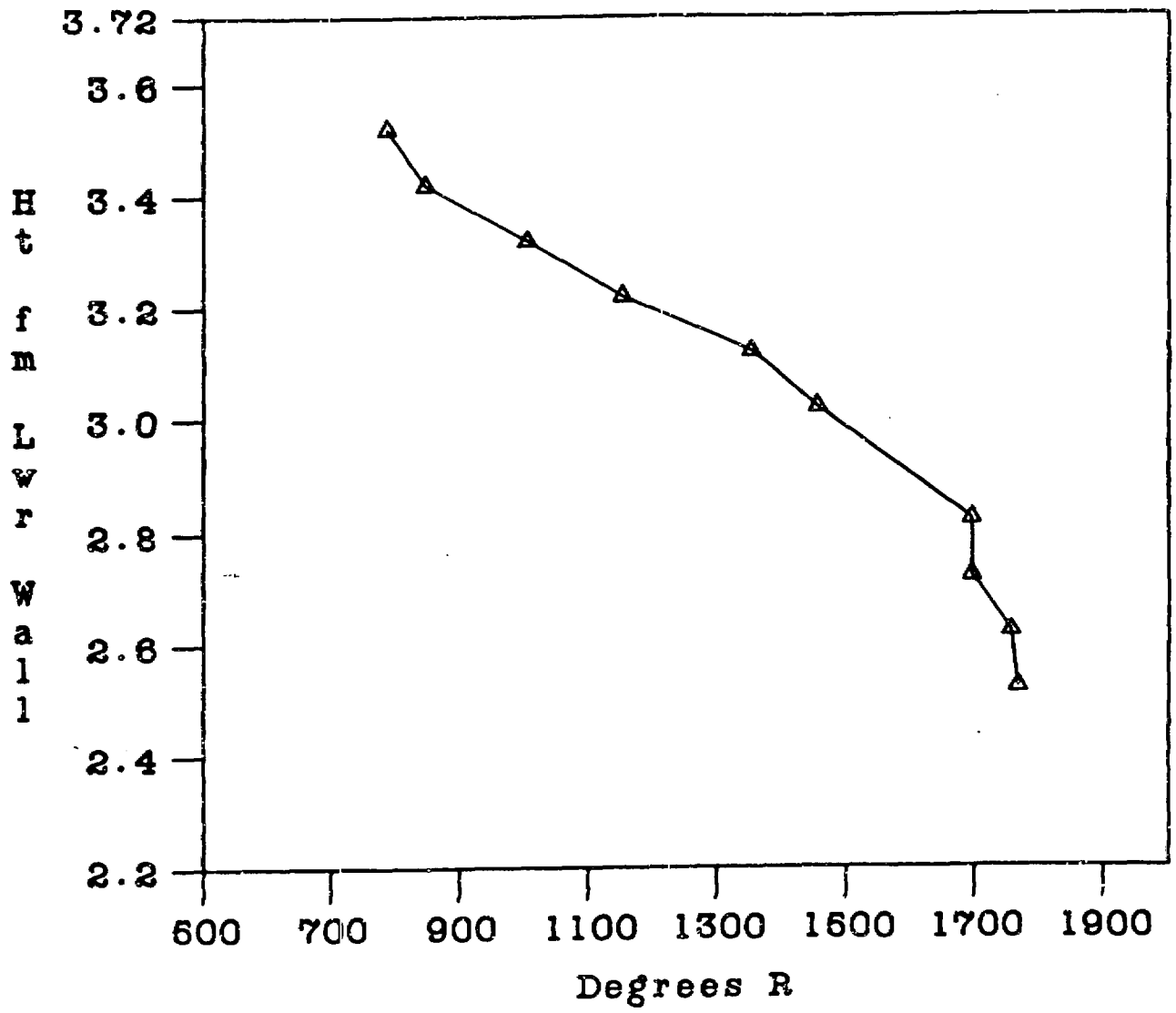

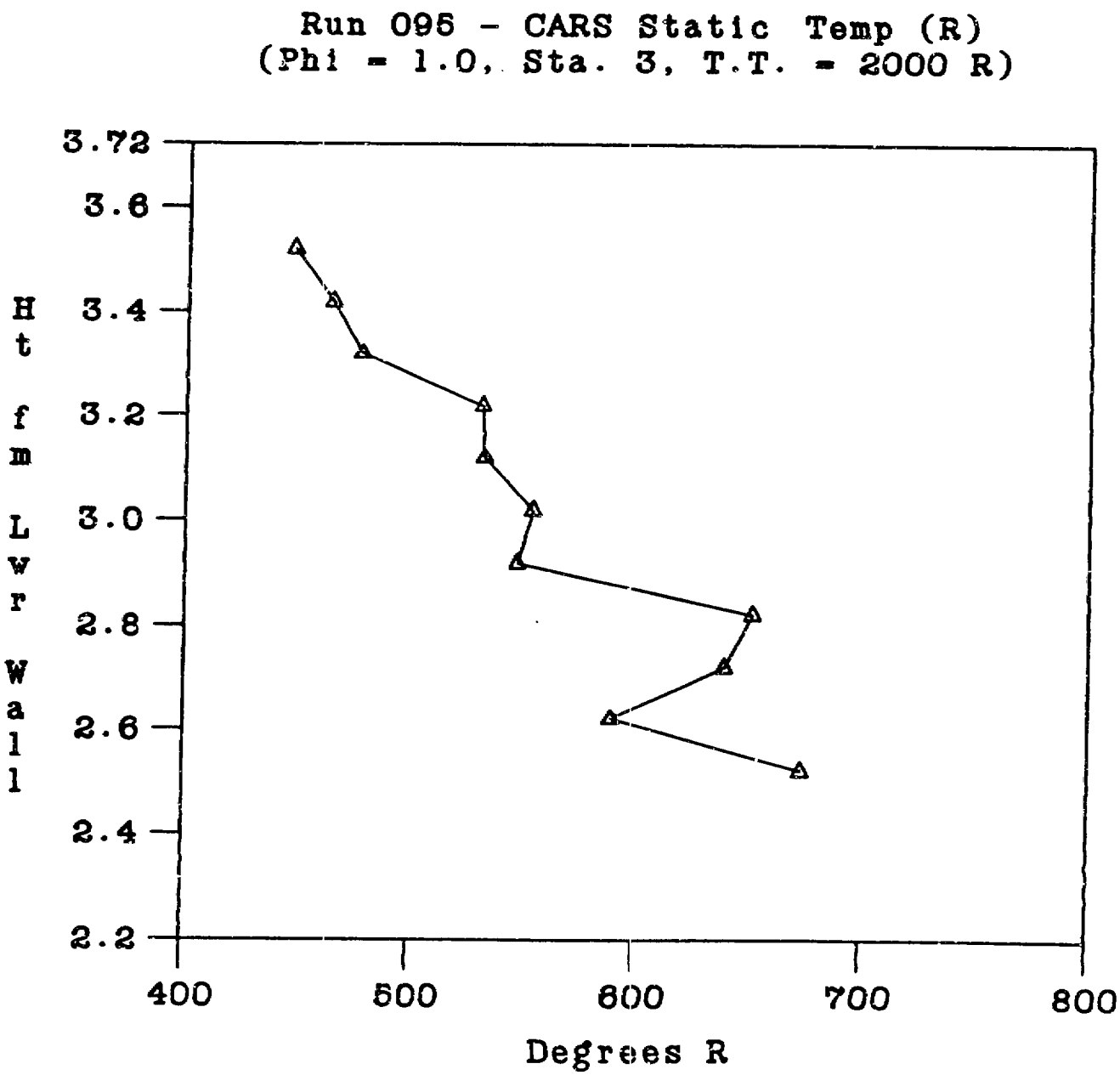
Run 095 - CARS Static Temp (R)
(Phi = 1.0, Sta. 3, T.T. = 2000 R)
Ht fm Lwr Wall
3.72
3.6
3.4
3.2
3.0
2.8
2.6
2.4
2.2
400
500
600
700
800
Degrees R

Run 096 - CARS Static Temp (R)
(Phi = 0.5, Sta. 3, T.T. = 2000 R)

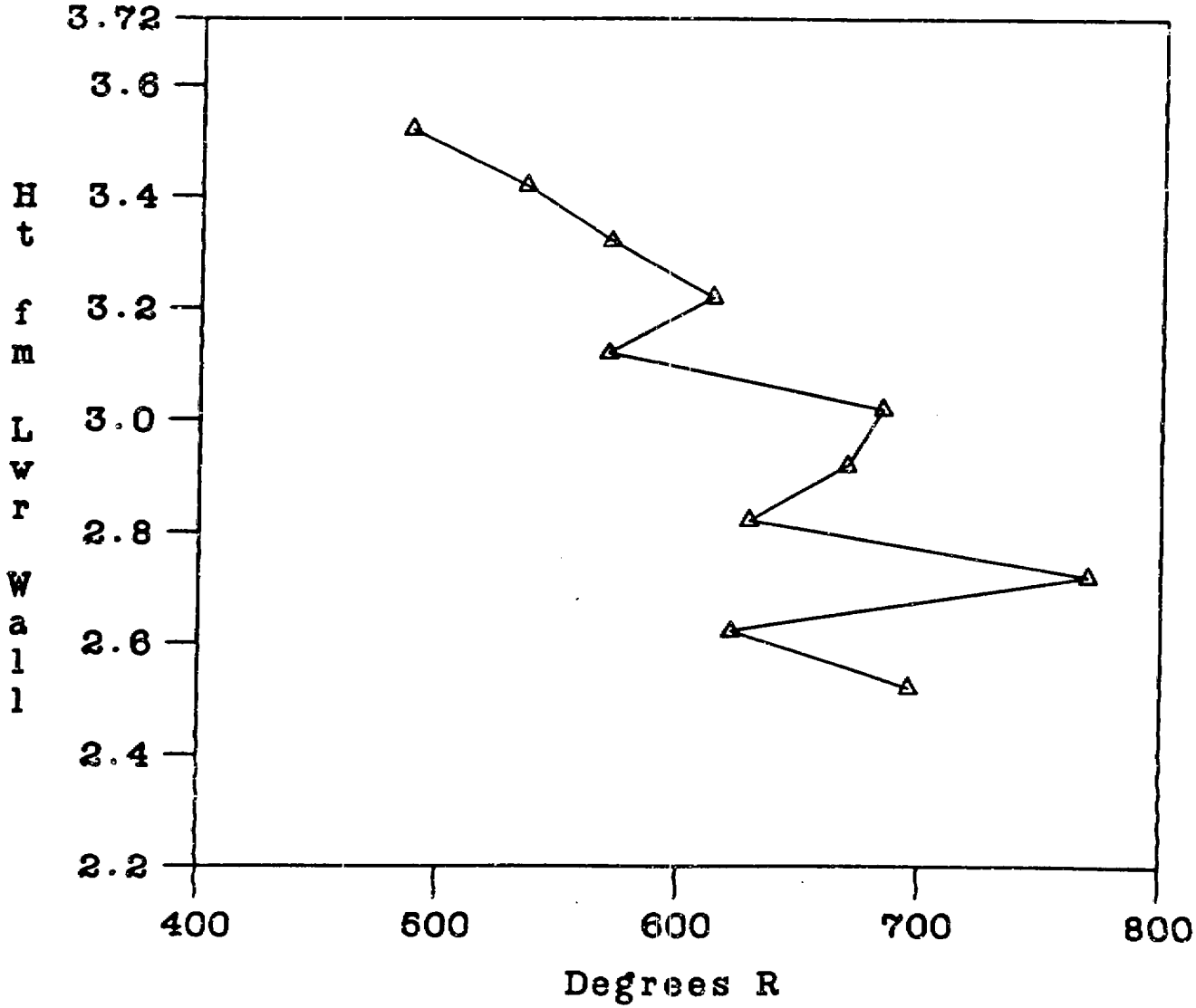

Run 112 - CARS Static Temp (R)
(Phi = 1.0, Sta. 2, T.T. = 2000 R, Wedge)

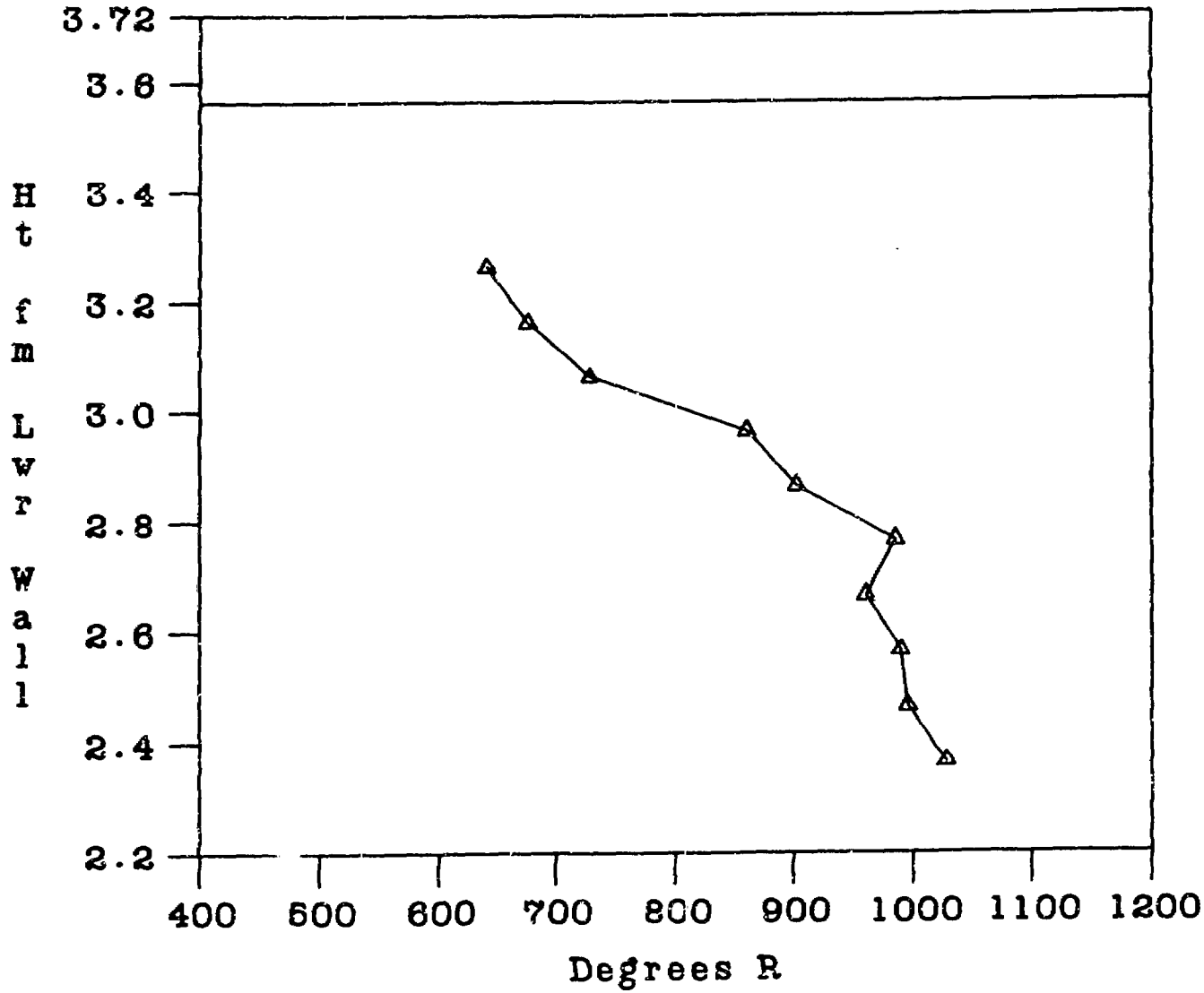

Run 113 - CARS Static Temp (R)
(Phi = 0.5, Sta. 2, T.T. = 2000 R, Wedge)

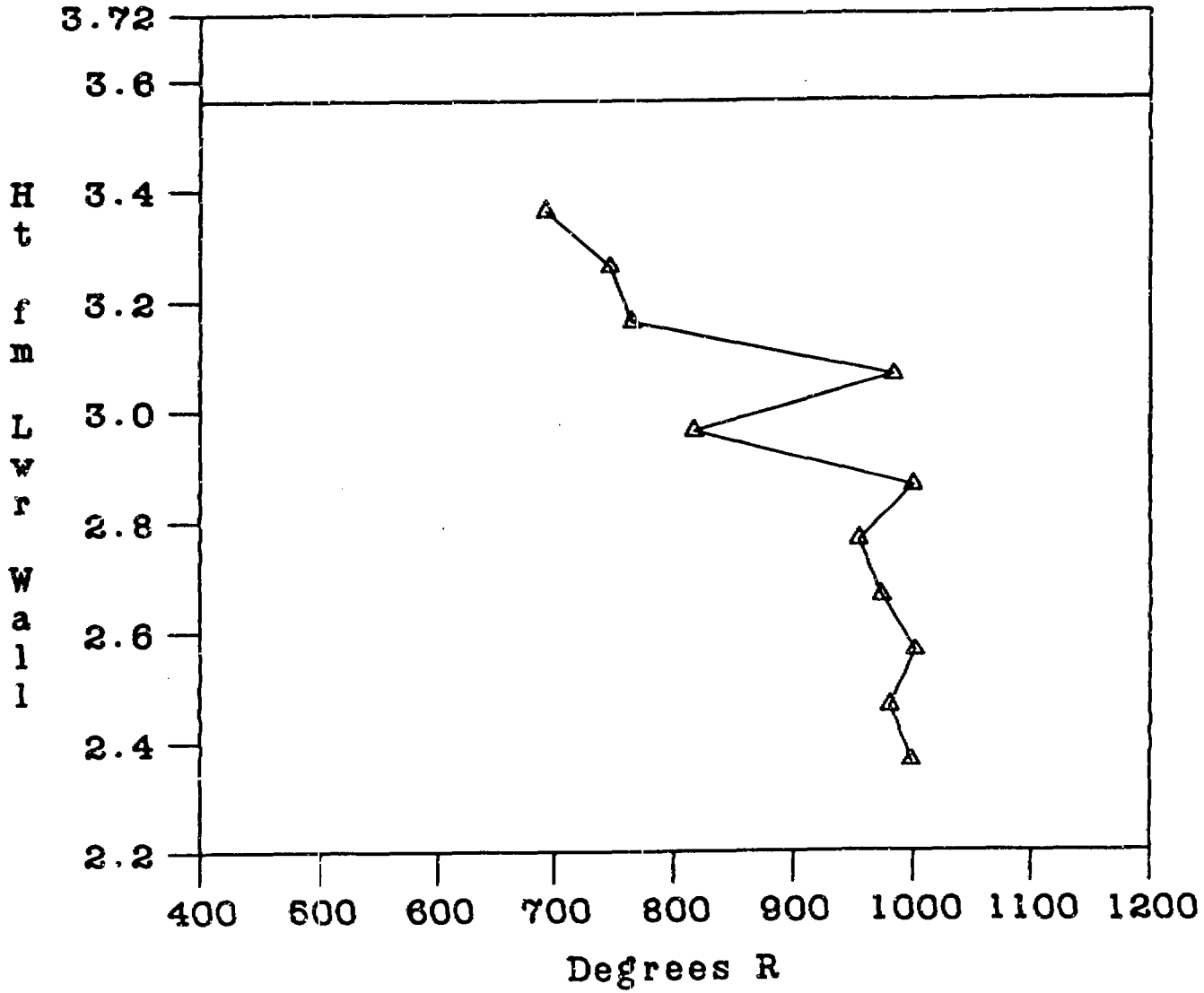

Run 114 - CARS Static Temp (R)
(N2 Injection, Sta. 2, T.T. = 2000 R, Wedge)

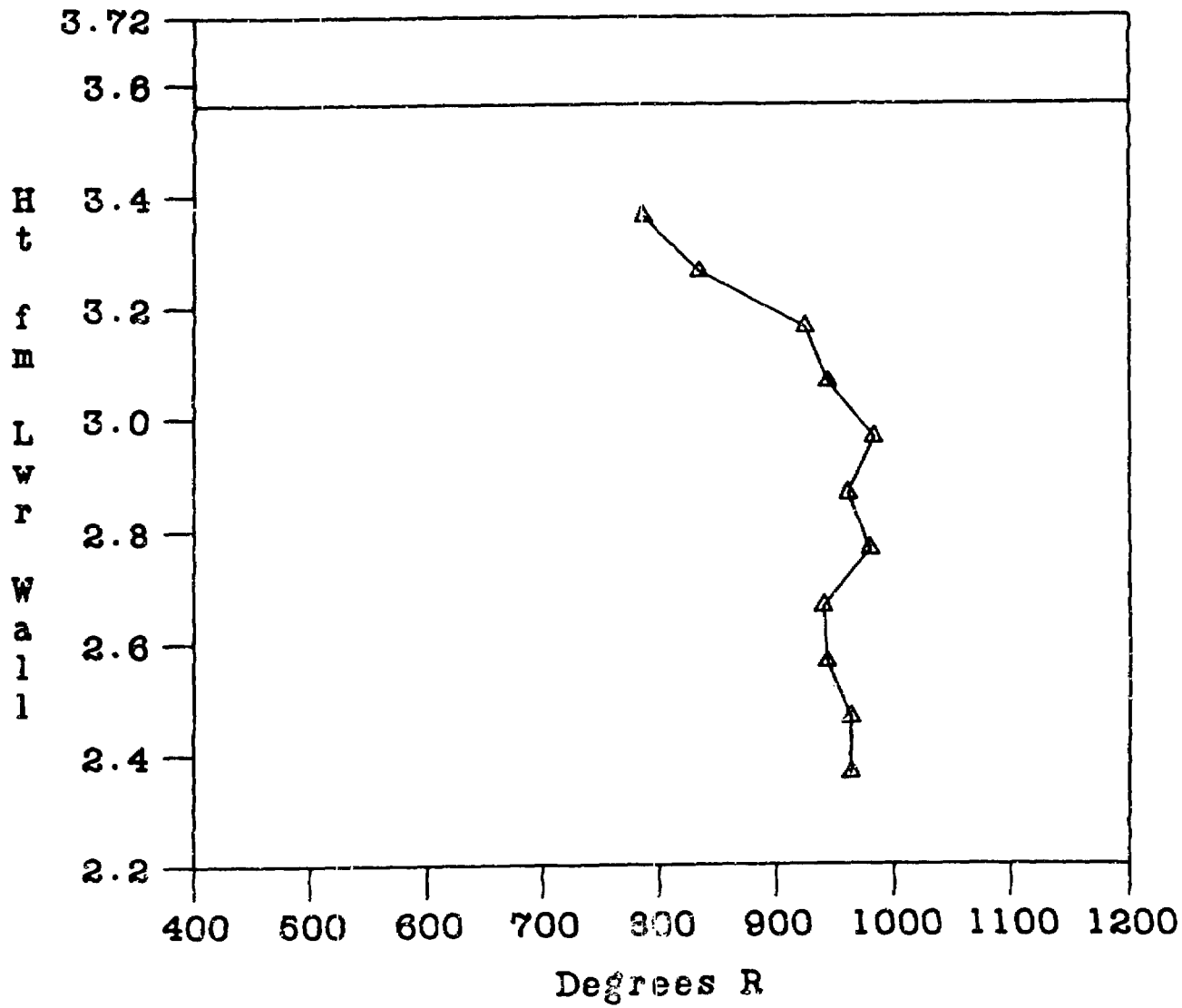

Run 121 - CARS Static Temp (R)
(Phi = 1.0, Sta. 2, T.T. = 4000 R, Wedge)

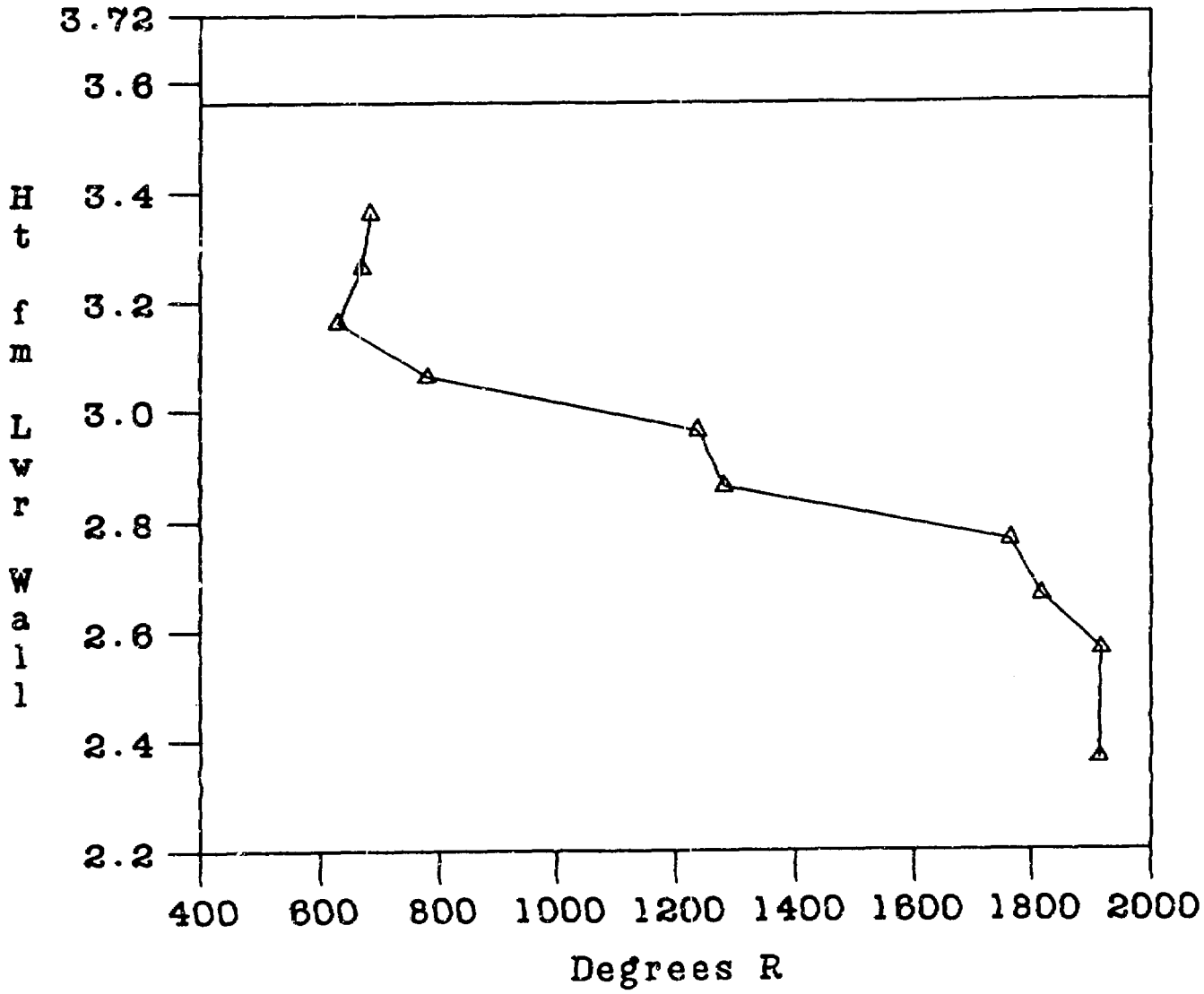

Run 122 - CARS Static Temp (R)
(Phi = 0.6, Sta. 2, T.T. = 4000 R, Wedge)

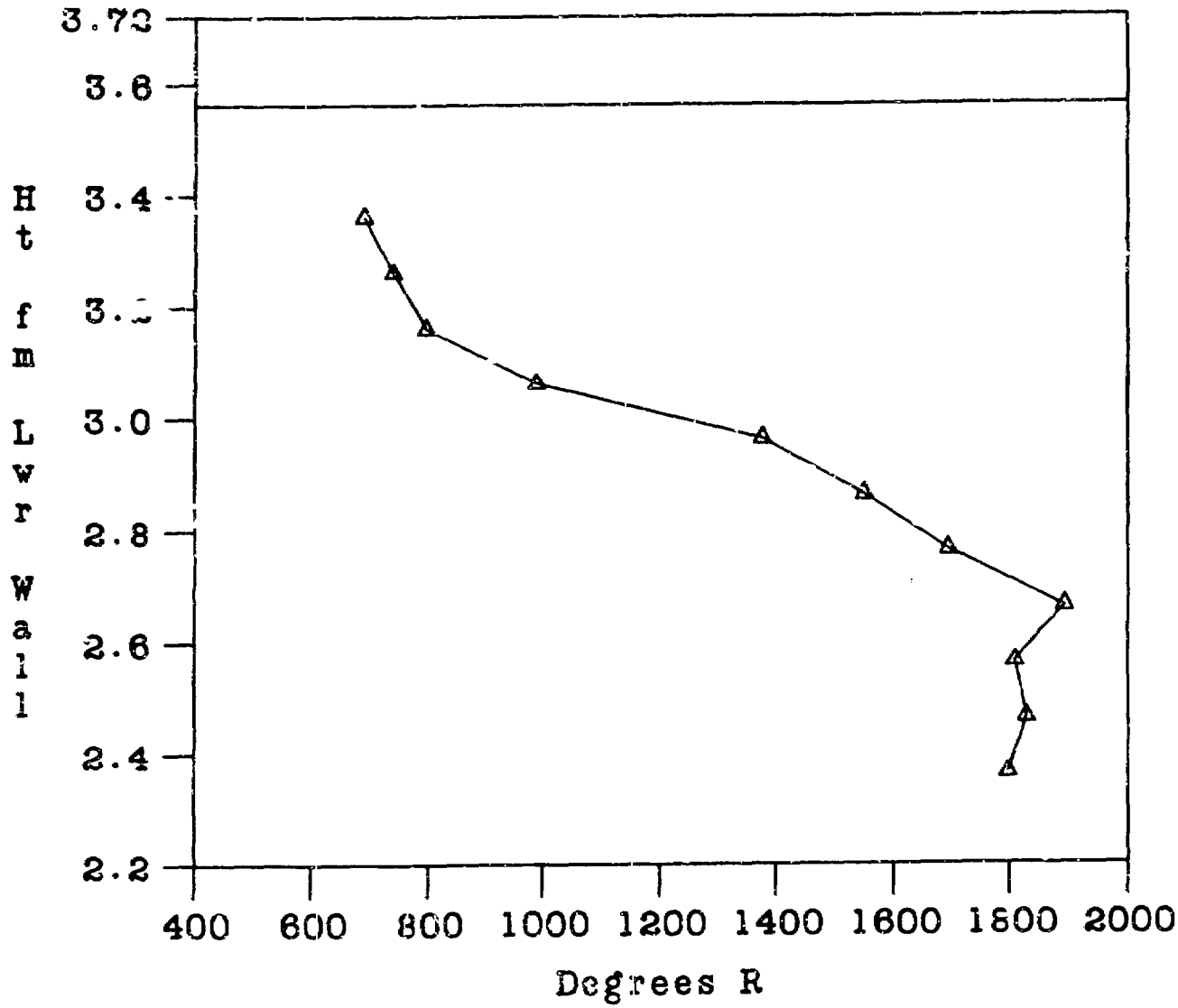

Run 123 - CARS Static Temp (R)
(Phi = 1.0, Sta. 3, T.T. = 2000 R, Wedge)

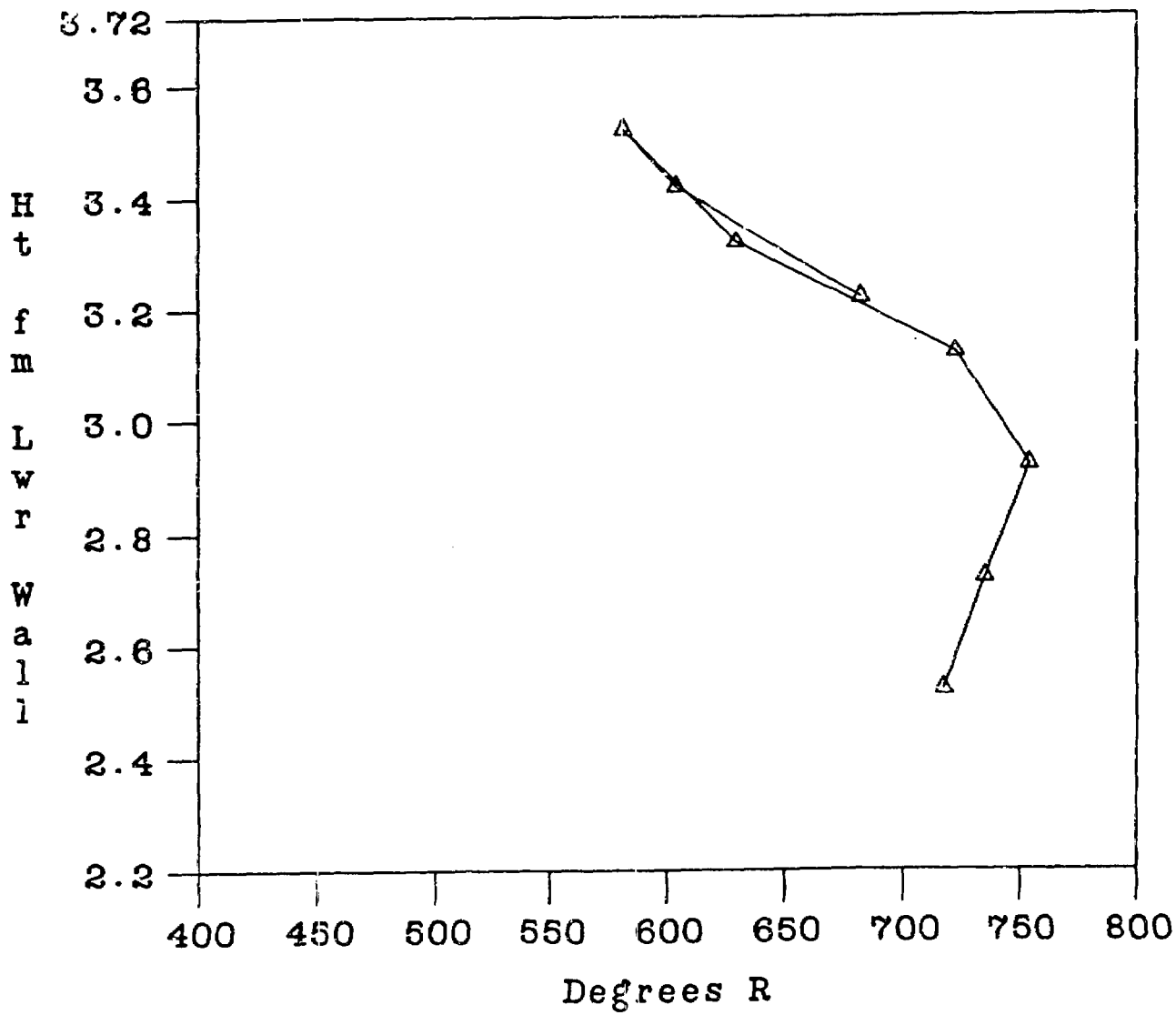

Run 124 - CARS Static Temp (R)
(Phi = 1.0, Sta. 3, T.T. = 2000 R, Wedge)

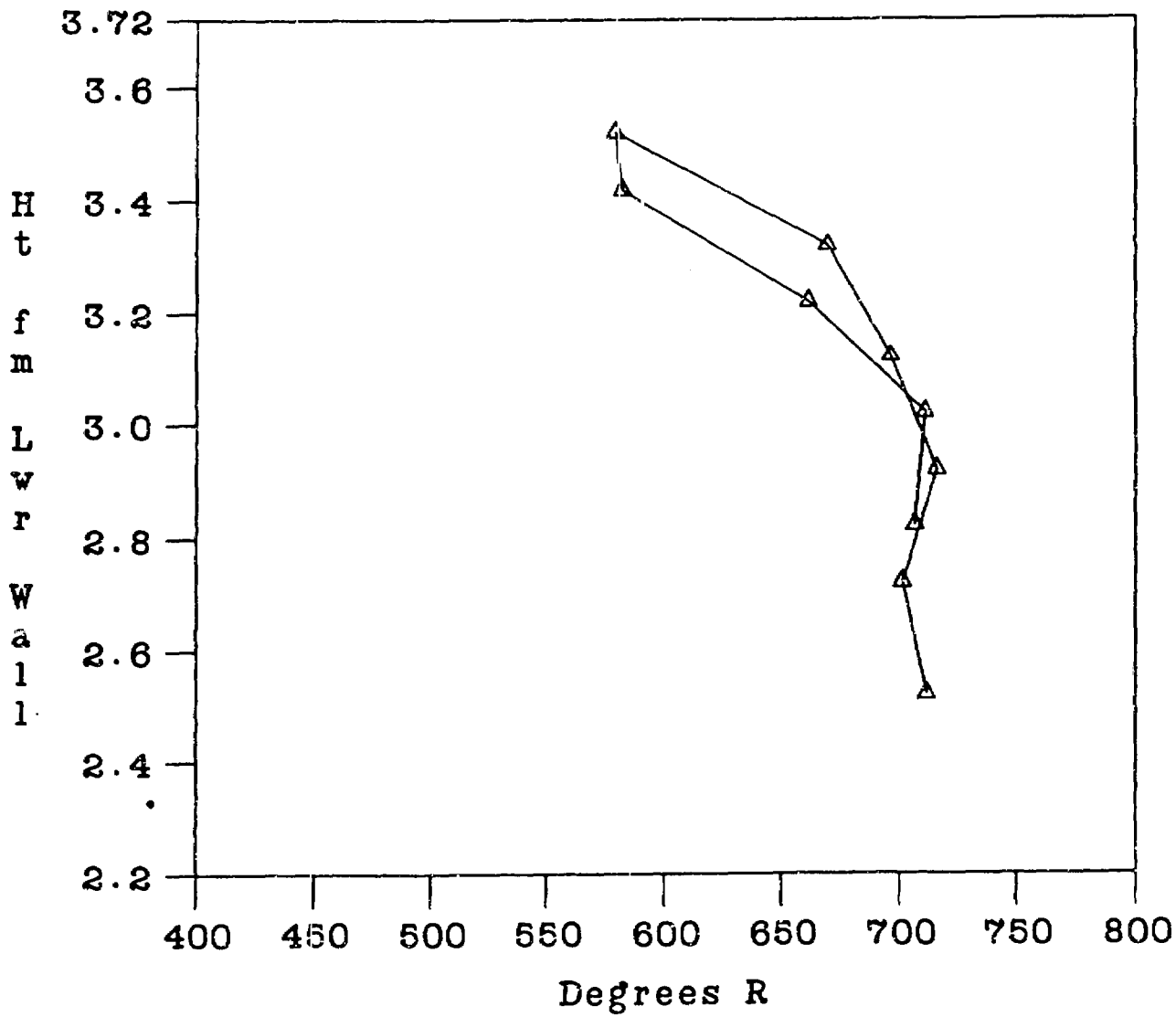

Run 125 - CARS Static Temp (R)
(Phi = 0.5, Sta. 3, T.T. = 2000 R, Wedge)

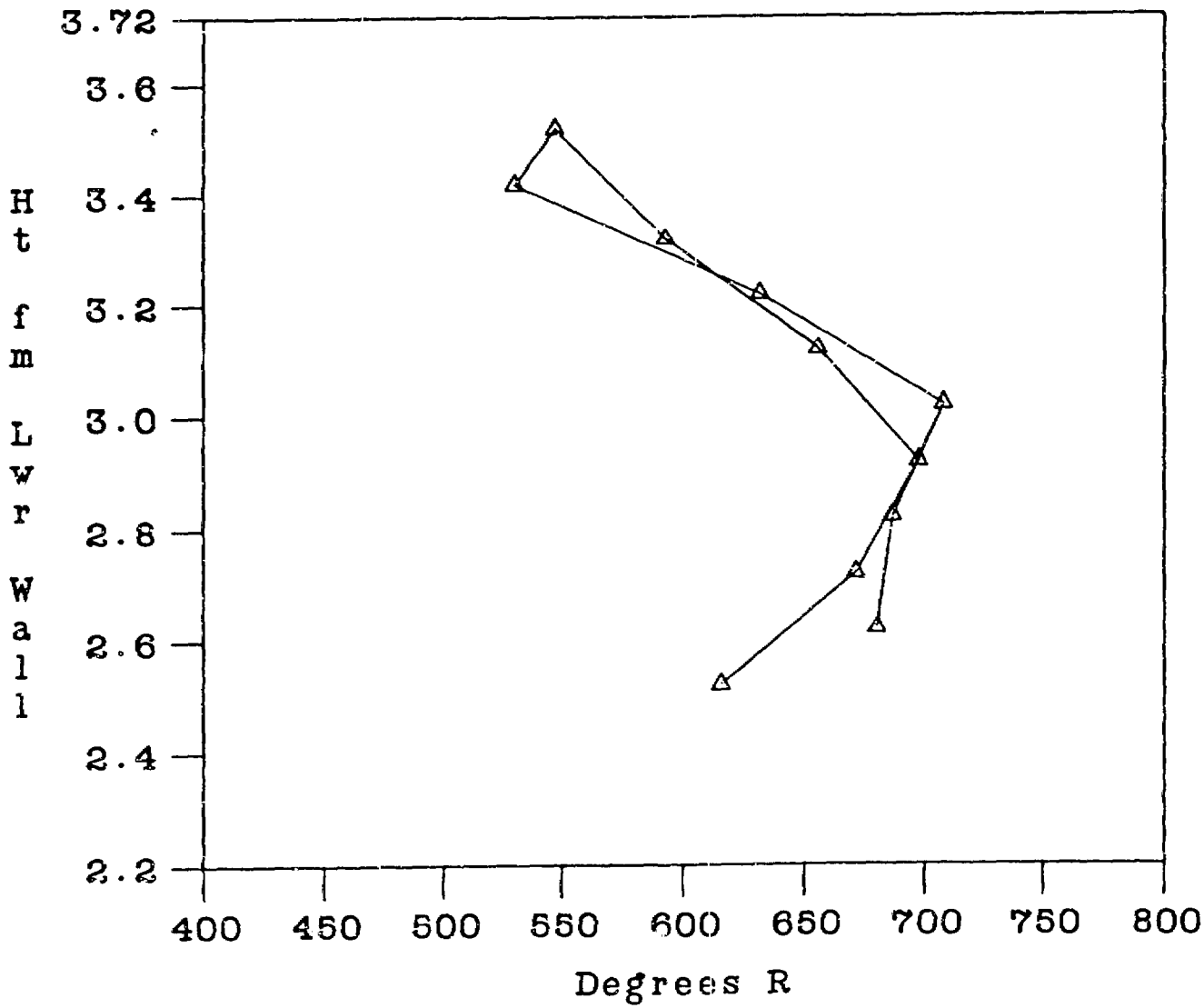

Run 126 - CARS Static Temp (R)
(Phi = 1.0, Sta. 3, T.T. = 4000 R, Wedge)

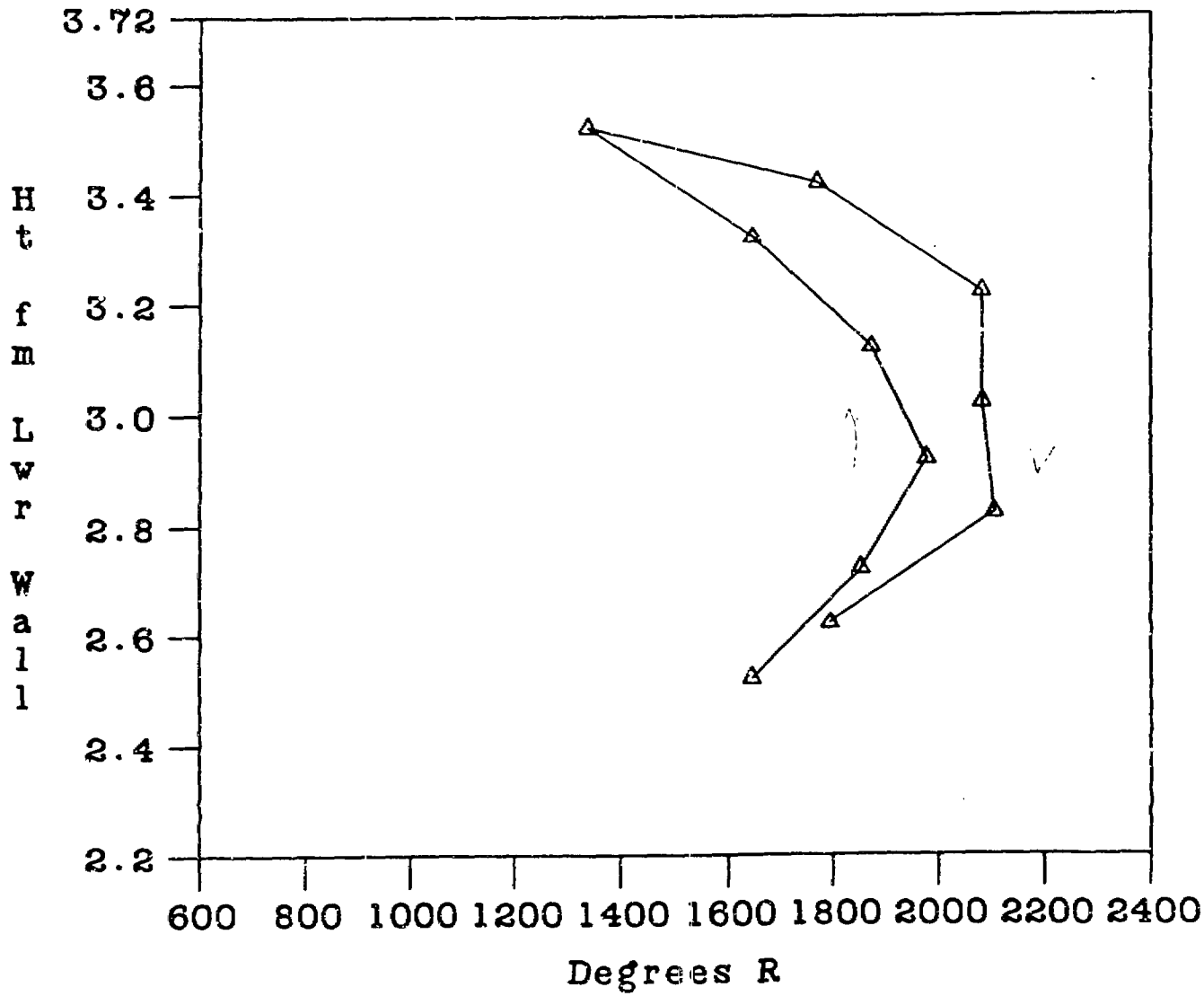

Run 127 - CARS Static Temp (R)
(Phi = 0.5, Sta. 3, T.T. = 4000 R, Wedge)

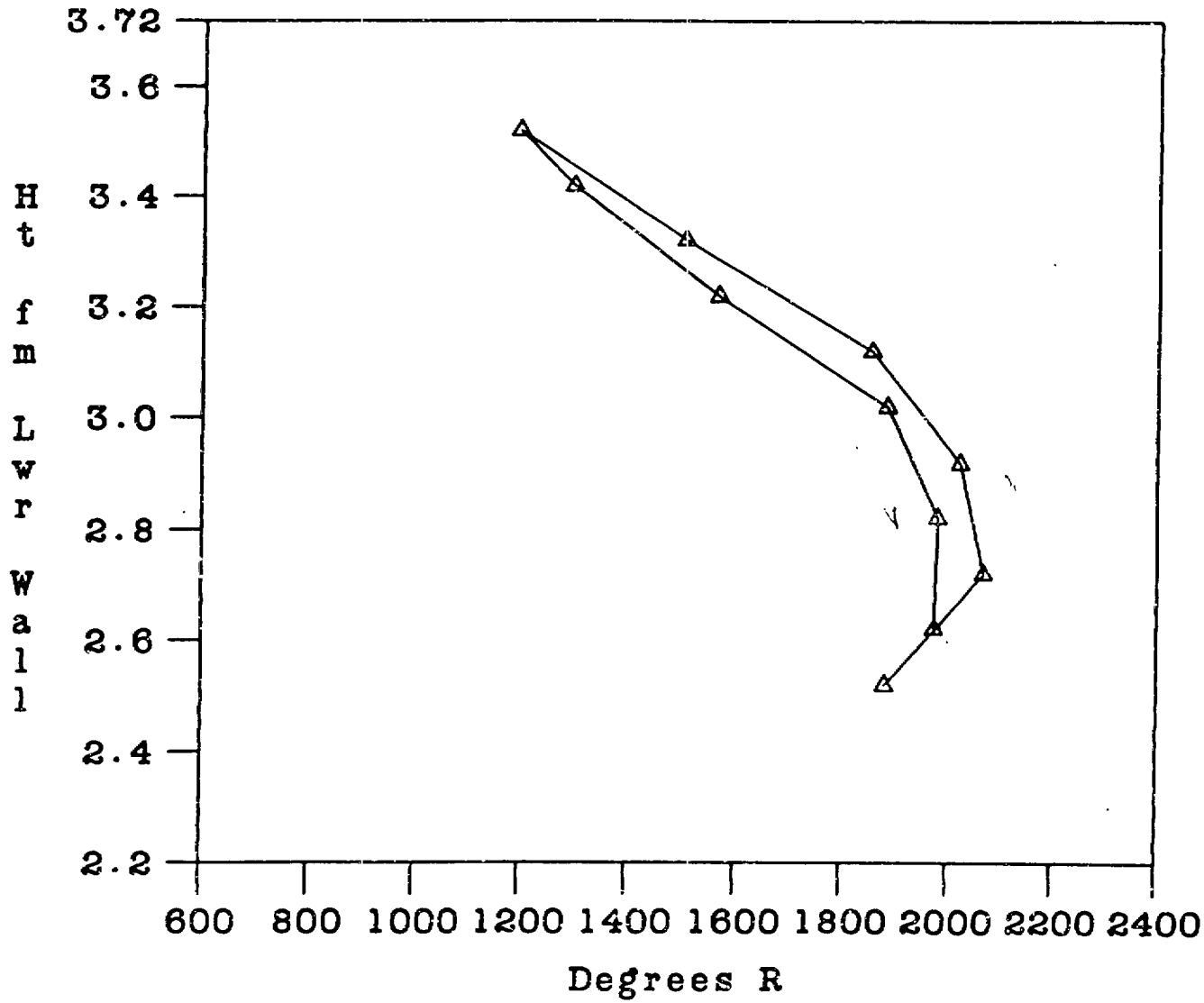

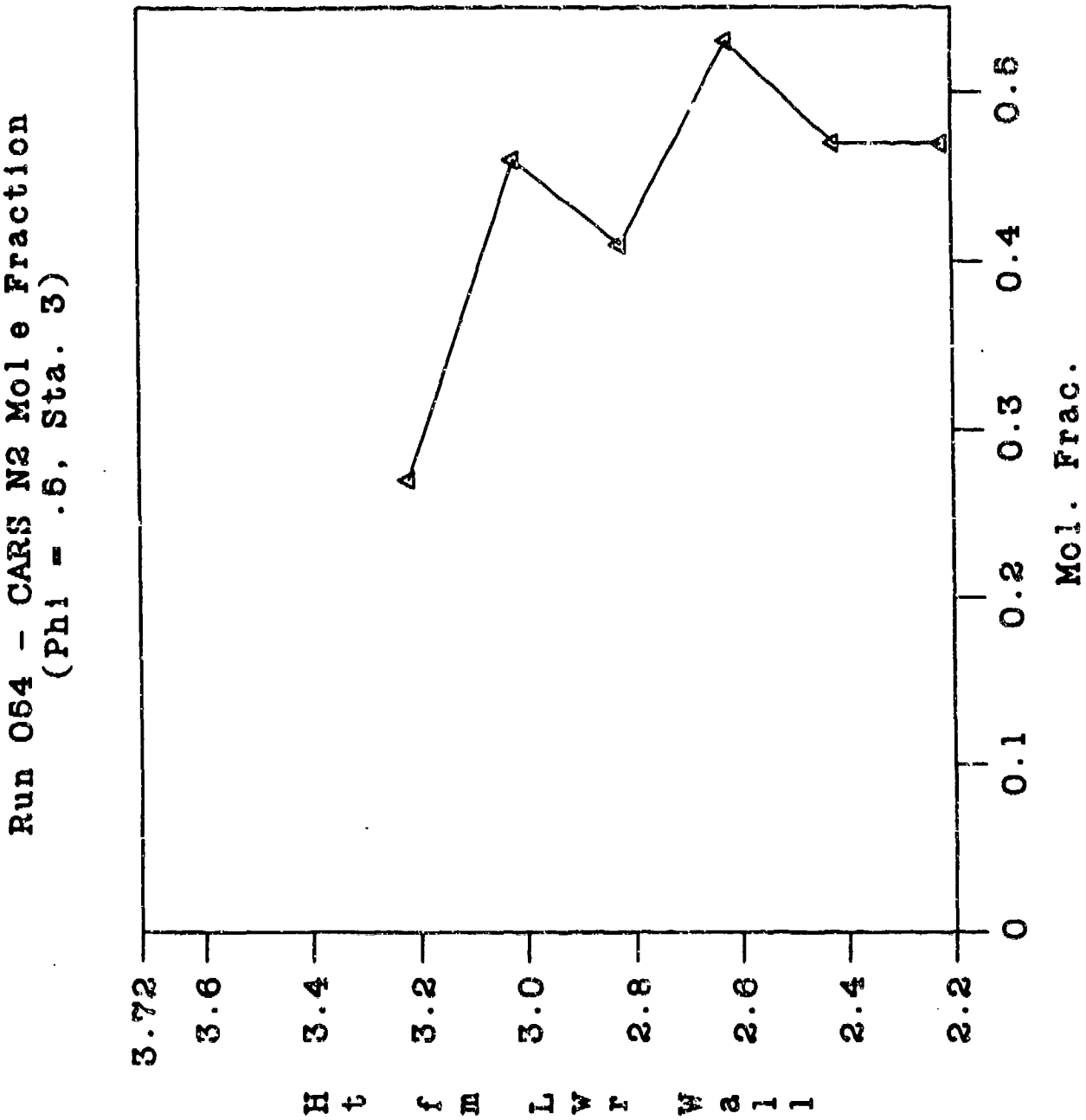
Run 064 - CARS N2 Mole Fraction
(Phi = .6, Sta. 3)
Height from Lower Wall
3.72
3.6
3.4
3.2
3.0
2.8
2.6
2.4
2.2
0
0.1
0.2
0.3
0.4
0.5
Mol. Frac.

Run 055 - CARS N2 Mol e Fraction
(Phi = 1.0, Sta. 3)

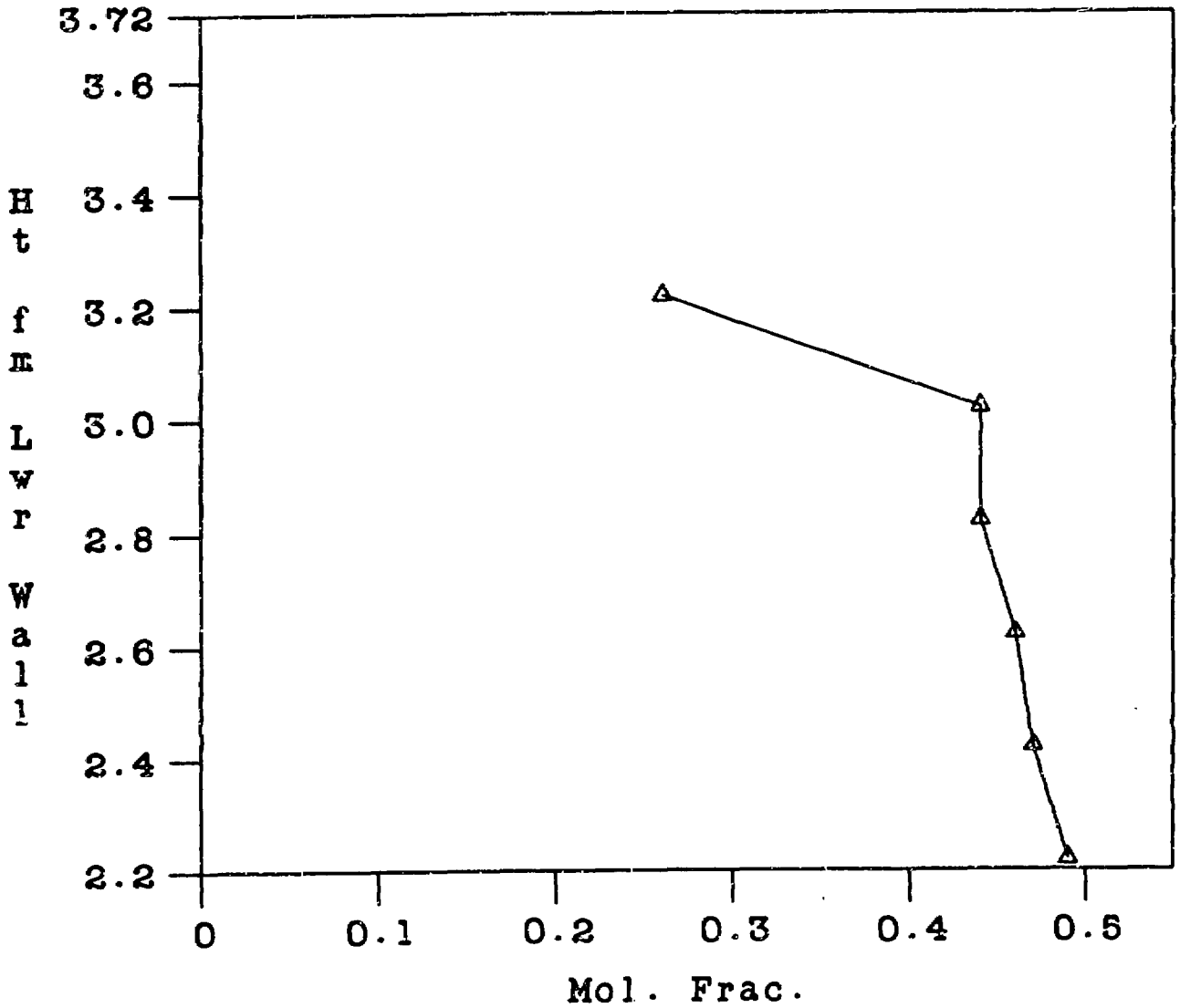

RUN 57 - CARS N2 Mole Fraction

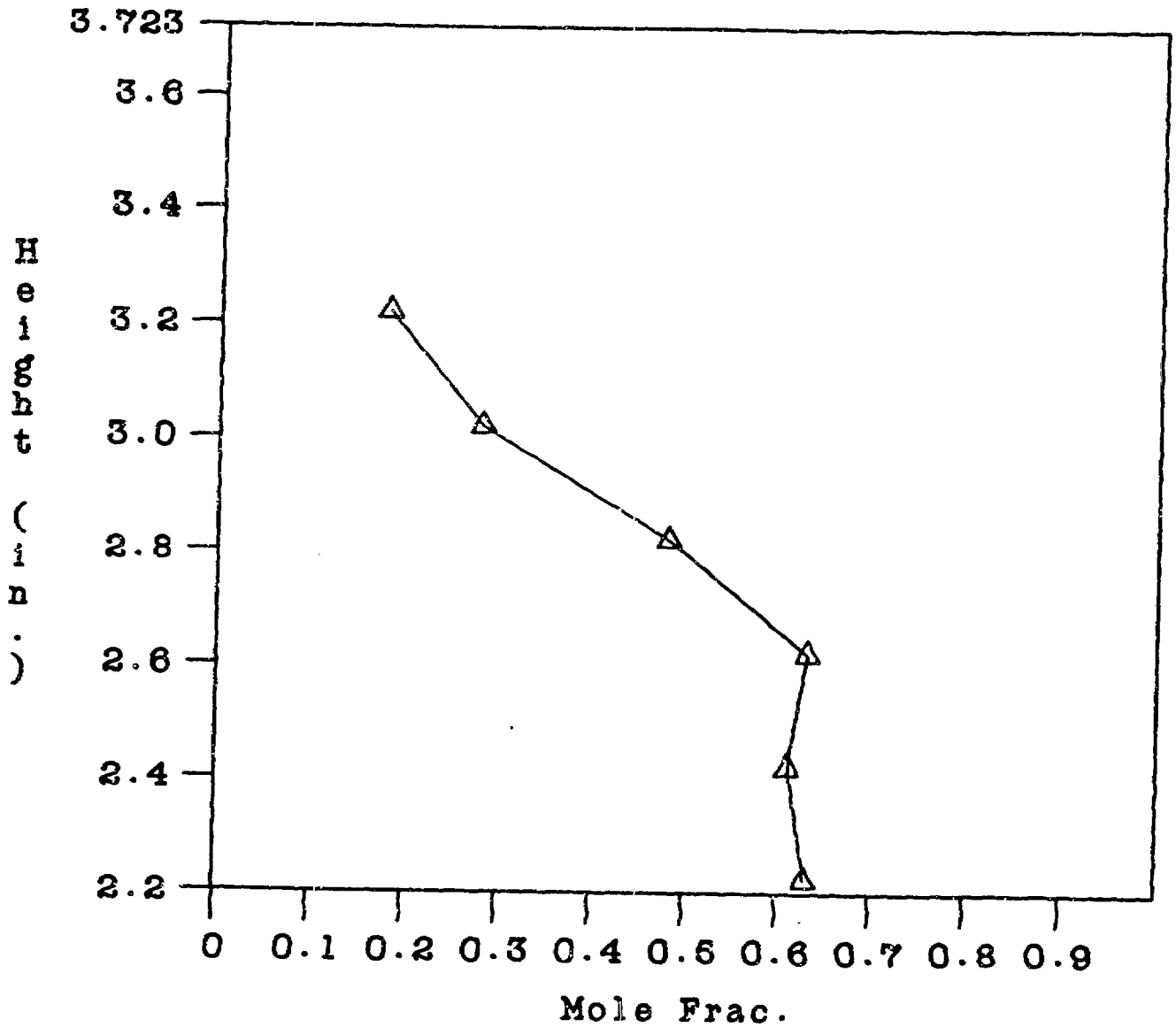

RUN 58 - CARS N2 Mole Fraction

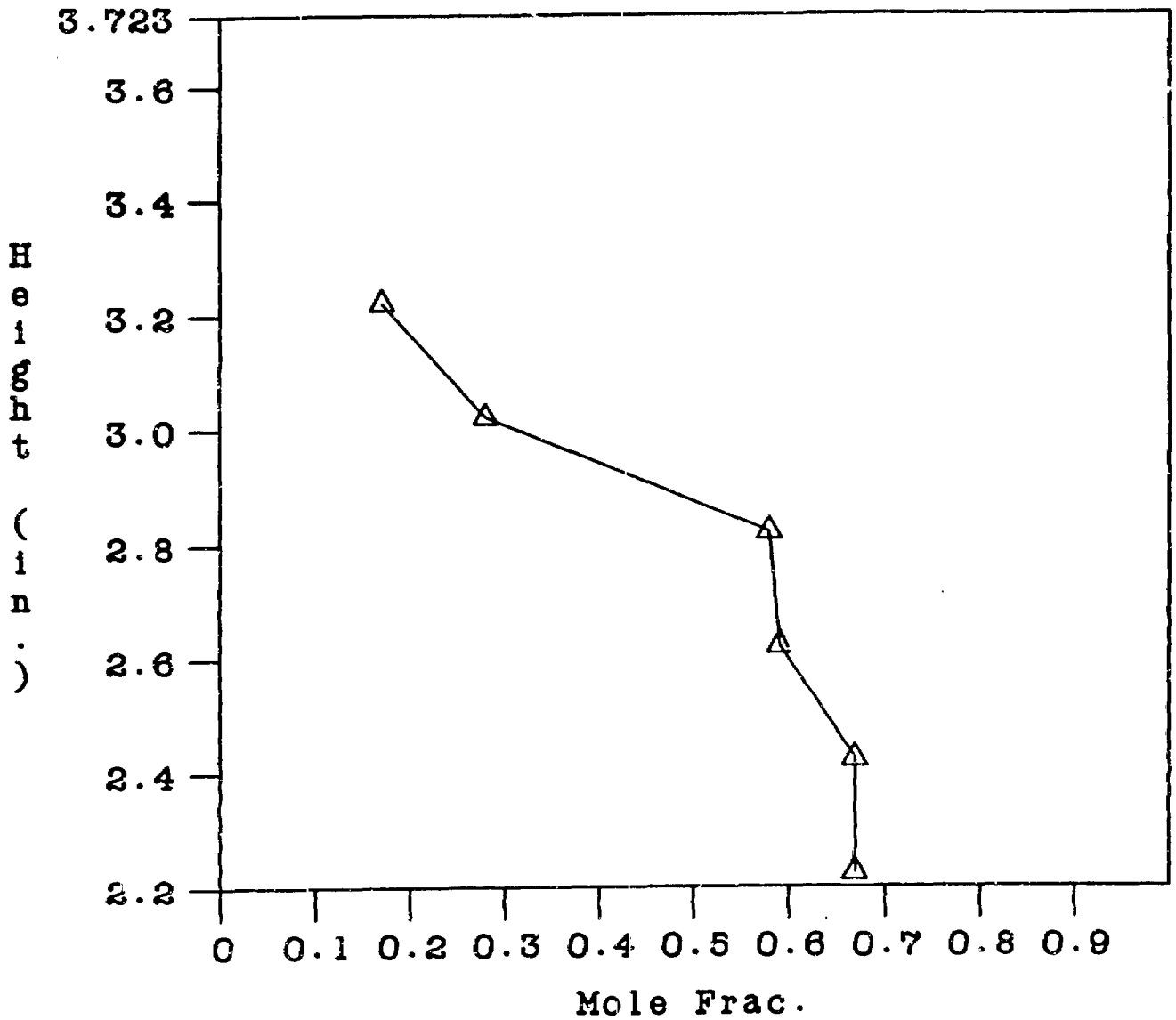

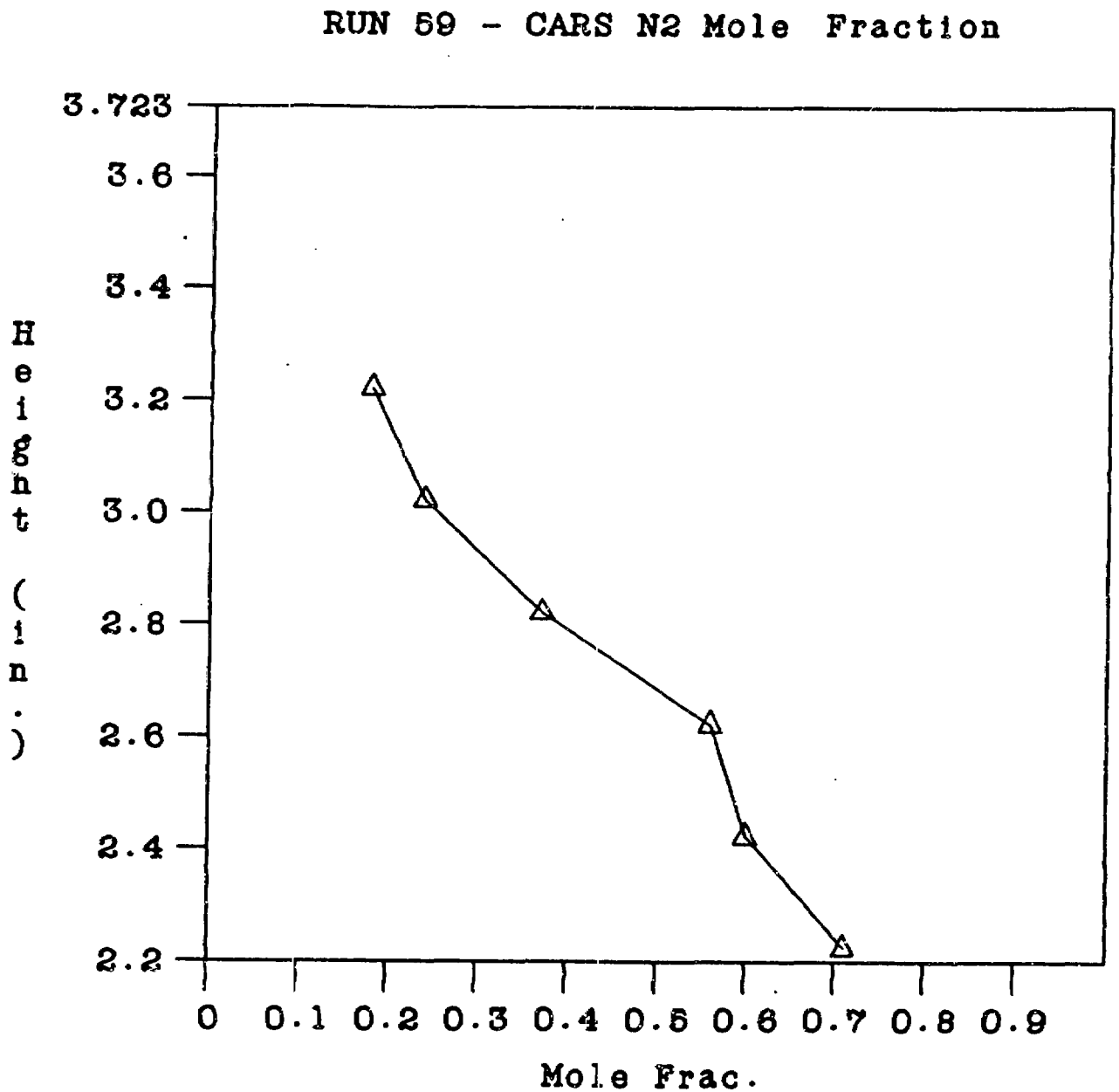
RUN 59 - CARS N2 Mole Fraction
3.723
3.6
3.4
3.2
3.0
2.8
2.6
2.4
2.2
Height (in.)
0
0.1
0.2
0.3
0.4
0.5
0.6
0.7
0.8
0.9
Mole Frac.

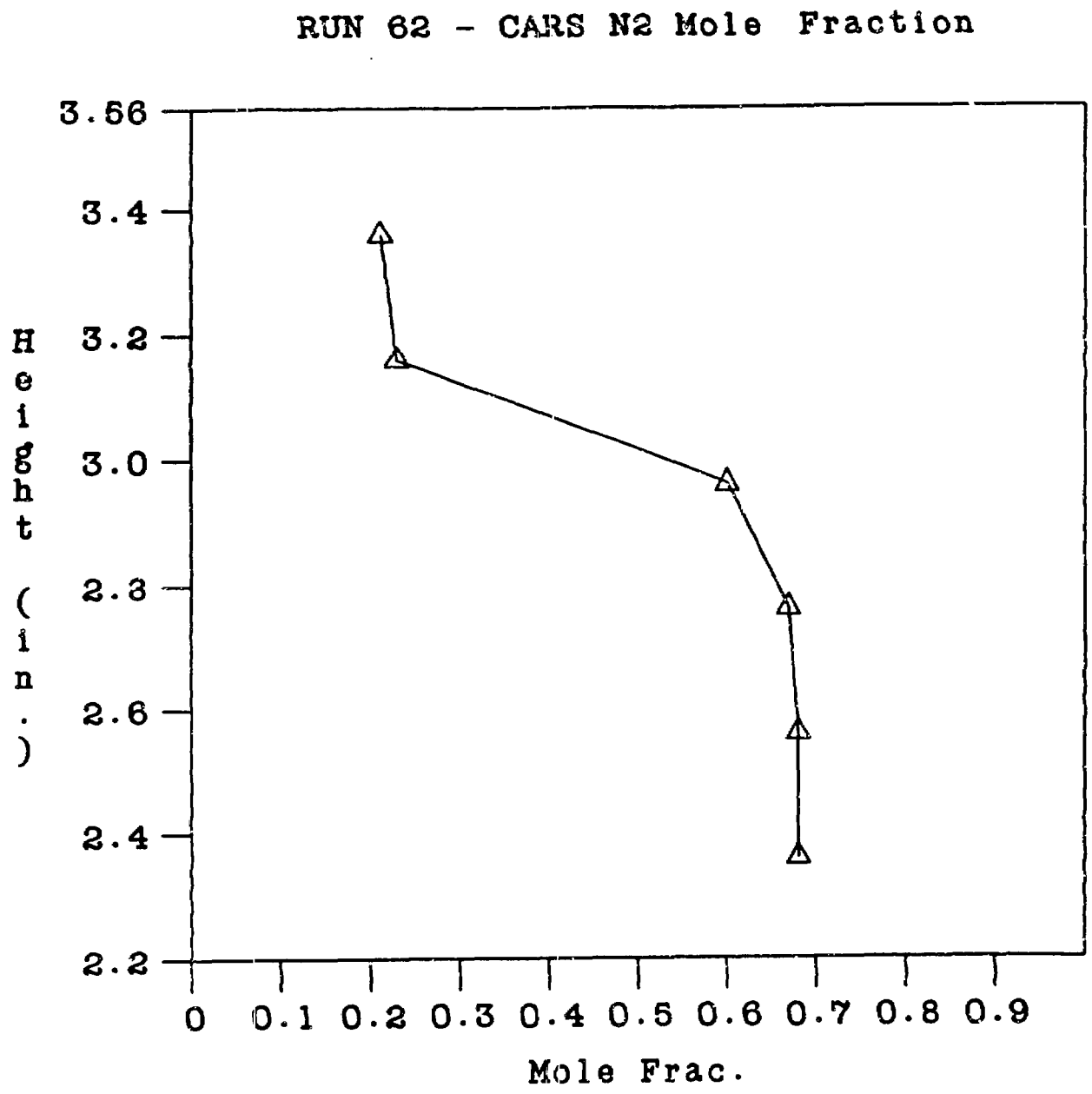
RUN 62 - CARS N2 Mole Fraction
3.56
3.4
3.2
3.0
2.8
2.6
2.4
2.2
Height (in.)
0
0.1
0.2
0.3
0.4
0.5
0.6
0.7
0.8
0.9
Mole Frac.

RUN 64 - CARS N2 Mole Fraction

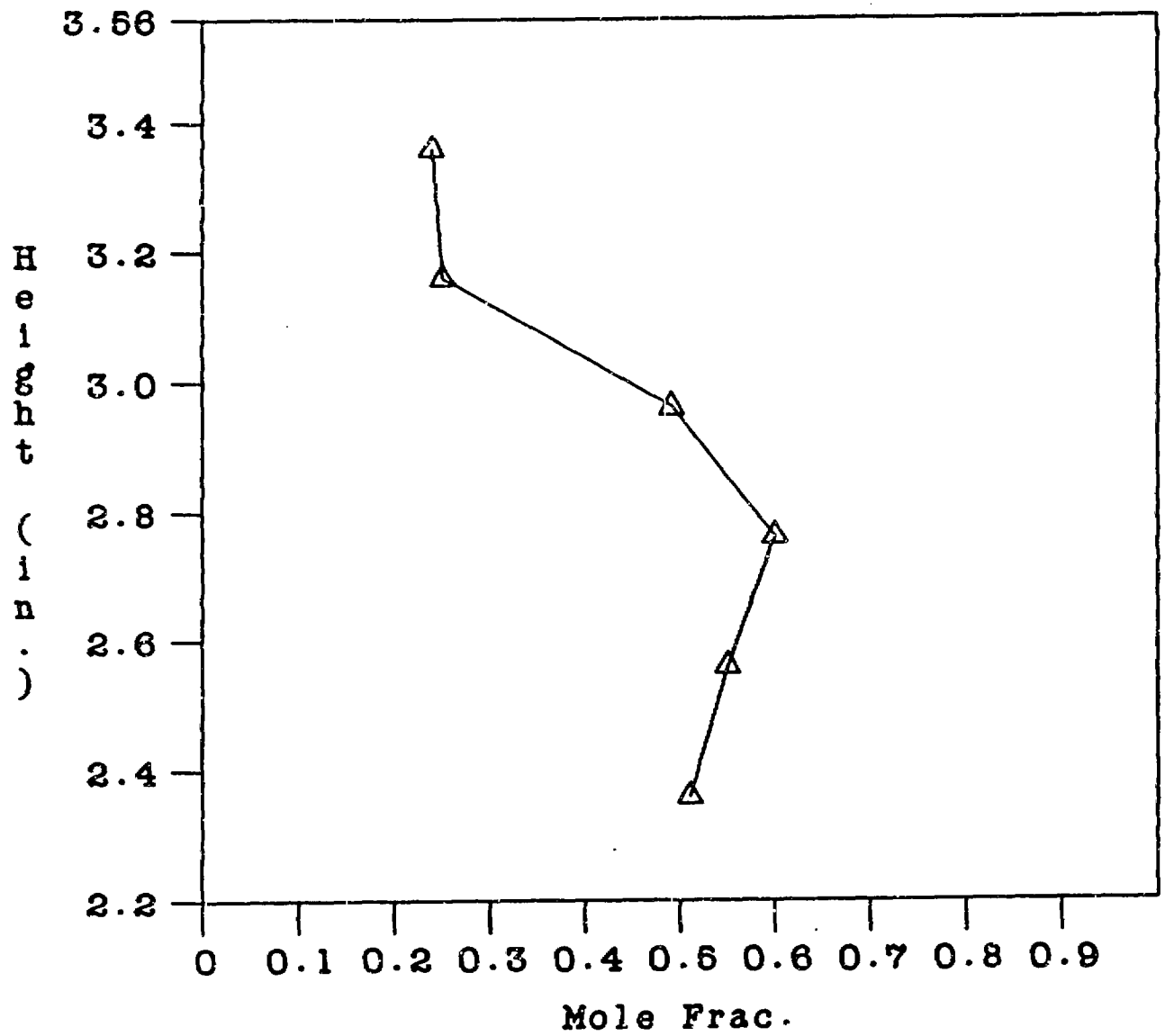

RUN 65 - CARS N2 Mole Fraction

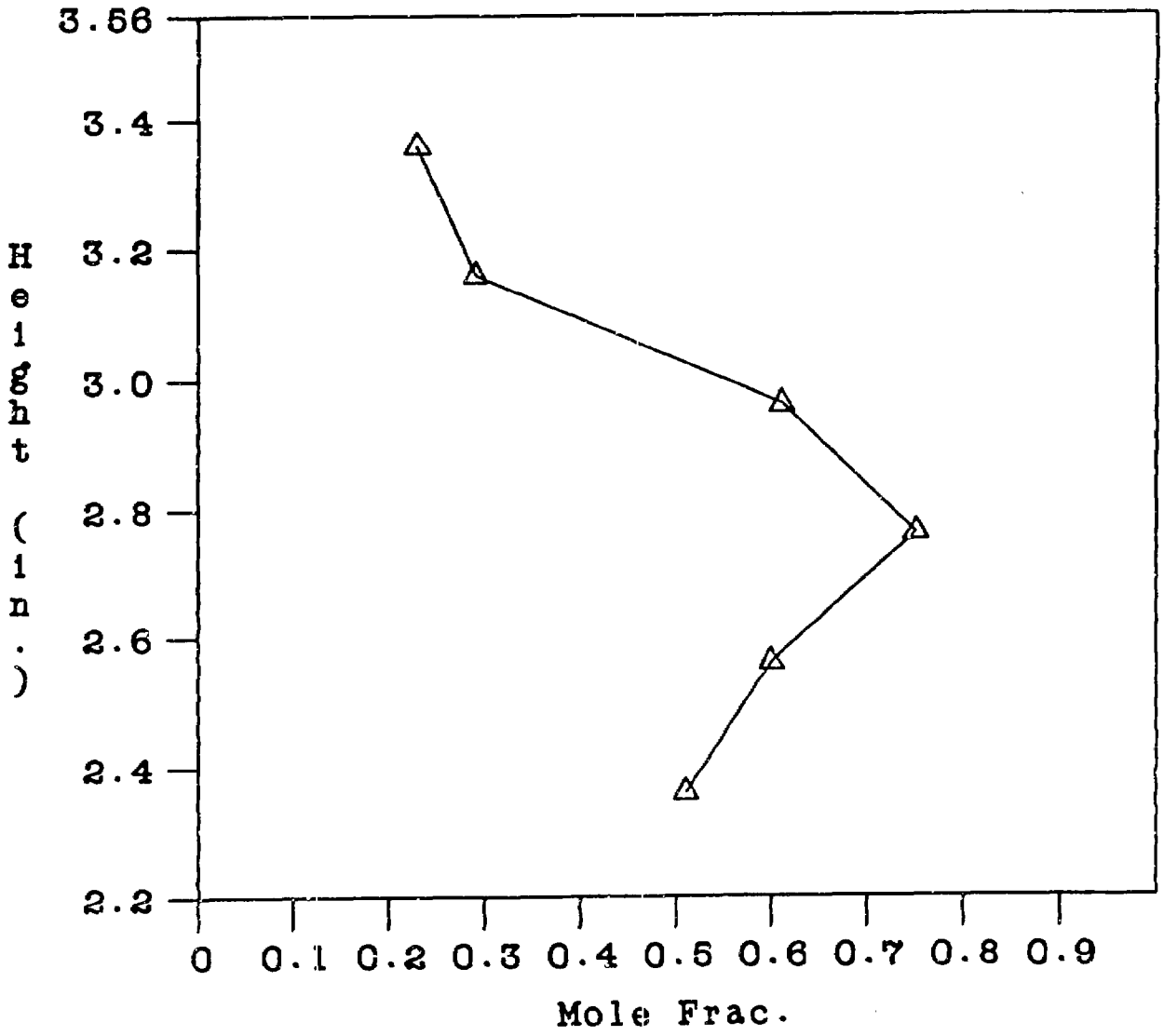

RUN 66 - CARS N2 Mole Fraction

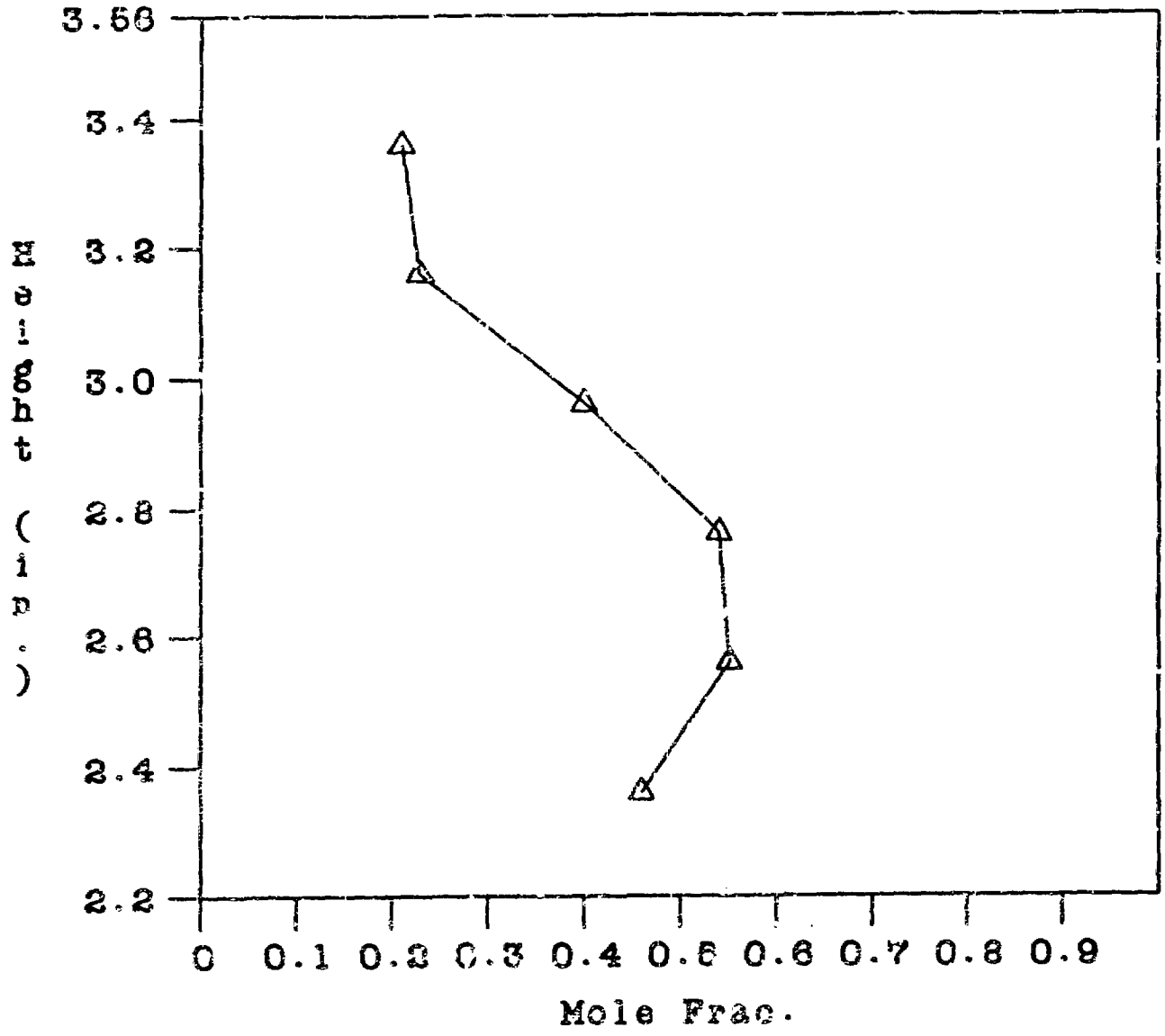

Run 074 - CARS N2 Mol e Fraction
(Phi =0.5, Sta. 2)

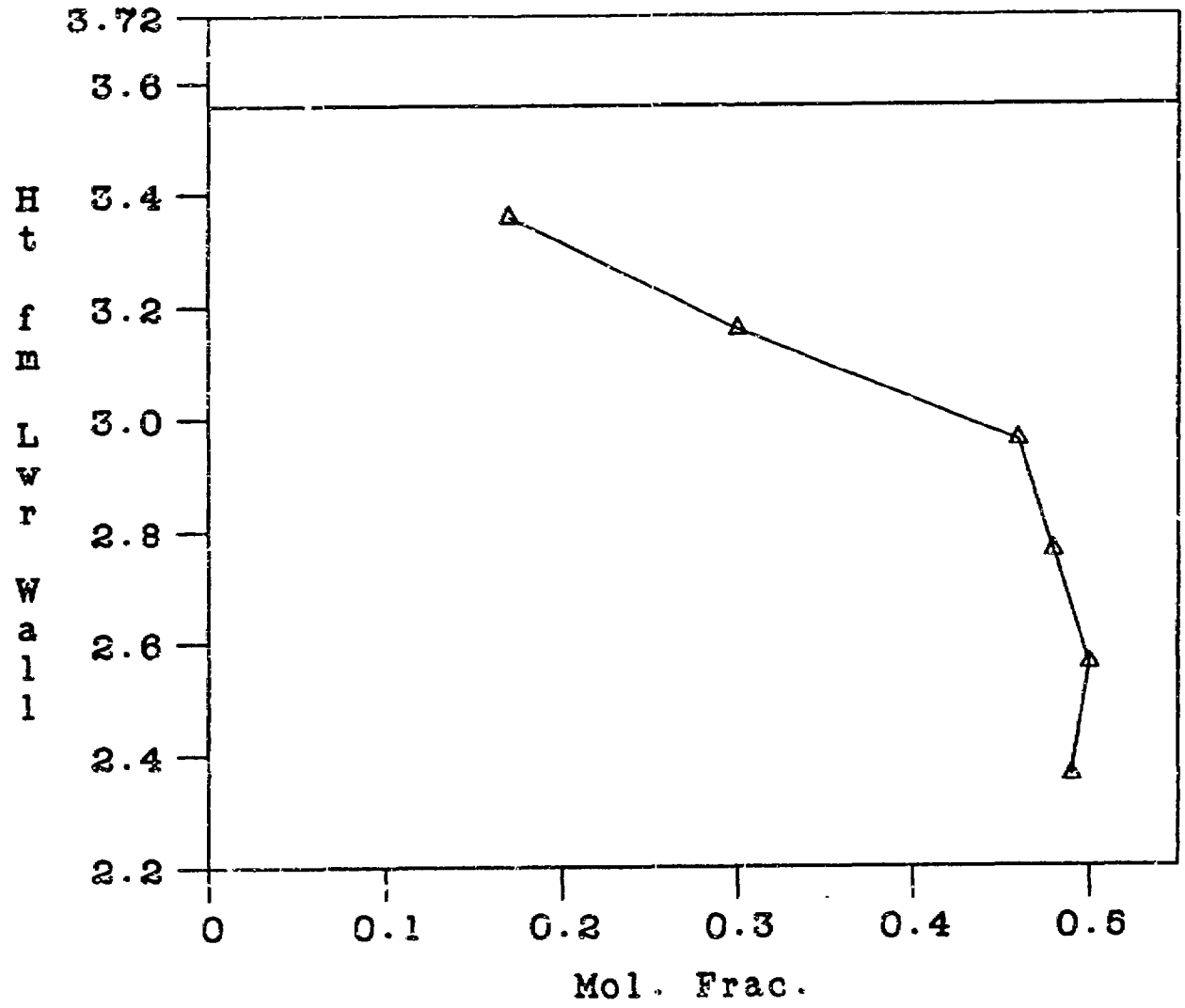

Run 081 - CARS N2 Mol e Fraction
(Phi = .5, Sta. 2)

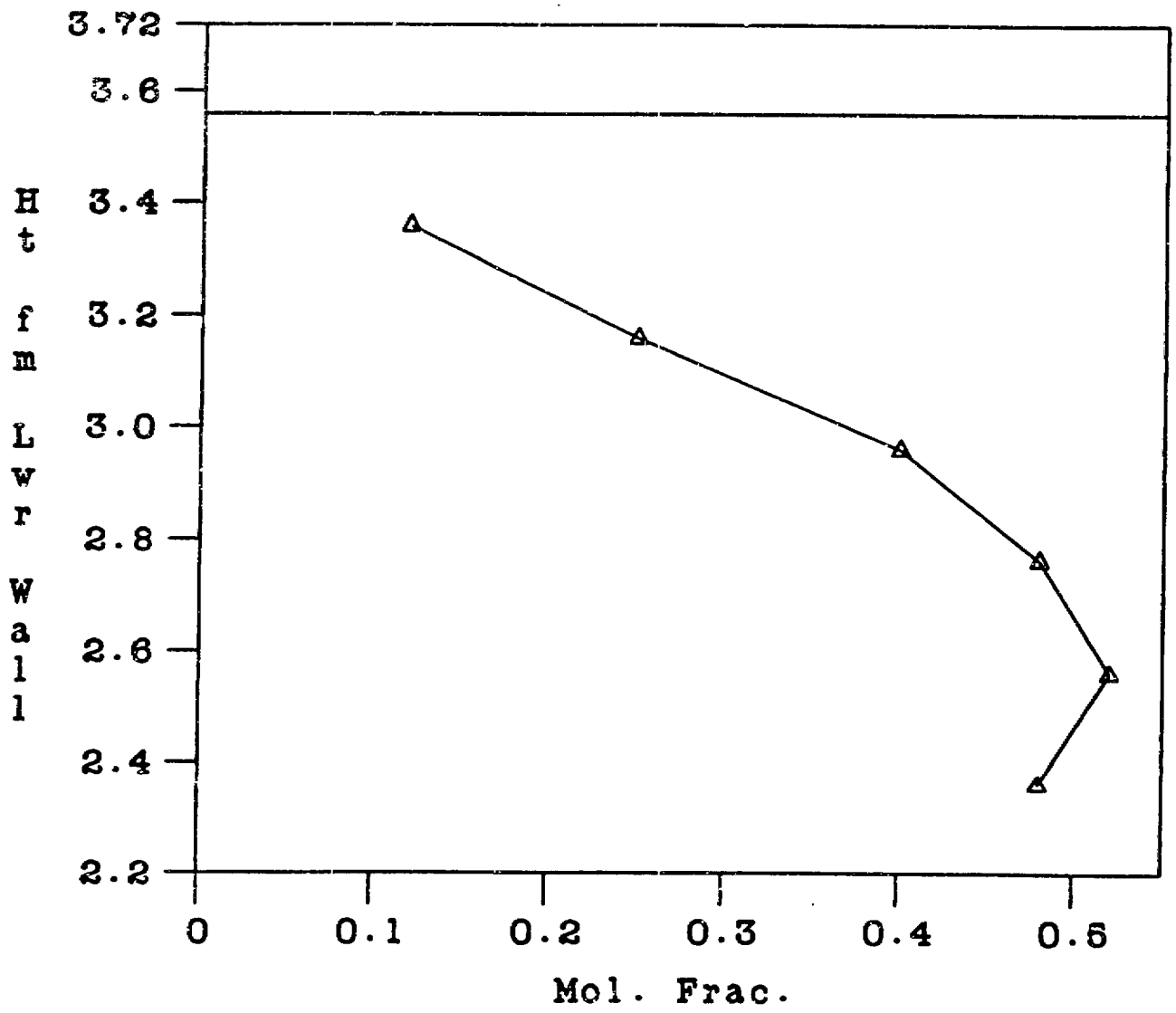

Run 084 - CARS N2 Mole Fraction
(Phi =1.0, Sta. 2)

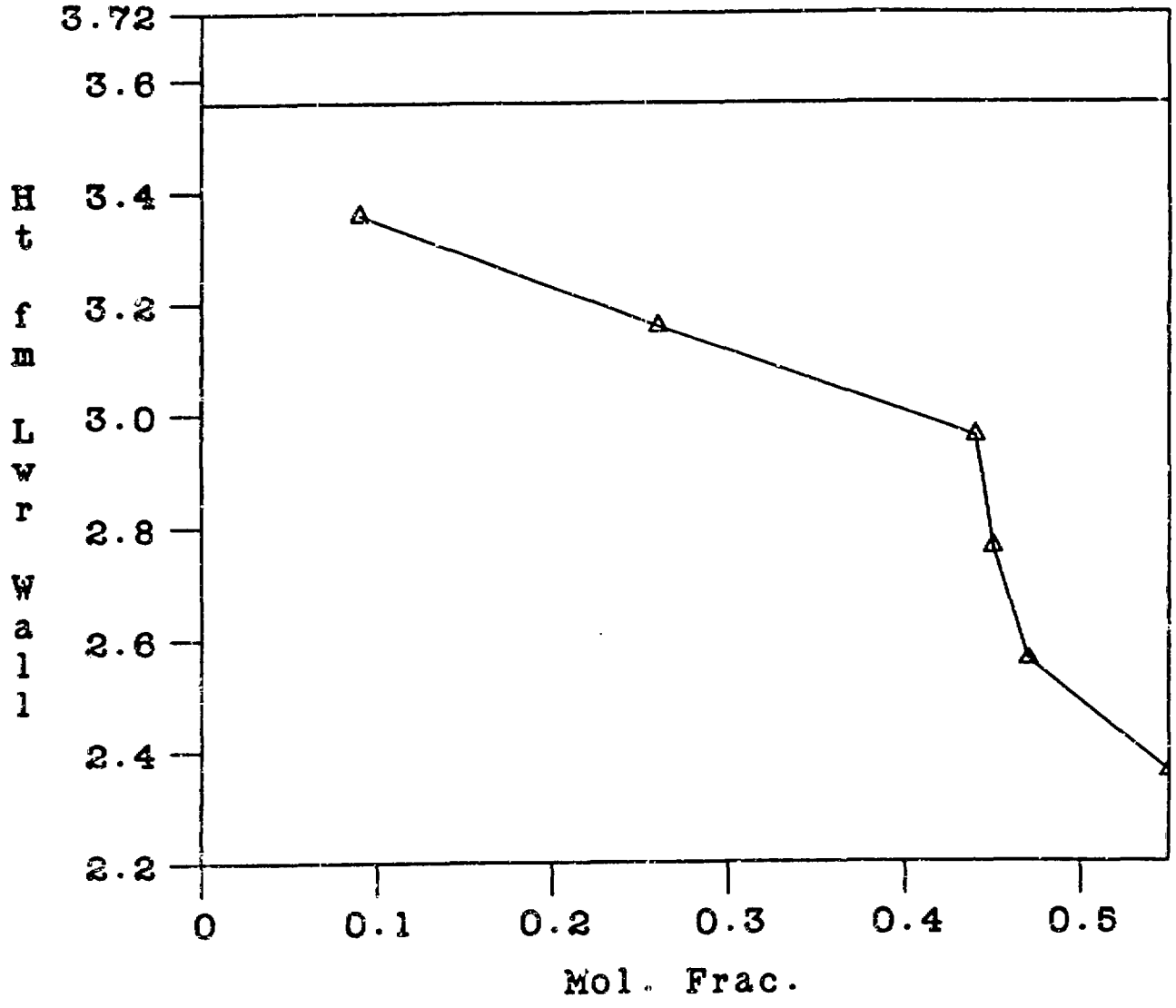

Run 092 - CARS N2 Mole Fraction
(Phi = 1.0, Sta. 3)

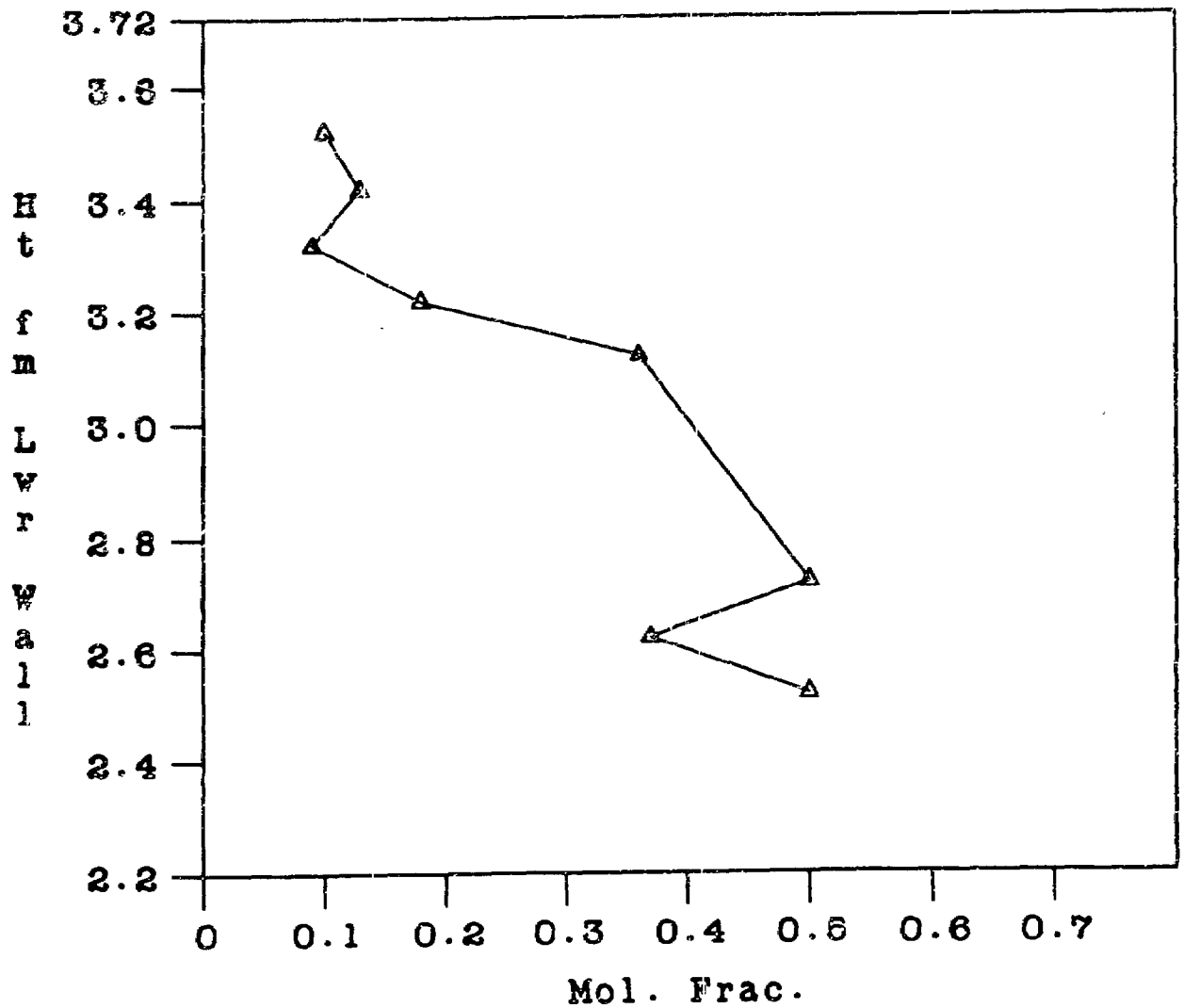

Run 093 - CARS N2 Mol e Fraction
(Phi = 0.5, Sta. 3)

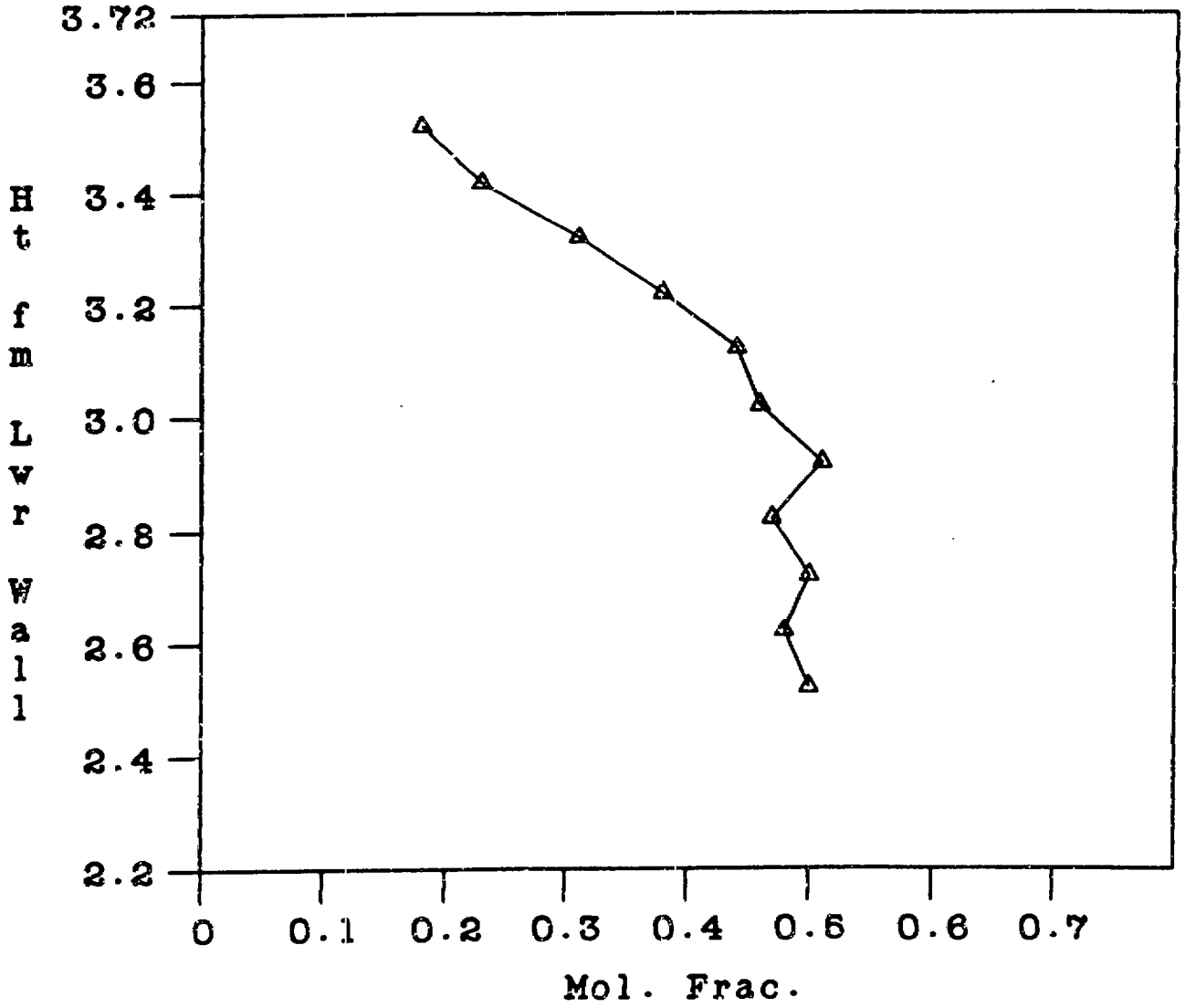

Run 094 - CARS N2 Mol e Fraction
(Phi = 1.0, Sta. 3)

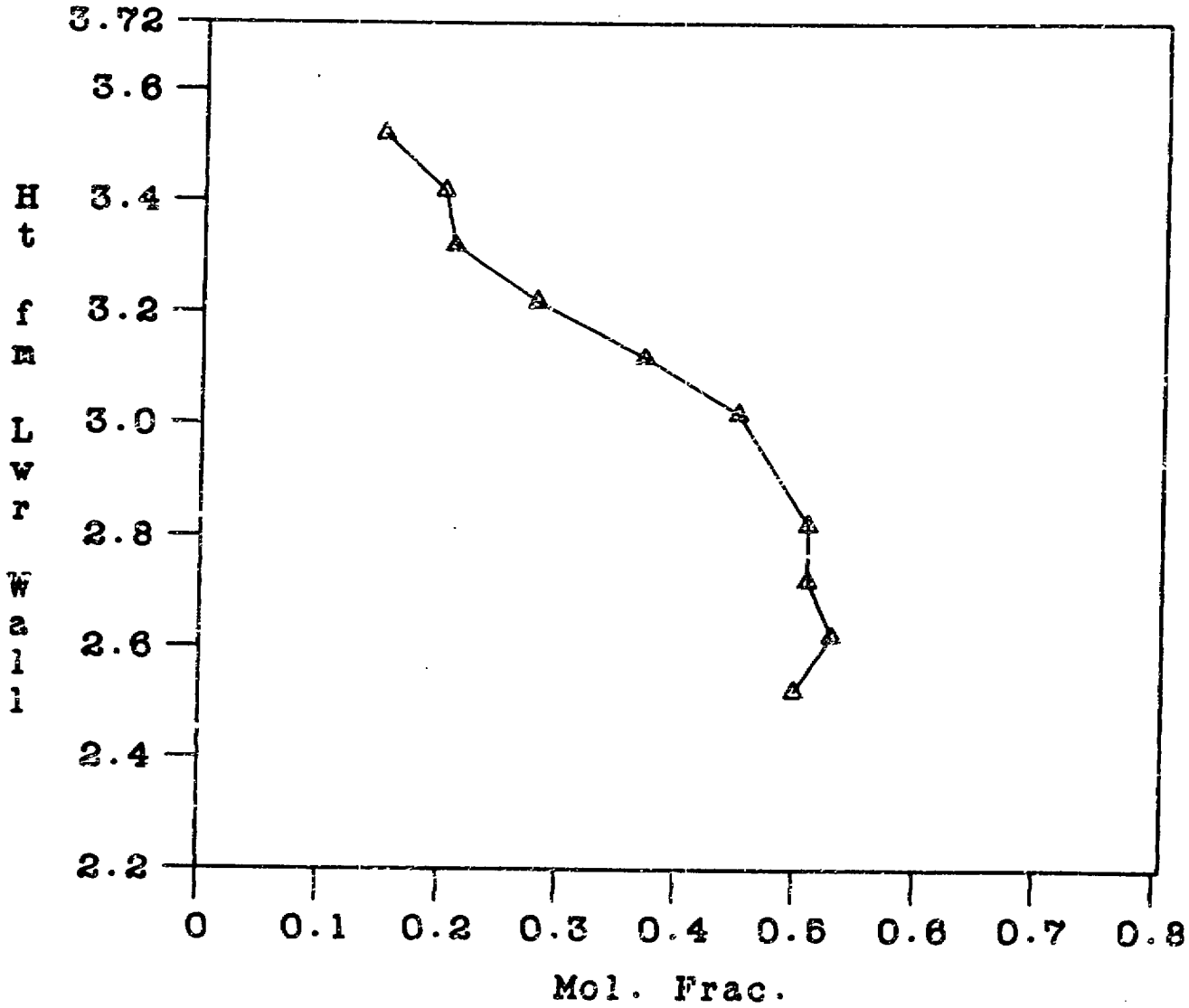

Run 095 - CARS N2 Mol e Fraction
(Phi = 1.0, Sta. 3, T.T. = 2000 R)

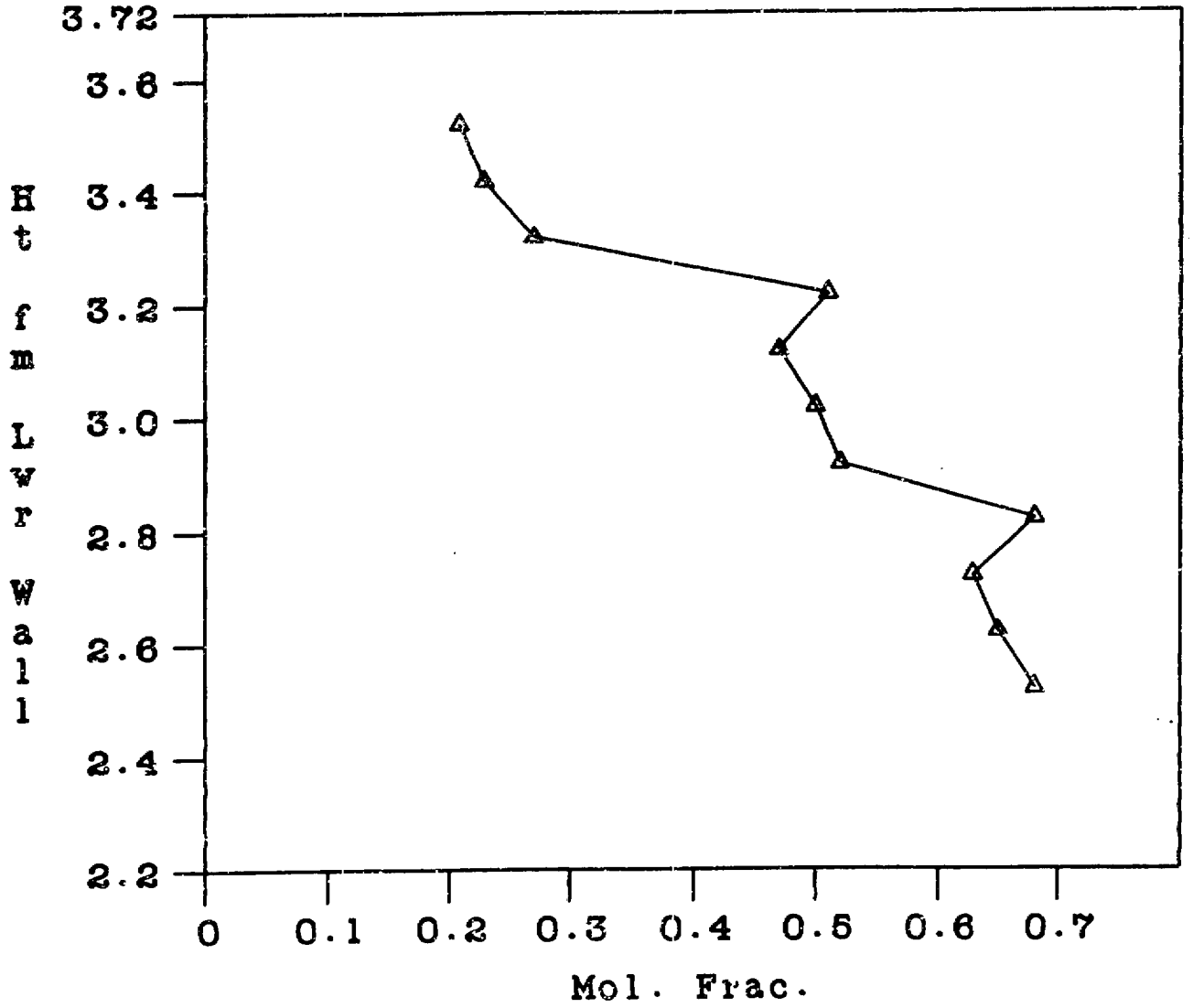

Run 096 - CARS N2 Mol e Fraction
(Phi = 0.5, Sta. 3, T.T. = 2000 R)

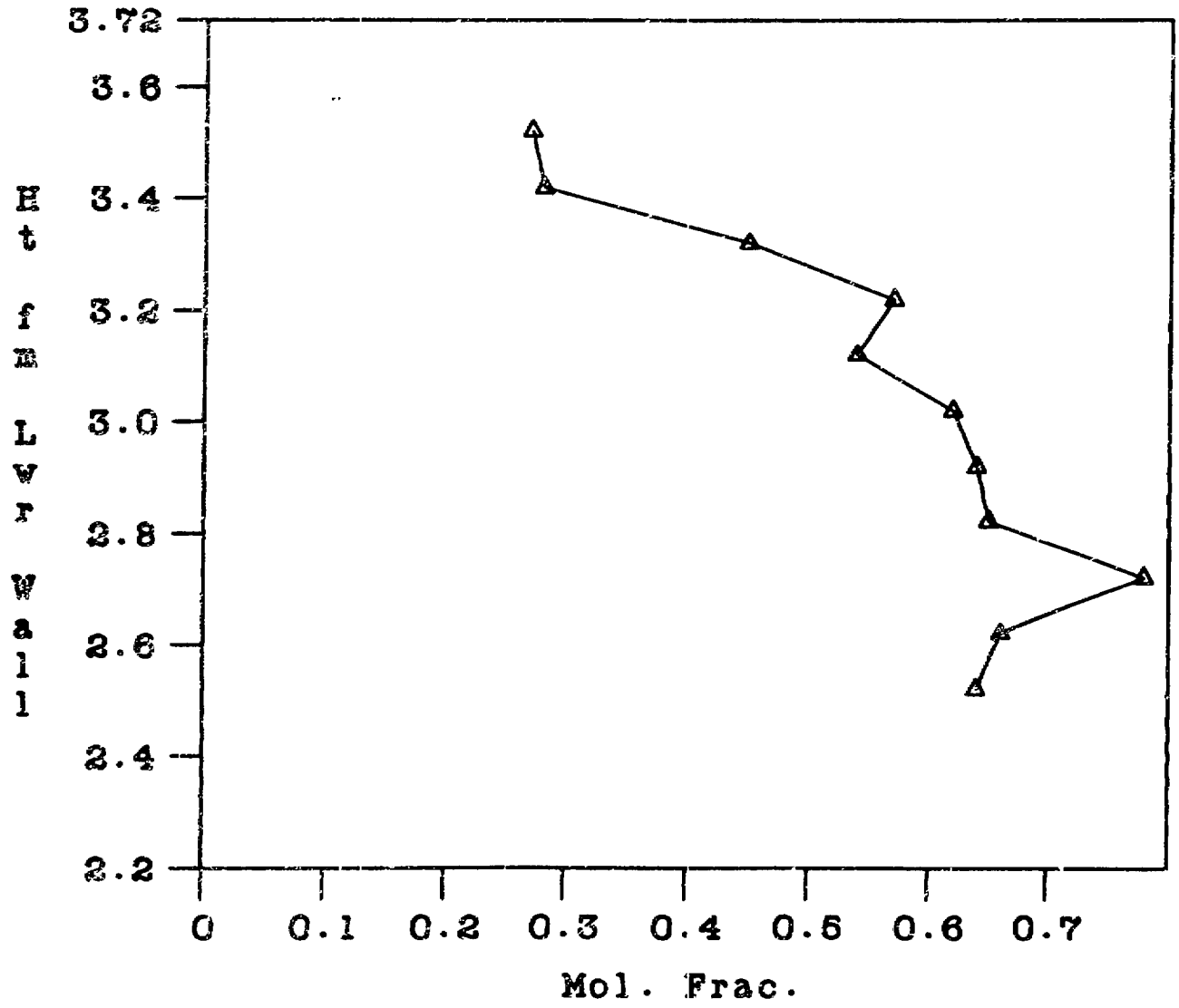

Run 112 - CARS N2 Concentration
(Phi = 1.0, Sta. 2, T.T. = 2000 R, Wedge)

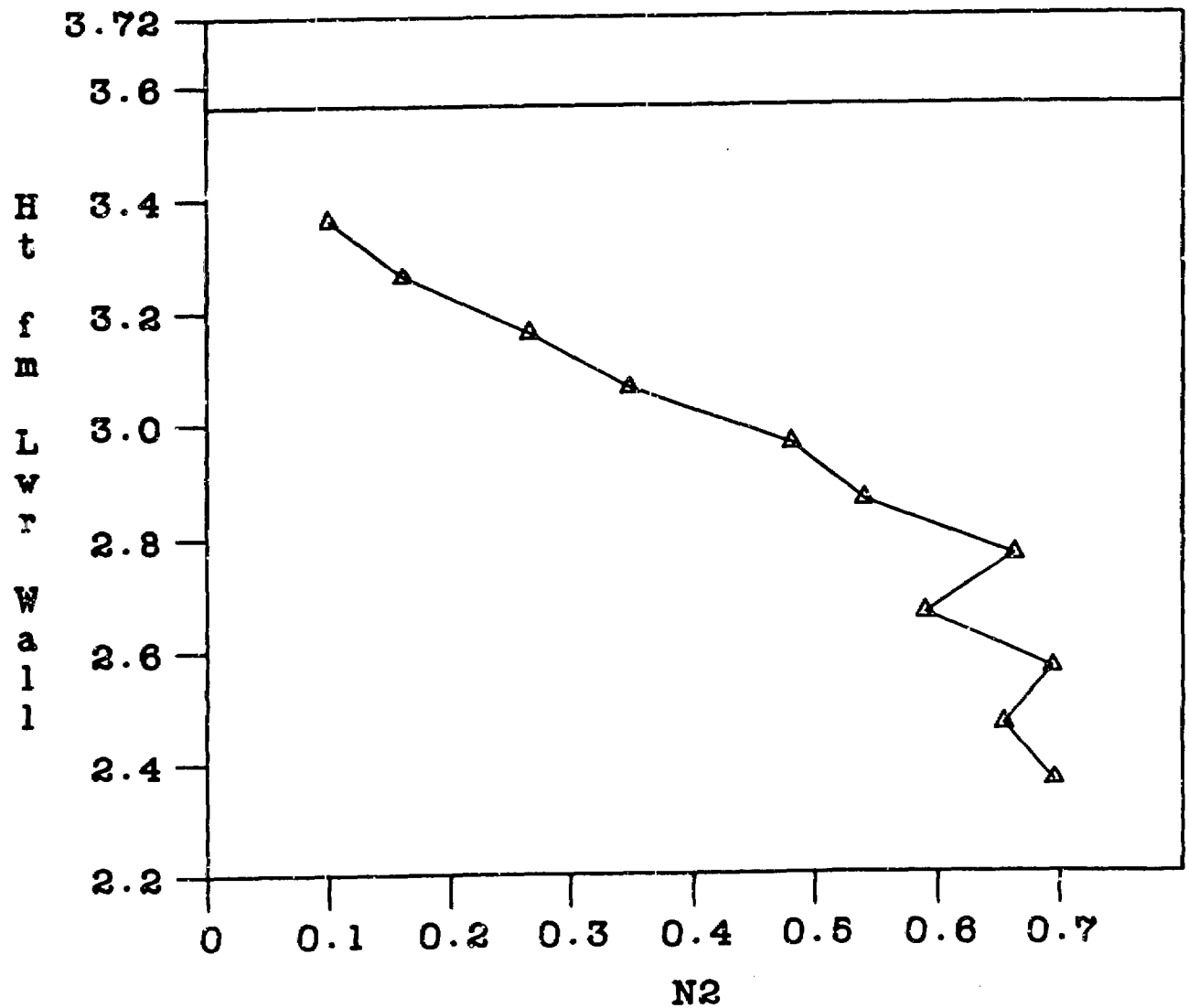

Run 113 - CARS N2 Concentration
(Phi = 0.5, Sta. 2, T.T. = 2000 R, Wedge)

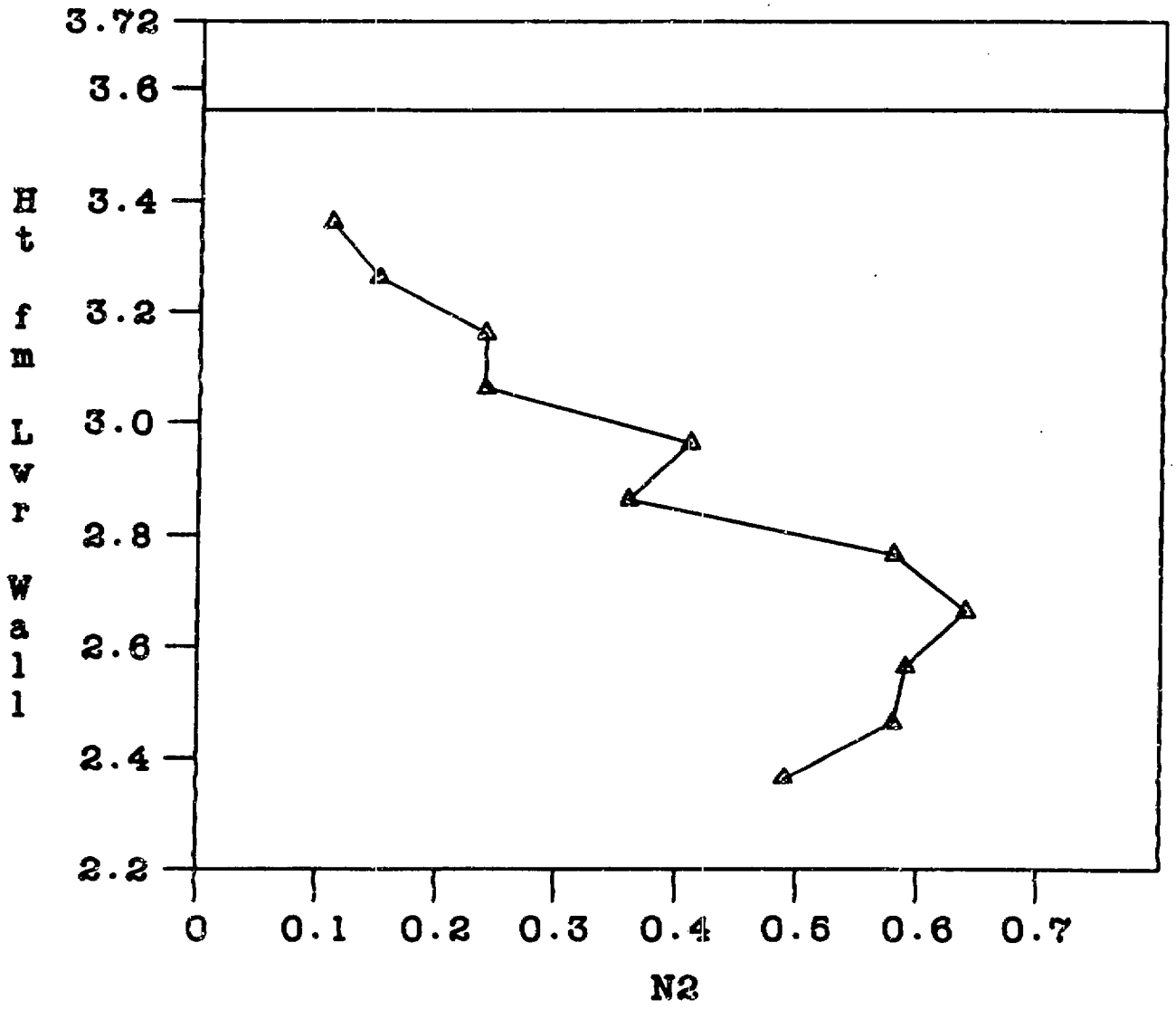

Run 114 - CARS N2 Concentration
(N2 Injection, Sta. 2, T.T. = 2000 R, Wedge)

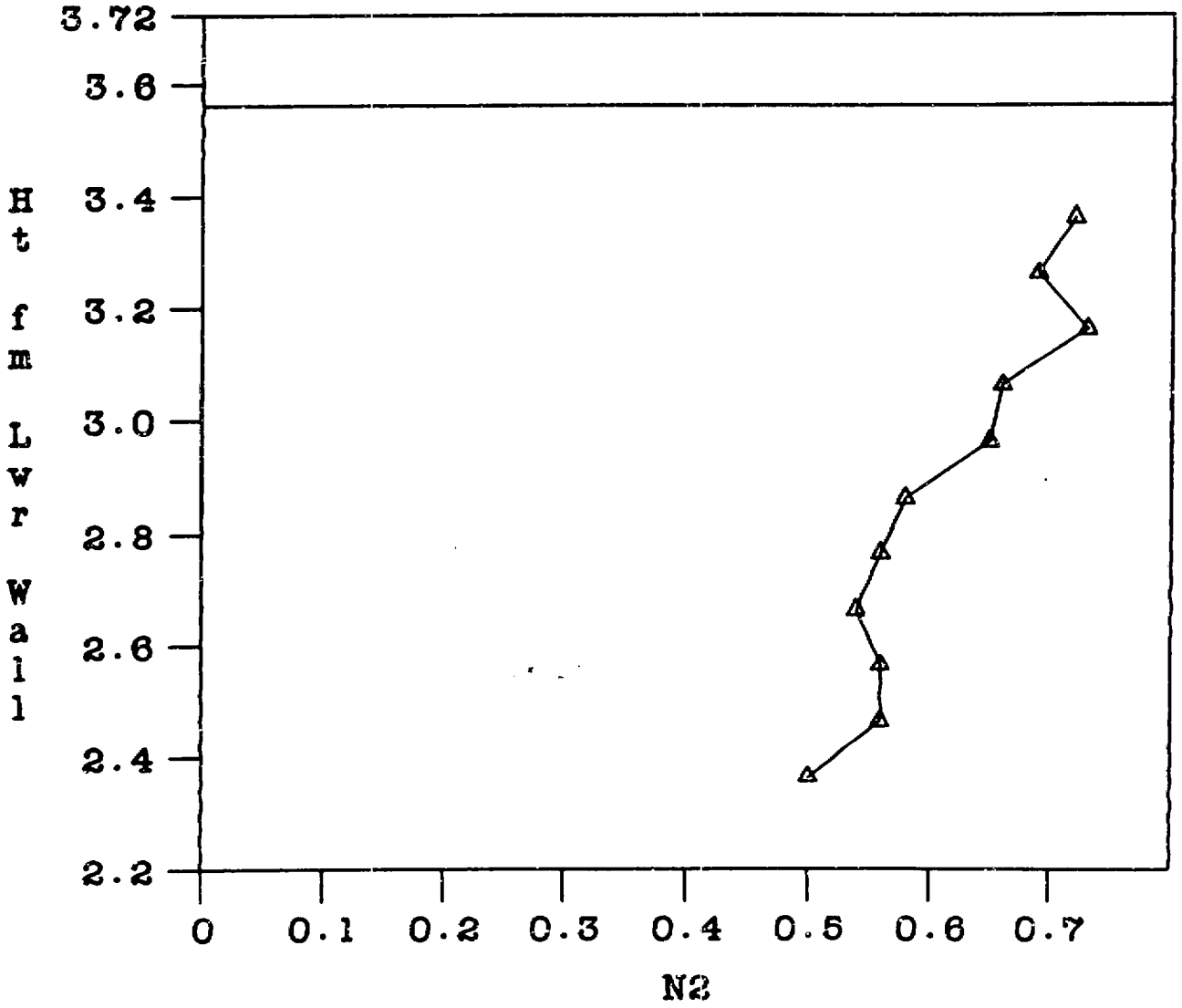

Run 121 - CARS N2 Concentration
(Phi = 1.0 Sta. 2, T.T. = 4000 R, Wedge)

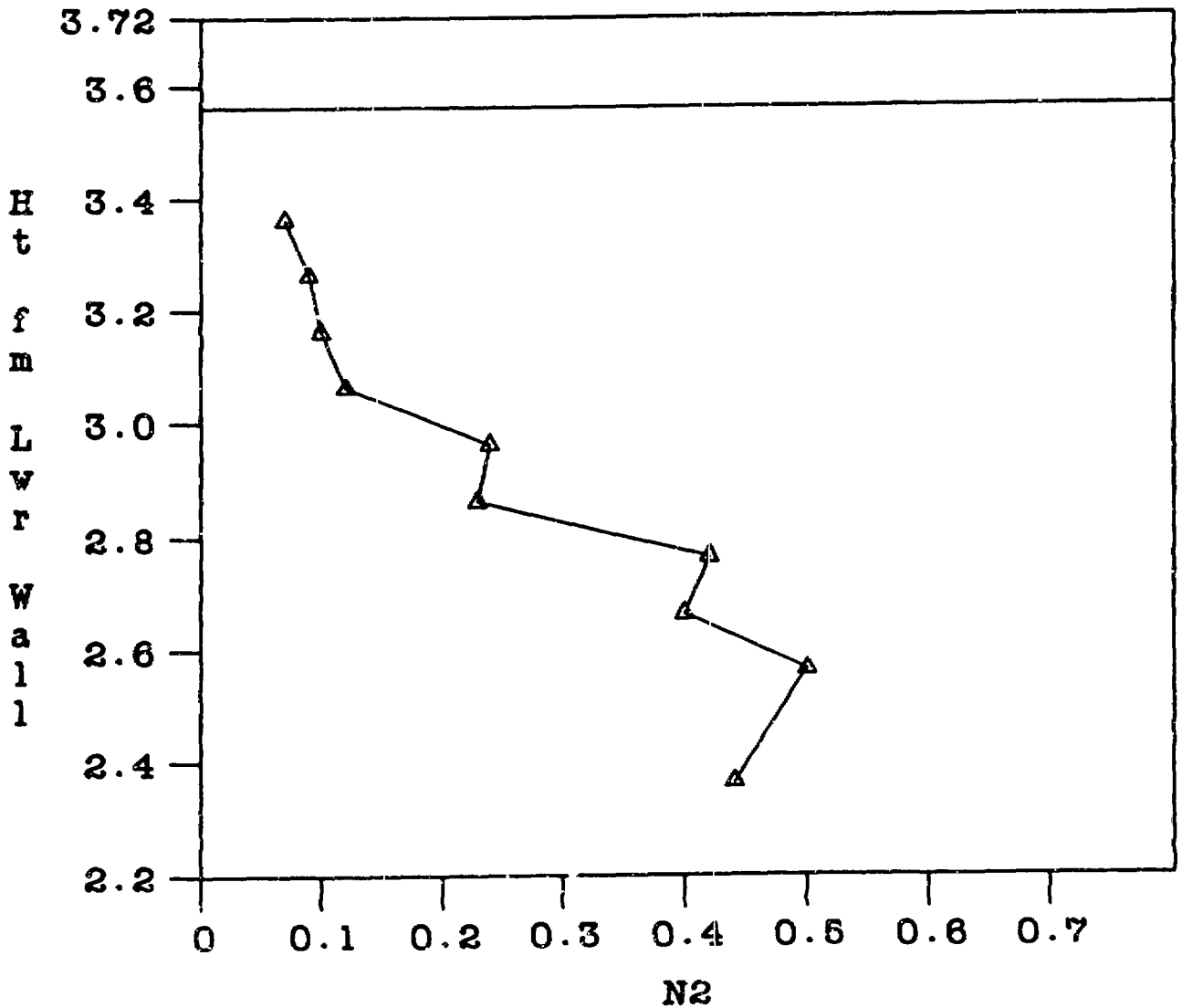

Run 122 - CARS N2 Concentration
(Phi = 0.5, Sta. 2, T.T. = 4000 R, Wedge)

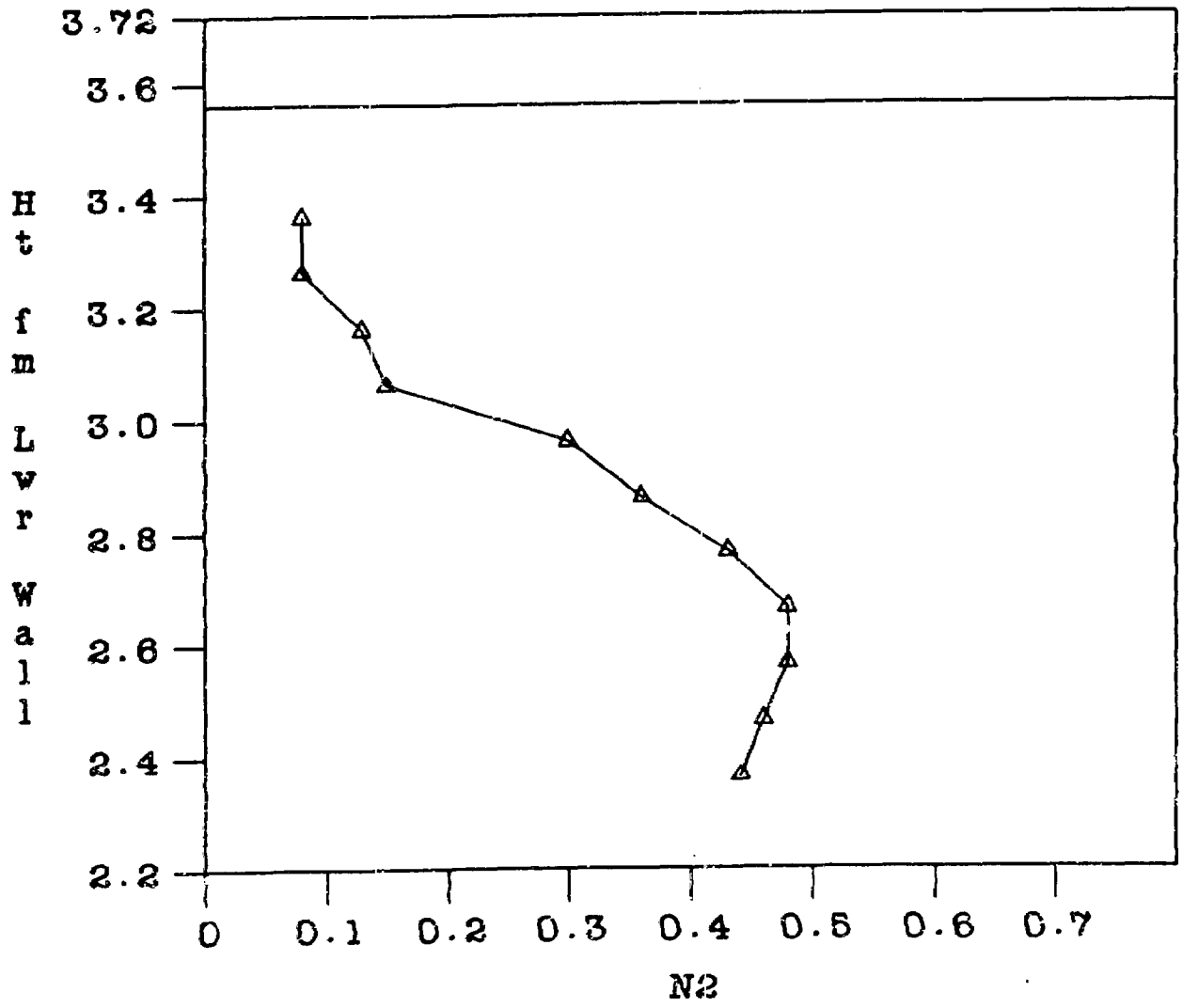

Run 123 - CARS N2 Concentration
(Phi = 1.0, Sta. 3, T.T. = 2000 R, Wedge)

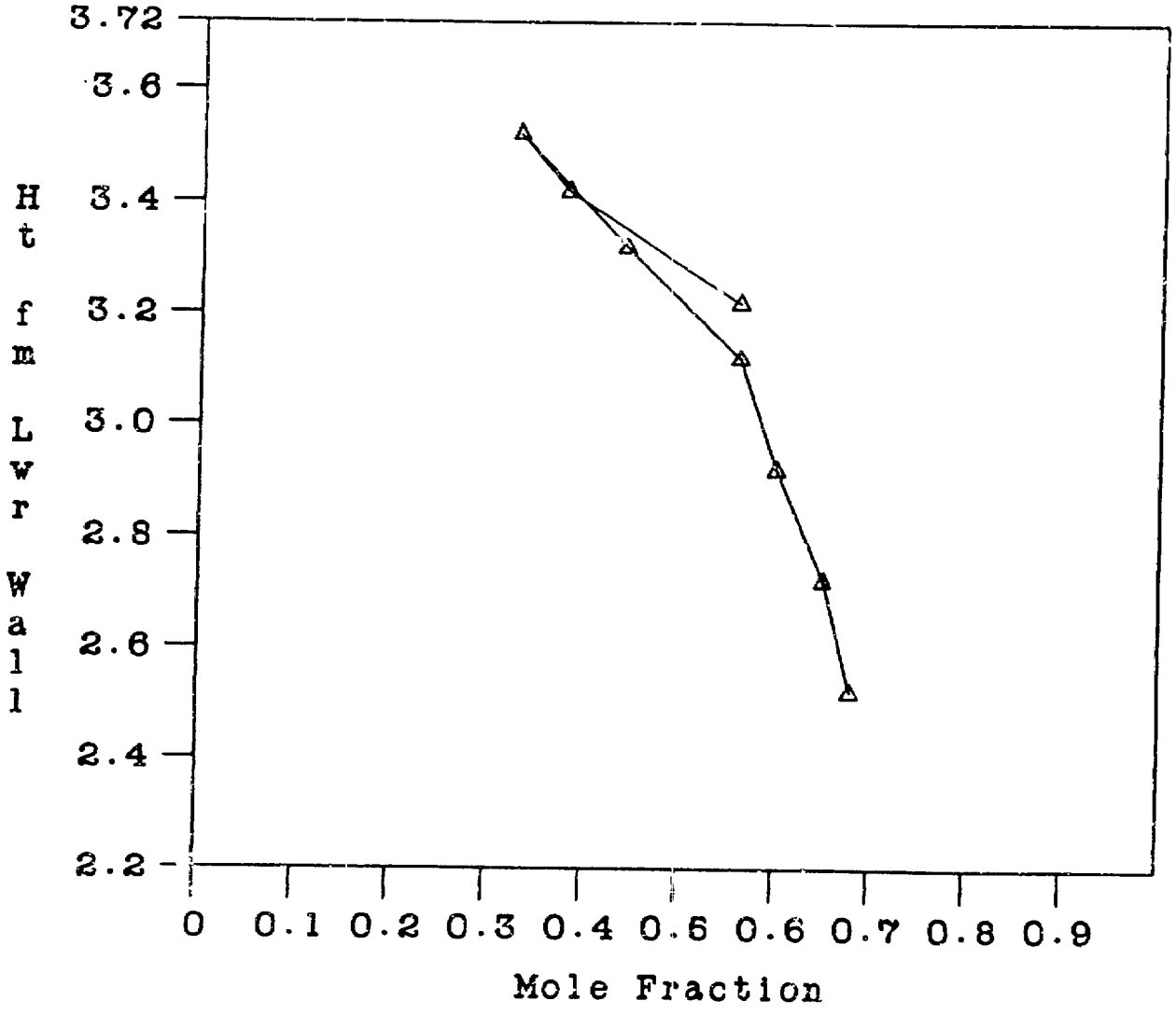

Run 124 - CARS N2 Concentration
(Phi = 1.0, Sta. 3, T.T. = 2000 R, Wedge)

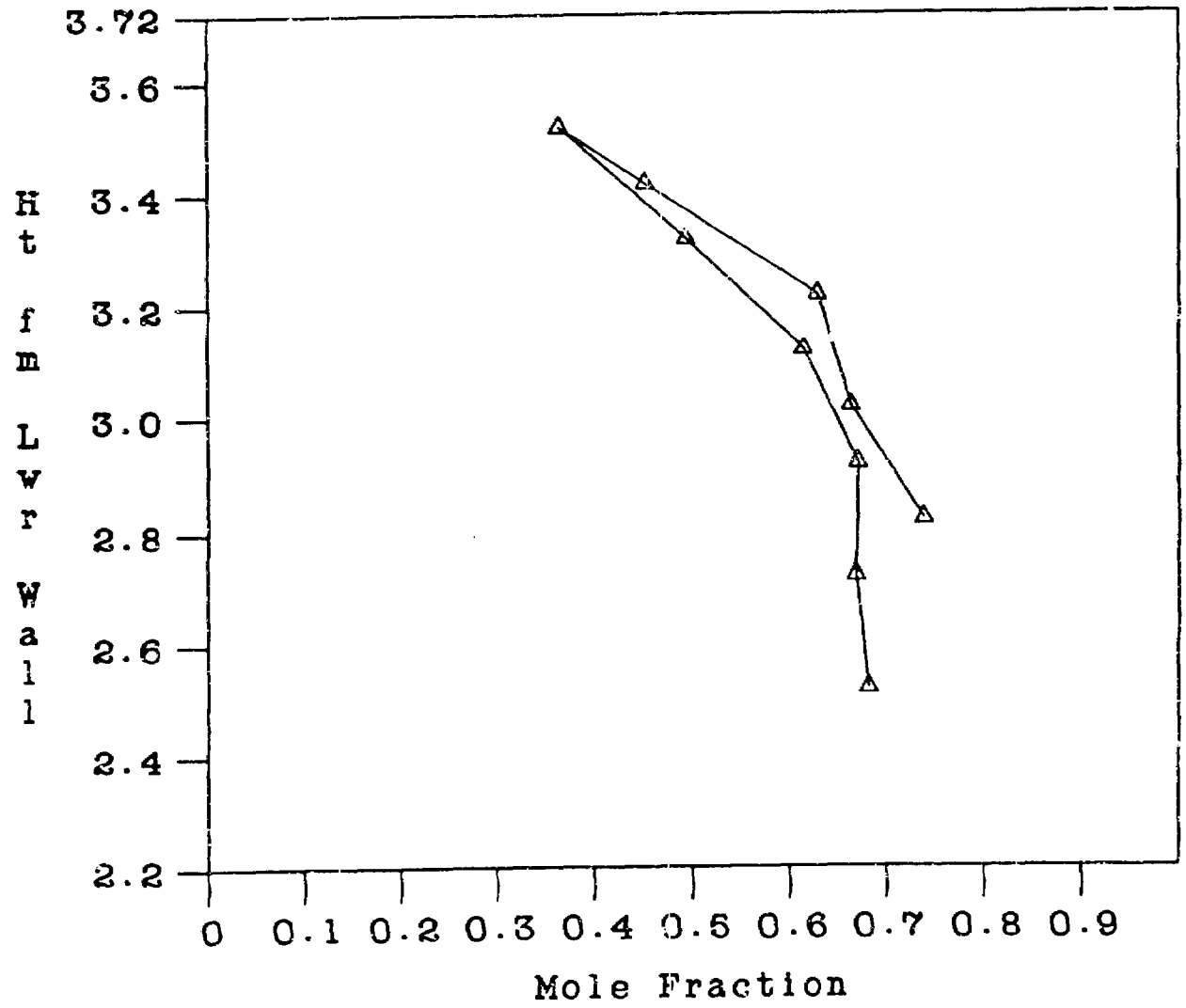

Run 125 - CARS N2 Concentration
(Phi = 0.5, Sta. 3, T.T. = 2000 R, Wedge)

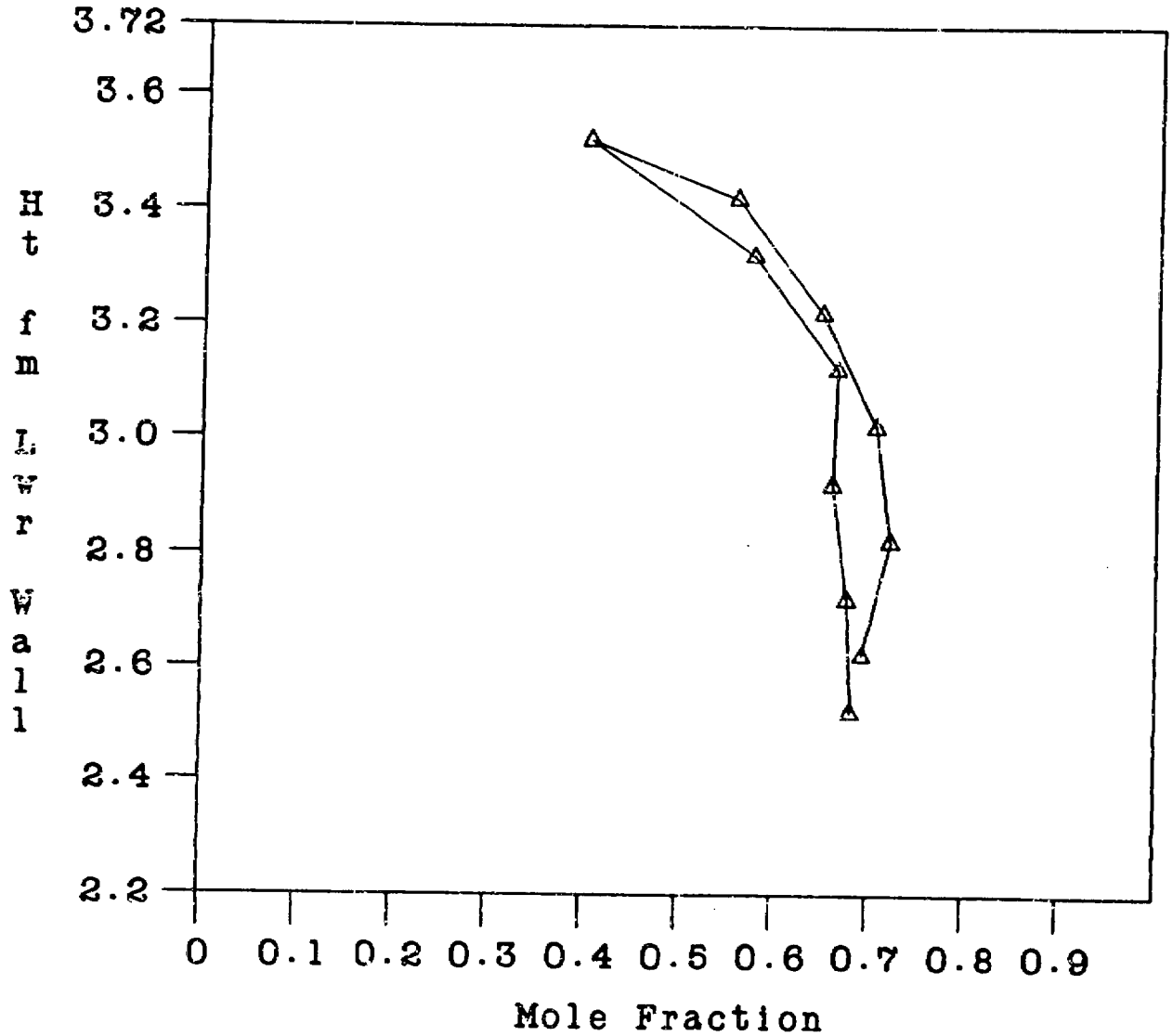

Run 126 - CARS N2 Concentration
(Phi = 1.0, Sta. 3, T.T. = 4000 R, Wedge)

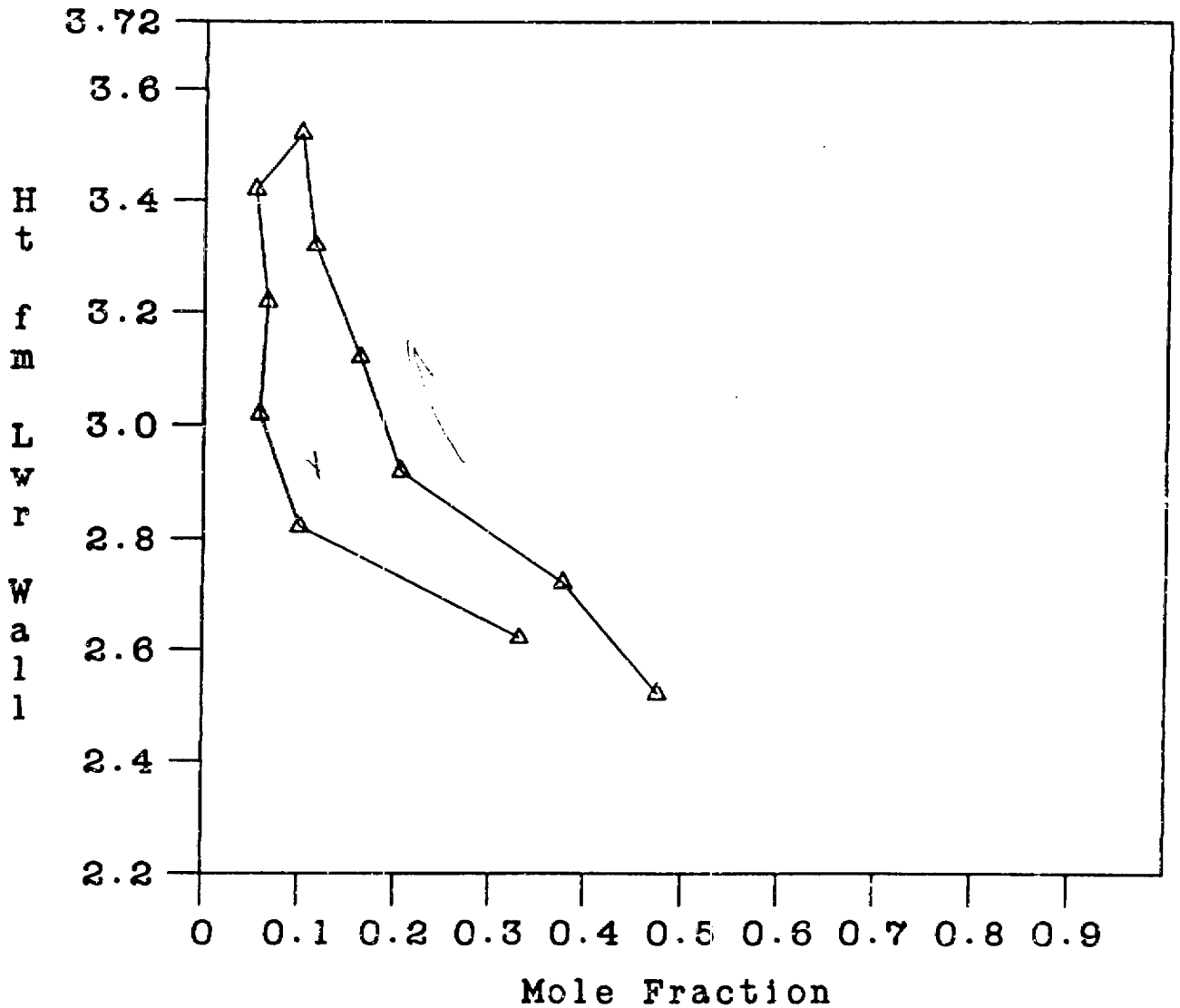

Run 127 - CARS N2 Concentration
(Phi = 0.5, Sta. 3, T.T. = 4000 R, Wedge)

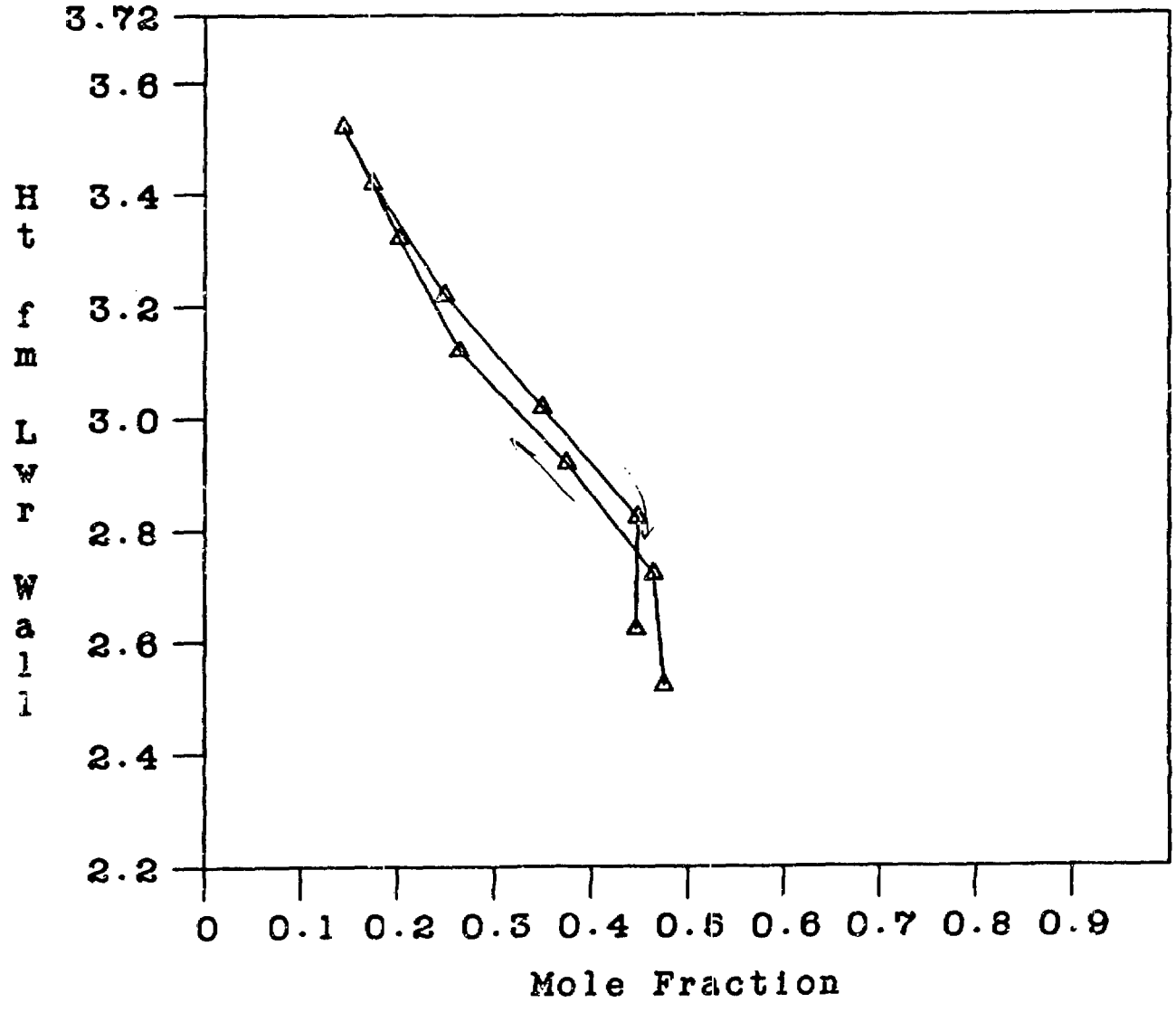

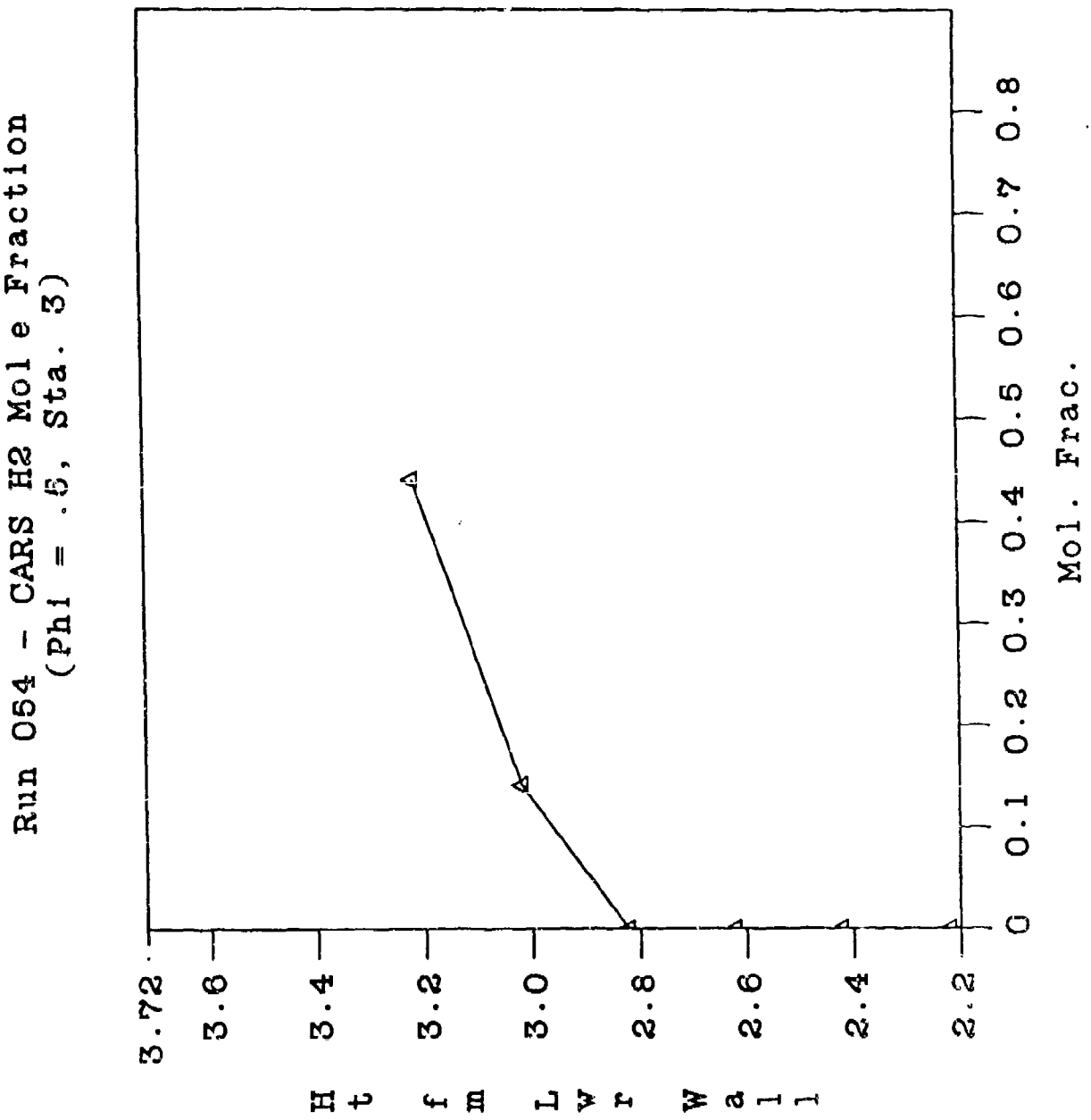
Run 054 - CARS H2 Mole Fraction
(Phi = .5, Sta. 3)
3.72
3.6
3.4
3.2
3.0
2.8
2.6
2.4
2.2
Height from Lower Wall
0
0.1
0.2
0.3
0.4
0.5
0.6
0.7
0.8
Mol. Frac.

Run 055 - CARS H2 Mole Fraction
(Phi = 1.0, Sta. 3)

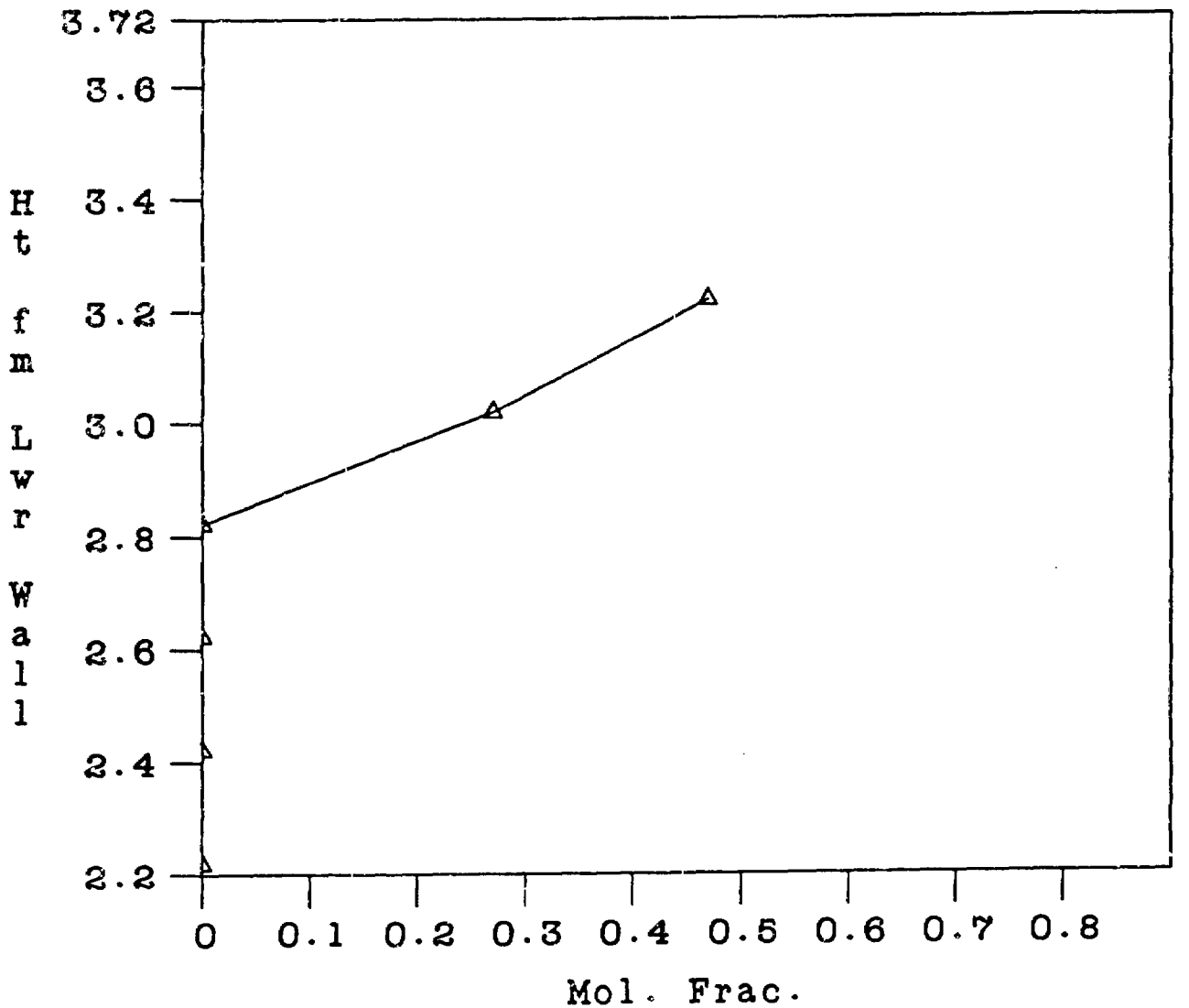

RUN 57 - CARS H2 Mole Fraction

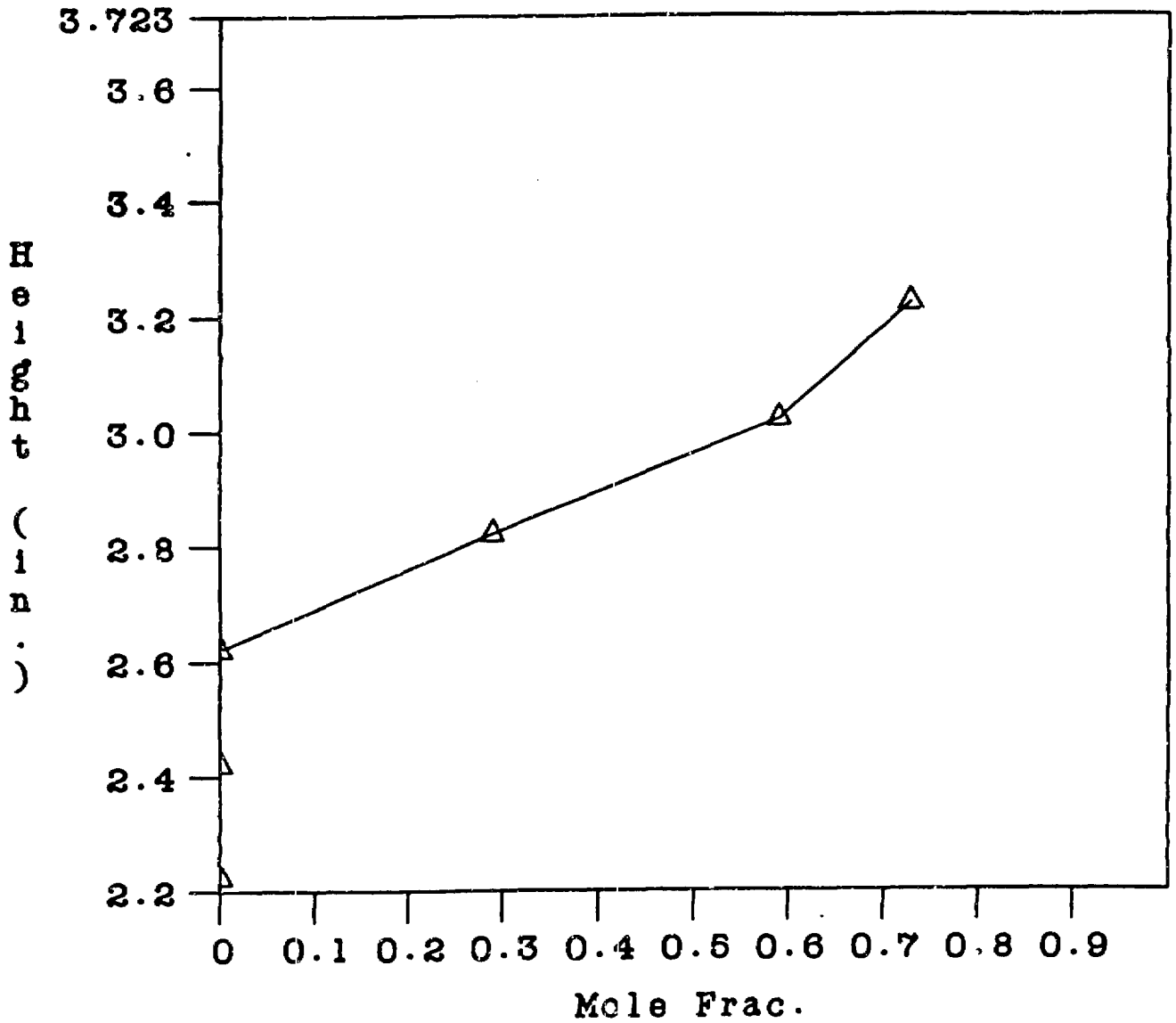

RUN 58 - CARS H2 Mole Fraction

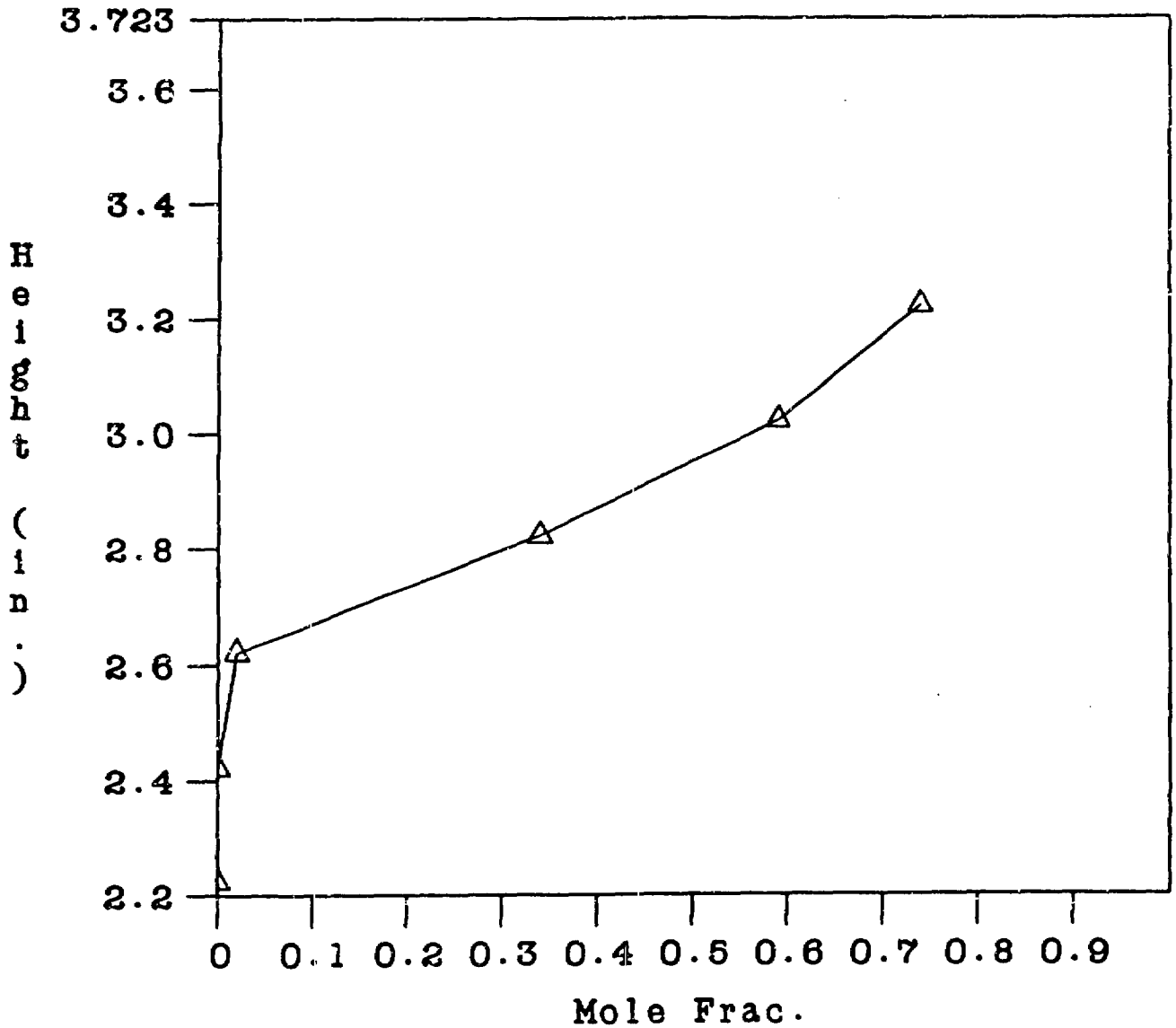

RUN 59 - CARS H2 Mole Fraction

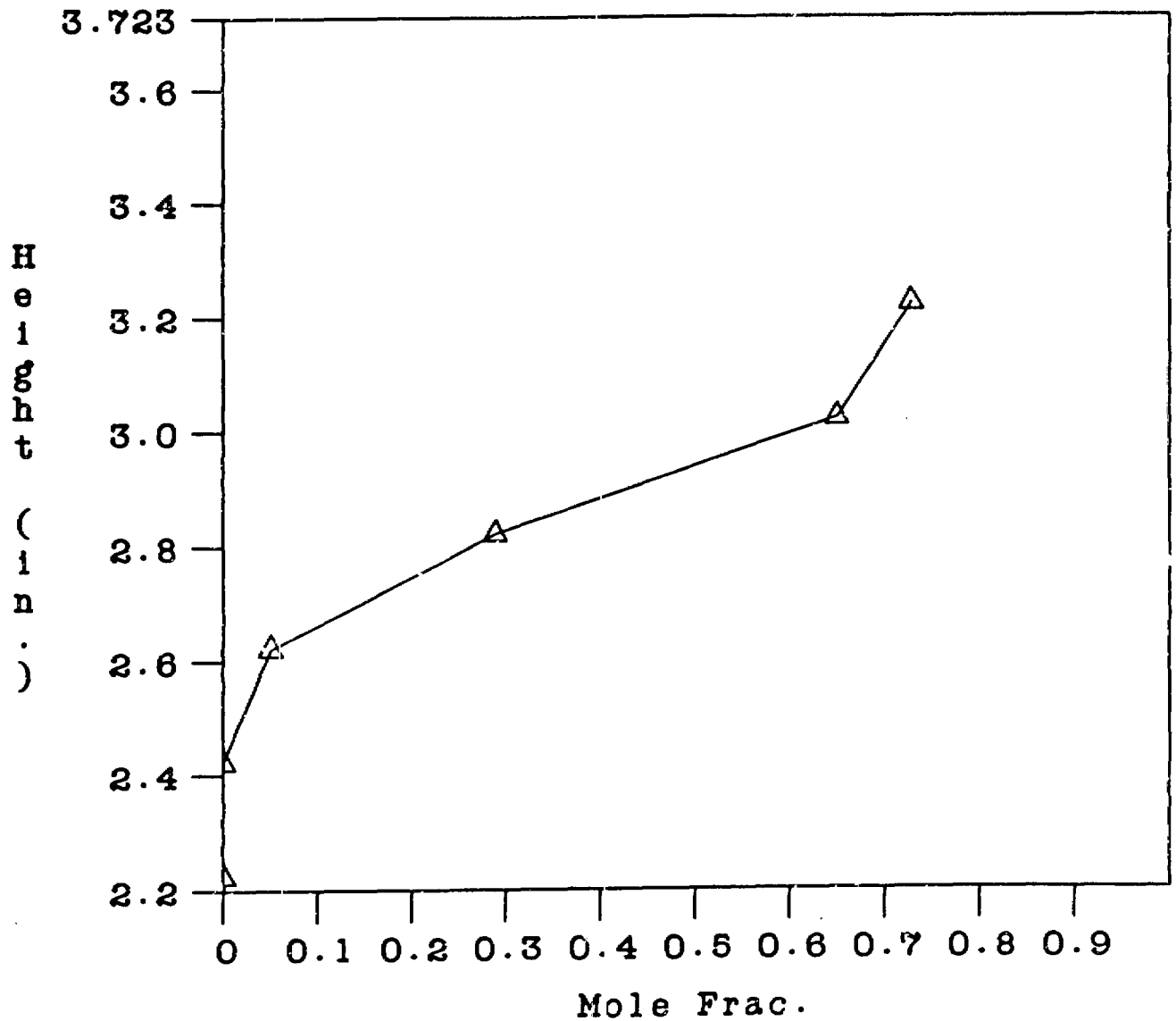

RUN 62 - CARS H2 Mole Fraction

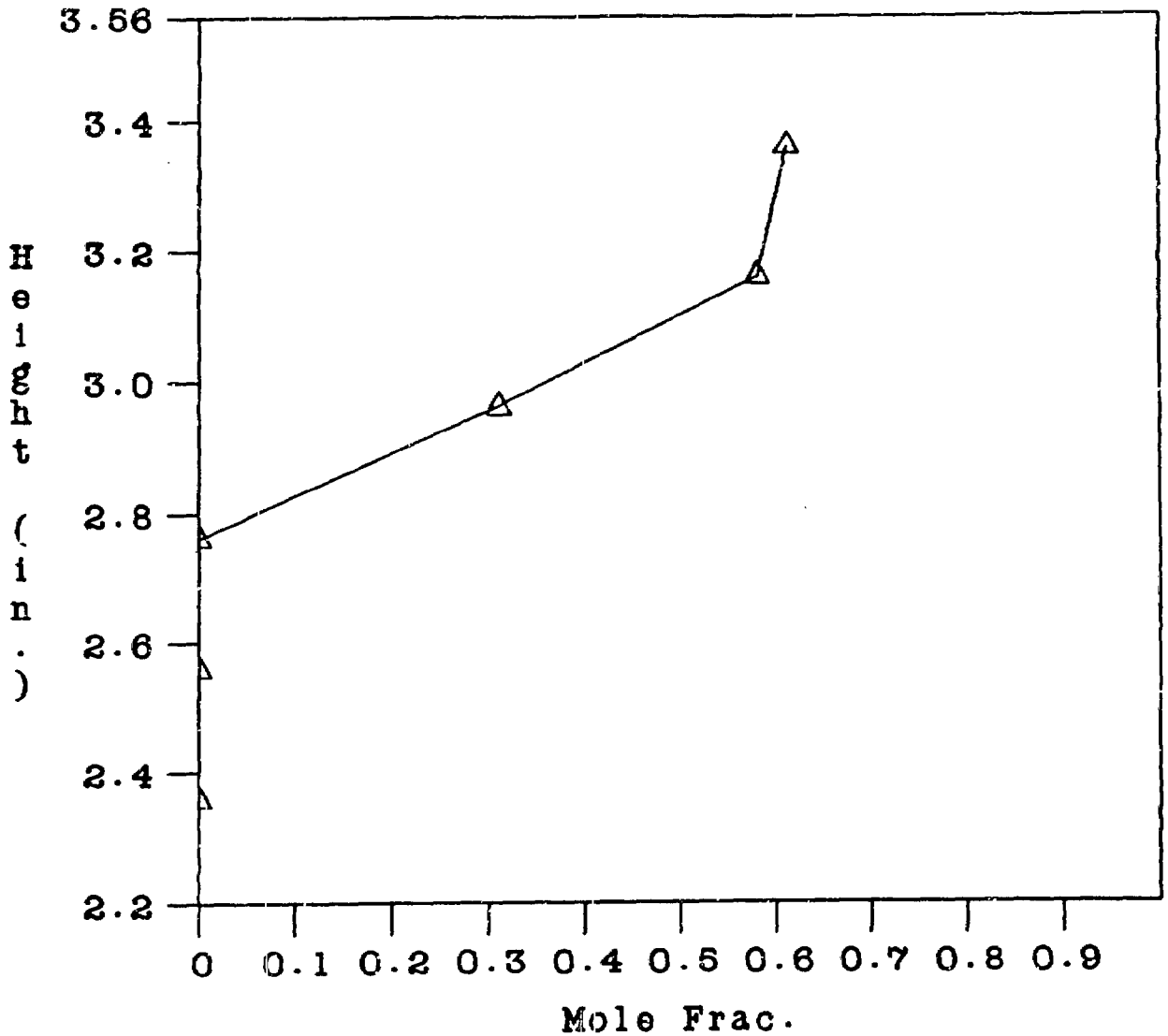

RUN 64 - CARS H2 Mole Fraction

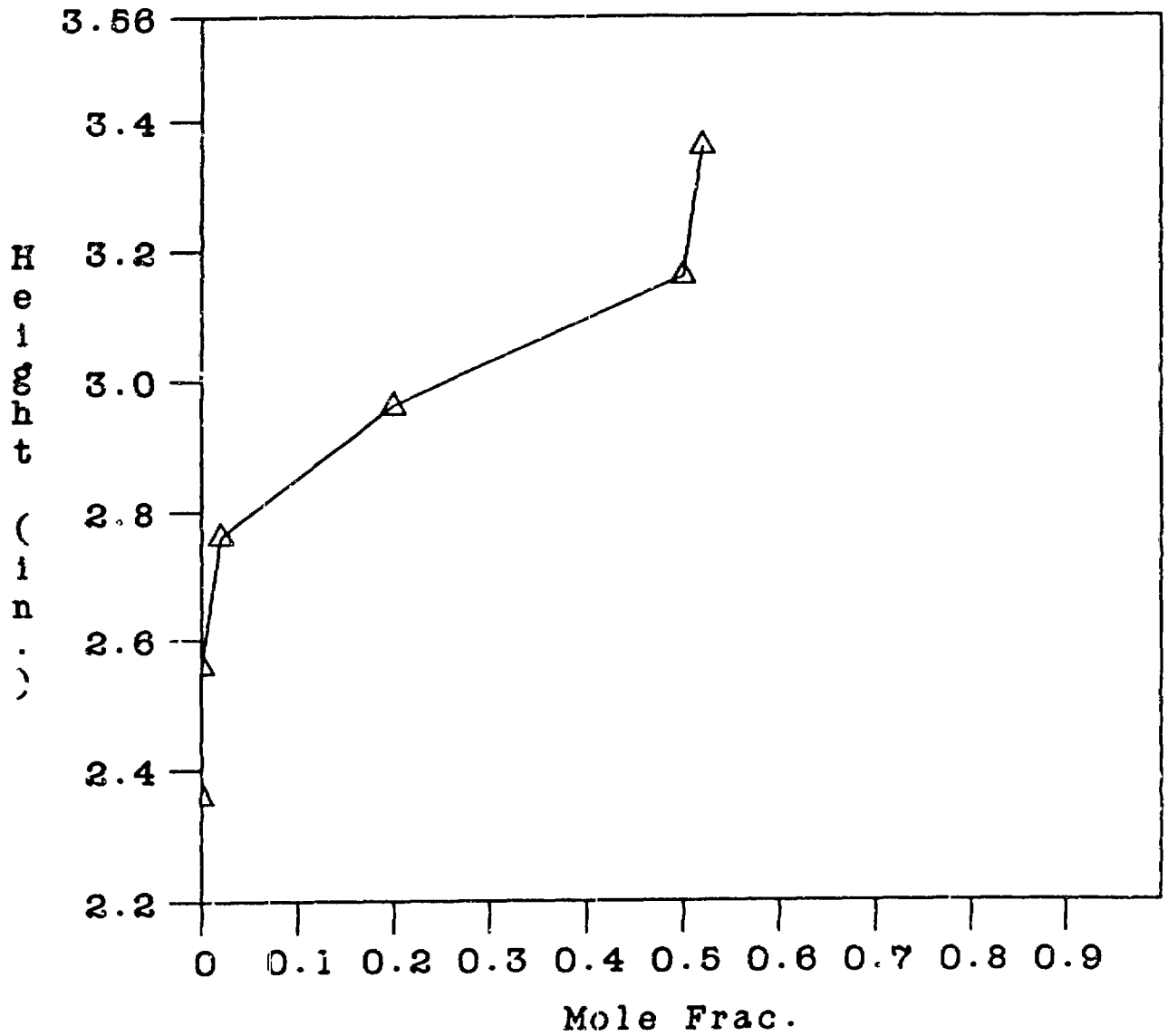

RUN 65 - CARS H2 Mole Fraction

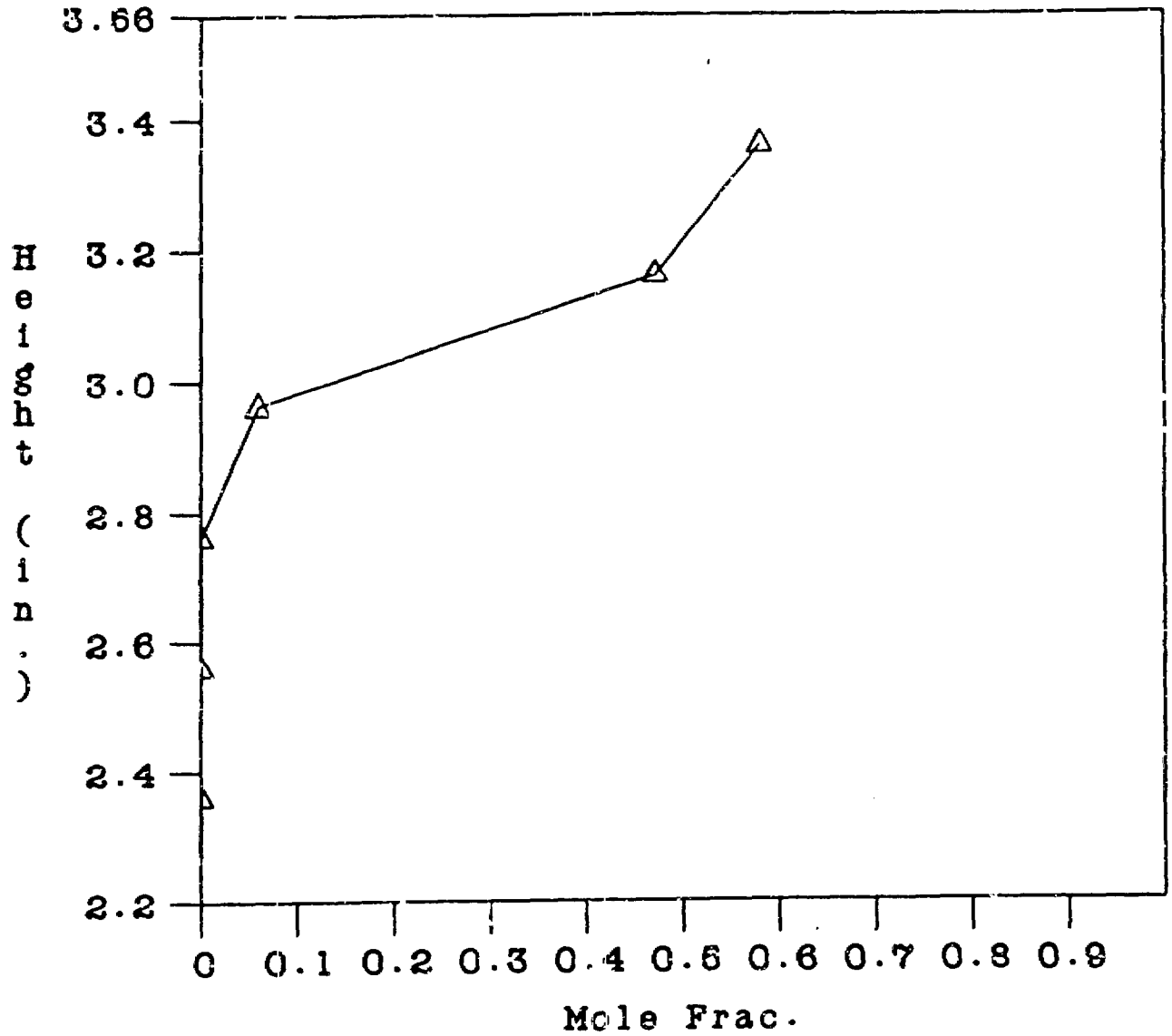

RUN 66 - CARS H2 Mole Fraction

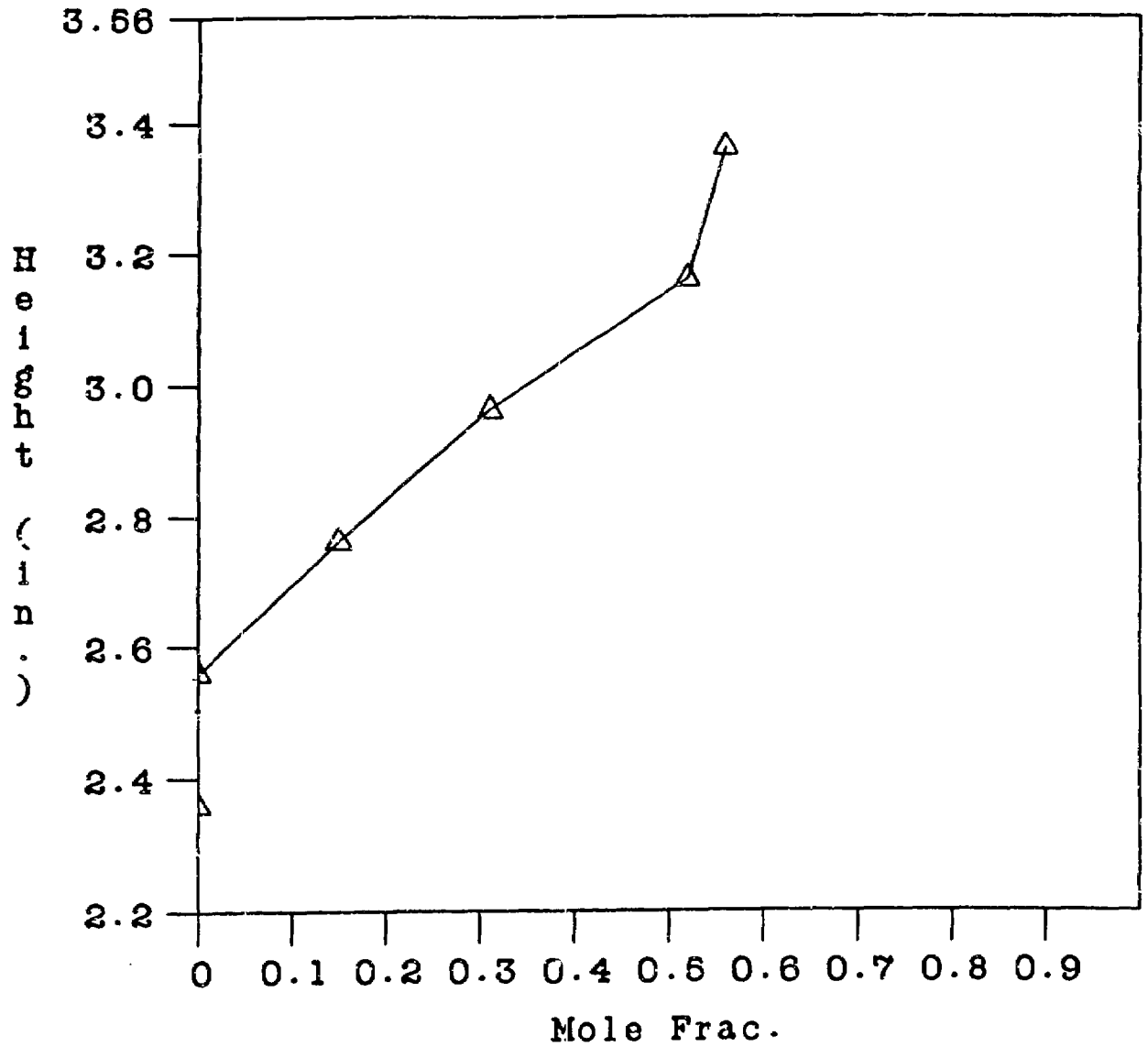

Run 074 - CARS H2 Mol e Fraction
(Phi =0.5, Sta. 2)

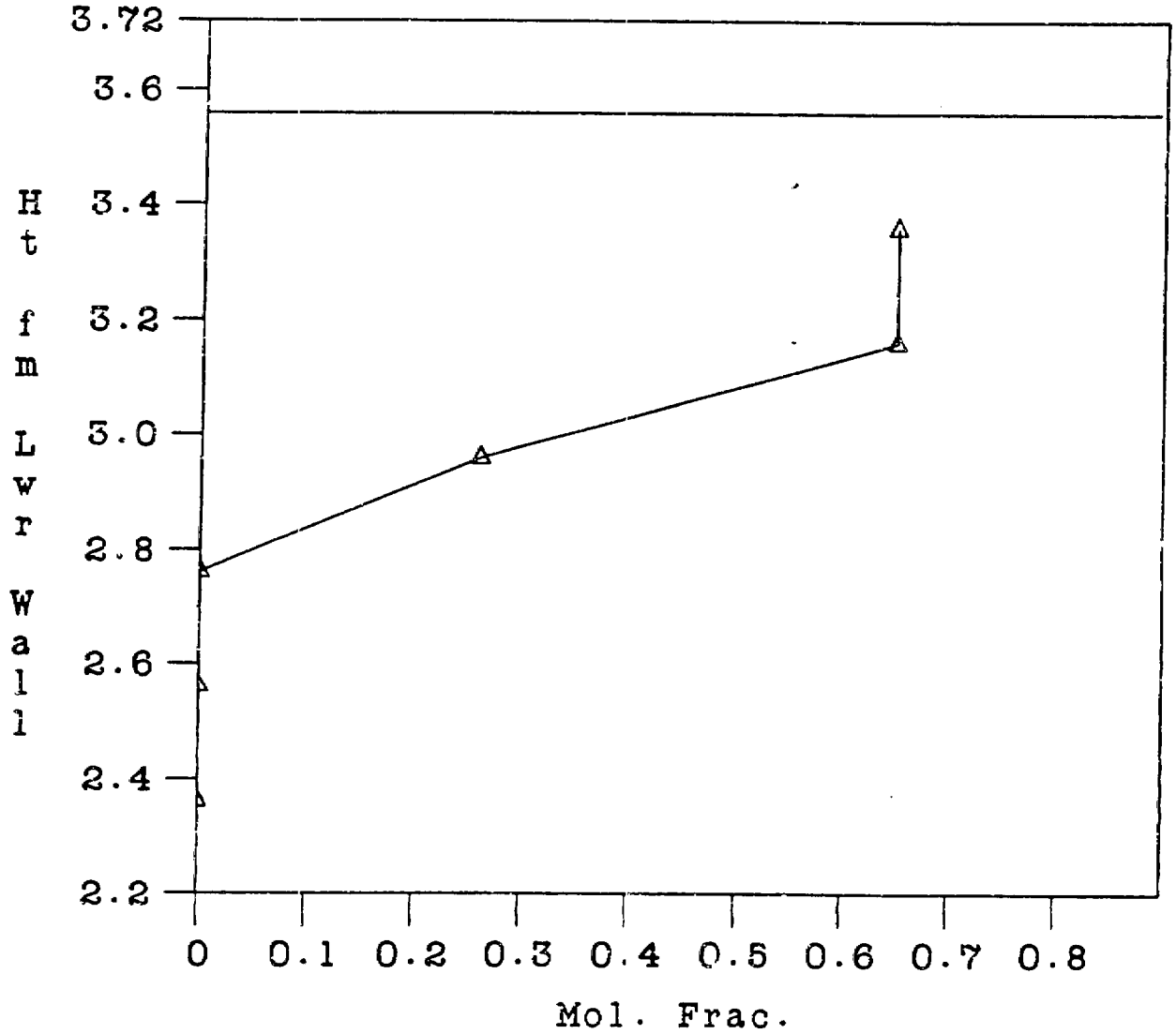

Run 081 -- CARS H2 Mol e Fraction
(Phi = .5, Sta. 2)

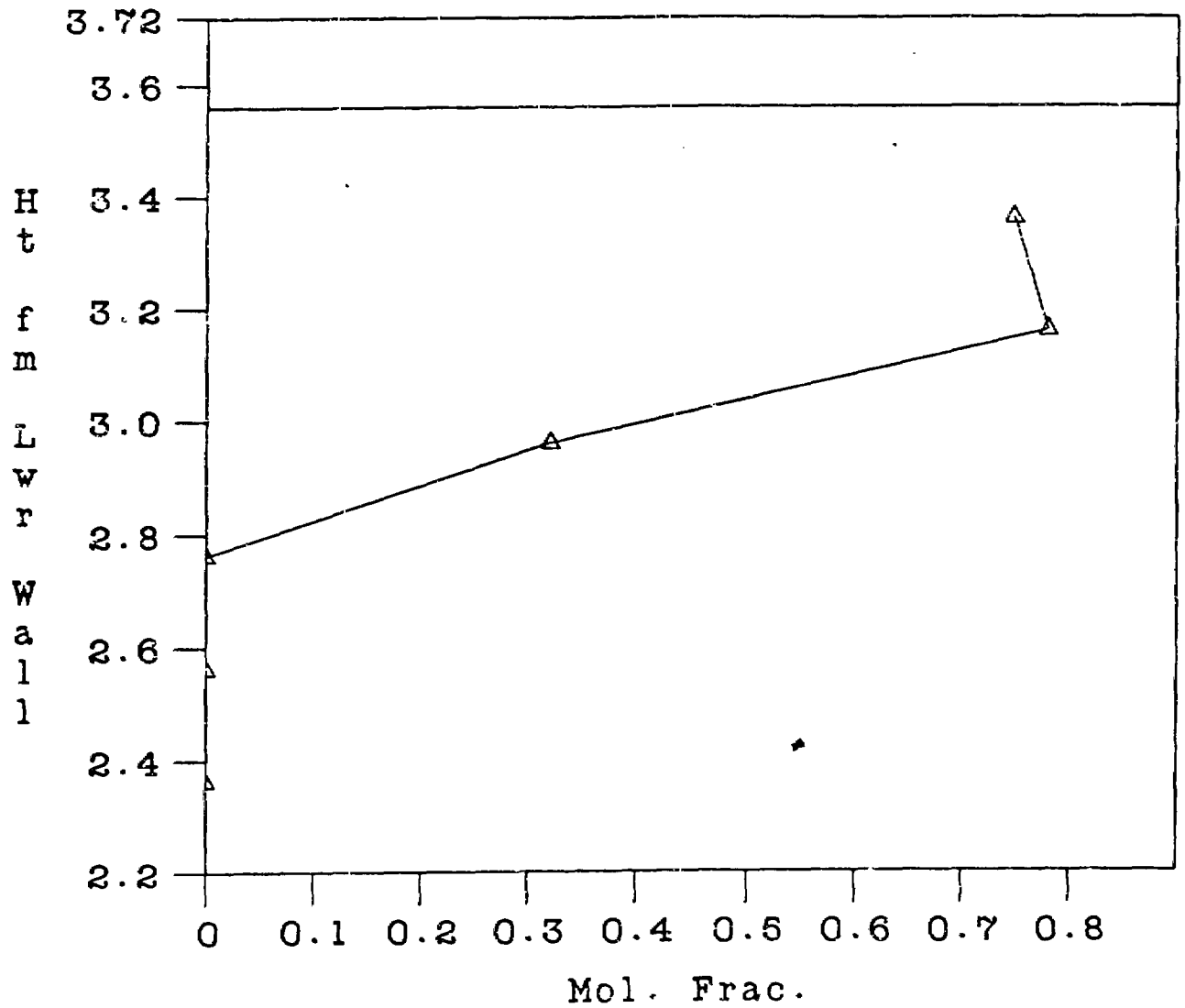

Run 082 - CARS H2 Mol e Fraction
(Phi = .5, Sta. 2)

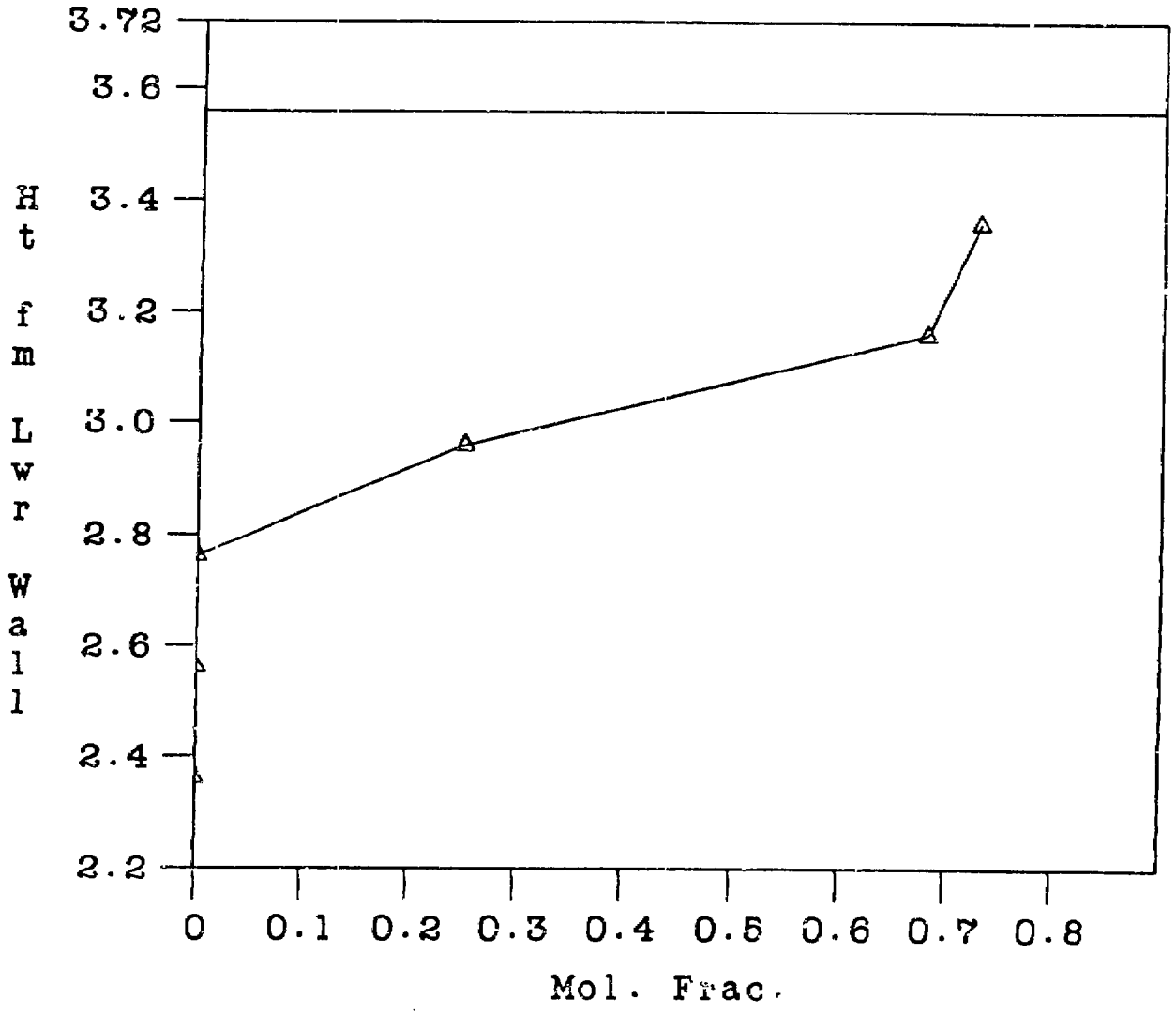

Run 084 - CARS H2 Mol e Fraction
(Phi =1.0, Sta. 2)

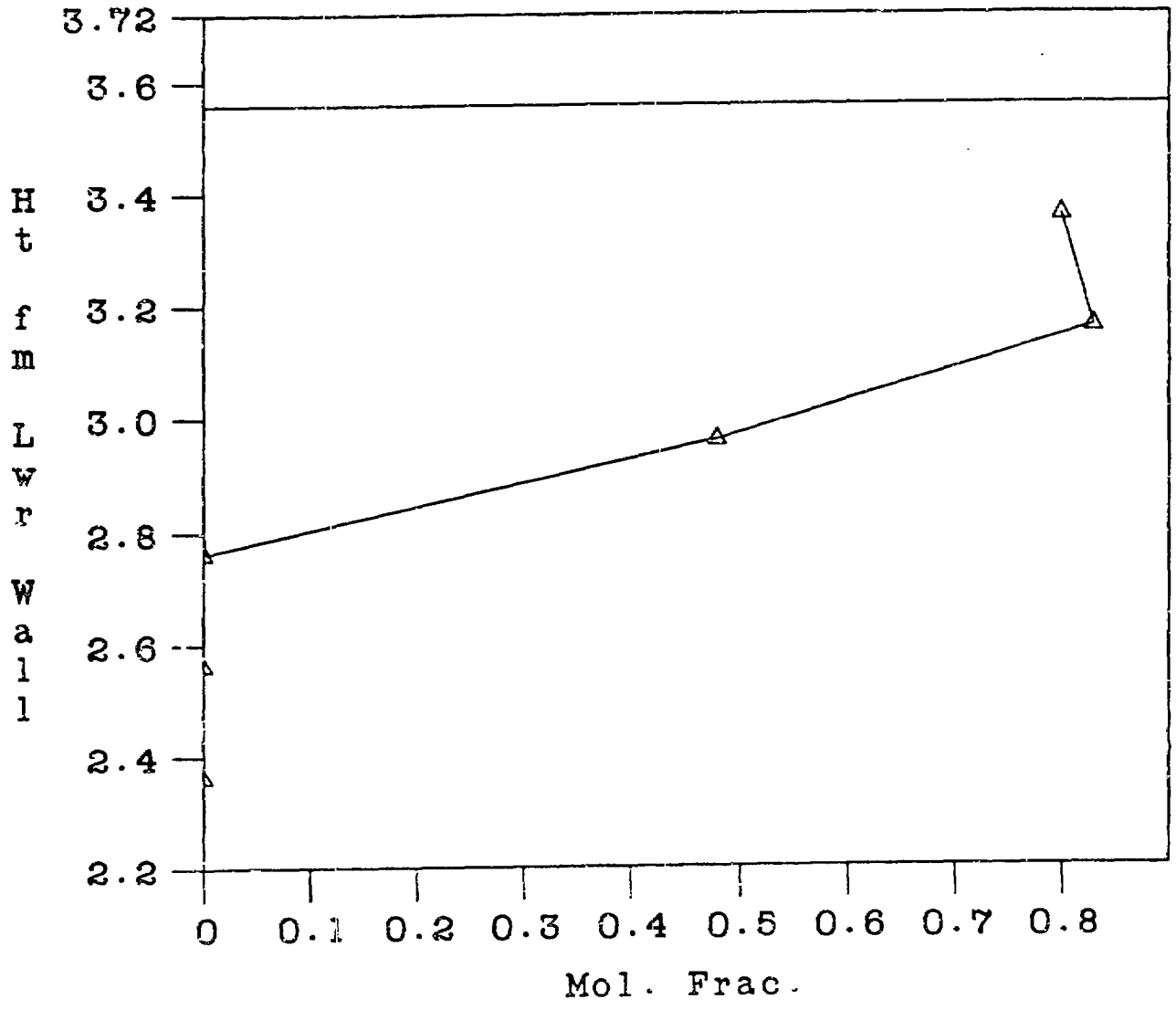

Run 092 - CARS H2 Mol e Fraction
(Phi = 1.0, Sta. 3)

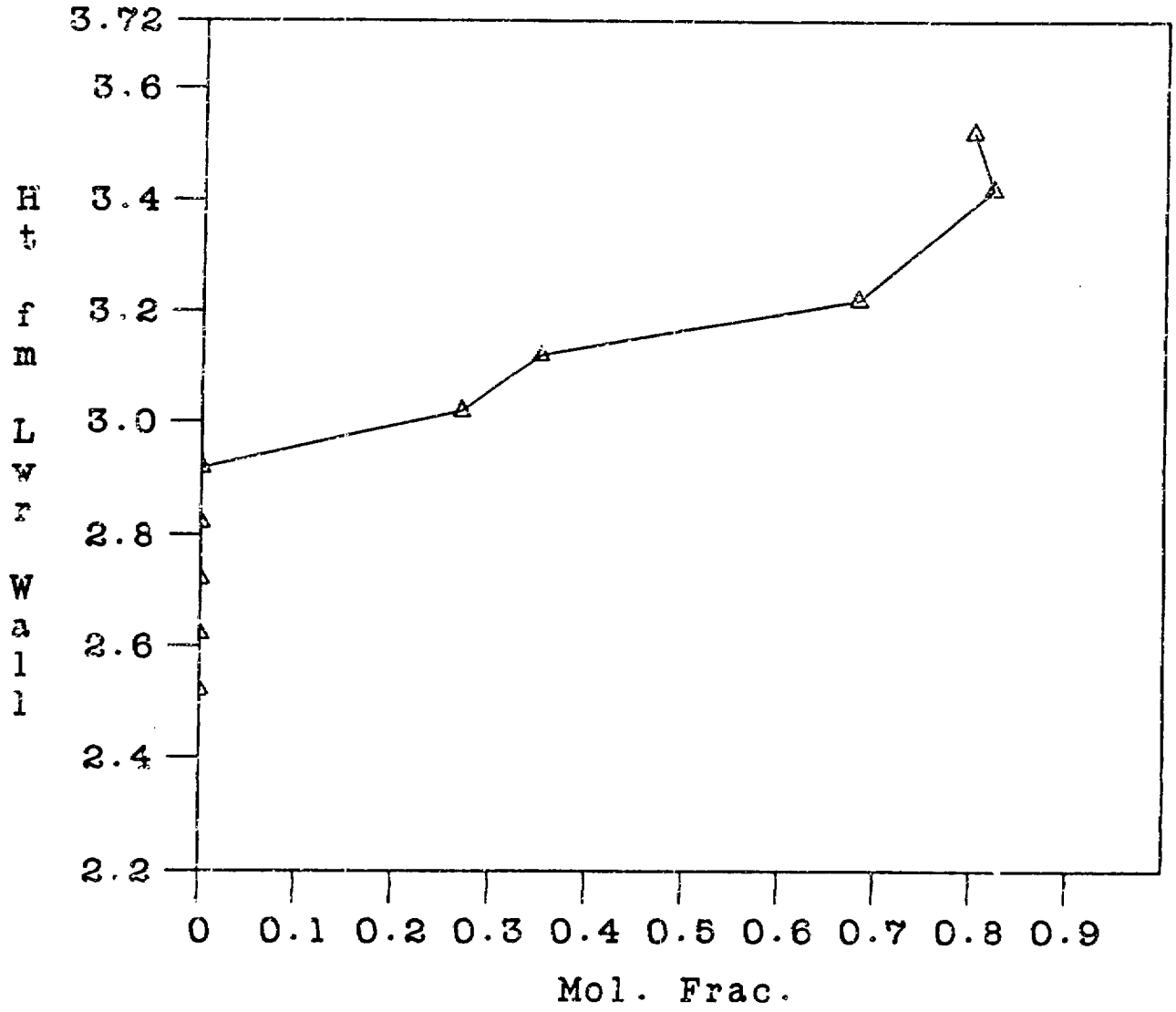

Run 093 - CARS H2 Mol e Fraction
(Phi = 0.5, Sta. 3)

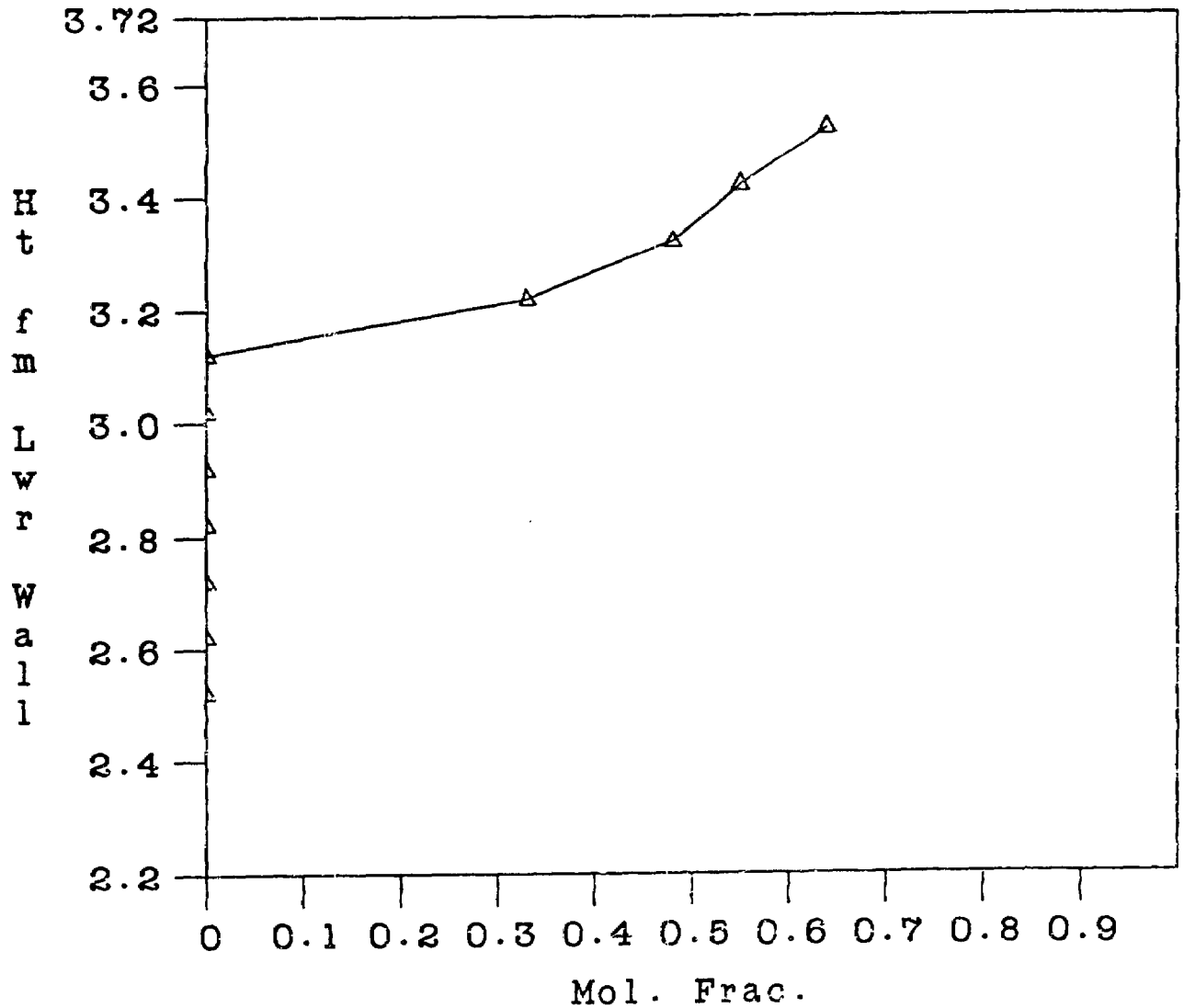

Run 094 - CARS H2 Mol e Fraction
(Phi = 1.0, Sta. 3)

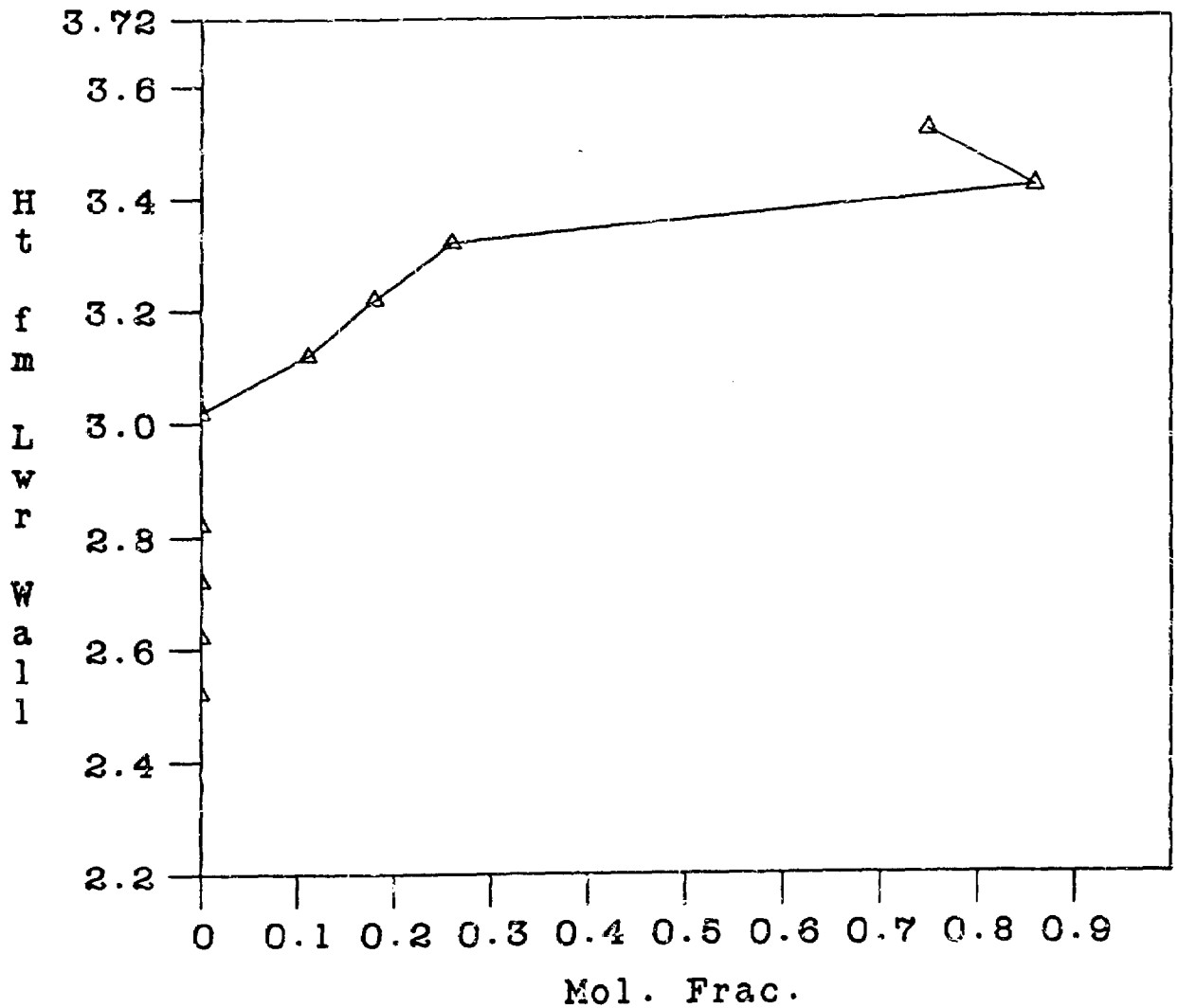

Run 095 - CARS H2 Mol e Fraction
(Phi = 1.0, Sta. 3, T.T. = 2000 R)

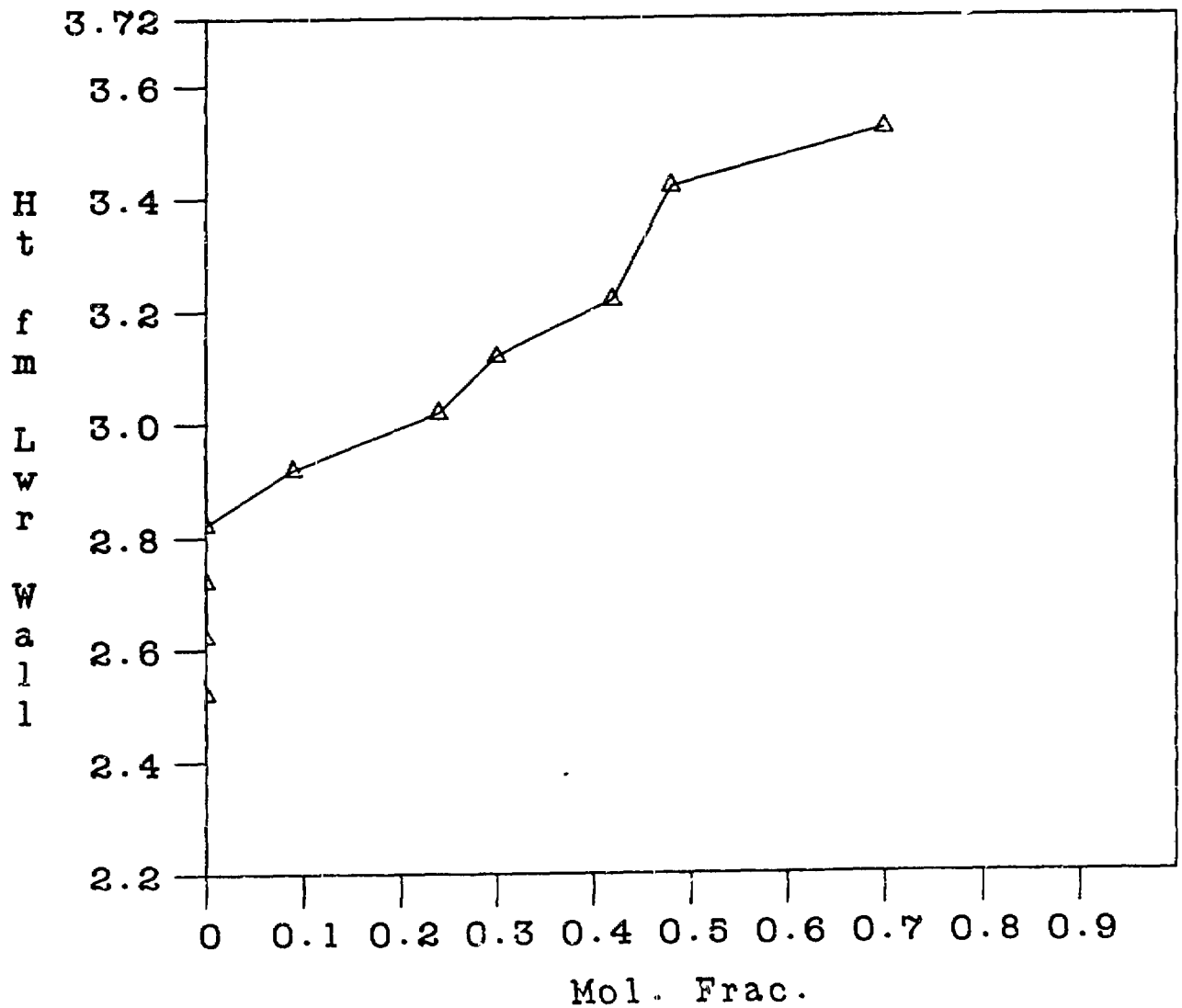

Run 096 - CARS H2 Mol e Fraction
(Phi = 0.5, Sta. 3, T.T. = 2000 R)

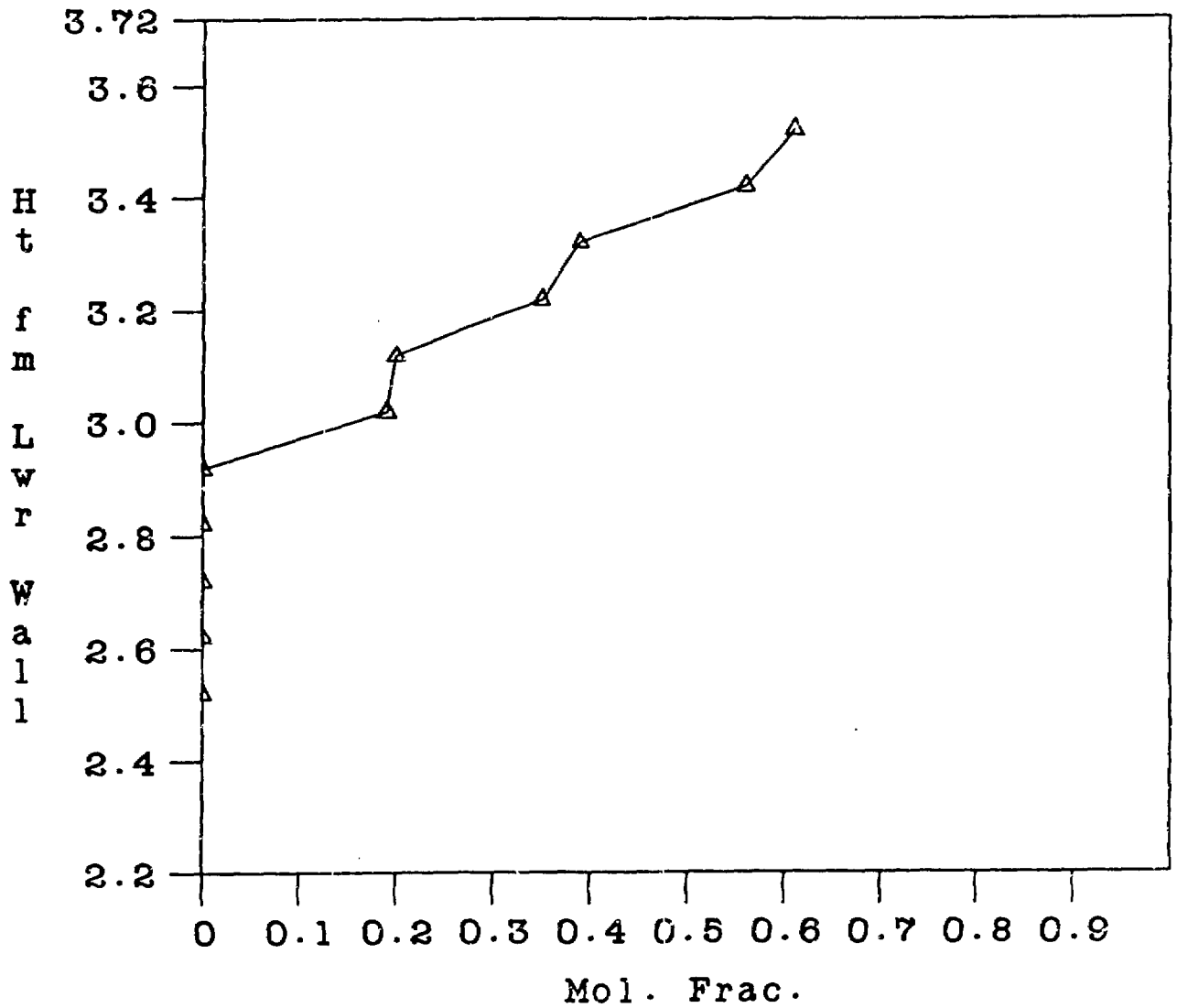

Run 112 - CARS H2 Concentration
(Phi = 1.0, Sta. 2, T.T. = 2000 R, Wedge)

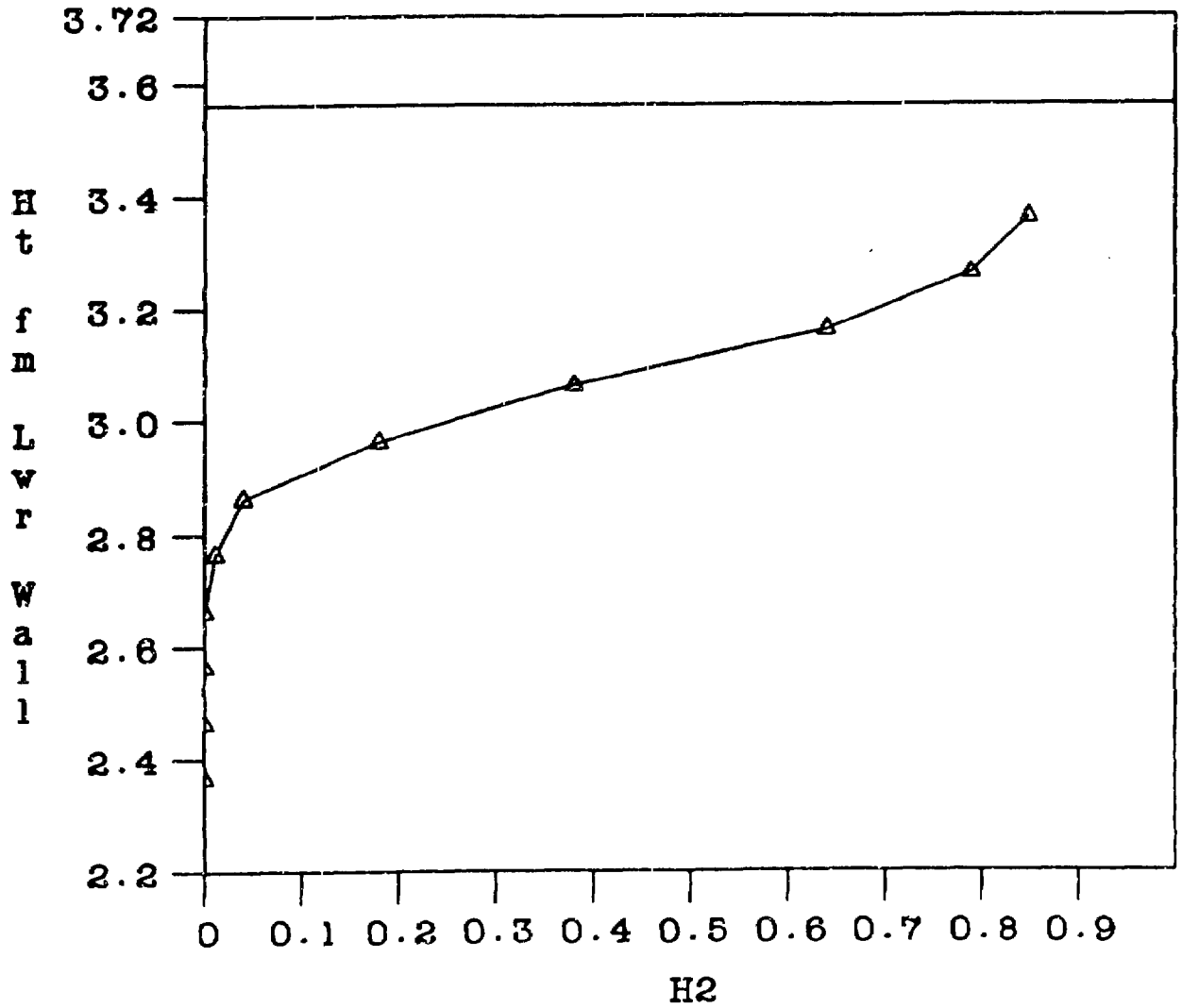

Run 113 - CARS H2 Concentration
(Phi = 0.5, Sta. 2, T.T. = 2000 R, Wedge)

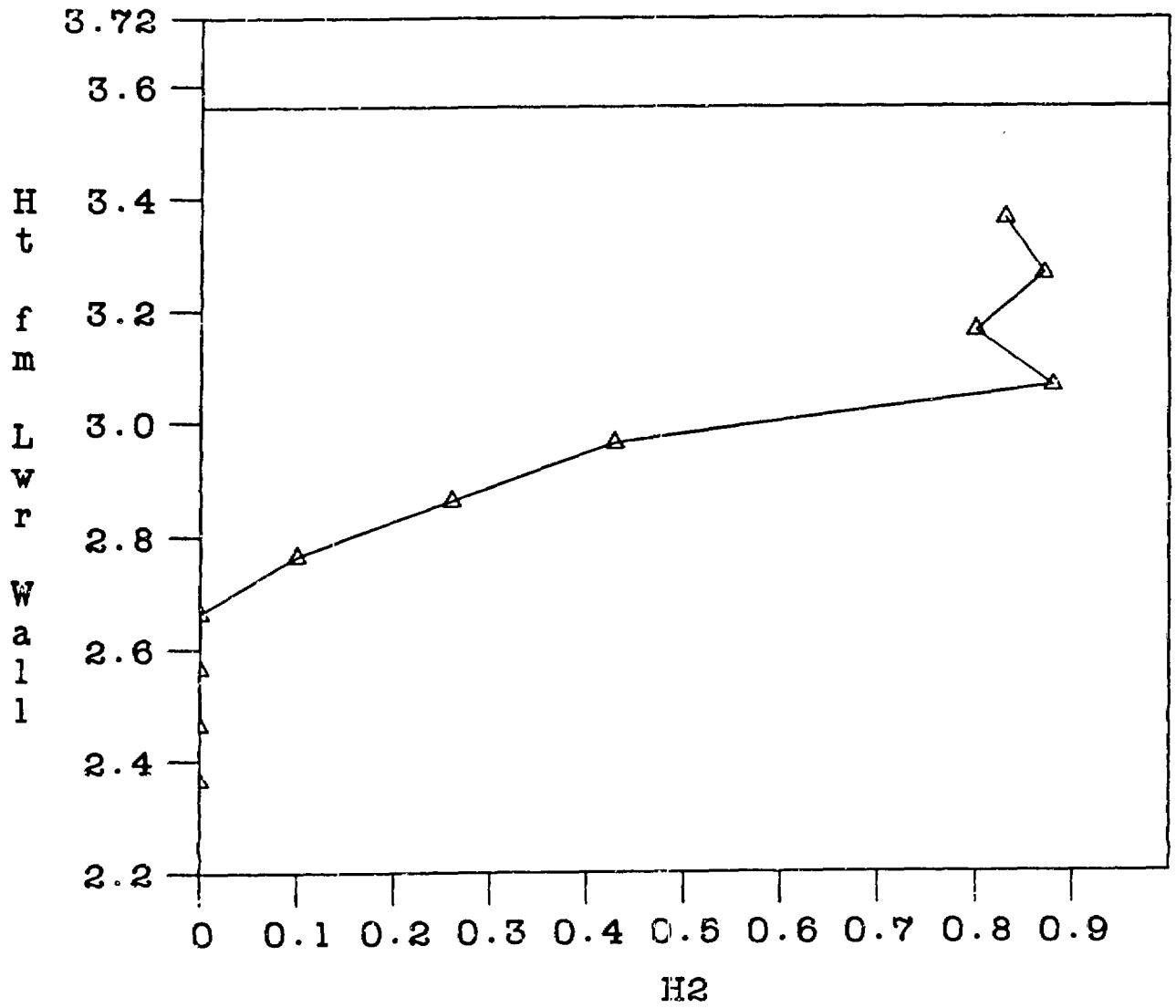

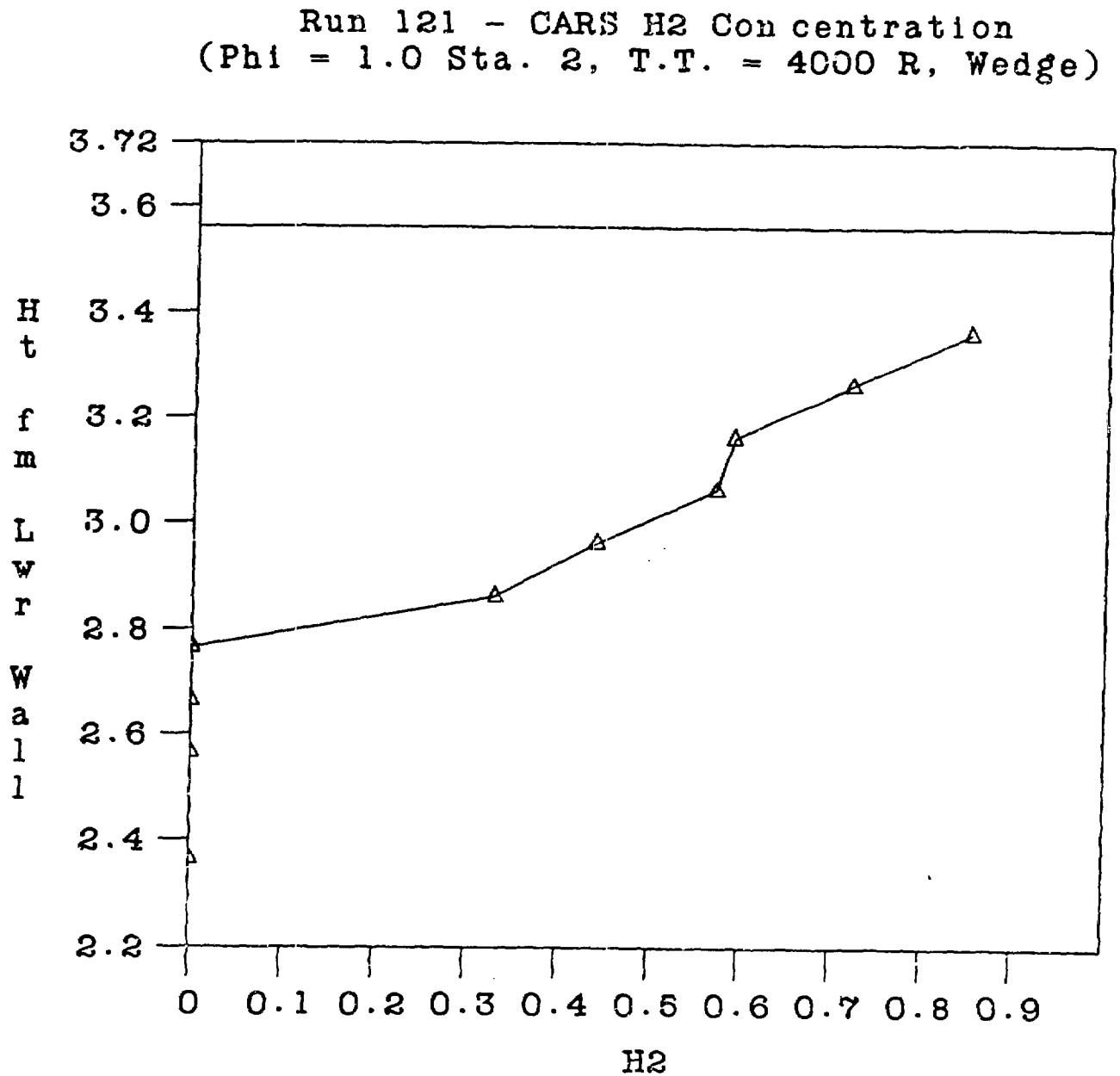
Run 121 - CARS H2 Concentration
(Phi = 1.0 Sta. 2, T.T. = 4000 R, Wedge)
Ht fm Lwr Wall
3.72
3.6
3.4
3.2
3.0
2.8
2.6
2.4
2.2
0
0.1
0.2
0.3
0.4
0.5
0.6
0.7
0.8
0.9
H2

Run 122 - CARS H2 Concentration
(Phi = 0.5, Sta. 2, T.T. = 4000 R, Wedge)

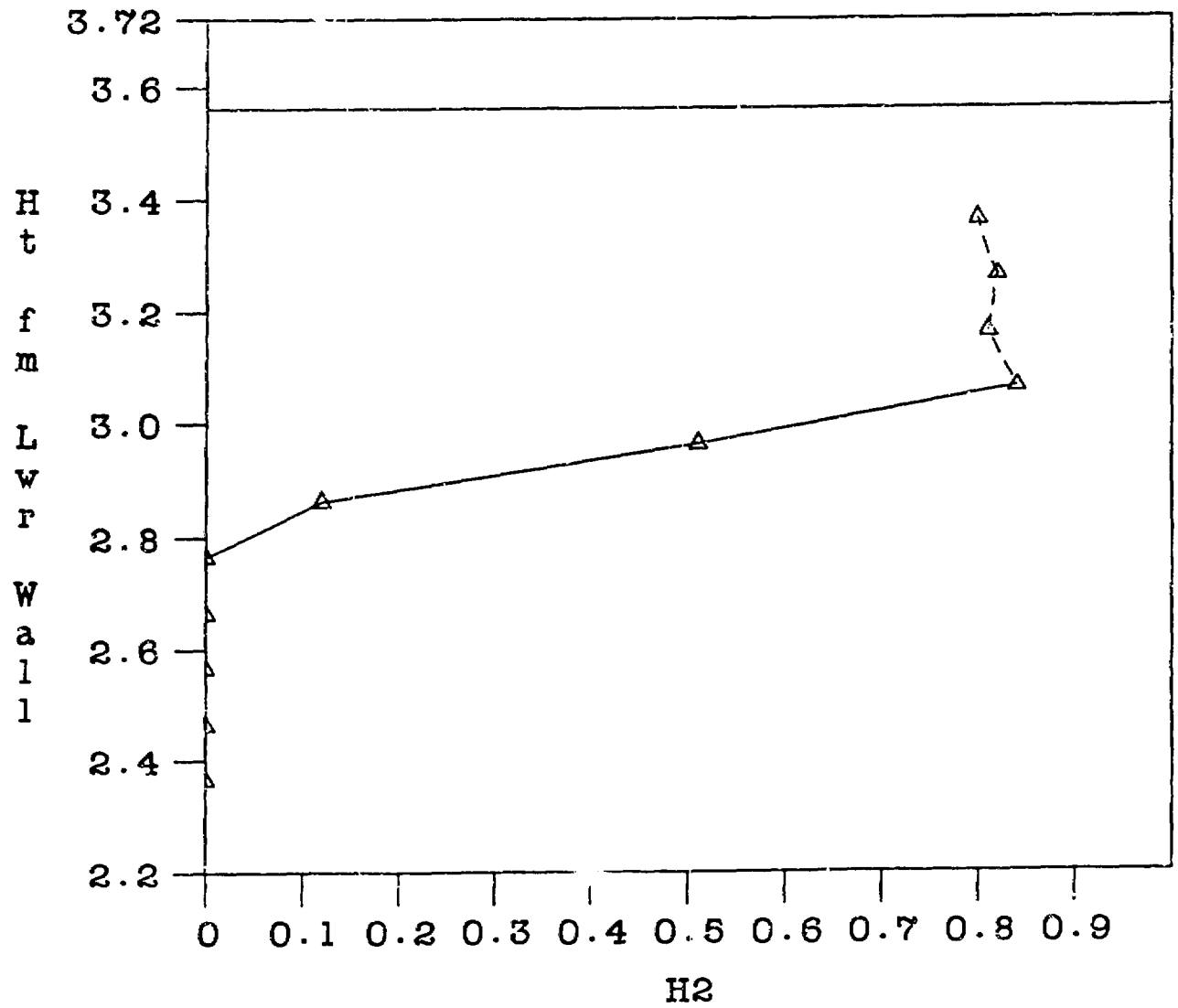

Run 124 - CARS H2 Concentration
(Phi = 1.0. Sta. 3, T.T. = 2000 R, Wedge)

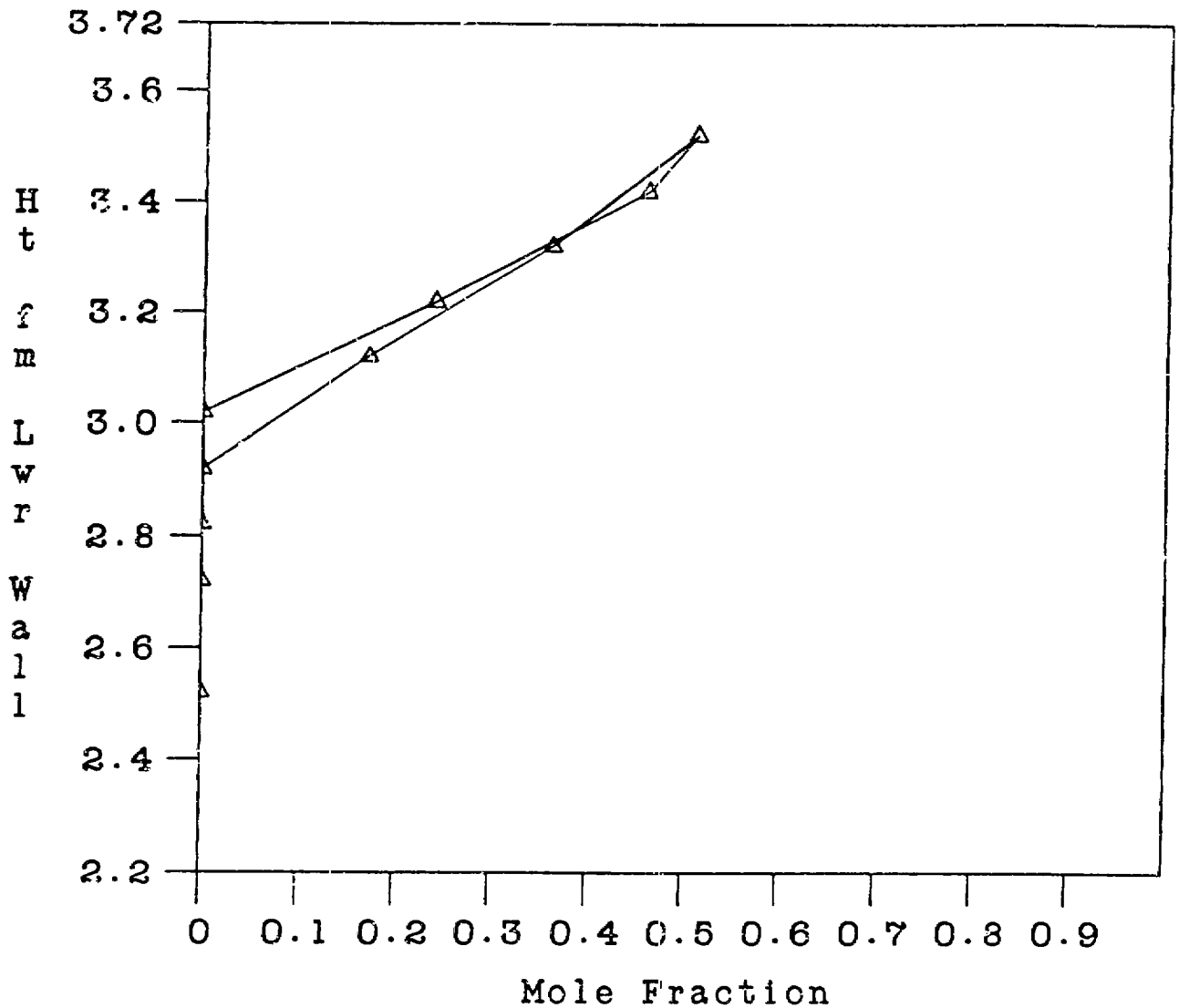

Run 125 - CARS H2 Concentration
(Phi = 0.5, Sta. 3, T.T. = 2000 R, Wedge)

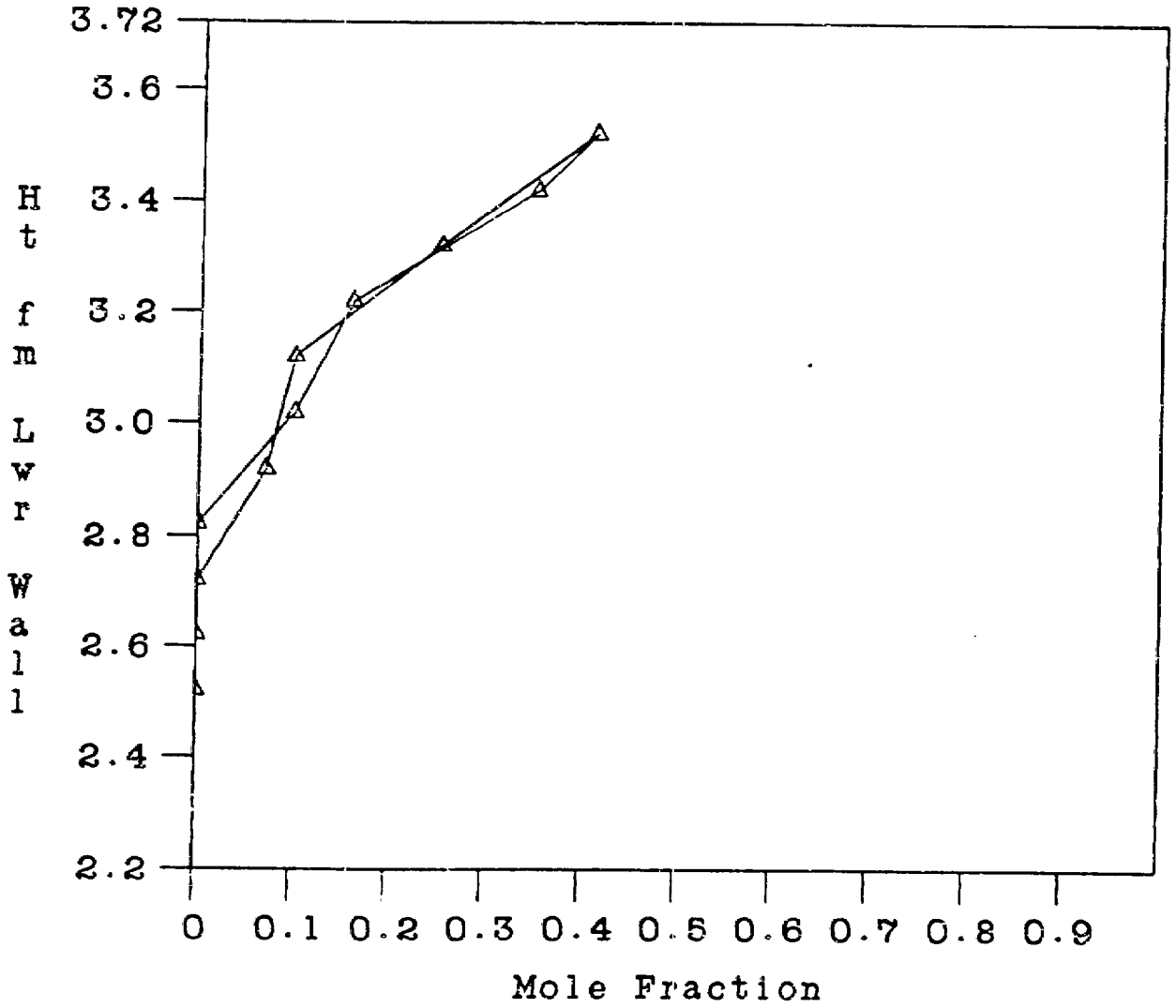

Run 126 - CARS H2 Concentration
(Phi = 1.0, Sta. 3, T.T. = 4000 R, Wedge)

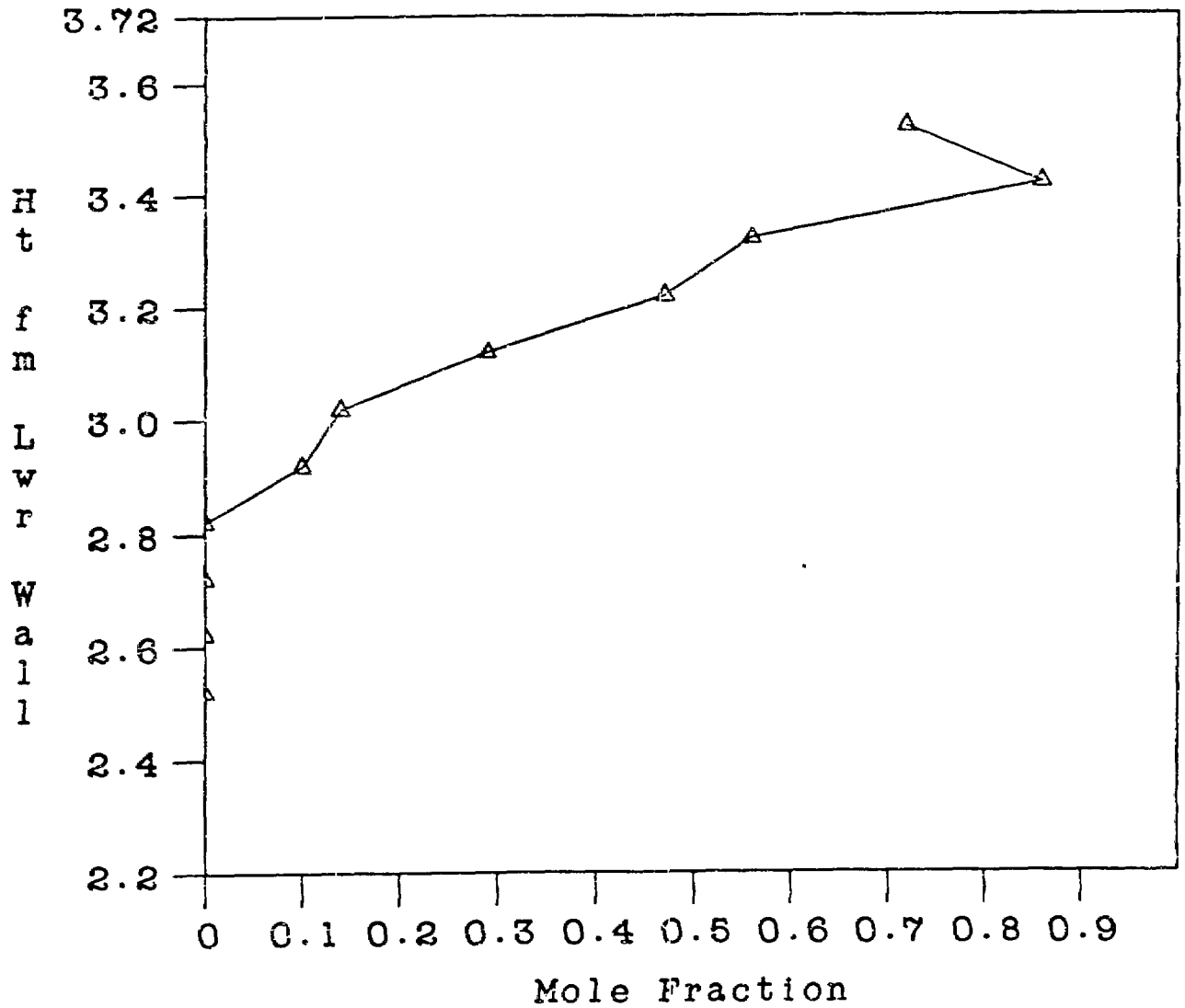

Run 127 - CARS H2 Concentration
(Phi = 0.5, Sta. 3, T.T. = 4000 R, Wedge)

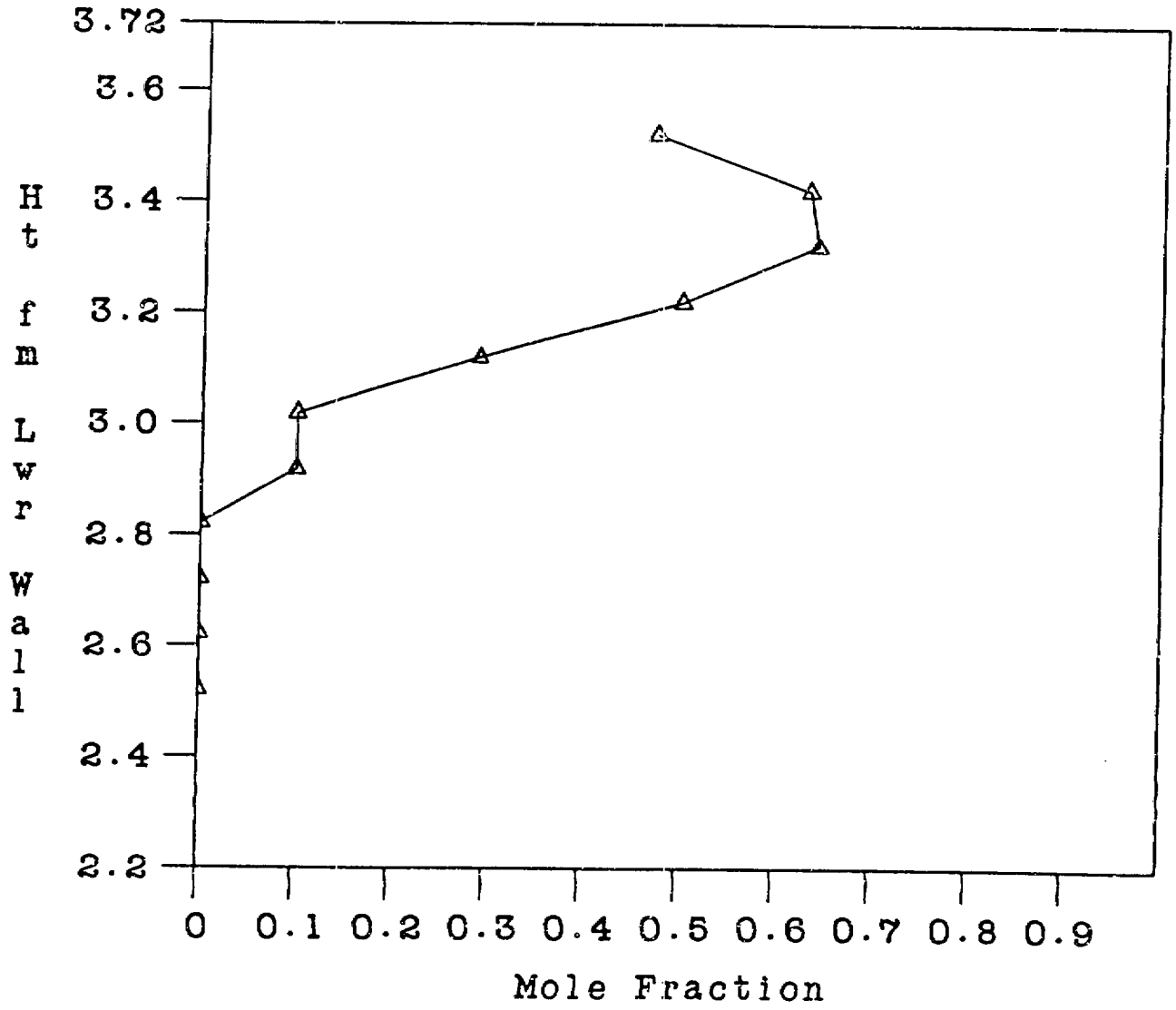

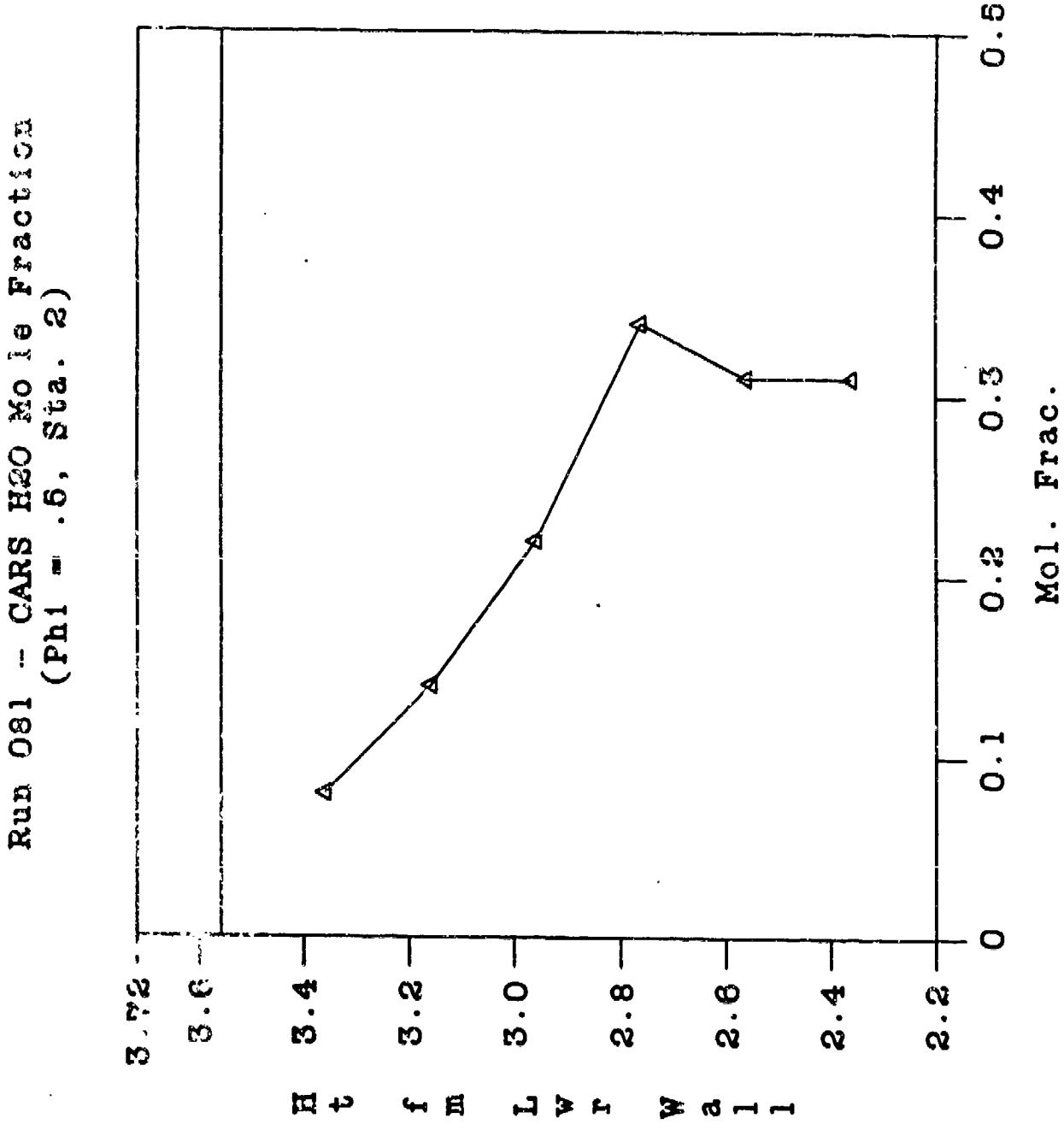
Run 081 -- CARS H2O Mole Fraction
(Phi = .6, Sta. 2)
3.72
3.6
3.4
3.2
3.0
2.8
2.6
2.4
2.2
Heff Layer Wall
0
0.1
0.2
0.3
0.4
0.5
Mol. Frac.

Run 084 - CARS H2O Mole Fraction
(Phi =1.0, Sta. 2)

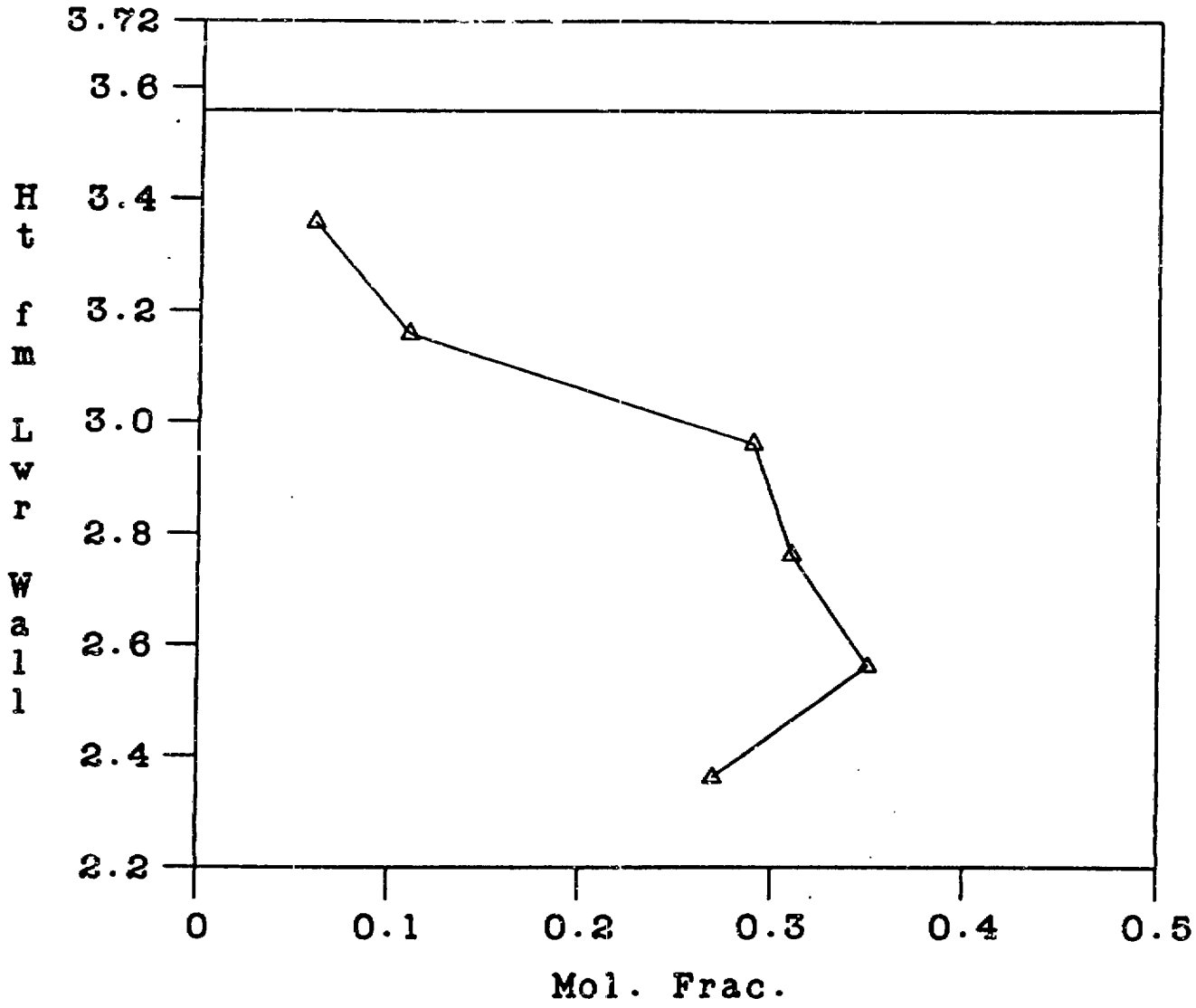

Run 092 - CARS H2O Mo le Fraction
(Phi = 1.0, Sta. 3)

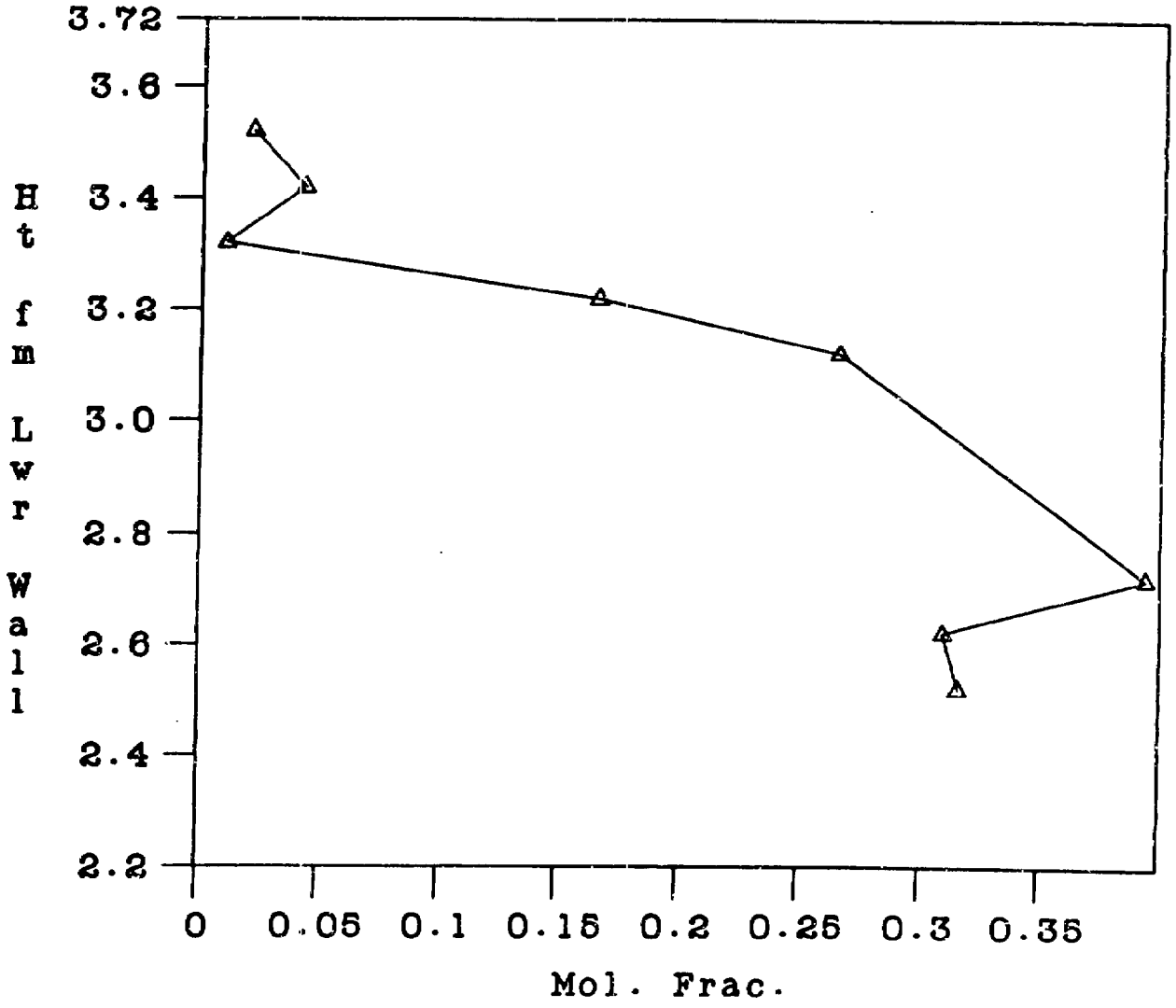

Run 093 - CARS H2O Mo le Fraction
(Phi = 0.5, Sta. 3)

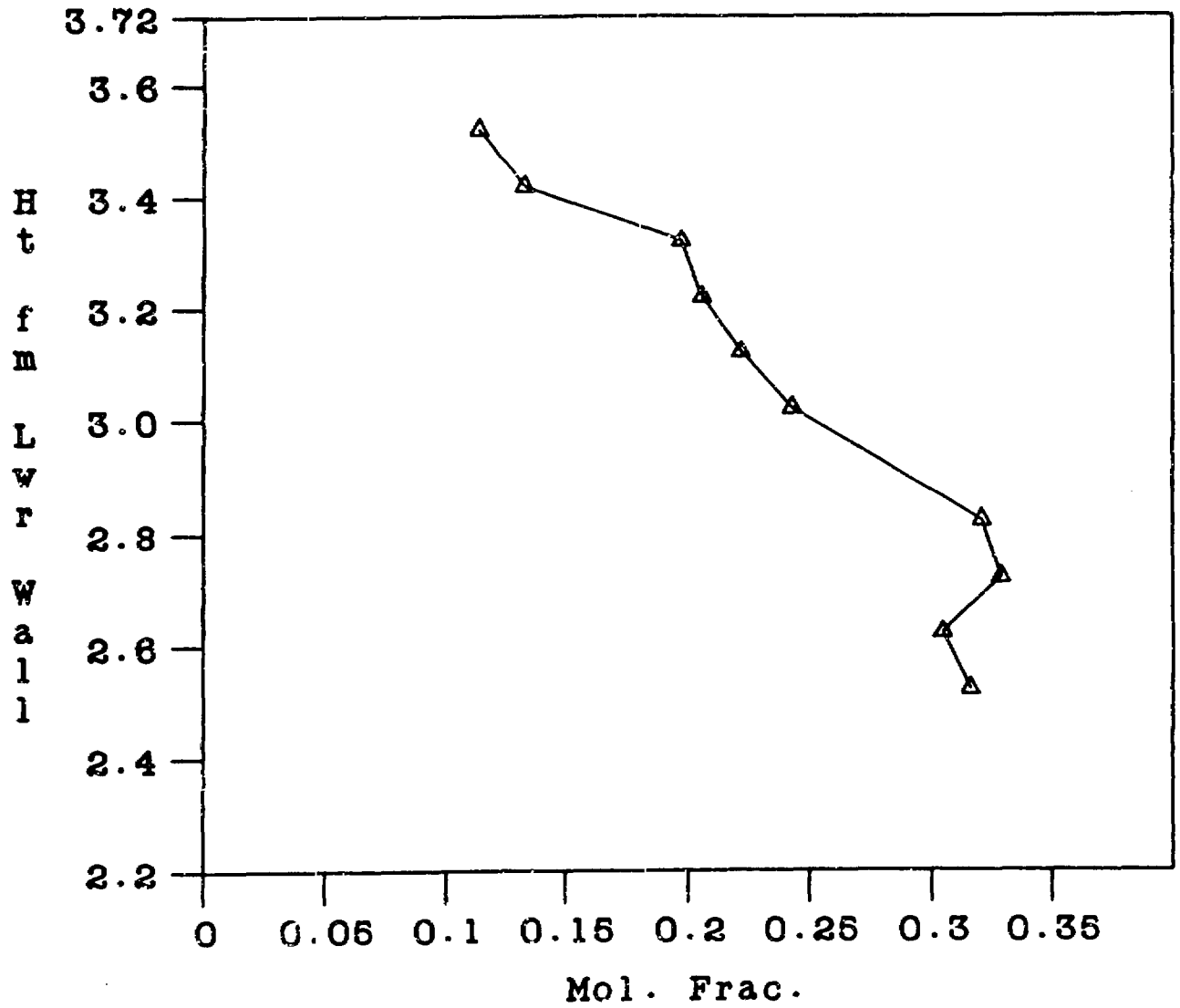

Run 094 - CARS H2O Mo le Fraction
(Phi = 1.0, Sta. 3)

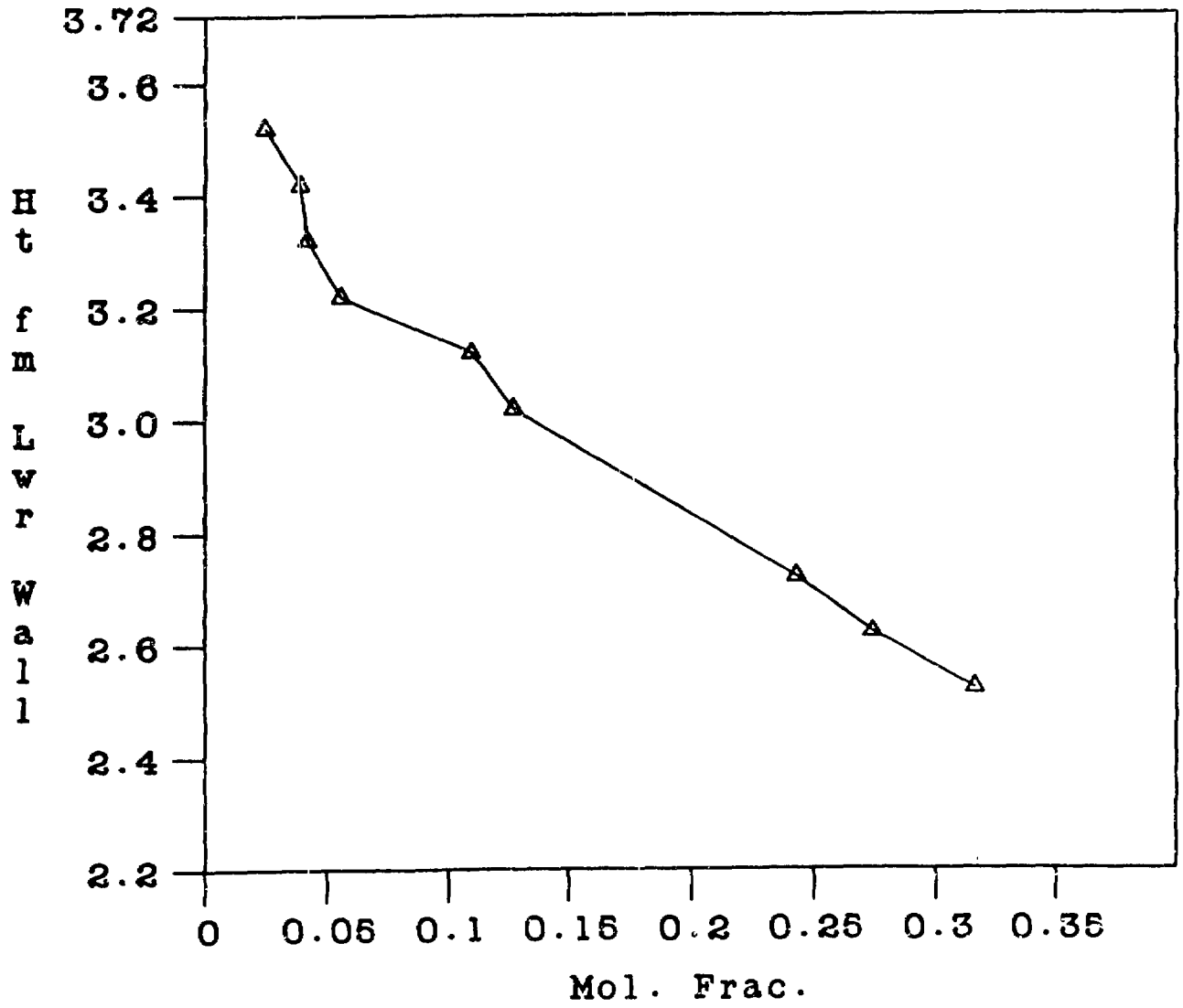

Run 096 - CARS H2O Mo le Fraction
(Phi = 0.5, Sta. 3)

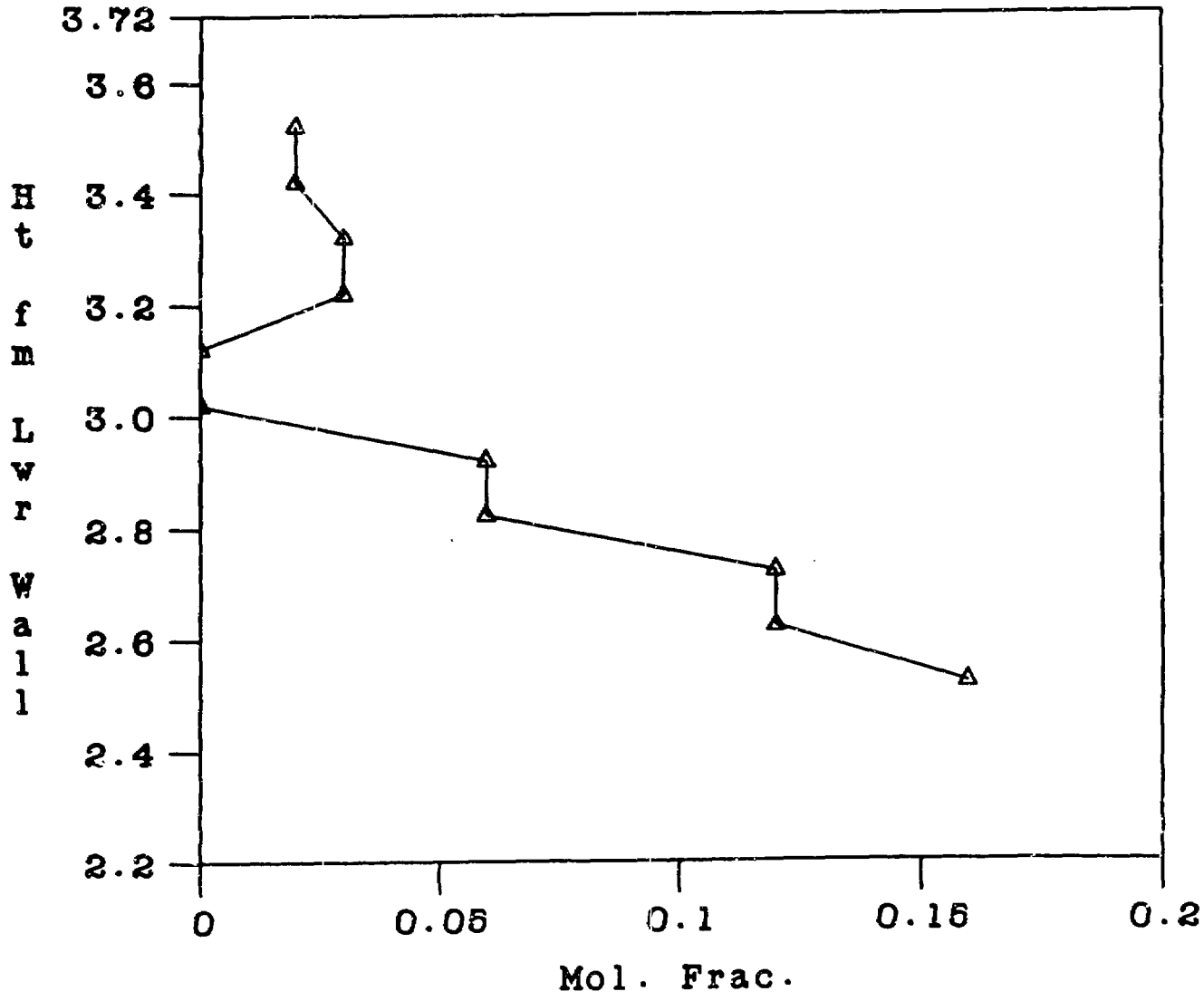

Run 112 - CARS H2O Concentration
(Phi = 1.0, Sta. 2, T.T. = 2000 R, Wedge)

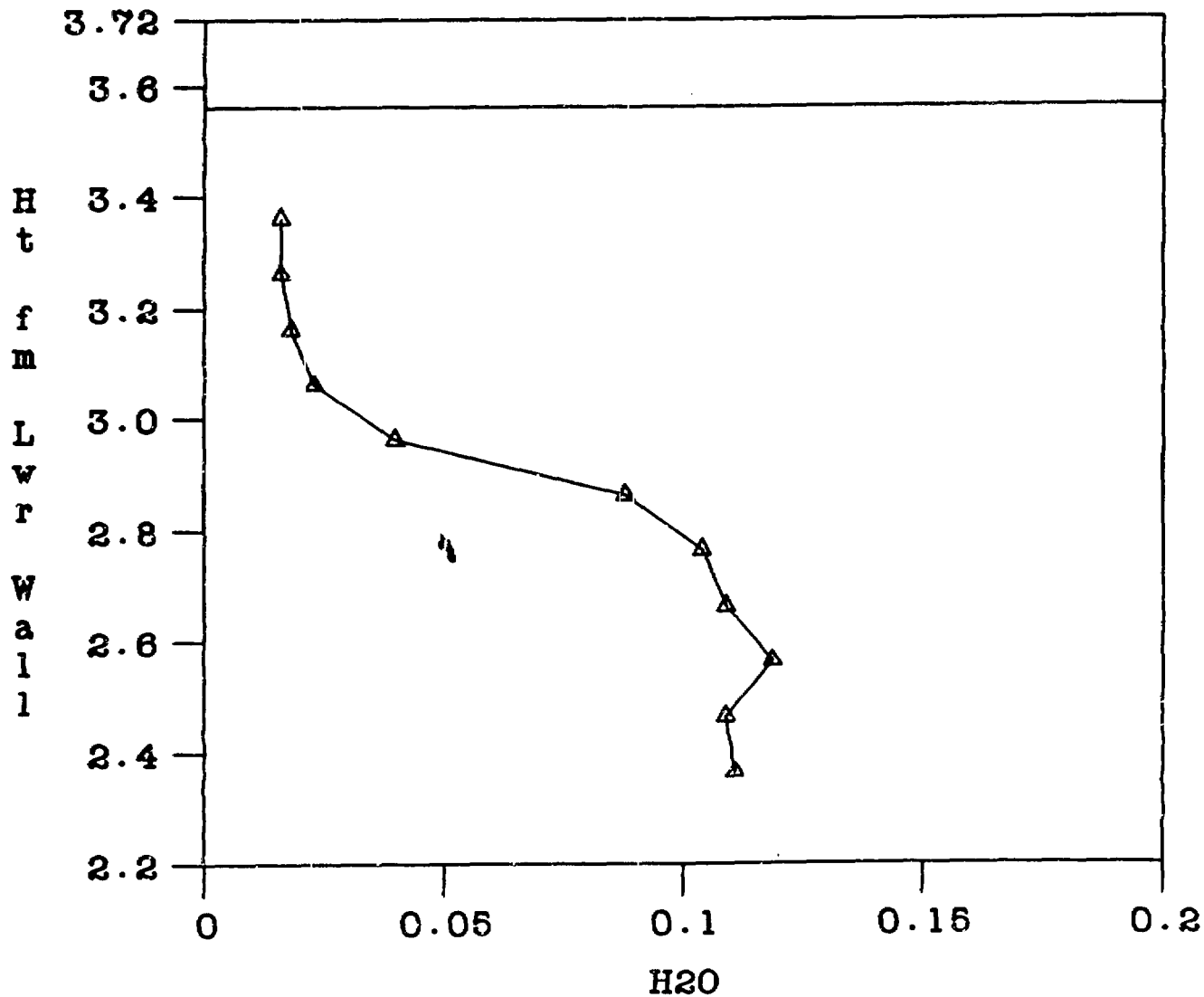

Run 113 - CARS H2O Concentration
(Phi = 0.6, Sta. 2, T.T. = 2000 R, Wedge)

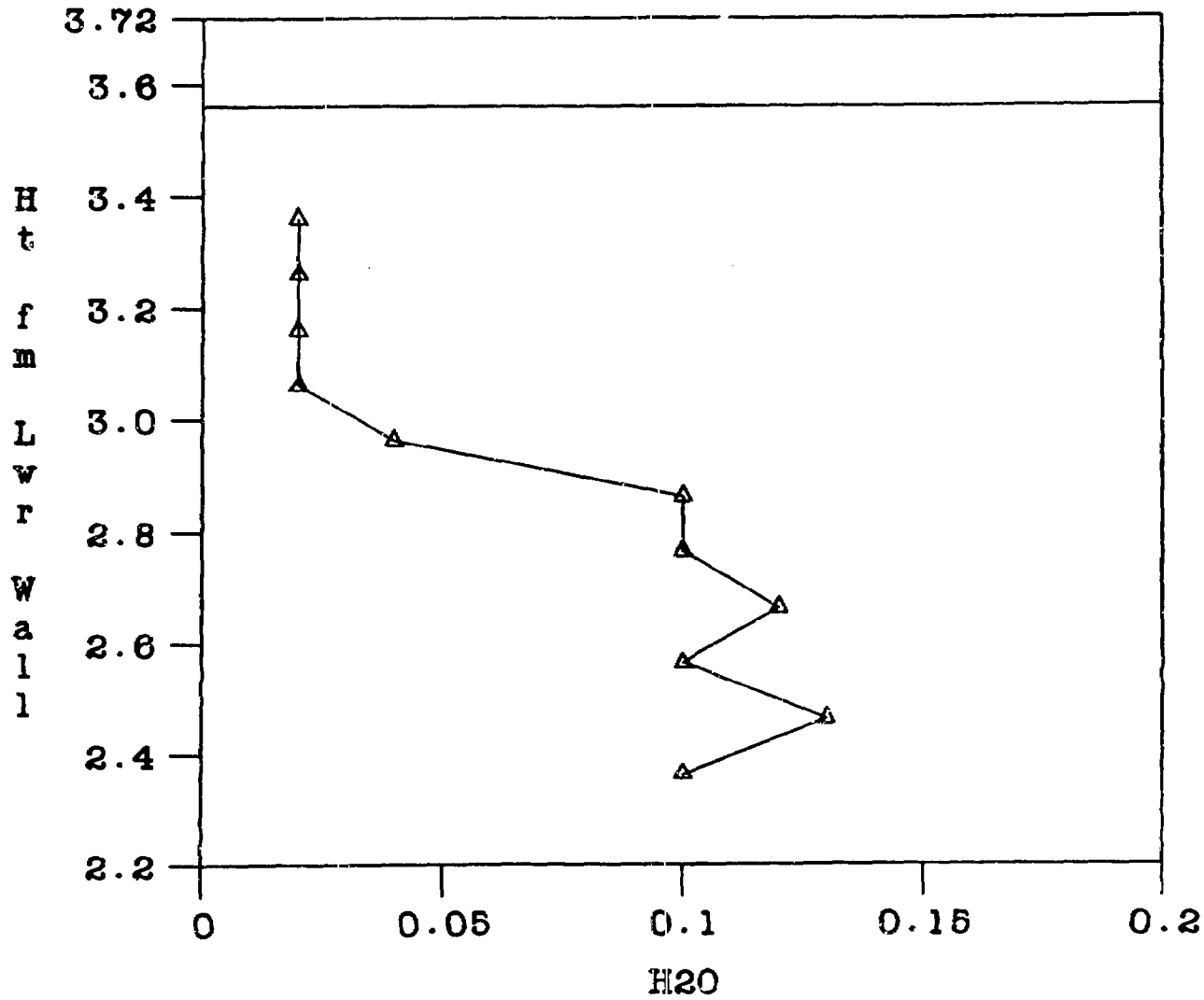

Run 114 - CARS H2O Concentration
(N2 Injection, Sta. 2, T.T. = 2000 R, Wedge)

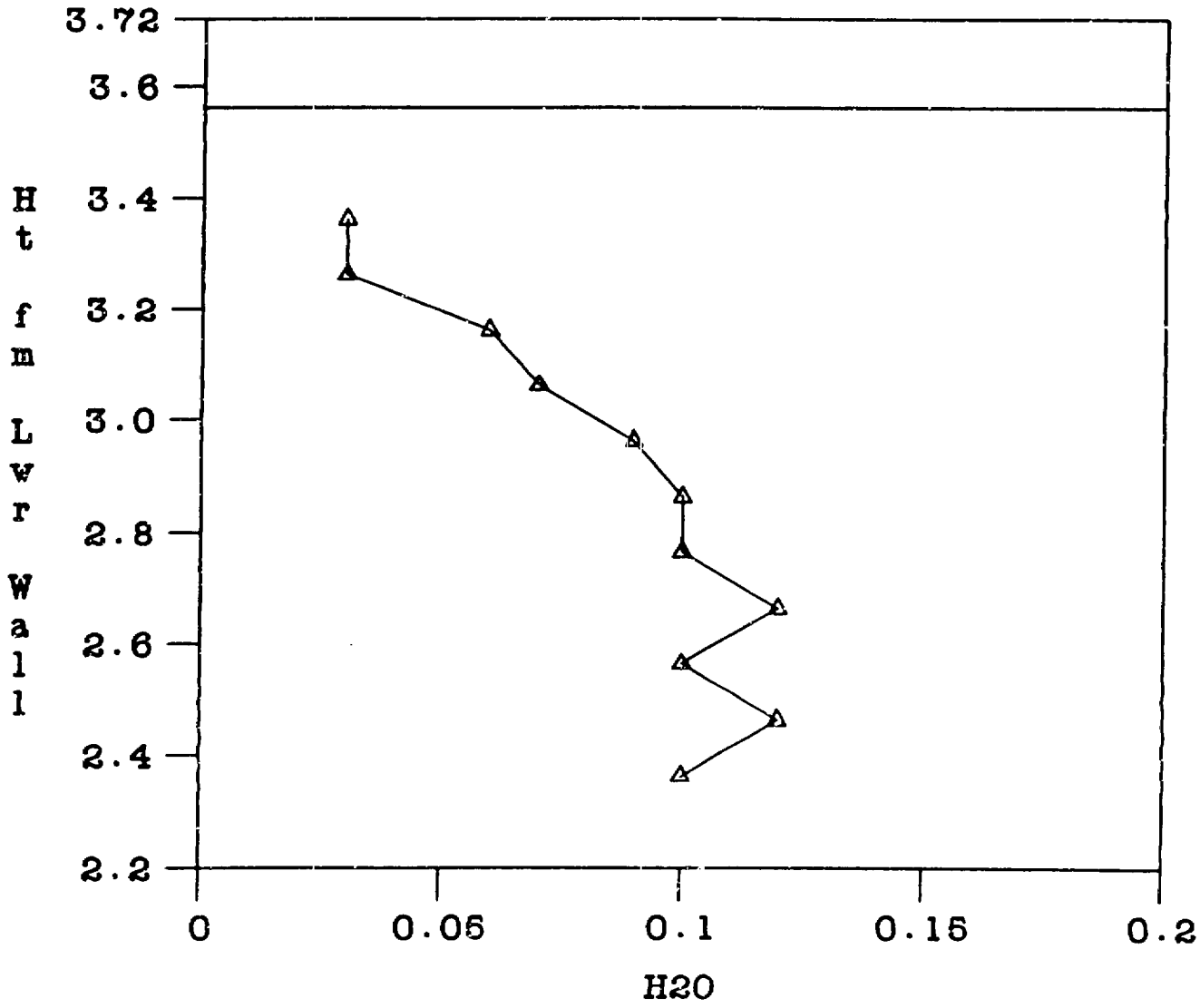

Run 121 - CARS H2O Concentration
(Phi = 1.0, Sta. 2, T.T. = 4000 R, Wedge)

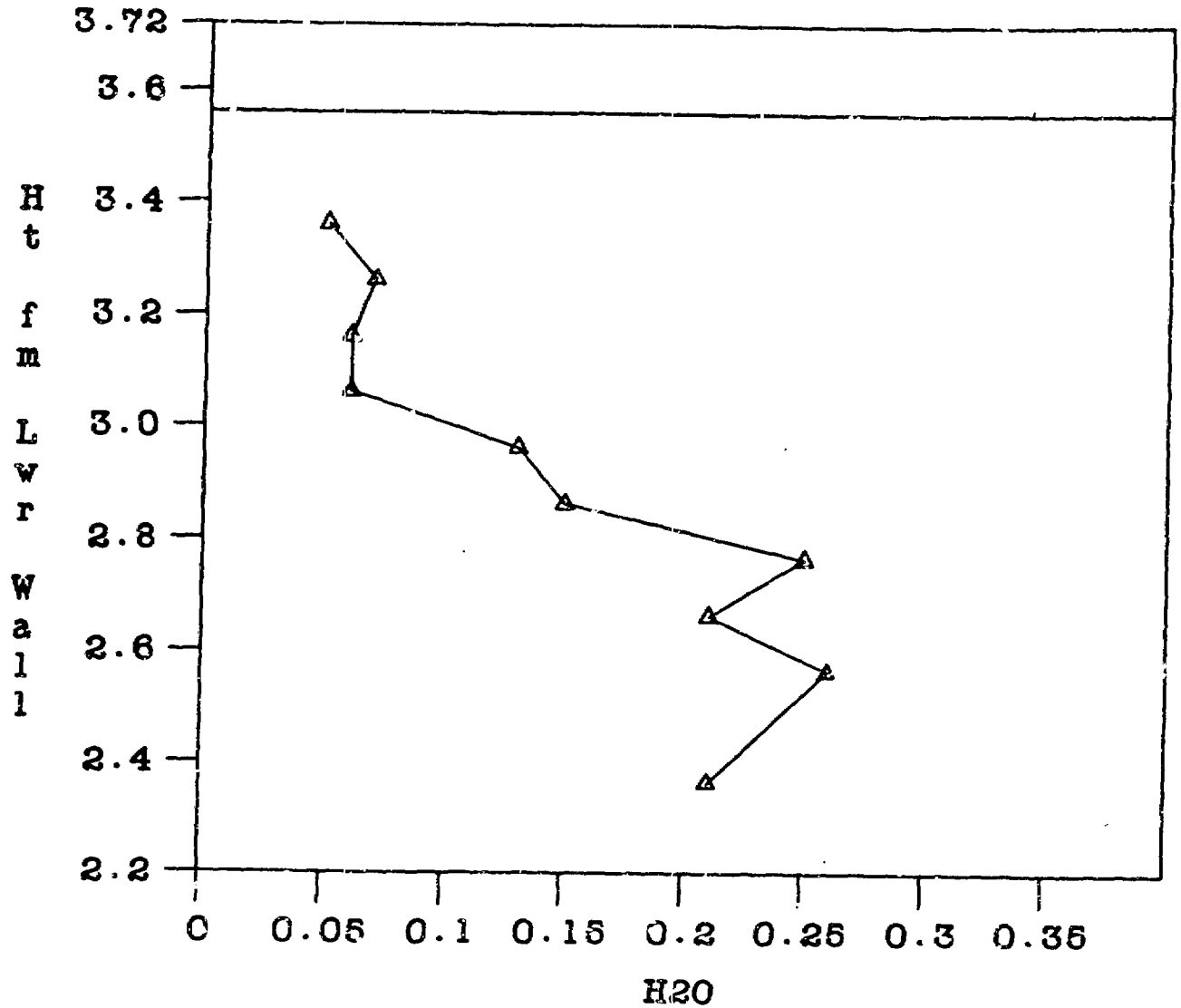

Run 122 - CARS H2O Concentration
(Phi = 0.5, Sta. 2, T.T. = 4000 R, Wedge)

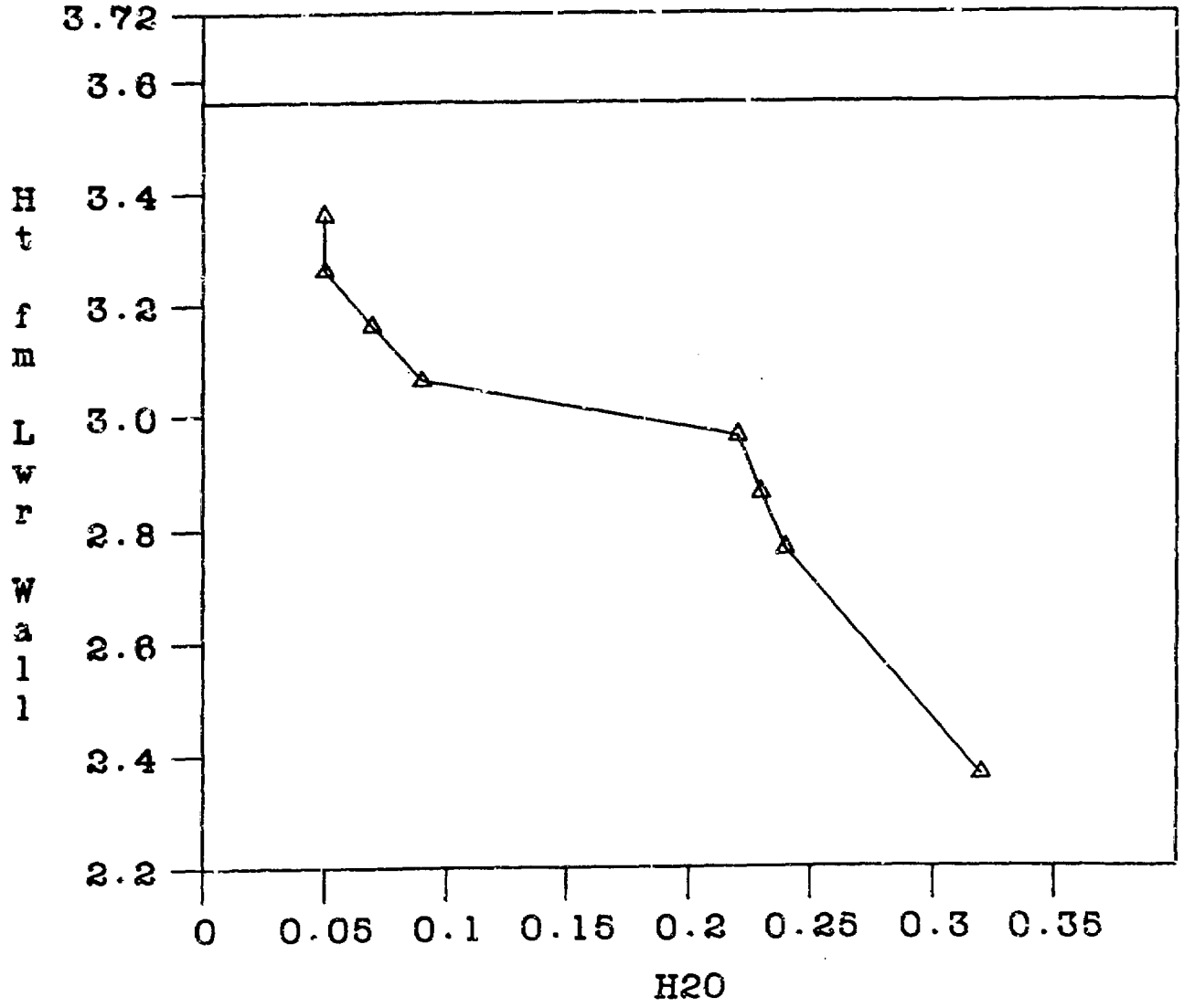

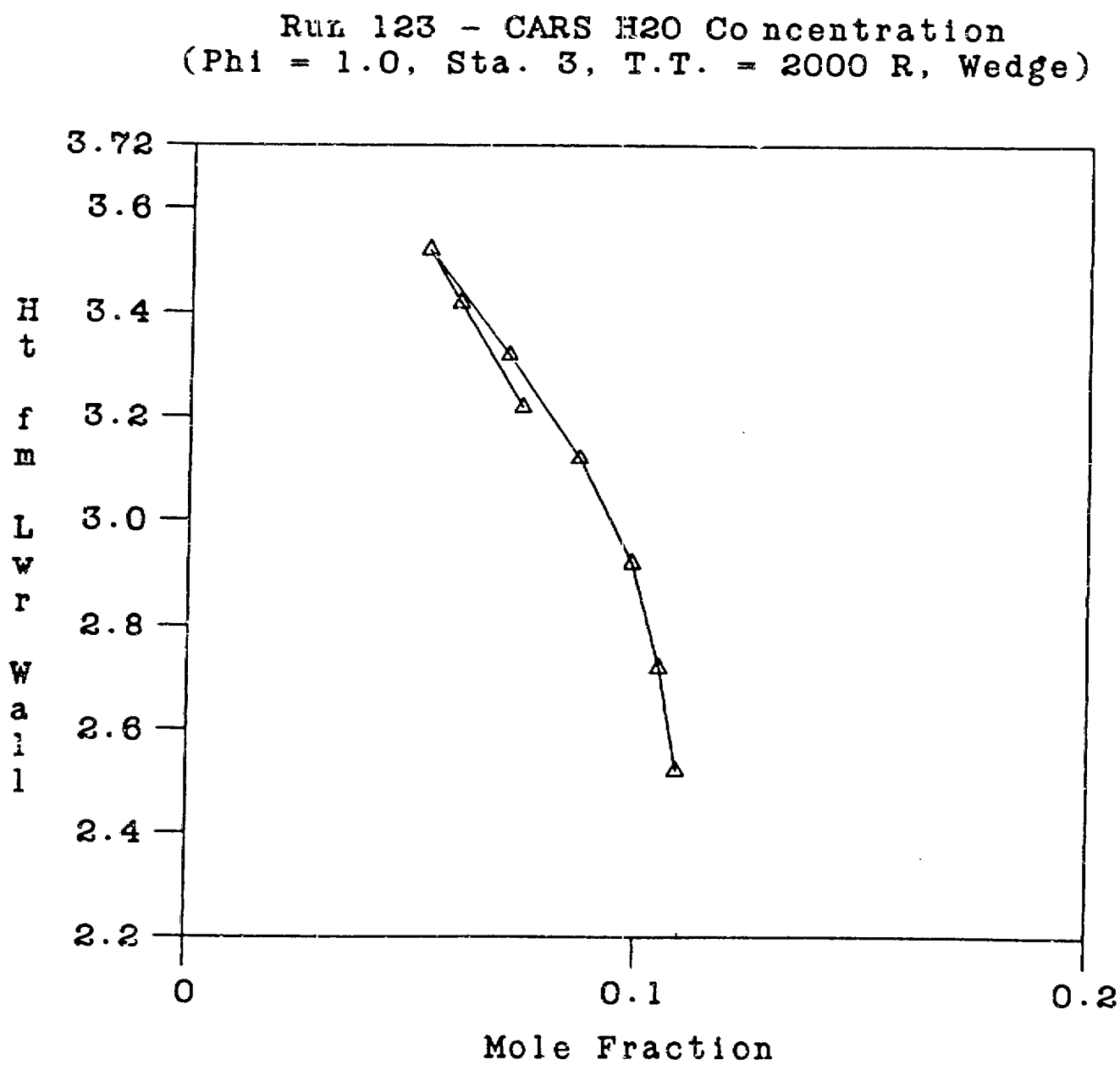
Run 123 - CARS H2O Concentration
(Phi = 1.0, Sta. 3, T.T. = 2000 R, Wedge)
3.72
3.6
3.4
3.2
3.0
2.8
2.6
2.4
2.2
Ht fm Lwr Wall
0
0.1
0.2
Mole Fraction

Run 124 - CARS H2O Concentration
(Phi = 1.0, Sta. 3, T.T. = 2000 R, Wedge)

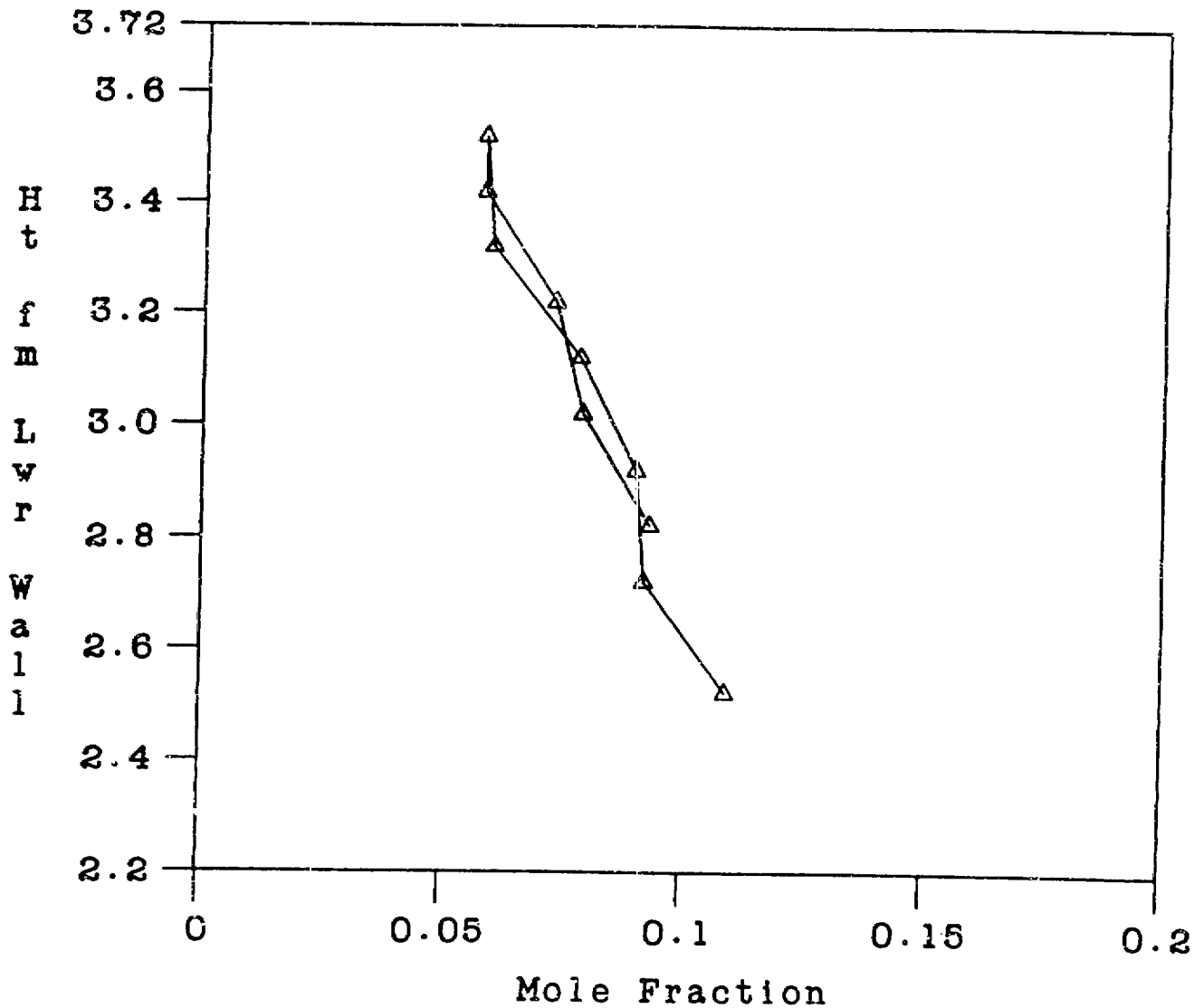

Run 125 - CARS H2O Concentration
(Phi = 0.5, Sta. 3, T.T. = 2000 R, Wedge)

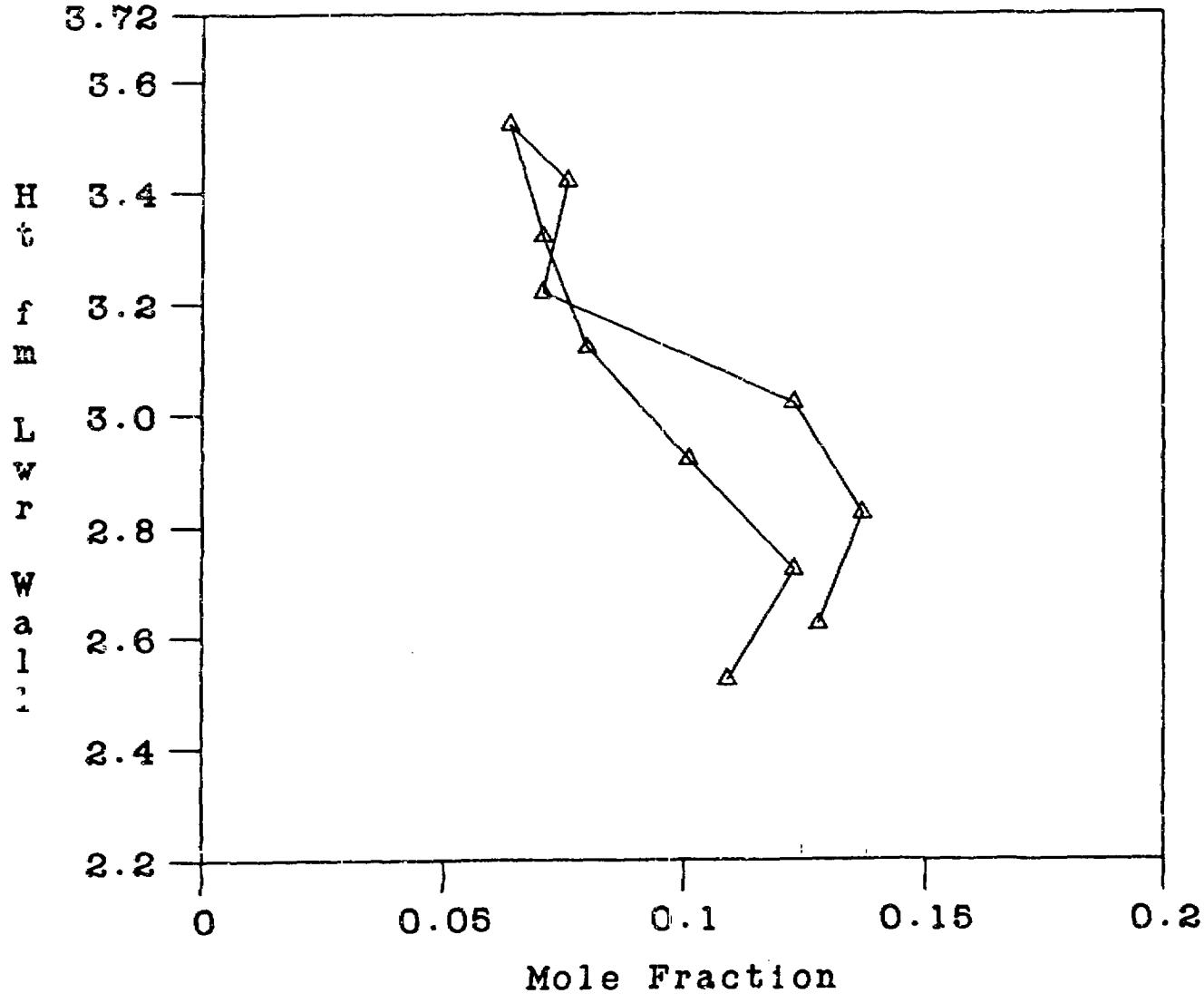

Run 126 - CARS H2O Concentration
(Phi = 1.0, Sta. 3, T.T. = 4000 R, Wedge)

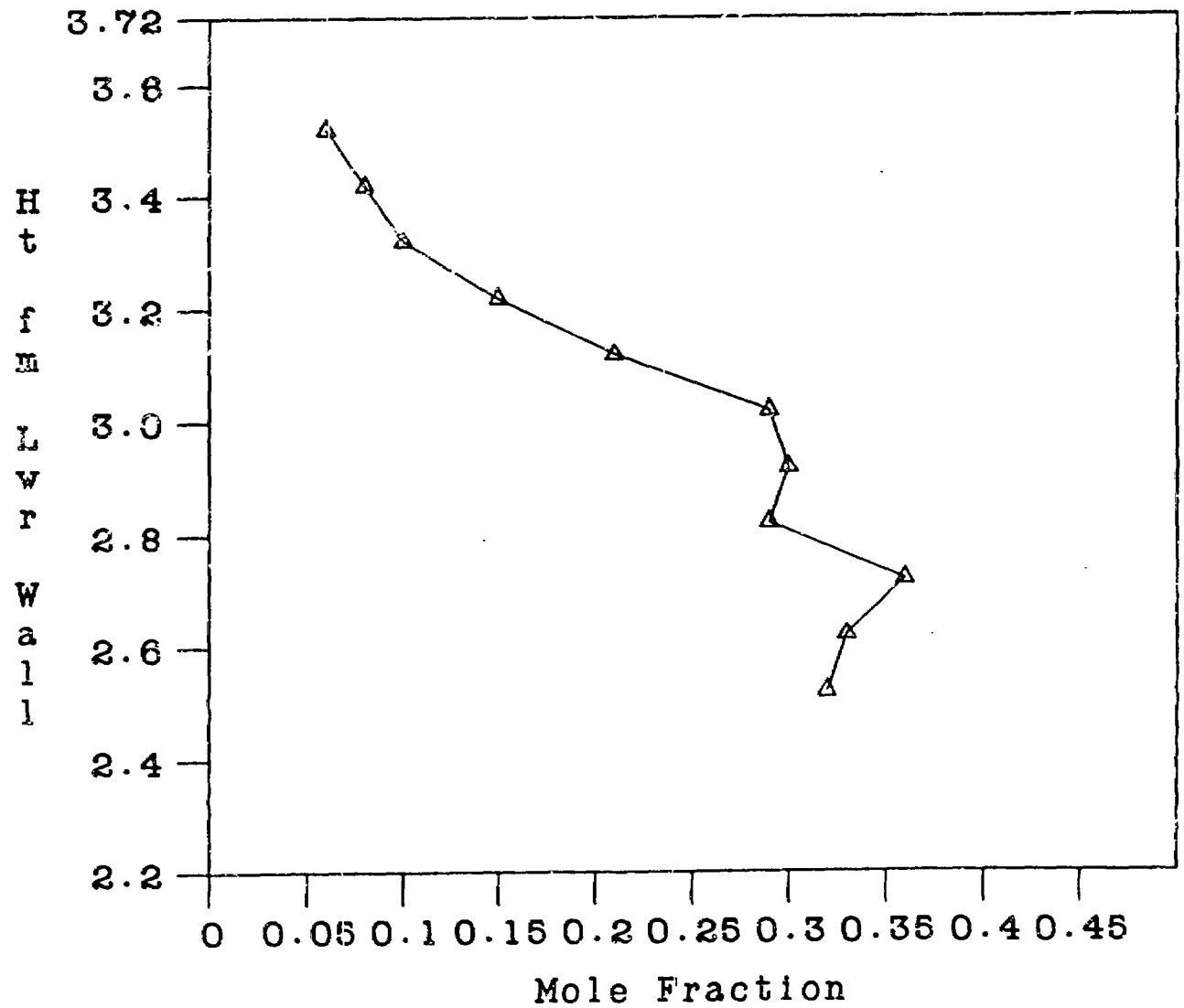

Run 127 - CARS H2O Concentration
(Phi = 0.5, Sta. 3, T.T. = 4000 R, Wedge)

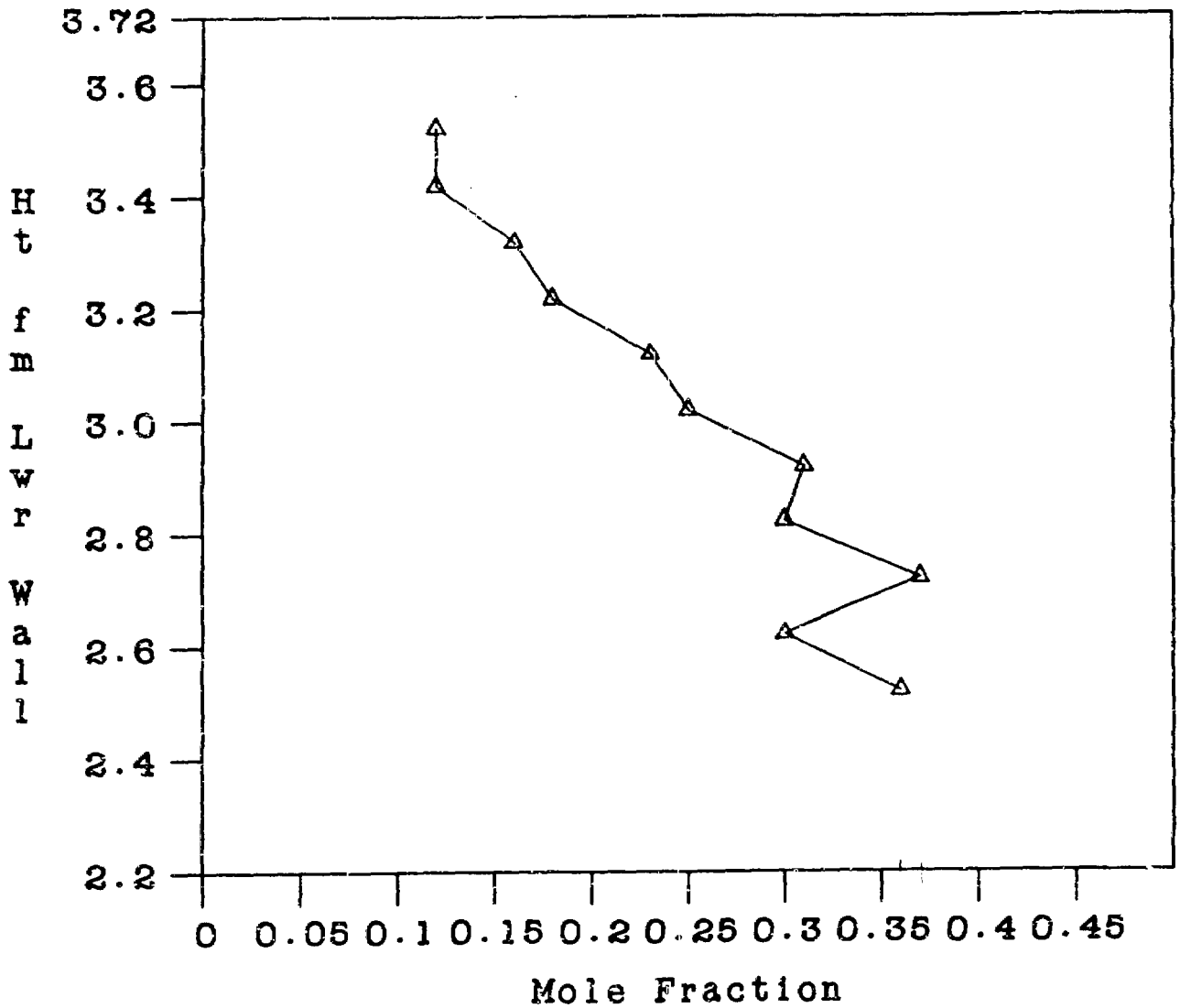

WALL STATIC PRESSURE

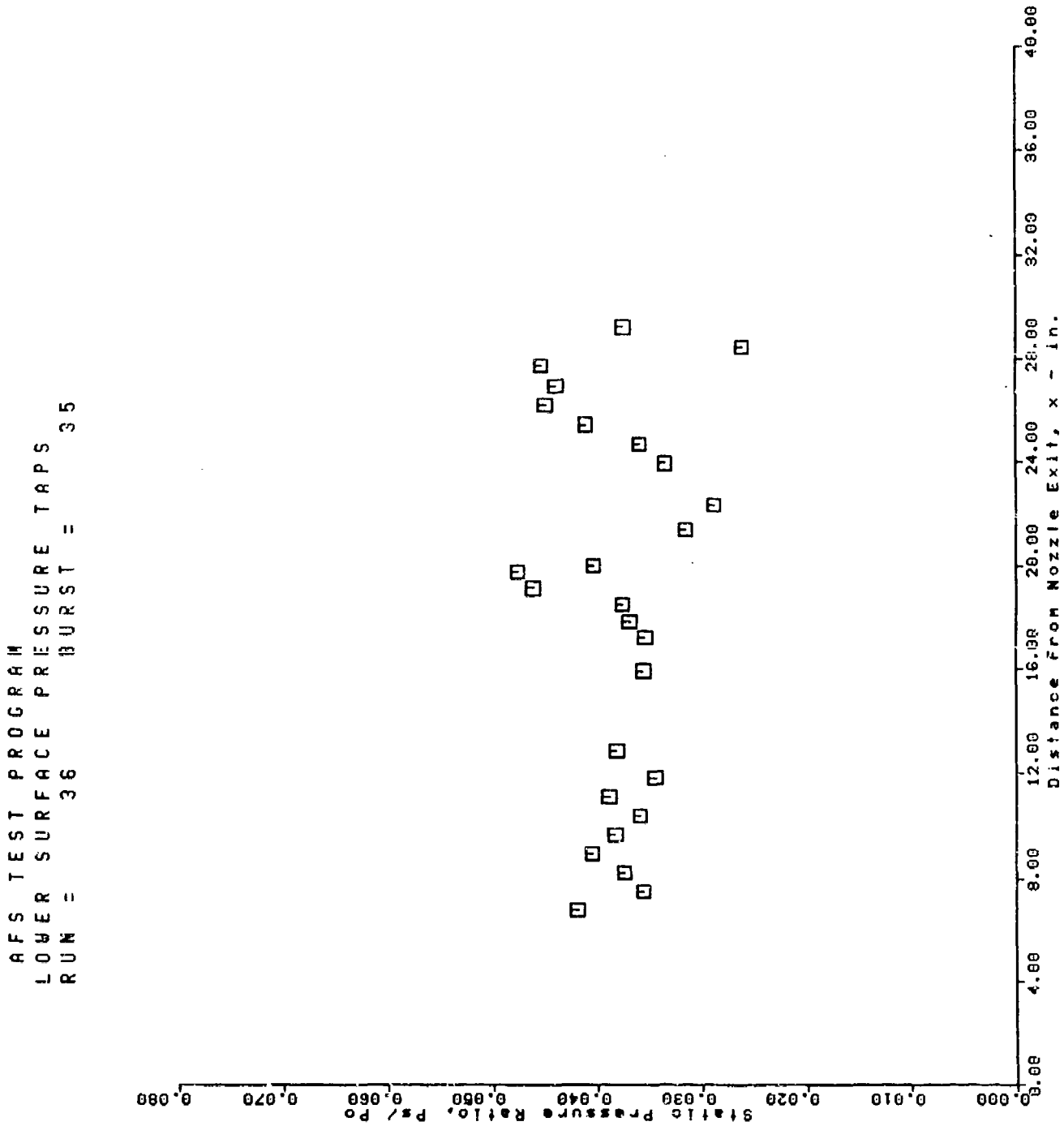

AFS TEST PROGRAM
UPPER SURFACE PRESSURE TAPS
RUN = 36 BURST = 35

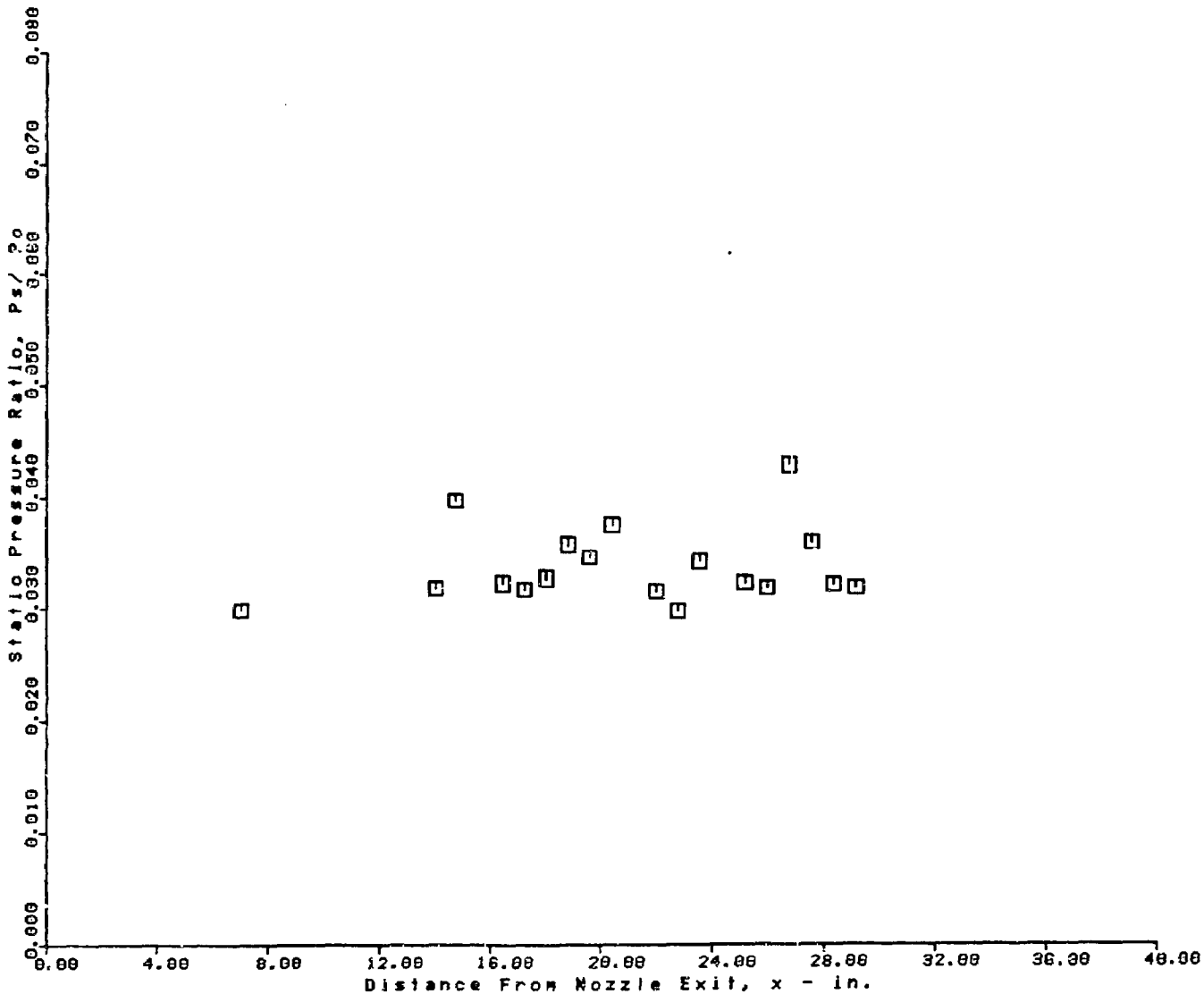

AFS TEST PROGRAM
LOWER SURFACE PRESSURE TAPS
RUN = 39 BURST = 41

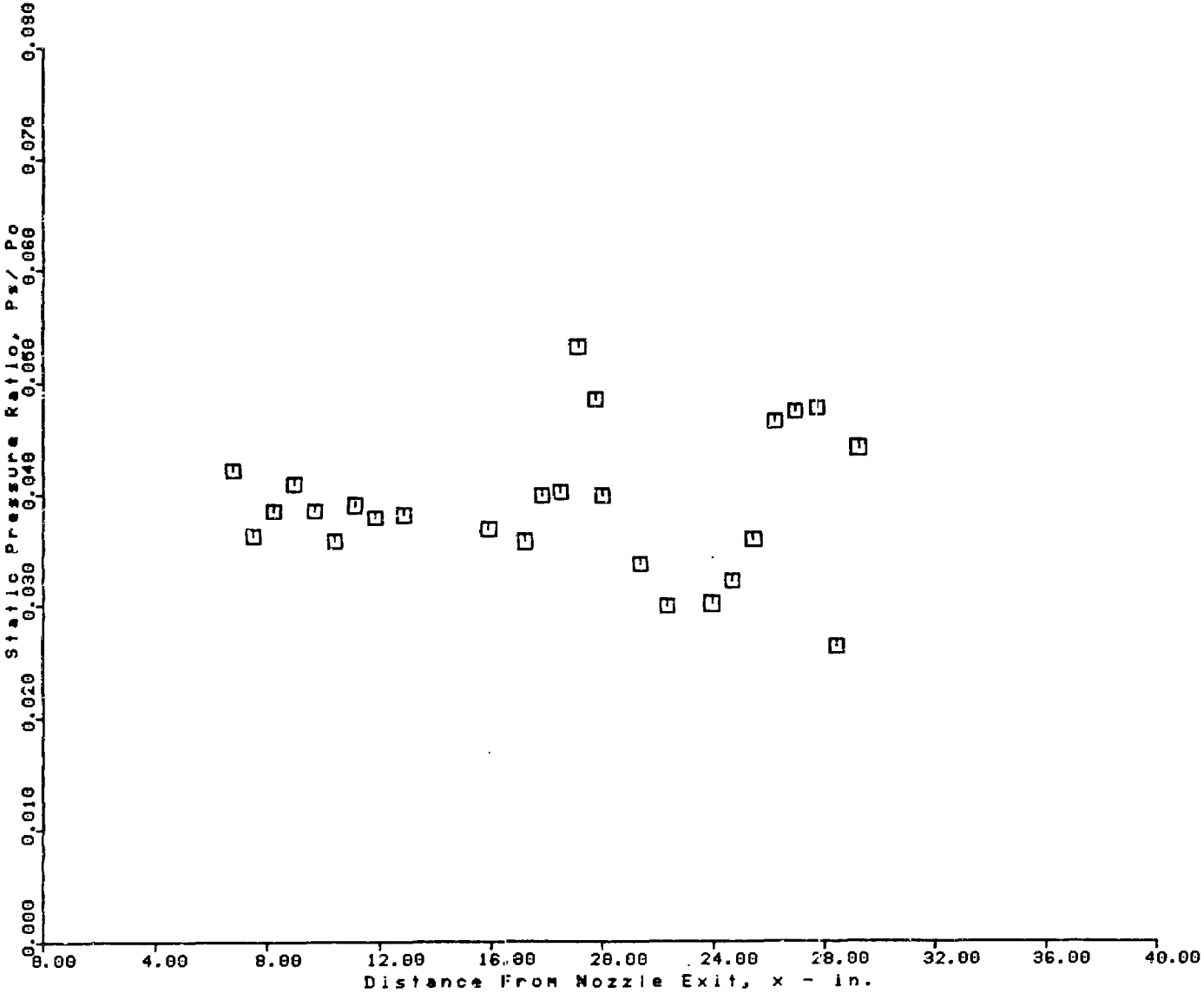

AFS TEST PROGRAM
UPPER SURFACE PRESSURE TAPS
RUN = 39 BURST = 41

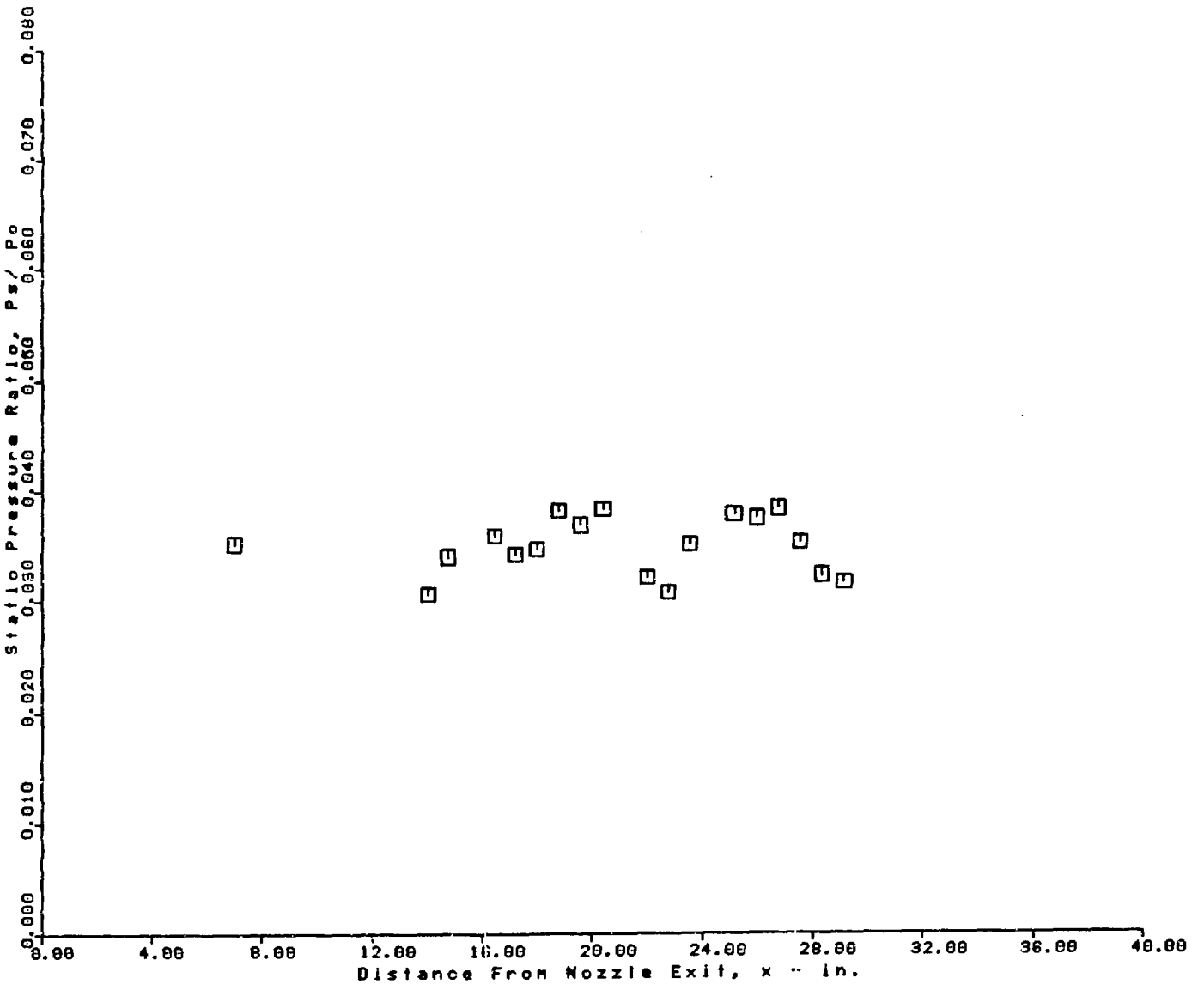

AFS TEST PROGRAM
LOWER SURFACE PRESSURE TAPS
RUN = 43 BURST = 39

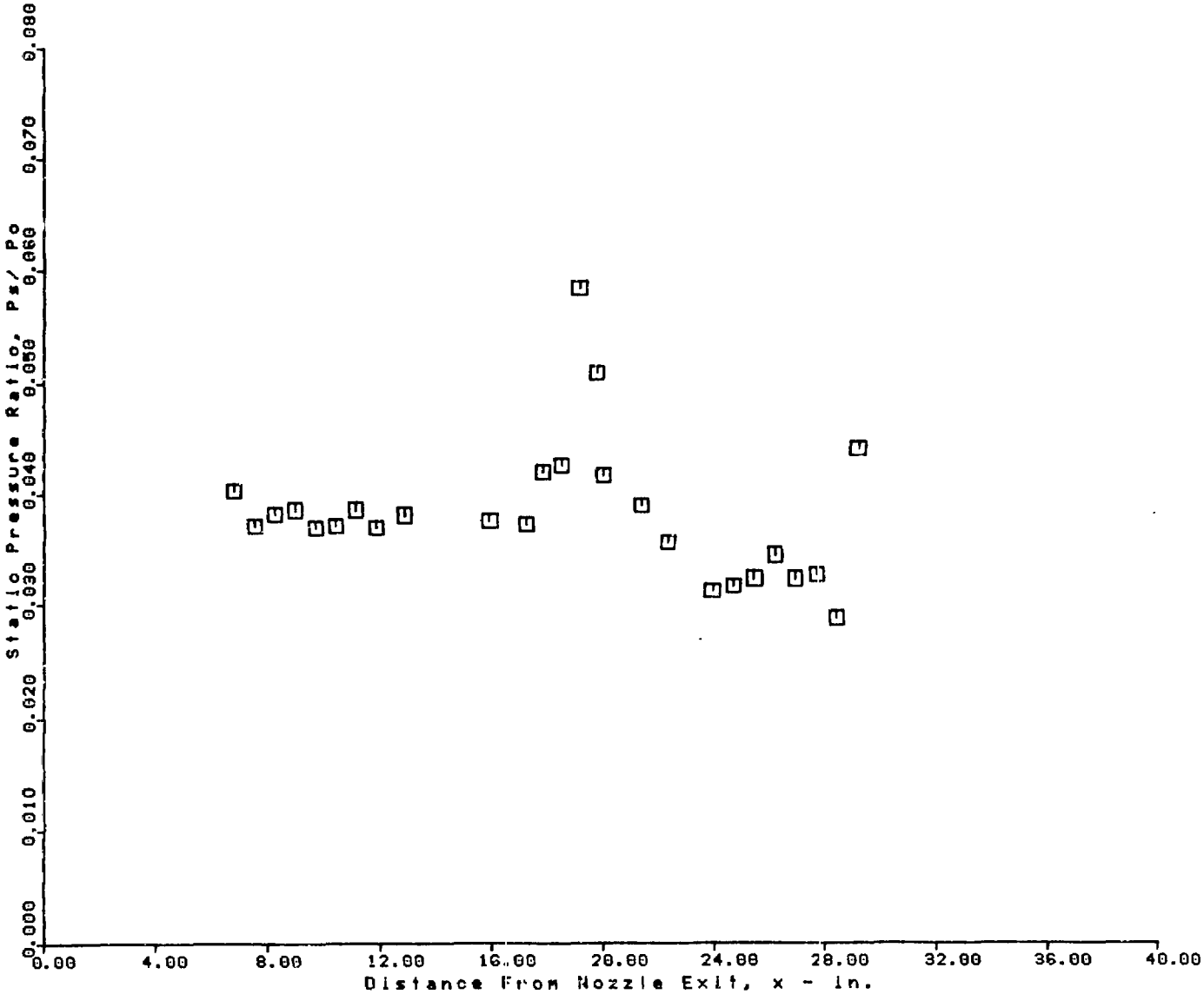

AFS TEST PROGRAM
UPPER SURFACE PRESSURE TAPS
RUN = 43 BURST = 39

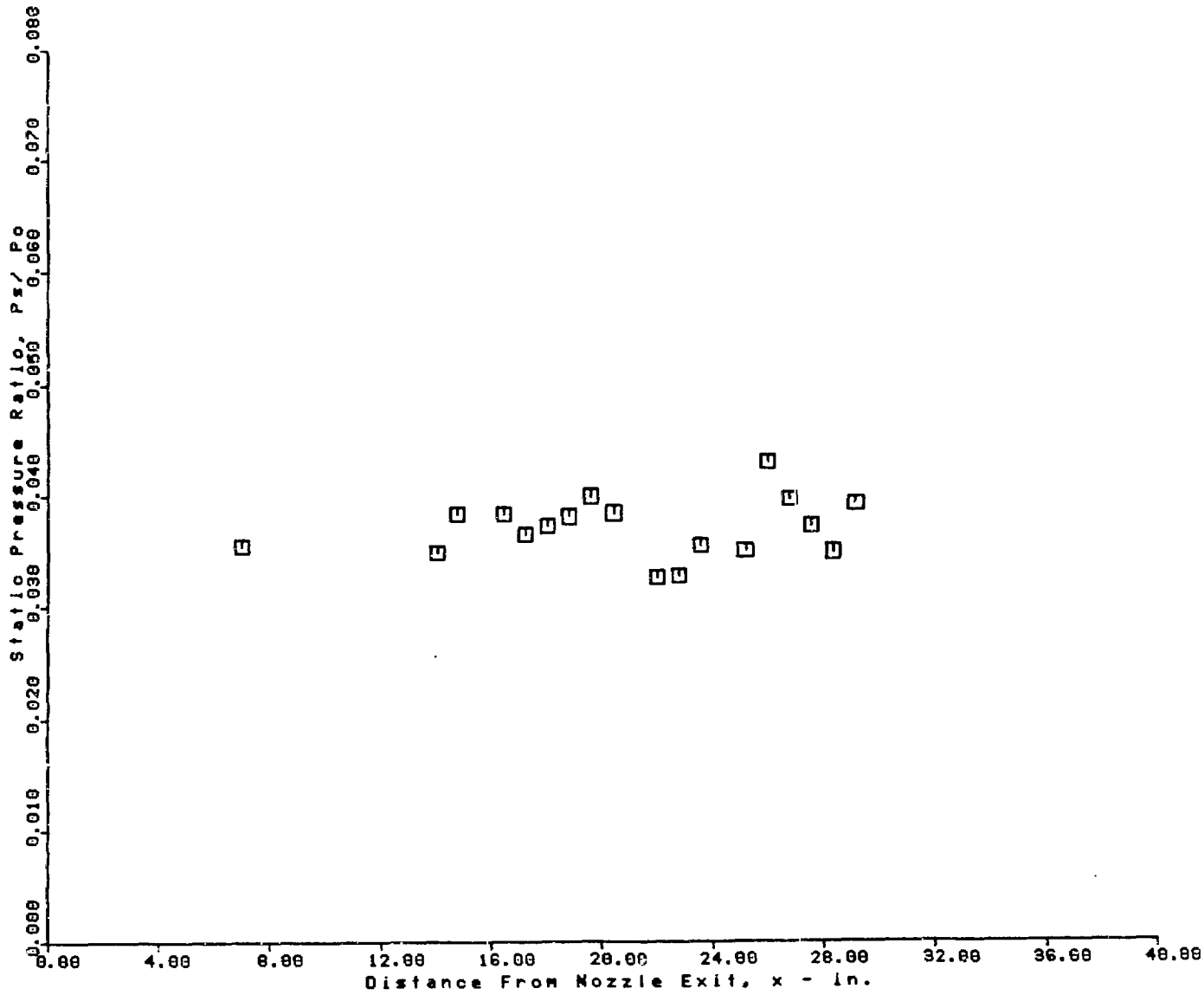

AFS TEST PROGRAM
LOWER SURFACE PRESSURE TAPS
RUN = 45 BURST = 28

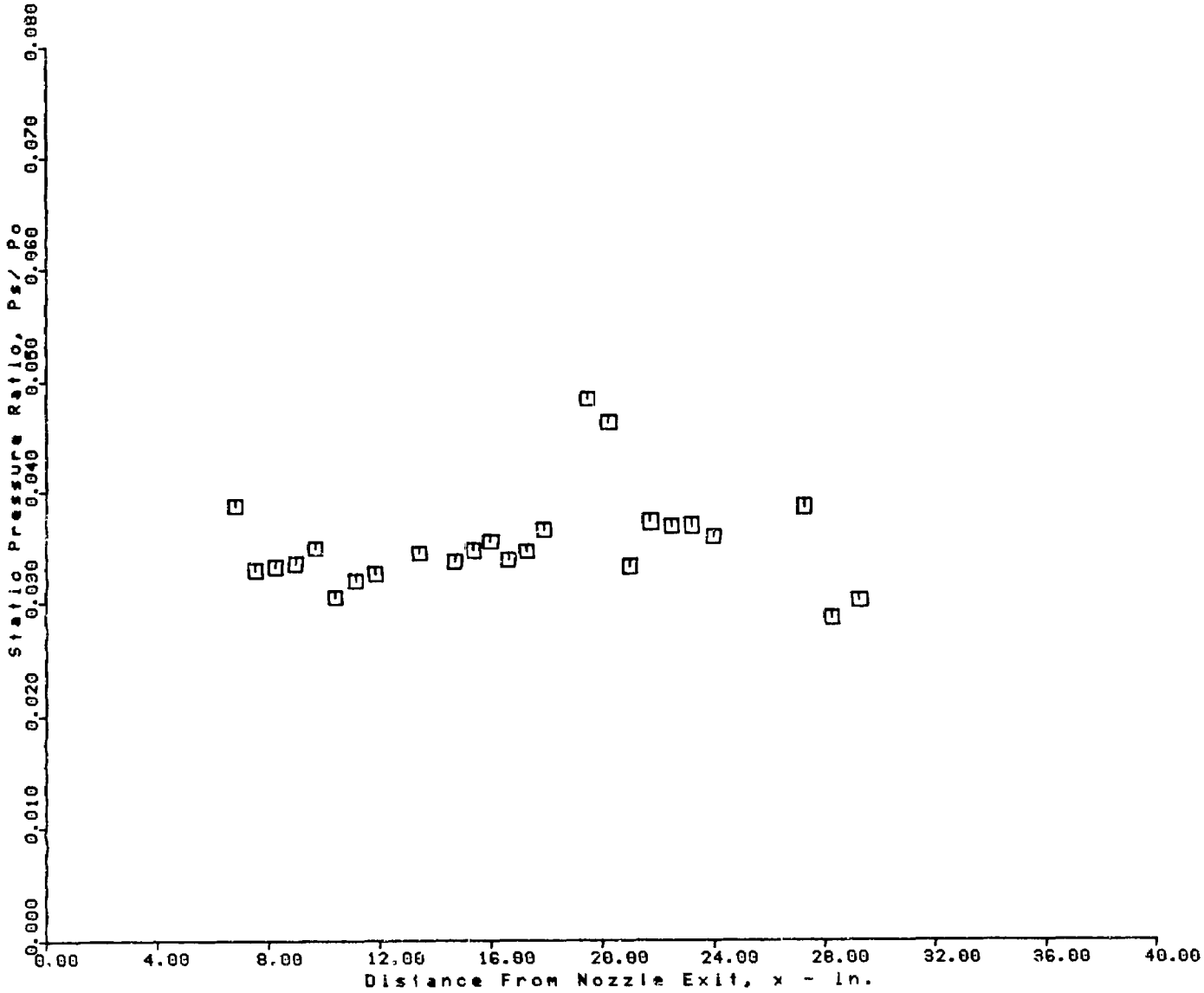

AFS TEST PROGRAM
UPPER SURFACE PRESSURE TAPS
RUN = 45 BURST = 28

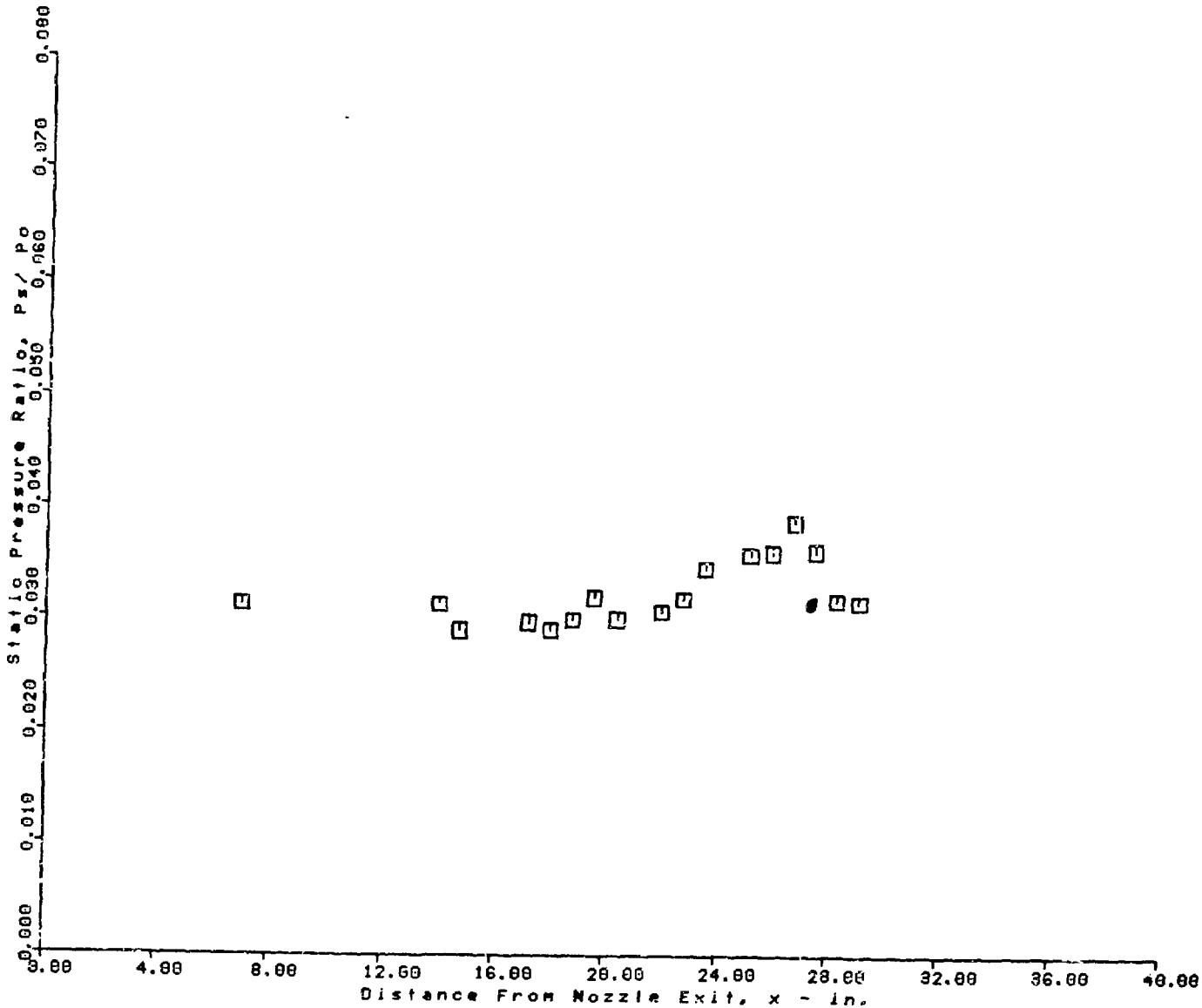

AFS TEST PROGRAM
LOWER SURFACE PRESSURE TAPS
RUN = 54 BURST = 50

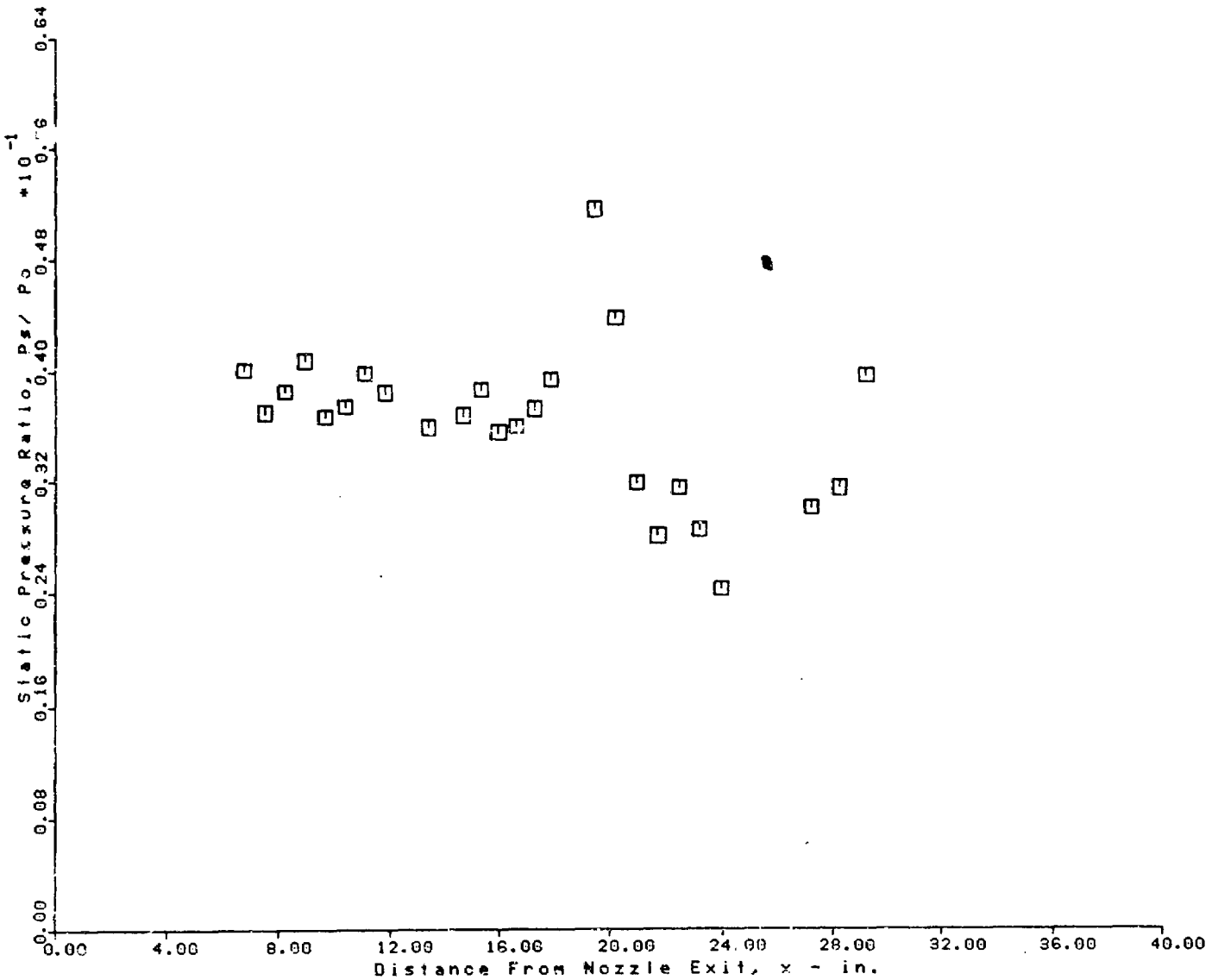

AFS TEST PROGRAM
LOWER SURFACE PRESSURE TAPS
RUN = 54 BURST = 50

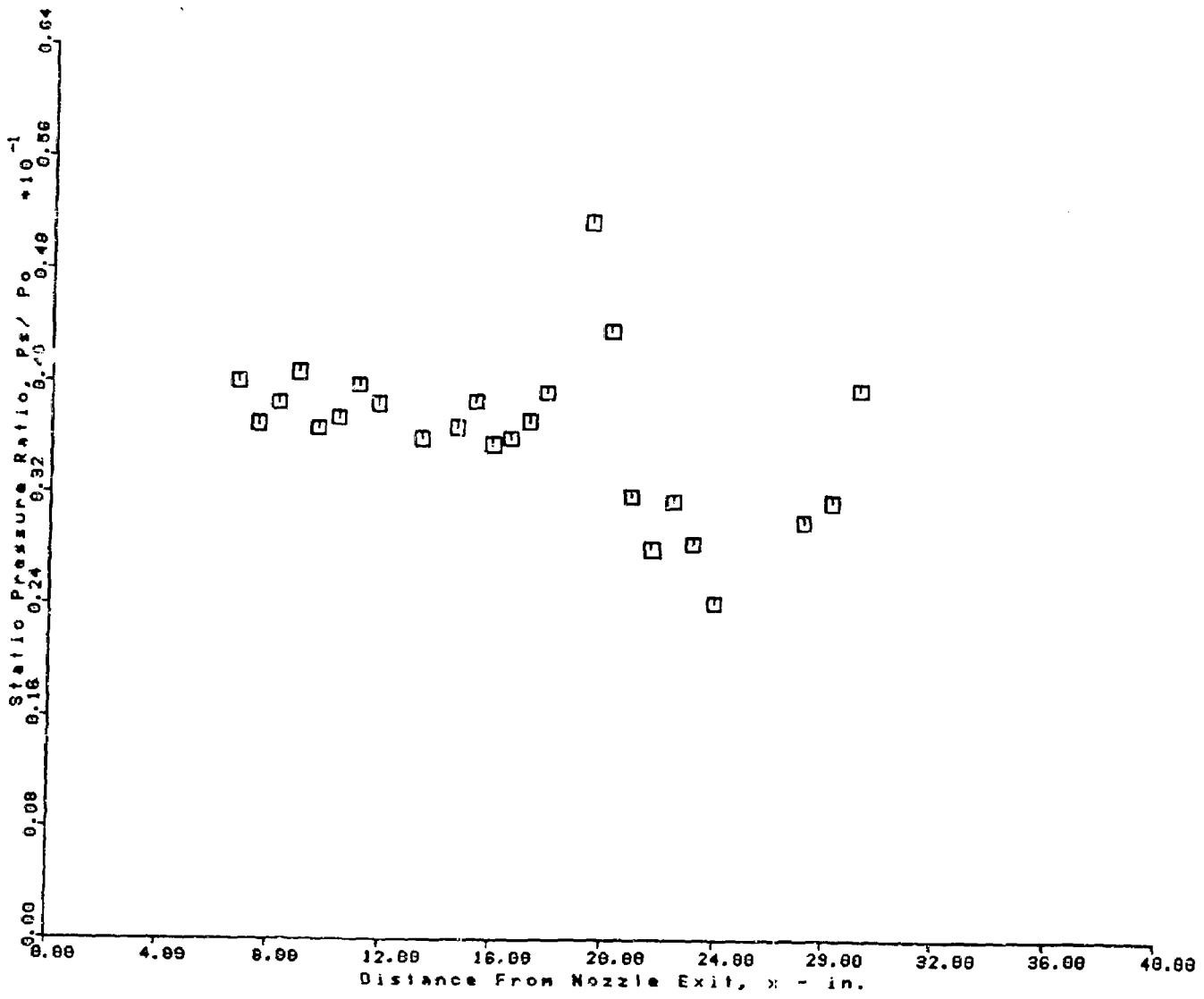

AFS TEST PROGRAM
UPPER SURFACE PRESSURE TAPS
RUN = 54 BURST = 50

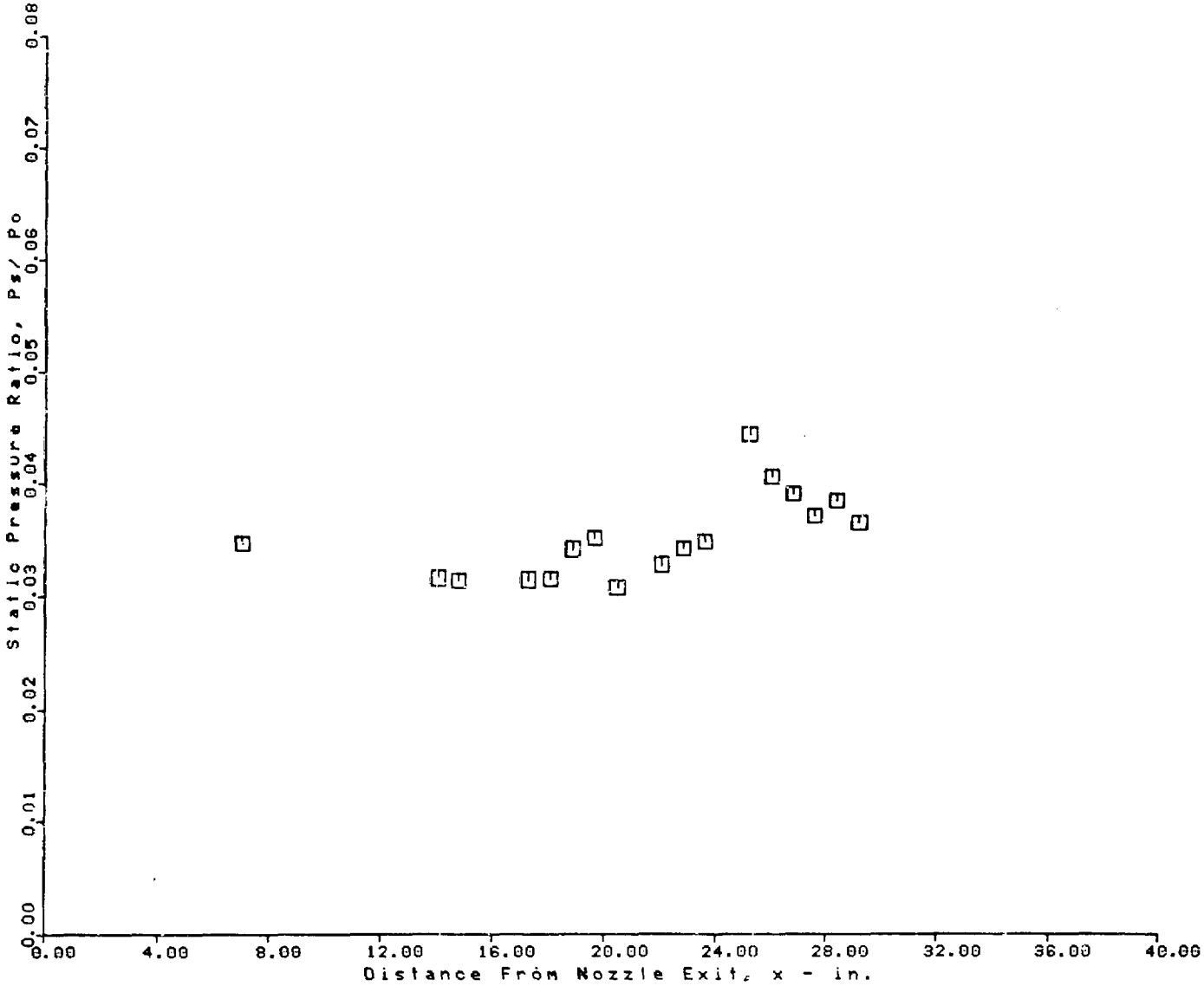

AFS TEST PROGRAM
LOWER SURFACE PRESSURE TAPS
RUN = 55 BURST = 30

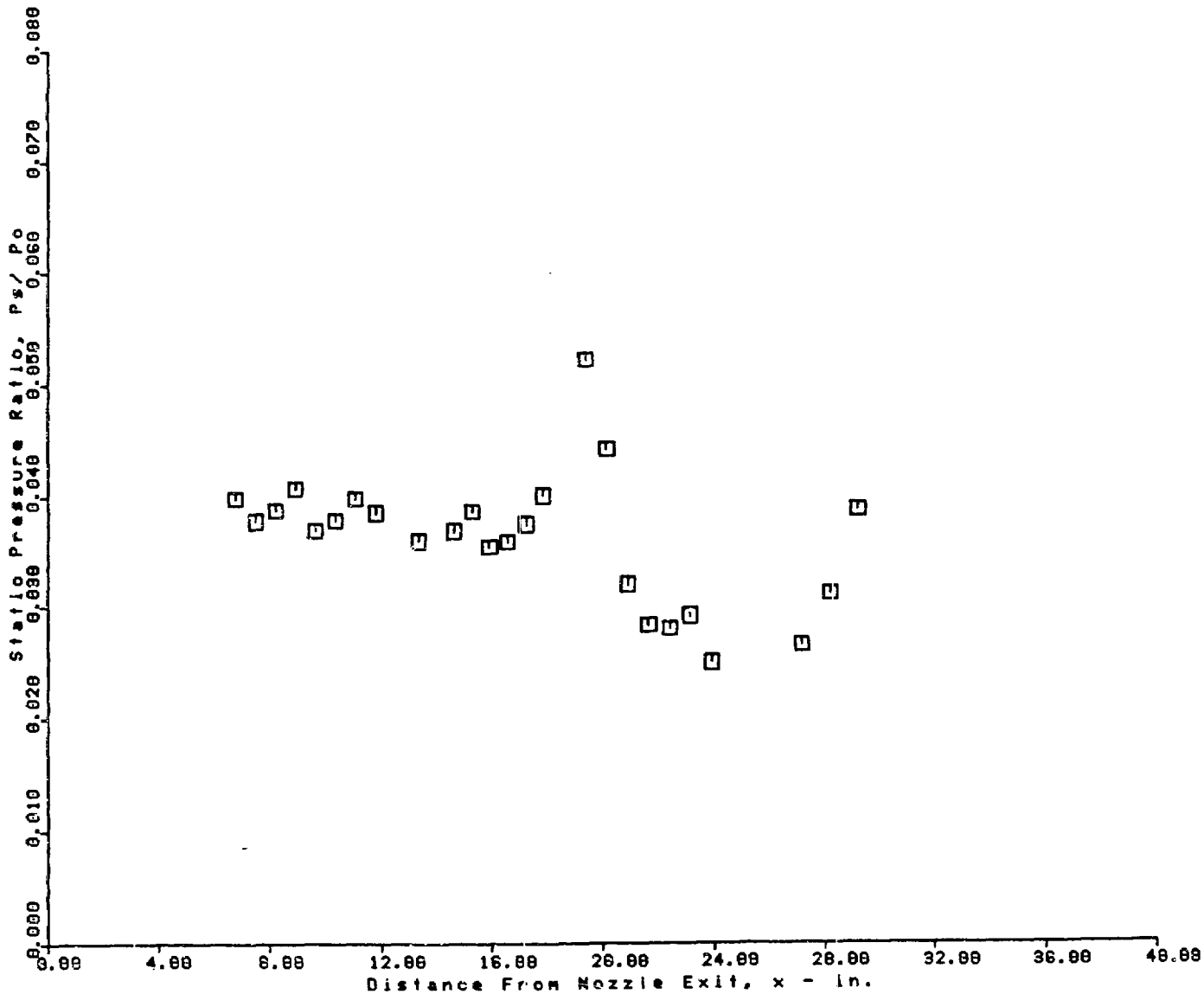

AFS TEST PROGRAM
UPPER SURFACE PRESSURE TAPS
RUN = 55 BURST = 30

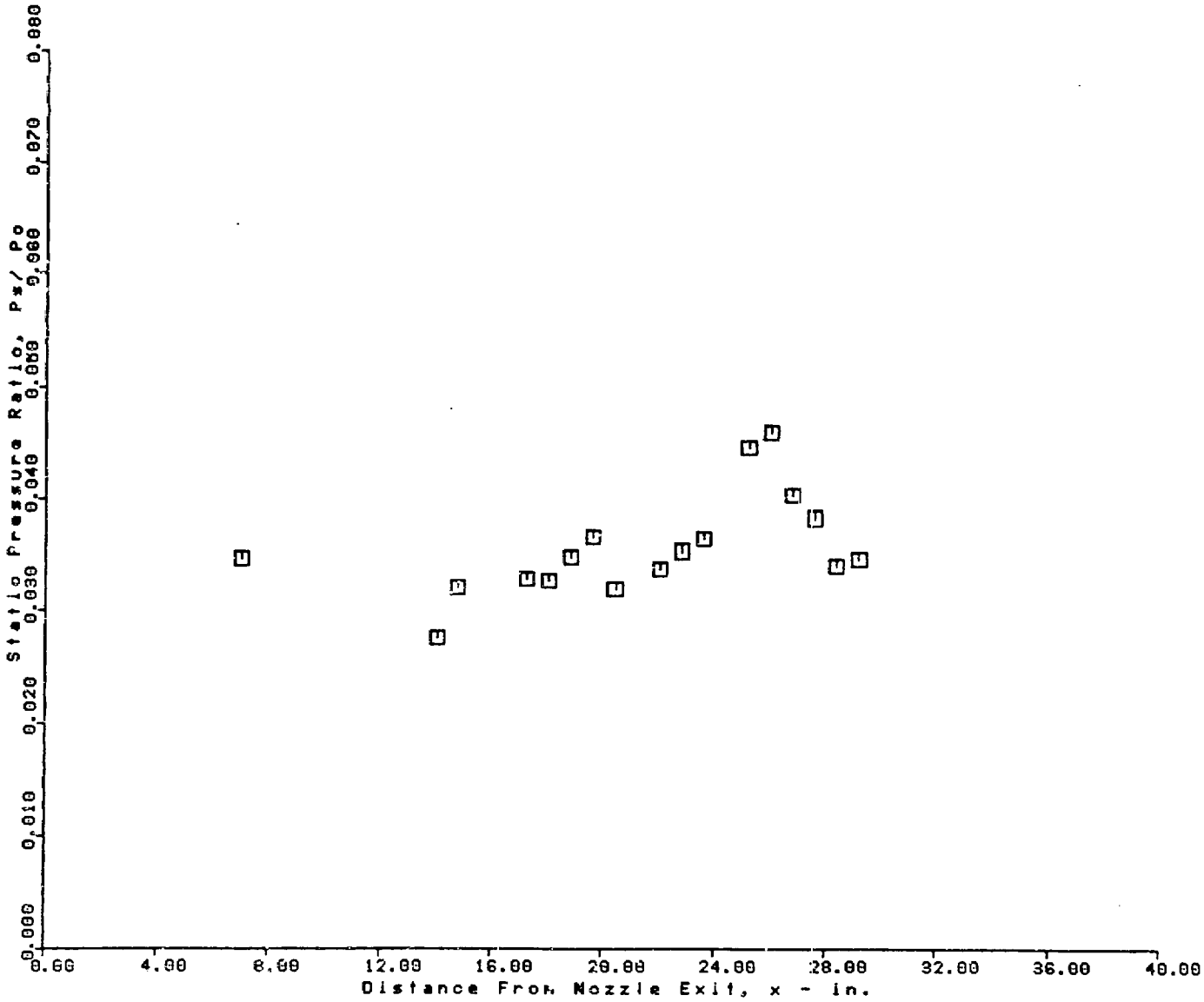

AFS TEST PROGRAM
LOWER SURFACE PRESSURE TAPS
RUN = 59 BURST = 38

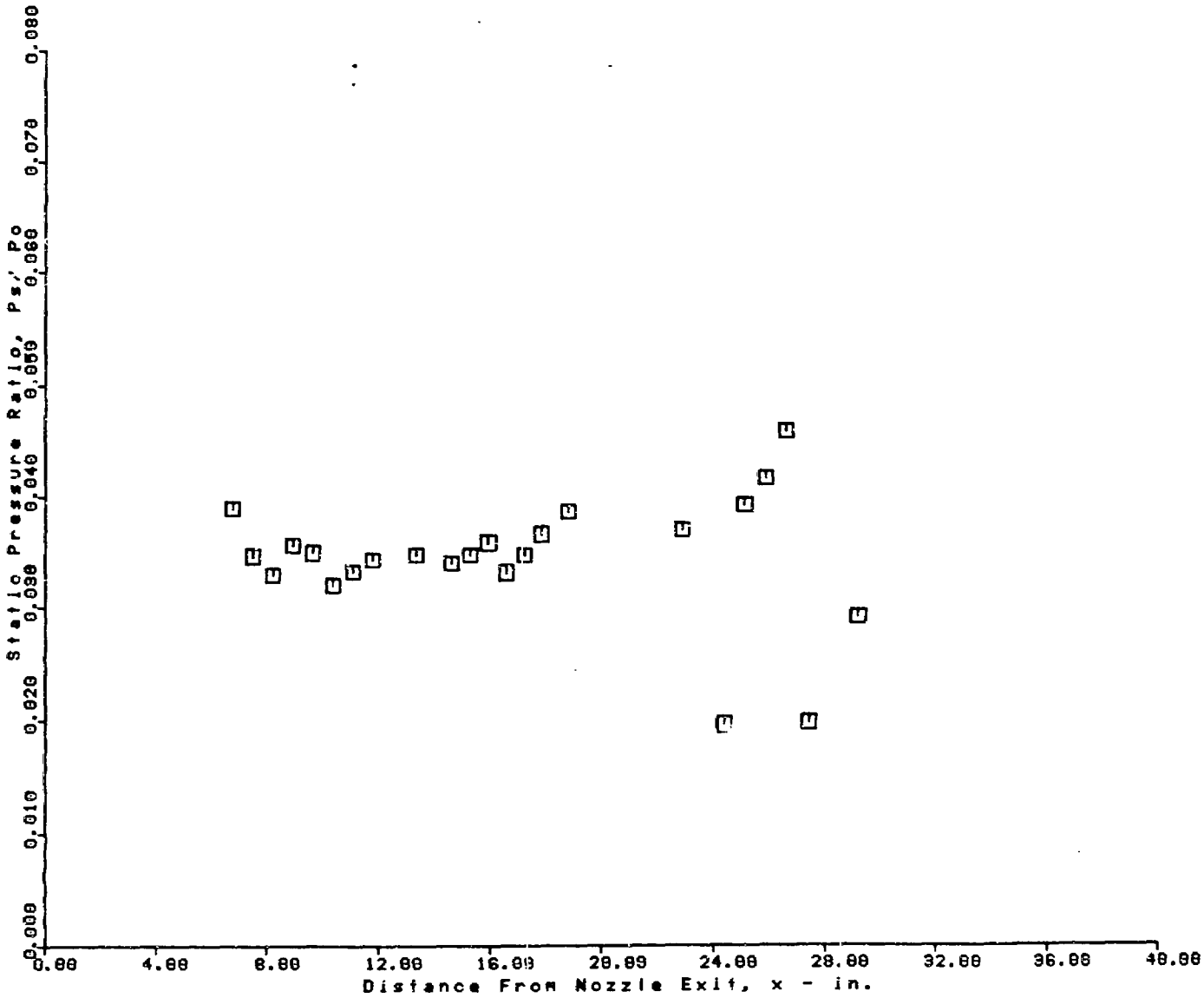

AFS TEST PROGRAM
UPPER SURFACE PRESSURE TAPS
RUN = 59 BURST = 30

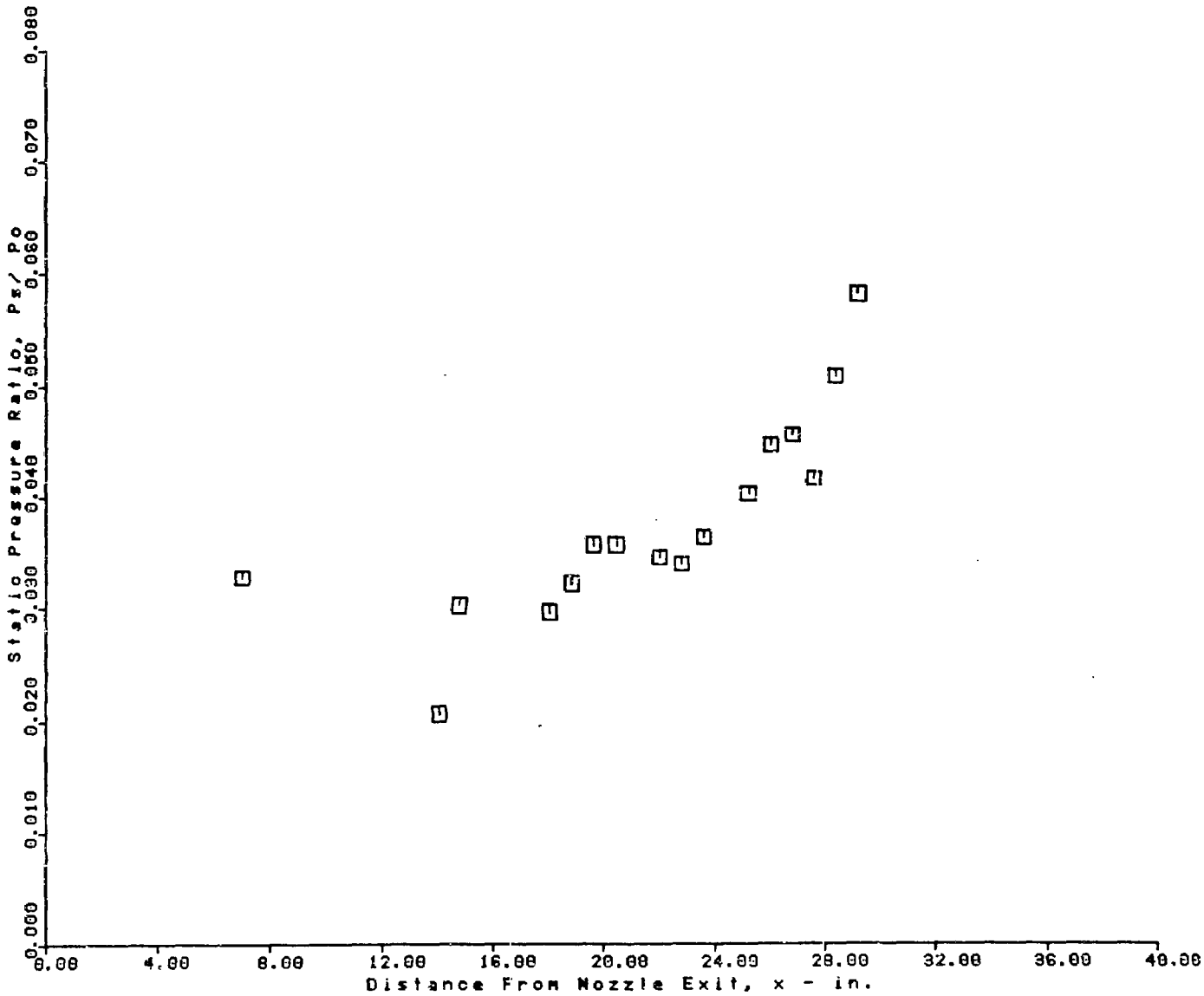

AFS TEST PROGRAM
LOWER SURFACE PRESSURE TAPS
RUN = 61 BURST = 30

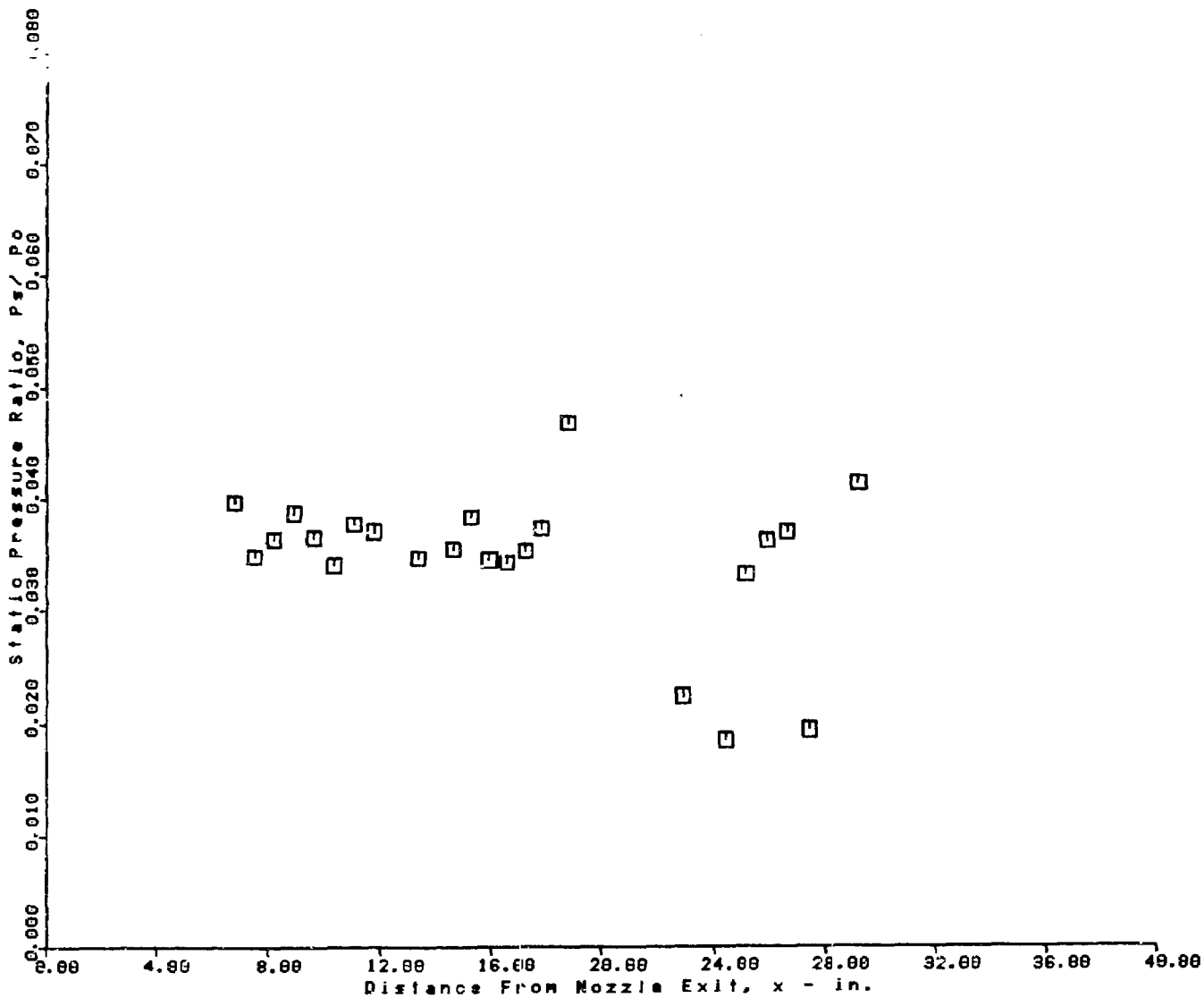

AFS TEST PROGRAM
UPPER SURFACE PRESSURE TAPS
RUN = 61 BURST = 30

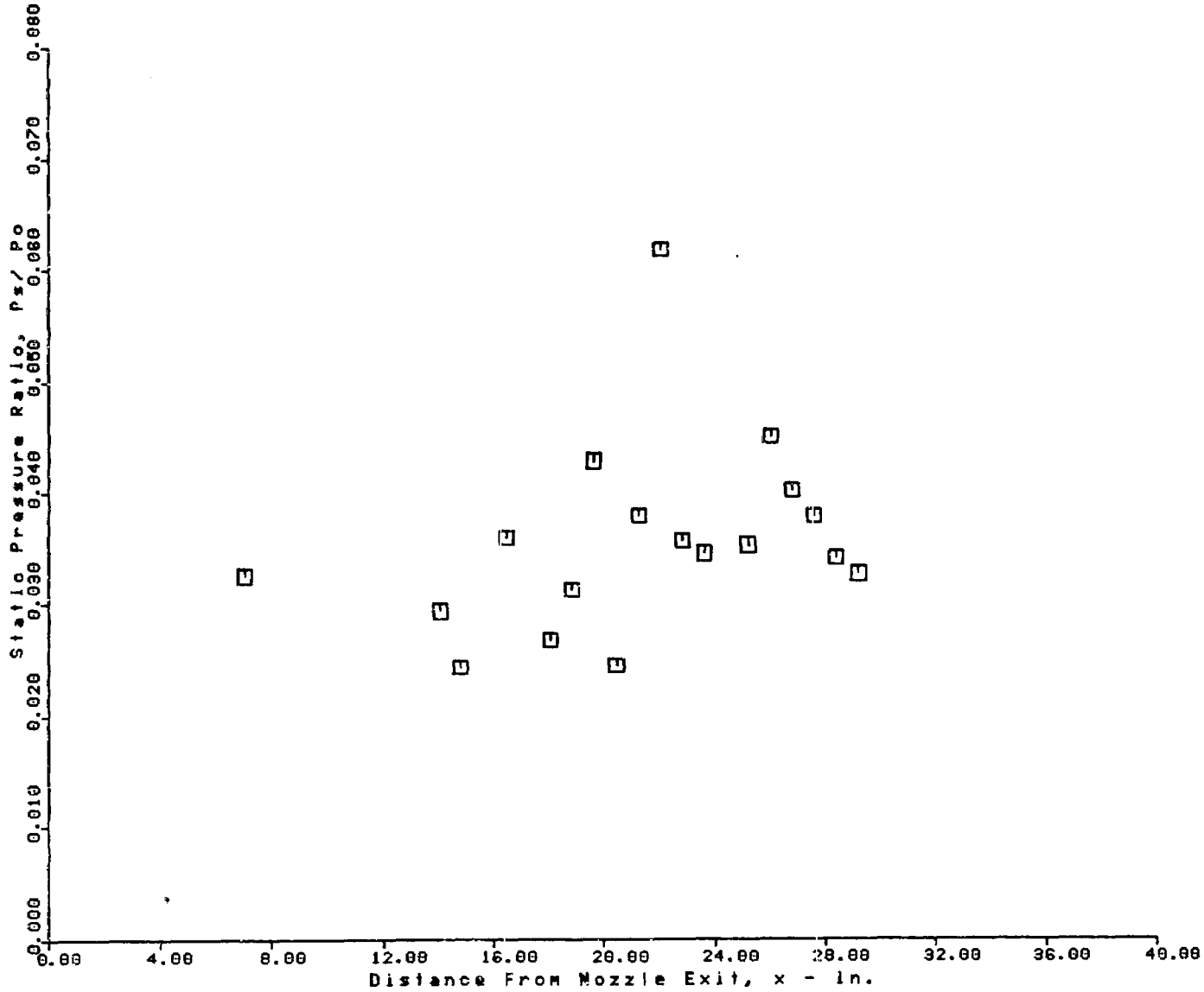

AFS TEST PROGRAM
LOWER SURFACE PRESSURE TAPS
RUN = 62 BURST = 30

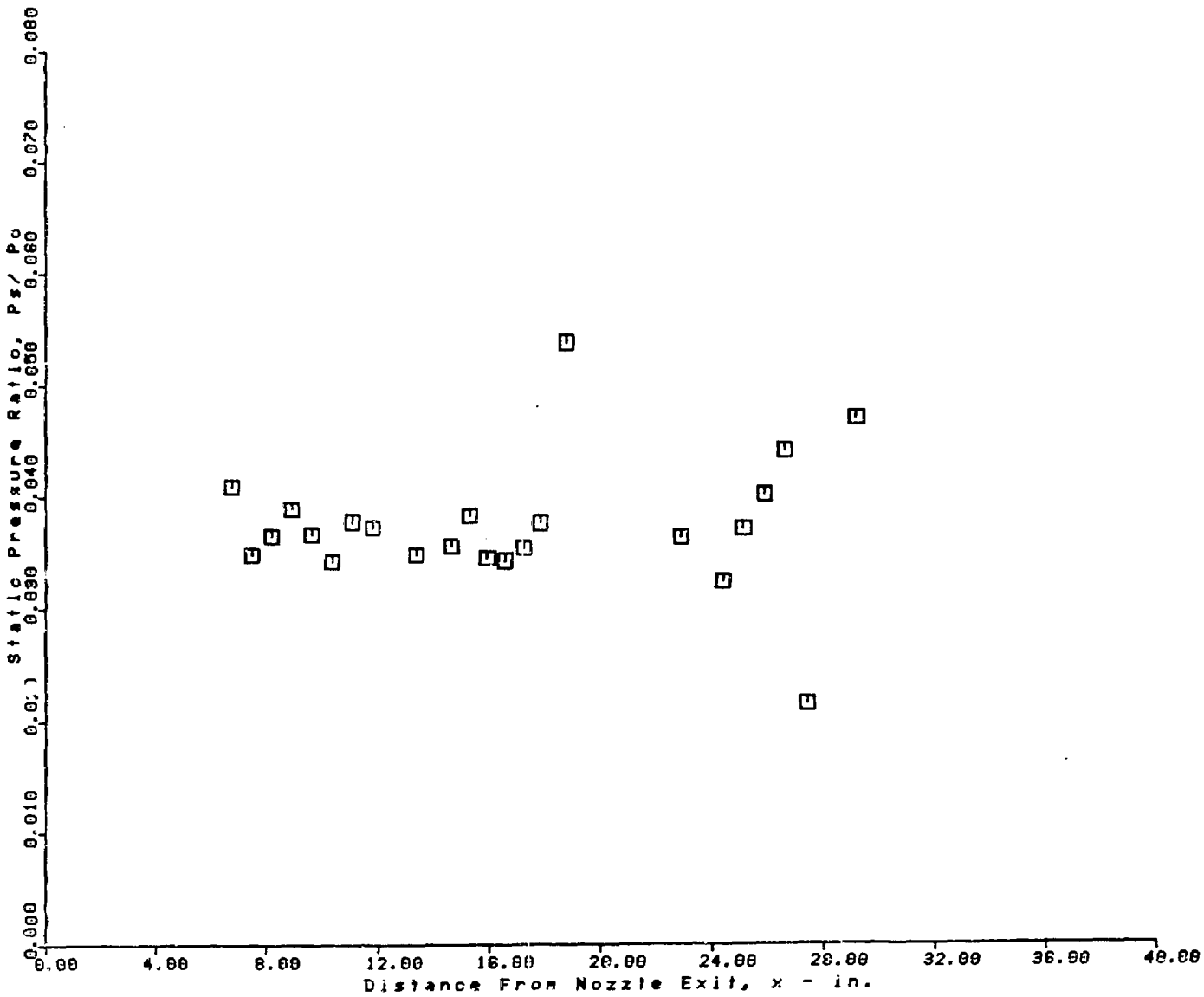

AFS TEST PROGRAM
UPPER SURFACE PRESSURE TAPS
RUN = 62 BURST = 30

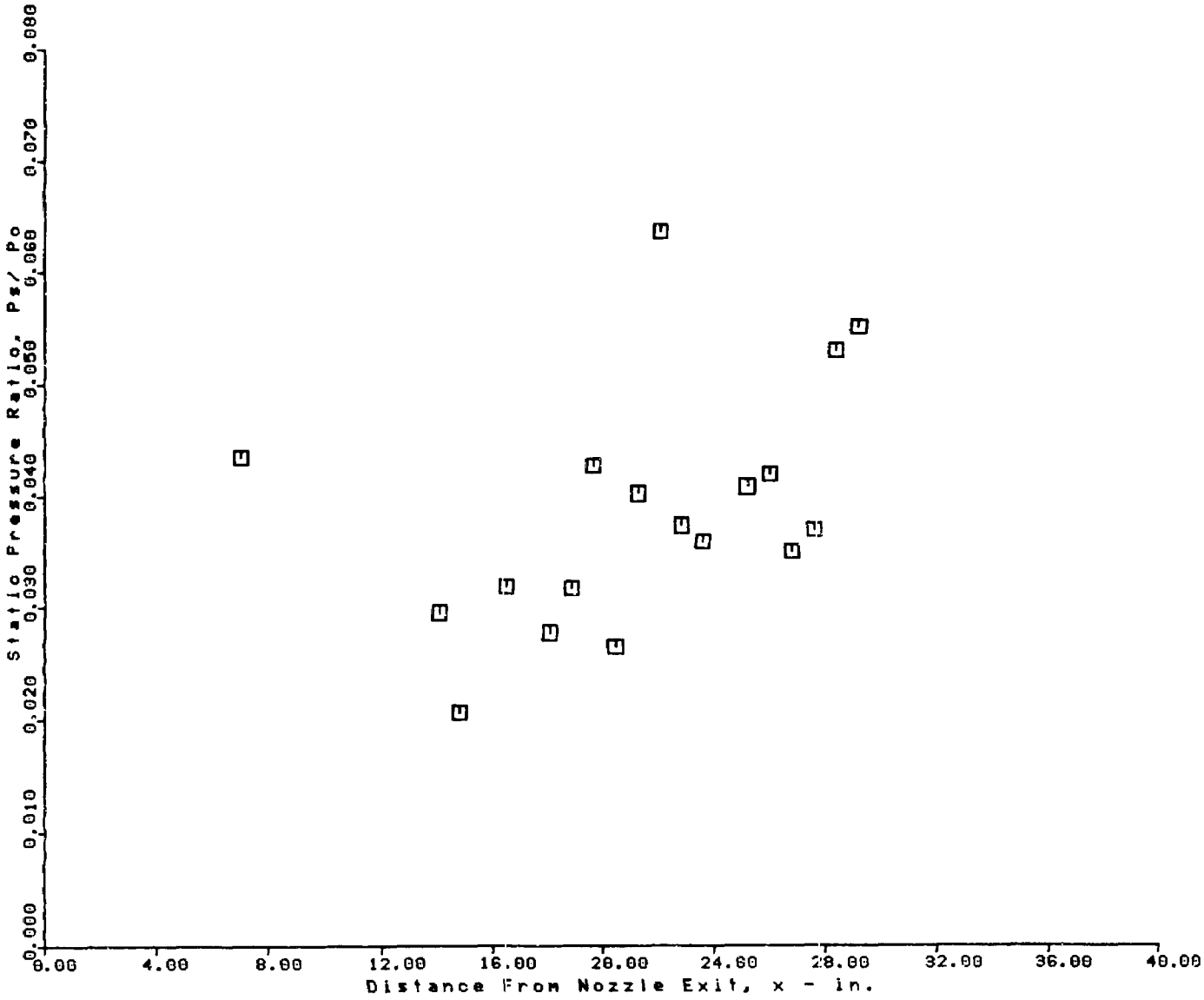

AFS TEST PROGRAM
LOWER SURFACE PRESSURE TAPS
RUN = 63 BURST = 35

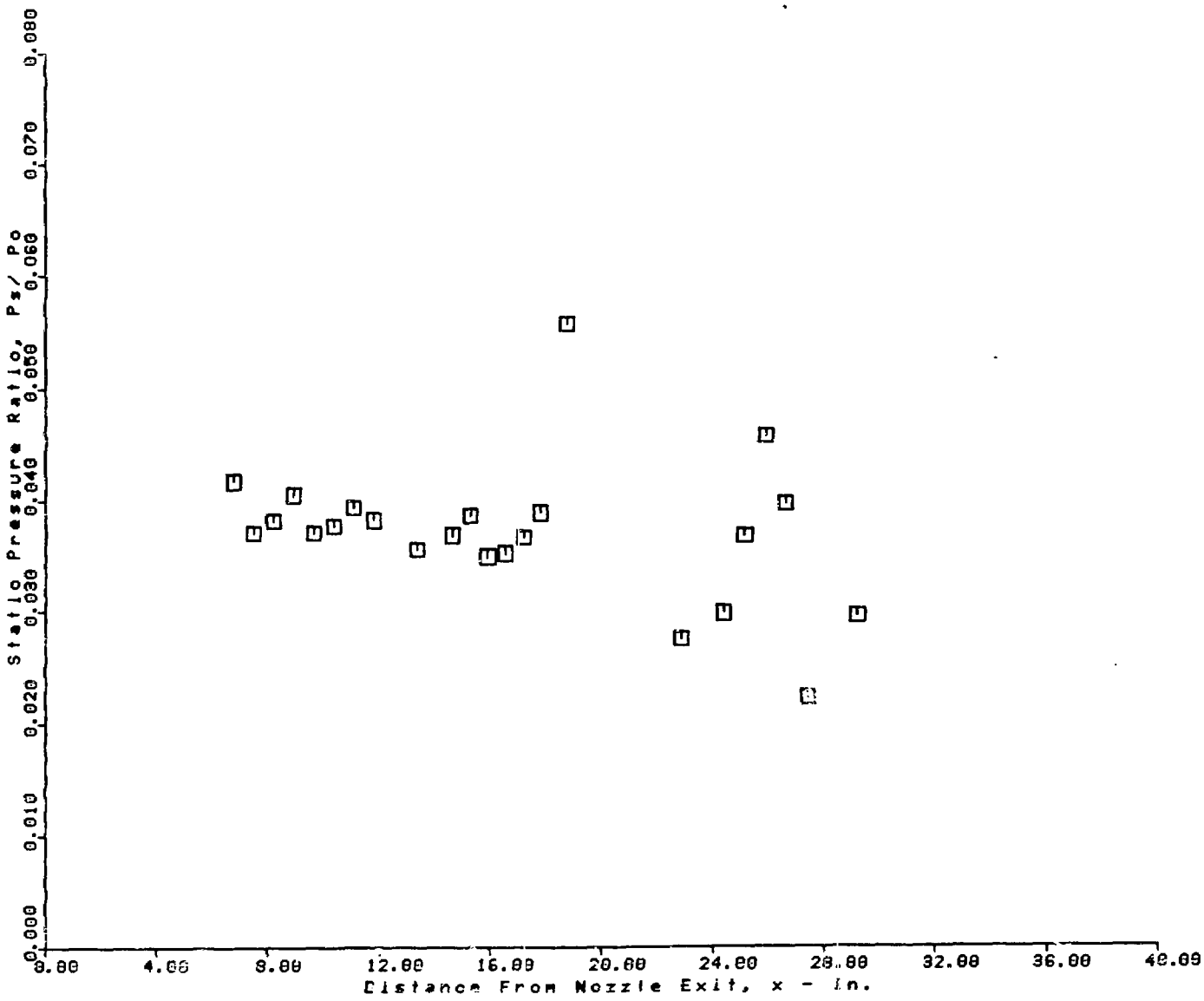

AFS TEST PROGRAM
UPPER SURFACE PRESSURE TAPS
RUN = 63 BURST = 35

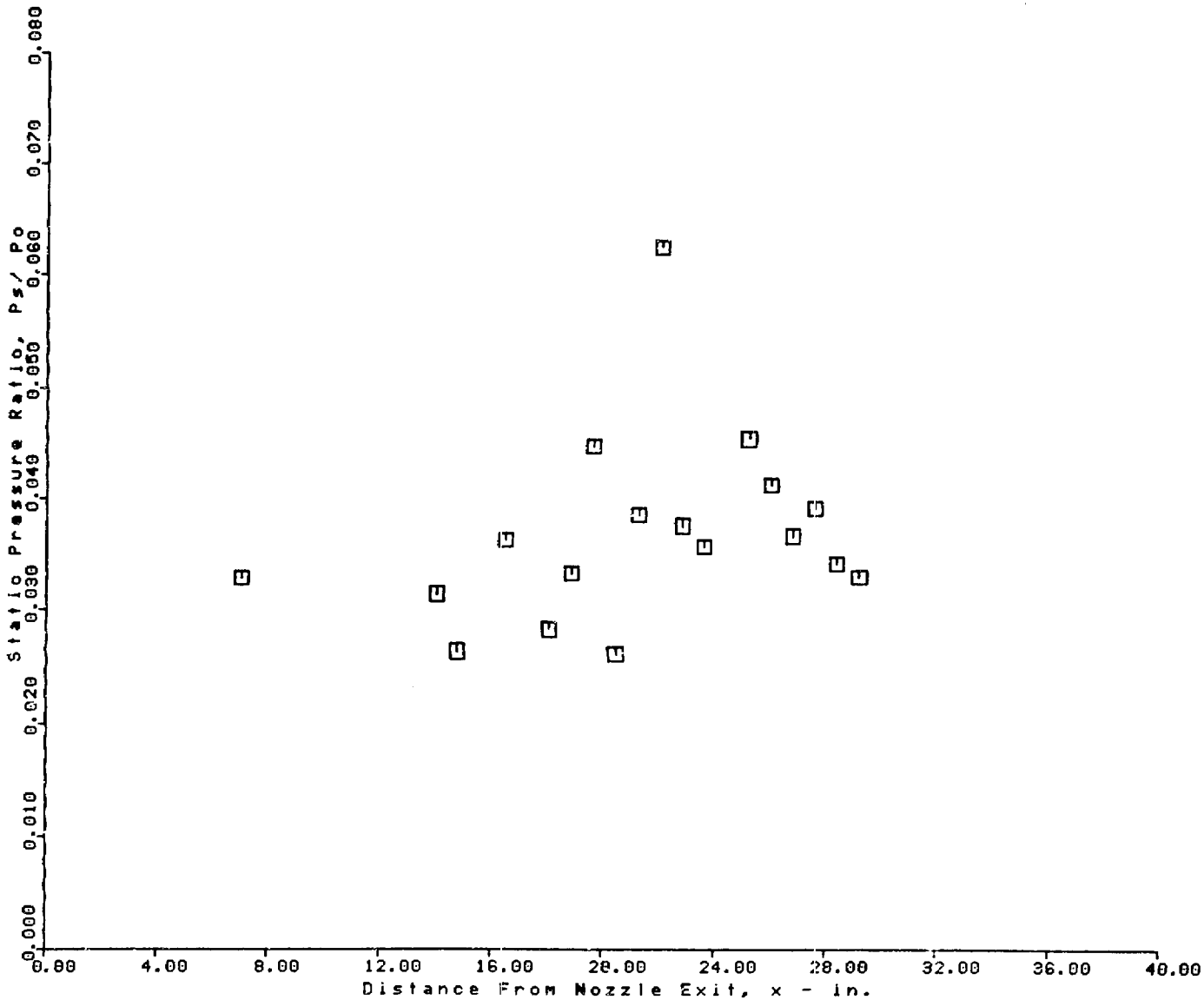

AFS TEST PROGRAM
LOWER SURFACE PRESSURE TAPS
RUN = 64 BURST = 38

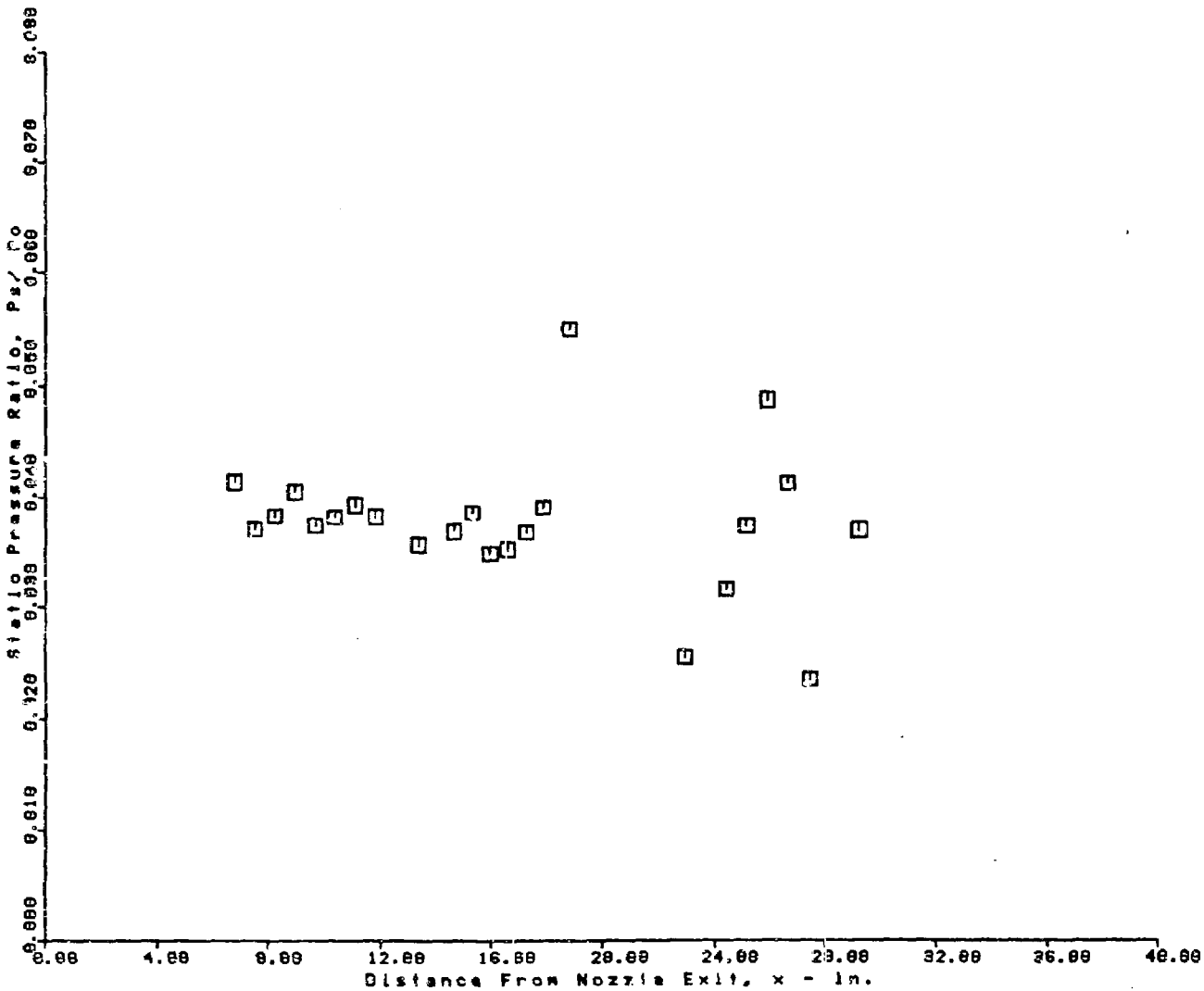

AFS TEST PROGRAM
UPPER SURFACE PRESSURE TAPS
RUN = 64 BURST = 38

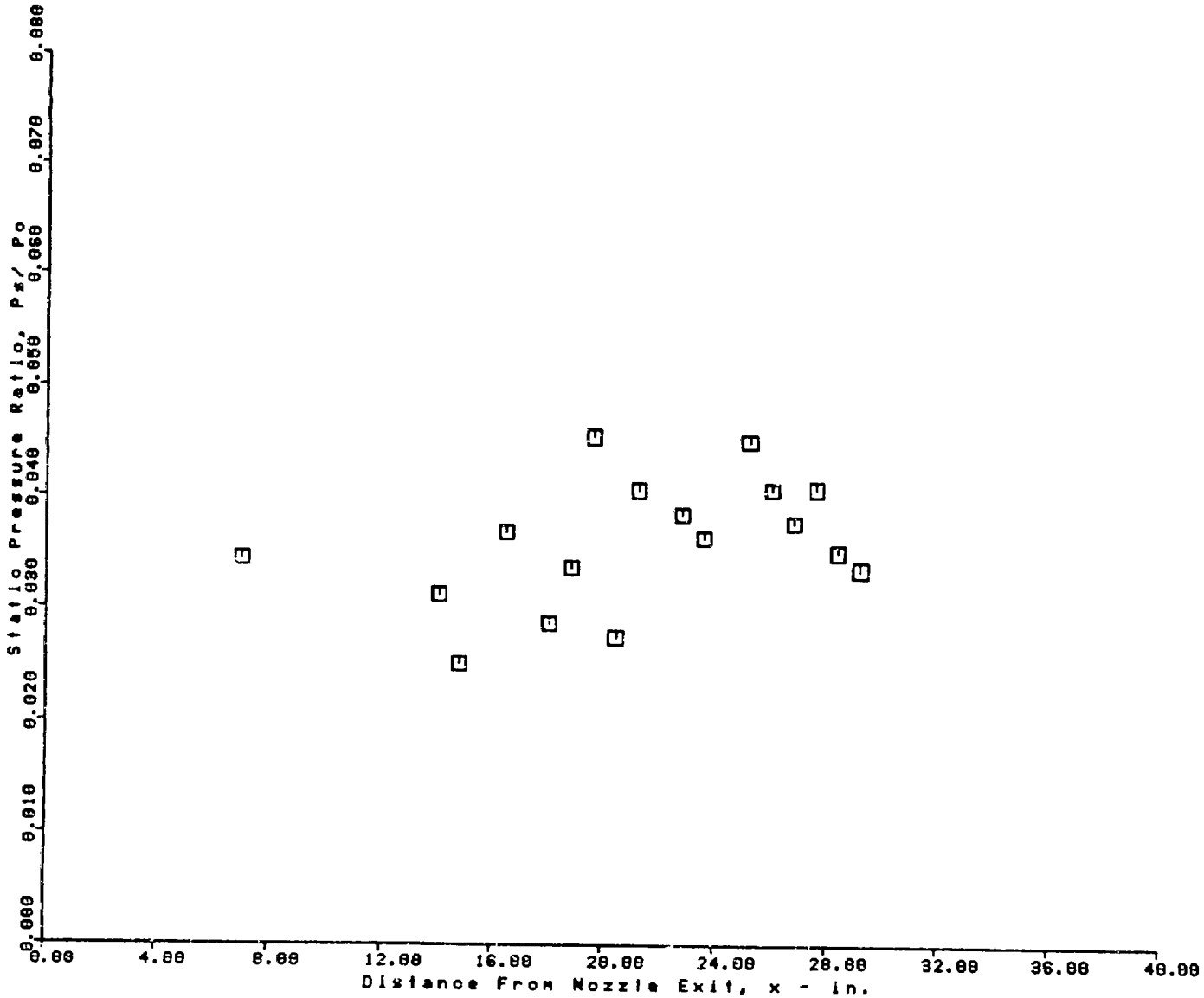

AFS TEST PROGRAM
UPPER SURFACE PRESSURE TAPS
RUN = 65 BURST = 32

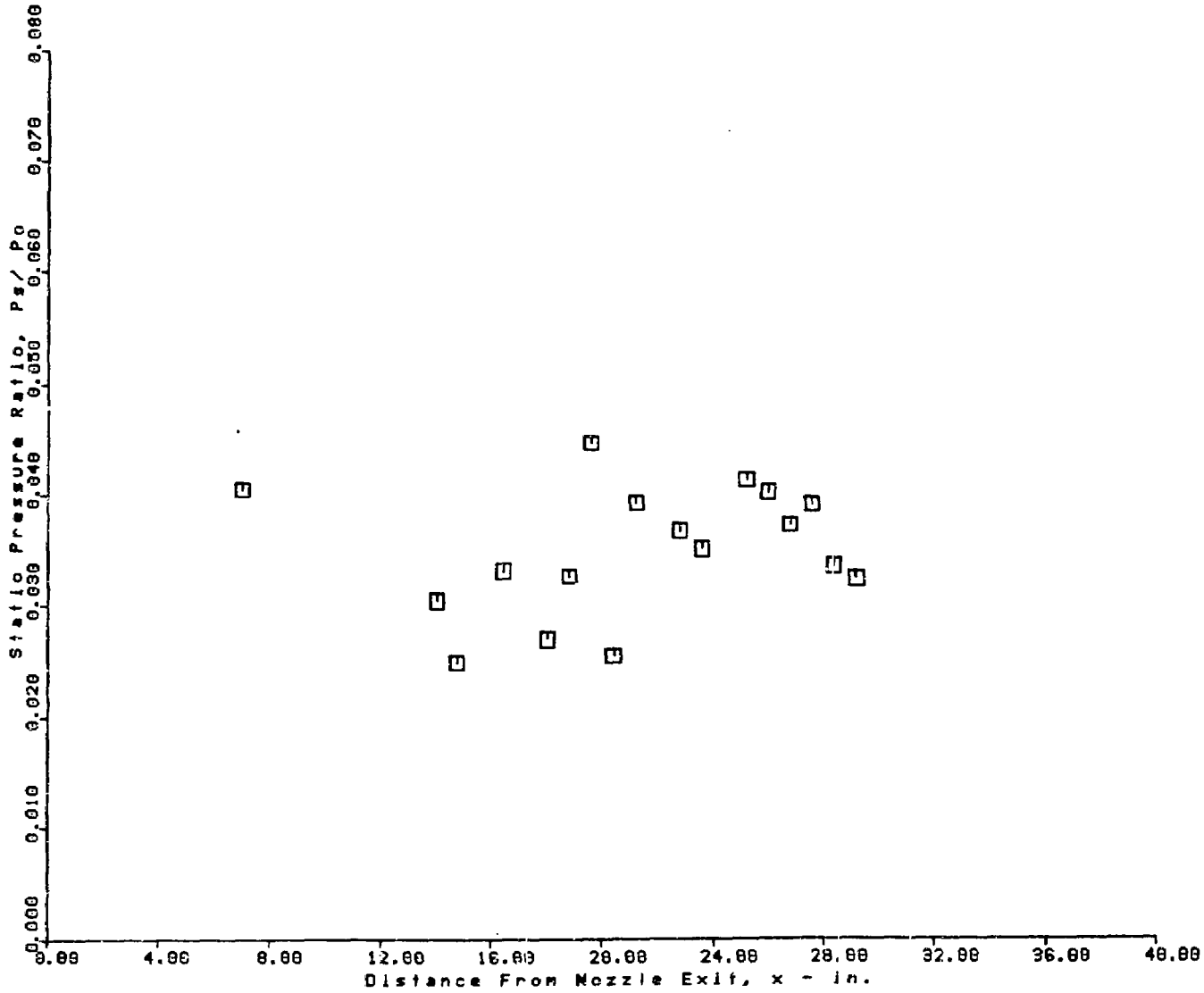

AFS TEST PROGRAM
LOWER SURFACE PRESSURE TAPS
RUN = 65 BURST = 32

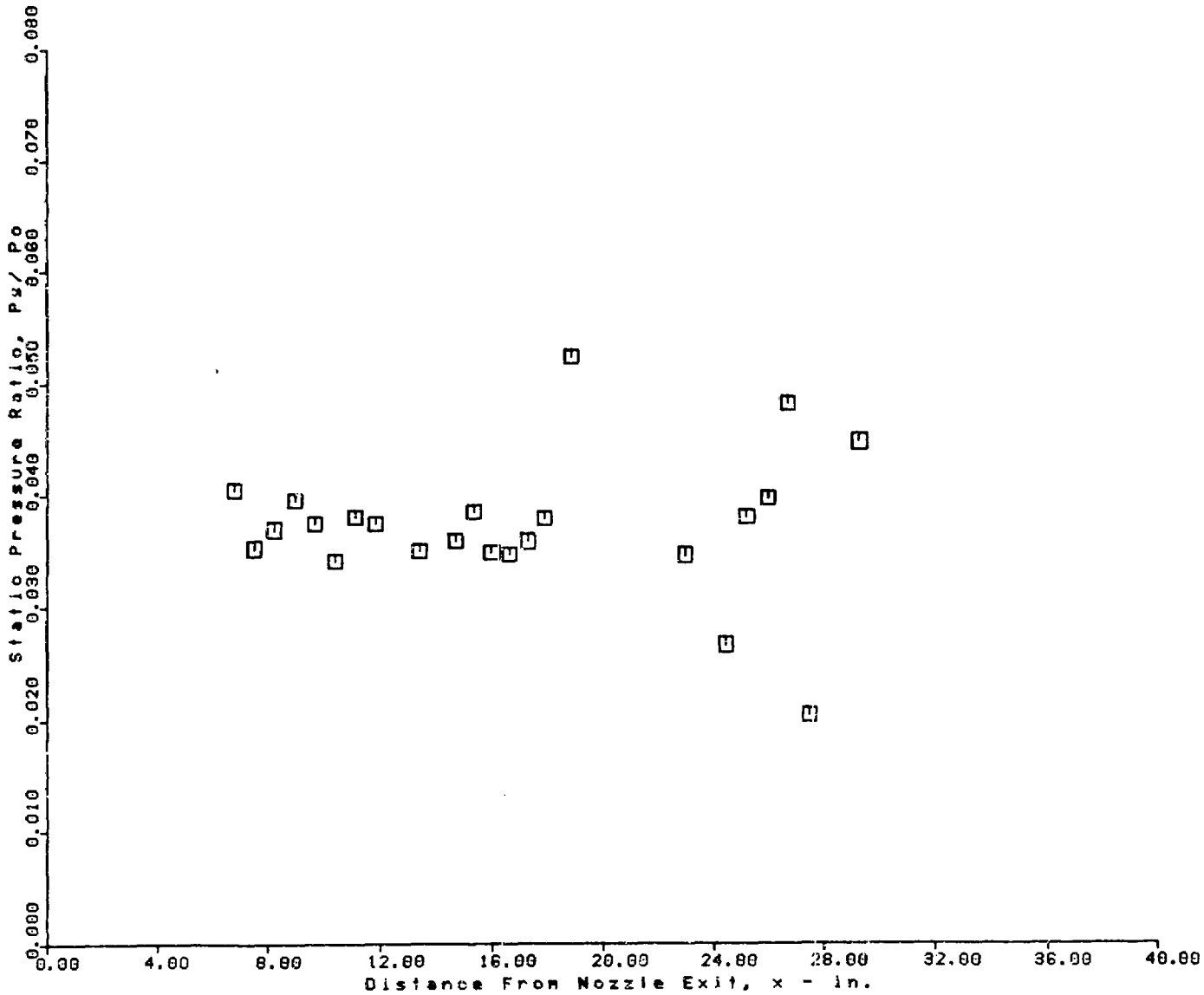

AFS TEST PROGRAM
LOWER SURFACE PRESSURE TAPS
RUN = 66 BURST = 32

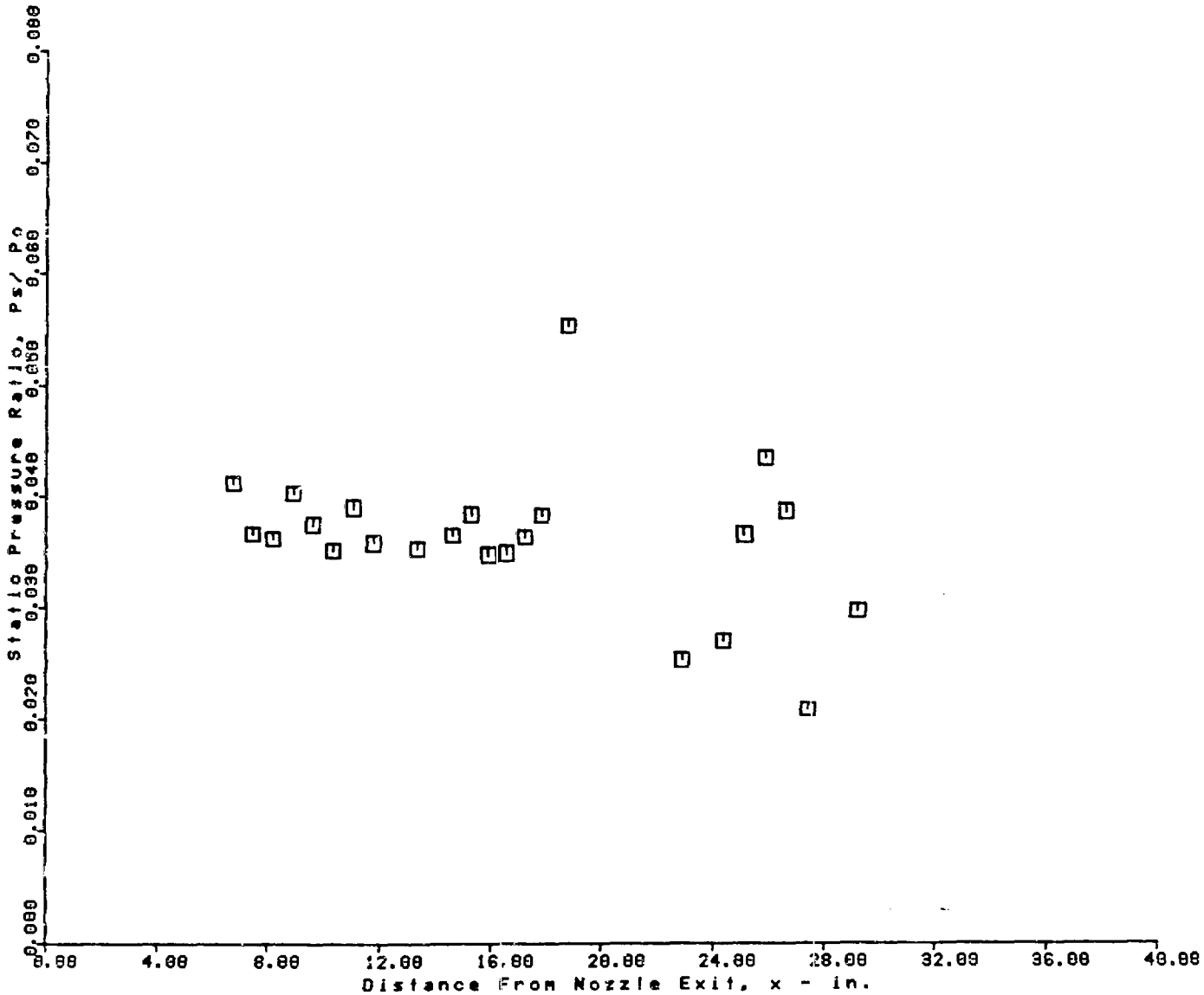

AFS TEST PROGRAM
UPPER SURFACE PRESSURE TAPS
RUN = 66 BURST = 32

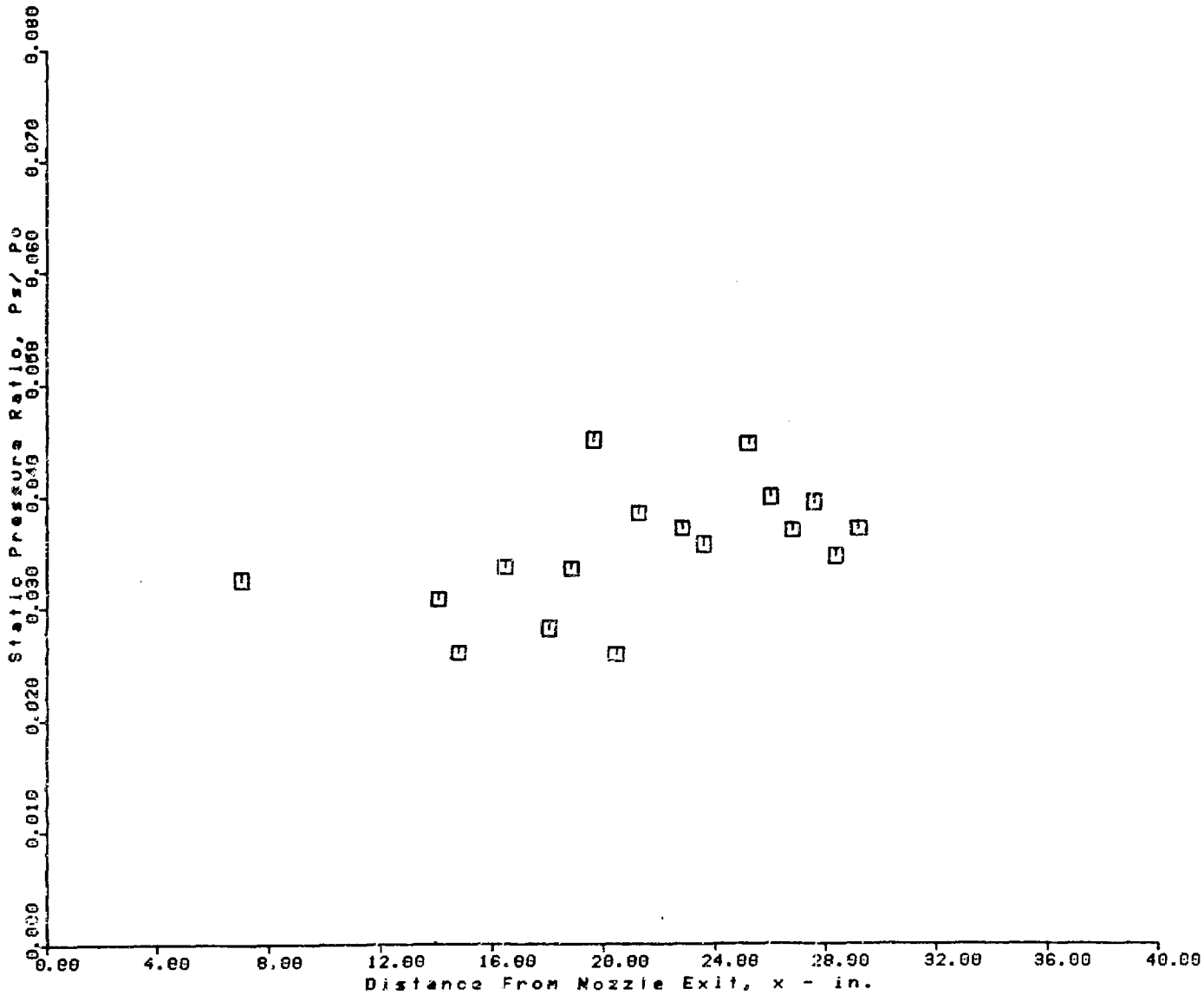

AFS TEST PROGRAM
LOWER SURFACE PRESSURE TAPS
RUN = 69 BURST = 50

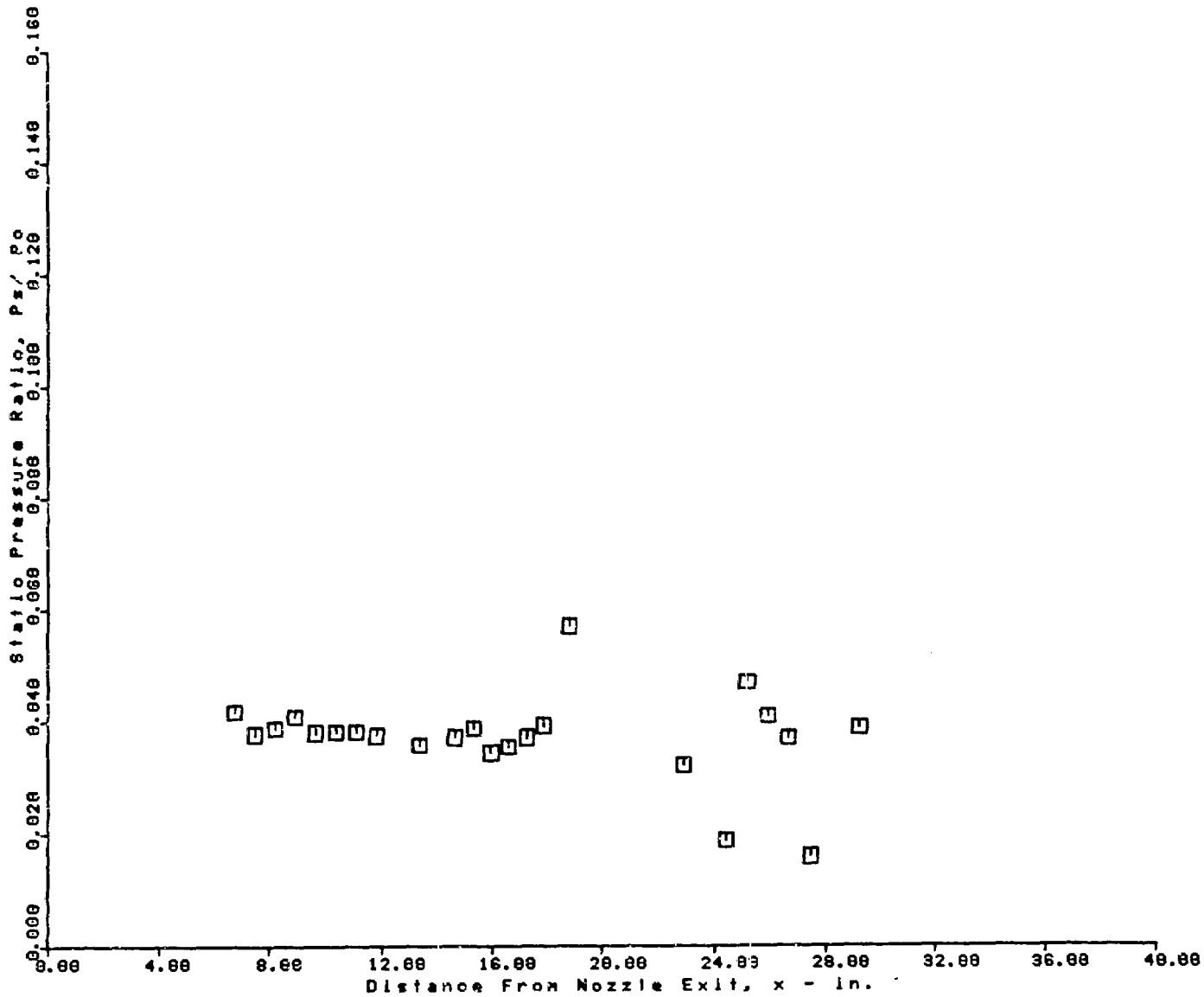

AFS TEST PROGRAM
UPPER SURFACE PRESSURE TAPS
RUN = 69 BURST = 50

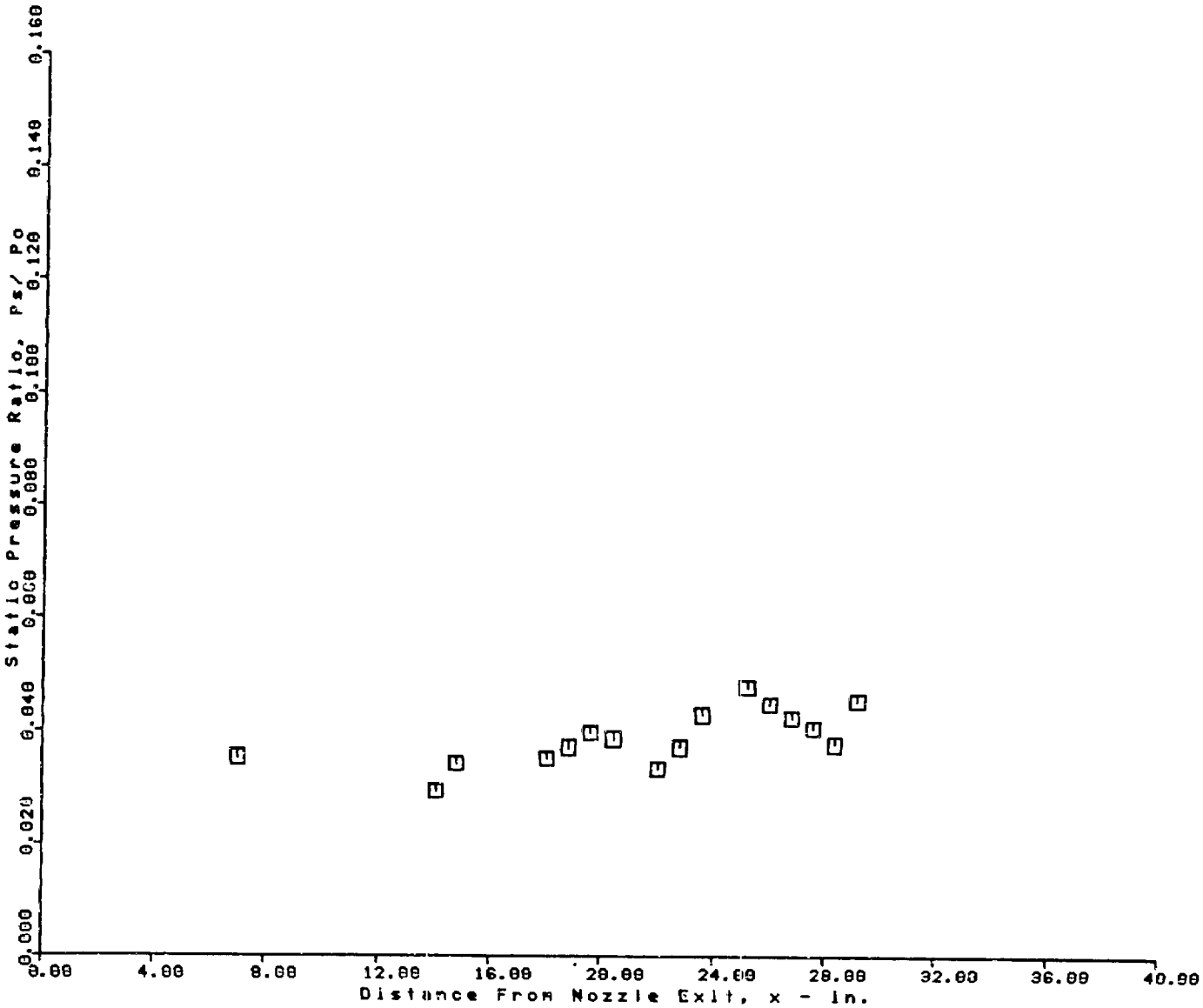

AFS TEST PROGRAM
LOWER SURFACE PRESSURE TAPS
RUN = 70 BURST = 50

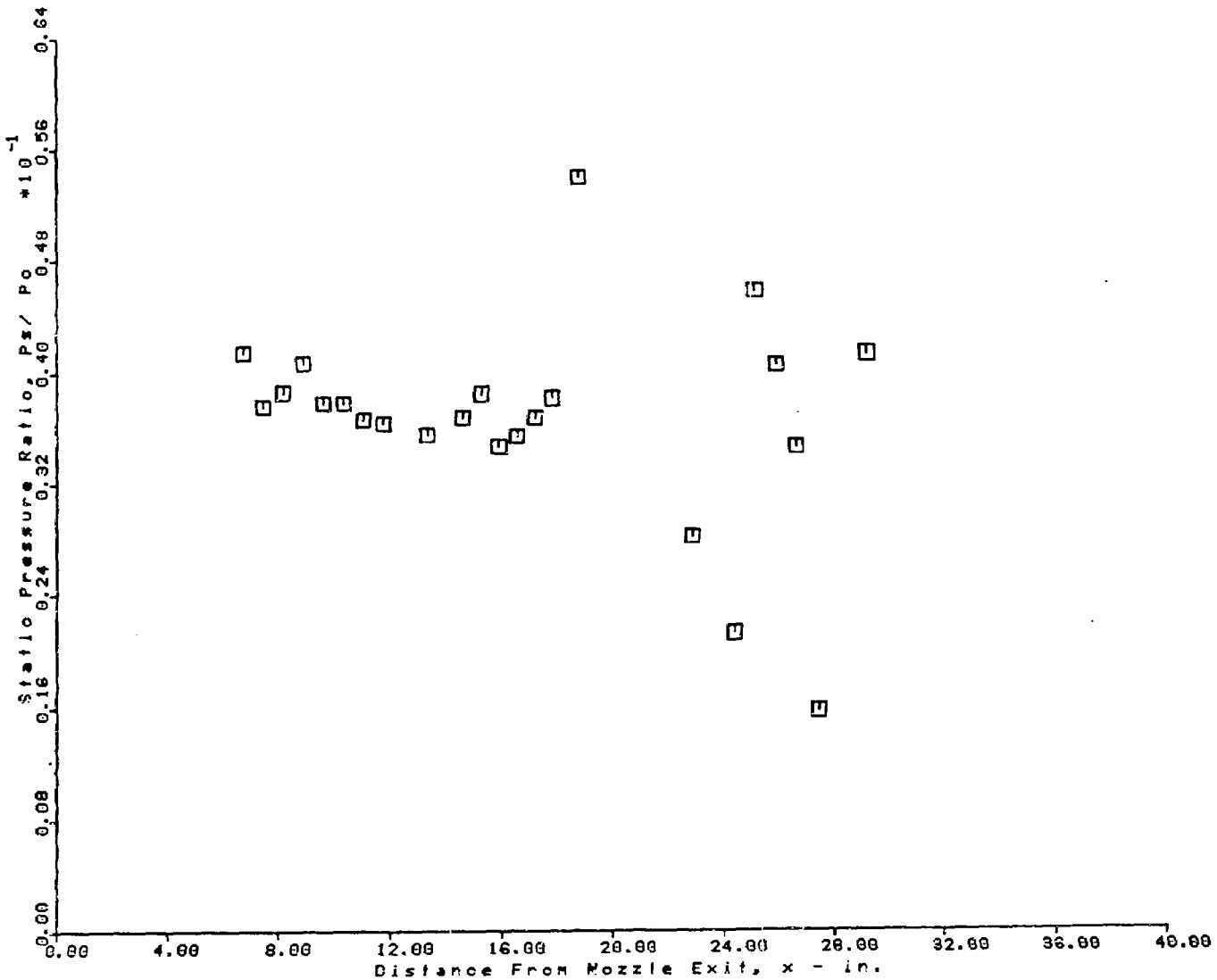

AFS TEST PROGRAM
UPPER SURFACE PRESSURE TAPS
RUN = 70 BURST = 50

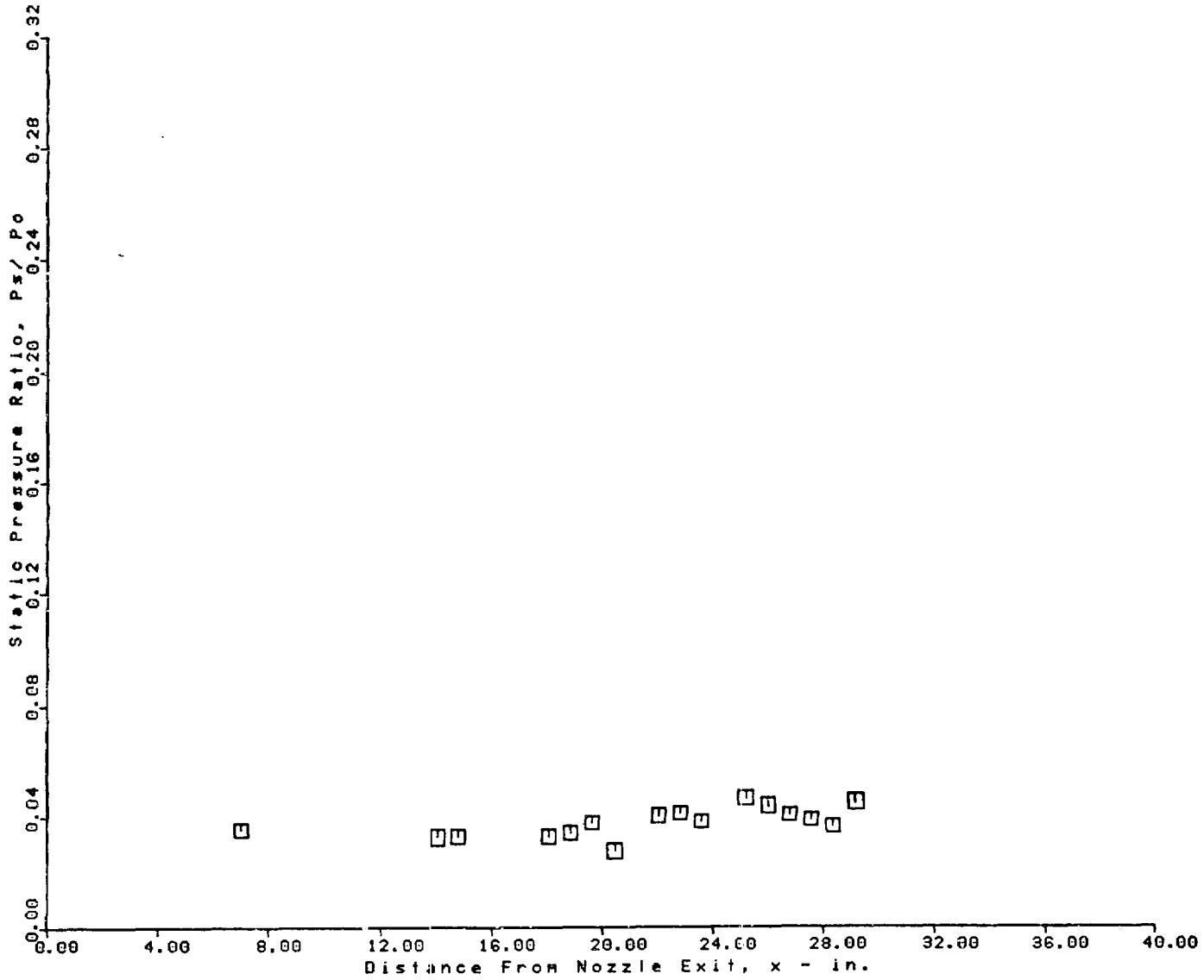

AFS TEST PROGRAM
LOWER SURFACE PRESSURE TAPS
RUN = 71 BURST = 50

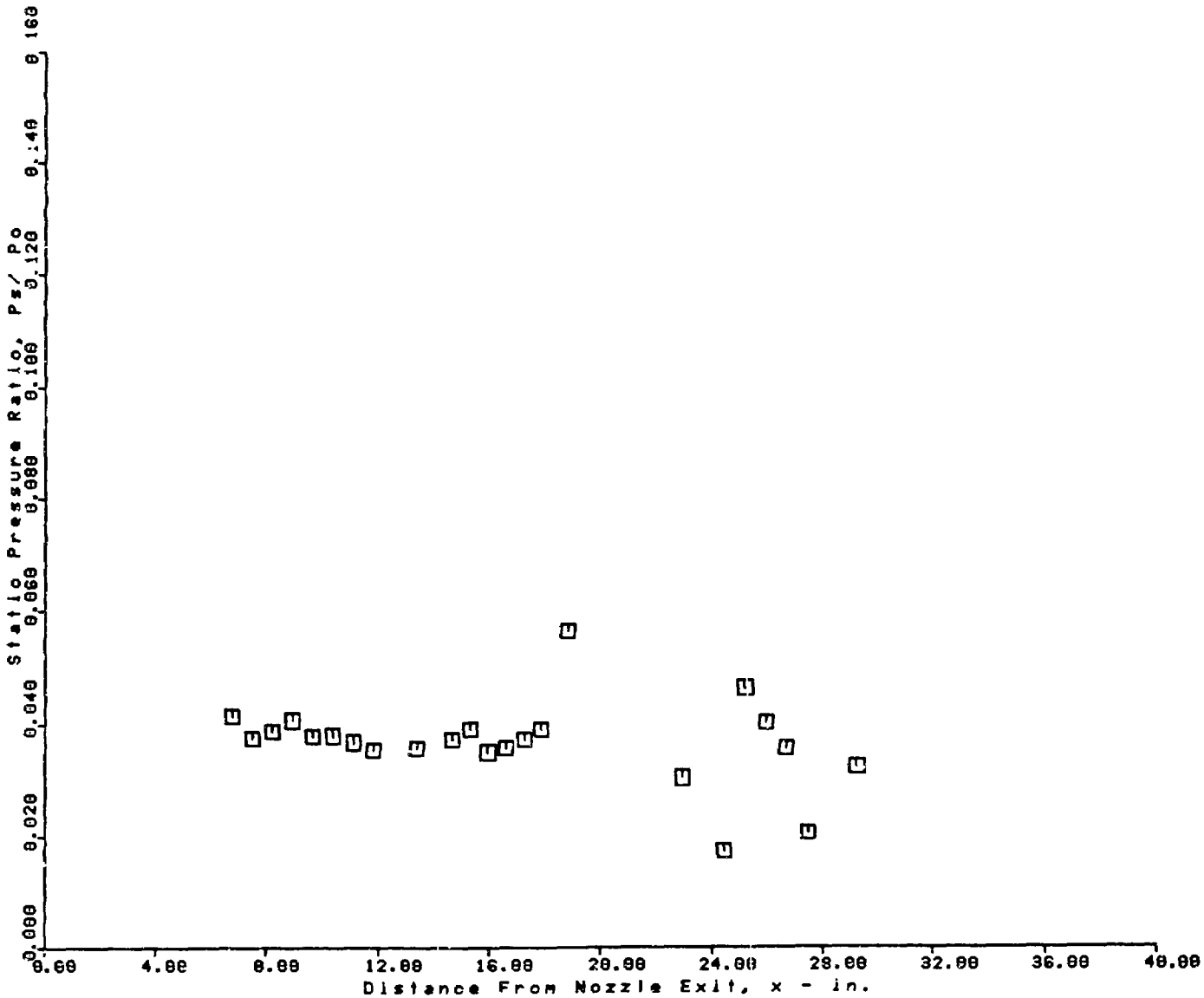

AFS TEST PROGRAM
UPPER SURFACE PRESSURE TAPS
RUN = 71 BURST = 50

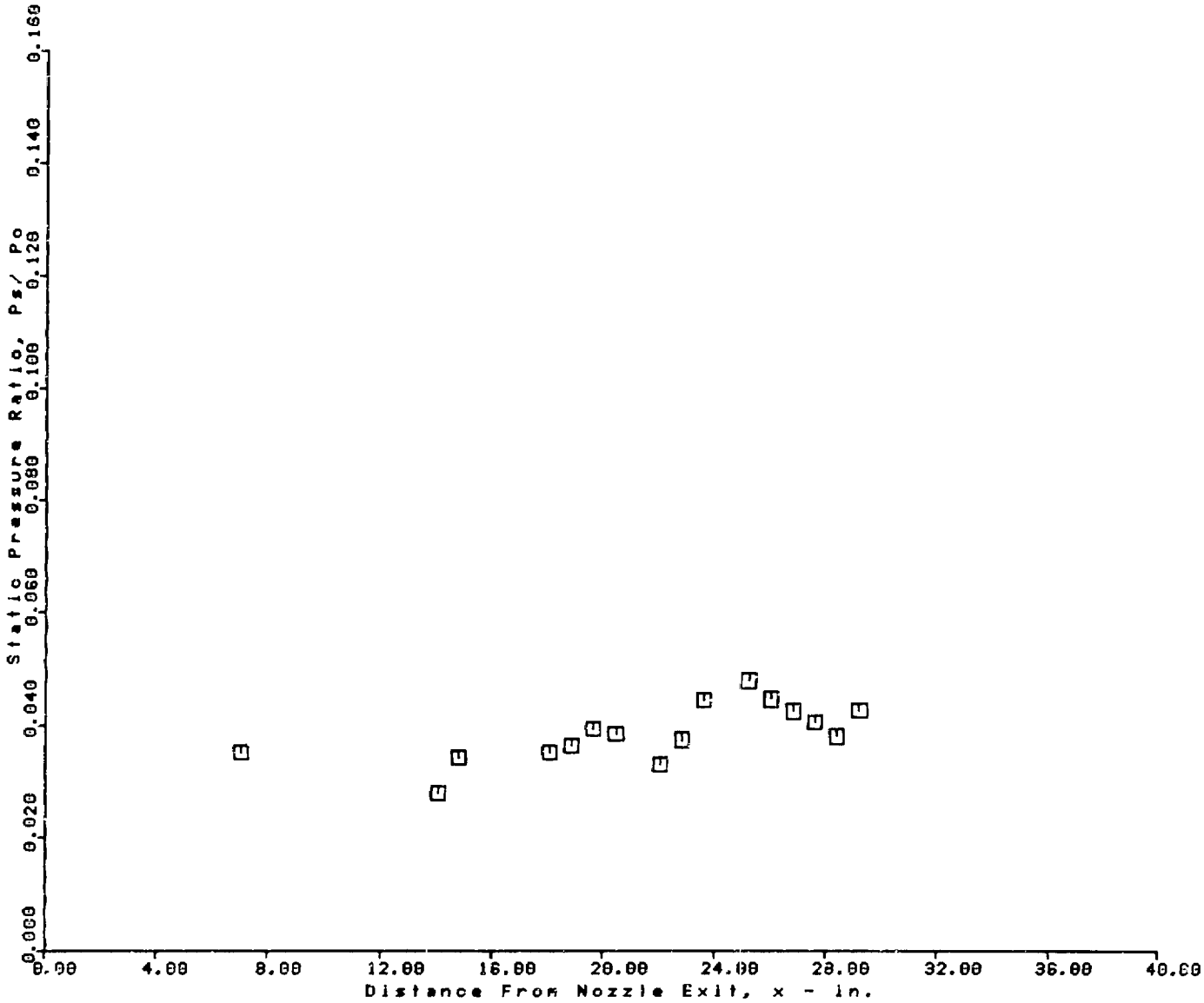

AFS TEST PROGRAM
LOWER SURFACE PRESSURE TAPS
RUN = 72 BURST = 50

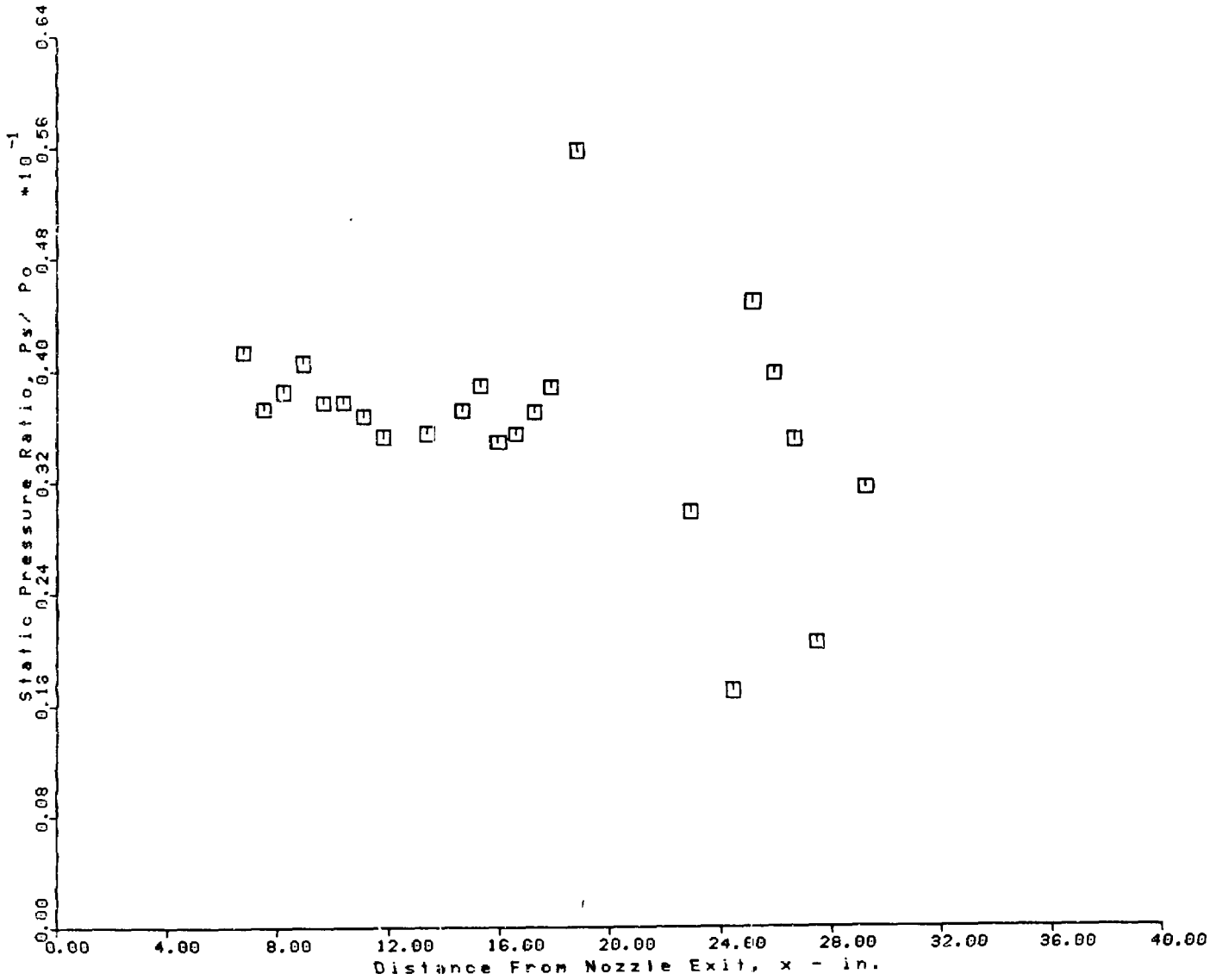

AFS TEST PROGRAM
UPPER SURFACE PRESSURE TAPS
RUN = 72 BURST = 50

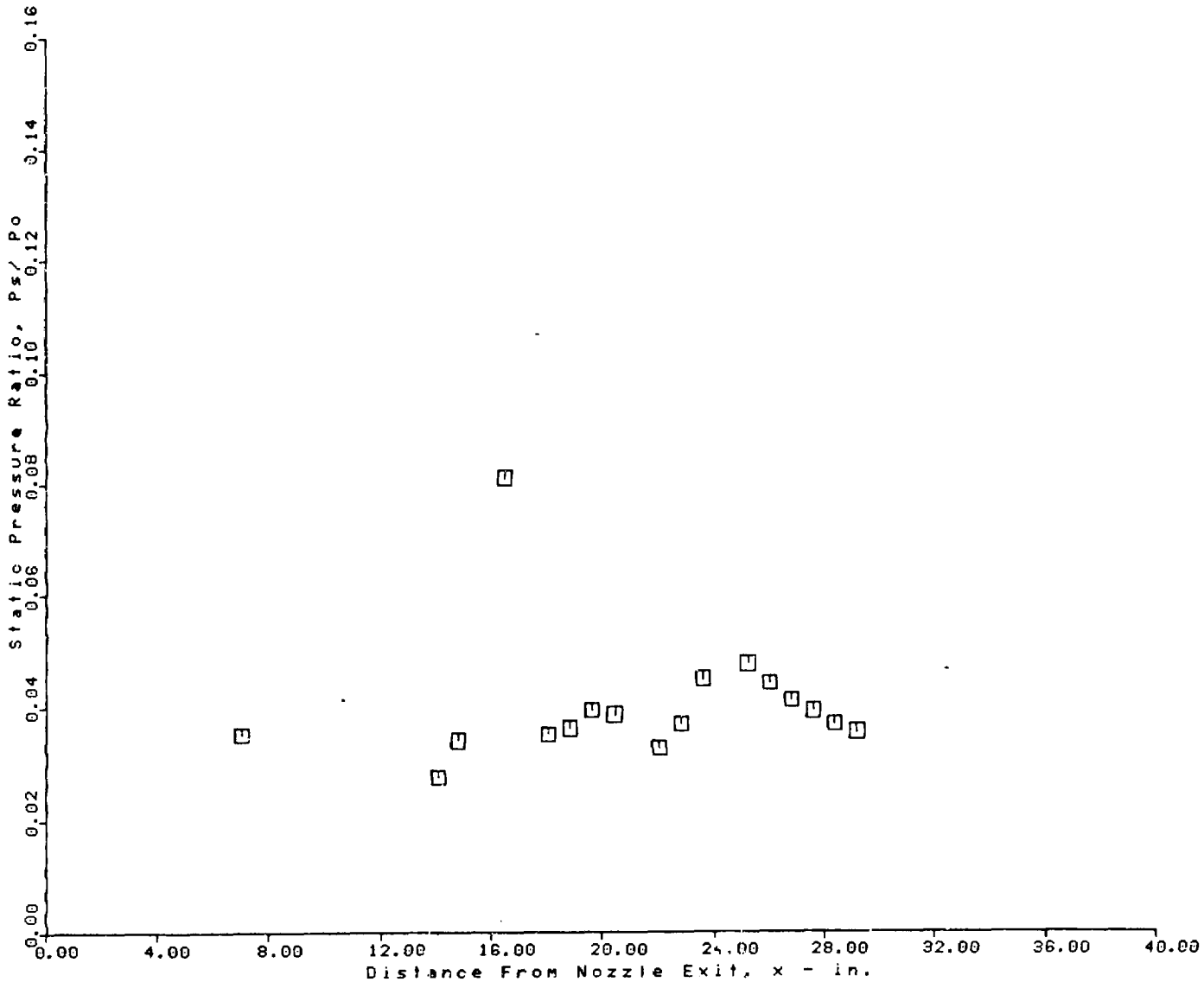

AFS TEST PROGRAM
LOWER SURFACE PRESSURE TAPS
RUN = 74 BURST = 50

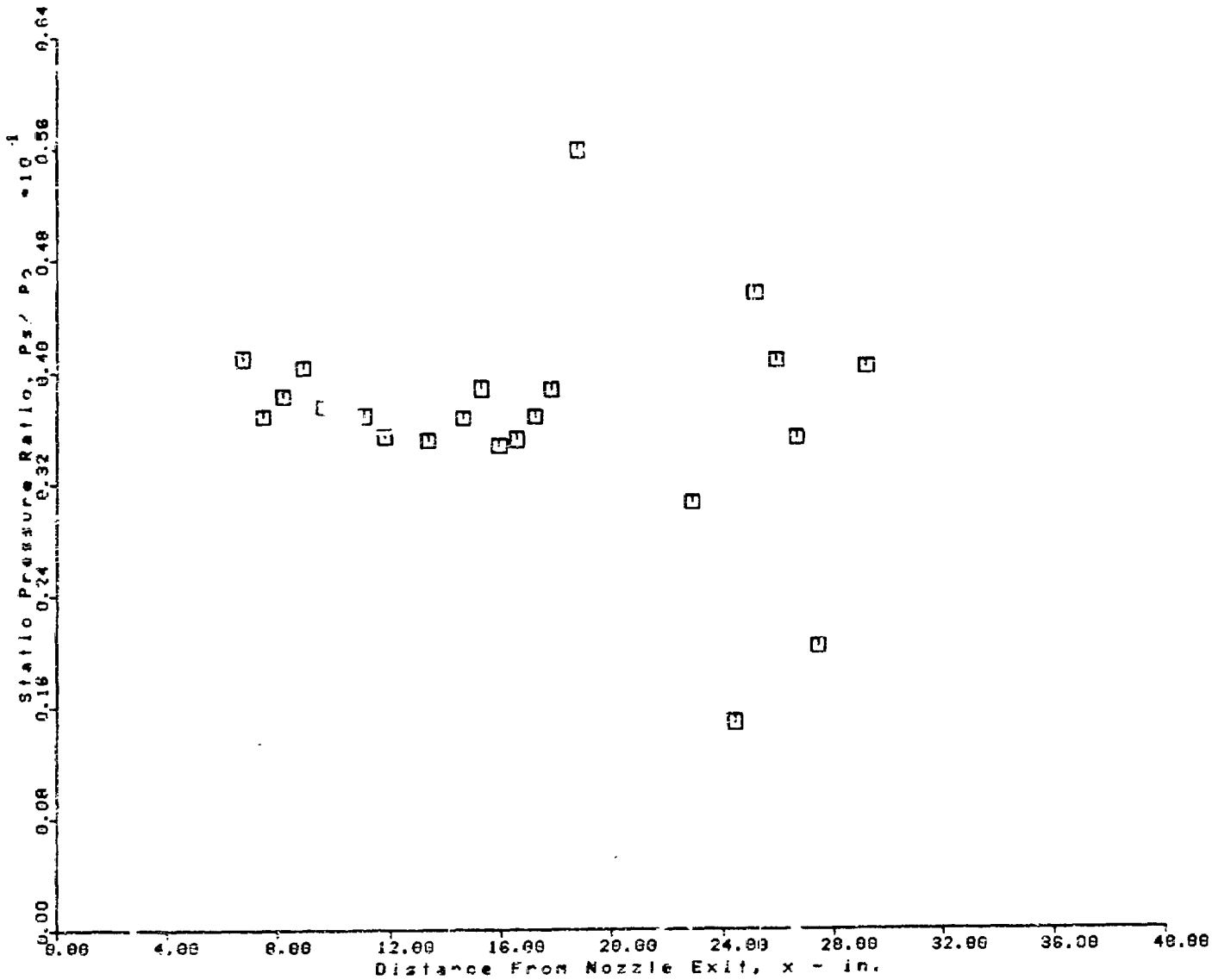

AFS TEST PROGRAM
UPPER SURFACE PRESSURE TAPS
RUN = 74 BURST = 50

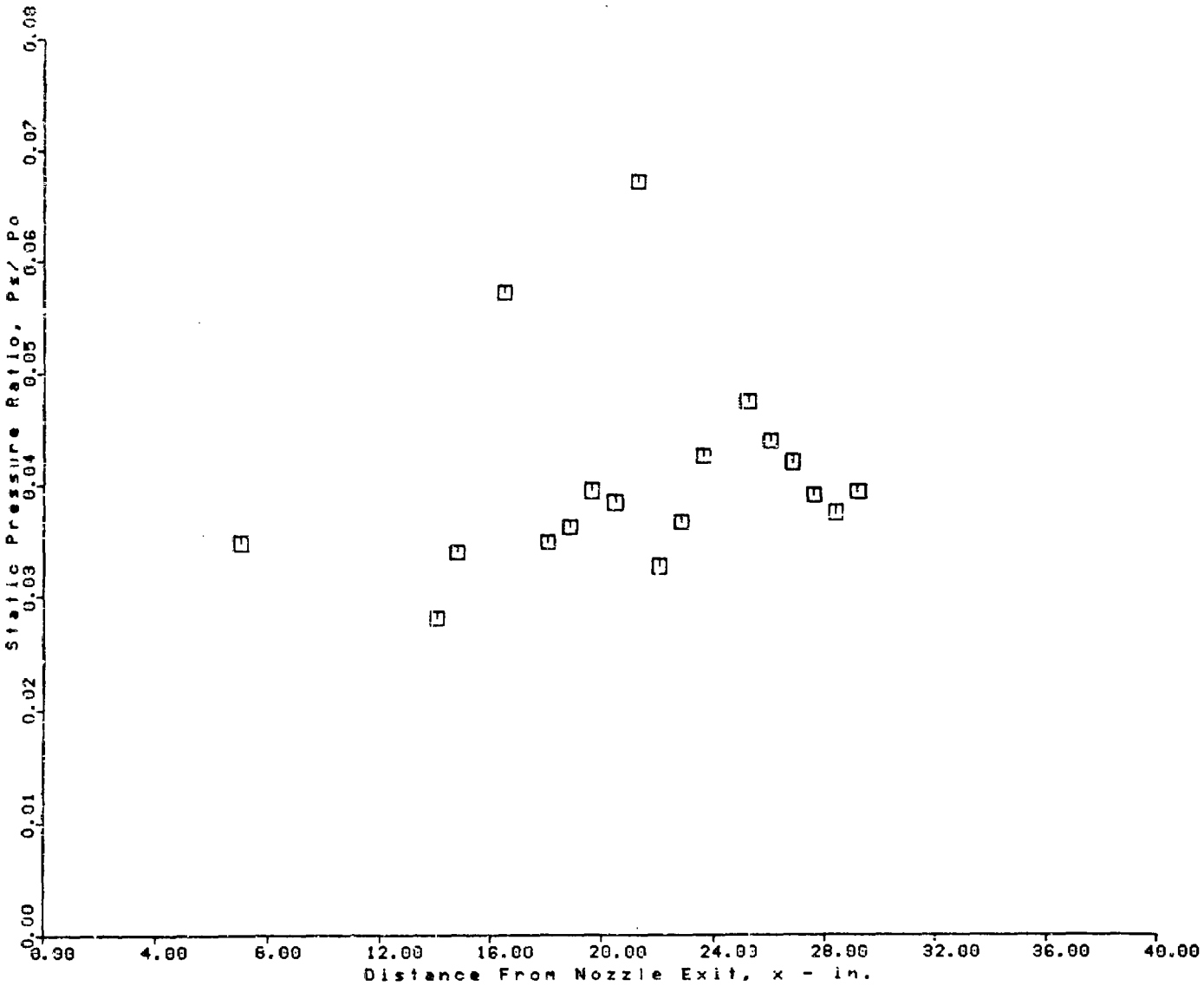

AFS TEST PROGRAM
LOWER SURFACE PRESSURE TAPS
RUN = 77 BURST = 50

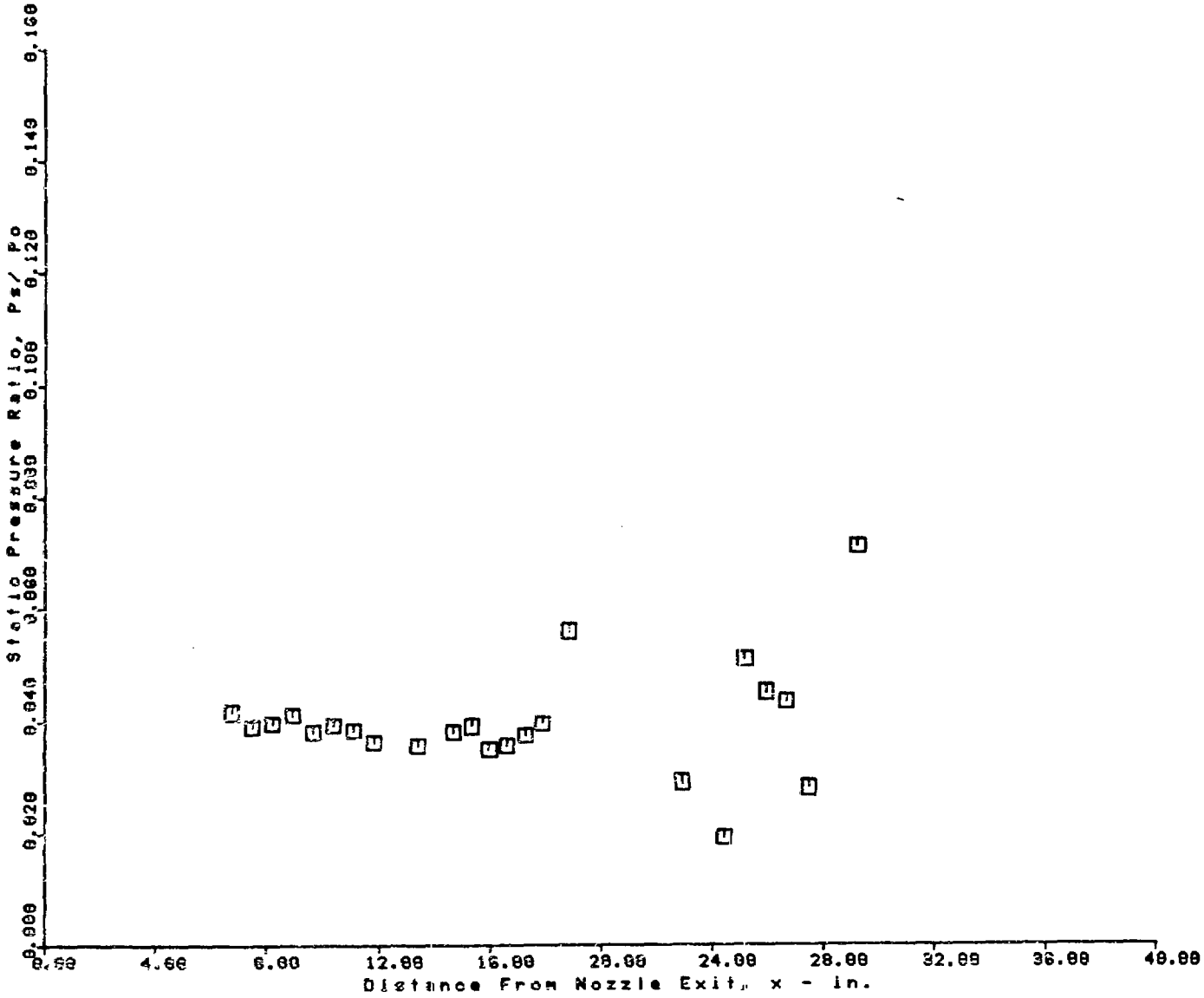

AFS TEST PROGRAM
UPPER SURFACE PRESSURE TAPS
RUN = 77 BURST = 58

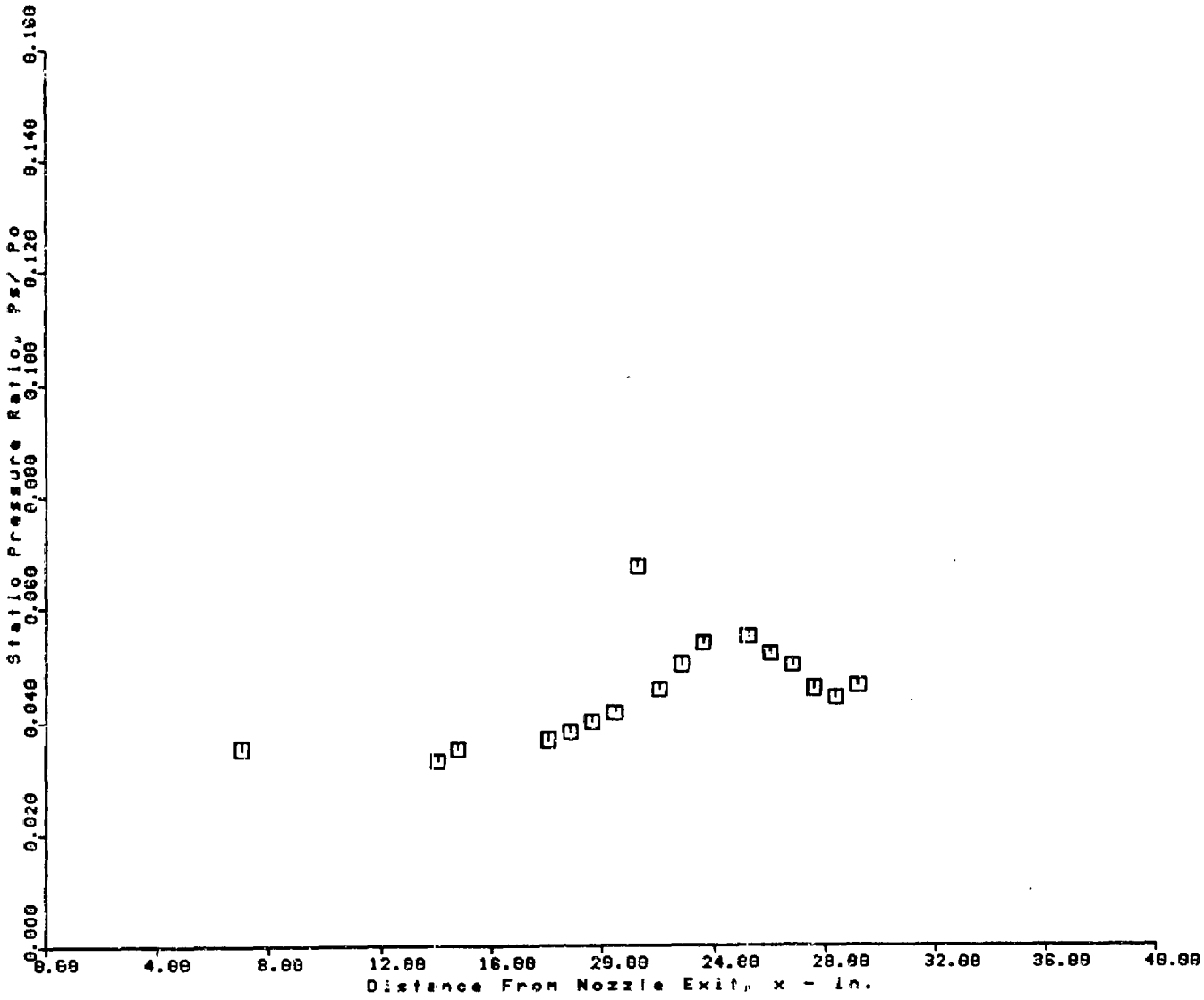

AFS TEST PROGRAM
LOWER SURFACE PRESSURE TAPS
RUN = 78 BURST = 58

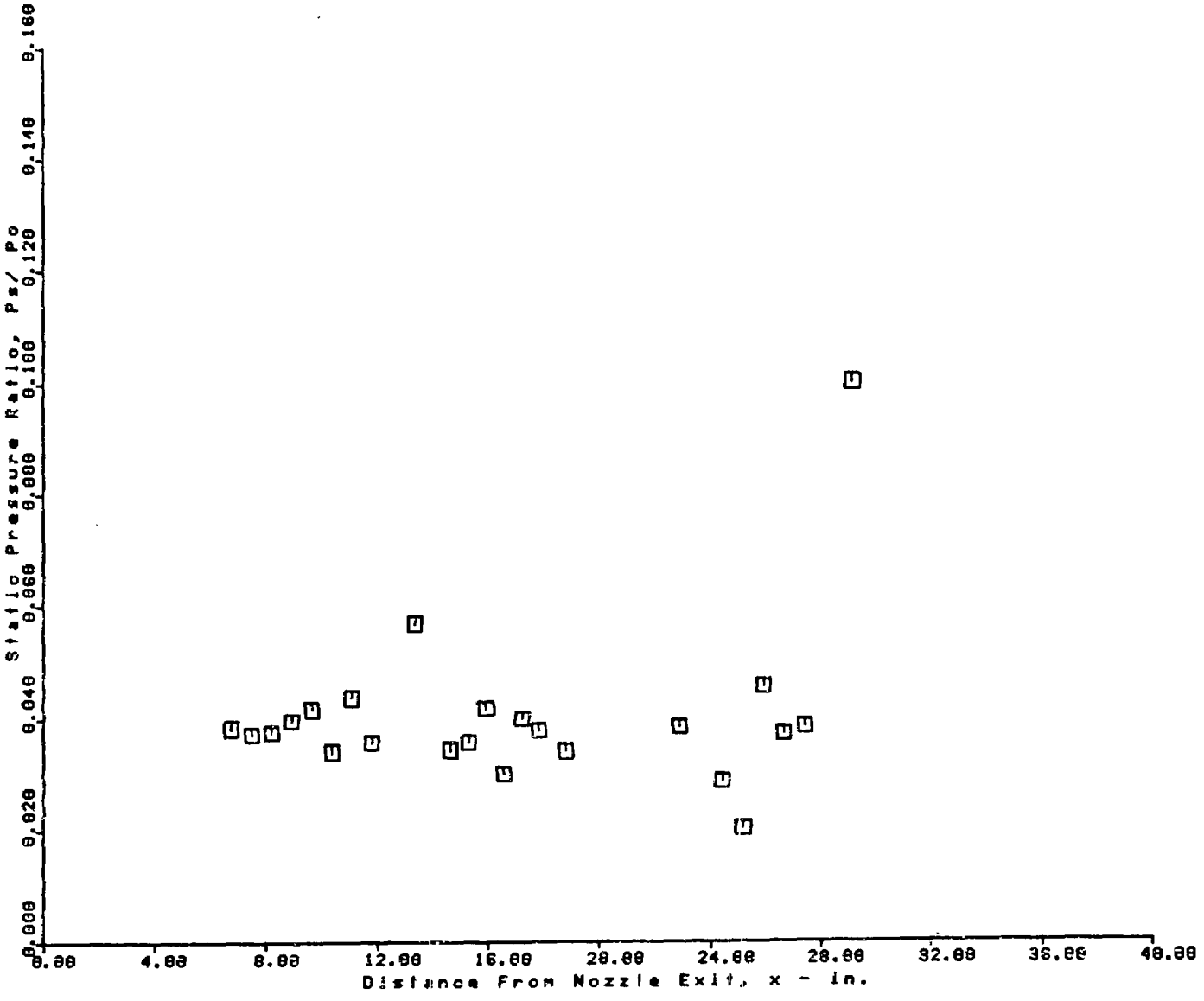

AFS TEST PROGRAM
UPPER SURFACE PRESSURE TAPS
RUN = 78 BURST = 58

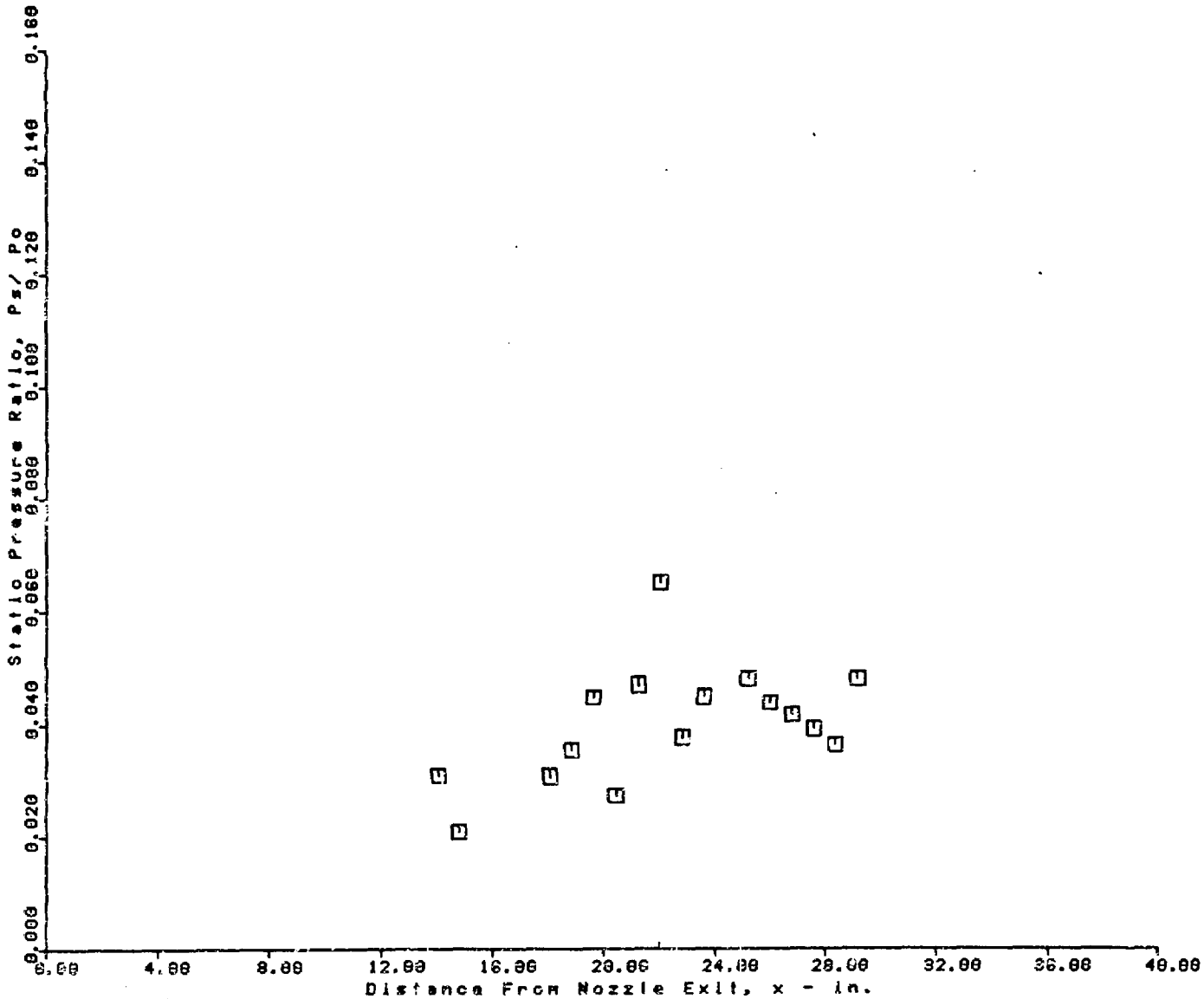

AFS TEST PROGRAM
LOWER SURFACE PRESSURE TAPS
RUN = 81 BURST = 50

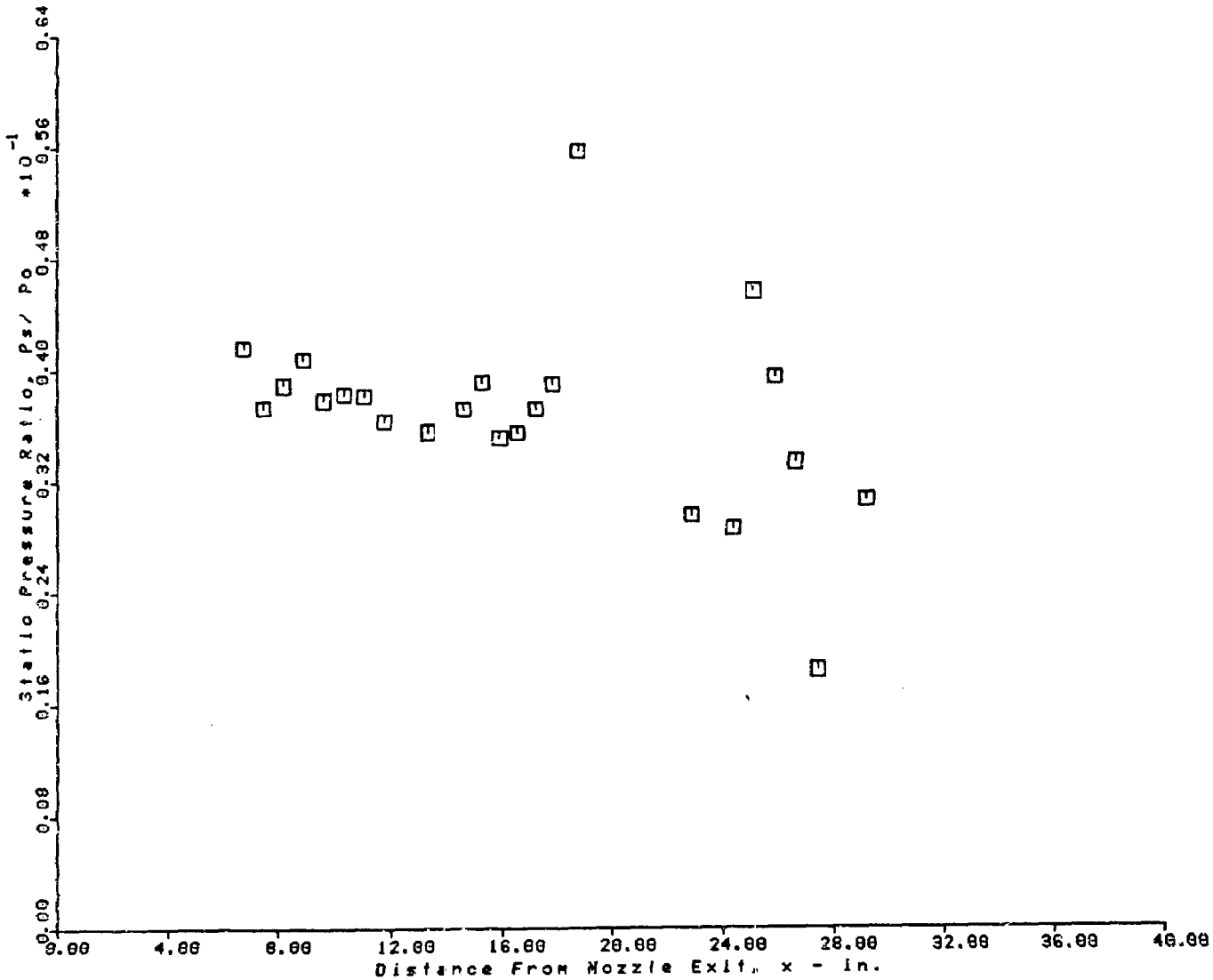

AFS TEST PROGRAM
UPPER SURFACE PRESSURE TAPS
RUN = 81 BURST = 50

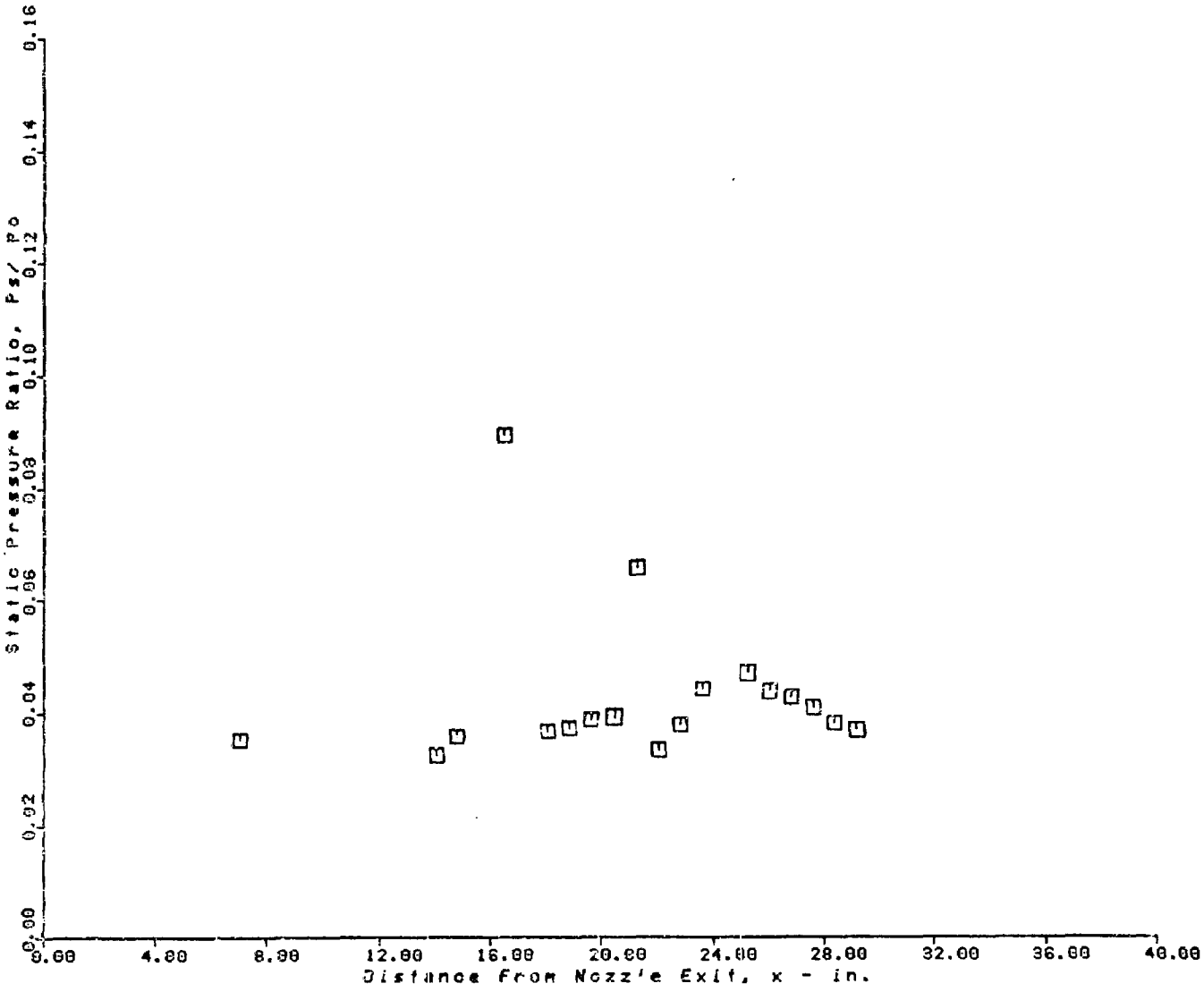

AFS TEST PROGRAM
UPPER SURFACE PRESSURE TAPS
RUN = 82 BURST = 50

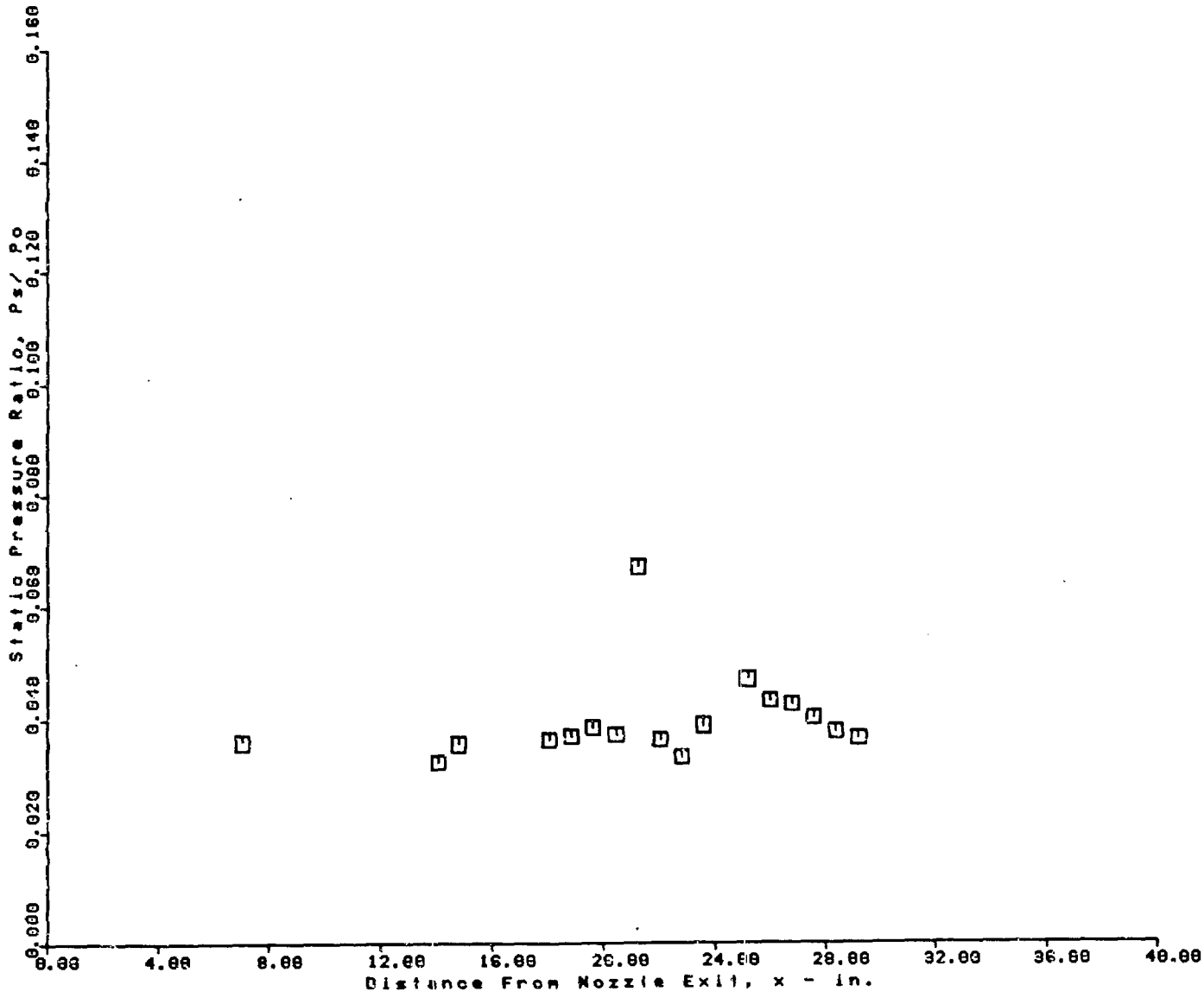

AFS TEST PROGRAM
LOWER SURFACE PRESSURE TAPS
RUN = 82 BURST = 50

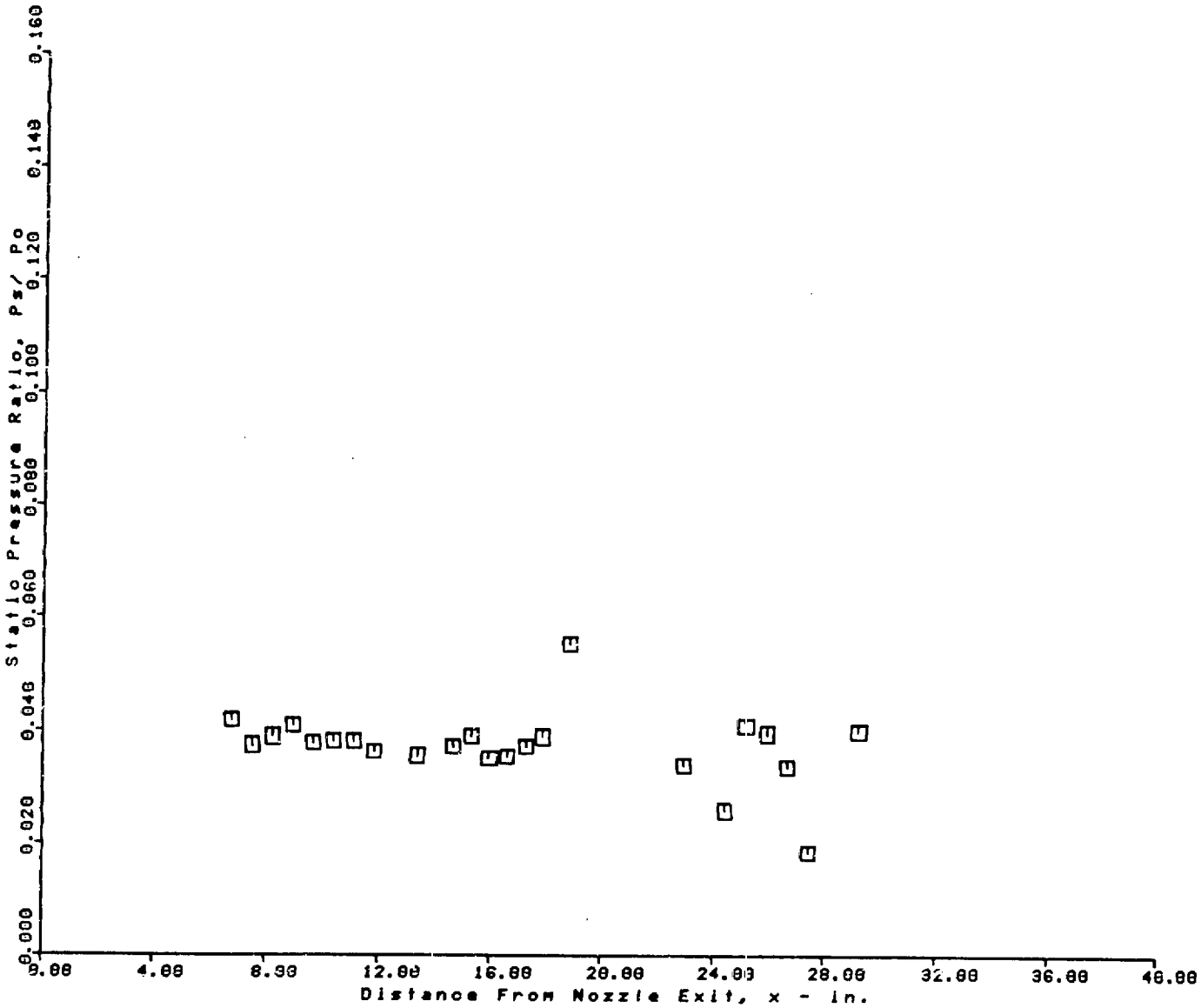

AFS TEST PROGRAM
LOWER SURFACE PRESSURE TAPS
RUN = 84 BURST = 50

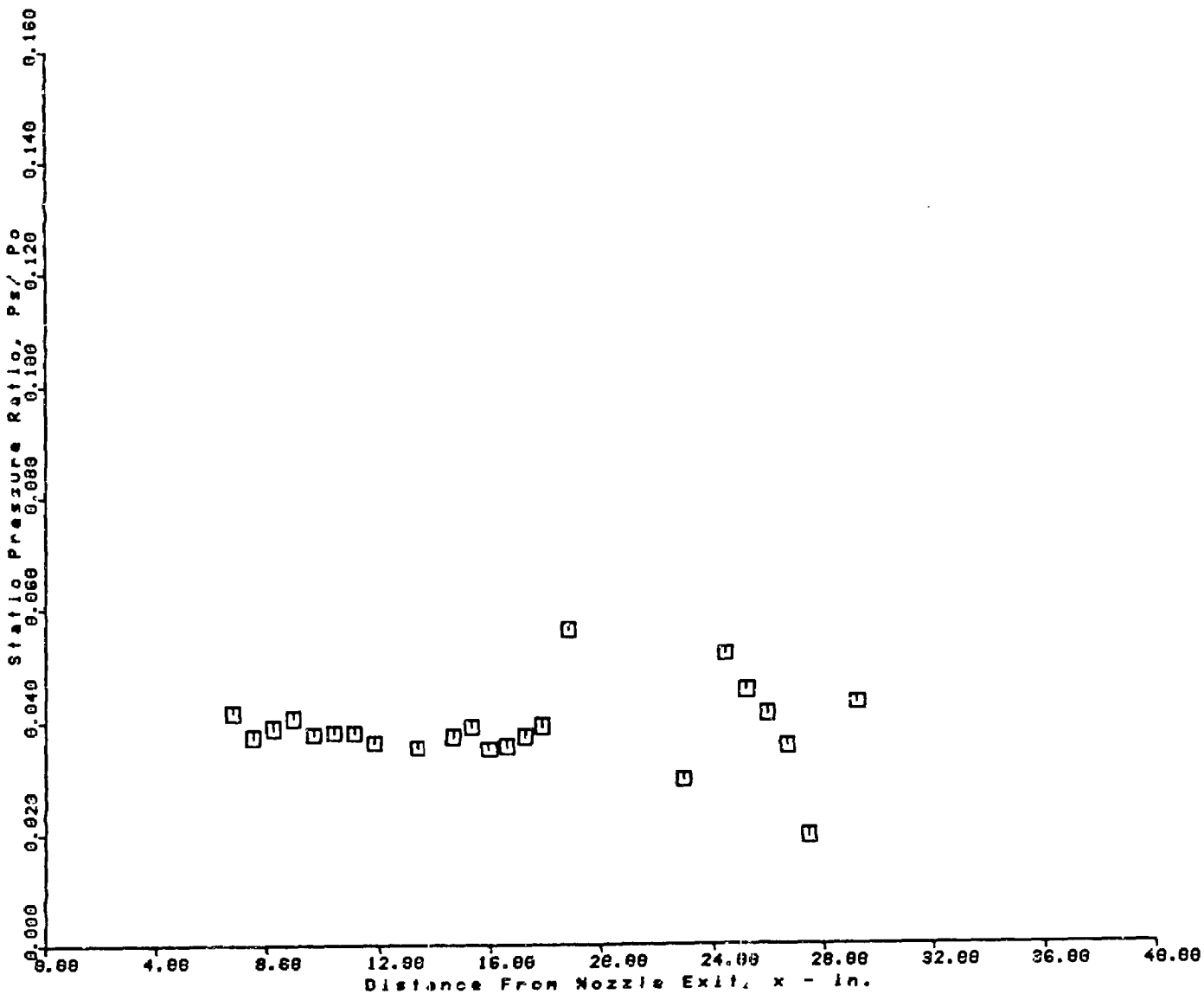

RFS TEST PROGRAM
UPPER SURFACE PRESSURE TAPS
RUN = 84 BURST = 58

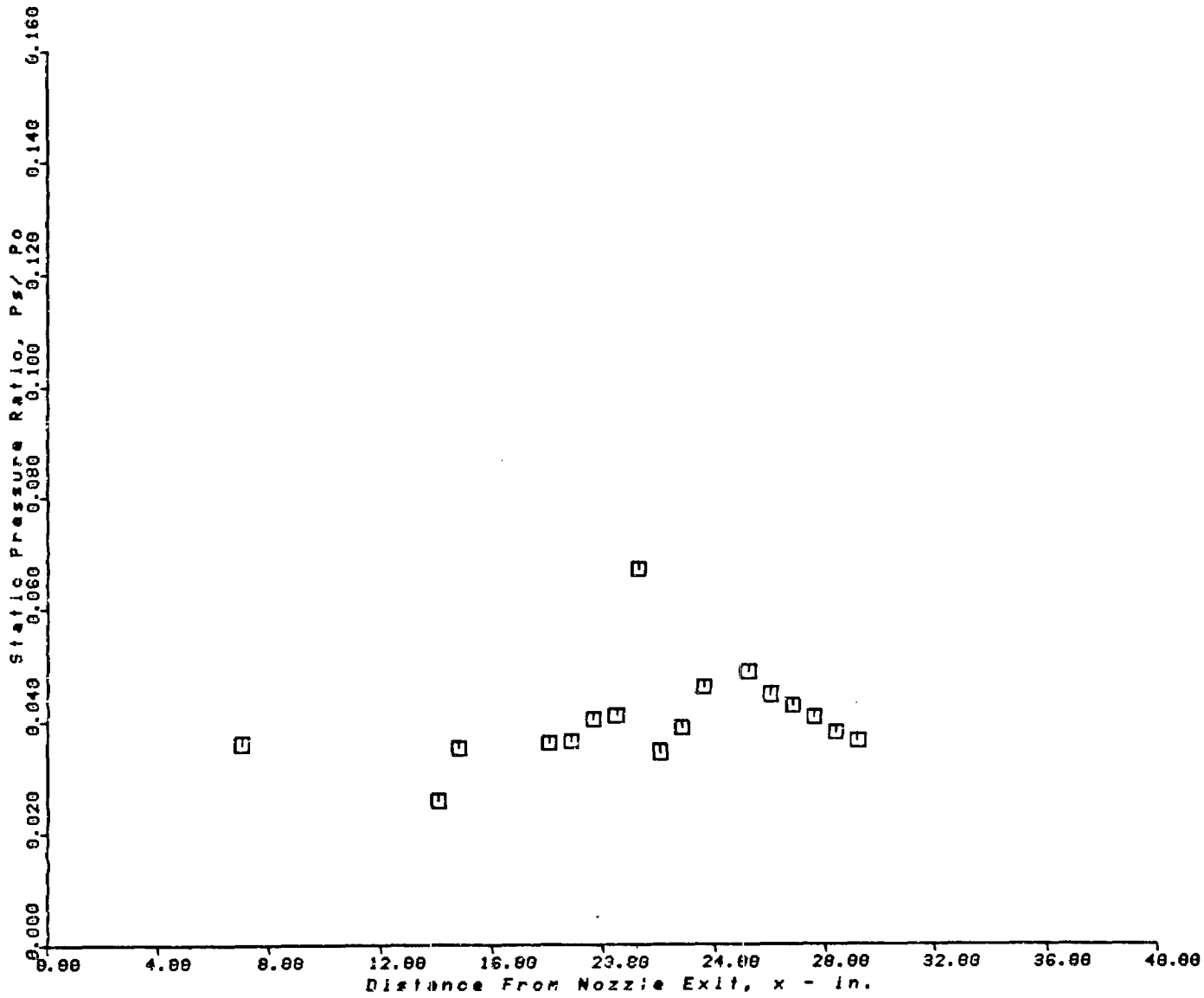

AFS TEST PROGRAM
LOWER SURFACE PRESSURE TAPS
RUN = 88 BURST = 58

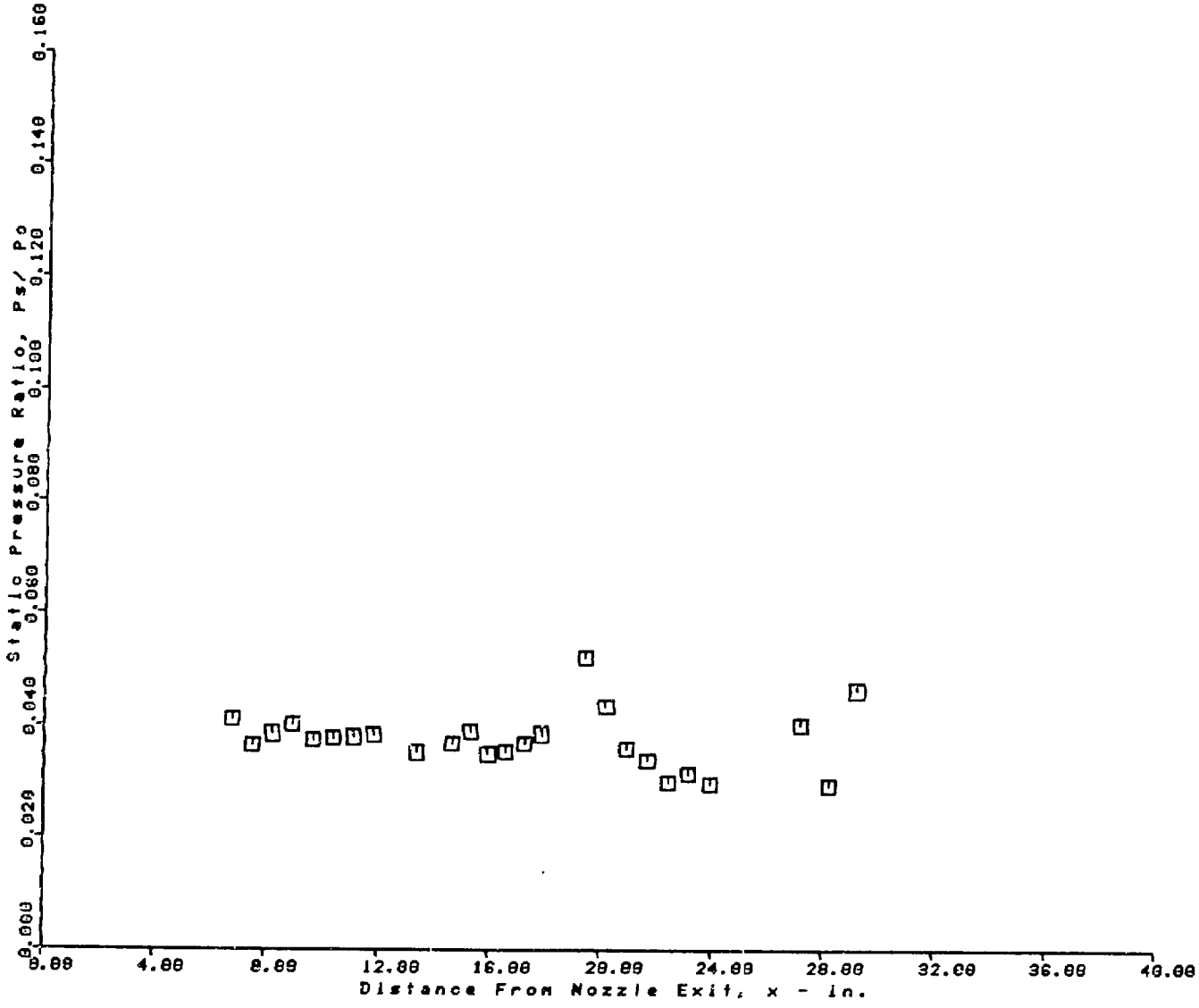

AFS TEST PROGRAM
UPPER SURFACE PRESSURE TAPS
RUN = 88 BURST = 50

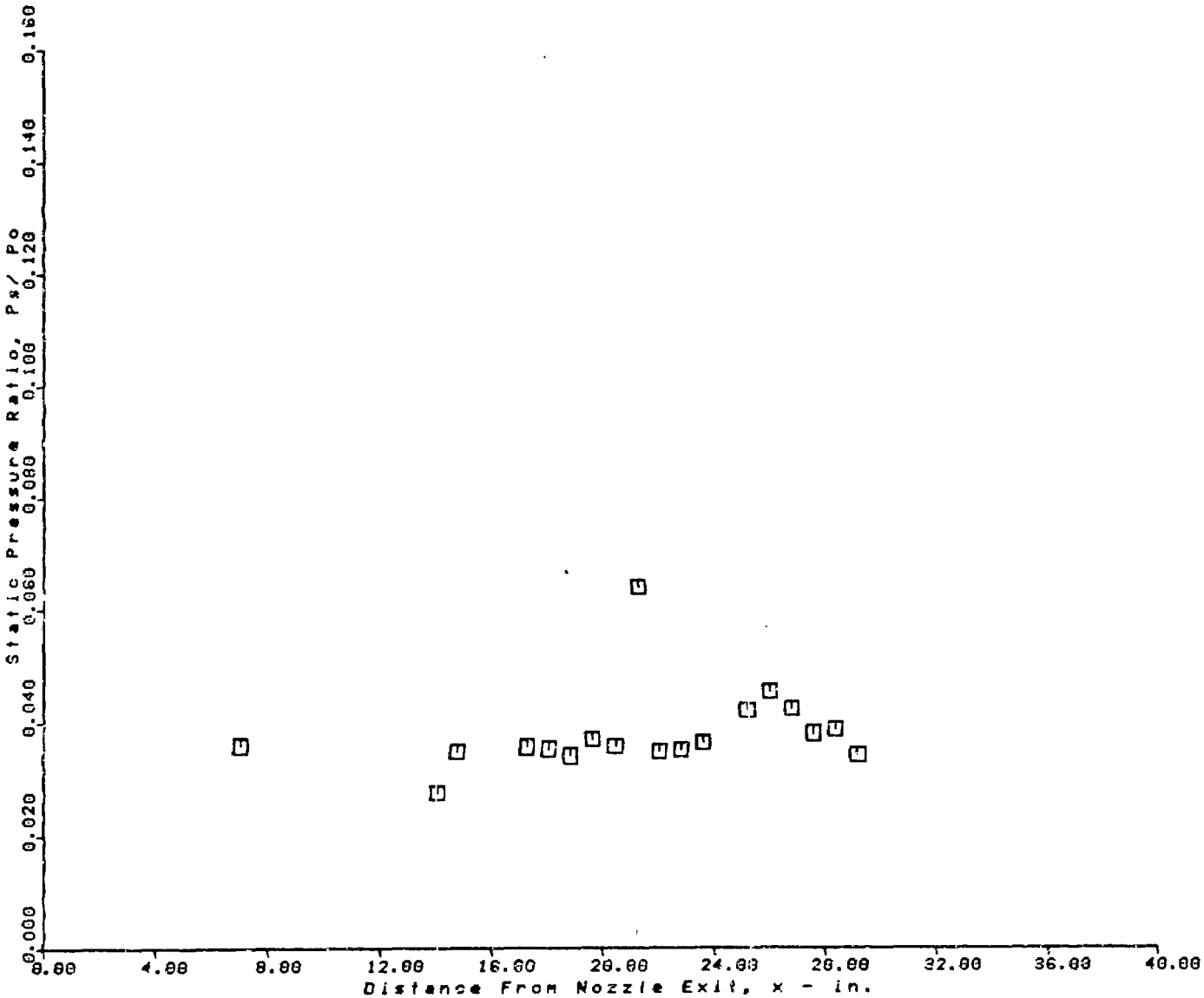

AFS TEST PROGRAM
LOWER SURFACE PRESSURE TAPS
RUN = 89 BURST = 58

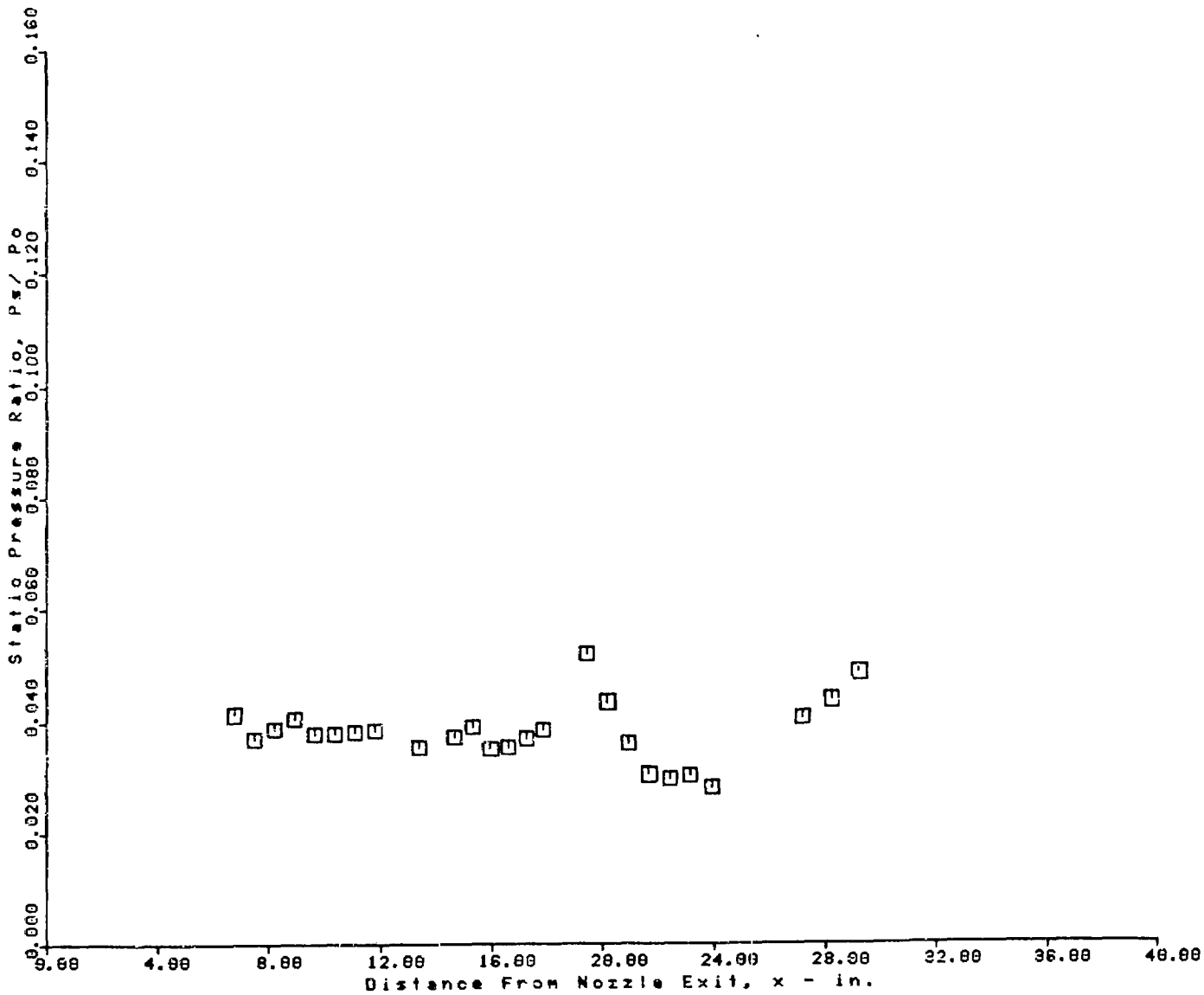

AFS TEST PROGRAM
UPPER SURFACE PRESSURE TAPS
RUN = 89 BURST = 58

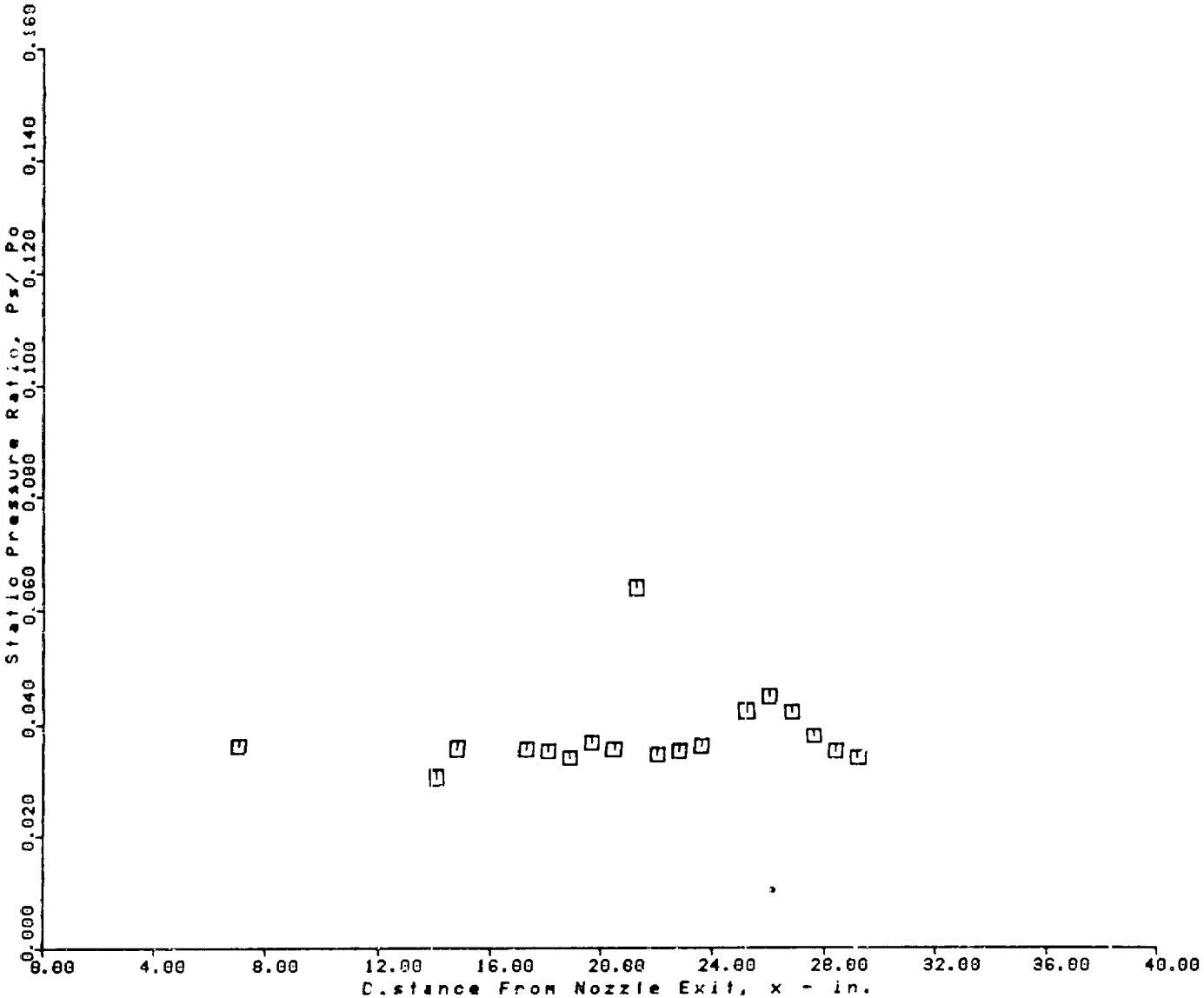

AFS TEST PROGRAM
UPPER SURFACE PRESSURE TAPS
RUN = 90 BURST = 50

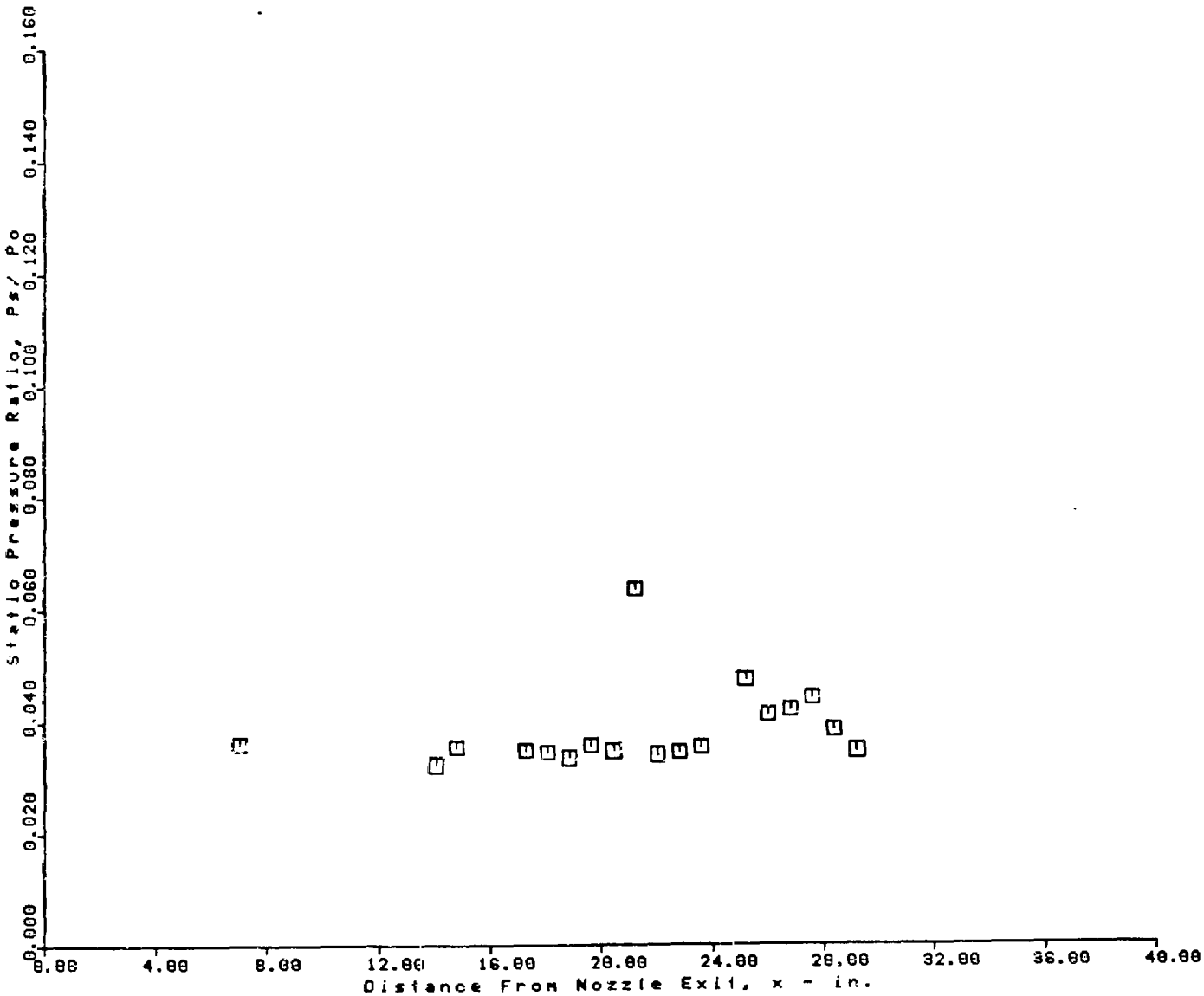

AFS TEST PROGRAM
LOWER SURFACE PRESSURE TAPS
RUN = 98 BURST = 58

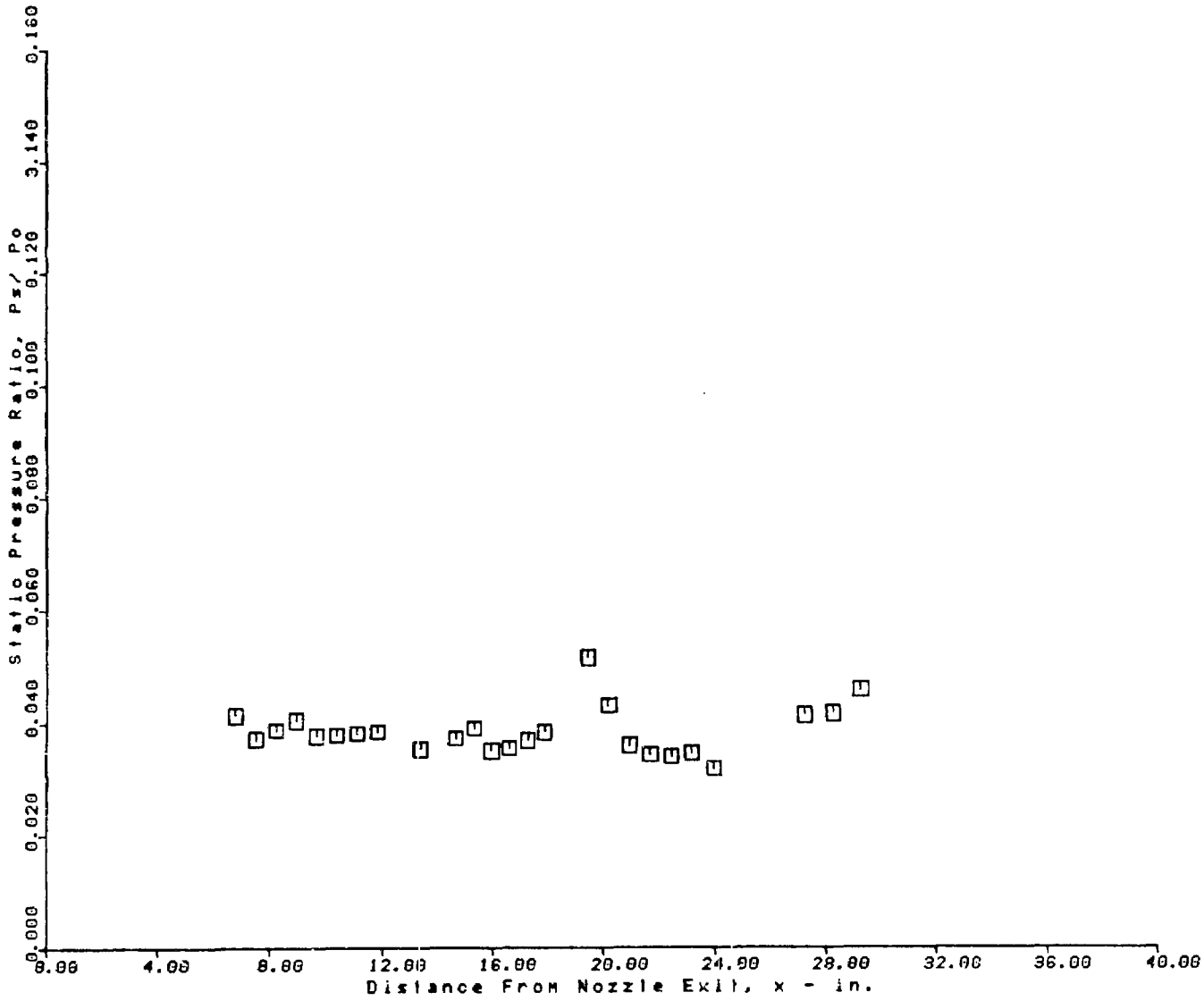

AFS TEST PROGRAM
LOWER SURFACE PRESSURE TAPS
RUN = 92 BURST = 50

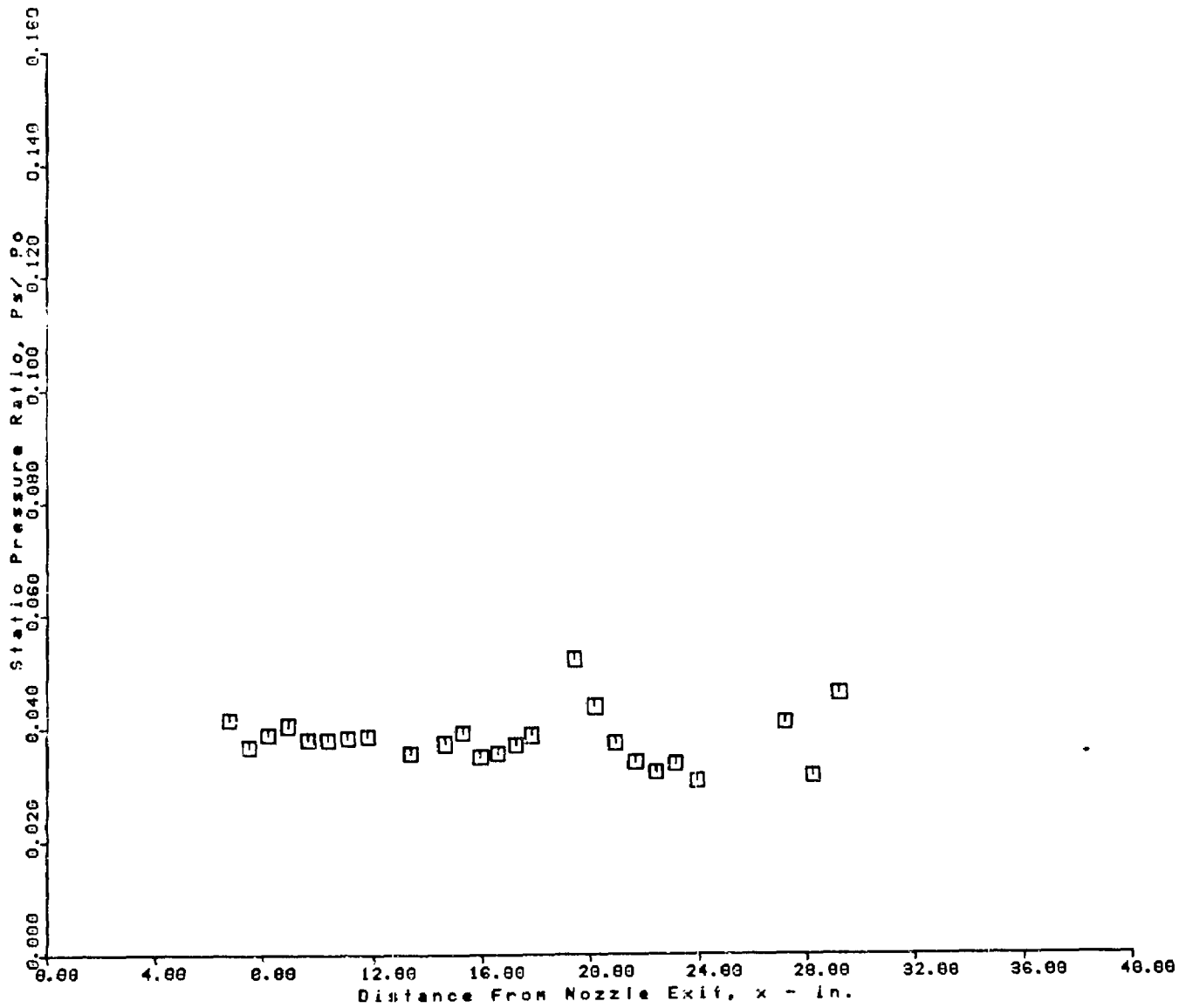

AFS TEST PROGRAM
UPPER SURFACE PRESSURE TAPS
RUN = 92 BURST = 50

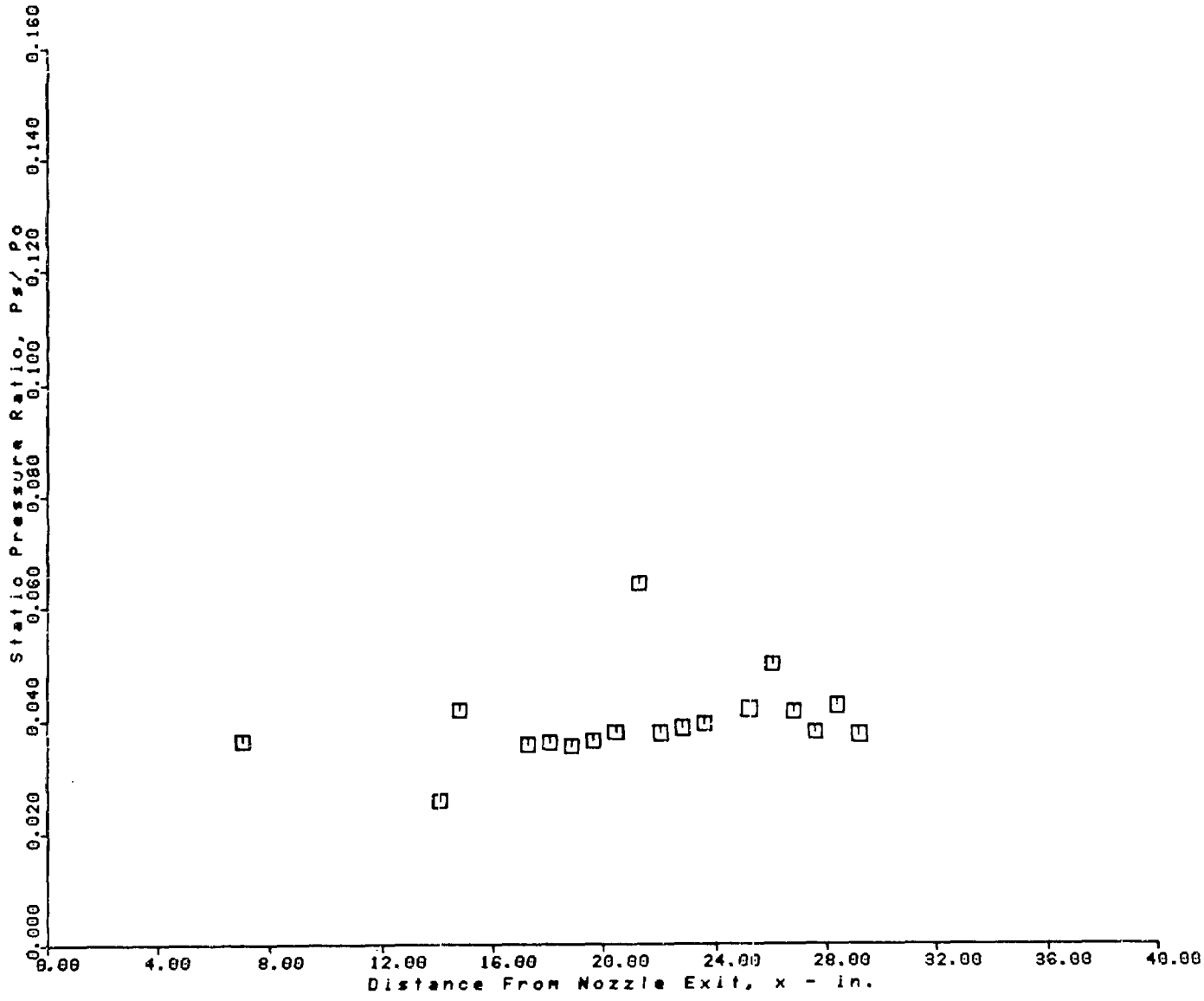

AFS TEST PROGRAM
LOWER SURFACE PRESSURE TAPS
RUN = 93 BURST = 50

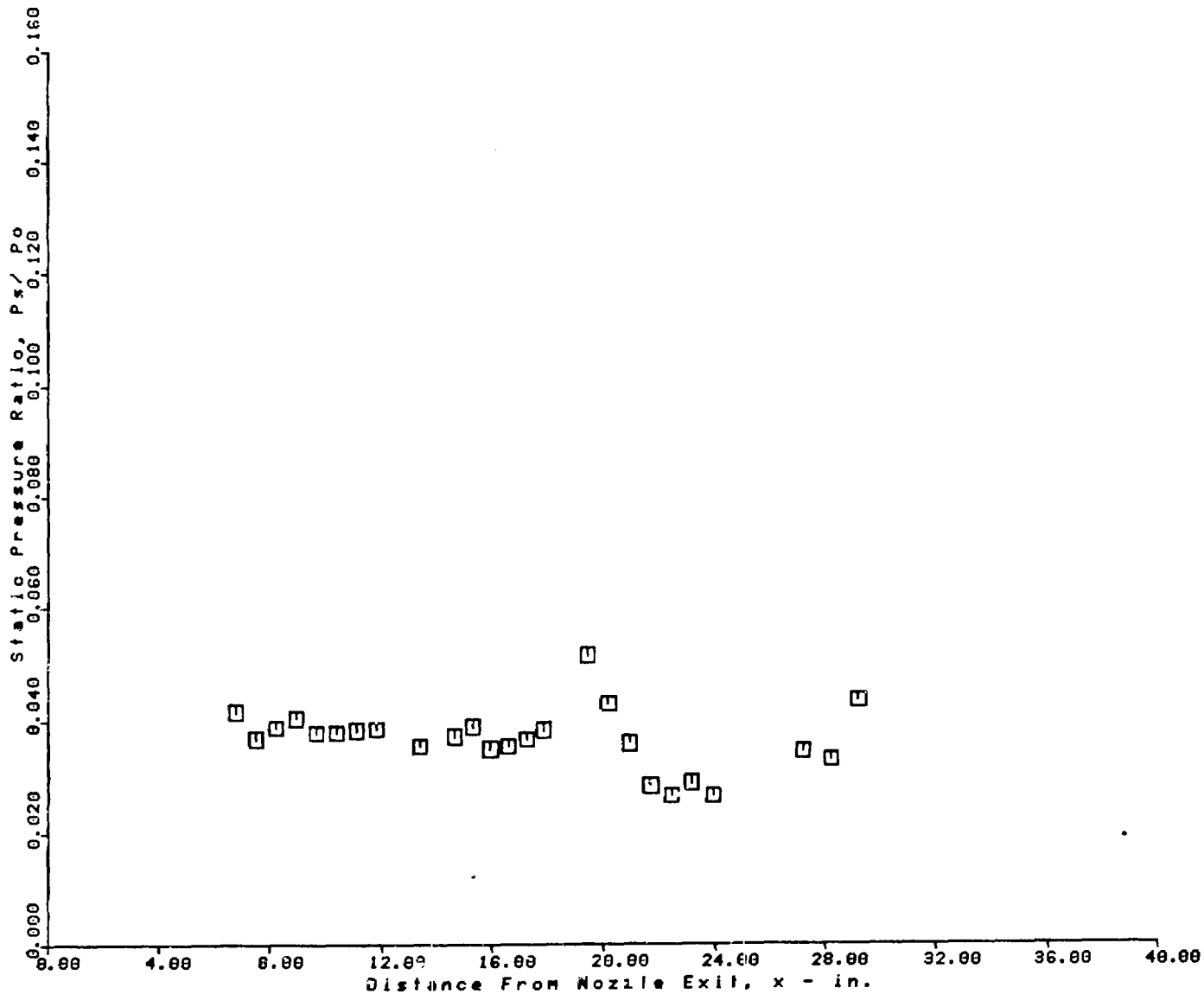

AFS TEST PROGRAM
UPPER SURFACE PRESSURE TAPS
RUN = 93 BURST = 58

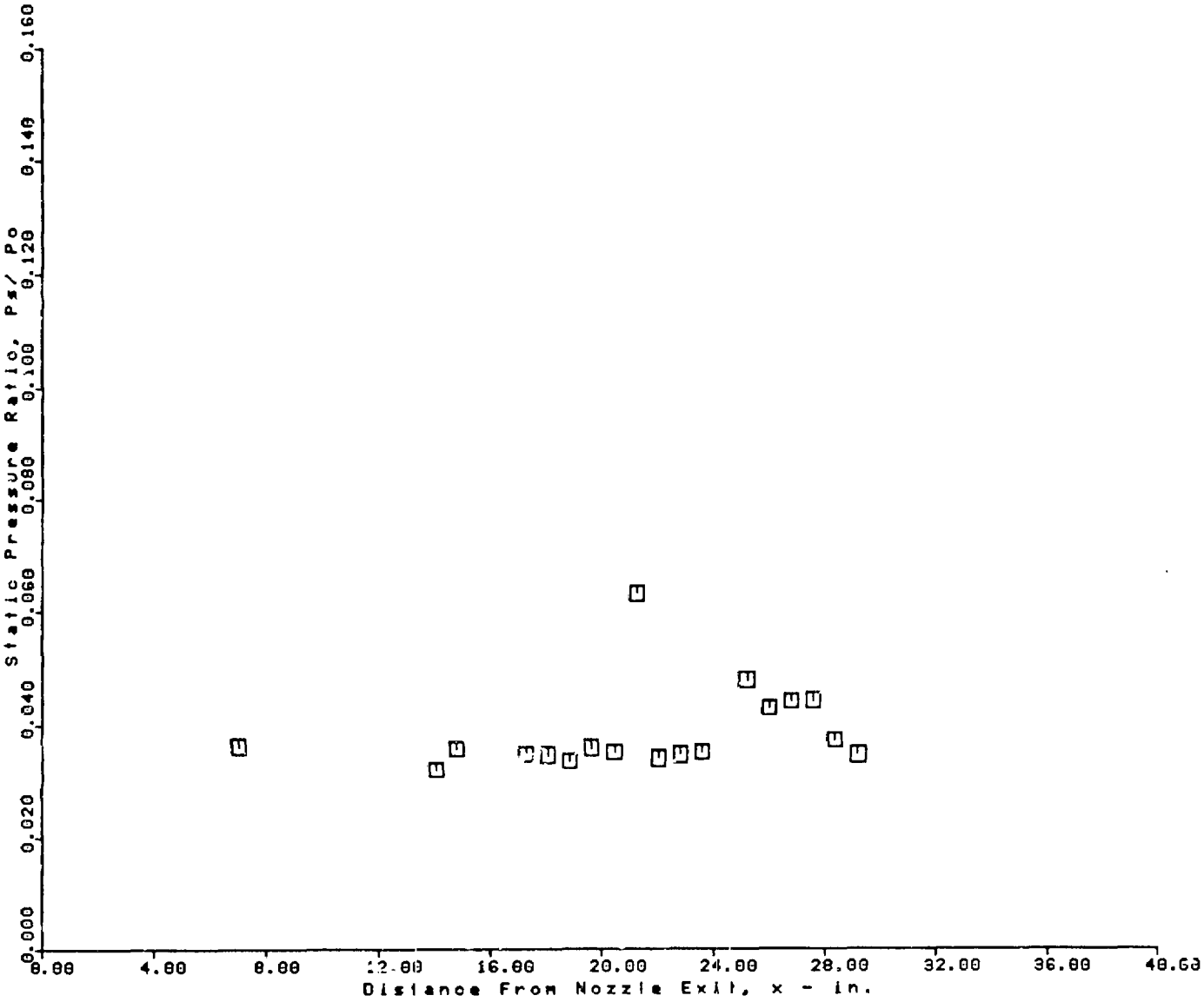

AFS TEST PROGRAM
LOWER SURFACE PRESSURE TAPS
RUN = 94 BURST = 50

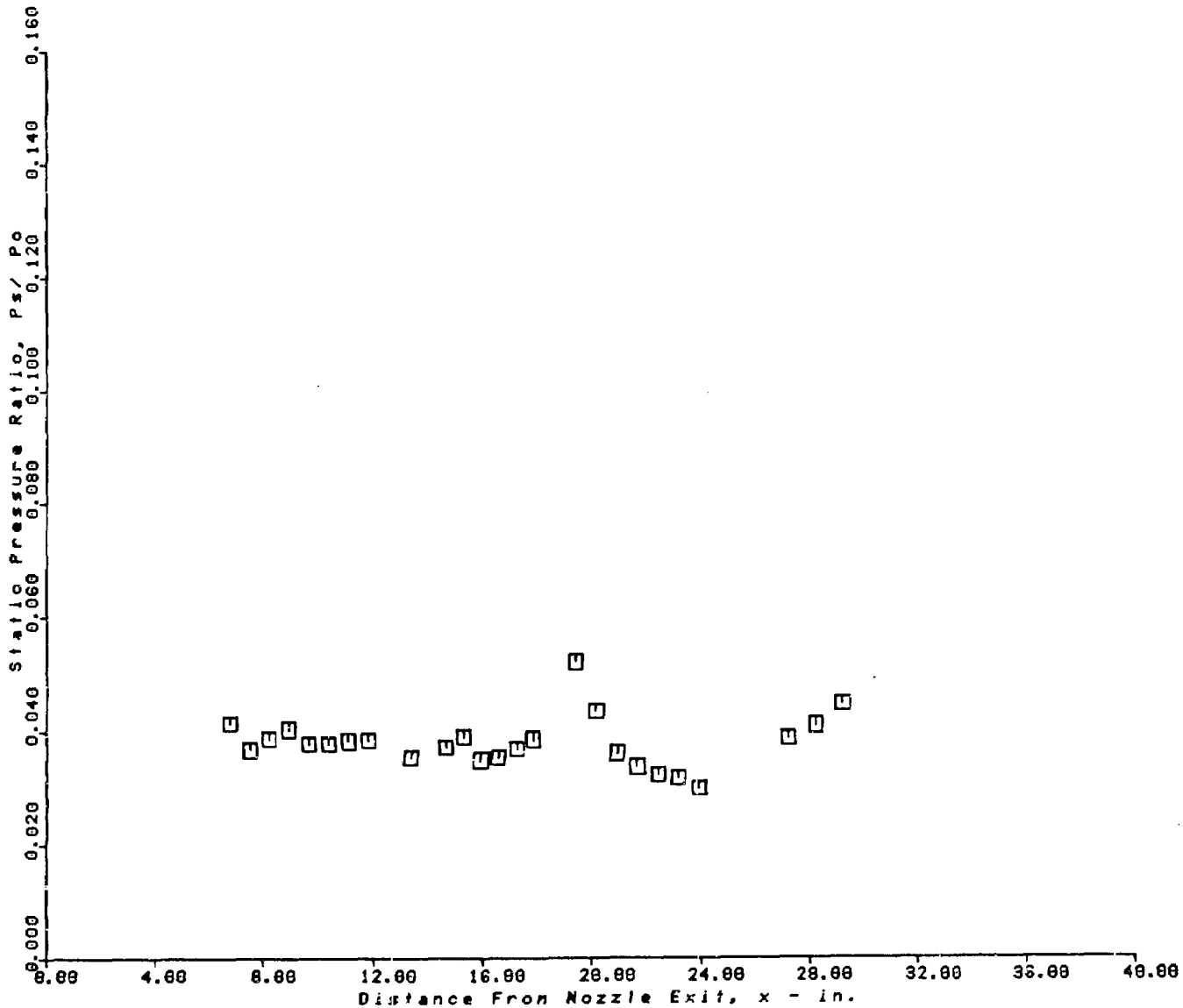

AFS TEST PROGRAM
UPPER SURFACE PRESSURE TAPS
RUN = 94 BURST = 58

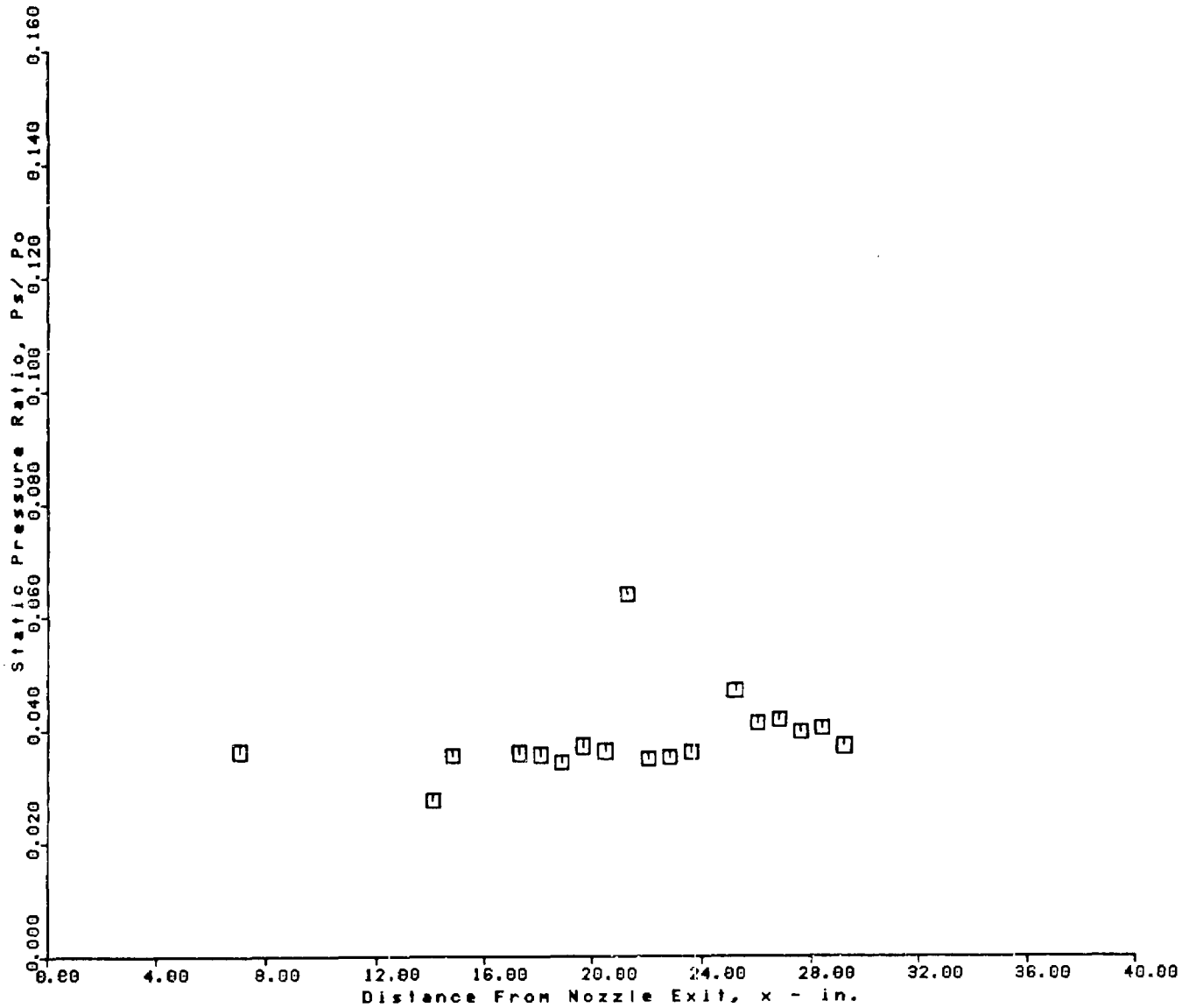

AFS TEST PROGRAM
LOWER SURFACE PRESSURE TAPS
RUN = 95 BURST = 50

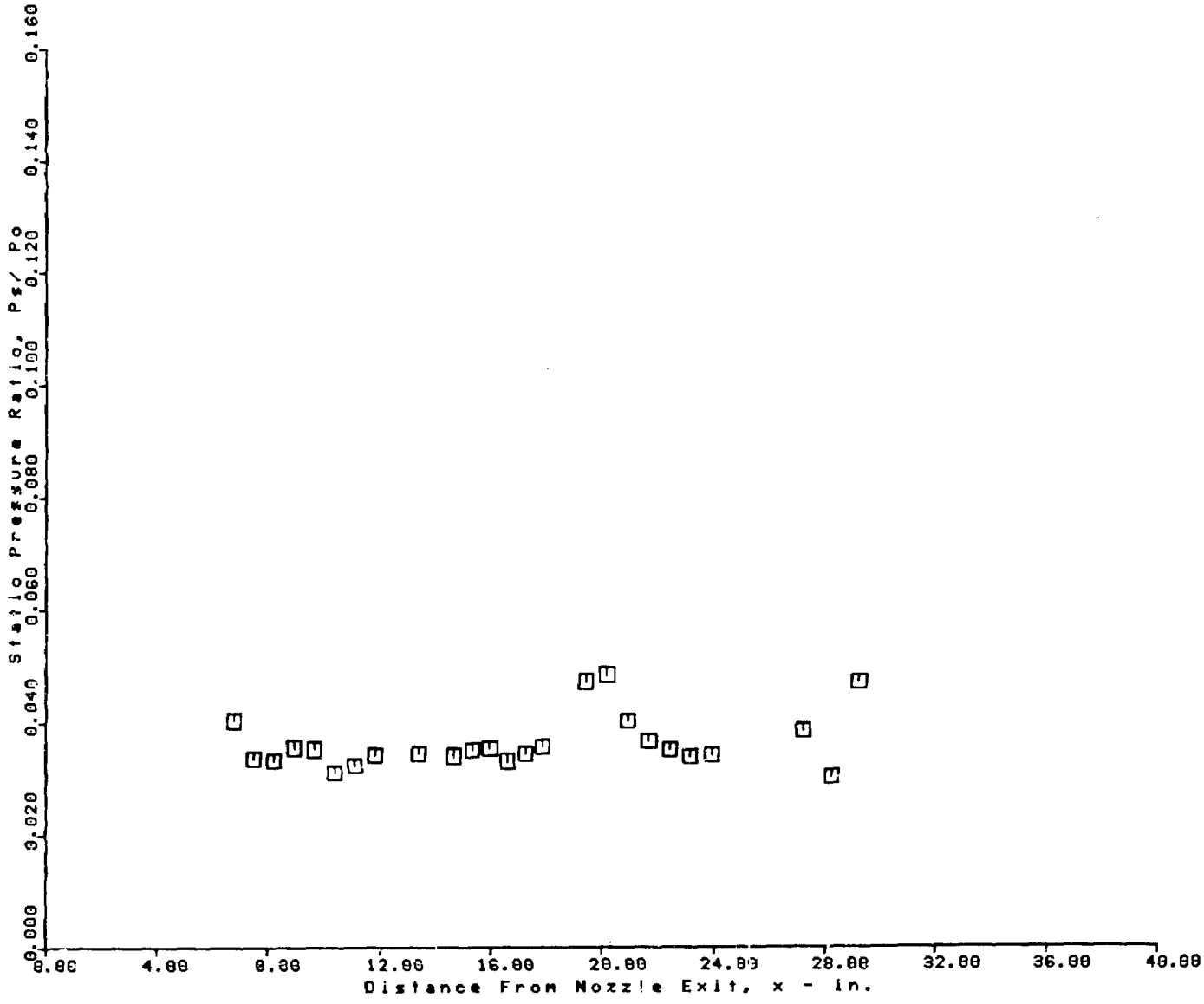

AFS TEST PROGRAM
UPPER SURFACE PRESSURE TAPS
RUN = 95 BURST = 50

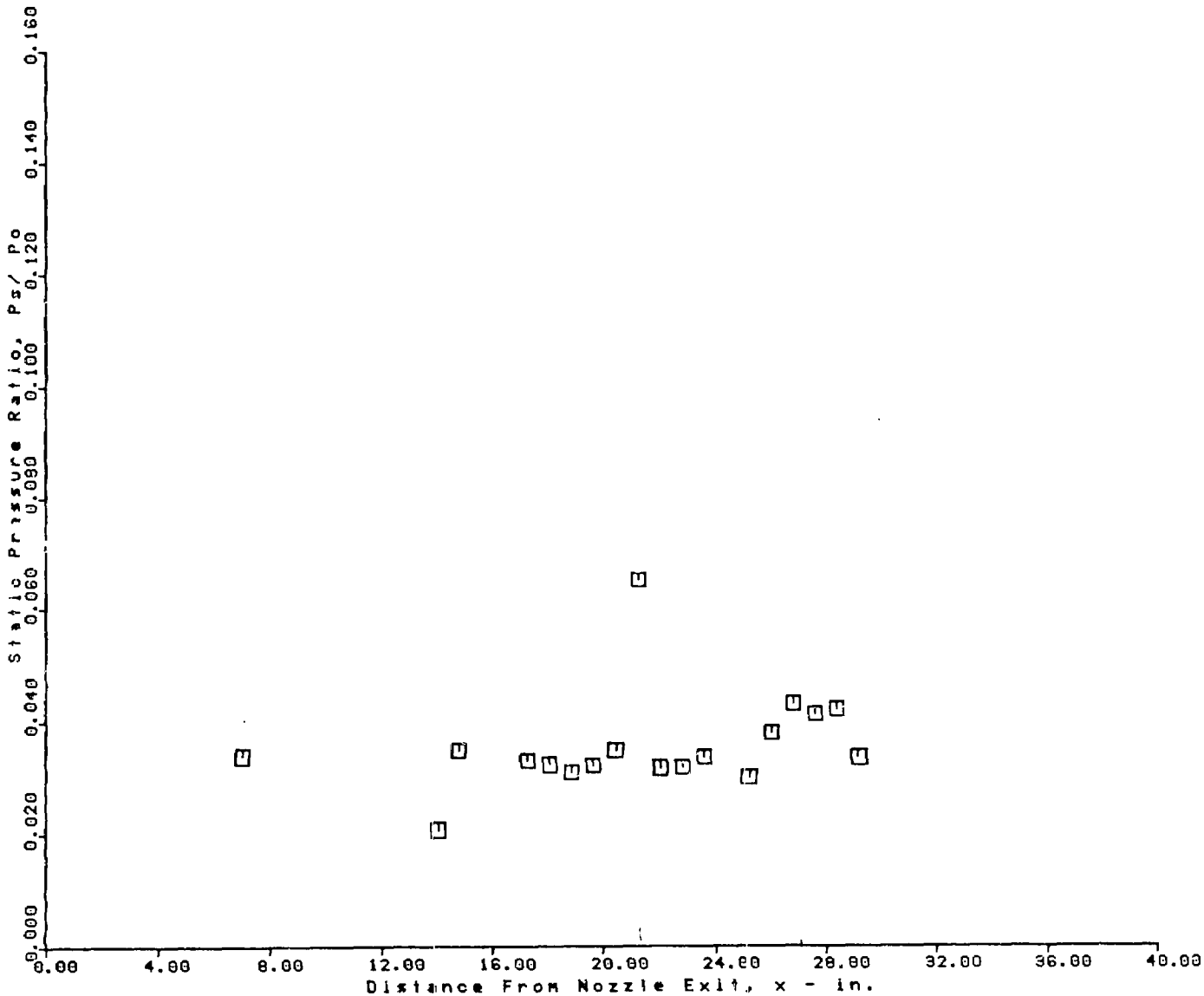

AFS TEST PROGRAM
LOWER SURFACE PRESSURE TAPS
RUN = 96 BURST = 50

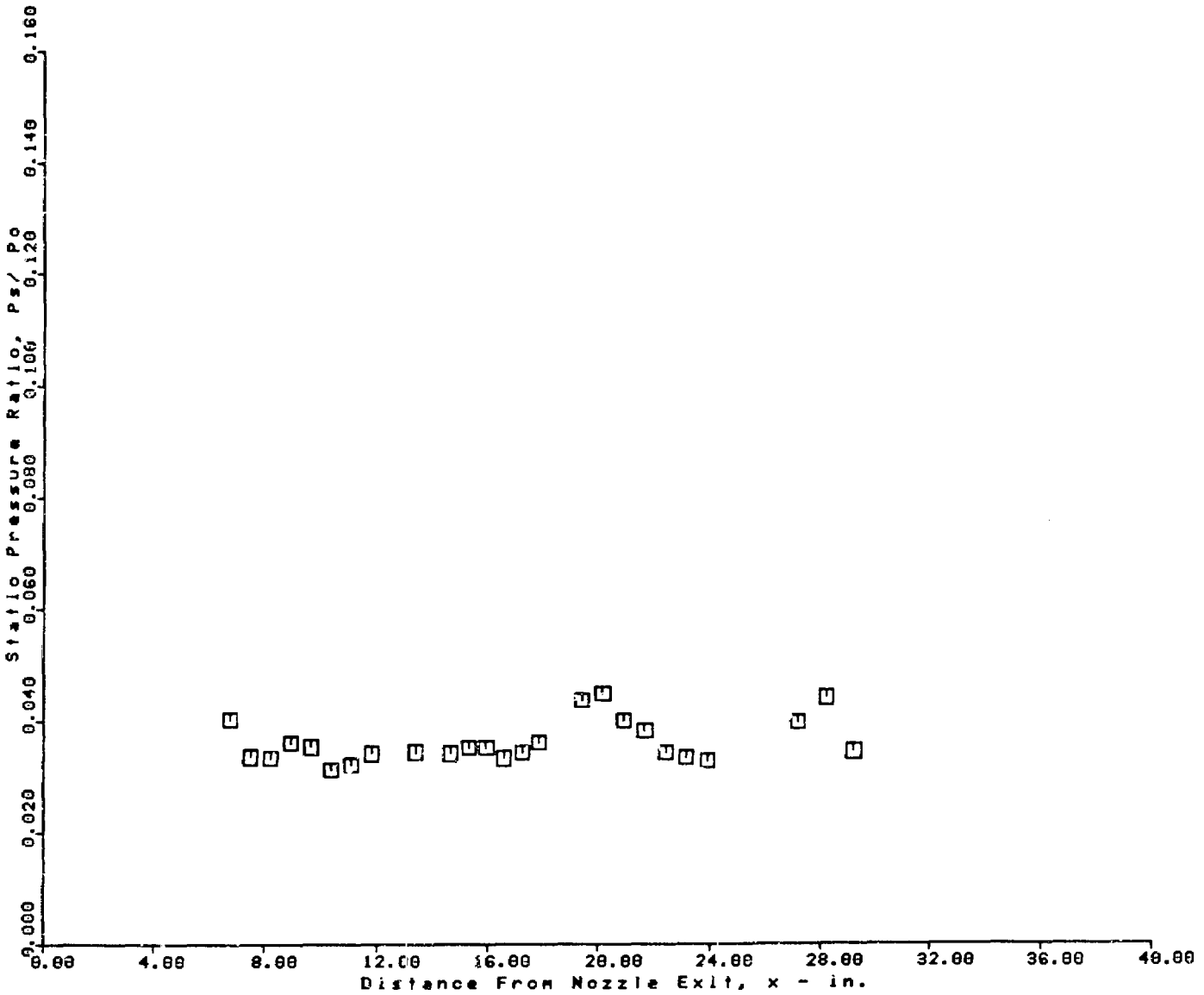

AFS TEST PROGRAM
UPPER SURFACE PRESSURE TAPS
RUN = 96 BURST = 50

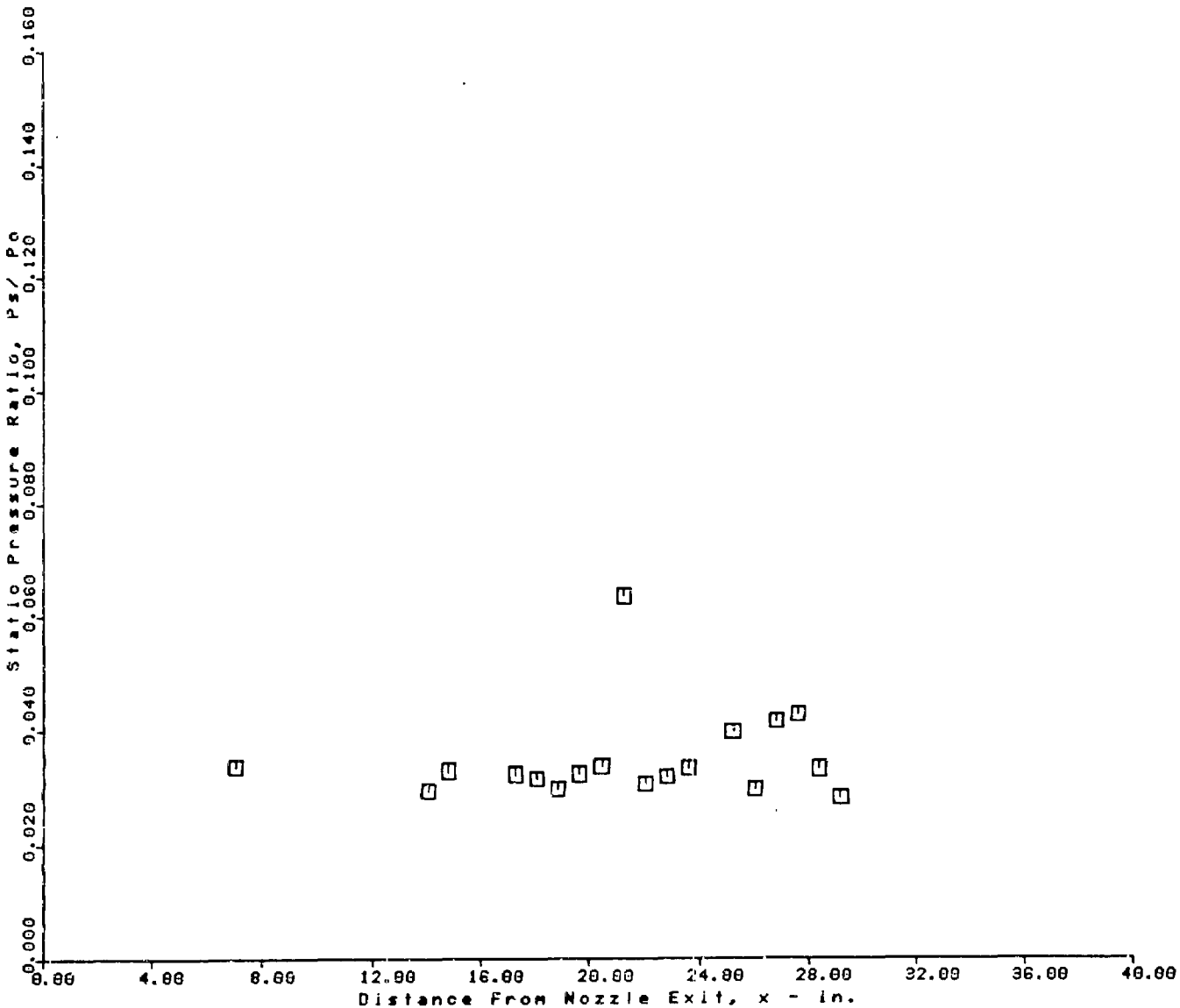

AFS TEST PROGRAM
LOWER SURFACE PRESSURE TAPS
RUN = 97 BURST = 50

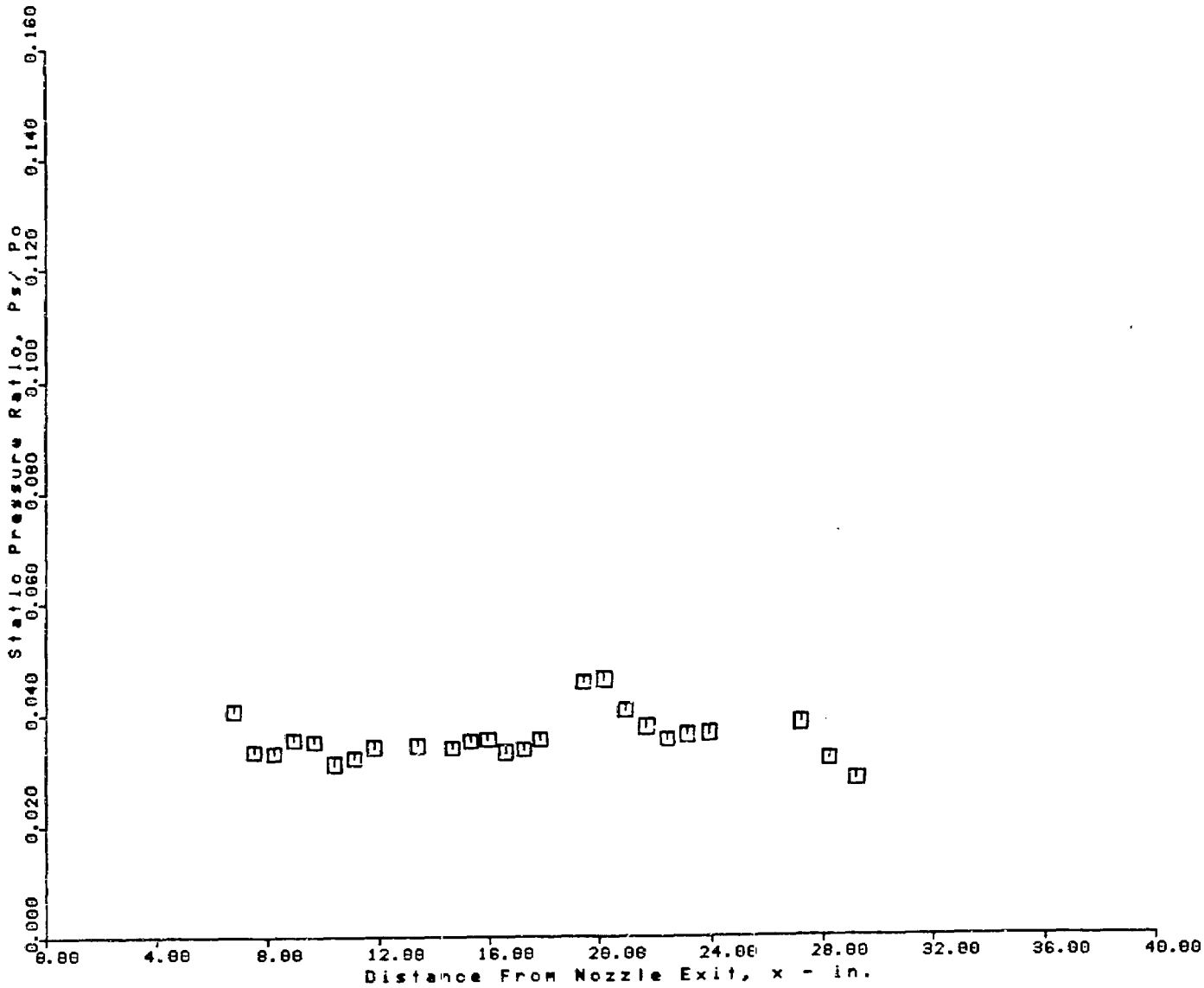

AFS TEST PROGRAM
UPPER SURFACE PRESSURE TAPS
RUN = 97 BURST = 50

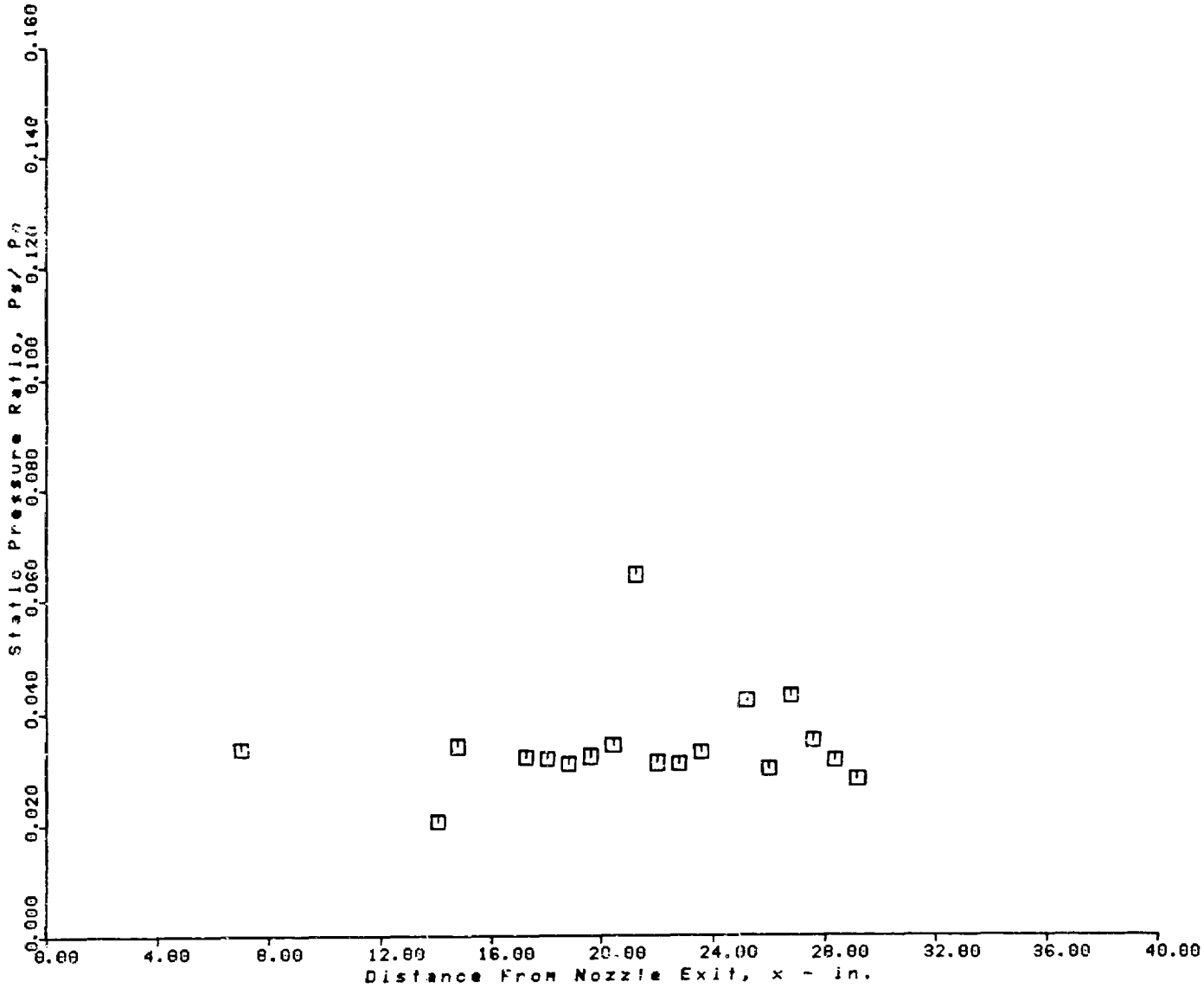

AFS TEST PROGRAM
LOWER SURFACE PRESSURE TAPS
RUN = 99 BURST = 50

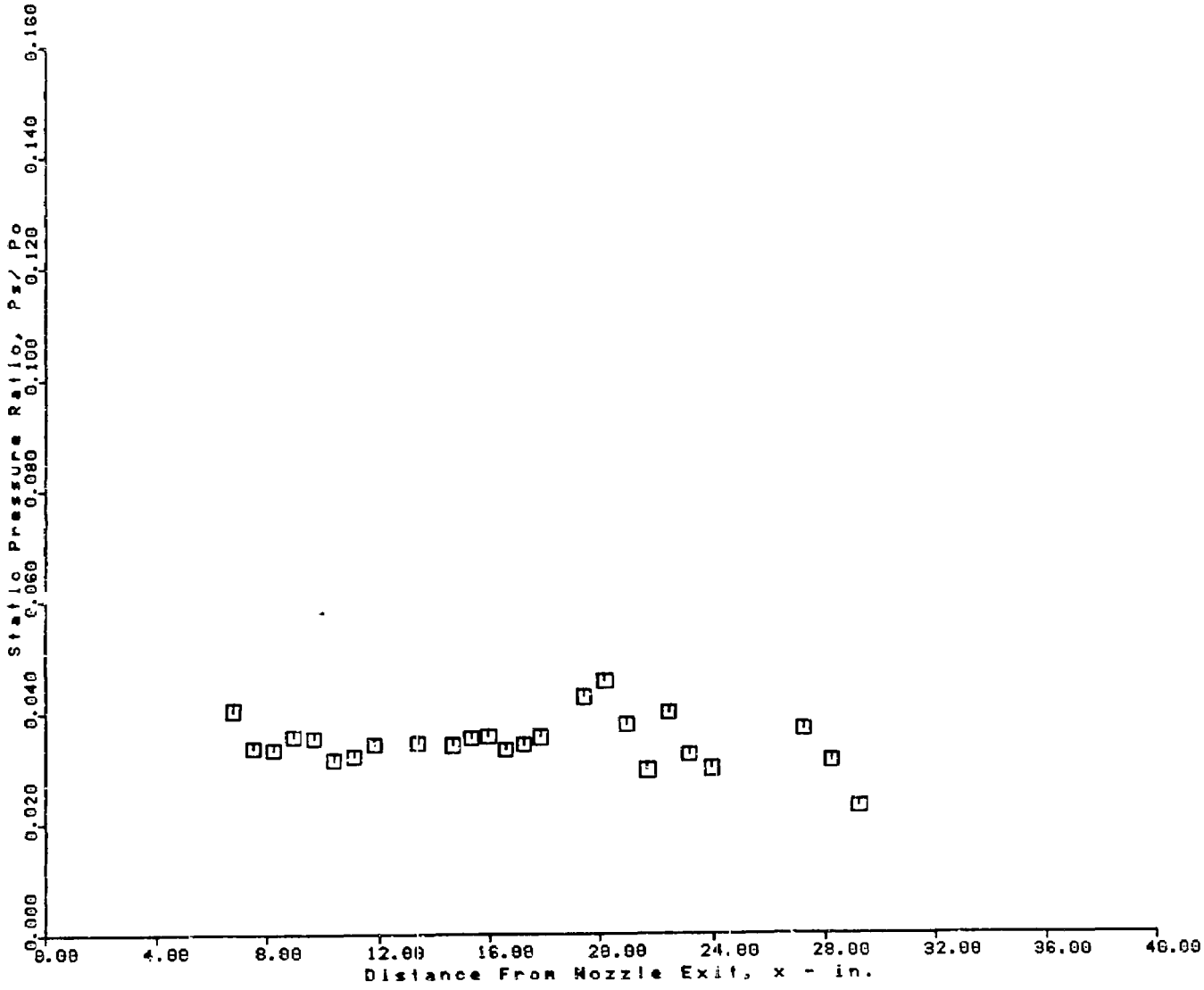

AFS TEST PROGRAM
UPPER SURFACE PRESSURE TAPS
RUN = 99 BURST = 58

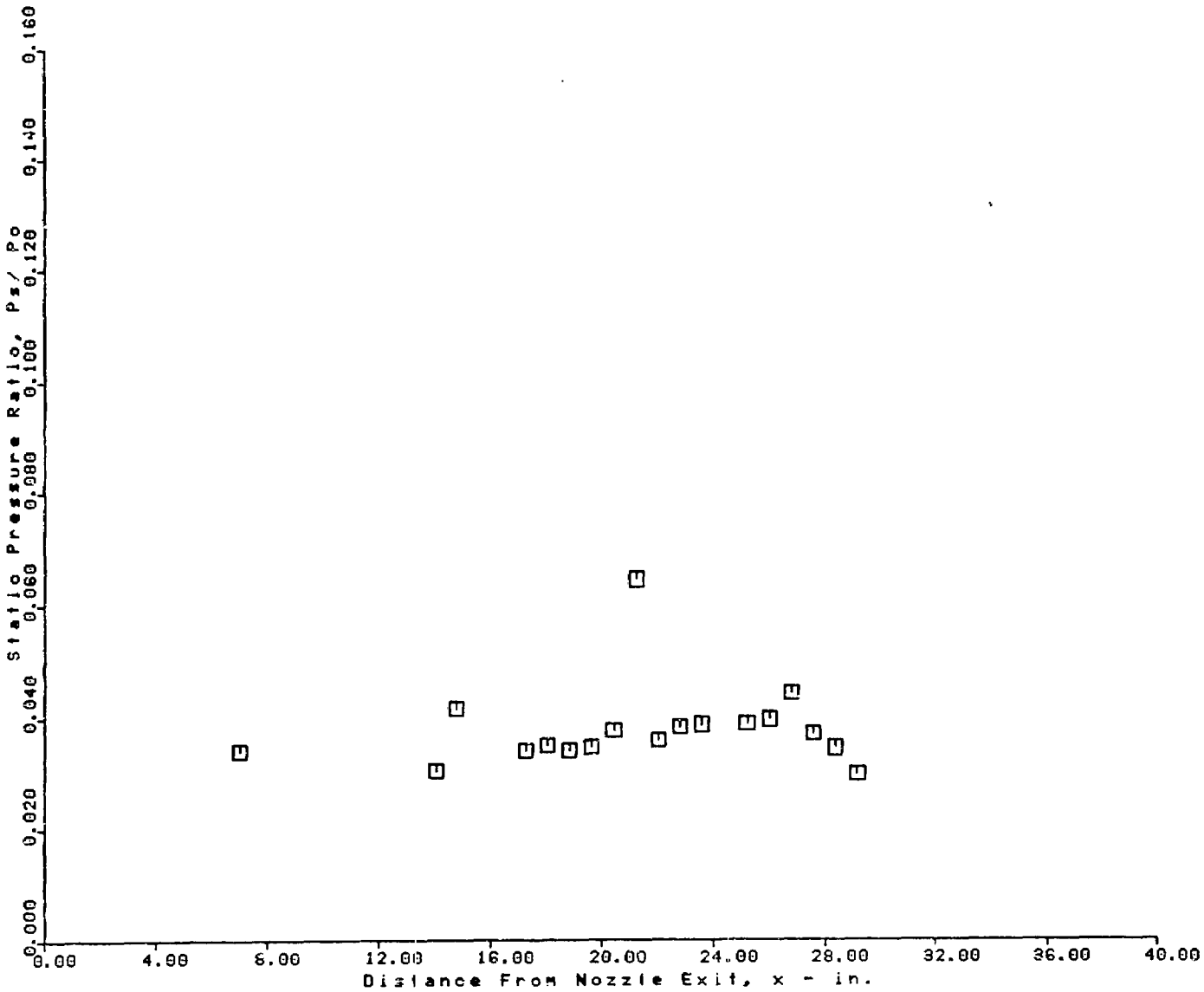

AFS TEST PROGRAM
LOWER SURFACE PRESSURE TAPS
RUN = 100 BURST = 50

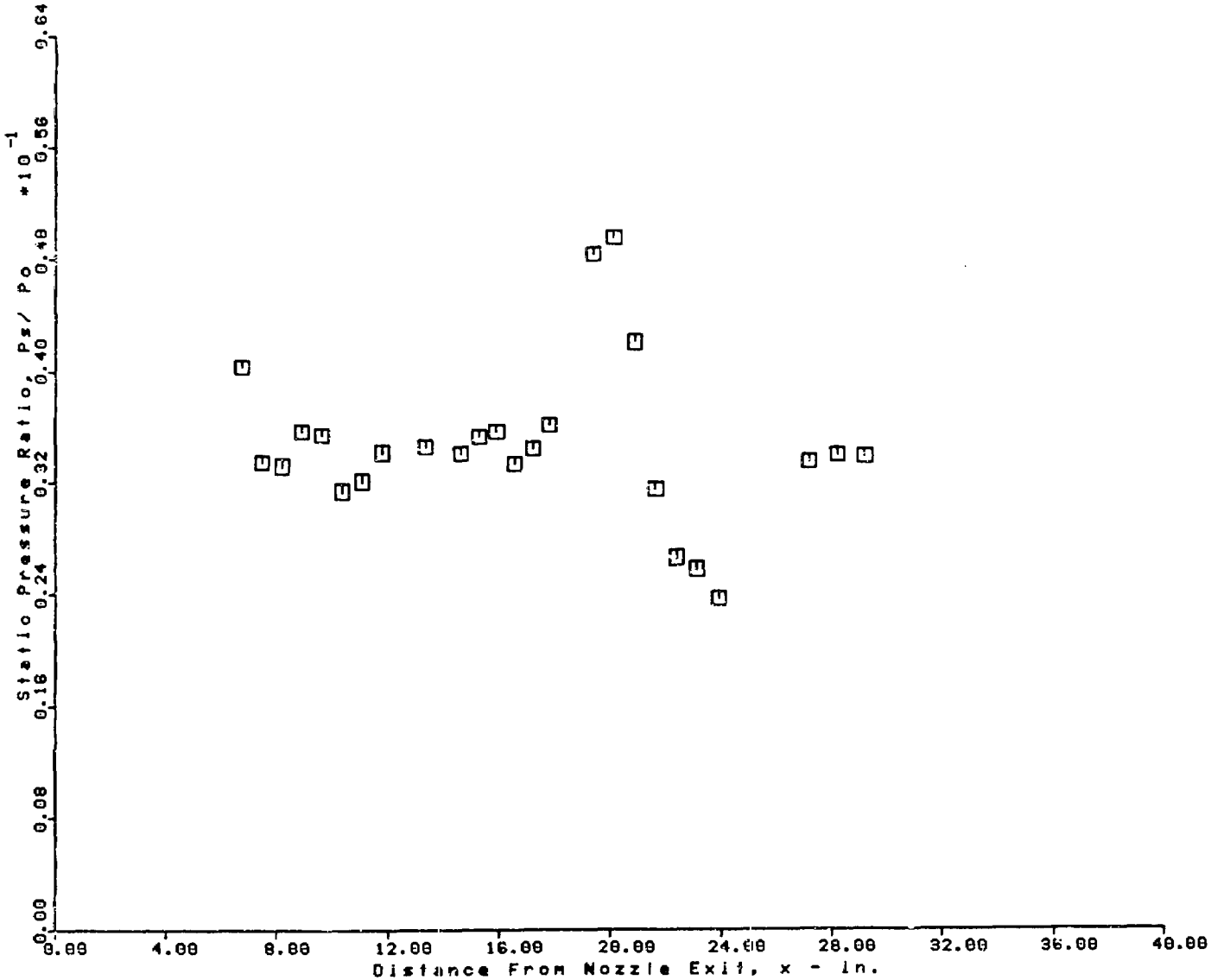

AFS TEST PROGRAM
UPPER SURFACE PRESSURE TAPS
RUN = 100 BURST = 50

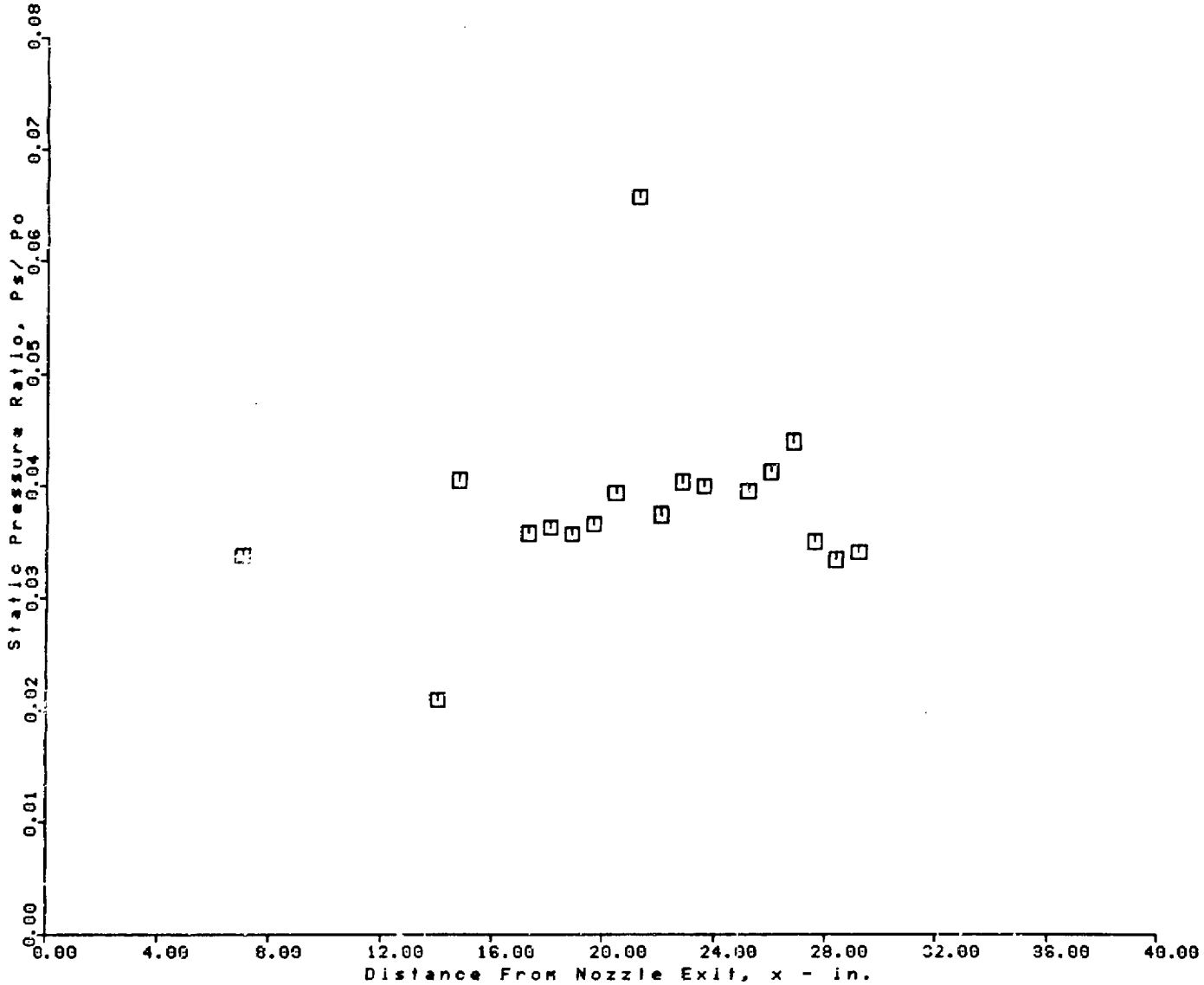

AFS TEST PROGRAM
LOWER SURFACE PRESSURE TAPS
RUN = 101 BURST = 50

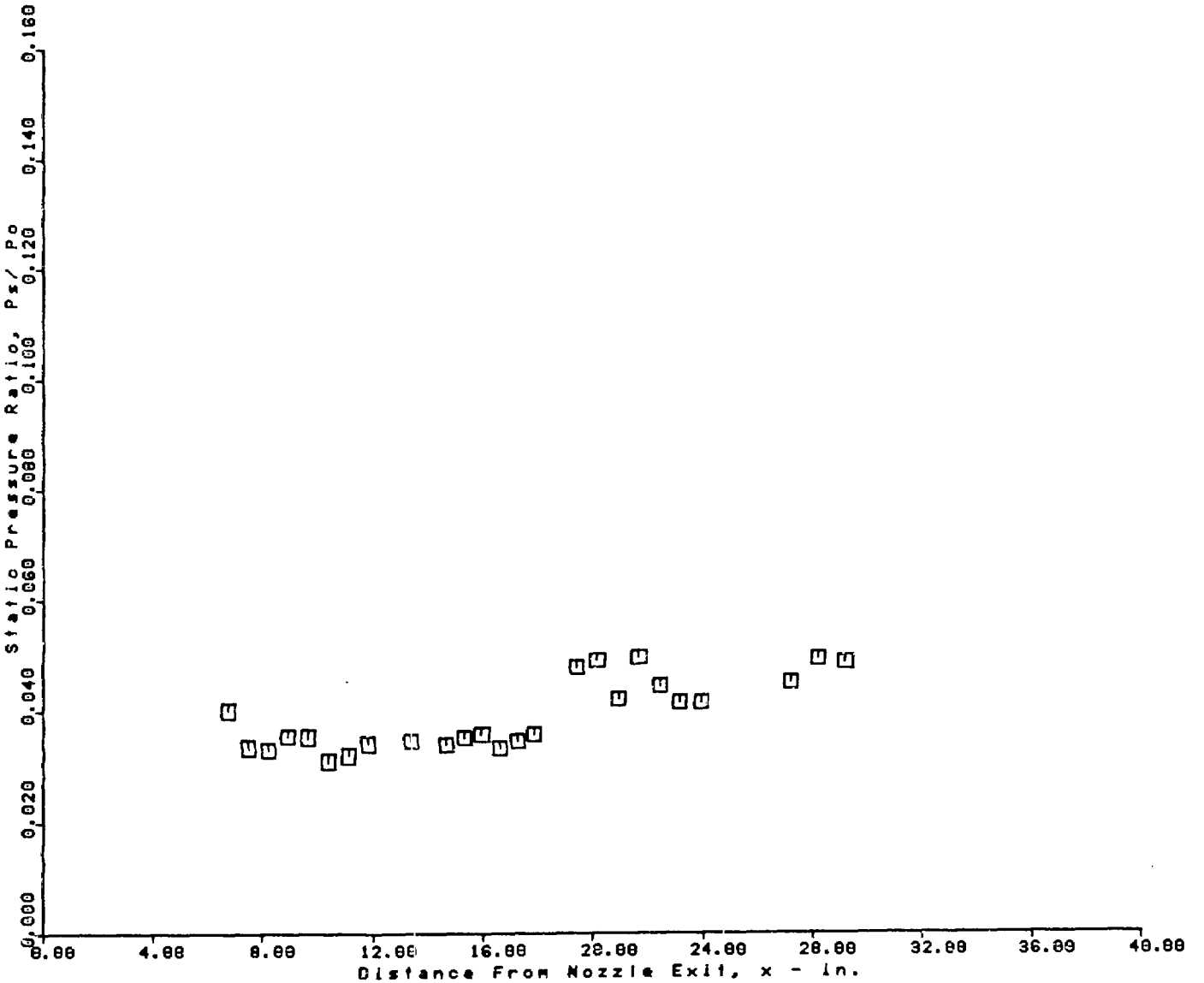

AFS TEST PROGRAM
UPPER SURFACE PRESSURE TAPS
RUN = 181 BURST = 50

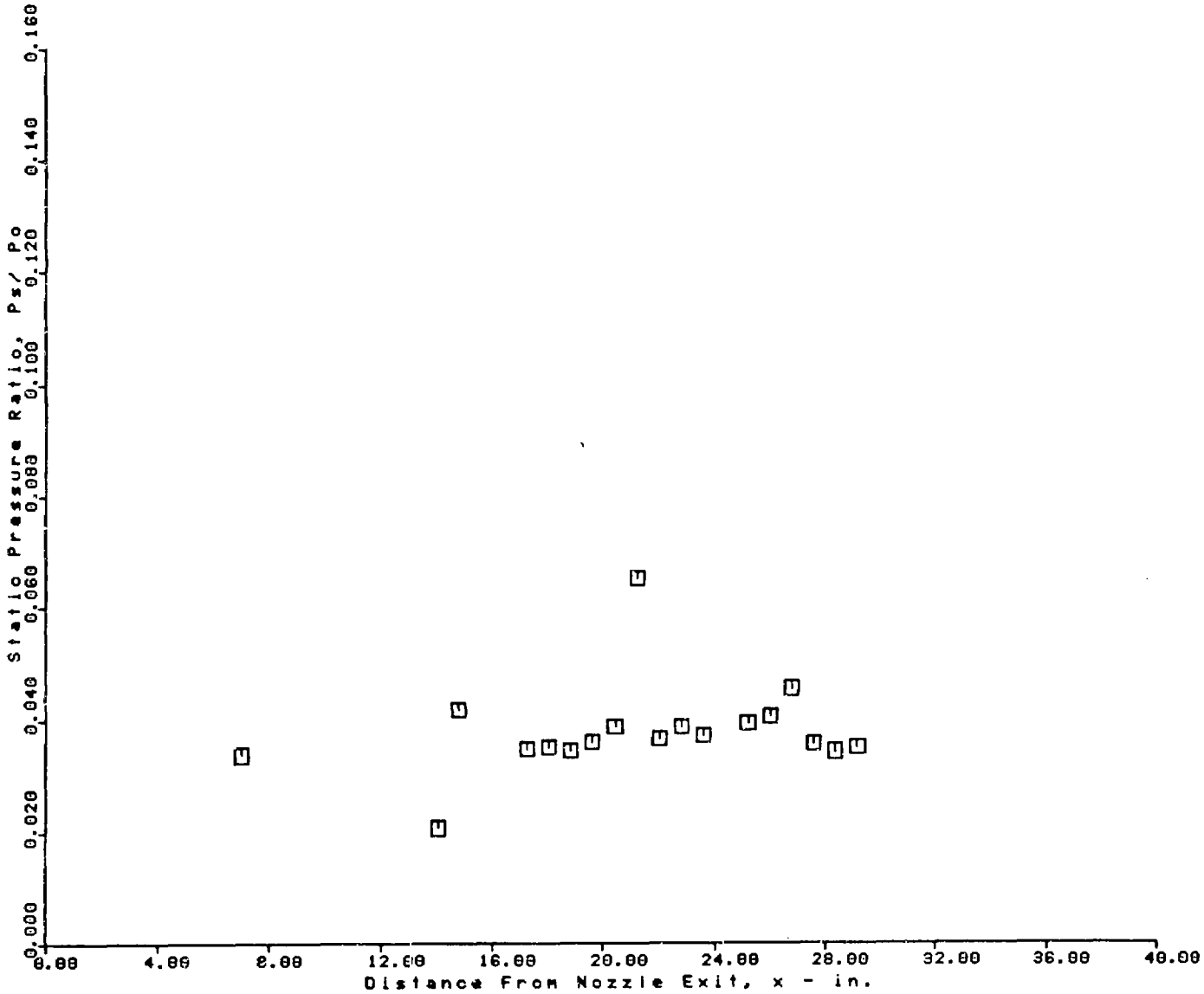

AFS TEST PROGRAM
LOWER SURFACE PRESSURE TAPS
RUN = 182 BURST = 50

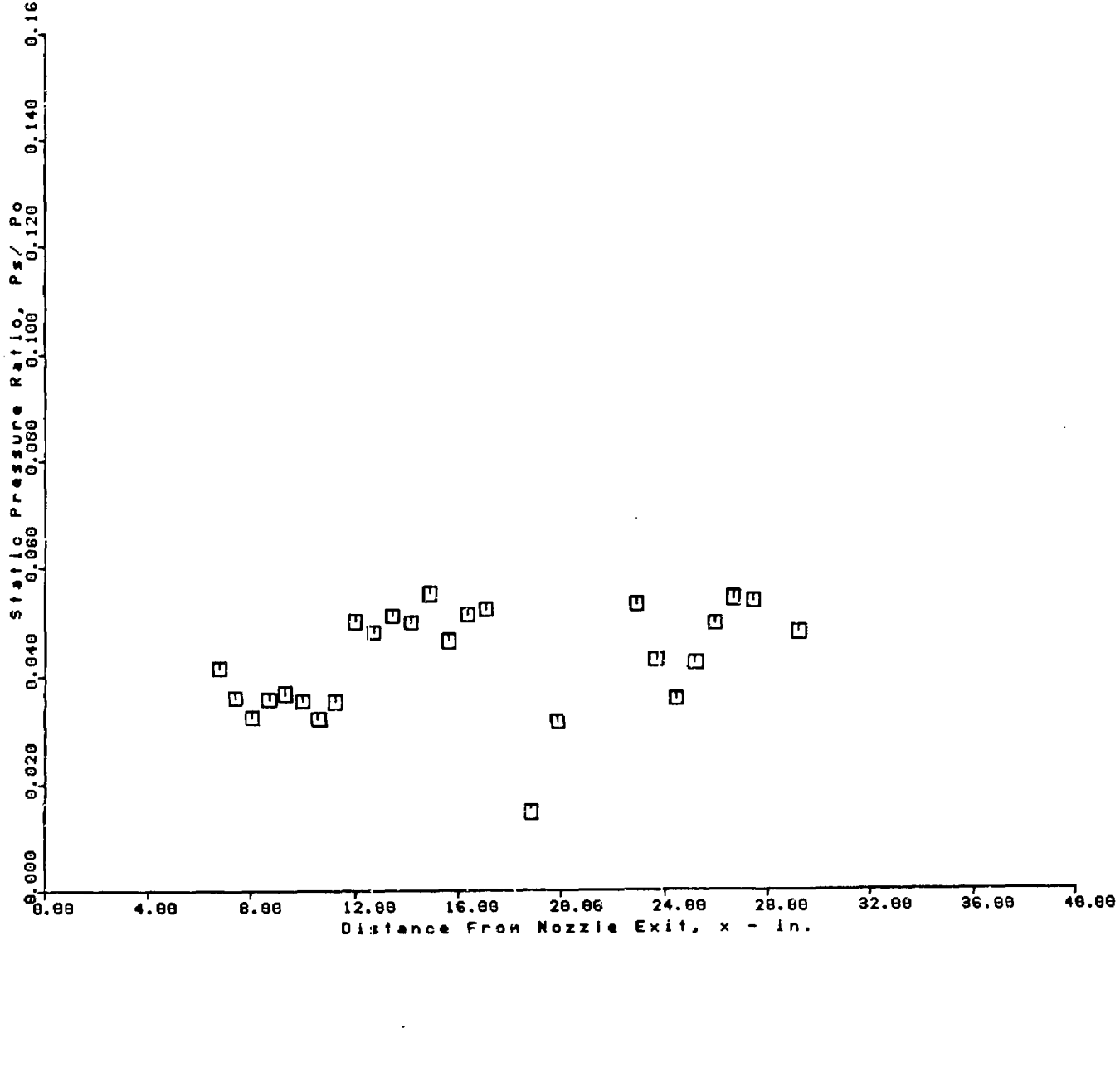

AFS TEST PROGRAM
UPPER SURFACE PRESSURE TAPS
RUN = 102 BURST = 50

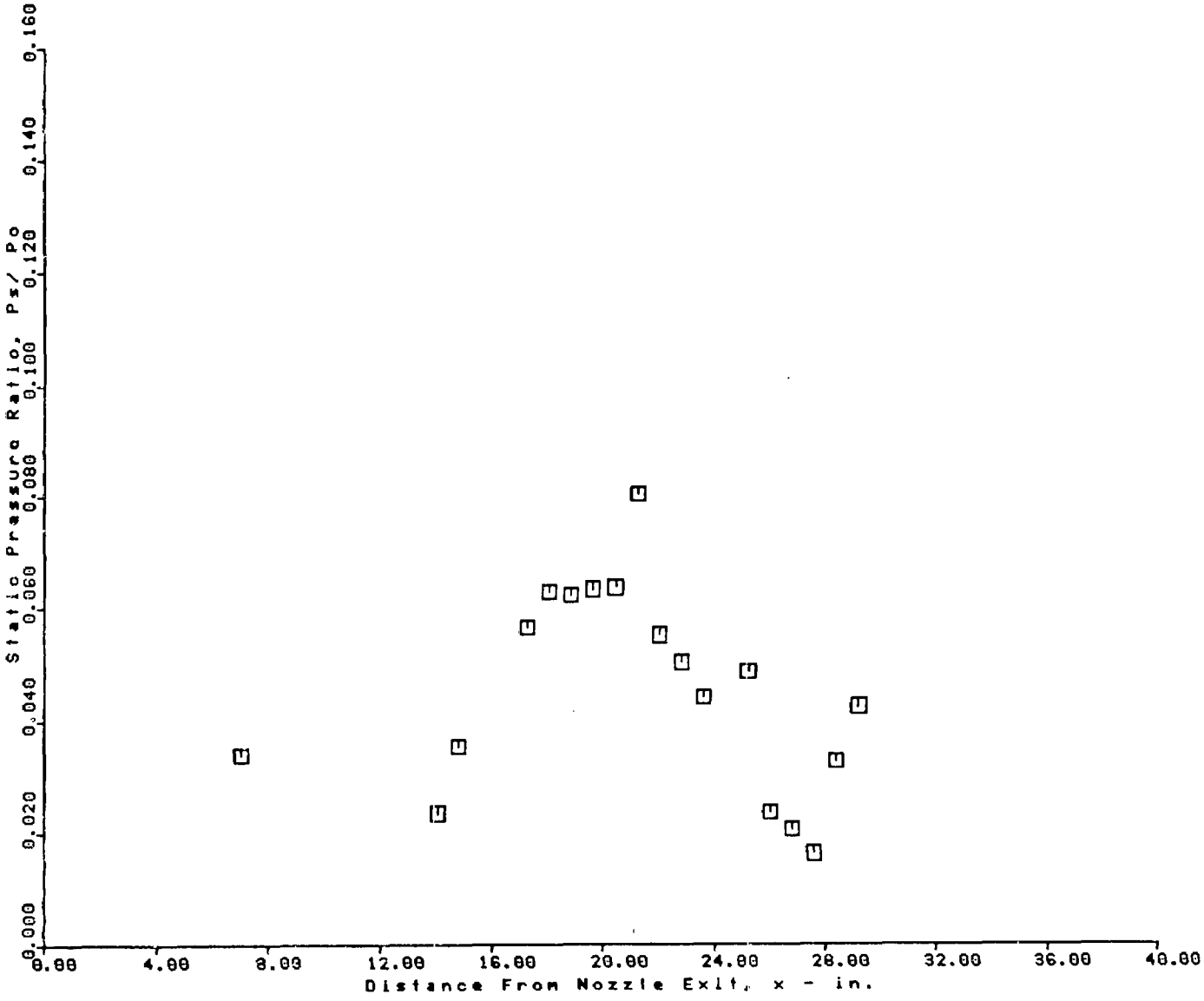

AFS TEST PROGRAM
LOWER SURFACE PRESSURE TAPS
RUN = 103 BURST = 50

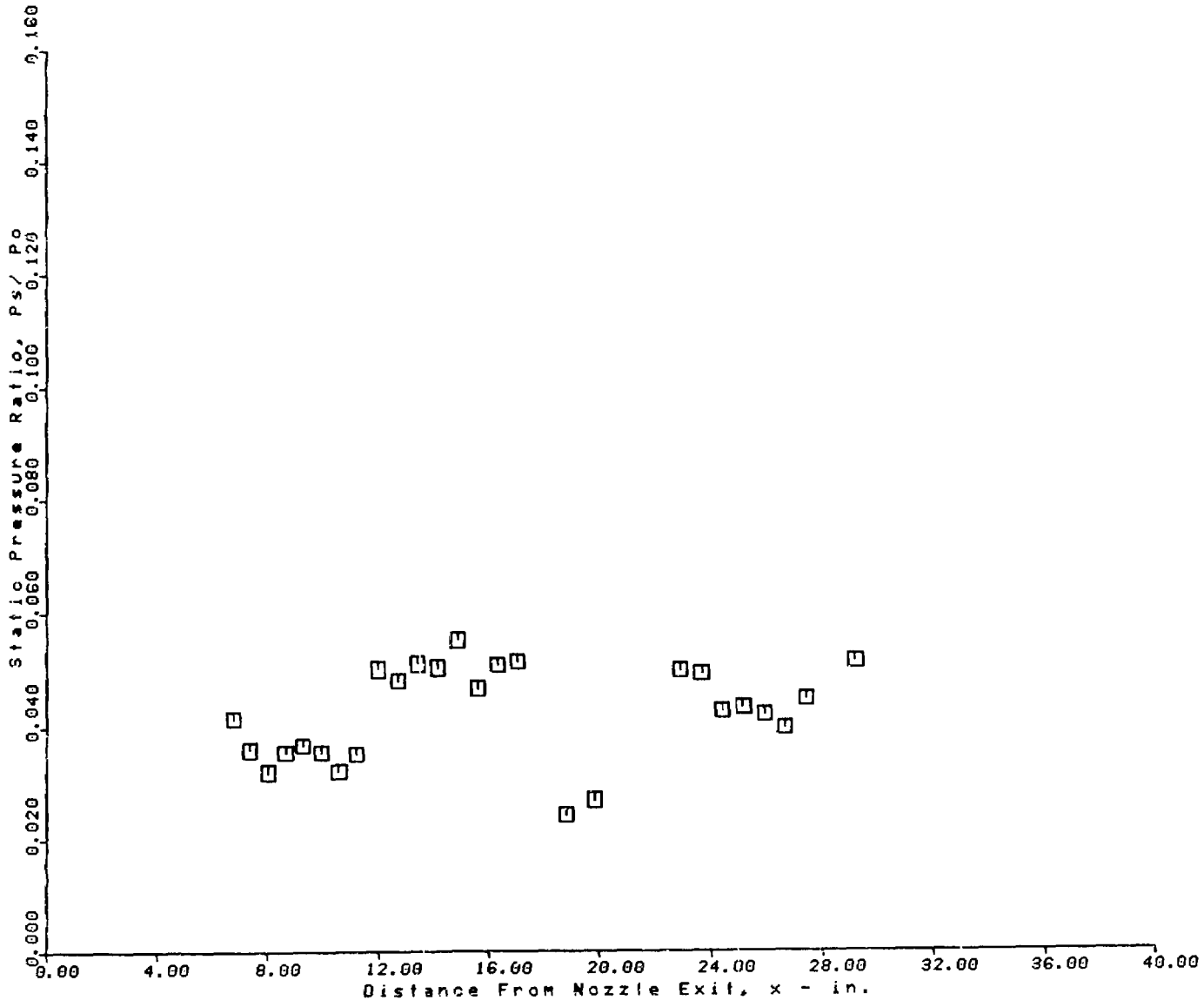

AFS TEST PROGRAM
UPPER SURFACE PRESSURE TAPS
RUN = 103 BURST = 50

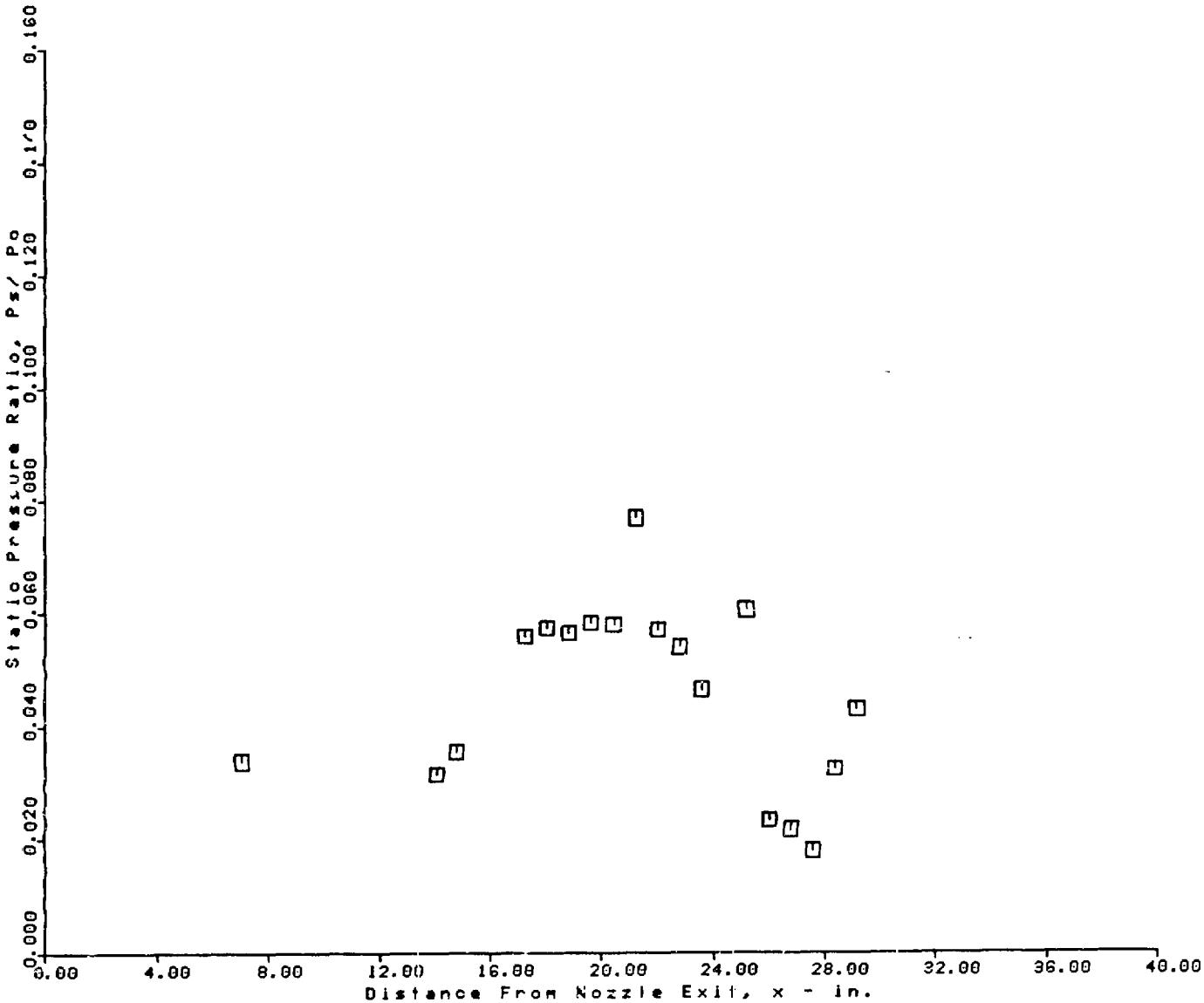

AFS TEST PROGRAM
LOWER SURFACE PRESSURE TAPS
RUN = 104 BURST = 58

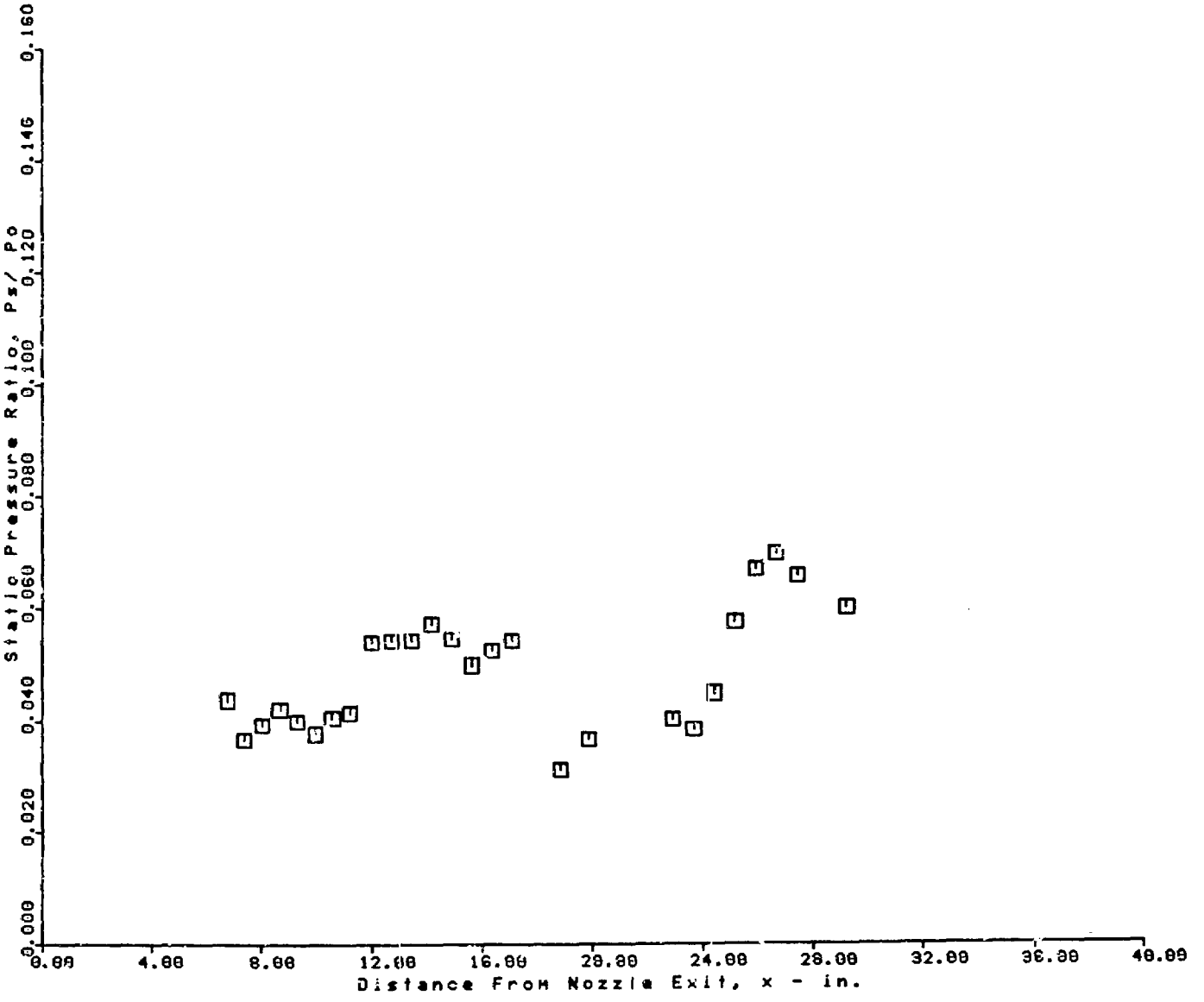

AFS TEST PROGRAM
UPPER SURFACE PRESSURE TAPS
RUN = 184 BURST = 50

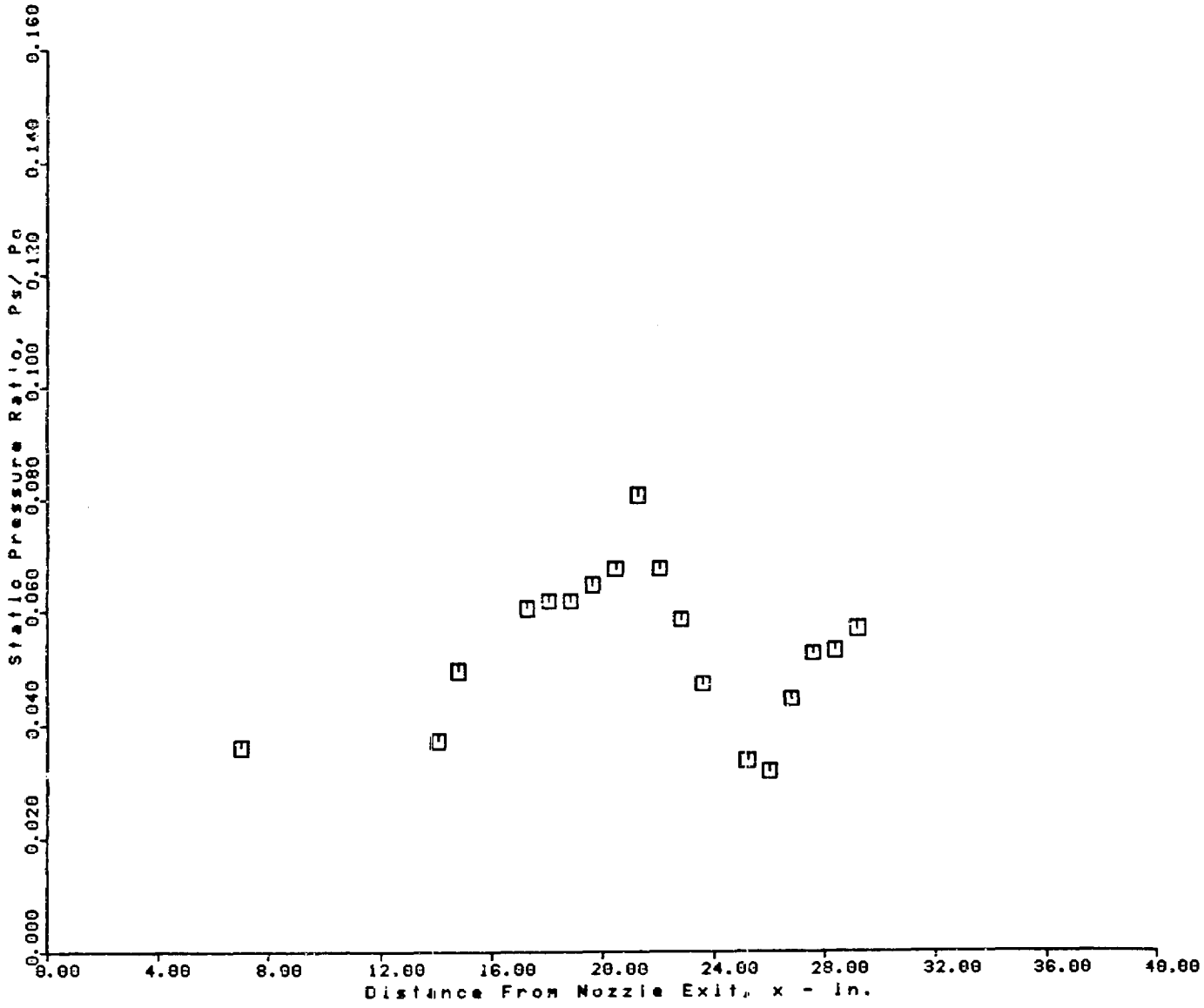

AFS TEST PROGRAM
LOWER SURFACE PRESSURE TAPS
RUN = 105 BURST = 58

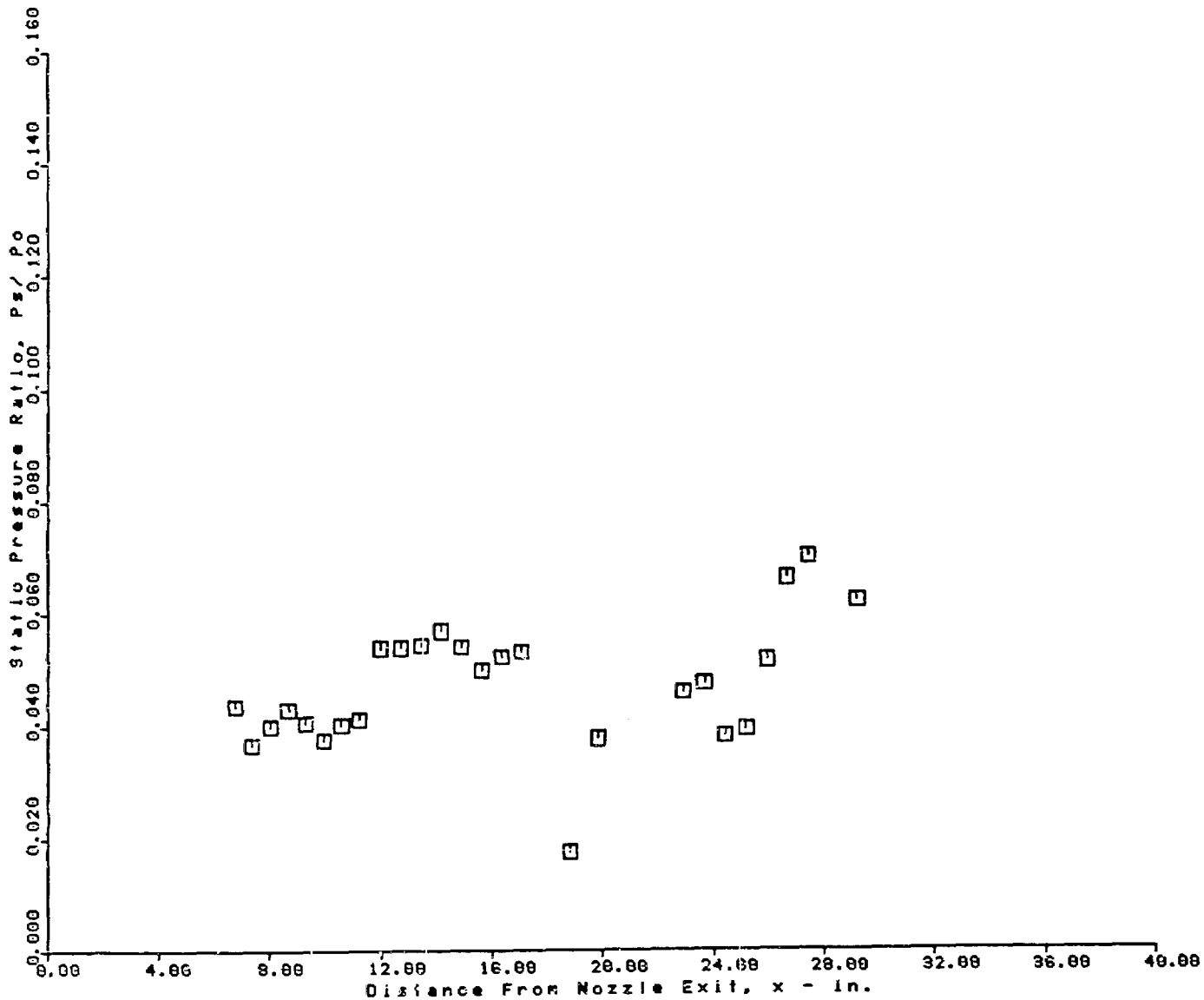

AFS TEST PROGRAM
UPPER SURFACE PRESSURE TAPS
RUN = 185 BURST = 50

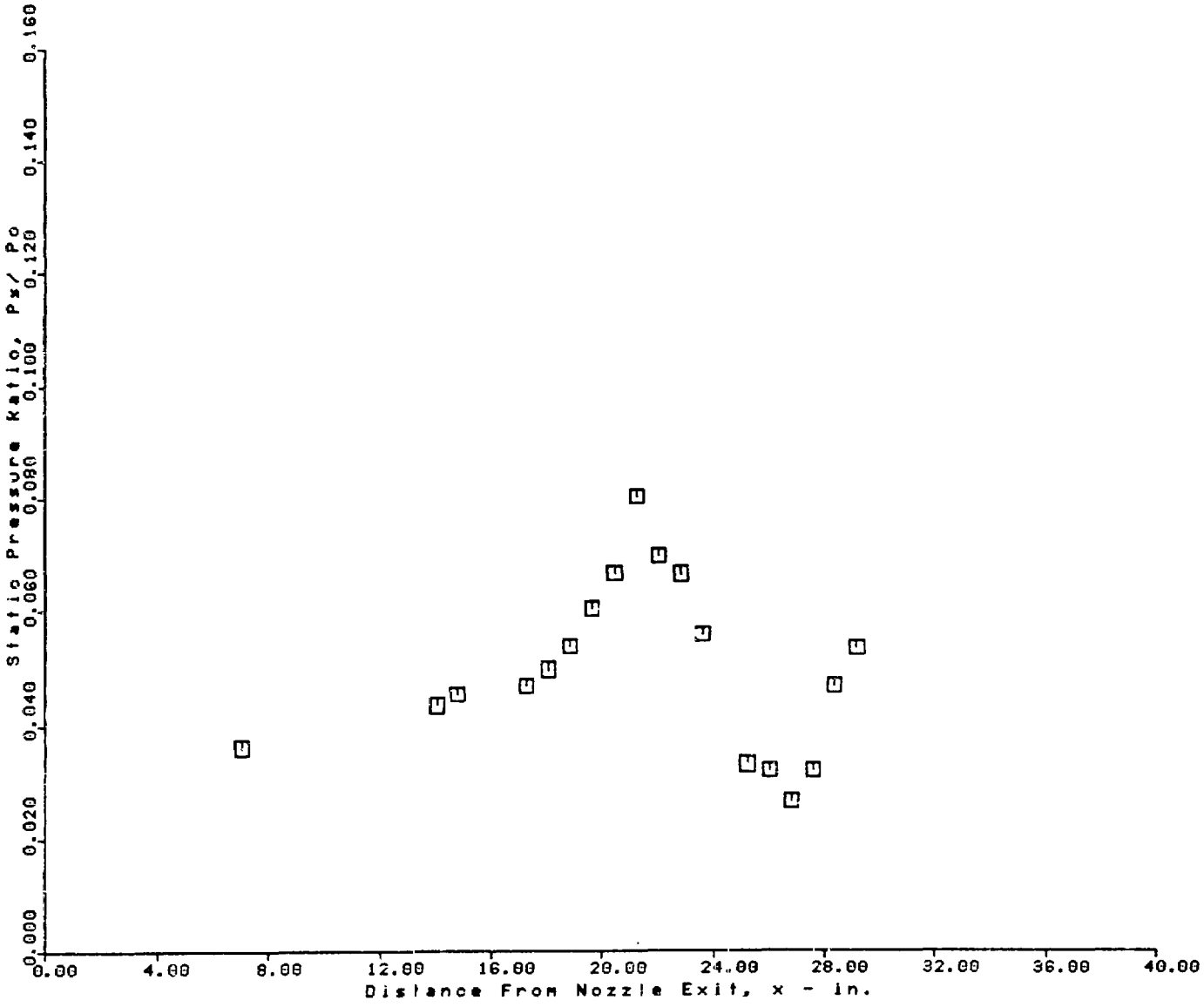

AFS TEST PROGRAM
LOWER SURFACE PRESSURE TAPS
RUN = 108 BURST = 50

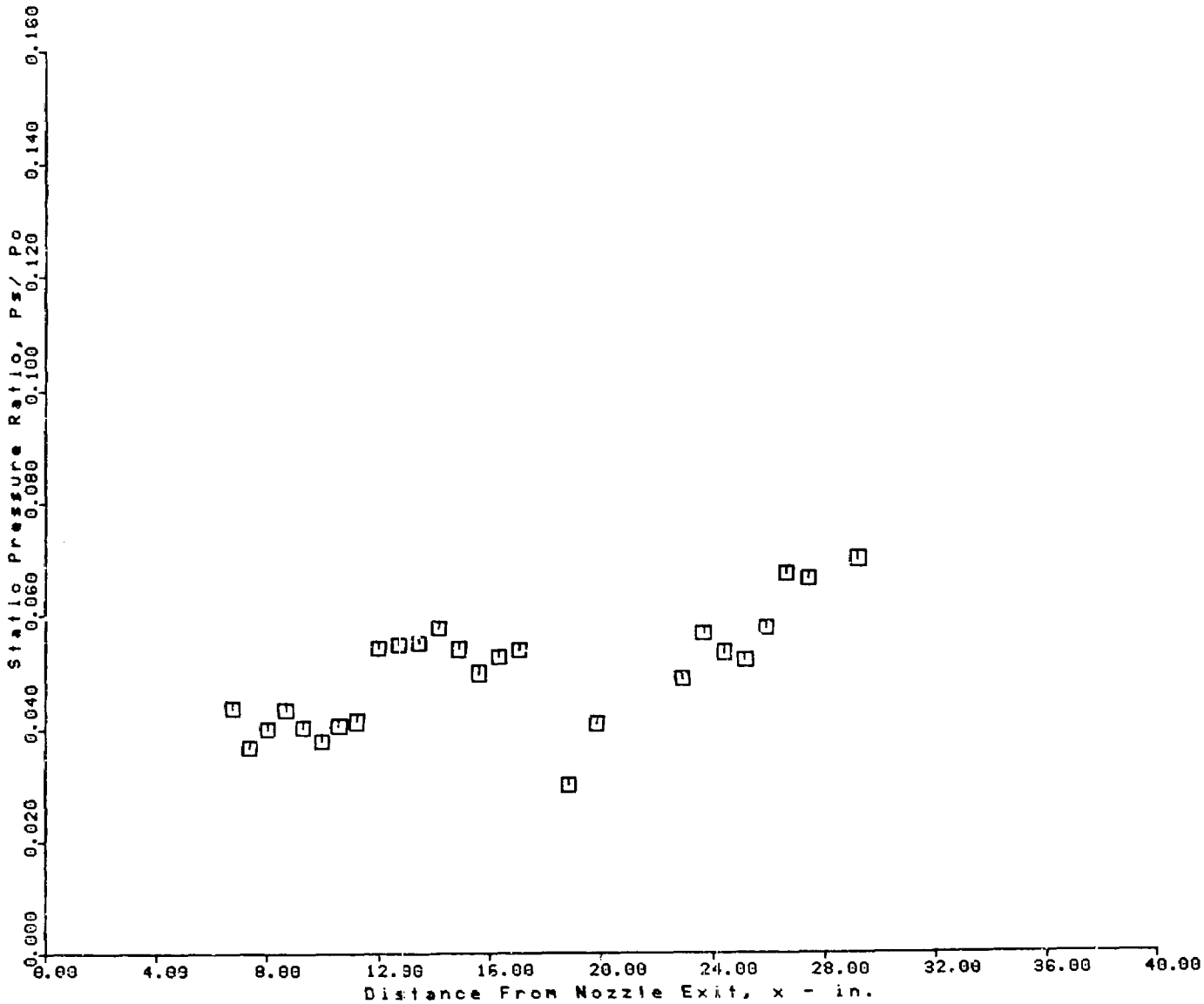

AFS TEST PROGRAM
UPPER SURFACE PRESSURE TAPS
RUN = 188 BURST = 50

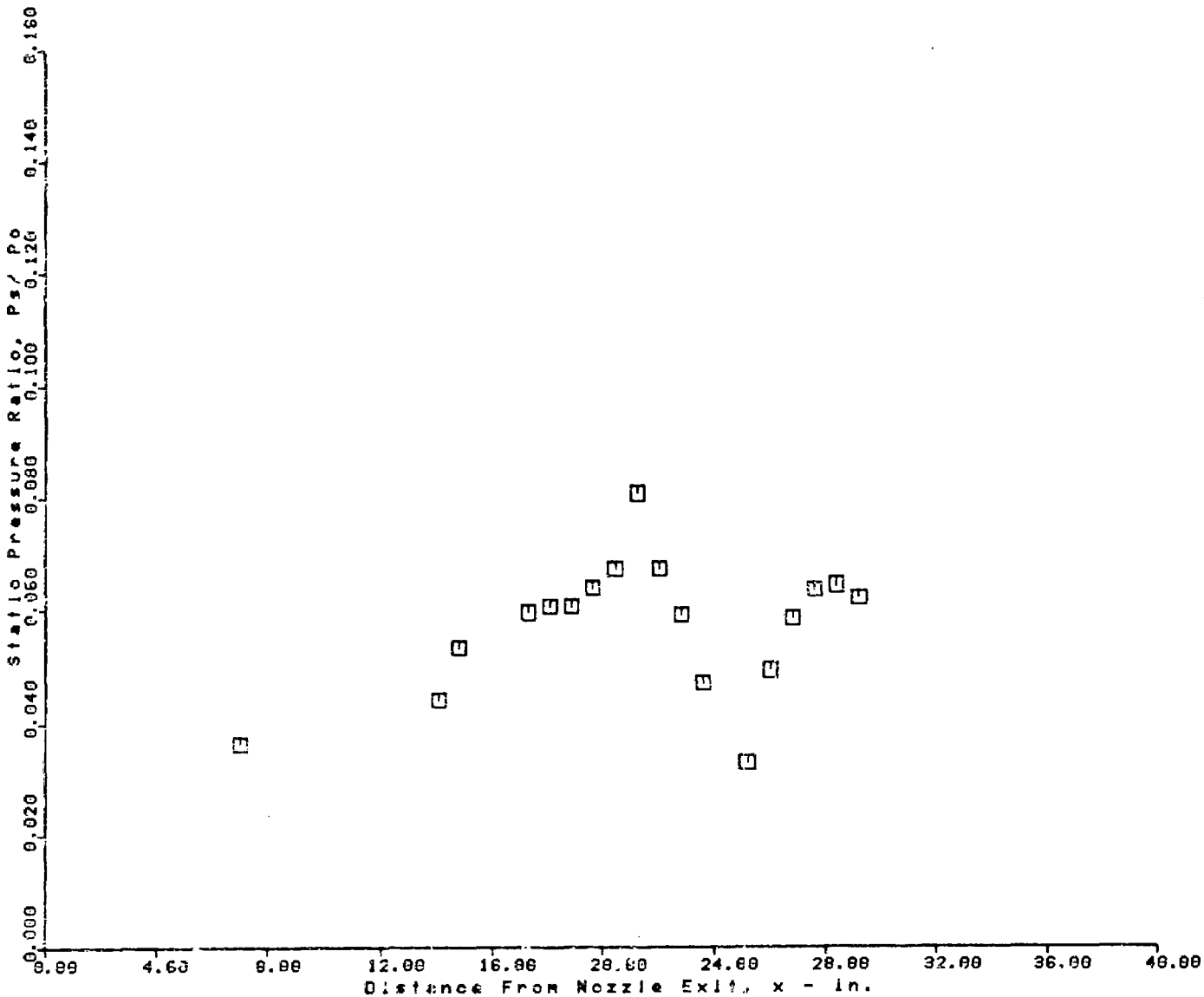

AFS TEST PROGRAM
LOWER SURFACE PRESSURE TAPS
RUN = 108 BURST = 50

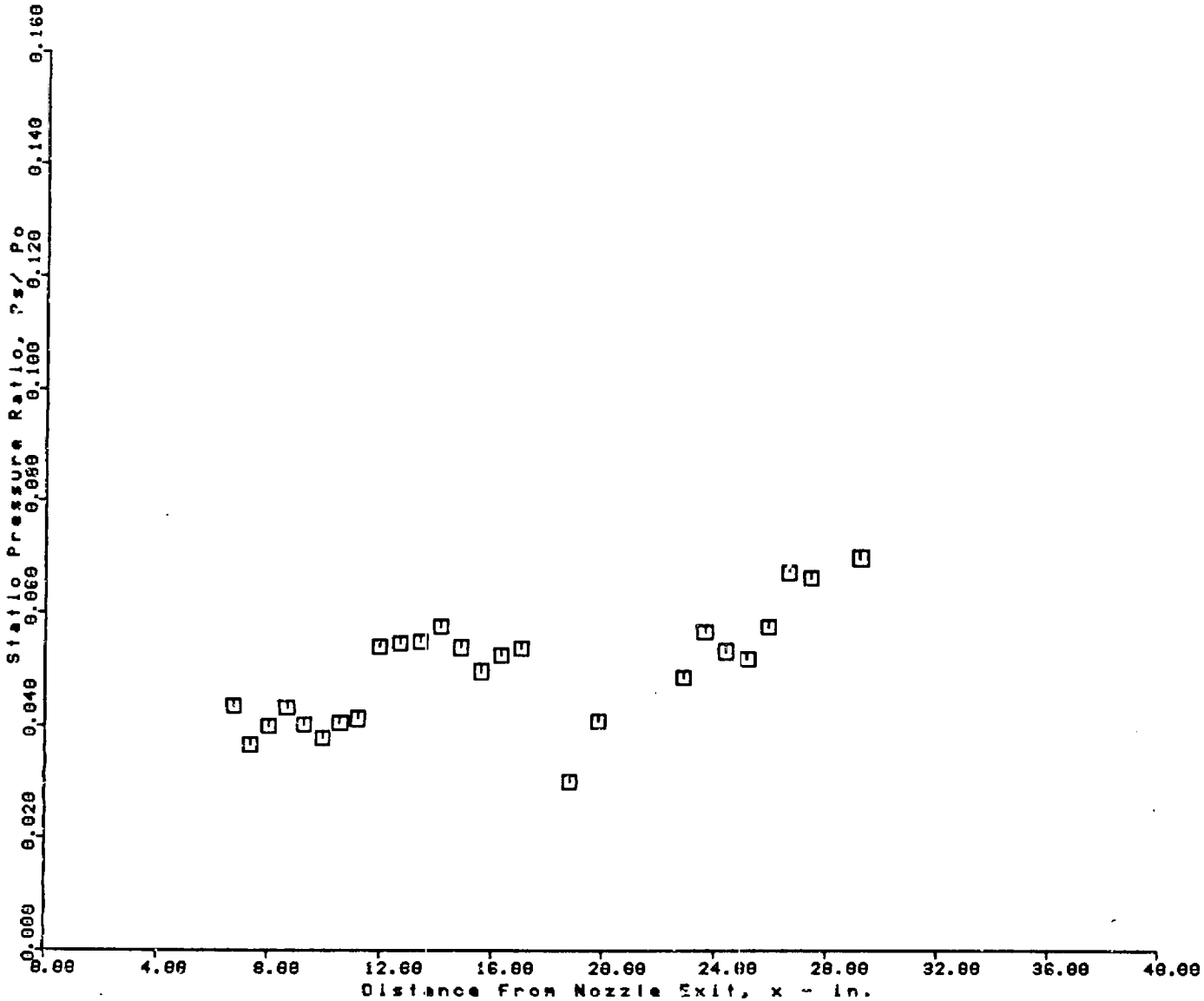

AFS TEST PROGRAM
UPPER SURFACE PRESSURE TAPS
RUN = 108 BURST = 50

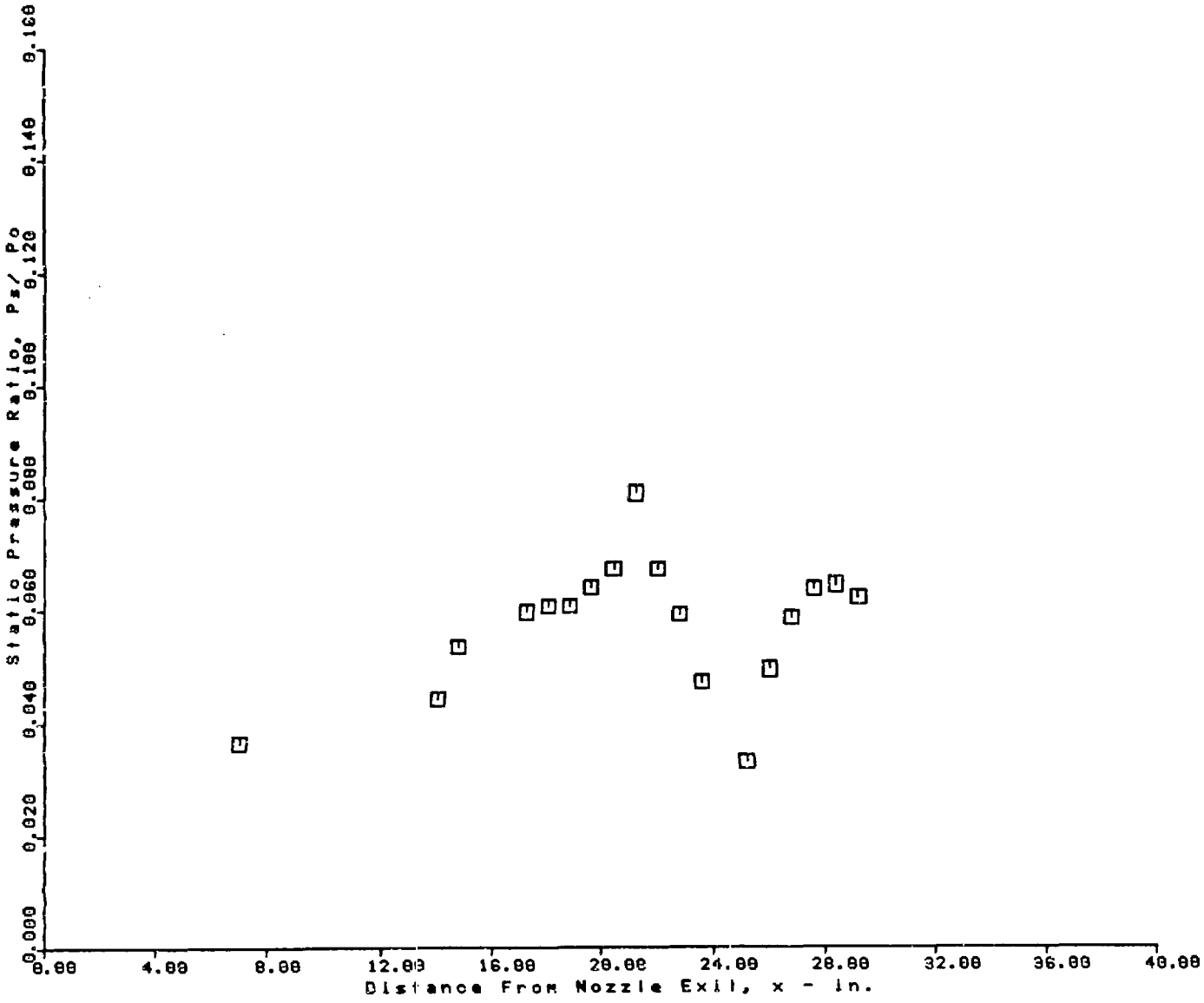

AFS TEST PROGRAM
LOWER SURFACE PRESSURE TAPS
RUN = 109 BURST = 50

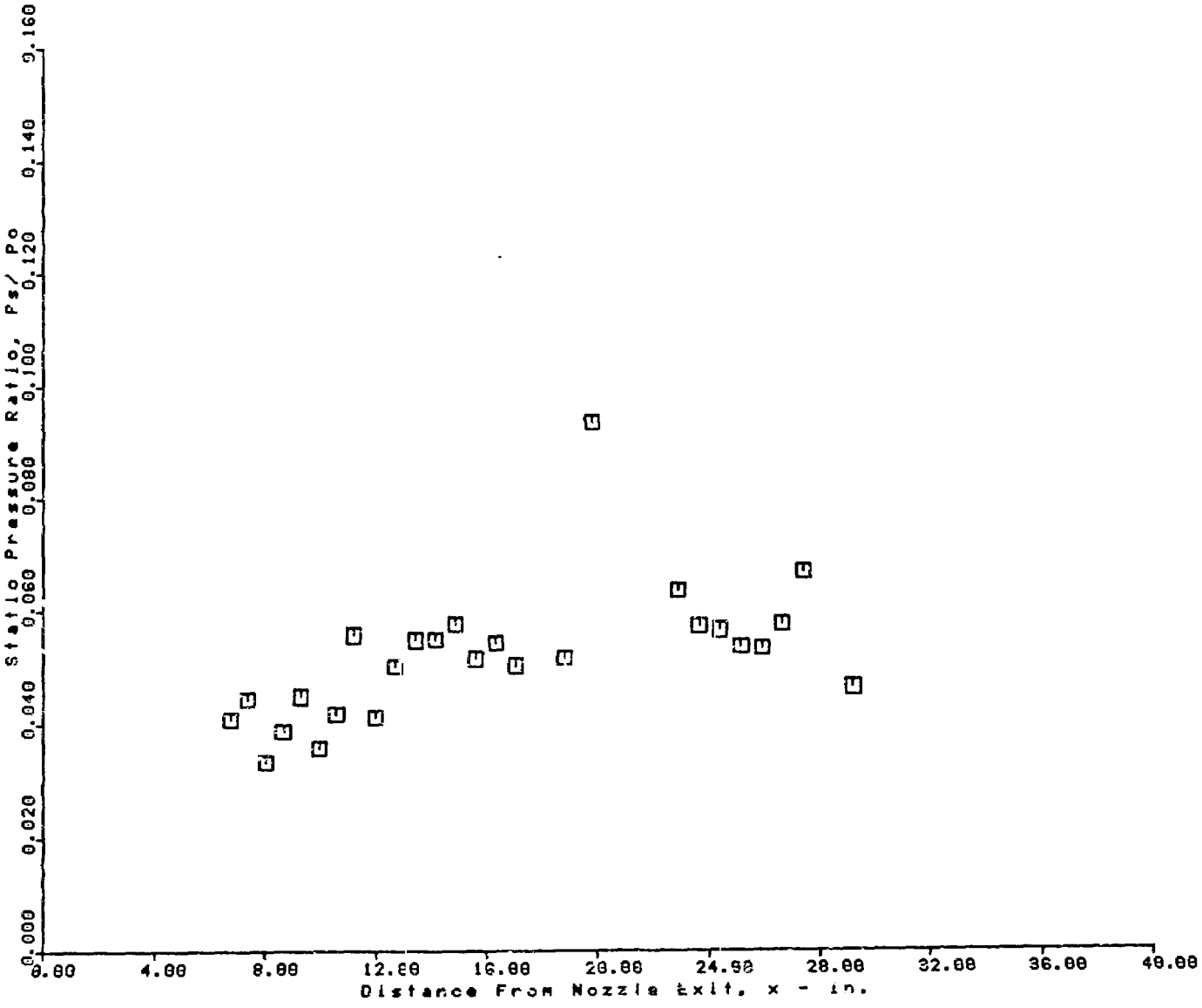

AFS TEST PROGRAM
UPPER SURFACE PRESSURE TAPS
RUN = 109 BURST = 50

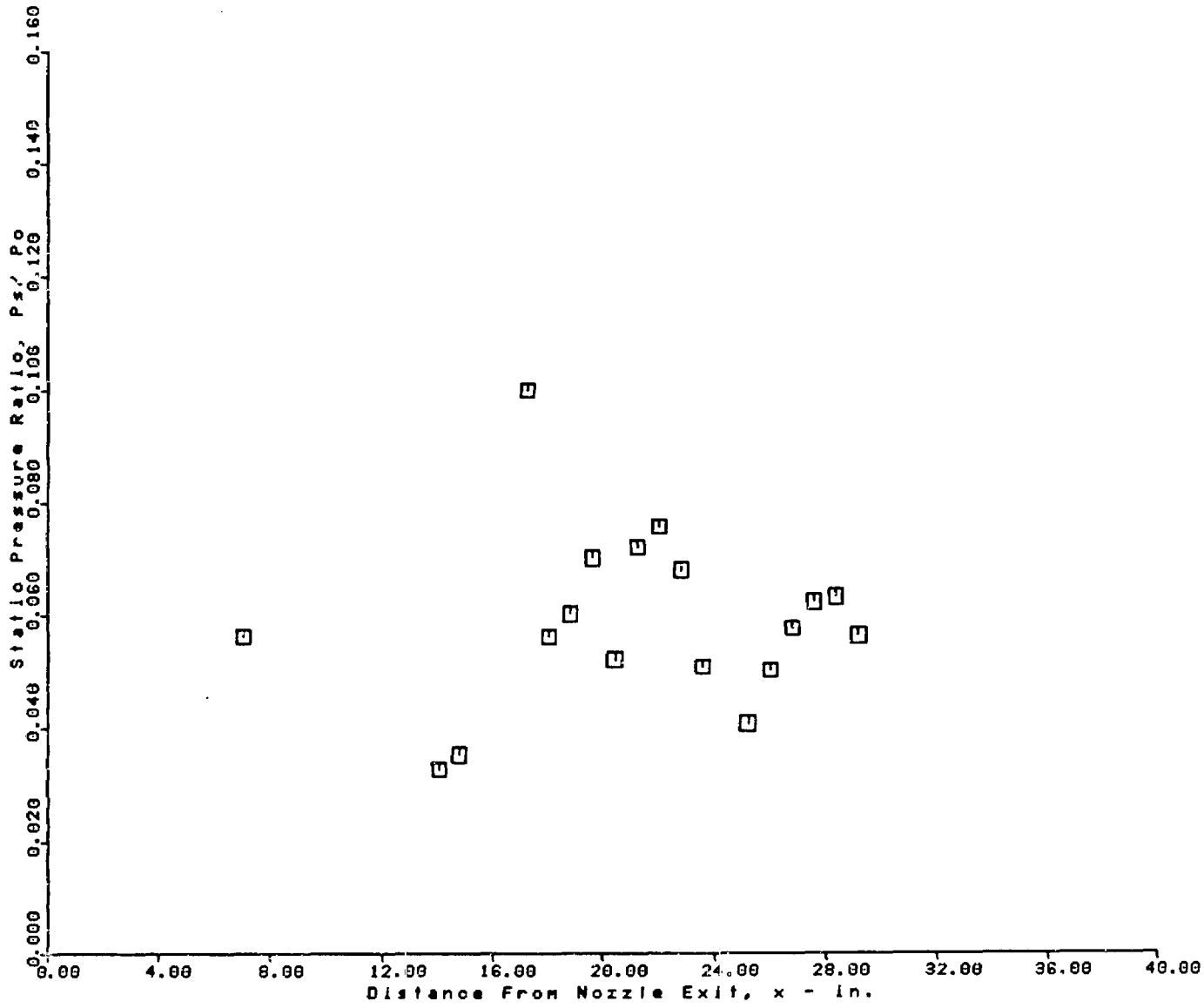

AFS TEST PROGRAM
LOWER SURFACE PRESSURE TAPS
RUN = 110 BURST = 50

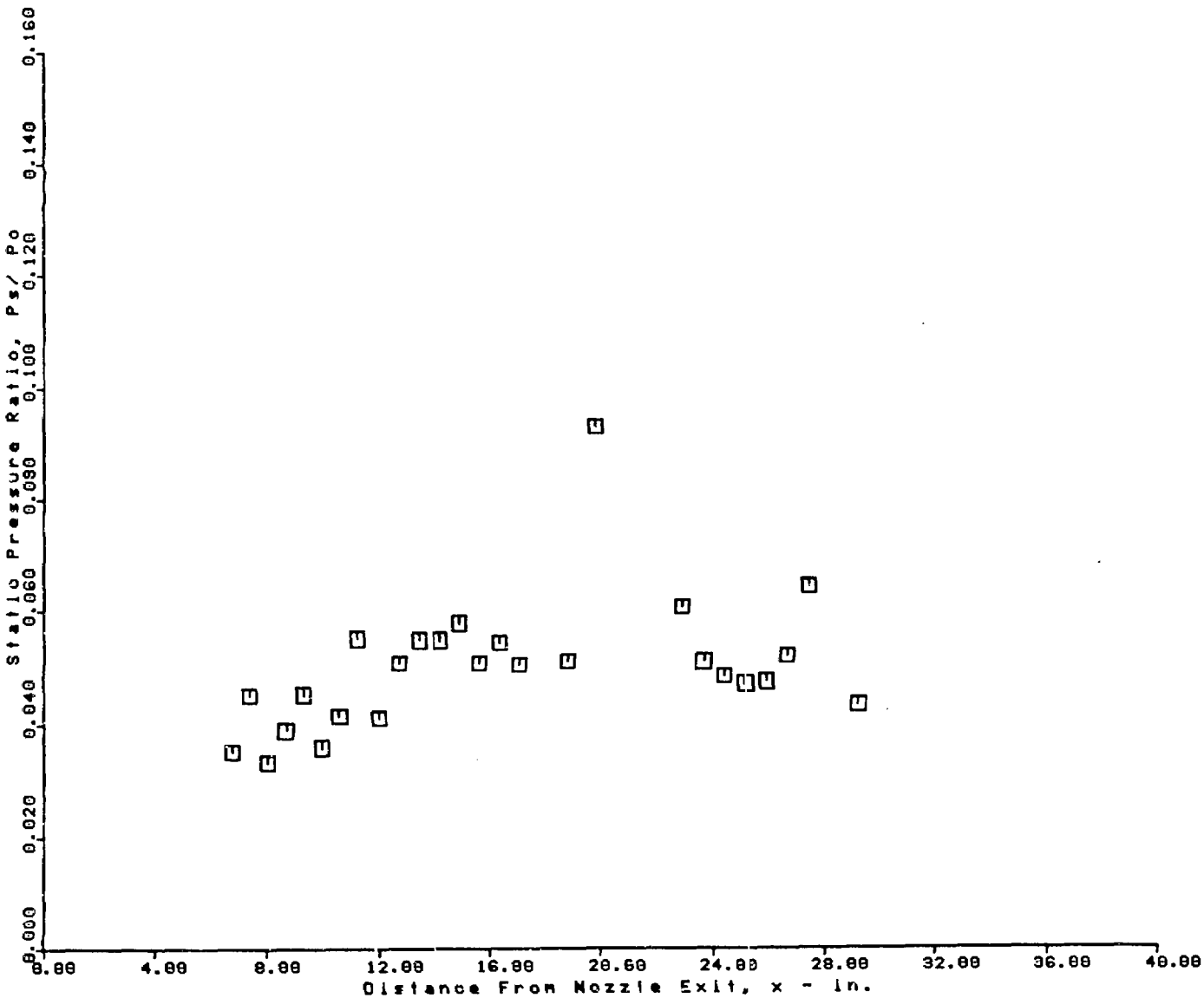

AFS TEST PROGRAM
UPPER SURFACE PRESSURE TAPS
RUN = 118 BURST = 58

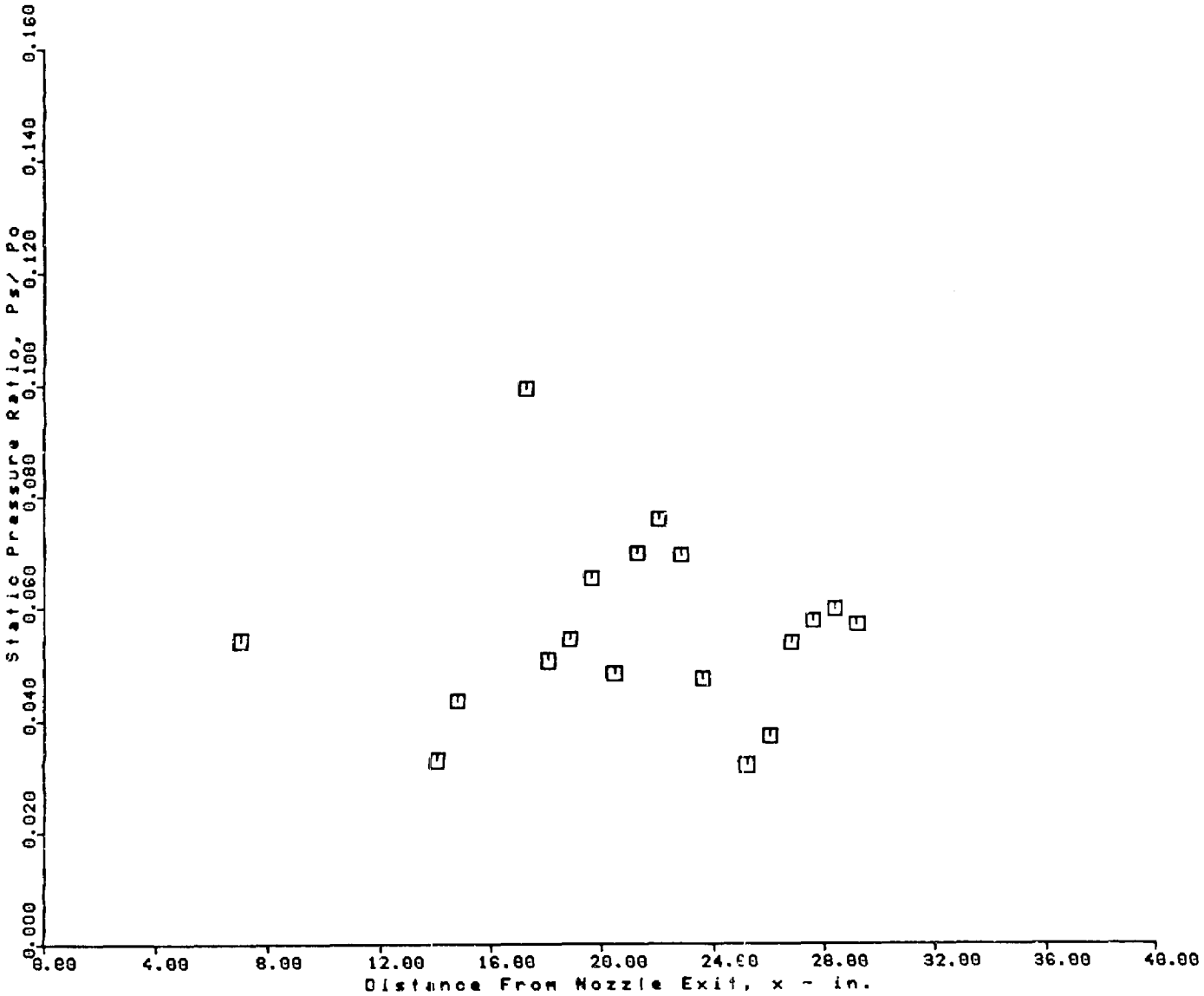

AFS TEST PROGRAM
LOWER SURFACE PRESSURE TAPS
RUN = 111 BURST = 50

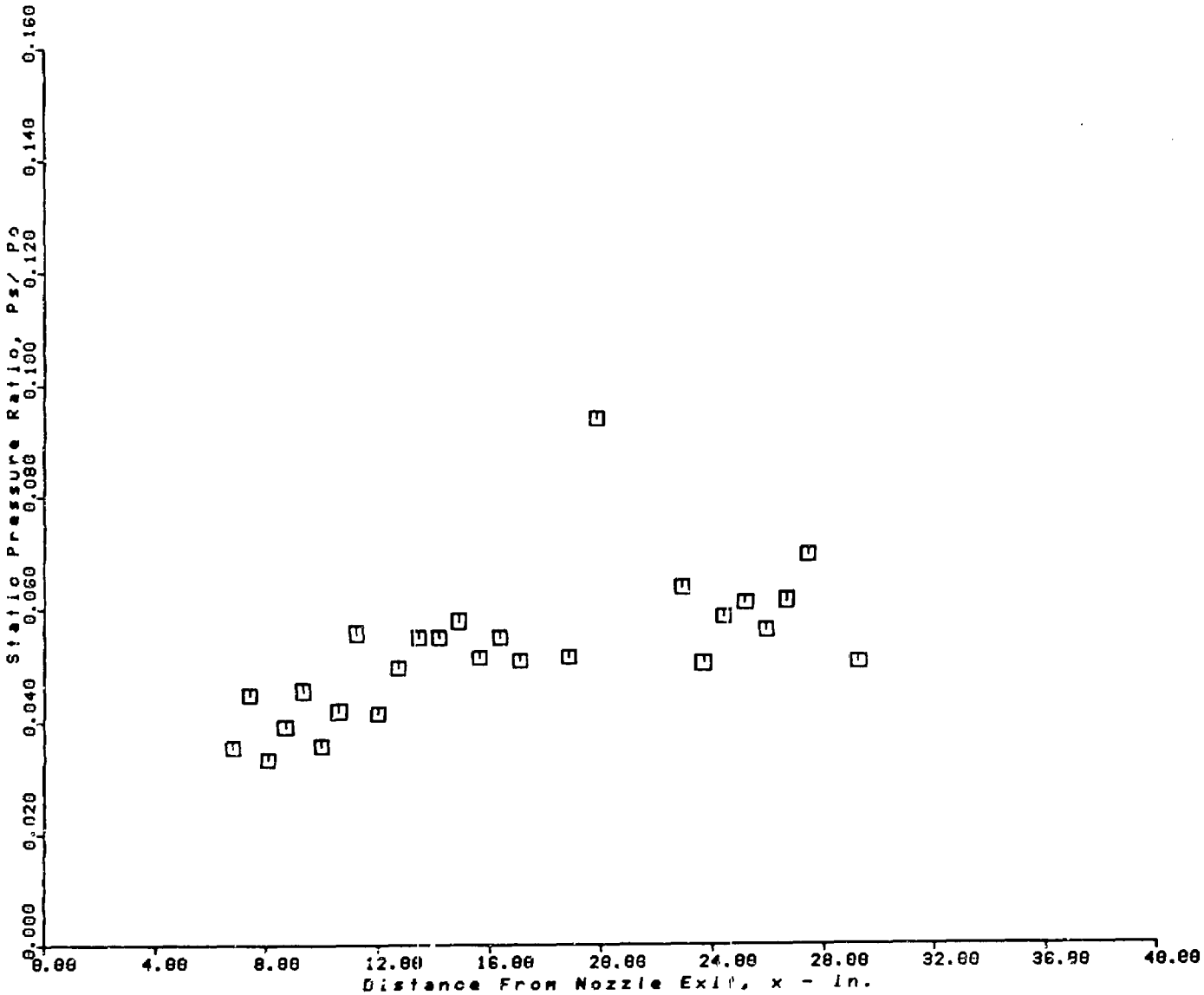

AFS TEST PROGRAM
UPPER SURFACE PRESSURE TAPS
RUN = 111 BURST = 50

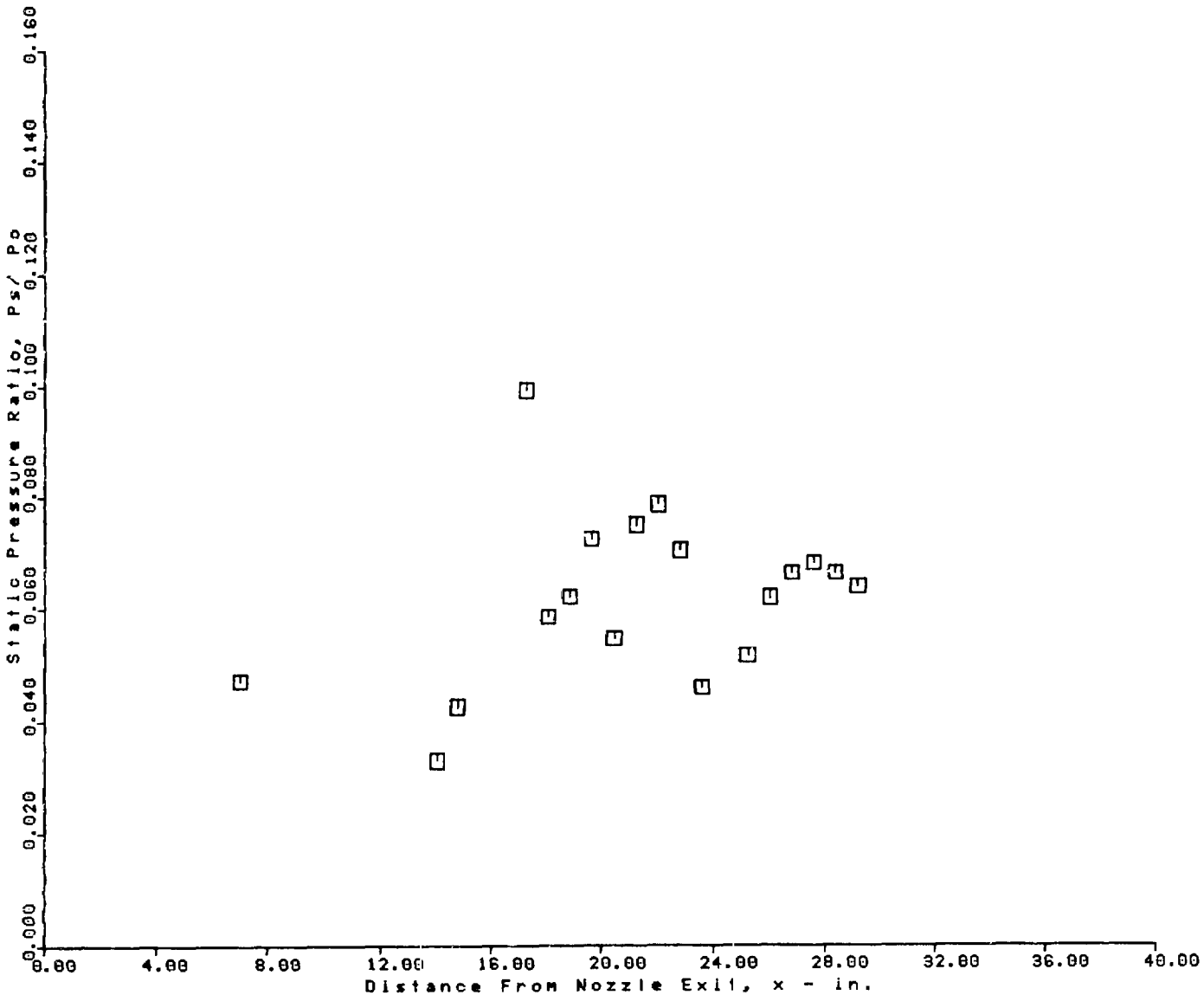

AFS TEST PROGRAM
LOWER SURFACE PRESSURE TAPS
RUN = 112 BURST = 50

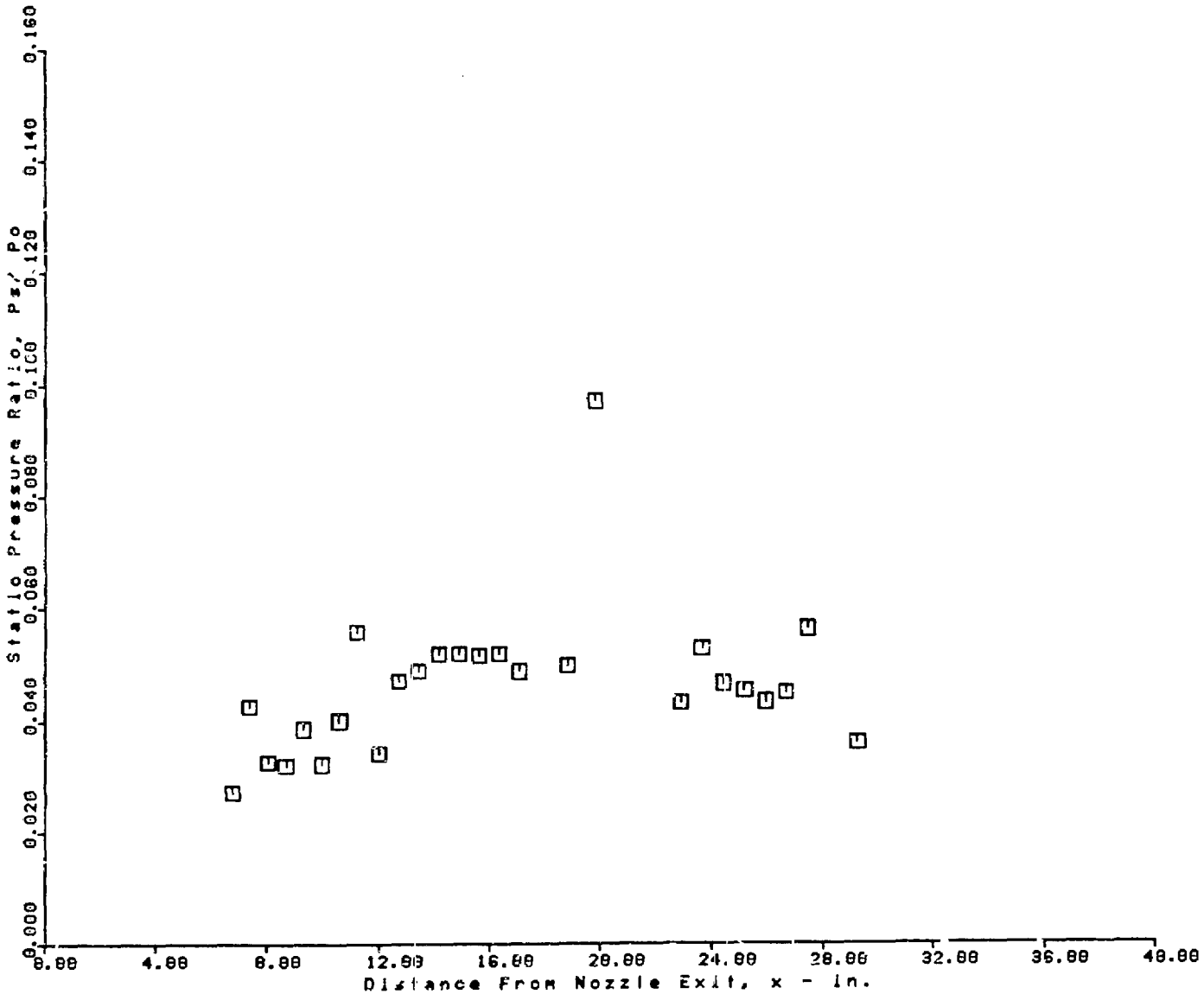

AFS TEST PROGRAM
UPPER SURFACE PRESSURE TAPS
RUN = 112 BURST = 50

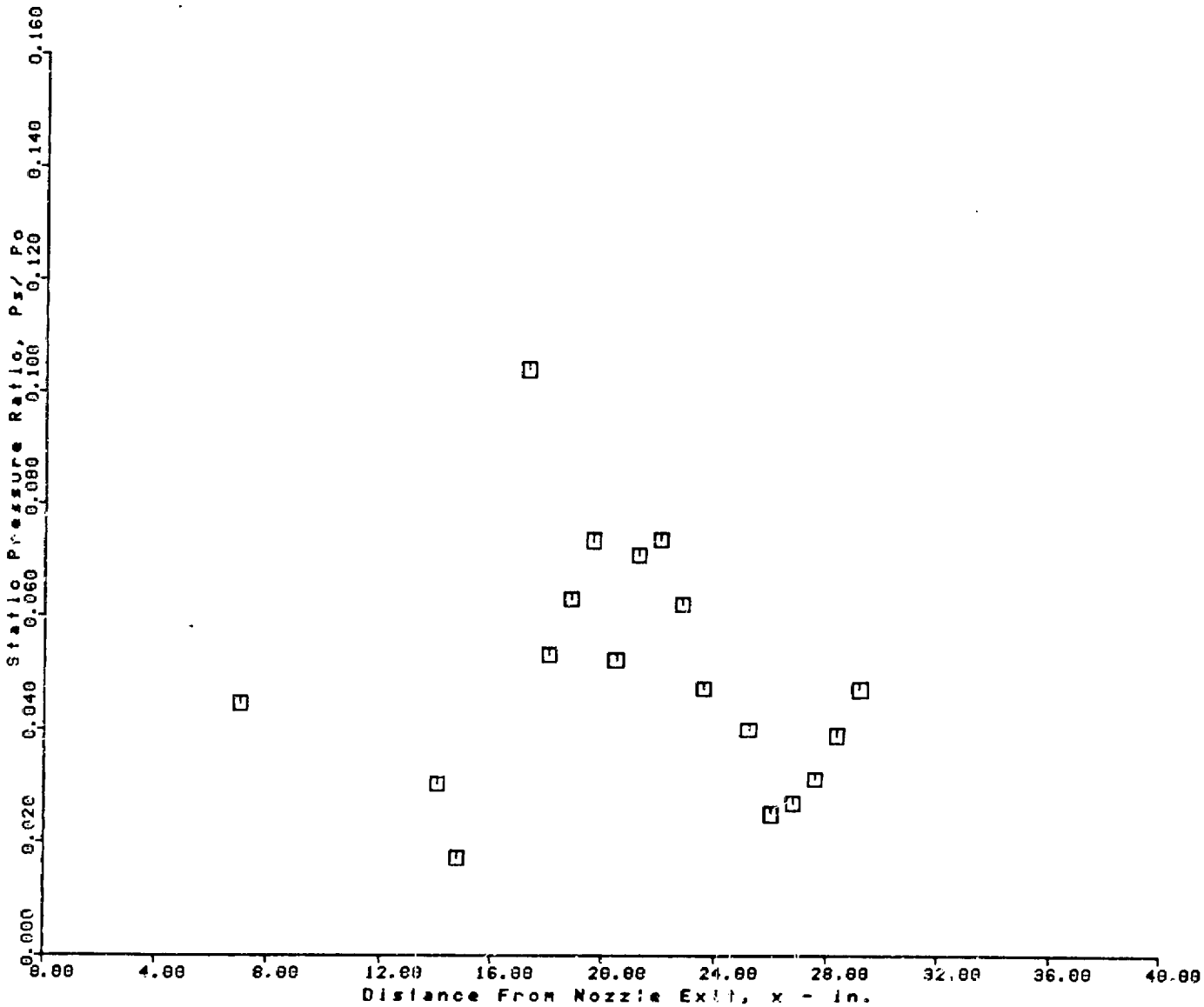

AFS TEST PROGRAM
LOWER SURFACE PRESSURE TAPS
RUN = 113 BURST = 50

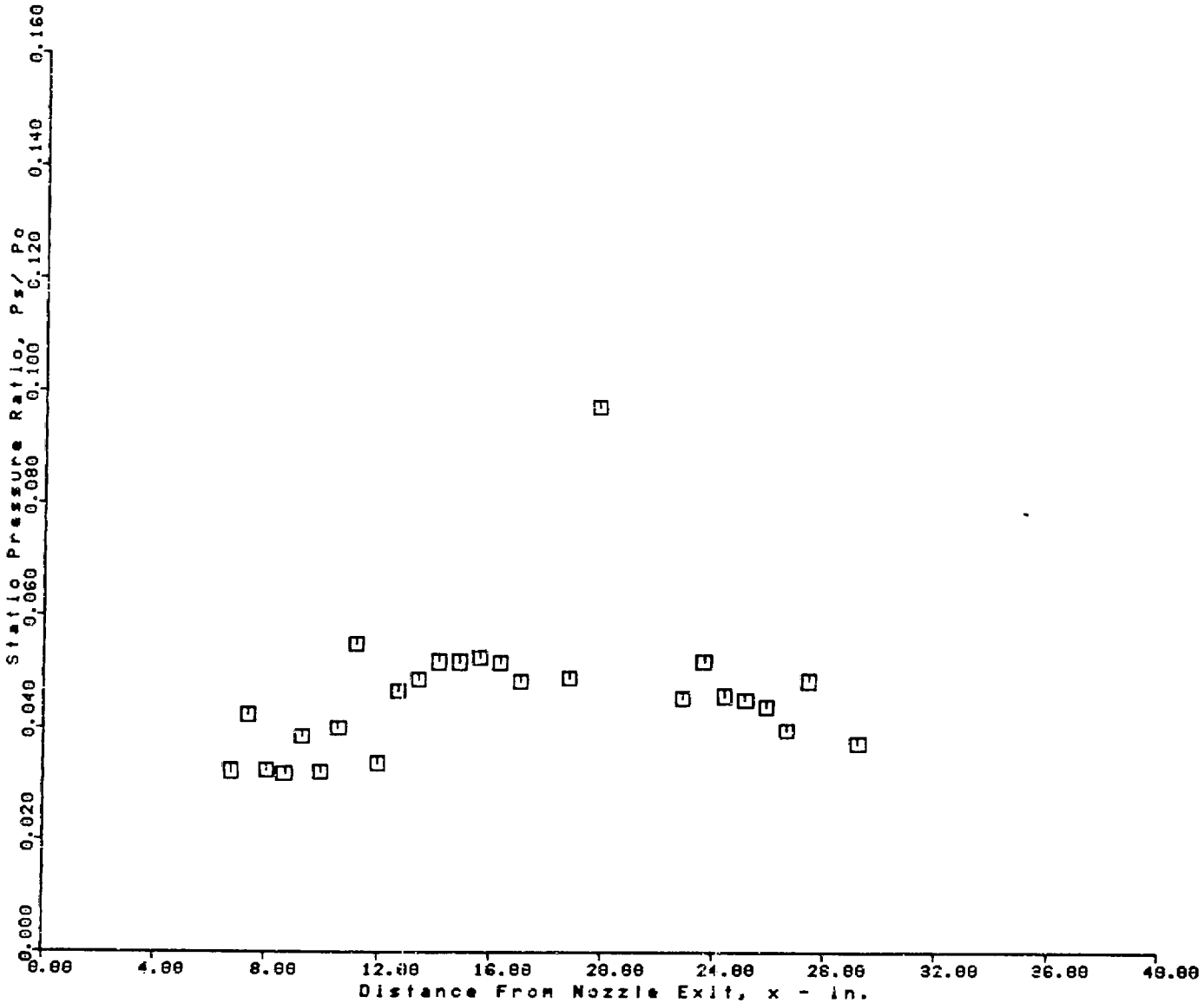

AFS TEST PROGRAM
UPPER SURFACE PRESSURE TAPS
RUN = 113 BURST = 50

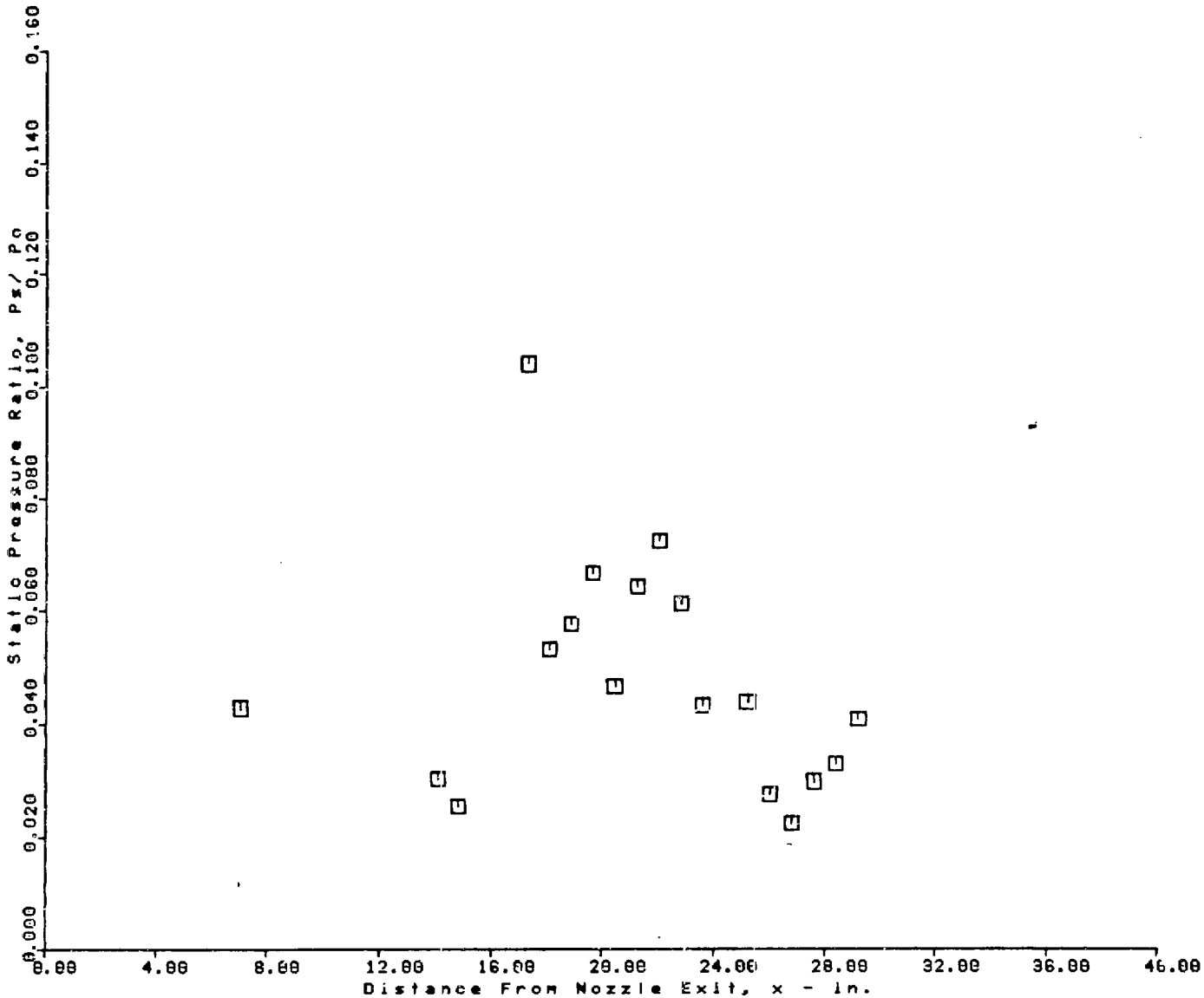

AFS TEST PROGRAM
LOWER SURFACE PRESSURE TAPS
RUN = 114 BURST = 50

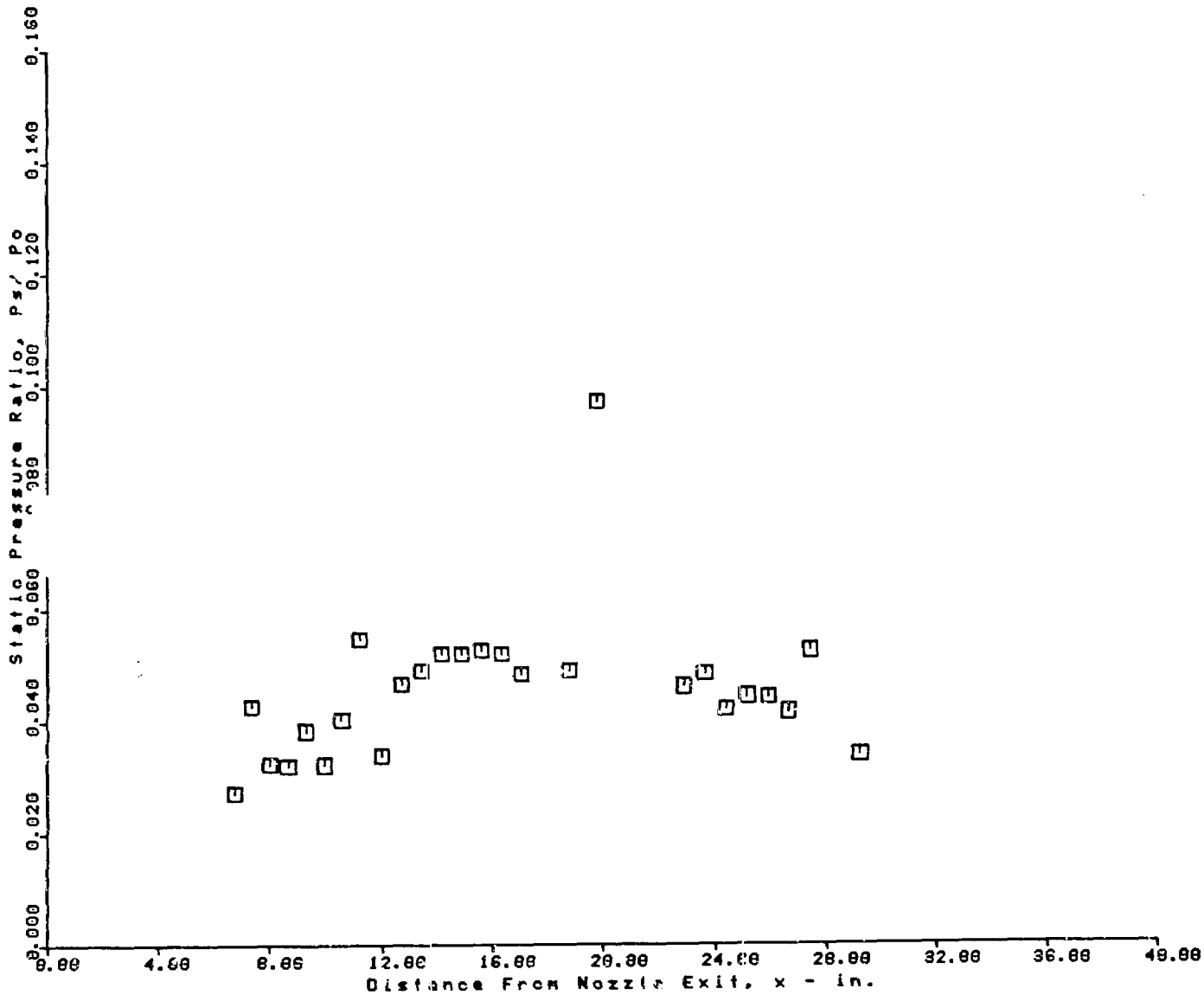

AFS TEST PROGRAM
UPPER SURFACE PRESSURE TAPS
RUN = 114 BURST = 50

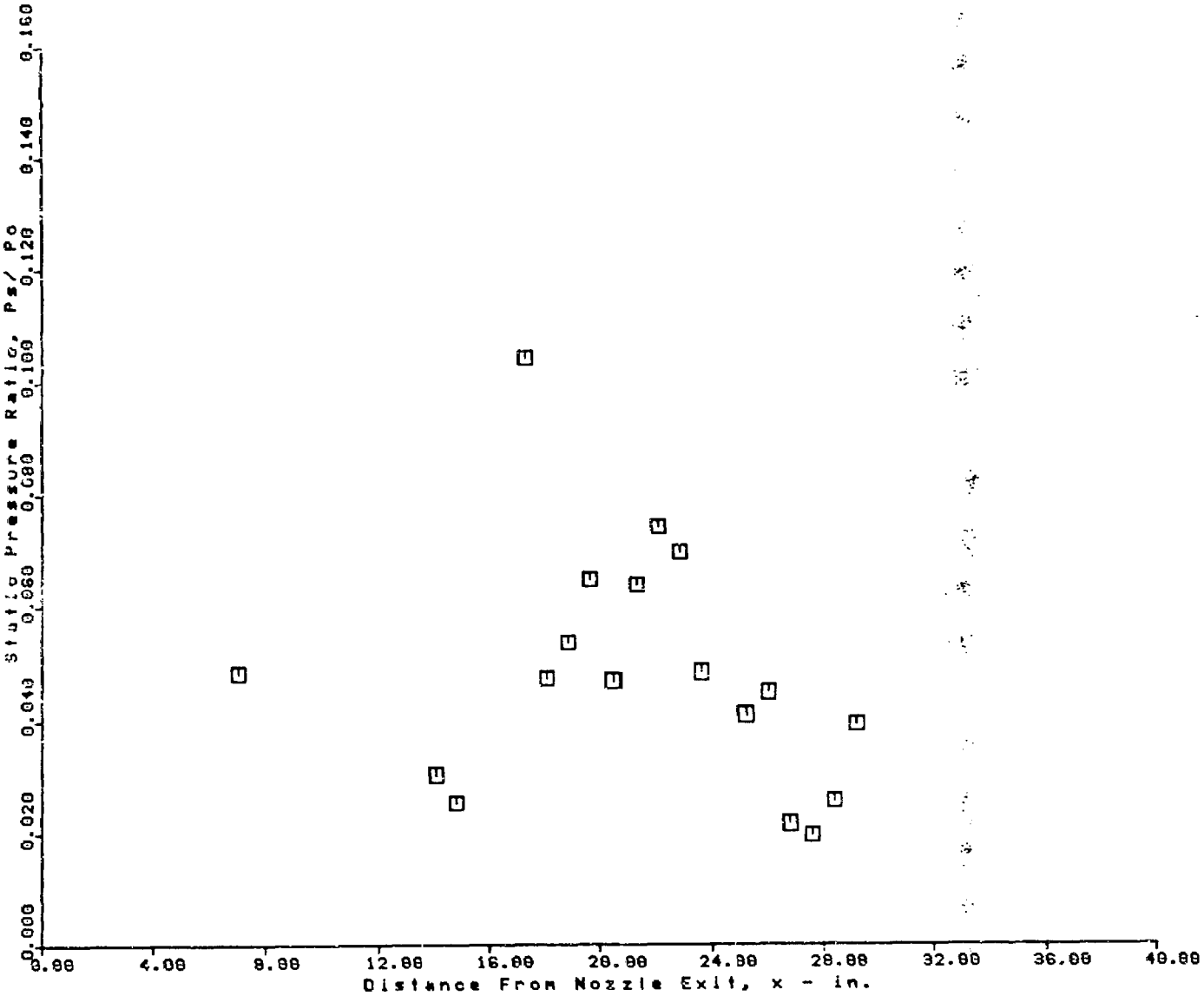

AFS TEST PROGRAM
LOWER SURFACE PRESSURE TAPS
RUN = 121 BURST = 50

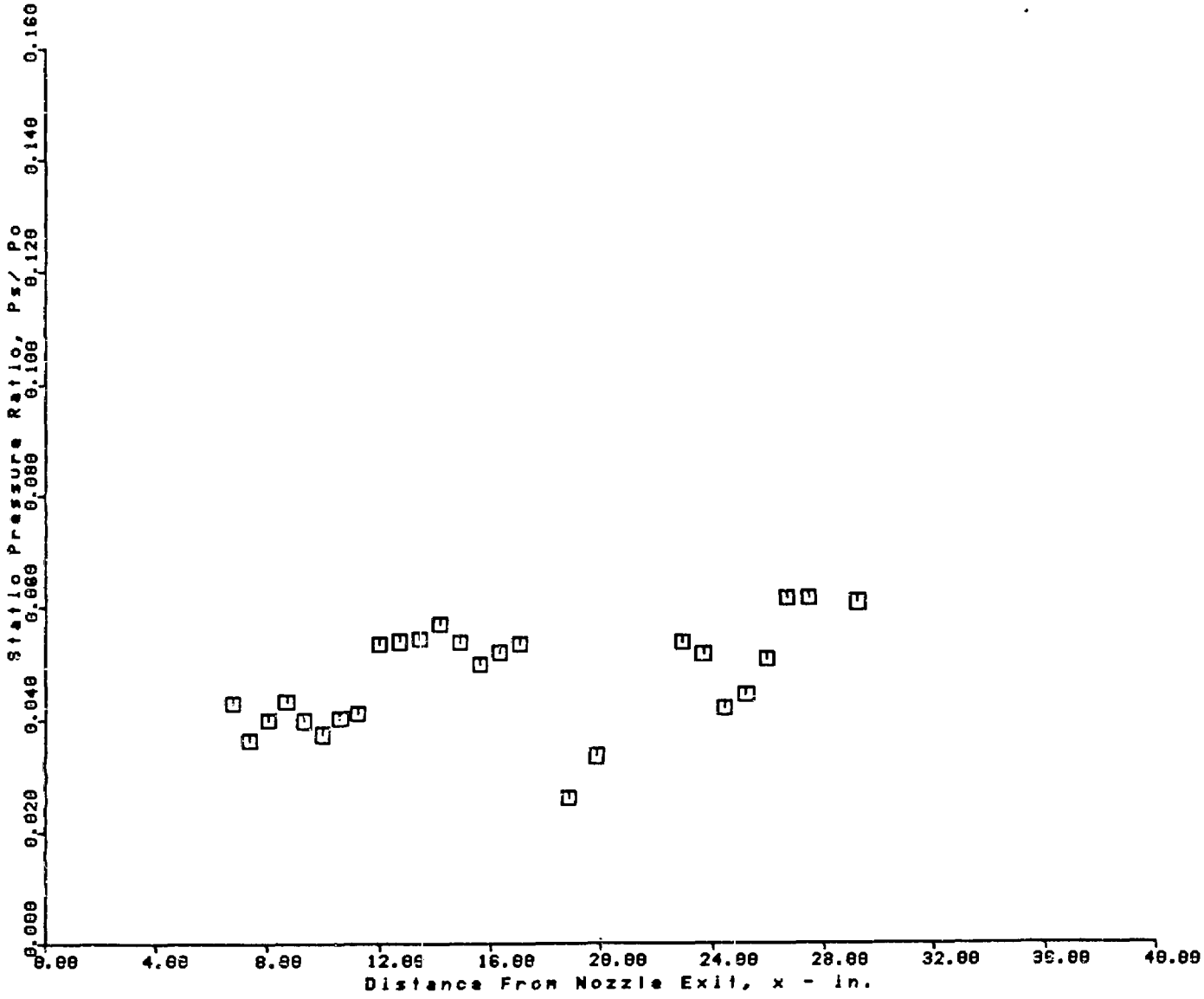

AFS TEST PROGRAM
UPPER SURFACE PRESSURE TAPS
RUN = 121 BURST = 58

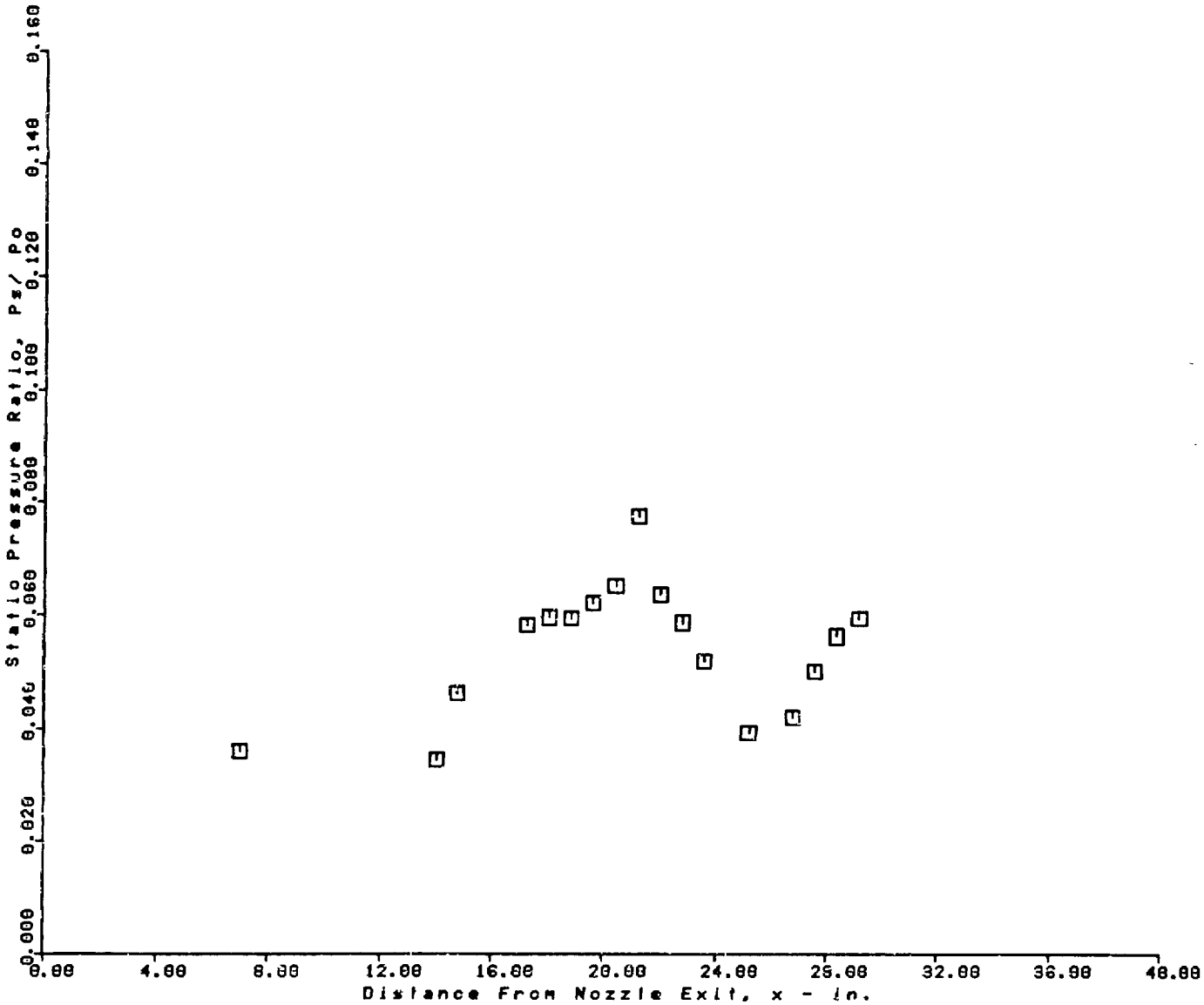

AFS TEST PROGRAM
LOWER SURFACE PRESSURE TAPS
RUN = 122 BURST = 50

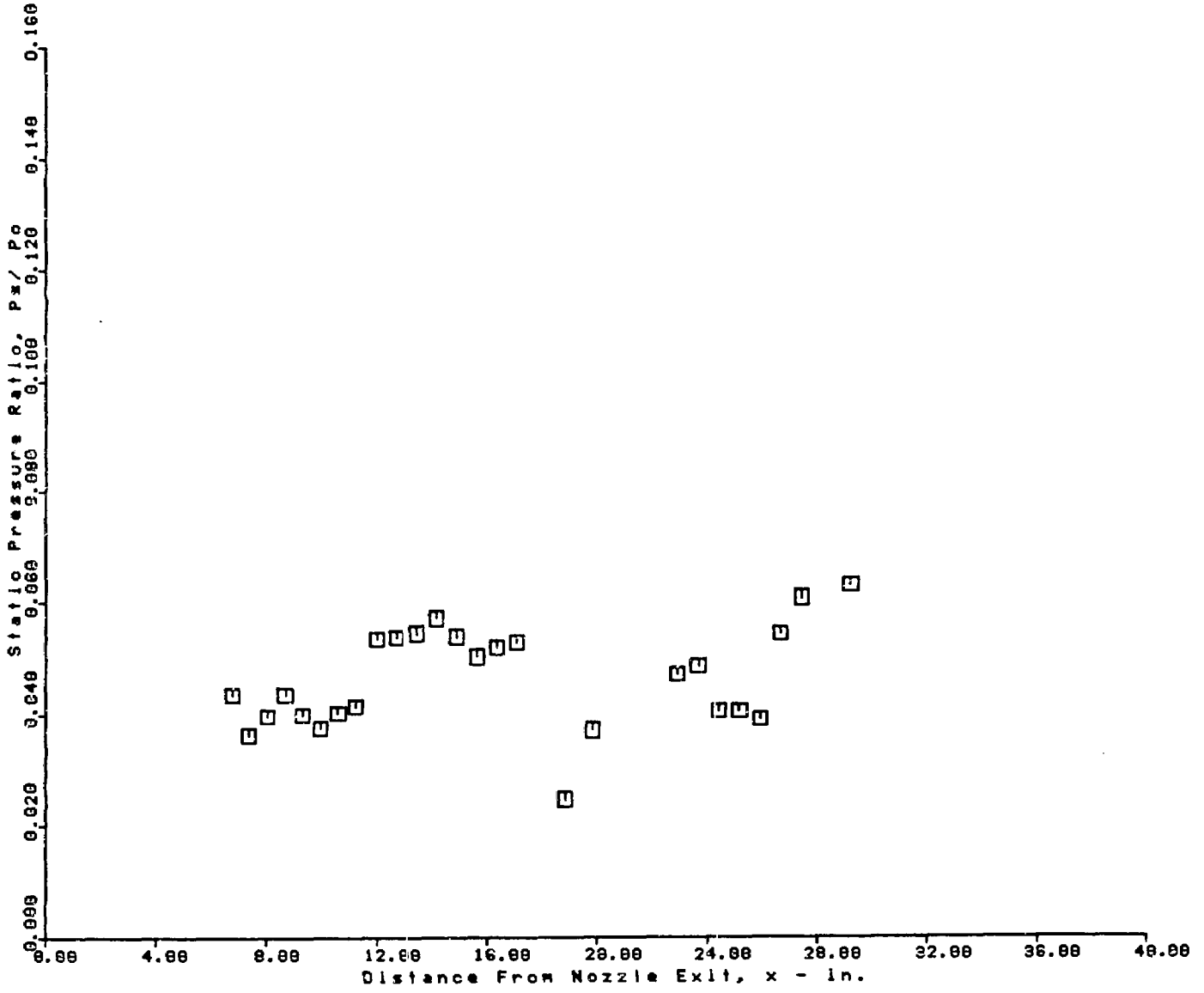

AFS TEST PROGRAM
UPPER SURFACE PRESSURE TAPS
RUN = 122 BURST = 58

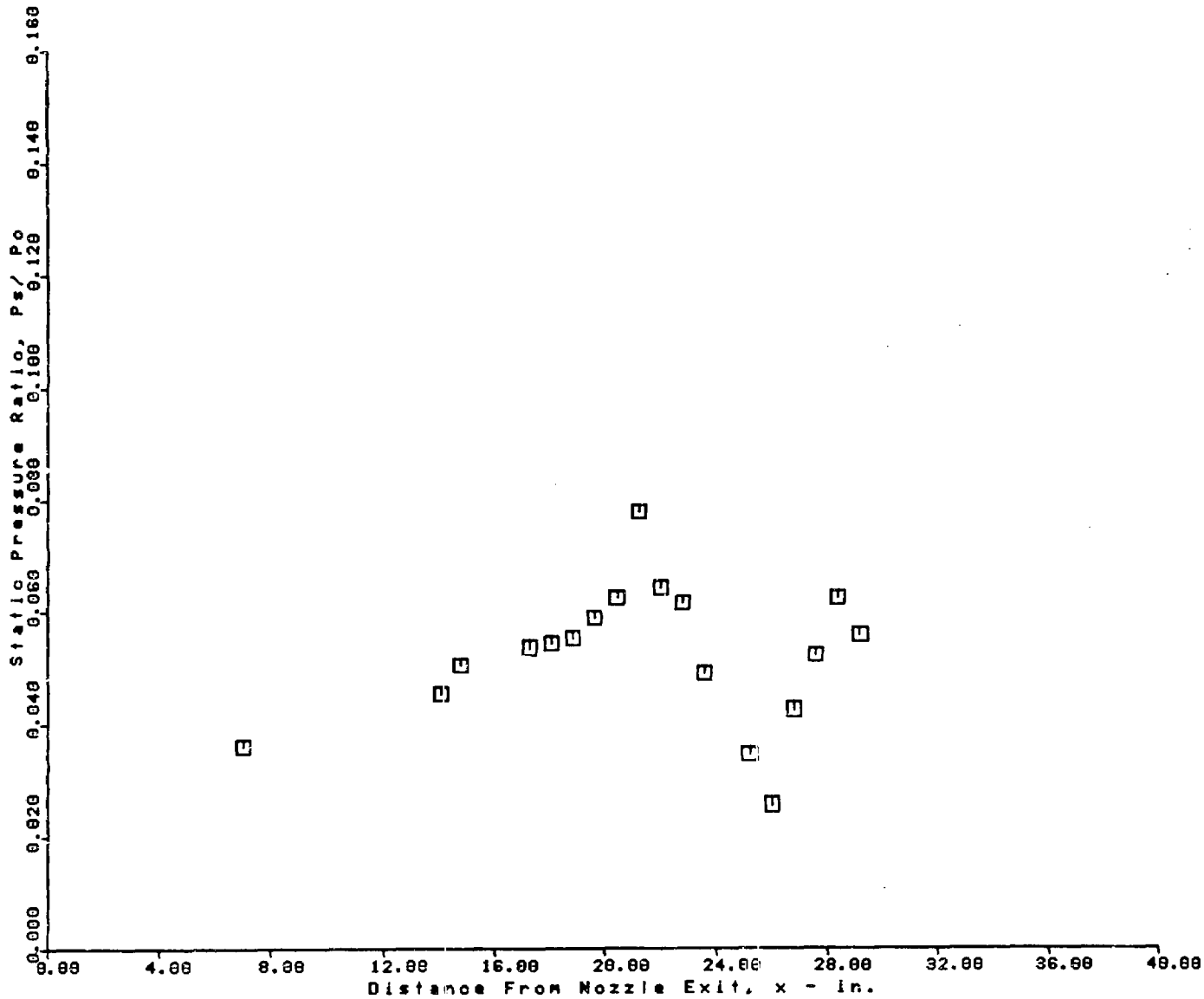

AFS TEST PROGRAM
LOWER SURFACE PRESSURE TAPS
RUN = 124 BURST = 50

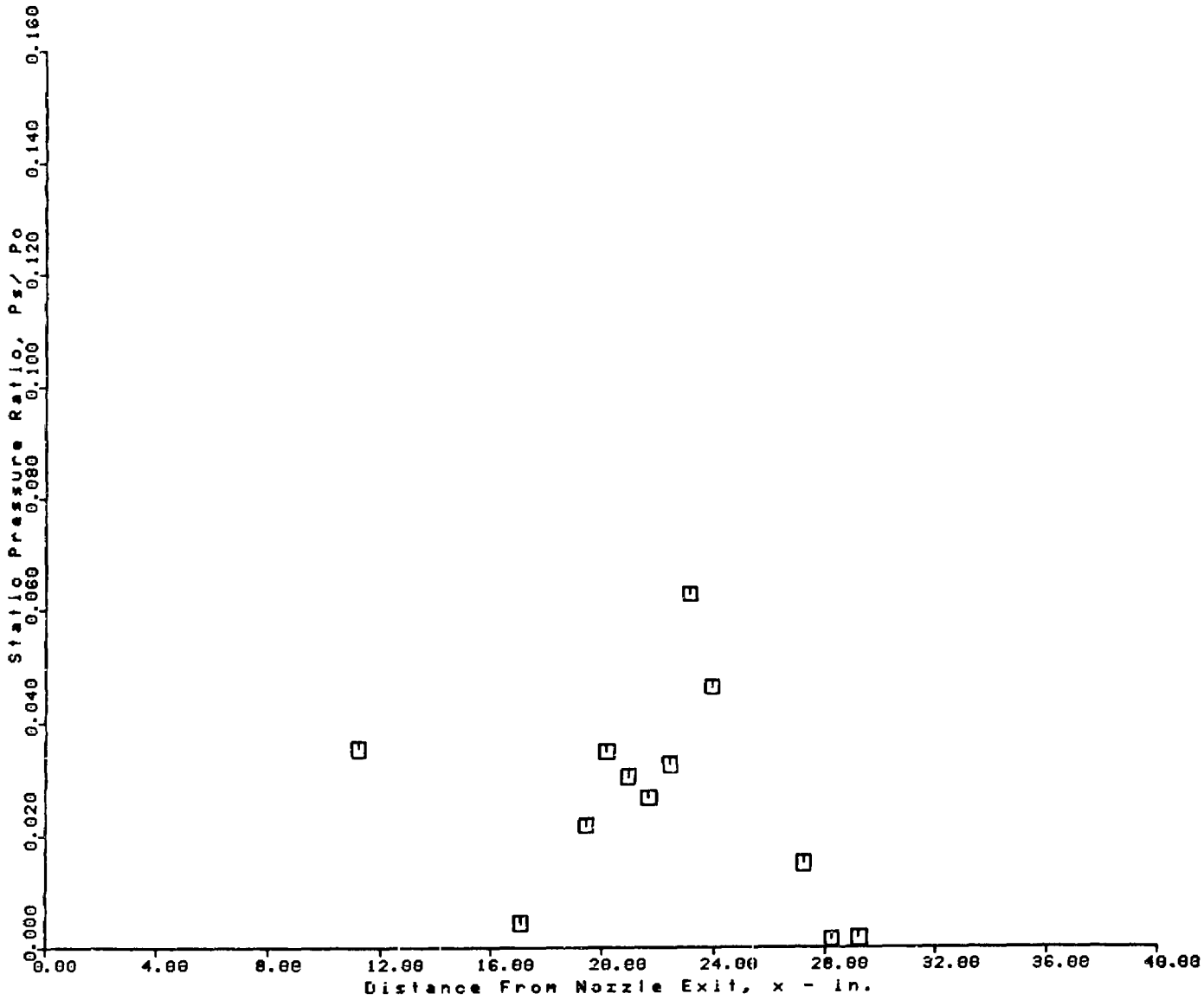

AFS TEST PROGRAM
UPPER SURFACE PRESSURE TAPS
RUN = 124 BURST = 50

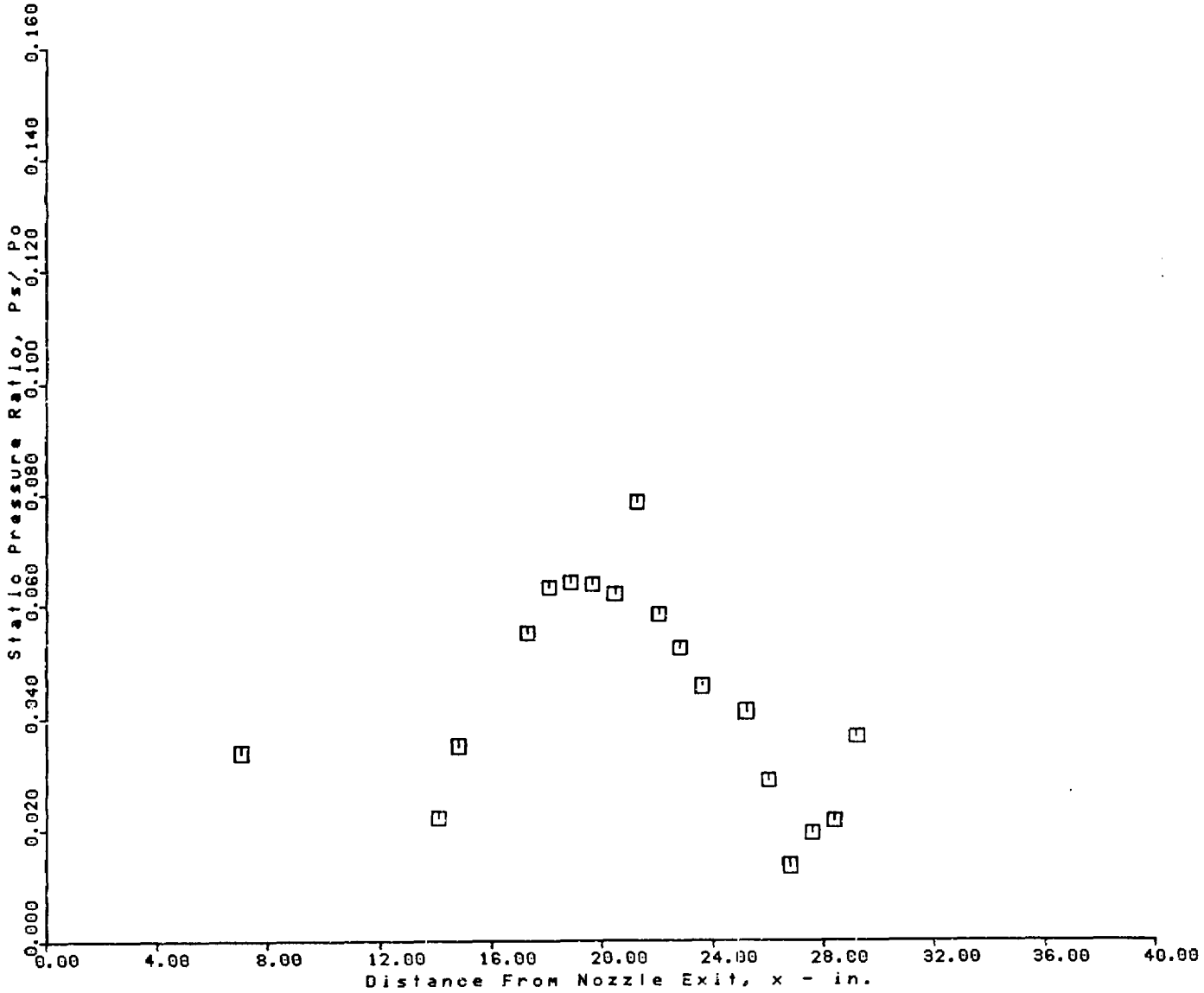

AFS TEST PROGRAM
LOWER SURFACE PRESSURE TAPS
RUN = 125 BURST = 50

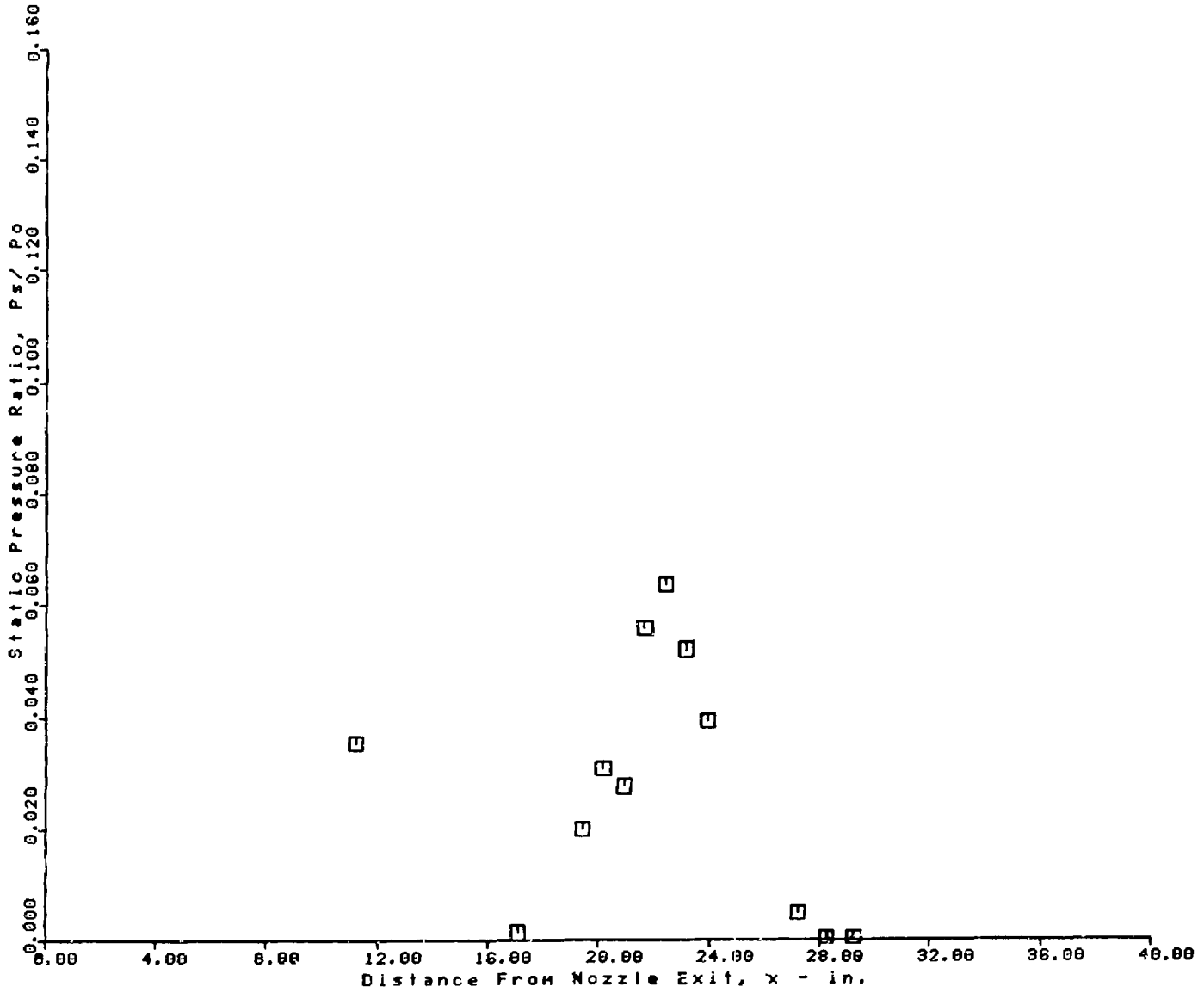

AFS TEST PROGRAM
UPPER SURFACE PRESSURE TAPS
RUN = 125 BURST = 50

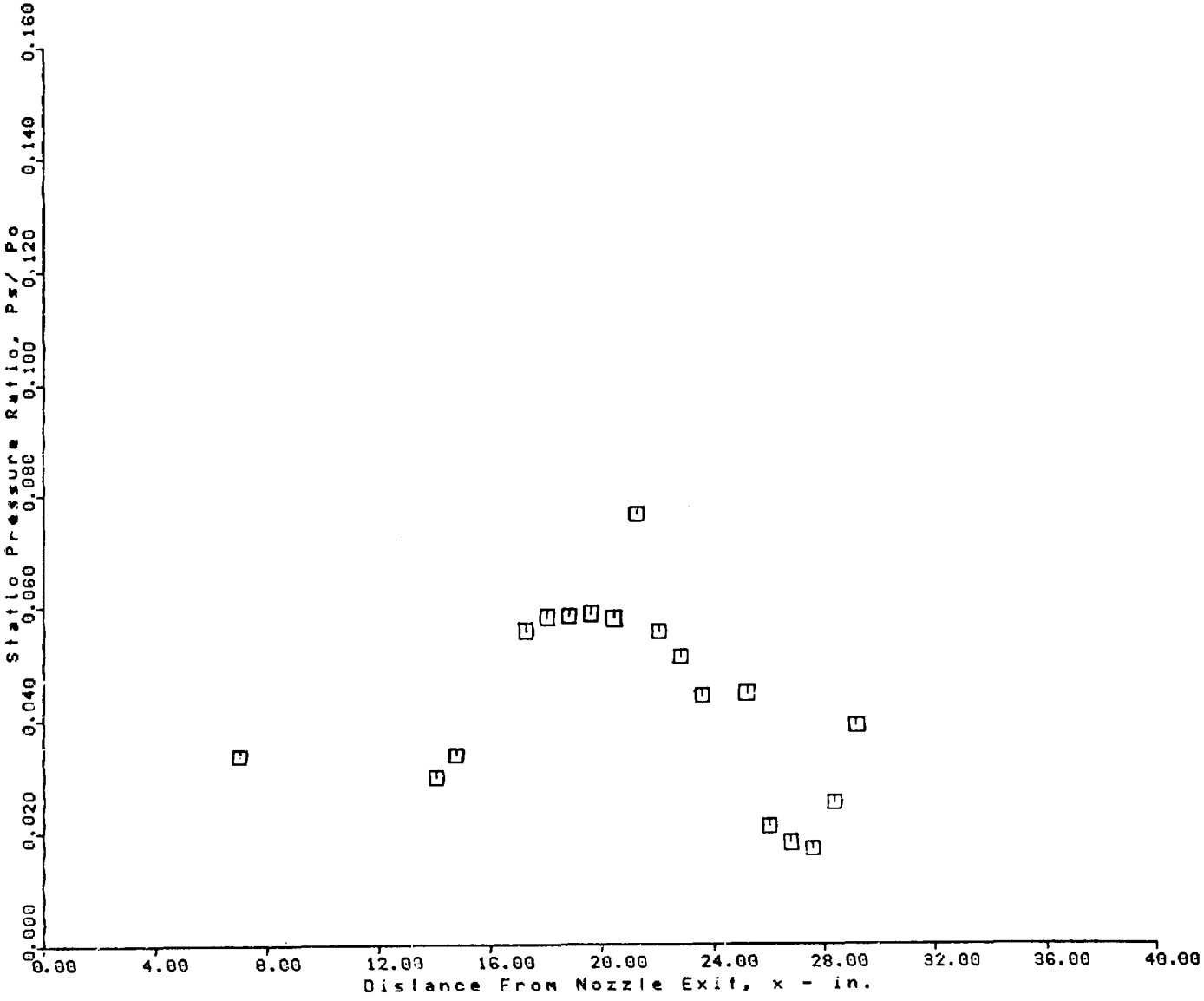

AFS TEST PROGRAM
LOWER SURFACE PRESSURE TAPS
RUN = 126 BURST = 58

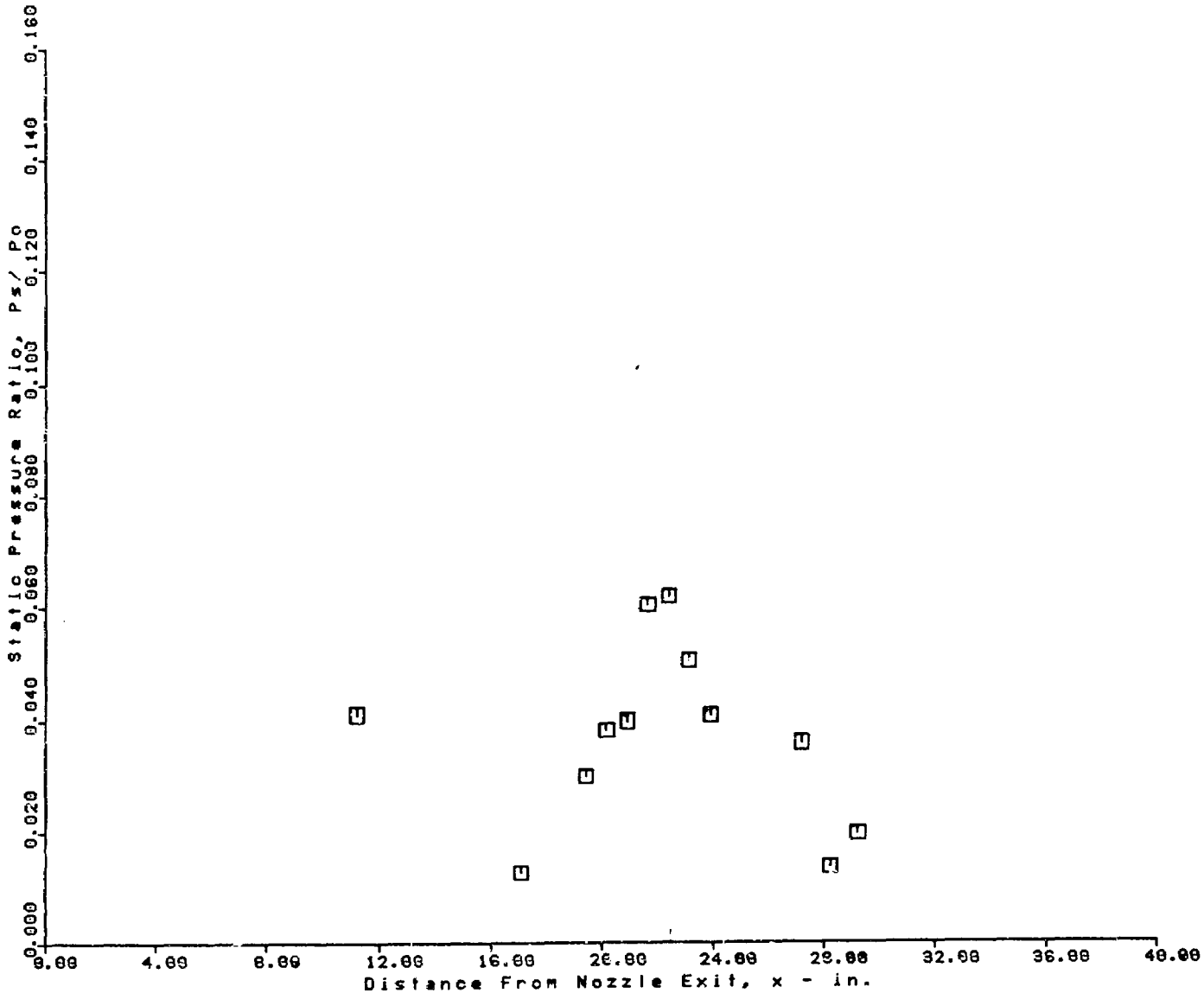

AFS TEST PROGRAM
UPPER SURFACE PRESSURE TAPS
RUN = 126 BURST = 50

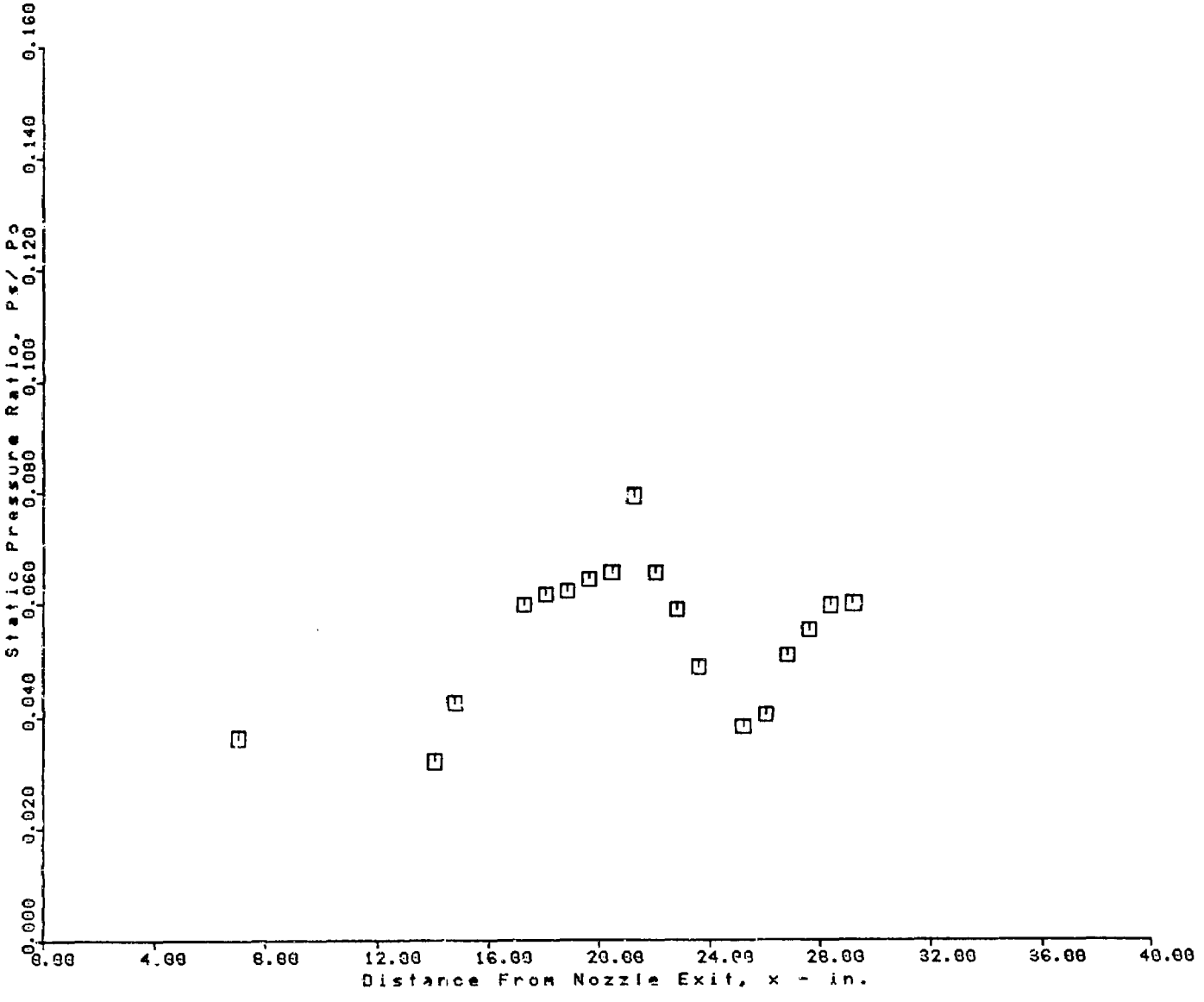

AFS TEST PROGRAM
LOWER SURFACE PRESSURE TAPS
RUN = 127 BURST = 58

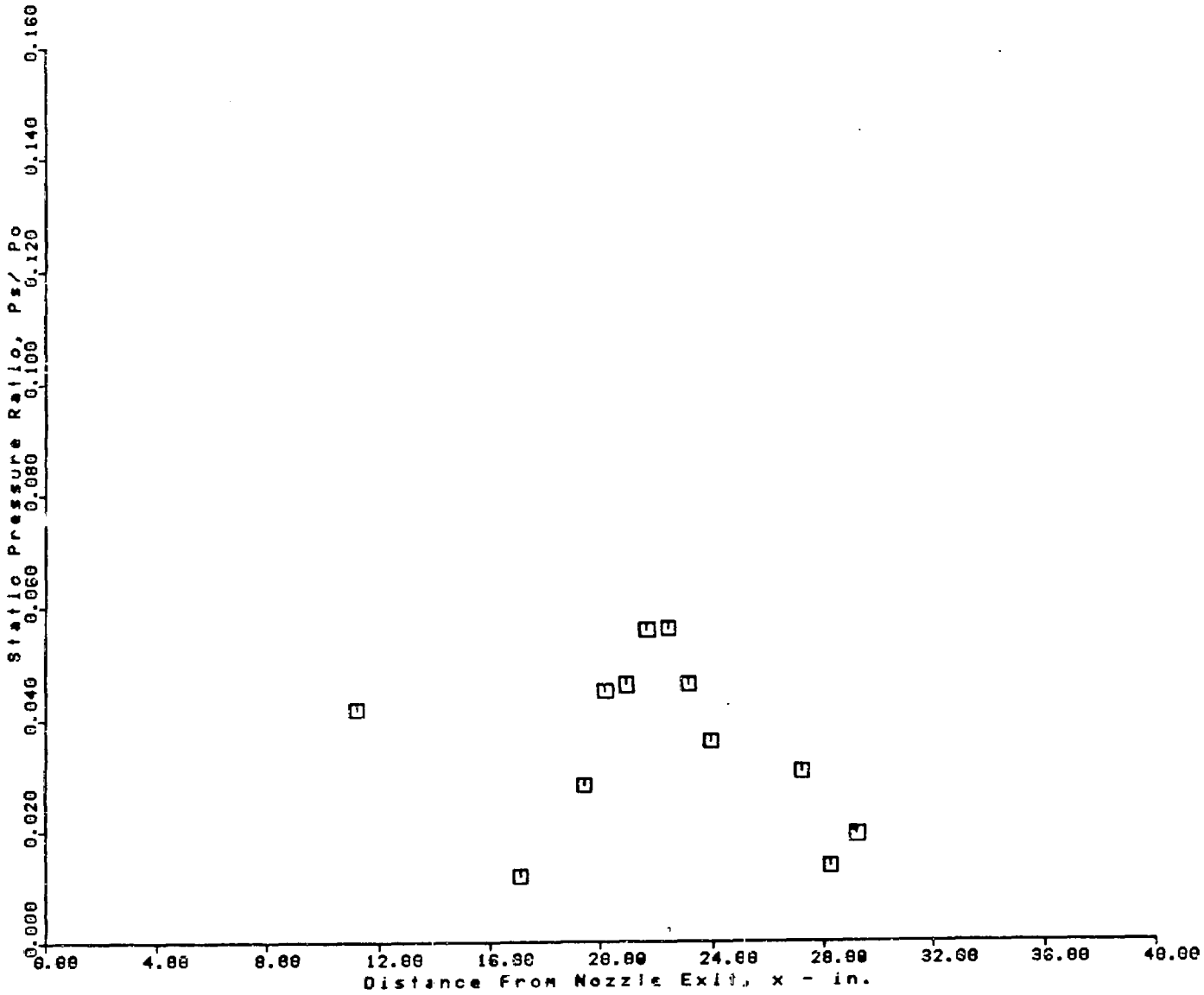

AFS TEST PROGRAM
UPPER SURFACE PRESSURE TAPS
RUN = 127 BURST = 50

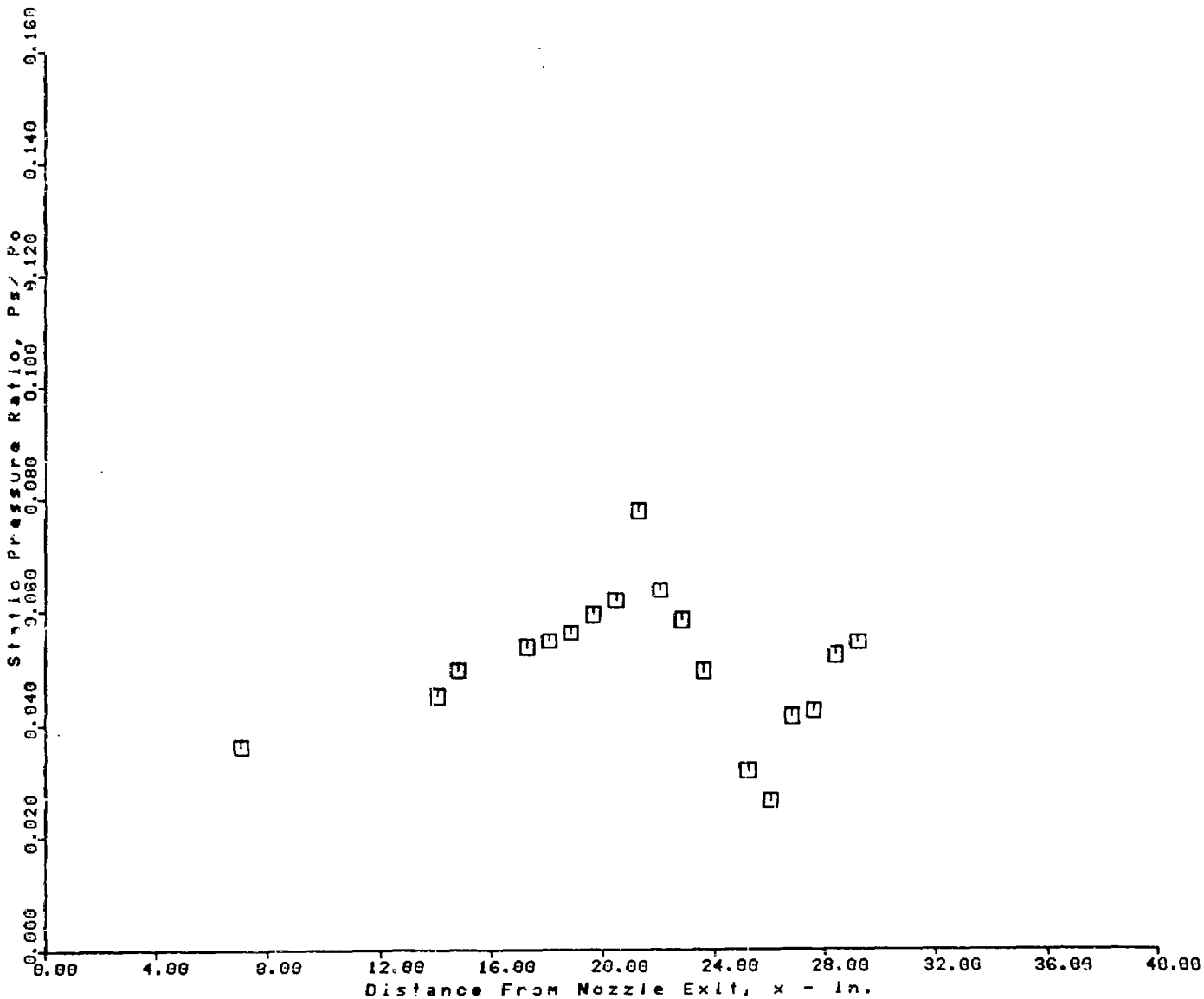

AFS TEST PROGRAM
LOWER SURFACE PRESSURE TAPS
RUN = 128 BURST = 58

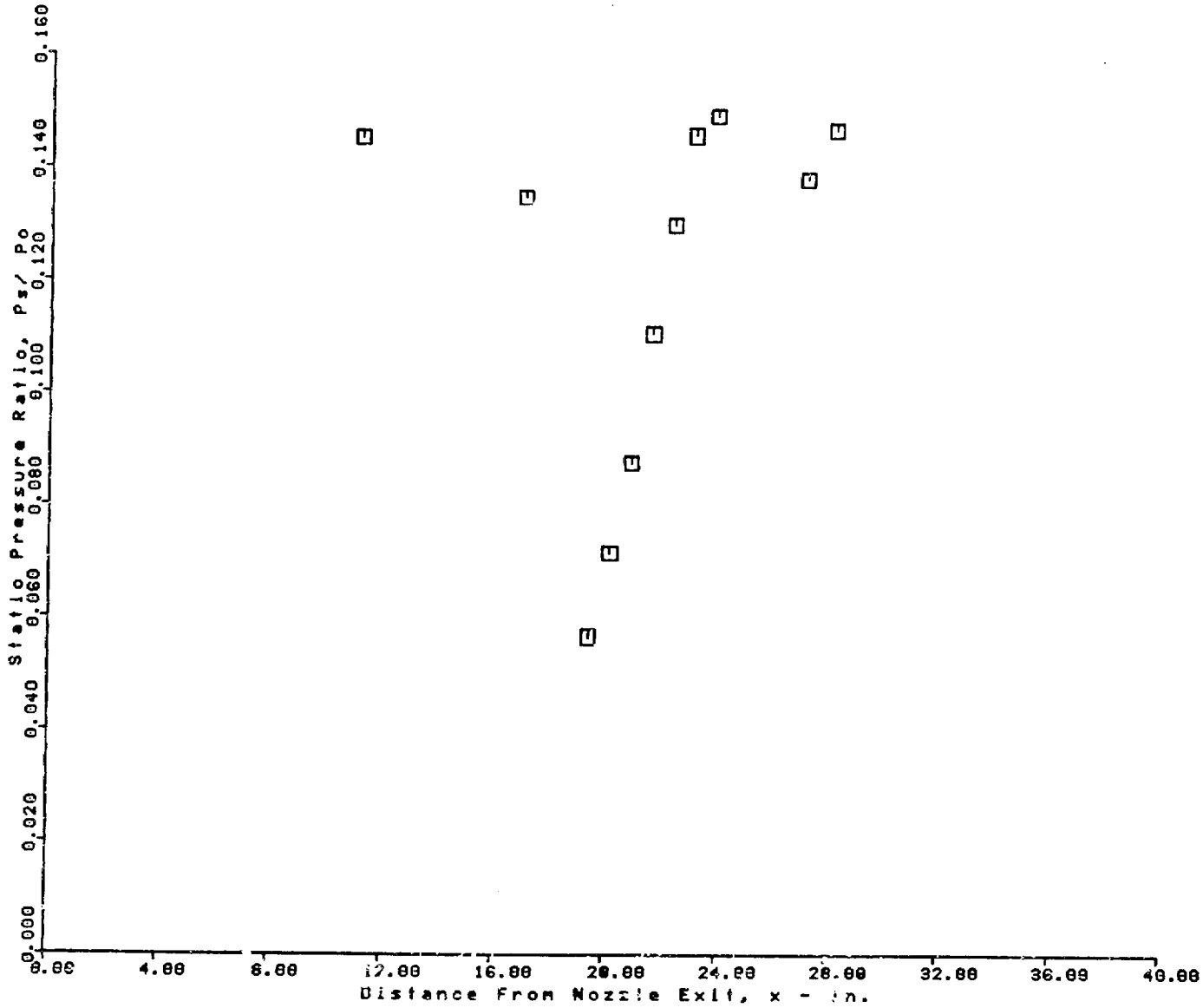

AFS TEST PROGRAM
UPPER SURFACE PRESSURE TAPS
RUN = 128 BURST = 50

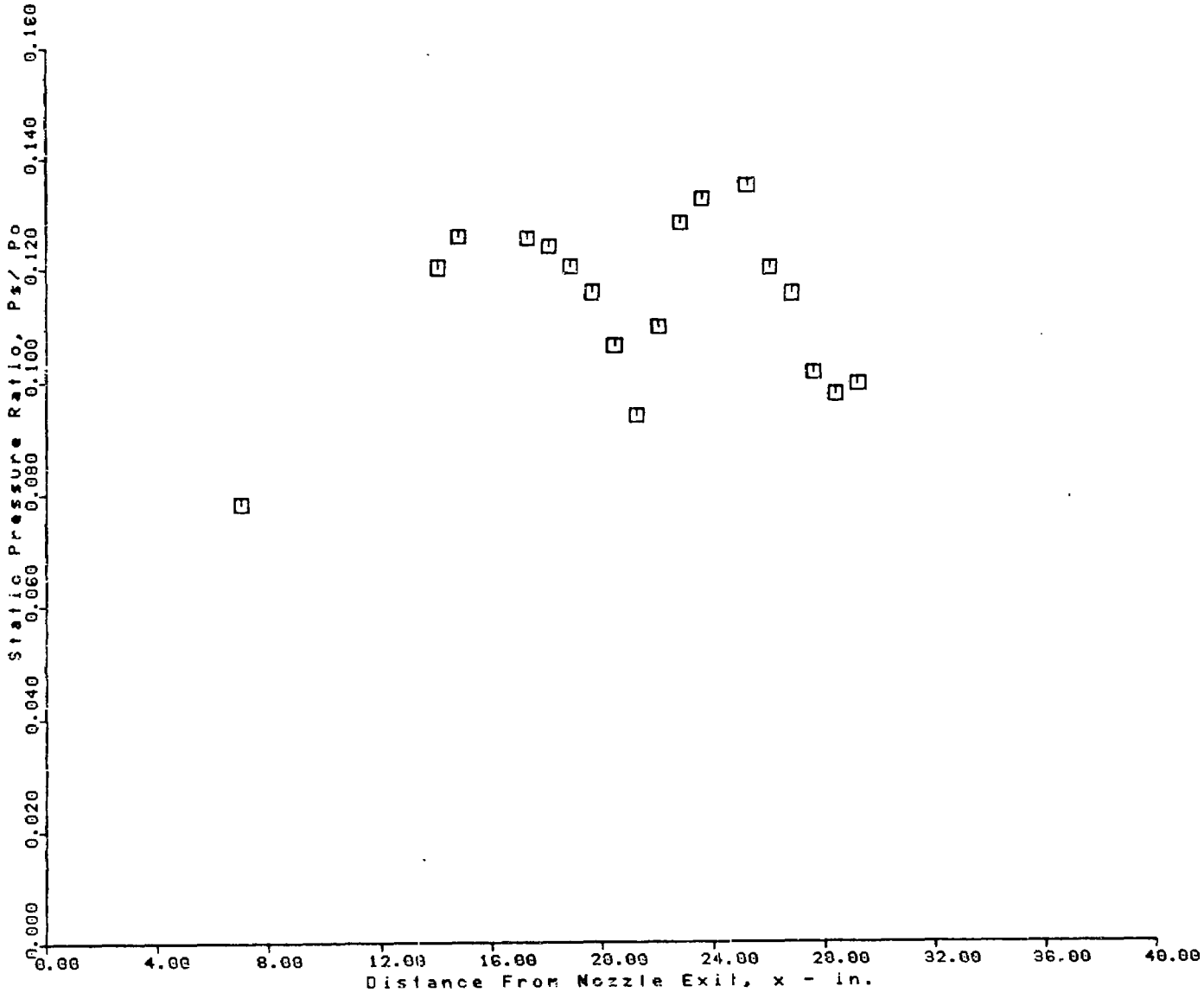

AFS TEST PROGRAM
LOWER SURFACE PRESSURE TAPS
RUN = 46 BURST = 38

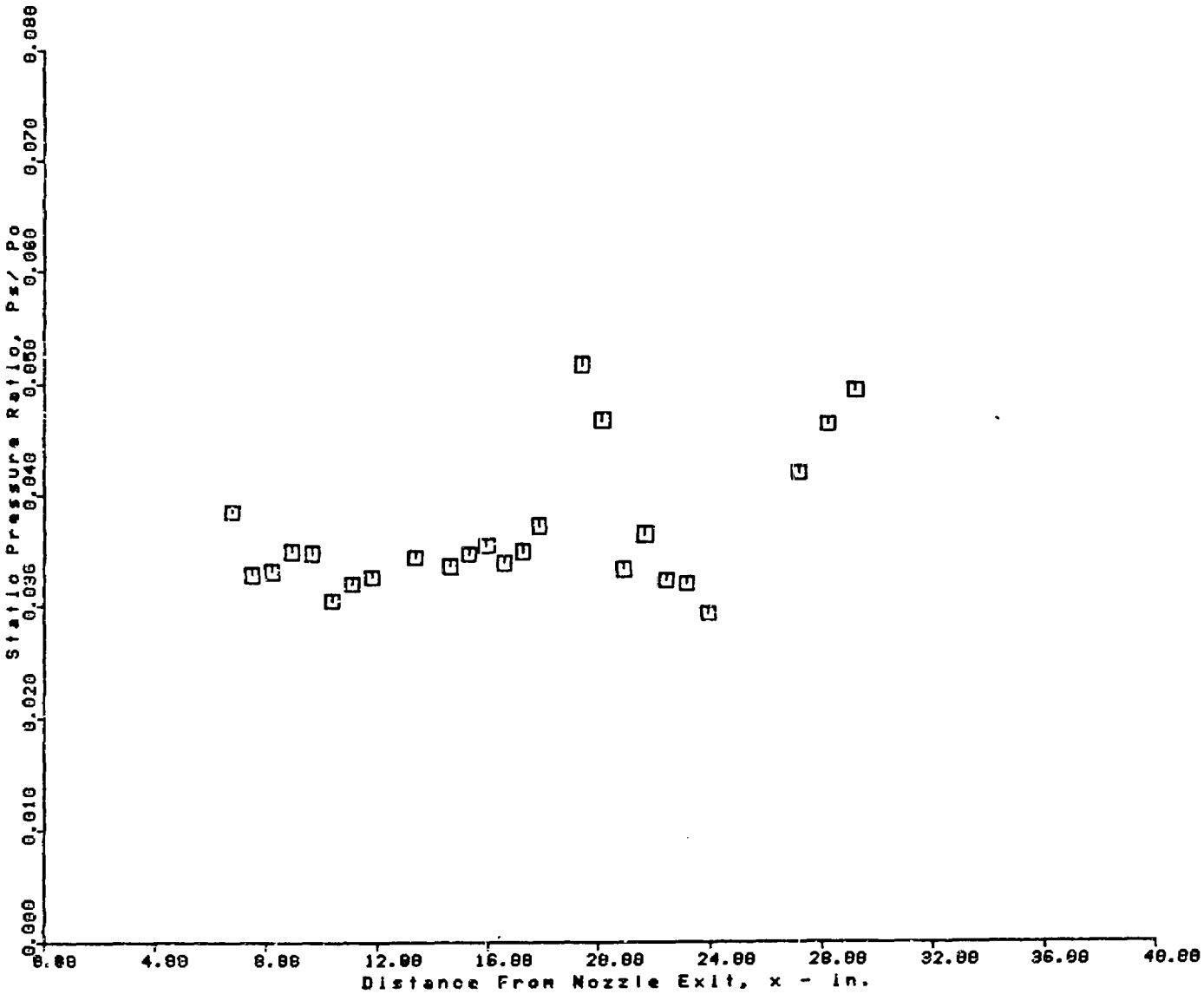

AFS TEST PROGRAM
UPPER SURFACE PRESSURE TAPS
RUN = 46 BURST = 30

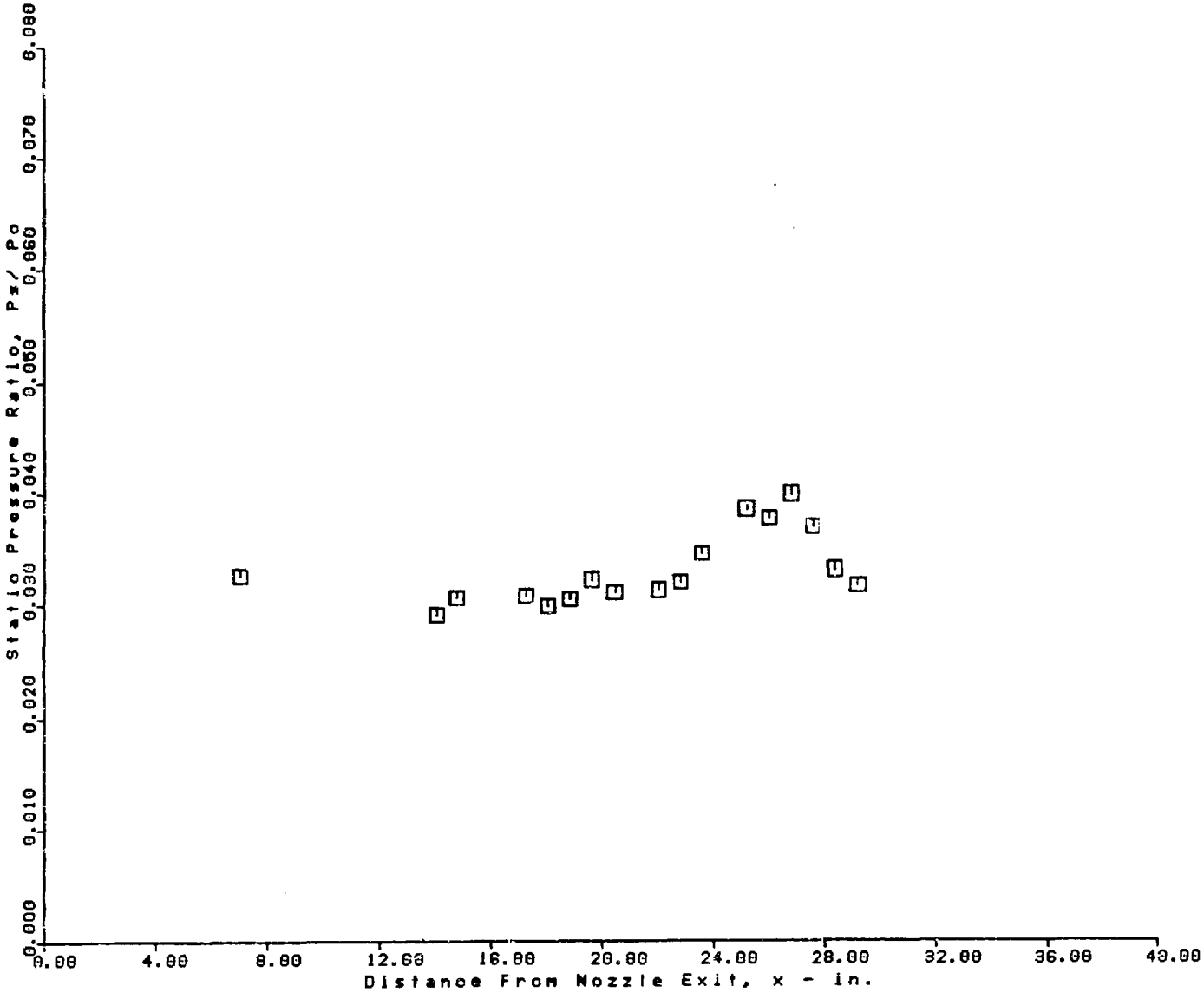

AFS TEST PROGRAM
LOWER SURFACE PRESSURE TAPS
RUN = 49 BURST = 45

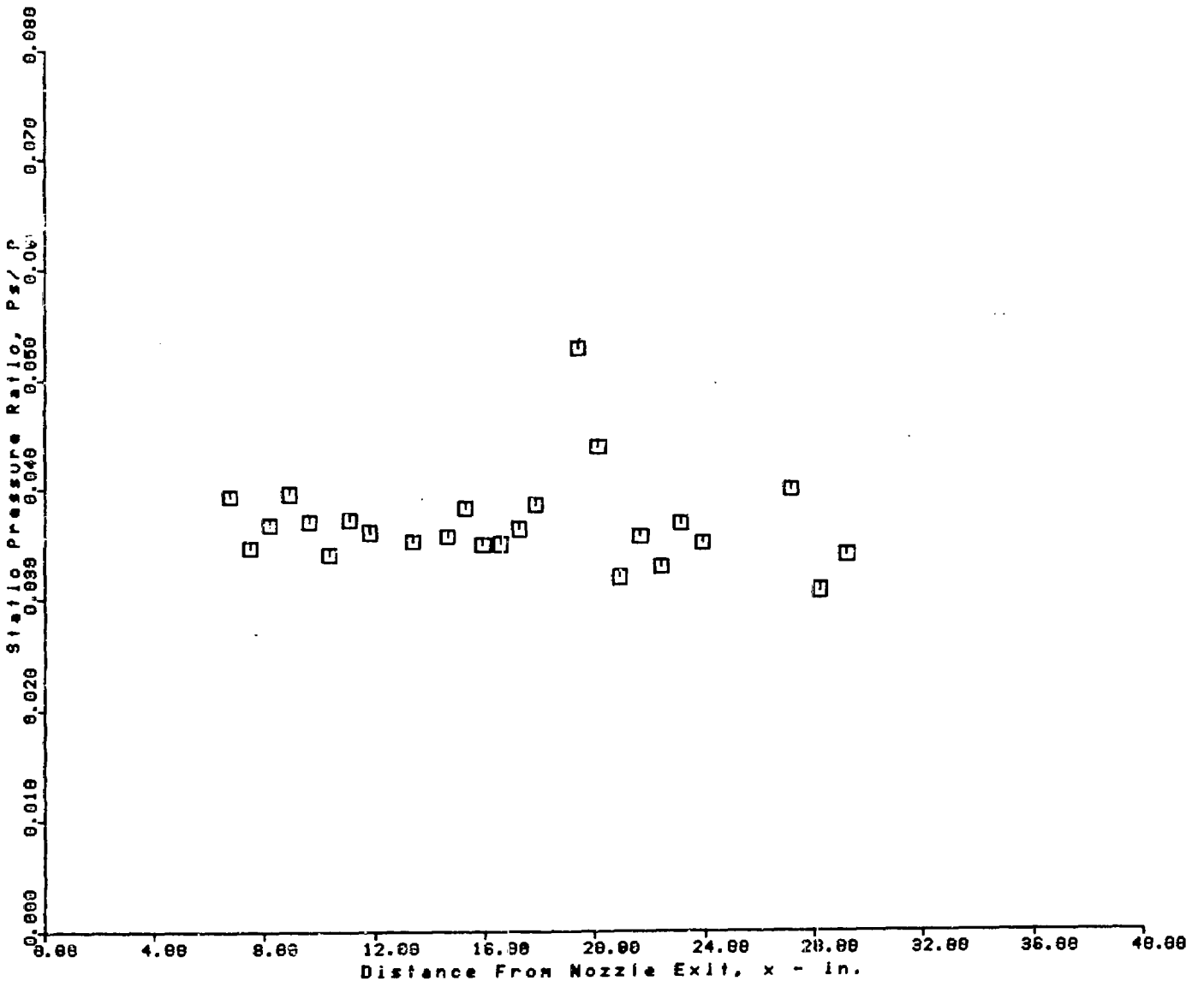

AFS TEST PROGRAM
UPPER SURFACE PRESSURE TAPS
RUN = 49 BURST = 45

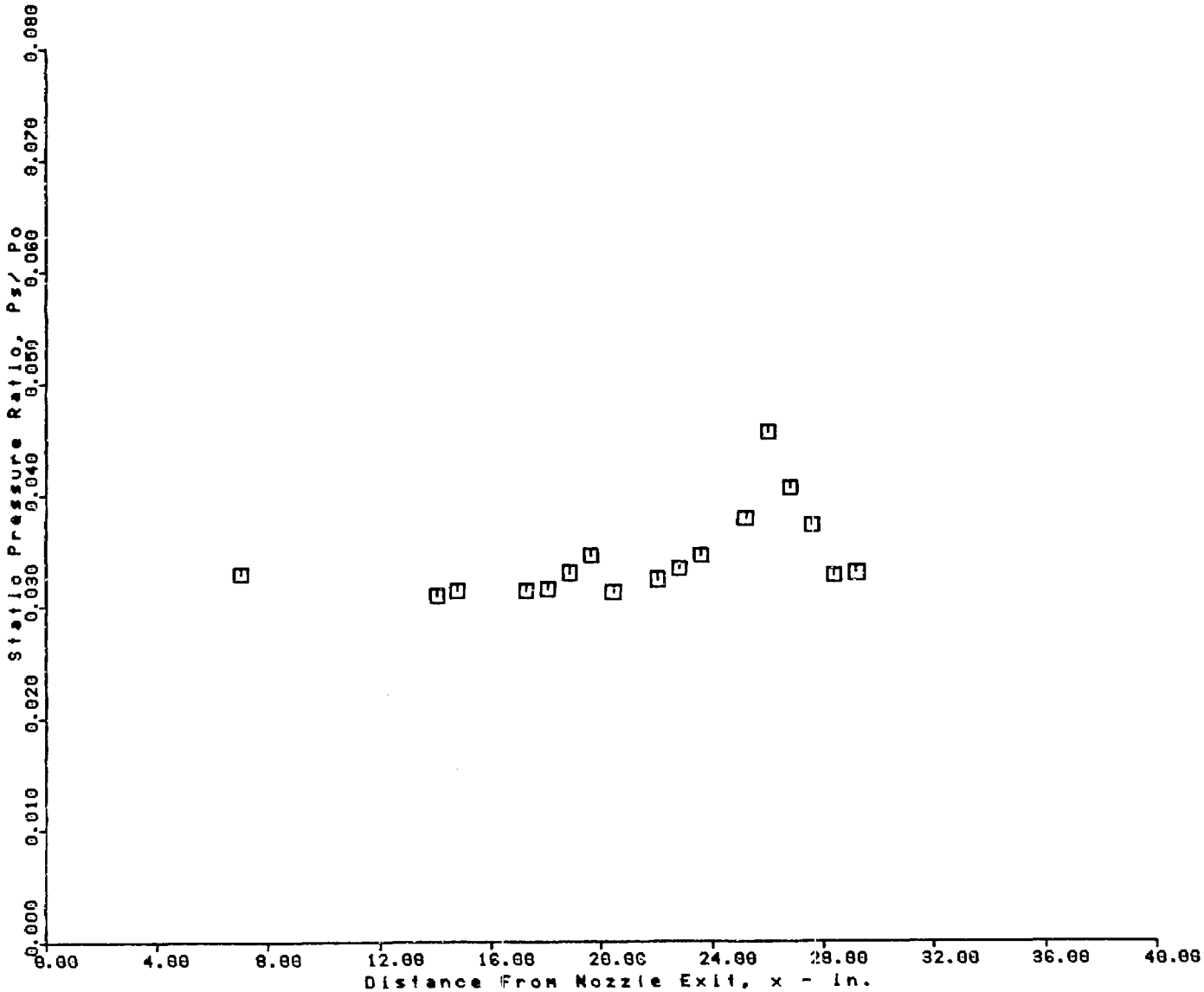

AFS TEST PROGRAM
LOWER SURFACE PRESSURE TAPS
RUN = 58 BURST = 32

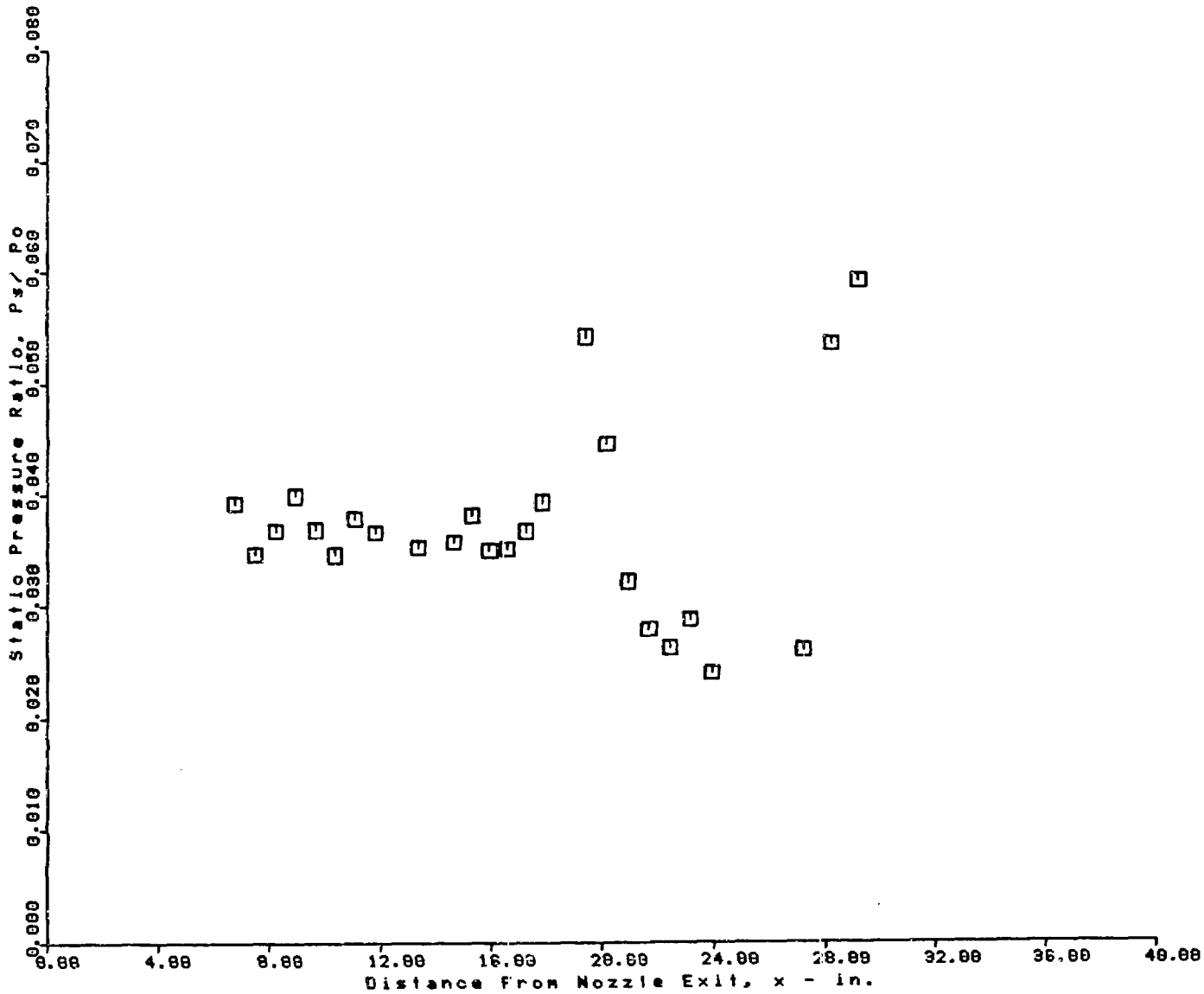

AFS TEST PROGRAM
UPPER SURFACE PRESSURE TAPS
RUN = 58 BURST = 32

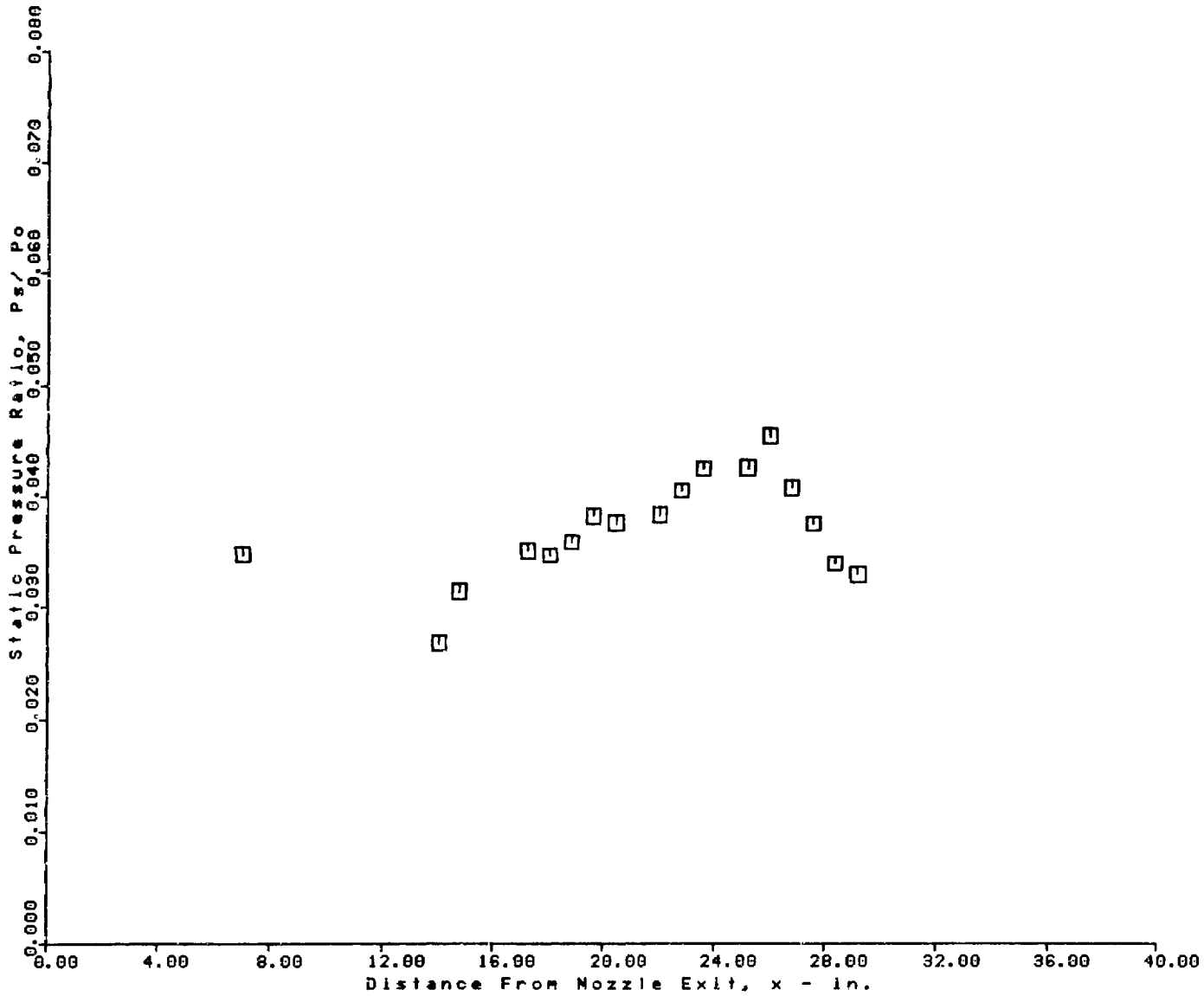

APPENDIX E
THERMAL COMPRESSION ANALYSES

This appendix comprises the listings for the two FORTRAN computer programs, S.FOR and S4.FOR, usable in calculating the test section flowfield structure, in accordance with the procedures set forth in TASK 3: Thermal Compression Analysis.

```
*********************************************************************
* This program calculates the pressure rise through a supersonic   *
* combustor using a thermal compression wave to simulate the       *
* pressure rise.  No attempt is made to model the mixing of the    *
* fuel and air stream.  The shock wave angles are determined from *
* the properties of the air.                                        *
*********************************************************************
      REAL THETA(25),BETA(25),ANGLE(25),PP1TR(25),DELTA(25)
      REAL XINT(25),PP1SR(25),M(25),YINT(25)
      REAL NU
      OPEN(2,FILE='SUPFLAT.DAT')
      OPEN(3,FILE='S.DAT')
      READ(2,10) M(1),THETA(2),GAM,H,FSH,FWA
 10   FORMAT(6F10.4)
      CLOSE (2)
      PI=3.1416
      PP1TR(1)=1.0
      PTPSR1=FPTPSR(M(1),GAM)
      XINT(1)=0.0
      YINT(1)=H
      PP1SR(1)=1.0
C Theta's are turning angles.  They are assigned positive angles.
C Convert input angle to radians.
      THETA(1)=0.0
      THETA(2)=THETA(2)*PI/180.
      FWA=FWA*PI/180.
C Calculate initial shock angle of thermal compression wave
      BETA(2)=FBETA(M(1),THETA(2),GAM,PI)
C Angle(I) is the wave angle, relative to horizontal, upstream of region
C Angle(I) takes on positive values
      ANGLE(2)=BETA(2)
C Find where the shock intersects the bottom wall
      XINT(2)=H/TAN(BETA(2))
      YINT(2)=0.0
C Calculate flow properties downstream of shock
      PP1SR(2)=FPSR(M(1),BETA(2),GAM)
      M(2)=FMACH(M(1),BETA(2),THETA(2),GAM)
      PP1TR(2)=FPTPSR(M(2),GAM)*PP1SR(2)/PTPSR1
C Find the conditions downstream of the reflected shock
      THETA(3)=THETA(2)
      BETA(3)=FBETA(M(2),THETA(3),GAM,PI)
      M(3)=FMACH(M(2),BETA(3),THETA(3),GAM)
      PP1TR(3)=FPTPSR(M(3),GAM)*PP1SR(2)*FPSR(M(2),BETA(3),GAM)/PTPSR1
      PP1SR(3)=FPSR(M(2),BETA(3),GAM)*PP1SR(2)
      ANGLE(3)=BETA(3)-THETA(2)
C Find where the shock intersects the upper surface
      XINT(3)=(XINT(2)*TAN(ANGLE(3))+H+FSH)/(TAN(ANGLE(3))-TAN(FWA))
      YINT(3)=XINT(3)*TAN(FWA)+H+FSH
C The shock must reflect as an expansion wave
C Find conditions downstream of the reflected expansion
      NU=FINDNU(M(3),GAM)+FWA
      M(4)=XMACH(NU,GAM)
      ANGLE(4)=(ASIN(1./M(3))+ASIN(1./M(4))-FWA)/2.
      PP1TR(4)=PP1TR(3)
      PP1SR(4)=PP1SR(3)*FPTPSR(M(3),GAM)/FPTPSR(M(4),GAM)
```

```
C Find where expansion intersects bottom wall
      XINT(4)=XINT(3)+YINT(3)/TAN(ANGLE(4))
      YINT(4)=0.0
C Expansion reflects as an expansion
      NU=NU+FWA
      M(5)=XMACH(NU,GAM)
      ANGLE(5)=(ASIN(1./M(4))+ASIN(1./M(5))-FWA)/2.
      PP1TR(5)=PP1TR(3)
      PP1SR(5)=PP1SR(4)*FPTPSR(M(4),GAM)/FPTPSR(M(5),GAM)
C Find where expansion intersects top wall
      XINT(5)=(XINT(4)*TAN(ANGLE(5))+H+FSH)/(TAN(ANGLE(5))-TAN(FWA))
      YINT(5)=XINT(5)*TAN(FWA)+H+FSH
C Expansion must reflect as a shock
      THETA(6)=FWA
      BETA(6)=FBETA(M(5),THETA(6),GAM,PI)
      M(6)=FMACH(M(5),BETA(6),THETA(6),GAM)
      PP1TR(6)=FPTPSR(M(6),GAM)*FPSR(M(5),BETA(6),GAM)*PP1SR(5)/PTPSR1
      PP1SR(6)=FPSR(M(5),BETA(6),GAM)*PP1SR(5)
        WRITE(3,*) ' REGION     X         Y        Mach     ST.P RATIO
     1TOT. P RATIO '
      DO 300 I=1,6
      WRITE(3,77) I , XINT(I),YINT(I),M(I),PP1SR(I),PP1TR(I)
 300  CONTINUE
  77  FORMAT(I2,'2X,3(F7.4,2X),F11.5,6X,F11.5)
      STOP
      END


      FUNCTION FINDNU(MACH,GAM)
      REAL MACH
      FINDNU=SQRT((GAM+1.)/(GAM-1.))*ATAN(SQRT((GAM-1.)*(MACH**2-1.)/
     1(GAM+1.)))-ATAN(SQRT(MACH**2-1.))
      RETURN
      END


      FUNCTION FBETA(MACH,THETA,GAM,PI)
      REAL MACH
C     tialize beta to 25 degrees
      BETA=0.436
 100   THETAN=ATAN((2.*COS(BETA)/SIN(BETA)*(MACH**2*(SIN(BETA))**2-1.0))
     1/((MACH**2)*(GAM+COS(2.*BETA))+2.))
      IF(ABS(THETAN-THETA)*180./PI .LT. 0.01) GO TO 120
      BETA=BETA+THETA-THETAN
      GO TO 100
 120  FBETA=BETA
      RETURN
      END


      FUNCTION FPSR(MACH,BETA,GAM)
      REAL MACH
      FPSR=(2.*GAM*MACH**2*(SIN(BETA))**2-GAM+1.0)/(GAM+1.0)
      RETURN
      END


      FUNCTION FPTPSR(MACH,GAM)
      REAL MACH
      FPTPSR=(1.+(GAM-1.)*MACH**2/2.)**(GAM/(GAM-1.))
```

```
      RETURN
      END

      FUNCTION FMACH(MACH,BETA,THETA,GAM)
      REAL MACH
      FMACH=SQRT((1.+((GAM-1.)/2.)*MACH**2*(SIN(BETA))**2)/((GAM*
     1(SIN(BETA))**2*MACH**2-(GAM-1.)/2.)*(SIN(BETA-THETA))**2))
      RETURN
      END

      FUNCTION XMACH(NU,GAM)
      REAL NU
      REAL LOWERM
      LOWERM=1.1
      UPPERM=100.
      DELTA=.0001
  200 GUESSM=(UPPERM+LOWERM)/2.
      GUESSN=FINDNU(GUESSM,GAM)
      IF (GUESSN .LT. NU) THEN
                LOWERM=GUESSM
      ELSE
                UPPERM=GUESSM
      ENDIF
      IF (ABS(GUESSN-NU) .GT. DELTA) GO TO 200
      XMACH=GUESSM
      RETURN
      END
```

```
Compile time:                        02.69  Execution time:                 00.00
Size of object code:                  4076  Number of extensions:              0
Size of local data area(s):           1097  Number of warnings:                0
Size of global data area:              900  Number of errors:                  0
Object/Dynamic bytes free:  401366/48876  Statements Executed:               0
```

```
      PROGRAM SUPCOM
*************************************************************************
* THIS PROGRAM TRACKS A THERMAL COMPRESSION SHOCK AND A                 *
* RAMP-GENERATED SHOCK THROUGH A SUPERSONIC COMBUSTOR                   *
* ALL GEOMETRIC ANGLES ARE INPUT AS POSITIVE VALUES IN DEGREES          *
*************************************************************************
      REAL THETA(50),BETA(50),ANGLE(50),PP1TR(50),DELTA(50)
      REAL XINT(25),YINT(25),PP1SR(50),M(50)
      REAL NU,MAVG,PSAVG
      OPEN(2,FILE='SUPRAM.DAT')
      READ(2,10) M(1),THETA(2),GAM,H,FSH
      READ(2,10) THETA(3),XRS,FWA,XRAMBR,DELTA(6)
10    FORMAT(5F10.4)
      CLOSE(2)
      PI=3.14 6
      PTPSR1=FPTPSR(M(1),GAM)
      PP1SR(1)=1.0
      PP1TR(1)=1.0
C THETA'S ARE TURNING ANGLES--THEY ARE ASSIGNED POSITIVE VALUES
C CONVERT INPUT ANGLES TO RADIANS
      THETA(1)=0.0
      THETA(2)=THETA(2)*PI/180.
      THETA(3)=THETA(3)*PI/180.
      FWA=FWA*PI/180.
C DELTA'S ARE FLOW ANGLES--FLOW UP IS POSITIVE --FLOW DOWN IS NEGATIVE
      DELTA(1)=0.0
      DELTA(2)=-1.*THETA(2)
      DELTA(3)=THETA(3)
C DELTA(6) IS THE BACK RAMP ANGLE--INPUT AS A POSITIVE VALUE
      DELTA(6)=-1.0*DELTA(6)*PI/180.
C FIND VERTICAL LOCATION OF THE RAMP PEAK
      YPEAK=XRAMBR*TAN(DELTA(3))
C FIND END OF RAMP
      XEND=XRS+XRAMBR+YPEAK/TAN(ABS(DELTA(6)))
C CALCULATE INITIAL SHOCK ANGLE DUE TO THERMAL COMPRESSION
      BETA(2)=FBETA(M(1),THETA(2),GAM,PI)
C CALCULATE SHOCK ANGLE DUE TO COMPRESSION RAMP
      BETA(3)=FBETA(M(1),THETA(3),GAM,PI)
C ANGLE(I) IS THE WAVE ANGLE, RELATIVE TO THE HORIZONTAL, UPSTREAM OF
C REGION I ANGLE(I) IS A POSITIVE VALUE
      ANGLE(2)=BETA(2)
      ANGLE(3)=BETA(3)
C  FIND WHERE SHOCKS INTERSECT
      XINT(1)=(H/TAN(BETA(3))+XRS)/(1.+TAN(BETA(2))/TAN(BETA(3)))
      YINT(1)=H-XINT(1)*TAN(BETA(2))
C CHECK IF SHOCKS REALLY INTERSECT IN DUCT
C STOP CALCULATION IF INTERSECTION POINT IS OUTSIDE OF DUCT
      IF(YINT(1).LT.YPEAK) GO TO 1000
C CALCULATE PROPERTIES DOWNSTREAM OF SHOCKS
      PP1SR(2)=FPSR(M(1),BETA(2),GAM)
      M(2)=FMACH(M(1),BETA(2),THETA(2),GAM)
      PP1TR(2)=FPTPSR(M(2),GAM)*PP1SR(2)/PTPSR1
      PP1SR(3)=FPSR(M(1),BETA(3),GAM)
```

```
35        M(3)=FMACH(M(1),BETA(3),THETA(3),GAM)
36        PP1TR(3)=FPTPSR(M(3),GAM)*PP1SR(3)/PTPSR1
37        I=2
38        J=4
39        K=3
40        L=5
41        CALL SHOCK(I,J,K,L,THETA,PP1TR,PP1SR,M,DELTA,BETA,ANGLE,GAM,PI)
42        ANGLE(4)=BETA(4)+DELTA(2)
43        ANGLE(5)=BETA(5)-DELTA(3)
C CHECK IF DOWNSHOCK WILL HIT RAMP ON THE BACK SIDE OF THE RAMP
44        IF(ANGLE(5).GT.ATAN((YINT(1)-YPEAK)/(XRS+XRAMBR-XINT(1)))) GO
         1TO 1010
C STOP CALCULATION IF UPSHOCK WOULD REFLECT AS A SHOCK FROM TOP WALL
C FOR THIS CASE
45        IF(DELTA(4).GT.FWA) GO TO 1100
46        PP1TR(4)=FPTPSR(M(4),GAM)*PP1SR(4)/PTPSR1
47        PP1TR(5)=FPTPSR(M(5),GAM)*PP1SR(5)/PTPSR1
C FIND WHERE UPSHOCK INTERSECTS UPPER WALL IF THERE ARE NO OTHER
C INTERSECTIONS THIS CALCULATION DOES NOT CONSIDER THE INTERACTION OF TH
C SHOCKS WITH THE SLIP STREAM BETWEEN THE FUEL AND THE AIR
48        XINT(2)=(H-YINT(1)+XINT(1)*TAN(ANGLE(4))+FSH)/(TAN(ANGLE(4))
         1-TAN(FWA))
49        YINT(2)=H+XINT(2)*TAN(FWA)+FSH
C FIND CONDITIONS DOWNSTREAM OF EXPANSION FROM UPPER WALL-REGION 13
50        DELTA(13)=FWA
51        N=-1
52        I=4
53        J=13
54        CALL EXPAND(I,J,N,DELTA,ANGLE,M,GAM)
55        PP1SR(13)=FPTPSR(M(4),GAM)*PP1SR(4)/FPTPSR(M(13),GAM)
56        PP1TR(13)=PP1TR(4)
57        DELTA(13)=FWA
C FIND ANGLE AND STRENGTH OF EXPANSION WAVE AT THE RAMP DISCONTINUTY
C SET N=1 SINCE THIS EXPANSION WAVE IS TRAVELING UPWARD
58        N=1
59        I=3
60        J=6
61        CALL EXPAND(I,J,N,DELTA,ANGLE,M,GAM)
C FIND WHERE EXPANSION WAVE INTERSECTS THE DOWN COMPRESSION WAVE
C THIS IS POINT 3
62        XINT(3)=(YINT(1)+XINT(1)*TAN(ANGLE(5))+XRAMBR*
         1(TAN(ANGLE(6))-TAN(DELTA(3)))+XRS*TAN(ANGLE(6)))/(TAN(ANGLE(6))
         1+TAN(ANGLE(5)))
63        YINT(3)=YINT(1)-(XINT(3)-XINT(1))*TAN(ANGLE(5))
64        PP1SR(6)=FPTPSR(M(3),GAM)*PP1SR(3)/FPTPSR(M(6),GAM)
65        PP1TR(6)=PP1TR(3)
C REGIONS 8 & 9 ARE DOWNSTREAM OF THE INTERSECTION OF THE SHOCK AND
C EXPANSION WAVE
66        I=5
67        J=8
68        K=6
69        L=9
C EXPANSION WAVE IS TRAVELING UPWARD - IMPLIES N=1
70        N=1
71        CALL EXSHO(I,J,K,L,PP1SR,N,THETA,DELTA,M,BETA,ANGLE,PP1TR,GAM,PI)
C FIND INTERSECTION OF DOWNSHOCK WITH THE BOTTOM WALL
C THIS IS INTERSECTION POINT 4
72        XINT(4)=(YPEAK*XEND/(XEND-(XRS+XRAMBR))-YINT(3)-XINT(3)
         1*TAN(ANGLE(9)))/(YPEAK/(XEND-(XRS+XRAMBR))-TAN(ANGLE(9)))
73        YINT(4)=YINT(3)-(XINT(4)-XINT(3))*TAN(ANGLE(9))
```

```
      IF(XINT(4).GT.XEND) GO TO 1020
C SHOCK MUST REFLECT AS A SHOCK--DOWNSTREAM OF SHOCK IS REGION 11
      THETA(11)=DELTA(6)-DELTA(9)
      DELTA(11)=DELTA(6)
      BETA(11)=FBETA(M(9),THETA(11),GAM,PI)
      M(11)=FMACH(M(9),BETA(11),THETA(11),GAM)
      PP1TR(11)=FPTPSR(M(11),GAM)*FPSR(M(9),BETA(11),GAM)*PP1SR(9)/
     1PTPSR1
      PP1SR(11)=FPSR(M(9),BETA(11),GAM)*PP1SR(9)
      ANGLE(11)=BETA(11)-DELTA(9)
C FIND INTERSECTION OF REFLECTED SHOCK WITH SLIPSTREAM (POINT 7)
      XINT(7)=YINT(3)-YINT(4)+XINT(4)*TAN(ANGLE(11))-XINT(3)
     1*TAN(DELTA(8))/(TAN(ANGLE(11))-TAN(ANGLE(8)))
      YINT(7)=YINT(4)+(XINT(7)-XINT(4))*TAN(ANGLE(11))
C USE REGION 8 CONDITIONS TO CALCULATE SHOCK ANGLE AFTER INTERSECTION WI
      THETA(10)=DELTA(6)-DELTA(8)
C DELTA(8) SHOULD BE MORE NEGATIVE THAN DELTA(6)
      IF(THETA(10) .LT. 0.0) GO TO 1030
      BETA(10)=FBETA(M(8),THETA(10),GAM,PI)
      M(10)=FMACH(M(8),BETA(10),GAM,PI)
      PP1SR(10)=FPSR(M(8),BETA(10),GAM)*PP1SR(8)
      PP1TR(10)=FPTPSR(M(10),GAM)*PP1SR(10)/PTPSR1
      ANGLE(10)=BETA(10)+DELTA(8)
      DELTA(10)=DELTA(6)
C CHECK WHERE SHOCK INTERSECTS SHOCK EMANATING FROM RAMP END
C USE AVERAGE CONDITIONS OF REGIONS 10 AND 11 AS INPUT TO SHOCK
C THIS IS POINT 8
      THETA(12)=-1.0*DELTA(6)
      MAVG=(M(11)+M(10))/2.
      BETA(12)=FBETA(MAVG,THETA(12),GAM,PI)
      M(12)=FMACH(MAVG,BETA(12),THETA(12),GAM)
      PP1SR(12)=FPSR(MAVG,BETA(12),GAM)*(PP1SR(10)+PP1SR(11))/2.
      PP1TR(12)=FPTPSR(M(12),GAM)*PP1SR(12)/PTPSR1
      ANGLE(12)=BETA(12)+DELTA(6)
      IF(ANGLE(12) .LT. ANGLE(10)) GO TO 1050
      XINT(8)=(XINT(4)*TAN(ANGLE(11))-(XRS+XEND)*TAN(ANGLE(12))-
     1YINT(4))/(TAN(ANGLE(11))-TAN(ANGLE(12)))
      YINT(8)=(XINT(8)-(XRS+XEND))*TAN(ANGLE(12))
      IF(XINT(8) .LE. XINT(7)) GO TO 1040
C FIND WHERE EXPANSION WAVE INTERSECTS SLIPLINE (POINT 5)
      XINT(5)=YINT(1)-YINT(3)-XINT(1)*TAN(DELTA(4))+XINT(3)*
     1TAN(ANGLE(8))/(TAN(ANGLE(8))-TAN(DELTA(4)))
      YINT(5)=YINT(3)+(XINT(5)-XINT(3))*TAN(ANGLE(8))
C       IF(ANGLE(10) .GT. ANGLE(8)) GO TO CHECK IF SHOCK INT. WITH EXP.
C DEFINE REGION 7 DOWNSTREAM OF INTERSECTION OF EXPANSION WAVE WITH
C SLIPLINE IDEALIZE AS AN EXPANSION WAVE SIMPLY PASSING THROUGH THE
C SLIPLINE SECONDARY WAVES ARE NOT GENERATED-SIMPLY FORCE DELTA(7)
C =DELTA(8) REGION 7 CONDITIONS ARE DETERMINED BY ADDING THE CHANGE
C IN FLOW ANGLE TO THE PRANDTL-MEYER FUNCTION OF REGION 4-SLIPLINE
C IS NOT TRACKED FARTHER.
      M(7)=XMACH((FINDNU(M(4),GAM)+THETA(8)),GAM)
      PP1SR(7)=PP1SR(4)*FPTPSR(M(4),GAM)/FPTPSR(M(7),GAM)
      PP1TR(7)=PP1TR(4)
      DELTA(7)=DELTA(8)
  200 M(12)=FMACH(M(11),BETA(12),THETA(12),GAM)
      XINT(6)=1.
      YINT(6)=1.
      WRITE(*,*) 'INTERSECTION POINTS'
      DO 210 I=1,8
      WRITE(*,205) XINT(I),YINT(I)
```

```
205   FORMAT(2F10.5)
210   CONTINUE
      WRITE(*,*) 'FLOW DATA'
      DO 215 I=1,13
      WRITE(*,213) I,M(I),PP1SR(I),PP1TR(I)
213   FORMAT(I3,3F10.5)
215   CONTINUE
      GO TO 5000
 1000 WRITE(*,*) 'INITIAL SHOCKS DO NOT INTERSECT PROPERLY'
      GO TO 5000
 1010 WRITE(*,*) 'DOWNSHOCK INTERSECTS RAMP UPSTREAM OF EXPANSION'
      GO TO 5000
 1020 WRITE(*,*) 'DOWNSHOCK INTERSECTS DOWNSTREAM OF RAMP'
      GO TO 5000
 1030 WRITE(*,*) 'DELTA(8) IS SHALLOWER THAN BACK RAMP ANGLE'
      GO TO 5000
 1040 WRITE(*,*) 'REFLECTED SHOCK DOES NOT INTERSECT SLIPSTREAM'
      GO TO 5000
 1050 WRITE(*,*) 'WAVE FROM RAMP END DOES NOT INTER. REFLECTED SHOCK'
      GO TO 5000
 1100 WRITE(*,*) 'UPSHOCK MUST REFLECT FROM UPPER WALL AS AN EXPANSION'
      GO TO 5000
 5000 STOP
      END


      SUBROUTINE SHOCK(I,J,K,L,THETA,PP1TR,PP1SR,M,DELTA,BETA,
     1ANGLE,GAM,PI)
*************************************************************************
* ITERATE TO FIND SHOCK ANGLES AFTER INTERSECTION                       *
* MUST GUESS FLOW ANGLE AND ITERATE UNTIL STATIC PRESSURES MATCH        *
* FIRST GUESS FLOW ANGLE IS THE AVERAGE OF THE TWO INCOMING FLOW ANGLES*
* NOTE: FLOW ANGLE IS NOT THE TURNING ANGLE                             *
* I DENOTES REGION UPSTREAM OF UPSHOCK                                  *
* J DENOTES REGION DOWNSTREAM OF UPSHOCK                                *
* K DENOTES REGION UPSTREAM OF DOWNSHOCK                                *
* L DENOTES REGION DOWNSTREAM OF DOWNSHOCK                              *
*************************************************************************
      REAL THETA(50),PP1TR(50),PP1SR(50),M(50),DELTA(50)
      INTEGER I,J,K,L
      REAL GAM,PI
      REAL BETA(50),ANGLE(50)
      REAL TAVG,PAVG,TAVGJ,TAVGL,PSRJ,PSRL,THETAJ,THETAL
      TAVG=(DELTA(I)+DELTA(K))/2.
C RAMP ANGLE AND T.C. TURNING ANGLE ARE INPUT AS POSITIVE
20    THETAJ=TAVG-DELTA(I)
      THETAL=DELTA(K)-TAVG
      BETA(J)=FBETA(M(I),THETAJ,GAM,PI)
      BETA(L)=FBETA(M(K),THETAL,GAM,PI)
      PP1SR(J)=FPSR(M(I),BETA(J),GAM)*PP1SR(I)
      PP1SR(L)=FPSR(M(K),BETA(L),GAM)*PP1SR(K)
      IF(ABS(PP1SR(J)-PP1SR(L)).LT..005) GO TO 40
C GUESS STATIC PRESSURE IS THE AVERAGE OF THE TWO CALCULATED VALUES
C CALCULATE CORRESPONDING FLOW ANGLES
      PAVG=(PP1SR(J)+PP1SR(L))/2.
      PSRJ=PAVG/PP1SR(I)
      PSRL=PAVG/PP1SR(K)
      THETAJ=FTHETA(M(I),PSRJ,GAM)
      THETAL=FTHETA(M(K),PSRL,GAM)
C CALCULATE FLOW ANGLE FOR EACH TURNING ANGLE
```

```
      TAVGJ=DELTA(I)+THETAJ
      TAVGL=DELTA(K)-THETAL
      TAVG=(TAVGJ+TAVGL)/2.
C LET THE FLOW ANGLE BE THE AVERAGE OF THE FLOW ANGLES
      GO TO 20
40    M(J)=FMACH(M(I),BETA(J),THETAJ,GAM)
      M(L)=FMACH(M(K),BETA(L),THETAL,GAM)
      THETA(J)=THETAJ
      THETA(L)=THETAL
C KEEP TRACK OF FLOW ANGLES
      DELTA(J)=TAVG
      DELTA(L)=TAVG
      ANGLE(J)=BETA(J)+DELTA(I)
      ANGLE(L)=BETA(L)-DELTA(K)
      RETURN
      END


      SUBROUTINE EXPAND(I,J,N,DELTA,ANGLE,M,GAM)
*************************************************************************
* I DENOTES THE REGION UPSTREAM OF THE EXPANSION                        *
* J DENOTES THE REGION DOWNSTREAM OF THE EXPANSION                      *
* MU IS THE ANGLE OF THE WAVE REPRESENTING THE EXPANSION FAN            *
* N=1 FOR AN UPEXPANSION--N=-1 FOR A DOWNEXPANSION                      *
*************************************************************************
      REAL M(50),DELTA(50),ANGLE(50)
      INTEGER I,J,N
      REAL GAM,NU
*************************************************************************
* SET ANGLE OF EXPANSION WAVE FROM RAMP AS THE AVERAGE ANGLE OF EACH    *
* END OF THE EXPANSION FAN.                                             *
*************************************************************************
      NU=FINDNU(M(I),GAM)
      NU=NU+ABS(DELTA(I)-DELTA(J))
      M(J)=XMACH(NU,GAM)
      ANGLE(J)=(ASIN(1/M(I))+N*DELTA(I)+N*DELTA(J)+ASIN(1/M(J)))/2.
      RETURN
      END


      SUBROUTINE EXSHO(I,J,K,L,PP1SR,N,THETA,DELTA,M,BETA,
     1ANGLE,PP1TR,GAM,PI)
*************************************************************************
* THIS SUBROUTINE CALCULATES THE FLOW PROPERTIES DOWNSTREAM OF THE      *
* INTERSECTION OF AN EXPANSION WAVE AND A SHOCK WAVE                    *
* I=REGION UPSTREAM OF THE EXPANSION WAVE                               *
* J=REGION DOWNSTREAM OF THE EXPANSION WAVE                             *
* K=REGION UPSTREAM OF THE SHOCK WAVE                                   *
* L=REGION DOWNSTREAM OF THE SHOCK WAVE                                 *
* N=EXPANSION WAVE DIRECTION:  1 FOR UP AND -1 FOR DOWN                 *
* ITERATE TO MATCH STATIC PRESSURE AND FLOW ANGLE                       *
* GUESS THE STATIC PRESSURE TO BE THE AVERAGE PRESSURE OF THE           *
* TWO INCOMING FLOWS                                                    *
* CALCULATE THE FLOW ANGLE DOWNSTREAM OF THE EXPANSION FROM THE         *
* CHANGE IN THE PRANDTL-MEYER FUNCTION                                  *
* CALCULATE THE FLOW ANGLE DOWNSTREAM OF THE SHOCK USING SHOCK          *
* RELATIONS                                                             *
* SET THE DOWNSTREAM FLOW ANGLE EQUAL TO THE AVERAGE OF THESE FLOW      *
* ANGLES.  THEN CALCULATE THE CORRESPONDING STATIC PRESSURES DOWN-      *
* STREAM OF THE WAVES                                                   *
```

```
*********************************************************************
      REAL PP1SR(50),M(50),ANGLE(50),DELTA(50),THETA(50)
      REAL BETA(50),PP1TR(50)
      INTEGER I,J,K,L,N
      REAL NU,PSRL,PSAVG,DELAVG,PTPSRJ,GAM,PI
      PSAVG=(PP1SR(I)+PP1SR(K))/2.
10    PTPSRJ=FPTPSR(M(I),GAM)*PP1SR(I)/PSAVG
      M(J)=FINDLM(PTPSRJ,GAM)
C FIND FLOW ANGLE DOWNSTREAM OF THE EXPANSION FROM THE CHANGE IN THE
C PRANDTL-MEYER FUNCTION
      THETA(J)=FINDNU(M(J),GAM)-FINDNU(M(I),GAM)
C MUST WATCH SIGN CONVENTION HERE TO TAKE CARE OF WAVE DIRECTION
      DELTA(J)=DELTA(I)-N*THETA(J)
C CALCULATE THE FLOW ANGLE DOWNSTREAM OF THE SHOCK FROM THE CHANGE IN
C STATIC PRESSURE
      PSRL=PSAVG/PP1SR(K)
      THETA(L)=FTHETA(M(K),PSRL,GAM)
C SHOCK TURNS FLOW DOWN
      DELTA(L)=DELTA(K)-N*THETA(L)
C GUESS FLOW ANGLE IS THE AVERAGE OF THE FLOW ANGLES IN REGIONS J & L
C CALCULATE CORRESPONDING PRESSURES
      DELAVG=(DELTA(L)+DELTA(J))/2.
      THETA(J)=ABS(DELAVG-DELTA(I))
      NU=FINDNU(M(I),GAM)+THETA(J)
      M(J)=XMACH(NU,GAM)
      PP1SR(J)=FPTPSR(M(I),GAM)*PP1SR(I)/FPTPSR(M(J),GAM)
      THETA(L)=ABS(DELAVG-DELTA(K))
      BETA(L)=FBETA(M(K),THETA(L),GAM,PI)
      M(L)=FMACH(M(K),BETA(L),THETA(L),GAM)
      PP1SR(L)=FPSR(M(K),BETA(L),GAM)*PP1SR(K)
      IF(ABS(PP1SR(L)-PP1SR(J)) .LT. 0.005) GO TO 20
      PSAVG=(PP1SR(L)+PP1SR(J))/2.
      GO TO 10
20    PP1TR(L)=FPTPSR(M(L),GAM)*PP1SR(L)/FPTPSR(M(1),GAM)
      ANGLE(J)=(ASIN(1./M(I))+ASIN(1./M(J))+N*DELTA(J)+N*DELTA(I))/2.
      ANGLE(L)=BETA(L)-N*DELTA(K)
      DELTA(L)=DELAVG
      DELTA(J)=DELAVG
      PP1TR(J)=PP1TR(I)
      RETURN
      END


      FUNCTION FPTPSR(MACH,GAM)
      REAL MACH
      FPTPSR=(1.+(GAM-1.)*MACH**2/2.)**(GAM/(GAM-1.))
      RETURN
      END


      FUNCTION FBETA(MACH,THETA,GAM,PI)
      REAL MACH
C Initialize beta to 25 degrees
      BETA=0.436
       J=1
100    THETAN=ATAN((2.*COS(BETA)/SIN(BETA)*(MACH**2*(SIN(BETA))**2-1.0))
     1/((MACH**2)*(GAM+COS(2.*BETA))+2.))
      IF(ABS(THETAN-THETA)*180./PI .LT. 0.01) GO TO 120
      BETA=BETA+THETA-THETAN
```

```
      J=J+1
      GO TO 100
120   FBETA=BETA
      RETURN
      END


      FUNCTION FPSR(MACH,BETA,GAM)
      REAL MACH
      FPSR=(2.*GAM*MACH**2*(SIN(BETA))**2-GAM+1.0)/(GAM+1.0)
      RETURN
      END


      FUNCTION FMACH(MACH,BETA,THETA,GAM)
      REAL MACH
      FMACH=SQRT((1.+((GAM-1.)/2.)*MACH**2*(SIN(BETA))**2)/((GAM*
     1(SIN(BETA))**2*MACH**2-(GAM-1.)/2.)*(SIN(BETA-THETA))**2))
      RETURN
      END


      FUNCTION FINDNU(MACH,GAM)
      REAL MACH
      FINDNU=SQRT((GAM+1.)/(GAM-1.))*ATAN(SQRT((GAM-1.)*(MACH**2-1.)/
     1(GAM+1.)))-ATAN(SQRT(MACH**2-1.))
      RETURN
      END


      FUNCTION XMACH(NU,GAM)
      REAL NU
      REAL LOWERM
      LOWERM=1.1
      UPPERM=100.
      DELTA=.0001
200   GUESSM=(UPPERM+LOWERM)/2.
      GUESSN=FINDNU(GUESSM,GAM)
      IF (GUESSN .LT. NU) THEN
                LOWERM=GUESSM
      ELSE
                UPPERM=GUESSM
      ENDIF
      IF (ABS(GUESSN-NU) .GT. DELTA) GO TO 200
      XMACH=GUESSM
      RETURN
      END


      FUNCTION FTHETA(MACH,PSR,GAM)
      REAL MACH
      FTHETA=ATAN(SQRT(((PSR-1.)/(GAM*MACH**2-PSR+1.0))**2
     1*(2.*GAM*MACH**2-(GAM-1.)-(GAM+1.)*PSR)
     1/((GAM+1.)*PSR+(GAM-1.))))
      RETURN
      END


      FUNCTION FINDLM(PTPSR,GAM)
      FINDLM=SQRT((PTPSR**((GAM-1.)/GAM)-1.)*2./(GAM-1.))
```

```
271        RETURN
272        END
```

Compile time:	04.45	Execution time:	00.00
Size of object code:	10980	Number of extensions:	0
Size of local data area(s):	2703	Number of warnings:	0
Size of global data area:	1600	Number of errors:	0
Object/Dynamic bytes free:	257516/46878	Statements Executed:	0

○ Region Identifier

1 Intersection Identifer

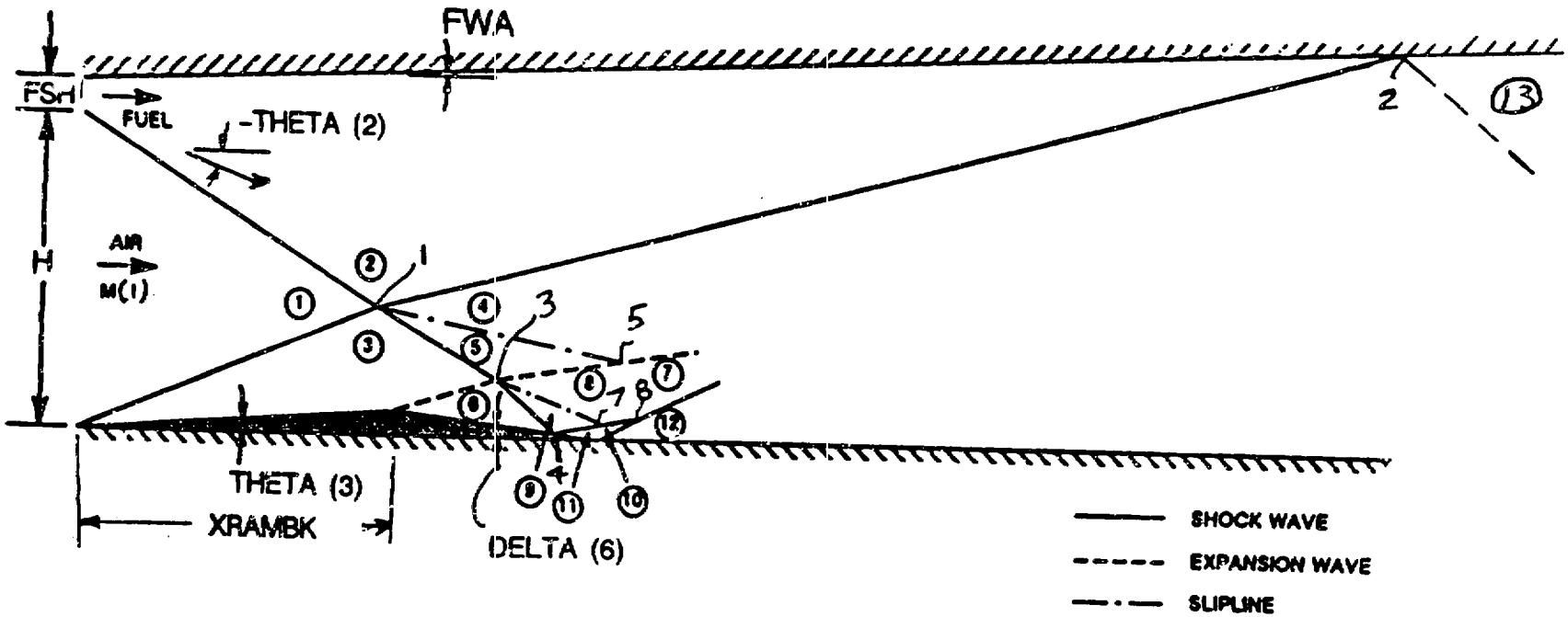

NOMENCLATURE FOR CALCULATION WITH RAMP

☆U.S. Government Printing Office:1991—548-076/44309